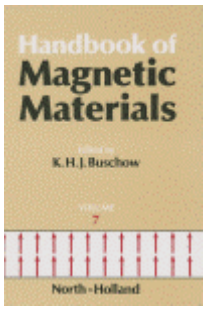

Handbook of Magnetic Materials, Volume 7

Elsevier, 1993

Edited by: K.H.J. Buschow
ISBN: 978-0-444-89853-1

PREFACE TO VOLUME 7

The original aim of Peter Wohlfarth when he started this Handbook series was to combine new development in magnetism with the achievements of earlier compilations of monographs, to produce a worthy successor to Bozorth's classical and monumental book **Ferromagnetism**. It is mainly for this reason that **Ferromagnetic Materials** was initially chosen as title for the Handbook series, although the latter aims at giving a more complete cross-section of magnetism than Bozorth's book.

During the last few years magnetism has even more expanded into a variety of different areas of research, comprising the magnetism of several classes of novel materials which share with ferromagnetic materials only the presence of magnetic moments. This is the reason why the Editor and the Publisher of this Handbook series have carefully reconsidered the title of the Handbook series and have come to the conclusion that the more general title **Magnetic Materials** is more appropriate than **Ferromagnetic Materials**. This change in title has become effective starting with Volume 6. It is with great pleasure that I can introduce to you now Volume 7 of this series.

A substantial step forward in the understanding of metallic magnetism has been reached by means of electronic band structure calculation. Progress in this area has been made not only due to the availability of high speed computing machines but also due to sophistication in the computational methodology. In Volume 7 two chapters are devoted to this subject, one chapter dealing primarily with the elements and one chapter dealing primarily with 4f and 5f systems, including examples of the large group of intermetallic compounds. In both chapters the authors have concentrated on explaining the physics behind these band calculations. Their chapters are written in a manner understandable also to those scientists having no experience with band calculations.

Thin film technology has become a key issue in high density magnetic and magneto-optical recording. Both topics will be dealt with in future volumes of this Handbook series. As a precursor and as a sound basis for these topics the present volume contains a chapter on the magnetism of ultrathin transition metal films, describing the richness in novel magnetic phenomena that has been encountered in the past few years in these materials.

Of equal interest are the novel magnetic phenomena observed when magnetic

moments are incorporated in a semiconducting matrix. A comprehensive description of these materials is found in the chapter on Diluted Magnetic Semiconductors.

A separate chapter is devoted to the progress made in the field of heavy fermions and valence fluctuations, the emphasis being on the important results obtained by means of neutron scattering.

The magnetic properties of various types of rare earth based intermetallic compounds were reviewed already in Volume 1 of this Handbook series. However, the compounds in which rare earth elements are combined with 3d transition metals have received renewed interest in the last decade, which is due in part to the success of novel permanent magnet materials. Proliferation of scientific results obtained with novel techniques, and made for a large part on single crystals, have led to a more complete understanding of the basic interaction in these materials. A comprehensive description of the progress made in this field since the appearance of Volume 1 is given in the chapter on Magnetic Properties of Binary Rare-Earth 3d-Transition-Metal Intermetallic Compounds.

Volume 7 of the Handbook on the Properties of Magnetic Materials, as the preceding volumes, has a dual purpose. As a textbook it is intended to be of assistance to those who wish to be introduced to a given topic in the field of magnetism without the need to read the vast amount of literature published. As a work of reference it is intended for scientists active in magnetism research. To this dual purpose, Volume 7 of the Handbook is composed of topical review articles written by leading authorities. In each of these articles an extensive description is given in graphical as well as in tabular form, much emphasis being placed on the discussion of the experimental material in the framework of physics, chemistry and materials science.

The task to provide the readership with novel trends and achievements in magnetism would have been extremely difficult without the professionalism of the North-Holland Physics Division of Elsevier Science Publishers and I would like to thank Anita de Waard and Fer Mesman for their great help and expertise.

K.H.J. Buschow
Philips Research Laboratories

CONTENTS

CONTENTS OF VOLUMES 1–6

Volume 1

Volume 2

Volume 3

Volume 4

Volume 5

Volume 6

chapter 1

MAGNETISM IN ULTRATHIN TRANSITION METAL FILMS

ULRICH GRADMANN

Physikalisches Institut
Technische Universität Clausthal
W-3392 Clausthal-Zellerfeld
Germany

Handbook of Magnetic Materials, Vol. 7
Edited by K. H. J. Buschow

CONTENTS

1. Introduction

In discussing magnetic thin metal films, we may distinguish intrinsic from defect-induced magnetic thin film phenomena. The first group includes phenomena which are connected with the finite thickness ('size effects' like the dependence of the Curie temperature and spontaneous magnetization on film thickness) and the existence of two surfaces ('surface' effects like magnetic surface anisotropies or modified magnetic moments in surfaces or interfaces). In addition, because films can be prepared only on substrates, the interaction with these substrates and their magnetic implications must be considered as intrinsic film phenomena. On the other hand. thin films are usually prepared by condensation from a highly supersaturated atomic beam and therefore contain a high level of defects. Depending on the vacuum level used in the preparation, a high level of impurities must be considered, too. A rich variety of interesting magnetic properties is connected with the resulting defect- and impurity-structure of thin magnetic films, in particular polycrystalline ones. They depend in a complicated manner on the preparation conditions, as discussed in the reviews of Jaggi, Methfessel and Sommerhalder (1962) and of Wijn (1988). The opportunities which are given by this broad spectrum of defect-induced magnetic thin film phenomena are widely used in magnetic thin film applications.

Because of their connexion with basic theoretical models, intrinsic magnetic film phenomena are of considerable interest for the understanding of fundamental magnetic phenomena, like magnetic order in lower dimensions. They have been discussed for a long time in this context only. However, following the success of molecular beam epitaxy (MBE) for semiconductors, the application of high-quality epitaxial magnetic thin films, and multilayers consisting of them, have been realized during the last years. MBE-grown magnetic multilayers are now candidates for high-density information storage. With increasing structural quality of these systems, intrinsic thin film properties become more and more important for applications, also.

The aim of the present review is a report on intrinsic magnetic thin film phenomena in epitaxial films of 3d-metals, the main concern being given by magnetic single films. Magnetic coupling phenomena in sandwiches and multilayers became recently a rapidly developing field, which deserves a separate review; we restrict ourselves to a short sketch of this timely subject, the full discussion of which is out of the scope of the review. In addition, magnetic multilayers will be reported, somewhere, as systems in which magnetic single film phenomena can be observed conveniently because of multiplication of the volume. In agreement with the general philosophy of this hand-

book, the review presents an experimental approach. Basic ideas of theoretical models will also be reported, however. In stressing intrinsic film phenomena, we are aware of the fact that the influence of the real and defect structure on the magnetic properties remains considerable even in the most sophisticated epitaxial films. Methods of epitaxial film preparation and structural testing will, therefore, be included. Being restricted to magnetic films which are dominated by intrinsic magnetic film phenomena, the report definitely excludes the extended body of application-oriented magnetic thin film research, in particular on polycrystalline films. Further, films containing rare earths are outside the scope of the review; they will be discussed in other contributions of the present volume.

Essential aspects of the subject are covered by several volumes of collected articles (Falicov and Moran-Lopez 1986, Falicov et al. 1990, Farrow et al. 1987, Jonker et al. 1989), and by special issues of Applied Physics edited by Pescia (1989). For a systematic collection of very thin epitaxial magnetic thin film data compare Gradmann (1988). For previous coherent presentations of the field see Gradmann (1974) and Gradmann et al. (1985).

The organization of the present review is based on the fact that any meaningful experimental research on intrinsic magnetic film properties depends on the preparation and structural testing of appropriate samples, and on experimental probes for magnetic order in films with monolayer sensitivity. After the present introduction, we therefore report on these preconditions of magnetic thin film analysis in the first main part consisting of sections 2–4 on guidelines of metal epitaxy, methods of structural analysis and probes of magnetic order, respectively. Magnetic thin film phenomena are then reported in the second main part in sections 5–9.

PART I. Preconditions of magnetic thin film analysis

2. Guidelines of metal epitaxy

Ultrathin magnetic metal films usually are prepared, using MBE or sputtering techniques, with growth rates which are many orders of magnitude larger than the rates of re-evaporation. Accordingly, growth proceeds in a quenching mode with high supersaturation, far from equilibrium, even at elevated temperatures of the epitaxial substrate, and is therefore far from being understood in detail. The resulting film structures therefore always have to be tested by the methods to be discussed in the next chapter. Extended reviews on epitaxial growth have been written by Matthews (1975a), Bauer and van der Merwe (1986) and Markov and Stoyanov (1987). We restrict our present discussion to some basic models and principles, which, though simplifying some aspects of a complicated subject, turned out to be useful in predicting and understanding epitaxial growth modes and film structures.

2.1. Surface energies and equilibrium growth modes

Bauer (1958) was the first to note that growth modes of thin films can be considered as a wetting problem, governed by $\Delta\gamma = \gamma_f + \gamma_i - \gamma_s$, where γ_s, γ_f and γ_i are the surface

energies of substrate and the growing film and the interface energy, respectively. If the film grows near equilibrium, it wets the surface and therefore starts growing by a monolayer if $\Delta\gamma < 0$; it starts growing by three-dimensional nuclei when $\Delta\gamma > 0$ (*Volmer–Weber mode of growth, island mode*). For the case of a stable monolayer, a further layer-by-layer growth (*van der Merwe mode, layer-by-layer mode*) is expected only if each layer wets the previous one, otherwise 3D nuclei are expected on one or a few flat layers (*Stranski–Krastanov mode*). Because of strain energies, which must be included in the surface energies of layer-grown film, whereas they can relax in 3D nuclei, plane van der Merwe mode is extremely rare. Because metallic interface energies are one order of magnitude lower than surface energies, the growth mode is governed essentially by surface energies. They are hard to measure. Some data for the magnetic 3d-metals Ni, Co and Fe are reported in table 1, in comparison with frequently used substrate metals. Considering all restrictions given by the application of these equilibrium considerations to the supersaturated growth, by the temperature dependence, anisotropy and overall uncertainty of surface energies, and by the application of the surface energy concept to monolayers, the data reduce to a rough rule that monolayer nucleation of Ni, Co and Fe can be expected on the high melting, high surface-energy substrates Mo, Re, Ta and W, but not on Cu, Ag and Au. It will be shown below that this rule fits to the available experience. Because A does not wet B if B wets A, flat multilayers cannot be grown near equilibrium.

TABLE 1

Free surface energies of metals and heats of adsorption for metals on metals. Experimental values γ (in mJ/m^2) for free surface energies of metals, from Mezey and Giber (1982), at lowest available temperatures; ground state values γ^0 from Miedema and Dorleijn (1980) for comparison. Heats of adsorption ΔH_{AB} for adsorption of adsorbate metal A on substrate metal B (in kJ/mol) from Miedema and Dorleijn (1980).

	Adsorbate A											
	Ag	Au	Mn	Cu	Pd	Ni	Co	Fe	Pt	Mo	Ta	W
γ ($mJ\,m^{-2}$)	1.25	1.55	1.6	1.85	2.1	2.45	2.55	2.55	2.55	2.95	3.05	3.3
γ^0 ($mJ\,m^{-2}$)	1.1	1.4		1.7		1.8	2.0	2.0		2.0	2.7	2.9
Substrate B	ΔH_{AB} ($kJ\,mol^{-1}$)											
Ag	225	275	185	230	230	250		200				
Au	255	295	235	260	245	280		250				
Mn	265	315	220	245	285	300		260				
Cu	265	325	230	265	280	295		250				
Pd	295	335	285	295	285	320		300				
Ni	285	345	285	295	305	340		315				
Co	285	355	285	295	315	345		320				
Fe	275	355	280	285	320	345		315				
Pt	320	360	320	320	310	355		340				
Mo	295	395	295	305	365	380		345				
Ta	345	460	315	335	430	415		305				
W	310	405	315	315	375	390		360				

An alternative approach to the growth modes is given by heats of adsorption of metals on metals, as determined from thermodynamic data and tabulated by Miedema and Dorleijn (1980). Monolayer nucleation of A on B is then expected if the magnitude of the heat for adsorption of A on B, $\Delta H_{A,B}$, is larger than $\Delta H_{A,A}$. We include in table 1 values of $\Delta H_{A,B}$; both criteria, from ΔH and from $\Delta\gamma$, agree in their main message on growth modes.

2.2. *Supersaturation and forced layer growth*

Because of the high supersaturation of the condensing atomic beam, the real growth process is determined to a large extent by kinetic principles. It is then a general experience, both for epitaxial and polycrystalline films, that condensation at low temperatures results in small grain sizes, at high temperatures in large grains. The cause for this is that the atomic beam condenses, for the case of high supersaturation (low temperatures, high growth rates), by many small critical nuclei. Markov and Kaischew (1976) showed how size and volume of critical nuclei in epitaxial films depend on surface energies and supersaturation and that effective monolayer nucleation can be expected as soon as the height of the critical nucleus becomes as low as the distance of atomic layers. Accordingly, monolayer nucleation can be induced by high supersaturation, which means either low substrate temperatures or high evaporation rates, resulting in what is called a *quasi van der Merwe or forced layer growth mode.* A quantitative confirmation of the theory was performed by Gradmann and Tillmanns (1977), who observed for γ-Fe films on Cu(111) a transition from island growth, as expected from wetting considerations (compare table 1), to layer growth, which could be induced either by high evaporation rates or reduced growth temperatures. It is this supersaturation-induced, forced layer growth which enables more or less layer-grown epitaxial films even in nonwetting systems near the wetting limit, and therefore enables the growth of metallic superlattices if the surface energies of the components are similar. The situation is qualitatively different in semiconductor superlattices, where the different components are frequently given by lattice-matched, nearly equal crystals, which differ only by having a different doping to change their electrical properties and show nearly identical surface and negligible interface energies, resulting in the well-known possibility of growing superlattices with a quality which may be hard to achieve in metallic systems. In turn, layer growth of metal epitaxial films turns out to be mostly a delicate balance between forcing layer growth by super-saturation, which requires low temperatures, and good crystalline order, which requires high ones. We should note at this point that the notion of epitaxy, as introduced by Royer (1928), means only oriented growth of some crystal on an epitaxial substrate, be it of the same material (*autoepitaxy*) or another one (*heteroepitaxy*), independent of growth mode and lattice matching. An epitaxial film can, according to this definition, consist of few large, defect-free crystallites in parallel orientation, which grow together to a continuous film only in a later state of growth ('coalescence'), e.g. epitaxial metal films on NaCl, molybdenite or mica. For a review compare Pashley (1956, 1965) and Matthews (1975). Optimum epitaxy of defect-free crystals and layer growth are competing, for metal films.

2.3. *Misfit and misfit dislocations*

A second important parameter determining epitaxial growth is the *lattice misfit*, f, defined in a one-dimensional model by

$$f = (b - a)/a, \tag{2.1}$$

where b and a are the lattice parameters of film and substrate, respectively. This definition applies too for interfaces, if the contacting lattice planes of both crystals show the same two-dimensional symmetry (homosymmetric interfaces). Besides parallel orientated crystals with common 3D-symmetry, homosymmetric epitaxial systems include systems like hcp (0001) on fcc (111), with densely packed hexagonal planes in contact, and bcc (100) on fcc (100) with bcc [001] parallel to fcc [011], with parallel oriented square nets in contact. Misfits for magnetic or nearly magnetic 3d-metals on homosymmetric epitaxial substrates are given in table 2. For appropriate misfit definitions and epitaxial orientations in heterosymmetric epitaxial systems compare the extended discussion of fcc (111) on bcc (110) metals given by Bauer and van der Merwe (1986).

The misfit to the substrate can be accommodated in the growing film by elastic strain or by misfit dislocations, which have been first discussed by Frank and van der Merwe (1949) and reported by Matthews (1975b). A schematic representation of an interface between misfitting crystals, resolved into a sequence of edge-type misfit dislocations, is shown in fig. 1. The periodic elastic strain is virtually restricted to a sheet the thickness of which equals roughly the distance of dislocations, p. By simple geometric arguments, p is connected with the in-plane atomic distances a in the substrate and b^* in a growing film by

$$p = ab^*/(a - b^*). \tag{2.2}$$

b^* represents a mean value, which may differ from the bulk lattice parameter if part of the misfit is accommodated by elastic strain in the growing film. For small misfits, it may be energetically favourable for the film to accommodate completely to the substrate by elastic strain, without any dislocations, forming what is called a *pseudomorphic film*, in which all film atoms occupy substrate positions in the plane. The elastic energy of a pseudomorphic monolayer is proportional to f^2, whereas the dislocation energy of the misfitting monolayer is proportional to the density of dislocations, which means to f. Therefore there is a *critical misfit*, below which the monolayer is pseudomorphic. Being of the order of 10% in general, the magnitude of the critical misfit is larger for $f < 0$, where the film is under expansive strain. It is smaller for $f > 0$, where the film is under compressive strain, as discussed by Markov and Milchev (1984a,b), who showed that this difference results from anharmonicity in the mechanical pair interaction. For thicker films, the critical misfit decreases with increasing film thickness, being roughly proportional to $1/d$. Even above this critical misfit, the accommodation of the misfit is shared between misfit dislocations and some residual elastic strain, as shown, e.g., in fig. 2. Misfit dislocations have been studied extensively by transmission electron microscopy (TEM), cf. Matthews (1975b). For the case of misfits of the order of 10%, the misfit interaction results in periodic misfit

TABLE 2

Lattice misfits $f = (b' - a')/a'$ (in %) between effective lattice parameters b' of magnetic films and a' of homosymmetric substrates. Lattice parameters from Pearson (1958).

(a) fcc and hcp films on fcc and hcp substrates. $a' = a$ for fcc, $a' = a\sqrt{2}$ (in-plane constant a) for hcp metals. For epitaxy of fcc on hcp, and vice versa, the table applies only if densely packed planes, (111) or (0001), respectively, are in contact.

Substrate metal		f (%) for different film metals			
	a'	Ni $b' = 3.524$	Co $b' = 3.550$	γ-Fe $b' = 3.59$	Pd $b' = 3.89$
Ni	3.524	0	0.7	1.9	10.4
Co	3.550	−0.7	0	1.1	9.6
γ-Fe	3.59	−1.8	−1.1	0	8.4
Cu	3.615	−2.5	−1.8	−0.7	7.6
Rh	3.803	−7.3	−6.6	−5.6	2.3
Ru	3.824	−7.5	−7.2	−6.1	1.7
Ir	3.839	−8.2	−7.5	−6.5	1.3
Pd	3.890	−9.4	−8.7	−7.7	0
Re	3.903	−9.7	−9.0	−8.0	−0.3
Pt	3.924	−10.2	−9.5	−8.5	−0.9
Al	4.048	−12.9	−12.3	−11.3	−3.9
Au	4.078	−13.6	−13.0	−12.0	−4.6
Ag	4.086	−13.8	−13.1	−12.1	−0.3

(b) bcc films on cubic substrates. $a' = a$ for bcc, $a' = a\sqrt{2}$ for fcc substrates. For bcc on fcc metals, the table applies only to (100) epitaxy, with [001] bcc parallel to [011] fcc, which means parallel orientation of quadratic nets.

Substrate metal		f (%) for different film metals		
	a'	α-Fe $b' = 2.866$	Cr $b' = 2.885$	V $b' = 3.039$
Pd	2.750	4.2	4.9	10.5
Pt	2.775	3.3	4.0	9.5
GaAs	2.827	1.4	2.1	7.5
Al	2.862	0.1	0.8	6.2
Fe	2.866	0	0.7	6.0
Au	2.884	−0.6	0.03	5.4
Cr	2.885	−0.7	0	5.4
Ag	2.889	−0.8	−1	5.2
V	3.039	−5.7	−5.1	0
Mo	3.147	−8.9	−8.3	−3.4
W	3.165	−9.4	−8.8	−4.0
Nb	3.301	−13.2	−12.6	−7.9
Ta	3.303	−13.2	−12.6	−12.6

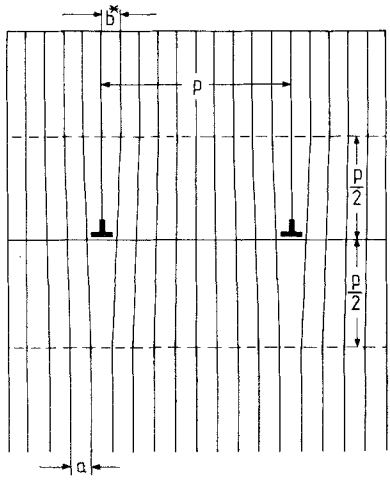

Fig. 1. Schematic representation of an interface between a substrate and a growing film with atomic spacings a and b^*, containing a sequence of edge-type misfit dislocations. For thicker films, the periodic elastic strain is limited to a sheet of thickness p, the distance between the dislocations.

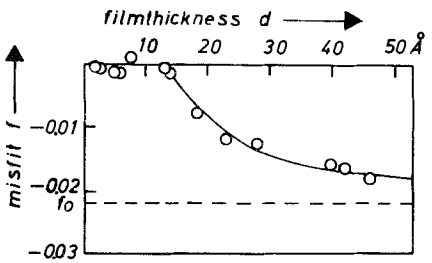

Fig. 2. Misfit $f=(b^*-a)/a$ of an fcc Co(111) film of mean lattice parameter b^* on a Cu(111) substrate of lattice parameter a, in comparison with the misfit f_0 of the bulk materials, versus Co thickness d. The film is pseudomorphic with the substrate up to 1.3 nm. A residual strain $(f-f_0)$ is retained even above 5 nm. Data taken by RHEED (from Gradmann 1974).

dislocation networks, which can be observed in situ by electron diffraction, where the periodic lattice distortion shows up in superstructure multiplets in the diffraction pattern (Gradmann 1964, Waller and Gradmann 1982).

2.4. Interdiffusion

Severe restrictions are imposed on the preparation of metallic film systems by interdiffusion. In an ideal case, interdiffusion of substrate and film is forbidden by the phase diagram. An inspection of binary phase diagrams including Fe, Co and Ni (Hansen and Anderko 1958), however, shows that insolubility is found only for Fe on Cu and Ag, for Co on Ag and Au and for Ni on Ag. Strictly speaking, atomically

sharp interfaces are stable for these systems only, and the wide interest in these epitaxial systems seems to be caused by this simple fact. In addition, broad miscibility gaps greater than 90% for Fe on Au, for Co on Cu and for Cu on Ni and Au open up good possibilities for nearly sharp interfaces in these systems. Because none of the substrates Cu, Ag and Au shows higher surface energies than Fe, Co and Ni (cf. table 1) the preparation of flat ultrathin films down to a monolayer in these systems is problematic. On the other hand, the comparatively small differences of surface energies open up good possibilities for constructing superlattices by forced layer growth. Another possibility for avoiding interdiffusion is provided by using W substrates, where the kinetic barrier for diffusion is so high that no interdiffusion could be observed up to the re-evaporation temperature of the magnetic films, as shown for Ni on W by Kolaczkiewicz and Bauer (1984) and for Fe on W by Gradmann et al. (1990a). Similar conditions have been shown for Ni on Re by Gradmann and Bergholz (1984) and can be expected in general for the high melting substrates Re, Ta and W. For Mo substrates, interface alloying has been reported by Tikhov and Bauer (1990) at temperatures of about 800 K. For other substrates, interdiffusion has to be checked carefully from case to case.

3. Methods of structural analysis

There is now a wide variety of experimental methods available for structural testing of ultrathin films, mostly in situ in UHV, none giving complete structural information; using complementary methods is required. In principle, all experimental methods of surface and interface analysis are applicable to ultrathin films and they cannot be reported completely. The following presentation comprises a short characterization of the methods that are most important for thin magnetic films, illustrated by applications on them. References to the literature are given for full descriptions. We start with high- and low-energy electron diffraction, which in combination with Auger electron spectroscopy form the most powerful techniques presently available for surface structural analysis. We proceed then with X-ray, and Mössbauer methods, which are applicable to the less accessible internal surfaces or interfaces. We end with electron microscopies, which form a most powerful method which is only beginning to be applied to metal epitaxial growth. It should be noted that the magnetic data themselves and their appropriate interpretation may provide valuable structural information too.

3.1. Low-energy electron diffraction (LEED)

In comparison with reflexion high-energy electron diffraction (RHEED) the advantage of LEED is the availability of a straightforward line of analysis, which can be used to some extent only for RHEED. We therefore start with LEED, where the sample is irradiated, mostly at normal incidence, by a low-energy primary electron beam (energy of the order of 100 eV). The structural analysis is based on the elastically scattered electrons only, which are separated from a strong inelastic background by a retarding field and visualized on a fluorescent screen after acceleration to some keV. General reviews of the method were given by Ertl (1986) and Zangwill (1988). In an alternative

setup, the diffracted Bragg beams are swept over a pinhole before a multiplier, in order to analyze their angular fine structure, which forms something like the Fourier transform of the real structure of the surface (*spot profile analysis, SPA-LEED*, for reviews see Henzler 1984, 1988).

Three types of information can be obtained from a LEED experiment: First, the spot pattern indicates crystalline order and in our case epitaxial growth, and its symmetry reflects the symmetry of the sample. It should be emphasized, however, that only the two-dimensional translational symmetry in the film plane can be deduced from visual inspection. Therefore, in cubic (100)-films a decision between fcc (100) and bcc (100) is impossible, because both are special cases of the bodycentered tetragonal lattice, with a c/a ratio of $\sqrt{2}$ and 1, respectively. Actually, epitaxial strain and surface relaxation of lattice plane distances along the surface normal make the exact cubic cases rare exceptions in epitaxial films. The situation is similar for fcc (111) in comparison with hcp (0001). To get the additional information on the third dimension, along the surface normal, LEED patterns have to be taken and their intensities $I(V)$ measured as a function of electron wavelengths or energies. In combination with their analysis along the well-developed dynamical (multiple-scattering) theory (compare for example van Hove and Tong 1979), this $I(V)$ analysis gives reliable data on relaxations, normal strains and the third component of a structure, as a second information from LEED analysis, as discussed in the review of Jona and Marcus (1988). Because the $I(V)$-curves can be taken as a fingerprint of surface structures, they can be useful for the analysis of films in the nucleation state, too (H. Li et al. 1990).

For real structure and defect analysis, the third type of information is most important, that which comes from a small angle analysis of the spot structure, performed in SPA-LEED. For the analysis of the experimental spot profiles, the so-called kinematical approximation of the scattering process turns out to work well. It starts from the assumption (Henzler 1984, 1988) that each surface atom can be considered as the source of a secondary wavelet, which actually sums up all multiple scattering processes ending up in this surface atom or atoms in a column below it, before the final emission. Because of the strong forward scattering of the electrons and the small elastic mean free path involved, this wavelet depends only on a very narrow column around this surface atom. The interference pattern of all wavelets of this type can then be treated by classical optical methods.

As an example of SPA-LEED-analysis, fig. 3 shows spot profiles of the specular beam from a W(110) surface, covered by 0.45 pseudomorphic monolayers of Fe(110), for various kinetic energies E of the electron beam. For $E = 130\,\text{eV}$, a sharp spike is observed only, just as observed at an ideal homogeneous W(110) surface for any energy. This pure central spike pattern is characteristic for an in-phase condition, in which wavelets from the free W surface and from the Fe-coated patches scatter in phase. With increasing energy, the relative intensity of the central spike is reduced and a broad diffraction shoulder evolves, which becomes a maximum near 139 eV, where the wavelets are out of phase. The periodic change of intensity between central spike and shoulder for varying energies was used by Albrecht et al. (1991a) to determine experimentally the relative scattering phases from uncoated and Fe-coated W(110) regions. Results are in excellent agreement with phases from dynamical LEED calculations.

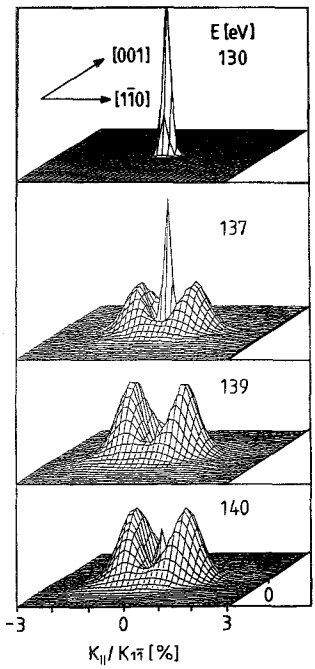

Fig. 3. SPA-LEED from 0.45 pseudomorphic monolayers Fe(110) on W(110), prepared at room temperature. Spot profiles of the specular beam, near normal incidence, for electron energies, E, between 130 and 140 eV, showing central spike and broad shoulder, with change of their relative intensities with changing electron energy (from Albrecht et al. 1991a).

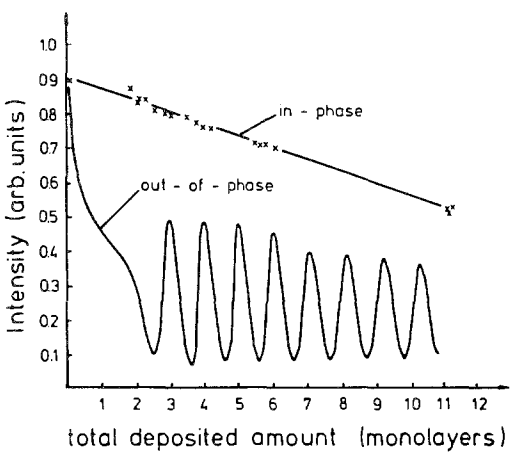

Fig. 4. Intensity of the central spike of the specular LEED beam, for epitaxy of Si(111) on Si(111) at 790 K, for in-phase and out-of-phase electron energies, respectively. After an initial nucleation phase of about three layers, the oscillations for the out-of-phase energies indicate a periodic repeat of similar terrace structures with monolayer period. The decreasing amplitude indicates an increasing number of involved levels (from Henzler 1988).

The broad shoulder, which is maximum for the out-of-phase conditions, contains the information on the real structure of the surface (it is the Fourier-transform of the autocorrelation function of the surface). For the example of fig. 3, it tells us that the Fe(110) monolayer islands are elongated along [001] with a width of about 13 nm along [1$\bar{1}$0].

The intensity of the central spike for out-of-phase energies depends sensitively on the structure of the surface. If a film grows layer-like in the sense that identical surface

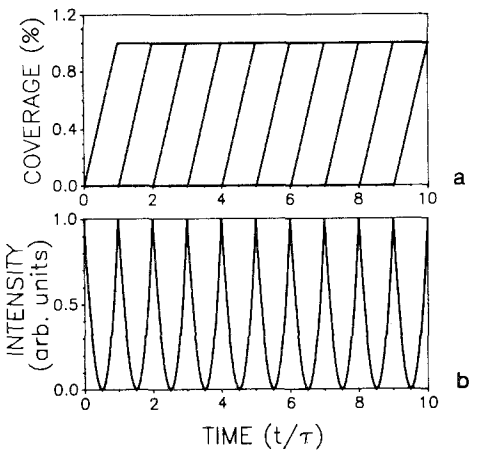

Fig. 5. Model calculations for the relative intensity of the central spike in electron diffraction spots, for perfect layer-by-layer growth. (a) Coverages of subsequent layers, versus total film thickness, or evaporation time, in monolayer-units τ. (b) Intensity of the central spike, for out-of-phase energies. Note the cusp-like maxima indicating the completion of a perfect atomically smooth surface (from Cohen et al. 1989).

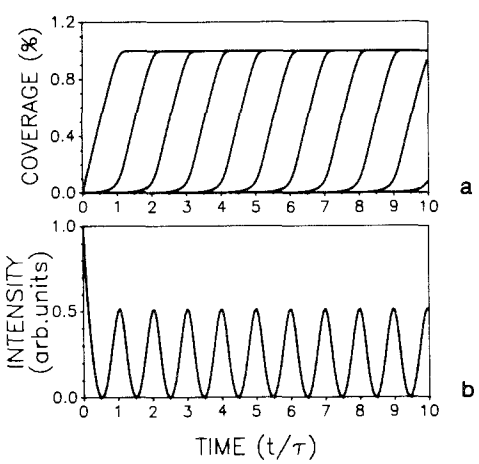

Fig. 6. As fig. 5, but for a modified layer growth where the layer $n+1$ starts growing before layer n has been completed (from Cohen et al. 1989).

structures repeat periodically as a function of mean film thickness d, the central spike for out-of-phase energies shows intensity oscillations, which became popular as 'RHEED-oscillations', but can be observed by LEED as well, cf. fig. 4. As shown in figs. 5 and 6, the amplitude of these oscillations is connected with relative areas of the atomic levels involved in the growing surface. However, nothing can be concluded from these oscillations about the geometric shape of these levels, which in turn must be deduced from the structure of the shoulder.

3.2. Reflexion high-energy electron diffraction (RHEED)

If high-energy electrons with kinetic energies of some 10 keV are reflected from crystalline surfaces after glancing incidence, the RHEED diffraction pattern can be visualized on a fluorescent screen without post-acceleration. This technique is known for many years, it has been described by Raether (1957) in some detail, shows comparable surface sensitivity to LEED, and provides in principle the same information on two-dimensional symmetries of crystalline surfaces as LEED. However, a quantitative evaluation of the observed intensities suffers first of all from the missing subtraction of the inelastic background and further from the much more complicated dynamical scattering problem, which has not yet been solved. For surface analysis, the technique therefore had been nearly completely displaced by LEED, up to the discovery of the 'RHEED-oscillations' by Neave et al. (1983), which are completely analogous to the LEED-oscillations discussed in the last section, cf. figs. 4, 5 and 6. Again they consist of periodic changes in specular reflectivity, under out-of-phase conditions, for periodically repeating surface morphologies as they occur during layer-like growth in MBE. The strong advantage of the technique is its easy applicability during film growth, which made it an extremely powerful method in controlling epitaxial growth processes in UHV. Extended discussions of the method can be found in articles of Farrow et al. (1987) and van der Veen and van Hove (1988). The problems in quantitative evaluation remain, however. In particular, the quantitative applicability of the kinematical approximation described in the last section, which is actually widely used for the discussion of the experiments (cf. Lent and Cohen 1984) suffers not only from the missing subtraction of the inelastic background. It suffers most of all from the fact that the forward-scattering, which for the case of normal incidence in LEED defines a narrow cylinder below each surface atom as the source of the wavelet starting from it, defines now for the case of grazing incidence in RHEED a largely elongated surface stripe in the surface, connected by multiple scattering cascades along the incident beam. This is due to the enlarged elastic mean free path. As a result, the electrons 'see' almost a projection of the structure onto a plane perpendicular to both the surface and the incident beam, as noted by Maksym (1988). RHEED oscillations from a magnetic metal film example are shown in fig. 7. For the case of Ni on Fe, which apparently forms something like an ill-defined bcc structure (Heinrich et al. 1989a), as concluded from the diffraction pattern, the quite regular oscillations indicate a layer-like growth, and the decreasing amplitude indicates an increasing number of levels present in the growth surface, with increasing thickness. The meaning of the enhanced period in the initial growth regime remains unclear. For the case of Fe on Ag(001),

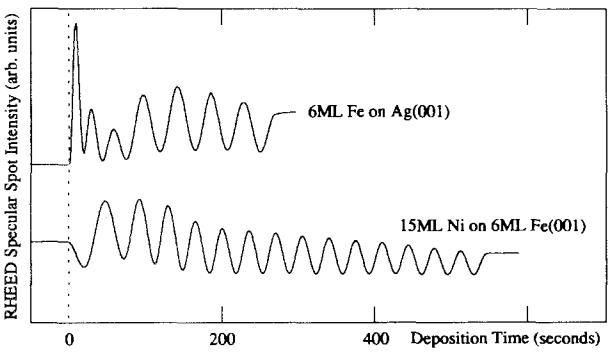

Fig. 7. RHEED-oscillations for Fe on Ag(001) and Ni on Fe(001) (from Heinrich et al. 1989a).

a regularly damped oscillation starts only after about four layers, and the complicated initial oscillation structure indicates a complicated nucleation process, as expected from the surface energies, without giving access to its details. One great advantage of RHEED-oscillations is given by the possibility of directly counting the number of layers and therefore of calibrating the film thickness.

3.3. Auger electron spectroscopy (AES) and photoelectron spectroscopy (PES)

The use of Auger electrons for surface analysis results from their low attenuation lengths, which are below 1 nm for electron energies of the order of 100 eV. For the case of layer-by-layer growth of a thin film, this has the consequence that the Auger amplitude of the growing film, plotted versus film thickness d, shows linear sections during the growth of each atomic layer, indicating the linear increase of coverage by it, and changes of slope when one layer is completed and the atoms start to be deposited in the next one. An extended presentation of the use of these *Auger kinks for growth mode analysis*, in combination with work-function measurement and thermal desorption, has been given by Tikhov and Bauer (1990) for the case of Fe, Co and Ni films on Mo(110). It turns out that Auger kinks can indicate other changes in the growth process than the completion of a monolayer, too, and extreme care is needed in their interpretation. This can be seen in fig. 8 for the example of Auger-amplitudes from Fe(110) on W(110), measured by use of LEED optics in the retarding field mode. For deposition at room temperature, the first kink is observed for $D = 1.64$ bulk monolayers, or 2.0 pseudomorphic monolayers. The completion of the first monolayer before the second one starts, which can definitely not be seen in the figure, has been seen by Gardiner (1983) by a weak Auger kink, using a cylindrical mirror analyzer, and most clearly by Przybylski et al. (1989) using Mössbauer spectroscopy, to be discussed below in sections 3.5 and 6.2.3. Accordingly, a possible suppression of the monolayer kink for a given detector geometry must be carefully excluded before identifying the first kink as a monolayer kink, and severe misinterpretations can result by neglect of this. This is of special importance if the monolayer kink is used for thickness calibration, as has frequently been done. Secondly, the first kink shifts to $D = 1.3$ for preparation at 475 K, indicating now apparently deposition in a third monolayer

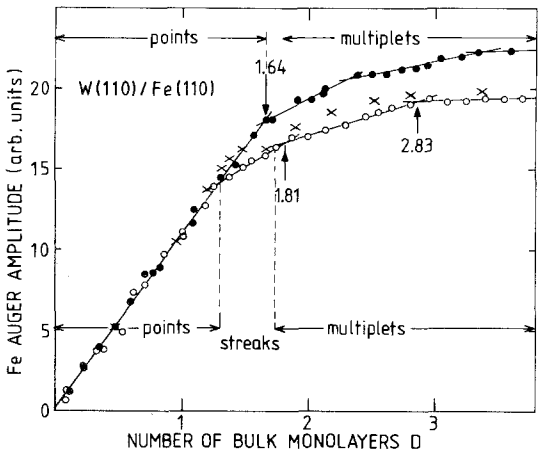

Fig. 8. Fe Auger amplitude (47 eV) for Fe(110) films on W(110), prepared at 295 K (full points) and 475 K (open circles, crosses), respectively, versus film thickness, given in bulk monolayer equivalents, D. The structure of the LEED pattern is indicated (from Przybylski et al. 1989).

before the second one is completed. Obviously, a possible misinterpretation of it as a monolayer kink represents a type of pitfall which has to be avoided carefully. The bare observation of Auger kinks cannot be taken as a proof for layer-by-layer growth.

A further application of Auger electrons in surface crystallography results if their angular distribution can be analyzed. Because of strong *forward scattering* by superimposed atoms, Auger electrons coming from the topmost layer show different angular distributions than those from deeper layers, and can be distinguished by that. A review of this forward-scattering method has been written by Egelhoff (1990). Both surface applications of AES rest on the emission of electrons with energies near 100 eV and their low attenuation length. They can therefore be realized with soft X-ray photoelectrons, too (Egelhoff 1990).

3.4. X-ray methods

Standard X-ray techniques suffer from low scattering cross sections in their application to ultrathin films. However, because the index of refraction becomes less than one for X-rays, total reflexion takes place at grazing incidence and penetration depths down to 2 nm can be realized. In combination with high-brilliance synchrotron sources, this opens forthcoming applications of X-rays on surfaces and ultrathin films, which have been reported by Cargill (1989). The use of standard X-ray techniques for multilayer testing has been described by C. H. Lee et al. (1989). The local symmetry of surface atoms can be analyzed by SEXAFS methods (Idzerda et al. 1990).

3.5. Conversion electron Mössbauer spectroscopy (CEMS)

Mössbauer spectroscopy, introduced in the field of magnetic films originally as a magnetic probe, turned out to be a sensitive structural probe, also. Monolayer sensitivity,

which is crucial for this application, can be achieved by detection of the resonant nuclear absorption via conversion electrons (CEMS, Korecki and Gradmann 1985, 1986a,b). The method is restricted to Fe-based films; it is applicable to interfaces. It is explained by an example, given in figs. 9 and 10, from Przybylski et al. (1989). Figure 9 shows CEMS spectra from Fe(110) films consisting of the pure Mössbauer isotope ^{57}Fe, prepared on W(110) at 300 K, coated by Ag, with the number of bulk Fe-monolayer equivalents, D, as parameter. Because of the misfit $f_{FeW} = -9.4\%$, the

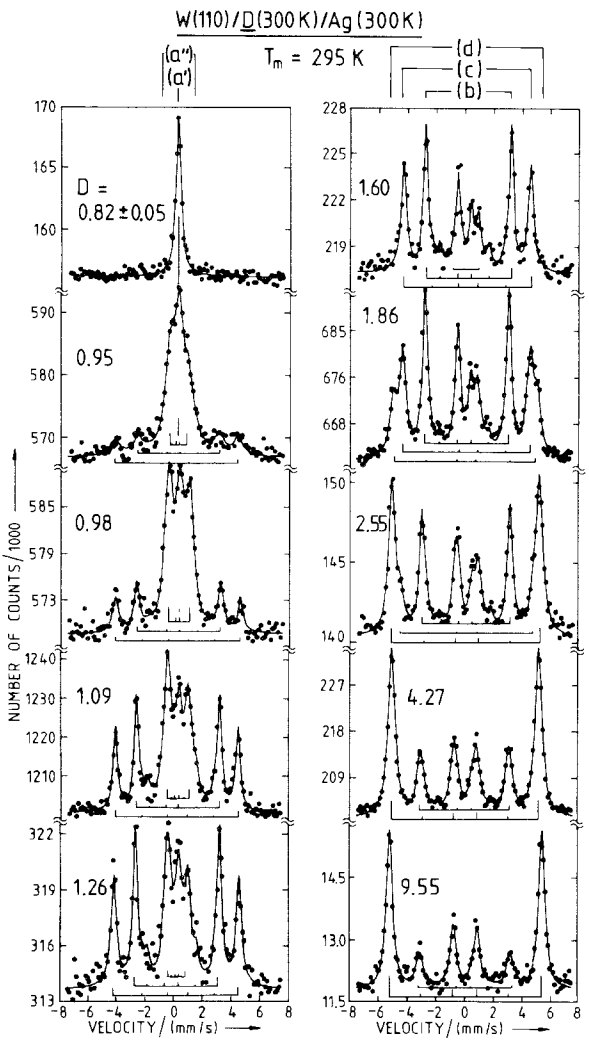

Fig. 9. Mössbauer spectra, taken at 295 K, of pure ^{57}Fe(110) films on W(110), prepared at 300 K, coated by Ag, with the number of bulk monolayer equivalents, D, as parameter (from Przybylski et al. 1989).

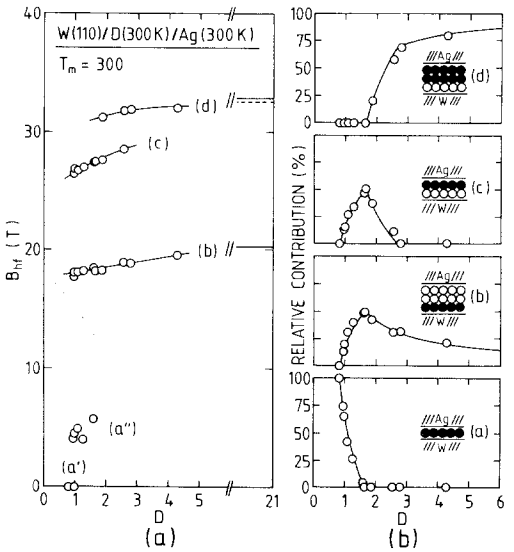

Fig. 10. (a) Magnetic hyperfine fields and (b) relative contributions of spectral components from fig. 9, versus D, compared with predictions from layer-by-layer growth (full curves in b) (from Przybylski et al. 1989).

pseudomorphic monolayer corresponds to $D = 0.82$. All spectra can be decomposed into four sixline-components, *a*, *b*, *c* and *d*, with magnetic hyperfine fields as given in fig. 10a versus D. A tentative attribution of them to the monolayer, the first layer in thicker films, the second atomic layer of a double layer, and further bulk-like material can be clearly confirmed by their relative intensities, which come out from the computer fit and are shown in fig. 10b to follow completely the predictions of a layer growth model (full lines). Layer-by-layer growth starting from a pseudomorphic monolayer is clearly confirmed. Deviations from this layer-by-layer growth for preparation at 475 K, as indicated by the Auger data of fig. 8, could be confirmed by CEMS, too. Application to structural changes by film annealing has been described by Przybylski et al. (1990b).

3.6. Electron microscopies

Detailed information on epitaxial growth processes and the morphology of film surfaces recently became available through the use of *scanning tunneling microscopy (STM)*. For example, its application to epitaxy of Au on Au(111) has been described by Lang et al. (1989). *Low-energy electron microscopy (LEEM)* has been dealt with in a review of Mundschau et al. (1989) and references given there. Whereas STM is unique by its atomic resolution, the advantage of LEEM is the rapid data access with the possibility of following growth processes in real time, combined with a resolution of about 40 nm. Application of LEEM to magnetic films is in progress.

4. Probes of magnetic order

There is now a wide variety of methods available to detect and measure magnetic properties of ultrathin films with monolayer or submonolayer sensitivity, in many cases in situ in UHV. The intention of this chapter is to give a short overview and discussion of capabilities of the most important methods, and to give references to further literature, and to examples of measurement in the following chapters.

4.1. Measurement of magnetic moment

In discussing the magnetic moment of a film, or of an atom in a certain position near the surface, one may ask for its magnitude, at fixed temperatures, or for its temperature dependence. Nearly any probe of magnetic order can be used for the latter, using the reasonable assumption that any ferromagnetic signal, caused by the magnetic moments, scales in temperature with them. The present section reports methods to measure the *magnitude of magnetic moments.*

Magnetometers for ultrathin films should be able to resolve the magnetization of monolayers. To estimate roughly the required sensitivity, consider a monolayer sample of area 0.1 cm^2, containing 10^{14} atoms, each with a moment of $1\mu_B = 1.165 \times 10^{-29}$ Wb m $= 0.927 \times 10^{-20}$ emu. Requiring a resolution of 1%, we calculate a required sensitivity of the order of $10^{12}\mu_B$, 10^{-17} Wb m or 10^8 emu as needed for ultrathin film analysis down to the monolayer.

The *vibrating sample magnetometer* (*VSM*, Foner 1959; for a review see Foner 1976) is the most popular one. Monolayer sensitivity can be achieved only with miniaturized coils (Foner 1975), whereas for standard geometries, as used in commercial equipment, the sensitivity is reduced to $10^{15}\mu_B$. The instrument therefore is used preferentially as a most convenient magnetometer for multilayers. In situ application has not been reported.

The *superconducting quantum interferometric device (SQUID)*, used as a detector for stray magnetic fields, detects $10^{12}\mu_B$ as required for monolayer analysis. Being appropriate for accurate absolute measurement at variable and low temperatures, the instrument is slow because of pointwise measurement of the magnetization loop. It has not yet been applied in UHV.

A *magnetic balance* of monolayer sensitivity, working in UHV, in which the translational force on a magnetic moment in a gradient field was measured with high sensitivity, has been used by Stuenkel (1963) for in situ research on polycrystalline Fe films, but never used since.

The translational force in a gradient field, superimposed to a magnetizing homogeneous field, is used in the *alternating field gradient (AFG) magnetometer* in a resonant mode. The sample is mounted on a flexible cantilever rod; with the frequency of the alternating field gradient in resonance with the cantilever–sample system, the oscillation amplitude, which is taken as a measure of the magnetic moment, is resonantly enhanced. The instrument was introduced, and applied for small particle magnetometry, by Zijlstra (1970), who used optical detection for the oscillation amplitude. The instrument was improved by Roos et al. (1980) using piezoelectric

detection techniques, and further developed recently by Flanders (1988). It provides a detection limit of $10^{12}\mu_B$ and can be used at low temperatures. Hysteresis loops can be taken in roughly one minute. Application in situ in UHV is in progress (Bayreuther 1990). Commercial versions of this promising instrument are available.

A high-sensitivity *static torque magnetometer* was used by Neugebauer (1962) in his pioneering study of polycrystalline Ni films, which were the first experiments on magnetic films in situ in UHV. What is measured is the torque felt by the sample in a magnetic field; because this torque is mediated by the combined coupling of the magnetic moment to the field, and by its coupling to the film plane by magnetic anisotropies, the method provides access to both magnetic moment and anisotropy. The method has never been applied to single-crystal films.

In the *torsion oscillation magnetometer (TOM)*, the magnetic torque on a sample, suspended on a thin torsion filament, is measured, near equilibrium position, via its influence on the period of torsion oscillations around this equilibrium. The instrument was used by Gradmann (1966) in the first experiments on epitaxial ferromagnetic films; it was adapted by Gradmann and Bergholz (1984) for measurements in UHV, during epitaxial film growth, and was used for extended research on ultrathin epitaxial magnetic films. As in the static torsion magnetometer of Neugebauer, the torque on the sample is mediated by the combination of the torque of the field on the magnetization and the coupling of the magnetization to the sample by magnetic anisotropies. For a quantitative description, assume that the magnetic anisotropy energy F, including shape anisotropy, is given by

$$F = LV\cos^2\theta, \tag{4.1}$$

where V is the film volume, L an anisotropy constant and θ the angle between the film normal and the saturation magnetization J_s of a magnetically saturated film. The magnetic torque constant R (torque per rotation angle) in a field H is then given by

$$1/R = 1/(J_sVH) + 1/(2LV). \tag{4.2}$$

Introducing an anisotropy field $H_L = 2L/J_s$, we see that $R = J_sVH$ for $H \ll H_L$, because J_s is rigidly fixed to the lattice, whereas $R = 2LV$ for $H \gg H_L$, because J_s is rigidly fixed to the field. Equation (4.2) may be alternatively written as

$$R/H = J_sV/(1 + H/H_L). \tag{4.3}$$

The magnetic saturation moment J_sV and anisotropy field can be determined independently. For the measurement of hysteresis loops compare the detailed discussion of the method given by Gradmann (1966) and Gradmann et al. (1976). The method cannot be used for vanishing anisotropies, e.g. if shape anisotropy is compensated by a perpendicular crystalline anisotropy. Further, straightforward analysis of the data is not possible if the magnitude of J becomes dependent on the field, as in the critical regime. For magnetic moments, the instrument has a sensitivity of $10^{12}\mu_B$. Up to now, it provides the only method to measure magnetic moments of epitaxial films in situ in UHV.

Spin-polarized neutron reflection from ferromagnetic films, at grazing incidence, has been shown by Bland and Willis (1987) to provide information on film magnetization

with monolayer sensitivity, also. The report of a very surprising magnetization of $1.0(0.15)\mu_B$ per atom in an epitaxial film of eight monolayers of Fe in a Ag(100) matrix by Bland et al. (1990a), obtained by this method, might however indicate some problems in the rather involved determination of magnetic film moments.

4.2. Measurement of magnetic anisotropies

As in bulk materials, magnetic anisotropies in ultrathin films can be measured by torque magnetometry or *ferromagnetic resonance (FMR)*; the same modes which can be observed by microwave absorption in FMR can be observed alternatively by inelastic or *Brillouin light scattering (BLS)*. Both methods are available in UHV and able to detect monolayers, cf. the reviews by Heinrich et al. (1988a, 1989b) and Cochran et al. (1988). In addition, anisotropies can be determined from hard axis loops, taken by the methods of the previous section or by the magnetooptical Kerr-effect, to be discussed in the next section.

4.3. Magneto-optical Kerr effect (MOKE)

The dependence of the polarization state of light reflected from ferromagnetic surfaces on the magnetization state of the latter, called magneto-optical Kerr-effect, has been used for many years to observe magnetic domains at bulk magnetic surfaces. After Bader et al. (1986) noted its easy use to take hysteresis loops from ultrathin films, the effect, called now the *surface magneto-optical Kerr effect (SMOKE)*, has found wide application in ultrathin film magnetism, down to the monolayer. A recent review has been published by C. Liu and Bader (1991) and references of the subject are given there. The effect seems to be to some extent proportional to the magnetic moment of an ultrathin film. However, strongly nonlinear dependence on film thickness has been reported by Weller et al. (1988) for NdFeCo films, with a maximum of the Kerr-rotation at 2 nm and a following zero at 4 nm film thickness. The effect therefore cannot be taken generally as a direct measure of magnetic moment. Its strong merit is the easy application in UHV and ready combination with other thin-film and surface techniques.

4.4. Spin-polarized electron techniques

The availability of sources and detectors of spin-polarized electrons make virtually any of the many low-energy electron techniques of surface analysis (Ertl 1986) a probe of the magnetic state of ferromagnetic surfaces. The resulting methods of experimental surface magnetism, like *spin-polarized electron reflection, photoemission, inverse photoemission* and *secondary electron emission*, and spin-polarized electron surface techniques in general, have been reviewed by Feder (1985). One main problem of the methods is the sensitivity of low-energy electrons to magnetic fields; magnetic stray fields have to be carefully avoided during measurements. For the case of bulk surfaces, this can be achieved by use of closed magnetic circuits; surface hysteresis loops can be taken with those techniques. They are not applicable for ultrathin magnetic films, which therefore can be analyzed using spin-polarized low-energy electron techniques in a

remanent state only. These electron-optical problems can be avoided by *electron capture spectroscopies (ECS)*, in which the neutralization of ions at ferromagnetic surfaces is used, resulting in a polarized neutral atom, with following polarization detection by nuclear methods (Rau 1982, for a recent review see Rau 1989) or by polarized light emission (Winter et al. 1989). The evaluation of the rich information contained in all these spin-polarization techniques in terms of magnetization is difficult. They provide powerful methods to detect surface magnetism and to measure its temperature dependence. They are restricted to external surfaces.

4.5. Nuclear methods

The merit of nuclear methods is to provide local probes of magnetic order, if the tracer isotopes can be included in the samples in definite positions. Two nuclear probes have been applied for magnetic analysis of surfaces and ultrathin films. Both use the magnetic hyperfine interaction to transfer the magnetic information from the surroundings to the tracer nucleus.

The first one is given by Mössbauer spectroscopy, which was first used for the analysis of ultrathin ferromagnetic films by Tyson et al. (1981), who used the usual transmission mode. Korecki and Gradmann (1985, 1986a) introduced the more surface-sensitive modification of *conversion electron Mössbauer spectroscopy (CEMS)* in the field, in which the resonant nuclear absorption is detected by the following emission of K-shell conversion electrons with a kinetic energy of 7.3 keV. For applications of the method, which has true monolayer sensitivity, compare section 6.2.3. However, the technique is slow, one spectrum taking roughly one day. A much more sensitive and rapid technique is given by *perturbed angular correlations (PAC)*, e.g. in γ-cascades of ^{111}Cd, which is populated by electron capture of ^{111}In. Voigt et al. (1990) used this technique to probe the magnetic hyperfine field of In/Cd probes on the surfaces of epitaxial Ni films on Cu(100) and its temperature dependence. The method is restricted to external surfaces. Note further that PAC applies to an external non-magnetic probe only, contrary to CEMS, which measures magnetic hyperfine fields at the nucleus of the magnetic atom itself.

4.6. Magnetic microscopies

Magnetic domains in ultrathin films have been observed by Pommier et al. (1990) using optical *Faraday-microscopy* and can certainly be observed by *Kerr-microscopy*, too. An enhanced local resolution of some 10 nm is provided by *scanning electron microscopy with spin-polarized analysis of secondary electrons (SEMPA)* (Koike and Hayakawa 1984, Unguris et al. 1985, Oepen and Kirschner 1988). This enables the analysis of magnetic domain wall structures (Scheinfein et al. 1989).

A spin-polarized version of the *low-energy electron microscope (LEEM)* (Telieps and Bauer 1985) has recently become operational (Altman et al. 1991) and opens the possibility of observing magnetization processes in ultrathin films in real time. The recent success of Wiesendanger et al. (1990) in observing antiferromagnetic surface structures by *spin-polarized scanning tunneling microscopy (STM)* opens up at least the hope that magnetic microscopy with atomic resolution will become available for

ferromagnetic surfaces, too. The potential impact of these microscopies on a detailed understanding of ultrathin film magnetism is evident.

PART II. Magnetic thin film phenomena

5. Magnetic anisotropies in ultrathin films

One of the most remarkable properties of ultrathin magnetic films is given by their unusual magnetic anisotropies. They are not only important for applications, but their presence is decisive too for the existence of long-range magnetic order in these two-dimensional systems. We therefore start our discussion of magnetic film phenomena with magnetic anisotropies.

5.1. Anisotropy contributions

In the following, we consider magnetic anisotropies in homogeneously magnetized samples, or homogeneously magnetized regions of a film. The anisotropy is given by the contribution to the free energy of the crystalline film which depends on the direction of the magnetization J_s. We describe this direction by the polar angle ϑ with respect to the sample normal and an azimuth angle φ with respect to some low symmetric direction in the plane. We thereby use a *homogeneous magnetization approximation*, assuming that the film thickness is small in comparison with any exchange length, and the direction of magnetization therefore depends on the in-plane local coordinates only, whereas it is homogeneous along the surface normal. We consider the following anisotropy contributions:

(a) *Magnetostatic anisotropy (shape anisotropy, stray field energy).* The thickness of our films is small in comparison with any characteristic length for changes of the magnetization direction (exchange length, wall width). This has an important consequence for the stray field energy. If magnetic poles are generated by a nonvanishing normal component of J_s, the stray fields, which they are the source of, are closed in a small volume of virtually homogeneous magnetization. The stray field energy with a volume density

$$f_M = (J_s^2/2\mu_0)\cos^2\vartheta \tag{5.1}$$

therefore becomes a local property of the in-plane local coordinates. Its nonlocal character, which causes severe difficulties in the micromagnetism of bulk ferromagnets, disappears in this approximation. The formation of domains, which is driven in bulk crystals by the minimization of the magnetostatic energy, can no longer be caused by this mechanism, and a single domain equilibrium state results. Only for the exceptional case that f_M is approximately compensated by a crystalline anisotropy, a domain system can be formed, as has been calculated by Yafet and Gyorgy (1988). The magnitude of these domains diverges rapidly for even small deviations from the exact compensation, thus leading back to the single-domain ground state. The usual shear of the magnetization loop, which is observed for thick plates, disappears for ultrathin films, cf. fig. 11 below. The domain systems predicted by Yafet and Gyorgy have been

detected by Allenspach et al. (1990), using SEMPA, in perpendicularly magnetized Co films on Au(111).

In using eq. (5.1) for the magnetostatic energy, we assume a demagnetizing factor 1, which is strictly speaking a property of homogeneous magnetic media only. Deviations, caused by the atomistic structure of the ferromagnet, must be considered for ultrathin films and can be incorporated by using a thickness-dependent demagnetizing factor, to be introduced in eq. (5.1), as discussed by Heinrich et al. (1988a). However, Draaisma and de Jonge (1988) showed that the deviation of the total magnetostatic energy in a film from the homogeneous-medium approximation $f_M V$ according to eq. (5.1) is proportional to the film surface, to a very good approximation. Following Draaisma and de Jonge, we therefore represent that deviation by a magnetostatic contribution to the surface energy (magnetic surface anisotropy) given by

$$\sigma_M = -k_s \delta (J_s^2/2\mu_0) \cos^2 \vartheta, \tag{5.2}$$

where δ is the spacing of lattice planes. Parameters k_s are shown in table 3 for different surfaces. Note that the correction is large for open surfaces like bcc (100) and fcc (100), whereas it is small for densely packed surfaces like fcc (111) and bcc (110). In our notation, σ_M is a magnetostatic contribution to the magnetic surface anisotropy in general, to be discussed under point (d).

(b) *The bulk magnetocrystalline contribution* of the density f_K is given in standard terms and has to be rewritten in polar coordinates.

(c) *Strain contributions* of density f_ε can be very strong, in particular for pseudomorphic films, where elastic strains of several percent can occur; examples are given in section 5.2.5. However, strain in epitaxial films, caused, for example, by differential thermal expansion with the substrate, or by defects induced by the growth process itself, is quite general. A complete strain analysis is difficult and has not been performed for any magnetic film system; some realistic estimates, which have been done for a few cases only, will be discussed below. As a rule, f_ε therefore must be taken as an empirical property, to be determined by magnetic measurements, as discussed below.

(d) *Magnetic surface anisotropy (MSA).* Any magnetic anisotropy reflects a deviation from isotropy in the crystalline surroundings of the magnetic atoms. Néel (1954)

TABLE 3
Parameters k_s of magnetostatic contribution to magnetic surface anisotropy, appearing in eq. (5.2) (from Draaisma and de Jonge 1988).

Surface	k_s
sc(100)	−0.0393
fcc(111)	0.0344
fcc(100)	0.1178
bcc(110)	0.0383
bcc(100)	0.2187
hcp(0001)	0.0338

was the first to note that the dramatic break of local magnetic symmetry in a surface must result in strong surface-type anisotropies. In a phenomenological sense, they are a magnetic contribution to the free surface (interface) energy of the crystal, depending on the magnetization direction in the surface. In a quadratic approximation, the surface anisotropy is given by

$$\sigma = K_s \cos^2 \vartheta + K_{s,p} \sin^2 \vartheta \cos^2 \varphi. \tag{5.3}$$

The leading first term, which describes what now is called an *out-of-plane surface anisotropy*, is present in all magnetic surfaces, by quite general symmetry reasons. In taking it proportional to $\cos^2 \vartheta$, we use a notation which was introduced by Néel and used afterwards in the first experimental analysis of MSA by Gradmann and Mueller (1968) and in subsequent reviews on the subject (Gradmann et al. 1984, Gradmann 1986a). This notation has the advantage that the stray-field energy, which is positive definite, appears positive, too, cf. eq. (5.1). Unfortunately, some authors preferred a notation with the reverse sign of K_s. The second term in eq. (5.3) is an *in-plane surface anisotropy*, which must be considered in lower-symmetry surfaces only, like Fe(110), to be discussed in section 5.2.5.

In addition to introducing MSA, Néel proposed a phenomenological pair-bonding model of magnetic anisotropies in general, which provides some connexion between magneto-elastic volume properties and the surface anisotropy constants. The basic idea is to derive both magnetic strain anisotropies and surface anisotropies from a pseudo-dipolar pair interaction between neighboring atoms given by

$$w = l \cos^2 \phi, \tag{5.4}$$

where ϕ is the angle between the magnetic moment and the pair axis. The bond parameter l can be determined from magneto-elastic data and then be used for a calculation of MSA. An excellent presentation of out-of-plane anisotropies in this model has been given by Jacobs and Bean (1963), for further discussion of in-plane surface anisotropies in Fe(110) surfaces, in Néel's model, see the paper of Elmers and Gradmann (1990). The merit of Néel's model lies rather in qualitative insight than in quantitative description. Bruno (1988) showed that it can even model the role of surface roughness. For the case of hcp (0001) surfaces, he showed that the surface anisotropy per atom in atomic steps is reduced by a factor of two in comparison with the free surface. A quantitative description of film anisotropies in the monolayer regime using first-principles band calculations became available more recently. A review has been given by Daalderop et al. (1990). Apparently, this approach will not be able to consider the real structure and roughness of interfaces. First-principles calculations and Néel's model are complementary.

Collecting contributions (a)–(d), we arrive, for a film of thickness d, with surface anisotropies $\sigma^{(1)}$ and $\sigma^{(2)}$ for both surfaces, for the free energy F per volume V, at

$$\begin{aligned} F/V = {} & [(J_s^2/2\mu_0)\cos^2 \vartheta + f_K(\vartheta, \varphi) + f_\varepsilon(\vartheta, \varphi)] \\ & + (1/d)[\sigma^{(1)}(\vartheta, \varphi) + \sigma^{(2)}(\vartheta, \varphi)]. \end{aligned} \tag{5.5}$$

In most cases, we can neglect the in-plane contributions and use a quadratic

approximation,

$$f_K(\vartheta, \varphi) + f_\varepsilon(\vartheta, \varphi) = K_V \cos^2 \vartheta, \tag{5.6}$$

for the sum of both volume-type crystalline contributions, with a common anisotropy constant K_V. The expression (5.5) then becomes

$$F/V = L \cos^2 \vartheta, \tag{5.7}$$

with a combined anisotropy constant

$$L = [(J_s^2/2\mu_0) + K_V] + (1/d)[K_s^{(1)} + K_s^{(2)}], \tag{5.8}$$

which actually consists of a real constant volume term and a surface term proportional to $1/d$. The anisotropy constant and its contributions may be visualized by anisotropy fields

$$H_L = 2L/J_s, \tag{5.9a}$$

$$H_M = J_s/\mu_0, \tag{5.9b}$$

$$H_V = 2K_V/J_S, \tag{5.9c}$$

$$H_s^{(i)} = 2K_s^{(i)}/(\delta J_s). \tag{5.9d}$$

The connexion (5.8) between the anisotropy constants can then be rewritten as a connexion between anisotropy fields according to

$$\mu_0 H_L = [J_s + \mu_0 H_V] + (1/D)\mu_0[H_s^{(1)} + H_s^{(2)}], \tag{5.10}$$

where D is the number of atomic layers in the film, $D = d/\delta$. We use eqs. (5.8) and (5.10) as starting points for our analysis. It should be emphasized that H_L (called $4\pi M_{s,\text{eff}}$ in part of the CGS-written literature, such as Heinrich et al. 1988a) is just the quantity which comes out of an anisotropy analysis of a film by TOM, FMR or BLS. A separation in volume and surface contributions is not possible for a single film but only for a series of similarly prepared films and plotting H_L versus $1/d$. Magnetic surface anisotropies determined in this way contain a magnetostatic contribution according to eq. (5.2) in addition to the crystalline, Néel-type contributions.

5.2. *Anisotropies in selected film systems*

In the following, we discuss magnetic anisotropies in the most important metallic epitaxy systems which have been analyzed up to now, each of which shows special aspects of the subject.

5.2.1. *Anisotropies in Ni(111) on Cu(111)*

Magnetic analysis of Ni(111) on Cu(111) was first performed using TOM by Gradmann (1966), who found that the data were not quantitatively conclusive in the sense that minor and not well reproducible Ni–Cu interdiffusion could not be avoided. This obscured the quantitative interpretation of the magnetic data. This has been confirmed by later work of Sill et al. (1985) on Ni–Cu-superlattices. The system nevertheless forms an instructive example for the interplay of different anisotropy contributions.

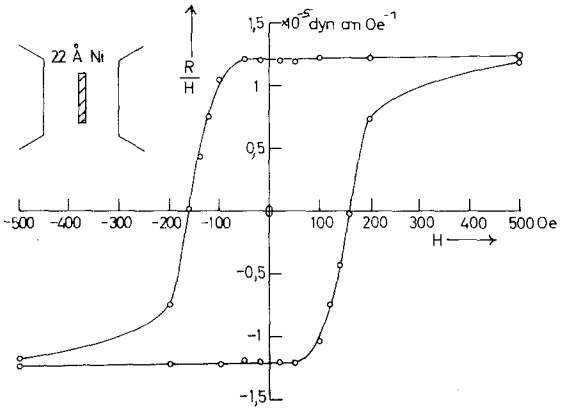

Fig. 11. Magnetization loop of a 2.2 nm thick Ni(111) film on Cu(111), coated by Cu(111), measured by TOM. R/H represents the magnetic moment to a good approximation; for an exact definition see eq. (4.3). Note that the film orients itself at right angles to the magnetic field, as indicated by the inset, as a result of a spontaneous perpendicular magnetization. Accordingly, the loop is taken with the field along the surface normal (from Gradmann 1966).

Gradmann (1966) observed that Ni(111) films prepared on Cu(111) and coated by Cu were magnetized in the plane for a film thickness above $d = 2.5$ nm, and below 1.0 nm, as expected from shape anisotropy, $J_s^2/2\mu_0 = 2.5 \times 10^5$ J/m^3 (anisotropy per atom $\varepsilon = 17$ μeV/atom). However, between 1.0 and 2.5 nm film thickness perpendicular magnetization was observed, as shown for a film of 2.2 nm in fig. 11. Apparently this provides the first example of *perpendicular magnetization in ultrathin films*. It resulted from the misfit $f_{\mathrm{NiCu}} = -2.5\%$, of which only a small part of roughly 0.5% was accommodated by misfit dislocations, as was shown then by RHEED. The residual strain of 2% results, because of the negative magnetostriction of Ni, in a negative strain anisotropy of -3.6×10^5 J/m^3 (-25 μeV/atom), which overrides shape anisotropy. With increasing accommodation for the misfit by misfit dislocations above 2.5 nm, shape anisotropy prevails, again resulting in an in-plane magnetization. The in-plane magnetization below 1.0 nm is surprising because the films are there pseudomorphic with Cu, resulting in an even larger strain anisotropy of -31 μeV/atom. It was recognized only later by Gradmann et al. (1984) that this results from a positive interface anisotropy $K_s = +0.22$ mJ/m^2 [$+104$ μeV/(surface atom)] which prevails for the thinnest films (magnetocrystalline anisotropy of the order of 0.1 μeV/atom can be neglected). This complicated interplay of counteracting anisotropy contributions, in combination with some minor interdiffusion, easily explains the unsatisfactory reproducibility of these early results. It may shed some light on contradictory results from different efforts in other epitaxial systems.

5.2.2. Anisotropies in NiFe(111) and γ-Fe(111) on Cu(111)

The problems encountered in Ni(111) on Cu(111) were overcome by Gradmann and Mueller (1968) by changing to alloy films of 48Ni/52Fe(111) on Cu(111). Interdif-

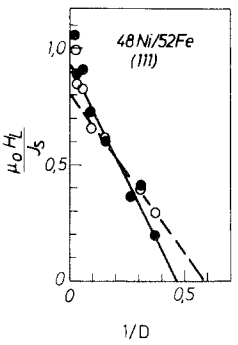

Fig. 12. Total anisotropy field $\mu_0 H_L/J_s$, normalized to the spontaneous magnetization J_s, versus $1/D$ (D: number of atomic layers), for 48Ni/52Fe(111)-films in a Cu(111)-matrix, measured by TOM (○) or FMR (●), respectively (from Gradmann 1977).

fusion is suppressed, the misfit is reduced to -0.8%, magnetostriction becomes positive and is reduced in magnitude. This enabled the separation of volume and surface contributions by a $1/D$ plot according to eq. (5.10) for the first time, cf. fig. 12. The resulting interface-anisotropy,

$$K_s[48\text{Ni}/52\text{Fe}(111)/\text{Cu}(111)] = -0.23\,\text{mJ/m}^2$$

$$(\varepsilon = -100\,\mu\text{eV/atom};\ \mu_0 H_s = -1.7\,\text{T, at } 250\,\text{K}),$$

is in fair agreement with a prediction from Néel's theory ($-0.41\,\text{mJ/m}^2$). The negative sign of K_s, as seen from the negative slope in fig. 12, means that the film normal becomes an easy axis of the surface anisotropy ('*perpendicular surface anisotropy*'). Note that according to fig. 12 H_L becomes negative for $D < 2$; this means perpendicular magnetization in the very thinnest films. This was actually observed for $D < 2$ in that the films, suspended on a thin torsion filament in the TOM, oriented spontaneously with the film plane at right angles to a magnetic field, like indicated for the Ni film by the inset in fig. 11. The temperature dependence of K_s and an equivalent analysis of 60Ni/40Fe(111) has been published by Gradmann (1986a). Perpendicular magnetization for $D < 2$ was observed too in fcc γ-Fe(111) on Cu(111) (Kuemmerle and Gradmann 1977, 1978) and on CuAu(111) (Gradmann and Isbert 1980). Although there is no doubt that this was again caused, in principle, by surface-type anisotropies, a clear separation of the latter from the volume contribution was not possible.

5.2.3. Anisotropies in Ni(111) on Re(0001) and W(110)

An extended study of magnetic anisotropies of Ni(111) films became possible by their preparation on Re(0001) and TOM in situ in UHV (Bergholz and Gradmann 1984, Gradmann et al. 1984). One big advantage of this technique is that the films can, after magnetometry, be flashed off the Re substrate, which therefore can be used for unlimited film series. As shown in fig. 13, the total anisotropy field H_L [cf. eq. (5.10)] depends linearly on $1/D$ to an excellent approximation. For an accurate determination of surface anisotropies, J_s had to be subtracted, which depends linearly on $1/D$, too.

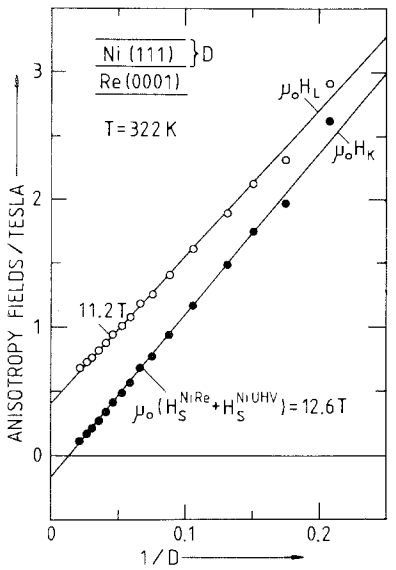

Fig. 13. Total anisotropy field $\mu_0 H_L$, and crystalline contribution $\mu_0 H_K = \mu_0 H_L - J_s$, versus $1/D$, for Ni(111) films on Re(0001) (from Gradmann et al. 1984).

The total surface anisotropy of both interfaces, $\mu_0 H_K = \mu_0 (H_s^{NiRe} + H_s^{NiUHV}) = 12.6$ T, can then be taken from the slope of $(\mu_0 H_L - J_S)$, for the uncoated film of fig. 13. The vertical intercept of $\mu_0 H_K$ represents a crystalline volume anisotropy, corresponding to a tensile strain of 0.7% in the plane. This seems a reasonable order of magnitude for a residual strain considering the misfit $f_{NiRe} = -9.7\%$ (compare table 2a). The surface anisotropy is positive, it supports shape anisotropy and therefore does not show up in unusual magnetization directions, but only in its quantitative determination using TOM. The surface character of the dominating anisotropy shows up very clearly in coating experiments like that shown in figs. 14a and b. Observed by in situ magnetometry during Cu-coating of a Ni(111) film, H_L changes rapidly with the number of Cu layers, D_{Cu}, and saturates for little more than one monolayer again. As expected from our model, the change in H_L varies linearly with $1/D_{Ni}$ (fig. 14b), resulting in a well-defined change of $\mu_0 H_s$ induced by the Cu-coating. By combining the results of similar coating experiments with different metallic coatings, single interface energies could be determined, as collected in table 4. Note the enormous anisotropy field of 9.9 T for the uncoated Ni(111) surface, its temperature dependence being described by Bergholz and Gradmann (1984). Whereas the magnitude of K_s decreases with approaching T_c, it is not clear whether it really disappears there. Ni(111) films on W(110) were analyzed recently by Y. Li et al. using FMR in UHV, see fig. 15. From their results, they concluded that $K_s^{NiW} + K_s^{NiUHV} = +0.46(6)\,\mathrm{mJ/m^2}$, at 300 K. Combining this with the data from Ni on Re, taken with TOM, one results in a surprisingly small value of $K_s^{NiW} = 0.02(2)\,\mathrm{mJ/m^2}$.

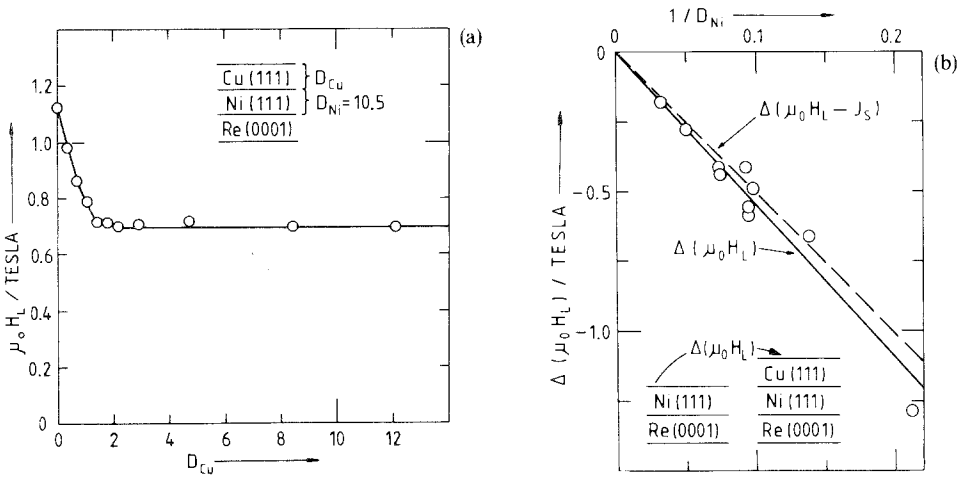

Fig. 14. Changes of anisotropies in Ni(111) films on Re(0001) by Cu coating, as discussed in the main text (from Bergter et al. 1985). (a) Anisotropy field $\mu_0 H_L$ of a 10.5 layer thick Ni film versus D_{Cu}, the number of coating Cu layers. (b) The saturation change of anisotropy field, $\Delta(\mu_0 H_L)$, caused by a thick Cu film on a Ni film of D_{Ni} atomic layers, versus $1/D_{Ni}$. The change of surface anisotropy can be concluded from the slope of the linear dependence (from Bergter et al. 1985).

TABLE 4
Interface anisotropies of Ni(111)-based interfaces, at 300 K, from data measured by TOM on Ni(111) on Re(0001) (Gradmann 1986a) and (*) by FMR on Ni(111) on W(110) (Y. Li et al. 1991).

Interface	K_s (mJ/m^2)	$\mu_0 H_s$ (T)
Ni(111)/UHV	0.48	9.9
Ni(111)/Cu	0.22	4.6
Ni(111)/Pd	0.22	4.6
Ni(111)/Re(0001)	0.19	4.0
Ni(111)/W(110)*	−0.02	−0.5

Néel's phenomenological model, which does not distinguish between the different coatings, results in $K_s = -0.19\,\mathrm{mJ/m^2}$, showing the right order of magnitude, but the wrong sign. First-principles calculations are missing for Ni(111).

5.2.4. Anisotropies in bcc Fe(100) on Ag(100)

The most extended work on perpendicular surface anisotropy and perpendicular magnetization in ultrathin single films has been done for bcc Fe(100) films on Ag(100). After pioneering work on the epitaxial growth of Ag on Fe(100) by Smith et al. (1982), who interpreted their LEED–AES-data as evidence for initial growth of a strained

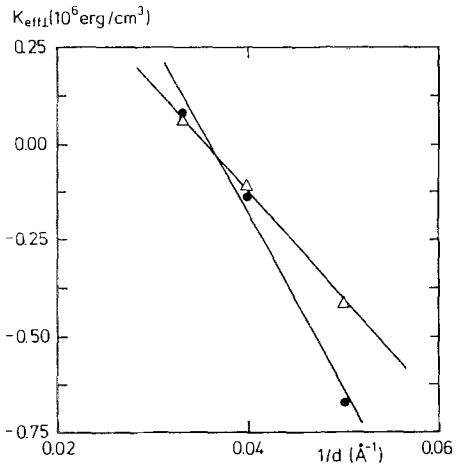

Fig. 15. Total crystalline anisotropy, $K_{eff} = -(L - J_s^2/2\mu_0)$, versus $1/d$ for Ni(111)-films on W(110), measured by FMR between 300 and 320 K (●) and 445 to 475 K, (Δ), respectively (from Y. Li et al. 1991).

fcc γ-Fe film, it was Jonker and Prinz (1986) who showed that it grows rather as a bcc α-Fe film, rotated by 45° with respect to the Ag substrate, resulting in a misfit of only 0.8% between the contacting square nets. It should be emphasized, however, that what is growing is certainly a centered tetragonal structure, with c/a near the fcc value of $\sqrt{2}$ instead of the bcc value of 1. The first experimental indication for perpendicular magnetization was published by Jonker et al. (1986), who observed by spin-polarized photoemission that up to a critical number of $D_c = 2.5$ monolayers no in-plane magnetization could be detected. They suggested perpendicular magnetization below D_c. This was in accordance with spin-dependent band-calculations of Gay and Richter (1986), who obtained, for one monolayer of Fe on Ag(100), an energetic preference of 0.4 meV/atom for a perpendicular magnetization against an in-plane magnetization. Note that the total surface anisotropy can be estimated using eq. (5.8) from $d_c = D_c\delta$. Assuming $K_V = 0$ one finds with $D_c = 2.5$ that $(K_s^{(1)} + K_s^{(2)}) = -0.65\,mJ/m^2$, corresponding to $-170\,\mu eV/atom$, in accordance with the calculations of Gay and Richter. A perpendicular magnetization below three layers could be confirmed by Koon et al. (1987) using Mössbauer spectroscopy. Further evidence came from Stampanoni et al. (1987), who observed magnetic order in those films using spin-polarized photoelectron emission, in a geometry where only perpendicular magnetization could be detected, in a perpendicular magnetic field. As shown in fig. 16, they observed, at low temperatures of 30 K, easy-axis loops indicating perpendicular magnetization for $D = 3.5$ and $D = 5$ atomic layers. The deviating behaviour for 1.5 and 0.8 ML must not be taken as an indication of a reversal of the anisotropies, but rather of superparamagnetism, indicating a non-ideal, island-like structure of the films, as expected from the surface energies in this nonwetting epitaxial system. Apparently, a closed film forms only at about 3 ML, in agreement with the RHEED-oscillations in fig. 7 and with the Mössbauer work of Koon et al. (1987), who obtained,

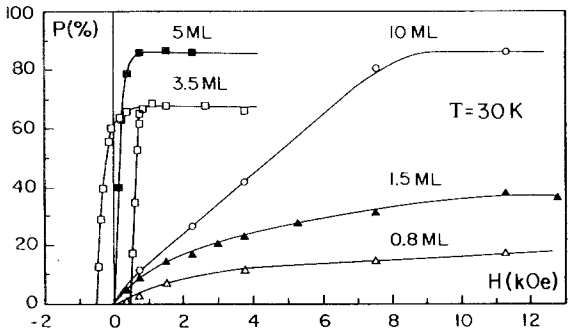

Fig. 16. Spin polarization, P (in %), of photoelectrons from Fe(100) films on Ag(100), versus magnetic field along the surface normal (from Stampanoni et al. 1987).

for a film of 2.5 layers, broadened spectral structures only, even at low temperatures, as shown in fig. 17 (monolayer spectra were never published; note for comparison the sharp Mössbauer spectra of really layer-grown Fe(110) on W(110) in fig. 9, and the sharp spectra obtained even in the true monolayer and at temperatures between 100 and 200 K, as shown in fig. 43, to be discussed below.

Direct measurement of the anisotropies in Fe(100) films with different coverages was performed in a careful study using RHEED, FMR and BLS by Heinrich et al. (1988a), and discussed later on in several review articles (Heinrich et al. 1989a,b). As usual for these techniques, the primary experimental information is given by the total

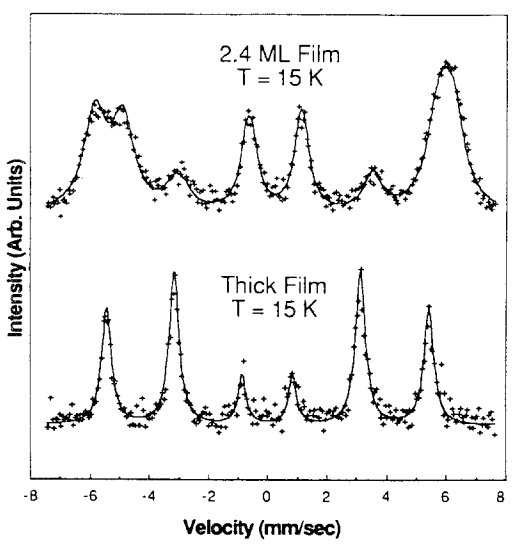

Fig. 17. Mössbauer spectrum of Fe(100)/Ag(100) multilayers, containing 2.4 ML Fe components, measured at 15 K; spectrum of a thick film for comparison (from Koon et al. 1987).

anisotropy with respect to the surface normal, L, or the equivalent anisotropy field $\mu_0 H_L$ (called $4\pi M^2_{s,eff}$ by Heinrich et al.), compare eqs. (5.8) and (5.10).

Unconventionally, Heinrich et al. discussed their results, by using the assumption of $K_V = 0$, in terms of surface anisotropies of single layers, see table 1 in the paper of Heinrich et al. (1989b). We have shown above in section 5.2.1 that severe misinterpretations can result from the neglect of K_V, which in particular includes all ill-defined but often strong strain anisotropies. We therefore prefer to analyze the experimental data of Heinrich et al., for the case of Au-coated films, in the usual plot of $\mu_0 H_L$ ($= 4\pi M_{s,eff}$) versus $1/D$, as shown in fig. 18. The excellent linearity shows the excellent quality of the experiment and enables the determination of $(K_s^{FeAg} + K_s^{FeAu}) = -0.84\,mJ/m^2$, as a common property of the whole series [the film for $1/D = 0.36$, prepared as the other films of the series on epitaxial Ag films, apparently suffered from island-structure; we use instead one special film at $1/D = 0.335$ ($D = 3$), which was prepared on a Fe whisker surface and apparently consisted of three completed layers]. Using one special film of $D = 7.6$ with free surface, Ag-coating and Au-coating, respectively, Heinrich et al. (1988a) determined further $K_s^{FeAu} - K_s^{FeAg} = 0.26\,mJ/m^2$ and $K_s^{FeUHV} - K_s^{FeAg} = -0.34\,mJ/m^2$. This enables finally the determination of single-interface energies given by

$$K_s^{FeAg} = -0.55\,mJ/m^2,$$

$$K_s^{FeAu} = -0.29\,mJ/m^2,$$

$$K_s^{FeUHV} = -0.89\,mJ/m^2,$$

as a result of this thin film analysis. The values differ slightly from that given by Heinrich et al. As for Ni(111), the magnitude of K_s is maximal for the free surface. Note in fig. 18 that the critical number of layers for magnetization switching, $D_c = 3$ at $\mu_0 H_L = 0$, is in rough agreement with the experiments of Jonker et al. (1986). For the uncoated films, an increased total surface anisotropy of $-1.44\,mJ/m^2$ is expected. Assuming an unchanged K_V, this results in the broken line in fig. 18 and a critical thickness of 5 ML, in agreement with the experiments of Stampanoni et al., cf. fig. 16 (some increase of D_c with lowered temperatures is reasonable). Surface anisotropies were determined for metal-coated surfaces of bulk Fe(100) crystals too, using FMR-line-shape analysis (Heinrich et al. 1988) and BLS-line shifts (Dutcher et al. 1988), resulting in:

$$K_s^{FeAg} = [-0.7] \text{ or } [-0.79(5)]\,mJ/m^2$$

and

$$K_s^{FeAu} = [-0.45] \text{ or } [-0.54(5)]\,mJ/m^2,$$

from FMR and BLS, respectively. These values are in fair agreement with the values obtained from films. This makes surface anisotropies in these interfaces exceptionally well defined quantities. Note that they include a magnetostatic contribution, which is high for these open bcc (100) surfaces, cf. table 3 and amounts to $-0.19\,mJ/m^2$.

The total surface anisotropy of the uncoated films of $-144\,mJ/m^2$ corresponds to $\varepsilon^{(1)} + \varepsilon^{(2)} = -0.38\,meV/atom$. The agreement of this number with the anisotropy in a

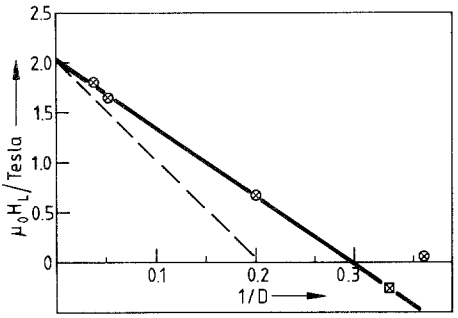

Fig. 18. Total anisotropy field $\mu_0 H_L$ versus $1/D$ for Au-coated Fe(100) films consisting of D atomic layers, prepared on Ag(100)-films (⊗) or a Fe(100) whisker surface (⊠), respectively. Broken line calculated for an uncoated film (experimental data from Heinrich et al. 1988a, modified evaluation).

monolayer of Fe on Ag(100) as calculated by Gay and Richter (1986), −0.40 meV/atom, seems accidental. This was first indicated by alternative calculations of Karas et al. (1989) on the free-standing Fe(100) monolayer, who showed that only small changes in the parameters of calculation could change the sign of ε in comparison with the results of Gay and Richter (1986). A more extended calculation of C. Li and Freeman (1991) results in $\varepsilon = +0.04$, −0.57 and −0.06 meV/atom for the freestanding monolayer, the monolayer on Au and the monolayer on Ag, respectively, with a simulation of the substrate by one monolayer only. Whereas the sign is in agreement with the experiment for the monolayer on Ag, the magnitude is obviously not large enough to overcome the magnetostatic energy of roughly +0.12 meV/atom. The perpendicular magnetization, which is observed up to $D = 5$, is not even reproduced for $D = 1$. C. Li and Freeman (1991) conclude that "the comparison of our calculated values with experiments is not significant at this time".

5.2.5. Anisotropies in Fe(110) on W(110) and on Au(111)

Because of the reduced (two-fold) in-plane local symmetry, Fe(110) films provide an example where in-plane surface anisotropies occur in addition to the usual out-of-plane anisotropies. They first became evident in experiments of Prinz et al. (1982), who found in Fe(110) films on GaAs(110) strong in-plane anisotropies, which turned the magnetization at right angles from the easy bulk direction [001] into [110], for films thinner than 5 nm. Because of their strong dependence on film thickness, these anisotropies were interpreted by Rado (1982) in terms of in-plane surface anisotropies. The same magnetization switching from [001] to [110] was observed by Gradmann et al. (1986) in Fe(110) films on W(110), for film thicknesses near 50 nm, and used for an estimate of the in-plane anisotropy constants. Gradmann et al. assumed in this estimate a balance between the in-plane surface anisotropy and the in-plane component of standard fourth-order crystalline anisotropy. It has been shown later in independent work on these films by Elmers and Gradmann (1990) using TOM and Baumgart et al. (1991) using BLS that considerable strain anisotropies have to be included in the analysis in order to avoid severe errors which were contained in the

early determination of the in-plane surface anisotropy from the switching thickness only. We show this as follows: Because the crystalline volume anisotropy contains fourth-order in-plane terms, we use for the in-plane anisotropy the ansatz

$$F/V = [K_{v,p} - (1/d)K_{s,p}] \sin^2 \varphi + [K_{v,pp} - (1/d)K_{s,pp}] \sin^4 \varphi. \tag{5.11}$$

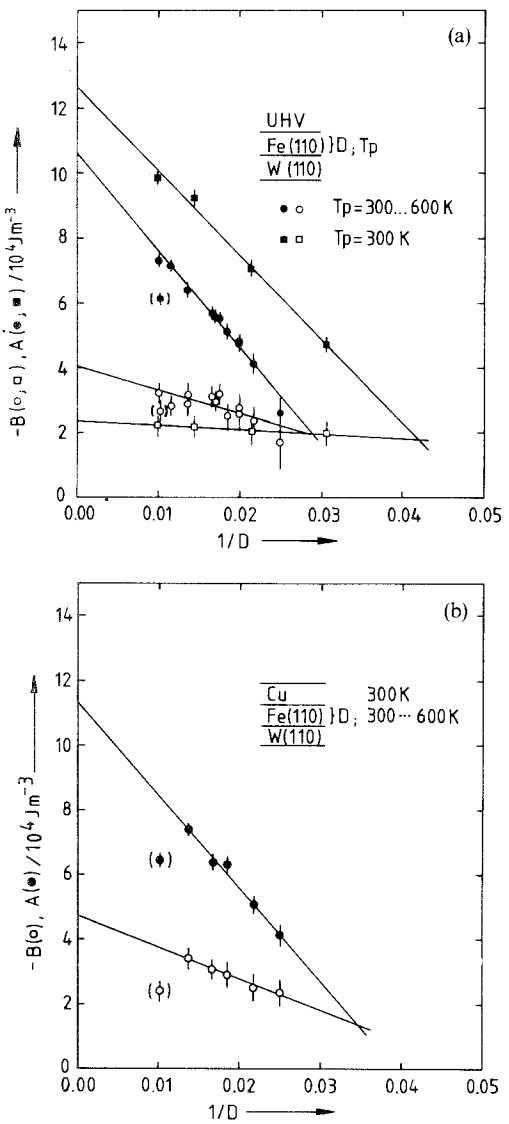

Fig. 19. Separation of volume and surface contributions of in-plane anisotropies in Fe(110) films on W(110), by TOM, prepared at temperature T_p. Total anisotropy constants $A = K_{v,p} - (1/d)K_{s,p}$ and $B = K_{v,pp} - (1/d)K_{s,pp}$ are plotted versus $1/D$. (a) Uncoated films, with different preparation conditions, as explained in the text; (b) Cu-coated films (from Elmers and Gradmann 1990).

Here we use a notation where $K_{s,p} = K_{s,p}^{(1)} + K_{s,p}^{(2)}$ represents the total film surface anisotropy from both interfaces, and a corresponding definition for $K_{s,pp}$. Standard volume anisotropy gives $K_{v,pp} = -\frac{3}{4}K_1$ and $K_{v,p} = K_1 + K_u$, where an additional uniaxial anisotropy K_u is introduced, caused by epitaxial strain in the film. As shown in fig. 19a and b, the data can be well explained with a constant value of K_u. Elmers and Gradmann (1990) suggested that the main contribution to K_u results from a residual in-plane strain of 0.39%, given by a coincidence structure of Fe on W, where 11 Fe atoms met 10 W atoms, resulting in a contribution of 3.7×10^4 J/m^3. With $K_1 = 4.8 \times 10^4$ J/m^3, this results in a common contribution to $K_{v,p}$ of 8.5×10^4 J/m^3, which is near the experimental value. Both in-plane anisotropy constants were determined for single films from hard-axis loops with the field along [110], for films above the switching thickness, as shown in fig. 20. The strictly linear dependence in fig. 19 allows a clear separation of volume and surface contributions in the sense of eq. (5.11). Results from both TOM and BLS experiments are collected in table 5. This table and fig. 19a show first of all a sensitive dependence on the preparation conditions. Elmers and Gradmann used, as a rule, an optimized growth mode (a) starting at 300 K in order to avoid island formation on top of the first, stable monolayer, with successive raising temperatures up to 600 K with increasing film thickness, to get a smooth surface. If preparation started (b) immediately with 600 K, a clear enhancement of $K_{v,p}$ resulted, apparently as a result of an enhanced density of volume defects, with a minor change only in $K_{s,p}$. Baumgart et al. started their preparation (c) at 500 K. The difference between the volume constants of the uncoated films grown by the two methods can be explained from these minor differences in preparation conditions. The minor differences in the in-plane surface constants are only slightly out of the error limits. This can be taken as a good confirmation of the concept of an in-plane surface anisotropy. The difference in the out-of-plane constant K_s is surprising. Some support for the K_s values measured by TOM comes from a comparison with predictions from Néel's model, which gives $K_s = -(4\sqrt{2}/3a^2)l$ and $K_{s,p} = -(2\sqrt{2}/3a^2)l$ [Néel's pair-bonding parameter l; data from eq. (40) in Elmers and Gradmann (1990) are corrected by a factor $\frac{1}{2}$]. The numerical data, which come from a comparison

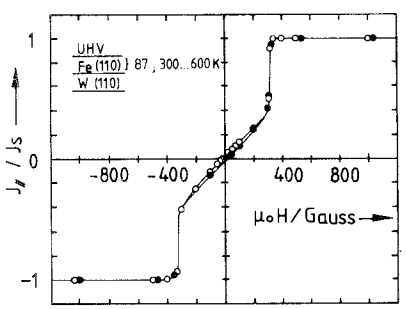

Fig. 20. Hard-axis loop with field along [110], for an uncoated Fe(110), film on W(110), consisting of $D = 87$ layers. The anisotropy constant A is determined from the initial slope, constant B from the jumping field (from Elmers and Gradmann 1990).

TABLE 5

Anisotropy constants in Fe(110) films on W(110). Experimental values from TOM (Elmers and Gradmann 1990) and BLS (Baumgart et al. 1991). The preparation conditions are described in the main text. The strain used for the theoretical values of the volume constants results from the assumption of a 10/11 coincidence lattice, compare the main text.

Coating	Preparation	Magnetic method	Volume constants ($\times 10^4$ J m^{-3})		Surface constants ($\times 10^{-3}$ J m^{-2})		
			$K_{v,p}$	$K_{v,pp}$	$K_{s,p}^{(1)}+K_{s,p}^{(2)}$	$K_{s,pp}^{(1)}+K_{s,pp}^{(2)}$	$K_s^{(1)}+K_s^{(2)}$
UHV	(a)	TOM	10.6(2)	−4.1(3)	0.61(3)	−0.16(4)	1.0(2)
	(b)	TOM	12.6(3)	−2.4(3)	0.52(5)	−0.03(5)	–
	(c)	BLS	12.1(8)	−3.1(3)	0.76(8)	−0.08(2)	0.0(3)
Cu	(a)	TOM	11.3(5)	−4.7(2)	0.58(5)	−0.20(2)	1.4(2)
Ag	(a)	TOM	10.8(2)	−3.5(2)	0.46(2)	−0.12(2)	1.1(2)
Pd	(c)	BLS	–	–	0.58(7)	−0.06(2)	–
Au	(a)	TOM	9.6(5)		−0.09(2)		1.2(2)
Theory with strain			8.5	−3.6			
without strain			4.8	−3.6			
Néel model					0.18		0.36

with strain anisotropy, are too low by a factor of three. However, the factor of two between $K_{s,p}$ and K_s agrees nicely with the data from TOM. Note a clear dependence of surface anisotropies on coatings. Note further that the neglect of strain anisotropies, which was used in the preliminary analysis of Gradmann et al. (1986), and in the analogous analysis of Fe(100) on Ag(100) by Heinrich et al. (1988a), results in qualitatively wrong and thickness-dependent numbers for the surface anisotropies (see also the last section). Use of a film series and use of an $1/d$ plot is undispensable.

In order to compare surface with volume anisotropies, we express both by energy per atom. Surface anisotropies are of the order of 10^{-3} mJ/m^2 = 257 μeV/atom. They are by nearly two orders of magnitude larger than bulk anisotropies which are of the order of 10^5 J/m^3 = 7.4 μeV/atom. This reflects the strong symmetry-breaking properties of the surface.

Magnetic anisotropies of ultrathin Fe(110) films in Au(111)/Fe(110)/Au(111) sandwiches were analyzed by Lugert and Bayreuther (1989) by taking magnetization loops both in-plane and out-of-plane at 10 K in a SQUID magnetometer. The films were ferromagnetic down to the monolayer, indicating a good approximation to layer growth. Because of the six-fold symmetry of the substrate, in-plane anisotropies could not be determined. However, the symmetric structure of the sandwich enabled the determination of the single interface anisotropy $K_s^{FeAu} = -0.7(1)$ mJ/m^2, resulting from a very clear linear dependence of the total anisotropy on $1/d$. Accordingly, perpendicular magnetization was observed below three layers. The same authors found, using Ag(111)/Fe(110)/Ag(111) sandwiches, that $K_s^{FeAg} \ll 0.1$ mJ/m^2, again at 10 K (Lugert and Bayreuther 1988). This strong difference of out-of-plane anisotropies

for Au- and Ag-covered Fe(110) interfaces at low temperatures is only in apparent contradiction to their small difference at 300 K, as shown in table 5. The difference rather indicates a different temperature dependence of both interface anisotropies. Accordingly, Lugerts single-interface anisotropies do not enable a determination of single interface anisotropies from the data of table 5.

5.2.6. Anisotropies in hcp Co(0001) on Au(111) and Pd(111)

The anisotropies in hcp Co(0001) on Au(111) and Pd(111) are characterized by the assistance of perpendicular surface anisotropies of -0.5 and $-0.25\,\mathrm{mJ/m^2}$, respectively, by the perpendicular volume anisotropy [$K_V = -5 \times 10^5\,\mathrm{J/m^3}$ in our notation, cf. eqs. (5.7) and (5.8)] both counteracting the shape anisotropy of $+12 \times 10^5\,\mathrm{J/m^3}$. Perpendicular magnetization results up to critical numbers of six and four monolayers, respectively, and make multilayers based on these combinations attractive candidates for perpendicular magnetic recording devices. Perpendicular magnetization in Pt/Co multilayers, which apparently are the most attractive candidates for perpendicular magneto-optic recording (Carcia et al. 1989), is out of the scope of this review.

(a) *Co(0001) on Pd(111).* The unique combination of crystalline and surface anisotropies in Co(0001) was first realized by Carcia et al. (1985) in texturized Pd/Co multilayers prepared by sputtering techniques. For an extended discussion including a comparison with Co/Pt multilayers we refer to the paper of Carcia (1988). As shown in fig. 21, the hard axis, as characterized by hard-axis loops, is along the surface normal for Co-thicknesses $T = 0.49$ and 0.72 nm and switches into the plane near 0.5 nm. A

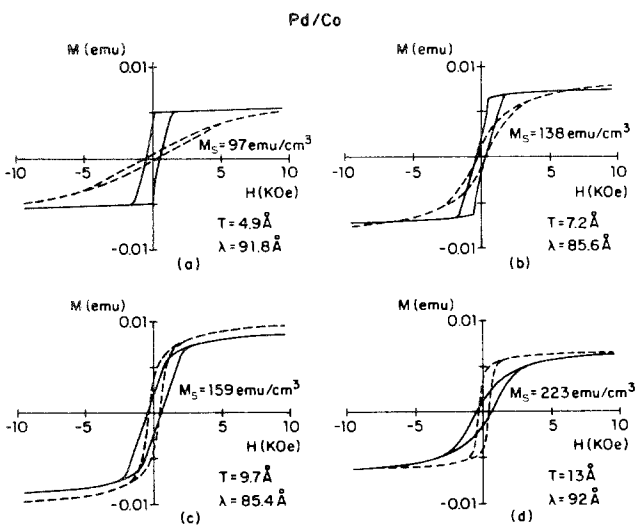

Fig. 21. Magnetization loops of Pd/Co multilayers, taken at 300 K, with the field in the film plane (dashed curves) or along the surface normal (full lines). Film periodicity λ, Co thickness T and saturation magnetization M_s are indicated (from Carcia 1988).

discussion of deviations from the ideal square loop as a result of magnetostatic couplings in these multilayers has been given by Draaisma and de Jonge (1987). As shown in fig. 22, the crystalline anisotropies from multilayers, determined from the magnetization work of the magnetization curves, for different thicknesses of the Pd-interlayer, follow a common linear dependence. The surface anisotropy constant was determined to be $K_s^{CoPd} = -0.16\,mJ/m^2$, from sputtered multilayers.

Multilayers of the same type were prepared later by Draaisma and de Jonge (1984) and den Broeder et al. (1989) by vapor deposition in UHV and analyzed by magnetometry and FMR. Their evaluation is shown in fig. 23, in comparison with corresponding first-principles calculations of Daalderop et al. (1990). The figure shows the anisotropy constant per film area, Kt, versus the thickness of the Co layer denoted by t. For films prepared at 50°C, a linear dependence is observed as expected from our anisotropy model, eq. (5.8), and the vertical intercept is twice the surface anisotropy $K_s^{CoPd} = -0.26\,mJ/m^2$, from evaporated multilayers, prepared at 50°C.

Surprisingly, the anisotropies could be enhanced considerably by preparation at an elevated temperature of 200°C. It has been suggested that this might be the result of some interface smoothing. However, the deviation from linearity for the films prepared at 200°C indicates structural complications which remain to be clarified. There is considerable correlation with the calculated anisotropies. It has been discussed by Draaisma et al. (1988) that atomic roughening reduces the magnitude of K_s. The differences from the sputtered films might therefore be explained by a compara-

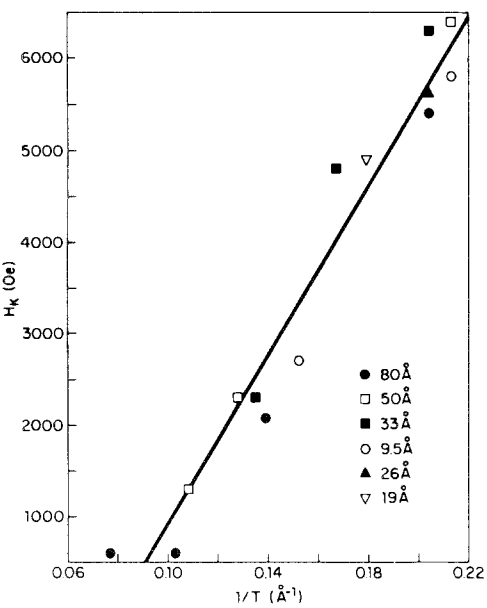

Fig. 22. Crystalline anisotropy field H_K ($= \mu_0 H_L - J_s$ in our notation, cf. eq. (5.10)), in Pd/Co multilayers, versus the reciprocal of the Co layer thickness T. Symbols denote the different the Pd thicknesses (from Carcia 1988).

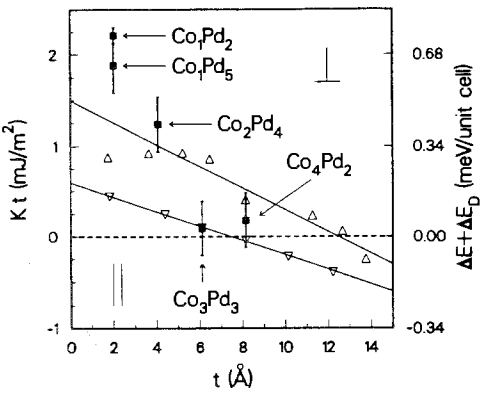

Fig. 23. Total anisotropy per period and film area, Kt, for evaporated, (111)-texturized, polycrystalline Co/Pd multilayers, versus thickness t of Co films in them. Data for samples prepared at 50°C (V) and 200°C (Δ) in comparision with first-principles calculations for CoPd multilayers (■) (from Daalderop et al. 1990).

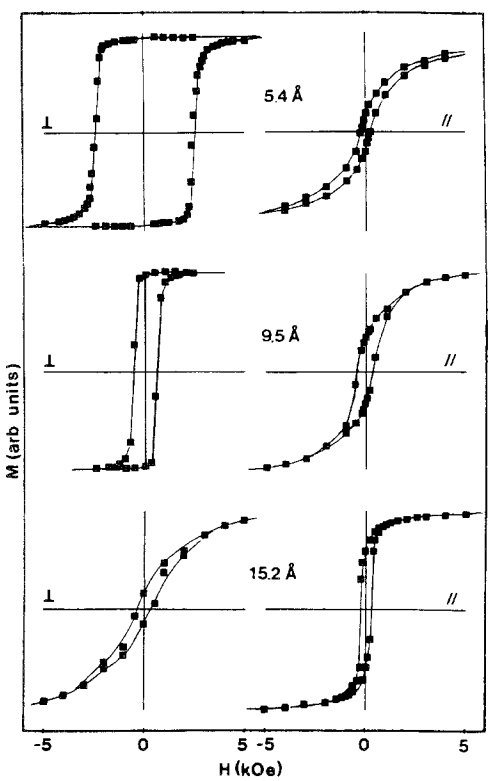

Fig. 24. Magnetization loops of Au(111)/Co/Au sandwiches with various thicknesses of Co, as indicated, taken with the field perpendicular or parallel to the film plane, at $T = 10$ K (from Bruno and Renard 1989).

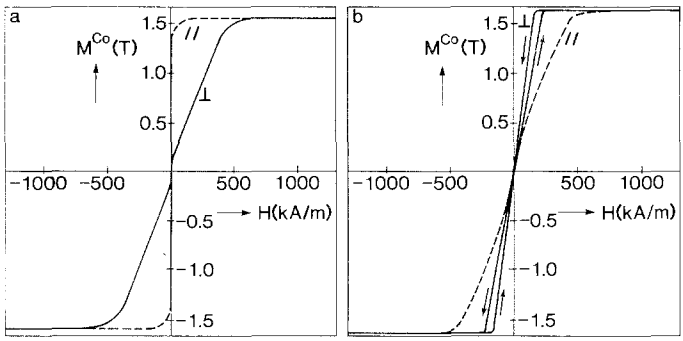

Fig. 25. Magnetization loops for sputtered Au/Co multilayers, with $d_{Co} = 1.1$ nm, $d_{Au} = 2.8$ nm, measured in fields parallel and perpendicular to the film plane, (a) before and (b) after annealing for 30 min at 250°C. Note the change of the hard-axis loop from the parallel to the perpendicular case (from den Broeder et al. 1988).

tively rougher interface for the latter. The slope in fig. 23 is 7×10^5 J/m^3, for the films prepared at 50°C. After subtraction of the shape anisotropy $J_s^2/2\mu_0 = 12 \times 10^5$ J/m^3, this results in $K_V = -5 \times 10^5$ J/m^3, which agrees surprisingly well with the volume anisotropy. Apparently, strain contributions play only a minor role in these multilayers.

(b) *Co(0001) on Au(111).* Co(0001) films, prepared on highly (111)-texturized Au films on glass and coated by Au, have been analyzed by Chappert et al. (1986) using FMR and Chappert and Bruno (1988) using SQUID magnetometry; their results have been reviewed by Bruno and Renard (1989). The transition to perpendicular magnetization below 1.0 nm is documented by the magnetization loops shown in fig. 24, taken at 10 K. Surface anisotropies resulted as $K_s^{CoAu} = -0.5$ or -0.7 mJ/m^2, at 300 or 10 K, respectively, from evaporated Au(111)/Co/Au sandwiches.

Den Broeder et al. (1988) analyzed corresponding Co/Au multilayers, prepared by sputtering, resulting in $K_s^{CoAu} = -0.1$ mJ/m^2 for the as-prepared multilayers, at 300 K. The difference between these values and that from evaporated film sandwiches disappeared after annealing the sputtered films, which resulted in an increase of K_s^{CoAu} to roughly -0.5 mJ/m^2. The result of the annealing process is shown by the magnetization loops in fig. 25. Apparently, the as-sputtered multilayers showed some interface roughness, and the interfaces sharpened by annealing, driven by the complete immiscibility of Co and Au. Again, the volume anisotropies could be explained completely from shape and standard magnetocrystalline contributions. It should be noted however that C. H. Lee et al. (1990), in an experimental analysis of evaporated Co(0001)/Au(111) superlattices, which included strain analysis using X-ray diffraction, could explain the measured magnetic anisotropies from thickness-dependent strain only, without any Néel-type magnetic surface anisotropy.

5.2.7. *Perpendicular magnetization in Co on Cu(111) and in Fe on Cu(111), CuAu(111), Cu(100), Au(100), Pd(100) and Ru(0001)*

In addition to the film systems of the preceding sections, where film anisotropies were measured using FMR, by TOM or by evaluating hard-axis loops, and surface

anisotropies could be determined in most cases as important contributions, there are a couple of cases where perpendicular magnetization was observed in ultrathin films without measuring the anisotropy. It should be clear from the discussion of the preceding sections that this perpendicular magnetization is a strong indication but not a proof of perpendicular surface anisotropy. We report in the following on these examples, which are of timely interest because of the potential application of perpendicular magnetization for magnetic recording.

(a) *Co on Cu(111).* Perpendicular magnetization was observed by Gradmann and Mueller (1970, 1971) in Co films in Cu(111), in the monolayer regime. Although the measurements were performed by TOM, an analysis in terms of surface anisotropies was not possible, probably because of badly controlled stacking faults in the (hcp or fcc?) films. Perpendicular magnetization of this monolayer is in agreement with calculations of Daalderop et al. (1990), who obtained for a Co monolayer between Cu an anisotropy energy per atom of $\varepsilon = -0.2$ meV/atom, which overrides the magnetostatic energy of $+0.09$ meV/atom and thus results in perpendicular magnetization.

(b) *fcc γ-Fe on Cu(111), CuAu(111) and Cu(100).* A general discussion of ferromagnetic order in fcc γ-Fe films on Cu is given below in section 8.1. Perpendicular magnetization was observed first for the case of γ-Fe(111) films on Cu(111) by Kuemmerle and Gradmann (1977, 1978) and on CuAu(111) by Gradmann and Isbert (1980) in monolayers and double layers, without measurement of anisotropies. For the case of Fe on Cu(100), a perpendicular remanent magnetization was first observed by Pescia et al. (1987a), using spin-polarized photoemission, for a film of five monolayers, observed at $T = 30$ K. Liu et al. (1988), using MOKE, then showed that the magnetization direction depends on the preparation conditions, and square loops with the field along the film normal could be observed only if the films are prepared below 320 K.

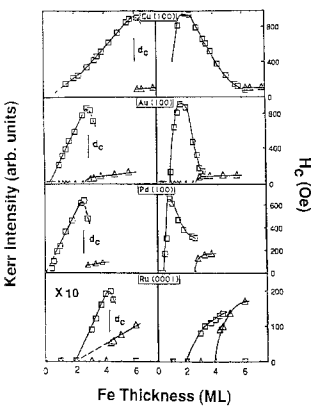

Fig. 26. Perpendicular magnetization in Fe films, prepared at 100 K on various substrates, as indicated. Characteristic data of magnetization loops, measured by MOKE. Loops are characterized by their saturation value (Kerr intensity, left) and their coercive fields (right). Squares (triangles) represent measurements by the polar (longitudinal) effect, which means perpendicular (in-plane) magnetization (from Liu and Bader 1991).

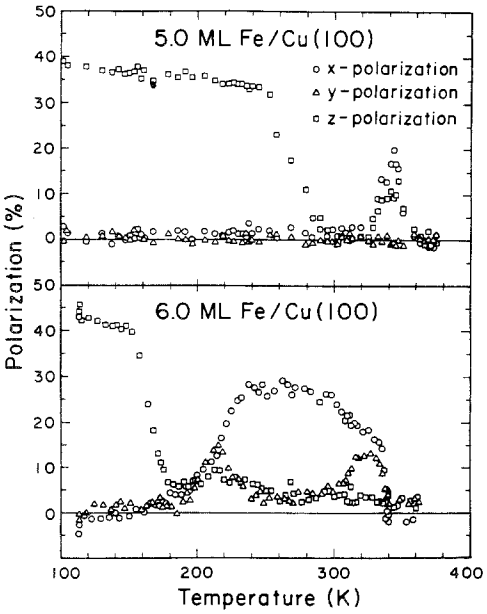

Fig. 27. In-plane (x,y) and out-of-plane (z) components of the photo-electron spin polarization from Fe films on Cu(100), versus temperature of measurement (from Pappas et al. 1991).

For preparation at 100 K, perpendicular magnetization was observed up to a critical number of six monolayers; this is shown in fig. 26, in combination with data from other systems. The transition between perpendicular and parallel magnetization has been observed recently by Pappas et al. (1990, 1991), using spin-polarized photo-electron emission, as a function of temperature, for films consisting of five and six monolayers (the thickness calibration from 1990 was corrected in 1991), prepared at 100 K. Using three independent spin-detectors, they could follow all three components of the magnetic moment of the films in the remanent state. As shown in fig. 27, the magnetization switched from the film normal to the film plane near 300 and 200 K, respectively. The interesting point is that remanent magnetization disappears for all components in some temperature window (290 to 320 K for the five-monolayer film). We discuss this phenomenon below.

(c) *bcc α-Fe(100) on Au(100) and Pd(100).* For bcc α-Fe(100) films on Au(100), prepared at room temperature, Duerr et al. (1989) observed in-plane magnetization, whereas Liu and Bader (1991) reported perpendicular magnetization up to two layers if the films were prepared at 100 K. Similarly, Liu and Bader (1991) showed that Fe(100) films on Pd(100) show perpendicular magnetization up to two layers when prepared at 100 K whereas they are magnetized in the plane when prepared at 300 K. The structural basis for these changes remains to be explained.

Perpendicular magnetization was observed in Fe films on Ru(0001) (Liu and Bader 1990b), also, cf. fig. 26.

6. Temperature dependence of magnetic order

In ultrathin films, both the ground-state magnetic moment including its spatial variation and the temperature dependence of magnetic order become different from what is known from bulk materials. We start our presentation of magnetic order with its temperature dependence, firstly because ground-state properties always have to be determined by extrapolation from experiments at finite temperatures, and secondly because the temperature dependence can be followed by many magnetic probes which are unable to measure the absolute magnitude of the magnetization.

6.1. Theoretical models for the temperature dependence of magnetic order

Despite their limited applicability to real films, theoretical models stimulated the field very much. A review of them is not the aim of the present paper. We will refer to related theories in the discussion of experiments and confine ourselves for the present to recalling some basic aspects. The problem of magnetic order in ultrathin films was raised by Bloch (1930) in his pioneering work on spin-waves. He noted for the two-dimensional *isotropic* Heisenberg model a divergence in spin-wave density which he interpreted as an indication for absence of magnetic order. A spin-wave theory of simple cubic films in a finite field was given first by Klein and Smith (1951) and improved by Doering (1961), who introduced correct boundary conditions, and Jelitto (1964), who extended it to general cubic lattices. A linear dependence of the magnetization on temperature in a considerable low temperature range was predicted by all these theories of the *isotropic* Heisenberg model. Davis (1965), however, showed that anisotropies may remove this linearity. The spin-wave approach, which is applicable to low temperatures only, was complemented by the molecular field model of Valenta (1962), which deviates from reality by neglecting any fluctuations but gives a rough idea of the influence of reduced magnetic coordination in films on the temperature dependence of magnetic order in them. The spatial structure of magnetization could first be addressed in this model. A straightforward treatment of this interesting aspect was given in a Green's-functions theory by Haubenreisser et al. (1969), which includes shape and crystalline anisotropies and applies up to T_c. As shown in fig. 28a and b, the overall thermal decrease of the magnetization is connected with the considerable inhomogeneity of it. The linear thermal decrease of the mean magnetization is lost, as shown in fig. 28c. More recently, Hasegawa (1987) proposed an itinerant approach to thin-film magnetism; unfortunately, however, he neglected spin-waves.

Theories of magnetism in thin films are complemented by theories of the ferromagnetic monolayer, starting with the famous exact solution of the two-dimensional Ising model, given without proof by Onsager (1944). A proof has been given later by Yang (1952). The central role of this model, which represents a uniaxial monolayer with infinite anisotropy, stems from the observation, derived from Monte Carlo simulations by Binder and Hohenberg (1976), that a 2D Heisenberg system with anisotropy becomes Ising-like, near T_c. Considering the strong anisotropies in films, which we discussed in the last chapter, the critical magnetization exponent $\beta = \frac{1}{8}$ of this model might therefore have a universal applicability in monolayers and ultrathin

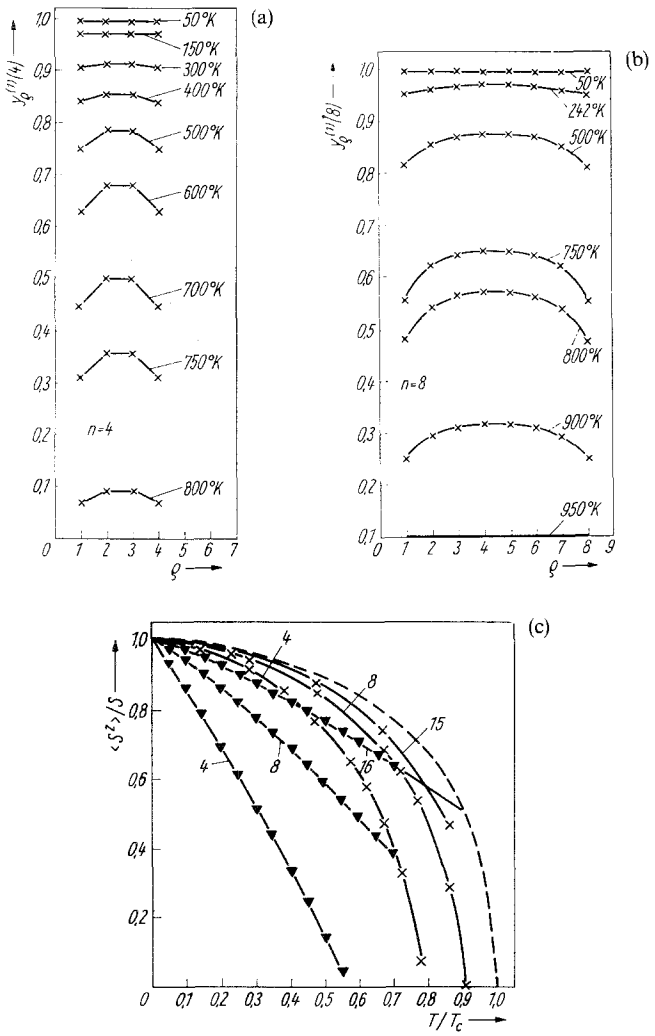

Fig. 28. Green's-function theory of magnetic order in Fe(100). Spatial dependence of the relative magnetization $Y_{\rho}^{(1)(n)}$ in layer ρ of a film consisting of n layers of local spins $S = 1$, (a) for $n = 4$, (b) for $n = 8$ layers. (c) Relative magnetization versus relative temperature, for numbers of atomic layers as indicated. Results from Green's function theory, $S = 1$, anisotropy field 100 Oe (×), in comparison with spin-wave theory (Jelitto 1964) for $S = \frac{1}{2}$, anisotropy field 20 Oe (▼). Broken line gives Green's-function theory for bulk Fe (from Haubenreisser et al. 1969).

films. The problem is the extension of the critical regime. Onsager's exact solution gives an interesting insight, as can be seen from a numerical comparison with the asymptotic power law, as given in fig. 29. Both agree only in a critical range of a few percent below T_c. Any interpretation of film experiments beyond this narrow critical range are at least problematic (Kohlhepp et al. 1992). Perhaps the most cited paper

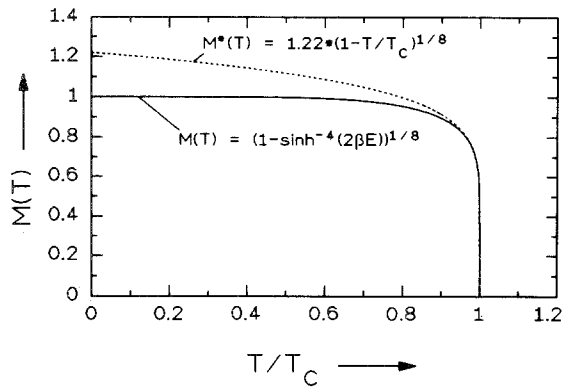

Fig. 29. Spontaneous magnetization in the two-dimensional Ising model. Exact solution $M(T)$ in comparison with the asymptotic power law $M^*(T)$.

in the monolayer literature is a letter of Mermin and Wagner (1966), who gave the supposition of Bloch (1930) of absence of long-range order in an *isotropic* Heisenberg system a rigorous proof. The proof applies to any film of finite thickness, with infinite extension in the plane; it does not exclude divergent susceptibilities and high sensitivities to anisotropies, which might trigger long-range order, at finite temperatures. The paper is therefore of restricted applicability for the reality of mostly anisotropic films. A transition to divergent susceptibility, which might correlate to the onset of ferromagnetism in real monolayers, has been discussed by Stanley and Kaplan (1966). Bander and Mills (1988) showed that even bare shape anisotropy, which is neglected in many theories, can trigger long-range magnetic order.

Summarizing, it turns out that the existence of long-range magnetic order in ultrathin films and its temperature dependence is tightly connected with magnetic film anisotropies. A general theory of temperature-dependent magnetization in models with realistic anisotropies remains to be given.

6.2. Temperature dependence of magnetic order in selected systems

6.2.1. 48Ni/52Fe(111) and Co(111) on Cu(111)

The first study of magnetic order in epitaxial films prepared in UHV was performed by Gradmann and Mueller (1968) using 48Ni/52Fe(111) films, prepared on Cu(111) and coated by Cu. By changing from Ni on Cu(111) to the fcc NiFe alloy, they could avoid interdiffusion and conveniently reduce the misfit from 2.5% to 0.7%. Flat epitaxial growth was checked by RHEED; the film thickness was measured with an accuracy of 4% using X-ray fluorescence. However, AES was not yet available, and deviations from layer-by-layer growth could not be checked in detail. Magnetic measurements were done ex situ by TOM, and ferromagnetism was detected down to the monolayer. Results for the magnetization are shown in fig. 30a–d, in comparison with spin-wave calculations of Jelitto (1964); good overall agreement is found. An external field of the order of 300 Oe, which had to be used for the calculations in order to get agreement with the experiments, seems a reasonable simulation of in-plane

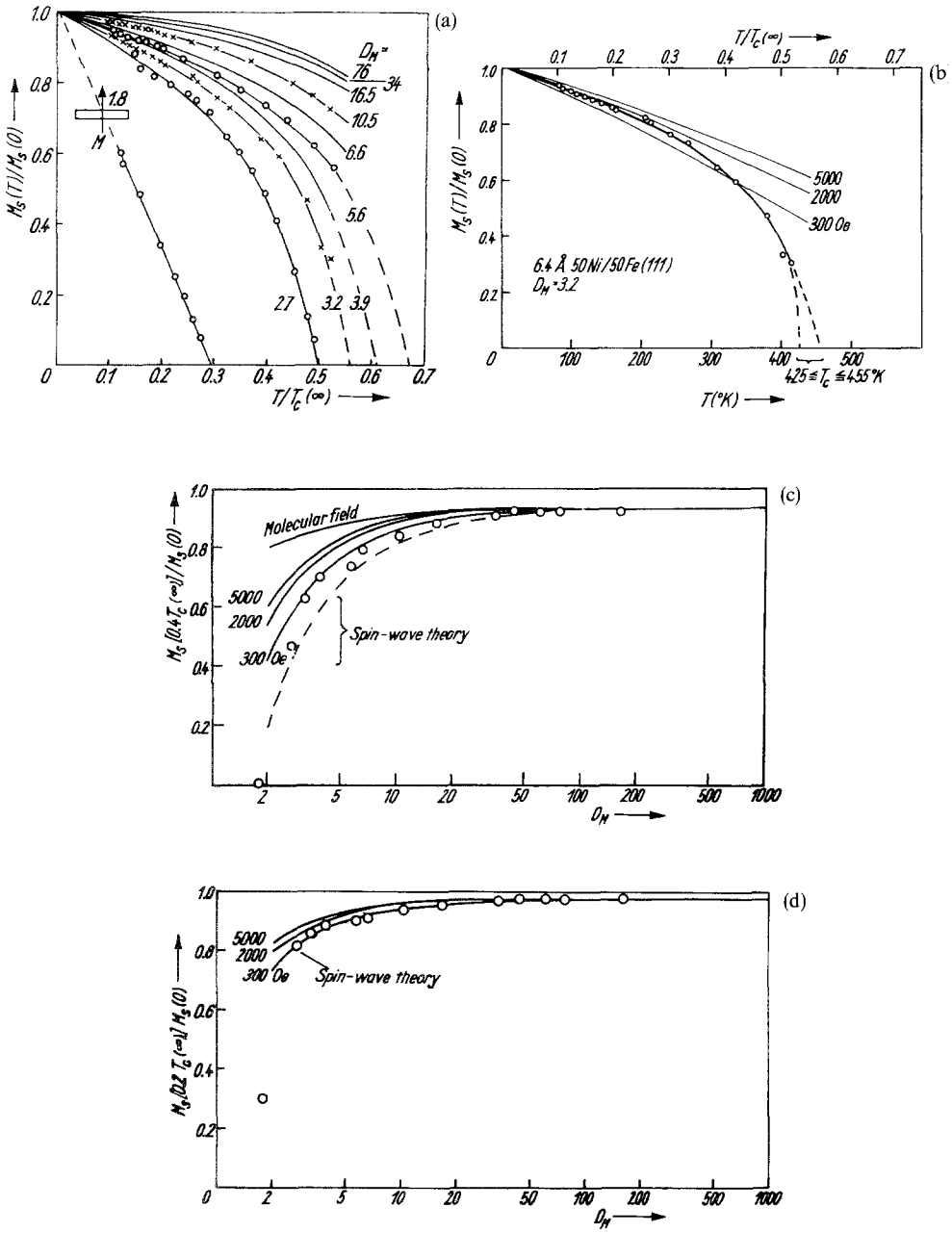

Fig. 30. Saturation magnetization M_s of 48Ni/52Fe(111) films on Cu(111), coated by Cu. (a) M_s versus temperature T, normalized to $T_c(\infty)$, the Curie temperature of bulk material. Number of atomic layers in the films D_M as indicated, from magnetic moment. The film $D = 1.8$ is magnetized perpendicularly. (b) M_s versus T for a film consisting of $D = 3.2$ layers; spin-wave calculations for different external fields (Jelitto 1964) for comparison. (c) M_s versus D for $T = 0.4T_c(\infty)$, (d) for $0.2T_c(\infty)$ (from Gradmann and Mueller 1968).

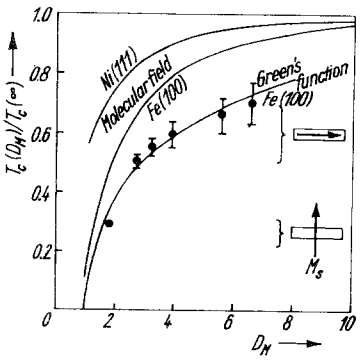

Fig. 31. Curie temperatures of 48Ni/52Fe(111) films on Cu(111) versus number of atomic layers D_M, from Gradmann and Mueller (1968) in comparison with Green's-function theory for Fe(100) from Brodkorb et al. (1966) and molecular-field theory of Ni(111) and Fe(100) from Valenta (1962).

anisotropies. Note the perpendicular magnetization of films consisting of $D = 0.9$ and 1.8 monolayers, respectively, which in addition show a striking linear dependence of M_s on temperature T, far beyond the range where it is predicted by spin-wave theory. In the light of investigations made by Qiu et al. (1989), who showed that such a linear dependence can result from an island structure, the existence of flat islands in these monolayer-films cannot be excluded. The enhanced thermal decrease of magnetic order is clearly in accordance with spin-wave theory. The linear decrease is confirmed to a good approximation (note however deviations in the film $D = 5.6$ in fig. 30a), and the dependence of T_c on D is in surprisingly good accordance with predictions from the Green's-function theory of Brodkorb and Haubenreisser (1966), cf. fig. 31. Results from Co films on Cu(111) (Gradmann and Mueller 1970, 1971) fitted well to the data for NiFe on Cu.

6.2.2. Ni(111) on Re(0001), W(110) and Cu(111)

After introducing TOM in situ in UHV, the experiments on the 'pseudo Ni' NiFe(111) could be complemented by Bergholz and Gradmann (1984) by work on Ni(111) films on Re(0001). Layer-by-layer growth, as expected from the surface energies, discussed in section 2.1. and table 1, was confirmed by AES, epitaxial growth by LEED. The misfit of -9.7% gives rise to periodic misfit dislocations with resulting periodic strain up to roughly ten layers. The magnetic film moment could be followed during growth, or measured in situ for a series of films with increasing thickness, as shown in fig. 32. In agreement with spin-wave predictions, a linear increase of the moment with increasing thickness is observed. The absence of a ferromagnetic moment below $D = 2$ means that the temperature of measurement equals the Curie temperature at $D = 2$. The magnetization, which could be measured above room temperature only, is shown in fig. 33 versus T, with D as a parameter. In properly reduced units, the data fit well to that of NiFe, as shown in fig. 34, except an indication of some saturation for the thinnest Ni films, which remains to be explained.

Layer-grown Ni(111) films on W(110) have been investigated by Y. Li et al. (1990, 1991) using FMR in situ in UHV, in the paramagnetic regime. They observed a

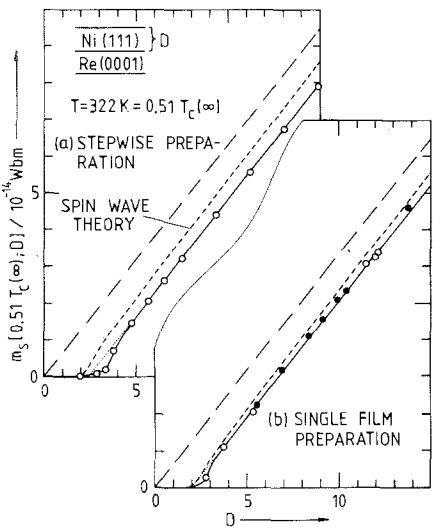

Fig. 32. Magnetic saturation moment m_s of Ni(111) films on Re(0001) at 322 K versus number of atomic layers D, for two different modes of preparation. Magnetic moment of bulk material (---) and results of spin-wave theory for the Heinsenberg model of fcc (111), $S=\frac{1}{2}$, $H=20$ Oe, from Jelitto (1964) for comparision (from Bergholz and Gradmann 1984).

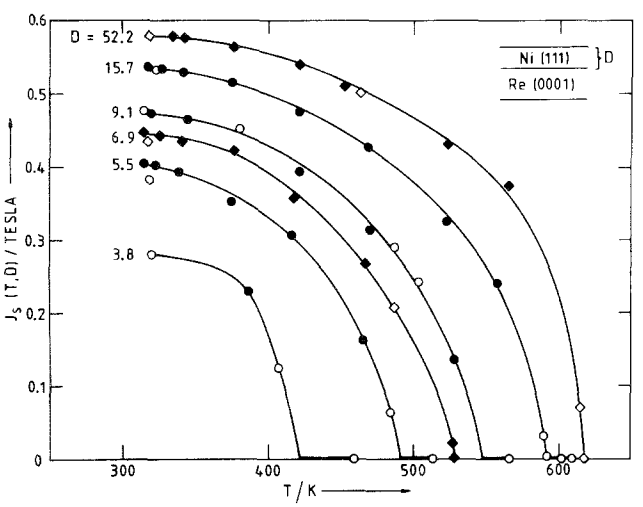

Fig. 33. Saturation magnetization $J_s(T,D)$ of Ni(111) films on Re(0001), versus temperature T, with the number of atomic layers D as parameter. Data taken with increasing T (closed symbols) and decreasing T (open symbols) (from Bergholz and Gradmann 1984).

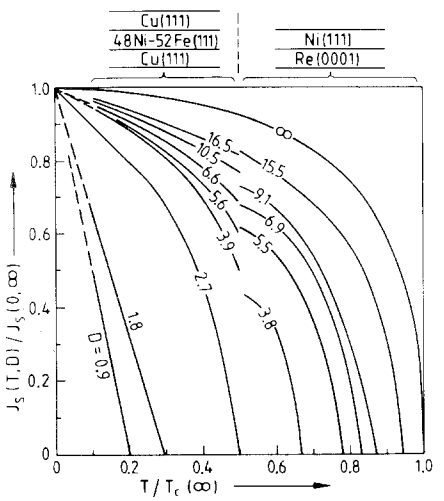

Fig. 34. Magnetization $J_s(T,D)$ versus temperature T, both normalized to bulk data, with number of atomic layers D as parameter, for Ni(111) on Re(0001) and 48Ni/52Fe(111) in Cu(111) (from Gradmann et al. 1985).

peak-like broadening of the resonance line, near T_c, which they discussed in terms of critical fluctuations, see fig. 35. Their results for $T_c(D)$ are shown in fig. 36 in comparison with data from Ni on Re, NiFe on Cu and from Ni(111) on Cu(111), as measured in situ by Ballentine et al. (1990) using MOKE. The Curie temperature of a W(110) monolayer on W(110) is included. The full curve provides a fit to the Ni/Re data by a power law $\Delta T_c \sim D^{-\lambda}$, as proposed first by Allan (1970), with an exponent

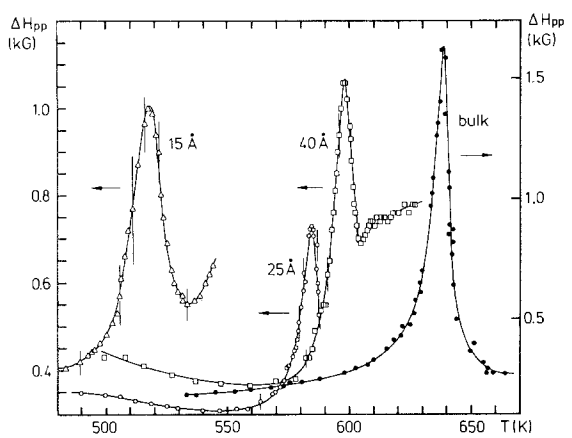

Fig. 35. Critical fluctuations in bulk Ni and in Ni(111) films on W(110) of thickness as indicated. The fluctuations are indicated by a resonant peak of the FMR-linewidth DH_{pp} just above the Curie temperature (from Y. Li et al. 1991).

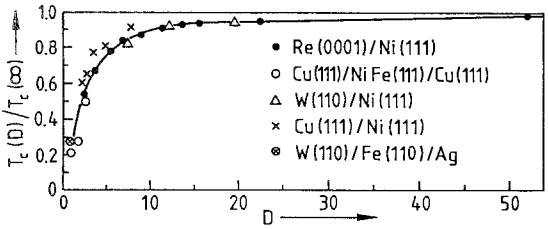

Fig. 36. Normalized Curie temperatures versus number of atomic layers D for different densely packed cubic transition metal films (from Gradmann et al. 1991).

$\lambda = 1.27(20)$ near the prediction $\lambda = 1/\nu = 1.4$ of Domb (1973). The Curie temperature in the densely packed films fcc (111) and bcc (110) presents a rather consistent view.

6.2.3. Fe(110) on Ag(111) and on W(110)

For the case of Fe films, the Mössbauer effect provides a unique tool for thermal analysis of magnetic order. The physical basis for this method is given by the fact that the magnetic hyperfine field B_{hf} at a ^{57}Fe nucleus shows to a very good approximation the same temperature dependence as the magnetization, because all its contributions are caused by the magnetic moment of the electron shell. This is well known from bulk materials (Preston et al. 1962) and is described in any textbook on Mössbauer effect (see, e.g., Wegener 1965). Small deviations were discussed by Vincze and Kollar (1972). This proportionality is generally assumed to apply in thin films also, and has been confirmed for this case recently by Lugert and Bayreuther (1988). It should be emphasized however, and will be shown below, that in inhomogeneously magnetized samples, like thin films, B_{hf} cannot be taken as a measure of the local magnetization value.

The use of the Mössbauer effect for local analysis of thermal decrease of magnetic order in thin films was pioneered by Tyson et al. (1981). They prepared epitaxial films of Fe(110) on Ag(111) films on mica, coated by Ag, including probes of some atomic layers of the Mössbauer isotope ^{57}Fe in a film which consisted otherwise of ^{56}Fe, and took Mössbauer spectra of them by standard transmission techniques. Because of a low signal-to-noise ratio, and of preparation problems, true monolayer probes could not be used. Figure 37 shows the hyperfine field against the ^{57}Fe probe position at (a) 295 K and (b) 4.2 K, for a film consisting of 30 layers. As indicated by the lines, an enhancement of B_{hf} towards the right interface (coated surface), at 4 K, is inverted at 300 K to a decrease. Both the enhancement at 4 K and the decrease at 300 K are rudimentary only at the left interface, near the Ag(111) substrate. This clearly reflects an island nucleation of the initial probe layer, the atoms of the probe crystallites being later in different planes of the completed film. This is just the mode of nucleation which is expected from the surface energies, as discussed in section 2.1 and table 1. Apparently, it takes place for Fe on Ag(100), too, as seen from figs. 7, 16 and 17.

Further analysis showed that $B_{hf}(T)$ in the Ag-coated interface of a 30-layer film

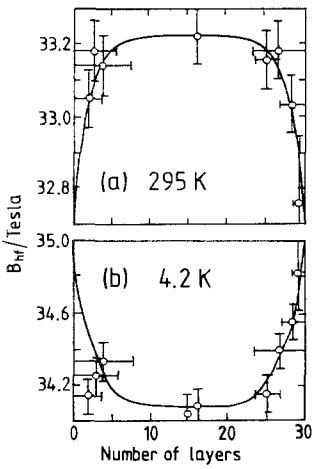

Fig 37. Magnetic hyperfine field B_{hf} versus position of ^{57}Fe probe layer in 30-layer Fe(110) films on Ag(111), (a) at 295 K, (b) at 4.2 K (after Tyson et al. 1981).

follows a Bloch law,

$$B_{hf}(T) = B_{hf}(0)[1 - b_s T^{3/2}], \tag{6.1}$$

with a spin-wave parameter $b_s = 12 \times 10^{-6}\,K^{-3/2}$, confirmed later for a film of 50 layers by Walker et al. (1984). These authors compared b_s with a bulk value of $3.4 \times 10^{-6}\,K^{-3/2}$, apparently taken from Argyle et al. (1963), who in turn got it from a fit of the magnetization for $T < 100$ K. Because of T^2 terms, which must be considered at higher temperatures but were neglected by Walker, one should rather compare the data with a pure $T^{3/2}$ fit of the bulk data, as has been pointed out by Korecki and Gradmann (1986b). If this is done for Mössbauer data from Butler et al. (1972), one obtains $b_{bulk} = 5.2 \times 10^{-6}\,K^{-3/2}$, from B_{hf}(0–300 K), and finally an enhancement of b_s by a factor 2, 3. This is very near the enhancement by a factor 2 which Rado (1957) had predicted from spin-wave theory, arguing that spin-waves have nodes in the surface, and their intensity therefore is two-fold enhanced in comparison with the mean value of the interior. His argument was given a rigorous basis by Mills and Maradudin (1967). It has been shown by Mathon (1988) that a weakened exchange coupling between the first and the second monolayer results in an enhancement of b_s beyond $2b_{bulk}$. Walker's result, properly evaluated, means in turn that the exchange coupling near the surface of Fe(110) is nearly unweakened.

Korecki and Gradmann (1985, 1986b) improved the Mössbauer technique by using the surface sensitive detection of the resonant nuclear absorption by the subsequent emission of conversion electrons from the K-shell (conversion electron Mössbauer spectroscopy, CEMS). They implemented the method in UHV and realized monolayer sensitivity. They applied the method to Fe(110) films on W(110) and performed a local analysis of $B_{hf}(T)$ by shifting a monolayer probe of ^{57}Fe through a film of 21 layers. Figure 38 shows that both the central and the topmost layer of an Ag-coated

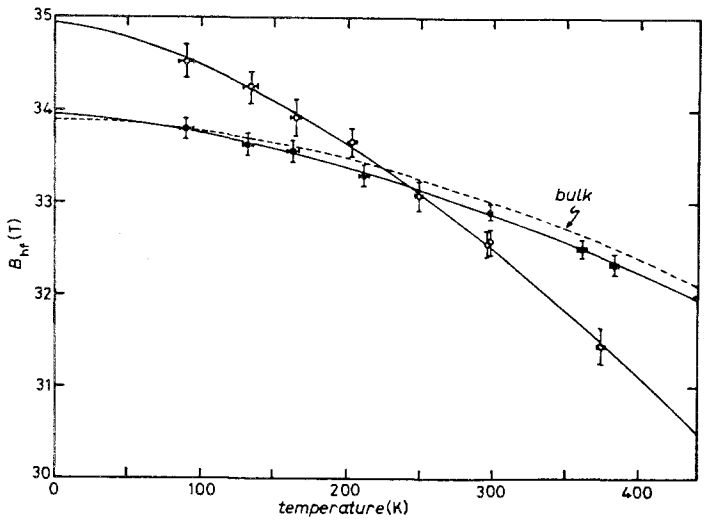

Fig. 38. Magnetic hyperfine field B_{hf} versus temperature in a Fe(110) film on W(110), coated by Ag, measured at a monolayer probe of ^{57}Fe just below the Ag coating (○) and in the center of the film (●), respectively. Bulk data for comparison. Fitting curves are $T^{3/2}$ laws (from Korecki and Gradmann 1986b).

film follow a $T^{3/2}$ law, with only minor deviation from the bulk behaviour in the center and enhanced thermal decrease at the surface. Figure 39 shows a profile of spin-wave parameters across the film which is now nearly symmetric because of the layer-by-layer growth, the more reliable data coming from the Ag-coated surface. The value $b_s = 13.3 \times 10^{-6}\,K^{-3/2}$ is in excellent agreement with Walker's result; the small difference is reasonable because Walker used a probe of 1.6 monolayers. It is a matter of discussion whether to compare b_s, for the film in fig. 39, with the value of bulk material, the mean value in the film or that in the center, given by 5.3, 7.2 and $6.2 \times 10^{-6}\,K^{-3/2}$,

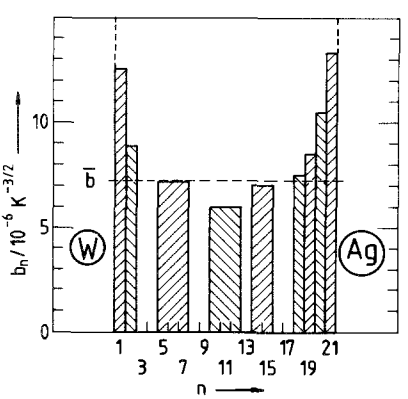

Fig. 39. Spin-wave parameters b_n versus position of ^{57}Fe probe layers in films of 21 monolayers Fe(110) on W(110), coated by Ag (from Przybylski et al. 1987).

respectively. Roughly speaking, the deviations from Rado's prediction are minor only for the Ag-coated Fe(110) surface.

Because of enhanced ^{56}Fe–^{57}Fe interdiffusion in the misfit-dislocation zone near the W substrate, the straightforward local analysis using ^{57}Fe-monolayer probes is not applicable for films below about ten monolayers. Some possibility of local analysis is provided by pure ^{57}Fe films, because the first monolayer on W differs in B_{hf} from the following material, as was shown already in fig. 10. The temperature dependence could therefore be followed by Korecki et al. (1990) for this first monolayer and the rest of the film separately. It turned out that $B_{hf}(T)$ for all films and both components could be fitted by a $T^{3/2}$ Bloch law according to eq. (6.1) and therefore be described phenomenologically by a spin-wave parameter b. Whereas the absence of a linear dependence seems reasonable with regard to the Green's functions results presented in fig. 28c, the $T^{3/2}$ dependence can be taken as an empirical fact only. Deviations certainly must be considered at $T < 90$ K, where experimental data are missing. Nevertheless, the b parameters can be taken as a phenomenological measure for the overall temperature dependence between 90 and 300 K. The temperature dependence of the mean hyperfine field is in good agreement with Green's-function calculations for Fe(100), shown in fig. 40, which may be surprising because of the different orientation. In combination with the monolayer-probe analysis for 21 layers, the data from the pure ^{57}Fe films result in a tentative inhomogeneity of $B_{hf}(300\,K)/B_{hf}(0\,K)$ as shown in fig. 41, which is in fair agreement with the predictions of Haubenreisser et al. (1969) for Fe(100). Note the homogeneity of the thermal decrease for the film $D = 3.4$. The same homogeneity was found, in a local analysis of spin-wave b parameters using CEMS, to hold up to $D = 4$ (Przybylski et al. 1989), which means that the strong exchange interaction suppresses any local changes of thermal decrease in these ultrathin films, when grown layer by layer. For comparison, Lugert and Bayreuther (1989) found for a Fe(110) film on Ag(111), consisting of four layers, two components with

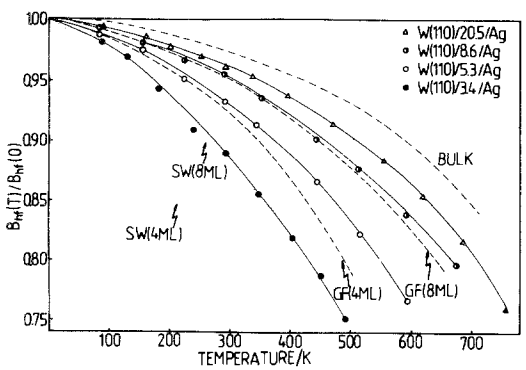

Fig. 40. Normalized values of the main component of hyperfine field B_{hf}, versus temperature, for Fe(110) films on W(110) consisting of numbers of atomic layers as indicated, coated by Ag. Solid lines to guide the eye. Spine-wave calculations SW (Jelitto 1964) and Green's functions calculations GF (Haubenreisser et al. 1969) for comparison (from Korecki et al. 1990).

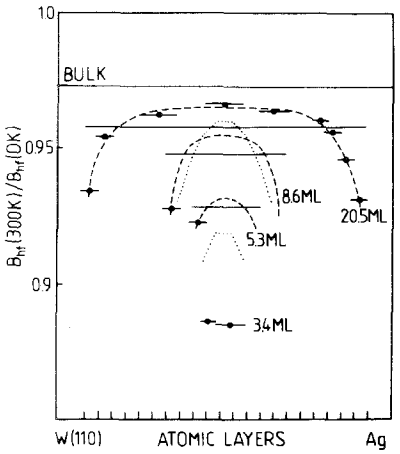

Fig. 41. Spatial distribution of the normalized hyperfine field, at 300 K, in Fe(110) films on W(110), coated by Ag, across films of numbers of monolayers as indicated. The data represent the local structure of thermal decrease of magnetic order. Broken lines serve to guide the eye, dotted lines are Green's function predictions for Fe(100) from Haubenreisser et al. (1969) (from Korecki et al. 1990).

b parameters of 13 and $32 \times 10^{-6} K^{-3/2}$, respectively. These differences reflect the island structure of these non-wetting Fe films.

The monolayer Fe(110) on W(110) was first analyzed using CEMS by Przybylski and Gradmann (1987), who prepared their films at 300 K, following their experience from thicker films, where deviations from layer-by-layer growth were observed at higher temperatures (Przybylski et al. 1989). For the monolayer, this was not an optimum choice, as was recognized only later by Przybylski and Gradmann (1988), who measured the Curie temperature as a function of the mean number of bulk monolayers, D, near the pseudomorphic monolayer (which is given by $D = 0.82$ because of the misfit of -9.4%). This was done for different preparation temperatures. As shown in fig. 42, $T_c(D)$ increases monotonically with D for films prepared at 300 K, whereas a constant value $T_c = 282$ K was observed for films prepared at 475 K. This value remains stable even when the films are annealed up to 800 K. Apparently, preparation at elevated temperatures and annealing results in extended monolayer patches, the Curie temperature of which is independent of the coverage, whereas for preparation at room temperature the film consists of small-sized monolayer patches and the increasing T_c must be interpreted in terms of increasing coalescence between them. This was confirmed by Albrecht and Gradmann (1993) using SPA-LEED for an analysis of the two-dimensional island structure in the submonolayer regime. Following spot profiles of the type shown in fig. 3 for varying preparation temperatures, they found a shrinking in the distance of the two broad peaks of the shoulders, with increasing preparation temperatures, indicating the recrystallization into large monolayer patches. The improvement of the monolayer structure by annealing clearly confirms its thermodynamic stability, which was discussed in detail by Gradmann et al. (1989). Subsequent monolayer analysis was consequently done with films prepared

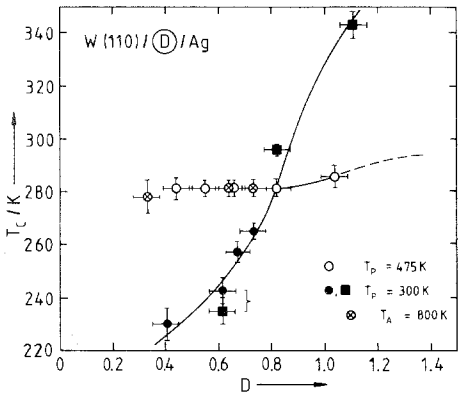

Fig. 42. Curie temperature T_c versus number of bulk monolayers, D, for ^{57}Fe(110) films on W(110), prepared at temperatures T_p as indicated, or annealed at T_A, and coated finally by Ag (from Gradmann et al. 1990).

near 500 K. Figure 43 shows CEMS spectra of an Fe-coated monolayer, prepared at 475 K, with a clear hyperfine sextet for $T < 210$ K. This is superimposed by a nonmagnetic single line, with increasing intensity of the latter up to $T_c = 282$ K. The nature of this nonmagnetic single line remains to be explained. It may be connected with atomic steps in the W(110) substrate, which might provide breaks in the exchange coupling and effectively cut the monolayer into loosely coupled stripes. The distance between monatomic steps is larger than 100 nm, as known from SPA-LEED analysis. Figure 44 shows the mean hyperfine field $\overline{B_{hf}}$ and the hyperfine field of the magnetic component, versus T. Both can be fitted in a wide range by power laws which are included in fig. 44 and documented by the logarithmic plot in fig. 45. Of course, these can hardly be taken as critical power laws but rather should be taken as phenomenological descriptions. Note that the fitting temperature in the power law of B_{hf}, 268 K, clearly deviates from $T_c = 282$ K. Accordingly, the power law for $B_{hf}(T)$ does *not* apply near T_c! All parameters of the fits change when the Ag coating is replaced by Cu or Au, as reported in detail by Gradmann et al. (1990). An excellent reproducibility of the data for fixed coating material is shown in fig. 46, which presents, for a film just above the monolayer, the temperature dependence for B_{hf} of all three components of the Mössbauer-spectrum [monolayer component (a), first and second layers (b) and (c) in double layer patches, respectively; compare with figs. 9 and 10]. The monolayer component shows exactly the same pattern as the true monolayer in fig. 44. Obviously, an interpretation of the critical behaviour of this comparatively well defined monolayer in terms of generalized models with two-dimensional translational symmetry is not appropriate. This should be taken as a hint to be extremely cautious in comparing the critical behaviour of films in the monolayer regime with less defined structure with theoretical models, which in general are based on two-dimensional translation symmetry.

The Curie temperature of the uncoated monolayer is reduced to 210 K (Przybylski

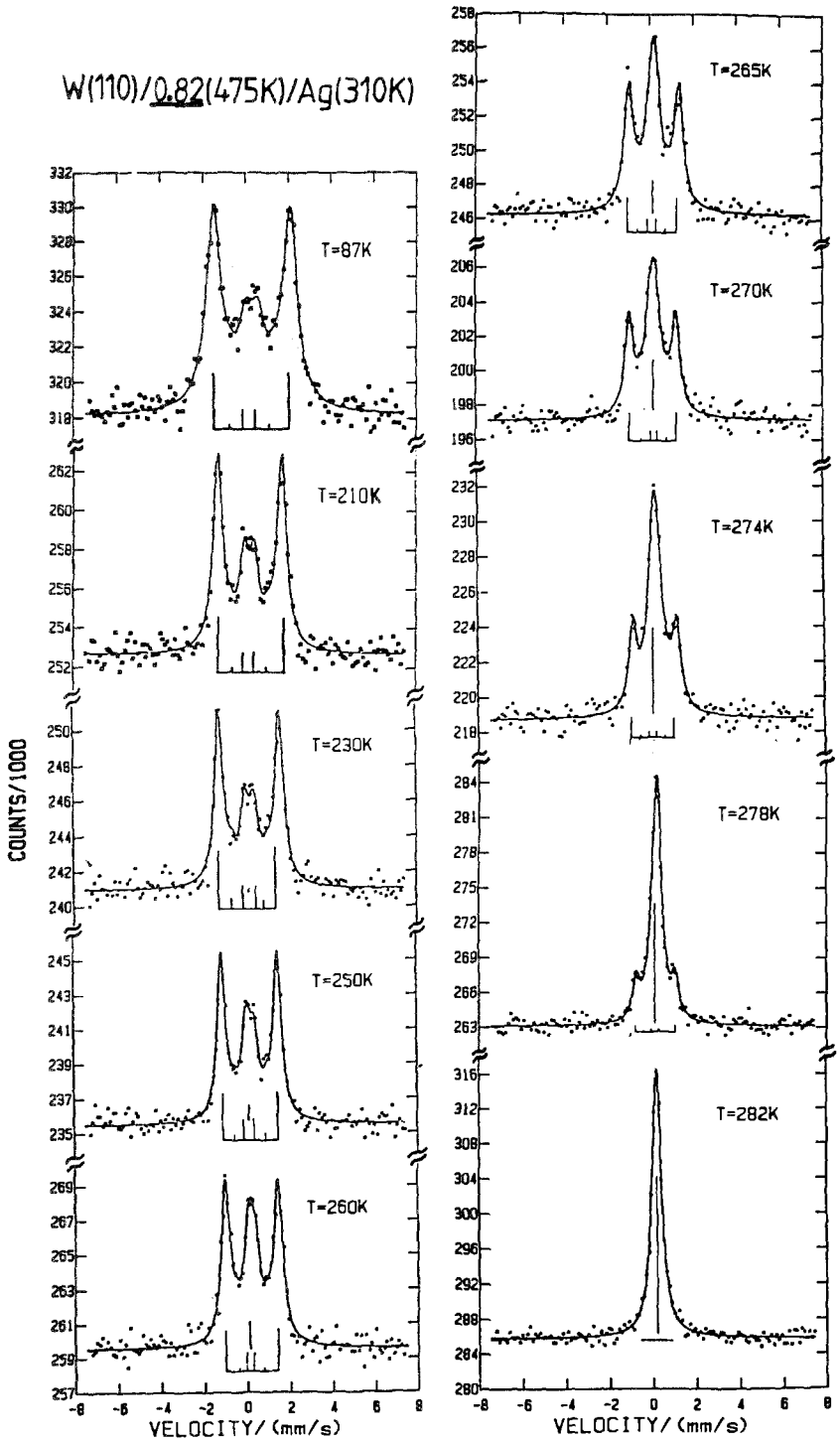
W(110)/0.82(475K)/Ag(310K)
T=87K
T=210K
T=230K
T=250K
T=260K
T=265K
T=270K
T=274K
T=278K
T=282K
COUNTS/1000
VELOCITY/(mm/s)
VELOCITY/(mm/s)

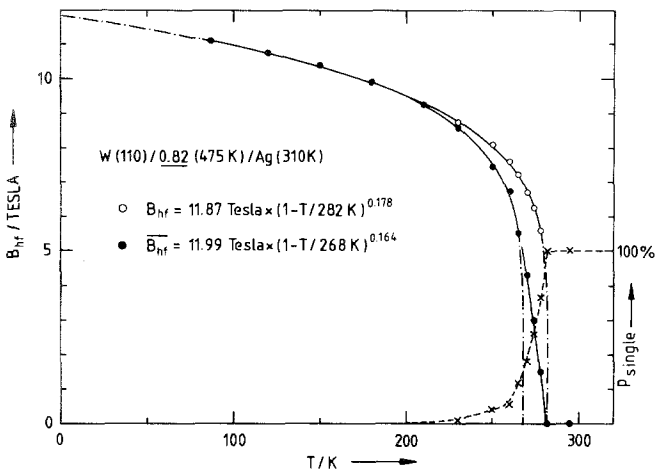

Fig. 44. Magnetic hyperfine field B_{hf} of the magnetic component (○), mean hyperfine field $\overline{B_{hf}}$ (●) and single line contribution p_{single} (×) versus temperature, T, for a pseudomorphic monolayer of ^{57}Fe on W(110), prepared at 475 K. Power law fits (–·–·–), which differ from the full guide-to-the-eye curve for B_{hf} in the critical region (from Gradmann et al. 1989).

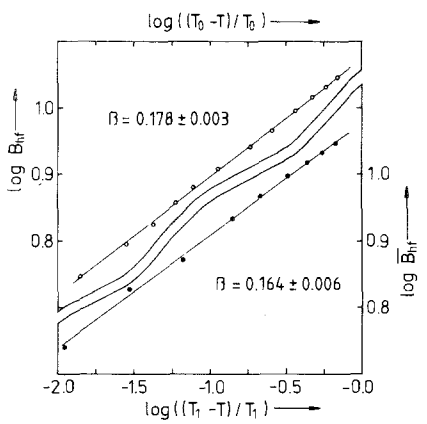

Fig. 45. Double-logarithmic plot of B_{hf} and $\overline{B_{hf}}$ from fig. 44. T_0 and T_1 are fitting parameters which give the most extended linear fit (from Gradmann et al. 1990).

and Gradmann 1987). Accordingly, the chemical state of the monolayer must be included in any forthcoming theory of T_c.

Magnetometry of the Ag-coated monolayer, performed by Elmers et al. (1989), confirmed the ferromagnetic order, with a slightly enhanced critical temperature of 291 K, as shown in fig. 47. As usual, the transition is comparatively sharp

Fig. 43. Mössbauer spectra of a pseudomorphic monolayer of ^{57}Fe on W(110), prepared at $T_{Fe} = 475$K, coated by Ag at $T_{Ag} = 310$K. Spectra are fitted by a superposition of one magnetic sextet and one nonmagnetic single line (from Gradmann et al. 1990).

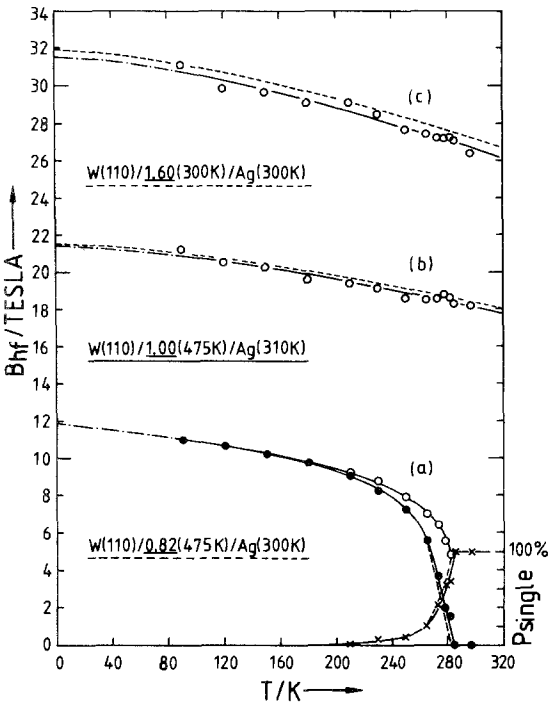

Fig. 46. Magnetic hyperfine fields in a ^{57}Fe(110) film on W(110), consisting of $D = 1.00$ bulk monolayer (1.2 pseudomorphic monolayers), versus temperature. The temperature dependence of components (a), (b) and (c) follows to an good approximation the dotted lines, which are taken from a true monolayer or a true double layer, respectively. They represent the monolayer patches and the first or second monolayer in double-layer patches, of which this epitaxial film is composed (from Gradmann et al. 1989).

in low fields and is smeared out in higher fields. A square hysteresis loop could be observed even at $220\,\mathrm{K} = 0.76T_c$. In the limited range where it could be measured, the remanent magnetization followed the same temperature dependence as B_{hf}, as shown in fig. 48. This enabled a extrapolation to the magnetic moment in the ground state, to be discussed in the next section.

In the temperature range between 90 and 220 K, $B_{hf}(T)$ for the Ag-coated monolayer can be described phenomenologically by a Bloch law with a parameter $b(1) = 56.3 \times 10^{-6}\,\mathrm{K}^{-3/2}$. A plot of the mean Bloch parameter $b(D)$ of films consisting of D layers, versus $1/D$, is shown in fig. 49 (taken from Przybylski et al. 1990a). The parameter $b(D)$ follows a linear dependence

$$b(D) = b(\infty) + [b(1) - b(\infty)]/D, \tag{6.2}$$

with $b(1) = 56 \times 10^{-6}\,\mathrm{K}^{-3/2}$ and $b(\infty) = b_{bulk} = 5.2 \times 10^{-6}\,\mathrm{K}^{-3/2}$, as given above. For an interpretation of this remarkable result, let us assume at first a homogeneous magnetization $J_s(0)$ in the ground state, where $J_s(T)$ is the magnetization of bulk Fe. The magnetic moment of a film of area A, consisting of D layers with distance δ, is

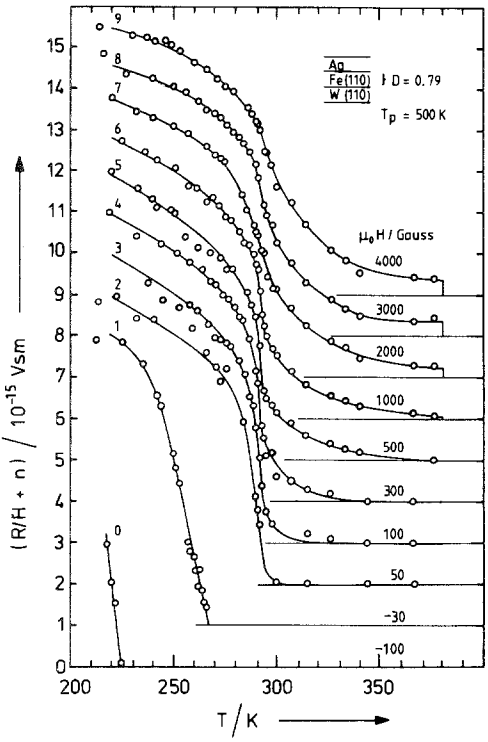

Fig. 47. Magnetometry of a pseudomorphic monolayer of Fe(110) on W(110) (consisting of 0.79 bulk monolayers), coated by Ag. The quantity R/H, measured by TOM versus temperature for different external fields, represents the magnetic moment to a good approximation, compare eq. (4.3). Curves are shifted along the vertical axis for clarity (from Elmers et al. 1989).

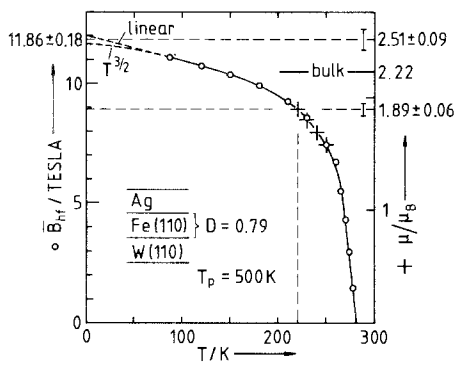

Fig. 48. Magnetometry and Mössbauer spectroscopy of a pseudomorphic monolayer Fe(110) on W(110), prepared at $T_p = 500$ K, coated by Ag. Magnetic moments per atom μ, in units of the Bohr magneton μ_B, could be determined by magnetometry in a limited temperature interval only between 220 and 250 K. The normalized moment μ/μ_B shows the same temperature dependence as B_{hf}, which could be measured in a more extended temperature range and therefore enables the extrapolation of both quantities to $T = 0$ (from Elmers et al. 1989).

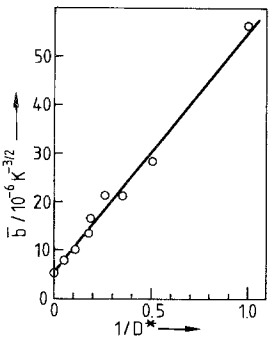

Fig. 49. Spin-wave parameters $\bar{b}$ in ^{57}Fe(110) films on W(110), coated by Ag, versus $1/D^*$, where D^* is the number of true monolayers ($D^* = D - 0.18$ differs from the number of bulk monolayers, because the first monolayer is pseudomorphic) (according to Korecki et al. 1990 and Przybylski et al. 1989).

then given by

$$m = AJ_s(T)\delta[D - \Delta D_{th}], \tag{6.3}$$

with

$$\Delta D_{th} = [b(1) - b(\infty)]T^{3/2}. \tag{6.4}$$

This is just the linear dependence shown for $m(D)$ in a growing Ni film in fig. 32. The extrapolation of $m(D)$ goes to zero at ΔD_{th}, and m is reduced, with respect to what was be expected from the bulk magnetization, by

$$\Delta m_{th} = AJ_s(T)\delta\Delta D_{th}. \tag{6.5}$$

Δm_{th} is the moment of ΔD_{th} bulk monolayers. The important point is its independence of D. For thin films up to $D = 4$, where b is homogeneous across the film, this means that the spectrum of thermally excited spin-wave modes is independent of D, because modes with $k_z = 0$ are frozen in (for the case of the isotropic Heisenberg model, see the paper of Gradmann 1974). For thick films, Δm_{th} represents the Rado-like reductions near both surfaces. It is remarkable that apparently the magnitude of Δm_{th} is the same in both limiting cases.

The numerical data for $b(1)$ and $b(\infty)$ result in $\Delta D_{th} = 0.27$, at $T = 300$ K. Figure 50, taken from Elmers (1989), shows the magnetic moment of the growing film at 300 K, which disappears in extrapolation at $D_c = -0.14(14)$. Apparently, this thermal decrease is superimposed upon a thickness-independent increase corresponding to the moment of 0.41(14) monolayers, which we interpret as an enhanced moment near the interfaces, to be discussed in the next section.

For the thinnest films, the separate hyperfine field of the first monolayer, (24 T, see figs. 9 and 10) enables separate measurement of b in it. It turns out that it agrees with b of the subsequent layers within the accuracy of the measurement (2%), for the very thinnest films with $D < 4$. For $D = 5$, it is enhanced by only 13%. The temperature dependence is rigidly locked in all layers of these layer-grown epitaxial films (Przybylski et al. 1989). In contrast, Lugert and Bayreuther (1988) reported for a four-layer epi-

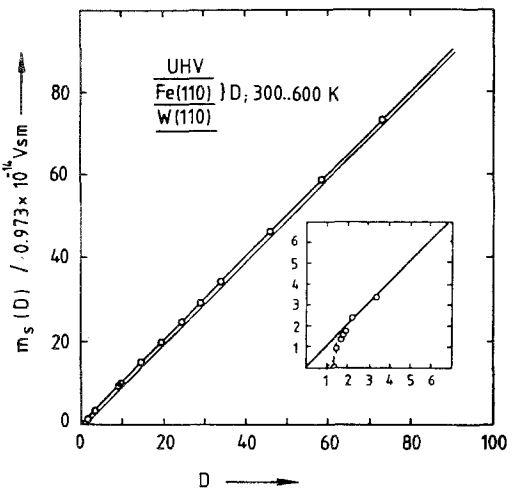

Fig. 50. Magnetic saturation moment m_s of uncoated Fe(110) layers, prepared in an optimized mode on W(110), measured in situ by TOM as a function of number of bulk atomic layers D. m_s is given in units of a bulk monolayer moment, 0.973×10^{-14} V s m (from Elmers 1989).

taxial Fe(110) film on Ag(111) two Mössbauer-components with $b = 13$ and $32 \times 10^{-6}\,K^{-3/2}$, which they attributed to the outer and inner layers of their film, respectively. With respect to the strict homogeneity of b in Fe(110) on W(110), this interpretation is improbable. We rather suggest that the inhomogeneity reflects the ill-defined rough and island structure of the films on Ag(111), in the nucleation state, which is indicated by other data too.

6.2.4. Fe(100) on Ag(100), Au(100) and Pd(100)

Magnetic investigation of bcc α-Fe(100) films on fcc Ag(100) and Au(100) seemed promising because of the low misfit, as may be inferred from table 2. Because of the interest in perpendicular magnetization, the measurements concentrated on the very thinnest films. The films are mostly addressed as bcc Fe, although they are strictly speaking tetragonal centered, with c/a supposedly near $\sqrt{2}$.

For the case of *Fe(100) on Ag(100)*, coherent films form, however, only at about three monolayers, as expected from the surface energies, discussed above in section 5.2.4, and in accordance with the observations available for Fe(110) on Ag(111), as discussed in the last sections. These structural problems apparently prevented reliable experiments on the temperature dependence of the magnetic order. For the case of *Fe(100) on Au(100)*, magnetic order was detected first by Bader and Moog (1987) using MOKE. The temperature dependence of magnetic order for films in the monolayer regime was then measured by Duerr et al. (1989) by SPLEED and spin-polarized secondary electron emission using the exchange asymmetry A_{ex} of reflected electrons or the polarization P of emitted electrons as a measure of magnetic order. They observed rounded phase transitions as shown in fig. 51a, which they fitted by power laws as shown in fig. 51a and b in a linear and a logarithmic plot, respectively. The

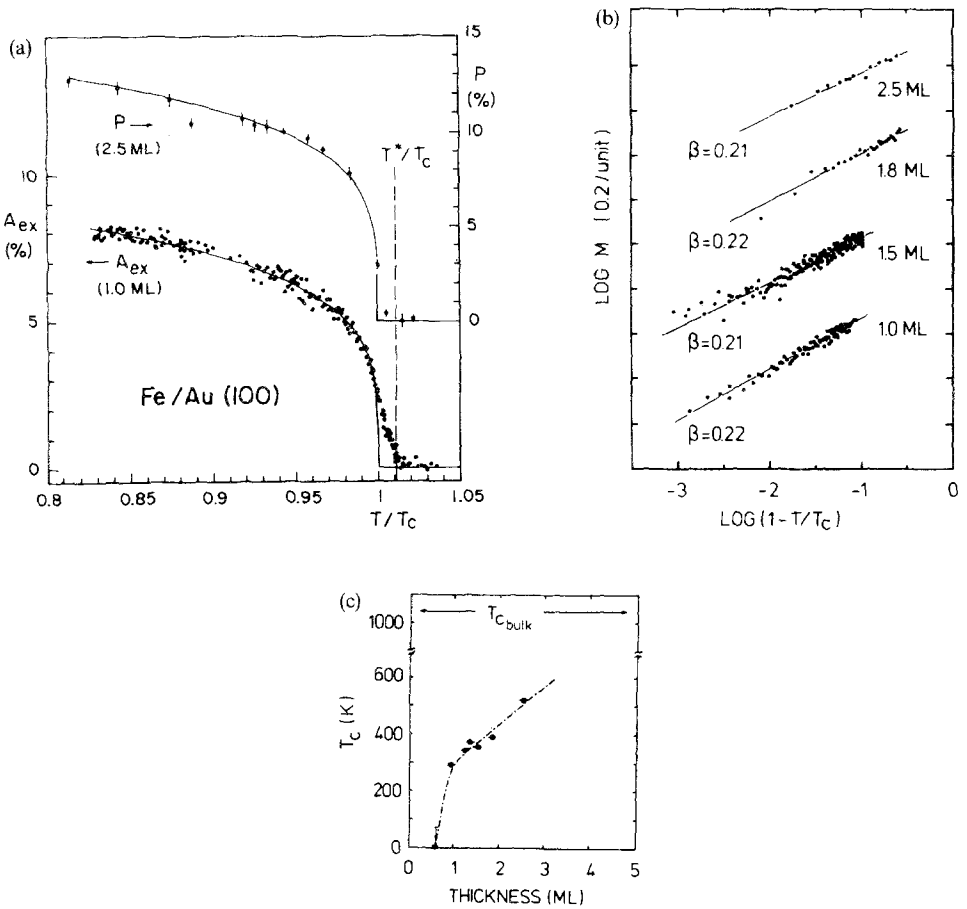

Fig. 51. SPLEED and spin-polarized secondary electron emission from Fe(100) films on Au(100). (a) Exchange asymmetry, A_{ex}, from SPLEED from 1.0 monolayers and secondary electron spin polarization, P, from 2.5 monolayers versus reduced temperature T/T_c, with $T_c = 315$ and 521 K, respectively. (b) Temperature dependence of P (for 2.5, 1.8 and 1.5 monolayers) and A_{ex} (for 1 monolayer) in a log P or log A_{ex} versus log $(1 - T/T_c)$ representation. T_c is a fitting parameter for getting most extended linear range. (c) Fitting parameter T_c versus number of monolayers; curve to guide the eye (from Duerr et al. 1989).

Curie temperature was determined as a fitting parameter, chosen to maximize the linear range in fig. 51b. This procedure seems to be not unproblematic, compare our discussion of fig. 44. It results in T_c as given in fig. 51c. Rau and Xing (1989) analyzed a two-layer film of Fe(100) on Au(100) using electron capture spectroscopy (ECS). As shown in fig. 52, they observed a sharp transition at 290 K and a power law with an exponent $\beta = 0.25(1)$. Whereas the exponent is not far away from that of Duerr et al. (0.21 to 0.22, compare with fig. 51b), $T_c(2)$ differs strongly (410 K from Duerr et al.). The different magnetic results must be caused by unknown structural differences, which however are not surprising. The observation of Duerr et al. (1989) that "deposition

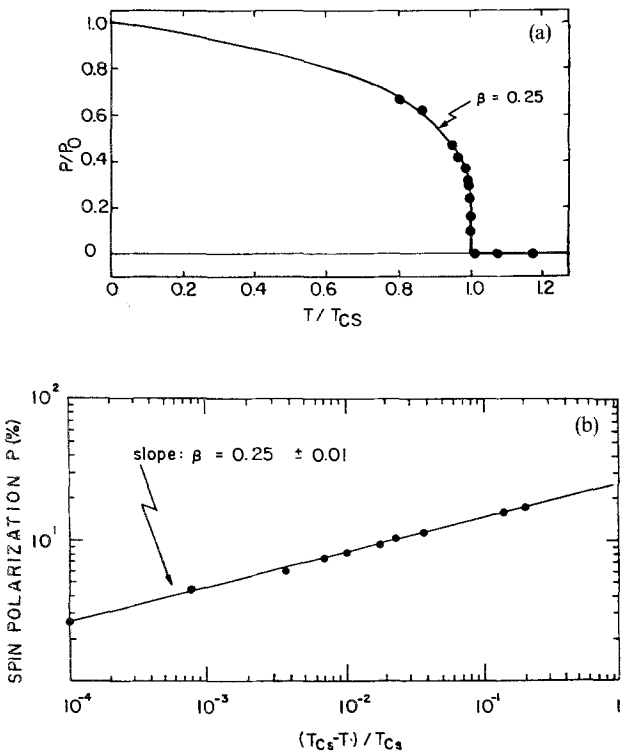

Fig. 52. Electron capture spectroscopy at two monolayers Fe(100) on Au(100). Elctron spin polarization, P, versus reduced temperature (a) in a linear plot of P versus T/T_{cs}, (b) in a log–log-plot of P versus $(T_{cs} - T)/T_{cs}$. The fitting curve gives a power law with $T_{cs} = 290.0$ K and $b = 0.25$ (from Rau 1989).

at 300 K is a necessary condition to obtain layer-by-layer growth" means that the films actually grew in a forced layer-growth mode, as expected from the surface energies (table 1). For details see section 2.2. In this mode, the structure in the monolayer regime depends sensitively on the preparation conditions (Gradmann and Tillmanns 1977), and structural differences to explain the different magnetic results are reasonable. Although the sharp transition in the experiment of Rau and Xing (1989) indicates a comparatively good layer structure, a discussion of the results in terms of universal models of 2D magnetism seems problematic.

The magnetization in films of *Fe(100) on Pd(100)* was measured by Liu and Bader (1990a) using MOKE. When prepared at 100 K, the films were perpendicularly magnetized. However, the magnetization of a monolayer could be switched from perpendicular to parallel to the plane when the sample was prepared at 300 K. The structural cause of the switching is unknown. Rounded transitions were observed and analyzed in a way analogous to that of Duerr et al. (1989) for Fe films on Au(100), as shown in fig. 51. The power-law exponents, however, were lower (0.13 to 0.16).

6.2.5. fcc Co(100) on Cu(100)

fcc Co(100) films on Cu(100) were measured by the group of Pescia, who reported for the monolayer, grown at room temperature, a magnetization which is nearly independent of temperature up to 400 K (Pescia et al. 1987b, Kerkmann 1989, Smardz et al. 1990). In sharp contrast, Schneider et al. (1990) and de Miguel et al. (1989), reported for Co(100)-films on Cu(100) a $T_c(D)$ which decreases linearily from 580 K for $D = 3$ to 120 K for $D = 1.5$ monolayers, the Curie temperature of the monolayer being definitely below 100 K. The structural cause for the discrepancy is not clear. We dispense a further discussion of this system.

6.2.6. bcc V(100) on Ag(100)

Rau (1989) investigated bcc V(100) films on Ag(100) using ECS. His results are remarkable, firstly because they provide an example where a metal which is nonmagnetic in bulk becomes ferromagnetic in a thin film, up to $D = 7$ layers! We come back to this aspect in the next chapter. Secondly, they are remarkable with respect to the temperature dependence of magnetic order, which is shown for the case of five monolayers in fig. 53. The data fit much better to the exact solution of the 2D Ising model, as demonstrated in fig. 29, than to an asymptotic power law, shown in fig. 53a for comparison. Accordingly, a power-law exponent $\beta = 0.128(10)$ was determined which agrees with the Ising value 0.125 within the limits of accuracy.

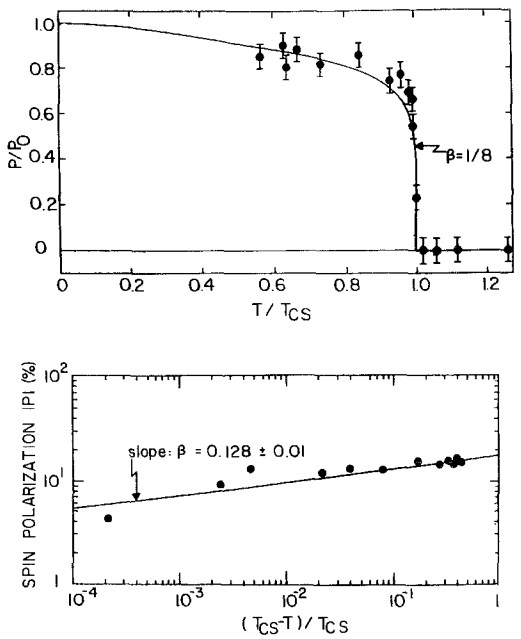

Fig. 53. Electron capture spectroscopy at five monolayers V(100) on Ag(100), presentation as in fig. 52. (from Rau 1989).

Measurements of the anisotropies in this unique system with true Ising behaviour are required.

7. Magnetic ground-state properties

The discussion of magnetic ground-state properties in ultrathin films is dominated by the strong progress in their calculations by first-principles self-consistent band theories. The present experimentally oriented paper does not intend a review of theoretical results in general, which has been given in several excellent theoretical review papers (Freeman and Fu 1986, 1987, Victora 1986, Bluegel et al. 1989, Freeman and Wu 1991). We concentrate on systems where comparison with experiments is available or possible. Theoretical results are given in terms of local densities of states, magnetic moments and magnetic hyperfine fields. Anisotropies have been calculated in selected systems, which have been discussed above (section 5.2). The main concern of the present section is magnetic moments. Band-structure calculations provide the spin polarization of the electron system. We take account of the small contribution to the magnetic moment that results from incomplete orbital quenching by a small additive correction which brings the polarization of bulk material to the experimental ground state moment ($2.22\mu_B$ for Fe). The magnetic hyperfine field B_{hf} is interesting because of its tight connection with the moment and because it provides a local probe. What comes out directly from the band calculations is the Fermi-contact contribution $B_{co} = B_{core} + B_{cond}$, which is a direct measure of the spin polarization of the electron density at the nucleus. It contains contributions B_{core} from the core polarization and B_{cond} from the conduction electrons.

The comparison between theory and experiment suffers from the tendency of theorists to perform calculations for simple model systems, even if they never will exist, like a free monolayer or a Fe monolayer on Ag, whereas experimentalists tend to measure on systems which they can prepare. Our presentation therefore will contain comparison of related systems, to show general tendencies. One guideline is that magnetic moments in surfaces and monolayers are enhanced by reduced coordination, making the surface atoms something between bulk and free atoms, with moments of 2.2 and $4.0\mu_B$, for the case of Fe.

7.1. Magnetic moments in monolayers at low temperatures

The ferromagnetic monolayer has attracted attention as a model system. Table 6 shows magnetic moments and hyperfine fields in Fe monolayers. The general tendency of enhanced moment, in comparison with the bulk, is most clearly seen in the free-standing monolayer Fe(100), with a moment of $3.07\mu_B$. A promising candidate for approaching this free monolayer seems to be given by Fe(100) on Mg(100). Layer-by-layer growth has been reported for this system by Urano and Kanaji (1988). The calculations of C. Li and Freeman (1991) show that the monolayer Fe(100) on Mg(100) apparently represents the free monolayer to a very good approximation, as a result of the clear separation between the electron bands of substrate and film, as shown in fig. 54a. The enhanced moment is connected with the strong band narrowing in

TABLE 6
Ground-state magnetic properties of magnetic monolayers, from theory (upright numerals) and experiment (slanted numerals). Magnetic moments per atom, μ, in units of the Bohr magneton, μ_B, core contribution, B_{co}, of magnetic hyperfine field and total magnetic hyperfine field, B_{hf}, both in T.

System	μ/μ_B	B_{co} (T)	B_{hf} (T)	Ref*
Bulk Fe	2.22	−30	−33.9	
Fe(100) free	3.07	−5.1		[1]
MgO(100)/1Fe(100)	3.04	−4.2		[1]
MgO(100)/2Fe(100)				
1st layer	2.82	−36.8		[1]
2nd layer (surf)	2.93	−28.4		[1]
Ag(100)/1Fe(100)	2.96	−15.7		[2]
Au(100)/1Fe(100)	2.97	−21.3		[2]
W(110)/Fe(110)/-	2.18	−14.8	−9.3	[3]
W(110)/Fe(110)/Ag	2.17	−17.7	−12.2	[3]
	2.53(12)		*−11.9(3)*	[4]
W(110)/Fe(110)/Au			*−15.9(3)*	[5]

*References:
[1] C. Li and Freeman (1991).
[2] C. Li et al. (1988).
[3] Hong et al. (1988).
[4] Gradmann et al. (1989).
[5] Gradmann et al. (1990).

the monolayer, which results in a full majority band, the monolayer becoming a strong ferromagnet. The formation of a double layer (fig. 54b) is connected with increasing bandwidth. However, strong ferromagnetism and high moments are retained. For other metallic substrates, this enhancement of moment is counteracted by hybridization, most effectively in Fe(110) on W(110).

The *enhancement of* μ which is found in many monolayer systems, both in theory and in experiment, is in many cases associated with a *reduction in the magnitude of* B_{hf} *or* B_{co}. The magnitude of B_{hf} must therefore not be taken as a measure of μ in comparing atoms in different surroundings. The details of the calculations show that the reduction of B_{hf} comes from B_{cond}; it therefore changes sensitively with the substrate. B_{core}, on the other hand, is proportional to μ and insensitive to a change of the substrate.

The Ag-coated monolayer on W(110) is unique in that both moment and hyperfine field can be compared between theory and experiment. The experimental moment, determined by the extrapolation scheme given in fig. 48, shows some enhancement against its bulk value and is definitely higher than the theoretical value. The agreement in B_{hf} is excellent (a small error of Gradmann et al. 1989 is corrected). The tendency towards increasing hyperfine field by changing from Ag to Au as a contact material, which is theoretically predicted for the uncoated monolayers on Ag(100) and Au(100), is confirmed in the experimental films on W(110), coated by Ag or Au, respectively.

7.2. *Surface magnetization at low temperatures*

7.2.1. *Dead layers at Ni surfaces?*

The surface magnetization of Ni played a stimulating role in surface and thin film magnetism, since Liebermann et al. (1970) discussed the possibility of a nonmagnetic 'dead layer' on top of Ni films. Whereas it is now clear that these 'dead layers' were an artifact of the electrolytic preparation of Liebermann, this idea stimulated intense work on surface magnetism in Ni surfaces. For the case of the Ni(100) surface, first self-consistent band calculations of C. S. Wang and Freeman (1980) using the linearized augmented plane wave (LAPW) method of band-structure calculation (Krakauer et al. 1979) indicated a reduction of the first layer moment μ_1 by 20%, with some minor oscillating enhancement of μ_2 and μ_3. Band calculations of Jepsen et al. (1980, 1982) in turn predicted an enhancement of μ_1 by 5%, with only minor oscillations in the following layers. The improved version of LAPW, FLAPW (Wimmer et al. 1981) was applied later to the problem and resulted in an increase of μ_1 by 30%. Ni(100) was the first sample for a straightforward application of spin-polarized LEED to the analysis of surface magnetism, resulting in an enhancement of μ_1, extrapolated to $T = 0$, of $+5(5)\%$. The surface magnetization in Ni(100) differs only slightly from the bulk value. There are definitely no dead layers.

7.2.2. *Surface magnetization in Fe*

The surface magnetization of Fe was again pioneered by theory. Using FLAPW, enhancements of μ_1 by 32% for Fe(100) (Ohnishi et al. 1983) and by 19% for Fe(110) (Freeman and Fu 1986) were calculated. The latter enhancement was obtained with nearly the same strenght (20%) with tight-binding methods by Victora and Falicov (1984). However, experimental analysis using SPLEED by Tamura et al. (1990) strongly suggests an enhancement by 38(2)%. Considering this discrepancy, one might recall that the data of fig. 50 indicate an enhancement of the moment in Ag-coated Fe(110) films on W(110) by 41(14%) of a monolayer, distributed on both interfaces. Because Elmers and Gradmann (1988) showed that the moment change induced by an Ag coating is only a tiny increase by 1(3)% of a monolayer, the enhancement in the uncoated films is 40(15)%. The moment in the Fe/W interface can be expected to be reduced in comparison with the monolayer moment, which in turn is enhanced by 14%. This would suggest a surface moment enhanced by more than 26(14)%, in agreement with both the theoretical and the experimental value from SPLEED.

7.2.3. *Enhanced moment in steps on Fe(110)*

If the magnetic moment is enhanced for atoms in surfaces because of reduced magnetic coordination, it should be enhanced a fortiori for atoms in atomic steps or for single atoms on top of smooth surfaces. Albrecht et al. (1992a,b) recently checked this idea. They first coated Fe(110) films on W(110) by some additional atomic layers, at low temperatures, creating a rough surface, as seen by SPA-LEED. The density of atomic steps could be estimated with an accuracy of about 10%. By annealing, the surface could be smoothed, including a removal of the steps. By measuring the reduction of magnetic moment by in situ magnetometry, they could estimate the

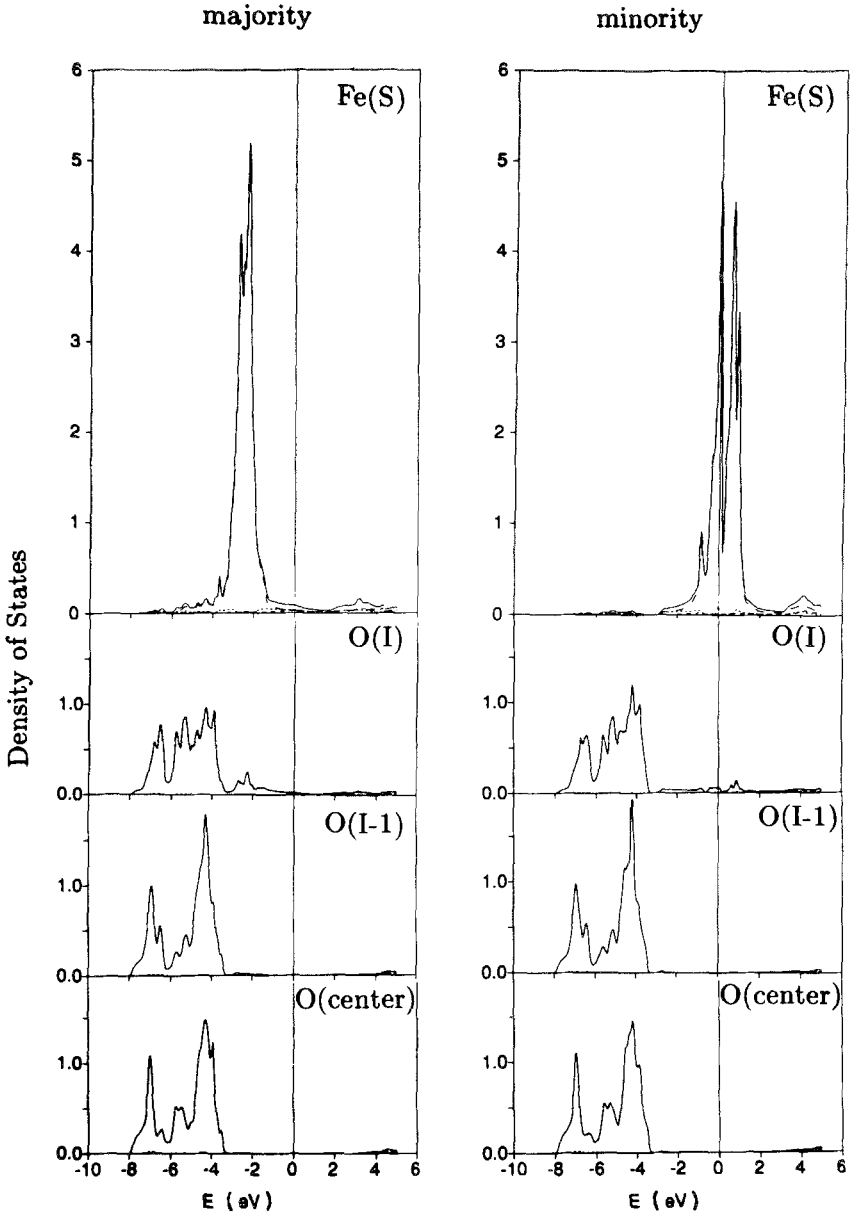

Fig. 54. Monolayer magnetism in Fe on MgO(100), from FLAPW calculations. (a) Layer-projected partial density of states of the conduction electrons in units of state/eV·atom for one monolayer Fe on MgO(100) (Fe above O-site). (b) As (a), but for the second and first of two atomic layers of Fe on Mg(100); Fe(S) and Fe(S − 1) represent surface and subsurface Fe layers, respectively, O(N) represents oxygen atoms in the Nth layer from the interface, O (center) one in the center of the slab (from C. Li and Freeman 1991).

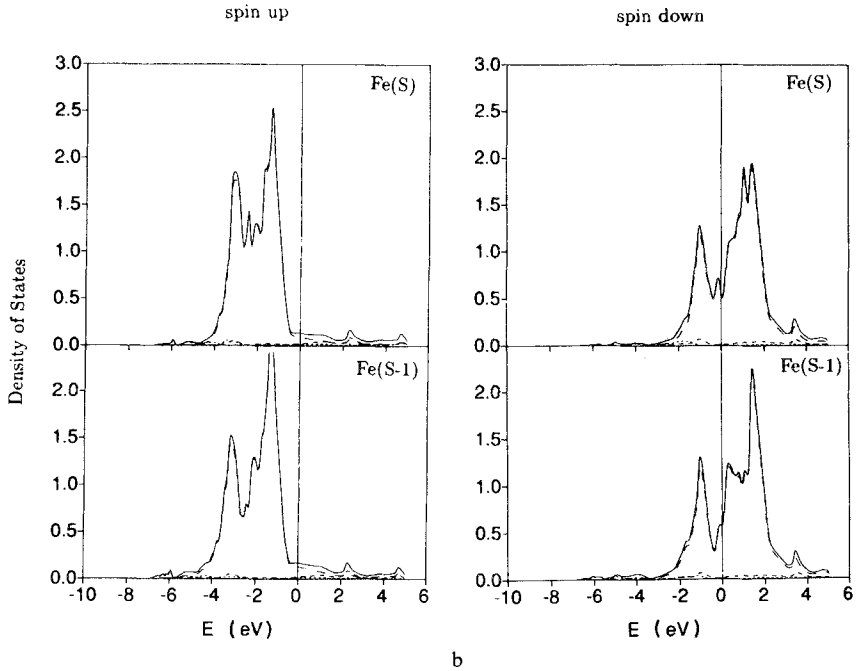

Fig. 54. (*continued*)

moment enhancement per step atom to be $1.1(4)\mu_B$. Because single atoms and kinks must be considered to contribute to the enhanced moment, too, this number must be taken as an upper limit for the moment enhancement in a step atom. The real value was very roughly estimated to be $0.7(4)\mu_B$. Albrecht et al. could explain this enhancement semiquantitatively using the theory of local moments as given by Anderson (1961) and generalized to degenerate states as described by Harrison (1984). This model results in a moment enhancement of $0.45\mu_B$ per step-atom, in fair agreement with the experiment.

7.2.4. Spatial oscillation of B_{hf} near the Fe surface

Ohnishi et al. (1984) predicted a spatial oscillation of B_{hf} near the Fe(100) surface, with a reduction in the first layer by about 25% and an enhancement of the same order in the second layer, resulting from an oscillating polarization of the conduction electrons. This in turn is a consequence of the simultaneous cut-off of the electron gas in real space at the surface, and in k-space at the Fermi edge. Consequently, the oscillation was predicted to disappear in a metal-coated Fe surface. Korecki and Gradmann (1986b) confirmed the oscillation for the case of Fe(110) using monolayer probe CEMS. As shown in fig. 55, the oscillation shows an amplitude of about 3%. The theoretical treatment of the phenomenon for the free surface by Fu and Freeman (1987) resulted in an amplitude of about 8%. Korecki and Gradmann (1986b) confirmed that the oscillation disappears in an Ag-coated surface. The magnetic moment does not oscillate at all.

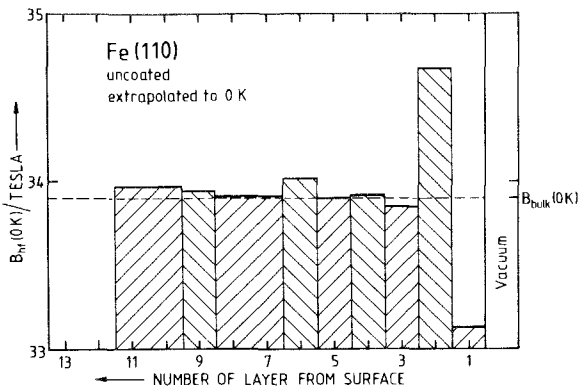

Fig. 55. Local oscillation of the ground-state magnetic hyperfine field $B_{hf}(0\,K)$ near the free Fe(110) surface (from Korecki and Gradmann 1986b).

7.2.5. Interface magnetization: Cu on Fe(110) and Ni(111)

Interface magnetization can be measured by following the magnetic moment of ultrathin films by magnetometry in situ during film growth and coverage (Bergholz and Gradmann 1984). A collection of results can be found in an article of Gradmann (1988). For example, it turns out that the change of magnetic moment of Fe(110) surface atoms induced by Cu or Ag is negligible ($< 1\%$, Elmers and Gradmann 1988). The situation is completely different for Cu on Ni(111) (Bergter et al. 1985). We explain the method using this example, for which comparison with theory was possible. Figure 56a shows the change in magnetic moment of a Ni(111) film on Re(0001), caused by a Cu coverage, versus the number of Cu layers, D_{Cu}, in units of the moment of one bulk monolayer Ni(111). A steep decrease caused by the first Cu layer is followed by a saturation at four Cu layers. Measurements were done at room temperature. The loss of magnetization therefore depends on the number of layers in the Ni film, D_{Ni}, as a result of some interplay with reduced T_c in the thinnest films, as shown in fig. 56b. The asymptotic value of 0.6 monolayer equivalents represents the effect at a bulk Ni(111) surface. Tersoff and Falicov (1983) calculated this decrease in a tight-binding approximation and obtained a reduction of 0.52 and 0.61 monolayer equivalents, caused by one or two layers of Cu, respectively. The agreement is surprisingly good. The connexion of the phenomenon with NiCu alloys is obvious: The basic phenomenon is the filling of d-holes in Ni by Cu conduction electrons. The absence of such an effect for Fe reflects the local character of the Fe moments.

7.2.6. Induced magnetization in Pd

It has been known for a long time that Ni and Fe impurities in the nearly ferromagnetic metal Pd from 'giant moments' (Aldred et al. 1970), consisting of a cluster of magnetized Pd around the central 3d-moment, with a correlation length of about 0.5 nm for the magnetization in Pd. It is reasonable to assume that the same type of induced magnetization in Pd occurs in Ni/Pd and Ni/Fe interfaces, as has been shown first

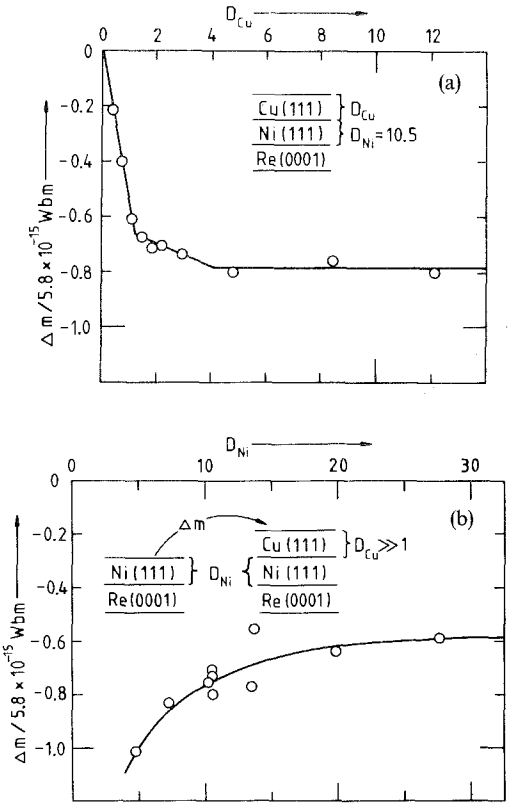

Fig. 56. Decrease of magnetic moment in a Ni(111) film induced by Cu coating. (a) Decrease $\bar{\Delta}m$, in units of the bulk monolayer moment of 5.8×10^{-15} Wb m, versus the number of coating Cu layers, D_{Cu}, for one special N(111) film consisting of $D_{Ni} = 10.5$ monolayers. (b) The saturation value from (a) versus D_{Ni} (from Bergter et al. 1985).

by Bergholz and Gradmann (1984) for the case of Pd(111) on Ni(111). Figure 57 shows the increase of magnetic moment per surface atom, in a 30-layer Ni(111) film on Re(0001), versus the number of coating Pd layers, D_{Pd}, as measured by magnetometry in situ during Pd coating. The full curve was calculated by Mathon (1986b) using a Landau–Ginzburg type theory. The theory contains two parameters. The first parameter is given by the correlation length of magnetization in Pd, which was taken from giant moments (0.5 nm). Obviously, the physics of the Pd magnetization is basically the same in giant moments and in interfaces. The second parameter is the strength of coupling, given by the saturation value of $0.5\mu_B$/atom, or alternatively by the initial slope of $0.1\mu_B$/atom, which gives the magnetic moment per Pd atom in the first monolayer. This coupling depends on the strain state of Pd. Bergholz and Gradmann measured the induced magnetization alternatively for epitaxial Pd(111) films on Re(0001), which were expanded in the plane by 0.3%, by pseudomorphic

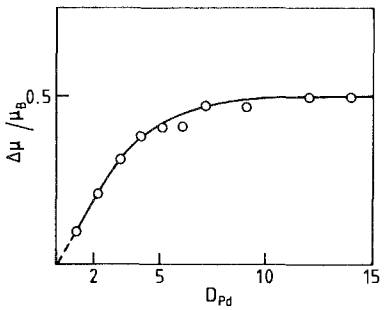

Fig. 57. Increase of magnetic moment in Ni(111) film on Re(0001), induced by Pd coating. Increase of magnetic moment per surface atom $\Delta\mu/\mu_B$ in units of Bohr magnetons, versus the number of coating atomic Pd layers D_{Pd}, as measured in situ by TOM, in comparison with a theoretical curve from Ginzburg–Landau theory (from Mathon 1988).

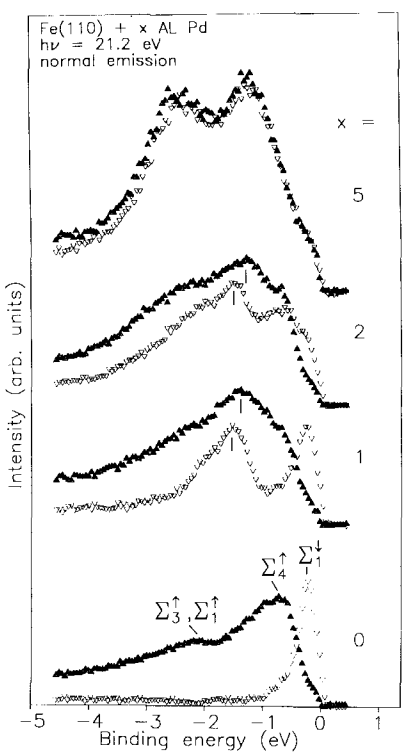

Fig. 58. Spin polarization in Pd(111) on Fe(110) from spin-polarized photoemission. Spin-resolved energy-distribution curves (solid or open symbols for majority or minority spin direction, respectively) for films consisting of x atomic layers of Pd(111), The indicated peak shift for $x = 1$ and $x = 2$ suggests negative spin polarization; Σ_n represents the symmetry of the state (from Weber et al. 1991).

growth on Re. By coating experiments with Ni, they concluded that there is an initial magnetization of Pd in the first monolayer of roughly $0.3\mu_B$/atom. These values for the induced moment in the first Pd layer on Ni(111) are in accordance with theoretical results of Bluegel et al. (1989), who calculated the moment in Pd(100), coated by one monolayer of Ni(100), and obtained 0.24 and $0.20\mu_B$ for the moment in the first and second Pd layer, respectively.

The same type of induced magnetization was detected also by Hillebrands et al. (1989) in Fe(110)/Pd(111) superlattices. It was analyzed more quantitatively by Celinski et al. (1990) in Fe(100)/Pd(100)/Fe(100) structures. As shown by RHEED, the Pd films were expanded in the plane by interaction with the Fe(100) substrate. Complete pseudomorphism with an expansion by the misfit of 5.1% was reported for films of up to eight layers. From detailed magnetic measurements using FMR and BLS, they concluded that there is a magnetic moment per Pd atom of $0.25\mu_B$, in agreement with Bluegel et al. (1989), who calculated $0.32\mu_B$ in the first layer of Pd(100) coated by a monolayer of Fe.

A direct verification of magnetization of Pd in Pd(111)/Fe(110) interfaces was given using spin-polarized photoelectron emission by Weber et al. (1991), who found a clear exchange splitting in a Pd-induced peak, as shown in fig. 58. The splitting disappears for five layers of Pd, in agreement with the observation of Celinski et al. (1990) that not more than four Pd layers are magnetized by Fe. The experiments of Bergholz and Gradmann (1984) on Ni indicate a slightly larger range of Pd polarization.

8. Magnetism of pseudomorphic films

In favourable cases, ultrathin epitaxial films can be grown pseudomorphically in the structure of the substrate, even when this deviates from the equilibrium structure of the bulk film material. These pseudomorphic films offer the unique possibility to study the physical properties of matter in unusual states. The chances to grow films in pseudomorphic phases are high if the binding energies in them differ only slightly from that in the equilibrium phases. Band calculations of Moruzzi et al. (1986) show that this is the case for fcc Fe, bcc Ni and bcc Co. Accordingly, pseudomorphic films of fcc Fe, bcc Co and bcc Ni have been prepared on appropriate substrates; their preparation and their magnetic properties are the subject of the present section.

It has been noted by Prinz (1985) that one might distinguish in epitaxial films between metastable phases and forced structures. For the first case, the presence of the deviating substrate structure depends on kinetic growth conditions which cause the film to grow in a metastable phase, that is in a state of local minimum of the free energy, which, however, is a little bit higher than in the equilibrium ground state. There is no basic limitation for the thickness of a true metastable film, which goes over to the ground state only after some nucleation, which in turn depends on defects and details of growth in an accidental manner. bcc Co on GaAs(110), to be discussed in the last part of this section, apparently provides an example of a true metastable phase. Forced structures, on the other hand, are stabilized by the mechanical interaction with the epitaxial substrate. Most pseudomorphic films apparently are more or

less of this second type. We therefore avoid to call these pseudomorphic films in general metastables, as has been done in the literature.

8.1. fcc γ-Fe

The most extended studies on magnetism in pseudomorphic films were done for fcc Fe-films on Cu. We start their discussion by a short report on magnetism in bulk fcc Fe, followed by sections on different types of γ-Fe films.

8.1.1. Magnetism in bulk fcc γ-Fe, fcc Fe-based alloys and γ-Fe precipitates in Cu

The fcc γ-phase of Fe exists only in the temperature range between 1183 and 1663 K. The paramagnetic susceptibility in this range follows a Curie–Weiss law with a negative Curie temperature, indicating antiferromagnetic interaction. γ-Fe particles with diameters up to 200 nm can be stabilized at room temperature by precipitation in Cu (Knappwost 1957). Particles with diameters above 2 nm are semicoherent with the Cu matrix, which means they accept the fcc structure of the matrix, but with an intrinsic lattice parameter of 0.359 nm (Newkirk 1957) which deviates slightly from $a_{Cu} = 0.3615$ nm. In agreement with the high-temperature susceptibility of the bulk phase, these precipitates are antiferromagnetic, as shown by neutron diffraction (Abrahams et al. 1962) and Mössbauer spectroscopy (Gonser et al. 1963), with a Néel temperature $T_N = 70$ K for large particles with a diameter of about 100 nm. Later, Tsunoda et al. (1988) showed that two states can be distinguished in these precipitates, γ-B and γ-C with diameters below 180 nm and above 120 nm, and with lattice parameters $a_{\gamma-B} = 0.3589$ nm and $a_{\gamma-C} = 0.3583$ nm, respectively, at room temperature. It

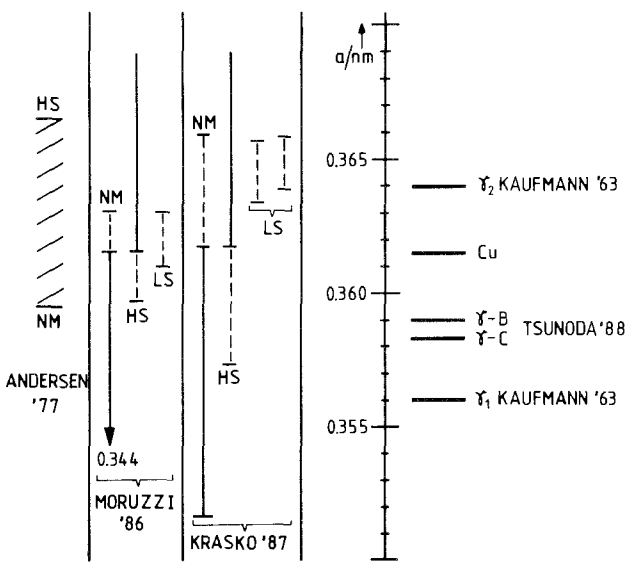

Fig. 59. Lattice parameters of different electronic states of fcc γ-Fe, as derived from experiments (left) or from band-structure calculations (right). Metastable nonmagnetic (NM), low-spin (LS) and high-spin (HS) states are indicated by broken lines, the stable ground state by a full line. For details see the main text.

is assumed that $a_{\gamma-C}$ is something like an intrinsic lattice parameter of 'bulk' γ-Fe. Very small γ-Fe particles in Cu ($d < 2$ nm) are coherent in the sense that they accept the lattice parameter of Cu, too. They are superparamagnetic (Berghout 1961, Window 1972). A visualization of the lattice parameters is shown in fig. 59.

A different approach to the magnetic state of γ-Fe was introduced by Kaufmann et al. (1963). Based on a thermodynamic analysis of the martensitic γ–α transition, they postulated the existence of two electronic states in fcc Fe, a low-volume ($a = 0.356$ nm), low-moment ($0.6\mu_B$) antiferromagnetic state γ_1 and a high-volume ($a = 0.364$ nm), high-moment ($2.8\mu_B$) ferromagnetic state γ_2. Weiss (1963) used this model of the two γ-states in his discussion of the Invar effect. This aspect of fcc Fe has been reviewed by Wassermann (1990).

The strong dependence of magnetic order in γ-Fe on the volume, contained in the Weiss model, has been modelled by several band calculations. In general, these are ground-state calculations which consider only nonmagnetic and ferromagnetic states. The antiferromagnetic state, which is observed in the precipitates, could not yet be modelled. Andersen et al. (1977), using canonical band theory, calculated the magnetic moment per Fe atom as a function of the lattice parameter and found a transition between a nonmagnetic state below 0.3595 nm to a high spin state ($2.6\mu_B$) above 0.3665 nm, cf. figs. 59 and 61. Moruzzi et al. (1986) used the local spin density approximation to calculate energies per atom, for fixed lattice parameters, as a function of

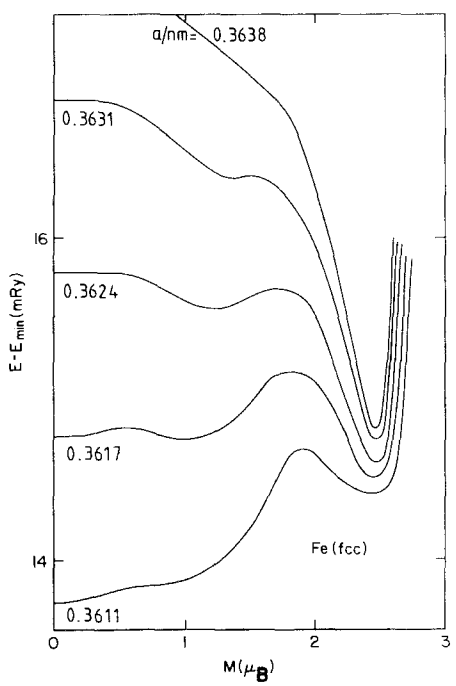

Fig. 60. Total energy E (relative to a minimum energy) versus magnetic moment, M, for fcc Fe at several values of the cubic lattice parameter a as parameter (from Moruzzi et al. 1986).

the magnetic moment ('fixed moment method', see also the chapter of Moruzzi and Marcus in this volume). Based on these calculations, they discussed magnetic phases for fixed lattice parameters. The results presented in fig. 60 show that for $a < 0.361$ nm the nonmagnetic state is stable, for $a > 0.362$ nm the high spin state ($2.5\mu_B$). In a very limited range of lattice parameters, a metastable low-spin state occurs which might be connected with the low-spin state of Weiss. Stability and metastability ranges of the magnetic states are indicated in fig. 59. It should be emphasized, however, that all calculations were done for constrained cubic lattice parameters and most structures therefore are unstable in the crystallographic sense. The crystalline ground state is nonmagnetic with a lattice parameter of 0.344 nm, well below the intrinsic parameter of the large precipitates (0.3583 nm). Finally, Krasko (1987) used a Stoner approach for calculations similar to that of Moruzzi et al. (1986) and refined the model by finding two separate metastable low-spin states, as shown in fig. 59. The crystalline ground-state lattice parameter is raised to 0.352 nm.

As seen in the overview in fig. 59, all theoretical models agree qualitatively with the experiments in predicting a transition from a nonmagnetic (antiferromagnetic) to a high-spin ferromagnetic state near the lattice parameter of Cu. The antiferromagnetic low-spin state of the large precipitates agrees with the theoretical models. The superparamagnetic properties of coherent small precipitates indicate that extended γ-Fe with the lattice parameter of Cu would be ferromagnetic, in accordance with the theoretical models.

8.1.2. Ferromagnetic γ-Fe films; general remarks

The isotropic expansion of the lattice parameter in fcc Fe beyond $a_{\gamma-C} = 0.3583$ nm in three dimensions, which forms the basis of the theoretical models, cannot be realized in experiment. What can be expected, as a consequence of the small misfit, $f_{\gamma-C/Cu} = -0.9\%$, of γ-Fe to Cu, is a two-dimensional coherence of the Fe films to the Cu substrate, up to a thickness of some ten atomic layers. This means isotropic expansion by 0.9% in two dimensions only. A Poisson-type contraction in the third dimension must be considered, which forms a clear difference to isotropic structural models of existing band models. In addition, this strict coherence can be expected in layer-grown films only, or in film structures consisting of very flat islands. Because the surface energy of Fe is larger than that of Cu (see section 2.1 and table 1), those films must be grown by forced layer growth, as has been described in section 2.2.

8.1.3. γ-Fe(110) films on Cu(110)

First evidence for ferromagnetism in γ-Fe films was reported by Wright (1971), who prepared Fe films electrolytically on Cu(110), detected ferromagnetic order and estimated the magnetic moment to $1.1\mu_B$/atom. Detailed structural analysis was not possible.

8.1.4. γ-Fe(111) films on Cu(111) and CuAu(111)

The first study on γ-Fe films prepared in UHV was performed by Kuemmerle and Gradmann (1977, 1978), using TOM ex situ at atmospheric pressures, for the case of Cu-coated films on Cu(111). The study was based on preparations in UHV by Grad-

mann and Tillmanns (1977), which included structural and growth-mode analysis using LEED and AES. The study included both very thin films up to four layers, prepared by forced layer growth at 20 and 100°C, and thicker films prepared at temperatures up to 400 K (the γ–α-transition, which starts below 1 nm at room temperatures, is shifted to about 50 nm at 400°C). All films were coherent with the Cu substrate. The AES data for the films prepared at higher temperatures, which were interpreted in terms of island growth, may have partially been caused by Cu segregation on top of flat Fe islands. This is indicated by a later LEED–AES study of Darici et al. (1988), who confirmed layer-by-layer growth at room temperatures, but found evidence for surface segregation of Cu at 473 K and higher temperatures. Microscopic interdiffusion is excluded by the phase diagram.

All γ-Fe(111) films on Cu(111) showed ferromagnetism with a common moment of 0.58(13)μ_B/atom at low temperatures. Curie temperatures of 350(50) K and 600(90) K for three and four layers, respectively, indicated a tentative T_c for 'bulk' γ-Fe of 900(300) K. Some of the very thinnest films below three layers showed perpendicular magnetization. A transition from in-plane to perpendicular magnetization with decreasing temperature was observed in one special film. Although the perpendicular magnetization was certainly caused by surface-type anisotropies, a straightforward analysis in those terms, including quantitative determination of surface anisotropies, was not possible because of the limited range of existence of the γ-phase in layer-grown films.

The experiments were extended by Gradmann and Isbert (1980) to γ-Fe(111) films on CuAu(111) films, the addition of Au to the Cu substrate introducing a lattice

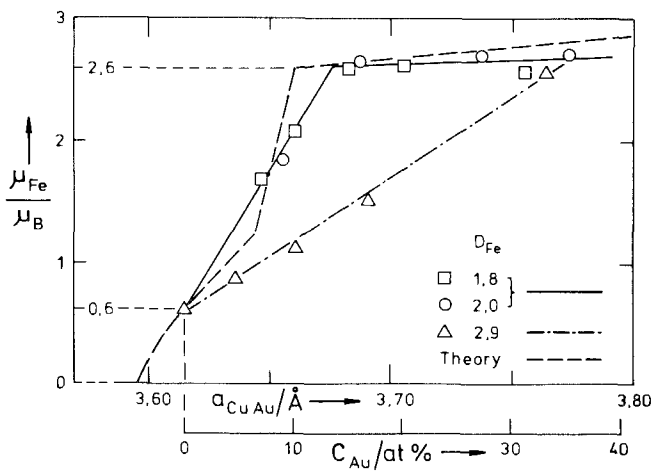

Fig. 61. Ferromagnetism in fcc Fe(111) films on CuAu(111). Magnetic moment per atom, μ_{Fe}, in the Fe film versus the mean lattice parameter a_{CuAu}, or Au concentration c_{Au} in the CuAu substrate. Full and dash–dotted lines are guides to the eye for films consisting of two or three layers, respectively. All films were magnetized perpendicularly. The dashed line gives a theoretical result from Andersen et al. (1977) for comparison (from Gradmann and Isbert 1980).

expansion. Layer-grown films only were investigated, consisting of two and three atomic layers; all of them showed perpendicular magnetization. Magnetic moments per atom are shown in fig. 61, versus Au concentration, c_{Au}, or the mean lattice parameter, respectively, which roughly followed Vegard's law, as confirmed by LEED. As expected, the moment rises steeply with increasing lattice parameter, from $0.6\mu_B$ on Cu to a saturation of $2.6\mu_B$, for lattice parameters which are different for the three-layer and the two-layer series, respectively. In view of this difference, the surprising quantitative agreement of the two-layer series with calculations of Andersen et al. (1977) seems to be fortuitous. Nevertheless, the basic phenomenon of increasing moment with increasing atomic distance is clearly confirmed, in semi-quantitative agreement with all theoretical models. The agreement is surprisingly good regarding the fact that a contraction along the surface normal, which could not yet be analyzed, must be considered, as a result of the in-plane expansion, forming a basic difference between the film structures and the isotropic models.

8.1.5. γ-Fe(100) films on Cu(100) and CuAu(100)

Extended structural studies have been performed on the initial stages of epitaxial growth for fcc Fe(100) on Cu(100), with conflicting results. Whereas Pescia et al. (1987b) claimed layer-by-layer growth at room temperature, starting with a pseudomorphic monolayer, Steigerwald and Egelhoff (1988) presented convincing evidence from angleresolved XPS against this growth mode, at room temperature. The controversy seems not to be clarified in detail. However, the following points might have been contributed: First, Pappas et al. (1991) have recently shown that the first kink in the Fe Auger amplitude of Fe on Cu can indicate the completion of a double layer rather than of a monolayer, in a similar way as discussed with fig. 8. Apparently, Pescia et al. (1987b) calibrated their film thickness using this first kink. The calibration therefore might have been in error. We further recall the message of fig. 8 that a kink in the Auger amplitude indicates some change in the growth process, which must not necessarily consist in the completion of a monolayer. Second we note that the growth mode in nonwetting systems like Fe on Cu is determined by the growth rate, in addition to the substrate temperature, as discussed in section 2.2. Because growth rates were not discussed in the controversy, their role remains open. Third, the bare existence of the controversy shows the sensitivity of the details of growth mode and film structure on growth conditions, in the monolayer regime of this system, just as expected for forced layer growth. We will discuss magnetic evidence on deviation from layer-by-layer growth below. Based on their careful growth analysis, Steigerwald and Egelhoff (1988) proposed a growth recipe for flat epitaxial films consisting of at least three atomic layers, which has been used since by several groups. It consists in depositing three monolayers at 100 K, to get a coherent film, with subsequent annealing to 345 K to achieve a smooth surface on a well-ordered film.

Different results have been reported for the maximum thickness, up to which the fcc structure can be retained. Whereas Pescia et al. (1987b) reported a limit of seven to eight layers, Darici et al. (1987) reported more than ten and Lu et al. (1989) even 18 layers. A complete report on the conflicting structural results can be found in the careful study by Lu et al. (1989). This study and its supplement by Jona and Marcus

(1989) provides in addition quantitative data on the relaxation of lattice-plane distances near the surface of 'thick' films consisting of 12 layers, which are in good agreement with earlier results from Darici et al. (1987). Jona and Marcus report layer distances $d_{bulk} = 0.177$ nm, $d_{12} = 0.184$ nm and $d_{23} = 0.176$ nm for the inner layers, between the first and the second and the second and the third one, respectively. These should be compared with the intrinsic parameter of the precipitates, $a_{\gamma-C}/2 = 0.1792$ nm, and with $a_{Cu}/2 = 0.1808$ nm. The following picture of the elastic state then evolves: In comparison with the large precipitates, the films are expanded in the plane by 0.9% and contracted along the surface normal by 1.2% which results only in a small increase of the volume of 0.6%. A remarkable result is the outward relaxation of the first monolayer by 3% withe respect to $a_{\gamma-C}/2$ or even 4% with respect to d_{bulk}. No other case of outward relaxation in fcc (100) surfaces is known; some connexion with the magnetic state is supposed.

To make the structural problems yet more complicated, Daum et al. (1988) observed reversible structural displacive phase transitions on films in the monolayer regime, which depend sensitively on the growth and vacuum conditions. They must be expected

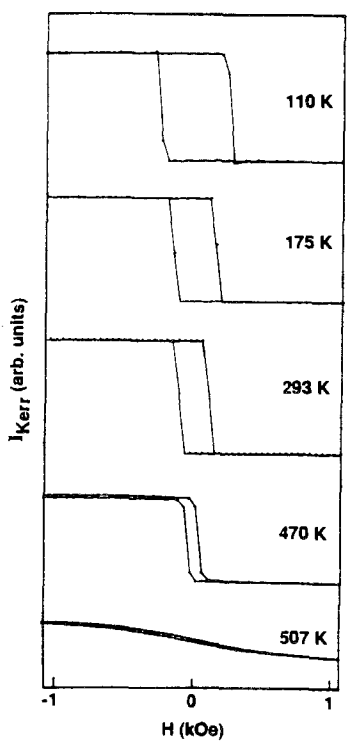

Fig. 62. Polar Kerr-effect hysteresis curves for 4.2 monolayers of fcc (100), grown on Cu(100) at 100 K. The data were taken at the indicated temperatures as the sample warmed up. The square loops indicate perpendicular magnetization (from Liu et al. 1988).

to influence the magnetic properties in a manner which has not yet been analyzed at all. As to the magnetic properties of γ-Fe(100) films on Cu(100), there is now general agreement that films prepared at 100 K are ferromagnetic at room temperature, with perpendicular magnetization up to roughly five atomic layers. This has been shown for the case of uncoated films by Liu et al. (1988), who observed, using MOKE, square loops in perpendicular fields, for films between 1.5 and 6 monolayers, as shown in figs. 62 and 63. For the 1.5 monolayer film, cf. fig. 63a, the magnetization loop taken at 106 K was changed by annealing at 240 K only. This shows the instability of these ultrathin film structures in the monolayer regime, which can be held layer-like only by forced layer growth at 100 K. For comparison, a film of four monolayers (fig. 63b) was stable up to 480 K, obviously because the energy barrier for recrystallization is too high at this thickness, in agreement with the structural investigations of Steigerwald and Egelhoff (1988). As a result of systematic variation of film thickness and growth temperatures, Liu et al. (1988) could present an overview for the conditions for observation of square hysteresis loops in a perpendicular field, which is shown in fig. 64. For large thicknesses, this regime of perpendicular square loop is limited, at six monolayers, by the switching to in-plane magnetization. At low thicknesses, it is limited by clustering in the film, which shifts to higher film thicknesses when increasing the temperature of preparation. Above 350 K, the preparation of perpendicularly magnetized films becomes impossible, apparently because of island formation.

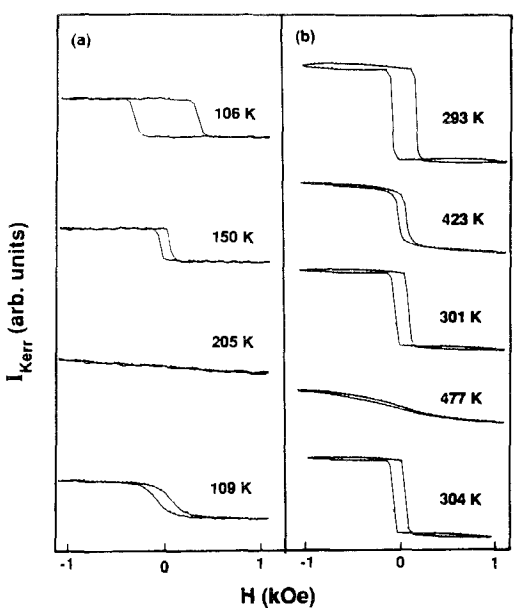

Fig. 63. Thermal cycles, from top to bottom, of polar Kerr-effect hysteresis loops taken from (a) 1.5 monolayers and (b) 4 monolayers fcc Fe on Cu(100), both prepared at 100 K. The low-temperature loop of the 1.5 monolayer film after warming up to 240 K indicates irreversible changes caused by intermixing (from Liu et al. 1988).

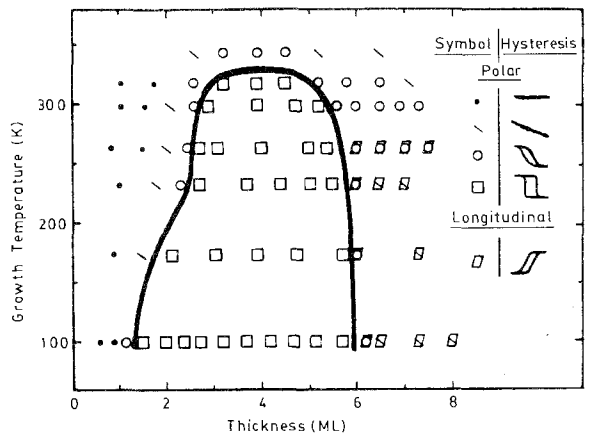

Fig. 64. The region of stability of perpendicular anisotropy for fcc Fe/Cu(100) outlined on a plot of film thickness versus growth temperature. The Kerr-effect measurements used to determine the stability boundaries were made at the growth temperature (from Liu et al. 1988).

In agreement with this experience with uncoated films, ferromagnetism with perpendicular magnetization has been confirmed for the case of Cu-coated films between three and five monolayers, prepared at 100 K, annealed and coated at room temperature, using BLS by Dutcher et al. (1989) and using FMR by Heinrich et al. (1988a). A review has been presented by Heinrich et al. (1989b). Further evidence for ferromagnetism in Cu-coated γ-Fe(100) films on Cu(100) comes from Mössbauer-work of Keune et al. (1989), who found ferromagnetism in a film of five layers, prepared at 36°C, with a hyperfine field of 35.2 T at 30 K, surprisingly near the low-temperature field of 34.9 T in bcc α-Fe, and in-plane magnetization. For comparison, Macedo and Keune (1988) found absence of ferromagnetism in their Mössbauer analysis of films prepared at 200°C, which behaved similar to medium-sized γ-Fe precipitates, in confirmation of earlier results in γ-Fe films prepared at elevated temperatures (Becker et al. 1985). This result fits to the finding that these γ-Fe films on Cu(100) are instable against island formation, at elevated temperatures, and can be prepared in a layered mode at room temperature or low temperatures only. There is only apparent contradiction with the work of Carbone et al. (1988), who could not detect remanent in-plane magnetization in films prepared at room temperature, using spin-resolved photoemission. As explained above in section 2.2, the mode of growth and resulting structure in nonwetting systems like Fe on Cu depends not only on the preparation temperature, but on the growth rate, too. The low growth rate of 0.1 nm/min, used by Carbone et al. (1988), favours island formation. Therefore their finding of absent in-plane remanent magnetization cannot be taken as a general property of fcc Fe films on Cu, but pertains to their own films only, with an unknown island structure.

The tendency to island formation at room temperature is reflected too in the early work of Pescia et al. (1987b), who detected magnetism and perpendicular magnetization, using spin-polarized photoemission, in films consisting of one, three and five monolayers, respectively, prepared at room temperature. The field dependence of the spin

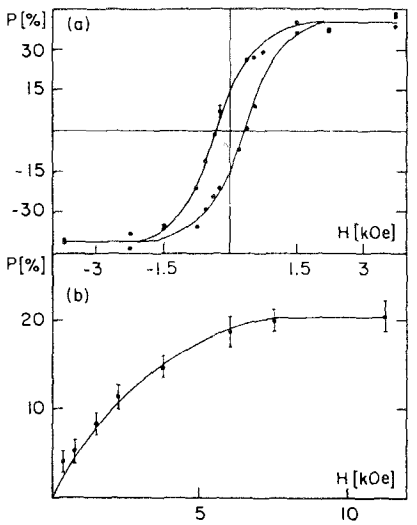

Fig. 65. Spin polarization, P, of photoelectrons from fcc Fe films on Cu(100) versus magnetic field, H, applied perpendicularly to the film plane, measured at $T = 30$ K. The film consists of (a) three monolayers, (b) one monolayer (from Pescia et al. 1987b).

polarization, P, for the monolayer, as shown in fig. 65, clearly shows superparamagnetic features, even at 30 K, and therefore indicates island structure. The five-monolayer film, which was magnetically stable at 30 K, showed superparamagnetic behaviour (not interpreted there in those terms), for temperatures above 215 K. The experience from fig. 64 that films prepared at room temperature are on the border between island and layer growth, even at five monolayers, is confirmed.

Films of γ-Fe on $Cu_3Au(100)$, prepared at room temperature, were measured using spin-resolved photoemission by Carbone et al. (1988), who found an extraordinarily high spin polarization of $> 50\%$, and using Mössbauer spectroscopy by Keune et al. (1989), who found an enhancement of B_{hf} in comparison with the films on Cu. Both results are in agreement with theoretical predictions on enhanced moments in expanded γ-Fe, as discussed in section 8.1.1, and with the magnetometric work of Gradmann and Isbert (1980) on γ-Fe(111) on CuAu(111), described in section 8.1.4.

Magnetic moments have not yet been measured for γ-Fe(100) films.

8.1.6. Concluding remarks on γ-Fe films

It should have become clear that epitaxial γ-Fe films and magnetic order in them are characterized by an extraordinarily rich variety of instabilities or metastabilities:

(1) fcc γ-Fe is instable in bulk and can be stabilized only as thin film or as precipitate.

(2) Layered γ-Fe films on Cu are metastable; they can be grown at room temperature or lowered temperatures only by forced layer growth and recrystallize to island structures when annealed.

(3) Films in the monolayer regime show displacive reconstructions, which depend sensitively on the surface conditions.

(4) Magnetic order depends sensitively on lattice parameters.

(5) Competition of shape anisotropy and surface-type perpendicular anisotropies induce an instability of the magnetization direction near five monolayers, for fcc Fe(100), and for a little bit thinner films for (111).

Having in mind all these instabilities and their complicated interplay, and in addition a sensitive dependence on structural defects of any kind, one cannot be surprised on the apparently contradictory results. Magnetic properties depend sensitively on structural details, which are not known. A quantitative experimental treatment of this tricky problem is certainly difficult.

In comparing films in (100) and (111) orientation, we note two points of interest: First, it is clear that neither (111) nor (100) films are strictly speaking fcc, the first showing hexagonal, the second ones tetragonal distortion. However, (111) films show the clearer symmetric distinction from bcc α-Fe, which can be described as a special case of a tetragonal, but not of a hexagonal lattice. In other words, the square net is a building block of both fcc (100) and bcc (100), whereas the hexagonal net of densely packed spheres is a building block of fcc (111) only, but not of bcc in any orientation. It is unknown whether this has implications on magnetic order in both orientations. Second, the densely packed orientation (111) seems to show more tendency to flat island formation, or even to forced layer structures, than the more open orientation (100). We suppose that the possibility to stabilize γ-Fe(111) films up to a thickness of 40 layers, at temperatures of 400°C, is connected with these two points in some way, which certainly remains to be clarified in detail.

8.2. bcc Co

bcc Co grown as pseudomorphic films on GaAs(110) has been reported by Prinz (1985). The cubic nature of the films, which was initially inferred from RHEED and the symmetry properties investigated by magnetometry and FMR by Prinz (1985), has been unequivocally confirmed by Idzerda et al. (1989) using a modification of EXAFS. In the latter method the near-edge absorption of X-rays is detected by the subsequent emission of Auger-electrons ('conversion-electron X-ray absorption fine structure', to be clearly distinguished from CEMS, where nuclear energy is converted to the emitted electron). The possibility to grow bcc Co films as thick as 36 nm, and the strong dependence of the transition to hcp Co on details of preparation indicates a really metastable structure. This agrees with the extremely small energy difference of 0.03 eV/atom between the bcc and the more stable fcc phase, as calculated by Min et al. (1986) for bulk bcc Co. References to previous band calculations, including the first calculation of bcc Co by Bagayoko et al. (1983), are given by J. I. Lee et al. (1986), who performed calculations for ultrathin film slabs of bcc Co(100) using the FLAPW method. This led to a magnetic moment of $1.76\mu_B$ in the center, enhanced by 10% to $1.94\mu_B$ in the free surface, the bulk value being in agreement with the result of other theoretical work. The experimental value of $1.53\mu_B$ per atom, as determined using vibrating sample magnetometry by Prinz (1985) is definitely lower, the cause of the difference is not clear. Band calculations show a band structure of bcc Co which is very similar to that of bcc Fe, except that bcc Co seems to be a strong

ferromagnet (nearly no majority d-holes). Spin-polarized photoemission experiments by Prinz et al. (1985) are in agreement with this theoretical picture.

8.3. bcc Ni

bcc Ni was first discussed theoretically by Moruzzi et al. (1986) who found a nonmagnetic ground state of bcc Ni, only 50 meV above the magnetic ground state of the stable fcc Ni, with a lattice parameter of 0.277 nm, 2.5% below that of Fe (0.287 nm). According to this theoretical work, an expansion by 1.4% to 0.281 nm would induce the inset to weak ferromagnetic order, with a saturation moment of about $0.5\mu_B$ at the lattice parameter of Fe, bearing some similarity to the behaviour of fcc Fe. bcc Ni has been prepared first by Heinrich et al. (1987) on Fe(100) surfaces. Wang et al. (1987), using quantitative LEED analysis, showed that roughly five layers of bcc Ni grow pseudomorphically on Fe(100), with the same lattice constant and multilayer relaxations as in the Fe(100) substrate. However, thicker films show a complicated structure that is neither bcc nor fcc. In a careful and extended study of Ni/Fe bilayers on Ag(100), Heinrich et al. (1988b) confirmed these structural findings. However, in contrast to the theory of Moruzzi et al. (1986), they found strong indication on a by 2% compressed state of the first five pseudomorphic Ni layers on Fe(100). Of course, the separation of the magnetic properties of Ni from that of the ferromagnetic Fe substrate is difficult. As a result of a careful analysis of FMR and BLS measurements on the bilayers, Heinrich et al. (1988b) "concluded tentatively that the pure unreconstructed bcc Ni is nonmagnetic, even at the temperatures of liquid nitrogen".

9. Indirect coupling and magnetoresistance in magnetic film systems

During the writing of this review, which concerns mainly intrinsic single film properties, indirect coupling and magnetoresistance pheomena in film systems became a rapidly developing field, which certainly needs a subsequent special review article. Whereas a full report on the subject is out of the scope of this review, we give a short sketch in the following section and refer the interested reader to the original articles for full information.

The interest in an indirect coupling between two ferromagnetic layers by an interlayer of nonmagnetic material goes back to the 1960s, when Bruyere et al. (1964) searched for an oscillating coupling, changing between ferro- and antiferromagnetic as a function of interlayer thickness, but found ferromagnetic coupling only. Because direct coupling through ferromagnetic bridges could not be excluded, the indirect nature of the coupling remained uncertain.

An antiferromagnetic coupling, the indirect nature of which is unequivocal, could first be established by Gruenberg et al. (1986) in (100)-oriented Fe/Cr/Fe sandwiches, using Brillouin light scattering (BLS). Binasch et al. (1989) showed that the antiferromagnetic orientation of the two coupled Fe layers results in an enhanced electrical resistance of the sandwich, which disappears when both films are forced to be magnetized parallel by an external field. Apparently, a specific scattering mechanism is connected with the change of conduction electrons between the majority and minority

spin systems, respectively. The resulting magnetoresistance in film systems is not restricted to the case of antiferromagnetically coupled layers, because it is based primarily on the existence of antiparallel magnetized neighbouring layers. Accordingly, enhanced magnetoresistance had been observed before by Velu et al. (1988) in uncoupled Co/Au/Co sandwiches, where peaking resistance was found near the coercivity, the antiparallel orientation of adjacent layers being caused by separate magnetization reversal. In addition, Dieny et al. (1991) observed magnetoresistance as a result of antiparallel magnetization of neighbouring magnetic layers, without antiparallel coupling, in what they called spin-valve structures. Basically, these consist of two ferromagnetic films, separated by a nonmagnetic, noncoupling interlayer. One of the magnetic layers is in contact with a thick antiferromagnetic layer and therefore shows exchange anisotropy (Meiklejohn and Bean 1956, Schlenker et al. 1986), which means a shifted hysteresis loop, caused by exchange interaction with the antiferromagnetic substrate. Accordingly, both films can be switched separately by an external field, and the magnetoresistance with it.

An amplification of the magnetoresistance in indirectly antiferromagnetically coupled systems by use of multilayers was achieved by Baibich et al. (1988), who observed in (100)-oriented Fe/Cr multilayers changes of the resistance of nearly 50%, at low temperatures, as shown in fig. 66.

Obviously, magnetoresistance provides an easy method to distinguish, in appropriate superlattices, between antiferromagnetic coupling, where magnetoresistance is observed, and ferromagnetic coupling, where it disappears. This method has been applied by Parkin et al. (1990) for the analysis of exchange coupling in Co/Ru, Co/Cr and Fe/Cr superlattices, prepared by sputtering of Si(111) substrates. They combined the magnetoresistance method with an alternative analysis by measuring magnetization curves

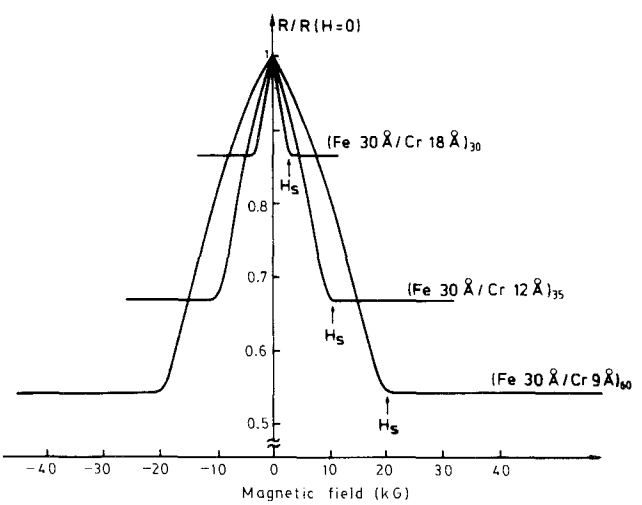

Fig. 66. Magnetoresistance $R/R(H)$ of three Fe(100)/Cr(100) superlattices at 4.2 K. The current and the applied field are along the same [011] axis in the plane of the sample (from Baibich et al. 1988).

and concluded to the strength of the coupling from the field needed to saturate the sample, which means the strength needed to make the moments of adjacent magnetic layers parallel. Results are shown in fig. 67 for Co/Ru and Fe/Cr superlattices. An oscillating character of the coupling was clearly established, for the first time, in these experiments. Note that the initial coupling for very thin interlayers is antiferromagnetic for the case of Ru, but ferromagnetic for the case of Cr. The method of Parkin is time-consuming because each point requires a separate sample to be prepared. The strength of the coupling can be determined in the antiferromagnetic regimes only. Coupling energies as large as $-5\,\mathrm{erg/cm^2}$ were observed for the case of a 0.3 nm thick Ru interlayer.

The alternative analysis of the indirect coupling in triple-layer sandwiches using BLS has two advantages: It enables the measurement of the coupling both in the ferro- and the antiferromagnetic regime, and it provides local resolution in the limits of the diameter of the reflected laser beam. Gruenberg et al. (1991) took advantage of this local resolution by using BLS and Fe/Cr/Fe sandwiches with Cr wedges for the analysis of the indirect coupling. The dependence of the interlayer coupling on

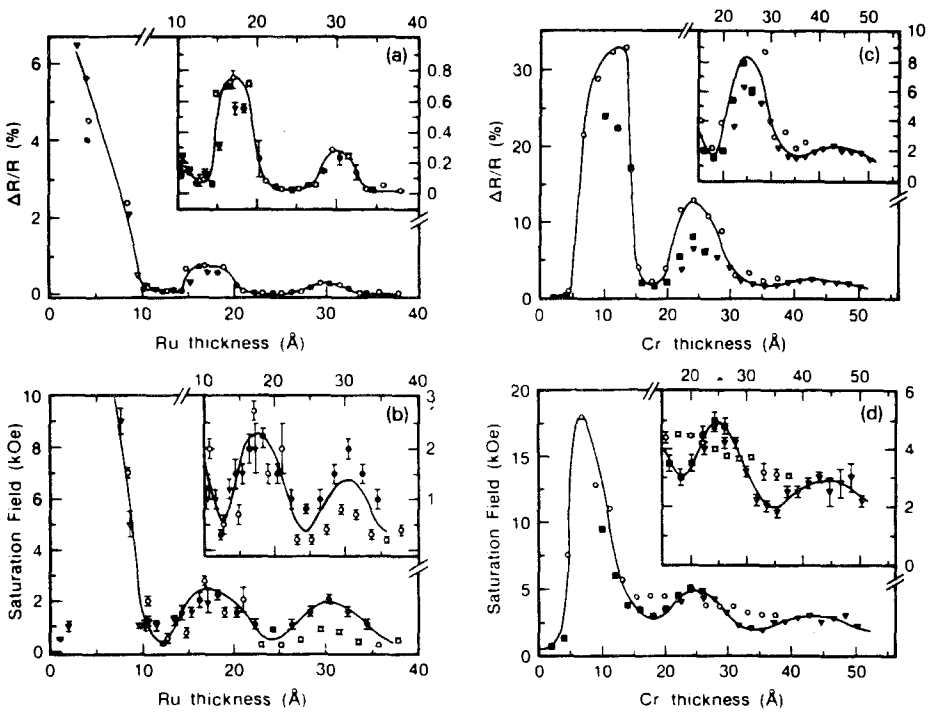

Fig. 67. Oscillations in transverse saturation magnetoresistance $\Delta R/R$ (a, c), measured at 4 K, and in the exchange coupling, as measured at 300 K by the saturation field of in-plane hysteresis loops (b, d) both versus the thickness of Ru or Cr interlayers, for sputtered superlattice structures on Si(111) of the form [20 Å Co/t Å Ru] × N (a, c) or [20 Å Fe/t Å Cr] × N (b, d). Different symbols represent different temperatures of preparation (from Parkin et al. 1990).

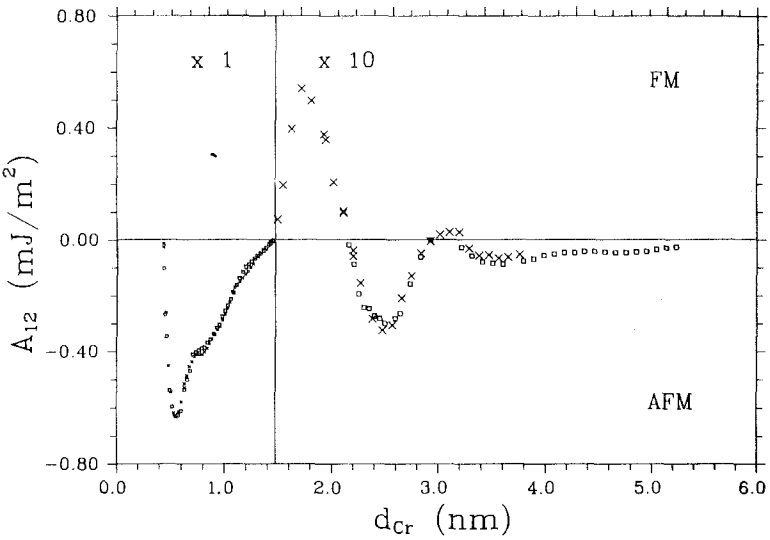

Fig. 68. Interlayer coupling constant A_{12} for sandwich structures of the form [5 nm Fe(100)/d_{Cr} Cr(100)/5 nm Fe(100)], determined by BLS (×) or from hysteresis loops (□) (from Gruenberg et al. 1991).

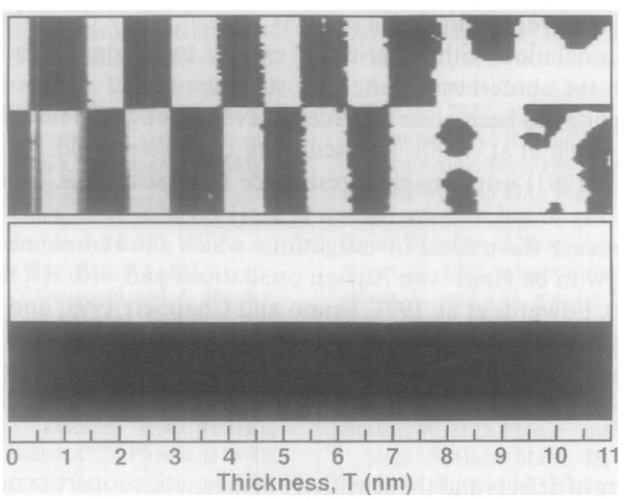

Fig. 69. Oscillating indirect coupling in Fe(100)/Cr(100)/Fe(100) structures on a Fe whisker, observed by SEMPA. Lower panel is taken from the clean whisker surface. Two domains, magnetized antiparallel along the horizontal axis, are seen. The upper panel is from a Fe/Cr/Fe sandwich including a Cr wedge of thickness T. Each image represents a region 490 × 280 μm^2 (from Unguris et al. 1991).

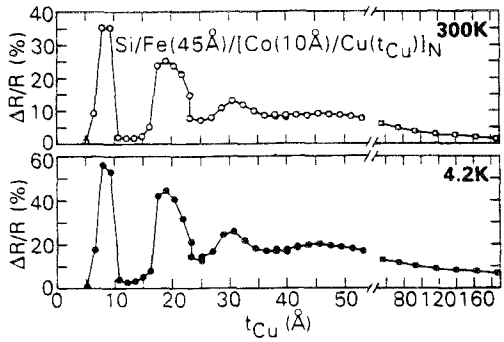

Fig. 70. Saturation transverse magnetoresistance in sputtered Co/Cu superlattices of the form [1 nm Co/t_{Cu} Cu] × N, versus t_{Cu}, measured at 300 and at 4.2 K, respectively (from Parkin et al. 1991).

the thickness of a Cr interlayer found by these authors is shown in fig. 68. The oscillating character was clearly confirmed, up to 3 nm interlayer thickness. Further detailed insight in the couplings was achieved by Ruehrig et al. (1991), who observed the domain structures in these wedge preparations using magneto-optical Kerr microscopy. In particular, the oscillating character of the coupling could be visualized. Finally, Unguris et al. (1991) analyzed the oscillating coupling between two Fe(100) layers by a wedge-shaped Cr spacer using scanning electron microscopy with polarization analysis (SEMPA). Using an Fe whisker as a substrate of their preparations, they could improve the quality of the sandwich structures and therefore observe up to six oscillations for Cr thicknesses up to 10 nm, as shown in fig. 69 for a sample prepared at room temperature. By using elevated preparation temperatures, they could further improve the film structure. As a result, they then observed a further superimposed oscillation with a period of exactly two monolayers Cr(100), in fine agreement with the antiferromagnetic spin structure of Cr.

Indirect coupling has been observed recently even through Cu interlayers (Cebollada et al. 1989, Heinrich et al. 1990). Its oscillating character could again be confirmed by Parkin et al. (1991) using magnetoresistance in superlattices, as shown in fig. 70, and independently found also by Mosca et al. (1991).

Despite of intense theoretical investigations which showed connections of the indirect coupling with de Haas–van Alphen oscillations and with RKKY-coupling (see Hasegawa 1990, Edwards et al. 1991, Bruno and Chappert 1991, and references given there), our understanding of the phenomenon is yet incomplete.

10. Conclusions

The high density of defects and the sensitivity of magnetic properties on them, resulting in a broad variety of magnetic film phenomena, infers part of the attraction of magnetic thin films. In stressing intrinsic magnetic thin film phenomena in the present review, we found that even in the best prepared film structures incompletely known structural details influence the magnetic properties in an essential manner. Whereas the main

lines of intrinsic magnetic film phenomena, like the temperature dependence of magnetic order with film thickness as parameter, are now basically understood, the detailed understanding of magnetic properties therefore requires a more detailed understanding of atomistic film structures, in particular in the ultrathin film regime. High-resolution diffraction and microscopical methods, which became available during the last years, will promote the progress towards a straightforward understanding of magnetic film phenomena in well defined film structures, based on a full atomistic structural analysis. Recently discovered coupling phenomena open up a new complexity of magnetic film phenomena, fascinating by their basic physical aspects and interesting for applications. Ultrathin magnetic films remain a promising field for future research.

Acknowledgments

The main part of the manuscript was written during a stay as a Visiting Professor at Stanford University, Department of Material Science and Engineering, under the auspices of the Volkswagen Stiftung. The author would like to thank the Department for its hospitality, the Volkswagen Stiftung for its generous support, Robert White for critically reading part of the manuscript, and Bruce Clemens, Michael Farle and Walter Harrison for fruitful discussions.

References

Abrahams, S.C., L. Guttmann and J.S. Kasper, 1962, Phys. Rev. **127**, 2052.

Albrecht, M., and U. Gradmann, 1993, to be published.

Albrecht, M., U. Gradmann, Th. Reinert and L. Fritsche, 1991, Solid State Commun. **78**, 671.

Albrecht, M., U. Gradmann, T. Furubayashi and W.A. Harrison, 1992a, Europhys. Lett. **20**, 65.

Albrecht, M., T. Furubayashi, U. Gradmann and W.A. Harrison, 1992b, J. Magn. & Magn. Mater. **104–107**, 1699.

Aldred, A.T., B.D. Rainford and M.W. Stringfellow, 1970, Phys. Rev. Lett. **24**, 897.

Allan, G.A.T., 1970, Phys. Rev. B **1**, 352.

Allenspach, R., M. Stampanoni and A. Bischof, 1990, Phys. Rev. Lett. **65**, 3344.

Altman, M.S., H. Pinkvos, J. Hurst, H. Poppa, G. Marx and E. Bauer, 1991, Mater. Res. Soc. Symp. Proc. **232**, 125.

Andersen, O.K., J. Madsen, U.K. Poulsen, O. Jepsen and J. Kollar, 1977, Physica B **86-88**, 249.

Anderson, P.W., 1961, Phys. Rev. **124**, 41.

Argyle, B.E., S.H. Charap and E.W. Pugh, 1963, Phys. Rev. **132**, 2051.

Bader, S.D., and E.R. Moog, 1987, J. Appl. Phys. **61**, 3729.

Bader, S.D., E.R. Moog and P. Gruenberg, 1986, J. Magn. & Magn. Mater. **53**, L295.

Bagayoko, D., A. Ziegler and J. Callaway, 1983, Phys. Rev. B **27**, 7064.

Baibich, M.N., J.M. Broto, A. Fert, F. Nguyen Van Dau, F. Petroff, P. Etienne, G. Creuzet, A. Friederich and J. Chazelas, 1988, Phys. Rev. Lett. **61**, 2472.

Ballentine, C.A., R.L. Fink, J. Araya-Pochet and J.L. Erskine, 1990, Phys. Rev. B **41**, 2631.

Bander, M., and D.L. Mills, 1988, Phys. Rev. B **43**, 11527.

Bauer, E., 1958, Z. Kristallogr. **110**, 37.

Bauer, E., 1991, private communication.

Bauer, E., and J.H. van der Merwe, 1986, Phys. Rev. B **33**, 3567.

Baumgart, P., B. Hillebrands and G. Güntherodt, 1991, J. Magn. & Magn. Mater. **93**, 325.

Bayreuther, G., 1990, private communication.

Becker, W., H.D. Pfannes and W. Keune, 1985, J. Magn. & Magn. Mater. **35**, 55.

Bergholz, R., and U. Gradmann, 1984, J. Magn. & Magn. Mater. **45**, 389.

Berghout, C., 1961, Z. Metallkd. **52**, 179.

Bergter, E., U. Gradmann and R. Bergholz, 1985, Solid State Commun. **53**, 565.

Binasch, G., P. Gruenberg, F. Saurenbach and

W. Zinn, 1989, Phys. Rev. B **39**, 4828.
Binder, K., and P.C. Hohenberg, 1976, IEEE Trans. Magn. **MAG-12**, 66.
Bland, J.A.C., and R.F. Willis, 1987, in: Thin Film Growth Techniques for Low-Dimensional Structures, eds R.F.C. Farrow, S.S.P. Parkin, F.J. Dobson, J.H. Neave and A.S. Arrott (Plenum Press, New York) p. 405.
Bland, J.A.C., A.D. Johnson, C. Norris and H.J. Lauter, 1990, J. Appl. Phys. **67**, 5397.
Bloch, F., 1930, Z. Phys. **61**, 206.
Bluegel, S., B. Drittler, R. Zeller and P.H. Dederichs, 1989, Appl. Phys. A **49**, 547.
Brodkorb, W., and W. Haubenreisser, 1966, Phys. Status Solidi **16**, 225, 577.
Bruno, P., 1988, J. Phys. F **18**, 1291.
Bruno, P., and C. Chappert, 1991, Phys. Rev. Lett. **67**, 1602.
Bruno, P., and J.-P. Renard, 1989, Appl. Phys. A **49**, 499.
Bruyere, J.C., O. Massenet, R. Montmory and L. Néel, 1964, C.R. Acad. Sci. Paris **258**, 1423.
Butler, M.A., G.K. Wertheim and D.N.E. Buchanan, 1972, Phys. Rev. B **5**, 990.
Carbone, C., G.S. Sohal and E. Kisker, 1988, J. Appl. Phys. **63**, 3499.
Carcia, P.F., 1988, J. Appl. Phys. **63**, 5066.
Carcia, P.F., A.D. Meinhaldt and A. Suna, 1985, Appl. Phys. Lett. **47**, 178.
Carcia, P.F., W.B. Zeper and F.J.A.M. Greidanus, 1989, Mater. Res. Soc. Symp. Proc. **150**, 115.
Cargill, G.S., 1989, in: Growth, Characterization and Properties of Ultra thin Magnetic Films and Multilayers, eds B.T. Jonker, J.P. Heremans and E.E. Marinero, Mater. Res. Soc. Symp. Proc. **151**, p. 231.
Cebollada, A., J.L. Martinez, J.M. Gallego, J.J. de Miguel, R. Miranda, S. Ferrer, F. Batallan, G. Fillion and J.P. Rebouillat, 1989, Phys. Rev. B **39**, 9726.
Celinski, Z., B. Heinrich, J.F. Cochran, W.B. Muir and A.S. Arrott, 1990, Phys. Rev. Lett. **65**, 1156.
Chappert, C., and P. Bruno, 1988, J. Appl. Phys. **64**, 5736.
Chappert, C., K. Le Dang, P. Beauvillain, H. Hurdequint and D. Renard, 1986, Phys. Rev. B **34**, 3192.
Cochran, J.F., B. Heinrich, A.S. Arrott, K.B. Urquhart, J.R. Dutcher and S.T. Purcell, 1988, J. de Physique C **8**, 1671.
Cohen, P.I., G.S. Petrich, P.R. Pukite, G.J. Whaley and A.S. Arrott, 1989, Surf. Sci. **216**, 222.
Daalderop, G.H.O., P.J. Kelly and M.F.H. Schuurmans, 1990, Phys. Rev. B **42**, 7270.
Darici, Y., J. Marcano, H. Min and P.A. Montano, 1987, Surf. Sci. **182**, 477.
Darici, Y., J. Marcano, H. Min and P.A. Montano, 1988, Surf. Sci. **195**, 566.
Daum, W., C. Stuhlmann and H. Ibach, 1988, Phys. Rev. Lett. **60**, 2741.
Davis, J.A., 1965, J. Appl. Phys. **36**, 3520.
de Miguel, J.J., A. Cebollada, J.M. Gallego, S. Ferror, R. Miranda, C.M. Schneider, P. Bressler, J. Garbe, K. Bethke and J. Kirschner, 1989, Surf. Sci. **211/212**, 732.
den Broeder, F.J.A., D. Kuiper, A.P. van de Mosselaer and W. Hoving, 1988, Phys. Rev. Lett. **60**, 2769.
den Broeder, F.J.A., D. Kuiper, H.C. Donkersloot and W. Hoving, 1989, Appl. Phys. A **49**, 507.
Dieny, B., V.S. Speriosu, S. Metin, S.S.P. Parkin, B.A. Gurney, P. Baumgart and D.R. Wilhoit, 1991, J. Appl. Phys. **69**, 4792.
Doering, W., 1961, Z. Naturforsch. Teil A **16a**, 1008, 1146.
Domb, C., 1973, J. Phys. A **6**, 1296.
Draaisma, H.J.G., and W.J.M. de Jonge, 1987, J. Appl. Phys. **62**, 3318.
Draaisma, H.J.G., and W.J.M. de Jonge, 1988, J. Appl. Phys. **64**, 3610.
Draaisma, H.J.G., F.J.A. den Broeder and W.J.M. de Jonge, 1988, J. Appl. Phys. **63**, 3479.
Duerr, W., M. Taborelli, O. Paul, R. Germar, W. Gudat, D. Pescia and M. Landolt, 1989, Phys. Rev. Lett. **62**, 206.
Dutcher, J.R., J.F. Cochran, B. Heinrich and A.S. Arrott, 1988, J. Appl. Phys. **64**, 6095.
Dutcher, J.R., J.F. Cochran, I. Jacob and W.F. Egelhoff Jr, 1989, Phys. Rev. B **39**, 10430.
Edwards, D.M., J. Mathon, R.B. Muniz and M.S. Phan, 1991, Phys. Rev. Lett. **67**, 493.
Egelhoff Jr, W.F., 1990, Crit. Rev. Solid State Mater. Sci. **16**, 213.
Elmers, H.J., 1989, Ph.D. Thesis (Clausthal).
Elmers, H.J., and U. Gradmann, 1988, J. Appl. Phys. **64**, 5328.
Elmers, H.J., and U. Gradmann, 1990, Appl. Phys. A **51**, 255.
Elmers, H.J., G. Liu and U. Gradmann, 1989, Phys. Rev. Lett. **63**, 566.
Ertl, G., 1986, Low Energy Electrons and Surface Chemistry, Verlag Chemie, Weinheim.
Falicov, L.M., and J.L. Moran-Lopez, eds, 1986, Magnetic Properties of Low-Dimensional Systems (Springer, Berlin).
Falicov, L.M., F. Mejia-Lira and J.L. Moran-Lopez, ed., 1990, Magnetic Properties of Low-Dimensional Systems II (Springer, Berlin).

Farrow, R.F.C., S.S.P. Parkin, P.J. Dobson, J.H. Neave and A.S. Arrott, eds., 1987, Thin Film Growth Techniques for Low-Dimensional Structures (Plenum Press, New York).
Feder, R., ed., 1985, Spin Polarized Electrons in Surface Physics (World Scientific, Singapore).
Feder, R., S.F. Alvarado, E. Tamura and E. Kisker, 1983, Surf. Sci. **127**, 83.
Flanders, P.J., 1988, J. Appl. Phys. **63**, 3940.
Foner, S., 1959, Rev. Sci. Instrum. **30**, 548.
Foner, S., 1975, Rev. Sci. Instrum. **46**, 1425.
Foner, S., 1976, Rev. Sci. Instrum. **47**, 520.
Frank, F.C., and J.H. van der Merwe, 1949, Proc. R. Soc. A **198**, 205, 216.
Freeman, A.J., and C.L. Fu, 1986, in: Magnetic Properties of Low-Dimensional Systems, eds L.M. Falicov and J.L. Moran-Lopez (Springer, Berlin) p. 16.
Freeman, A.J., and C.L. Fu, 1987, J. Appl. Phys. **61**, 3356.
Freeman, A.J., and R. Wu, 1991, J. Magn. & Magn. Mater. **100**, 497.
Fu, C.L., and A.J. Freeman, 1987, J. Magn. & Magn. Mater. **69**, L1.
Gardiner, T.M., 1983, Thin Solid Films **105**, 213.
Gay, J.G., and R. Richter, 1986, Phys. Rev. Lett. **56**, 2728.
Gonser, U., C.J. Meechan, A.H. Muir and H. Wiedersich, 1963, J. Appl. Phys. **34**, 2373.
Gradmann, U., 1964, Phys. Kondens. Mater. **3**, 91.
Gradmann, U., 1966, Ann. Phys. **17**, 91.
Gradmann, U., 1974, Appl. Phys. **3**, 161.
Gradmann, U., 1977, J. Magn. & Magn. Mater. **6**, 173.
Gradmann, U., 1986a, J. Magn. & Magn. Mater. **54**, 733.
Gradmann, U., 1986b, in: Magnetic Properties of Low-Dimensional Systems, eds L.M. Falicov and J.L. Moran-Lopez (Springer, Berlin).
Gradmann, U., 1988, Magnetic properties of metallic surfaces, interfaces and very thin films, in: Landolt–Boernstein, New Series, ed. O. Madelung, III/19g, p. 1ff.
Gradmann, U., and R. Bergholz, 1984, Phys. Rev. Lett. **52**, 771.
Gradmann, U., and H.O. Isbert, 1980, J. Magn. & Magn. Mater. **15-18**, 1109.
Gradmann, U., and J. Mueller, 1968, Phys. Status Solidi **27**, 313.
Gradmann, U., and J. Mueller, 1970, Z. Angew. Phys. **20**, 87.
Gradmann, U., and J. Mueller, 1971, Czech. J. Phys. B **21**, 553.
Gradmann, U., and P. Tillmanns, 1977, Phys. Status Solidi A **44**, 539.
Gradmann, U., W. Kuemmerle and R. Tham, 1976, Appl. Phys. **10**, 219.
Gradmann, U., R. Bergholz and E. Bergter, 1984, IEEE Trans. Magn. **20**, 1840.
Gradmann, U., R. Bergholz and E. Bergter, 1985, Thin Solid Films **126**, 107.
Gradmann, U., J. Korecki and G. Waller, 1986, Appl. Phys. A **39**, 101.
Gradmann, U., M. Przybylski, H.J. Elmers and G. Liu, 1989, Appl. Phys. A **49**, 563.
Gradmann, U., G. Liu, H.J. Elmers and M. Przybylski, 1990, Hyperf. Interact. **57**, 1845.
Gradmann, U., H.J. Elmers, M. Albrecht and G. Liu, 1991, in: Magnetwerkstoffe und Magnetsysteme, ed. H. Warlimont, (DGM-Verlag, Oberursel) p. 201.
Gruenberg, P., R. Schreiber, Y. Pang, M.B. Brodsky and H. Sowers, 1986, Phys. Rev. Lett. **57**, 2442.
Gruenberg, P., S. Demokritov, A. Fuss, M. Vohl and J.A. Wolf, 1991, J. Appl. Phys. **69**, 4789.
Hansen, M., and K. Anderko, 1958, Constitution of Binary Alloys (McGraw-Hill, New York).
Harrison, W.A., 1984, Phys. Rev. B **29**, 2917.
Hasegawa, H., 1987, Surf. Sci. **182**, 591.
Hasegawa, H., 1990, Phys. Rev. B **42**, 2368.
Haubenreisser, W., W. Brodkorb, A. Corciovei and G. Costache, 1969, Phys. Status Solidi **31**, 245.
Heinrich, B., A.S. Arrott, J.F. Cochran, S.T. Purcell, K.B. Urquhart and K. Myrtle, 1987, J. Cryst. Growth **81**, 562.
Heinrich, B., K.B. Urquhart, J.R. Dutcher, S.T. Purcell, J.F. Cochran and A.S. Arrott, 1988a, J. Appl. Phys. **63**, 3863.
Heinrich, B., S.T. Purcell, J.R. Dutcher, K.B. Urquhart, J.F. Cochran and A.S. Arrott, 1988b, Phys. Rev. B **38**, 12879.
Heinrich, B., A.S. Arrott, J.F. Cochran, K.B. Urquhart, K. Myrtle, Z. Celinski and Q.M. Zhong, 1989a, in: Growth, Characterization and Properties of Ultrathin Magnetic Films and Multilayers, eds B.T. Jonker, J.P. Heremans and E.E. Marinero, Mater. Res. Soc. Symp. Proc. **151**, p. 177.
Heinrich, B., J.F. Cochran, A.S. Arrott, S.T. Purcell, K.B. Urquhart, J.R. Dutcher and W.F. Egelhoff Jr, 1989b, Appl. Phys. A **49**, 473.
Heinrich, B., Z. Celinski, J.F. Cochran, W.B. Muir, J. Rudd, Q.M. Zhong, A.S. Arrott, K. Myrtle and J. Kirschner, 1990, Phys. Rev. Lett. **64**, 673.
Henzler, M., 1984, Appl. Phys. A **34**, 205.

Henzler, M., 1988, in: The Structure of Surfaces II, eds J.F. van der Veen and M.A. van Hove (Springer, Berlin) p. 431.
Hillebrands, B., P. Baumgart and G. Güntherodt, 1989, Appl. Phys. A **49**, 589.
Hong, S.C., A.J. Freeman and C.L. Fu, 1988, Phys. Rev. B **38**, 12156.
Idzerda, Y.U., W.T. Elam, B.T. Jonker and G.A. Prinz, 1989, Phys. Rev. Lett. **62**, 2480.
Idzerda, Y.U., B.T. Jonker, W.T. Elam and G.A. Prinz, 1990, J. Appl. Phys. **67**, 5385.
Jacobs, I.S., and C.P. Bean, 1963, in: Magnetism III, eds G.T. Rado and H. Suhl (Academic Press, New York) p. 271.
Jaggi, R., S. Methfessel and S. Sommerhalder, 1962, Magnetic properties of thin films, in: Landolt-Boernstein, 6th Ed., eds K.H. Hellwege and A.M. Hellwege, II, 9, p. 1ff.
Jelitto, R.J., 1964, Z. Naturforsch. Teil A **19**, 1567, 1580.
Jepsen, O., J. Madsen and O.K. Andersen, 1980, J. Magn. & Magn. Mater. **15-18**, 867.
Jepsen, O., J. Madsen and O.K. Andersen, 1982, Phys. Rev. B **26**, 2790.
Jona, F., and P.M. Marcus, 1988, in: The Structure of Surfaces II, eds J.F. van der Veen and M.A. van Hove (Springer, Berlin) p. 90.
Jona, F., and P.M. Marcus, 1989, Surf. Sci. **223**, L897.
Jonker, B.T., and G.A. Prinz, 1986, Surf. Sci. **172**, L568.
Jonker, B.T., K.H. Walker, E. Kisker, G.A. Prinz and C. Carbone, 1986, Phys. Rev. Lett. **57**, 142.
Jonker, B.T., J.P. Heremans and E.E. Marinero, eds, 1989, Growth, Characterization and Properties of Ultrathin Magnetic Films and Multilayers, Mater Res. Soc. Symp. Proc. **151**.
Karas, W., J. Noffke and L. Fritsche, 1989, J. Chim. Phys. **86**, 861.
Kaufmann, L., E.V. Clougherty and R.J. Weiss, 1963, Acta Met. **11**, 323.
Kerkmann, P., 1989, Appl. Phys. A **49**, 523.
Keune, W., T. Ezawa, W.A.A. Macedo, U. Glos, K.P. Schletz and U. Kirschbaum, 1989, Physica B **161**, 269.
Klein, M.J., and R.S. Smith, 1951, Phys. Rev. **81**, 378.
Knappwost, A., 1957, Z. Phys. Chem. **12**, 30.
Kohlhepp, J., H.J. Elmers, S. Cordes and U. Gradmann, 1992, Phys. Rev. B **45**, 12287.
Koike, K., and K. Hayakawa, 1984, Jpn. J. Appl. Phys. **23**, L187.
Kolaczkiewicz, J., and E. Bauer, 1984, Surf. Sci. **144**, 495.
Koon, N.C., B.T. Jonker, F.A. Volkening, J.J. Krebs and G.A. Prinz, 1987, Phys. Rev. Lett. **59**, 2463.
Korecki, J., and U. Gradmann, 1985, Phys. Rev. Lett. **55**, 2491.
Korecki, J., and U. Gradmann, 1986a, Hyperf. Inter. **28**, 931.
Korecki, J., and U. Gradmann, 1986b, Europhys. Lett. **2**, 651.
Korecki, J., M. Przybylski and U. Gradmann, 1990, J. Magn. & Magn. Mater. **89**, 325.
Krakauer, H., M. Posternak and A.J. Freeman, 1979, Phys. Rev. B **19**, 1706.
Krakauer, H., A.J. Freeman and E. Wimmer, 1983, Phys. Rev. B **28**, 610.
Krasko, G.L., 1987, Phys. Rev. B **36**, 8565.
Kuemmerle, W., and U. Gradmann, 1977, Solid State Commun. **24**, 33.
Kuemmerle, W., and U. Gradmann, 1978, Phys. Status Solidi A **45**, 171.
Lang, C.A., M.M. Dovek, J. Nogami and C.F. Quate, 1989, Surf. Sci. **224**, L947.
Lee, C.H., Hui He, F.J. Lamelas, W. Vavra, C. Uher and R. Clarke, 1989, in: Characterization and Properties of Ultrathin Magnetic Films and Multilayers, eds B.T. Jonker, J.P. Heremans and E.E. Marinero, Mater. Res. Soc. Symp. Proc. **151**, p. 111.
Lee, C.H., Hui He, F.J. Lamelas, W. Vavra, C. Uher and R. Clarke, 1990, Phys. Rev. B **42**, 1066.
Lee, J.I., C.L. Fu and A.J. Freeman, 1986, J. Magn. & Magn. Mater. **62**, 93.
Lent, C.S., and P.I. Cohen, 1984, Surf. Sci. **139**, 121.
Li, C., and A.J. Freeman, 1991, Phys. Rev. B **43**, 780.
Li, C., A.J. Freeman and C.L. Fu, 1988, J. Magn. & Magn. Mater. **75**, 201.
Li, C., A.J. Freeman, H.J.F. Jansen and C.L. Fu, 1990, Phys. Rev. B **42**, 5433.
Li, H., Y. Si. Li, J. Quinn, D. Tian, J. Sokolov, F. Jona and P.M. Marcus, 1990, Phys. Rev. B **42**, 9195.
Li, Y., M. Farle and K. Baberschke, 1990, Phys. Rev. B **41**, 9596.
Li, Y., M. Farle and K. Baberschke, 1991, J. Magn. & Magn. Mater. **93**, 345.
Liebermann, L.N., J. Clinton, D.M. Edwards and J. Mathon, 1970, Phys. Rev. Lett. **25**, 4.
Liu, C., and S.D. Bader, 1990a, J. Appl. Phys. **67**, 5758.
Liu, C., and S.D. Bader, 1990b, Phys. Rev. B **41**, 553.
Liu, C., and S.D. Bader, 1991, J. Magn. & Magn. Mater. **93**, 307

Liu, C., E.R. Moog and S.D. Bader, 1988, Phys. Rev. Lett. **60**, 2422.
Lu, S.H., J. Quinn, D. Tian, F. Jona and P.M. Marcus, 1989, Surf. Sci. **209**, 364.
Lugert, G., and G. Bayreuther, 1988, Phys. Rev. B **38**, 11068.
Lugert, G., and G. Bayreuther, 1989, Thin Solid Films **175**, 311.
Macedo, W.A.A., and W. Keune, 1988, Phys. Rev. Lett. **61**, 475.
Maksym, P.A., 1988, in: Thin Film Growth Techniques for Low-Dimensional Structures, eds R.F.C. Farrow, S.S.P. Parkin, P.J. Dobson, J.H. Neave and A.S. Arrott (Plenum Press, New York) p. 95.
Markov, I., and R. Kaischew, 1976, Kristall und Technik **11**, 685.
Markov, I., and A. Milchev, 1984a, Surf. Sci. **136**, 519.
Markov, I., and A. Milchev, 1984b, Surf. Sci. **145**, 313.
Markov, I., and S. Stoyanov, 1987, Contemp. Phys. **28**, 267.
Mathon, J., 1986a, Phys. Rev. B **34**, 1775.
Mathon, J., 1986b, J. Phys. F **16**, 669.
Mathon, J., 1988, Rep. Prog. Phys. **51**, 1.
Matthews, J.W., ed., 1975a, Epitaxial Growth, Parts A and B (Academic Press, New York).
Matthews, J.W., 1975b, chapter 8 in Matthews, 1975.
Meiklejohn, W.H., and C.P. Bean, 1956, Phys. Rev. **102**, 1413.
Mermin, N.D., and H. Wagner, 1966, Phys. Rev. Lett. **17**, 1133.
Mezey, L.Z., and J. Giber, 1982, Surf. Sci. **117**, 220.
Miedema, A.R., and J.W.F. Dorleijn, 1980, Surf. Sci. **95**, 447.
Mills, D.L., and A.A. Maradudin, 1967, J. Phys. Chem. Solids **28**, 1855.
Min, B.I., T. Oguchi and A.J. Freeman, 1986, Phys. Rev. B **33**, 7852.
Moruzzi, V.L., P.M. Marcus, K. Schwarz and P. Mohn, 1986, Phys. Rev. B **34**, 1784.
Mosca, D.H., F. Petroff, A. Fert, P.A. Schroeder, W.P. Pratt Jr and R. Laloee, 1991, J. Magn. & Magn. Mater. **94**, L1.
Mundschau, M., E. Bauer, W. Telieps and W. Swiech, 1989, Surf. Sci. **213**, 381.
Neave, J.H., B.A. Joyce, P.A. Dobson and N. Norton, 1983, Appl. Phys. A **31**, 1.
Néel, L., 1954, J. Phys. Radium **15**, 225.
Neugebauer, C.A., 1962, Phys. Rev. **116**, 1441.
Newkirk, J.B., 1957, Trans. AIME **209**, 1214.
Oepen, H.P., and J. Kirschner, 1988, J. Phys. **49**, C8, 1853.
Ohnishi, S., M. Weinert and A.J. Freeman, 1983, Phys. Rev. B **28**, 6741.
Ohnishi, S., M. Weinert and A.J. Freeman, 1984, Phys. Rev. B **30**, 36.
Onsager, L., 1944, Phys. Rev. **65**, 117.
Pappas, D.P., K.P. Kaemper and H. Hopster, 1990, Phys. Rev. Lett. **64**, 3179.
Pappas, D.P., K.P. Kaemper, H. Hopster, D.E. Fowler, A.C. Luntz, C.R. Brundle and Z.X. Shen, 1991, J. Appl. Phys. **69**, 5209.
Parkin, S.S.P., N. More and K.P. Roche, 1990, Phys. Rev. Lett. **64**, 2304.
Parkin, S.S.P., R. Bhadra and K.P. Roche, 1991, Phys. Rev. Lett. **66**, 2152.
Pashley, D.W., 1952, Proc. R. Soc. A **210**, 355.
Pashley, D.W., 1956, Adv. Phys. **5**, 173.
Pashley, D.W., 1965, Adv. Phys. **14**, 327.
Pearson, A., 1958, A Handbook of Lattice Spacings and Structures of Metals and Alloys (Pergamon Press, Oxford).
Pescia, D., ed., 1989, Appl. Phys. A **49**, 437ff.
Pescia, D., G. Zampieri, M. Stampanoni, G.L. Bona, R.F. Willis and F. Meier, 1987a, Phys. Rev. Lett. **58**, 933.
Pescia, D., M. Stampanoni, G.L. Bona, A. Vaterlaus, R.F. Willis and F. Meier, 1987b, Phys. Rev. Lett. **58**, 2126.
Pommier, J., P. Meyer, G. Penissard, J. Ferre, P. Bruno and D. Renard, 1990, Phys. Rev. Lett. **65**, 2054.
Preston, R.S., S.S. Hanna and J. Heberle, 1962, Phys. Rev. **128**, 2207.
Prinz, G.A., 1985, Phys. Rev. Lett. **54**, 1051.
Prinz, G.A., G.T. Rado and J.J. Krebs, 1982, J. Appl. Phys. **53**, 2087.
Przybylski, M., and U. Gradmann, 1987, Phys. Rev. Lett. **59**, 1152.
Przybylski, M., and U. Gradmann, 1988, J. Phys. C **8**, 1705.
Przybylski, M., U. Gradmann and J. Korecki, 1987, J. Magn. & Magn. Mater. **69**, 199.
Przybylski, M., I. Kaufmann and U. Gradmann, 1989, Phys. Rev. B **40**, 8631.
Przybylski, M., J. Korecki and U. Gradmann, 1990a, Hyperf. Inter. **57**, 2053.
Przybylski, M., U. Gradmann and K. Krop, 1990b, Hyperf. Inter. **60**, 995.
Qiu, Z.Q., S.H. Mayer, C.J. Gutierrez, H. Tang and J.C. Walker, 1989, Phys. Rev. Lett. **63**, 1649.
Rado, G.T., 1957, Bull. Am. Phys. Soc. **2**, 127.
Rado, G.T., 1982, Phys. Rev. B **26**, 2087.
Rado, G.T., and J.C. Walker, 1982, J. Appl. Phys. **53**, 8055.
Raether, H., 1957, Handbuch der Physik,

Vol. XXXII, ed. S. Fluegge (Springer, Berlin) p. 495.
Rau, C., 1982, J. Magn. & Magn. Mater. **30**, 141.
Rau, C., 1989, Appl. Phys. A **49**, 579.
Rau, C., and G. Xing, 1989, J. Vac. Sci. & Technol. A **7**, 1889.
Roos, W., K.A. Hempel, C. Voigt, H. Dederichs and R. Schippan, 1980, Sci. Instrum. **51**, 612.
Royer, L., 1928, Bull. Soc. Fr. Mineral. Crist. **51**, 7.
Ruehrig, M., R. Schaefer, A. Hubert, R. Mosler, J.A. Wolf, S. Demokritov and P. Gruenberg, 1991, Phys. Status Solidi **125**, 635.
Scheinfein, M.R., J. Unguris, R.J. Celotta and D.T. Pierce, 1989, Phys. Rev. Lett. **63**, 668.
Schlenker, C., S.S.P. Parkin, J.C. Scott and K. Howard, 1986, J. Magn. & Magn. Mater. **54-57**, 801.
Schneider, C.M., P. Bressler, P. Schuster and J. Kirschner, 1990, Phys. Rev. Lett. **64**, 1059.
Sill, L.R., M.B. Brodsky, S. Bowen and H.C. Hamaker, 1985, J. Appl. Phys. **57**, 3663.
Smardz, L., V. Koeller, D. Kerkmann, F. Schumann, D. Pescia and W. Zinn, 1990, Z. Phys. B **80**, 1.
Smith, G.C., G.A. Padmore and C. Norris, 1982, Surf. Sci. **119**, L287.
Stampanoni, M., A. Vaterlaus, M. Aeschlimann and F. Meier, 1987, Phys. Rev. Lett. **59**, 2483.
Stanley, H.E., and T.A. Kaplan, 1966, Phys. Rev. Lett. **17**, 913.
Steigerwald, D.A., and W.F. Egelhoff Jr, 1988, Phys. Rev. Lett. **60**, 2558.
Stünkel, D., 1963, Z. Phys. **176**, 207.
Tamura, E., R. Feder, G. Waller and U. Gradmann, 1990, Phys. Status Solidi B **157**, 627.
Telieps, W., and E. Bauer, 1985, Surf. Sci. **162**, 163.
Tersoff, J., and L.M. Falicov, 1983, Phys. Rev. B **26**, 6186.
Tikhov, M., and E. Bauer, 1990, Surf. Sci. **232**, 73.
Tsunoda, Y., S. Imada and N. Kunitomi, 1988, J. Phys. F **18**, 1421.
Tyson, J., A.H. Owens, J.C. Walker and G. Bayreuther, 1981, J. Appl. Phys. **52**, 2487.
Unguris, J., G.G. Hembree, R.J. Celotta and D.T. Pierce, 1985, J. Microsc. **139**, RP1.
Unguris, J., R.J. Celotta and D.T. Pierce, 1991, Phys. Rev. Lett. **67**, 140.
Urano, T., and T. Kanaji, 1988, J. Phys. Soc. Jpn. **57**, 3043.
Valenta, L., 1962, Phys. Status Solidi **2**, 112.
van der Veen, J.F., and M.A. van Hove, eds, 1988, The Structure of Surfaces II (Springer, Berlin).
van Hove, M.A., and S.Y. Tong, 1979, Surface Crystallography by LEED (Springer, Berlin).
Velu, E., C. Dupass, D. Renard, J.-P. Renard and J. Seiden, 1988, Rapid Commun. **37**, 668.
Victora, R.H., 1986, in: Magnetic Properties of Low-Dimensional Systems, eds L.M. Falicov and J.L. Moran-Lopez (Springer, Berlin).
Victora, R.H., and L.M. Falicov, 1984, Phys. Rev. B **26**, 6186.
Vincze, I., and J. Kollar, 1972, Phys. Rev. B **6**, 1066.
Voigt, J., X.L. Ding, R. Fink, G. Krausch, B. Luckscheiter, R. Platzer, U. Woehrmann and G. Schatz, 1990, Appl. Phys. A **51**, 317.
Walker, J.C., R. Droste, G. Stern and J. Tyson, 1984, J. Appl. Phys. **55**, 2500.
Waller, G., and U. Gradmann, 1982, Phys. Rev. B **26**, 6330.
Wang, C.S., and A.J. Freeman, 1980, Phys. Rev. B **21**, 4585.
Wang, C.S., and A.J. Freeman, 1981, Phys. Rev. B **24**, 4364.
Wang, Y.Q., Y.S. Li, F. Jona and P.M. Marcus, 1987, Solid State Commun. **61**, 623.
Wassermann, E.F., 1990, in: Ferromagnetic Materials, Vol. 5, eds K.H.J. Buschow and E.P. Wohlfarth (Elsevier, Amsterdam) p. 238.
Weber, W., D.A. Wesner and G. Güntherodt, 1991, Phys. Rev. Lett. **66**, 942.
Wegener, H., 1965, Der Moessbauer-Effekt (Bibliographisches Institut, Mannheim).
Weiss, R.J., 1963, Proc. Phys. Soc. **82**, 281.
Weller, D., P. Schrijner and W. Reim, 1988, IEEE Trans. Magn. **24**, 1731.
Wiesendanger, R., H.J. Güntherodt, G. Güntherodt, R.J. Gambino and R. Ruf, 1990, Z. Phys. B **80**, 5.
Wijn, H.P.J., 1988, Crystalline Films of 3d-Transition Elements and of Alloys of these Elements, in: Landolt-Boernstein, New Series, ed. O. Madelung, II/19g, p. 35ff.
Wimmer, E., H. Krakauer, M. Weinert and A.J. Freeman, 1981, Phys. Rev. B **24**, 864.
Window, B., 1942, Philos. Mag. **26**, 681.
Winter, H., H. Hagedorn, R. Zimny, H. Nienhaus and J. Kirschner, 1989, Phys. Rev. Lett. **62**, 296.
Wright, J.G., 1971, Philos. Mag. **24**, 217.
Yafet, Y., and E.M. Gyorgy, 1988, Phys. Rev. B **38**, 9145.
Yang, C.N., 1952, Phys. Rev. **85**, 808.
Zangwill, J., 1988, Physics at Surfaces (Cambridge Univ. Press, Cambridge).
Zijlstra, H., 1970, Rev. Sci. Instrum. **41**, 1241.

chapter 2

ENERGY BAND THEORY OF METALLIC MAGNETISM IN THE ELEMENTS

V. L. MORUZZI and P. M. MARCUS

Thomas J. Watson IBM Research Center
Yorktown Heights, NY 10598
U.S.A.

Handbook of Magnetic Materials, Vol. 7
Edited by K. H. J. Buschow

CONTENTS

1. Introduction

Since the first edition of *Ferromagnetic Materials* (Wohlfarth, 1980), a great expansion of the knowledge of magnetism in the elements has taken place by extending theory and experiment to large ranges of lattice and magnetic cell size and shape. Stable ferromagnetic phases can be found in all the 3d and 4d transition elements and antiferromagnetic phases in at least half of them, when expansion of the lattice is considered.

Some of these magnetic phases have been produced by epitaxial growth, which can expand a lattice, but the greatest number has been found by application of the band theory of magnetism. This theory now has a sound basis and a computationally practicable form to obtain reliable ground-state properties of crystalline elemental solids. The theory makes use of a set of Schrödinger-like one-electron equations to describe the ground state of a system with given nuclear positions. The equations contain an effective one-electron potential, i.e., a function of electron position, which adds exchange and correlation effects to Hartree-type Coulomb terms to describe electron–electron interactions. Several forms of the effective potential have been deduced from various physical approximations; among these forms are the $X\alpha$ form based on a statistical treatment of the exchange interaction and the local-density approximation (LDA) in the density functional theory of the ground state. The LDA results agree better with experiment and have a sounder physical basis, so that recent work is mostly with the LDA; however, useful results have been obtained with the $X\alpha$ approximation, as will be noted later.

The reliable result of density functional theory is the total energy of the system and properties derived from the total energy, such as lattice and magnetic structure, electron–electron interactions. Several forms of the effective potential have been de- of the system, and quantities such as band structures, densities of states and Fermi surfaces should not be expected to agree quantitatively with the theory. These quantities may be regarded as intermediate computational results in the process of calculating total energies, and will not be described here.

The application of the theory made here is to infinite crystals of the elements, particularly to changes of total energy when small changes in the valence electrons are made by straining the lattice or changing its magnetization. The latter change makes use of the spin-polarized form of the effective potential. With infinite periodic systems the computational techniques of band theory can be applied. However the size of the calculation needed to establish the magnetic ground states over substantial ranges

of volume makes simplifying approximations necessary in the work reported here. Among these approximations are: the potential is assumed spherically symmetric around each nucleus, the lattice is rigid, the spins are treated as collinear and the Hamiltonian is non-relativistic. These computational approximations could be removed at the cost of increased computation, but are quite good for the applications made here.

In section 2 the development of the band theory of magnetism is sketched and references are listed that find magnetic properties of 3d and 4d transition elements by band calculations. Table 1 lists the references by individual elements and the corresponding references include a compact description of the results and features of that reference.

In section 3 the explicit equations of density-functional theory in the spin-polarized local-density approximation are given and the important idea of constrained solutions of these equations is discussed. In particular the type of constraint called the fixed-spin-moment procedure, which is essential for determining magnetic structure, is described.

In section 4 the computation of ground-state magnetic properties by the augmented spherical wave method is described, including the procedure for locating magnetic phases and their stability limits. The useful simple Stoner formulation is given and related to the general theory.

In section 5 details of the calculation and the calculated results for magnetic properties (ferromagnetic and antiferromagnetic) of all the 3d and 4d transition elements in bcc and fcc structure are given. Comparison of equilibrium results with experiment are made, tables of quantitative results and plots of energy and magnetic moments as functions of volume in different magnetic phases are given.

2. Development of the energy-band theory of magnetism

The modern first-principles (i.e., without empirical parameters; also called parameter-free or ab initio) theory of the ground state of a system of nuclei and electrons based on density-functional theory starts with the work of Hohenberg and Kohn (1964), who deduced rigorous Schrödinger-like one-electron ground-state equations with an effective one-electron potential. The ground-state description is completed with a formula for the total energy in terms of the solutions of the one-electron equations. An exact explicit form for the effective potential is not known, but Kohn and Sham (1965) introduced the simple plausible local-density approximation (LDA), which assumes the effective potential at a point can be given by the value in a homogeneous electron gas (jellium) of the same density. This LDA combined with quantitative expressions for the energy of jellium, gives the explicit one-electron equations called the Kohn–Sham (KS) equations. A commonly used form of the LDA effective potential based on a detailed study of the jellium ground-state is due to Hedin and Lundqvist (1971). Subsequently a spin-polarized form of the theory, the local-spin-density approximation (LSDA), was developed by Von Barth and Hedin (1972). The LSDA is needed to find magnetic ground states and the Von Barth–Hedin form is used in the calculations reported here, but with the modified parameters given by Janak (1978)

to provide continuity with the LDA of Hedin and Lundqvist (1971) at zero polarization. Alternative forms of the LSDA were suggested by Gunnarsson and Lundqvist (1976) and by Vosko et al. (1980).

The derivation of the KS equations shows that their most favorable application is to calculate changes in the total energy of condensed matter under small changes of the system, such as those produced by changes of lattice structure (e.g., strain) or changes in magnetization density. Such changes correspond to changes primarily in the valence electron distribution, in which the gradients of the density are small, so the LSDA based on the homogeneous electron system should hold well. The calculation of bulk ground-state properties of periodic solids reported here is just such a favorable application.

A significant early paper in the band theory of magnetism is by Hattox et al. (1973), which solved the spin-polarized $X\alpha$ equations for the total energy of bcc vanadium over a large range of volume. The $X\alpha$ theory (Slater 1974) does not have a rigorous starting point as does the LSDA, which starts from density-functional theory, and $X\alpha$ theory contains an adjustable parameter α, which makes a correction for the effects of correlation. However the formulation of the $X\alpha$ equations is very similar to the KS equations – they are one-electron equations with an explicit spin-density dependent potential whose self-consistent solutions are used to evaluate a total-energy expression of the same form as in KS theory. The work by Hattox et al. (1973) anticipated many of the features of the later development of the band theory of magnetism, e.g., the evaluation of total energies over extended volume ranges, the location of the theoretical equilibrium volume and of the critical volume for existence of a ferromagnetic phase, the demonstration of a first-order phase transition to the ferromagnetic phase and of the existence of a two-phase range of volume in which two solutions of the $X\alpha$ equations existed at the same volume with different magnetic moments. Also the quantitative results for lattice constants and magnetic moments are close to those found in later work with the LSDA.

The first paper based on the KS equations which showed a phase transition to a ferromagnetic phase appears to be by Madsen and Andersen (1976) for fcc Fe. The calculations, which made simplifying assumptions about hybridization, were later extended to several metals by Poulsen et al. (1976). Quantitative application of the Stoner approach, which used solutions of the nonmagnetic KS equations and derived the magnetic behavior by applying perturbation theory to those solutions, was made by Gunnarsson (1976) for several metals. Janak and Williams (1976) found total energies, equilibrium lattice constants and magnetic moments from spin-polarized solutions of the KS equations for bcc Fe and fcc Ni; Janak (1978) then extended the same calculation to fcc Co.

A significant development was the book published by Moruzzi et al. (MJW) (1978), which found total energies, equilibrium (zero-pressure) lattice constants and bulk moduli for all metallic elements through atomic number $Z=49$, including the 3d and 4d transition series. This systematic study permitted reliable tracking of trends with Z. Comparison of non-spin-polarized results with experiment revealed clearly the expanded lattice constants and lower bulk moduli measured for the five elements which are magnetic in their ground equilibrium states, i.e., Cr, Mn, Fe, Co, Ni. These

differences of nonmagnetic theory from experiment were substantially reduced by spin-polarized calculations for Fe, Co, and Ni. The discrepancies for Cr and Mn, which have complex atomic and magnetic structures in the ground equilibrium state, are discussed in section 5.4.

Since 1978 the development of the much faster linearized methods of solving the energy-band problem (Andersen 1975, Andersen et al. 1984, Williams et al. 1979) along with increased computer power have made possible a large extension of the work of MJW. Calculation of total energy, E, and spin magnetic moment, M, in magnetic and nonmagnetic phases became possible over large ranges of volume V, leading to much richer magnetic behavior of the elements. In particular Kübler (1980a,b, 1981, 1983) applied the augmented spherical-wave method to calculations of $E(V)$ and $M(V)$ over extended ranges of V in nonmagnetic, ferromagnetic and antiferromagnetic phases of the magnetic elements in cubic structures. These calculations showed clearly the occurrence of abrupt transitions between magnetic phases at critical values of V. (There is an error in the position of the antiferromagnetic phase for fcc Fe in Kübler 1981; see Kübler 1983, C. S. Wang et al. 1985 or Moruzzi and Marcus 1990a.)

A large number of calculations subsequently extended the early work on magnetic phases of the 3d and 4d transition elements by means of spin-polarized band calculations. These calculations are too numerous to describe individually, but are given in the references along with a compact description of the contents of each paper. However we mention explicitly an important recent stage in finding magnetic phases of the elements, namely the fixed-spin-moment (FSM) procedure, which will be discussed in more detail in section 3.2. This procedure is the basis of the results for ferromagnetic phases given in section 5.3 and for antiferromagnetic phases given in section 5.4. The FSM procedure has permitted precise location of the stability limits of magnetic phases, and of the shapes of $M(V)$ curves up to these limits. The first application of the FSM procedure was made by Schwarz and Mohn (1984) to the magnetic phase transition as a function of volume of the intermetallic compound YCo_2. The first application to the magnetic phase transitions of elements was made by Moruzzi et al. (1986a,b).

Although we do not discuss the great variety of methods, models and approximations used to find magnetic properties of the transition elements by means of band calculations, we provide a guide to that literature by means of table 1 and the references, which are selective before 1980 and attempt to be more complete after 1980. Table 1 lists the reference numbers for individual 3d or 4d elements of papers (enumerated below) which calculate magnetic properties from band theory. The references include a compact characterization of each paper, which gives the elements studied, the lattice structure, the type of magnetic phase, whether spin susceptibilities and total energies were found, whether spin-polarized equations were solved, notes some features of the potential used and whether the Stoner formulation and the FSM procedure were used. A key to the symbols in the characterization is in the caption of table 1. Note that excitation properties of the elements such as band structures, densities of states, and Fermi surfaces are not referred to, although many papers include that information. The reference list does not include band structure papers on the transition elements

TABLE 1

References to band calculations of magnetic ground-state properties of 3d and 4d transition elements. Each element has a separate list of reference numbers. The symbols used in the compact description in the references have the following meaning: S1 = bcc, S2 = fcc, S3 = hcp, S3A = hexagonal with variation of axial ratio, S4 = tetragonal, S4A = tetragonal with variation of axial ratio. M1 = ferromagnetic (FM) phase, M1V = FM phase over extended volume range, M1A = FM phase with variation of axial ratio, M2 = antiferromagnetic (AF) phase, M2A = AF phase with variation of axial ratio, M22 = AF phase of the 2nd kind, M3V = ferrimagnetic phase over extended volume range, MOA = orbital moment with variation of axial ratio. SU = static spin susceptibility $\chi(0)$, SUV = $\chi(0)$ as a function of volume, SUQ = static spin susceptibility $\chi(Q)$ as a function of wave number. E = total energy, EV = E over an extended volume range, EA = variation of E with axial ratio. SP = spin-polarized band calculation, FP = full potential (no shape approximation), SR = semi-relativistic band calculation (no spin–orbit interaction), FR = fully relativistic calculation, FSR = core treated fully relativistically, valence electrons semirelativistically. PSP = pseudopotential, NLP = non-local exchange–correlation potential. $X\alpha$ = use of $X\alpha$ form of exchange–correlation potential, FSM = fixed-spin moment procedure. ST = application of Stoner formulation. SO = spin–orbit interaction used as a perturbation.

Element	References*
Sc	[19, 25, 54, 55, 71]
Ti	[19, 25, 54, 55, 71]
V	[19, 22, 23, 25, 53, 55, 58, 63, 71]
Cr	[13, 19, 25, 38, 42, 55, 58, 63, 71, 74, 79]
Mn	[7, 8, 9, 10, 15, 18, 19, 20, 25, 37, 40, 48, 55, 57, 58, 63, 64, 65, 71]
Fe	[1, 3, 5, 11, 14, 17, 19, 21, 22, 24, 25, 27, 30, 31, 33, 34, 35, 36, 39, 40, 41, 46, 48, 49, 51, 53, 55, 58, 60, 62, 63, 64, 67, 68, 69, 70, 71, 72, 73, 78]
Co	[4, 6, 19, 22, 25, 26, 33, 43, 44, 45, 47, 48, 50, 51, 52, 53, 54, 55, 60, 61, 62, 71, 75]
Ni	[1, 2, 16, 17, 19, 22, 25, 27, 32, 33, 48, 50, 51, 53, 54, 55, 60, 62, 66, 71, 72, 77]
Y	[19, 25]
Zr	[19, 25]
Nb	[8, 19, 25, 28, 59]
Mo	[19, 25, 29, 59]
Tc	[19, 25, 59]
Ru	[19, 25, 59]
Rh	[1, 8, 19, 25, 56, 72, 76, 80]
Pd	[1, 12, 17, 19, 22, 25, 48, 56, 72]

*References:

[1] Andersen et al. (1977); Fe [S1, S2, S3, M1V, SU; SP, ST], Ni [S2, M1, SU; SP, ST], Rh, Pd [S2; SP, ST].
[2] Anderson et al. (1979); Ni [S2, M1; SP, SR].
[3] Bagayoko and Callaway (1983); Fe [S1, S2, M1V; SP, FP].
[4] Bagayoko et al. (1983); Co [S1, M1, E; SP, FP].
[5] Bagno et al. (1989); Fe [S1, EV; SP, NLP].
[6] Blaha et al. (1988); Co [S3, M1; SP, FP, SR].
[7] Brener et al. (1988a); Mn [S1, S2, M1V, M2V; SP, FP].
[8] Brener et al. (1988b); Mn [S1, S2, M1V; SP, FP], Nb [S1, M1V; SP, FP], Rh [S2, M1V; SP, FP].
[9] Cade (1980); Mn [S2, M2; SP].
[10] Cade (1981); Mn [S2, S4, M2; SP].
[11] Callaway and Wang (1977); Fe [S1, M1; SP, FP].
[12] H. Chen et al. (1989); Pd [S2, M1V; SP, FP].
[13] J. Chen et al. (1988); Cr [S1, M2V, EV; SP, FP, FSR].
[14] Christensen et al. (1988); Fe [S2, M1; ST], Fe [S1, S2, EV; SP].
[15] Duschanek et al. (1989); Mn [S1, S2, S4, M1V, M2V, EV; SP, FSM].

TABLE 1 (*continued*)

[16] Eckardt and Fritsche (1987); Ni [S2, M1; SP].
[17] Fritsche et al. (1987); Ni [S2, M1; SP, FR], Fe [S1, M1; FP, FR], Pd [S2, M1; SP, FR, ST].
[18] Fry et al. (1987); Mn [S1, M1*V*, SU*Q*; SP].
[19] Fry et al. (1988); Sc, Ti, Mn, Co, Ni, Y, Zr, Tc, Ru, Rh, Pd [S1, SU*Q*; ST], V, Cr, Fe, Nb, Mo [S2; ST].
[20] Fuster et al. (1988); Mn [S1, S2, M1*V*, SU*Q*; SP, FP].
[21] Greenside and Schlüter (1983); Fe [S1, M1*V*, *E*; SP, FP, PSP].
[22] Gunnarsson (1976); V [S1; ST], Fe [S1, M1; ST], Co, Ni [S2, M1; ST], Pd [S2; ST].
[23] Hattox et al. (1973); V [S1, M1*V*, *EV*; SP, $X\alpha$].
[24] Hathaway et al. (1985); Fe [S1, M1*V*, *EV*; SP, FP, FSR].
[25] Janak (1977); Sc [S1, S2, SU; ST], V, Cr, Zr, Nb, Mo, Fe [S1, SU; ST], Ti, Y, Mn, Co, Ni, Tc, Ru, Rh, Pd [S2, SU; ST].
[26] Janak (1978); Co [S2, M1, *E*; SP].
[27] Janak and Williams (1976); Fe [S1, M1, *E*; SP], Ni [S2, M1, *E*; SP].
[28] Jani et al. (1988); Nb [S1, M1*V*; SP, FP].
[29] Jani et al. (1989); Mo [S1, M1*V*; SP, FP].
[30] Jansen and Peng (1988); Fe [S1, S2, M1, *E*; SP, FP].
[31] Jansen et al. (1984); Fe [S1, M1, *EV*; SP, FP, SR].
[32] Jarlborg and Freeman (1980); Ni [S2, S4, M1; SP, FSR].
[33] Jarlborg and Peter (1984); Fe [S1, M1; SP, ST], Co [S2, S3, M1; SP, ST], Ni [S2, M1; SP, ST].
[34] Johnson et al. (1984); Fe [S1, M1; SP, SR].
[35] Krasko (1987); Fe [S2, M1*V*, *EV*; ST].
[36] Krasko (1989); Fe [S1, S2, M1*V*, *EV*; ST].
[37] Kübler (1980a); Mn [S2, M1, M2, *E*; SP].
[38] Kübler (1980b); Cr [S1, M1, M2, *E*; SP].
[39] Kübler (1981); Fe [S1, S2, M1*V*, M2*V*, *EV*; SP].
[40] Kübler (1983); Fe, Mn [S1, S2, M1*V*, M2*V*, *EV*; SP].
[41] Kübler (1989); Fe [S3, M1*V*, M2*V*, *EV*; SP, FSM].
[42] Kulikov and Kulatov (1982a); Cr [S1, M2; SP].
[43] Kulikov and Kulatov (1982b); Co [S3; SP, $X\alpha$].
[44] Lee et al. (1986); Co [S1, M1; SP, FP, FSR].
[45] Li et al. (1988); Co [S2, M1; SP, FP, FSR].
[46] Madsen and Andersen (1976); Fe [S1, S2, S3, M1*V*; SP, ST].
[47] Marcus and Moruzzi (1985); Co [S1, S2, M1*V*, *EV*; SP, FSM].
[48] Marcus and Moruzzi (1988a); Fe, Co, Pd [S2, M1*V*, SU*V*, *EV*; SP, FSM], Ni, Mn [S1, M1*V*, SU*V*, *EV*; SP, FSM].
[49] Marcus and Moruzzi (1988b); Fe [S2, M1*V*, *EV*; SP, FSM].
[50] Marcus et al. (1986); Co, Ni [S1, S2, M1*V*, *EV*; SP, FSM].
[51] Marcus et al. (1987); Fe, Co, Ni [S1, S2, *EV*; SP, FSM].
[52] Min et al. (1986); Co [S1, S2, S3, M1, *EV*; SP, FSR, ST].
[53] Moruzzi (1986); Ni, V [S1, M1*V*; SP, FSM], Co, Fe [S2, M1*V*; SP, FSM].
[54] Moruzzi and Marcus (1988a); Sc, Ti, Co, Ni [S1, M1*V*, *EV*; SP, FSM].
[55] Moruzzi and Marcus (1988b); Sc, Ti, V, Cr, Mn, Fe, Co, Ni [S1, M1*V*, *EV*; SP, FSM].
[56] Moruzzi and Marcus (1989a); Rh, Pd [S2, M1*V*, SU*V*, *EV*; SP, FSM].
[57] Moruzzi and Marcus (1989b); Mn [S1, M1*V*, S2*V*, M3*V*, *EV*; SP, FSM].
[58] Moruzzi and Marcus (1990a); V, Cr [S1, M1*V*, M2*V*, *EV*; SP, FSM], Fe [S2, M1*V*, M2*V*, *EV*; SP, FSM], Mn [S1, S2, M1*V*, M2*V*, *EV*; SP, FSM].
[59] Moruzzi and Marcus (1990b); Nb, Mo [S1, M1*V*, M2*V*, *EV*; SP, FSM], Ru [S2, M1*V*, M2*V*, *EV*; SP, FSM], Tc [S1, S2, M1*V*, M2*V*, *EV*; SP, FSM].
[60] Moruzzi et al. (1978); Fe [S1, M1, *E*; SP], Co, Ni [S2, M1, *E*; SP].
[61] Moruzzi et al. (1986a); Co [S1, S2, M1*V*, *EV*; SP, FSM].
[62] Moruzzi et al. (1986b); Fe, Co, Ni [S1, S2, M1*V*; SP, FSM].
[63] Moruzzi et al. (1988a); V, Cr, Mn, Fe [S1, M1*V*, *EV*; SP, FSM].

TABLE 1 (*continued*)

[64] Moruzzi et al. (1989); Fe, Mn [S2, M1*V*, M2*V*, *EV*; SP, FSM].
[65] Oguchi and Freeman (1984); Mn [S2, S4, M2A, *E*A; SP].
[66] Papaconstantopoulos et al. (1989); Ni [S3, M1; SP, SR].
[67] Peng and Jansen (1988); Fe [S1, M1, M2, M22, *E*; SP, FP].
[68] Peng and Jansen (1990); Fe [S4V, M1*V*, *EV*; SP, FP, SR].
[69] Podgórny (1989a); Fe [S2, M1; SP, SR].
[70] Podgórny (1989b); Fe [S2, M1*V*, *EV*; SP, FSM].
[71] Podgórny and Goniakowski (1990); Sc, Ti, V, Cr, Mn, Fe, Co, Ni [S3, M1*V*, SU; SP, FSM].
[72] Poulsen et al. (1976); Fe, Ni, Rh, Pd [S1, S2, S3, M1*V*; SP, ST].
[73] Roy and Pettifor (1977); Fe [S2, M1; ST].
[74] Skriver (1981); Cr [S1, M2*V*; SP, ST].
[75] Szpunar and Strange (1985); Co [S3A, M1A, MOA, EA; SP, SR, SO].
[76] Tripathi et al. (1988); Rh [S2, M1*V*; SP, FP].
[77] C. S. Wang and Callaway (1977); Ni [S2, M1; SP, FP].
[78] C. S. Wang et al. (1985); Fe [S1, S2, M1*V*, M2*V*, *EV*; SP, FP, FSR].
[79] Xu (1984); Cr [S2; SP, FSR, ST].
[80] Yahaya and Fletcher (1979); Rh [S2; ST, *X*α].

if no magnetic properties are found. Also omitted are references to the extensive literature on magnetic behavior of disordered systems, or at finite temperatures, or dealing with noncollinear spins, with surface and layer magnetism, magnetic anisotropy, or with magnetic excitations such as spin waves and magneto-optic transitions.

3. Formulation of the ground-state equations with constraints

3.1. The spin-polarized Kohn–Sham equations

The properties of the transition elements given here are all found from calculations of total energies using solutions of the KS equations under particular constraints to be described later. These equations, which employ the local-density approximation as their principal physical approximation, give reliable values of changes of total energy in condensed matter when the nuclear configuration changes. We give these equations in spin-polarized form and discuss the terms in them to help understand the significance of the new results, but refer to systematic reviews elsewhere for the derivation (Kohn and Vashishta 1983).

Consider a system of N nuclei with charges Z_j at positions $\boldsymbol{R}_j$ and N electrons in a volume V. The Schrödinger-like KS equations in the LSDA for one-electron wave functions $\psi_{i\alpha}(\boldsymbol{r})$ in atomic units are

$$[-\tfrac{1}{2}\nabla^2 + V_\alpha^{\text{eff}}(\boldsymbol{r})]\psi_{i\alpha}(\boldsymbol{r}) = \varepsilon_{i\alpha}\psi_{i\alpha}(\boldsymbol{r}), \quad i = 1, N_\alpha, \ \alpha = 1, 2. \tag{1}$$

In eq. (1) α is the spin index, and the equations are coupled through the effective one-electron potential V_α^{eff}. This potential is the sum of two contributions

$$V_\alpha^{\text{eff}}(\boldsymbol{r}) = V_{\text{H}}(\boldsymbol{r}) + V_{\text{xc}\alpha}(\boldsymbol{r}). \tag{2}$$

The Hartree potential $V_{\text{H}}(\boldsymbol{r})$ is given by Coulomb terms due to the nuclei and to the

electron density function

$$V_{\mathrm{H}}(\boldsymbol{r}) = -\sum_{j=1}^{N} \frac{Z_j}{|\boldsymbol{r}-\boldsymbol{R}_j|} + \int_V \frac{n(\boldsymbol{r}')\,\mathrm{d}^3 r'}{|\boldsymbol{r}-\boldsymbol{r}'|}, \tag{3}$$

where the total electron density at $\boldsymbol{r}$ is

$$n(\boldsymbol{r}) = \sum_{\alpha=1}^{2} n_\alpha(\boldsymbol{r}) = \sum_{\alpha=1}^{2} \sum_{i=1}^{N_\alpha} |\psi_{i\alpha}(\boldsymbol{r})|^2, \tag{4}$$

$$\sum_{\alpha=1}^{2} N_\alpha = N. \tag{5}$$

In eq. (5) $N_\alpha = \int_V n_\alpha(\boldsymbol{r})\,\mathrm{d}^3 r$ is the total number of electrons of spin α and in eq. (4) the N_α lowest energy states of spin α are occupied. The exchange–correlation potential is

$$V_{\mathrm{xc}\alpha}(\boldsymbol{r}) = \left(\frac{\partial[n\varepsilon_{\mathrm{xc}}(n_1, n_2)]}{\partial n_\alpha} \right)_{n_1 = n_1(\boldsymbol{r}), n_2 = n_2(\boldsymbol{r})}, \tag{6}$$

and the exchange–correlation energy density $\varepsilon_{\mathrm{xc}}(n_1, n_2)$ is a known function of the two spin densities from the theory of the homogeneous electron gas (Von Barth and Hedin 1972). The energy $\varepsilon_{\mathrm{xc}}(n_1, n_2)$ corresponds to a decrease in the Coulomb energy of interaction of the electron distribution with itself due to the presence of both the exchange hole around a given electron (which keeps electrons of the same spin away from the given electron because of the Pauli exclusion principle), and the correlation hole (which keeps electrons of both spins away from the given electron because of the Coulomb repulsion). At any atomic position increased polarization of the electron distribution produces a larger decrease of $\varepsilon_{\mathrm{xc}}$ by the exchange hole, but produces a smaller decrease of $\varepsilon_{\mathrm{xc}}$ by the correlation hole. The exchange effects dominate and the net effect of increased polarization is to lower $\varepsilon_{\mathrm{xc}}$, e.g., at typical d-band densities of 0.03 electrons/bohr^3 the energy density decrease at complete polarization of the electron density due to exchange is six times the energy density increase due to correlation.

However the net decrease in the energy of the system achieved by unbalancing the spins is offset by an increase in the kinetic energy of the system, expressed by an increase in the sum of the occupied energy eigenvalues $\varepsilon_{i\alpha}$. The solutions of the KS equations balance the two opposing effects throughout the system to minimize the total energy. When the minimizing solution has a net magnetization per atom, the system is magnetic, and the driving force producing that magnetism is the Coulomb energy lowering due to exchange.

It is plausible that the term in eq. (1) involving $\varepsilon_{\mathrm{xc}}$ should have the form of eq. (6), since the gradient of the exchange–correlation energy density $n\varepsilon_{\mathrm{xc}}(n_1, n_2)$ would act like a potential, i.e., displacement in a direction that increases $n\varepsilon_{\mathrm{xc}}$ increases the potential energy of an electron. The formal derivation of eq. (1) minimizes the total energy with respect to the distributions $n_1(\boldsymbol{r})$ and $n_2(\boldsymbol{r})$.

3.2. Constrained solutions and the total-energy function

The formulation is completed by specifying boundary conditions and constraints on the solutions of eq. (1), and by giving the formula for the total energy in terms of the

solutions of eq. (1). The boundary conditions for periodic crystals introduce the Bloch phase factors relating solution values on the surfaces of the unit cell and label the solutions by a discrete set of wave numbers. The constraints are additional conditions imposed on the solutions. Thus the volume of the system, or the size and shape of the unit cell for periodic crystals, are constraints. In principle the size and shape of the unit cell for a given set of atoms which are periodically repeated could be obtained by minimizing the total energy. But we do not have the computational power to handle such a general problem, and we must simplify the computation by imposing a constraint to a particular unit cell. In fact for the results presented here a constraint to a bcc or fcc structure was imposed with a particular value of the volume, V, of the unit cell in each solution of the KS equations; then V was varied to evaluate E as a function of V.

An important additional constraint for magnetic systems imposes a magnetic moment on the system. Thus we impose the condition that

$$N_1 - N_2 = M, \tag{7}$$

where M is the magnetic moment of the system in Bohr magnetons. Since the systems treated here are electrically neutral, we also have

$$N_1 + N_2 = \sum_{j=1}^{N} Z_j. \tag{8}$$

Thus from eqs. (7) and (8) the constraint of a given total spin moment is equivalent to specifying N_1 and N_2 separately in the calculation, and is easily carried out by filling the N_1 lowest energy states of spin one and the N_2 lowest states of spin two. This procedure is the fixed spin-moment (FSM) procedure (Schwarz and Mohn 1984; Moruzzi et al. 1986a) and it gives rise to a total energy as a function of two variables, $E(V, M)$. In section 5.3 the FSM procedure is applied to bcc and fcc crystal lattices using one-atom cells to find ferromagnetic states of the elements. In section 5.4 the FSM procedure is applied to two-atom cells of the elements to find antiferromagnetic states.

After a self-consistent solution of eq. (1) has been found with the constraints to particular values of V and M, we insert the solution in the formula for the total energy. Thus we evaluate E as a function of V and M from

$$E(V, M) = \sum_{\alpha=1}^{2} \sum_{i=1}^{N_\alpha} \varepsilon_{i\alpha} - \tfrac{1}{2} \int_V \int_V \frac{n(\boldsymbol{r}) n(\boldsymbol{r}')}{|\boldsymbol{r} - \boldsymbol{r}'|} \mathrm{d}^3 r \, \mathrm{d}^3 r' - \int_V \mathrm{d}^3 r \sum_{\alpha=1}^{2} n_\alpha(\boldsymbol{r}) (V_{\mathrm{xc}\alpha} - \varepsilon_{\mathrm{xc}\alpha}) + \sum_{j,j'} \frac{Z_j Z_{j'}}{|\boldsymbol{R}_j - \boldsymbol{R}_{j'}|}. \tag{9}$$

In eq. (9) the sum of the eigenvalues of occupied one-electron states is corrected for double counting of electron–electron interactions – in the direct Coulomb interactions by the second term on the right, and in the exchange–correlation contribution by the third term on the right. The fourth term on the right is the Coulomb energy of interaction of nuclear charges.

Note that a solution of eq. (1) with any of the constraints is always a ground-state calculation, i.e., the solution gives a constrained ground state, not an excited state

of the system. Hence we retain the reliability of the density-functional theory for ground-state properties and the value of E from eq. (9) has variational accuracy with respect to errors in the solutions of eq. (1). This variational accuracy in the solution of eq. (1) can compensate for computational approximations, of which there are many, but not, of course, for errors in the LSDA.

4. The computation of ground-state magnetic properties

4.1. Features of the augmented spherical wave (ASW) method

The ASW method (Williams et al. 1979) is an efficient and accurate method of solving the KS equations for periodic systems (the band problem) and calculating accurate total energies for those systems. The ASW method gains efficiency by linearization of the energy dependence of matrix elements of the Hamiltonian and by sphericalization of the electronic charge and effective electron potential around each nucleus within an equivalent sphere. The equivalent sphere has as radius the Winger–Seitz radius r_{ws} and has a volume equal to the volume per atom.

The linearization of the method is a consequence of the use of energy-independent basis functions. Linear combinations of the basis functions are used to represent the solutions of the KS equations. With such basis functions the matrix elements of the Hamiltonian are linear in the electron energy. Hence fast matrix-eigenvalue determination procedures can be used to find the eigenvalues and eigenvectors, rather than procedures which find the roots of determinantal equations, i.e., values of electron energies which make the secular determinant vanish. In the Korringa–Kohn–Rostoker (KKR) method used in Moruzzi et al. (1978) (MJW) each matrix element had a general nonlinear dependence on electron energy and required such a root-finding calculation. The sphericalization of charge and potential greatly simplifies the evaluation of matrix elements of the Hamiltonian and the evaluation of the total energy.

The high accuracy required for total-energy calculations, where small differences between solutions with different boundary conditions and different constraints are the important results, is achieved by the careful choice of basis functions. These functions are designed to be continuous and have continuous derivatives everywhere. They are in fact made up entirely of spherical waves, an envelope spherical wave in the background, which is matched in value and gradient to spherical-wave expansions within each atomic sphere. The spherical waves inside each equivalent sphere satisfy the correct differential equation, although not at the correct energy of the total wave function.

The procedure for finding magnetic phases starts with the self-consistent solution of eqs. (1)–(6) calculated under the constraints of a given cubic lattice structure, a given volume per atom, V, and a given magnetic moment per atom, M, as in eqs. (7) and (8), i.e., the FSM procedure. Any such solution is appropriately called a *state* of the system, and has a total energy E found from eq. (9). A set of such states for a given element with a given structure, e.g., bcc or fcc, provides a known ground-state energy function $E(V, M)$ from which magnetic properties can be deduced. Establishing that function in sufficient detail usually requires several hundred complete band calcula-

tions iterated to self-consistency. This amount of calculation has become practicable because the ASW method requires roughly one hundredth as much calculation as the KKR method for equivalent information, and also because the basic computer speed has increased substantially since 1978.

4.2. States, magnetic phases, and phase lines

An arbitrary state of an element in a given structure in general requires application of a pressure, p, and a magnetic field, H, to maintain that state, where

$$p = -\left(\frac{\partial E(V,M)}{\partial V}\right)_M, \tag{10}$$

and

$$H = \left(\frac{\partial E(V,M)}{\partial M}\right)_V. \tag{11}$$

The applied magnetic field H acts only on the spin moments and has no orbital effects; it is in general a very large field, since it is producing changes in the saturation magnetization of the material. However the quantities of interest at any V are the M values at which E has minima, i.e., where $(\partial E/\partial M)_V = 0$, $(\partial^2 E/\partial M^2)_V > 0$. At such a point in the V–M plane, the applied field vanishes and the state maintains itself without application of a field. Also the state is stable or metastable, since small fluctuations of M increase E. Such a state of the bulk periodic system is appropriately called a *magnetic phase*. The designation magnetic phase includes the nonmagnetic phase, which is a magnetic phase with the corresponding minimum of total energy at $M = 0$. There must be at least one minimum on every $E(M)_V$ curve, since E increases strongly for positive or negative M values that approach complete polarization of the electron distribution. With the notation $E(M)_V$ the function $E(V,M)$ as a function of M at given V is meant. Examples of calculated $E(M)_V$ curves which exhibit one or more minima may be found in Moruzzi et al. (1986b, 1988a).

During the iterations to self-consistency at a given $M \neq 0$ (or equivalently at given unequal N_1 and N_2 values), two Fermi levels are required, one for each spin, to accommodate N_1 and N_2 electrons. However at the minimum of E, where $H = 0$, the two Fermi levels are equal. Transfer of electrons from spin 1 at Fermi energy ε_{F1} to spin 2 at Fermi energy ε_{F2} produces an energy change in the system $dE = (\varepsilon_{F2} - \varepsilon_{F1})\,dN$. At a minimum of E, $dE = 0$, hence $\varepsilon_{F1} = \varepsilon_{F2}$. This result is consistent with the usual floating moment iteration to a self-consistent solution using a single Fermi energy applied to the total density of states. That solution thus corresponds to a minimum of E.

The line of minima in the V–M plane is conveniently called a *phase line* along which the functions $E(V)$ and $M(V)$ will describe the magnetic behavior. A more accurate notation would be $E_m(V)$ and $M_m(V)$ where m refers to the line of minima of $E(M)_V$ as V varies in the V–M plane. The subscript m is dropped for compactness. Plots of the functions $E(V)$ and $M(V)$ will be given in section 5.2 for the 3d and 4d transition series. In general a pressure is needed to maintain a volume on the phase

line. However at a minimum of $E(V)$ the pressure also vanishes and such a state is appropriately called an *equilibrium state*. There may be more than one equilibrium state, e.g., on different magnetic phase lines; the one of lowest energy will be the *ground equilibrium state*, which is usually shortened to the ground state. However in more precise terminology all the states found at any values of V and M are ground states. To be clear we shall refer to the state at the minimum $E(V, M)$ with respect to both M and V as the equilibrium state; if there is more than one equilibrium state it will be necessary to refer to the lowest such state as the ground equilibrium state.

A particular feature of the $M(V)$ phase lines will be evident in the many examples in section 5 and can be proved quite generally (Moruzzi 1986, Marcus and Moruzzi 1988a), i.e., at the stability limits, where a magnetic phase begins or ends, $\mathrm{d}M/\mathrm{d}V$ is in general infinite, corresponding to a vertical tangent. Thus along a phase line $(\partial E/\partial M)_V = 0$, hence

$$\mathrm{d}\left[\left(\frac{\partial E}{\partial M}\right)_V\right] = \left(\frac{\partial^2 E}{\partial V \partial M}\right)\mathrm{d}V + \left(\frac{\partial^2 E}{\partial M^2}\right)\mathrm{d}M = 0 \tag{12}$$

and the slope of the phase line is

$$\frac{\mathrm{d}M}{\mathrm{d}V} = -\left(\frac{\partial^2 E}{\partial V \partial M}\right) \Big/ \left(\frac{\partial^2 E}{\partial M^2}\right). \tag{13}$$

Now at the stability limits of a phase, a minimum and maximum of $E(M)_V$ merge to give an inflection point with $(\partial^2 E/\partial M^2) = 0$, hence from eq. (13) at that point $\mathrm{d}M/\mathrm{d}V = \infty$. An exception occurs in the degenerate case of the nonmagnetic phase line, where $(\partial^2 E/\partial V \partial M)$ also vanishes and the nonmagnetic phase line has zero slope up to its stability limit.

In addition to determining the values of p and H from eqs. (10) and (11), the higher derivatives of the function $E(V, M)$ determine additional properties of the magnetic phases. Thus we have

$$B = V\left(\frac{\mathrm{d}^2 E(V)}{\mathrm{d}V^2}\right) \tag{14}$$

for the bulk modulus B along the phase line $E(V)$ and the Grüneisen constant γ, a dimensionless measure of the anharmonic behavior of the crystal (using the definition of Dugdale and MacDonald (1953) which modifies a form due to Slater and fits low-temperature data better, see Moruzzi et al. (1988b)) is given by

$$\gamma = -1 - \frac{V(\mathrm{d}^3 E(V)/\mathrm{d}V^3)}{2(\mathrm{d}^2 E(V)/\mathrm{d}V^2)}. \tag{15}$$

We can also find the magnetic spin susceptibility χ at any point of the V–M plane from

$$\chi = \left(\frac{\partial M}{\partial H}\right)_V = \left(\frac{\partial^2 E(V, M)}{\partial M^2}\right)_V^{-1}. \tag{16}$$

In terms of the Pauli spin susceptibility of the nonmagnetic phase $\chi_0(V)$ the exchange-

enhanced ratio $\chi(V)/\chi_0(V)$ is given by

$$\frac{\chi(V)}{\chi_0(V)} = \frac{1}{2\mu_B^2 N_d(\partial^2 E(V,M)/\partial M^2)_V}, \tag{17}$$

where $N_d(\varepsilon_F, V)$ is the density of states of one spin at the common Fermi level along the nonmagnetic phase line.

In section 5.4 the procedure which holds the total moment per atom fixed will be generalized to hold the total moment of a two-atom cell fixed; then the individual atomic moments can float, but with a constant sum. This generalization will lead to antiferromagnetic and ferrimagnetic phase lines.

4.3. The Stoner formulation

A further property of the function $E(V, M)$ that has a useful application is that $E(V, M)$ is even in M in the absence of significant spin–orbit interaction, i.e.,

$$E(V, M) = E(V, -M). \tag{18}$$

Consider now two contributions to the increase ΔE in E when M (the excess of spin 1 over spin 2 per atom) is increased from zero at a given V. One contribution is from the change in the sum of the one-electron energies $\varepsilon_{i\alpha}$ when $\frac{1}{2}M$ electrons are moved from occupied spin 2 states below the Fermi level to unoccupied spin 1 states above the Fermi level, assuming the energies $\varepsilon_{i\alpha}$ and densities of states for spins 1 and 2 electrons retain the values they have at $M = 0$ (a rigid-band assumption). This contribution is clearly even in M since it is the same for $|M|$ and $-|M|$. Since ΔE is even in M, the remaining contribution to ΔE which takes account of all other changes due to M is then also even in M and its leading term in M is an M^2 term. The Stoner model assumes that combination of the rigid-band contribution and the M^2 term of the remaining contribution is an adequate description of the effects of change of M; it will certainly be good for small enough M. Then we can write ΔE in the form

$$\Delta E \equiv E(V, M) - E(V, 0) = \left(\int_{\varepsilon_F}^{\varepsilon(M)} - \int_{\varepsilon(-M)}^{\varepsilon_F} \right) \varepsilon' N_d(\varepsilon')\, d\varepsilon' - \tfrac{1}{4} I M^2, \tag{19}$$

where

$$\int_{\varepsilon_F}^{\varepsilon(M)} N_d(\varepsilon')\, d\varepsilon' = \int_{\varepsilon(-M)}^{\varepsilon_F} N_d(\varepsilon')\, d\varepsilon' = \tfrac{1}{2} M \tag{20}$$

and ε_F is the common Fermi level of the two spin bands at $M = 0$, $N_d(\varepsilon')$ is the density of states for either spin around that common Fermi level. Thus general symmetry arguments provide directly a Stoner-type theory (Stoner 1939, Edwards and Wohlfarth 1968). The form of e.g. (19) can be written compactly as (Andersen et al. 1977)

$$\Delta E = \tfrac{1}{2} \int_0^M \frac{M'\, dM'}{\bar{N}_d(M')} - \tfrac{1}{4} I M^2 \tag{21}$$

where $\bar{N}_d(M)$ is the average value of $N_d(\varepsilon)$ over the energy interval from $\varepsilon(-M)$ to $\varepsilon(M)$,

$$\bar{N}_d(M) \equiv \frac{M}{\varepsilon(M) - \varepsilon(-M)}. \tag{22}$$

Then the inverse susceptibility (magnetic modulus) at any M from eqs. (16) and (21) is given by

$$\chi^{-1} = \frac{\partial^2 \Delta E(V, M)}{\partial M^2} = \frac{1}{2\bar{N}_d(M)} - \frac{I}{2} \tag{23}$$

or at $M = 0$, i.e., in the nonmagnetic phase

$$\chi = \frac{2\bar{N}_d(0)}{1 - \bar{N}_d(0)I} = \frac{2N_d(\varepsilon_F)}{1 - N_d(\varepsilon_F)I}. \tag{24}$$

The susceptibility is enhanced by the magnetic contribution to the energy, arising, as noted above, from the exchange lowering of energy as spin distributions are unbalanced; the susceptibility goes singular when

$$N_d(\varepsilon_F)I = 1, \tag{25}$$

which is the Stoner criterion for onset of ferromagnetism. This criterion and eqs. (19) and (20) assume I is not a significant function of M over the range of M of interest, although it may be a function of V. The Stoner parameter I can be evaluated by perturbation theory based on non-spin-polarized solutions of the KS equations, without evaluating total energies (Janak and Williams 1976, Janak 1977); it can also be evaluated directly from the function $E(V, M)$ using eq. (19), which permits the basic assumption of independence of M to be tested (Marcus and Moruzzi 1988b).

5. ASW results for 3d and 4d transition elements

5.1. Convergence criteria and approximations

The systematic results reported in this section for $E(V)$ and $M(V)$ along the magnetic phase lines of the 3d and 4d transition elements in bcc and fcc structure all employed the spin-polarized ASW method with the exchange–correlation potential of Von Barth and Hedin (1972) and the parametrization of Janak (1978), the FSM procedure, the same set of points in k-space, and the same convergence criteria on iteration. The calculations used a uniform mesh of 405 points for the bcc lattice and 570 points for the fcc lattice in the irreducible 1/48th of the Brillouin zone. The iterations, which generate a new charge distribution from an old one by solving eqs. (1) to (6), were stopped when successive iterations gave average charge densities over the periodic cell which differed by less than one part in 10^5. The accuracy of the total energy is then better than one mRy per atom, which is adequate for discussing changes of magnetic structure corresponding to tens of mRy per atom.

The calculations with the AWS method were restricted to bulk cubic structures, which have highly symmetric local environments, because of the approximation which

sphericalized the potential in the equivalent sphere. The calculations make the following approximations for practicability and efficiency: (1) the LSDA is used to obtain explicit equations; (2) the lattice is assumed rigid (no thermal or zero-point motion); (3) the spins are treated as collinear (their vector character is ignored); (4) the calculation is non-relativistic; (5) the potential is made spherical around each nucleus in an equivalent sphere. The last three of these approximations could be removed by known procedures and the accuracy of the total-energy calculation maintained at the cost of increased computation; these refinements are made in some of the references in table 1. However the approximations are quite good for the systems studied here and the large number of calculations required for a comprehensive study like this one made it desirable to keep the calculations efficient. The results provide a systematic body of information of uniform accuracy in which trends with atomic number can be reliably followed; they constitute a useful reference point for further refinement.

The introduction of zero-point motion of the lattice and thermal excitations in the system would require detailed knowledge of phonon and magnon excitations and a large expansion of the calculation to carry out appropriate statistical averaging. Some progress in this extension of the band theory of magnetism has been made (Sandratski and Guletski 1989, Peng and Jansen 1988, Liechtenstein et al. 1987). However it is

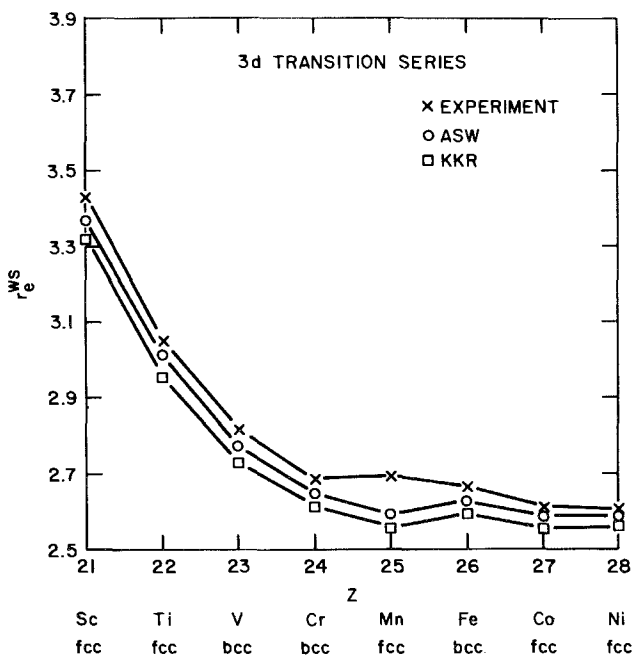

Fig. 1. Equilibrium ground-state Wigner–Seitz radius r_e^{WS} (bohr) for the 3d transition series versus atomic number Z; the volume per atom for any structure is used to define r_e^{WS}; for each element the more stable structure between bcc and fcc is used; experiment (crosses), spin-polarized ASW (open circles), KKR results (open squares); the table 3 caption gives the relation between the lattice constant in Å and r_{WS} in bohrs.

not clear that the desired accuracy of better than one mRy in the total energy per atom can be maintained. An alternative simpler procedure for comparing rigid-lattice theory with experiment is to use measurements down to low temperatures to extrapolate to the rigid-lattice values. Improvement in the more fundamental approximation contained in the LSDA is more difficult, but some progress has been reported (Bagno et al. 1989).

5.2. *Results near equilibrium and trends with atomic number*

We describe first the results of the new calculations near the ground equilibrium state, both because it provides continuity with the previous work of MJW (Moruzzi et al. 1978), and because these results are the most accessible to experiment. The information in the plots is supplemented by tables of quantitative results from the energy calculations. These tabular results go beyond MJW by including both bcc and fcc structures for each element and by using spin-polarized calculations in all cases.

The trends at the equilibrium state in the 3d and 4d transition series as functions of atomic number Z are plotted in figs. 1 to 4. In each case the more stable of the bcc and fcc structures is used; in two cases in each series the choice is dictated by experiment (see table 2). Figures 1 and 2 show the trends in the equilibrium Wigner–Seitz or equivalent-sphere radius r_e^{WS}, which is proportional to the lattice constant a (the caption to table 3 gives the factor between a in Å and r_e^{WS} in bohrs). The ASW

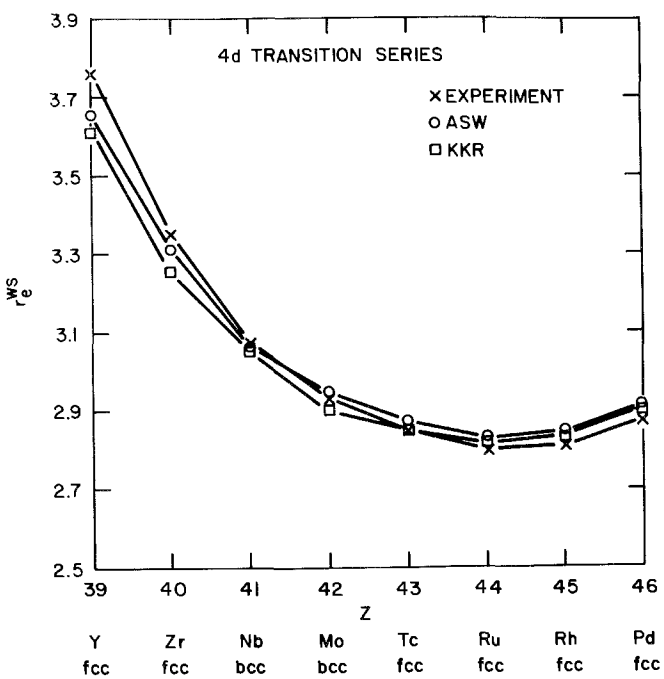

Fig. 2. The same plots as in fig. 1 for the 4d transition series.

values are compared with the KKR values in MJW and with experiment (Taylor and Kagle 1963). The ASW values of r_e^{ws} track the KKR values closely, but are slightly larger (up to 1% in the 3d series, up to 2% in the 4d series). Both the ASW and the KKR values track the experimental values well with the exception of Mn. The theoretical values for bcc Fe, fcc Co and fcc Ni include the volume increase due to magnetization, since the equilibrium state is ferromagnetic. However the theoretical value for Mn is for the nonmagnetic equilibrium state of the fcc lattice, whereas the experimental value comes from the many-atom equilibrium magnetic cell of α-Mn, whose magnetic character increases the volume per atom.

The effects of magnetization are more dramatic on the bulk moduli B plotted in figs. 3 and 4 for the ASW results and experiment (Simmons and Wang 1971). The ASW values of B track the experimental values closely for the nonmagnetic 4d series in fig. 4 (theory is 4 to 5% high) and follow a smooth curve with a maximum. However the ASW values of B for the 3d series show a large abrupt drop from such a curve

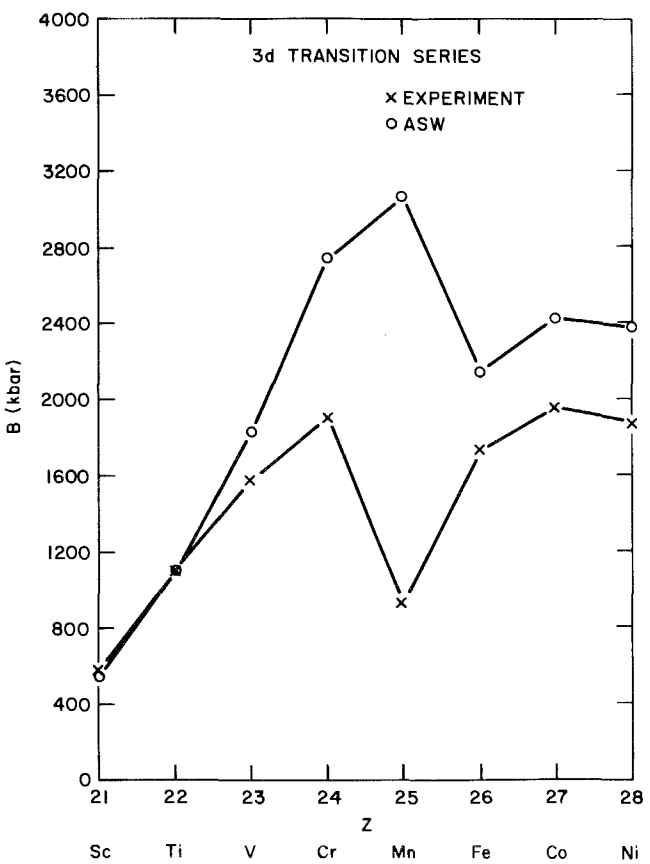

Fig. 3. Bulk moduli B (kbar) in the ground equilibrium state for the 3d transition series from spin-polarized ASW calculations (open circles) compared with experiment (crosses) versus Z; same structures as in fig. 1.

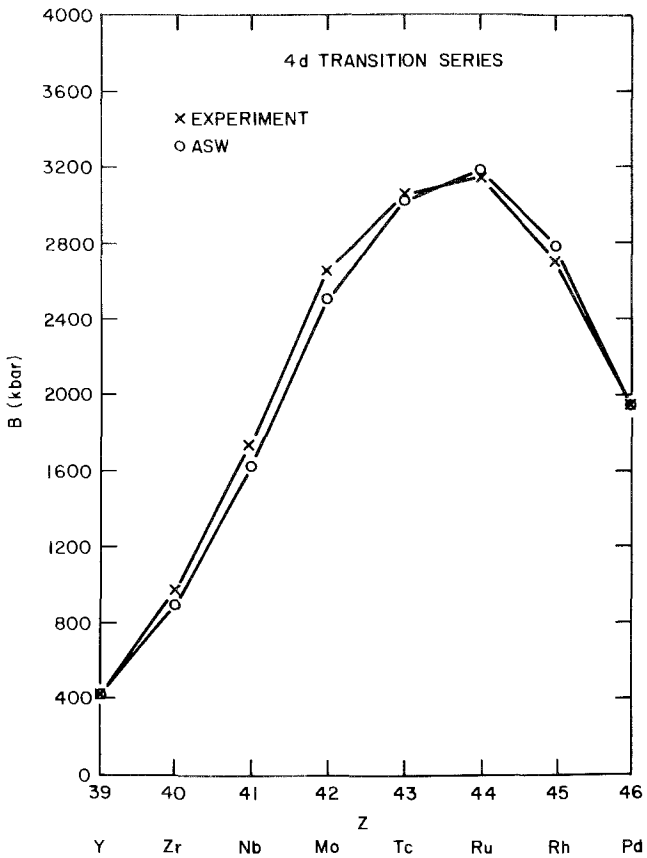

Fig. 4. The same plots as fig. 3 for the 4d transition series.

for the three ferromagnetic elements Fe, Co and Ni. The experimental values show an earlier abrupt drop in B which includes Cr and Mn as well as Fe, Co and Ni. The much lower experimental B values for Cr and Mn are qualitatively explained by the fact that each is magnetic at equilibrium with a complicated many-atom magnetic cell, whereas the calculated values for bcc Cr and fcc Mn are for the *nonmagnetic* equilibrium state. It should be noted that while the calculated B values for Fe, Co and Ni track the experimental values, they are high by about 25%, a substantial discrepancy compared to the 3d and 4d elements with nonmagnetic equilibrium states and at this time unexplained.

The cohesive energies given in MJW are omitted here, since they depend on total-energy calculations which use the LSDA in isolated atoms, where the approximation is much poorer than for atoms in condensed matter. However values of the cohesive energy may be deduced from the entries in table 2, which repeats the total energies for LSDA atoms from MJW-table 1.1 and also gives the total energies per atom of the bcc and fcc equilibrium states. Table 2 also provides an estimate of whether the

TABLE 2
ASW total energies per atom of 3d and 4d transition elements. The total energies per atom E in Ry are listed for the free LSDA atom in column 2 (from Moruzzi et al. 1978), for the bcc and fcc structures in columns 3 and 4; the last column gives the more stable structure; a dash means the values are too close to decide between bcc and fcc. Values of E marked with an asterisk are ferromagnetic equilibrium states.

Element	LSDA atom	bcc structure	fcc structure	More stable structure
Sc	−1517.322	−1517.669	−1517.672	fcc
Ti	−1694.591	−1695.024	−1695.023	–
V	−1883.529	−1883.958	−1883.936	bcc
Cr	−2084.386	−2084.689	−2084.689	bcc
Mn	−2297.211	−2297.556*	−2297.560	fcc
Fe	−2522.369	−2522.818*	−2522.818	–
Co	−2760.288	−2760.747*	−2760.754*	fcc
Ni	−3011.233	−3011.639*	−3011.643*	fcc
Y	−6658.819	−6659.177	−6659.182	fcc
Zr	−7073.319	−7073.812	−7073.810	–
Nb	−7502.361	−7502.904	−7502.872	bcc
Mo	−7946.087	−7946.579	−7946.546	bcc
Te	−8404.435	−8404.979	−8404.992	fcc
Ru	−8877.807	−8878.341	−8878.375	fcc
Rh	−9366.418	−9366.859	−9366.877	fcc
Pd	−9870.419	−9870.701	−9870.701	–

bcc or fcc equilibrium state is more stable. In four cases, marked by a dash, the E values are too close for a reliable theoretical estimate. The failure to find a clear preference for bcc Fe over fcc Fe is probably a failure of the LSDA combined with the error in the spherical approximation. Work which corrects these errors and finds that bcc Fe is more stable is Bagno et al. (1989). In six cases, marked by an asterisk, the equilibrium state is ferromagnetic.

Tables 3 and 4 tabulate the coefficients of a cubic expansion of $E(r_{WS})$ around r_e^{WS} for the 3d and 4d series in bcc and fcc structures. These coefficients provide values of the lattice constants, a, bulk moduli, B, and Grüneisen constants, γ (related to the pressure derivative of the bulk modulus). For fcc Co and Ni and for bcc Mn, Fe, Co and Ni the equilibrium state is ferromagnetic and the corresponding magnetic moment is listed. For bcc Fe, fcc Co and fcc Ni the experimental value (corrected to the spin-only value with the experimental g factor) is also listed and is within 3% of theory.

5.3. *Energies and magnetic moments of ferromagnetic phases*

The main body of ASW results is contained in the $E(V)$ and $M(V)$ functions along the magnetic phase lines for the individual elements. An overall view of the trends in the ferromagnetic moments for the 3d elements in bcc structure is provided by fig. 5. The four lower-Z elements have nonmagnetic equilibrium states and would require expansions of the lattice to reach a transition to the ferromagnetic phase.

TABLE 3

Coefficients of cubic fit to ASW total energies around equilibrium for bcc lattices. The ASW calculated values of changes in total energy per atom $E-E_c$ in Ry for the 3d and 4d series in bcc structure are fitted around the equilibrium values r_e^{WS} and E_c to the cubic polynomial $E-E_c = E_2(r-r_e)^2 - E_3(r-r_e)^3$ where E_c is given in table 1. From r_e^{WS}, E_2, E_3 the values of the cubic lattice constant a (Å), bulk modulus B (kbar), and Grüneisen constant γ are given, where $a^{bcc}(Å) = 1.0748 r_e^{WS}(\text{bohr})$, $a^{fcc}(Å) = 1.3542 r_e^{WS}(\text{bohr})$, $B_e(\text{kbar}) = 7804.4 E_2(\text{Ry/bohr}^2)$, $\gamma = r_e^{WS}(\text{bohr}) E_3(\text{Ry/bohr}^3)/2E_2(\text{Ry/bohr}^2) = -\frac{1}{2} + \frac{1}{2}dB/dp$. The ASW (th) and experimental (ex) values (where available) of equilibrium magnetic moments M_e in Bohr magnetons are given in the last two columns. The experimental values are corrected to spin-only values with the measured g factor.

Element	r_e^{WS}	E_2	E_3	a	B	γ	M_e	
							th	ex
Sc	3.374	0.2378	0.1287	3.627	550	0.913		
Ti	3.003	0.4019	0.2254	3.228	1045	0.842		
V	2.776	0.6518	0.5023	2.984	1832	1.070		
Cr	2.644	0.9239	0.9404	2.842	2727	1.346		
Mn	2.590	0.9164	1.2806	2.784	2761	1.810	0.70	
Fe	2.626	0.7203	0.9942	2.823	2141	1.812	2.15	2.12
Co	2.602	0.7900	0.9336	2.797	2369	1.538	1.68	
Ni	2.585	0.7442	1.1983	2.778	2247	2.081	0.38	
Y	3.673	0.1820	0.0614	3.948	387	0.620		
Zr	3.272	0.3423	0.1425	3.517	816	0.681		
Nb	3.064	0.6335	0.4025	3.293	1614	0.973		
Mo	2.947	0.9443	0.7662	3.167	2501	1.196		
Tc	2.886	1.0646	0.9771	3.101	2879	1.324		
Ru	2.857	1.0787	1.3390	3.071	2947	1.773		
Rh	2.865	0.9655	1.1610	3.079	2630	1.722		
Pd	2.922	0.6937	0.7431	3.957	1853	1.565		

The four upper-Z elements have ferromagnetic equilibrium states, which could be removed by compressing the lattice. The transitions themselves are of three types: first order (discontinuous moment), second order (continuous moment), composite [second-order transition to a low-spin (LS) magnetic phase followed by a first-order transition to a high-spin (HS) magnetic phase as the lattice expands].

Figures 6 to 37 give the ASW results element by element through the 3d and then the 4d series, first in bcc structure followed immediately by fcc structure. Each plot for a particular element in a particular structure contains the functions $E(V)$ and $M(V)$ for each ferromagnetic phase (which includes the nonmagnetic phase). The energy scale (on the left in mRy) has a zero reference level at the equilibrium state and the moment scale (on the right in Bohr magnetons μ_B) has a zero level displaced upward. The volume dependence is provided by the Wigner–Seitz radius (in bohrs), which gives the bcc and fcc lattices similar ranges.

The values of special radii that appear in the plots are listed in table 5 for the bcc structure and table 6 for the fcc structure. These radii are the equilibrium state radius and the stability limits of the nonmagnetic, low-spin and high-spin ferromagnetic

TABLE 4
Coefficients of cubic fit to ASW total energies around equilibrium for fcc lattices. The same quantities as in table 3 for fcc lattices.

Element	r_e^{WS}	E_2	E_3	a	B	γ	M_e	
							th	ex
Sc	3.361	0.2337	0.1184	4.551	543	0.852		
Ti	3.013	0.4208	0.2657	4.080	1090	0.951		
V	2.807	0.6582	0.5481	3.802	1830	1.169		
Cr	2.667	0.8534	0.9065	3.612	2497	1.417		
Mn	2.583	1.0124	1.1921	3.498	3059	1.521		
Fe	2.541	1.0186	1.4028	3.441	3128	1.750		
Co	2.583	0.7998	1.0964	3.497	2417	1.770	1.56	1.61
Ni	2.585	0.7870	1.0161	3.500	2376	1.669	0.60	0.61
Y	3.655	0.1934	0.0848	4.950	413	0.801		
Zr	3.306	0.3752	0.1888	4.476	886	0.832		
Nb	3.105	0.6195	0.3998	4.204	1557	1.002		
Mo	2.954	0.9466	0.9500	4.000	2501	1.482		
Tc	2.873	1.1078	1.0674	3.890	3009	1.384		
Ru	2.829	1.1494	1.2690	3.832	3170	1.562		
Rh	2.841	1.0127	1.2381	3.847	2782	1.737		
Pd	2.912	0.7273	1.0238	3.943	1949	2.049		

phases. The stability limits of antiferromagnetic phases are also given and will be discussed in section 5.4. The table contains the relative expansion of the lattice constant $\Delta r/r$ in % required to reach a phase transition from equilibrium, and is negative when the equilibrium phase is ferromagnetic; algebraically larger values of $\Delta r/r$ mean weaker magnetic interactions in that element. The column (TO1) listing the type of transition from the nonmagnetic to the ferromagnetic phases shows that second-order transitions occur at the ends of the transition series, that first-order transitions occur in the middle of the series and composite transitions in between the other two. The transitions in Rh and Pd are marked W for weak, since the moments are less than one Bohr magneton, hence the energy minima in $E(M)_V$ are shallow and it is difficult to follow the magnetic phase to its stability limit to fix the order. (The transition is probably second order, since these elements end a transition series.)

Examination of the special radii and especially of the % expansion required to reach a phase transition from equilibrium leads to some qualitative comparative comments about the occurrence of ferromagnetism in the transition series, i.e., magnetism is more favored by the 3d elements over the 4d elements, and by the higher-Z over the lower-Z members of each series. In five out of eight cases for each series the bcc structure favors the ferromagnetic phase more than the fcc structure, in two cases the fcc structure favors ferromagnetism more, and in one case there is no difference.

The transition to the ferromagnetic phase is of different type in the bcc than the fcc structure for V, Cr, Mn, Fe, Co in the 3d series and for Nb, Mo and Ru in the

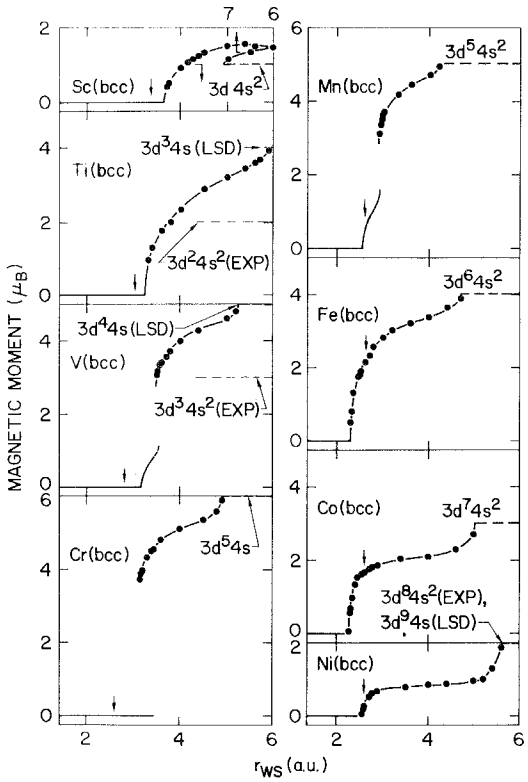

Fig. 5. Magnetic moments (Bohr magnetons) versus r_{WS} (bohrs) for the 3d transition series from spin-polarized ASW calculations in bcc structure. The equilibrium radius r_e^{WS} is indicated by an arrow; the electron configuration and moment of the free atom are shown (dashed lines) for LSDA and from experiment.

4d series. The $E(V)$ and $M(V)$ curves differ most between bcc and fcc Fe and between bcc and fcc Mn.

In fig. 38 the spin susceptibility enhancement factor in the nonmagnetic phase of fcc Rh and fcc Pd is plotted as a function of volume. The calculation used eq. (17) of section 4 and the $E(V, M)$ function (Moruzzi and Marcus 1989a). These factors diverge at the stability limit of the nonmagnetic phase.

Of particular interest are bcc Mn (fig. 14), bcc Co (fig. 18) and bcc Ni (fig. 20), which are predicted to have ferromagnetic equilibrium states. In each case these lattice structures are not the most stable structures, but stabilization of these structures by epitaxial growth has been reported: bcc Mn on Fe(001) by Heinrich et al. (1986); of bcc Ni on Fe(001) by Z. Q. Wang et al. (1987) and by Heinrich et al. (1988); of bcc Co on GaAs(110) by Idzerda et al. (1989). Also of great interest is fcc Fe (fig. 17), which has a nonmagnetic ground equilibrium state, but has a metastable equilibrium state when the lattice constant is expanded about 5%. Epitaxial growth on Cu(001), which stretches the lattice 5%, has been shown to produce ferromagnetic Fe (Pescia

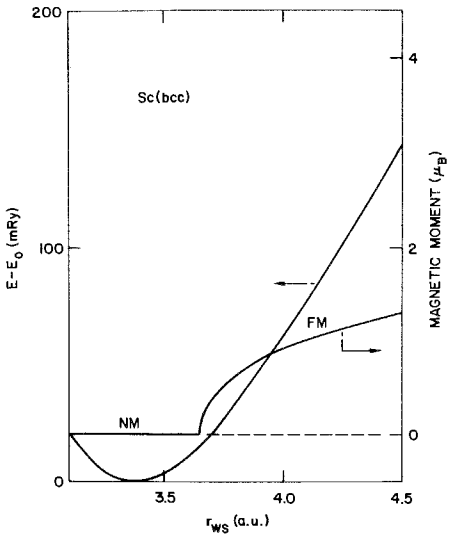

Fig. 6. The total energy E per atom (change in mRy from the equilibrium value; scale at left) and magnetic moment per atom (Bohr magnetons; scale at right) for bcc Sc versus r_{WS} (bohrs) along the nonmagnetic and ferromagnetic phase lines from spin-polarized band calculations.

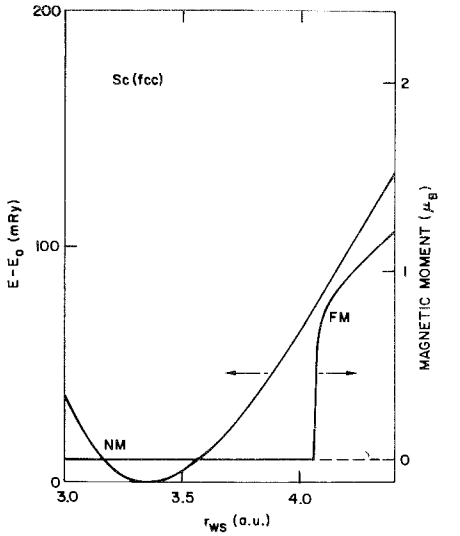

Fig. 7. $E(r_{WS})$ and $M(r_{WS})$ for fcc Sc, description as in fig. 6.

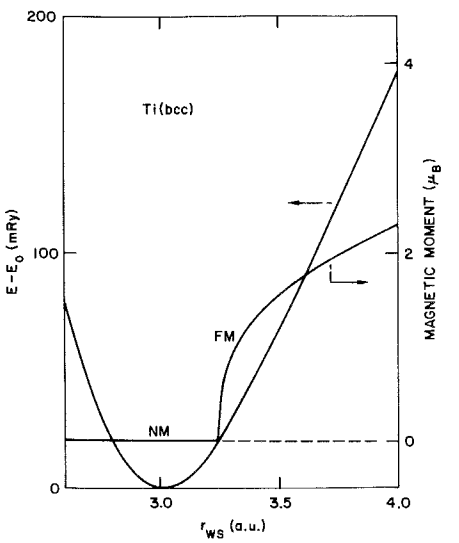

Fig. 8. $E(r_{WS})$ and $M(r_{WS})$ for bcc Ti, as in fig. 6.

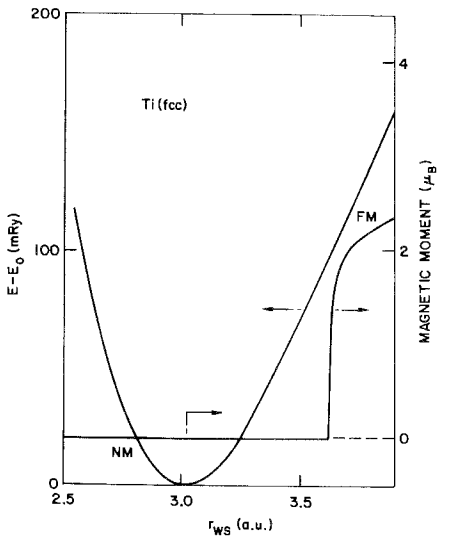

Fig. 9. $E(r_{WS})$ and $M(r_{WS})$ for fcc Ti, as in fig. 6.

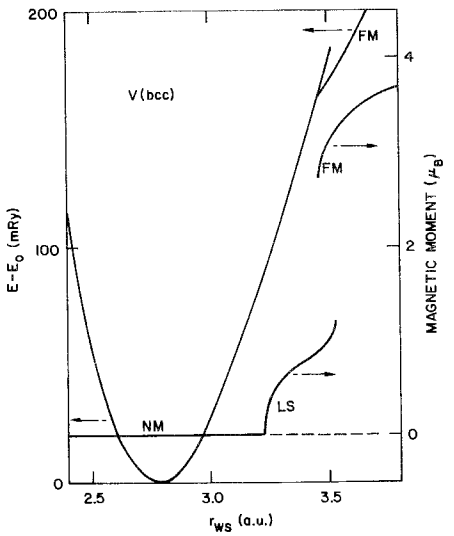

Fig. 10. $E(r_{WS})$ and $M(r_{WS})$ for bcc V, as in fig. 6.

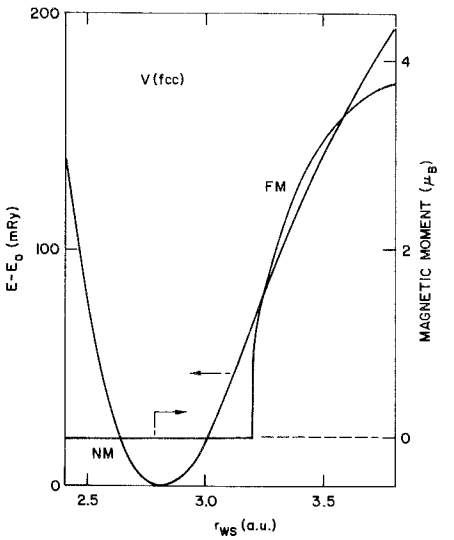

Fig. 11. $E(r_{WS})$ and $M(r_{WS})$ for fcc V, as in fig. 6.

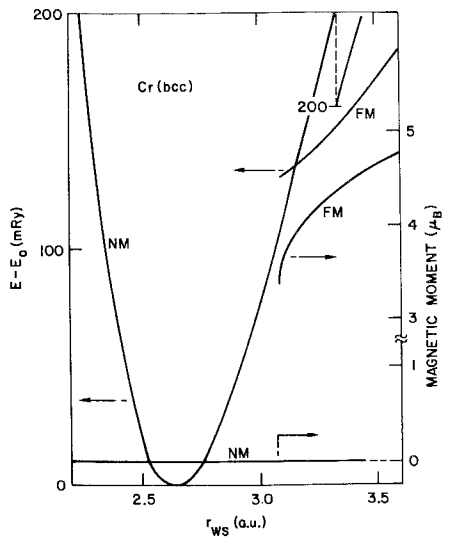

Fig. 12. $E(r_{WS})$ and $M(r_{WS})$ for bcc Cr, as in fig. 6.

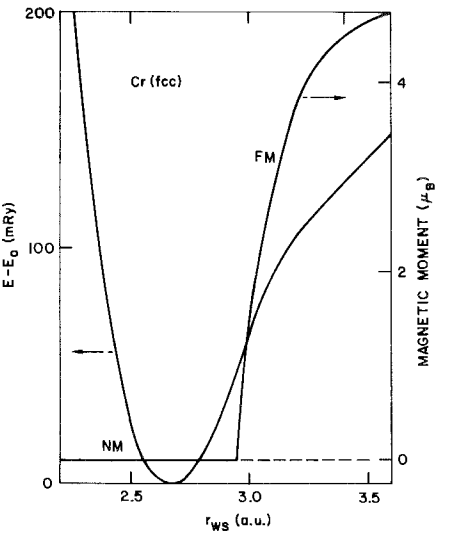

Fig. 13. $E(r_{WS})$ and $M(r_{WS})$ for fcc Cr, as in fig. 6.

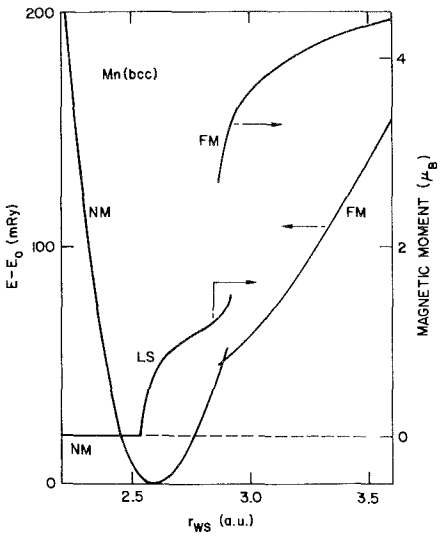

Fig. 14. $E(r_{WS})$ and $M(r_{WS})$ for bcc Mn, as in fig. 6.

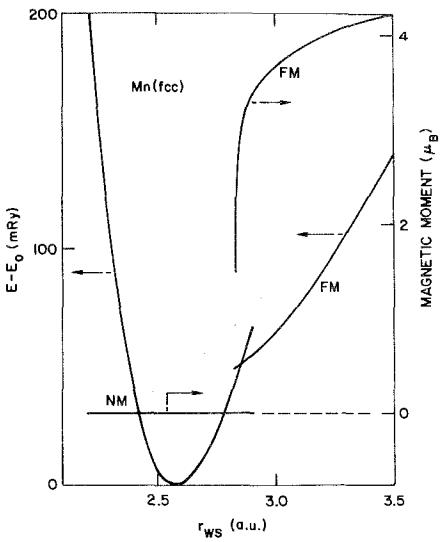

Fig. 15. $E(r_{WS})$ and $M(r_{WS})$ for fcc Mn, as in fig. 6.

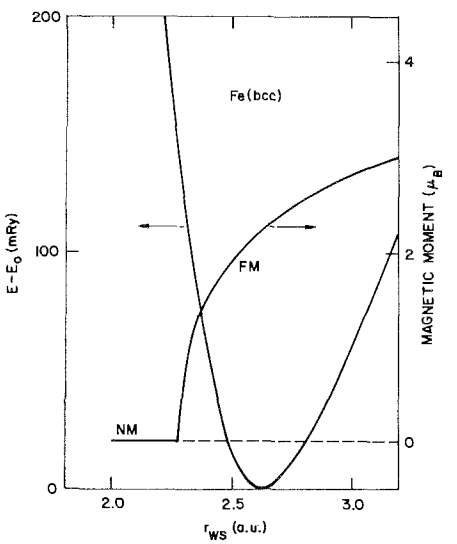

Fig. 16. $E(r_{WS})$ and $M(r_{WS})$ for bcc Fe, as in fig. 6.

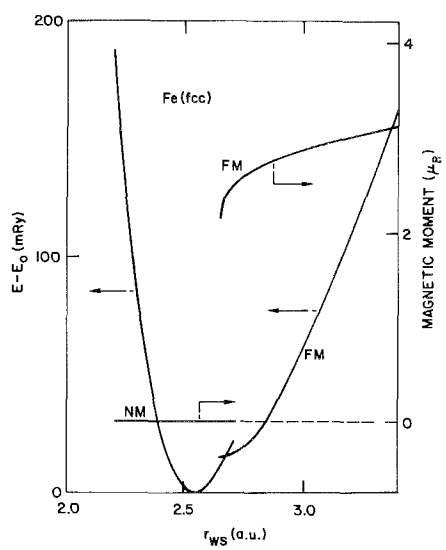

Fig. 17. $E(r_{WS})$ and $M(r_{WS})$ for fcc Fe, as in fig. 6.

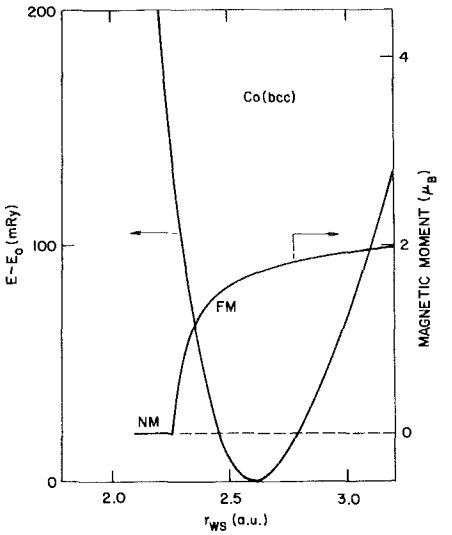

Fig. 18. $E(r_{WS})$ and $M(r_{WS})$ for bcc Co, as in fig. 6.

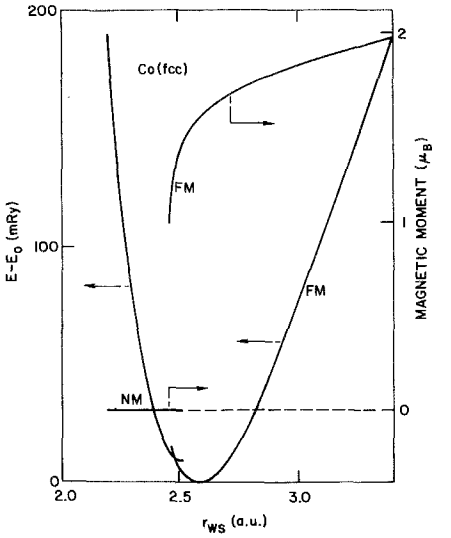

Fig. 19. $E(r_{WS})$ and $M(r_{WS})$ for fcc Co, as in fig. 6.

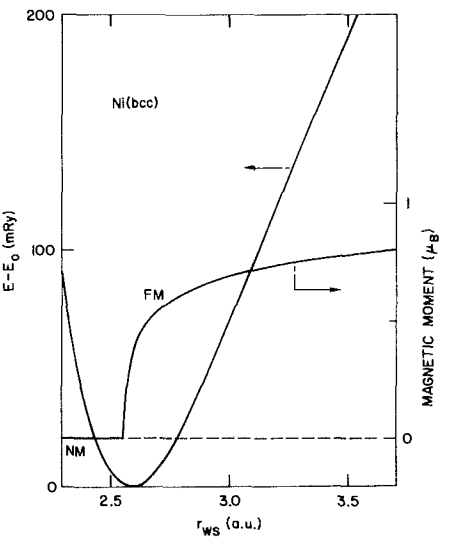

Fig. 20. $E(r_{WS})$ and $M(r_{WS})$ for bcc Ni, as in fig. 6.

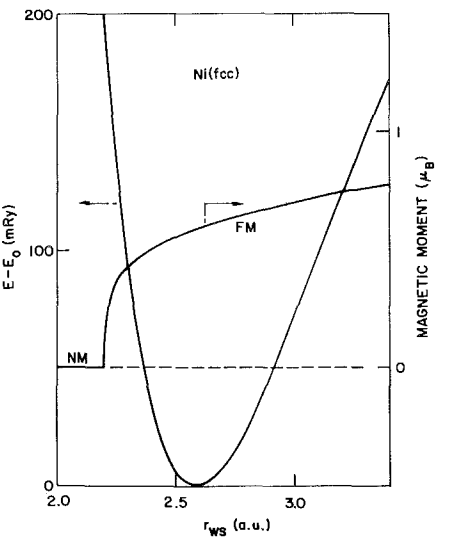

Fig. 21. $E(r_{WS})$ and $M(r_{WS})$ for fcc Ni, as in fig. 6.

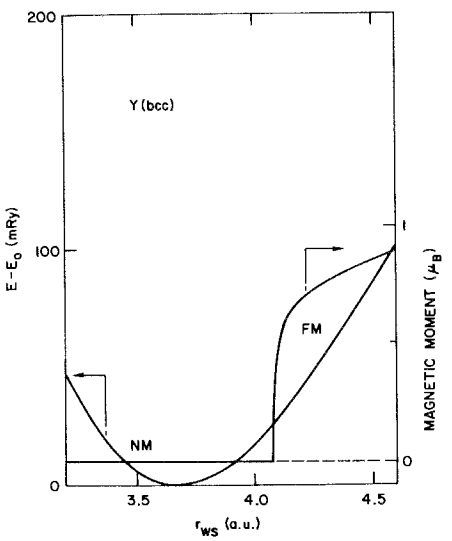

Fig. 22. $E(r_{WS})$ and $M(r_{WS})$ for bcc Y, as in fig. 6.

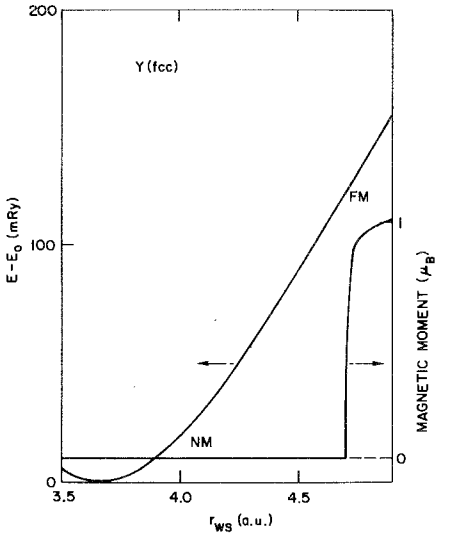

Fig. 23. $E(r_{WS})$ and $M(r_{WS})$ for fcc Y, as in fig. 6.

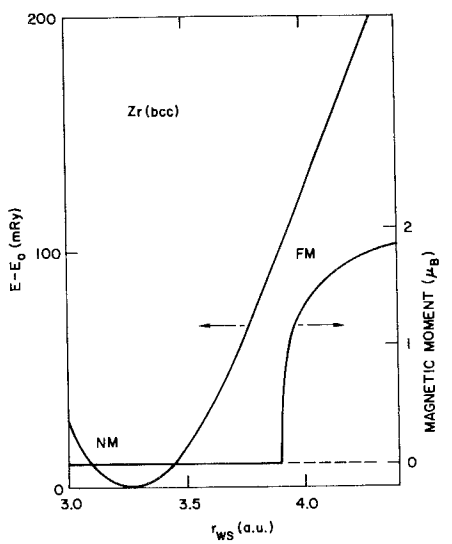

Fig. 24. $E(r_{WS})$ and $M(r_{WS})$ for bcc Zr, as in fig. 6.

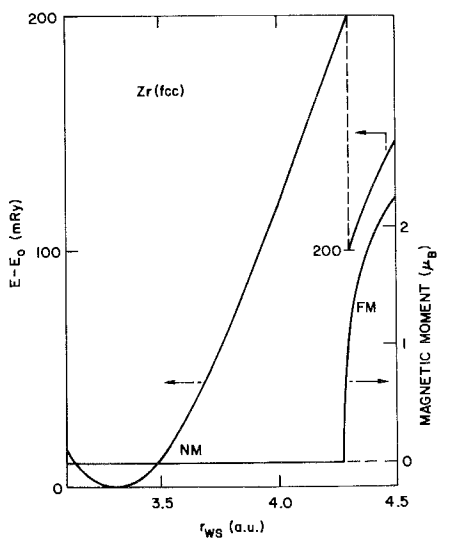

Fig. 25. $E(r_{WS})$ and $M(r_{WS})$ for fcc Zr, as in fig. 6.

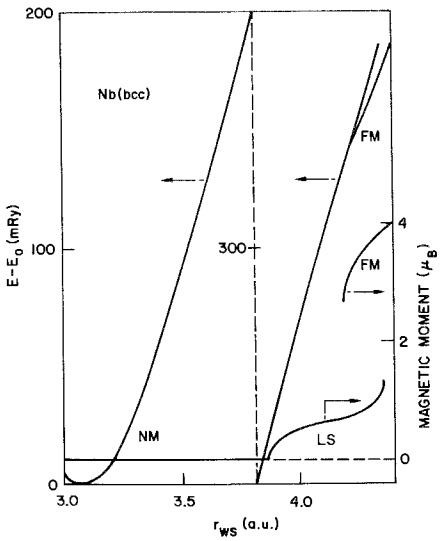

Fig. 26. $E(r_{WS})$ and $M(r_{WS})$ for bcc Nb, as in fig. 6.

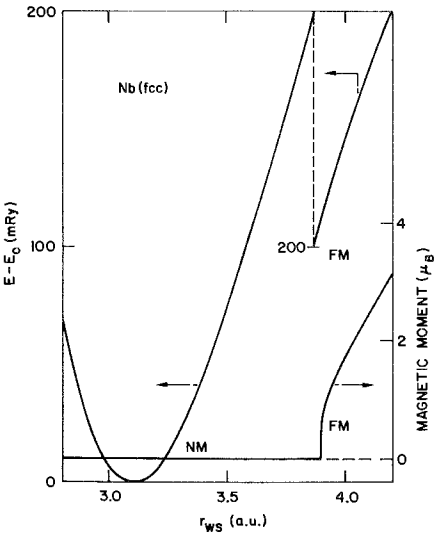

Fig. 27. $E(r_{WS})$ and $M(r_{WS})$ for fcc Nb, as in fig. 6.

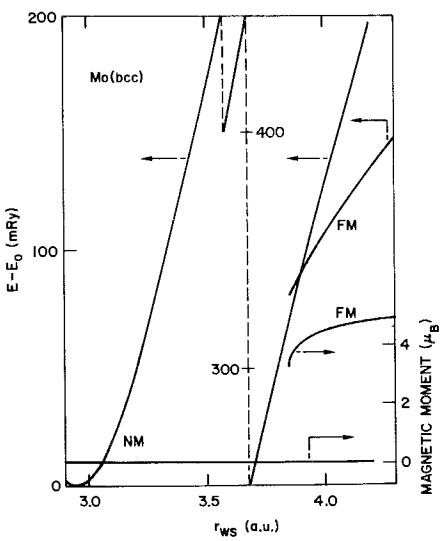

Fig. 28. $E(r_{WS})$ and $M(r_{WS})$ for bcc Mo, as in fig. 6.

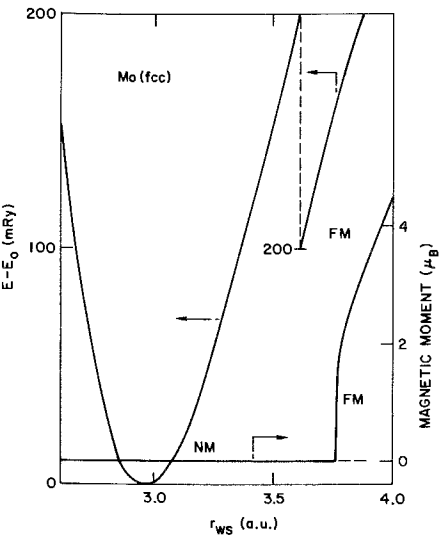

Fig. 29. $E(r_{WS})$ and $M(r_{WS})$ for fcc Mo, as in fig. 6.

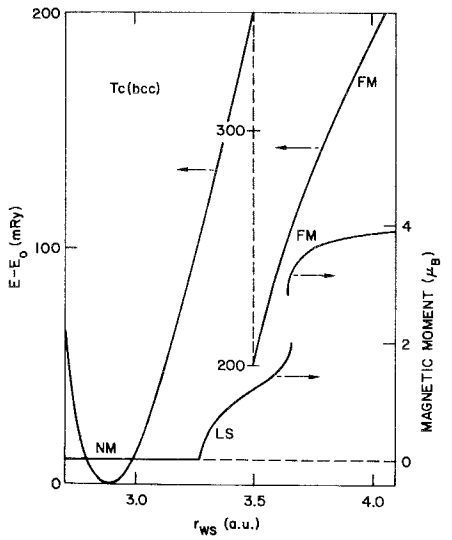

Fig. 30. $E(r_{WS})$ and $M(r_{WS})$ for bcc Tc, as in fig. 6.

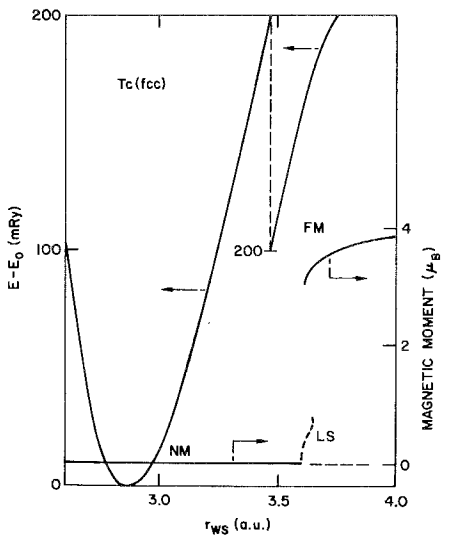

Fig. 31. $E(r_{WS})$ and $M(r_{WS})$ for fcc Tc, as in fig. 6.

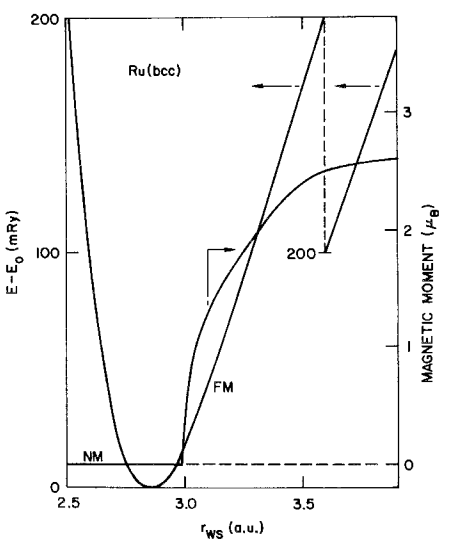

Fig. 32. $E(r_{WS})$ and $M(r_{WS})$ for bcc Ru, as in fig. 6.

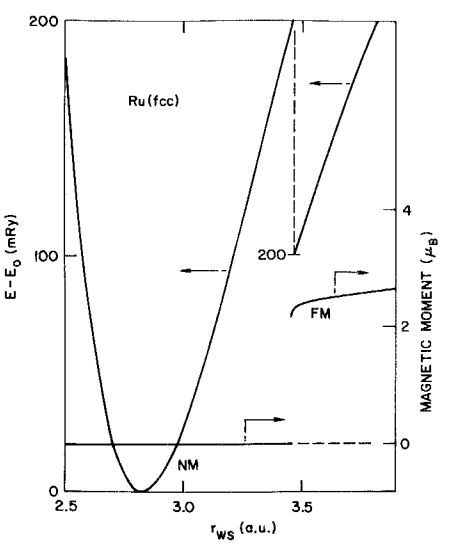

Fig. 33. $E(r_{WS})$ and $M(r_{WS})$ for fcc Ru, as in fig. 6.

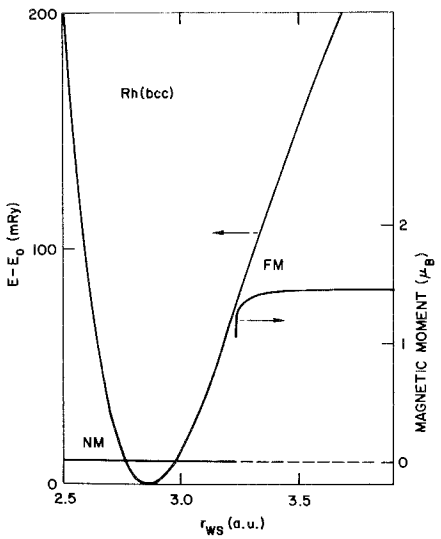

Fig. 34. $E(r^5_{WS})$ and $M(r_{WS})$ for bcc Rh, as in fig. 6.

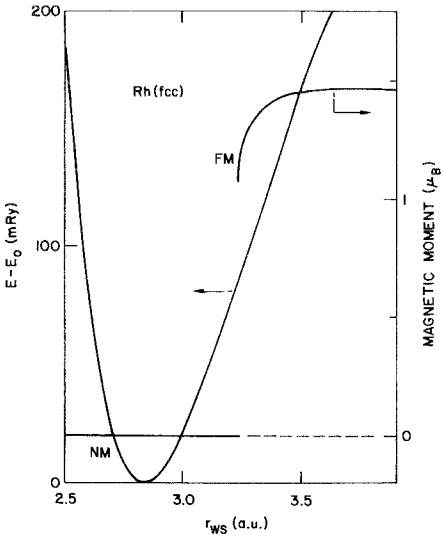

Fig. 35. $E(r_{WS})$ and $M(r_{WS})$ for fcc Rh, as in fig. 6.

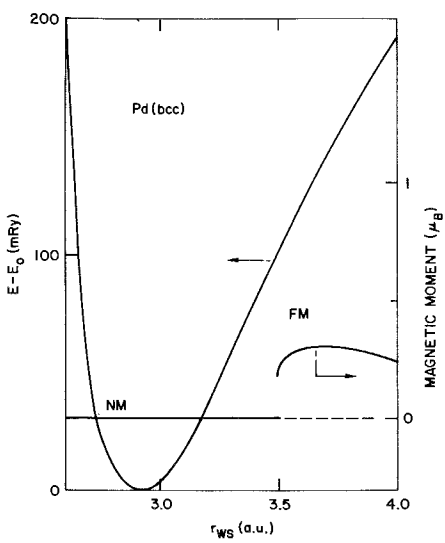

Fig. 36. $E(r_{WS})$ and $M(r_{WS})$ for bcc Pd, as in fig. 6.

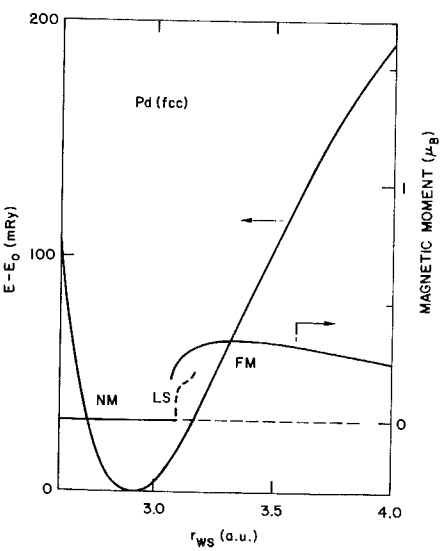

Fig. 37. $E(r_{WS})$ and $M(r_{WS})$ for fcc Pd, as in fig. 6.

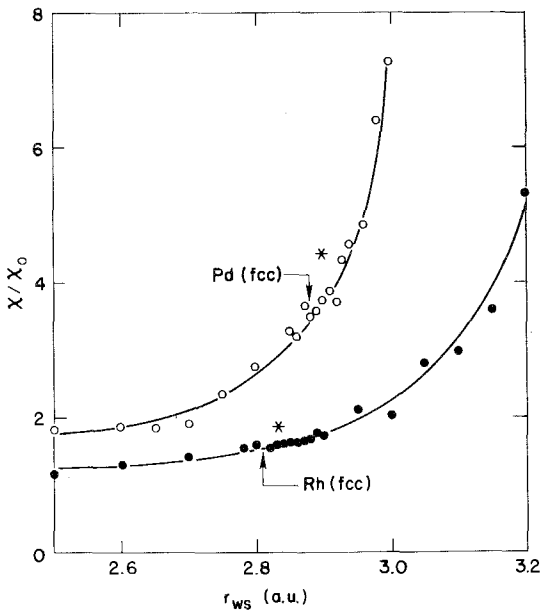

Fig. 38. Spin susceptibility enhancement factor χ/χ_o versus r_{ws} for fcc Rh and fcc Pd from spin-polarized ASW calculations; * is from Janak (1977).

et al. 1987). Ferromagnetic phases of bcc Ru, Sc and Ti and fcc Ru may also be in range of such stabilization.

5.4. *Energies and magnetic moments of antiferromagnetic phases*

The calculations of section 5.3 are extended to antiferromagnetic spin arrangements by generalizing the FSM procedure to two-atom cells. The spin-polarized ASW calculation is applied to the two-atom cell with the partial constraint that the total moment of the whole cell is fixed; when the moment is fixed at $M = 0$ antiferromagnetic states can be found. For $M = 0$ two self-consistent solutions of the KS equations may exist at the same volume, namely, a nonmagnetic one in which the magnetization density vanishes everywhere or an antiferromagnetic one in which the magnetization density has one sign around one nucleus and the opposite sign around the other nucleus. The choice of which solution is found depends on the initial spin distribution, i.e., the antiferromagnetic solution is generated by iteration from initial spin distributions that are inverted between the two atoms. The converged self-consistent solution then has a total spin of one sign in the part of the cell around one atom and an equal spin distribution of the other sign around the other atom. These sublattice spin values are found in the ASW from the total spin in each equivalent sphere.

This partially constrained procedure has been applied to type-I antiferromagnetism in the bcc structure in which the spins form a CsCl-type lattice of two interpenetrating simple cubic lattices and also to type-I antiferromagnetism in the fcc structure in

TABLE 5

Critical radii and transition order for ferromagnetic and antiferromagnetic phases in bcc structure. The critical Wigner–Seitz radii for magnetic transitions for the 3d and 4d transition series in bcc structure in bohrs (the WS superscript is omitted for simplicity); r_e is the equilibrium radius (also in table 2); r_{NM} is the stability limit of the nonmagnetic phase; r_{FM}^{LS} gives the lower and upper stability limits of the low-spin ferromagnetic phase for composite transitions (when the NM–LS transition is second-order, r_{NM} = the lower value of r_{FM}^{LS}); r_{FM}^{HS} is the lower stability limit of the high-spin ferromagnetic phase; C = composite transition; W = a weak transition (change in M less than one μ_B); $\Delta r/r(\%)$ = percent change in lattice constant between the equilibrium state and the onset of the ferromagnetic phase; TO1 is the transition order for the NM to the FM phase; TO2 is the transition order for the NM to the AF phase. For antiferromagnetic transitions r_{FIM} gives the stability limits on a ferrimagnetic phase; r_{AF} = the onset of an antiferromagnetic phase; the composite antiferromagnetic transition is first a ferrimagnetic phase, then a first-order transition to an antiferromagnetic phase.

Element	r_e	r_{NM}	r_{FM}^{LS}	r_{FM}^{HS}	$\Delta r/r(\%)$	TO1	r_{FIM}	r_{AF}	TO2	$\Delta r/r(\%)$
Sc	3.37	3.65		3.65	8.3	2				
Ti	3.00	3.24		3.24	8.0	2				
V	2.78	3.17	3.17–3.53	3.47	14.0	C		3.15	2	13.3
Cr	2.64	3.44		3.09	17.0	1		2.72	1	3.0
Mn	2.59	2.53	2.53–2.92	2.86	−2.3	C	2.69–2.82	2.79	C	3.9*
Fe	2.63	2.27		2.27	−13.7	2				
Co	2.60	2.25		2.25	−13.5	2				
Ni	2.58	2.56		2.56	−0.8	2				
Y	3.67	4.08		4.08	11.1	2				
Zr	3.27	3.90		3.90	16.2	2				
Nb	3.06	3.86	3.86–4.35	4.18	26.1	C		3.91	2	27.7
Mo	2.95	4.20		3.85	30.5	1		3.40	2	15.3
Te	2.89	3.27	3.27–3.66	3.64	13.1	C		3.50	1	21.1
Ru	2.86	2.99		2.99	4.5	2				
Rh	2.86	3.24		3.23	12.9	W				
Pd	2.92	3.51		3.49	19.5	W				

*% stretch to ferrimagnetic phase.

which the spins form a CuAu-type lattice with spin signs alternating on successive (001) planes. The bcc antiferromagnetic type-I arrangement preserves cubic symmetry around each atom, but the fcc type-I arrangement has a special axis (along [001] if the spin planes are (001)), which allows a tetragonal distortion to lower the energy. Hence the results given here for the fcc lattice are not complete, since they constrain the lattice to fcc structure, and the type-I antiferromagnetic phases shown in the plots are unstable with respect to a tetragonal distortion (Oguchi and Freeman 1984).

When M is allowed to vary in the two-atom cell an $E(M)_V$ function is found that provides additional information about the magnetic phases. If $E(M)_V$ has a minimum at $M = 0$ for the antiferromagnetic solution, that solution is stable, but if $E(M)_V$ has a maximum at $M = 0$ the antiferromagnetic solution is unstable. Just such an instability occurs (Moruzzi and Marcus 1990a) in the case of bcc Fe. If a minimum of $E(M)_V$ occurs at *finite* M, then another magnetic phase is found which may be ferromagnetic

TABLE 6

Critical radii and transition order for ferromagnetic and antiferromagnetic phases in fcc structure. The critical Wigner–Seitz radii for magnetic transitions for the 3d and 4d transition series in fcc structure in bohrs (the WS superscript is omitted for simplicity). The definitions of r_e, r_{NM}, r_{FM}^{LS}, r_{FM}^{HS}, TO1, TO2, r_{AF} are the same as for table 5. There are no ferrimagnetic phases.

Element	r_e	r_{NM}	r_{FM}^{LS}	r_{FM}^{HS}	$\Delta r/r(\%)$	TO1	r_{AF}	TO2	$\Delta r/r(\%)$
Sc	3.36	4.05		4.05	20.5	2			
Ti	3.01	3.62		3.62	20.3	2			
V	2.81	3.20		3.20	13.9	2			
Cr	2.67	2.95		2.95	10.5	2			
Mn	2.58	2.90		2.83	9.7	1	2.58	2	0.0
Fe	2.54	2.70		2.65	4.3	1	2.54	2	0.0
Co	2.58	2.50		2.46	−4.7	1			
Ni	2.58	2.20		2.20	−14.7	2			
Y	3.66	4.70		4.70	28.4	2			
Zr	3.31	4.37		4.37	32.0	2			
Nb	3.10	3.90		3.90	25.8	2			
Mo	2.95	3.76		3.76	27.5	2			
Tc	2.87	3.60	3.60–3.64	3.62	25.4	C	3.35	2	16.7
Ru	2.83	3.46		3.45	21.9	1	3.35	2	18.4
Rh	2.84	3.25		3.24	14.1	W			
Pd	2.91	3.10		3.08	5.8	W			

(equal moments of the same sign on both atoms) or ferrimagnetic (unequal moments on the two atoms) as shown in fig. 43 for bcc Mn (Moruzzi and Marcus 1989b).

The results of these antiferromagnetic calculations on the 3d and 4d transition series in bcc and fcc structure are listed in tables 5 and 6 and plotted in figs. 39 to 50. Out of the sixteen cases of 3d elements in tables 5 and 6, there are five stable or metastable antiferromagnetic phases, four of them close to the equilibrium lattice. Out of the sixteen cases of 4d elements in the tables there are also five antiferromagnetic phases, but all are greatly expanded from the equilibrium lattice. All of these antiferromagnetic phases satisfy a simple rule – they arise when there is a first-order transition between ferromagnetic phases. In a first-order transition there are two $E(V)$ curves which intersect at an angle leaving a cusp-shaped region below the combined energy curves that is spanned by the lower-energy curve of the antiferromagnetic phase, e.g., fig. 39. The antiferromagnetic energy curve resembles the common tangent line which gives the energy curve of the two-phase volume range for a transition at constant volume between the two ferromagnetic phases. In this case there is a mixing of the two sublattices at the atomic level. Since the first-order ferromagnetic transitions occur near the middle of the transition series (note that composite transitions have a first-order part), all the antiferromagnetic phases are also near the middle of the transition series.

Plots of these ten antiferromagnetic cases are in figs. 39 to 50, which add antiferromagnetic energy-per-atom curves and sublattice magnetic moment-per-atom curves to the earlier ferromagnetic plots. For fcc Fe and fcc Mn (figs. 44 and 45) the

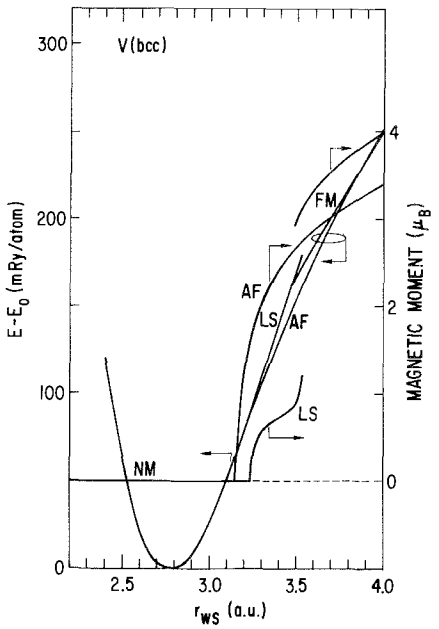

Fig. 39. $E(r_{ws})$ and $M(r_{ws})$ for bcc V with antiferromagnetic (AF) phase curves added to fig. 10.

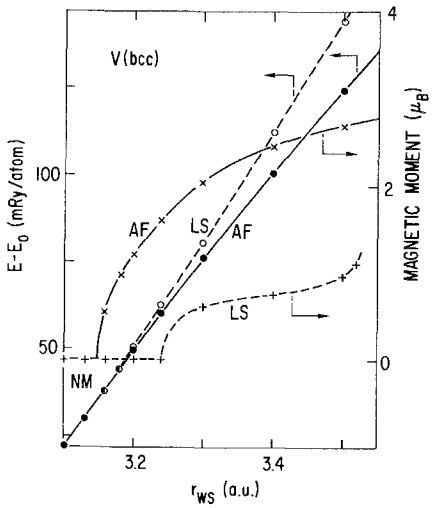

Fig. 40. Detail of AF and FM transitions for bcc V, enlarged from fig. 39.

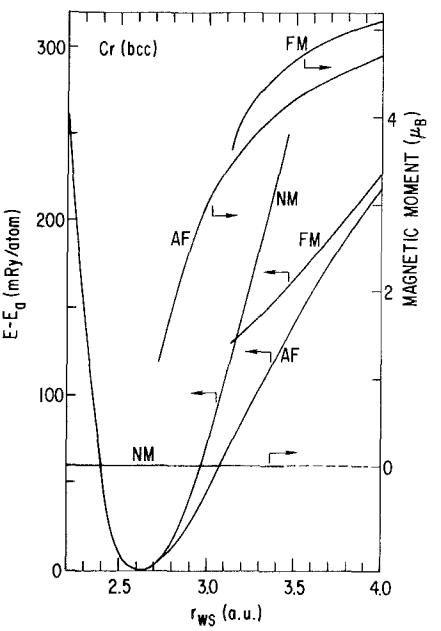

Fig. 41. $E(r_{ws})$ and $M(r_{ws})$ for bcc Cr with AF phase curves added to fig. 12.

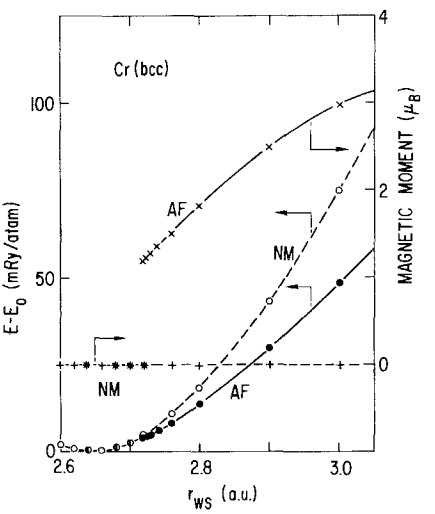

Fig. 42. Detail of AF and FM transitions for bcc V, enlarged from fig. 41.

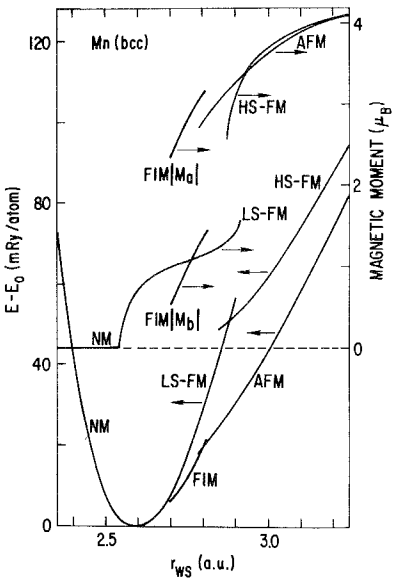

Fig. 43. $E(r_{WS})$ and $M(r_{WS})$ for bcc Mn with AF phase curves added to fig. 14.

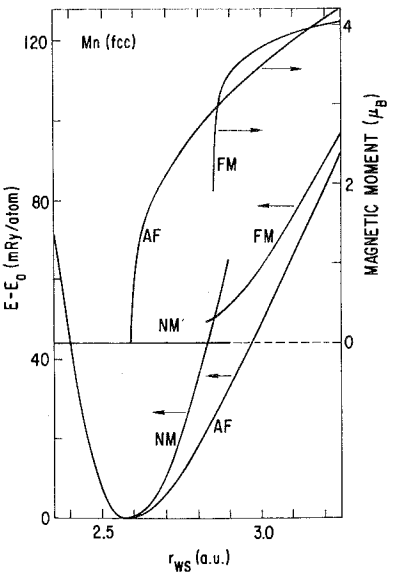

Fig. 44. $E(r_{WS})$ and $M(r_{WS})$ for fcc Mn with AF phase curves added to fig. 15.

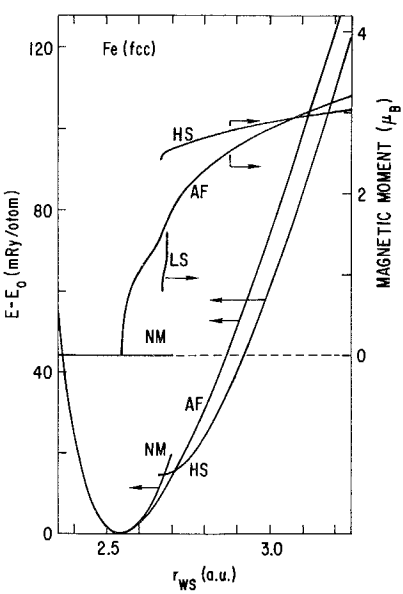

Fig. 45. $E(r_{WS})$ and $M(r_{WS})$ for fcc Fe with AF phase curves added to fig. 17.

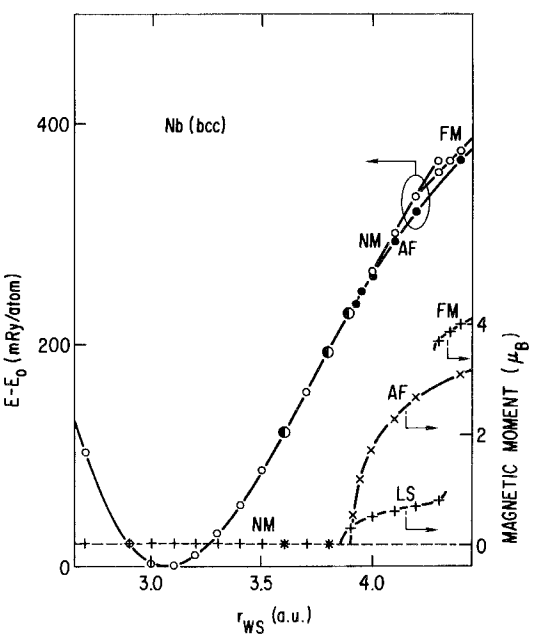

Fig. 46. $E(r_{WS})$ and $M(r_{WS})$ for bcc Nb with AF phase curves added to fig. 26.

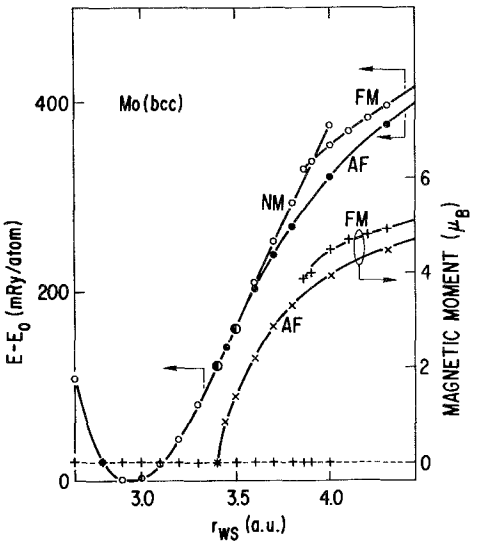

Fig. 47. $E(r_{ws})$ and $M(r_{ws})$ for bcc Mo with AF phase curves added to fig. 28.

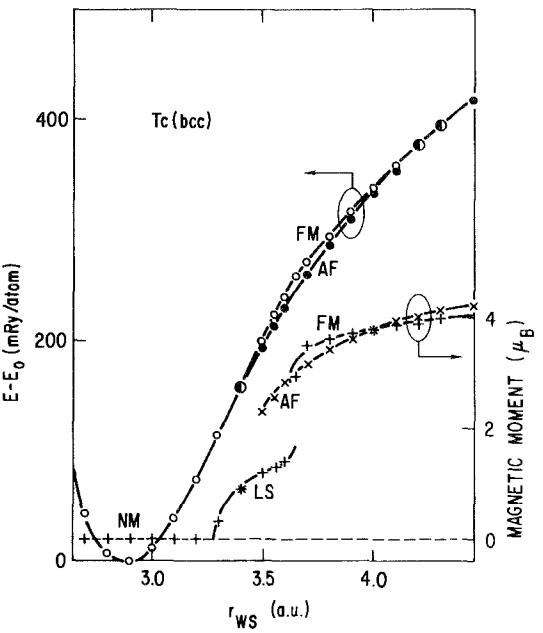

Fig. 48. $E(r_{ws})$ and $M(r_{ws})$ for bcc Tc with AF phase curves added to fig. 30.

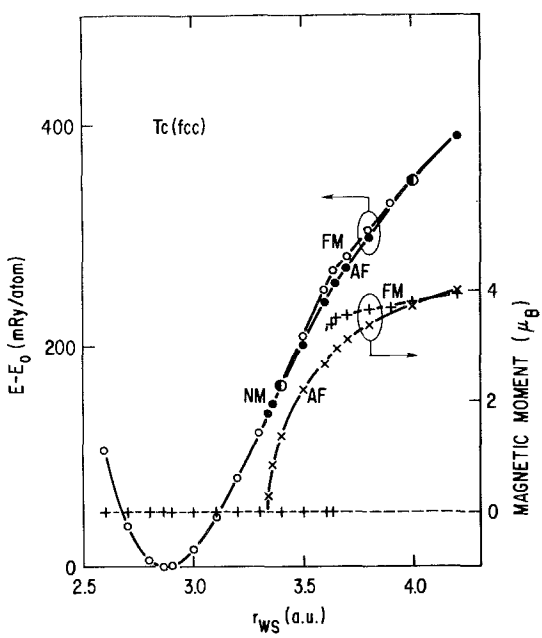

Fig. 49. $E(r_{ws})$ and $M(r_{ws})$ for fcc Tc with AF phase curves added to fig. 31.

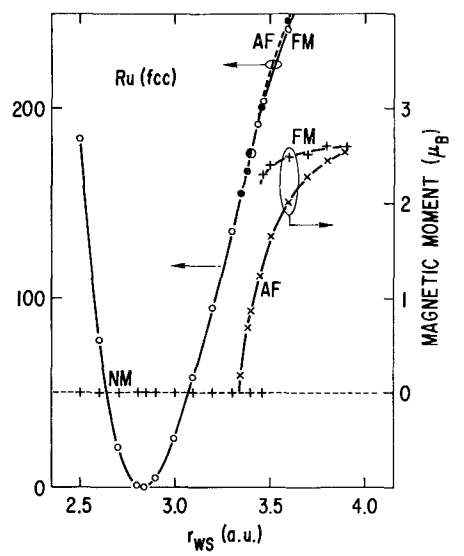

Fig. 50. $E(r_{ws})$ and $M(r_{ws})$ for fcc Ru with AF phase curves added to fig. 33.

antiferromagnetic phase begins at the equilibrium state volume, so even a small expansion of the lattice produces an antiferromagnetic phase, as has been shown in epitaxial growth of Fe on Cu(001). The antiferromagnetism of fcc Fe grown epitaxially on Cu(001) at temperatures above room temperature has been reported by Macedo and Keune (1988).

The sublattice moment curves of bcc Cr and bcc Mn (figs. 41, 42 and 43) are unusual in that they show a *first-order* transition to the antiferromagnetic phase in the case of bcc Cr and to the ferrimagnetic phase in the case of bcc Mn. If we generalize the rule which undercuts a first-order transition in one-atom cells (a ferromagnetic transition) by a second-order transition in a two-atom cell (an antiferromagnetic transition), then we might expect to undercut the first-order transition in the two-atom cell by a magnetic phase in a many-atom cell with more than two atoms. In fact both Cr and Mn are known to have many-atom equilibrium states with complex magnetic structure. For the magnetic ground state of Cr see Fawcett (1988); for the magnetic ground state of α-Mn see Kasper and Roberts (1956).

References

Andersen, O.K., 1975, Phys. Rev. B **12**, 3060.

Andersen, O.K., J. Madsen, U.K. Poulsen, O. Jepsen and J. Kollar, 1977, Physica B **86-88**, 249.

Andersen, O.K., O. Jepsen and D. Glötzel, 1984, Highlights of Condensed Matter Theory, eds F. Bassani, F. Fumi and M.P. Tosi (North-Holland, Amsterdam) pp. 59-176.

Anderson, J.R., D.A. Papaconstantopoulos, L.L. Boyer and J.E. Schirber, 1979, Phys. Rev. B **20**, 3172.

Bagayoko, D., and J. Callaway, 1983, Phys. Rev. B **28**, 5419.

Bagayoko, D., A. Ziegler and J. Callaway, 1983, Phys. Rev. B **27**, 7046.

Bagno, P., O. Jepsen and O. Gunnarsson, 1989, Phys. Rev. B **40**, 1997.

Blaha, P., K. Schwarz and P.H. Dederichs, 1988, Phys. Rev. B **38**, 9368.

Brener, N.E., G. Fuster, J. Callaway, J.L. Fry and Y.Z. Zhao, 1988a, J. Appl. Phys. **63**, 4057.

Brener, N.E., J. Callaway, G. Fuster, G.S. Tripathi and A.R. Jani, 1988b, J. Appl. Phys. **64**, 5601.

Cade, N.A., 1980, J. Phys. F **10**, L187.

Cade, N.A., 1981, J. Phys. F **11**, 2399.

Callaway, J., and C.S. Wang, 1977, Phys. Rev. B **16**, 2095.

Chen, H., N.E. Brener and J. Callaway, 1989, Phys. Rev. B **40**, 1443.

Chen, J., D.J. Singh and H. Krakauer, 1988, Phys. Rev. B **38**, 12834.

Christensen, N.E., O. Gunnarsson, O. Jepsen and O.K. Andersen, 1988, J. Phys. Colloq. **49**, C8.

Dugdale, J.S., and D.K.C. MacDonald, 1953, Phys. Rev. **89**, 832.

Duschanek, H., P. Mohn and K. Schwarz, 1989, Physica B **161**, 139.

Eckardt, H., and L. Fritsche, 1987, J. Phys. F **17**, 925.

Edwards, D.M., and E.P. Wohlfarth, 1968, Proc. R. Soc. London Ser A **303**, 127.

Fawcett, E., 1988, Rev. Mod. Phys. **60**, 209.

Fritsche, L., J. Noffke and H. Eckardt, 1987, J. Phys. F **17**, 943.

Fry, J.L., Y.Z. Zhao, N.E. Brener, G. Fuster and J. Callaway, 1987, Phys. Rev. B **36**, 868.

Fry, J.L., Y.Z. Zhao, P.C. Pattnaik, V.L. Moruzzi and D.A. Papaconstantopoulos, 1988, J. Appl. Phys. **63**, 4060.

Fuster, G., N.E. Brener, J. Callaway, J.L. Fry, Y.Z. Zhao and D.A. Papaconstantopoulos, 1988, Phys. Rev. B **38**, 423.

Greenside, H.S., and M.A. Schlüter, 1983, Phys. Rev. B **27**, 3111.

Gunnarsson, O., 1976, J. Phys. F **6**, 587.

Gunnarsson, O., and B.I. Lundqvist, 1976, Phys. Rev. B **13**, 4274.

Hathaway, K.B., H.J.F. Jansen and A.J. Freeman, 1985, Phys. Rev. B **31**, 7603.

Hattox, T.M., J.B. Conklin, J.C. Slater and S.R. Trickey, 1973, J. Phys. Chem. Solids **34**, 1627.

Hedin, L., and B.I. Lundqvist, 1971, J. Phys. C **4**, 2064.

Heinrich, B., A.S. Arrott, J.F. Cochran, C. Liu and K. Myrtle, 1986, J. Vac. Sci. Technol. A **4**, 1376.

Heinrich, B., S.T. Purcell, J.R. Dutcher, K.B. Urquhart, J.F. Cochran and A.S. Arrott, 1988, Phys. Rev. B **38**, 12879.

Hohenberg, P., and W. Kohn, 1964, Phys. Rev. **136**, B864.

Idzerda, Y.U., W.T. Elam, B.T. Jonker and G.A. Prinz, 1989, Phys. Rev. Lett. **62**, 2480.

Janak, J.F., 1977, Phys. Rev. B **16**, 255.

Janak, J.F., 1978, Solid State Commun. **25**, 53.

Janak, J.F., and A.R. Williams, 1976, Phys. Rev. B **14**, 4199.

Jani, A.R., N.E. Brener and J. Callaway, 1988, Phys. Rev. B **38**, 9425.

Jani, A.R., G.S. Tripathi, N.E. Brener, J. Callaway, 1989, Phys. Rev. B **40**, 1593.

Jansen, H.J.F., and S.S. Peng, 1988, Phys. Rev. B **37**, 2689.

Jansen, H.J.F., K.B. Hathaway and A.J. Freeman, 1984, Phys. Rev. B **30**, 6177.

Jarlborg, J., and M. Peter, 1984, J. Magn. & Magn. Mater. **42**, 89.

Jarlborg, T., and A.J. Freeman, 1980, J. Magn. & Magn. Mater. **22**, 6.

Johnson, W.B., J.R. Anderson and D.A. Papaconstantopoulos, 1984, Phys. Rev. B **29**, 5337.

Kasper, J.S., and B.W. Roberts, 1956, Phys. Rev. **101**, 537.

Kohn, W., and L.J. Sham, 1965, Phys. Rev. **140**, A1133.

Kohn, W., and P. Vashishta, 1983, in: Theory of Inhomogeneous Electron Gas, eds S. Lundqvist and N.H. March (Plenum Press, New York) pp. 79–147.

Krasko, G.L., 1987, Phys. Rev. B **36**, 8565.

Krasko, G.L., 1989, Solid State Commun. **70**, 1099.

Kübler, J., 1980a, J. Magn. & Magn. Mater. **20**, 107.

Kübler, J., 1980b, J. Magn. & Magn. Mater. **20**, 277.

Kübler, J., 1981, J. Phys. Lett. A **81**, 81.

Kübler, J., 1983, Proceedings of the Institute von Laue-Langevin, Workshop on 3rd Metallic Magnetism, eds D. Givord and K. Ziebeck (Grenoble, unpublished).

Kübler, J., 1989, Solid State Commun. **72**, 631.

Kulikov, N.I., and E.T. Kulatov, 1982a, J. Phys. F **12**, 229.

Kulikov, N.I., and E.T. Kulatov, 1982b, J. Phys. F **12**, 2267.

Lee, J.I., C.L. Fu and A.J. Freeman, 1986, J. Magn. & Magn. Mater. **62**, 93.

Li, C., A.J. Freeman and C.L. Fu, 1988, J. Magn. & Magn. Mater. **75**, 53.

Liechtenstein, A.J., M.I. Katsnelson, V.P. Antropov and V.A. Gubanov, 1987, J. Magn. & Magn. Mater. **67**, 65.

Macedo, W.A.A., and W. Keune, 1988, Phys. Rev. Lett. **61**, 475.

Madsen, J., and O.K. Andersen, 1976, Proc. 21st Ann. Conf. on Magnetism and Magnetic Materials, eds J.J. Becker, G.H. Lauder and J.J. Rhyne (AIP, New York) p. 327.

Marcus, P.M., and V.L. Moruzzi, 1985, Solid State Commun. **55**, 971.

Marcus, P.M., and V.L. Moruzzi, 1988a, J. Appl. Phys. **63**, 4045.

Marcus, P.M., and V.L. Moruzzi, 1988b, Phys. Rev. B **38**, 6949.

Marcus, P.M., V.L. Moruzzi and K. Schwarz, 1986, in: Computer-Based Microscopic Description of the Structure and Properties of Materials, eds J. Broughton, W. Krakow and S.T. Pantelides, Materials Research Society Symposium Proc., Vol. 63, p. 117.

Marcus, P.M., V.L. Moruzzi, Z.Q. Wang, Y.S. Li and F. Jona, 1987, in: Physical and Chemical Properties of Thin Metal Overlayers and Alloy Surfaces, eds D.M. Zehner and D.W. Goodman, Materials Research Society Symposium, Proc. Vol. 83, p. 21.

Min, B.I., T. Oguchi and A.J. Freeman, 1986, Phys. Rev. B **33**, 7852.

Moruzzi, V.L., 1986, Phys. Rev. Lett. **57**, 2211.

Moruzzi, V.L., and P.M. Marcus, 1988a, Phys. Rev. B **38**, 1613.

Moruzzi, V.L., and P.M. Marcus, 1988b, J. Appl. Phys. **64**, 5598.

Moruzzi, V.L., and P.M. Marcus, 1989a, Phys. Rev. B **39**, 471.

Moruzzi, V.L., and P.M. Marcus, 1989b, Solid State Commun. **71**, 203.

Moruzzi, V.L., and P.M. Marcus, 1990a, Phys. Rev. B **42**, 8361.

Moruzzi, V.L., and P.M. Marcus, 1990b, Phys. Rev. B **42**, 10322.

Moruzzi, V.L., J.F. Janak and A.R. Williams, 1978, Calculated Electronic Properties of Metals (Pergamon Press, New York).

Moruzzi, V.L., P.M. Marcus, K. Schwarz and P. Mohn, 1986a, J. Magn. & Magn. Mater. **54–57**, 955.

Moruzzi, V.L., P.M. Marcus, K. Schwarz and

P. Mohn, 1986b, Phys. Rev. B **34**, 1784.
Moruzzi, V.L., P.M. Marcus and P.C. Pattnaik, 1988a, Phys. Rev. B **37**, 8003.
Moruzzi, V.L., J.F. Janak and K. Schwarz, 1988b, Phys. Rev. B **37**, 790.
Moruzzi, V.L., P.M. Marcus and J. Kübler, 1989, Phys. Rev. B **39**, 6957.
Oguchi, T., and A.J. Freeman, 1984, J. Magn. & Magn. Mater. **46**, L1.
Papaconstantopoulos, D.A., J.L. Fry and N.E. Brener, 1989, Phys. Rev. B **39**, 2526.
Peng, S.S., and H.J.F. Jansen, 1988, J. Appl. Phys. **64**, 5607.
Peng, S.S., and H.J.F. Jansen, 1990, J. Appl. Phys. **67**, 4567.
Pescia, D., M. Stampanoni, G.L. Bona, A. Vaterlaus, R.F. Willis and F. Meier, 1987, Phys. Rev. Lett. **58**, 2126.
Podgórny, M., 1989a, J. Magn. & Magn. Mater. **78**, 352.
Podgórny, M., 1989b, Physica B **161**, 105.
Podgórny, M., and J. Goniakowski, 1990, Phys. Rev. B **42**, 6683.
Poulsen, U.K., J. Kollar and O.K. Andersen, 1976, J. Phys. F **6**, L241.
Roy, D.M., and D.G. Pettifor, 1977, J. Phys. F **7**, L183.
Sandratski, L.M., and P.G. Guletski, 1989, J. Magn. & Magn. Mater. **77**, 306.
Schwarz, K., and P. Mohn, 1984, J. Phys. F **14**, L129.
Simmons, G., and H. Wang, 1971, Single-Crystal Elastic Constants and Calculated Aggregate Properties: A Handbook (The MIT Press, Cambridge, 2nd Ed.).
Skriver, H.L., 1981, J. Phys. F **11**, 97.
Slater, J.C., 1974, Quantum Theory of Molecules and Solids, Vol. 4 (McGraw-Hill, New York).
Stoner, E.C., 1939, Proc. R. Soc. London Ser. A **169**, 339.
Szpunar, B., and P. Strange, 1985, J. Phys. F **15**, L165.
Taylor, A.D., and B.T. Kagle, 1963, Crystallographic Data on Metal and Alloy Structures (Dover, New York).
Tripathi, G.S., N.E. Brener and J. Callaway, 1988, Phys. Rev. B **38**, 10454.
von Barth, U., and L. Hedin, 1972, J. Phys. C **5**, 1629.
Vosko, S.H., L. Wilk and M. Nussair, 1980, Can. J. Phys. **58**, 200.
Wang, C.S., and J. Callaway, 1977, Phys. Rev. B **15**, 298.
Wang, C.S., B.M. Klein and H. Krakauer, 1985, Phys. Rev. Lett. **54**, 1852.
Wang, Z.Q., Y.S. Li, F. Jona and P.M. Marcus, 1987, Solid State Commun. **61**, 623.
Williams, A.R., J. Kübler and C.D. Gelatt Jr, 1979, Phys. Rev. B **19**, 6094.
Wohlfarth, E.P., ed., 1980, Ferromagnetic Materials - A Handbook on the Properties of Magnetically Ordered Substances (North-Holland, Amsterdam).
Xu, J.-L., A.J. Freeman, T. Jarlborg and M.B. Brodsky, 1984, Phys. Rev. B **29**, 1250.
Yahaya, M., and G.C. Fletcher, 1979, J. Phys. F **9**, 1295.

chapter 3

DENSITY FUNCTIONAL THEORY OF THE GROUND-STATE MAGNETIC PROPERTIES OF RARE EARTHS AND ACTINIDES

M. S. S. BROOKS

Commission of the European Communities
European Institute Transuranium Elements
Postfach 2340, D-7500 Karlsruhe
Germany

and

Borje JOHANSSON

Condensed Matter Theory Group
Institute of Physics, University of Uppsala
Box 530, S-75121, Uppsala
Sweden

Handbook of Magnetic Materials, Vol. 7
Edited by K. H. J. Buschow

CONTENTS

1. Introduction

Any article on the theory of magnetism in the rare earths and actinides must inevitably concern itself with one of the major problems in magnetism. Since the elemental metals and compounds of these two series are usually conductors we shall be very much concerned with whether the electrons responsible for conduction are also the electrons responsible for the magnetism. In both the 4f and 5f series the f shell is usually (but not in some intermetallics) responsible for the magnetism.

It is well established that the 4f shell (with the possible exception of cerium in some circumstances) does not contribute significantly to conduction or chemical bonding. Well-developed theory describes the magnetism of the 4f shell in rare earth metals and compounds extremely well. This type of theory starts always with the assumption that the 4f shell is similar to the 4f shell of the isolated atom, modified only weakly by interaction with the environment in the solid. But the exchange interactions between the 4f and conduction, principally 5d, electrons are responsible for an induced conduction-electron spin density which is in principle calculable. The conduction-electron spin density then couples the 4f moments on different atoms and therefore, although small, is very important.

The 5f shell cannot be reasonably described in the same way. In the elemental metals Th–Pu, which do not order magnetically at any temperature, the weight of the evidence is that the 5f states contribute to both conduction and bonding. The heavier metals, beyond Am, do order magnetically and there is evidence that a sound theoretical description would be similar to that for the rare-earth metals. The experimental data, especially magnetic data, for the heavier metals is however very sparse and we shall be concerned with these elements only briefly. That there is not, however, any simple association here between the appearance of ordered magnetism and the nature of the 5f shell can be established by studies of the magnetism of light actinide metals in compounds. Here the evidence is that in many cases the 5f electrons contribute to both magnetism and to conduction and bonding.

We shall discuss these various aspects of the 4f and 5f shells and their interactions with conduction electrons in order: first the principle magnetic properties of the 4f and 5f shells in isolated atoms in section 2, and then of the elemental metals in section 3. In sections 4 and 5 we discuss the magnetism of the compounds. In this introduction we confine ourselves to some remarks on cohesive properties that are relevant to the theoretical treatment of magnetism.

The measured equilibrium atomic volumes of the 3d, 4d and 5d transition metals,

rare earths and actinides are shown in fig. 1.1. The bond-lengths between the transition metal atoms are shortest for those atoms with half-filled, or nearly half-filled, d shells. The small deviations from the parabolic trend in lattice constant expected from the Friedel (1969) theory that occur for the magnetic 3d elements are due to magnetovolume effects. In contrast the equilibrium atomic volumes of the rare earths – with the exception of those of europium and ytterbium – are almost constant throughout the series. The same plot for the actinides is quite different. In the first half of the series the trend in atomic volume, with increasing atomic number, is similar to that of a d transition-metal series. However, between plutonium and americium, there is a large jump in volume and after this the trend is similar to that of the rare earths.

The cohesive energies of the 3d, 4d and 5d transition metals, rare earths and actinides are shown in fig. 1.2. Again the trend for the 4d and 5d transition metals is approximately parabolic with a maximum in the middle of the series. This appears to be inversely related to the trend in atomic volume shown in fig. 1.1. The fact that the cohesive energy is a function of the d occupation number and is large near the middle of the series suggests that the d electrons make a large, even dominant, contribution to the metallic bonding. If the cohesive energies of strontium and cadmium

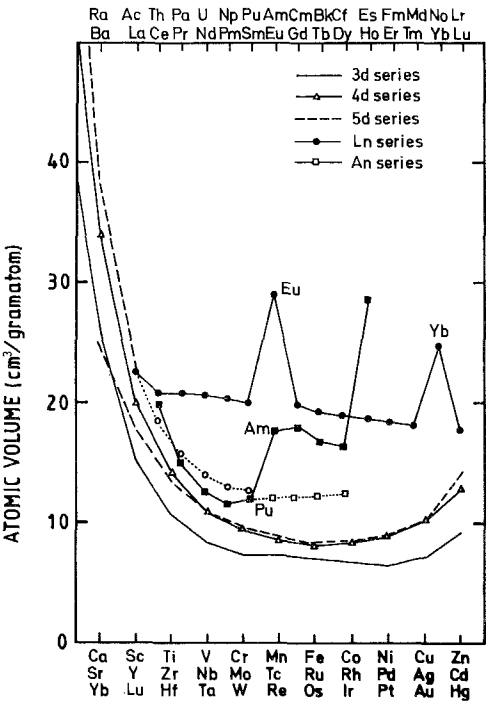

Fig. 1.1. The experimental equilibrium atomic volumes of the 3d, 4d and 5d transition metals, the lanthanides and the actinides. Very rough estimates of the collapsed volumes of the light rare earths (open circles) and the heavy actinides (open squares) have been added for comparison.

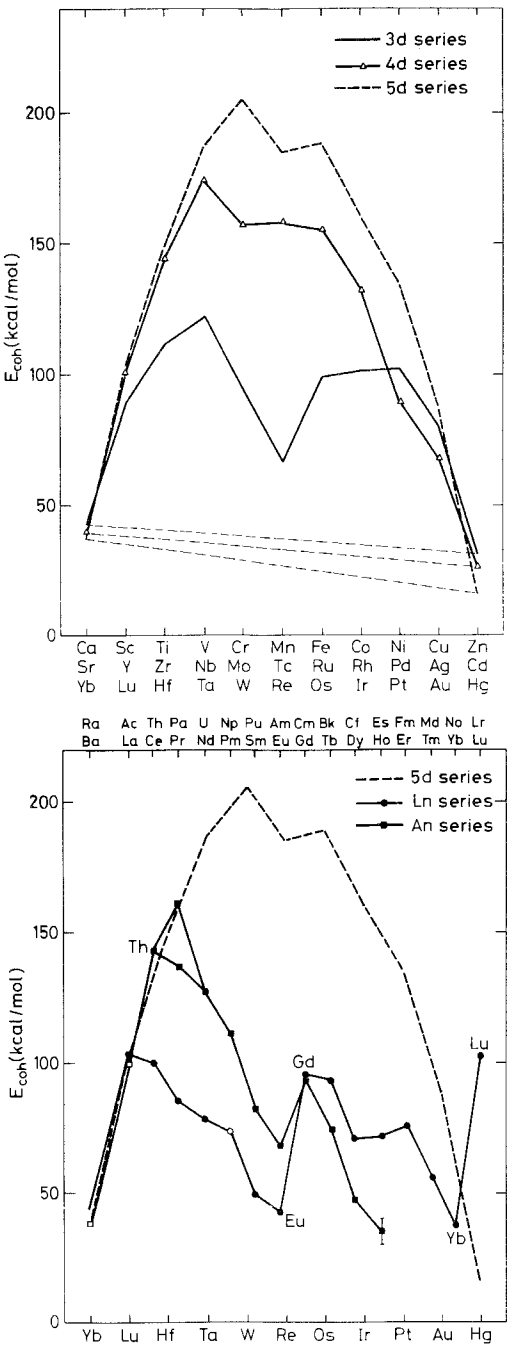

Fig. 1.2. The measured cohesive energies of (a) the 3d, 4d and 5d transition metals, and (b) the 5d transition metals, rare earth and actinide series.

are taken to be representative of the s–p part of the cohesive energy for the 4d series then this part of the cohesive energy is obtained, for any member of the series, by linear interpolation – as shown in the figure. The remaining d electron contribution is large. A similar interpolation between calcium and zinc (fig. 1.2) leads to the same conclusion for the 3d transition series. Here, however, there remain obvious deviations from a pure parabolic trend, most pronounced for manganese, near the middle of each series. But these deviations are due primarily to that part of the cohesive energy which arises from multiplet effects in the free atoms (Brooks and Johansson 1983).

The rare earths are trivalent metals – except for Eu and Yb which are divalent at ambient pressure and temperature – with three valence electrons (of primarily 5d and 6s character) whilst the 4f electrons are part of the chemically inert ionic core. Consequently the lattice constants are not affected by the number of 4f electrons except for the incomplete screening of nuclear charge as each additional 4f electron is added. The paramagnetic moments of the metals are, to a very good approximation, equal to the paramagnetic moments of the free ions. At low temperatures weak interactions between the ionic moments and with their conduction electron environment produce ordering into various and spectacular magnetic structures.

Consequently, the trend in the cohesive energies of the rare earths, fig. 1.2, is very different from that of the d elements. It decreases throughout the first half of the series, rises sharply at gadolinium, and again decreases quasi-regularly in the second half of the series until it once more rises sharply at the last element, lutetium. The minima at europium and ytterbium occur because they are divalent. Then the cohesive energies of Eu and Yb are quite similar to that of barium, the divalent element preceding the rare earth series. There is also very little correlation between the atomic volumes and the cohesive energies of the rare earths. This is again due to the energetics of the free atoms. The cohesive energy, unlike the atomic volume and the bulk modulus, is a combined property of the solid and the free atom. Therefore the electronic structure of both solids and free atoms must be studied in some detail if either absolute values of, or trends in, cohesive energies are to be understood.

The similarity between the trends in atomic volume of the light actinides and d transition metals suggested (Zachariasen 1973) that the light actinides were part of a 6d transition series. The population of the 5f shell was not supposed to begin until later in the series in order to explain a volume trend for the heavier elements that was typical of the rare earths. More recent research has produced a radical change in viewpoint, and a corresponding increase in our understanding of the chemical and physical properties of the actinides. It is now known that the trend in the atomic volumes of the light actinides does not mean that they form a 6d transition metal series, but that the light actinides are part of a *5f transition* series. Cohesive energy calculations (Eriksson et al. 1990c) have confirmed the measured valence states of the rare earths and suggest that several of the heavier actinide metals are divalent. Lawrencium – element 103 – was found to be the first member of the 6d transition series, in analogy to the position of lutetium relative to the 5d series.

Free rare-earth and 3d transition-metal ions are adequately described by the Russel–Saunders coupling scheme in which Coulomb correlation is the largest part of the

ionic valence electron Hamiltonian. Spin–orbit interaction may then be safely projected onto eigenstates characterized by total spin and total orbital angular momentum which it couples to give a total angular momentum of $\boldsymbol{J} = \boldsymbol{L} + \boldsymbol{S}$. The ground-state moment is that of the lowest multiplet – the product of J with the Landé factor g_J. The susceptibility at moderate temperatures obeys a Curie–Weiss law with an effective paramagnetic moment $g_J[J(J+1)]^{1/2}\mu_B$. The ratio of paramagnetic to saturated moments is $[J(J+1)]^{1/2}/J$, a relationship that is entirely due to the assumption that the ion is in an isotropic environment. This ratio for the rare-earth metals is measured to be close to ideal, indicating that the shielding of the localized f electrons is very effective – the remaining magnetic interactions being only small perturbations. In the first approximation, the total angular momentum is conserved. However, when the crystal field splitting of the ground-state multiplet is large, the moment ratio can be quite different from the free ion ratio. In general it decreases as the degeneracy of the crystal field ground state decreases until it is zero for a singlet ground state.

The magnetic moments of the 3d transition metals are entirely different in nature to the magnetic moments of the rare earth metals. Nearly all elemental transition metals are enhanced Pauli paramagnets because the cost in kinetic energy upon moment formation is larger than the energy gained from spin alignment – they do not satisfy the Stoner criterion (Stoner 1938, Gunnarsson 1976, 1977, 1978, Vosko et al. 1975, Vosko and Perdew 1975). But Fe, Co and Ni – with their narrow d bands at the end of the 3d series – do satisfy the Stoner criterion and their ground-state moments have been calculated to good accuracy in self-consistent spin-polarized energy band calculations (Moruzzi et al. 1978, Andersen et al. 1977, 1985). The light actinide metals (Pa–Pu) are also enhanced paramagnets. The ground states have also been computed in parameter free self-consistent energy band calculations (Skriver et al. 1978, 1980, Brooks et al. 1984) and it has been shown that, according to the Stoner criterion, they should not order ferromagnetically. The heavy actinides (Cm and beyond) are suspected to be localized magnets, similar to the rare-earth metals although sound experimental data is sparse.

Of the actinide compounds, the insulators and ionic compounds tend to have localized moments, e.g., the magnetism of uranium dioxide is well understood (Osborn et al. 1988, Amoretti et al. 1989) although neptunium dioxide remains something of a puzzle (Amoretti et al. 1992) with a hint that quadrupole effects may be large in actinides. Although the magnetism in these cases is rare-earth-like, both spin–orbit coupling and crystal field energies are considerably larger than in the rare earths.

Moment formation in metallic actinide compounds appears to be sensitive to volume in a manner summarized in the Hill plots (Hill 1970). There appear to be critical An–An spacings below which ground-state ordered moments are not stable. The systematic absence of magnetism in compounds with small An–An separation raises again the possibility that moment formation is controlled by the Stoner criterion, and it has been shown that UC, for example, should be a Pauli paramagnet (Brooks 1984). The magnetic moments of metallic actinide compounds also appear to be sensitive to volume (fig. 1.3) and it is suspected that some of the NaCl-type compounds with small lattice parameters are itinerant magnets (Brooks and Kelly 1983) even though the moments are located almost entirely at the actinide site.

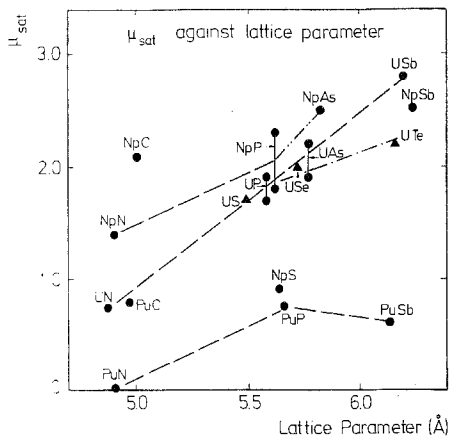

Fig. 1.3. The magnetic moments of NaCl-type light actinide carbides, pnictides and chalcogenides plotted against lattice constant.

Actinide–transition-metal intermetallics (An–M) provide several examples of the magnetic transition as a function of either the actinide or the transition metal. In the intermetallics the interest is in the M d–An f hybridization and its influence upon the magnetism. There is now considerable evidence that M d–An f hybridization influences the localization of the 5f states as much as does the lattice constant in the NaCl-type monochalcogenides and pnictides (Johansson et al. 1986).

The useful technical properties of rare earth transition metal intermetallics have encouraged much basic research into their electronic structure (Buschow 1977, 1979, 1980, Givord 1987, Hilscher 1982b). One of the most interesting characteristics of these intermetallics is the combination of itinerant transition-metal magnetism with the localized and anisotropic magnetism of the rare-earth ions. This has naturally led to investigations of the coupling between the transition-metal and rare-earth magnetic moments. The site-resolved moments have been studied in neutron diffraction experiments (Boucherle et al. 1982) and it has become clear that the spins on the transition-metal and rare-earth sites are often coupled antiparallel. The attention of theorists is now being directed to the origins and magnitude of the intersite coupling (Brooks et al. 1991a).

Some experimental results illustrate the relationship between the rare earths and actinides more graphically than others. Firstly, crystallography under pressure has shown that the heavy actinides transform from dhcp to fcc structures at moderate pressures, indicating that they have a trivalent rare-earth-like electronic structure with localized 5f electrons and spd conduction bands (Akella et al. 1979, Benedict et al. 1984, Haire et al. 1984, Peterson et al. 1983, Benedict 1987). At higher pressures the volumes of Am, Cm, Bk and Cf collapse, with relative volume change of 12–22%, to orthorhombic structures (fig. 1.1). Volume collapses had previously been found for the light rare earths Ce and Pr (Zachariasen and Ellinger 1975, Endo et al. 1977,

Mao et al. 1981, Smith and Akella 1982, Grosshans et al. 1983) under pressure, and under high pressures low-symmetry orthorhombic structures are the most stable, suggesting that itinerant f electrons – as in the light actinides – are determining the crystal structure. It appears, in a rather dramatic fashion, as if compression can be used to turn a heavy actinide into a light actinide – or 5f transition metal – or a light rare earth, for that matter, into a 4f transition metal.

The photoemission and inverse photoemission spectra (Lang et al. 1981, Baer and Schneider 1987) for Tb, Dy and Ho are shown in fig. 1.4. where the *fingerprint* of the localized 4f states is unmistakable, the 4f spectral density lying well below and above the Fermi level. The photoemission spectra for the Pu and Am (Naegele et al. 1984) – the only heavy actinide for which they are available – are shown for comparison in

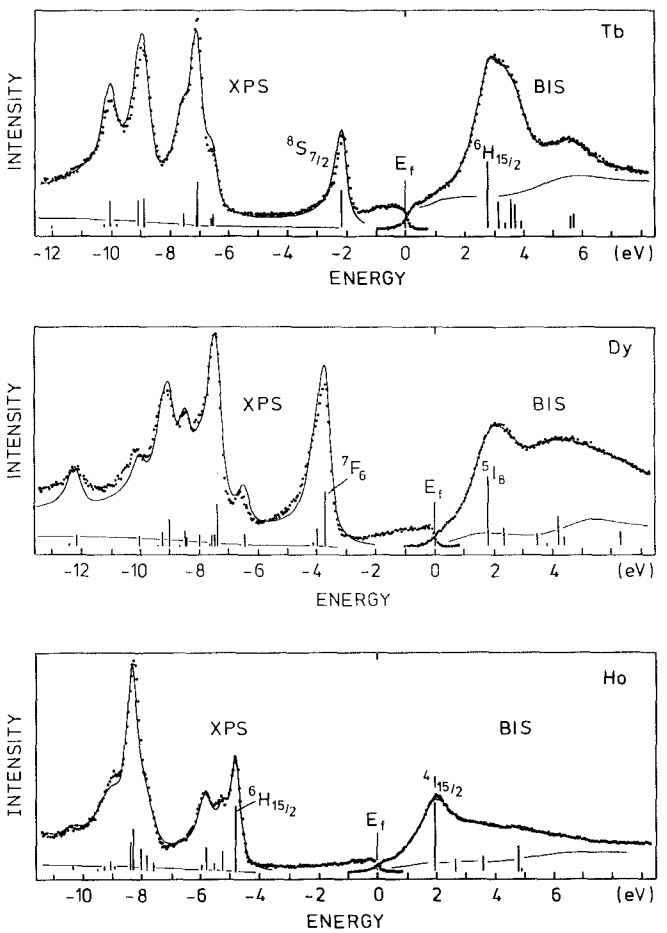

Fig. 1.4. Photoemission and inverse photoemission spectra of the heavy rare-earth metals Tb, Dy and Ho (after Baer and Schneider 1987).

fig. 1.5. The sharp shift of spectral density away from the Fermi level in Am illustrates the entirely different types of electronic structure of light and heavy actinides.

Finally positron-annihilation experiments (Gustafson and Mackintosh 1964, Gustafson et al. 1969) made through the γ–α phase transition of Ce as a function of both temperature and pressure indicate that the 4f occupation number does not change significantly at the transition. Compton scattering experiments (Kornstädt et al. 1980) have been similarly interpreted. The conclusion drawn by Gustafson et al. (1969) was that, in contrast to the assumptions underlying the Pauling–Zachariasen promotional model (Lawson and Tang 1949, Schuck and Sturdivant 1950) the phase transition is due to a change in the nature of the f state rather than f occupation number – a Mott transition which also occurs with the localization of 5f electrons in americium.

Throughout this article we shall be quoting and using the results of calculations made using density functional (DF) theory (Hohenberg and Kohn 1964, Kohn and Sham 1965) since this is the theory used for nearly all electronic structure calculations in solids. Density functional theory, as used in practice, is a *ground-state* theory – a variational principle for the ground-state energy in terms of the electron density, or electron spin density. The eigenvalues that are obtained in this theory are the functional derivatives of the total energy with respect to the density or spin density. They are not in general simply related to measured quantities, although the temptation to compare the two is rarely resisted. DF theory contains an unknown functional for the exchange and correlation energy into which most of our lack of knowledge of the contribution of many-body interactions to the total energy (the classical Coulomb energy is calculated exactly) has been placed. One important field of research is the

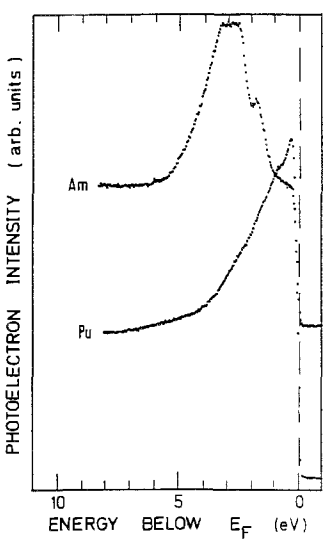

Fig. 1.5. Photoemission spectra of Pu and Am metals (After Naegele et al. 1984).

attempt to improve this *exchange and correlation energy* functional, although a very simple functional is actually used in most self-consistent energy band calculations. The functional is replaced by an approximate one which has been derived for a homogeneous electron gas with constant density. At each point in space, the functional and its functional derivatives having been used to obtain the potential in terms of the density, the constant density is then replaced by the real density – the *local density or spin density approximation (LDA or LSDA)* (Gunnarsson and Lundqvist 1976, Hedin and Lundqvist 1971, von Barth and Hedin 1972). The primitive nature of this approximation would not lead to the expectation that a quantitatively accurate theory would result if it were not for the fact that computed ground-state properties of solids, obtained in this manner, often agree very well with measurements. One of the areas where genuine problems arise is with narrow band systems, in particular the 4f bands in cerium or the 5f bands in actinides. Some advance has been made in identifying what the problems are and, although we shall not discuss DF theory in any detail, we will mention and deal with these problems when they arise.

2. Transition metals, rare earths and actinides

Most atoms loose their magnetic moments in the solid state; the exceptions are some transition metals, the rare earths, and the actinides. The 3d, 4d and 5d transition metals, when not magnetic, have relatively large magnetic susceptibilities. Nearly all of the rare earths are magnetic, the magnetism arising from the 4f shell. But the f shells interact via the conduction electrons – principally the 5d electrons. Viewed in terms of these conduction electrons the rare-earth metals are early 5d transition metals since the 5d shell is rather less than half-filled and the 4f shell chemically inert. The actinides are more complex. It is believed that the light actinides are 5f transition metals while the heavy actinides have an essentially chemically inert 5f shell. They are therefore more like early 6d transition metals – which is consistent with the limited data on the bulk ground-state properties.

2.1. The resonance interaction in transition metals

The radial Schrödinger equation is

$$\left[-\frac{\mathrm{d}^2}{\mathrm{d}r^2} + V(r) + \frac{l(l+1)}{r^2} \right] u_l(r) = E u_l(r), \tag{2.1}$$

where $V(r)$ is the spherically averaged effective potential due to the nucleus and other electrons and $u_l(r) = rR_l(r)$ is the radius times the radial solution for the angular momentum l. The centrifugal potential is large near the nucleus and vanishes at large distances (fig. 2.1). For sufficiently small r, it is much larger than $V(r) - E$ and $R_l \approx r^l$. There is another, unphysical, solution $R_l \approx r^{-l-1}$. Orbitals with large values of angular momentum are therefore pushed away from the nucleus.

Secondly, the energy is raised by $\int u_l^2 [l(l+1)/r^2] \mathrm{d}r$ compared with $l = 0$. The result is that states with large l and a given principle quantum number lie higher in energy

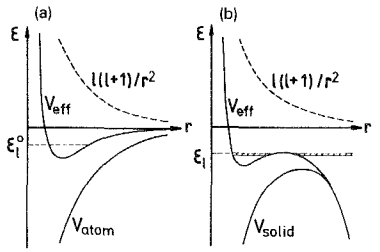

Fig. 2.1. (a) The total effective potential of an atom as the sum of the Coulomb potential and the repulsive centrifugal potential. (b) The modified Coulomb potential in the solid lowers the total potential in the interstitial region of the crystal and the state becomes a resonance.

than those of smaller l and become occupied later. Hence 3d states, for example, fill after the 4s and 4p states become occupied. If it were not for the centrifugal term they would be core electrons before the 4s and 4p states started to fill.

In addition, in the periodic table the 3d and 4f are the first d and f states and need have no nodes to orthogonalize them to lower states. Their kinetic energies are therefore relatively small, and their wave functions and densities relatively contracted. Since the size of the atom is determined by the 4s and 4p states – whose density lies further out as they have more nodes in the wave function – the 3d density lies mostly within the atom. But, because of the centrifugal potential, it is also pushed away from the nucleus. The spherical average of the 3d densities is therefore a shell at intermediate distance from the nucleus and it is small at the boundary of the atom (fig. 2.1).

The 3d, 4f and 5f states are therefore very similar to core states which are not quite bound as they lie too high in energy. But we notice that the direct effect of the centrifugal potential is to push their density away from the nucleus. It does not bind them. What it does is to raise the energy of what would be a core state to somewhere close to zero energy so that the electrons can tunnel through to the free electron states outside the atom. Such states are called resonances.

The actual potential in which the d or f electrons move is the same as that in which any other electrons move. But the d or f states – being more localized – sample the potential closer to the nucleus than s and p states. They shield the s and p states from the nucleus, which pushes the s and p states further out. They in turn do not shield the d and f states so well, which pushes them further in. The final total potential is all part of a self-consistent process.

In the interstitial region of a crystal, where the potential is flat, the radial part of the wave function is a spherical wave with a phase shift due to the atomic potential

$$u(r, E) + [\cot \eta_l j_l(\kappa r) - n_l(\kappa r)], \quad r > S, \tag{2.2}$$

where j_l and n_l are spherical Bessel and Neumann functions, η_l is the lth wave phase shift, S is the radius of the atom and $\kappa = (2E)^{1/2}$. The typical energy dependence of the phase shifts is shown in fig. 2.2. Whereas the s and p wave phase shifts are smooth almost linear functions of energy, the $l = 2$ wave phase shift passes through $\pi/2$ at a

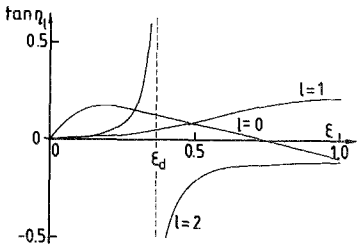

Fig. 2.2. The energy dependence of the s and p wave phase shifts compared with the d wave phase shift in a transition metal.

resonant energy E_0. For a narrow resonance

$$\tan \eta_l = \frac{\frac{1}{2}\Gamma}{E_0 - E} \tag{2.3}$$

where the width of the resonance is

$$\Gamma = \frac{2\kappa_0^5}{225} M^2, \tag{2.4}$$

where $\kappa^2 = 2E_0$ and the *reduced matrix element* (Heine 1980), M, is

$$M = \left| \int_0^S V(r) u(r) r^4 \, dr \right|, \tag{2.5}$$

which is an integral entirely within the atomic sphere. Physically, the solutions to the wave equation inside the atom are not exact eigenstates but have width Γ, and $\hbar/\Gamma$ is the time to escape to free electron states outside.

At low kinetic energy eq. (2.2) may be approximated to

$$u(r, E) \to M\left[\frac{E_0 - E}{M^2} r^2 + \frac{1}{5r^3} \right], \quad r > S. \tag{2.6}$$

The bonding function is obtained from $u'(S, E_b) = 0$ and the energy of the bottom of the band is

$$E_b = E_0 - \frac{3}{10} \frac{M^2}{S^5}. \tag{2.7}$$

The anti-bonding function is obtained from $u(S, E_m) = 0$ and the energy of the top of the band is

$$E_t = E_0 + \frac{1}{5} \frac{M^2}{S^5}, \tag{2.8}$$

hence the bandwidth is

$$\Delta_d = \frac{1}{2} \frac{M^2}{S^5}. \tag{2.9}$$

Therefore the bandwidth depends upon M or Γ. One would expect that the bandwidth would be proportional to the square of the hopping or transfer integral between atoms A and B

$$\int u(r - R_A) V(r - R_B) u(r - R_B),$$

and for sp states this integral picks up its principal contribution from the region between the atoms where the s and p functions overlap. But Γ depends upon M which is an *intra-atomic* integral. Resonant orbitals peak so strongly within the atoms that the integrand is large within the atoms.

This aspect of resonant orbital theory is put to good use in the LMTO method (Andersen 1975, Andersen and Jepsen 1977, Andersen et al. 1985, Skriver 1983a), where there is a very useful approximate description of resonant states when they hybridize little with s and p states. The unhybridized energy band eigenvalues are

$$E_{li}^{k} = C_l + \Delta_l S_{li}^{k}, \tag{2.10}$$

where C_l – the band centre – and Δ – the bandwidth parameter – depend upon potential, but S_{li}^{k} – the structure constants – depend only upon structure and are independent of the scale of the lattice. The bandwidth parameter is

$$\Delta_l = \tfrac{1}{2} S R_l^2(C_l) = \frac{1}{\mu_l S^2}, \tag{2.11}$$

where $R_l(C_l)$ is the wave function evaluated at the atomic sphere boundary at the energy C_l. The bandwidth parameter is Δ_l and μ_l is the band mass parameter which is unity for free electrons, but may become very large for narrow resonances. The bandwidth parameter depends only upon the size of the atomic sphere and the value of the wave function at the sphere boundary. It is therefore, as above, an *atomic property* and measures the probability of the electron reaching the boundary of the atom. The bandwidth is obtained from the second moment of the energy bands $M_{ll}^2 = \int (E - C_l)^2 N_l(E)\, dE$ and may be written as

$$W_l = \Delta_l M_{ll}^2, \tag{2.12}$$

where M_{ll}^2 is the second moment of the l diagonal structure constants which is 28 for all fcc d bands and 45 for all fcc f bands. The calculated band mass parameters for the transition metals, rare earths and actinides are plotted in fig. 2.3. The bandwidths are obtained by scaling μ_l^{-1} by M_{ll}^2/S^2. The band masses increase across any series due to contraction of the orbitals as the extra added electron is incompletely shielded. They also decrease down a column of the periodic table as additional orthogonality nodes push wave functions outwards.

The most evident characteristic of transition metals, apart from their magnetism, is that the resonant electrons are very strongly bonding in the sense that they decrease the lattice constant. Another way to state this is that the resonant electrons exert a negative *electronic pressure* (Pettifor 1976). The force theorem (Mackintosh and Andersen 1979) states that any distortion of the system changes the total energy to first

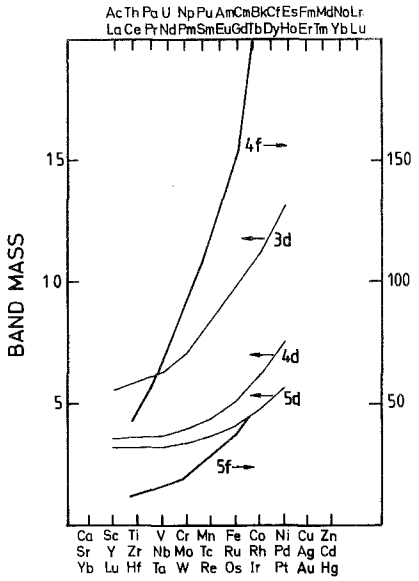

Fig. 2.3. The calculated band masses of the 3d, 4d and 5d transition metals, rare earths and actinides (after Andersen and Jepsen 1977 and Brooks 1979).

order by

$$\delta E = \delta \int EN(E)\,\mathrm{d}E \tag{2.13}$$

whence the electronic pressure formula (Andersen et al. 1985) is

$$3PV = 3V\sum_l P_l,$$

$$3P_lV = \int_{-\infty}^{E_F} N_l(E)SR_l^2(E,S) \times \{[D_l(E)+l+1][D_l(E)-l] + S^2[E-\varepsilon_{xc}+\mu_{xc}-V(S)]\}\mathrm{d}E, \tag{2.14}$$

where $D_l(E)$ is the logarithmic derivative at $R = S$. LSDA enters eq. (2.14) through ε_{xc} and μ_{xc}, the exchange–correlation energy density and contribution to the potential, respectively. This formula is actually used in LMTO (Andersen et al. 1985, Skriver et al. 1978, 1980, Brooks et al. 1984) calculations to compute the pressure as a function of volume and from this the lattice constants and bulk moduli. The decomposition of the pressure into partial wave components is extremely useful as it allows the chemical bond to be analysed in a new way. It should not however be assumed that the total energy may be decomposed in the same way. Here we are concerned with virtual work processes which may be decomposed but the work, once part of the internal energy, is no longer decomposable (Christensen and Heine 1985). An ap-

proximate form of eq. (2.14) is (Christensen and Heine 1985, Andersen et al. 1985)

$$3PV = \frac{2n_l}{\mu_l}[(C_l - V(S)) + \mu_{xc}(S) - \varepsilon_{xs}(S)] + n_l[\langle E\rangle_l - C_l]\left[2l + 1 + \frac{2}{\mu_l}\right], \qquad (2.15)$$

for a resonant band. The physical interpretation of eq. (2.15) is that the first term – the band centre term – is positive, due to the exclusion principle, when neighbouring shells overlap and negative when the atoms are well separated when it becomes the van der Waals interaction. The second term is the band filling term which is attractive when the bonding orbitals are filling and is zero for empty and filled ideal bands.

We may go back one step to eq. (2.14) to examine the behaviour of the logarithmic derivatives for the values of D_l corresponding to V_l and C_l, i.e., $D_l = l$ and $D_l = -l-1$, or B_l and A_l, i.e., $D_l = 0$ and $D_l = -\infty$ (corresponding to bond and antibond, respectively). Here we note that

$$[D_l + l + 1][D_l - l] + (E - V)S^2 = D_l(D_l + 1) + (E - V_l)S^2,$$

with $V_l = V + l(l+1)/S^2$. Hence the pressure at the bottom of the band is positive if the electron is allowed to pass classically out of the atomic sphere but negative if it tunnels. The magnitude of the pressure is proportional to the partial wave density at the sphere boundary – the escape probability or inverse of the band mass. The contribution to the pressure for A states is always repulsive. The wave functions for these different cases are illustrated in fig. 2.4. At the bonding energy the wave function is a minimum between the atoms if the region is classically forbidden. The slope of the wave function is negative at S. Thus the energy of a tunneling state must be lowered if the solid is compressed to maintain the bonding condition. The opposite is true of free states. The transition metals and actinides are therefore bonded by resonant, or tunnelling, electrons (Andersen et al. 1985).

The usual chemical picture of bonding corresponds to neglecting the band centre term – or replacing it with an empirical short-range repulsion – whence all bonding states are taken to bond. However from the above we see that if the states do not tunnel the band centre term may be large and positive.

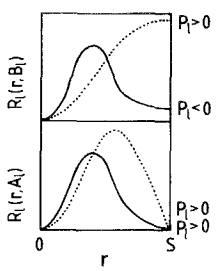

Fig. 2.4. The radial wave functions at the bottom (B) and top (A) of an energy band. The dotted lines are for the case where both B and A are greater than the total effective potential at the atomic sphere boundary. The full lines are for the case where A and B are less than the total effective potential at the sphere boundary. The corresponding sign of the electronic pressure, from eq. (2.14) is indicated (after Andersen et al. 1985).

2.2. *Summary of the magnetic properties of the rare earths and actinides*

Free rare-earth and 3d transition-metal ions are adequately described by the Russel–Saunders coupling scheme in which Coulomb correlation is the largest part of the ionic valence electron Hamiltonian. Spin–orbit coupling may then be safely projected onto eigenstates characterized by total spin and total orbital angular momentum which it couples to give a total angular momentum of $\boldsymbol{J} = \boldsymbol{L} + \boldsymbol{S}$. The saturated ground-state moment, $\boldsymbol{\mu}_s$, is then the product of J with the Landé factor, g_J. The calculated moments and their orbital and spin contributions are plotted in fig. 2.5. Evidently one of the principal characteristics of rare-earth magnetism is the large orbital contribution to the moment which arises because the 4f states are highly degenerate.

The magnetic moments of the 3d transition metals, in contrast, are due to a splitting of the up and down spin states at the Fermi level and they can only be obtained from self-consistent spin-polarized energy band calculations. The orbital contributions to the moments of the magnetic transition metals have been calculated (Ebert et al. 1988, Eriksson et al. 1990b). In contrast to the rare-earth magnetism the orbital magnetism in the 3d transition metals is very weak since the orbital moments are quenched; the energy band states are orbitally nondegenerate and in first order do not support orbital magnetism. The light actinide metals (Pa–Pu), in contrast again, are Pauli paramagnets – and, according to the Stoner criterion, they should not order ferromagnetically (Skriver et al. 1978). The heavy actinides (Cm and beyond) are suspected to be localized magnets, similar to the rare-earth metals although sound experimental data is sparse.

Magnetic moment formation and magnitude in metallic actinide compounds is the subject of much current research. There appear to be critical An–An spacings below

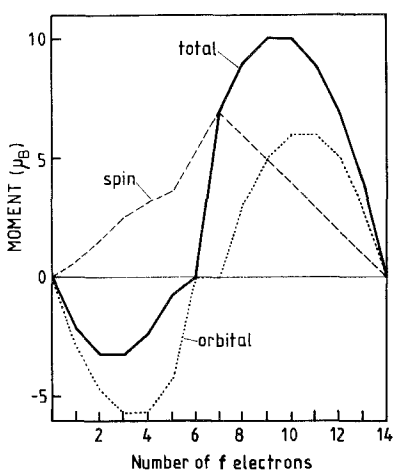

Fig. 2.5. The total, spin and orbital contributions to the z component of the magnetic moment of an f shell in Russel–Saunders coupling as a function of the number of f electrons.

which ground state ordered moments are not stable, as a typical Hill plot (Hill 1970) (fig. 2.6) demonstrates. The systematic absence of magnetism in compounds with small An–An separation raises again the possibility that the onset of magnetic ordering is due to the competition between kinetic and spin polarization energies. Calculations show that many Pa compounds, for example, do not obey the Stoner criterion. The magnetic moments of metallic actinide compounds also appear to be sensitive to volume as we have shown in fig. 1.3. Actinide transition metal intermetallics provide several examples of the magnetic transition as a function of either the actinide or the transition metal and, for example, the paramagnetism of $PuCo_2$ might also be due to a failure to satisfy the Stoner criterion, albeit a relativistic version thereof. But the

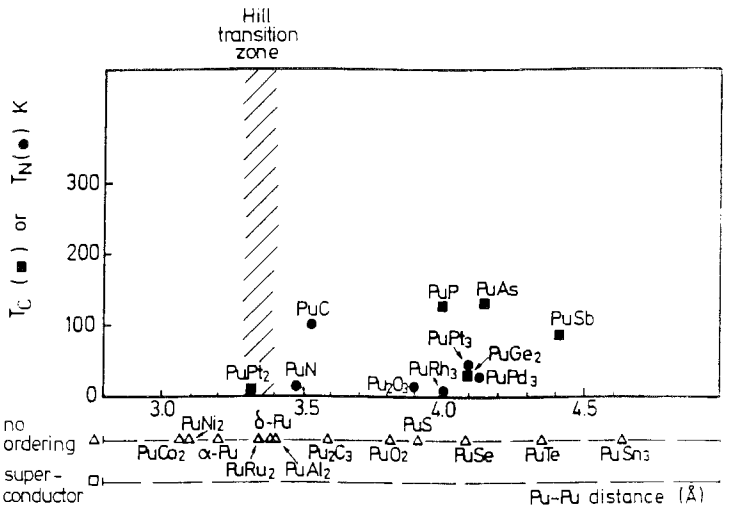

Fig. 2.6. A Hill plot (Hill 1970) for Pu compounds demonstrating the transition from magnetism to superconductivity as a function of Pu–Pu distance.

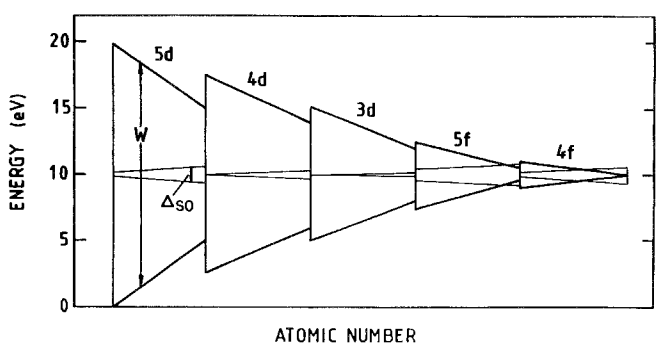

Fig. 2.7. The spin–orbit splitting and bandwidths of the 3d, 4d and 5d transition metals, the rare earths and actinides.

magnetic actinide compounds, even those with small lattice constants such as UN (Brooks and Kelly 1983), normally have – in contrast to normal transition metals – very large orbital moments. The reason is that 5f spin–orbit interaction in the actinides is far larger than that of the 3d spin–orbit interaction in the much lighter 3d transition metals. This is illustrated in fig. 2.7, where we have plotted the spin–orbit interaction and bandwidths for the transition metals, rare earths and actinides. The bandwidths of the actinides are less than those of the 3d transition metals, whereas the spin–orbit interaction is far larger. In first order the orbital moment of an itinerant magnet is zero, but in second order the spin–orbit interaction mixes an orbital moment into the ground state. This involves mixing states from across the energy bands, and when the bandwidth is large the mixing is small and vice versa. The narrow 5f bands and the large spin–orbit interaction in actinides produces the ideal situation for itinerant electrons to support the strong orbital magnetism which is one of the remarkable features of actinide magnetism.

2.3. The 4f and 5f shells of isolated atoms

In a discussion of the properties of f states, one should at the outset distinguish between radial and angular properties. The angular properties are common to all f states, whereas it is the difference between the radial wave functions that distinguishes between 4f and 5f states.

The special properties of f shells are primarily due to the centrifugal potential in the radial Schrödinger equation as explained in section 2.1. The extent of the radial density as a function of atomic number depends upon the self-consistent potential. This potential contains the attraction due to the nuclear charge which is shielded by the charge from the occupied electron states. The shielding of the nuclear charge by the f density is less than perfect and as the number of f electrons increases the effective potential becomes more attractive. At the beginning of the rare-earth series, the 4f density of lanthanum lies essentially outside the xenon core. But as the number of f electrons increases the f density is drawn inside the 5s and 5p shells. These outer core shells effectively shield the f states from the environment in the solid. In the actinides the effect of imperfect shielding occurs less rapidly than in the rare earths and the atomic f states are not occupied before protactinium. The f states behave like a partially filled inner shell with relatively little interaction with the environment. The difference in radial extent due to the extra node in the 5f wave function implies that the rare earths provide a more chemically inert shell than the actinides.

The angular properties of the f states are well known. In free atoms, and to a certain extent in solids, it follows from the invariance of the electron–electron interaction under rotations of all the electrons simultaneously, that the total angular momentum of the electrons, $\boldsymbol{L}$, is a constant of the motion since $\boldsymbol{L}$ generates such rotations. Further, the total spin, $\boldsymbol{S}$, is also a constant of the motion and is an operator suitably symmetric under permutation of the electrons. The eigenstates of the electron–electron interaction may therfore be classified according to the eigenstates of L and S. In the Russel–Saunders coupling scheme the spin–orbit interaction is assumed to be far smaller than the electron–electron interaction and it is therefore treated as a first-order

perturbation. In this approximation the eigenstates of the Hamiltonian are invariant under rotations of spin space and real space simultaneously, i.e., they are eigenstates of the total angular momentum, J. Since the eigenstates of the Hamiltonian are eigenstates of the total angular momentum in the above-mentioned approximation, the matrix elements of any vector operator are proportional to the matrix elements of the total angular momentum, a considerable simplification that essentially determines the theory of magnetic properties of rare earths, outlined in section 2.2. In an applied field the added Zeeman term in the Hamiltonian is

$$\mu_B \boldsymbol{H}\cdot(\boldsymbol{L} + 2\boldsymbol{S}), \tag{2.16}$$

and, at zero temperature, the saturated magnetic moment is given by

$$\boldsymbol{\mu} = \mu_B g_J \boldsymbol{J}. \tag{2.17}$$

The g-factor, g_J, depends upon the expectation value of S_z in the ground state and this is given in terms of the matrix element theorem above, or Wigner–Eckart theorem, by

$$g_J = 1 + \frac{(\alpha J \| \boldsymbol{S} \| \alpha J)}{(\alpha J \| \boldsymbol{J} \| \alpha J)}, \tag{2.18}$$

where $\| \boldsymbol{O} \|$ is the reduced matrix element of the operator, O, and contains its dynamics. It is a simple matter to evaluate the reduced matrix elements which are given by

$$g_J = 1 + \frac{J(J+1) + S(S+1) - L(L+1)}{2J(J+1)} \tag{2.19}$$

whence the expression for the magnetic moment, eq. (2.17), is familiar as the classical vector coupling rule. The magnetic moments, calculated in this way are clearly independent of the principle quantum number of the f shell.

The approximations leading to Russel–Saunders coupling are quite good for rare-earth atoms but spin–orbit interaction is greater in the actinides and first-order perturbation theory is not always sufficient. However, the other extreme is to assume that spin–orbit interaction is larger than the electron–electron interaction in which case the states are first classified by the total individual electron angular momentum $\boldsymbol{j}_i = \boldsymbol{l}_i + \boldsymbol{s}_i$, the so-called j–j coupling scheme which is used for nuclei. When the weaker electron–electron interaction is taken into account the eigenstates of the Hamiltonian are, of course, again eigenstates of the total angular momentum, $\boldsymbol{J}$, since space is isotropic, but the reduced matrix elements are changed due to the change in dynamics. For the ground states, which are the states of maximum multiplicity, the g-factors for j–j coupling are given by

$$g_j = 1 + \frac{j(j+1) + s(s+1) - l(l+1)}{2j(j+1)} \tag{2.20}$$

for each electron, and the total moments are obtained by adding the individual moments $\mu_j = \mu_B g_j j$ with $\boldsymbol{J} = \sum_i \boldsymbol{j}_i$ maximized. That the j–j limit is not appropriate for actinides is easily demonstrated by the example of Cm, which has seven 5f electrons

and has a $J = 7/2$ ground state in both LS and j–j coupling. The 5f shell is half-filled and, in LS coupling at least, the orbital moment is zero in a first approximation making the Cm ion relatively insensitive to crystal fields. The g-factors in j–j and LS coupling are 8/7 and 2, respectively. Experimentally (Kanellakopulos et al. 1975), metallic Cm has a spin of 7/2 and a g-factor of 2.

The exchange interactions of the atoms depend in general upon both orbital and angular properties but the *isotropic* part of the exchange interaction depends only upon radial integrals for an f shell. The exchange energy of the open shells in the Hartree–Fock (HF) approximation (Slater 1968) is

$$E^{\mathrm{ex}} = -\tfrac{1}{2} \sum_{lm,l'm'} \langle l'm', lm|g|lm, l'm'\rangle n_{lm} n_{l'm'} \delta_{s_{lm}, s_{l'm'}}, \tag{2.21}$$

where g is the Coulomb interaction, lm labels the orbitals and, in an extended system, n_{lm} – which are *local* occupation numbers – are in general *non-integral*. This expression is evaluated in terms of Slater integrals through a multipole expansion of the Coulomb interaction. The exchange energy may be separated into two parts, one of which depends upon the number of electrons and the other of which depends upon the total spin. The latter is called the *spin polarization energy*, E_{SP}. Under the assumption that the spin orbitals are equally populated with occupation numbers $n_{lm}^{\pm} = q_l^{\pm}/(2l+1)$, where $q_l^{\pm}$ is the number of electrons with l character and spin $\pm$, the Hartree–Fock spin polarization energy becomes

$$E_{\mathrm{SP}}^{\mathrm{HF}} = -\tfrac{1}{4} \sum_{l,l'} V_{ll'} m_l m_{l'} \tag{2.22}$$

in terms of the *partial spin moments*, m_l. The exchange integrals $V_{ll'}$ are given in terms of radial Slater exchange integrals $G_{ll'}^k$ (Slater 1968) by

$$V_{ll'} = \sum_k \begin{pmatrix} l & l' & k \\ 0 & 0 & 0 \end{pmatrix}^2 G_{ll'}^k \tag{2.23}$$

where $(\cdots)$ is a Wigner $3j$ symbol, and $G_{ll'} = F_{ll'}$ – the Slater–Coulomb integrals – when $l = l'$. The isotropic exchange interactions $V_{ll'}$ therefore depend only upon the orbital quantum number of the shell and radial integrals.

Li and Coey (1991) have derived the isotropic exchange interaction between the f and other angular momentum states and obtained the expression (which was evaluated for a number of rare earths)

$$J_{4f-nl} = \frac{1}{\sqrt{7(2l+1)}} \left[\sum_k \langle f \| C^{(k)} \| f \rangle \begin{Bmatrix} 3 & 3 & 0 \\ l & l & k \end{Bmatrix}^2 G^k(4f, nl) \right] \tag{2.24}$$

where $\{\cdots\}$ is a $6j$ symbol. It is easy to show, by evaluating the reduced matrix element of the spherical tensor harmonic, $C^{(k)}$, that J_{4f-nl} in eq. (2.24) is equivalent to V_{3l} in eq. (2.23). These HF exchange integrals for d and f states of rare-earth and actinide atoms are plotted in figs. 2.8 and 2.9.

In LSDA the *spin polarization energy* may also be expressed in terms of radial integrals, which are quite different from the Slater integrals (Brooks and Johansson

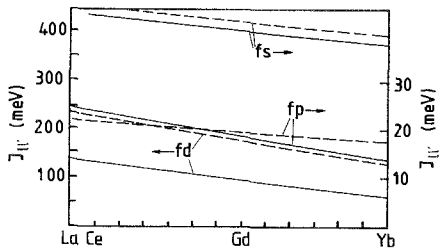

Fig. 2.8. Calculated exchange integrals across the rare-earth series for free atoms. The full lines are the LSDA exchange integrals, eq. (2.26), and the dashed lines the Hartree–Fock exchange integrals, eq. (2.23).

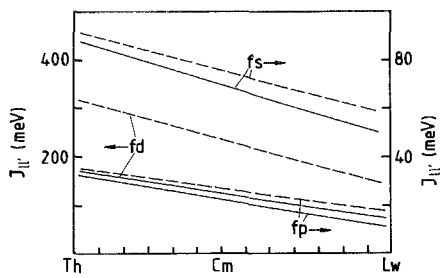

Fig. 2.9. The same exchange integrals as in fig. 2.8 but for the actinide series.

1983),

$$E_{\mathrm{SP}}^{\mathrm{LSDA}} = -\tfrac{1}{4}\sum_{l,l'} J_{ll'} m_l m_{l'}, \tag{2.25}$$

where the LSDA *atomic exchange integral matrices* are given by

$$J_{ll'} = \tfrac{2}{3}\int r^2 \phi_l^2(r)\phi_{l'}^2(r) A[n(r)]/n(r)\,\mathrm{d}r \tag{2.26}$$

and $A(r)$ is well-known (von Barth and Hedin 1972) function of the density. Evidently $V_{ll'}$ is the HF equivalent of $J_{ll'}$. The LSDA exchange integrals for the f states of rare-earth and actinide atoms are also plotted in figs. 2.8 and 2.9 where they are compared with the HF exchange integrals. Since for free atoms the eigenstates are bound states, there are solutions only at discrete energy eigenvalues and only one possible exchange interaction for a given value of ll'. In the solid state where the conduction electron bands are scattering states the radial wave functions are continuous functions of energy and the exchange integrals are energy dependent. Under these circumstances one must beware of expecting the exchange integrals not to change between free atom and solid.

The reason that the f–d exchange integrals decrease across each series is the contraction (lanthanide and actinide) of the f shell, which decreases the overlap with the d states. The overlap between 4f and 5d densities occurs over a relatively small region

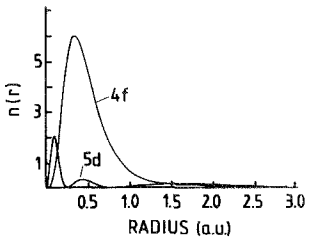

Fig. 2.10. The 4f and 5d radial densities for a free Gd atom. The overlap region of the 4f and 5d densities is shaded.

of space corresponding to the outer part of 4f density and the inner part of the 5d density (fig. 2.10). As the 4f shell contracts the region of overlap decreases.

The HF and LSDA exchange integrals are by no means identical. The HF integrals are perfectly straightforward quantities, but the origin of the LSDA integrals is more obscure. If the correlation contribution to the exchange and correlation energy is neglected, which is a reasonable approximation for f shells where the electron density is high, the integrals depend in the first instance on the exchange energy of a homogeneous electron gas – which is proportional to the density to the power of $\frac{4}{3}$. The gas is then allowed to spin-polarize and, since the spin-up and spin-down densities each have their own exchange energies, the exchange energy contains spin-up and spin-down contributions, each proportional to the $\frac{4}{3}$ power of its own density. The exchange energy of the paramagnetic state is then subtracted from the exchange energy of the polarized state and the difference is the spin polarization energy. The spin polarization energy is then expanded to second order in the ratio of magnetization to total densities – a process made necessary by the $\frac{4}{3}$ power dependence of the spin polarization energy – in order to obtain a quadratic (or interaction) form for the spin polarization energy. The expansion is, of course, only valid for small values of the ratio $\zeta(r) = m(r)/n(r)$. The resulting moment densities are then expanded in spherical harmonics to obtain the l dependence the moment densities related to the total lth partial moments. The result is eq. (2.25). Then, when the integrals are made, the density of the homogeneous electron gas is replaced by the real density, $n(r)$.

That the two approximations yield different results is, under these circumstances, hardly surprising. The LSDA integrals are local, the HF integrals are not. The *exchange hole* in the HF integrals is closely related to the shape of the wave function whereas in the LSDA integrals it is spherical about the electron. The difference is to some extent alleviated in eq. (2.23) since it was assumed that all orbitals of a shell were equally occupied thus removing some of the effects of the nonspherical nature of the wave functions and densities. But we note that this has, at least overtly, nothing to do with correlation since the exchange contribution in LSDA is calculated using the Hartree–Fock approximation – the only difference is that it is the HF approximation for a homogeneous electron gas.

Experience has shown that the LSDA integrals lead to splittings of energy bands and calculated magnetic moments that are in better agreement with measurements than if the HF approximation is used. Exactly why this should be is not perfectly

understood, although it is often discussed (e.g., Gunnarsson 1978). The results of research on the magnetism of actinides, however, suggest that LSDA runs into difficulties when the nodal properties of the wave functions become important to the exchange interactions (Gunnarsson and Jones 1985).

2.4. *Charge, spin and magnetization densities*

The charge and spin densities are the essential electronic and magnetic structure of a material in its ground state and are probed experimentally by diffraction experiments. The magnetization density, which is responsible for the magnetic scattering of neutrons, is almost entirely due to the valence electrons (as core polarization is, relatively, very small). The magnetic form factors may be obtained from self-consistent energy band calculations, which yield the magnetization density, and compared with experiments. The atomic magnetic scattering amplitude is just the Fourier transform of the atomic magnetization density

$$F(\boldsymbol{Q}) = \int \boldsymbol{M}(\boldsymbol{r}) \exp(\mathrm{i}\boldsymbol{Q}\cdot\boldsymbol{r})\,\mathrm{d}\boldsymbol{r} \tag{2.27}$$

where $\boldsymbol{Q}$ is the scattering vector. The *magnetic form factor* is the scattering amplitude divided by the total moment so that it is normalized to unity although in experiments the scattering in the forward direction is proportional to the total moment – and it is assumed that the moment density is unidirectional. In the dipole approximation eq. (2.27) reduces to a readily computable form

$$F(\boldsymbol{Q}) = [\langle j_0 \rangle_s m_s^z + \langle j_0 + j_2 \rangle_l m_l^z]/m^z, \tag{2.28}$$

where the total ground-state moment is the integral of the moment density given by

$$m^z(r) = \mu_B[l^z(r) + 2s^z(r)] \tag{2.29}$$

in terms of the orbital angular momentum and spin densities. Here

$$\langle j_i \rangle_\alpha = 4\pi \left[\int j_i(Qr) r^2 n_\alpha(r)\,\mathrm{d}r \right] \Big/ m_\alpha^z, \tag{2.30}$$

where $\alpha = s, l$ denotes the spin or orbital density and moment.

The form factors are smooth functions since, in the dipole approximation at small scattering vectors, the form factor is insensitive to irrelevant oscillations that do not affect the overall radial extension. The partial 4f, 5d and 5f, 6d spin-only form factors for Ce and U are shown in fig. 2.11. It is difficult to measure the form factor at values of $\sin(\theta)/\lambda$ less than 0.2 and it is normally concluded that a spin density with the spatial extension of the 5d or, even more, 6d density does not influence the measured form factor over the measurable range. Since the measured form factor is very close to the partial f form factor the measured moment is the f moment. This is the explanation usually put forward for the difference between the moments measured in bulk magnetization and neutron scattering experiments. Therefore the magnitude and sign of the conduction electron polarization may be deduced. It is known, for example, that in the elemental rare earth metals the conduction electron polarization is *parallel* to

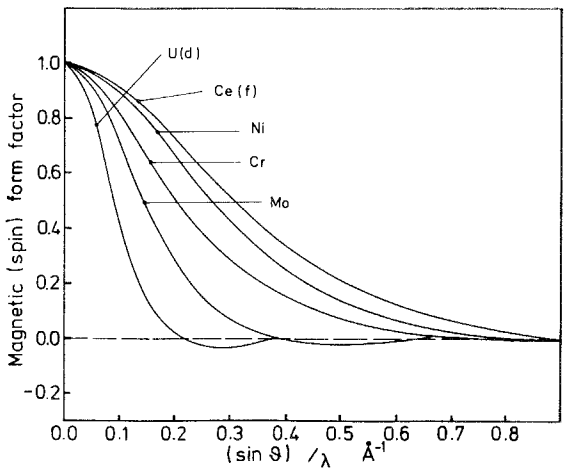

Fig. 2.11. The calculated magnetic form factors of the partial d densities of Ni, Cr, Mo and U free atoms compared with the form factor of the partial f densities of a Ce free atom.

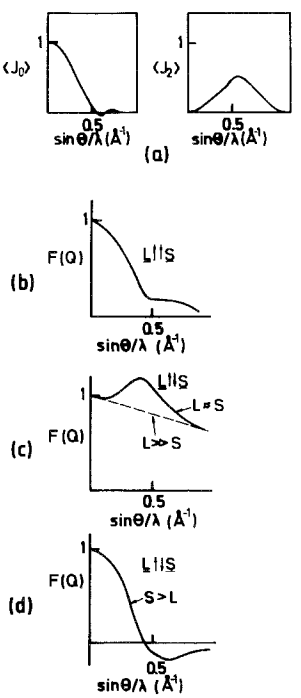

Fig. 2.12. Magnetic form factor analysis: (a) shows the wave vector dependence of the functions $\langle j_0 \rangle$ and $\langle j_z \rangle$ in eqs. (2.28) and (2.30); (b) is the corresponding form factor, eq. (2.28), when m_l^z and m_s^z are parallel; (c) is the form factor when m_l^z and m_s^z are antiparallel with the magnitude of m_l^z greater, or equal, to the magnitude of m_s^z; (d) as for (c) but with the magnitude of m_l^z less than the magnitude of m_s^z.

the *4f spin* moment. The physical reason that the f and d partial form factors can be separated in this way is that their spatial spin densities are also well separated.

Neutron diffraction is also useful as a probe of orbital magnetism. Typical radial integrals of the products of the spherical Bessel functions with the density given in eq. (2.30), are plotted in fig. 2.12a. It may be seen from eq. (2.28) that the $\langle j_2 \rangle$ contributes only when there is an orbital contribution to the moment. Furthermore, the way in which $\langle j_2 \rangle$ contributes depends critically upon the relative signs and magnitudes of the spin and orbital moments. We illustrate this schematically in figs. 2.12b,c and d where we have drawn form factors for m_s^z and m_l^z parallel, $m_s^z < m_l^z$ but m_s^z and m_l^z antiparallel, and $m_s^z > m_l^z$ with m_s^z and m_l^z again antiparallel. It is relatively difficult to extract the orbital moment when the spin and orbital contributions are parallel, as in a heavy rare earth, since the tail in the measured form factor arising from the dependence of $\langle j_2 \rangle$ upon the scattering vector, appears only as a bump at large scattering vectors. But when orbital and spin moments are antiparallel, especially if they are almost cancelling, the tail in the form factor arising from the orbital contribution to the magnetization density develops into a prominent bump which has been observed in several actinide compounds (e.g., Lander and Aeppli 1991).

The origin of the different shapes of the orbital and spin moment contributions is that, although the angular momentum and spin densities have similar spatial distributions, their concomitant contributions to the magnetization density are quite different. The orbital magnetization density lies much closer to the nucleus and therefore appears in the form factor, which is a Fourier transform, further out.

3. The elemental metals

The conduction bands transmit the exchange interactions between local atomic moments. The exchange interaction between any pair of electrons is usually written in terms of their spins as $-2J_{12}\boldsymbol{s}_1\cdot\boldsymbol{s}_2$, where J_{12} is the exchange integral. For rare earths the exchange interaction Hamiltonian between conduction electrons and local 4f moments is

$$\mathscr{H}_{\text{s-f}} = -\sum_{\text{4f}} -2\tilde{J}_{\text{4f2}}\boldsymbol{s}_{\text{4f}}\cdot\boldsymbol{s}_2 = -2\tilde{J}_{\text{4f-c}}\boldsymbol{S}_{\text{4f}}\cdot\boldsymbol{s}_{\text{c}} = -2\tilde{J}_{\text{4f-c}}(g-1)\boldsymbol{J}_{\text{4f}}\cdot\boldsymbol{s}_{\text{c}}, \tag{3.1}$$

where $\tilde{J}_{\text{4f-c}}$ is an average taken over the ground-state J multiplet, $\boldsymbol{J}_{\text{4f}}$ is the total 4f angular momentum and $\boldsymbol{s}_{\text{c}}$ is the conduction electron spin. The exchange interaction is often called the s–f interaction for historical reasons since it was first used for exchange between nucleus and conduction electrons (Ruderman and Kittel 1954), where the contact interaction with the nucleus picks out the s-wave part of the conduction electron wave functions. The name is preserved although it is not intended that the conduction electrons states be pure s states. In fact, in rare-earth metals and compounds the 5d states are more important. In principle, the s–f exchange integral is, explicitly,

$$\tilde{J}_{\text{4f-c}}(n'\boldsymbol{k}', n\boldsymbol{k}) = \int \Psi_{n'k'}(\boldsymbol{r})\Phi_{\text{4f}}(\boldsymbol{r}' - R_i)\frac{e^2}{|\boldsymbol{r}-\boldsymbol{r}'|}\Psi_{n\boldsymbol{k}}(\boldsymbol{r}')\Phi_{\text{4f}}(\boldsymbol{r} - R_i)\,\mathrm{d}\boldsymbol{r}\,\mathrm{d}\boldsymbol{r}'. \tag{3.2}$$

The exchange integrals are always positive and they align the conduction and 4f *spin* moments. In the ordered phase at zero temperature the rare-earth moment may be replaced by its expectation value in the mean field (MF) approximation. The s–f Hamiltonian still has both diagonal and off diagonal elements among conduction electron states since the unperturbed states are for the paramagnetic phase. The diagonal contribution to the conduction band energies splits the spin-up and spin-down conduction bands

$$\varepsilon_{nk}^{\pm} = \varepsilon_{nk} \mp \langle J_{4f}^{z} \rangle (g-1)\tilde{J}_{4f-c}(nk, nk). \tag{3.3}$$

In second order the energies are further modified by a contribution involving interband transitions. This second-order contribution is due to the change of wave functions induced by magnetic ordering since the unperturbed wave functions are for the paramagnetic ground state, and the induced potential is non-uniform. In section 3.2, when we discuss self-consistent spin-polarized calculations, we will see that this type of analysis is not necessary. In a self-consistent calculation for a crystal the wave functions and spin densities are continuously modified, the problem being solved by iteration, and the final – converged – wave functions are eigenstates of the potential due to a non-uniform, but periodic, spin density. The first-order splitting of the conduction bands, eq. (3.3), leads to an approximate conduction electron moment

$$\langle \mu_z \rangle_c = \mu_B N(\varepsilon_F)(g_J - 1)\langle J_{4f}^{z} \rangle \tilde{J}_{4f-c}, \tag{3.4}$$

where $N(\varepsilon)$ is the state density per f.u. in the *paramagnetic* phase.

The Hamiltonian approach above finds its analogy in density functional theory. Here the total energy, which is in general a functional of the spin densities, may be approximated by the quadratic form of eq. (2.25) where the atomic exchange integral matrices are given by eq. (2.26) and plotted in figs. 2.8 and 2.9. In the solid the atomic exchange integrals are not accurate and should be replaced by the *energy-dependent exchange integrals* with the conduction electron wave functions evaluated at the correct energy

$$J_{4f-c}(nk, nk) = \tfrac{2}{3}\int r^2 \phi_{4f}^2(r)\phi_{5d}^2(r, E_{nk}) A[n(r)]/n(r)\,dr, \tag{3.5}$$

where it has been assumed that the 5d density dominates at the Fermi energy. The energy dependence of the 5d conduction band states in rare earths can change the 4f–5d exchange integrals considerably. Figure 3.1 shows the calculated 4f density and the 5d density at the bottom and top of the 5d bands (the bonding and antibonding states of section 2.1, eq. (2.7) and (2.8)). The magnitude of J_{4f-c} depends upon the small overlap region of the 4f and 5d densities which clearly varies enormously as the bonding 5d density is moved outwards away from the 4f density in contrast to the situation in the free atom shown in fig. 2.7. The energies of the conduction electron bands in the field of the 4f states are then given by

$$\varepsilon_{nk}^{\pm} = \varepsilon_{nk} \mp \tfrac{1}{2} J_{4f-c}(nk, nk)\langle \mu_{4f}^{z} \rangle = \varepsilon_{nk} \mp (g_J - 1) J_{4f-c}(nk, nk)\langle J_{4f}^{z} \rangle. \tag{3.6}$$

The approximations leading to eq. (3.3) are similar to those leading to eq. (3.6) – the LSDA version of the rigid-band splitting of the Stoner theory (Gunnarsson 1976, 1977, Janak 1977). The theory of energy band splitting in itinerant electron metals by Slater

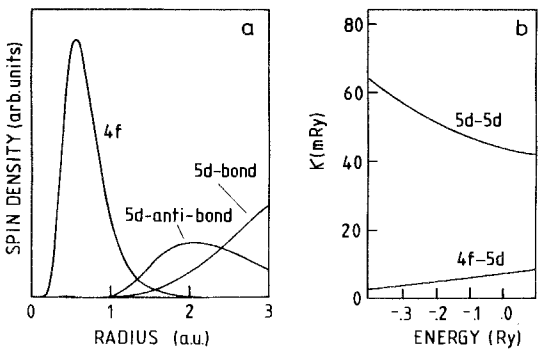

Fig. 3.1. (a) The calculated 4f and 5d radial densities for Gd metal. The d density is shown for the bottom (bond) and top (antibond) of the 5d bands. (b) The corresponding calculated 5d–5d and 4f–5d exchange interactions as a function of energy from the bottom of the 5d bands.

(1968) corresponds to the treatment we have outlined in eqs. (2.21)–(2.23), and calculations by Li and Coey (1991) from eq. (2.24) are essentially the same. These HF theories have used free atom exchange integrals but in principle could be extended to include the energy dependence of the wave functions in the solid.

3.1 Self-consistent energy band calculations for the rare-earth metals

The 4f states in the rare earths remain localized but the 5d and 6s states become delocalized, are Bloch states, and are best treated by band structure calculations. Although the conduction electrons make only a small contribution to the magnetic moment they play an essential role in the magnetism as the mediators of magnetic interactions. It is therefore important that theorists are able to calculate the conduction band electronic structure accurately.

Three approaches have been made to the calculation of conduction electron band structure in the rare earths. In the first, the 4f states have been treated as part of the band structure (e.g., Harmon 1979). This treatment is most suitable for Gd where the seven filled spin-up 4f states lie self-consistently below, and the empty spin-down f states above, the Fermi energy. The splitting between these two sets of 4f states is easily estimated to be seven times the 4f–4f exchange integral ($J_{4f4f} \simeq 0.69$ eV) or 4.8 eV. According to Singh (1991) fully self-consistent calculations yield a splitting of 5 eV between up and down spin 4f bands, the up spin states lying about 4.5 eV below E_F and the down 4f bands about 0.5 eV above E_F. The spin-down 4f bands are quite close to the Fermi level, raise the state density at the Fermi energy through hybridization with the 5d states, and they increase the calculated state density at the Fermi energy to 27 states/Ry compared with a value deduced from measurements (Wells et al. 1974) and assuming no enhancement, of 21.35 states/Ry. The 4f character at the Fermi energy in Gd is, according to Singh (1991), about 5 states/Ry and it is reasonable to assume that it is responsible for the difference between theory and measurement. Precisely this problem had been detected earlier by Harmon (1979) who artificially raised the 4f spin-down bands to remove their influence upon the state density at

the Fermi energy. It is tempting to attribute the error in the position of the spin-down bands to the absence of a large Hubbard U repulsion (Hubbard 1963) in LSDA.

The example of Gd identifies the main problem associated with leaving the 4f states in the band structure. The position in energy of the 4f bands is incorrect and the hybridization with other conduction electron states is too large. The situation is far worse for the other metals since in spin-polarized calculations a spin shell is not filled and the 4f bands, which act as a sink for electrons, always cut the Fermi level leading to specific heat coefficients which are larger than those measured by an absurd amount.

The second approach has been to treat the 4f states as part of the core as is compatible with their localized status. This not only reduces the calculated specific heat coefficients but actually makes self-consistent calculations more stable since the sensitivity of the energy of the 4f bands to their own occupation may easily lead to oscillations in 4f occupation number. This approach has been used very successfully for the computation of cohesive properties by Skriver (1983b). Those details of the conduction bands which influenced the crystal structure were reproduced very well. For example, the partial 5d occupation numbers increased across the series, with a corresponding decrease in the 6s occupation, due to incomplete screening by the added 4f electrons. The increase in 5d occupation is what causes the structural sequence hcp → Sm-structure → dhcp → fcc as the atomic number is decreased or the pressure is increased.

A natural extension is to spin-polarize the core in order to be better able to compute magnetic properties. Now the 4f moments, being part of the core, cannot be computed self-consistently but the moments are known in the limit that Russel–Saunders coupling is a good approximation. The problem of how to fix the number of spin-up and spin-down 4f electrons remains. The total number of 4f electrons is not a problem as it is known to change from seven for Gd to twelve for Tm in the trivalent metals, the divalency of Eu and Yb can easily be handled, and the rare earth in most intermetalic compounds is trivalent. The spin occupation numbers are determined by applying the standard Russel–Saunders coupling scheme to the 4f shell. Then S is maximized, L is maximized for a given maximum S, and the total momentum $\boldsymbol{J}$ is $\boldsymbol{J} = \boldsymbol{L} + \boldsymbol{S}$. The magnetic moment is given by $\boldsymbol{\mu}_{4f} = g_J \boldsymbol{J}$ where g_J is the Landé factor, eq. (2.19). The ground-state spin component of the total 4f moment is obtained from the Wigner–Eckart theorem (section 2.3) μ^s_{4f}, is obtained from the projection of the spin along the direction of total angular momentum,

$$\mu^s_{4f} = 2(g_J - 1)J. \tag{3.7}$$

The 4f spin-up and spin-down occupation numbers are then determined by

$$\begin{aligned} n_{4f} &= n^+_{4f} + n^-_{4f}, \\ \mu^s_{4f} &= n^+_{4f} - n^-_{4f}, \end{aligned} \tag{3.8}$$

where $n^{\pm}_{4f}$ are the up and down spin occupation numbers and n_f is the total number of 4f electrons. The foregoing is consistent with the de Gennes factor and model theories of s–f interactions where, at the mean field level, the projection of the 4f spin along the total 4f moment direction enters the 4f–conduction electron exchange interaction.

Clearly the occupation numbers n_{4f}^{+}, n_{4f}^{-} are part of the input to the calculations and are not determined ab initio as are the partial occupation numbers of the conduction electron states. The fact that the 4f occupation numbers are not determined ab initio will obviously cause difficulty if the Russel–Saunders scheme is not correct but for the heavy rare earths, with $\boldsymbol{L}$ and $\boldsymbol{S}$ parallel, there is no obvious difficulty since the resulting projection of $\boldsymbol{S}$ along $\boldsymbol{J}$ is equal to $\boldsymbol{S}$. But for the light rare earths, with $\boldsymbol{S}$ and $\boldsymbol{L}$ anti-parallel, this is not so and the occupation numbers for spin-up and spin-down states must be made non-integral, although their sum is of course integral. Nevertheless, since LSDA in its present form is a mean field theory, what is required are the spin up and down potentials along the moment direction and these should be obtained from the quantum mechanical average of the spin density along this direction. Therefore, as long as the Russel–Saunders scheme is reliable, the projection of the spin density along the total moment direction should be the appropriate quantity with which to split the potential. The foregoing is, of course, completely consistent with the de Gennes factor and model theories of s–f interactions where, at the mean field level, the projection of the 4f spin along the total 4f moment direction enters the 4f–conduction electron exchange interaction.

The third approach, which is more recent, is to incorporate the self-interaction correction (SIC) in the energy band calculations (Heaton et al. 1983). SIC, as its name suggests, uses complete cancellation between the Coulomb interaction of an electron with itself and its exchange and correlation self-energy – a cancellation which is incomplete in LSDA. The result is that localized states are localized further, and the energies of occupied and unoccupied states are split. Svane and Gunnarsson (1990) have applied SIC to the transition metal oxides, obtaining a drastic improvement in band gaps and calculated moments compared with the results of LSDA. The most favourable aspect of SIC in its application to rare earths is the existence of separate occupied and unoccupied states. Szotek et al. (1993) have applied the scheme to praseodymium metal. The occupied 4f states are pulled well below the conduction bands whereas unoccupied 4f bands lie about 1 eV above the Fermi energy.

Since most of the available LSDA calculations have been for Gd metal it is most worthwhile to summarize these results. Firstly, calculations for the *paramagnetic* ground state have been made by Lindgard (1976), Harmon (1979) and Brooks et al. (1992). The state density at the Fermi energy per atom was found to be 28 by Harmon (1979), 25 by Lindgard (1976), and 22 by Brooks et al. (1992). Calculations with the 4f states polarized in the bands have been made by Harmon (1979), Sticht and Kübler (1985), Temmerman and Sterne (1990), Krutzen and Springelkamp (1989), Richter and Eschrig (1989), and Singh (1991). There seems to be general agreement that the state density at the Fermi energy is 25–37 states/(Ry atom spin), to which there is a 4f contribution of about 5–6 states/(Ry atom spin). The exception is Harmon (1979) who finds that the state density drops to about 11 in the polarized case. Calculations with the 4f states polarized in the core (Brooks et al. 1992) or an exchange splitting applied (Skriver and Mertig 1990) yield a state density at the Fermi energy of 12 states/Ry atom spin). The latter calculations yield results that are on the correct side of experiment.

The calculated magnetic moments from most calculations are in good agreement

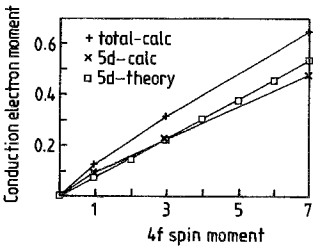

Fig. 3.2. The self-consistently calculated total and partial 5d moments per cell (two atoms) for Gd metal as a function of 4f spin moment. The approximate partial 5d moment was obtained from eq. (3.1).

with measurements (Roeland et al. 1975) of $7.63\mu_B$. The authors of this chapter (Brooks et al. 1992) obtained $7.65\mu_B$, Singh (1991) obtained $7.57\mu_B$, and Temmerman and Sterne (1990) $7.68\mu_B$. One difference, however, between the two types of polarized calculations is that when the 4f states are in bands the 4f moments turn out to be slightly less than seven, and the conduction electron moments to be correspondingly greater.

In all cases the calculated moment is within a few percent of experiment and it is reasonable to claim that the splitting of the conduction bands is approximately correct. This is not unimportant as it indicates that LSDA exchange interactions are of about the correct strength in rare earths. Brooks et al. (1992) have calculated the conduction electron moment as a function of 4f moment when the Gd spin is changed from one to seven (fig. 3.2). The conduction electron moment is approximately (but not exactly) a linear function of 4f spin which indicates that a Stoner model for the conduction bands should be useful (but not exact). The reason that the conduction electron moment increases less rapidly for larger values of 4f moment is that the state density at the Fermi energy starts to fall as the splitting of the conduction bands increases.

Studies of the Fermi surface of Gd have been made by Harmon (1979), Singh (1991), and Auluck and Brooks (1991). Although not perfect, reasonable agreement with measurements (Mattocks and Young 1977a) was obtained, except that some measured smaller orbits provide some difficulty. Of the other metals, calculations for ferromagnetic Tb (Auluck and Brooks 1991) were used to identify the single measured dHvA frequency (Mattocks and Young 1977b) which could be done with only a shift of 0.002 Ry in the Fermi energy. The detailed dHvA experiments (Wulff et al. 1988) on dhcp praseodymium have led to studies (Wulff et al. 1988, Auluck and Brooks 1991) of its Fermi surface although most interest has centred on the mass enhancement (Wulff et al. 1988). There are some small discrepancies between the two LMTO calculations but an overall good agreement with the frequencies of the measured orbits. The calculated Fermi surface of Lu (Johanson et al. 1982, Tibbetts and Harmon 1982) is also in semi-quantitative agreement with experiment.

3.2. A model for the influence of the localized moments upon the band structure

The exchange integrals may be used to analyse the effect of the localized 4f magnetism upon the conduction electron band structure. In LSDA the exchange and correlation

potential is given by (von Barth and Hedin 1972)

$$v_{xc}^{\pm}(r) = A(n(r))\left[\frac{2n^{\pm}(r)}{n(r)}\right]^{1/3} + B(n(r)), \tag{3.9}$$

where A and B are functionals of the total electron density (von Barth and Hedin 1972), $n(r) = n^{+}(r) + n^{-}(r)$. Since the total spin-up and spin-down potentials contain $v_{xc}(r)$, additively, the difference between spin-up and spin-down potentials is

$$\Delta v_{xc} = v_{xc}^{+}(r) - v_{xc}^{-}(r). \tag{3.10}$$

The difference in the spin-up and spin-down potentials is a functional of the local total spin-up and spin-down densities. Since the 4f spin density is highly non-uniform, so is its effect upon the spin-up and spin-down potentials. The effect of exchange with 4f electrons, felt by the conduction electrons, is therefore also highly non-uniform and no approximation of the nature of a Stoner splitting or uniform molecular field need be made in the self-consistent calculations, as described in the previous section. Nevertheless, the influence of the localized 4f states upon the conduction band structure, including conduction electron exchange enhancement, may be modelled in a transparent way.

The bare exchange integrals are obtained approximately by first expanding the exchange split potential, eq. (3.9), to first order in the magnetic moment density which is resolved into its partial angular momentum components, assuming that spin-up and spin-down densities do not differ, that only states close to the Fermi energy contribute to the magnetic moment, and applying first-order perturbation theory by averaging with the wave function at the energy for which the splitting is required. The effective energy splitting at the Fermi energy is then

$$\Delta\varepsilon(E_F) = \sum_q \sum_l \left[\frac{N_{ql}(E_F)}{N(E_F)} \sum_{l'} J_{qll'}(E_F)\mu_{ql'} + J_{4f-l}(E_F)\right], \tag{3.11}$$

where J_{4f-l} is given by

$$J_{4f-l}(E_F) = \tfrac{2}{3}\int r^2 \phi_{4f}^2(r)\phi_l^2(r, E_F) A[n(r)]/n(r)\,dr, \tag{3.12}$$

where the sum over l, l' excludes $l = 3$ and q labels the atom. The intra-conduction electron exchange integrals are

$$J_{ll'}(E) = \tfrac{2}{3}\int r^2 \phi_l^2(r, E)\phi_{l'}^2(r, E_F) A[n(r)]/n(r)\,dr. \tag{3.13}$$

The latter integrals are evaluated at the Fermi energy for both states l and l'. Then one obtains essentially the average splitting of the partial l bands per unit of spin moment, $\mu_{l'}$, obtained from the potential difference, of eq. (3.10) at the Fermi energy. The integrals, $J_{ll'}(E_F)$, for the rare-earth metals are calculated to be:

for dhcp Pr; $J_{5d5d} = 38$ mRy; $J_{5d6p} = 36$ mRy; $J_{5d6s} = 39$ mRy,

for hcp Gd; $J_{5d5d} = 39$ mRy; $J_{5d6p} = 40$ mRy; $J_{5d6s} = 42$ mRy,

and are therefore more or less constant across the series. The integrals, $J_{4f-l}(E_F)$, are:

for dhcp Pr; $J_{4f-5d} = 8.6\,\text{mRy}$;
for hcp Gd; $J_{4f-5d} = 6.5\,\text{mRy}$.

Since rare-earth contraction, which changes 4f5d overlap, is fairly smooth the integrals may reasonably be interpolated by:

$J_{4f-5d} \simeq 8.6 - 0.42(x-2)\,\text{mRy}$; or
$J_{4f-5d} \simeq 117 - 5.71(x-2)\,\text{meV}$,

where x is the number of 4f electrons.

Self-consistent calculations for Gd in which the 4f spin was varied between 0 and 7 confirmed that the 5d moment was almost a linear function of the 4f spin. The 4f5d exchange integrals actually change slightly with increasing 4f spin. For example, in Gd with $\mu^s_{4f} = 0$, $J_{4f-5d} = 88\,\text{meV}$ whereas when $\mu^s_{4f} = 7$, $J_{4f-5d} = 94\,\text{meV}$. The 5d moments may be estimated from the corresponding exchange splitting of the 5d bands at the Fermi energy, eq. (3.11), at various levels of approximation. If it is assumed that the partial 5d state density dominates, the ratio $N_{qd}(E_F)/N(E_F)$ is one half for hcp Gd and one quarter for dhcp Pr. The 5d moment at a site is then given by

$$\mu_{5d} = J_{4f-5d}\mu^s_{4f}\frac{N_{5d}(E_F)/2}{[1 - J_{5d5d}N_{5d}(E_F)/2]}, \tag{3.14}$$

where J_{5d5d} is calculated to be 531 meV for Gd and $\mu^s_{4f} = 7$ is the 4f spin. The approximation of eq. (3.14) yields results to within a few percent of the actual 5d moments obtained in the self-consistent spin-polarized calculations (fig. 3.2). The partial 5d state density at the Fermi energy is calculated to be about 16 states/(Ry atom) in the paramagnetic state and is more or less constant across the heavy rare-earth series. The 5d moment for Gd is calculated to be $\mu_{5d} = 0.53\mu_B$ from eq. (3.14) and to be $\mu_{5d} = 0.48\mu_B$ self-consistently in a 405 k-point spin-polarized calculation. The reasons for the slightly different values are (1) above $\mu^s_{4f} = 3$, $N_d(E_F)$ starts to fall being only 9.2 states/(Ry atom) for $\mu^s_{4f} = 7$, and (2) $N_{5p}(E_F) = 5.5$ which is not negligible compared with $N_{5d}(E_F) = 16.5$. In a more complete multi-band theory (Brooks et al. 1992) eq. (3.14) is modified by 5d–5d and 5p–5p exchange interactions which yield an effective Stoner factor $IN_{tot}(E_F)/2$ where $I = 272\,\text{meV}$. With $N_{tot}(E_F) = 16 + 5.5 = 21.5$ states/(Ry atom), the Stoner enhancement factor is then 1.79 for the calculated values of $J_{5p5p} = 734\,\text{meV}$ and $J_{5p5d} = 544\,\text{meV}$ compared with the 5d5d enhancement factor of 1.47 in eq. (3.14).

We recall that self-consistent spin-polarized calculations (section 3.1) yielded a total conduction electron moment for Gd of $0.65\mu_B$ from a 405 k-point calculation which compares well with the measured value of $0.63\mu_B$ (Roeland et al. 1975) and suggests that LSDA gives reasonable values for the conduction band splitting. Lindgard (1976) used magnetization data to deduce the conduction electron polarization and, from his calculated state density at the Fermi energy, evaluated the exchange interaction from $\mu_{cond} = \bar{S}_{4f}N(E_F)J_{4f-c}$. In this way he obtained an effective $J_{4f-c} = 82\,\text{meV}$ for the series – quite close to the values of J_{4f-5d} given above.

Comparison with detailed dHvA data for dhcp Pr is also interesting. Here Wulff

et al. (1988) find an effective exchange interaction of about 9 mRy. The way in which this comes about is quite complex and informative. Firstly, the bare $J_{4f-5d} = 8.6$ mRy and it might appear that this agrees well with experiment, but $J_{5d5d} = 38$ mRy is large and the enhanced interaction according to eq. (3.14) would be too large. The partial 5d state density is 50 states/(cell Ry) compared with a total of 66 states/(cell Ry) and, according to eq. (3.11), this reduces the effective 4f–5d interaction. If we define

$$\bar{J}_{4f-5d}(E_F) = \sum_q J_{4f-5d}(E_F) \frac{N_{5d}(E_F)}{N(E_F)}, \tag{3.15}$$

the effective bare exchange interaction is only 6.6 mRy. This interaction is then enhanced by the 5d–5d interaction, which is itself reduced to 29 mRy by eq. (3.15) when 4f is replaced by 5d. The enhanced 4f–5d exchange interaction then becomes 8 mRy, if the 6s and 6p contributions are neglected close to the experimentally deduced value.

3.3. The Curie temperatures of the rare-earth metals

A simple mean field theory (Bloch et al. 1975) is normally used to estimate the Curie temperatures. The Helmholtz free energy of the 5d bands at high temperature is expanded,

$$\Delta F = F_d(\mu_d, T) - F_d(0, T) = \tfrac{1}{2} A(T) \mu_{5d}^2 + \cdots, \tag{3.16}$$

where

$$A(T) = \frac{1}{\chi_{5d}^0} - \tfrac{1}{2} J_{5d5d} - \frac{J_{4f-5d}^2 (g_J - 1)^2 J(J+1)}{3kT} \tag{3.17}$$

is the effective field acting on the 5d bands. Thus the susceptibility of the 5d bands is enhanced by the exchange interactions with the 4f states where the temperature dependence has been obtained by expanding the usual molecular field Brillouin function for small values of moment. For a second-order transition the Curie temperature is obtained by setting $A(T)$ to zero. The enhanced value of $\chi_{5d} = \chi_{5d}^0 / [1 - \chi_{5d}^0 J_{5d5d}/2]$ is 23.5 states/(Ry atom) and eq. (3.17) yields $T_C = 823$ K for Gd which is far too high. If, furthermore, the more complete multiband enhancement factor of 1.79 for the conduction band susceptibility is used in eq. (3.17), one finds $T_C = 1002$ K for Gd. The Curie temperatures of the other rare earths scale with the de Gennes factor, $G = (g_J - 1)^2 J(J+1)$, in eq. (3.17) and are all far too high. The foregoing is not compatible with the excellent results obtained for the Fermi surface and the saturation magnetization of Gd.

It is normal that the Curie temperatures calculated according to mean field approximations such as eq. (3.17) are too high. The magnetic field stabilizing μ_d in eq. (3.16) is $H = \partial F / \partial \mu_d = A(T) \mu_{5d} + \cdots$, which should be improved by adding a term to $A(T)$ to account for degrees of freedom in the d bands omitted in the mean field approximation (Lonzarich and Taillefer 1985). In weak itinerant magnets a mode–mode coupling term due to the effect of spin fluctuations in the d bands is added to $A(T)$ (Murata and Doniach 1972, Mohn and Wohlfarth 1987). However, the always finite 4f moments change the situation in the rare earths. Even at high temperature 5d moments form, but

since they are local and orientationally disordered there is no phase transition. The *local* susceptibility, χ_{ii}, is defined in terms of the single conduction electron Green function by (Heine et al. 1981, Moriya 1984)

$$\chi_{ii} = \frac{1}{\pi} \mathrm{Im} \int_{-\infty}^{E_F} \sum_m \langle i, m | G_0(E)^2 | i, m \rangle \, \mathrm{d}E, \tag{3.18}$$

where m denotes an orbital at the ith site. At a lower temperature, just above where long-range order occurs the correct susceptibility to use excludes the local susceptibility χ_{ii} then

$$A'(T) = \frac{1}{\chi^0_{5d}} - \left[\tfrac{1}{2} J_{5d5d} + \frac{J^2_{4f-5d}(g_J - 1)^2 J(J+1)}{3kT} \right] \left[1 - \frac{\chi_{ii}}{\chi^0_{5d}} \right] \tag{3.19}$$

replaces eq. (3.17). The Curie temperature is obtained from $A'(T_C) = 0$. The additional term in eq. (3.19), which is small when χ_{ii} is small, replaces the local fluctuation correction used for weak itinerant magnets and has a quite different temperature dependence (Brooks et al. 1992, Mohn and Wohlfarth 1987). It is entirely equivalent to excluding on site effective 4f–4f interactions (or self-energies) as is done in model theories for the rare-earth metals.

Initial estimates of χ_{ii} were quite primitive, the calculated matrix elements of the single-electron Green function were restricted to being between 5d states in the approximation that all 5d orbitals, $\{m\}$, were shifted equally by the exchange split potential. The calculation of χ_{ii} was complex and necessarily restricted to a zone sampling of 75 k-points. Whereas $\chi^0_{5d} = 16$, $\chi_{ii} = 12$ states/(Ry atom), with the appropriate numbers in eq. (3.19) for Gd, $T_C = 172$ K with 5d–5d enhancement alone. With the enhancement from multiband Stoner theory, which includes the 5p–5p and 5p–5d contributions to $\chi(q = 0)$ but not in χ_{ii}, $T_C = 195$ K compared with a measured paramagnetic Curie temperature of 317 K. In both cases the considerable reduction of T_C is too large.

The Curie temperatures of the other metals scale with the de Gennes factor and the 4f–5d exchange interaction since eq. (3.19) does. The calculated Curie temperatures are, although too low, in improved agreement with experiment.

3.4. The actinide metals

The light actinide metals, Th–Pu, are part of a 5f transition series which may be regarded as the analogue of the 3d, 4d and 5d transition metal series. The heavy actinides, Am–Lr, form a second rare earth series in which the 5f electrons are localized and have little effect upon cohesive properties.

An overview of the electronic structure of the pure actinide metals is shown in fig. 3.3 (Skriver et al. 1978, Brooks et al. 1984). The 7s band in Fr takes the first electron, the 6d band in Ra through Th takes most of the next three electrons. Therefore in Th only the 7s and 6d bands are occupied. Th is a d band transition metal similar to Ti, Zr and Hf. However, the unoccupied 5f band is so close to the Fermi energy that it influences the occupied part of the band structure through hybridization, and this effect has proven to be important for details of the Fermi

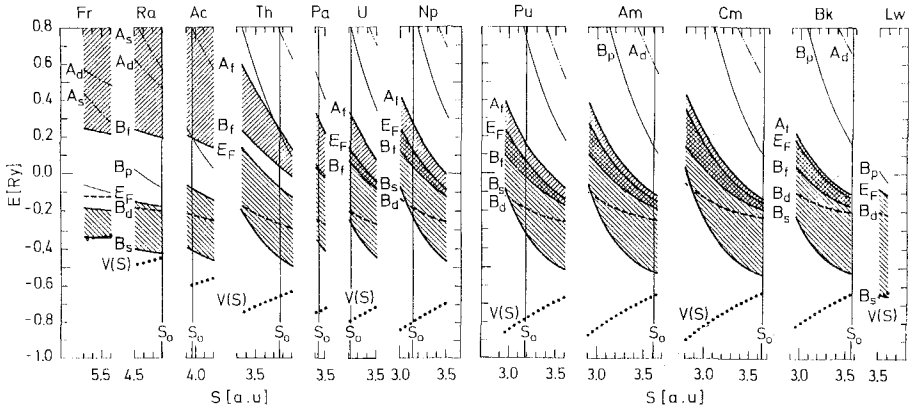

Fig. 3.3. The energy bands of Fr, Ra and the actinides calculated self-consistently as a function of atomic radius, S, by Skriver (after Brooks et al. 1984). The bottom and top of the relevant bands are B_l and A_l, respectively; S_0 is the measured atomic radius and $V(S)$ is the potential at the sphere boundary (not including the centrifugal potential, see figs. 2.1 and 2.4).

surface. In Pa the first real occupancy of itinerant 5f states occurs. From here on the 5f band gradually fills up.

The 5f bandwidth obtained from the canonical estimate $W_f = 45/\mu_f S^2$ where μ_f is the band mass is shown in fig. 3.4. For fixed atomic radius the bandwidth decreases with increasing atomic number. This occurs because each extra proton added to the nucleus makes the electronic orbitals contract owing to the increased nuclear potential and thereby lowers the amplitude, $R_l(S)$, of the partial wave at the sphere. Since $\mu_l =$

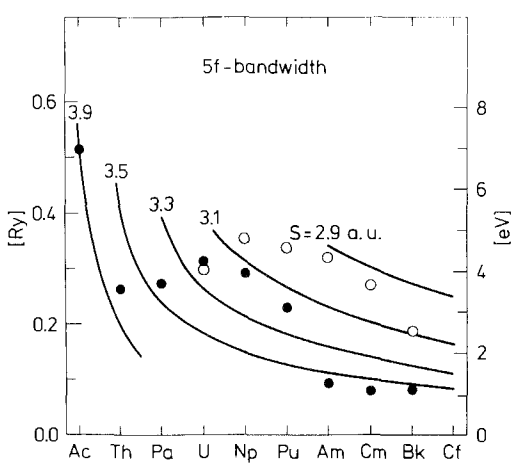

Fig. 3.4. The 5f bandwidth calculated as a function of both atomic number and radius by Skriver (after Brooks et al. 1984). The full and open circles indicate the 5f bandwidths at the measured and calculated atomic radii, respectively.

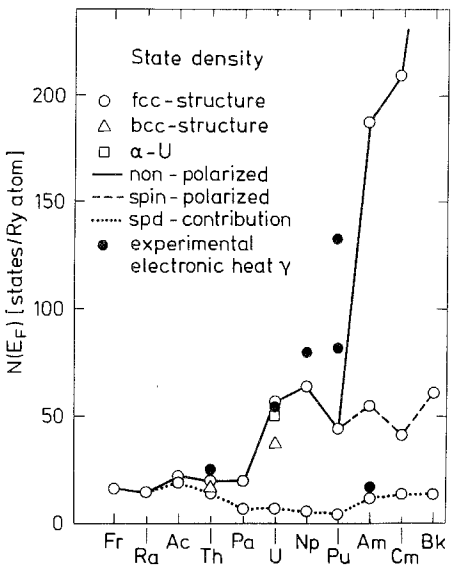

Fig. 3.5. The state density at the Fermi level calculated at the measured atomic radius by Skriver (after Brooks et al. 1984), compared to the measured electronic specific heat.

$2/S^3 R_l^2(C,S)$ the narrowing of the bands follows. This narrowing effect is most pronounced at the beginning of the series because later the extra electron added to the system enters the 5f shell and partially screens the nuclear charge seen by the other 5f electrons. A similar trend is found for the 6d and 7s states, which are located outside the 5f shell and therefore also see the nuclear charge partially screened. For fixed atomic number the bandwidth decreases with increasing atomic radius. This narrowing occurs because the overlap between orbitals centred at neighbouring atoms, and hence $R_l(C,S)$ decreases as the atoms are pulled apart.

The 5f bandwidths evaluated at the measured equilibrium atomic radius, fig. 3.4, are nearly constant from Th to Pu. The atomic radius adjusts itself so tht $R_l(C,S)$ remains almost independent of atomic number. The atomic volume follows the 5f orbitals indicating that the 5f electrons determine the volume of the early actinides. The calculated state densities at the Fermi energy have been collected and compared to observed electronic specific heat coefficients, γ, in fig. 3.5. One should bear in mind that most of the calculations assume an fcc structure, and therefore one cannot expect too detailed an agreement between theory and experiment. In the beginning of the series, i.e. for Fr–Th, the 5f contribution is rather unimportant and we find for instance that Th has an $N(E_F) = 20$ states/(Ry atom) which is typical for transition metals. In Pa the 5f contribution starts to dominate the state density and by Am $N(E_F)$ has increased one order of magnitude over the value for Th. The measured electronic specific heat coefficients show a similar trend up to, and including, Pu. However in Am it is down by one order of magnitude over the value for Pu, and is in fact close to the spd contribution to the state density. Hence, in this respect Am behaves like

a rare-earth metal. The interpretation of the above-mentioned observations is that the 5f electrons in Pa–Pu are metallic, hence the high electronic specific heat in the same sense that the 3d, 4d and 5d electrons in the ordinary transition series are metallic, and that this metallic 5f state turns into a localized state between Pu and Am, hence the low electronic specific heat, rendering Am and the later actinides into a second rare-earth series.

4. Magnetism of rare-earth compounds

The relative scarcity of first-principles theory of the magnetism of rare-earth compounds is due, as for the elemental metals, to the difficulty of handling the 4f electrons self-consistently within energy band theory. It is for this reason that most early studies have been for lutetium or yttrium compounds (Cyrot et al. 1979, Cyrot and Lavagna 1979, Yamada and Shimizu 1985, 1986, Yamada 1988, Schwarz and Mohn 1984, Szpunar and Wallace 1986, Szpunar 1985, Szpunar and Smith 1990, Coehoorn 1991, Jaswal 1990, Sellmyer et al. 1988). Studies of Y and Lu compounds do, in fact, simulate the conduction electron band structure of many rare-earth compounds well, and it is now also possible to include the effects of the 4f magnetism (Brooks et al. 1989) although earlier work seems to have suffered from convergence problems (Malik et al. 1977, Gu and Ching 1987).

4.1. Rare-earth–transition-metal intermetallics: a simple model of the electronic structure

A general picture of the electronic structure of Laves phase compounds between rare earth and late 3d transition metals, is best obtained from a simple approach. Firstly we consider a molecule, RFe_2, where R is a rare-earth element. For simplicity we choose R = Lu so that we can neglect the presence of the 4f electrons. For Lu we consider the 5d, 6s and 6p valence states and for Fe the 3d, 4s and 4p states. Since in the solid the s and p projected orbitals will form broad and rather featureless bands, these will be neglected for simplicity and we focus our attention on the 5d and 3d states. In the free atom the energy of the Fe 3d states lies far lower than that of the Lu 5d states, as shown schematically in fig. 4.1a. When we form the RFe_2 molecule the 5d and 3d states will hybridize, yielding then bonding–antibonding level scheme illustrated in fig. 4.1b. Thus in the molecule the bonding level will obviously be dominated by the 3d states, while the antibonding level has mainly 5d character. The degree of mixing between the 3d and 5d states depends on the overlap matrix element and on the energy separation between the 3d and 5d levels. If this energy separation is increased the mixing will decrease and the opposite holds when the separation is decreased.

The next step is to assemble the molecules to form the Laves phase crystal. In a simplified picture the bonding and antibonding molecular state will broaden into energy band states, as illustrated in fig. 4.2. There are now two sets of bands which will be referred to as bonding and antibonding in accordance with the molecular terminology used above. In reality there is generally no such clear separation in

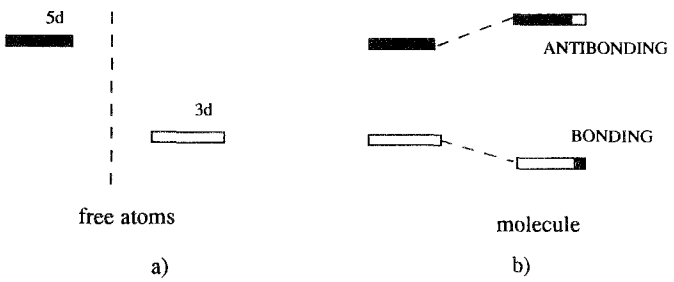

Fig. 4.1. (a) Schematic representation of the relative position between lutetium 5d and iron 3d atomic levels. (b) Bonding and antibonding levels for the $LuFe_2$ molecule. The amount of mixing between the original 3d and 5d states is illustrated by the black and white areas.

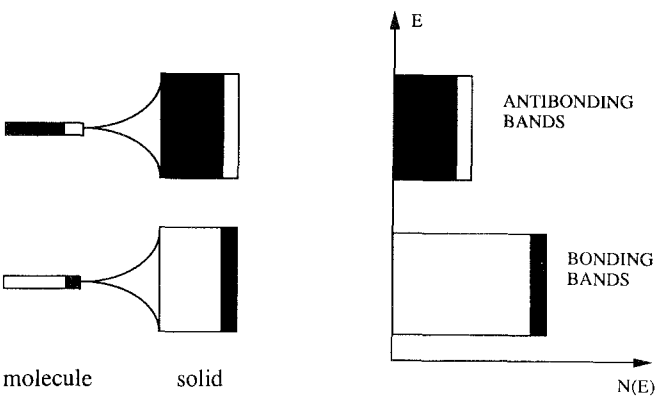

Fig. 4.2. Illustration of the broadening of the bonding and antibonding molecular levels into energy bands upon condensation of $LuFe_2$ molecules to a solid (left) and the associated density of states $N(E)$ (right). The amount of mixing between the 3d and 5d states is illustrated by the black and white areas.

energy between these two parts of the electronic structure, but it is used here for clarity. An associated state density is drawn schematically to the right in the same figure, where we have accounted for the fact that there are twice as many 3d states as 5d states in the RFe_2 compound. The main point here is that the bonding part, although dominated by the 3d states, contains a fair amount of 5d character and vice versa for the antibonding states which are dominated by the 5d states, but contain 3d character. Again if the 3d–5d energy separation is decreased (increased) the amount of mixing will increase (decrease).

It is common practice to discuss electronic structure in terms of the filling of the 3d bands in connection with compounds composed of early and late transition metals. However, as the simple approach above shows this must be understood as filling of the bonding part of the state density for the compound, and should therefore not necessarily be associated with a real transfer of electrons from the 5d states into the 3d states. Actual calculations show that there is hardly any change in the R and Fe

d-occupation numbers between the pure elements and the compounds. Rather, any charge transfer modifies rapidly the energy distance between the 3d and 5d bands, changing the mixing between them, untill self-consistency is achieved. It turns out that the d-occupation numbers obtained in this way differ little from those of the pure elements. In practice the separation into 3d and 5d partial state occupations is dependent upon the geometrical division of space into the R-atom and Fe-atom spheres, therefore the concept of electron transfer between the atoms is not completely well-defined.

The next step is to introduce the effects due to the 4f states. For most rare-earth compounds the 4f electrons retain their atomic character in the solid. Therefore the energy location of the 4f states relative to the 5d and 3d state energies is not important. In practice, it is only for some cerium compounds that 4f states need to be considered simultaneously with, and on the same footing as, the other valence states. If the 3d–5d hybridization happens to have the general shape sketched in fig. 4.2, then the energy position of the cerium 4f state is particularly important. If it is situated in the gap between the bonding and antibonding states, then this energy mismatch will lead to little hybridization between the 4f states and the 3d states, and the 4f electron occupying this 4f state is likely to be of a localized nature. On the other hand, if the 4f state is situated in an energy region with high 3d state density, then hybridization is important and may lead to delocalization of the 4f–3d hybridized states. Since it is not obvious from the outset how well separated the bonding–antibonding states will be, and since the energy position of the 4f states is not easily assessed, it becomes necessary to perform accurate electronic structure calculations before an appropriate level scheme can be given.

When the 4f electrons remain localized in the compound they will influence the magnetic properties of the valence electrons through the exchange potential. Since the 4f wave function has limited range this coupling will take place essentially within the rare-earth atom and mainly with the 5d electrons, which have a larger density and overlap with the 4f states than have the 5p or 5s states. The local exchange interactions are positive and the 4f and 5d spins will align parallel. The strength of the coupling will clearly be dependent upon the number of unpaired 4f spins. Therefore, a large 4f spin moment is likely to enhance the local 5d spin moments quite significantly. Since the 5d states in their turn are hybridized with the 3d states, this means that the 4f spin moments couple indirectly to the 3d spin moments. In a Heisenberg model Hamiltonian this coupling between the 4f and 3d electrons is often denoted by J_{RM} and is a technologically important material parameter for permanent magnets.

For a specific example we consider the RFe_2 systems, and for simplicity we first consider the case of a nonmagnetic $4f^{14}$, configuration, i.e. $LuFe_2$. We assume that the 3d electrons spin-polarize, and for simplicity we also assume that the magnetization is saturated. The energy level densities from fig. 4.2 are then modified as illustrated in fig. 4.3. This means that the energy separation between the bonding and antibonding subbands becomes different for the two spin directions, therefore the 3d–5d hybridization is different for the majority and minority spins. For the majority bonding band there is therefore now a decrease of its 5d content. This has the effect that the spin-up (majority) occupation of the 5d part becomes less than the spin-down (minority)

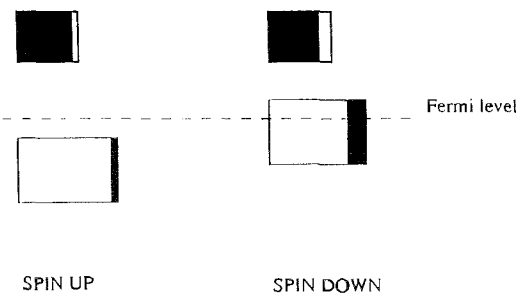

Fig. 4.3. Spin-up (majority) and spin-down (minority) densities of states for a saturated ferromagnetic state. Notice that the amount of hybridization between the 3d and 5d states becomes different for the two spin directions. This is illustrated by the black and white areas.

occupation of the 5d part. Thus there is a total spin-down 5d moment on the rare-earth atom. The 3d and 5d spin moments are in opposite directions, the system is a ferrimagnet rather than a ferromagnet.

For a standard rare-earth system, the localized $4f^n$ spin configuration will interact with the surrounding 5d electron spin cloud by means of local exchange–correlation and this will enhance the total 5d spin-down moment. Therefore the 5d spin-up band will become further pushed away from the majority bonding (3d) band, and the associated hybridization will be further decreased. This means that the local 3d spin-up moment will increase in size. However, since we started from a saturated magnetic state, the total conduction electron moment is fixed and only its distribution between the R and Fe atoms changes. Thus although the individual 5d and 3d moments both increase in size, there is for this situation an exact cancellation between the two 4f spin-induced changes of the local moments.

Thus the presence of the 4f spin moment induces a redistribution of the spin moment between the rare-earth and iron sites, while the total moment remains constant. This cancellation between the two 4f induced extra spin moments also occurs to a large extent for nonsaturated magnetism, and explains the successful interpretation of experimental magnetic moment data in terms of a constant conduction electron spin moment and an atomic $4f^n$ magnetic moment through a series of compounds.

$CeFe_2$ is entirely different and the standard rare-earth model is abandoned, the 4f states being included in the conduction bands since 4f–3d hybridization is important. The model system with a saturated magnetic moment, fig. 4.3, now has to be extended to include the 4f states. This is illustrated in fig. 4.4 and it is obvious that when the 4f states are treated as itinerant the total conduction electron moment for this saturated magnet has to decrease by one μ_B, simply as a consequence of the required band filling. In the same way as above for the 5d electrons, due to the difference in 3d–4f hybridization between the spin-up and spin-down states, there will be an induced 4f spin moment in the opposite direction to the 3d moment. Thus the active participation

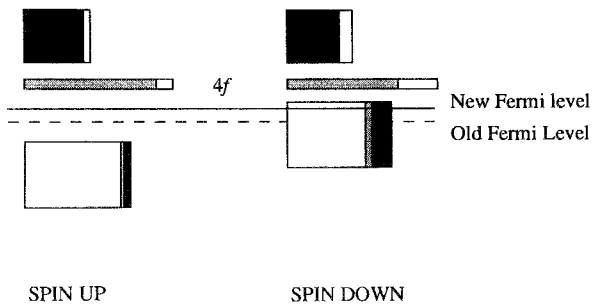

Fig. 4.4. Same as in fig. 4.3, expect that now also the 4f level is included. The amount of 3d–4f hybridization is illustrated by the dashed and white areas. The 'old Fermi level' refers to the case where the 4f level is regarded as part of the core, while the 'new Fermi level' is for the case of a strong 3d–4f hybridization and the 4f electrons are part of the valence electrons. (For clarity the 4f level has been placed in the hybridization gap. In the case of $CeFe_2$ the 4f (spin-down) resonance is in fact situated just above the Fermi level and overlaps in energy with the 3d states.)

of the 4f electron in the band formation means that the total magnetic moment will not be in accordance with the standard model value but will appear anomalous when compared with other homologeous rare-earth compounds. Since the number of Fe 3d electrons is practically constant, and since it is also clear from fig. 4.4 that the number of 3d spin-up electrons is reduced due to the 4f–3d hybridization, the Fe 3d moment becomes reduced. This reduction and the reduction of the total conduction electron spin moment are the most likely the reasons why the Curie temperature of many of the cerium intermetallic ferromagnets are anomalously low relative to the corresponding standard rare-earth systems.

For more complicated rare-earth–transition-metal intermetallic systems than the Laves phase compounds a very similar picture to the one above should apply. Even for the technologically important class of materials, $R_2Fe_{14}B$, the notion of the 3d–5d hybridization is an essential ingredient for the understanding of its behaviour. This is again the mechanism which governs the 4f–3d coupling, an important quantity for the magnetic anisotropy.

4.2. *$LuFe_2$*

Among the RFe_2 systems one expects $LuFe_2$ to have the simplest electronic structure because of the filled 4f shell. Furthermore, Givord et al. (1980) have published neutron diffraction data for this compound and attempted to resolve the magnetism into its atomic partial moments. However, they were unable to resolve a moment on the Lu site. Both Yamada and Shimizu (1986) and the authors (Brooks et al. 1989) calculate that there is a moment of about $-0.4\mu_B$ on lutetium of which $-0.3\mu_B$ is of partial 5d character. The calculated form factor suggests that the 5d contribution might easily be missed by experiment because the 5d form factor is too small at the scattering vectors used. On the other hand, on the basis of X-ray dichroism experiments (Baudelet et al. 1990) it has been claimed that there is a moment at the lutetium site and that

it is of opposite sign to the iron moment. The calculated partial d-occupation numbers for iron and lutetium were 6.6 and 1.5, respectively, i.e. close to the numbers for the pure metals. The energy distance between the centre of the 3d band and the centre of the 5d band was calculated to be 4.8 eV. This can be compared with the difference in the atomic ionization energy for a d electron which is about 5.4 eV larger for Fe than for Lu.

The Stoner product, $IN(E_F)$, was calculated to be 1.15, and the system is then unstable to ferromagnetism. Since the state density at the Fermi level is heavily dominated by the iron 3d states it is clear that the iron atoms cause the ferromagnetism. The calculated total moment of $2.85\mu_B$/f.u. compares with measured values of $2.85\mu_B$/f.u. (Givord et al. 1980) and $2.93\mu_B$/f.u. (Buschow 1977, 1979). Analysis of the neutron diffraction data yielded an Fe 3d spin moment of $1.67\mu_B$ and an orbital moment of $0.07\mu_B$ (Givord et al. 1980). The computed values (with spin–orbit coupling included) are $1.62\mu_B$ for the Fe 3d spin moment and $0.07\mu_B$ for the Fe 3d orbital moment (Brooks et al. 1989). It therefore seems clear that the local spin density approximation is able to describe the valence electron magnetism in a satisfactory way for this filled 4f shell cubic RFe_2 Laves phase system.

4.3. *RFe_2 (R = Gd–Yb) systems*

Due to the localized nature of the 4f electrons it is appropriate to isolate the treatment of the 4f states from the conduction electron states. However, it is essential to account for the coupling between the 4f and the conduction electron magnetism. The 4f spin density polarizes the conduction electron spin density through local exchange interactions, as we have described for the metals. Therefore, if the 4f spin density can be calculated accurately, the local spin density approximation could be used to compute self-consistently energy bands for all the valence electrons except the 4f electrons, and derive the spin densities in any rare-earth compound for which the local 4f spin moment is known.

The combination of localized 4f magnetism and itinerant magnetism of the spd band structure in heavy rare-earth–transition-metal intermetallics is handled by treating localized 4f states as outer core states, as in the elemental metals (section 3). This is done in order to fix the number of 4f electrons to an integer, as in the infinite U limit of the Hubbard model (Hubbard 1963). Again the number of spin-up and spin-down 4f electrons is an input to the calculation but, subject to this constraint, the 4f spin densities are calculated self-consistently. The 4f spin densities contribute to the total spin densities, and hence to the spin-up and spin-down potentials. In the absence of hybridization between the 4f states and the conduction band states, the interaction between the 4f electrons and the conduction electrons is electrostatic plus local exchange. The problem of how to fix the number of spin-up and spin-down 4f electrons is solved by using the Russel–Saunders coupling scheme for the $4f^n$ configuration, as described in section 2.3. For the elements Gd–Yb this results in a spin-up occupation of seven and a spin-down occupation which increases by one for each increase of the atomic number starting with zero for Gd.

In fig. 4.5 we show the obtained total conduction electron spin moment through

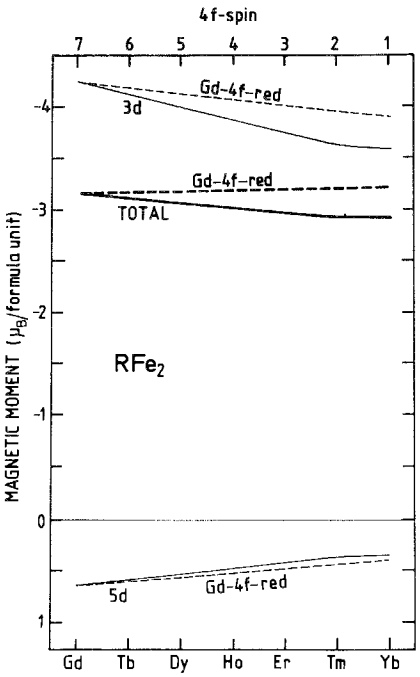

Fig. 4.5. The calculated conduction electron spin contribution to the moments of the RFe_2 series. The negative spin for the total and Fe 3d contribution was chosen because they are antiparallel to the R 4f moment and the total moment is therefore positive. The broken lines, labelled Gd-4f-red, are for the ideal system $GdFe_2$ with reduced 4f spin.

the series and its decomposition into a 3d and 5d contribution. As already shown by the simple model in section 4.1, these two d moments have opposite directions. The individual 5d and 3d moments depend much more strongly on the rare-earth element than does the total moment. The reason for this is the partial cancellation that occurs between the 4f induced conduction electron spin moments. This cancellation can be even better studied by means of calculations for $GdFe_2$, where, however, the magnitude of the 4f spin moment is allowed to vary from seven to zero. In such a calculation one finds for example that the number of 5d electrons is independent on the size of the 4f spin moment. In fig. 4.5 the dependence of the total, 3d and 5d spin moments on the 4f spin moment has been plotted. First we notice that the local 5d spin polarization increases when the 4f spin moment is increased. Also the 3d moment increases appreciably in size. Since these two are of opposite sign there is a strong cancellation effect, and, indeed, the total moment remains practically constant upon variation of the size of the 4f spin polarization. This is exactly the behaviour derived from the model in section 4.1 when the magnetism is saturated.

The calculated total moments are compared with experiment in fig. 4.6. Here we have added the rare-earth moment to the calculated conduction electron moment. Agreement with experiment is excellent except for $YbFe_2$. The data for $TbFe_2$–$TmFe_2$

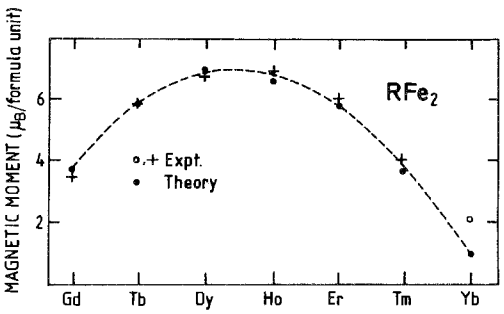

Fig. 4.6. Comparison between the measured and calculated total magnetic moments for the RFe_2 series.

are for single-crystal samples, while the result for $YbFe_2$ is for a less well-defined sample, which might explain the less satisfactory agreement for the latter compound. Due to the 3d–5d hybridization a significant spin density is produced at the R sites, even when the 4f moments are zero. This hybridization is believed to be responsible for the important coupling between the 4f and 3d spin directions. The essential point to realize is that in the local spin density approximation the R 4f and R 5d spins are coupled by local exchange interactions to give a parallel spin alignment. The interaction between the R 4f and Fe 3d spins is mediated by the R 5d spin and it aligns the 4f and 3d spins antiparallel.

4.4. Anomalous Ce intermetallic compounds

Compounds like $CeFe_2$ and $CeCo_5$ are anomalous in several respects (Eriksson et al. 1988a, Nordström et al. 1990). Firstly, their lattice constants are considerably smaller than would be expected for a standard localized $4f^1$ configuration. Secondly, their Curie temperatures are low in comparison with the other isostructural rare-earth compounds such as the corresponding lanthanide and praseodymium compounds. In addition, the magnetic moments deviate from the values one would expect for normal trivalent ions at the cerium sites. Self-consistent local density electronic structure calculations (Eriksson et al. 1988a) for the CeM_2 (M = Fe, Co and Ni) cubic Laves phase systems, where the 4f states were treated as a part of the conduction electron complex have shown that their peculiar lattice constant trends can be explained. There is a minimum in lattice constant for $CeCo_2$ – in contrast to the trivalent RM_2 systems where the lattice constant decreases monotonically from RFe_2 to RNi_2.

The theroy suggests that only $CeFe_2$ should to be a magnet, in agreement with experiment. For the spin-polarized calculation (Eriksson et al. 1988a) for $CeFe_2$ a total spin moment of $2.16\mu_B$/f.u. was obtained. We now compare this value with the above calculated total conduction electron moment for $GdFe_2$ of $3.15\mu_B$/f.u. (irrespective of whether the $4f^7$ configuration is treated as fully spin-polarized or unpolarized). Thus the conduction electron spin moment has decreased by $1\mu_B$/f.u. for $CeFe_2$ compared to $GdFe_2$. This is most interesting in view of the simple model presented in section 4.1. As we have already seen above, it is not unreasonable to assume that if 4f states were removed from the conduction states in $CeFe_2$ and placed in the core, the spd

ferromagnetism will be essentially saturated and the conduction electron moment will be about 3.1–3.2μ_B/f.u. as for $GdFe_2$. When the 4f electrons are itinerant a 4f electron is transferred from the core to the valence band states. Since the magnet is assumed to be saturated, this extra valence electron must enter the spin-down states, thus reducing the total moment by 1μ_B/f.u. This is also what was calculated self-consistently for $CeFe_2$.

Of course the real situation is not quite as simple as a fully saturated magnetic state would suggest, but the main reason for the decreased spin moment in $CeFe_2$ originates from the effect of one additional valence electron. Notice that this is not a valence transition from a trivalent state (where the 4f electron is in the core) to a tetravalent state in the traditional sense, although it is true that the number of cerium valence electrons is three when the 4f electron is in the core and four when the 4f electron is treated as one of the conduction electrons. The point is that in the first case the 4f state is treated as inert, and in the second case as part of the bonding complex built up from hybridizing s, p, d and f states, while in the conventional meaning of the tetravalent state one would have only s, p and d conduction states. Put in another way, it is not the 4f *occupation number* that changes, but the *nature* of the 4f state. This change from one behaviour to another for the 4f states can be looked upon as a Mott transition within the 4f configuration (Johansson 1974), i.e. on one side the 4f electron is localized (as for an insulator) and does not contribute to the bonding, while on the other it is itinerant (as for a metal) and actively engaged in the metallic bonding.

Addition of spin–orbit interaction to the band Hamiltonian (Eriksson et al. 1988a) produced a 3d orbital moment of about 0.08μ_B/Fe-atom, i.e. almost as for $LuFe_2$ (Brooks et al. 1989). The calculated orbital moment for the Ce 4f states was found to be 0.15μ_B/atom and addition of spin–orbit interaction changed the spin moments only slightly. The calculated total moment for $CeFe_2$ became 2.41μ_B/f.u. compared with the measured value of 2.3μ_B/f.u. (Hilscher 1982a).

Calculations (Nordström et al. 1990) for the ferromagnet $CeCo_5$ yielded similar results to those for $CeFe_2$, namely a 4f spin moment of opposite sign to the cobalt spin moment. $LaCo_5$ was used as a reference system and it was found that its cobalt moment is larger than for $CeCo_5$. This reduction for $CeCo_5$ is caused by the hybridization between the Ce 4f and the Co 3d states which induces a 4f spin moment antiparallel to the cobalt moment *and* reduces the cobalt moment (see below). Therefore the calculations give a total magnetic spin moment which is less for $CeCo_5$ than for $LaCo_5$. Such a moment reduction is actually observed experimentally (Buschow 1977, 1979) and is the opposite of what would be expected for a localized $4f^1$ cerium configuration in this compound. This is again evidence for a system with itinerant 4f states and the series of experiments suggested for $CeFe_2$ (Eriksson et al. 1988a) would also be of crucial importance in this case. It is also interesting to note that the Curie temperature (Buschow 1977, 1979) for $CeCo_5$ is anomalous since it is about 200 K less than would have been expected from a comparison with the other RCo_5 compounds. In the calculation without the spin–orbit interaction (scalar relativistic) the total spin moment for $LaCo_5$ was 6.6μ_B/f.u. and for $CeCo_5$ it was 5.7μ_B/f.u. As above for the RFe_2 systems, we assume for simplicity that the RCo_5 compounds

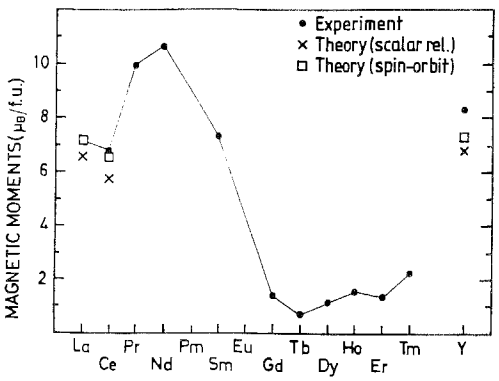

Fig. 4.7. Experimental (closed circles) and calculated magnetic moments (crosses and squares) per formula unit for the RCo_5 (R = La–Tm) series and YCo_5.

have an essentially saturated ferromagnetic moment. Again the extra electron in Ce (compared to La) must enter the spin-down band and therefore the spin moment should decrease by $1\mu_B$/f.u., which is nearly the case. In fig. 4.7 we compare the calculated moments with experiments (Alameda et al. 1981, Velge and Buschow 1968, Gupta et al. 1984) for $LaCo_5$, $CeCo_5$ and YCo_5. As can be seen the calculations reproduce well the observed difference in moments between $LaCo_5$ and $CeCo_5$.

4.5. Spin moments in $Nd_2Fe_{14}B$

Due to its extraordinary properties as a permanent magnet, $Nd_2Fe_{14}B$ has attracted an immense amount of scientific interest (Buschow 1988). Besides a large number of experimental investigations there have also been several theoretical attempts to describe different aspects of the basic properties which make this compound so attractive for technical applications. There have been theoretical studies of the crystallographic anisotropy (Radwanski and Franse 1989, Zhong and Ching 1987) the critical temperature (Mohn and Wohlfarth 1987) as well as its magnetic moments (Gu and Ching 1987, Szpunar and Szpunar 1985, Sellmyer et al. 1988, Jaswal 1990, Coehoorn 1991, Nordström et al. 1991, Hummler and Fähnle 1992).

A major problem theory has to deal with the fact that in this compound there is an interplay between the localized 4f magnetism and the itinerant magnetism basically originating from the transition-metal 3d electrons. A second problem is the large size of the unit cell, which consists of four formula units or 68 atoms. Inevitably this large number means that basic electronic structure calculations become exceedingly extensive. A prerequisite for an understanding of the different properties of the permanent magnet, $Nd_2Fe_{14}B$, is that the electronic structure and the ground-state magnetic density is known. Several electronic structure calculations have already been performed for this system (e.g., Gu and Ching 1987, Szpunar and Szpunar 1985, Jaswal 1990, Sellmyer et al. 1988, Coehoorn 1991). However, the 4f states may only be treated as part of the band structure for a half-filled shell at most, as was done by Coehoorn (1991) for $Gd_2Fe_{14}B$. When the 4f states are treated as part of the core

they should be spin-polarized, otherwise the band structure will not differ from that found for $Y_2Fe_{14}B$ by Coehoorn (1991). More recently both the 4f states of Nd and the 3d states of Fe have been spin-polarized (Nordström et al. 1991, Hummler and Fähnle 1992). When the neodymium 4f shell is spin-polarized by Russel–Saunders coupling the total moment of the unperturbed $4f^3$ shell of Nd is $3.27\mu_B$/atom. This consists of a projected orbital part of $5.72\mu_B$/atom and a projected spin contribution of $-2.45\mu_B$/atom. To implement this spin moment into density functional theory we populate the majority 4f spin with 2.72 electrons and the minority 4f spin with 0.28 electrons. Two different calculations were performed, one with a 4f spin moment in accordance with the just mentioned Russel–Saunders coupling (calc. I) and one without a 4f spin polarization (calc. II). This gives us the possibility of registering the influence of the spin moment on the six different iron sites (denoted by c, k1, k2, j1, j2 and e). For the two neodymium sites, f and g, the unpolarized 4f calculation gives a conduction electron moment of 0.36 and $0.35\mu_B$/atom, respectively, while in the spin-polarized 4f case we obtain 0.57 and $0.53\mu_B$/atom. Thus the size of the conduction electron rare-earth moment increases by about 50% due to the 4f spin moment.

In fig. 4.8 the results of calculations (Nordström et al. 1991) are compared with the experimental data (Givord et al. 1985) for the Fe sites from a spin-polarized neutron experiment. As can be seen the agreement is satisfactory. The largest iron moment is calculated to be situated on the j1 site, the second largest on the c site and the two smallest on the j1 and e sites, all in agreement with data. Also the theoretical finding that the moments are spread between 2.1 and $2.9\mu_B$/atom agrees with data. When we compare the unpolarized 4f calculation (calc. II) with the spin-polarized 4f calculation (calc. I) we notice that the inclusion of the 4f–3d coupling improves the agreement with experiment. By adding the Russel–Saunders total 4f moment for Nd to the calculated conduction electron moment a magnetic moment of $38.1\mu_B$/f.u. is obtained. The experimental value (Givord et al. 1984) at 4 K is $37.1\mu_B$/f.u. In $Nd_2Fe_{14}B$ there is however a spin reorientation at low temperatures, therefore the measured

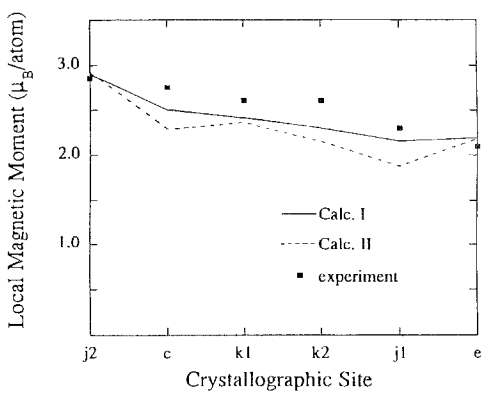

Fig. 4.8. The calculated local 3d spin moments for the crystallographically inequivalent iron sites for the two types of calculations together with experimental data from Givord et al. (1985).

moments may not be fully aligned (Givord et al. 1985). This could explain the slight overestimate of the total moment. In the second calculation, where the influence of the 4f spin on the conduction electrons is neglected, a total moment of $37.1\mu_B$/f.u. is obtained which happens to agree perfectly with the experimental value.

4.6. RCo_2 compounds

In studies of the influence of the 4f moments upon the conduction electron magnetism it is always useful to change only the 4f moment to isolate its effect. Calculations for $YbCo_2$–$GdCo_2$, in which the 4f moment on the Gd, μ_f^s, was changed from zero to seven and then back again to zero, revealed the metamagnetism already familiar from work on YCo_2, and evident in $Y(Fe_{1-x}Co_x)_2$ alloys (section 4.7). The resulting computed conduction electron moments are shown in fig. 4.9a. For μ_f^s increasing from zero to three (corresponding to Lu–Er) the moment induced on the Co is small but at $\mu_f^s = 4$ (Ho) the conduction electron moment jumps to $1.75\mu_B$/f.u. When μ_f^s is increased further to seven there is no change in the total conduction electron moment (which is saturated) but the 3d and 5d contributions, which are antiparallel, both increase. In $GdCo_2$ itself the computed 3d moment is $-1.25\mu_B$/Co, which for Co in the present compound is saturated. When μ_f^s is then reduced from seven to zero the saturated conduction electron moment remains stable.

The results of similar calculations for the real systems are shown in fig. 4.9b. Here the lattice constants change from compound to compound and the corresponding small changes in electronic structure make the isolation of the effect of changing R 4f moment impossible. Hence the small irregularities in the small induced moments for $YbCo_2$ to $DyCo_2$, but the low conduction electron moment states are stable when the calculations are started with only the R 4f spin nonzero. The transition to the high conduction electron moment state does not occur until $TbCo_2$, suggesting that volume effects play a role in determining the effective critical field in $HoCo_2$ and

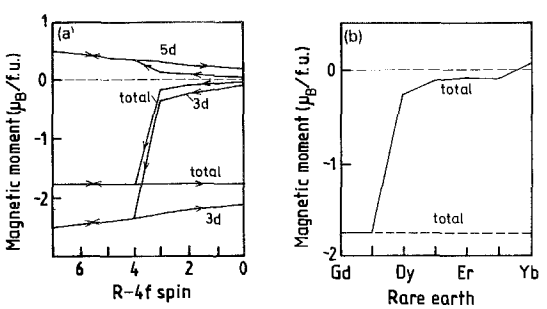

Fig. 4.9. (a) The calculated partial Co 3d, Gd 5d, and total conduction electron moments of $GdCo_2$ as a function of 4f spin moment. The arrows denote the direction in which the 4f spin is being changed. (b) The calculated total conduction electron moments of $GdCo_2$–$YbCo_2$. The conduction electron moments obtained when the self-consistent spin-polarized calculations were started with zero conduction electron moment but the correct 4f spin are indicated by the full line. The conduction electron moments when the calculations were started with a large spin density on the Co atom are indicated by the broken line.

$DyCo_2$. Once again, if the calculations are started with a high spin on the Co, the high spin state remains stable and we obtain another hysteresis curve.

The calculated total moments, obtained by adding the 4f total moments to the calculated conduction electron moments for the high moment states in fig. 4.9b, are shown in fig. 4.10 along with the range of measured values taken from the review article by Buschow (1980). Agreement with experiment is not particularly good but the trend in total moment with the maximum in the middle, which arises from the maximum in the R 4f moment, is obtained. Since the conduction electron moment in the low moment state is very small, the total moment for this ground state would lie close to the R 4f moment, which is in less good agreement with experiment. The computed conduction electron moment has the constant, and saturated, value of $-1.75\mu_B$, throughout. Both R 5d and M 3d moments increase as the 4f spin increases. But they are antiparallel and the changes nearly cancel leaving a total conduction band moment which is almost constant across the series – an effect which is due to 3d–5d hybridization (Brooks et al. 1989, 1991a).

The hysteresis in the conduction electron moments is essentially due to metamagnetism of the conduction bands in RCo_2 compounds (Wohlfarth and Rhodes 1962, Shimizu 1964, 1965, Yamada 1988). The total energy of a metamagnet as a function of energy is shown schematically in fig. 4.11 for several values of applied field. Curve 1 corresponds to YCo_2 in zero applied field and Schwarz and Mohn (1984) have estimated the critical field (curve 4) above which only the high moment state is locally stable. Upon removal of the field the high moment state remains locally stable, although it is not the ground state (curve 1).

In RCo_2 compounds the field arises from polarization of the 5d states by the 4f spin and subsequent hybridization with the 3d states. In $GdCo_2$ and $TbCo_2$ the high moment conduction electron state is obtained when the calculations are started with only a 4f moment, corresponding to curve 5. The large 4f spin-polarizes the 5d states enough to saturate, through hybridization with the 3d states, the Co moments.

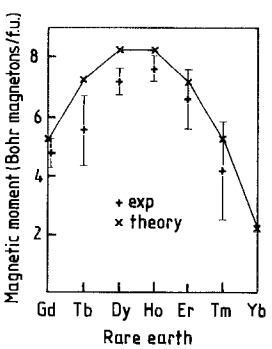

Fig. 4.10. The calculated total magnetic moments of $GdCo_2$–$YbCo_2$ compared with measurements. The vertical lines indicate the range of measured values of the moments from review articles by Buschow (1977, 1979).

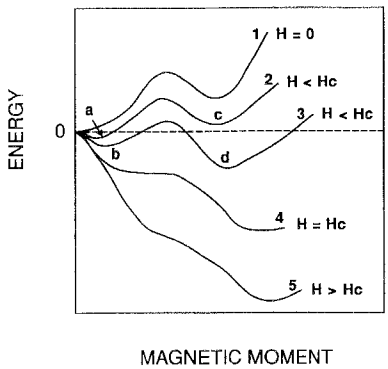

Fig. 4.11. Total energy curves for a metamagnet as a function of moment for several values of applied field (after Wohlfarth and Rhodes 1962). The parts of the curves indicated by a, b, c and d are locally stable states.

For the other compounds, the results correspond to either curve 2 or curve 3. When the calculations are started with zero moment on Co the low moment state corresponding to a or b is obtained. Hysteresis was obtained by re-starting the calculations with a large moment on the Co, moving to the local minimum at c or d. The effective field from the 4f states exceeds the critical field for metamagnetism only for $GdCo_2$ and $TbCo_2$.

The partial Co 3d state density for $YbCo_2$ in its paramagnetic state is shown in fig. 4.12. It is very similar to the state density of YCo_2 calculated by Yamada (1988). The Fermi level lies in a dip in the state density with a large double peak just below and a somewhat broader peak above. The criterion for the local stability of a metamagnetic state is given in terms of the high field unenhanced susceptibility

$$\frac{1}{\chi^0} = \frac{1}{4}\left[\frac{1}{N^+(E_F)} + \frac{1}{N^-(E_F)}\right] \tag{4.1}$$

by

$$\frac{I\chi^0}{2} \geqslant 1. \tag{4.2}$$

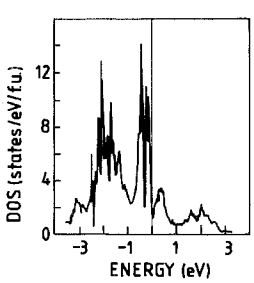

Fig. 4.12. The calculated partial Co 3d state density in $YbCo_2$.

At a finite splitting of the energy bands in fig. 4.12, both spin-up and spin-down state densities become large enough to satisfy this criterion. A similar situation occurs for $Y(Fe_{1-x}Co_x)_2$ alloys (section 4.7).

4.7. *$Y(Fe_{1-x}Co_x)_2$ alloys*

Yttrium, which is a 4d transition element, is – due to its similarity in number of valence electrons and chemical behaviour – often referred to as a member of the rare-earth series and forms Laves-phase compounds with Mn, Fe, Co and Ni. For compounds of yttrium with Mn, Fe and Co, no local 4f moments need be considered and the magnetism of the conduction bands may be studied in isolation. Of these systems YCo_2 (C15) is a strongly exchange enhanced paramagnet, YNi_2 (C15) is a weak paramagnet with a temperature independent susceptibility, YFe_2 (C15) orders ferromagnetically and YMn_2 (C15) is an antiferromagnetic at low temperatures. A metamagnetic transition with a critical field varying from 90, 100 to 350 T has been predicted (Cyrot et al. 1979, Schwarz and Mohn 1984, Yamada and Shimizu 1985) for YCo_2 and observed by Goto et al. (1990) and Sakakibara et al. (1990) at 60–80 T. The electronic structure and the magnetic moment of YFe_2 has also been calculated (Yamada et al. 1984, Mohn and Schwarz 1984) and agrees well with measurements (Buschow and van Stapele 1970). Evidently, yttrium compounds with Fe are magnetic whereas with Co they are nonmagnetic; therefore the pseudobinary alloys $Y(Fe_{1-x}Co_x)_2$ offer the possibility of studying the onset of magnetism as a function of concentration.

These alloys have been simulated in calculations (Eriksson et al. 1988d, 1989b) by constructing ordered compounds with the same stoichiometry intermediate between Y_2Fe_4 and Y_2Co_4. Thus the ternary compounds Y_2Fe_3Co, $Y_2Fe_2Co_2$, $Y_2Fe_3Co_3$ were studied. Although these compounds are not substitutionally disordered, as are the real alloys, they provide a reasonable system in which to study moment magnitude and formation as a function of Fe and Co concentrations. The calculated total moments (Eriksson et al. 1988d, 1989b) of the ordered compounds $Y(Fe_{1-x}Co_x)_2$ with

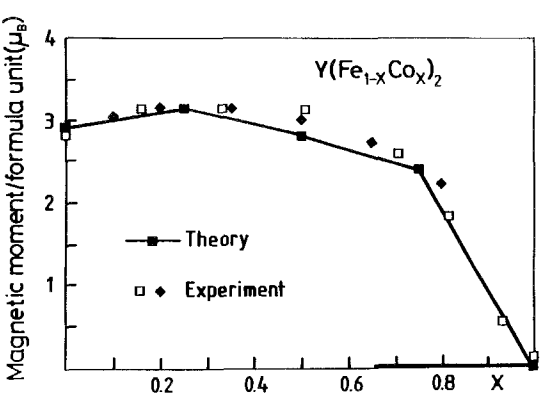

Fig. 4.13. The calculated and measured magnetic moments of $Y(Fe_{1-x}Co_x)_2$ alloys (after Eriksson et al. 1988d, 1989b).

$x = 0.0, 0.25, 0.5, 0.75, 1.0$ are compared with the measured moments of the real alloys (Hilscher 1982a,b) in fig. 4.13. At each end of the concentration range, the calculated paramagnetic state for $YCo_2$and the ferromagnetic moment of YFe_2 are in agreement with established theory and experiment (Yamada et al. 1984, Mohn and Schwarz 1984, Buschow and van Stapele 1970). The trend of the total magnetic moment, with a maximum at approximately 30% Co substitution, is also reproduced. The calculations reveal that the maximum in the total moment is due to a maximum in the Fe 3d moment, whereas the Y and Co moments remain more or less constant at $-0.4\mu_B$ and $1.3\mu_B$, respectively, as a function of concentration. The explanation for antiparallel alignment of the moment at the yttrium site has been given in section 4.1.

The band structure for the five ordered compounds is found to be very similar (fig. 4.14), with a band originating from 3d orbitals lying below the more broad yttrium 4d band. The separation between these two features is very small and consequently the hybridization between them is very strong. As iron is substituted with cobalt, valence electrons are added and the 3d band fills. However, the overall features of the paramagnetic state densities remains intact, suggesting that a rigid band model is a good approximation.

The origin of the magnetization curve (fig. 4.13) may easily be understood from the simple model state density shown in fig. 4.15. Since there are four transition-metal atoms in a primitive cell, each with ten 3d states, the lower square – the 3d derived state density – holds a total of 40 electrons, out of which approximately 3.2 are calculated to be yttrium 4d electrons. There is therefore room for 36.8 3d electrons per primative cell, or 18.4 3d electrons/f.u. in these bands – i.e. 9.2 3d electrons/f.u. in the spin-up bands. Since incomplete screening of the valence electrons causes the 3d orbitals to contract, the 3d moment increases with x in $Y(Fe_{1-x}Co_x)_2$, until the majority spin band is filled, where a maximum is followed by a decrease in the moment with x, since now the minority spin band has to be filled – a Slater–Pauling curve. Therefore the maximum in the 3d moments corresponds to 9.2 electrons in the majority spin band per formula unit. The 3d-occupation number per formula

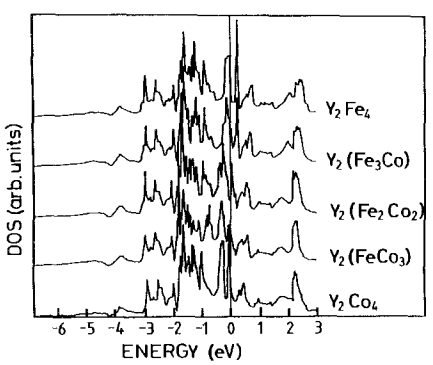

Fig. 4.14. The calculated state densities (DOS) of $Y_2(Fe_{1-x}Co_x)_2$ compounds with the Fermi energy at zero energy.

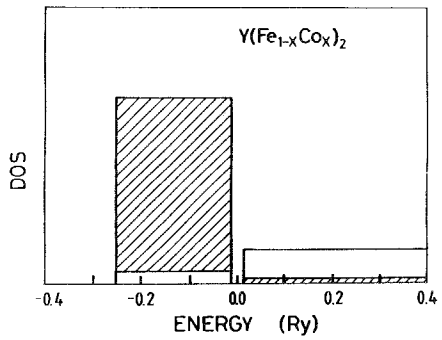

Fig. 4.15. The model state density corresponding to fig. 4.14 for $Y_2(Fe_{1-x}Co_x)_2$ alloys.

unit was found (Eriksson et al. 1988d, 1989b) to obey the linear relation $n_{3d} = 2[6.64(1-x)+7.74x]$ and, by applying a Stoner splitting to the bands, Eriksson et al. (1988d, 1989b) found that there are 9.2 electrons in the majority spin band per formula unit for x about 0.3.

The moment on Co is almost saturated with a majority band occupation of 4.5. The Fe moment is not quite $1\mu_B$ more than the Co moment and therefore not quite saturated at any Co concentration. Therefore, although the Co moments are *induced* by the Fe magnetism, the Co moment is more saturated, a circumstance which suggests that the induced magnetic state of Co in these alloys is the high spin metamagnetic state.

Moment formation via the Stoner criterion from the paramagnetic state in $Y(Fe_{1-x}Co_x)_2$, investigated by calculating the Stoner product as a function of concentration, suggested a critical concentration of 65% Co substitution compared with measured values of about 95% (Eriksson et al. 1989b) and the self-consistently calculated moments shown in fig. 4.13. The situation is familiar from the work of Mohn and Schwarz (1984) on YCo_2. With *locally* stable ferromagnetic and paramagnetic states the transition is first order as a function of concentration. Fixed spin moment calculations (Eriksson et al. 1989b) for Y_2FeCo_3 showed that there are indeed two energy minima with the high spin state having the lowest energy.

4.8. $GdFe_{12}$

The iron-rich ternary compounds $RFe_{12-x}M_x$ crystallize in the body-centred tetragonal $ThMn_{12}$ structure. The binary compounds RFe_{12} do not exist but they are stabilized by using small amounts of Ti, W, V, Cr or Mo instead of iron (de Mooij and Buschow 1988, Ohashi et al. 1988). Calculations have been made for $GdFe_{12}$ and the influence of the 4f moment upon the conduction electron moments studied by changing the 4f spin (Trygg et al. 1991). There are three Fe sites – (f), (i) and (j) – and one Gd site in the structure. The Fe moments at the (f) and (j) sites were not saturated when the 4f spin was zero and increase with the 4f spin. The Fe moment at the (i) site was saturated even for zero 4f spin and not susceptible to the 4f moment. The Fe moment at the (f) site was found to be smaller and more susceptible to 4f spin than the moment at the (j) site.

The saturated spin at the Fe(i) site is due to its low *close* coordination by other Fe atoms, which increases its local 3d state density. Although this might superficially appear to be the most highly coordinated Fe site (Coehoorn 1990, Li and Coey 1991) with 4(f), 5(i) and 8(j) neighbours it has, in fact, only one *close* Fe neighbour (at 2.41 Å), with the next four Fe atoms further away at more than the average Fe–Fe spacing. We recall (section 2.1, eq. (2.12) that the local state density is related to the inverse of the bandwidth which itself depends not only upon the coordination but also the *distance* of the neighbours. The bandwidths of d and f states are particularly sensitive to the near neighbour distances, depending upon the reciprocal of the distance to the power of $2l+1$, The local state density is therefore essentially determined by nearest-neighbour distances unless the next-nearest neighbours are also very close. In addition the (i) site has only one Gd site nearby, compared with two for the (f) and (j) sites, making it less susceptible to the induced spin density on the Gd site.

The Fe(j) site has four Fe neighbours at intermediate distance. The Fe(f) site has the highest coordination of *close* Fe atoms and the correspondingly smallest moment as its local 3d state density is reduced. It has four neighbours at the same distance as the (j) site but two additional Fe close neighbours (at 2.38 Å).

As in the RFe_2 compounds, the moments at the Gd and Fe sites were polarized anti-parallel. When the 4f spin was zero a total conduction electron moment of $24.62\mu_B$ was calculated whereas for a 4f spin of 7/2 the total conduction electron moment was $24.61\mu_B$. Thus an increase in the 4f spin increased the moments on both types of atom, leaving the total magnetic moment about constant.

4.9. The interatomic exchange interactions

3d–5d hybridization not only produces significant 5d spin density at the R sites but is also responsible for the crucial coupling between the R and M moments. The essential point to realise is that the R 4f and R 5d spins are coupled by local exchange interactions (which are always ferromagnetic) and that the interaction between R 4f and M 3d spins is mediated entirely by the R 5d spin. The exchange energy between 4f and 5d states may be written in the form

$$E_{4f5d} = -J_{4f5d}\bar{S}_{4f}\bar{S}_{5d}, \tag{4.3}$$

where $\bar{S}$ denotes the average spin and the exchange integrals are given by eq. (3.13), and the interpolation formula following that equation, and therefore depend upon the 4f–5d overlap densities. The exchange integrals decrease across the series due to lanthanide contraction. This may be seen clearly from fig. 3.1 where the 4f and 5d densities are plotted. The f–d overlap decreases when the f density contracts. Neutron scattering experiments on the RFe_2 series have resolved the low lying spin wave modes and the generic form of the spectra is shown in fig. 4.16. The lowest mode (labelled 1) at zero wave vector is the uniform mode and the highest (labelled 3) the exchange resonance mode of a ferrimagnet. The mode of interest here is the dispersionless mode (labelled 2) which corresponds to the precession of the R 4f moments in the molecular field due to the M-moments. The molecular field is therefore about 10 meV. A connection between eq. (4.3) and experiment is established through this

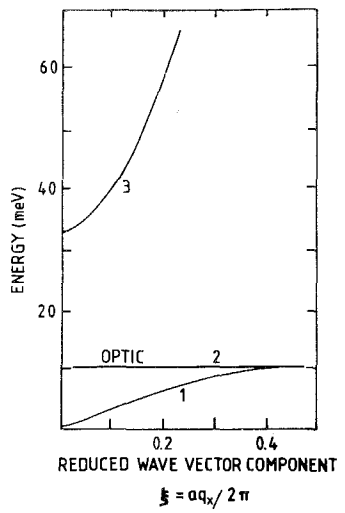

Fig. 4.16. Generic form of the spin wave spectra of the RFe_2 compounds (R = Gd–Yb). After Koon and Rhyne (1980).

spin wave gap. Equation (4.3) may be re-written in terms of the total 4f angular momentum via the Wigner–Eckart theorem, section 2.3.

$$E_{4f5d} = -2(g_J - 1)J_{4f5d}\bar{J}_{4f}\bar{S}_{5d}, \tag{4.4}$$

and, since the selection rule for spin waves is $\Delta J = \pm 1$, the change in energy is the

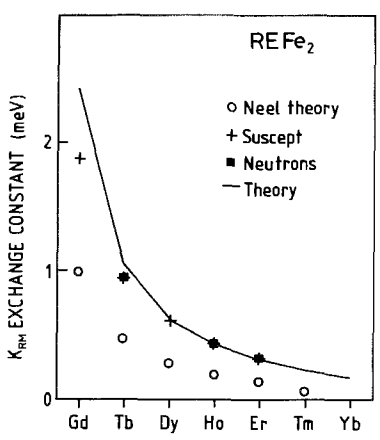

Fig. 4.17. A comparison of the calculated and measured interatomic exchange interactions. Of the measured data: + are obtained from perpendicular susceptibility measurements (Liu et al. 1991); * are obtained from analysis of neutron scattering data (Koon and Rhyne 1980, Nicklow et al. 1976); ○ are obtained from analysis of the Curie temperature (Beloritzky et al. 1988).

gap – given by

$$\Delta = 2(g_J - 1)J_{4f5d}\bar{S}_{5d}. \tag{4.5}$$

All the quantities in eq. (4.5) have been computed. The 5d moments may be read from fig. 4.5, and the exchange integrals are given by the interpolation formula $94 - 3.4(x-1)$ meV, where $x = 1$ for Gd, 2 for Tb, etc. The results are compared with experiment in fig. 4.17. The experimental results were deduced (Nicklow et al. 1976, Koon and Rhyne 1980) by fitting to neutron measurements and the results of high field susceptibility measurements (Liu et al. 1991). A considerable amount of work has also been done on a Néel theory in an attempt to deduce the intersite molecular fields from the systematics of the Curie temperatures (Belorizky et al. 1988). The values of the decrease in exchange interaction is due to both a decrease in the bare exchange integrals – caused by lanthanide contraction – and the decrease in 5d spin across the series, which itself is caused by the decrease in 4f moment. Although the parameters in eq. (4.5) appear to be properties of the R atoms, in fact the R 5d density arises from hybridization with the M 3d states and this is the origin of the interatomic interactions.

4.10. Curie temperatures

The exchange enhanced paramagnetism of the Co 3d bands in RCo_2 compounds was first investigated by Bloch and Lemaire (1970) and Gignoux et al. (1983). Other studies (Bloch et al. 1975, Cyrot et al. 1979) attempted to explain the trend in Curie temperatures across the heavy rare-earth series and the first-order magnetic transitions observed for $ErCo_2$, $HoCo_2$ and $DyCo_2$, and the second-order magnetic transitions observed for $TbCo_2$ and $GdCo_2$, in terms of a molecular field theory in which the 3d band susceptibility is enhanced by the field from the localized 4f moment.

In the simplest possible mean field theory, the Curie temperatures are given by (e.g., Bloch et al. 1975)

$$kT_c = \chi_d \frac{J_{4f5d}^2 (g_J - 1)^2 J(J+1)}{3}, \tag{4.6}$$

where χ_d is the d band susceptibility – equal to the partial d band state density at the Fermi level and which we calculate to be about 10 states/(Ry atom) in $GdFe_2$ and fairly constant across the series. The Curie temperature of $GdCo_2$ turns out to be 413 K compared with the measured value (Bloch and Lemaire 1970) of 395 K. We estimate from eq. (4.6) the remaining Curie temperatures to be Tb – 255 (229), Dy–159 (150), Ho – 94 (100), Er – 49 (60), Tm – 21 and Yb – 5, all in K with the measured values (Bloch and Lemaire 1970) in parentheses. The magnetic transition is actually first order in $ErCo_2$ to $DyCo_2$ (Bloch and Lemaire 1970, Bloch et al. 1975) and second order in $TbCo_2$ and $GdCo_2$.

5. Magnetism in actinide compounds

Magnetism in actinide compounds is characterized by two unusual features. The first is the presence of correlations associated with very narrow bands and the second is

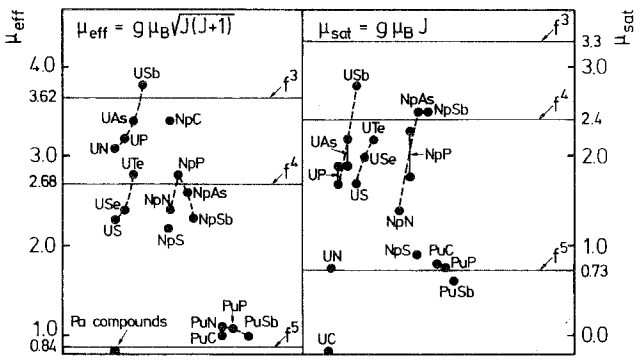

Fig. 5.1. The effective (left-hand side) and saturated (right-hand side) moments of actinides NaCl-type compounds. The Russel–Saunders values for f^3, f^4 and f^5 configurations are shown for comparison.

the effect of relatively large spin–orbit interaction for the 5f electrons. An overview of the measured moments of some NaCl-type compounds is given in fig. 5.1, with the 5f moments calculated using Russel–Saunders coupling shown for comparison. Clearly, the moments of the actinide compounds are much affected by their environment. Some of the moments were plotted against lattice constant in fig. 1.3. Although not perfect, there is a correlation between lattice constant and magnitude of the moment which suggests that the moments are forming from bands – the narrower the band, the higher the state density at the Fermi energy and corresponding moment – although there may be other explanations.

The bandwidths and spin–orbit splitting for the transition metals, rare earths and actinides were plotted in fig. 2.7. The perspective provided by fig. 2.7 is intended to make it clear that, in contrast to the theory for the transition metals, spin–orbit interaction plays a first-order role in the theory of magnetism and moment formation in the actinides. In the following we first examine conventional Stoner theory and spin-polarized energy band theory and their modification by relativistic effects.

5.1. Moment formation in actinide compounds

Studies of the linear response to an applied magnetic field in LSDA have produced a general expression for the magnetic susceptibility (Vosko et al. 1975, Vosko and Perdew 1975) which, under reasonable simplifying assumptions, reduce to

$$\frac{1}{\chi} = \frac{1}{\chi^0} - \frac{I}{2}, \tag{5.1}$$

where χ^0 is the unenhanced (or band) susceptibility which is equal to $N(E_F)$, the *total* state density at the Fermi energy per primitive cell. The LSDA effective exchange integral – or Stoner parameter – in eq. (5.1) is

$$I = \sum_{qll'} \frac{N_{ql}(E_F)}{N(E_F)} J_{qll'}(E_F) \frac{N_{ql'}(E_F)}{N(E_F)} \tag{5.2}$$

in terms of intra-atomic *energy-dependent* exchange integrals (eq. (3.13)). Here q labels

the atom and $N_{ql}(E_F)$ is the site and angular momentum resolved partial state density. The exchange integrals are energy dependent because energy band wave functions are continuous functions of energy, unlike the discrete solutions for bound electrons in free atoms (section 2.3). Since the exchange integrals are energy dependent, they vary from compound to compound, depending upon whereabouts in the energy bands the Fermi energy lies, but for uranium in NaCl compounds typical values for J_{ff} are 0.5eV, for J_{fd} about 0.35 eV, and for J_{dd} about 0.6 eV.

The major approximation entering eq. (5.2), apart from LSDA itself, is that the response at each site is the same as the response to a *uniform applied field* in the paramagnetic state (Janak 1977). The effect of hybridization between components of the compound upon the induced moment is therefore not fully included. The static ferromagnetic spin susceptibility diverges when the product of the Stoner parameter times the state density *per spin* at the Fermi energy is equal to one. The Stoner criterion indicates whether or not a ferromagnetically ordered ground state is stable for a pure spin system. The Stoner criterion is a sufficient, but not necessary, condition for the existence of ferromagnetism. It is possible for a finite moment to be stable but for an infinitesimal moment to be unstable. In such a case there is no substitute for a fully self-consistent spin-polarized energy band calculation. Another type of exception is much more important in the present context. In itinerant systems in which the spin–orbit splitting is large compared with the relevant bandwidth the pure spin Stoner criterion is unlikely to be accurate since the z-component of spin is not conserved. Nevertheless, the prediction of moment formation in actinide compounds is one of the main tasks of LSDA for which it has not been without success.

5.1.1. NaCl-type compounds

In uranium monochalcogenides and pnictides the uranium state densities at the Fermi energy dominate, and the partial 5f state density is far larger than the partial 6d state density. The 5f spin drives moment formation and it is sufficient to evaluate the 5f contribution to I in eq. (5.2). Then a typical value of I for a uranium pnictide or chalcogenide is about 0.5 eV or 0.04 Ry. Consequently, for the uranium monochalcogenides and monopnictides, a density of states per spin at the Fermi energy of $1/I = 25/(\text{Ry f.u.})$ is a sufficient condition for the formation of a spontaneous ferromagnetic spin moment. UC does not order. The calculated density of states per spin at the Fermi energy is 15/(Ry f.u.) and the effective Stoner parameter is found to be slightly lower (0.46 eV) than the average for UX compounds. The product IN is only 0.52 and a moderately enhanced paramagnetic susceptibility should be observed. Self-consistent energy band calculations (Brooks 1984) indicate that it should be a Pauli paramagnet. The Fermi surface (Auluck and Brooks unpublished), which is similar to that of ThC (Hasegawa and Yamagami 1990), consists of two hole ellipsoids centred at X and an electron sheet centred at W (fig. 5.2). The calculated extremal areas and masses on the three sheets are in reasonable agreement with dHvA experiments (Onuki et al. 1990a, b), indicating the presence of 5f states at the Fermi energy.

Of the UX compounds, UN has the next lowest product $IN = 1.8$ and would be ferromgnetic if it were not anti-ferromagnetic. Thus the Stoner criterion correctly yields the onset of magnetism in UX compounds, the boundary being between UC

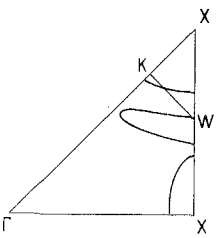

Fig. 5.2. The calculated Fermi surface of uranium carbide.

and UN. The Stoner criterion is fulfilled for all of the other monochalcogenides and pnictides.

5.1.2. The UM_2 series with $M = Mn, Fe, Co, Ni$

Moment formation in the series UM_2, where M = Mn, Fe, Co, Ni has also been studied in some detail (Eriksson et al. 1988c, 1989b) with a cubic Laves phase used throughout. The calculated partial 5f state densities of these compounds are shown in fig. 5.3. UFe_2 fulfils the Stoner criterion whereas UCo_2 does not, in apparent agreement with measurements although $IN(E_F)$ is calculated to be 0.86 for UCo_2 leading to a very strong enhancement of the paramagnetic susceptibility which has not been observed. UNi_2 does not fulfil the Stoner criterion whereas it is actually magnetic. However the actual crystal structure of UNi_2 is hexagonal and in self-consistent spin-polarized calculations (Severin et al. 1991) a finite moment is found

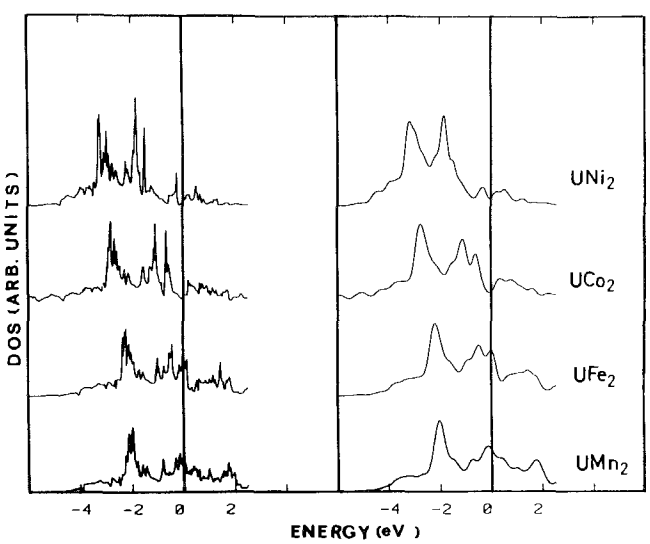

Fig. 5.3. The calculated partial 5f state densities of UMn_2–UNi_2 (left-hand side) and the same state densities (right-hand side) Gaussian broadened (0.3 eV) for comparison with photoemission experiments. The Fermi energy is at zero energy.

to be stable. The calculated Stoner product for UMn_2 was 1.04 whereas it is a strongly enhanced Pauli paramagnet. Actually this compound undergoes a large orthorhombic distortion at 235 K, which may have something to do with the descrepancy but the latter could equally be due to the approximations leading to eq. (5.2).

5.1.3. The $AnIr_2$ series

The $AnIr_2$ (An = Th–Cm) series is also isostructural in the cubic Laves phase (C15) and $NpIr_2$ is the first compound to order magnetically becoming antiferromagnetic at 5.8–7.5 K (Eriksson et al. 1989d), $ThIr_2$ is a superconductor below 6.5 K and UIr_2 is an almost temperature independent paramagnet with a specific heat coefficient of 62 mJ/(mol K^2), and is probably a spin fluctuation compound (Sechovsky and Havela 1988). The calculated (Eriksson et al. 1989d) Stoner products were 0.15 and 0.22 for $ThIr_2$ and $PaIr_2$, respectively, but 0.89 for UIr_2 in agreement with the suggestion (Sechovsky and Havela 1988) that it is a spin fluctuation material. The calculated Stoner products for the other compounds are greater than one.

5.1.4. The UMAl series with M = Fe, Co, Ni, Ru, Rh, Ir, Pt

The compounds UMAl (M = Fe, Co, Ni, Ru, Rh, Ir, Pt) crystallize in the hexagonal ZrNiAl structure, a modified form of the Fe_2P type. Measurements suggest that the 5f electrons in these compounds are itinerant (Sechovsky and Havela 1988). The available data is well documented (Sechovsky and Havela 1988) with UFeAl and URuAl paramagnetic, UCoAl metamagnetic (Eriksson et al. 1989e, Wulff et al. 1990), UNiAl is antiferromagnetic, and the remaining three are ferromagnetic (Sechovsky and Havela 1988). Extremely large anisotropy in the magnetic susceptibility of these compounds has been reported (Sechovsky and Havela 1988). The structure is shown in fig. 5.4. The uranium atoms lie in layers in the x–y plane, with a spacing of 3.5–3.6 Å, much less than the z–z separation of 4 Å. Evidently the uranium atoms find themselves in a highly anisotropic environment to which the 5f states are likely to be particularly sensitive. The transition-metal atoms are quite isolated from one another and one

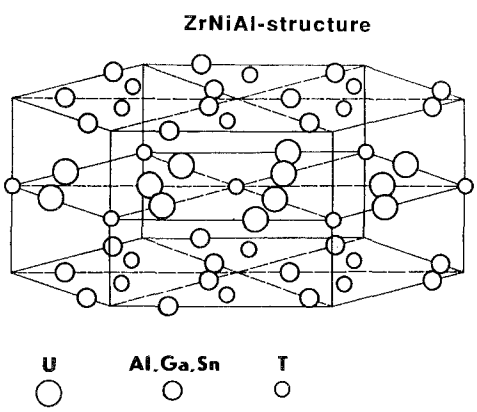

Fig. 5.4. The ZrNiAl structure.

would therefore expect the transition-metal (M) d bands to be narrow. Finally, in the energy range of the conduction bands, the aluminium states are almost entirely of s–p character and, to a first approximation, the aluminium atoms should act as spacers in this series.

There are 17 valence electrons in a formula unit of UFeAl, and it has been calculated (Gasche et al. 1991a, 1991b) that there are 5.3 electrons in the broad s–p conduction bands, leaving 11.7 in the d and 5f bands. When hybridization is introduced it has three main effects: it broadens the bands, pushes them apart and mixes the character. The further apart the bands are, the weaker the hybridization between them is. What was originally the pure Fe 3d band is pushed below, and the uranium 5f band above, the Fermi energy. Therefore the Fermi energy sits in a hybridization gap as may be seen from the calculated state densities shown in fig. 5.5. Into the Fe 3d-derived bands are now admixed states with 6.5 Fe 3d, 2.7 U 5f, and 0.8 s–p character. Similarly the U 5f-derived bands now contain an admixture of 3.5 Fe 3d states. This mixing allows the 3d-derived bands to sink below the Fermi energy whilst containing only 6.5 3d

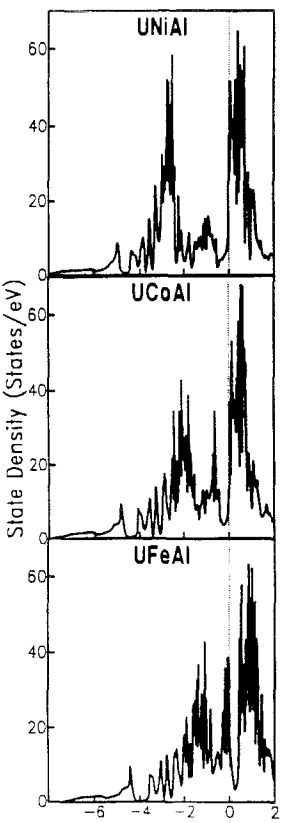

Fig. 5.5. The state densities of UMAl (M = Fe, Co, Ni). The Fermi energy is at zero.

electrons and the uranium 5f-derived band to rise above the Fermi energy whilst maintaining a 5f occupancy of 2.7.

UCoAl has one more electron than UFeAl. The 3d-derived bands then contain 7.5 electrons of 3d character and the Fermi energy rises into the tail of the 5f-derived bands. UNiAl has one more electron and the Fermi level lies in the 5f-derived bands. As the Fermi energy rises into the 5f-derived bands the state density at the Fermi energy increases and the Stoner criterion is eventually fulfilled. Although the model that we have used is necessarily approximate it correctly explains why UFeAl and UCoAl are paramagnets and UNiAl is magnetic. The calculated Stoner products are (Gasche et al. 1991a, 1991b):

UFeAl – 0.57; UCoAl – 0.81; UNiAl – 2.52; URuAl – 0.35; URhAl – 1.23; UIrAl – 1.46; UPtAl – 2.94.

It is interesting to note that the electron occupation numbers conform to the elemental values of 6.5 for Fe, 7.5 for Co, 8.5 for Ni and 2.6–2.7 for uranium in all of these compounds, despite the great variation in 5f-derived band occupation. The same model explains the transition to ferromagnetism between URuAl and URhAl, and the increase in moment between UIrAl and UPtAl. Finally we postulate that UMnAl, if it existed in this structure, would be magnetic with the moment on the Mn site.

5.1.5. The $AnRh_3$ series

The $AnRh_3$ (An = Th–Cm) series crystallizes in the $CuAu_3$ structure and the trend in the volume across the series is similar to that of the elemental metals as far as URh_3 but climbs for the Np and Pu compounds. There is a volume discontinuity between Pu and Am which is only 4.4 $Å^3$ compared with 8 $Å^3$ for the elemental metals. $ThRh_3$ and URh_3 are temperature independent paramagnets, $NpRh_3$ is highly enhanced with a specific heat coefficient of 95 mJ/(mol K^2) compared with 10 for the Th and U compounds, and $PuRh_3$ is an antiferromagnet (Brodsky 1978). The calculated values (Johansson et al. 1986, Eriksson et al. 1989a) for $IN(E_F)$ are less than one for $ThRh_3$–URh_3, in agreement with measurements, and greater than one for the other compounds – therefore erroneous for $NpRh_3$. The anomaly is actually corrected by the relativistic corrections to the Stoner criterion below.

The nature of the 5f electron states in URh_3 and UPd_3 has been explored in dHvA experiments (Arko et al. 1985, Ubachs et al. 1986). In URh_3, a Fermi velocity smaller than the Fermi velocity of Nb indicated significant 5f character in the conduction states. The measured Fermi velocities – only slightly lower than in d transition metals – and the agreement between the results of energy band calculations and experiment (Arko et al. 1975, 1985) for the Fermi surface geometries – suggest that the 5f electrons are itinerant. Furthermore, URh_3 has a temperature independent magnetic susceptibility (Nellis et al. 1981), a monotonically decreasing resistence as a function of temperature (Crabtree 1985) with no features indicative of Kondo or crystal field effects, and a photoemission spectrum with 5f state density at the Fermi energy (Arko et al. 1987). In UPd_3, in contrast, there are two types of orbit (Ubachs et al. 1986) with effective masses of 0.8 and 2.0. These small values of the electron mass, and the low measured value of the linear specific heat coefficient (Andres et al. 1978) are consistent

with a negligible contribution of 5f state density at the Fermi energy. A crystal field excitation consistent with an f^2 ground state has been observed in neutron scattering experiments (Buyers and Holden 1985) and 5f spectral density in photoemission (Baer et al. 1980, Reihl et al. 1982b) and resonant photoemission (Arko et al. 1987) experiments is centred about 1 eV below the Fermi energy.

5.1.6. Pseudobinary alloys $URh_{3-3y}Pd_{3y}$

The contrasting electronic structures of UPd_3 and URh_3 make the study of $URh_{3-y}Pd_y$ random alloys especially interesting. Photoemission experiments (Arko et al. 1987) on $URh_{2.0}Pd_{1.0}$ show a 5f peak at the Fermi energy which is narrow but similar to the URh_3 spectra. For $URh_{1.0}Pd_{2.0}$ the experimental partial 5f spectrum is much wider than that in $URh_{2.0}Pd_{1.0}$. However by subtracting these two spectra (with appropriate weighting factors) one obtains a spectrum that very much resembles that of UPd_3. This suggests that there are two distinct types of 5f response in $URh_{1.0}Pd_{2.0}$. For increasing values of y, we do in fact expect gradual 5f band narrowing since 5f–4d hybridization decreases. The linear specific heat coefficient (Ubachs et al. 1986, Dunlap et al. 1987), increases and when y approaches 2.01, reaches a heavy fermion value of 220 mJ/(mol K^2). With a further increase of y the 5f electrons finally become fully localized.

The pseudobinary alloys under study crystallize in the cubic Cu_3Au structure for y smaller than 2.7, and in the hexagonal $TiNi_3$ structure when y is greater than 2.79. Calculations (Eriksson et al. 1988d) were made at the same molecular volume but for the Cu_3Au structure.

Theoretical studies were made for the compounds $URhPd_2$ and URh_2Pd, with one Pd and two Rh atoms occupying the three Cu sites in the $CuAu_3$ primitive cell for URh_2Pd, and the reverse for $URhPd_2$ (Eriksson et al. 1988d). The calculated state densities are plotted in fig. 5.6. The main features of the density of states for URh_3 can be described by a 'bonding' 4d band (marked by A) separated by approximately 6 eV from an 'antibonding' 6d band (marked by B). The 5f states are located at the top of the 'bonding' 4d states and hybridize strongly with them. This hybridization is crucial for the 5f bandwidth – an estimate of the unhybridized 5f bandwidth in URh_3 is only 0.3 eV, which is much narrower than the calculated fully hybridized 5f bandwidth of about 3 eV. As the Pd concentration increases the 'bonding' d states move down in energy decreasing their overlap with the 5f levels. This causes a reduction of 5f–4d hybridization and 5f bandwidth. In the UPd_3 system the 5f states are situated in the gap between the 'bonding' and the 'antibonding' d states. Consequently the 5f bandwidth is far narrower than in URh_3, strongly increasing the tendency of the 5f electrons to localize.

Since there is an unusually strong ligand effect on the 5f bandwidth in these systems, and narrowing and movement of the partial 5f relative to 4d state densities, a rigid band model should not be used over a large concentration range. It is the nearest-neighbour environment of the uranium atom which determines the nature of the 5f states, which is consistent with the fact that for all these systems the U–U distances are considerably larger than the Hill limit. The largest contributions to the 5f bandwidths are from the f–d and f–f hybridization, with f–d hybridization dominant for

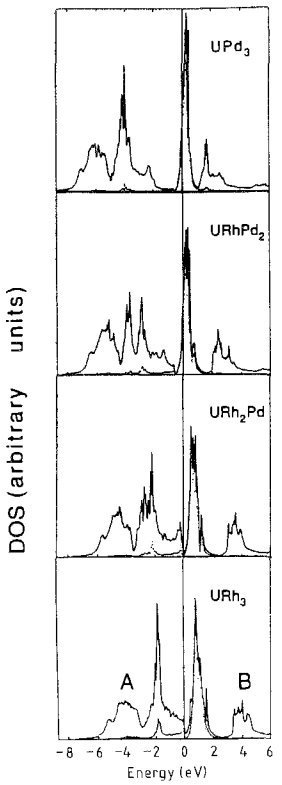

Fig. 5.6. The calculated densities of the pseudobinary alloys $URh_{3-y}Pd_y$ showing the bonding (A) and antibonding (B) state densities.

the Cu_3Au structure. Calculations (Eriksson et al. 1988d) show that the contribution from near neighbours accounts for more than 99.5% of the total f–d or f–f hybridization and therefore to the 5f bandwidth.

Since the elements that are varied in these alloys (Rh and Pd) are next to each other in the periodic table their band masses differ by less than 15% across the range of compounds studied. Thus their hopping matrix elements are similar, whereas their band centres differ by as much as 1.3 eV. In a substitutional alloy this corresponds to the case of diagonal disorder but relatively small off-diagonal disorder.

The calculated Stoner product (Eriksson et al. 1988d) for these compounds is plotted in fig. 5.7. Stoner theory predicts URh_3 and URh_2Pd to be paramagnetic, and the contrary for $URhPd_2$ and UPd_3. Self-consistent spin-polarized calculations for the ferromagnetic states of both UPd_3 and $URhPd_2$, yielded saturated U 5f moments which is consistent with localized 5f states (Eriksson et al. 1988d). However an interpolation of the state density, between UPd_3 and URh_3 does not yield satisfactory values of the Stoner product. The calculations for the ordered intermediate compounds (albeit with a spurious long-range order) give a more exact description of the environment of a uranium atom surrounded by eight Rh and four Pd atoms (and vice versa) in

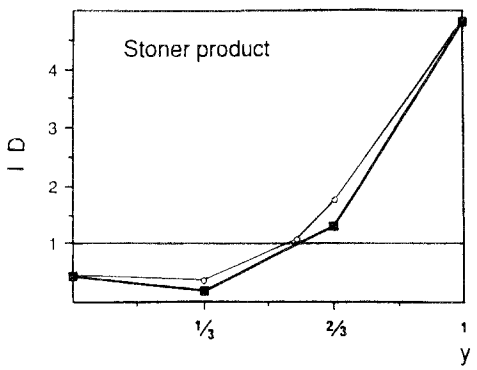

Fig. 5.7. The calculated Stoner products for the pseudobinary alloy $U(Rh_{1-y}Pd_y)_3$ as a function of y.

the alloys and it is this near-neighbour environment which is important. The intermediate compounds are both close to the Stoner limit of one, which might be identified with the critical concentration for localization of 5f electrons on a uranium atom.

5.1.7. $U(Fe_{1-x}Ni_x)_2$, $U(Fe_{1-x}Co_x)_2$, $U(Fe_{1-x}Mn_x)_2$ alloys

UMn_2 (C15) and UCo_2 (C15) are paramagnetic whereas UFe_2 (C15) and UNi_2 (C14) are ferromagnets. Detailed calculations of these systems have been performed and the magnetic ground-state properties were investigated (Eriksson et al. 1989b). The electronic specific heat coefficient of UFe_2 is 55 mJ/(mol K^2) (Sechovsky and Hilscher 1985, Frings 1984), which suggests itinerant electrons in narrow bands at the Fermi energy. The suggestion of itinerant 5f electrons in the UM_2 (M = Mn, Fe, Co, Ni) systems is supported by other experiments such as photoemission spectroscopy (Naegele et al. 1980, Ghijsen et al. 1985, Naegele 1985, Hoechst et al. 1986, Sarma et al. 1987) where a peak pinned at the Fermi energy was observed in all these systems, and identified as delocalized 5f states. These systems crystallize in the cubic Laves-phase (C15) (except UNi_2 which is (C14)).

There is great similarity between these and the $Y(Fe_{1-x}Co_x)_2$ alloys discussed in section 4.7. Compounds with Fe should be magnetic whereas compounds with Co should be nonmagnetic. However, this is not the case for the nickel systems and an explanation to this discrepancy has been proposed with the uranium 5f electrons as band states (Eriksson et al. 1989b), implying that the magnetism in UNi_2 is of 5f origin (Eriksson et al. 1989b, Severin et al. 1991).

The magnetic properties of the pseudobinary compounds $U(Fe_{1-x}Co_x)_2$, $U(Ni_{1-x}Co_x)_2$, $U(Fe_{1-x}Ni_x)_2$, $U(Fe_{1-x}Cr_x)_2$, $U(Fe_{1-x}Ti_x)_2$, $U(Fe_{1-x}Mn_x)_2$ are known (Andreev et al. 1988). A study of the magnetic properties of pseudobinary alloys offers the possibility of studying the onset of magnetism as a function of concentration. In the $U(Fe_{1-x}Mn_x)_2$ and the $U(Fe_{1-x}Cr_x)_2$ systems a rigid band model also seems appropriate, mainly by comparison of the state densities for the different compounds. This is used in computing the Stoner product for a general x in these compounds, since we interpolate the Stoner product between ordered compounds, in order to

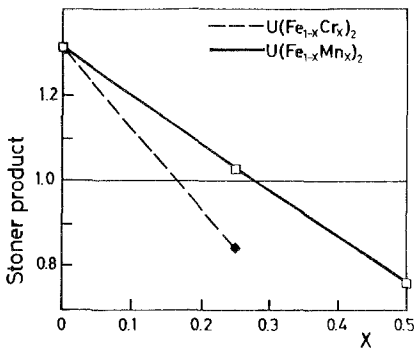

Fig. 5.8. The calculated Stoner products for the pseudobinary alloys $U(Fe_{1-x}Cr_x)_2$ and $U(Fe_{1-x}Mn_x)_2$ as a function of x.

distinguish between magnetic ordering and paramagnetism. The agreement between the experimental values of the critical concentration of the disappearance of ferromagnetism in both these systems gives additional support to a rigid band model can be used to describe the electronic structure in these alloy systems. Inspection of fig. 5.8 shows that the Stoner product in $U(Fe_{1-x}Cr_x)_2$ decreases twice as fast with x as it does for $U(Fe_{1-x}Mn_x)_2$. This can also be understood in a rigid band model where the substitution of iron by another 3d element merely shifts the Fermi energy according to the correct number of valence electrons. Since chromium has two valence electrons less than iron, whereas manganese has one electron less, the substitution of chromium for iron shifts E_F twice as fast with x, as a substitution with manganese would do, and correspondingly the Stoner product decreases twice as fast with x. For all studied systems the validity of the rigid band approximation is found to be good, although we emphasize that the description of an alloy system by studying an ordered ternary compound should be more appropriate than the simple rigid band model. However since the shape and extension of the 3d wave function of iron, manganese and chromium in these types of alloys and compounds is found to be very similar, and therefore the electronic structure is also very similar, this ensures the validity of the rigid band model. This should however be used cautiously since in a system where the original atom and its replacement have very different wave functions and electronic structure a rigid band analysis may break down. For instance, the paramagnetic ground state of the pseudo-binary alloy $U(Fe_{1-x}Ni_x)_2$ could in a first approximation be explained by a rigid band model since this system has exactly the same number of valence electrons as the paramagnetic compound UCo_2.

5.1.8. Relativistic effects upon moment formation

Although the *pure spin* LSDA Stoner criterion, eq. (5.2), predicts the onset of magnetism in actinide compounds reasonably well, there is another aspect of the magnetism that is revealed experimentally by the observation of anisotropic spin fluctuations in UCo_2, and magnetic anisotropy and magnetostriction of UFe_2. These properties arise from the large spin–orbit interaction at the uranium sites. $NpFe_2$, $NpNi_2$ and $PuFe_2$ are

ferromagnets whereas $PuCo_2$ and $PuNi_2$ are paramagnets and $NpCo_2$ a very weak anti-ferromagnet. The results of earlier relativistic energy band calculations for actinide NaCl-type compounds showed that spin–orbit interaction produces a dip in the density of states when the number of 5f electrons approaches six per atom, corresponding approximately to the filling of 5f $j = l - \frac{1}{2}$ sub-bands. Such a dip could inhibit magnetism and it is necessary to study the magnetic instability in the relativistic case.

Since the z-component of the spin is not a good quantum number in such calculations, the normal Stoner criterion cannot be used to describe the ferromagnetic instability. This is easily seen if the uniform unenhanced susceptibility is written in terms of the unperturbed Green function, G^0, and the Pauli matrix, σ^z, as

$$\chi^0 = -\left(\frac{1}{\pi}\right) \mathrm{Im}\,\mathrm{Tr}\,\sigma^z G^0 \sigma^z G^0, \tag{5.3}$$

which follows directly from linear response theory. When σ^z is diagonal in the unperturbed representation the right-hand side of eq. (5.3) becomes the density of states at the Fermi energy, $N(E_F)$. But here things are less simple because σ^z has nonzero interband matrix elements, producing a van Vleck contribution to the uniform susceptibility which is absent in the nonrelativistic case.

However, the spin–orbit interaction is a single particle effect and it is possible to reformulate to take it into account. Equation (5.2) has been generalized to cover the relativistic case (Eriksson et al. 1988c, 1989c) where it has a similar form. Another way to write eq. (5.2) is

$$I = \sum J_{qll'} \frac{\chi^0_{ql} \chi^0_{ql'}}{(\chi^0)^2}, \tag{5.4}$$

where χ^0_{ql} is the partial response resolved according to atom and angular momentum. Now χ^0_{ql} is no longer simply equal to $N_{ql}(E_F)$. In practice, the exchange integrals, $J_{qll'}$, must be calculated by applying a spin splitting (transformed into the jj-coupled relativistic representation) and calculating the response – and hence χ^0 and χ^0_{ql} – from a single iteration of a fully relativistic energy band calculation. The resulting effective Stoner products (Eriksson et al. 1989c) are shown in table 5.1, which resolves some of the anomalies noted above.

TABLE 5.1
Relativistic and nonrelativistic Stoner products for selected materials. NR = scalar relativistic, R = relativistic Stoner theory.

	NR	R
$PuFe_2$	1.7	1.4
$PuCo_2$	1.3	0.9
Np	1.3	0.3
Pu	0.9	0.3
YRh_3	0.4	0.4

5.2. *Spin-polarized calculations*

The standard approximation, which has been extremely successful for light elements, is to omit spin–orbit interaction in spin-polarized energy band calculations. Only pure spin moments are allowed to develop but these moments are calculated self-consistently. In the self-consistent spin-polarized calculations the spin-up and spin-down potentials are not shifted rigidly but have different shapes, leading to spin-up and spin-down bands with slightly different widths and shapes – the LSDA version of the spin-unrestricted Hartree–Fock approximation. The spin-up (majority) band is usually narrower than the spin-down (minority) band. The spin-up and spin-down densities of states for UFe_2, $NpFe_2$ and $PuFe_2$, for example, are shown in fig. 5.9. It has been found that spin-polarized calculations of this type do not yield the correct moments for any materials containing actinides if there are moments on the actinide atoms. This is due to the neglect of spin–orbit interaction and its direct result – the formation of an orbital contribution to the moment. The development of the ability to calculate self-consistently all of the contributions and the total moments is one of the major challenges facing actinide theory.

Before describing some of these more sophisticated efforts, we review here some of the results of spin-polarized calculations. We have several reasons for doing this. Firstly, although the calculated magnetic moments in many cases turn out to be incorrect, it is possible to identify magnetovolume effects which depend mainly on

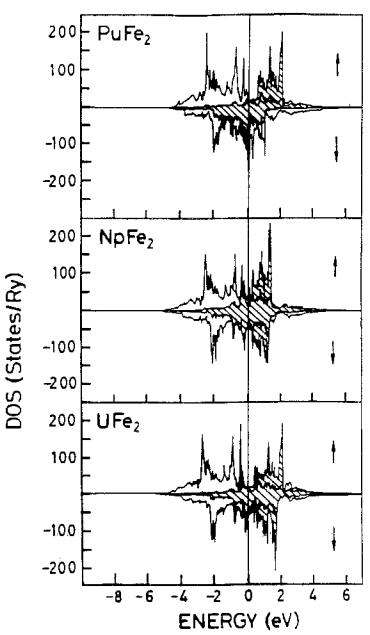

Fig. 5.9. The spin-resolved state densities for spin-polarized $AnFe_2$ (An = U, Np, Pn). The Fermi energy is at zero energy.

the calculated spin moment. Secondly, in some cases a saturated 5f moment is obtained and this often occurs in cases where there is other evidence that the 5f electrons are localized – the best known case being Am metal (Skriver et al. 1980). Thirdly, spin-polarized calculations must be made in some cases to investigate the possibility of metamagnetism.

5.2.1. NaCl-type compounds

The calculated spin moments (Brooks 1985) of some NaCl-type compounds are listed in table 5.2. The moments increase across an actinide series, with increasing f-electron number, and increase across a chalcogenide or pnictide series, with increasing anion size – reproducing the trends in fig. 1.3 but generally larger than experiment.

If itinerant magnetism exists in actinide compounds it is most likely to be found in those compounds with the smallest lattice parameters and the broadest 5f bands – making UN the best candidate among the UX compounds. A body of experimental evidence suggests that the electrons responsible for the moment in UN are itinerant (Fournier et al. 1980, Reihl et al. 1982a). From self-consistent spin-polarized energy band calculations for antiferromagnetic (Brooks and Kelly 1983) UN the calculated sublattice moment is $1.05\mu_B$ – about 25% larger than the measured moment. The discrepancy in the magnitude of the moment is not small. In addition the calculated volume dependence of the moment is too small by a factor of five.

5.2.2. Intermetallic compounds

Zero-temperature equation of state calculations for the $AnRh_3$ intermetallic compounds (Eriksson et al. 1989a, Johansson et al. 1986) reproduced the increase in measured lattice constant for the heavier actinides Np–Cm. The measured and calculated lattice constants are plotted in fig. 5.10. The Th–U compounds are paramagnetic and good results for the lattice constants are obtained from nonpolarized calculations. A small moment was obtained for $NpRh_3$ whereas it is an enhanced paramagnetic. The magnetovolume expansion for the compounds Pu–Cm is very pronounced and it drastically improves the calculated lattice constants. The experimental evidence, particularly the magnetic entropy of $PuRh_3$, is that the 5f electrons in these three

TABLE 5.2
The calculated magnetic moments (spin only) of uranium NaCl-type compounds from spin-polarized energy band calculations (Brooks 1985).

	m(expt)	m_f^s	m_d^s
US	1.7	2.05	0.20
USe	2.0	2.56	0.39
UTe	2.2	2.66	0.44
UP	1.8	1.91	0.10
UAs	2.1	2.36	0.21
USb	2.5	2.50	0.28
UN	0.75	1.05	0.02

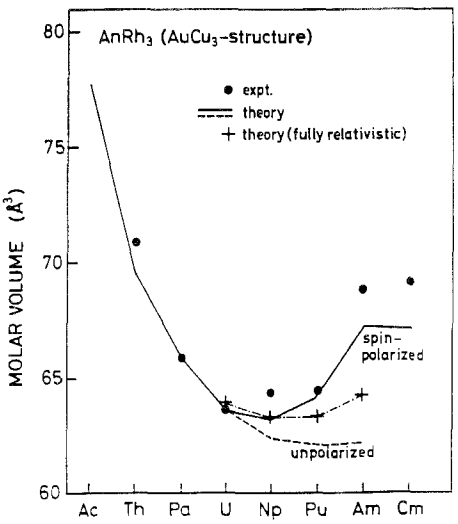

Fig. 5.10. The calculated atomic volumes of the $AnRh_3$ series (after Eriksson et al. 1989a) showing the large magnetovolume and relativistic effects for the Np–Cm compounds.

compounds are localized. The magnetovolume expansion obtained in spin-polarized calculations reduces the 5f bonding contribution to the equation of state which occurs when the 5f electrons localize.

Similar effects are found in the $AnIr_2$ systems (fig. 5.11). The electronic pressure formula, eq. (2.15), may be easily modified (Andersen et al. 1979, Eriksson et al. 1989d) to include the effects of moment formation in the 5f states

$$3PV_{5f}^{pol} = 3PV_{5f}^{para}\left\{1 - \frac{\mu_{5f}^2}{[n_{5f}(14 - n_{5f})]}\right\}, \tag{5.5}$$

where n_{5f} is the number of 5f electrons and μ_{5f} the 5f spin moment. When the 5f states polarize, the spin-up electrons occupy more anti-bonding states, reducing the magnitude of the (negative) 5f electronic pressure. The computed 5f spin increases

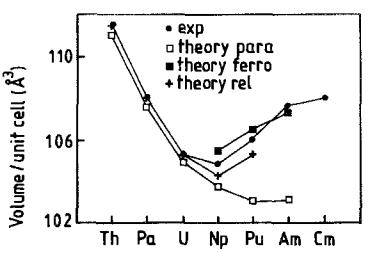

Fig. 5.11. The calculated atomic volumes of the $AnIr_2$ series showing the large magnetovolume and relativistic volume effects for the Np–Cm compounds (after Eriksson et al. 1989d).

from $2.7\mu_B$ to $5.8\mu_B$ between $NpIr_2$ and $AmIr_2$. It may be seen from eq. (5.5) that the 5f electronic pressure vanishes for a half-filled spin-up band, which is almost achieved for $AmIr_2$. For the Np and Pu compounds the electronic pressure reduction is less but there are still considerable magnetovolume effects.

5.2.3. Metamagnetism

UCoAl has the hexagonal ZrNiAl structure (Sechovsky and Havela 1988). The ground state of UCoAl has been shown to be nonmagnetic (Sechovsky et al. 1984, 1986, Havela et al. 1988) and the U–U spacing is in fact close to the Hill limit. However, in the presence of a magnetic field of less than 0.8 T a maximum in the magnetization develops at about 17 K. A further increase in the field drives the compound into a metamagnetic state with a moment of $0.34\mu_B$ along the c-axis. The moment does not saturate with the field, reaching $0.6\mu_B$ at 35 T (Sechovsky et al. 1984, 1986, Havela et al. 1988).

The calculated paramagnetic state density is shown in fig. 5.12 (Eriksson et al. 1989e). The 3 eV wide Co bands lie mainly below the Fermi energy but hybridize strongly with the 5f states which are pinned at the Fermi energy. The Stoner product was calculated to be 0.61 and the ground state paramagnetic. But in metamagnetic systems a sudden increase in moment for *finite* band splitting may increase the spin polarization energy more than the subsequent increase in kinetic energy. Under these circumstances, the criterion for a locally stable metamagnetic state is eq. (4.1). The criterion may be satisfied if the state densities are large just below and above the Fermi energy, which is evidently the case in fig. 5.12.

A search for the metamagnetic state was made using the fixed spin moment (FSM) method (Eriksson et al. 1989e), where the total energy is calculated as a function of the moment (Williams et al. 1984, Schwarz and Mohn 1984). The results are shown in fig. 5.13.

Agreement with experiment for the total moment is again made difficult by the

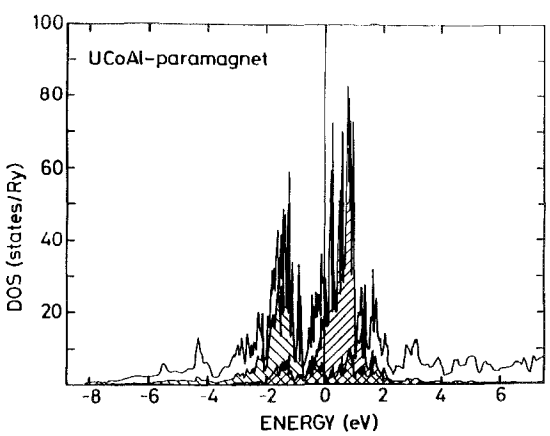

Fig. 5.12. The state density of UCoAl.

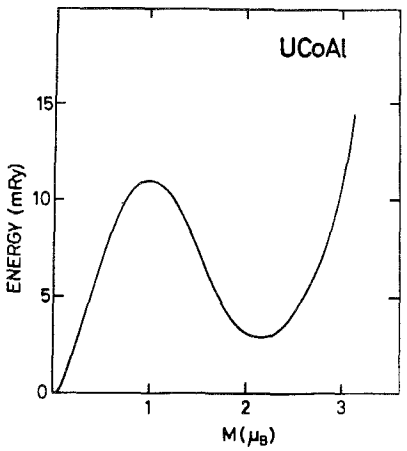

Fig. 5.13. The total energy of UCoAl as a function of magnetic moment (after Eriksson et al. 1989e).

intrusion of orbital effects but, with the complex state densities to be found in actinide–transition-metal intermetallics, it should not be surprising if many examples of metamagnetism are found.

5.3. *The sign of the moments in compounds and orbital effects*

Attempts to determine the magnitudes of magnetic moments are sometimes difficult in complex lattices because of the necessity to resolve the contributions from the different sites. No such ambiguity arises in the NaCl-type uranium compounds since the magnetic moments are almost entirely on the uranium sites. UN has the smallest U–U distance of any of the NaCl-type uranium compounds, and the pressure derivatives of the moment and Curie temperature are the same (Fournier et al. 1980, Fournier and Troc 1985). It therefore appears to be an itinerant antiferromagnet for which there is also evidence from photoemission (Reihl et al. 1982a). Of the ferromagnets, US has the smallest U–U lattice constant. It becomes ferromagnetic below 177 K with a zero temperature moment of $1.55\mu_B$ (Gardner and Smith 1968) with a 5f contribution, determined by neutron diffraction, of $1.7\mu_B$ (Wedgwood 1972, Wedgwood and Kuznietz 1972). The difference of $-0.15\mu_B$ is due to the diffuse (see the discussions in section 2.4 and below) conduction electrons polarized *antiparallel* to the total moment. There is now ample evidence that it has, although it is cubic, enormous magnetic anisotropy at low temperatures (Lander et al. 1991). Under pressure, the Curie temperature decreases at -0.23 K/kbar (Huang et al. 1979) – providing some evidence that US might be an itinerant ferromagnet.

Spin-polarized calculations for transition metals Fe, Co and Ni do not yield exactly the correct total moments, and analysis of the experimental data (Stearns 1986, Bonnenberg et al. 1986) for these metals yields an orbital contribution to the moment of $0.08\mu_B$, $0.14\mu_B$ and $0.05\mu_B$ for Fe, Co and Ni, respectively. The orbital contributions to the moments are *parallel* to the spin contributions of $2.13\mu_B$, $1.52\mu_B$ and $0.57\mu_B$

for Fe, Co and Ni, respectively. Such a situation is shown graphically on the left-hand side of fig. 5.14a.

In fig. 5.14a we have further resolved the spin contributions to the magnetic moments into *local* and *diffuse* parts (the orbital moments belong almost entirely to the 3d or *local* electrons). Here, in accordance with common usage, by *local* part we mean the 3d contribution and by *diffuse* part we mean the sp contribution, which is also that part of the moment whose density lies mainly in the interstitial region of the crystal and is not detected in neutron diffraction experiments under normal circumstances (see the discussion in section 2.4). In order to understand the importance of the sign of the orbital contribution to the moments it is first necessary to be clear about the relative signs of the local and diffuse parts of the spin contributions. In Fe, Co and Ni the diffuse part of the moment is *antiparallel* to the local part. The origin of the relative signs of the diffuse and local moments is hybridization between the 3d and sp electrons – or *local* and *diffuse* electrons. In Fe, Co and Ni the 3d band is more than half-filled and, of course, the Fermi energy lies close to the bottom of the broad, free-electron-like, sp bands. The hybridization is therefore similar to that between an early transition metal (the sp conduction band system) and a late transition metal (the 3d band system) and results in the relative sign of the local and diffuse moments being antiparallel, as argued in detail in section 4.1. In the elemental metals

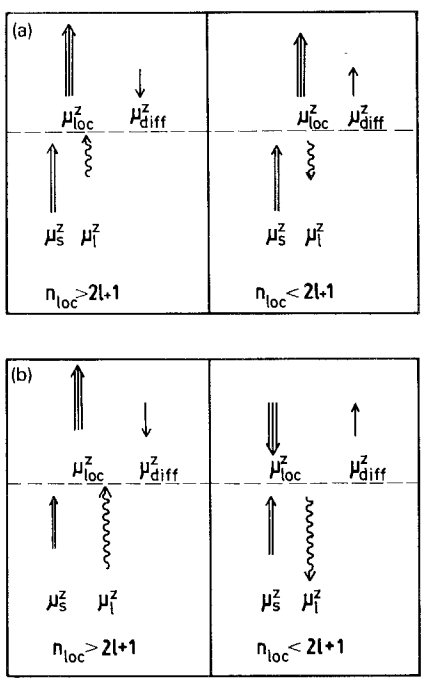

Fig. 5.14. The sign and composition of magnetic moments (see text): (a) orbital moment less than the spin moment; (b) orbital moment greater than the spin moment.

the sp bands actually cross the 3d bands and the simple arguments used in section 4.1 for the hybridization between two sets of non-overlapping d bands are not mathematically correct, but the more difficult mathematics for overlapping bands can be carried through (see, e.g., Anderson 1961, Heine and Samson 1980, Mayou et al. 1986, Terakura 1977) and this results in essentially the same physics.

The fact that the diffuse and local moments are antiparallel in Fe, Co and Ni – the only ferromagnetic elemental transition metals – has led to the effect of hybridization between local and diffuse electrons being loosely associated with antiparallel polarization between the two. In addition, in the original Anderson model (Anderson 1961) for moment formation on impurities, a nondegenerate *truly localized* level was allowed to hybridize with free-electron conduction bands. In this case the spin-up energy *level* is entirely below, and the spin-down energy level entirely above the Fermi energy when there is a moment. The result is that the diffuse moment is *always* antiparallel to the *truly localized* impurity moment. However, the situation is very different when the 3d electrons form energy bands since the dispersion of these bands allows them to cross the Fermi energy. If an early transition metal, such as vanadium, were magnetic, its diffuse and local moments would be *parallel*, for then the hybridization would be similar to that between two early transition metals – the 3d band system and the sp band system. The relative sign of the diffuse and local moments actually changes at about where the 3d band becomes half-filled. The same applies to the actinides which, being *early* transition metals, have 5f moments polarized *parallel* to the 5d moments which constitute nearly all of the diffuse moment. Some confusion arose from early work on actinides (Eib et al. 1978, Erbudak and Meier 1980) in which it appeared that the relative polarization of 5f and 6d electrons was anti-parallel but must have been due to an artifact in the cluster calculations (Keller 1973) used at the time to interpret the experiments and, as we shall see below, to the neglect of the orbital moments when comparison was made with experiment. Furthermore, exchange interactions between the local and diffuse moments are always positive and would always lead to parallel polarization in the absence of hybridization. In Fe, Co and Ni the spin moments are not large and the exchange interactions between local and diffuse moments small enough that hybridization dominates. In the actinides both mechanisms lead to parallel polarization of the local and diffuse moments as shown on the right-hand side of fig. 5.14a.

We now return to the orbital contributions to the magnetic moments. In an itinerant system the orbital contribution is a van Vleck moment, induced by spin–orbit interaction, and belongs almost entirely to the local electrons which are in narrow bands. In Fe, Co and Ni the orbital contributions to the moments are *parallel* to the spin contributions since the 3d bands are more than half filled, as shown on the left-hand side of fig. 5.14a. Light actinides have a less than half-filled 5f band, therefore the induced orbital moment is *antiparallel* to the 5f spin moment as shown on the right-hand side of fig. 5.14a. Thus there are *two* sign changes occurring between the right- and left-hand sides of the figure (the transition metal and actinide) – for both diffuse and orbital moments.

We now address the problem of the *size* of the orbital moments. Since the calcualted spin moments of the NaCl-type compounds are larger than the measured moments

(previous section), in the absence of detailed relativistic calculations it would be tempting to argue that, since spin–orbit splitting is larger for uranium 5f bands (0.77 eV) than for nickel 3d bands (0.22 eV) whereas the 5f bands are much narrower than nickel 3d bands, the corresponding induced orbital moment should be about $0.25\mu_B$ in UN – a large value for an itinerant magnet. The corresponding total moment of UN, $0.75\mu_B$, would then be in agreement with experiment. This in its turn suggests that the calculated moments of the other uranium pnictides and chalcogenides also tend to be too large because spin–orbit interaction induces an antiparallel orbital moment just large enough to explain the difference between the calculated spin moments and measured moments – as shown on the right-hand side of fig. 5.14a. The essential difference between the nature of the magnetism in light actinide compounds and transition metals would then be: (a) the presence of a larger induced orbital moment, probably with concomitant increased magnetic anisotropy, but with opposite sign, and (b) a change of sign of the diffuse contribution to the spin moment.

Satisfying though it at first seems, this hypothesis cannot be correct. Firstly, it is not consistent with the measured volume dependence of the moment in UN. According to Fournier et al. (1980) the measured moment of UN decreases from $0.75\mu_B$ at ambient pressure to $0.54\mu_B$ under 30 kbar. According to polarized calculations for the antiferromagnetic state (Brooks and Kelly 1983) the spin moment is at least $0.85\mu_B$ at this pressure, which would require an orbital moment of $-0.3\mu_B$ to yield the correct total moment. Therefore the orbital component must become more negative (increase in magnitude) under pressure to be consistent with calculated spin moment and the measured pressure dependence of the total moment. Now we recall that the orbital moment is a van Vleck moment, mixed into the spatially nondegenerate ground state by spin–orbit interaction. Its magnitude must decrease as the ratio of spin–orbit splitting to bandwidth decreases. The size of the spin–orbit splitting is relatively insensitive to volume but, under pressure, the 5f bands broaden rapidly. It is therefore unlikely that the magnitude of the orbital component of the moment could increase under pressure.

The second anomaly concerns the measured relative magnitudes of 5f and total moments in neutron scattering and magnetization experiments (Wedgwood and Kuznietz 1972, Lander 1978) and essentially the same problem occurs in the interpretation of spin-polarized photoemission experiments on uranium chalcogenides (Erbudak et al. 1979a,b, Eib et al. 1978, Erbudak and Meier 1980). In all of these experiments the 'spd' (mostly 6d in U compounds) or diffuse electron spin moment is observed to be *antiparallel* to the total moment as is also deduced from magneto-optical spectroscopy (Reim and Schoenes 1990). Yet the calculated diffuse moment (right-hand side of fig. 5.14) is always parallel to the total spin moment in actinide NaCl-type compounds. The addition of an antiparallel orbital component just large enough to bring the calculated moments into agreement with experiment yields a total moment with the same sign as the spin moment, and therefore parallel to the conduction electron moment (see fig. 5.14a).

Only if the orbital component of the moment were about $-1.75\mu_B$ in UN – an enormous value for an itinerant system and more typical of what one would expect for localized 5f electrons – would the spin component given by the band calculations

be consistent with the measured total moment and other data. The anomalies in the pressure dependence of the moment would be removed, however, only if the 5f moment were very pressure dependent – which is not typical of a localized 5f moment. The decrease in moment under pressure (Fournier et al. 1980) could, however, be due to the rapid quenching of a predominant orbital moment in an itinerant magnet by pressure. The observation of an antiparallel conduction electron moment in the uranium chalcogenides would also no longer be anomalous since the sign of the total moment would be determined by the orbital component. This situation – which is consistent with all known data – is shown graphically on the right-hand side of fig. 5.14b, where now the orbital moments are larger than the spin moments. The left-hand side of fig. 5.14b describes, for completeness, a late transition metal with a large orbital moment – none of which exist.

At first sight this analysis suggests that band theory does not describe 5f states. Since it is quite normal for rare earths to have large orbital moments it became customary to use the observation of a large orbital moment or magnetic anisotropy to argue that the corresponding electrons, by analogy, were localized (see, e.g., Chan and Lam 1974, Lander 1979). But other experimental evidence suggests that the 5f electrons, at least in UN and probably US, are itinerant. One of the surprises provided by self-consistent *relativistic* energy band calculations for actinides is that they do yield very large orbital moments. A large number of relativistic energy band calculations have now been made, yielding orbital contributions which are larger than the spin contributions to the moments in compounds containing actinides (e.g. Brooks and Kelly 1983, Brooks 1985, Eriksson et al. 1990a, 1991, Severin et al. 1991, Norman and Koelling 1986, Norman et al. 1988). The reason is that the induced orbital moment is more sensitive to the ratio of bandwidth to spin–orbit interaction (fig. 2.7) than would have been suspected from relativistic calculations which yield approximately the observed small orbital moments in Fe, Co and Ni (Singh et al. 1976, Ebert et al. 1988, Eriksson et al. 1990b).

5.4. Spin–orbit interaction and spin polarization: orbital magnetism

The spin–orbit splitting of the 5f states in uranium is about 0.77 eV, which is comparable with the Stoner splitting in uranium compounds. The spin–orbit splitting is recovered by adding to the potential a term

$$\Delta\mathscr{H} = \xi \boldsymbol{l}\cdot\boldsymbol{s}. \tag{5.6}$$

Neither the z component of the spin nor of the orbital angular momentum is a good quantum number when using eq. (5.6). The matrix of $\Delta\mathscr{H}$ connects spin-up and spin-down states in the basis set for the band structure calculation, therefore it is no longer possible to solve for spin-up and spin-down bands separately. The size of the matrix problem is doubled but the solutions are nondegenerate since time reversal symmetry is removed by the splitting between spin-up and spin-down potentials. A more exact way to solve the relativistic band structure problem is through the spin-polarized Dirac equation and several calculations of this type have been made (see, e.g., Ebert et al. 1988, Fritsche et al. 1987, Krutzen and Springelkamp 1989).

When either the net spin or spin–orbit interaction is zero the quantum current density,

$$j = 2c\mu_B \,\mathrm{Im}[\psi \times \nabla\psi], \tag{5.7}$$

is also zero in the ground state. In the presence of both spin polarization and spin–orbit interaction there is a net current, and it is from this current that the orbital moment arises. The orbital moment density may be calculated from the orbital angular momentum density given by

$$l_z(r) = \frac{1}{4\pi} \sum_{q,l,m} \sum_{s} \int^{E_F} N_{qlms}(E) m \phi^2_{qlms}(r, E)\, \mathrm{d}E, \tag{5.8}$$

where s is the spin index, N_{qlms} is the $qlms$-projected state density and q labels the atom.

The first attempt to calculate an orbital moment for an itinerant electron metal was by Singh et al. (1976) for Fe, and Ni with reasonable results although the orbital moments were very small. Subsequently Brooks and Kelly (1983) applied eq. (5.8) to uranium nitride and obtained an orbital moment larger than the spin moment – thus removing the relationship between the existence of a large orbital moment and localization of the 5f electrons. Similar calculations (Brooks 1985) for the uranium monochalcogenides, which are ferromagnets, showed that a large orbital contribution to the moment is a common feature of uranium compounds and established magnetic form factor analysis (next section) as a suitable test of the calculated total moment density for the ground states of actinide compounds. For actinide compounds in these and other, unpublished, calculations the calculated total orbital moment was larger than, and antiparallel to, the spin moment. The calculated moment decomposition in the actinide chalcogenides (Brooks 1985) is shown in table 5.3.

In all subsequent calculations for actinide compounds the orbital contribution at the actinide site has been found to be large (e.g., Eriksson et al. 1989b, Norman and Koelling 1986, Norman et al. 1988, Severin et al. 1991). In particular, a series of actinide compounds where a thorough analysis has been made is the $AnFe_2$ series.

TABLE 5.3

The calculated total and decomposed 5f contributions to the magnetic moments of the uranium monochalcogenides (Brooks 1985) compared with experiment: m_t, m_s and m_l are the total, spin and orbital moments. The experimental values of the 5f moments are obtained from neutron scattering experiments (Lander 1978). SO denotes spin–orbit coupling; SO + OP denotes spin–orbit coupling plus orbital polarization (see text).

	m(expt)	SO		SO + OP		m_t
		m_s	m_l	m_s	m_l	
US	1.7	2.1	−3.2	2.2	−4.0	−1.8
USe	2.0	2.4	−3.4	2.4	−4.3	−1.9
UTe	2.2	2.6	−3.4	2.6	−4.6	−2.1

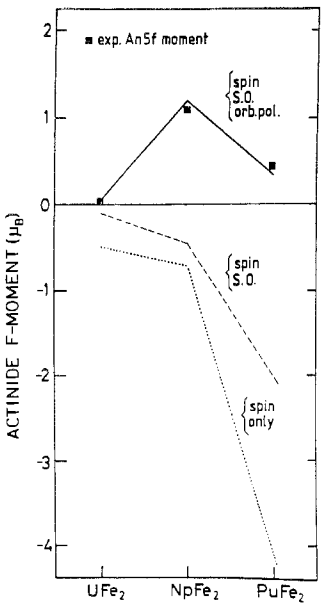

Fig. 5.15. The calculated magnetic moments of $AnFe_2$ compounds (An = U, Np, Pu) in several approximations: dotted line: spin-polarized; dashed line: relativistic with spin–orbit coupling; full line: relativistic with orbital polarization (see section 5.7) (after Eriksson et al. 1989b).

The results are shown in fig. 5.15. Here, as in the other compounds, the induced orbital moments are very large compared with those obtained for 3d transition metals. However, although the calculated orbital moments are very large in actinides, it seems to be generally true that they are still too small compared with experiment as may be seen from fig. 5.15, especially for Pu compounds.

Equation (5.8) has also been applied in calculations for Fe, Co and Ni (Eriksson et al. 1990a, Ebert et al. 1988) and some rare-earth–cobalt compounds (Nordström et al. 1990, 1992, Coehoorn and Daalderop 1992, Daalderop et al. 1992, Szpunar and Szpunar 1985, Szpunar and Wallace 1986, Szpunar 1985, Szpunar and Strange 1985, Szpunar and Smith 1990).

Once again, although calculated and measured orbital contributions to the moment are in reasonable agreement, there is a tendency for the calculated orbital moments to be too small.

5.5. *Magnetic anisotropy*

Spin–spin interaction in LSDA is isotropic. Thus all calculated magnetic properties are isotropic and it follows that the energy of magnetic excitations in ferromagnetic systems must approach zero for small wave vectors – the Goldstone theorem. What is a reasonable description for lighter itinerant systems cannot be correct for actinide compounds which have extraordinarily large magnetic anisotropy and magnetic excitations which, when observable, have large energy gaps.

The direction chosen as the quantization (or z) axis for the basis spherical harmonics used to represent the orbitals is irrelevant in calculations in which there is either net spin or no spin–orbit interaction, i.e., the system is magnetically isotropic. In the presence of spin–orbit interaction and a net spin, different energy bands are obtained for choices of quantization axis along inequivalent direction s in the crystal, i.e., the system is magnetically anisotropic. The magnetic anisotropy energy is usually calculated by making two sets of calculations with the quantization axis along hard and easy axes and subtracting the total energies for the two directions (H. Brooks 1940, Brooks et al. 1986, Daalderop et al. 1990, Coehoorn and Daalderop 1992). Such calculations have been for Fe, Co and Ni (Daalderop et al. 1990, Jansen 1988a, 1988b, 1990), for some rare-earth compounds (Nordström et al. 1992, Daalderop et al. 1992) and, for actinide compounds, for US (Brooks et al. 1986, Lander et al. 1990, 1991). For example, the energy difference between the 1 1 0 and 1 0 0 directions of US was first calculated self-consistently (Brooks et al. 1986),

$$E_{(\text{self-consistent})} = E_{100} - E_{111} = 204\,\text{meV}.$$

The Hellmann–Feynman – or force – theorem states that the energy difference is the difference in the sum of the energy eigenvalues if the calculation for the second of the two directions is not made self-consistently. This calculation yielded

$$E(\text{Hellmann–Feynman}) = E_{100} - E_{111} = 182\,\text{meV}.$$

Measurements yield a value of the first anisotropy constant, K_1, of $\simeq 10^{10}$ ergs/cm^3, which is about half of that calculated. The anisotropy energy of US is about two orders of magnitude greater than that of a rare-earth metal – which is hexagonal and an order of magnitude greater than that of $TbFe_2$.

5.6. *Analysis of magnetic form factors*

The magnetic form factor is just the normalized Fourier transform of the magnetization density as already outlined in section 2.4.

Calculations for actinide NaCl-type compounds show the moment on the anion to be negligible and the form factor is essentially that of the actinide. The calculated and measured form factors of UN are shown in fig. 5.1.6. Also shown is what should happen to the form factor if the crystal were put under pressure and the orbital moment were quenched more rapidly than the spin moment. The situation has already been sketched schematically in fig. 2.12 and discussed in section 2.4. It is the dependence of $\langle j_2 \rangle$ upon wave vector in fig. 2.12a that is responsible for the unmistakable tail in the measured form factor and $\langle j_2 \rangle$ contributes to the form factor only if there is an orbital contribution to the moment. The origin of the different shapes of the orbital and spin contributions to the form factor is that, although the orbital moment density (eq. (5.8)) has the same spatial distribution as the spin density, its contribution to the magnetization density is quite different. Neutrons are scattered by the magnetic field due to the electrons which has the shame shape as the magnetization density. The spin density contributes a term of the form $\langle j_0 \rangle$ to the form factor, where the average is over the density whereas the orbital density contributes a term which is the sum of

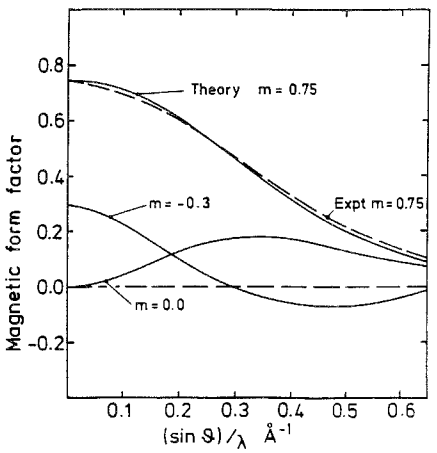

Fig. 5.16. The calculated magnetic amplitude of UN for different values of the total moment which varies with atomic volume (after Brooks and Kelly 1983).

$\langle j_0 \rangle$ and $\langle j_2 \rangle$. Since the wave vector dependence of $\langle j_0 \rangle$ and $\langle j_2 \rangle$ are shown in fig. 2.12a, it is quite easy to construct the different types of form factors that will be observed when the relative magnitudes of the spin and orbital moments are changed – depending, for example, upon whether the spin is greater or less than, parallel to, or antiparallel to, the orbital component. These are all shown in figs. 2.12b–d. Fig. 2.12b is typical for a heavy rare earth and it is clearly difficult to measure the orbital contribution as it appears as a small tail. Fig. 2.12c is more typical for a light actinide – $L > S$ and antiparallel. In this case it is easier to measure the orbital contribution. Fig. 2.12d is more unusual, but since the spin moment in $CeFe_2$ is calculated to be larger than the orbital moment (Eriksson et al. 1988a) and they are antiparallel, this could provide an example.

The above-mentioned calculations for UN led to a search for compounds where the orbital contribution was more quenched. In actinide–transition-metal intermetallics the negative electronic pressure arising from 3d–5f hybridization reduces the lattice constant and performs the task (Brooks et al. 1988). Fig. 5.17 shows the calculated equation of state and site resolved magnetic moments in UFe_2 as a function of volume (Johansson et al. 1990). Subsequently experiments were made on UFe_2 (Lebech et al. 1989, Wulff et al. 1989) and the measured uranium form factor, shown in fig. 5.18, bears a remarkable resemblence to the predicted form factor of UN under pressure, fig. 5.16. The cancellation between spin and orbital moments is almost complete. A Fourier transform of the form factor yields the magnetization density in real space (Lebech et al. 1989, Wulff et al. 1989) and this is shown in fig. 5.19. Here the possibility of zero total moment is shown graphically – the area under the curve is zero but the spin and orbital contributions to the magnetization density are large in different parts of space – the orbital magnetization density being closer to the nucleus.

Even more detailed studies have been made for UNi_2 (Severin et al. 1991). Here

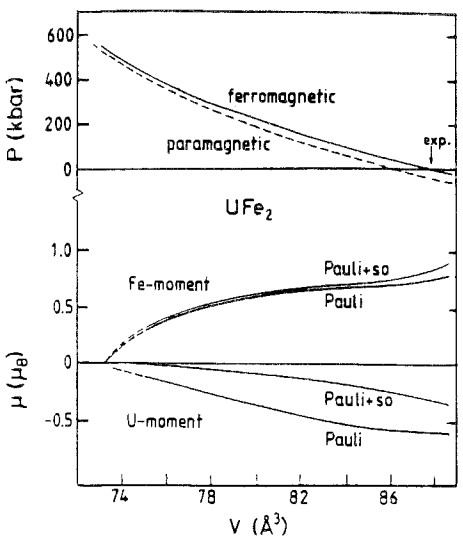

Fig. 5.17. In the upper part of the figure the calculated equation-of-state for the ferromagnetic and paramagnetic states in UFe_2 is plotted. The experimental equilibrium volume is denoted with an arrow. The calculated moments for U and Fe are plotted as a function of volume. The curves denoted by Pauli are the results of spin-polarized calculations and the curves denoted by Pauli + s.o. are from calculations with spin–orbit coupling included self-consistently. The main contributions originate from the Fe 3d and U 5f moments but the curves shown include all partial wave contributions to the moments.

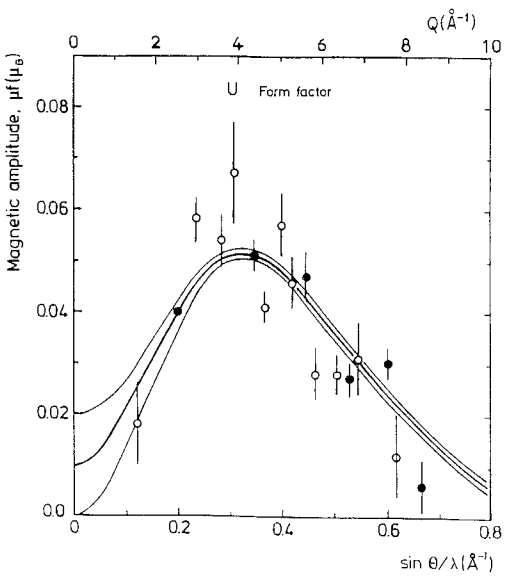

Fig. 5.18. The measured uranium magnetic amplitude of UFe_2 (after Lebech et al. 1989, 1991) as a function of scattering angle. The extrapolation to zero scattering angle gives the total uranium moment. The solid lines indicate the limits of the extrapolated moment.

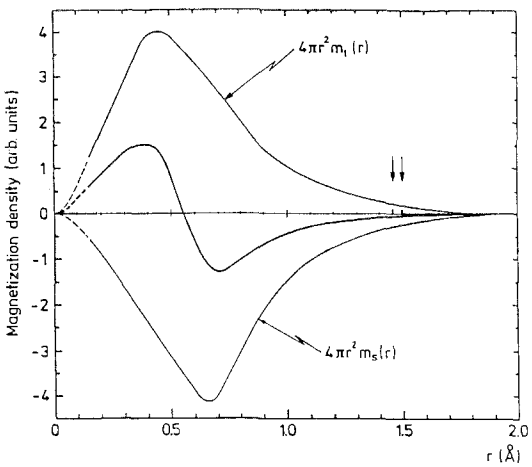

Fig. 5.19. The orbital and spin contributions and the total magnetization density as a function of radius at the uranium site in UFe_2, obtained by Fourier transforming the uranium form factor. The total area under the total magnetization is zero – corresponding to zero total moment (after Wulff et al. 1989).

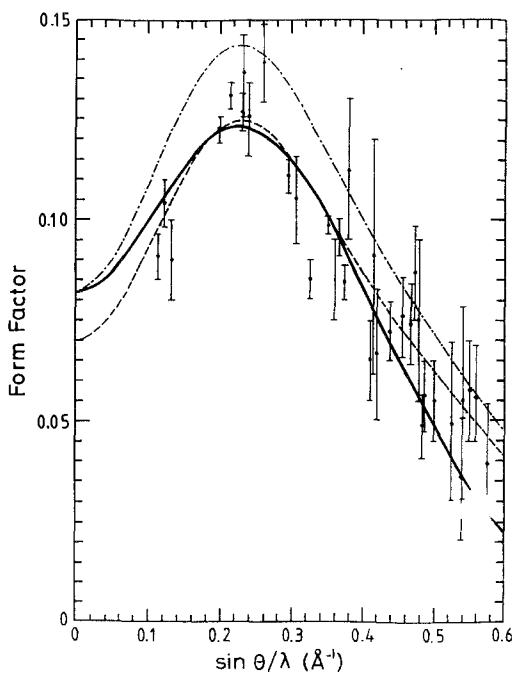

Fig. 5.20. Experimental data for the magnetic amplitude in UNi_2 and the corresponding fit (bold curve) (after Fournier et al. 1986). The dot-dashed curve corresponds to a constrained calculation in such a way that the total moment equals the experimentally observed value. The dashed curve corresponds to a similar calculation where the total moment is fixed to be $0.07\mu_B$ (after Severin et al. 1991).

there is appreciable scattering only at the uranium site (Fournier et al. 1986). The total moment is very small but the compound is nevertheless magnetic. The calculated and measured magnetic amplitudes are shown in fig. 5.20.

5.7. *Orbital polarization*

It was not emphasized in section 5.6, but despite some success with the form factors the calculated absolute values of the orbital moments are almost always too small (Brooks and Kelly 1983, Brooks 1985). This seems also to be true in Fe, Co and Ni (Eriksson et al. 1990b, Jansen 1990, Coehoorn and Daalderop 1992), although the larger discrepancies for the actinides are more obvious. One factor that could be missing is interaction between the orbital moments which is not allowed for in LSDA. Such interaction is well known to be important in atoms where it is responsible for Hund's second rule.

The exchange energy of an open shell, eq. (2.21), is usually approximated by assuming equal orbital occupation (Slater 1968) within a shell and leads to an approximation for the spin polarization energy, eq. (2.22), due to *isotropic* exchange – which is similar to the LSDA spin polarization energy, eq. (2.25). When the orbitals within a shell are not equally populated the spin polarization energy in the Hartree–Fock approximation depends upon the occupation of the individual orbitals.

One way to approximate orbital interactions which has had some success has been suggested by Brooks (1985) and Eriksson et al. (1990d). In a free atom the Hartree–Fock approximation to the Coulomb energy of an open shell is (Slater 1968)

$$E^{\text{shell}} = \tfrac{1}{2} \sum_{lm,l'm'} [\langle lm, l'm' | g | l'm', lm \rangle - \langle l'm', lm | g | lm, l'm' \rangle n_{lm} n_{l'm'} \delta_{s_{lm}, s_{l'm'}}], \tag{5.9}$$

where g is the Coulomb interaction and lm labels the orbitals. The second term is just the exchange energy, eq. (2.21), for integral occupation numbers. If the shell is filled according to Hund's rules for the ground state, the shell energy, eq. (5.9), may be evaluated and written as a function of occupation number

$$E(n) = \sum_K D^K(n) F^K, \tag{5.10}$$

where $K = 2, 4, 6$ for an f shell and F^K is a Slater Coulomb integral. The coefficient $D^2(n)$ for $n = 1$–7 is plotted in fig. 5.21.

If the orbitals had been *equally* populated (corresponding to a spherically symmetric charge density) rather than according to Hund's rules, the occupation numbers would have been $n/(2l+1)$ and the corresponding shell energy would have been (Slater 1968)

$$E^{\text{av}}(n) = \sum_K E^K(n) F^K, \tag{5.11}$$

where

$$E^K(n) = D^K(7) n \frac{(n-1)}{42} \tag{5.12}$$

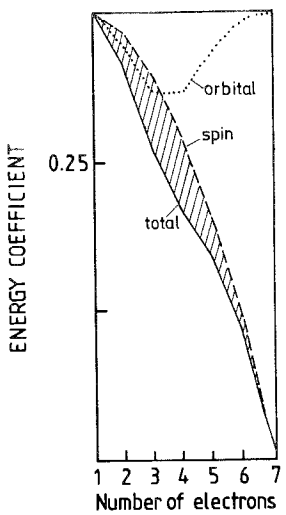

Fig. 5.21. The calculated energy coefficient for D^2, eq. (5.10), as a function of the number of f electrons for a less than half filled shell (the curve marked total). Also shown is the energy coefficient, E^2, from eq. (5.12) corresponding to an assumed equal occupation of orbitals. The difference between these two curves is the shaded region which is plotted as the curve marked orbital and corresponds to the energy gained by preferential filling of orbitals with larger values of orbital angular momentum.

is the coefficient of the average energy for a pair of electrons, multiplied by the number of pairs. The coefficient $E^2(n)$ is also plotted in fig. 5.21. There is no direct contribution to this coefficient for a filled spin shell or a spin shell with equal occupation numbers and eq. (5.11) is, in fact, the exchange energy that leads to the spin polarization energy in the Slater theory of spin polarization (Slater 1968, and eq. (2.22)). The difference between the average energy eq. (5.11), and the Hund's rule ground-state energy in the Hartree–Fock approximation, eq. (5.10), is also plotted in fig. 5.21. The latter energy is the difference between the energy of the ground state including orbital interactions and the energy with all orbital levels occupied equally for which there is only isotropic exchange.

The energy difference peaks for quarter filled shells and is zero for half-filled shells and is, therefore, an orbital polarization energy. Its functional dependence upon occupation number may be approximated quite well by $-\frac{1}{2}E^3L_z^2$ where E^3 is a Racah parameter (a linear combination of Slater–Coulomb integrals). Although the orbital polarization energy in this approximation is not a functional of the density it is a function, through L^z – the total orbital angular momentum of the shell, of the orbital occupation numbers. The differential of the orbital polarization energy with respect to occupation number leads to different orbital energy levels when there is an orbital moment (Eriksson et al. 1990d). E^3, the Racah parameter, may be re-evaluated during the iterative cycles of a self-consistent calculation along with the orbital occupation numbers, so that no free parameters are introduced.

This approximation has been applied to a number of systems. Although approximate, it removes the discrepancies in table 5.3 and brings theory into agreement with

experiment. The results for the $AnFe_2$ series are shown in fig. 5.15. (Eriksson et al. 1990a) where it also produces agreement with experiment. Applications to non-actinides such as Fe, Co and Ni and some cobalt compounds have also improved agreement with experiment for the orbital moments (Eriksson et al. 1990b, Coehoorn and Daalderop 1992, Daalderop et al. 1992, Nordström et al. 1992). Norman (1990) has applied this and similar approximations to the transition-metal oxides.

References

Akella, J., Q. Johnson, W. Thayer and R.N. Shock, 1979, J. Less-Common Met. **68**, 95.

Alameda, J.M., D. Givord and Q.J. Lu, 1981, J. Appl. Phys. **52**, 2079.

Amoretti, G., A. Blaise, R. Caciuffo, J.M. Fournier, M.T. Hutchings, R. Osborn and A.D. Taylor, 1989, Phys. Rev. B **40**, 1856.

Amoretti, G., A. Blaise, R. Caciuffo, D. Di Cola, J.M. Fournier, M.T. Hutchings, G.H. Lander, R. Osborn, A. Severing and A.D. Taylor, 1992, J. Phys.: Condens. Matter **4**, 3459.

Andersen, O.K., 1975, Phys. Rev. B **12**, 3060.

Andersen, O.K., and O. Jepsen, 1977, Physica B **91**, B317.

Andersen, O.K., J. Madsen, U.K. Poulsen, O. Jepsen and J. Kollar, 1977, Physica B **86–88**, B 249.

Andersen, O.K., H.L. Skriver, H. Nohl and B. Johansson, 1979, Pure and Appl. Chem. **52**, 93.

Andersen, O.K., O. Jepsen and D. Glötzel, 1985, in: Highlights of Condensed Matter Theory, Proceedings of the International School of Physics 'Enrico Fermi', eds F. Bassani, F. Fumi and M.P. Tosi (North-Holland, Amsterdam) p. 59.

Anderson, P.W., 1961, Phys. Rev. **124**, 41.

Andreev, A.V., L. Havela and V. Sechovsky, 1988, J. Phys. (France) **49**, C8-483.

Andres, K., D. Davidov, P. Dernier, F. Hsu, W.A. Reed and G.J. Nieuwenhuys, 1978, Solid State Commun. **60**, 7.

Arko, A.J., M.B. Brodsky, G.W. Crabtree, D. Karin, D.D. Koelling, L.R. Windmiller and J.B. Ketterson, 1975, Phys. Rev. B **12**, 4102.

Arko, A.J., D.D. Koelling and J.E. Schirber, 1985, in: Handbook on the Physics and Chemistry of the Actinides, eds A.J. Freeman and G.H. Lander (North-Holland, Amsterdam) Vol. 2, p. 175.

Arko, A.J., B.W. Yates, B.D. Dunlap, D.D. Koelling, A.W. Mitchel, D.L. Lam, C.G. Olson, M. del Guidice, Z. Fisk and J.L. Smith, 1987, Theoretical and Experimental Aspects of Valence Fluctuations and Heavy Fermions, Bangladore, 1987, eds L.C. Gupta and S.K. Malic (Plenum Press, New York).

Auluck, S., and M.S.S. Brooks, 1991, unpublished.

Baer, Y., and W.D. Schneider, 1987, in: Handbook on the Physics and Chemistry of Rare-Earths, Vol. 10, eds K.A. Gschneider, L. Eyring and S. Hüffner (North-Holland, Amsterdam) p. 1.

Baer, Y., H.R. Ott and K. Andres, 1980, Solid State Commun. **36**, 387.

Baudelet, F., C. Brouder, E. Dartyge, A. Fontaine, J.P. Kappler and G. Krill, 1990, Europhys. Lett. **13**, 751.

Belorizky, E., J.P. Gavigan, D. Givord and H.S. Li, 1988, Europhys. Lett. **5**, 349.

Benedict, U., 1987, in: Handbook on the Physics and Chemistry of the Actinides, Vol. 4, eds A.J. Freeman and G.H. Lander (North-Holland, Amsterdam) p. 227.

Benedict, U., J.R. Peterson, R.G. Haire and C. Dufour, 1984, J. Phys. F **14**, L43.

Bloch, D., and R. Lemaire, 1970, Phys. Rev. B**2**, 2648.

Bloch, D., D.M. Edwards, M. Shimizu and J. Voiron, 1975, J. Phys. F **5**, 1217.

Bonnenberg, D., K.A. Hempel and H.P.J. Wijn, 1986, in: Landolt-Börnstein Numerical Data and Functional Relationships in Science and Technology, Group 3, Vol. 19, Pt. a, ed. H.P.J. Wijn (Springer, Berlin),

Boucherle, J.X., D. Givord and J. Schweizer, 1982, J. Phys. (France) C **7**, 199.

Brodsky, M.B., 1978, Rep. Prog. Phys. **41**, 1547.

Brooks, H., 1940, Phys. Rev. B **58**, 909.

Brooks, M.S.S., 1979, J. Phys. (France) C **4**, 156.

Brooks, M.S.S., 1984, J. Phys. F **14**, 639.

Brooks, M.S.S., 1985, Physica B **130**, B 6.

Brooks, M.S.S., and B. Johansson, 1983, J. Phys. F **13**, L197.

Brooks, M.S.S., and P.J. Kelly, 1983, Phys. Rev. Lett. **51**, 1708.

Brooks, M.S.S., B. Johansson and H.L. Skriver, 1984, in: Handbook on the Physics and Chemistry of the Actinides, Vol. 1, eds A.J.

Freeman and G.H. Lander (North-Holland, Amsterdam) p. 153.
Brooks, M.S.S., B. Johansson, O. Eriksson and H.L. Skriver, 1986, Physica B **144**, 1.
Brooks, M.S.S., O. Eriksson, B. Johansson, J.J.M. Franse and P.H. Frings, 1988, J. Phys. F **18**, L33.
Brooks, M.S.S., O. Eriksson and B. Johansson, 1989, J. Phys.: Condens. Matter **1**, 5861.
Brooks, M.S.S., L. Nordström and B. Johansson, 1991a, J. Phys.: Condens. Matter **3**, 2357.
Brooks, M.S.S., T. Gasche, S. Auluck, L. Nordström, L. Severin, J. Trygg and B. Johansson, 1991b, J. Appl. Phys. **70**, 5972.
Brooks, M.S.S., S. Auluck, T. Gasche, J. Trygg, L. Nordström, L. Severin and B. Johansson, 1992, J. Magn. & Magn. Mater. **104–107**, 1496.
Buschow, K.H.J., 1977, Rep. Prog. Phys. **40**, 1179.
Buschow, K.H.J., 1979, Rep. Prog. Phys. **42**, 1373.
Buschow, K.H.J., 1980, in: Ferromagnetic Materials, ed. E.P. Wohlfarth (North-Holland, Amsterdam) p. 297.
Buschow, K.H.J., 1988, in: Ferromagnetic Materials, Vol. 4, eds E.P. Wohlfarth and K.H.J Buschow (North-Holland, Amsterdam) p. 1.
Buschow, K.H.J., and R.P. van Stapele, 1970, J. Appl. Phys. **41**, 4066.
Buyers, W.J.L., and T.M. Holden, 1985, in: Handbook on the Physics and Chemistry of the Actinides, Vol. 2, eds A.J. Freeman and G.H. Lander (North-Holland, Amsterdam) p. 239.
Chan, S.K., and D.L. Lam, 1974, in: The Actinides: Electronic Structure and Related properties, Vol. 1, eds A.J.Freeman and J.B.Darby (Academic Press, New York) p. 1.
Christensen, N.E., and V. Heine, 1985, Phys. Rev. B **32**, 6145.
Coehoorn, R., 1990, Phys. Rev. B **41**, 11790.
Coehoorn, R., 1991, Lecture notes Nato-ASI in: Supermagnets, Hard Magnetic Materials eds G.J. Long and F. Grandjean (Kluwer Academic, Dordrecht).
Coehoorn, R., and G.H.O. Daalderop, 1992, J. Magn. & Magn. Mater. **104–107**, 1081.
Crabtree, G.W., 1985, J. Magn. & Magn. Mater. **52**, 169.
Cyrot, M., and M. Lavagna, 1979, J. Phys. (France) **40**, 763.
Cyrot, M., D. Gignoux, F. Givord and M. Lavagna, 1979, J. Phys. (France) **40**, C5-171.
Daalderop, G.H.O., P.J. Kelly and M.F.H. Schuurmans, 1990, Phys. Rev. B **42**, 11919.
Daalderop, G.H.O., P.J. Kelly and M.F.H. Schuurmans, 1992, J. Magn. & Magn. Mater. **104–107**, 737.
de Mooij, D.B., and K.H.J. Buschow, 1988, J. Less-Common Met. **136**, 207.
Dunlap, B.D., F.J. Litterst, S.K. Malik, H.A. Kierstead, G.W. Crabtree, W. Kwok, D.L. Lam and A.W. Mitchel, 1987, in: Theoretical and Experimental Aspects of Valence Fluctuations and Heavy Fermions, Bangladore, 1987, eds L.C. Gupta and S.K. Malic (Plenum Press, New York).
Ebert, H., P. Strange and B.L. Gyorffy, 1988, J. Phys F **18**, L135.
Eib, W., M. Erbudak, F. Greuter and B. Reihl, 1978, Phys. Lett. A **68** 391.
Endo, S., H. Sasaki and T. Mitsui, 1977, J. Phys. Soc. Jpn. **42**, 4572.
Erbudak, M., and F. Meier, 1980, Physica B **102**, 134.
Erbudak, M., F. Greuter, F. Meier, B. Reihl, O. Vogt and J. Keller, 1979a, J. Appl. Phys. **50**, 2099.
Erbudak, M., F. Greuter, F. Meier, B. Reihl, O. Vogt and J. Keller, 1979b, Solid State Commun. **30**, 439.
Eriksson, O., L. Nordström, M.S.S. Brooks and B. Johansson, 1988a, Phys. Rev. Lett. **60**, 2523.
Eriksson, O., B. Johansson and M.S.S. Brooks, 1988b, J. Phys. (France) C **8**, 295.
Eriksson, O., M.S.S. Brooks and B. Johansson, 1988c, J. Phys. (France) C **8**, 695.
Eriksson, O., B. Johansson, M.S.S. Brooks and H.L. Skriver, 1988d, Phys. Rev. B **38**, 12858.
Eriksson, O., B. Johansson, M.S.S. Brooks and H.L. Skriver, 1989a, Phys. Rev. B **40**, 9508.
Eriksson, O., B. Johansson, M.S.S. Brooks and H.L. Skriver, 1989b, Phys. Rev. B **40**, 9519.
Eriksson, O., M.S.S. Brooks and B. Johansson, 1989c, Phys. Rev. B **39**, 13115.
Eriksson, O., B. Johansson, M.S.S. Brooks and H.L. Skriver, 1989d, Phys. Rev. B **39**, 5647.
Eriksson, O., B. Johansson and M.S.S. Brooks, 1989e, J. Phys.: Condens. Matter **1**, 4005.
Eriksson, O., M.S.S. Brooks and B. Johansson, 1990a, Phys. Rev. B **41**, 9087.
Eriksson, O., B. Johansson, R.C. Albers, A.M. Boring and M.S.S. Brooks, 1990b, Phys. Rev. **42**, 2707.
Eriksson, O., M.S.S. Brooks and B. Johansson, 1990c, J. Less-Common. Met. **158**, 207.
Eriksson, O., M.S.S. Brooks and B. Johansson, 1990d, Phys. Rev. B **41**, 7311.
Eriksson, O., M.S.S. Brooks, B. Johansson, R.C. Albers and A.M. Boring, 1991, J. Appl. Phys. **69**, 5897.
Fournier, J.M., and R. Troc, 1985, in: Handbook on the Physics and Chemistry of the Actinides,

Vol. 2, eds A.J. Freeman and G.H. Lander (North-Holland, Amsterdam) p. 29.
Fournier, J.M., J. Beille, A. Boeuf and F.A. Wedgwood, 1980, Physica B **102**, 282.
Fournier, J.M., A. Boeuf, P.H. Frings, M. Bonnet, J.X. Boucherle, A. Delapalme and A.A. Menovsky, 1986, J. Less-Common Met. **121**, 249.
Friedel, J., 1969, in: The Physics of Metals, ed. J.M. Ziman (Cambridge Univ. Press, Cambridge) p. 341.
Frings, P.H., 1984, Doctoral Thesis (University of Amsterdam).
Fritsche, L., J. Noffke and H. Eckardt, 1987, J. Phys F **17**, 943.
Gardner, W.E., and T.F. Smith, 1968, in: Proc. 2nd Int. Conf. on Low Temperature Physics, Vol. 2, eds D.M. Finlayson and D.M. McCall (St. Andrews) p. 1377.
Gasche, T., S. Auluck, M.S.S. Brooks and B. Johansson, 1991a, J. Magn. & Magn. Mater. **104–107**, 37.
Gasche, T., S. Auluck, M.S.S. Brooks and B. Johansson, 1991b, J. Appl. Phys. **70**, 6850.
Ghijsen, J., R.L. Johnson, J.C. Spirlet and J.J.M. Franse, 1985, J. Electron Spectrosc. Relat. Phenom. **37**, 163.
Gignoux, D., F. Givord and R. Lemaire, 1983, J. Less-Common Met. **94**, 1.
Givord, D., 1987, Europhysics News **18**, 93.
Givord, D., A.R. Gregory and J. Schweizer, 1980, J. Magn. & Magn. Mater **15–18**, 293.
Givord, D., H.S. Li and R. Perrier de la Bâthie, 1984, Solid State Commun. **51**, 837.
Givord, D., H.S. Li and F. Tasset, 1985, J. Appl. Phys. **57**, 4100.
Goto, T., K. Fukamichi, T. Sakakibara and H. Komatsu, 1990, J. Magn. & Magn. Mater. **90–91**, 700.
Grosshans, W.A., Y.K. Vohra and W.B. Holtzapfel, 1983, J. Phys. F **15**, L147.
Gu, S.Q., and W.Y. Ching, 1987, Phys. Rev. B **36**, 8350.
Gunnarsson, O., 1976, J. Phys. F**6**, 587.
Gunnarsson, O., 1977, Physica B **91**, 329.
Gunnarsson, O., 1978, J. Appl. Phys. **49**, 1399.
Gunnarsson, O., and R.O. Jones, 1985, Phys. Rev. B **31**, 7588.
Gunnarsson, O., and B.I. Lundqvist, 1976, Phys. Rev. B **13**, 4274.
Gupta, H.O., S.K. Malik and W.E. Wallace, 1984, J. Magn. & Magn. Mater. **42**, 239.
Gustafson, D.R., and A.R. Mackintosh, 1964, J. Chem. & Phys. Solids **25**, 389.
Gustafson, D.R., J.D. McNutt and L.O. Roellig, 1969, Phys. Rev. **183**, 435.
Haire, R.G., J.R. Peterson, U. Benedict and C. Dufour, 1984, J. Less-Common Met. **102**, 119.
Harmon, B.N., 1979, J. Phys. (France) C **5**, 65.
Hasegawa, A., and H. Yamagami, 1990a, J. Phys. Soc. Jpn. **59**, 218.
Hasegawa, A., and H. Yamagami, 1990b, Physica B **163**, 273.
Havela, L., V. Sechovsky, F.R. de Boer, E. Brück, P.A. Veenhuizen, J.B. Bouwer and K.H.J. Buschow, 1988, J. Magn. & Magn. Mater. **76–77**, 89.
Heaton, R.A., J.G. Harrison and C.C. Lin, 1983, Phys. Rev. B **28**, 5992.
Hedin, L., and B.I. Lundqvist, 1971, J. Phys. C **4**, 1971.
Heine, V., 1980, in: Solid State Physics, Vol. 35, eds H. Ehrenreich, F. Seitz and D. Turnbull (Academic Press, New York) p. 1.
Heine, V., and J.H. Samson, 1980, J. Phys. F **10**, 2609.
Heine, V., J.H. Samson and C.M.M. Nex, 1981, J. Phys. F **11**, 2645.
Hill, H.H., 1970, in: Plutonium 1970, ed. W.M. Miner (Met. Soc. AIME, New York) p. 2.
Hilscher, G., 1982a, J. Magn. & Magn. Mater. **25**, 229.
Hilscher, G., 1982b, J. Magn. & Magn. Mater. **27**, 1.
Hoechst, M., K. Tan and F.U. Hillebrecht, 1986, J. Vac. Sci. Technol. A **4**, 1585.
Hohenberg, P., and W. Kohn, 1964, Phys. Rev. **136**, 864.
Huang, C.Y., R.J. Laskowski, C.E. Olsen and J.L. Smith, 1979, J. Phys. (France) **40**, C4-26.
Hubbard, J., 1963, Proc. R. Soc. London A **276**, 238.
Hummler, K., and M. Fähnle, 1992, Phys. Rev. **45**, 3161.
Imer, J.M., D. Malterre, M. Grioni, P. Weibel, B. Dardel and Y. Baer, 1991, Phys. Rev. **44**, 10455.
Janak, J.F., 1977, Phys. Rev. B **16**, 255.
Jansen, H.J.F., 1988a, J. Appl. Phys. **64**, 5604.
Jansen, H.J.F., 1988b, Phys. Rev. B **38**, 8022.
Jansen, H.J.F., 1990, J. Appl. Phys. **67**, 4555.
Jaswal, S.S., 1990, Phys. Rev. B **41**, 9697.
Johanson, W.R., G.W. Crabtree, A.S. Edelstein and O.D. McMasters, 1981, Phys. Rev. Lett. **46**, 504.
Johanson, W.R., G.W. Crabtree and F.A. Schmidt, 1982, J. Appl. Phys. **53**, 2041.
Johansson, B., 1974, Philos. Mag. **30**, 469.
Johansson, B., O. Eriksson, M.S.S. Brooks and H.L. Skriver, 1986, Phys. Scripta T **13**, 65.

Johansson, B., O. Eriksson and M.S.S. Brooks, 1990, High Pressure Research **2**, 303.

Kanellakopulos, B., A. Blaise, J.M. Fournier and M. Müllet, 1975, Solid State Commun. **17**, 713.

Keller, J., 1973, AIP Conf. Proc **10**, 514.

Kennedy, S.J., and B.R. Coles, 1990, J. Phys.: Condens. Matter **2**, 1990.

Kohn, W., and L.J. Sham, 1965, Phys. Rev. A **140**, 1133.

Koon, N.C., and J.J. Rhyne, 1980, in: Crystalline Electric Field and Structural Effects, eds J.E. Crow, P. Guertin and T. Mihalisin (Plenum Press, New York) p. 125.

Kornstädt, U., R. Lässer and B. Lengeler, 1980, Phys. Rev. B **21**, 1898.

Krutzen, B.C.H., and F. Springelkamp, 1989, J. Phys. F **6**, 587.

Lander, G.H., 1978, in: Rare Earths and Actinides, 1977, eds W. D. Corner and B. K. Tanner (Inst. of Phys. Bristol) p. 173.

Lander, G.H., 1979, J. Magn. & Magn. Mater. **15–18**, 1208.

Lander, G.H., and G. Aeppli, 1991, J. Magn. & Magn. Mater. **100**, 151.

Lander, G.H., M.S.S. Brooks, B. Lebech, P.J. Brown, O. Vogt and K. Mattenberger, 1990, Appl. Phys. Lett. **57**, 989.

Lander, G.H., M.S.S. Brooks, B. Lebech, P.J. Brown, O. Vogt and K. Mattenberger, 1991, J. Appl. Phys. **69**, 4803.

Lang, J.K., Y. Baer and P.A. Cox, 1981, J. Phys. **11**, 121.

Lawson, A.W., and T.Y. Tang, 1949, Phys. Rev. **76**, 301.

Lebech, B., M. Wulff, G.H. Lander, J. Rebizant, J.C. Spirlet and J. Delapalme, 1989, J. Phys.: Condens. Matter **1**, 10229.

Lebech, B., M. Wulff and G.H. Lander, 1991, J. Appl. Phys. **69**, 5891.

Li, H.-S., and J.M.D. Coey, 1991, in: Handbook of Magnetic Materials, Vol. 6, ed. K.H.J. Buschow (North-Holland, Amsterdam) p. 1.

Lindgard, P.A., 1976, in: Magnetism in Metals and Metallic Compounds, eds J.T. Lopuzanski, A. Pekalsky and J. Przystawa (Plenum Press, New York) p. 203.

Liu, J.P., F.R. de Boer and K.H.J. Buschow, 1991, to be published.

Lonzarich, G.G., and L. Taillefer, 1985, J. Phys. C **18**, 4339.

Mackintosh, A.R., and O.K. Andersen, 1979, in: Electrons at the Fermi Surface, ed. M. Springford (Cambridge Univ. Press, Cambridge) p. 149.

Malik, S.K., F.J. Arlinghaus and W.E. Wallace, 1977, Phys. Rev. B **16**, 1242.

Mao, H.K., R.M. Hazen, P.M. Bell and J. Wittig, 1981, J. Appl. Phys. **52**, 4572.

Mattocks, P.G., and R.C. Young, 1977a, J. Phys. F **7**, 1219.

Mattocks, P.G., and R.C. Young, 1977b, J. Phys. F **7**, L19.

Mayou, D., D. Nguyen Manh, A. Pasturel and F. Cyrot-Lackmann, 1986, Phys. Rev. B **33**, 3384.

Mohn, P., and K. Schwarz, 1984, Physica F **130**, 26.

Mohn, P., and E.P. Wohlfarth, 1987, J. Phys. F **17**, 2421.

Moriya, T., 1984, J. Magn. & Magn. Mater. **45**, 79.

Moruzzi, V.L., J.F. Janak and A.R. Williams, 1978, Calculated Electronic Properties of Metals (Pergamon, New York).

Murata, K.K., and S. Doniach, 1972, Phys. Rev. Lett. **29**, 285.

Naegele, J., 1985, Physica B **130**, 52.

Naegele, J., L. Manes, J.C. Spirlet, L. Pellegrini and J.M. Fournier, 1980, Physica B **102**, 122.

Naegele, J., L. Manes, J.C. Spirlet and W. Müller, 1984, Phys. Rev. Lett. **52**, 1834.

Nellis, W.J., A.R. Harvey and M.B. Brodsky, 1981, in: Magnetism and Magnetic Materials, AIP Conf. Proc. No. 10, eds C.D. Graham Jr and J.J. Rhyne (AIP, New York) p. 1076.

Nicklow, R.M., N.C. Koon, C.M. Williams and J.B. Milstein, 1976, Phys. Rev. Lett. **36**, 532.

Nordström, L., O. Eriksson, M.S.S. Brooks and B. Johansson, 1990, Phys. Rev. B **41**, 911.

Nordström, L., B. Johansson and M.S.S. Brooks, 1991, J. Appl. Phys. **69**, 5708.

Nordström, L., M.S.S. Brooks and B. Johansson, 1992, J. Magn. & Magn. Mater. **104–107**, 1942.

Norman, M.R., 1990, Phys. Rev. Lett. **64**, 1162.

Norman, M.R., and D.D. Koelling, 1986, Phys. Rev. B **33**, 3803.

Norman, M.R., B.I. Min, T. Oguchi and A.J. Freeman, 1988, Phys. Rev. B **33**, 3803.

Ohashi, K., Y. Tawara, R. Osugi, J. Sakurai and Y. Komura, 1988, J. Less-Common Met. **139**, L1.

Onuki, Y., I. Umehara, Y. Kurosawa, K. Satoh and H. Matsui, 1990a, J. Phys. Soc. Jpn. **59**, 229.

Onuki, Y., I. Umehara, Y. Kurosawa, K. Satoh, H. Matsui, A. Hasegawa and H. Yamagami, 1990b, Physica B **163**, 273.

Osborn, R., A.D. Taylor, Z.A. Bowden,

M.A. Hackett, W. Hayes, M.T. Hutchings, G. Amoretti, R. Caciuffo, A. Blaise and J.M. Fournier, 1988, J. Phys. C **21**, L931.
Peterson, J.R., U. Benedict, C. Dufour, I. Birkel and R.G. Haire, 1983, J. Less-Common Met. **93**, 353.
Pettifor, D.G., 1976, Commun. Phys. **1**, 141.
Radwański, R.J., and J.J.M. Franse, 1989, J. Magn. & Magn. Mater. **80**, 14.
Reihl, B., G. Hollinger and F.J. Himpsel, 1982a, J. Magn. & Magn. Mater **29**, 303.
Reihl, B., N. Martensson, D.E. Eastman, A.J. Arko and O. Vogt, 1982b, Phys. Rev. B **26**, 1842.
Reim, W., and J. Schoenes, 1990, in: Ferromagnetic Materials, Vol. 5, eds E.P. Wohlfarth and K.H.J. Buschow (North-Holland, Amsterdam).
Richter, M., and H. Eschrig, 1989, Solid State Commun. **72**, 263.
Roeland, L.W., G.J. Cock, F.A. Muller, C.A. Moleman, K.A. McEwen, R.C. Jordan and D.W. Jones, 1975, J. Phys. F **5**, L233.
Ruderman, M.A., and C. Kittel, 1954, Phys. Rev. **96**, 99.
Sakakibara, T., T. Goto, K. Yoshimura and K. Fukamichi, 1990, J. Phys.: Condens. Matter **2**, 3381.
Sarma, D.D., F.U. Hillebrecht and M.S.S. Brooks, 1987, J. Magn. & Magn. Mater. **63–64**, 509.
Schuck, A.F., and J.H. Sturdivant, 1950, J. Chem. Phys. **18**, 145.
Schwarz, K., and P. Mohn, 1984, J. Phys. F **14**, L129.
Sechovsky, V., and L. Havela, 1988, in: Ferromagnetic Materials, Vol. 4, eds E.P. Wohlfarth and K.H.J. Buschow (North-Holland, Amsterdam) p. 309.
Sechovsky, V., and G. Hilscher, 1985, Physica B **130**, 201.
Sechovsky, V., L. Havela, N. Pillmayr, G. Hilscher and A.V. Andreev, 1984, J. Magn. & Magn. Mater. **63–64**, 99.
Sechovsky, V., L. Havela, F.R. de Boer, J.J.M. Franse, P.A. Veenhuizen, J. Sebet and A.V. Andreev, 1986, Physica B **142**, 283.
Sellmyer, D.J., M.A. Engelhardt, S.S. Jaswal and A.J. Arko, 1988, Phys. Rev. Lett. **60**, 2077.
Severin, L., L. Nordström, M.S.S. Brooks and B. Johansson, 1991, Phys. Rev. B **44**, 9392.
Shimizu, M., 1964, Proc. Phys. Soc. **84**, 397.
Shimizu, M., 1965, Proc. Phys. Soc. **86**, 147.
Singh, D.J., 1991, Phys. Rev. B **44**, 7451.
Singh, M., J. Callaway and C.S. Wang, 1976, Phys. Rev. B **14**, 1214.
Skriver, H.L., 1983a, Muffin Tin Orbitals and Electronic Structure (Springer, Heidelberg).
Skriver, H.L., 1983b, in: Systematics and Properties of the Lanthanides, ed. S.P. Sinha (Reidel, Dordrecht) p. 213.
Skriver, H.L., and I. Mertig, 1990, Phys. Rev. **41**, 6553.
Skriver, H.L., O.K. Andersen and B. Johansson, 1978, Phys. Rev. Lett. **41**, 42.
Skriver, H.L., O.K. Andersen and B. Johansson, 1980, Phys. Rev. Lett. **44**, 1230.
Slater, J.C., 1968, Phys. Rev. **165**, 165.
Smith, G.S., and J. Akella, 1982, J. Appl. Phys. **53**, 9212.
Stearns, M.B., 1986, in: Landolt-Börnstein Numerical Data and Functional Relationships in Science and Technology, Group 3, Vol. 19, Pt. a, ed. H.P.J. Wijn (Springer, Berlin).
Sticht, J., and J. Kübler, 1985, Solid State Commun. **53**, 529.
Stoner, E.C., 1938, Proc. R. Soc. London **165**, 372.
Svane, A., and O. Gunnarsson, 1990, Phys. Rev. Lett. **65**, 1148.
Szotek, Z., W.M. Temmerman and H. Winter, 1991, Physica B, to be published in 1993.
Szpunar, B., 1985, Physica B **130**, 29.
Szpunar, B., and V.H. Smith Jr, 1990, J. Solid State Chem. **88**, 217.
Szpunar, B., and P. Strange, 1985, J. Phys. F **15**, L165.
Szpunar, B., and J.A. Szpunar, 1985, J. Appl. Phys. **57**, 4130.
Szpunar, B., and W.E. Wallace, 1986, Lanthanide and Actinide Research **1**, 335.
Temmerman, W.M., and P.A. Sterne, 1990, J. Phys.: Condens. Matter **2**, 5229.
Terakura, K., 1977, J. Phys. F **7**, 1773.
Tibbetts, T.A., and B.N. Harmon, 1982, Solid State Commun. **44**, 1409.
Trygg, J., B. Johansson and M.S.S. Brooks, 1991, J. Magn. & Magn. Mater. **104–107**, 1447.
Ubachs, W., A.P.J. van Deursen, A.R. de Vroomen and A.J. Arko, 1986, Solid State Commun. **60**, 7.
Velge, W.A.J.J., and K.H.J. Buschow, 1968, J. Appl. Phys. **39**, 1717.
von Barth, U., and L. Hedin, 1972, J. Phys. C **5**, 1629.
Vosko, S.H., and J.P. Perdew, 1975, Can. J. Phys. **53**, 1385.
Vosko, S.H., J.P. Perdew and A.H. MacDonald, 1975, Phys. Rev. Lett. **35**, 1725.
Wedgwood, F.A., 1972, J. Phys C **5**, 2427.

Wedgwood, F.A., and M. Kuznietz, 1972, J. Phys. C **5**, 3012.
Wells, P., P.C. Lanchester, W.D. Jones and R.G. Jordon, 1974, J. Phys. F **4**, 1729.
Williams, A.R., V.L. Moruzzi, J. Kübler and K. Schwarz, 1984, Bull. Am. Phys. Soc. **29**, 278.
Wohlfarth, E.P., and P. Rhodes, 1962, Philos. Mag. **7**, 1817.
Wulff, M., G.G. Lonzarich, D. Fort and H.L. Skriver, 1988, Europhys. Lett. **7**, 629.
Wulff, M., G.H. Lander, B. Lebech and J. Delapalme, 1989, Phys. Rev. B **39**, 4719.
Wulff, M., J.M. Fournier, A. Delapalme, B. Gillon, A. Sechovsky, L. Havela and A.V. Andreev, 1990, Physica B **163**, 331.
Yamada, H., 1988, Physica B **149**, 390.
Yamada, H., and M. Shimizu, 1985, J. Phys. F **15**, L175.
Yamada, H., and M. Shimizu, 1986, J. Phys. F **16**, 1039.
Yamada, H., J. Inoue, J. Terao, S. Kanda and M. Shimizu, 1984, J. Phys. F **14**, 1943.
Zachariasen, W.H., 1973, J. Inorg. Nucl. Chem. **35**, 3487.
Zachariasen, W.H., and F.H. Ellinger, 1975, Acta Crystallogr. A **33**, 155.
Zhong, X.F., and W.Y. Ching, 1987, Phys. Rev. B **40**, 5992.

chapter 4

DILUTED MAGNETIC SEMICONDUCTORS

J. KOSSUT and W. DOBROWOLSKI

Institute of Physics of the Polish Academy of Sciences
Warsaw
Poland

Handbook of Magnetic Materials, Vol. 7
Edited by K. H. J. Buschow

CONTENTS

1. Introduction

The substantial growth of interest in semiconducting mixed crystals containing magnetic impurities can be traced back to the middle of the seventies, although scattered papers on these materials appeared in the literature considerably earlier. Diluted magnetic semiconductors (DMS)[1], as they became to be known, have been the subject of several review articles (see, e.g., Gałązka 1978, Gaj 1980, Takeyama and Narita 1980, J. Mycielski 1981, Furdyna 1982, Grynberg 1983, Brandt and Moshchalkov 1984, Lyapilin and Tsidil'kovskii 1985, Dietl 1987, Gałązka 1987, Furdyna 1988, A. Mycielski 1988, Furdyna and Kossut 1988). Nevertheless, recent developments in this field have appeared that still have to be studied from a fair amount of scattered original papers (e.g., 29 papers concerning DMS were presented at the most recent International Conference on the Physics of Semiconductors held in Thessaloniki in August 1990). One of the aims of this chapter is to review these new aspects of diluted magnetic semiconductor physics and provide a literature guide that would help the student of the subject to keep abreast of new results. This does not mean that we intend to neglect the presentation of the established achievements in the field. We will also provide an update of various numerical data that are relevant to DMS materials.

Although this series of volumes is primarily devoted to magnetic properties of materials, the specific nature of DMS makes it impossible to leave out those properties that are typical for semiconductors. Moreover, the two sides of the problem are interrelated and simply cannot be considered in isolation from each other. For these reasons this chapter is organized in the following way: in the introductory part the reader will find information concerning crystal structures and lattice constants of diluted magnetic semiconductors. The next section is devoted to the properties of these semiconducting mixed crystals in the absence of an external magnetic field. In this section we concentrate on quantities typically considered when discussing semiconducting materials, such as, e.g., energy gaps separating valence and conduction bands. Magnetic properties are presented in section 3, which is followed by section 4 where properties that single out DMS as a separate group of materials are discussed, namely those that are connected with a mutual dependence of the magnetic and semiconducting properties. This interdependence stems from strong exchange coupling between the conduction band electrons and/or valence band holes with the localized

[1] The term 'semimagnetic semiconductors' is also widely used to denote DMS.

electrons from 3d shells of 'magnetic' ions which form localized magnetic moments.

The materials that are most commonly considered as the members of the DMS family are substitutional solid solutions of II–VI semiconductors and transition-metal monochalcogenides, e.g., CdTe and MnTe. This was certainly the group of DMS studied most often in the past, in particular those containing manganese. In recent years, studies involving materials containing other transition-metal ions (e.g., iron and cobalt) started to become more and more popular. However, the number of papers on these new compounds appearing in the current literature is still smaller than that on traditional manganese-based DMS. Apart from the II–VI materials alloyed with transition-metal chalcogenides also IV–VI semiconductors were investigated quite intensively. It was in the latter DMS materials that the reciprocal influence of the 'semiconducting' band carriers on the magnetic properties was most clearly demonstrated (see section 3.2.5). Also, II–V semiconductors were sometimes used as host matrices for the preparation of DMS. Similarly, though less frequently, it was attempted to incorporate 'magnetic' ions other than those from the transition-metal series. These more exotic materials will, thus, find only a residual place in the present review.

1.1. Crystal structures and ranges of compositions of DMS mixed crystals

In all cases that are of present interest the 'magnetic' transition-metal ions are substituted for the cations in a host semiconductor. Certainly, their position is not a perfect lattice position in the cation sublattice – there are considerable lattice distortions visible in more detailed studies of the crystallographic structure of DMS (see section 1.2). This fact probably limits the amount of transition-metal ions that can be incorporated in a stable form of various DMS. Moreover, the lattice structure of, e.g., manganese chalcogenides is often different from the tetrahedrally coordinated (either cubic zinc-blende or hexagonal wurtzite) structure of II–VI semiconductors. For example, in the case of MnTe – which is the most common component of DMS – the crystal structure is of the NiAs type. Surprisingly, it is in alloys of MnTe and II–VI semiconductors that the highest molar fractions of the magnetic component were achieved. The miscibility of manganese with II–VI hosts is particularly large, as compared to other transition-metal ions. The possibility of obtaining crystals in which the amount of the magnetic component can be varied in a semi-continuous fashion within wide limits, is one of the reasons why DMS acquired such a large interest in the scientific community. The available molar range of transition-metal chalcogenide depends, of course, on the specific components being chosen. Table 1 lists the range of molar fractions in which various DMS alloys were obtained. Table 1 also provides information concerning the crystallographic structure of these compounds. With new growth techniques becoming available (molecular beam epitaxy – MBE – being the most important) it is possible to obtain materials which were previously considered only in the sense of 'hypothetical' crystals that did not exist in nature and whose physical properties were obtained by extrapolation to, e.g., $x=1$. Growth of the zincblende form of MnSe (which normally crystallizes in the rocksalt structure) by MBE represents the best example of these new opportunities (see Kolodziejski et al. 1986a). The growth techniques used to achieve such materials are, of course, non-

equilibrium methods. Therefore, the upper limits given in table 1 have to be regarded as the greatest amount of the magnetic component that has been successfully incorporated in DMS materials rather than true thermodynamic solubility limits.

1.2. Dependence of lattice constants on composition

A systematic study of lattice parameters has been done only in the case of DMS based on II–VI compounds. The lattice parameters were found to vary in proportion

TABLE 1
Crystal structures and ranges of composition of DMS mixed crystals.

Compound	Ref.*	Crystal structure	Composition range
$Zn_{1-x}Mn_xS$	[1,2]	zincblende	$0 < x < 0.1$
	[1,2]	wurtzite	$0.1 < x < 0.45$
$Zn_{1-x}Mn_xSe$	[1,2]	zincblende	$0 < x < 0.30$
	[1,2]	wurtzite	$0.3 < x < 0.57$
	[3]	zincblende	$0 < x < 1$
$Zn_{1-x}Mn_xTe$	[1,2]	zincblende	$0 < x < 0.86$
$Cd_{1-x}Mn_xS$	[1,2]	wurtzite	$0 < x < 0.45$
$Cd_{1-x}Mn_xSe$	[1,2]	wurtzite	$0 < x < 0.50$
	[4]	zincblende	$0 < x < 0.75$
$Cd_{1-x}Mn_xTe$	[1,2]	zincblende	$0 < x < 0.77$
$Hg_{1-x}Mn_xS$	[1,2]	zincblende	$0 < x < 0.37$
$Hg_{1-x}Mn_xSe$	[1,2]	zincblende	$0 < x < 0.38$
$Hg_{1-x}Mn_xTe$	[1,2]	zincblende	$0 < x < 0.75$
$(Cd_{1-x}Mn_x)_3As_2$	[5–7]	tetragonal	$0 < x < 0.12$
$(Zn_{1-x}Mn_x)_3As_2$	[5–7]	tetragonal	$0 < x < 0.15$
$Pb_{1-x}Mn_xS$	[8–10]	rocksalt	$0 < x < 0.05$
$Pb_{1-x}Mn_xSe$	[8–10]	rocksalt	$0 < x < 0.17$
$Pb_{1-x}Mn_xTe$	[8–10]	rocksalt	$0 < x < 0.40$
$Zn_{1-x}Fe_xS$	[11–14]	zincblende	$0 < x < 0.26$
$Zn_{1-x}Fe_xSe$	[11–14]	zincblende	$0 < x < 0.21$
$Zn_{1-x}Fe_xTe$	[11–14]	zincblende	$0 < x < 0.01$
$Cd_{1-x}Fe_xSe$	[11–14]	wurtzite	$0 < x < 0.20$
$Cd_{1-x}Fe_xTe$	[11–15]	zincblende	$0 < x < 0.03$
$Hg_{1-x}Fe_xSe$	[11–14]	zincblende	$0 < x < 0.20$
$Hg_{1-x}Fe_xTe$	[11–14]	zincblende	$0 < x < 0.02$
$Zn_{1-x}Co_xS$	[16]	zincblende	$0 < x < 0.15$
$Zn_{1-x}Co_xSe$	[16]	zincblende	$0 < x < 0.05$
$Cd_{1-x}Co_xSe$	[17,18]	wurtzite	$0 < x < 0.08$

*References:

[1] Furdyna (1988).
[2] Giriat and Furdyna (1988).
[3] Gunshor et al. (1987).
[4] Samarth et al. (1989).
[5] Żdanowicz et al. (1983).
[6] Denissen (1986).
[7] Pietraszko and Łukaszewicz (1979).
[8] Schultz and Weiss (1984).
[9] Bauer (1987).
[10] Madelung (1982).
[11] Swagten et al. (1990).
[12] A. Mycielski (1988).
[13] Twardowski (1990a).
[14] Twardowski (1991).
[15] Sarem et al. (1990).
[16] Lewicki et al. (1989).
[17] Nawrocki et al. (1991).
[18] Bartholomew et al. (1989).

with the molar fraction of the magnetic component. For example, in the case of a zincblende structure the lattice parameter obeys Vegard's law

$$a = (1 - x)a_{\text{II-VI}} + xa_{\text{TM-VI}}, \tag{1.1}$$

where x is the molar fraction of the transition-metal chalcogenide, $a_{\text{TM-VI}}$ and $a_{\text{II-VI}}$ represent the lattice constants of the endpoint binary compounds: a transition-metal chalcogenide in the (hypothetical) zincblende phase and a II–VI host, respectively. An example of such linear behavior is shown in fig. 1 for the MnTe family of II–VI DMS. It is quite remarkable that all three compounds shown in fig. 1 can be extrapolated to a single value of the lattice constant of cubic MnTe, although this latter material normally does not crystallize in the zincblende structure but, as mentioned above, in the NiAs structure. As we shall see in section 2, extrapolations of the energy gap versus molar fraction to $x = 1$ for various II–VI matrices also lead to one value of the energy gap in this 'hypothetical' manganese compound.

In view of the diversity of possible lattice structures (zinc-blende and wurtzite) that various II–VI DMS can acquire, it is useful to introduce the notion of the cation–cation distance in terms of which a description can be given without specifying the explicit structure of the material. This approach is particularly convenient (see Furdyna and Kossut 1986) in the case of DMS whose structure changes from zincblende to wurtzite as the amount of the magnetic component increases. This happens in the case of, e.g., $Zn_{1-x}Mn_xSe$ (see table 1). The possibility to describe zincblende and wurtzite structures in a unified way is closely related to inherent similarities of these two structures (both being examples of tetrahedrally bonded structures). The mean value of the cation–cation distance in the case of the zincblende structure is given by $d = 2^{1/2}\,a$, and in the case of the wurtzite structure by either $d = a$ or $d = (\frac{3}{8})^{1/2}c$ (both definitions becoming equivalent for the ideal wurtzite structure, i.e., when $a = (\frac{3}{8})^{1/2}c$). Figure 2 shows the variation of the cation–cation distance in II–VI-based DMS containing manganese. It is again remarkable that even in the region where the crystal structure changes, the dependence of the cation–cation distance on the molar fraction is smooth. It must be mentioned at this point that in the transition region between the zincblende and wurtzite phases the crystals usually display pronounced polytypism

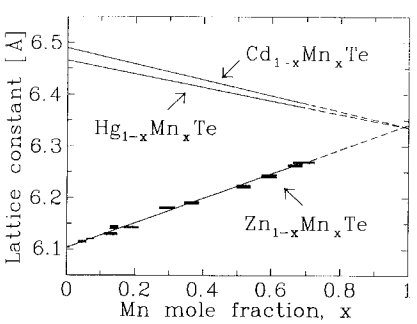

Fig. 1. Lattice constant as a function of MnTe molar fraction in the telluride family of DMS (after Furdyna 1988).

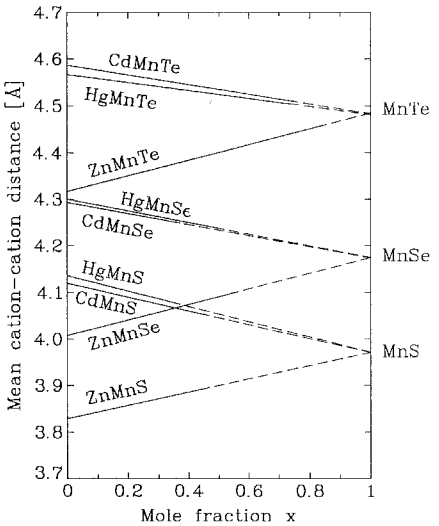

Fig. 2. Mean cation–cation distances in the II–VI family of DMS with Mn (after Furdyna 1988).

that may result in a considerable scatter of values of, e.g., the fundamental energy gap (Bylsma et al. 1986).

Unfortunately, there is a lack of lattice parameter data as functions of the composition of IV–VI-based DMS materials. It can be expected that Vegard's law should be even more strictly obeyed in the case of MnSe and MnS compounds because their

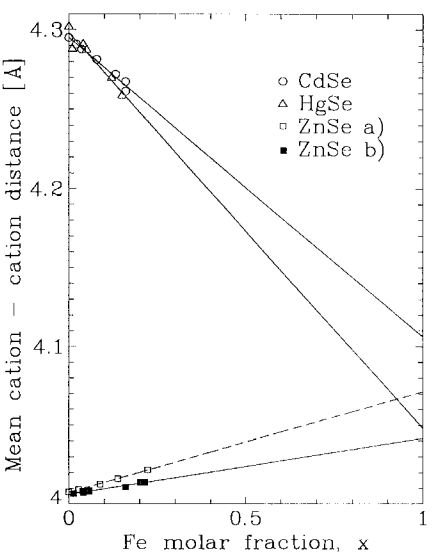

Fig. 3. Mean cation–cation distance in selenide DMS that contains iron. Data for $Cd_{1-x}Fe_xSe$ are from Dynowska et al. (1990). The data for $Hg_{1-x}Fe_xSe$ are unpublished results of Dynowska et al., and the data for $Zn_{1-x}Fe_xSe$ are from Jonker et al. (1988).

TABLE 2
Coefficients for the linear (Vegard's law) dependence of the cation–cation distance in Mn and Fe containing II–VI diluted magnetic semiconductors.

Compound	Mean cation–cation distance d (Å)	Ref.*
$Zn_{1-x}Mn_xS$	$3.830 + 0.139x$	[1]
$Zn_{1-x}Mn_xSe$	$4.009 + 0.164x$	[1]
$Zn_{1-x}Mn_xTe$	$4.315 + 0.168x$	[1]
$Cd_{1-x}Mn_xS$	$4.123 - 0.151x$	[1]
$Cd_{1-x}Mn_xSe$	$4.296 - 0.123x$	[1]
$Cd_{1-x}Mn_xTe$	$4.587 - 0.105x$	[1]
$Hg_{1-x}Mn_xS$	$4.139 - 0.167x$	[1]
$Hg_{1-x}Mn_xSe$	$4.301 - 0.123x$	[1]
$Hg_{1-x}Mn_xTe$	$4.568 - 0.080x$	[1]
$Zn_{1-x}Fe_xSe$	$4.007 + 0.064x$	[2]
	$4.006 + 0.036x$	[3]
$Cd_{1-x}Fe_xSe$	$4.295 - 0.184x$	[4]
$Cd_{1-x}Fe_xTe$	$4.583 - 0.267x$	[6]
$Hg_{1-x}Fe_xSe$	$4.298 - 0.250x$	[5]

*References:
[1] Yoder-Short et al. (1985). [4] Dynowska et al. (1990).
[2] Jonker et al. (1987). [5] Dynowska et al., unpublished data.
[3] Twardowski (1990b). [6] Sarem et al. (1990).

crystallographic structure matches that of the matrix which crystallizes also in the rocksalt structure.

Figure 3 shows the variation of the mean cation–cation distance in II–VI DMS containing Fe. The extrapolation to $x = 1$ displays a much larger scatter of the extrapolated values than in the case of manganese compounds. One of the reasons for this fact is that the existing data belong to a much smaller range of crystal compositions, $x < 0.15$. Furthermore, in the case of $Zn_{1-x}Fe_xSe$ part of the data points was obtained on MBE-growth layers whose lattice constants were to some degree distorted by strains introduced by the lattice mismatch with the substrate.

The numerical constants that appear in the Vegard's law for the mean cation–cation distance are gathered in table 2 for all DMS compounds for which such data are available in the literature.

1.3. Local distortions of the crystalline lattice

In the preceding section we have discussed the behaviour of mean values of lattice parameters as studied by standard X-ray diffraction techniques. These methods confirmed a strict adherence to Vegard's law. On the other hand, extended X-ray absorption fine structure (EXAFS) studies revealed a picture of the lattice of DMS that is much more complicated. The EXAFS technique is able to provide detailed information concerning distances between pairs of atoms of specified types. Similar to III–V ternary compounds (where the phenomenon was discovered first by Mikkelsen and Boyce 1982) the distance between a cation and an anion (i.e., the bond length) in the

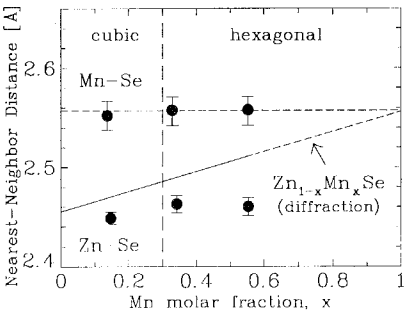

Fig. 4. The MnSe and ZnSe bond lengths from EXAFS data of Bunker (1987). Also shown is the mean nearest-neighbor distance deduced from X-ray diffraction experiments displaying a linear variation with the Mn contents.

entire region of crystal compositions of DMS ternary compound preserves the value characteristic for the binary compound. This is clearly shown in fig. 4 for $Zn_{1-x}Mn_xSe$. This constancy of the bond length can only mean that the real crystal lattice is highly distorted locally. According to the analysis of very recent X-ray data of Abrahams et al. (1989) it is likely that in $Cd_{1-x}Mn_xTe$ the cation sublattice as well as the anion sublattice are distorted, contrary to the original assumption of Balzarotti et al. (1984, 1985) who stated that the cations form an undistorted fcc sublattice. The existence of local distortions in the DMS crystal lattice has important implications. For instance, the selection rules for various optical transitions (which are derived under the assumption that there are strict symmetries that the lattice has to possess) must be relaxed.

2. Band structure of DMS in the absence of a magnetic field

2.1. General considerations

The band structure of DMS is derived naturally from the band structure of the parent nonmagnetic semiconductor. Figure 5 shows schematically the sequence of the conduction and valence band edges in wide-gap semiconductors (say, zinc- and cadmium-based II–VI compounds) with zincblende and wurtzite structures. In both cases the minimum of the conduction band and the maximum of the valence band occur at the center of the Brillouin zone. Note that in the case of the wurtzite structure the degeneracy of light and heavy hole bands is lifted since this structure may be viewed, in a first approximation, as the zincblende structure with additional axial deformation. The splitting by the crystal field results, e.g., in the existence of two distinct exciton lines observable in optical experiments with $Cd_{1-x}Mn_xSe$.

Quite different ordering of the bands occurs in narrow-gap mercury compounds. Their crystal structure being also that of zincblende, these compounds are known to possess an inverted band structure (see fig. 6a) with symmetry-induced degeneracy of the conduction and heavy hole valence bands both of which have their respective edge states of p-like symmetry (in contrast to the 'normal' ordering of the bands

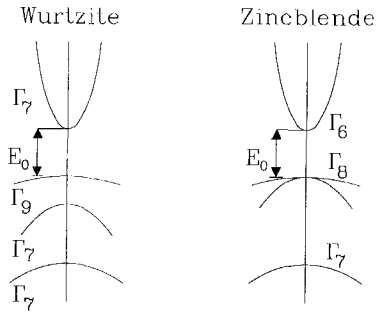

Fig. 5. Schematic representation of the band structure in the vicinity of the fundamental band edges at the center of the Brillouin zone in wide-gap II–VI semiconductors with wurtzite and zincblende crystal structure.

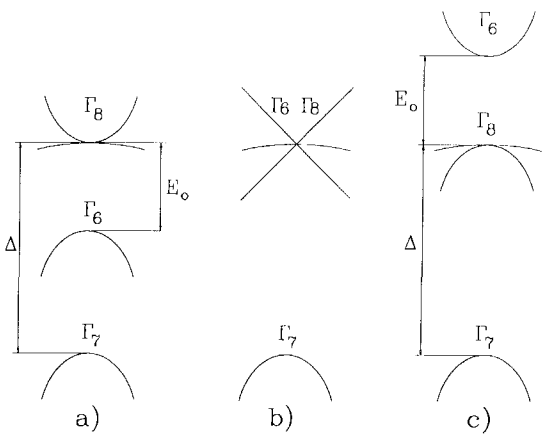

Fig. 6. Schematic representation of the band structure in narrow-gap II–VI zincblende semiconductors in the vicinity of the fundamental band gap in the center of the Brillouin zone. (a) Semimetallic configuration with symmetry-induced degeneracy of the conduction and heavy hole bands; (b) coincidental degeneracy of the conduction, heavy and light hole bands; (c) semiconducting (open gap) configuration. E_0 denotes the interaction energy gap, Δ spin–orbit splitting of the p-like Γ_{15} band.

when mostly s-like conduction Γ_6 band is separated by an energy gap from fourfold degenerate p-like valence band – see fig. 6c).

Figure 7 presents the scheme of the position of the band edges in IV–VI semiconductors (lead chalcogenides) with rocksalt structure. The band extrema occur at the L point of the Brillouin zone. The valence and the conduction bands are nearly mirror-like reflections of each other. The surfaces of constant energy are, to a good approximation, ellipsoids of revolution. In lead chalcogenides the conduction band edge is formed by the states of odd parity whereas the valence band edge states are of even parity. In the case of tin chalcogenides the sequence of the conduction and valence bands is reversed: L_6^+ (even parity wave functions) becomes the conduction band edge, while L_6^- (odd parity wave functions) is the valence band edge.

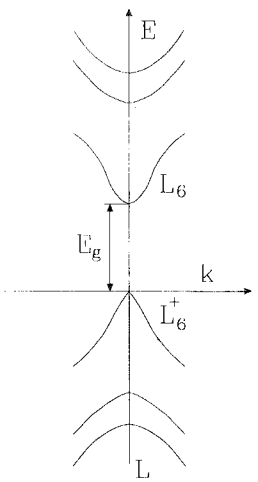

Fig. 7. Schematic representation of the band structure in lead chalcogenides in the vicinity of the fundamental energy gap at the L point of the Brillouin zone. Apart from the conduction L_6^- and valence L_6^+ bands also four remote bands are shown.

When a transition-metal atom is substituted for a cation in DMS, in the crudest approximation, two of its valence s electrons form sp bonds. They are responsible for modifications of the conduction and valence band edges to be described shortly. The description of their effect on the band structure of the host semiconductor can be done in terms of a suitable average medium theory, e.g., the virtual crystal approximation or another appropriate theoretical procedure (see, e.g., Hass and Ehrenreich 1983, Ehrenreich et al. 1987, Wei and Zunger 1987a,b, Gunnarson et al. 1989, Masek and Velicky 1987, Hui et al. 1989) employed in the case of semiconducting mixed crystals. On the other hand, the electrons originating from the partially filled d shell of a transition-metal atom retain their considerably more localized character although the spatial extension of their wave functions does increase, due to hybridization with electronic states of the host semiconductor. They give rise to new narrow photoemission features observed in many experimental studies (e.g., Webb et al. 1981, Ley et al. 1987, Oelhafen et al. 1982, Taniguchi et al. 1986, 1987, Franciosi et al. 1985a,b, 1989, Franciosi 1987, Wall et al. 1987, Orłowski et al. 1984, Velicky et al. 1986). Again, $A^{II}_{1-x}Mn_xB^{VI}$ alloys were studied most extensively in this respect. The energy of the state that is derived mostly from the ground state of Mn^{2+} $3d^5$ electrons is approximately 3.5 eV below the valence band edge, i.e., relatively far from the band edges which determine basic properties of a semiconductor, such as conductivity. It is interesting to note that the position of this manganese-derived state is rather insensitive to II–VI semiconducting host. The fact that the energy of the manganese 3d level is roughly the same, even in DMS differing in their anion constituents (e.g., in $Cd_{1-x}Mn_xTe$ and $Cd_{1-x}Mn_xSe$) is somewhat puzzling, particularly in view of the recent hypothesis (Langer and Heinrich 1985, Caldas et al. 1984) which equates the position of the 3d level of a transition-metal impurity and a common reference point

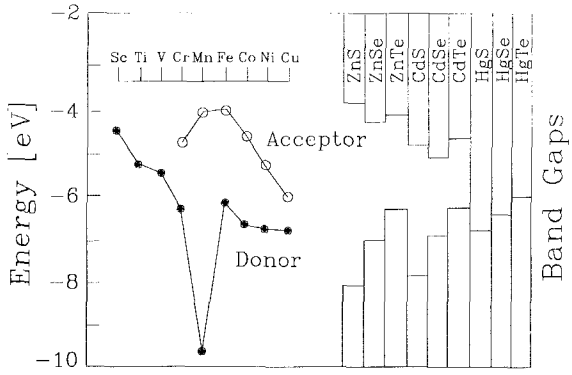

Fig. 8. Position of the acceptor-like and donor-like impurity levels of transition-metal impurities in various II–VI semiconductors showing also the relative energetic position of the conduction and valence band edges of the hosts (from Zheng et al. 1990).

for an energy scale from which valence and conduction band offsets between various semiconductors can be deduced (see fig. 8). An excited state that corresponds to placing an extra electron on the 3d shell is also observable in the inverted photoemission experiments which place it at about 3.5 eV above the top of valence band in $Cd_{1-x}Mn_xTe$ (Wall et al. 1989). As we shall see below, the positions of these two states are very important in determining exchange constants via the hybridization mechanism of the p–d type as well as of the d–d type (e.g., Mn–Mn) (Bhattacharjee et al. 1983, Hass et al. 1986, Larson et al. 1985, 1988).

Other possible excitations of Mn^{2+} ions exist that do not change the number of electrons occupying the 3d shell but only flip the spin direction of some of such electrons. In fact such transitions to these states often govern the optical properties of DMS whose energy gaps exceed 2.2 eV. We shall return to this problem in section 2.3.

Returning to the position of the ground state derived from the 3d states of a transition-metal atom let us note that in the majority of cases it is split by the crystal field of the semiconductor matrix. In the case of Mn with a half-filled 3d shell the ground state is an orbital *singlet*, and cannot be further split by the crystal field. Such splitting does exist in the case of other transition metals whose ground states are not orbital singlets. Very often the states introduced by transition-metal atoms into the semiconductor host band structure are situated within the fundamental band gap. They are also quite often electrically active, either donating or accepting band electrons. Manganese is unique in this sense since its ground state is located deep within the valence band – see fig. 8 – and is neither a donor nor an acceptor. A discussion of theoretical aspects of transition-metal impurities is semiconductors can be found, e.g., in the review by Zunger (1986).

2.2. Dependence of the band gap on composition

The variation of the fundamental band gap with the concentration in diluted magnetic semiconductors can be described, in a first approximation, by a linear dependence.

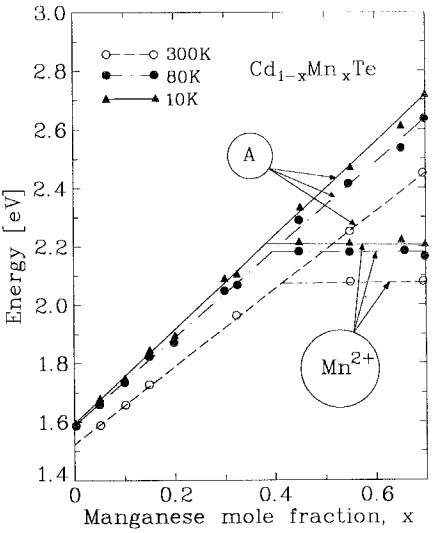

Fig. 9. Energy position of piezomodulated reflectivity features as functions of Mn molar fraction in $Cd_{1-x}Mn_xTe$ at three temperatures. 'A' represents the transitions across the fundamental energy gap, 'Mn^{2+}' represents the internal optical transition between the ground and excited levels of Mn ions (from Lee and Ramdas 1984).

Figure 9 shows the values of the fundamental optical energy gap determined experimentally in $Cd_{1-x}Mn_xTe$ at several temperatures. The saturation observed for $x > 0.4$ results from very efficient optical transitions within the Mn^{2+} ions (see section 2.3) whereas the gap variation is given by the position of a weaker feature labelled A in fig. 9 observed by Lee and Ramdas (1984) in the piezomodulated reflectivity experiments. When an extrapolation to $x = 1$ is made the value of the energy gap in hypothetical zincblende MnTe is obtained. Its value at low temperatures is about 3.5 eV. The same extrapolated value is obtained in the case of $Zn_{1-x}Mn_xTe$ and $Hg_{1-x}Mn_xTe$. In the latter alloy the addition of Mn ions causes an upward shift of the Γ_6 light hole band with respect to the Γ_8 level (see fig. 6). The shift results, at first, in a decrease of the Γ_6–Γ_8 distance, i.e., of the absolute value of the, so-called, interaction gap. The reduction of the interaction gap value is reflected in a decrease of the effective mass value at the conduction band edge. When the content of manganese grows from $x = 0$, a molar fraction is reached where an accidental degeneracy of the conduction, heavy hole and light hole bands takes place (triple degeneracy point) – see fig. 6b. When the Mn molar fraction is further increased the Γ_6 level acquires a position above the Γ_8 level and becomes the conduction band while the Γ_8 level corresponds to light and heavy hole band edges and a real energy gap opens up – see fig. 6c. This behavior is quite analogous to that known from the more familiar case of $Hg_{1-x}Cd_xTe$. However, in the case of manganese substituted for mercury atoms, the changes of the Γ_8–Γ_6 energy distance occur at a rate that is twice as large as in $Hg_{1-x}Cd_xTe$: the point of coincidence of the Γ_8 and Γ_6 levels corresponds to $x = 0.07$ in $Hg_{1-x}Mn_xTe$ while in $Hg_{1-x}Cd_xTe$ it occurs for $x = 0.16$.

Similar reversal of the sequence of the conduction and valence bands upon alloying occurs in the $Pb_{1-x}Sn_xTe$ system where at a certain concentration of tin the L_6^- level (which in PbTe is the edge of the conduction band) becomes the valence band edge and, vice versa, the L_6^+ level (valence band maximum in PbTe) becomes the conduction band edge. On the other hand, alloying lead chalcogenides with manganese results in an increase of the energy gap, i.e., the L_6^- and L_6^+ levels move further away from each other.

The coefficients that describe the behavior of the fundamental energy gap in DMS containing manganese are gathered in table 3. There are also two entries for DMS containing iron.

It was found (see, e.g., Kendelewicz 1980, 1981) that the energy distances between the conduction and the valence bands at various characteristic points of the Brillouin zone, other than those of the absolute minimum or maximum of the bands, change also linearly with x upon alloying with Mn.

The possibility of tuning the band gap of DMS, a feature characteristic for many other semiconducting alloy systems, represents an advantageous feature since by

TABLE 3

Fundamental energy gap in DMS as a function of alloy composition. The symbols $E^\perp$ and $E^\parallel$ refer to the $(\Gamma_{9v}-\Gamma_{7c})$ and $(\Gamma_{7v}-\Gamma_{7c})$ energy gaps, respectively, i.e., to the results of optical measurements making use of light polarized, respectively, perpendicular and parallel to the c axis of the wurtzite structure of $Cd_{1-x}Mn_xSe$.

Alloy	E_g (eV)	T (K)	Range of x	Ref.*
$Zn_{1-x}Mn_xS$	3.8–3.9			[1]
$Zn_{1-x}Mn_xSe$	2.8 minimum at $x \sim 0.01$	2.2	$x = 0$	[2]
	2.8 minimum for $0 < x < 0.2$	6.5	$x = 0$	[3]
	$dE/dx \approx 0.58$		$x > 0.3$	[3]
$Zn_{1-x}Mn_xTe$	$2.377 + 3.656x$	1.6	$0.01 \leqslant x < 0.15$	[4]
	$2.381 + 0.68x$ minimum for $x < 0.01$	2.2	$x > 0.02$	[4]
	$2.271 + 0.518x$	300	$0 \leqslant x \leqslant 0.6$	[5]
	$2.365 + 0.721x$	80	$0 \leqslant x < 0.6$	[5]
	$2.376 + 0.820x$	10	$0 \leqslant x < 0.6$	[5]
$Cd_{1-x}Mn_xS$	2.45 minimum at $x \sim 0.03$ $dE/dx \sim 0.9$ $x \geqslant 0.1$	298	$x = 0$	[6]
$Cd_{1-x}Mn_xSe$	$1.70 + 1.08x$	300	$0 < x < 0.5$	[7]
	$E^\perp$ $1.705 + 1.23x$	297	$0 < x < 0.3$	[8]
	$E^\parallel$ $1.725 + 1.23x$	297	$0 < x < 0.3$	[8]
	$E^\perp$ $1.800 + 1.33x$	86	$0 < x < 0.3$	[8]
	$E^\parallel$ $1.829 + 1.33x$	86	$0 < x < 0.3$	[8]
	$1.807 + 1.318x$	LN_2	$0 < x < 0.3$	[9]
	$1.821 + 1.54x$	2	$0 \leqslant x \leqslant 0.277$	[10]

TABLE 3 (*continued*)

Alloy	E_g (eV)	T (K)	Range of x	Ref.*
	$E^{\perp}$ 1.74 + 1.16x	300	$0 < x < 0.5$	[11]
	$E^{\parallel}$ 1.756 + 1.13x	300	$0 < x < 0.5$	[11]
	$E^{\perp}$ 1.807 + 1.34x	80	$0 < x < 0.5$	[11]
	$E^{\parallel}$ 1.833 + 1.31x	80	$0 < x < 0.5$	[11]
	$E^{\perp}$ 1.818 + 1.42x	10	$0 < x < 0.5$	[11]
	$E^{\parallel}$ 1.842 + 1.40x	10	$0 < x < 0.5$	[11]
$Cd_{1-x}Mn_xTe$	1.585 + 1.51x	77	$0 < x < 0.5$	[12]
	1.595 + 1.587x	LHe	$0 < x < 0.2$	[13]
	1.50 + 1.44x	300	$0 < x \leqslant 0.6$	[14]
	1.586 + 1.393x	76	$0 < x \leqslant 0.7$	[15]
	1.53 + 1.26x	300	$0 < x < 0.7$	[16]
	1.528 + 1.316x	300	$0 < x \leqslant 0.7$	[17]
	1.586 + 1.50x	80	$0 < x \leqslant 0.7$	[17]
	1.595 + 1.592x	10	$0 < x \leqslant 0.7$	[17]
$Hg_{1-x}Mn_xSe$	$-0.272 + 4.4x$	LHe	$0 < x \leqslant 0.11$	[18, 19]
	$dE/dT = 6.8 - 22x$ (for $T < 40$ K) ($\times 10^{-4}$ eV K^{-1})			[19]
$Hg_{1-x}Mn_xTe$	$-0.303 + 4.3x$	LHe	$0 < x \leqslant 0.2$	[20–23]
	$dE/dT = 5.8 - 24x$ (for $T < 60$ K) ($\times 10^{-4}$ eV K^{-1})			[25]
$Pb_{1-x}Mn_xS$	$0.266 + 3.2x$ (for $4 < T < 300$ K) $+ 10^{-3}[(0.044 - 2.3x)^2 T^2 + 400]^{1/2}$		$x \leqslant 0.032$	[24]
$Pb_{1-x}Mn_xSe$	$0.130 + 2.8x$ (for $4 < T < 300$ K) $+ 10^{-3}[(0.442 - 2.2x)^2 T^2 + 400]^{1/2}$		$x \leqslant 0.05$	[25]
$Pb_{1-x}Mn_xTe$	$0.190 + 0.38x$	4	$x \leqslant 0.01$	[26]
$Zn_{1-x}Fe_xSe$	2.8 + 0.21x	1.8	$x \leqslant 0.06$	[27]
$Cd_{1-x}Fe_xSe$	1.82 + 1.2x	1.8	$x \leqslant 0.034$	[28]

* References:

[1] Becker (1988).
[2] Twardowski et al. (1983).
[3] Bylsma et al. (1986).
[4] Twardowski et al. (1984).
[5] Lee et al. (1986).
[6] Ikeda et al. (1968).
[7] Wiedemeier and Sigai (1970).
[8] Antoszewski and Kierzek-Pecold (1980).
[9] Giriat and Stankiewicz (1980).
[10] Wiśniewski and Nawrocki (1983).
[11] Lee et al. (1987).
[12] Gaj et al. (1978a).
[13] Twardowski et al. (1979).
[14] Bottka et al. (1981).
[15] Vecchi et al. (1981).
[16] Lautenschlager et al. (1985).
[17] Lee and Ramdas (1984).
[18] Takeyama and Gałązka (1979).
[19] Dobrowolska et al. (1981).
[20] Kaniewski and Mycielski (1982).
[21] Bastard et al. (1978).
[22] Jaczyński et al. (1978a).
[23] Dobrowolska and Dobrowolski (1981).
[24] Karczewski et al. (1982).
[25] Le Van Khoi et al. (1991).
[26] Bauer (1987).
[27] Twardowski et al. (1987b).
[28] Scalbert et al. (1989b).

adjusting the composition one can achieve a gap value required by particular application needs. An even greater degree of freedom than in the case of ternary alloys is offered by quaternary systems, such as $Hg_xCd_yMn_zTe$ ($x + y + z = 1$). The band gap energy can in such a case be obtained by a simple interpolation scheme (Williams et al. 1978)

$$E_g(x, y, z) = \frac{xyE_g(Hg_{1-v}Cd_vTe) + yzE_g(Cd_{1-w}Mn_wTe) + xzE_g(Hg_{1-u}Mn_uTe)}{xy + yz + zx}, \tag{2.1}$$

where

$$u = \tfrac{1}{2}(1 - x + z),$$

$$v = \tfrac{1}{2}(1 - x + y),$$

$$w = \tfrac{1}{2}(1 - y + z).$$

It has been verified experimentally in several quaternary DMS systems that equations analogous to eq. (2.1) provide a good description of the variations upon alloying observed of many other parameters ranging from lattice constants to various differences between characteristic band energies (see, e.g., Kim et al. 1982, Niewodniczańska-Zawadzka et al. 1985, Takeyama and Narita 1986a, Quintero and Woolley 1985, Chehab and Woolley 1985, 1987, Donofrio et al. 1985, Brun del Re 1983). An example of the band gap variation with the composition of quaternary $Cd_xZn_yMn_zTe$ is shown in fig. 10.

The energy gap in DMS, as in other semiconducting compounds, exhibits a considerable temperature dependence. Corresponding phenomenological coefficients that approximate this dependence by linear relationships are gathered by Becker (1988). There are noticeable deviations from the linear dependence of the energy gap on the

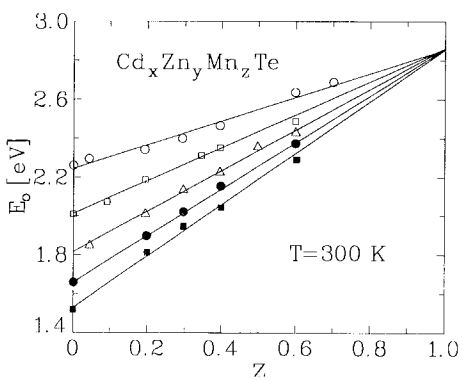

Fig. 10. The fundamental energy gap as a function of the molar fraction of Mn in quaternary $Cd_xZn_yMn_zTe$ at 300 K for fixed $x:y$ ratios. Experimental values – open circles: $x = 0$; full circles: $x = 3y$; open squares: $3x = y$; filled squares: $y = 0$; open triangles: $x = y$ (from Brun del Re et al. 1983).

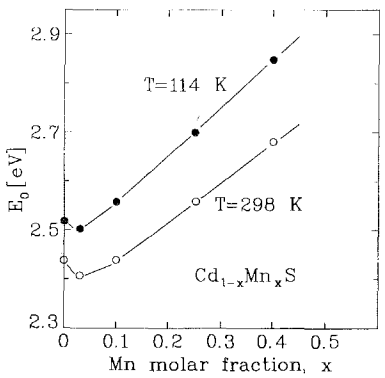

Fig. 11. Fundamental energy gap in $Cd_{1-x}Mn_xS$ as a function of composition at two temperatures showing a pronounced bowing effect (from Ikeda et al. 1968).

molar fraction of the magnetic constituents. While such deviations, known as 'bowing', are often encountered in the case of alloys of III–V semiconductors, it is peculiar to DMS materials that the magnitude of the bowing depends on the temperature as shown in fig. 11. It was suggested by Bylsma et al. (1986) and Gaj and Golnik (1987) that this strange behavior of bowing can be ascribed to second-order corrections to the energy of the band edge states originating from the s–d and p–d exchange interaction with the localized magnetic moments. Such corrections do not vanish in the absence of magnetic fields (as the first-order correction does) and are proportional to the magnetic susceptibility of DMS. They are also thought to be responsible for the anomalous temperature dependence of the energy gap at low temperatures ($Cd_{1-x}Mn_xTe$: Diouri et al. 1985, Lee and Ramdas 1984, Gaj and Golnik 1987; $Zn_{1-x}Mn_xSe$: Bylsma et al. 1987; $Zn_{1-x}Mn_xTe$ and $Cd_{1-x}Mn_xSe$: Morales et al. 1984, 1985, Bryja and Gaj 1988) which can not be described solely in terms of the Varshni formula (Varshni 1967) usually employed in various semiconductors. In DMS the band gap displays an extra 'blueshift' below 77 K. Such anomalies were previously observed in the magnetic semiconductors MnS (Chou and Fan 1974) and MnTe (Kendelewicz 1980).

2.3. *Intra-ionic optical transitions in* $A^{II}_{1-x}Mn_xB^{VI}$

As already mentioned, electrons from a partially filled d shell of a transition-metal ion placed in a semiconducting matrix give rise to states that are only slightly hybridized with the band states. The description of 3d electronic states, therefore, can be often made in terms of atomic orbitals modified by the presence of a crystal field of an appropriate symmetry. In particular, manganese with its exactly half-filled d shell forms a ground state that is an orbital singlet ($L = 0$) denoted by ^6S which does not split further in the presence of the crystal field nor by the spin–orbit interaction. In the presence of these interactions the ground state of d electrons in Mn ions is traditionally labelled as $^6A_1$. It is, of course, a spin sextet ($S = 5/2$). The lowest lying excited states which correspond to flipping the spin of one of the five d electrons of

manganese, are subject to splitting by the crystal field interaction as shown by the scheme presented in fig. 12. The relative position of the crystal field split states was studied intensively in the past for various symmetries of the host material in which Mn ions are embedded – see, e.g., Abragam and Bleaney (1970).

Although optical transitions from the ground ^6S state to lowest excited states are forbidden for a free Mn ion, the spin–orbit interaction and the absence of the inversion symmetry may relax this selection rule when Mn ions are placed into a crystalline host matrix. Also, the lattice distortions existing in real DMS, mentioned in section 1, may be a source of further relaxation of this strict selection rule. In fact, optical transitions from the $^6A_1$ ground state to the first excited $^4T_1$ state, as well as the other states originating from the ^4G multiplet of the free Mn ion (all are marked by arrows in fig. 12), are very probable and correspond to very strong absorption of light. Since they occur at an energy of 2.2 eV (cf., fig. 9) these transitions are responsible for the red tint of wide-gap DMS, e.g., of $Cd_{1-x}Mn_xTe$ with x exceeding 0.4. In $Zn_{1-x}Mn_xTe$ the intra-ionic transition is visible in the entire range of compositions since the energy gap is considerably greater in this compound than in $Cd_{1-x}Mn_xTe$.

The nature of optical transitions observed near 2.2 eV was in the past subject of considerable debate. In view of several theoretical calculations of the band structure of wide-gap DMS it was suggested that the feature at 2.2 eV is in fact related to the transfer of an electron from the top of the valence band to the d shell of Mn which would then acquire a $3d^6$ configuration. This identification was ruled out in an elegant experiment of Lee et al. (1988) who observed the transition in question by means of piezomodulated reflectivity in the presence of a magnetic field. Since the experiments did not reveal any variation of the transition energy with the field it was concluded that the extended valence band states (which are known to exhibit a giant shift in

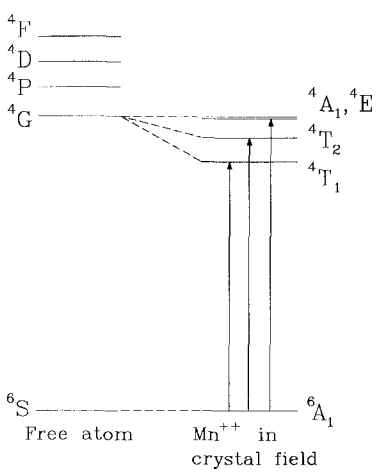

Fig. 12. Energy level scheme of the $3d^5$ state of an Mn^{2+} ion in the presence of a tetrahedral crystal field showing the ground ^6S and first excited ^4G levels. The arrows mark possible optical transitions.

the presence of a magnetic field – see section 4) cannot be the initial states of this transition.

The transitions within the Mn 3d shell are the source of an efficient emission of light observed in the electroluminescence in $Zn_{1-x}Mn_xSe$ and $Zn_{1-x}Mn_xS$ (for a review of the energy transfer mechanisms responsible for the electroluminescent properties of zinc-based DMS see, e.g., Gumlich 1981). Because of this intense emission an application in flat panel displays has been found for these materials.

Let us now, turning to Fe as the constituent of DMS, note that contrary to the case of Mn even the ground state of the 3d electrons is subject to splitting by the crystal field of a semiconducting matrix. This is because Fe with its six d electrons possesses a nonvanishing orbital moment $L = 2$. The resulting scheme of the energy levels in the case of a zincblende environment is depicted in fig. 13. The lowest lying state is a singlet, thus, the Fe containing materials display paramagnetic behavior of the Van Vleck type. The existence of low lying excited states of Fe completely changes the absorption spectra in the infrared of wide-gap DMS containing iron as compared to their Mn counterparts. While, e.g., $Cd_{1-x}Mn_xTe$ is transparent in these ranges of photon energies, the compounds containing Fe ions possess very characteristic absorption bands occurring in the near-infrared as well as in the far-infrared. These absorption bands are due to optical transitions between various crystal field and spin–orbit interaction split levels of Fe, respectively. From such spectroscopic investigations of absorption by transition-metal impurities in various semiconductor matrices the majority of information concerning the crystal field parameters and the spin–orbit

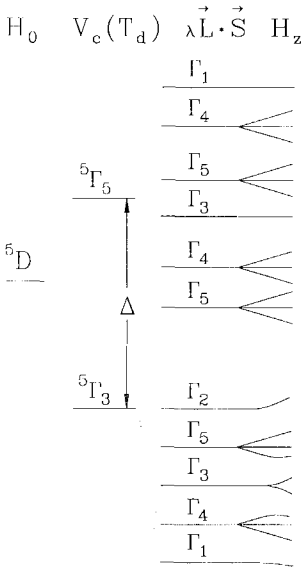

Fig. 13. Energy levels scheme of the $3d^6$ ground state of an Fe^{2+} ion in a tetrahedral field and in the presence of spin–orbit interaction. The splitting of the levels by an external magnetic field is also shown.

TABLE 4
Crystal field and spin–orbit interaction parameters for Fe in cubic and hexagonal DMS (in cm^{-1}).

Compound	$Dq = \Delta/10$	λ	v	v'	Ref.*
$Zn_{1-x}Fe_xSe$	293	−95	0	0	[1]
$Cd_{1-x}Fe_xSe$	257	−93.8	31	38	[1]
$Cd_{1-x}Fe_xTe$	248	−100	0	0	[2]
$Hg_{1-x}Fe_xSe$	293	−85, −95	0	0	[1]
$Hg_xCd_yFe_zSe$	280	−80	0	0	[1]

*References:
[1] Twardowski et al. (1990a).
[2] Testelin et al. (1989).

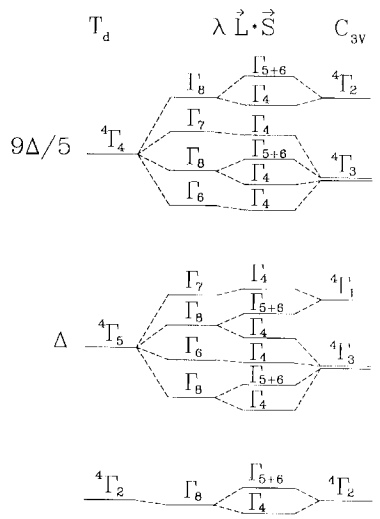

Fig. 14. Energy level diagram of the ground state of a Co^{2+} ion in the presence of tetrahedral (left-hand side) and trigonal (right-hand side) crystal fields showing splittings induced by spin–orbit interaction.

interaction parameters are obtained. Table 4 lists these parameters for Fe in several semiconducting hosts. A schematic representation of the energy levels of Co in cubic and hexagonal surroundings is shown in fig. 14.

2.4. *Inhomogeneous mixed valence regime in $Hg_{1-x}Fe_xSe$ – anomalies of conduction electron scattering rate at low temperatures*

The case of HgSe with substitutional iron atoms requires special attention (for a review of the properties of HgSe with iron, see, e.g., Reifenberger and Kossut 1987, A. Mycielski 1988, 1987, Dobrowolski et al. 1988, Kossut et al. 1990). Contrary to other II–VI compounds with iron and those DMS that contain manganese where

the 3d-derived state was situated either deep within the valence band or in the forbidden gap (cf. fig. 8), Fe in HgSe (and presumably also in HgS – although there is no clear experimental evidence in the latter case) gives rise to a state that is degenerate with the conduction band continuum and located approximately 200 eV above the band minimum (A. Mycielski et al. 1986) – see fig. 15a. Such a peculiar location of the iron level in HgSe is confirmed by photoemission studies of Wall et al. (1987) and Dzwonkowski et al. (1986). This state is weakly hybridized with the conduction band states and, thus, relatively long living. The longevity of the Fe d state is clearly evidenced by the extreme narrowness of the EPR lines observed by Wilamowski et al. (1988). Although it is a very stable state, the resonant Fe state can donate one of its six d electrons to the conduction band becoming a positively charged center (with respect to the lattice). This process of autoionization may be represented by

$$Fe^{2+} \rightarrow Fe^{3+} + e^{-}_{cond}.$$

Due to the autoionization, $Hg_{1-x}Fe_xSe$ samples are always n-type with an electron concentration which is either proportional to the number of Fe atoms present in the crystal (when this number is smaller than the number of available conduction band states whose energy is smaller than the energy of the resonant Fe state) or stabilized by the pinning of the Fermi level to the Fe state. The dependence of the conduction electron concentration is presented in fig. 16.

Pinning of the Fermi level occurs for $x > x^*$, with x^* being approximately equal to 0.0003, corresponding to a volume Fe concentration of $4.5 \times 10^{18}\,cm^{-3}$. This situation is shown in fig. 15b. The region where Fe contents exceed x^* may be referred to as 'an inhomogeneous mixed valence regime' since a fraction of iron atoms is in the Fe^{2+} state (neutral with respect to the lattice) while the remaining part is in the ionized Fe^{3+} state. The presence of iron in Fe^{3+} state in $Hg_{1-x}Fe_xSe$ crystals with $x \geqslant 0.0003$ is directly confirmed by the EPR measurements of Wilamowski et al. (1988)

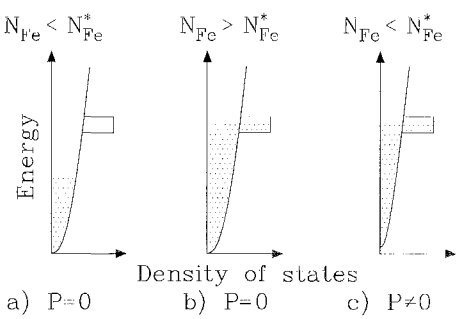

Fig. 15. Schematic representation of the density of conduction band states in $Hg_{1-x}Fe_xSe$ showing the additional density of resonant Fe impurity states for (a) small concentrations of Fe, and (b) for large Fe concentrations exceeding $N^*_{Fe} \approx 4.5 \times 10^{18}\,cm^{-3}$ with the Fermi level pinned to the impurity state. (c) Hydrostatic pressure reduces the density of states in the conduction band causing the pinning of the Fermi level in spite of $N_{Fe} < N^*_{Fe}$. The hatched area represents states that are occupied by electrons at a low temperature.

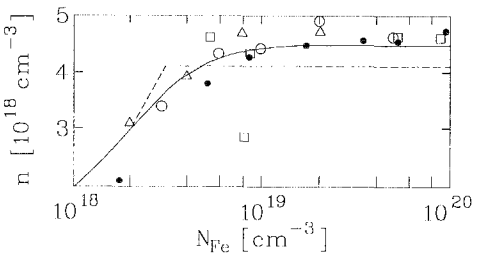

Fig. 16. Conduction electron concentration in $Hg_{1-x}Fe_xSe$ at 4.2 K as a function of Fe concentration. Experimental points – solid points: Pool et al. (1987); circles: Dobrowolski et al. (1987); triangles: Skierbiszewski et al. (1989); squares: Gluzman et al. (1986a,b). Lines are calculated with (solid line) and without (broken line) taking the interdonor Coulomb interaction into account (after Wilamowski et al. 1990).

(the Fe^{2+} state does not produce any EPR signal – see fig. 17) as well as by the Mössbauer effect studies of Nowik et al. (1988).

This simple picture of the relative position of the Fe state and the conduction band states explains correctly not only the observed dependence of the conduction electron concentration on Fe molar fraction but also the quite unusual (for a strongly degenerate electron gas) dependence of this quantity on the temperature, as shown in fig. 18.

It was quite surprising to find in experiments (Pool et al. 1987, Dobrowolski et al. 1987, Gluzman et al. 1986a,b) that the mobility of electrons in the range of Fe concentrations corresponding to the onset of the mixed valence regime is anomalously high at low temperatures. At the same time no anomalies of the mobility are seen at elevated temperatures (above ~ 100 K), as shown in fig. 19. It is found by Lenard et al. (1990) that the rapid variation of the mobility with the temperature saturates below approximately 0.5 K. The dependence of the low-temperature values of the mobility on the concentration of Fe atoms is presented in fig. 20. Similarly, the

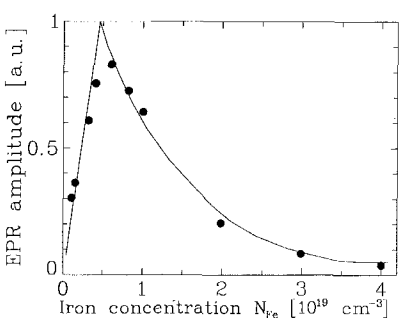

Fig. 17. The amplitude of the electron paramagnetic resonance of Fe^{3+} as a function of Fe concentration in $Hg_{1-x}Fe_xSe$ showing a linear increase for $N_{Fe} < N^*_{Fe}$ due to increasing number of paramagnetic centers and a decrease for $N_{Fe} > N^*_{Fe}$ due to damping of the resonance (after Wilamowski et al. 1990).

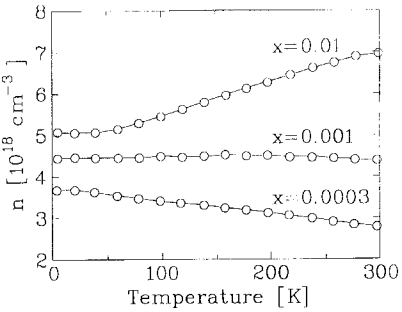

Fig. 18. Temperature dependence of the electron concentration of conduction electrons for three compositions of $Hg_{1-x}Fe_xSe$ as shown. The lowest Fe content corresponds to the situation when the Fermi level at $T=0$ is below the Fe resonant impurity state, the two higher Fe contents to when the Fermi level is pinned to the impurity state. In the case of the highest Fe concentration nearly all impurity states are occupied by electrons at $T=0$ (after Pool et al. 1987).

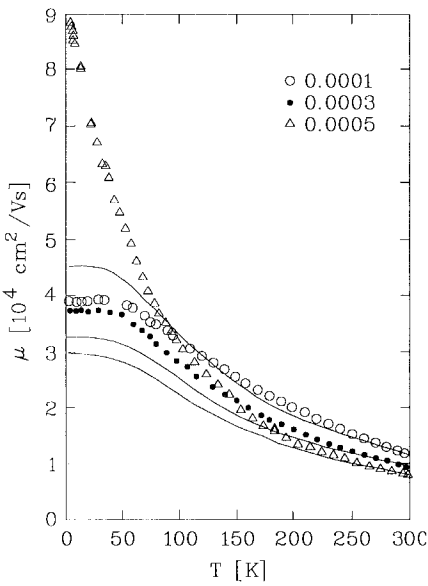

Fig. 19. Temperature dependence of the electron mobility in $Hg_{1-x}Fe_xSe$ for three values of the Fe molar fraction (points). The lines show the results of calculations assuming the scattering from randomly distributed charged impurities (after Pool et al. 1987).

conduction electron lifetime as measured by the Dingle temperature obtained from Shubnikov–de Haas experiments (Dobrowolski et al. 1987, 1989, Vaziri et al. 1985, Vaziri and Reifenberger 1985) and de Haas–van Alphen experiments (Miller and Reifenberger 1988a), was found to be unexpectedly long. This is compatible with the reduced values of the scattering rate suggested by mobility data.

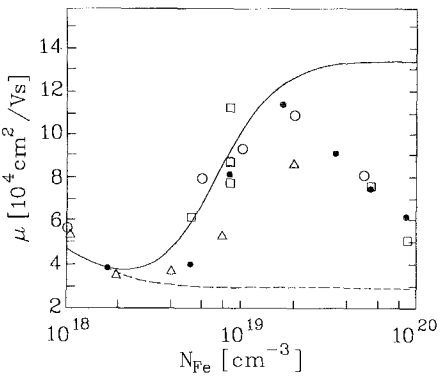

Fig. 20. Electron mobility in $Hg_{1-x}Fe_xSe$ at 4.2 K as a function of Fe concentration. Experimental points – solid points: Pool et al. (1987); circles: Dobrowolski et al. (1987); squares: Gluzman et al. (1986a,b); triangles: Skierbiszewski et al. (1989). The lines were calculated for charged impurity scattering without (broken line) and with (solid line) spatial correlations of the impurity charges included in the short-range correlation model (after Wilamowski et al. 1990).

In order to explain these anomalies a hypothesis was put forward by J. Mycielski (1986) that in the mixed valence regime the spatial positions of the scattering charged impurities (i.e., Fe^{3+} ions) are not distributed completely at random but that they are correlated, because of the mutual Coulomb repulsion between like charges. In other words, the reduction of the total scattering rate is related to a suppression of structure factor $S(q)$ of the system of scattering centers in the region of wave vector q that is of importance in the context of elastic scattering (i.e, for $q<2k_F$, where k_F is the Fermi wave vector). Let us note here that for a completely random distribution of the scattering centers in space the corresponding structure factor is equal to unity for all values of q. Working on this assumption Wilamowski et al. (1990) were able to describe quantitatively the majority of the phenomena observed in the region where the low-temperature mobility increases sharply with x (see fig. 20). For instance, the formation of a Coulomb gap in the one-particle density of impurity states (Shklovskii and Efros 1984) does explain the absence of resonant scattering which otherwise should be very effective in limiting the electronic mobility. The Coulomb gap as obtained in computer simulations of the system for three different concentrations of Fe atoms in HgSe is shown in fig. 21. Moreover, sizable corrections to the Fermi energy stemming from inter-donor Coulomb interaction help to understand, as fig. 22 shows, the details of results obtained in electronic transport experiments of Skierbiszewski et al. (1989) performed in the presence of a hydrostatic pressure which reduces the conduction band density of states (as shown in fig. 15c). The pinning of the Fermi level, therefore, can occur in the presence of pressure at smaller Fe concentrations than at ambient pressure.

The degree of spatial correlation that is needed to account for the observed reduction of the scattering rate is rather short ranged. The screening of the Coulomb potentials by the conduction electron gas is one of the factors that limits the range of the correlation. The correlation length estimated by Wilamowski et al. (1990) for

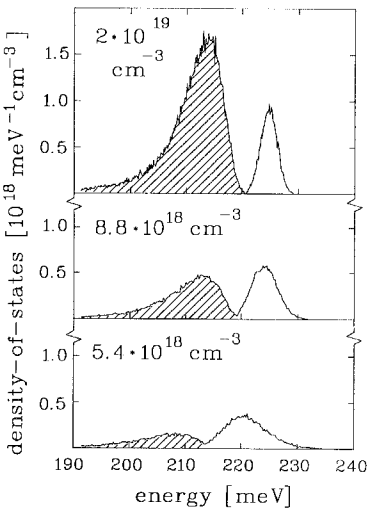

Fig. 21. The density of impurity states in $Hg_{1-x}Fe_xSe$ for three different Fe concentrations showing the formation of a Coulomb gap in the vicinity of the Fermi level (after Wilamowski et al. 1990).

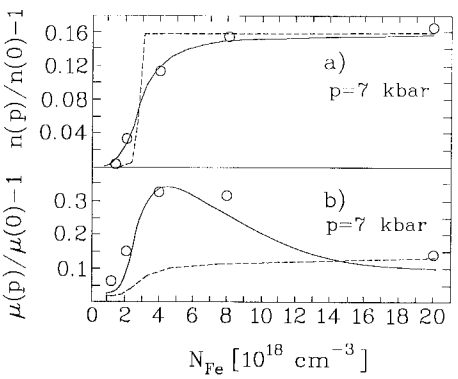

Fig. 22. Relative changes of electron concentration and mobility induced by hydrostatic pressure as a function of Fe concentration in $Hg_{1-x}Fe_xSe$ at 4.2 K. Lines are calculated without (broken lines) and with (solid lines) short-range correlations of the positions of donor charges (after Wilamowski et al. 1990).

the parameters of the HgSe:Fe sample showing the greatest mobility enhancement is only ~ 40 Å (which is only slightly greater than the average distance between the donor sites). This is clearly seen in fig. 23 which presents the calculated charged impurity pair correlation function which has a depletion at short distances while being equal to one (i.e., corresponding to essentially random distribution of charged donors) at a distance larger than the correlation length. At the same time, the Thomas–Fermi screening radius in HgSe with $4.5 \times 10^{18}\,\mathrm{cm}^{-3}$ conduction electrons is 60 Å, i.e., on the order of the distance between the charged Fe^{3+} centers.

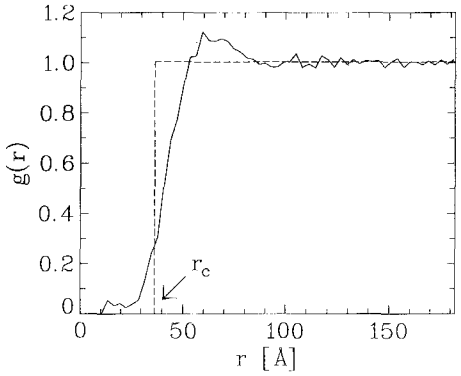

Fig. 23. Pair correlation function in $Hg_{1-x}Fe_xSe$ ($x = 0.0005$) as a function of distance from the central charged donor calculated within the short-range correlation model (dashed line) and obtained in a numerical simulation (after Kossut et al. 1990).

While being very attractive, the hypothesis involving spatial correlation of the impurity charges in HgSe:Fe in the mixed valence regime is by no means the only one proposed to explain the observed anomalies. For example, von Ortenberg et al. (1990) suggest that the observed mobility values may be associated with special characteristics of the scattering from a single Fe scatterer. The proposed mechanism of scattering differs, obviously, from that of a purely Coulomb potential of a charged impurity. The hypothesis of von Ortenberg et al. (1990) describes well the decrease of the mobility for concentrations of Fe in HgSe greater than $\sim 2 \times 10^{19}\,cm^{-3}$. For this highly concentrated samples the hypothesis of correlated system of scattering charges predicts a greater degree of mobility enhancement than observed in experiments. It is not unreasonable, however, that additional scattering mechanisms (such as, e.g., spin disorder and/or chemical disorder scattering) start to be operative and contribute efficiently to the total scattering rate. Without doubt this problem requires further analysis. A study by Szuszkiewicz et al. (1990) of the charged impurity structure factor by means of observation of free carrier optical absorption may shed light on this controversy.

The effect of pinning of the Fermi level to the resonant Fe state and associated with it the reduction of the conduction electron scattering rate was observed in related materials such as $Hg_{1-x}Fe_xSe_{1-y}Te_y$ (Dobrowolski et al. 1988) and $Hg_{1-x}Mn_xSe$:Fe (Dobrowolski et al. 1989). The fact that the scattering of conduction electrons can be so weak in all the above-mentioned materials makes them ideal objects for studies on Landau quantization in the presence of strong magnetic fields. In fact, oscillatory patterns of the magnetic susceptibility in experiments on the de Hass–van Alphen effect were observed at fields as low as 0.2 T (Miller and Reifenberger 1988b). We shall return to this problem in section 4.

Because of the fact that the concentration of conduction electrons can be varied neither by thermal annealing nor by additional doping, it is difficult to determine by normal procedures how the interaction energy gap depends on the composition of narrow-gap $Hg_{1-x}Fe_xSe$ (pure HgSe has, as mentioned earlier, an inverted semi-

metallic band ordering). The observed decrease of the electron concentration in samples with $x > 0.05$ (Pool et al. 1987, Gluzman et al. 1986a,b, Paranchich et al. 1990) suggests that the interaction gap decreases with increasing amount of Fe atoms present in the crystals (a decrease of the interaction gap causes the effective mass in the conduction band and the density of states in this band to become smaller). This, in turn, results in a smaller number of electrons that can be accommodated in the conduction band below the energy of an Fe impurity state. However, without knowledge of the details of the dependence of the energy of the resonant Fe state (with respect to the band edge) on the composition, it is not possible to extract any reliable quantitative information concerning the energy gap variation from these data. Very recent experiments of Paranchich et al. (1990) on the absorption coefficient in the IR range of the spectrum seem to be consistent with a rather rapid closure of the interaction gap with growing Fe content, which places the triple degeneracy point at $x = 0.15$–0.16. Unfortunately, such a rapid closure of the interaction gap is inconsistent with values of the effective electron mass measured by Miller and Reifenberger (1988a). This important point needs to be clarified.

3. Magnetic properties

3.1. An overview

The main role in the determination of magnetic properties of DMS is played by electrons from partially filled 3d shells of transition-metal atoms. It has to be remembered, however, that semiconductors that most often constitute host matrices of DMS are weak diamagnets (e.g., see Ivanov-Omskii et al. 1969). Although weak, this diamagnetism has to be included in a quantitative analysis of magnetic data. In the very dilute limit the transition-metal ions can be regarded as isolated entities. In this range of crystal compositions magnetic properties of DMS are governed by the sequence and the distances between the energy levels of 3d electrons described in the preceding section for the cases of Mn, Fe and Co in an environment of a specified symmetry. Thus, Mn-containing DMS are simple paramagnets with $S = 5/2$, while in Fe-containing DMS Van Vleck paramagnetism is observed. Figure 24 illustrates this qualitative difference between DMS with Mn and those with Fe. In the case of Mn the susceptibility displays a rapid variation with temperature which roughly corresponds to a $1/T$ dependence given by the Curie law. On the other hand, the same amount of Fe in exactly the same semiconducting host is characterized by a susceptibility that depends only very weakly on the temperature. This week dependence of the magnetic susceptibility observed for Fe in HgSe indicates that in this particular case we do not deal with pure Van Vleck paramagnetism but that there is a sizable admixture of another type of magnetism. In a slightly different semiconducting matrix, namely in HgTe, iron results in the susceptibility shown in fig. 25 which, at low temperatures, is practically independent of the temperature – a behavior typical for Van Vleck paramagnetism. Cobalt in a cubic crystal surrounding displays a paramagnetic behavior with $S = 3/2$, which is connected with a fourfold degeneracy of the Co ground state (cf. fig. 14 in the preceding section).

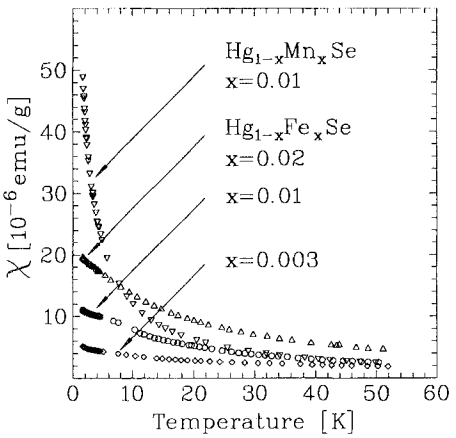

Fig. 24. Magnetic susceptibility as a function of temperature in $Hg_{1-x}Fe_xSe$ and $Hg_{1-x}Mn_xSe$ (after Arciszewska 1991).

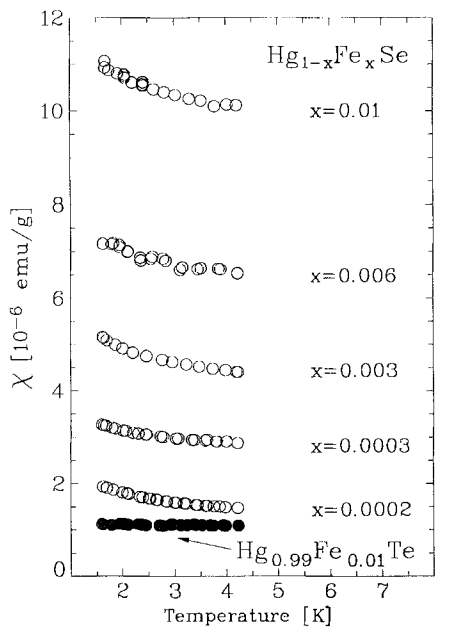

Fig. 25. Temperature variation of the susceptibility in $Hg_{1-x}Fe_xSe$ and $Hg_{1-x}Fe_xTe$ showing Van Vleck paramagnetism in the latter case (after Arciszewska 1991).

The case of Fe in HgSe requires a more careful analysis. As argued in section 2.4, for Fe concentrations smaller than $n^*_{Fe} \sim 4.5 \times 10^{18}\,cm^{-3}$ all iron ions are stripped of one d electron. They acquire, thus, a Mn^{2+}-like (i.e., paramagnetic) $3d^5$ configuration. When the Fe concentration exceeds n^*_{Fe} only a fraction of the iron ions have $3d^5$ configuration. The rest is in the $3d^6$ configuration since they cannot be ionized

because of a lack of available states in the conduction band below the Fermi level. Therefore, magnetism observed in $Hg_{1-x}Fe_xSe$ shows an admixture of paramagnetism. This admixture is the origin of the weak temperature variation of the magnetic susceptibility shown in figs. 24 and 25 in $Hg_{1-x}Fe_xSe$ at low temperatures. We contrast this situation with the case of $Hg_{1-x}Fe_xTe$, where all Fe ions are in the $3d^6$ configuration and where the corresponding susceptibility dependence is completely flat. A very similar mechanism may be responsible for the weak temperature dependence of the susceptibility in DMS in which the Fe level is situated within the forbidden gap, e.g., in $Cd_{1-x}Fe_xTe$, provided that below this level there are acceptor states ready to accept 3d electrons released in the autoionization process.

The cubic nature of the crystal field that acts upon the Fe ion in, e.g., CdTe, becomes visible as a slight anisotropy of the magnetic susceptibility in the region of high magnetic fields. Figure 26 shows results of the measurements of magnetization in $Cd_{1-x}Fe_xTe$ by Testelin et al. (1989) for two different orientations of the magnetic field with respect to the crystal axes. The anisotropy of the high field magnetization is fairly well accounted for by a calculation based on the Hamiltonian of the system which includes effects of the cubic crystal field, spin–orbit interaction and the direct influence of the magnetic field on the total (i.e., consisting of orbital and spin parts) magnetic moment of iron.

When the 'magnetic' transition-metal atoms are incorporated in DMS in larger proportions, deviations from such simple magnetic behavior become observable. They are connected with the fact that the probability of finding an isolated atom, i.e., with no nearest magnetic neighbors, becomes smaller and smaller and an increasing number of magnetic ions must be viewed as being members of clusters. The mean size of such clusters grows with the amount of transition-metal atom present in the crystal. The probabilities of finding a cluster of a specified size and type as a function of the molar fraction of, say Mn in DMS, can be found, e.g., in the review by Oseroff and Keesom (1988) together with corresponding eigenvalues of the energy.

Ultimately, when the concentration of magnetic atoms is further increased, the description in terms of isolated clusters breaks down. It is possible to amend the

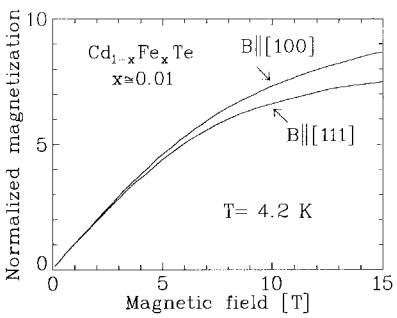

Fig. 26. Normalized magnetization in $Cd_{1-x}Fe_xTe$ at 4.2 K as a function of the magnetic field for two field orientations with respect to the crystal axes (after Testelin et al. 1989).

description by placing the clusters in a suitably chosen molecular field as done, for example, in the analysis of Larson et al. (1986). In this range of high concentrations of magnetic atoms their magnetic moments freeze into a spin-glass state. The susceptibility exhibits a distinct anomaly at a freezing temperature, as shown in fig. 27, and details of the susceptibility behavior depend on the thermal history of the sample. An example is shown in fig. 27 where the susceptibility data are presented for $Cd_{1-x}Mn_xTe$ cooled in the presence of a magnetic field and without a field. No anomaly is found in the specific heat at the freezing temperature (see, e.g., Khattak et al. 1981). The spin-glass freezing temperature T_f is found to be an increasing function of the concentration x of magnetic atoms in DMS (see fig. 28). Let us note that the T_f versus x lines in fig. 28 intersect the ordinate axis at a value that roughly corresponds to the critical percolation concentration of a lattice of magnetic ions with only nearest-neighbor interactions. For the highest concentrations of transition-metal atoms attainable in DMS there are clear indications of magnetically ordered phases appearing at low temperatures. These conclusions were inferred from the measurements of the susceptibility and the specific heat (where an anomaly is found at the transition temperature) but, first of all, from the neutron diffraction studies where extra peaks were observed in $Cd_{1-x}Mn_xTe$, $Zn_{1-x}Mn_xTe$ and $Zn_{1-x}Mn_xSe$ (see, the review of Giebultowicz and Holden 1988). An example of such peaks is presented in fig. 29. Their positions in reciprocal space makes it possible to identify the observed low-temperature superstructure as the antiferromagnetic ordering of type III of an fcc lattice, according to Anderson's classification (P. W. Anderson 1953). The actual arrangement of spins in this type of antiferromagnetic ordering is depicted in fig. 30.

It is difficult to draw meaningful borderlines between regions displaying various magnetic behaviors (as attempted in the early studies as, e.g., in Gałązka et al. 1980).

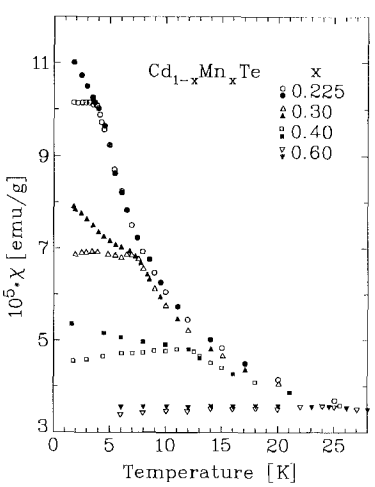

Fig. 27. Magnetic susceptibility in $Cd_{1-x}Mn_xTe$ as a function of the temperature in samples cooled in the absence of a magnetic field (empty symbols) and in a field of 15 kOe (filled symbols) – after Oseroff and Gandra (1985).

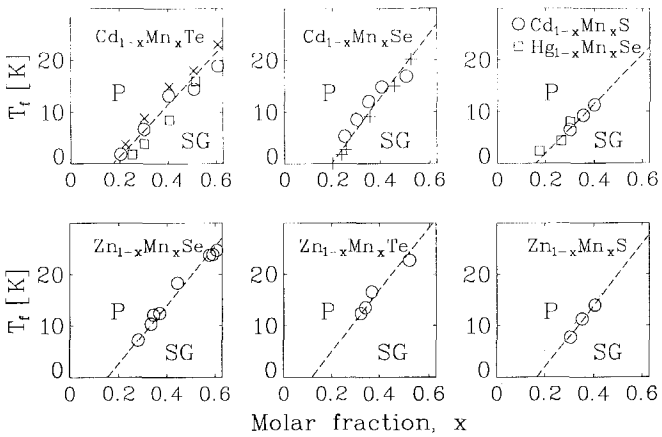

Fig. 28. Dependence of the spin-glass freezing temperature on the composition of II–VI DMS (after Oseroff and Keesom 1988).

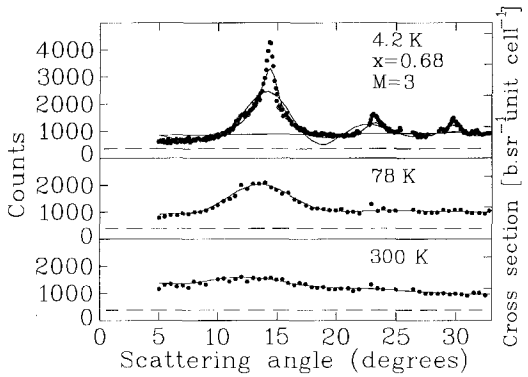

Fig. 29. Variation with temperature of diffuse neutron scattering peaks in $Zn_{1-x}Mn_xTe$. The lines represent fits to various models of the antiferromagnetic ordered structure (after Holden et al. 1982).

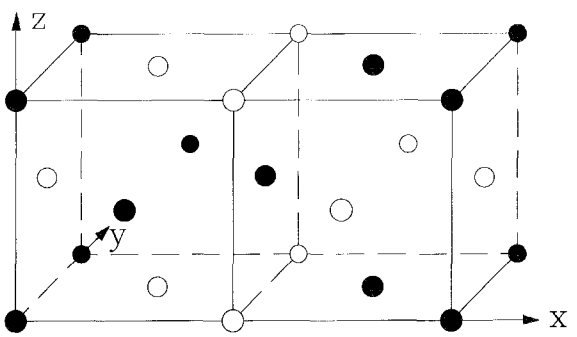

Fig. 30. Unit cell of the antiferromagnetic ordered type-III structure (empty symbols represent spin-up sites, solid symbols represent spin-down sites).

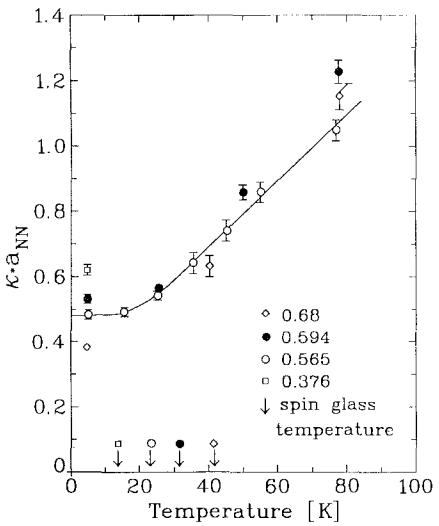

Fig. 31. Inverse correlation length κ in $Zn_{1-x}Mn_xTe$ from neutron scattering experiments as a function of temperature multiplied by the nearest-neighbor separation of Mn sites, a_{NN} (after Giebultowicz and Holden 1988).

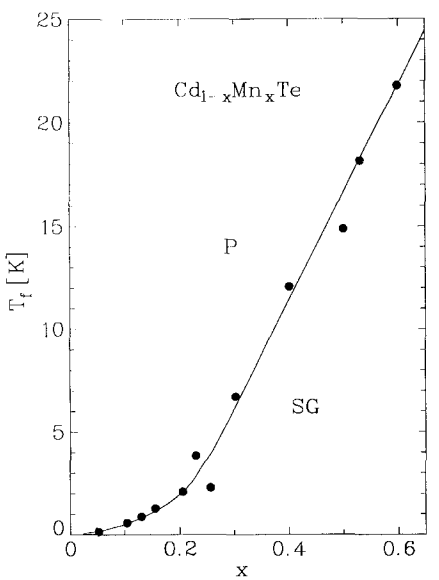

Fig. 32. Spin-glass freezing temperature in $Cd_{1-x}Mn_xTe$ as a function of composition showing a change of slope at low temperatures where interactions between remote magnetic moments manifest their presence (after Oseroff and Keesom 1988).

One of the reasons that make such phase diagrams misleading is the fact that the correlation length of the antiferromagnetic ordered phase, as estimated from the neutron diffraction studies is quite small, see fig. 31. One deals rather with antiferromagnetic grains than truly macroscopic magnetically ordered regions. Also, the neutron scattering experiments indicate that the antiferromagnetic superstructure maxima appear with decreasing temperature in a smooth fashion without any obvious criticality. Nevertheless, theoretical simulations of diluted systems of antiferromagnetically interacting spins in a lattice with frustration performed by Ching and Huber (see Giebultowicz et al. 1986) have shown that such noncritical temperature behavior of the neutron diffraction peaks is compatible with the anomaly seen in the magnetic susceptibility. Secondly, the borderline between the spin-glass and paramagnetic phases is also elusive. As the temperature is lowered the spin-glass phase is observable in samples with magnetic atom concentrations that are smaller than the percolation threshold for networks connected by nearest-neighbor interactions. This is shown in fig. 32. Clearly, interactions between more distant neighbors start to manifest their presence at such low temperatures. The borderline between paramagnetic and spin-glass phases in fig. 32 merely leads to a change of slope at the nearest-neighbor percolation threshold.

3.2. Coupling between magnetic moments in DMS

The vast majority of information that is available on the nature of the form of the interaction between magnetic moments in DMS concerns the II–VI materials containing manganese. Other hosts and/or magnetic components of DMS were considerably less studied both experimentally as well as theoretically. The contents of this section will, therefore, emphasize the results found in the first group of materials.

In the case of Mn-based diluted magnetic semiconductors it was established that the dominating interactions are those between nearest neighbors and that they are antiferromgnetic in sign and isotropic. The interaction between next-nearest (second) neighbors is also antiferromagnetic and is estimated to be approximately one order of magnitude weaker (for numerical values of exchange constants, see table 5). This particular ratio of the exchange constants for nearest and the next-nearest neighbors is the principal reason for the realization of the type-III antiferromagnetic arrangement of spins in the fcc lattice. An anisotropic Dzialoshinskii–Moriya interaction was also found to be present in DMS. It was necessary to consider the possibility of existence of this type of interaction in view of the anomalously broadened EPR lines observed by Samarth and Furdyna (1988) in various DMS (see also, Claessen et al. 1990). This interaction may also be of importance for the formation of the spin-glass state (as numerical simulations of Giebultowicz et al. 1985 suggest). However, its strength is more than one order of magnitude smaller than the Heisenberg exchange constant characterizing the nearest-neighbor isotropic interaction. In particular, the theoretical estimate of Larson and Ehrenreich (1989) fixes the value of the Dzialoshinskii–Moriya interaction constant in $Cd_{1-x}Mn_xTe$ at 0.3 K. This value is, as shown by Larson and Ehrenreich (1989), in excellent agreement with that needed to understand the EPR line width of Samarth and Furdyna (1988).

TABLE 5

Coupling constants of the Heisenberg interaction between nearest (NN) and next-nearest neighboring (NNN) magnetic atoms in DMS. Method of measurement: step = magnetization step (also those recorded in optical properties); susc = high-temperature susceptibility; neut = inelastic neutron scattering; magn = high-field magnetization fitted within the pair approximation; spec = specific heat; tf = deduced from spin-glass freezing temperature.

Compound	$-J_{NN}$ (K)	Method	Ref.*	$-J_{NNN}$ (K)	Method	Ref.*
$Zn_{1-x}Mn_xS$	16.9 ± 0.6	step	[1]	0.6	step	[1]
	16.1 ± 0.2	neut	[2]	4.8 ± 0.1	susc	[3]
				~ 0.7	tf	[4]
$Zn_{1-x}Mn_xSe$	9.9 ± 0.9	step	[5]	3.0 ± 2.4	susc	[7]
	13	step	[8]	2.4	susc	[6]
	12.6	step	[9]	0.7	tf	[15]
	12.2 ± 0.3	step	[10]			
	12.3 ± 0.2	neut	[2]			
	13.5 ± 0.95	susc	[6]			
$Zn_{1-x}Mn_xTe$	10.0 ± 0.8	step	[11]	0.6	step	[24]
	10.1 ± 0.4	step	[12]	4.6 ± 0.9	susc	[7]
	9.25 ± 0.3	step	[13]	3.6 ± 2	susc	[7]
	8.8 ± 0.1	step	[5]			
	9.0 ± 0.2	step	[10]			
	9.52 ± 0.05	neut	[14]			
	7.9 ± 0.2	neut	[15]			
	12.0	susc	[11]			
	11.85 ± 0.25	susc	[16]			
$Cd_{1-x}Mn_xS$	8.6 ± 0.9	step	[5]	5.2 ± 0.3	step	[17]
	10.5 ± 0.3	step	[9]			
	10.6 ± 0.2	step	[17]			
	11.0 ± 0.2	step	[1]			
	9.65 ± 0.2	step	[1]			
$Cd_{1-x}Mn_xSe$	8.3 ± 0.7	step	[8]	1.6 ± 1.5	step	[18]
	7.9 ± 0.56	step	[18]	4.6 ± 2.0	susc	[7]
	8.1 ± 0.2	step	[17]	5.4 ± 1.5	susc	[7]
	9.0	susc	[8]			
	10.6 ± 0.2	susc	[16]			
	7.7 ± 0.3	step	[19]			
$Cd_{1-x}Mn_xTe$	~ 10	step	[8]	1.9 ± 1.1	step	[18]
	6.3 ± 0.3	step	[18]	1.1 ± 0.2	step	[38]
	6.1 ± 0.3	step	[9]	0.67	neut	[21]
	6.2 ± 0.2	step	[10]	1.2 ± 1.0	susc	[7]
	7.5	neut	[20]	0.55 ± 0.05	spec	[22]
	6.7	neut	[21]			
	6.9 ± 0.15	susc	[16]			
	7.7 ± 0.3	step	[22]			
	6.1 ± 0.2	step	[19]			
$Hg_{1-x}Mn_xSe$	6 ± 0.5	step	[23]			
	5.3 ± 0.5	step	[24]			
	10.9 ± 0.7	susc	[16]			
$Hg_{1-x}Mn_xTe$	5.1 ± 0.5	step	[23]	1	susc	[26]
	4.3 ± 0.5	step	[24]	0.7 ± 0.3	spec	[27]

TABLE 5 (*continued*)

Compound	$-J_{NN}$ (K)	Method	Ref.*	$-J_{NNN}$ (K)	Method	Ref.*
	15	susc	[25]			
	15.7	susc	[26]			
	7.15 ± 0.25	susc	[16]			
$(Zn_{1-x}Mn_x)_3As_2$	~ 100	tf	[27]	~ 2	tf	[27]
$(Cd_{1-x}Mn_x)_3As_2$	~ 30	tf	[28]	~ 5	tf	[28]
$Pb_{1-x}Mn_xS$	0.537	magn	[29]	0.05	magn	[29]
	1.28	susc	[30]			
$Pb_{1-x}Mn_xSe$	~ 1	magn	[31]			
	1.67	susc	[30]			
$Pb_{1-x}Mn_xTe$	~ 1	magn	[31]			
	0.84	susc	[30]			
$Zn_{1-x}Fe_xSe$	22.0 ± 2.0	susc	[32]			
$Cd_{1-x}Fe_xSe$	11.3 ± 1.5	susc	[33]			
	18.8 ± 2.0	susc	[32]			
$Hg_{1-x}Fe_xSe$	15.0 ± 1.0	susc	[33]			
	18.0 ± 2.0	susc	[34]			
$Zn_{1-x}Co_xS$	47.5 ± 0.6	neut	[35]	2.25 ± 0.2	step	[39]
	47.0 ± 6.0	susc	[36]			
$Zn_{1-x}Co_xSe$	54.0 ± 8.0	susc	[36]	3.04 ± 0.1	step	[39]
	49.5 ± 1.0	neut	[38]			
$Zn_{1-x}Co_xTe$	38.0 ± 2.0	neut	[37]			

*References:

[1] Shapira et al. (1989).
[2] Giebultowicz et al. (1987).
[3] Spasojevic et al. (1989).
[4] Twardowski et al. (1987a).
[5] Lascaray et al. (1987).
[6] Furdyna et al. (1988).
[7] Lewicki et al. (1988).
[8] Shapira et al. (1984).
[9] Shapira and Oliveira (1987).
[10] Foner et al. (1989) and Shapira (1990).
[11] Shapira et al. (1986).
[12] Aggarwal et al. (1986).
[13] Barilero et al. (1987).
[14] Corliss et al. (1986).
[15] Twardowski et al. (1987a).
[16] Spałek et al. (1986).
[17] Bartholomew et al. (1987).
[18] Larson et al. (1986).
[19] Isaacs et al. (1988).
[20] Giebultowicz et al. (1984).
[21] Giebultowicz et al. (1989).
[22] Gałązka et al. (1980).
[23] Gałązka et al. (1988).
[24] Lascaray et al. (1989).
[25] Savage et al. (1973).
[26] Davydov et al. (1980).
[27] Denissen et al. (1987).
[28] Denissen et al. (1986).
[29] Karczewski et al. (1985).
[30] J. R. Anderson et al. (1990).
[31] Górska and Anderson (1988).
[32] Twardowski et al. (1988).
[33] Lewicki et al. (1987).
[34] Twardowski et al. (1990a).
[35] Giebultowicz et al. (1990a).
[36] Lewicki et al. (1989).
[37] Giebultowicz et al. (1990b).
[38] Wang et al. (1990).
[39] Shapira et al. (1990) (the value for $Zn_{1-x}Co_xS$ is either for second- or third-nearest neighbors; for $Zn_{1-x}Co_xSe$ the value for third neighbors was also determined, $J_3 = -0.8$ K).

The physical nature of the nearest-neighbor antiferromagnetic exchange interaction was established by Hass et al. (1986) and Larson et al. (1988) in the course of their theoretical work on the wide-gap DMS band structure. The interaction consists largely of the superexchange mechanism with a small (less than 5%) admixture of indirect couplings of the Bloembergen–Rowland type, i.e., via virtual excitation of pairs of holes and electrons in the valence and conduction band, respectively. The critical comparison of the data for various materials done by the Eindhoven group (see, e.g., de Jonge et al. 1987) does show that there are differences in the range of interactions between the magnetic moments in wide-gap DMS and narrow-gap DMS. These differences are most obvious when one compares the strength of the interaction in wide-gap DMS with that in narrow-gap DMS. Figure 33 shows, as an illustration of the differences in question, plots of the logarithm of the freezing temperatures as a function of the logarithm of the concentration of magnetic atoms in various DMS. Remarkably, all data points for wide-gap II–VI-based Mn-containing DMS can be described by straight lines with slopes corresponding to the decay of the exchange interaction constants. The latter varies as $R^{-6.8}$, R is the mean distance between the magnetic atoms. Parenthetically, this fast disappearance of the interaction with inter-spin distance is as rapid as the exponential behavior predicted for the superexchange mechanism of Larson et al. (1988). We show this in fig. 34 taken from the unpublished thesis of Swagten (1990). On the other hand, the slopes of the lines showing the data for narrow-gap semiconductors in fig. 33 are significantly smaller, which means that the exchange interactions in these compounds have a longer range. It still has to be proven if this longer range is directly connected to the smallness of the band gap. For a small band gap one can expect such gap-dependent mechanisms as indirect exchange interaction via conduction electrons (Rudermann–Kittel–Kasuya–Yosida – RKKY – mechanism) and/or via virtual excitation of conduction electron–valence

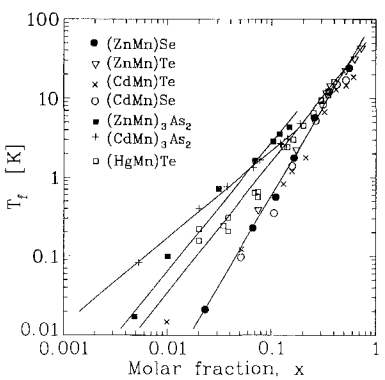

Fig. 33. Variation of the logarithm of the spin-glass freezing temperature with the logarithm of the Mn molar fraction in various DMS. Wide-gap II–VI DMS fall on one common line, while narrow-gap II–VI and II–V DMS deviate from this common dependence (after de Jonge et al. 1987 with data for mercury compounds added from Nagata et al. 1980, Brandt et al. 1983 and A. Mycielski et al. 1984).

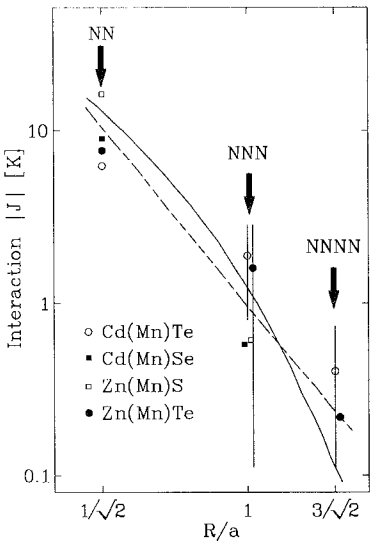

Fig. 34. Exchange constant as a function of separation between magnetic atoms showing experimental values for nearest (NN), second (next-nearest – NNN) and third (NNNN) magnetic neighbors in wide-gap II–VI DMS. The solid line represents the exponential behavior predicted by the superexchange theory of Larson et al. (1988) – eqs. (3.1) and (3.2). The broken line shows the dependence $R^{-6.8}$ obtained from scaling of the spin-glass freezing temperature (after Swagten 1990).

hole pairs (Bloembergen–Rowland mechanism) to contribute more significantly to the total interaction than in the case of a material with a wide energy gap. That the RKKY interaction is of some importance is also the conclusion of a careful analysis of the electron paramagnetic resonance line width in the narrow-gap quaternary system $Hg_xCd_yMn_zTe$ studied by Woolley et al. (1989). The same conclusion was derived from a comparative susceptibility study of $Hg_{1-x}Mn_xTe$ and $Hg_xCd_yMn_zTe$ made by A. Mycielski et al. (1984). Let us note additionally that DMS that are based on lead chalcogenides also seem to be characterized by exchange interactions whose range is, as reported by Twardowski et al. (1987a), even longer than in the case of narrow-gap II–VI semiconductors containing Mn. It is tempting to speculate that the indirect coupling discussed theoretically by, e.g., L. Liu and Bastard (1982) and Dugaev and Litvinov (1990) for these specific materials are in fact responsible for the long range of the exchange interaction.

The remaining part of this section, after some additional theoretical preliminaries, is devoted to a presentation of methods for the precision determination of exchange coupling constants and to a critical comparison of results obtained in each of these methods. Finally, we discuss briefly the case of mixed crystals of $Pb_xSn_yMn_zTe$ where the presence of Sn introduces a large number of electrically active defects that produce a great concentration of holes. These in turn are the source (via RKKY mechanism) of an effective ferromagnetic coupling of the Mn atoms.

3.2.1. Theoretical considerations

As mentioned above, the isotropic Heisenberg-like coupling of magnetic moments in nearest-neighbor positions is by far the strongest interaction that governs the magnetic properties of concentrated DMS. Based on the extensive calculations of the band structure of $Cd_{1-x}Mn_xTe$ including the effect of hybridization of s and p band states of the host semiconductor with d states of manganese, Larson et al. (1988) succeeded in deriving a simple formula which expressed the coupling constant of the Heisenberg-like exchange interaction $-2J^{dd}(R_{ij})\boldsymbol{S}_i\boldsymbol{S}_j$ in terms of various characteristic energies in the crystal,

$$J^{dd}(R_{ij}) = -2V_{pd}^4[U_{eff}^{-1}(E_v^0 - \varepsilon_d - U_{eff})^{-2} - (E_v^0 - \varepsilon_d - U_{eff})^{-3}]f(r), \tag{3.1}$$

where ε_d is the energy of the occupied (majority spin) states of the 3d orbital, $\varepsilon_d + U_{eff}$ is the energy of an unoccupied (minority spin) state of the 3d orbital (differing from the state at ε_d by accommodating one more electron on the d shell), E_v^0 is the p-like valence band edge, and V_{pd} is a single hybridization constant. The function $f(r)$ with $r = R_{ij}$ in units of cubic lattice parameter describes the dependence of the coupling constant on the inter-manganese distance. It can be approximated by

$$f(r) = 51.2\exp(-4.89r^2). \tag{3.2}$$

The usefulness of the above formula becomes apparent when one tries to analyse trends in $J^{dd}(R_{ij})$ when the chemical composition of the DMS crystal is varied. It accounts qualitatively for the experimentally confirmed fact that the exchange constant increases in II–VI Mn-based DMS when the group-II atoms are varied from Hg, to Cd, to Zn. Similarly, eq. (3.1) predicts correctly the qualitative variation of the exchange constant upon changes of anions in a II–VI compound: it is found that J increases when the chalcogen becomes lighter, i.e., it increases in the sequence Te, Se, S. However, quantitative agreement is not reached, most probably, because of our poor knowledge of the parameters appearing in eq. (3.1). So far no attempt was made to analyse chemical trends exhibited in various semiconducting hosts by the values of exchange constants between transition metal atoms different from Mn. For example, Co and to some extent Fe are found to be much more strongly coupled via exchange interaction than Mn atoms in DMS (cf. table 5).

3.2.2. High-temperature susceptibility

The first method of determination of values of the Mn–Mn spin interaction constants in II–VI DMS that yielded reliable results made use of the high-temperature behavior of the magnetic susceptibility (Spałek et al. 1986). In this region of temperatures the susceptibility obeys the Curie–Weiss law,

$$\chi = C(x)/[T - \Theta(x)], \tag{3.3}$$

where $C(x)$ is the Curie constant,

$$C(x) = N_0(g\mu_B)^2S(S+1)x/(3k_B), \tag{3.4}$$

with N_0 denoting the number of cation sites per unit volume, μ_B being the Bohr

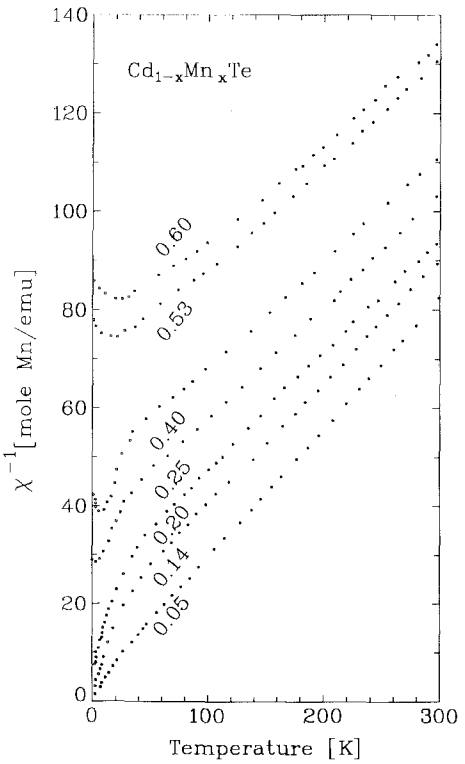

Fig. 35. Magnetic susceptibility in $Cd_{1-x}Mn_xTe$ as a function of temperature showing a linear dependence in the high-temperature region (after Oseroff 1982).

magneton, k_B the Boltzmann constant, and g and S standing for the Landé factor and the spin of the magnetic atom, respectively. The quantity Θ depends on the exchange interaction constant and can be expressed by

$$\Theta(x) = -\tfrac{2}{3}S(S+1)x\sum_n z_n J_n, \tag{3.5}$$

where z_n denotes the number of nth neighbors and J_n the corresponding Heisenberg-like isotropic exchange constant. Assuming that the interaction is of short range and involves only interactions between nearest neighbors we can express the magnetic susceptibility of DMS at high temperatures in terms of the single exchange constant J_1. The linear behavior of χ^{-1} with T at high temperatures predicted by eq. (3.3) is indeed observed in DMS[2] – see fig. 35. Deviations from linearity, clearly visible in the low temperature region, can, at least qualitatively, be understood in terms of higher order expansion of χ into a series involving J/k_BT.

[2] Twardowski et al. (1988) have generalized the high temperature series expansion of the susceptibility to encompass the case of magnetic atoms with nonvanishing orbital momentum, e.g. Fe.

The values of J determined from Θ obtained by extrapolation of the linear portions of χ^{-1} versus T plots are listed in table 5. Comparing the values thus obtained one immediately notices that they are usually slightly larger than those obtained by other methods. The discrepancies are associated with an interaction between more distant magnetic moments which contribute terms with $n > 1$ to the sum in eq. (3.5). These contributions are absent in the methods of determination of the exchange constant described below since they involve isolated nearest-neighbor pairs of magnetic moments.

3.2.3. Magnetization steps

When the concentration of magnetic atoms in DMS is in the range from $x = 0.01$ to approximately $x = 0.05$ the probability of finding a pair of nearest neighbors is already appreciable while larger clusters are still not very frequently found. Therefore, the magnetic properties of DMS in this region of concentrations can be viewed as a superposition of contributions due to isolated atoms and due to exchange-coupled pairs. In the case of Mn pairs in DMS interacting via Heisenberg-like exchange the energy level scheme is particularly simple. It consists of a ladder of levels (shown in fig. 38) each characterized by the total spin of the pair S_T ($S_T = 0, 1, 2, 3, 5$). The separations between the levels are determined by the magnitude of the exchange constant. The ground state of the pair is, in the case of antiferromagnetic coupling, a singlet,

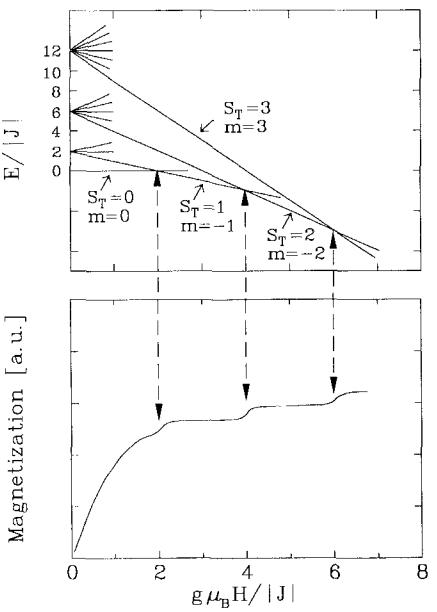

Fig. 36. Energy levels of an interacting Mn^{2+} pair (only the ground and three excited states are shown of total six states) as functions of the magnetic field. The crossing of the lowest levels (a change of the ground state) is reflected in a step-like increase of the magnetization shown in the lower part of the figure.

$S_T = 0$. Thus, a pair does not contribute to the magnetization at low temperatures (lower than, roughly, the energy separation between the ground state and the first excited $S_T = 1$ triplet). This statement is, strictly speaking, valid only in very weak magnetic fields. When the magnetic field is sufficiently strong to bring the $m = -1$ component of the $S_T = 1$ state in the vicinity of the ground state (see fig. 36) the pair begins to contribute to the total magnetization. In particular, at a well-defined field strength $B_1 = -2J_1/(g\mu_B)$ the state with $S_T = 1$, $m = -1$ becomes the ground state of the pair. At this field a sudden step-like increase of the magnetization is expected. Similar steps on the magnetization versus magnetic field curve are expected at higher fields each corresponding to a change of the ground state. In total, five magnetization steps are predicted for Mn pairs – only three of those are shown in fig. 36. An example of an experimental magnetization curve in $Cd_{1-x}Mn_xSe$ is shown in fig. 37 where two steps are visible, the remaining occurring at higher fields being not available in the experiment. The height of each step gives information concerning the number of pairs present in the material and, consequently, about the distribution of magnetic atoms in the host matrix. However, this information is by far less direct than that given by the value of the magnetic field at which the steps appear. The values of the exchange constants determined in this way are listed in table 5.

So far we have assumed that the exchange interaction takes place only between nearest neighbors. Larson et al. (1986) considered also the interactions between more distant magnetic atoms in the context of the magnetization step. Inclusion of the remote magnetic neighbors into the analysis based on the effective field approximation resulted in a rounding of the sharp magnetization step-like features as well as in a shift of the critical fields. By making a detailed fitting to the experimental data the above authors were able to extract from their data also the value of the next-nearest neighbor interaction constant, J_2. Let us mention that, because of the shifts due to interaction with the second-nearest neighbors and/or the presence of larger clusters, the position of the magnetization step only approximately corresponds to the value of J_1. On the other hand, the difference between the fields at which two consecutive

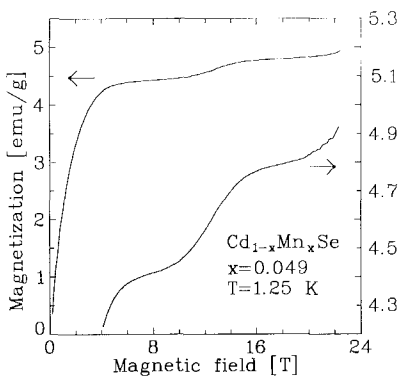

Fig. 37. Magnetization in $Cd_{1-x}Mn_xSe$ showing two steps. They are particularly clear on the lower curve with expanded vertical axis. (after Isaacs et al. 1988).

steps appear is found to be a more precise measure of this quantity than the value of the field corresponding to a single step (Aggarwal et al. 1986).

Determination of the exchange constants from the position of the magnetization steps so far was done only for Mn atoms in various DMS. An estimate of Swagten et al. (1990) places the position of the first magnetization step in $Zn_{1-x}Fe_xSe$ at about 35 T, which is out of the range of fields used so far by experimenters.

Very recently, the magnetization step method was used to determine the values of the exchange constants between second- and third-nearest neighbors in $Zn_{1-x}Co_xS$ and $Zn_{1-x}Co_xSe$ (Shapira et al. 1990). The magnetization steps corresponding to the first-nearest neighbors in these compounds are expected to be situated in immensely large magnetic fields and were not possible to be observed. This is related to the fact that the first-nearest neighbor exchange constants in Co-containing materials are the largest encountered in DMS (cf. table 5 where J_1 values determined from the high-temperature susceptibility as well as from inelastic neutron scattering measurements are included).

3.2.4. Inelastic neutron scattering

Another precise determination of the values of nearest-neighbor exchange constants makes use of inelastic neutron scattering experiments in DMS (for a review of this method the reader is referred to Giebultowicz et al. 1990a). In these experiments intensity peaks are observed that correspond to the scattered neutrons whose energy is changed by an amount equal to the distances between the levels within an exchange-coupled pair of magnetic atoms (see fig. 38 for a schematic representation of the mechanism of the scattering in question). These peaks are distinguishable from other

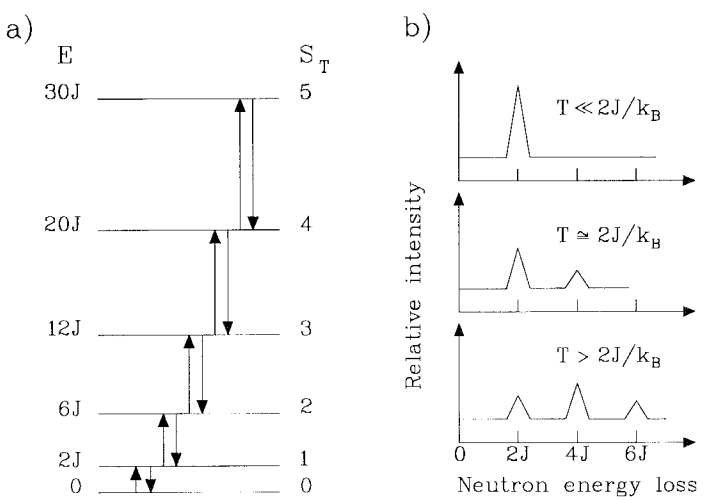

Fig. 38. (a) Energy levels of the interacting Mn^{2+} pair showing excitations with energy supplied or taken away by inelastic scattered neutrons, and (b) corresponding peaks of the intensity of the scattered neutrons (after Giebultowicz et al. 1990a).

features seen in the inelastic scattering of neutrons because of their characteristic dependence on the temperature and on the neutron momentum transfer. As in the case of the magnetization steps described in the preceding subsection the samples that are best suited for these investigations contain magnetic atoms in such numbers that the nearest-neighboring pairs can be found with a quite high probability while larger clusters are still not abundant. This requirement limits the method to $x = 0.01$–0.05. One has to remember that for $x = 0.05$ only $\sim 15\%$ of isolated pairs occur.

The method of inelastic neutron scattering has been used to determine the values of J_1 in zinc chalcogenides with manganese as a magnetic component as well as in $Zn_{1-x}Co_xSe$ (Giebultowicz et al. 1990b). Unless special measures are taken the method is not easy to apply in DMS which contains, e.g., Cd or Hg since they are efficient neutron absorbers.

When the concentration of magnetic atoms in DMS is high the inelastic neutron scattering detects collective excitations of the spins in the spin-glass region (for a review see Giebultowicz et al. 1990a), i.e., in more concentrated DMS where the pair spectra are not observable. Ching and Huber (1982) developed a simulation procedure capable of describing such magnon-like excitations. Comparison of the results of the simulations with the energy of the excitations observed in the neutron experiments makes it possible to determine the value of the nearest-neighbor coupling constant in this high-concentration regime. They are found to be smaller in $Zn_{0.35}Mn_{0.65}Te$ while they are larger in $Cd_{0.33}Mn_{0.67}Te$ than in respective alloys with only a few percent of Mn present. This fact is shown to be consistent with lattice constant variation in these two compounds as the MnTe molar fraction is increased (cf. section 1). As a matter of fact, a linear relationship is found between the lattice constant and the J_1 values determined in inelastic neutron scattering measurements.

3.2.5. RKKY in $Pb_xSn_yMn_zTe$

In $Pb_{1-x}Mn_xTe$ the magnetic moments localized on Mn atoms are weakly antiferromagnetically coupled (cf. Górska and Anderson 1988 and table 5). Comparably small antiferromagnetic exchange constants are found in other lead chalcogenides with Mn. The exact mechanism of this interaction is not completely clear. The magnetic behavior found in these compounds is that of a paramagnet with spin-glass properties observed at very low temperatures. On the other hand, in $Sn_{1-x}Mn_xTe$ a transition to the ferromagnetic ordered phase was observed (Cochrane et al. 1974). The ferromagnetic sign of the exchange interaction between the Mn atoms in the latter compound is ascribed to an indirect mechanism via polarization of spins of mobile band carriers, i.e., to the Rudermann–Kittel–Kasuya–Yosida (RKKY) interaction. Indeed, the concentrations of band carriers – holes in the valence band, to be precise – that are typically found in $Sn_{1-x}Mn_xTe$ are very high, on the order of 10^{20}–10^{21} cm^{-3}. Their presence is related to the metal vacancies. Unfortunately, in $Sn_{1-x}Mn_xTe$ it is difficult to vary the concentration of holes by the methods usually employed. Therefore, the case of quaternary $Pb_xSn_yMn_zTe$ crystals is attractive as the concentration of holes in this material can be as high as in $Sn_{1-x}Mn_xTe$ and at the same time it can be varied between relatively wide limits – spanning more than one order of magnitude – by an isothermal annealing technique. Moreover, since the band structure of the

material is fairly well known it offers an opportunity to analyze the effects due to the RKKY interactions in a truly quantitative way.

The experiments of Story et al. (1986) and Swagten et al. (1988a) on $Pb_xSn_yMn_zTe$ revealed that this material has a ferromagnetically ordered phase and that the transition temperature depends sensitively on the concentration of holes. This dependence is shown in fig. 39. The concentration of holes can also be altered by means of a hydrostatic pressure. Interestingly, parallel to these changes of the ferromagnetic transition temperature are also observed (see Suski et al. 1987). The changes of the concentration of holes induced either by annealing or by the application of pressure are reversible as are induced changes of the magnetic transition temperature.

The band structure of $Pb_xSn_yMn_zTe$ is shown schematically in fig. 40. As in the case of other IV–VI compounds the conduction and valence band edges occur at the L point of the Brillouin zone. Therefore, one has to consider four equivalent valleys. Note that in the Sn-rich compounds that are of present interest, the ordering of the conduction band and the valence band is reversed compared to that in Pb-rich compounds, cf. fig. 7. Because of the smallness of the density of states in the valleys corresponding to the edge of the valence band, the number of carriers (holes) that exist in $Pb_xSn_yMn_zTe$ studied in the present context is too high to be accommodated in the L-valleys alone. When the concentration of holes exceeds approximately

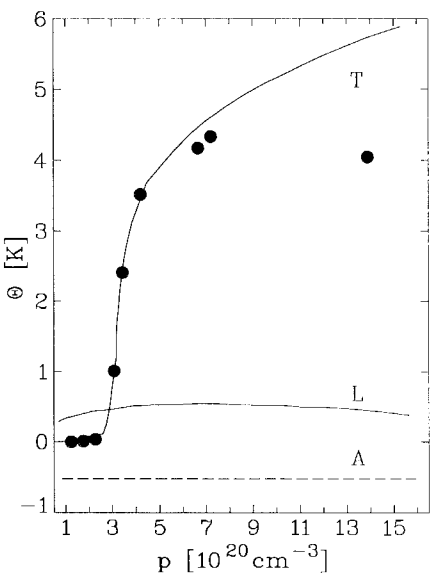

Fig. 39. Ferromagnetic transition temperature in $Pb_xSn_yMn_zTe$ as a function of hole concentration. The broken line shows the antiferromagnetic temperature characteristic for weak interaction in PbMnTe. The solid line labelled L shows the calculated temperature when only the light holes from the L valence band maxima are included in the RKKY coupling. The solid line labelled T shows the result when holes from L maxima and heavy holes from Σ maxima are included in the calculation (after Story et al. 1990).

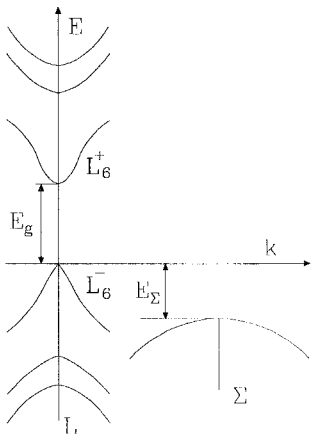

Fig. 40. Band structure in $Pb_xSn_yMn_zTe$ showing the L and Σ maxima of the valence band (after Story et al. 1990).

$2 \times 10^{20}\,cm^{-3}$ they 'spill over' to the side maxima of the valence band that are situated along the Σ direction in the Brillouin zone, as shown in fig. 40. The effective masses in this side valence band maxima are considerably greater than in the L maxima. The corresponding density of states is, thus, sufficiently large to account for the observed order of magnitude of the transition temperature. The sudden jump of the Θ versus p curve visible in fig. 39 occurs when the Fermi level of holes reaches the maximum of the Σ-pocket of valence band states. The results of detailed calculations of Story et al. (1990) are shown in fig. 39 for two cases, first neglecting the existence of the Σ maximum and including only the L-point valence band maxima. The second curve, labelled T in fig. 39, shows the results that take both valence band maxima into consideration. One point that leaves some doubts about this quantitative calculation is that account is made for the finite lifetime of the band carrier. This is done along the lines proposed by de Gennes (1962), i.e., by adding to the expression for the effective coupling constant an exponential factor involving the hole mean free path, λ,

$$J_{RKKY}(R) = J^0_{RKKY}(R)\exp(-R/\lambda), \tag{3.6}$$

where $J^0_{RKKY}(R)$ is the effective exchange constant for the coupling mediated by holes that suffer no scattering due to imperfections of the crystalline lattice. It seems, however, that the relevant physical events that limit the range of the effective interaction are not the scattering events that relax the momentum of a hole but only those scattering events that destory the spin coherence of a hole as it moves in the crystal. Therefore, the proper quantity to be inserted into eq. (3.6) is not the conductivity mean free path but some other length scale related to the spin relaxation time of a hole. This latter length may be quite different from the mean free path as measured by the mobility. This point requires further clarification, particularly in view of the tendency of spin-glass phase formation in DMS materials.

3.3. *Magnetic properties of thin DMS films and superlattices*

Early studies of magnetic properties of thin films of DMS by Venugopalan et al. (1984) indicated that the coupling between Mn atoms in these structures seemed to be reduced as the thickness of the film was diminished. Kolodziejski et al. (1986a) reported the growth of monolayers of MnSe sandwiched between ZnSe layers. The magnetic properties were again found to be indicative of weaker inter-Mn spin coupling than in the case of 3d samples. These results were thought to be interesting in view of the Mermin and Wagner (1966) theorem which predicted the absence of long-range magnetic ordering in 2d for isotropic interactions between the magnetic atoms. Direct measurements of the susceptibility in a $Cd_{1-x}Mn_xTe/CdTe$ superlattice structure performed by Awschalom et al. (1987a) has shown that the cusp marking the transition to the spin-glass phase observed in samples with thick magnetic layers (~ 80 Å) broadens when the thickness is reduced and, then, disappears entirely for the thickness of the magnetic layers (i.e., $Cd_{1-x}Mn_xTe$ barriers) smaller than ~ 20 Å. This is interpreted as the manifestation of the fact that a quasi two-dimensional system cannot support the long-range order and in particular the spin-glass phase, which is consistent with the lower minimal dimensionality for the spin-glass formation, d_1 being greater than or equal two. Similarly, PbTe/EuTe superlattices studied by Heremans and Partin (1988) did not order antiferromagnetically when the thickness of the EuTe layers was made smaller than eight monolayers.

In contrast to the above conclusions, suggesting weaker magnetic coupling in the reduced dimensionality conditions, very recent studies of neutron diffraction from thin layers of $Cd_{1-x}Mn_xSe$ (Giebultowicz et al. 1990c) as well as from MnSe/ZnSe

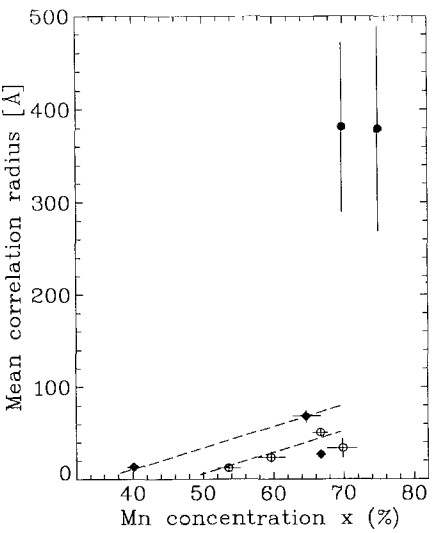

Fig. 41. Mean correlation length of antiferromagnetic ordered domains in bulk $Cd_{1-x}Mn_xTe$ (empty triangles) and $Zn_{1-x}Mn_xTe$ (empty circles) and thin epilayers of $Cd_{1-x}Mn_xSe$ (solid points) obtained by neutron scattering measurements (after Giebultowicz et al. 1990c).

bilayers (where magnetic MnSe layers were as thin as three monolayers) have revealed that the antiferromagnetic ordering that appears below a well-defined temperature is long-range. The correlation length is found to be by an order of magnitude greater than in three-dimensional cases (see fig. 41). Moreover, the transition is clearly shown to be of second order. The authors of these findings associate their surprising results with an anisotropy present in the structures which is related to the lattice mismatch between the layers constituting their structures. This anisotropy reduces the degree of frustration of antiferromagnetic interaction between the spins on an fcc lattice and facilitates a truly long-range antiferromagnetic order. Studies of DMS structures under the conditions of reduced dimensionality are only at their beginning and one may expect new fascinating phenomena to be discovered in the near future.

4. Effect of sp–d exchange interaction

In this section we discuss various consequences of a strong exchange coupling that exists in DMS between band carriers and localized 3d electrons of transition-metal atoms. Actually, it is this coupling that is responsible for most of the peculiarities of DMS, e.g., for the greatly enhanced spin splitting of the band states in the presence of a magnetic field. We start with a description of the physical origin and the form of the sp–d exchange interaction, then the related modifications of the band structure of DMS are presented. Some of the most important consequences of these modifications observed experimentally in DMS constitute the topics of the remaining part of this section.

4.1. Coupling of localized 3d electrons and mobile band carriers

In general, two mechanisms of sp–d exchange interaction have been considered in the context of diluted magnetic semiconductors (see also chapter 5 in the volume edited by Furdyna and Kossut 1988). The first of these mechanisms is a direct exchange due to Coulomb interaction between delocalized electrons in mostly s- and p-like conduction or valence band states of a host semiconductor and those from 3d shells of transition metal atoms. This exchange interaction is ferromagnetic in sign. As shown by S. H. Liu (1961) the resulting Hamiltonian can be cast in a familiar Heisenberg-like isotropic form,

$$H_{\text{exch}} = -J_{nd}\boldsymbol{S}\cdot\boldsymbol{J}, \tag{4.1}$$

where $\boldsymbol{S}$ and $\boldsymbol{J}$ represent the total spin operator of d-shell electrons and the total angular momentum of the band states (labelled in eq. (4.1) by the index n). J_{nd} stands for an exchange constant. Strictly speaking, the Hamiltonian of the exchange interaction was shown to have the simple form of eq. (4.1) only when (i) the band carriers are in s-like ($J = 1/2$) states – then the form of eq. (4.1) is valid for any transition-metal atom – or (ii) the band carriers are in p-like states ($J = 3/2$ or $1/2$), but then the 3d state must have a vanishing orbital momentum $L=0$ (S-state ions).

In the course of investigations on DMS that contains Mn (i.e., S-state ions) it became apparent that the coupling constant between the p-like electrons (which

traditionally is denoted by β) is antiferromagentic in sign while the constant for the s-like electrons (traditionally denoted by α) is ferromagnetic. Also, the magnitude of β typically is considerably greater than that of α. To account for the antiferromagnetic sign of the p–d integral β it was suggested by Bhattacharjee et al. (1983) that the mechanism responsible for the exchange in this case is the hybridization mechanism of Schrieffer and Wolff (1966) (see also Schrieffer 1967) and not the direct Coulomb interaction. On the other hand, the ferromagnetic and weaker interaction with s-like electrons (described by the α integral) is mainly due to the direct Coulomb interaction of the electrons. This point of view is now widely accepted particularly in view of the theoretical work of Larson et al. (1988) on the band structure of $Cd_{1-x}Mn_xTe$.

The considerations of Bhattacharjee et al. (1983) and Larson et al. (1988) mentioned above, as well as later developments of Bhattacharjee (1990a,b) involving a dependence of the exchange constant on the band electron momentum, restricted the attention to the case of manganese, i.e., to an S-state ($L = 0$) ion. In recent years more data became available also for DMS containing other transition-metal atoms, particularly iron and cobalt. It was necessary then to reconsider the hybridization mechanism for $L \neq 0$ atoms. This was done by Blinowski and Kacman (1990) who found that, in general, the coupling of p-like electrons with 3d electrons in Fe^{2+} and Co^{2+} configurations can be, with a good accuracy, approximated by an isotropic Heisenberg-like exchange Hamiltonian. On the other hand, the Cr^{2+} configuration leads to an interaction Hamiltonian which apart from Heisenberg-like terms contains also an anisotropic part. These authors predict that the hybridization mechanism should disappear, because of symmetry, in the case of Sc^{2+} and Ti^{2+} configurations leaving only the ferromagnetic direct Coulomb interaction as the nonvanishing contributor to the p–d exchange constant. It remains to be seen whether this prediction will find confirmation in experiments on DMS that contain Ti or Sc.

In the case of p-like electrons interacting with Mn ions Larson et al. (1988) derived the formula that expresses the p–d exchange constant β in terms of the same band structure parameters as in the case of eq. (3.1) for the inter-manganese exchange

$$\beta = -32V_{pd}^2[(\varepsilon_d + U_{eff} - E_v^0)^{-1} + (E_v^0 - \varepsilon_d)^{-1}], \tag{4.2}$$

which can be used as a guide in tracing chemical trends exhibited by β in various DMS materials.

Table 6 contains a list of experimentally established values of s–d and p–d exchange constants in DMS. The values in wide-gap DMS are usually determined with an accuracy that is considerably higher than in the case of narrow-gap DMS. This can also be seen as a small scatter of exchange constant values obtained by various authors, in contrast with large discrepancies characterizing these values in the case of narrow-gap semiconductors. This situation is partly connected with a considerably more complicated band structure in the latter compounds where a strong mixing of p- and s-like states usually occurs. As was the case of the exchange coupling of the magnetic atoms themselves the p–d constant shows also a characteristic variation as the composition of DMS crystals is changed, revealing similar chemical trends. This is not surprising in view of the fact that both p–d and d–d exchange interactions have a common physical origin in the hybridization of the electronic states. Let us stress

TABLE 6
s–d and p–d exchange constants in DMS.

Compound	α (eV)	β (eV)	Ref.**
$Zn_{1-x}Mn_xSe$	0.26	−1.32	[1,2]
$Zn_{1-x}Mn_xTe$	0.19	−1.09	[3]
$Cd_{1-x}Mn_xS$	–	−1.8	[4]
$Cd_{1-x}Mn_xSe$	0.261	−1.24	[5]
$Cd_{1-x}Mn_xTe$	0.22	−0.88	[6]
$Hg_{1-x}Mn_xSe$*	0.4	−0.7	[7]
	0.9	−1.54	[8]
	0.96	−1.35	[8]
	0.32	−0.92	[8]
	0.35	−0.9	[9]
$Hg_{1-x}Mn_xTe$*	0.4	−0.6	[10, 11]
		−0.65	[12]
	0.75	−1.5	[13]
	0.7	−1.4	[14]
	0.45	−0.8	[15]
	0.6		[16]
	0.61	−0.62	[17]
	0.3	−0.9	[18]
	0.36		[19]
$Zn_{1-x}Fe_xSe$	0.22	−1.74	[20]
$Cd_{1-x}Fe_xSe$	0.25	−1.45	[21]
	0.225	–	[22]
	0.26	−1.53	[23]
	0.23	−1.9	[20]
		−1.6	[24]
$Cd_{1-x}Co_xSe$	0.32		[25]
	0.279	−1.87	[26]

*We have reversed the signs of α and β compared to those given in the original papers to be compatible with the convention adopted in this chapter.

**References:

[1] Twardowski et al. (1983).
[2] Heiman et al. (1984).
[3] Twardowski et al. (1984).
[4] Nawrocki et al. (1987).
[5] Arciszewska and Nawrocki et al. (1986).
[6] Gaj et al. (1979).
[7] Dobrowolska et al. (1981).
[8] Takeyama and Gałązka (1979).
[9] Byszewski et al. (1980).
[10] Dobrowolska and Dobrowolski (1981).
[11] Bauer et al. (1985).
[12] Pastor et al. (1979).
[13] Bastard et al. (1978).
[14] Jaczyński et al. (1978a).
[15] Gel'mont et al. (1988c).
[16] Johnson et al. (1984).
[17] Wróbel et al. (1987).
[18] Sandauer and Byszewski (1982).
[19] Belayev et al. (1988).
[20] Twardowski et al. (1990b).
[21] Shih et al. (1990).
[22] Heiman et al. (1988).
[23] Scalbert et al. (1990).
[24] Twardowski et al. (1990c).
[25] Bartholomew et al. (1989).
[26] Nawrocki et al. (1990).

that, as it will become evident in a moment, in order to extract values of α and β from experimentally observed quantities one must know the magnetization of the investigated samples. When this information is not directly available and one resorts to, e.g., interpolation schemes to estimate the magnetization values for the composition, magnetic field range and temperature of interest, an additional source of error is introduced into the procedure of determining the s–d and p–d exchange constants.

As stated in section 2 the band structure of DMS in the absence of a magnetic field resembles qualitatively that of a host nonmagnetic semiconductor. On the other hand, the s–d and p–d interaction described by eq. (4.1) modify substantially the band structure of the parent semiconductor in the presence of an external magnetic field. One of the first and most spectacular pieces of evidence for this modification was obtained in $Hg_{1-x}Mn_xTe$ by Bastard et al. (1978), who measured the magneto-optical transitions between spin-split Landau levels of the light hole and conduction bands. As shown in fig. 42 the transitions that do not involve spin-flip of an electron are completely analogous to those observed in $Hg_{1-x}Cd_xTe$ with Cd contents chosen in such a way that the resulting interaction energy gap is the same as in a given $Hg_{1-x}Mn_xTe$ sample. At the same time the magneto-optical transition that changes the spin of the band carrier takes place at a completely different energy than in $Hg_{1-x}Cd_xTe$. This means that the spin splitting is considerably greater in the case of $Hg_{1-x}Mn_xTe$. Moreover, the spin splitting, as can be seen in fig. 42, depends sensitively on the temperature in $Hg_{1-x}Mn_xTe$ while in the nonmagnetic counterpart, i.e. in $Hg_{1-x}Cd_xTe$, it practically remains constant in the temperature range of interest.

In order to understand these results, it was proposed (Bastard et al. 1978, Jaczyński et al. 1978a; see also Bastard 1978, Jaczyński et al. 1978b) that the s–d and p–d exchange interaction must be properly accounted for in calculations of the band structure of DMS in the presence of a magnetic field. Two approximations were introduced to facilitate these calculations. In the first approximation, which is analogous

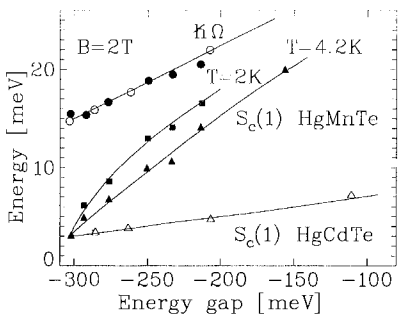

Fig. 42. Energies of various interband magneto-optical transitions in $Hg_{1-x}Mn_xTe$ (solid symbols) and nonmagnetic $Hg_{1-x}Cd_xTe$ (open symbols) observed at $B=2$ T as functions of the interaction energy gap at two temperatures. Circles show the (temperature independent) transitions between the first Landau levels in the conduction and valence bands without spin flip (i.e., involving only valence and conduction band cyclotron frequencies). Squares ($T=2$ K) and triangles ($T=4.2$ K) show data for the transition between the first Landau levels with spin flip (i.e., including additionally the spin splitting of the initial and final Landau levels). The lines are guides to the eye (after Bastard et al. 1978).

to the molecular field approximation, known from the physics of magnetism, the localized spin in eq. (4.1) is replaced by its thermal average. This step is substantiated by the large spatial extent of the band electron wave function. The mobile carrier, thus, 'sees' a large number of localized magnetic moments and experiences an average influence of the entire ensemble. Within this approximation we write the Hamiltonian describing the exchange interaction of the band electron with magnetic moments localized on substitutional transition-metal atoms which are randomly distributed in the crystal lattice as

$$H_{\text{exch}} = -\sum_i J_{nd}(r - R_i)\boldsymbol{J}\cdot\langle \boldsymbol{S}\rangle, \tag{4.3}$$

where the sum is over all sites where magnetic moments are localized and where $\langle \cdots \rangle$ denotes the thermal average. The exchange integral J_{nd} was taken to be a function of the distance between the band electron in question and the magnetic moment located at site R_i. As discussed in section 3, localized magnetic moments in DMS form either a paramagnetic system or are frozen in a spin-glass state. In both cases the average value of the magnetic moment vanishes in the absence of an external magnetic field. This fact explains qualitatively why peculiarities associated with the presence of magnetic moments in DMS become obvious only when a magnetic field is applied. Let us note that in the presence of a magnetic field the only component of $\boldsymbol{S}$ that does not vanish on the average is that along the field direction. Therefore, the modifications of the physical properties of DMS induced by the exchange interaction scale in the majority of cases with the *magnetization.*

The second simplification is also connected with the large spatial extent of the electronic wave function. It restores the translation invariance of the crystalline lattice in the spirit of the virtual crystal approximation by replacing the sum in eq. (4.3) by the sum over all cation sites of the crystal lattice, however weighing the value of J_{nd} in proportion to the concentration of the magnetic centers, i.e., by writing, instead of eq. (4.3)

$$H_{\text{exch}} = -J_{nd}xJ_z\langle S_z\rangle, \tag{4.4}$$

where J_{nd} is now a constant equal to α for s-like electrons, β for p-like electrons and x is the molar fraction of the magnetic component. With eq. (4.4) representing the net effect of the magnetic moments on the band structure it is easy to make further calculations of the semiconductor band structure in the presence of the magnetic field. We shall present the results separately for DMS with a narrow gap and those with a wide forbidden gap.

4.2. Band structure of narrow-gap DMS in the presence of a magnetic field

Since narrow-gap semiconductors are characterized by small values of the effective masses and by large g-factors it is necessary to consider simultaneously a direct effect of an external magnetic field on the band carriers together with the modifications arising via the exchange interaction. In order not to further complicate the picture we shall, for the sake of this presentation, consider a single s-like conduction band with a parabolic dispersion relation $E(k)$ and spin equal to 1/2. This is a simplification

that has to be avoided in any quantitative analysis of data obtained in real narrow-gap semiconductors such as $Hg_{1-x}Mn_xTe$. In reality, one has to take into account both the nonparabolicity of the dispersion law $E(k)$ as well as the mixing of states having various symmetries. A method of calculation of the band structure that accounts for these acts is presented in detail by Kossut (1988). We shall therefore not repeat it here.

For a simple conduction band it is easy to obtain the eigenenergies of the electrons. They may be represented by

$$E(l, k_z, \sigma) = \hbar\omega_c(l + \tfrac{1}{2}) + \sigma(g^*\mu_B H + \alpha x\langle S_z\rangle), \tag{4.5}$$

where ω_c is the cyclotron frequency, $l = 0, 1, 2, \ldots$ is the Landau quantum number, k_z is the wave vector component along the magnetic field direction, $\sigma = \pm\frac{1}{2}$ is the z-component of the electronic spin, μ_B denotes the Bohr magneton, and g^* represents the Landé factor of the band electrons without the correction due to exchange interaction. We see from eq. (4.5) that the effect of the exchange interaction is to modify the spin splitting of the band electrons. In reality the modification can be very substantial. For example, in $Hg_{1-x}Mn_xTe$ with $x > 0.07$ (open gap configuration of bands – fig. 6c) where g^* is large and negative, the contribution of the exchange interaction at low temperatures can be comparable to the absolute value of g^*. Because α is positive, this additional term is opposite in sign to g^*. This leads to a considerable reduction of the g-factor and, in extreme cases, to a change of sign of the spin splitting (e.g., Dobrowolska and Dobrowolski 1981, Geyer and Fan 1980, Bastard et al. 1981). In $Hg_{1-x}Mn_xTe$ with semimetallic band ordering (i.e., for $x < 0.07$) the exchange contribution to the spin splitting is proportional to β and, since the p–d exchange constant is negative, the resulting g-factor is greatly enhanced as can be observed in fig. 42. Often the spin splitting is found to be greater than the Landau splitting $\hbar\omega_c$ which already is very large because of the smallness of the effective mass in this narrow gap material. This can be observed in fig. 43a for fields smaller than 10 T.

It is sometimes convenient to define an effective g-factor that includes the effect of the exchange interaction. For a parabolic s-like band we have on the basis of eq. (4.5)

$$g_{\text{eff}} = g^* + \frac{\alpha x\langle S_z\rangle}{\mu_B H}. \tag{4.6}$$

The contribution of the exchange interaction to an effective g-factor is, as eq. (4.6) indicates, proportional to $\langle S_z\rangle$, i.e., to the magnetization. Therefore, the effective g-factor is a sensitive function of the temperature. This sensitivity is clearly seen in figs. 43a and 43b. The Landau levels shown in fig. 43 were calculated including, apart from the exchange interaction, also the effects of the nonparabolicity and band state mixing (i.e., they were calculated within the Pidgeon and Brown (1966) model modified by the sp–d exchange). A strong temperature variation of the spin splitting was, as mentioned, clearly observed experimentally, as fig. 42 showed. In the magnetic field range where the magnetization varies linearly with the magnetic field the second term in eq. (4.6) is proportional to the magnetic susceptibility. In higher fields, where the magnetization saturates, the exchange contribution to the effective g-factor decreases. Therefore, in the highest fields in fig. 43 the sequence of the spin-split Landau levels resembles that observed in nonmagnetic semiconductors and/or at elevated temper-

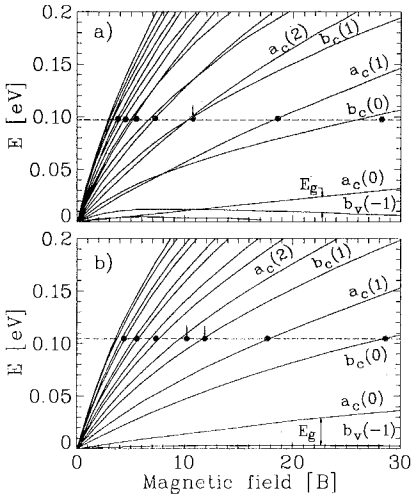

Fig. 43. Energies of the Landau levels in the conduction band in $Hg_{1-x}Mn_xTe$ with $x = 0.02$ calculated at (a) $T = 4$ K and (b) $T = 36$ K. The labels a and b denote two sets of solutions differing by the projection of the total momentum $J_z = \pm\frac{1}{2}$, the numerals after the symbols refer to the Landau quantum number. The uppermost valence band heavy hole Landau level $b_v(-1)$ is also shown. Note that the band gap at low temperature opens only in magnetic fields greater than ~ 8 T. Broken line shows the position of the Fermi level for which the positions of Shubnikov–de Haas maxima observed by Byszewski et al. (1979) are marked by solid points. Arrows mark the peak that splits at elevated temperatures.

ature. This fact is responsible for intersections of the spin-split Landau levels at a low temperature, visible in fig. 43a. The existence of these intersections (and the temperature shift of the fields of their occurrence) help to understand many anomalous features observed in quantum transport experiments in narrow-gap DMS. For example, as fig. 43 shows, they provide a natural explanation of the puzzling fact that in the magnetoresistance of $Hg_{1-x}Mn_xTe$ more Shubnikov–de Haas maxima can be resolved at an elevated temperature than at a low temperature. This is in complete contrast to the behavior found in nonmagnetic semiconductors where lowering the temperature usually leads to a better resolution of the quantum oscillations simply because the thermal broadening of the Landau levels is then reduced.

Figure 43 shows one more unusual feature of the band structure of semimetallic $Hg_{1-x}Mn_xTe$ with $x < 0.07$ in the presence of a magnetic field. As mentioned, in this range of crystal compositions the conduction band and the heavy hole valence band are degenerate at the Γ point of the Brillouin zone. Normally, in nonmagnetic semiconductors, the application of a magnetic field lifts this degeneracy by shifting the heavy hole Landau levels to lower energies while the conduction electron Landau levels move to higher energies. Therefore, the gap appears between the conduction and valence band states. Quite a different situation occurs in $Hg_{1-x}Mn_xTe$ where the exchange part of the spin splitting of the uppermost heavy hole Landau level is so strong that it moves up in energy faster than the lowest conduction band Landau level. As a result a band overlap is induced by the field. As the field increases and

the magnetization saturates, the uppermost heavy hole Landau level ceases to be shifted to higher energies at such a fast rate and, finally, it starts to move down. This causes the gap to open in the region of very intense fields. The occurrence of the band overlap is limited to the low-temperature domain. For higher temperatures (i.e., when the exchange contribution to the g-factor of the heavy holes is not very large) the band gap opens even in small magnetic fields, as can be seen in fig. 43b.

One of the interesting consequences of the exchange-induced changes of the g-factor is a peculiar temperature dependence of the amplitude of quantum oscillations. In nonmagnetic semiconductors the amplitude of, say, the Shubnikov–de Haas oscillations of the magnetoresistance is a monotonic and decreasing function of the temperature. This is related to the thermal broadening of the Landau levels which suppresses the oscillations. In DMS, on the other hand, the amplitude of the Shubnikov–de Haas oscillations was found to exhibit a nonmonotonic temperature dependence with one (or more) distinct points at which it disappears completely – see fig. 44. An explanation of this puzzling behavior makes use of rapid changes of the g-factor with the temperature, being so characteristic for DMS. The expression for the amplitude of the first harmonic of quantum oscillations contains a factor

$$\cos(\pi g_{\mathrm{eff}} m^*/2m_0),$$

where m^* is the effective mass of the conduction electrons and m_0 is the free electron mass (cf. Roth and Argyres 1966). Whenever the arguments of the cosine equals an odd multiple of $\pi/2$ the amplitude drops to zero. The temperature at which the oscillations in DMS fade out completely is thought to correspond to the equality $g_{\mathrm{eff}} = m^*/m_0$. For both lower and higher temperatures the above condition is not met and the amplitude of quantum oscillations differs from zero. Nonmonotonic behavior of the Shubnikov–de Haas effect amplitude was detected not only in $Hg_{1-x}Mn_xTe$ but also in other narrow-gap DMS (see Takeyama and Gałązka 1979, Neve et al. 1981, Lubczyński et al. 1991, Takeyama and Narita 1986b, Vaziri et al. 1985, Miller and

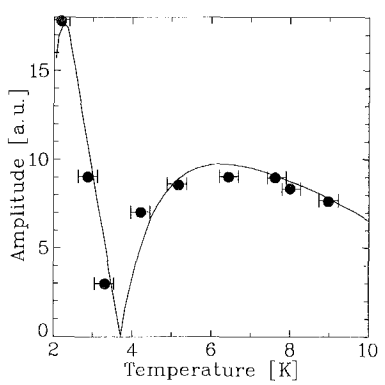

Fig. 44. The amplitude of Shubnikov–de Haas oscillations in $Hg_{1-x}Mn_xTe$ ($x = 0.02$) as a function of temperature (solid points). The solid line is calculated using a temperature-dependent g-factor (after Jaczyński et al. 1978a).

Reifenberger 1988b). A detailed analysis of the effect is often difficult since other reasons for the disappearance of the amplitude can not be excluded as pointed out by Reifenberger and Schwarzkopf (1983) and by Miller and Reifenberger (1988b).

It is interesting to devote some attention to the case of $Hg_{1-x}Fe_xSe$. As mentioned in section 2.4 the scattering rate of conduction electrons in these mixed crystal can be strongly reduced when the concentration of iron exceeds $4.4 \times 10^{18}\,cm^{-3}$, i.e., when Fe^{2+} and Fe^{3+} ions coexist in the material. Therefore, the broadening of the Landau levels is relatively small in these samples. As a result very well resolved spin splitting of the Landau levels is observable making possible a precise determination of the g-factor. An example of well resolved oscillations of magnetoresistance with clearly visible spin splitting of the Landau levels is shown in fig. 45. As discussed by Blinowski and Kacman (1990) the p–d exchange constant should, in principle, be different for iron ions in the two charge states Fe^{2+} and Fe^{3+}. In this context experiments involving hydrostatic pressure, by means of which one can influence the ratio of the number of Fe^{3+} and Fe^{2+} ions in one $Hg_{1-x}Fe_xSe$ sample, are promising. A preliminary study of Skierbiszewski et al. (1990b) indicates that the exchange constants for Fe^{2+} and Fe^{3+} ions are in fact different.

The band structure of other narrow-gap DMS, e.g., those involving PbTe or other IV–VI compounds as well as those based on II–V materials is similarly perturbed by the exchange interaction. Since the s–d and p–d coupling constants are smaller in IV–VI than in II–VI compounds with Mn the quantitative effect is weaker in, e.g., $Pb_{1-x}Mn_xTe$ than in $Hg_{1-x}Mn_xTe$ with comparable x values. For this reason determination of the values of appropriate exchange constants is only imprecise if possible at all (the complex band structure of lead chalcogenides makes this task even less trivial). On the other hand, in II–V compounds, e.g., $(Cd_{1-x}Mn_x)_3As_2$ the exchange constants are found to be larger than in II–VI compounds, which makes the g-factor

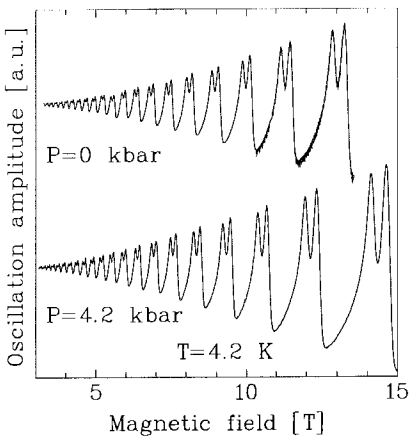

Fig. 45. Shubnikov–de Haas oscillations in $Hg_{1-x}Fe_xSe$ ($x \approx 0.0005$) at two values of hydrostatic pressure showing prominent spin splitting (after Skierbiszewski et al. 1990b).

modifications due to exchange easier to observe. Details of the calculations for these two groups of materials can be found in the original papers of Niewodniczańska-Zawadzka (1983) (see also Bauer 1987) and Neve et al. (1982), respectively.

4.3. *Band structure and optical properties of wide-gap DMS in the presence of a magnetic field*

In wide-gap II–VI semiconductors the masses and g-factors characterizing the band carriers are, respectively, considerably greater and smaller than in narrow-gap mercury compounds. Moreover, the cyclotron splitting and the spin splitting in the host wide-gap II–VI materials are small in comparison with the contribution to the spin splitting due to the exchange interaction appearing when transition-metal atoms are introduced into these hosts. Consequently, one can neglect the term involving $\hbar\omega_c$ as well as g^* in eq. (4.5). Thus, the conduction band rigidly splits in the presence of the field into two subbands. The g-factor describing this splitting is simply given by the second term of eq. (4.6). The situation is more complicated in the case of the fourfold degenerate valence band. As pointed out first by Gaj et al. (1978b), exchange interaction induces an anisotropy of the E versus $\boldsymbol{k}$ relationship. A diagonalization of the eigenvalue problem is easy only for certain orientations of the wave vector with respect to the direction of the magnetization. For $\boldsymbol{k}$ parallel to the magnetic field (i.e., magnetization) direction one obtains as a result that the valence band splits rigidly into four components with energies

$$E_{1,2} = -\frac{\hbar^2 k^2}{2m^*_{\mathrm{hh}}} \pm \tfrac{1}{2} x\beta \langle S_z \rangle, \tag{4.7}$$

$$E_{3,4} = -\frac{\hbar^2 k^2}{2m^*_{\mathrm{lh}}} \pm \tfrac{1}{6} x\beta \langle S_z \rangle, \tag{4.8}$$

where m^*_{hh} and m^*_{lh} denote heavy and light hole effective masses, respectively. An analytical solution can also be found when $\boldsymbol{k}$ is perpendicular to the field direction. Figure 46 shows a scheme of the band structure of $Cd_{1-x}Mn_xTe$ for this orientation of the wave vector as well as for the case when $\boldsymbol{k}$ makes an angle of 10° with the direction of the magnetic field and when the solutions were found numerically. It is worth noting that a clear distinction between light and heavy hole, possible for $\boldsymbol{k}//\boldsymbol{B}$, cannot be made in the cases presented in fig. 46. Also the splittings in this case are k-dependent. The splitting of the spin–orbit split-off Γ_7 band induced by the exchange interaction is also rigid, i.e., independent of k, as in the case of the Γ_6 conduction band.

The most important interband optical transitions are those between the band edge states. They are shown in fig. 47 together with corresponding selection rules for various polarizations of the light with respect of the magnetization axis. Since the exchange-induced splitting is large even at moderate magnetic fields it is not difficult to resolve it and directly observe by studying the position of the free exciton line in various light polarizations. An example is shown in fig. 48 where the energy of the two spin-split components of the heavy hole exciton (labelled a and b) is plotted as a function of the magnetic field applied to $Zn_{1-x}Mn_xTe$. Also plotted are the observed

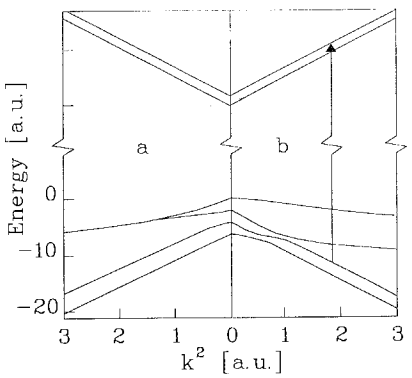

Fig. 46. Schematic representation of the dispersion relations for the conduction and valence band edges in $Cd_{1-x}Mn_xTe$-like crystals for two orientations of the wave vector and external magnetic field directions: (a) $\boldsymbol{k}$ perpendicular to $\boldsymbol{B}$, and (b) $\boldsymbol{k}$ inclined by 10° to the field direction (after Gaj et al. 1978b).

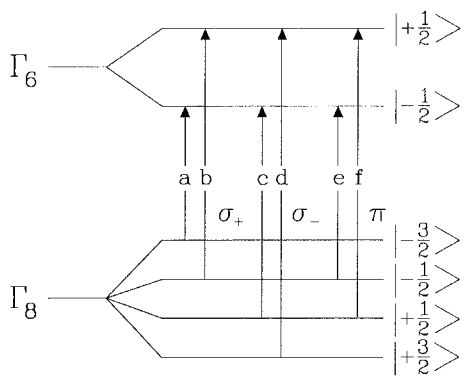

Fig. 47. Zeeman splitting of the conduction Γ_6 and valence Γ_8 band edges in $Cd_{1-x}Mn_xTe$. Arrows show optical transitions allowed in the dipole approximation for various light polarizations.

energies of the light hole exciton spin-split components. Figure 48 shows that these dependencies exhibit a characteristic saturation which resembles the saturation attained by the magnetization as the magnetic field grows. In fact, when the energy of excitonic features are plotted not as a function of the magnetic field but as a function of the magnetization (independently measured) one obtains a straight line shown for $Cd_{1-x}Mn_xTe$ in fig. 49. This strict adherence to linearity may be viewed as a direct confirmation of the applicability of various approximations (e.g., the molecular field approximation neglecting all but the S_z components of localized impurity spins in eq. (4.3)) used in the derivation of the spin splitting formulae. The slope of the line gives very direct access to the information concerning the values of the exchange constants (cf. Gaj et al. 1979).

The one-to-one correspondence between the splitting of excitonic features and the magnetization enables to use optical measurements to study magnetic properties.

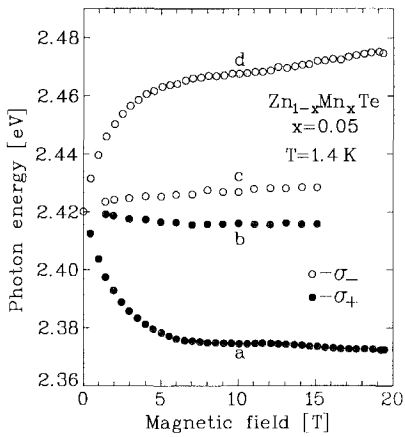

Fig. 48. Energies of various components of 1s excitonic transitions observed in magnetoreflectance in Faraday σ polarizations in $Zn_{1-x}Mn_xTe$ with $x = 0.05$. The symbols correspond to the transitions marked in fig. 47 (after Aggarwal et al. 1986).

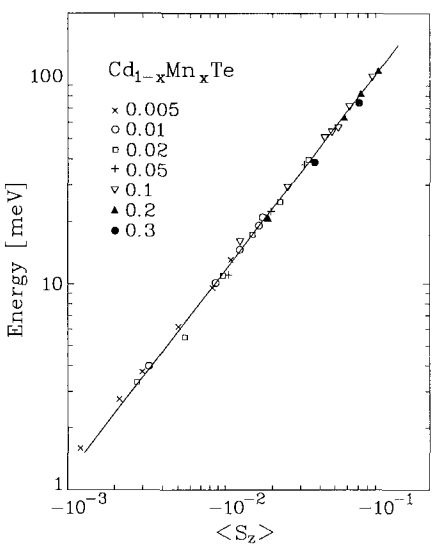

Fig. 49. Splitting of the two strong σ components (corresponding to transitions marked a and d in fig. 47) of the exciton Zeeman structure in $Cd_{1-x}Mn_xTe$ as a function of magnetization. Manganese molar fractions are given in the figure beside the corresponding symbols (after Gaj et al. 1979).

This often gives a considerable advantage since optical measurements are very precise. Moreover, they often can be performed on samples whose magnetic properties are otherwise difficult to assess (e.g., because of their small size or mass). An example of this opportunity is illustrated in fig. 50, which shows a clear magnetization step (cf. section 3.2.3). In fact, all five magnetization steps were experimentally observed only

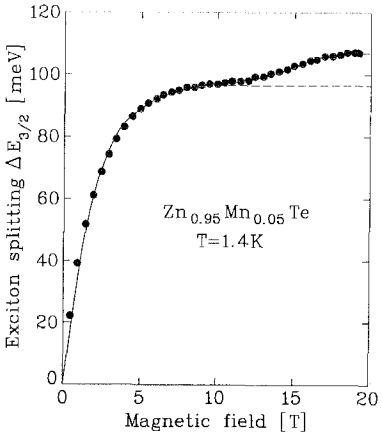

Fig. 50. Heavy hole exciton splitting in $Zn_{1-x}Mn_xTe$ at 1.4 K as a function of magnetic field showing a clear 'magnetization step' (after Aggarwal et al. 1986).

by means of optical detection (Foner et al. 1989). Measurements of the optical properties were also employed by the researchers studying the spin glass phase in DMS (e.g., Kett et al. 1981), particularly, the temporal behavior of the magnetic response in the spin-glass regime (see, e.g., Zhou et al. 1989).

The giant spin splitting of the band states, apart from being responsible for the fact that the fundamental absorption edge of light for right and left circular polarizations (σ^- and σ^+ polarizations) takes place at different energies, is also a source of a strong Faraday rotation of the polarization plane of linearly polarized light passing through wide-gap DMS samples. The magnitude of the effect is so large that the phenomenon is often referred to as a 'giant Faraday rotation' (see chapter 7 in the volume of DMS edited by Furdyna and Kossut 1988, and, e.g., Gaj et al. 1978a, Bartholomew et al. 1986). The strong Faraday rotation gives us the hope that $Cd_{1-x}Mn_xTe$ will become useful in various nonreciprocal devices in optical circuitry (Turner et al. 1983, Butler 1987, Butler et al. 1986).

4.4. Bound magnetic polarons in DMS

The concept of a free and bound magnetic polaron has been put forward in the context of magnetic semiconductors (for the history and development of the idea of magnetic polarons the reader is referred to the reviews of, e.g., von Molnar 1987, Nagaev 1983, Kasuya and Yanase 1968, Yanase 1972, Kuivalainen et al. 1979 and the extensive reference lists therein). A magnetic polaron was visualized as a charged carrier whose kinetic energy is counterbalanced by a self-induced polarization cloud of magnetic moments surrounding it and interacting with it via s–d or p–d interaction. Thus, the polaron represents an object which is considerably more localized than a carrier that does not interact with surrounding magnetic moments. Already at very early stages of development it was realized that the free polaron (self-trapped state) is much more difficult to be a stable object in real materials. On the other hand, bound

magnetic polarons with a major part of kinetic energy balanced by an additional 'binding' potential, usually due to an impurity, were shown to be, in principle, observable in magnetic substances. However, a first clearcut evidence of existence of bound magnetic polarons was obtained only after optical studies of DMS were initiated. The review of the results obtained in DMS concerning magnetic polarons can be found in the review chapter by Wolff (1988) and, even more recently, by Thibblin (1989).

The evidence of existence of bound magnetic polarons mentioned above was obtained by Nawrocki et al. (1981) by studying the spin-flip Raman scattering of light from donor bound electrons in n-$Cd_{1-x}Mn_xSe$. Nearly at the same time acceptor bound magnetic polarons were evidenced in luminescence from $Cd_{1-x}Mn_xTe$ in the presence of a magnetic field (Golnik et al. 1980). In their spin-flip Raman scattering study Nawrocki et al. (1981) observed that the Stokes-shifted line corresponding to the transition between the spin-split states of the ground state of a donor in $Cd_{1-x}Mn_xSe$ did not vanish as the external magnetic field strength was reduced to zero. This zero-field spin splitting is interpreted as resulting from a nonvanishing net magnetization in the region where the donor wave function has appreciable values. A theoretical formulation of Dietl and Spałek (1983) stressed the importance of thermal fluctuations of the magnetization in determining the properties of bound magnetic polarons. Such fluctuations, neglected in the mean field approaches to the bound magnetic polaron problem, appear because of the finite size of the system. Similar conclusions were reached by Heiman et al. (1983). An example of the Stokes shift energy obtained in spin-flip Raman scattering experiments in $Cd_{1-x}Mn_xSe$ by these authors is shown in fig. 51 together with a lines calculated within a theory that, although formulated independently, is completely analogous to that of Dietl and Spałek (1983). An extensive verification of the theory stressing the importance of magnetization fluctuations was done by Peterson et al. (1985) using a broad set of experimental data. Let us mention

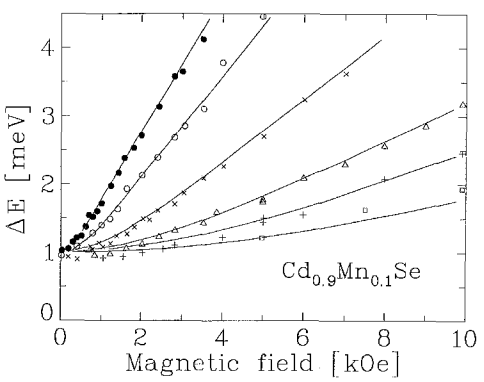

Fig. 51. Low field spin-flip Raman scattering energies in $Cd_{1-x}Mn_xSe$ as functions of the magnetic field showing nonzero values at $B = 0$ due to bound magnetic polaron. Various symbols correspond to different temperatures of the experiments – solid points: $T = 1.9$ K; open circles: $T = 3.4$ K; crosses: $T = 6.9$ K; triangles: $T = 12.8$ K; plus signs: $T = 18$ K; squares: $T = 28.3$ K (after Heiman et al. 1983).

that the presence of the fluctuations destroys the critical dependence of the bound magnetic polaron energy on the temperature. Also, the significance of the fluctuations is reduced when the strength of an external magnetic field is increased. All these features of the bound magnetic polaron dependence on temperature and/or magnetic field found their experimental confirmation.

Acceptor-bound magnetic polarons, although without any doubt shown to exist in DMS (Golnik et al. 1983, Nhung et al. 1985), are more difficult to describe theoretically. This is because the number of magnetic moments within the Bohr orbit of an acceptor-bound carrier is much smaller than in the case of donors whose Bohr radii are greater. Therefore, the role of fluctuations is even more pronounced in the case of acceptors. Calculations often resort to numerical or variational methods (see Golnik et al. 1983, Benoit a la Guillaume 1987). An attempt to improve this situation was made by Dietl (1983) – see also Jaroszyński and Dietl (1985) – who introduced correcting factors into the theory of donor-bound polarons of Dietl and Spałek (1983). A formalism that takes proper account of the complicated symmetry of an acceptor state in DMS was developed in recent years by Gel'mont et al. (1988b) and Berkovskaya et al. (1988).

The existence of bound magnetic polarons follows not only from the optical properties of DMS but also from additions to the thermal activation of the hopping conductivity in p-$Hg_{1-x}Mn_xTe$ (Dietl et al. 1983, Belayev et al. 1988) and from the thermally activated transport properties at very low temperatures in $Cd_{1-x}Mn_xTe$ where the carriers are excited from acceptors to the valence band (Jaroszyński and Dietl 1985).

Bound magnetic polarons were reported to be observed by Choi et al. (1990) in zero-gap p-$Hg_{1-x}Mn_xTe$ where acceptors are resonant with the conduction band continuum of states.

Free magnetic polarons in DMS are much more elusive than bound magnetic polarons. There are indications that they may exist in $Cd_{1-x}Mn_xTe$ (Golnik et al. 1983), or in $Hg_{1-x}Mn_xTe$ (Stępniewski 1986). Reports of the observation of free magnetic polarons in $Pb_{1-x}Mn_xS$ by Karczewski and von Ortenberg 1984 (see also Pascher et al. 1983, 1987 for similar results in $Pb_{1-x}Mn_xTe$) remain to be reconfirmed in view of the results of Zasavitskii and Sazonov (1988).

Another line of interesting investigations involving bound magnetic polarons includes time-resolved studies where the process of formation and development of a polaronic state is observed (see, e.g., Harris and Nurmikko 1983, Awschalom et al. 1985). In their time-resolved studies Oka and collaborators (Oka et al. 1987) observed that under the conditions of light-induced creation of carriers, at first free polarons are formed in $Cd_{1-x}Mn_xTe$ with $x = 0.2$–0.4. Only after some finite time they become trapped by an impurity and develop into bound magnetic polarons.

Finally, let us mention studies of a bound magnetic polaron analogue in Fe-containing DMS. As shown by Heiman et al. (1988), since the magnetic moment of an Fe^{2+} ion vanishes in its ground state, the spin splitting of an impurity bound electron in $Cd_{1-x}Fe_xSe$ decreases to zero together with the external magnetic field. This does not mean, of course, that donor-bound electrons do not interact at all via s–d interaction with 3d electrons of Fe impurities inside the Bohr radius. The interaction results

in anticrossing behavior of the inelastic Raman scattering lines associated with crystal field split levels of Fe impurities observed in $Cd_{1-x}Fe_xSe$ by Scalbert et al. (1989a).

4.5. Optically induced magnetization

As shown by experiments of, e.g., Gaj (1985) and Warnock et al. (1985) it is possible to induce a considerable spin polarization of band carriers in DMS by an optical pumping method using circularly polarized light. In principle, these spin-polarized photoexcited carriers can influence, via s–d or p–d exchange interaction, the polarization of magnetic moments. Recently, optical pumping was used in conjunction with the detection of magnetic properties using a superconducting quantum-interference device (SQUID). Experiments were performed on $Hg_{1-x}Mn_xTe$ by Krenn et al. (1985) – see also Krenn (1986) and Krenn et al. (1987, 1989) – and on $Cd_{1-x}Mn_xTe$ by Rozen and Awschalom (1986) and Awschalom et al. (1987b). Both groups detected light-induced magnetizations at minute levels. The typical magnitude of the induced magnetization was comparable to that caused by an external field on the order of 10^{-2} Oe. On the basis of these studies it is thought now that the polarization of Mn spins in $Hg_{1-x}Mn_xTe$ is induced by a mean field related to a net spin direction of the band electrons excited by light, i.e., it is associated with the diagonal elements of the s–d interaction Hamiltonian. The second possible mechanism of the magnetic polarization, the one connected with dynamic spin-flip transitions involving off-diagonal elements of the s–d interaction Hamiltonian is shown to occur only under very special conditions. The above-mentioned investigations gave also a better insight into relevant relaxation processes of optically oriented localized magnetic moments in DMS.

4.6. Transport properties of DMS in the vicinity of the metal-to-insulator transition

Exchange interaction between localized magnetic moments and band carriers may relax the momentum of the latter, contributing to the resistance of a material. However, compared to other momentum relaxation mechanisms, e.g., to that due to the scattering by Coulomb potentials of charged impurities or scattering by various phonon modes, the spin-disorder scattering is relatively inefficient in DMS. It is appreciable only under very special experimental conditions (see, e.g., Wittlin et al. 1980) or as a small correction that has to be extracted from a background due to dominant scattering mechanisms. Another method of obtaining information on spin-dependent scattering is to study the amplitude of quantum oscillatory effects (e.g., the Shubnikov–de Haas effect) and analyse subtle effects occurring close to the spin-splitting zero of the amplitude (see, e.g., Vaziri et al. 1985, Lubczyński et al. 1991).

The above remarks do not, of course, mean that s–d and p–d exchange interactions do not have any influence on charge transport phenomena in DMS. On the contrary, the influence is found to be a profound one. It is, however, connected to the creation of magnetic polarons and/or giant spin splitting of the electronic states. In fact, the giant spin splitting of the electron states helps crucially to understand the mechanism responsible for the behavior of the magnetoresistance observed in samples with a

concentration of impurities close to (but slightly larger than) the critical Mott concentration for localization. In this region of electron concentrations (known as the weakly localized regime) two effects contribute to the behavior of the magnetoresistance: quantum interference of backscattered electron waves and electron–electron interaction within the conduction electron gas. Detailed studies of this effect in $Cd_{1-x}Mn_xSe$ and CdSe in the weak localization regime were performed by Sawicki et al. (1986), and by Sawicki and Dietl (1988) – for a review see also Dietl (1990) – and showed that the quantum corrections to the conductivity in the latter material are due to the constructive interference effect. In the presence of weak magnetic fields this interference effect is partially destroyed which results in a small negative magnetoresistance observed in CdSe. Contrary to this result a negative and much stronger magnetoresistance characterizes n-$Cd_{1-x}Mn_xSe$ samples in the weakly localized regime. This fact is interpreted as evidence of the major role played by electron–electron interactions between the spin-polarized conduction electrons.

Another consequence of the giant spin splitting is a redistribution of carriers between the spin-split components of a band in which the conductivity takes place. This redistribution, by increasing the kinetic part of the carrier energy, slows down their tendency to localization. Thus, application of a magnetic field may drive a transition from the insulating to the metallic phase – a situation quite unusual in typical semiconductors where a reverse transition usually takes place. This strange phenomenon is actually observed in p-$Hg_{1-x}Mn_xTe$ (e.g., by Wojtowicz et al. 1986). The transition is particularly sharp in the case of this material enabling the precise determination of the exponents describing the conductivity near criticality (see fig. 52). Their values indicate that electron–electron interactions play a very important role at the magnetic

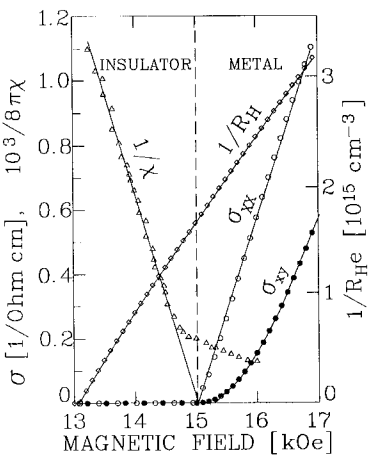

Fig. 52. Values extrapolated to zero temperature of the transverse (σ_{xx}: full circles) and longitudinal (σ_{zz}: open circles) conductivity; inverse of dielectric susceptibility $1/\chi$: triangles (left-hand scale); and inverse of the Hall constant $1/R_H$: diamonds (right-hand scale) in p-$Hg_{1-x}Mn_xTe$ ($x = 0.08$) as functions of the magnetic field in the vicinity of the metal–insulator transition. Note that the critical field for $1/R_H$ is different from that deduced from the susceptibility and conductivity (after Jaroszyński et al. 1989).

field driven Anderson transition in p-$Hg_{1-x}Mn_xTe$. Critical behavior was also found in the electric susceptibility and, more interestingly, in the Hall constant in this material. The Hall effect measurements yielded results that are unique in semiconductors (Jaroszyński et al. 1989). The Hall effect displays a critical behavior; however, the value of the critical field is significantly different from that of the conductivity (cf. fig. 52). So far this puzzling observation remains not understood.

The magnetic field induces also a more conventional transition from a metallic to an insulating phase. This occurs in open-gap n-HgMnTe where the spin splitting, as we argued earlier, is considerably smaller due to the negative sign and a smaller absolute value of the s–d coupling constant α compared to the p–d constant β that is of relevance in p-type samples. Therefore, diamagnetic effects dominate in n-type samples in the region of magnetic fields close to the insulator-to-metal transition as was shown, e.g., in a study by Wróbel et al. (1990).

4.7. DMS quantum wells and superlattices

Diluted magnetic semiconductors were employed as components of quantum wells and superlattices only very recently. Nevertheless, there are already meaningful physical results obtained on such structures. The review papers of Kolodziejski et al. (1986b), Furdyna et al. (1987) and Nurmikko et al. (1986, 1988) to some extent summarize the early efforts. More recent achievements in $CdTe/Cd_{1-x}Mn_xTe$ are described by L. L. Chang (1989). Earlier in this chapter we have discussed novel magnetic properties encountered when studying thin structures involving DMS (see section 3.3). Here we shall briefly discuss the consequences that the two-dimensional nature of quantum wells and superlattices has as far as transport and optical properties of DMS are concerned.

First of all, it has to be realized that, because of the relatively strong lattice variation with composition (see section 1.2), the majority of the DMS superlattices studied represent strained systems. This fact adds to the complexity of the analysis of experimental data. Optical studies of $Cd_{1-x}Mn_xTe/CdTe$ (see, e.g., Zhang et al. 1985, 1986, Nurmikko et al. 1985) and $Zn_{1-x}Mn_xSe/ZnSe$ (studied by Bylsma et al. 1987) showed very clearly two types of excitonic features observed in the luminescence that are due to the strain-induced splitting of heavy and light hole bands. The study of optical properties performed in the presence of a magnetic field in $Cd_{1-x}Mn_xTe/CdTe$ superlattices revealed a vigorous spin splitting although the carriers are confined to nonmagnetic CdTe wells in these structures. The splitting was shown to be (see, e.g., Zhang et al. 1985; see also S.-K. Chang et al. 1988) too large to be attributable to the effect of normal penetration of the tails of electronic wave functions into the magnetic barriers due to the finite barrier heights. Therefore, it was necessary to consider the effect of trapping of electrons and/or holes at the interfaces. It was further shown that the trapping of holes is particularly important so that their two-dimensional character is even more substantial than that caused by the confinement in the CdTe wells. In this context it was suggested that a two-dimensional analogue of a bound magnetic polaron is formed at the interfaces (Goncalves da Silva 1985, 1986, Wu et al. 1986, Gan 1986). The intensity of the luminescence from DMS quantum wells

is very intense due to the localization of excitonic states. In the case of $Zn_{1-x}Mn_xSe$/ZnSe and $Cd_{1-x}Mn_xTe$ a stimulated emission was observed by Bylsma et al. (1985) and Isaacs et al. (1986), respectively. In the case of a $Cd_{1-x}Mn_xTe$/CdTe superlattice the latter authors were able to tune the quantum well laser frequency by means of a magnetic field.

One of the most striking effects exhibited by DMS superlattices is the field-induced change of the type of the superlattice, i.e., a change of the region of localization of the charge carriers. This possibility arises as a consequence of the giant spin splitting in DMS. Because of large shifts of the band edges in the presence of a magnetic field, the offset between spin-split band edges can be reversed for one spin orientation. Figure 53 shows schematically the mechanism of this reversal of the localization of heavy holes with $m = 3/2$ in strained $ZnSe/Zn_{1-x}Fe_xSe$. The effect proposed originally by Brum et al. (1986) is found to occur in real systems including $ZnSe/Zn_{1-x}Fe_xSe$ (X. Liu et al. 1989), $ZnSe/Zn_{1-x}Mn_xSe$ (X. Liu et al. 1990) and $CdTe/Cd_{1-x}Mn_xTe$ (Deleporte et al. 1990).

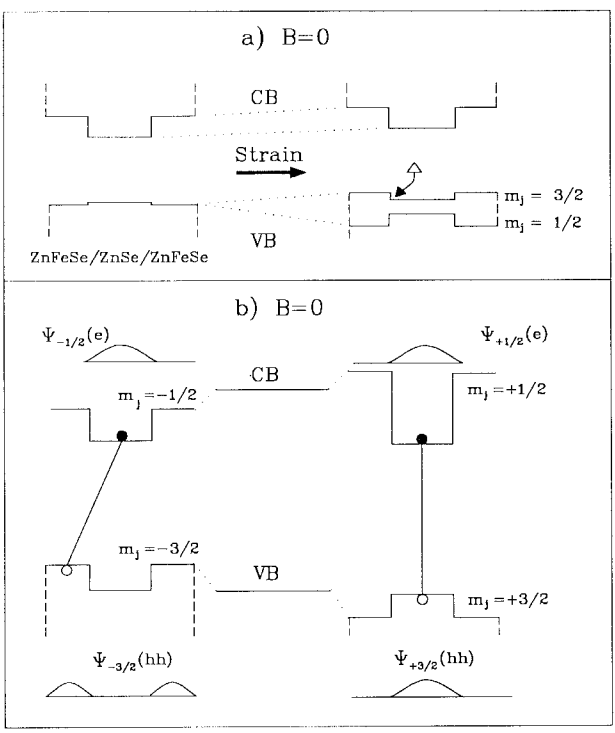

Fig. 53. Schematic representation of band edges in $ZnSe/Zn_{1-x}Fe_xSe$ quantum wells (a) in the absence of a magnetic field showing the strain-related shifts (shown not to scale) of the band edges, and (b) in the presence of the field showing the spin splitting of the conduction ($m = \pm 1/2$) and heavy hole ($m = \pm 3/2$) valence band. The general shapes of the wave functions are sketched indicating the regions of their localization. Lines show transitions in σ^+ and σ^- polarizations (after X. Liu et al. 1989).

It is worth noting that confinement of charge carriers was also achieved in thin sheets associated with grain boundaries in $Hg_{1-x}Mn_xTe$ and $Hg_xCd_yMn_zTe$ (Grabecki et al. 1984). In fact, these naturally occurring quasi two-dimensional electronic systems were of sufficiently good quality in DMS that clear plateaus of the integer quantum Hall effect were observed by Grabecki et al. (1987).

Diluted magnetic semiconductors in superlattice and quantum well configurations seem to bear the promise of observations to be made of other completely new and potentially important phenomena. One of the first papers on this subject by von Ortenberg (1982) introduced a novel notion of a spin superlattice where, because of the giant spin splitting, the adjacent layers of a superlattice will confine carriers with opposite spins[3]. Some further interesting effects that may be expected in superlattices and quantum wells containing DMS are discussed by Furdyna et al. (1987) and Kossut and Furdyna (1987). Their realization depends crucially on developments in superlattice growth and doping techniques.

Acknowledgements

We are grateful to M. Arciszewska, E. Dynowska and M. Nawrocki for making their unpublished data available to us and for consenting to present them in this work.

References

Abragam, A., and B. Bleaney, 1970, Electron paramagnetic resonance of transition ions (Clarendon Press, Oxford).

Abrahams, S.C., P. Marsh and P.M. Bridenbaugh, 1989, Acta Crystallogr. C **45**, 545.

Aggarwal, R.L., S.N. Jasperson, P. Becla and J.K. Furdyna, 1986, Phys. Rev. B **34**, 5894.

Anderson, J.R., G. Kido, Y. Nishina, M. Górska, L. Kowalczyk and Z. Gołacki, 1990, Phys. Rev. B **41**, 1014.

Anderson, P.W., 1953, Phys. Rev. **79**, 705.

Antoszewski, J., and E. Kicrzek-Pecold, 1980, Solid State Commun. **34**, 733.

Arciszewska, M., 1991, Acta Phys. Pol. A **79**, 341.

Arciszewska, M., and M. Nawrocki, 1986, J. Phys. Chem. Solids **47**, 309.

Arushanov, E.K., A.A. Gubanova, A.F. Knyazev, A.V. Lashkul, K.G. Licunov and V.V. Sologub, 1988, Fiz. Tekh. Poluprovodn. **22**, 338.

Awschalom, D.D., J.M. Halbout, S. von Molnar, T. Siegrist and F. Holtzberg, 1985, Phys. Rev. Lett. **55**, 1128.

Awschalom, D.D., J.M. Hong, L.L. Chang and G. Grinstein, 1987a, Phys. Rev. Lett. **59**, 1733.

Awschalom, D.D., J. Warnock and S. von Molnar, 1987b, Phys. Rev. Lett. **58**, 812.

Balzarotti, A., M.T. Czyżyk, A. Kisiel, N. Motta, M. Podgórny and M. Zimnal-Starnawska, 1984, Phys. Rev. B **30**, 2295.

Balzarotti, A., N. Motta, A. Kisiel, M. Zimnal-Starnawska, M.T. Czyzyk and M. Podgórny, 1985, Phys. Rev. B **31**, 7526.

Barilero, G., C. Rigaux, Nguyen Hy Hau, J.C. Picoche and W. Giriat, 1987, Solid State Commun. **62**, 345.

Bartholomew, D.U., J.K. Furdyna and A.K. Ramdas, 1986, Phys. Rev. B **34**, 6943.

Bartholomew, D.U., E.-K. Suh, S. Rodriguez, A.K. Ramdas and R.L. Aggarwal, 1987, Solid State Commun. **62**, 235.

Bartholomew, D.U., E.-K. Suh, A.K. Ramdas, S. Rodriguez, U. Debska and J.K. Furdyna, 1989, Phys. Rev. B **39**, 5865.

Bastard, G., 1978, in: Physics of Narrow Gap

[3]Spin superlattice was, in fact, recently realized (see Dai et al. 1992).

Semiconductors, Proc. Internat. Conf. Warsaw, 1977, eds J. Raułuszkiewicz, M. Górska and E. Kaczmarek (Polish Scientific Publishers, Warsaw) p. 63.

Bastard, G., C. Rigaux, Y. Guldner, J. Mycielski and A. Mycielski, 1978, J. Phys. (Paris) **39**, 87.

Bastard, G., C. Rigaux, Y. Guldner, A. Mycielski, J.K. Furdyna and D.P. Mullin, 1981, Phys. Rev. B **24**, 1961.

Bauer, G., 1987, in: Diluted Magnetic (Semimagnetic) Semiconductors, Mat. Res. Soc. Symp. Proc., Vol. 89, eds R.L. Aggarwal, J.K. Furdyna and S. von Molnar (Mater. Res. Soc., Pittsburgh) p. 107.

Bauer, G., J. Kossut, R. Faymonville and R. Dornhaus, 1985, Phys. Rev. B **31**, 2040.

Becker, W.M., 1988, in: Diluted Magnetic Semiconductors, volume eds J.K. Furdyna and J. Kossut, Vol. 25 of Semiconductors and Semimetals, series eds R.K. Willardson and A.C. Beer (Academic Press, New York) ch. 2, p. 35.

Belayev, A.E., Yu.G. Semenov and N.V. Shevchenko, 1988, JETP Lett. **48**, 675.

Benoit a la Guillaume, C., 1987, Physica B+C **146**, 234.

Berkovskaya, Yu.F., E.M. Vakhabova, B.L. Gel'mont and I.A. Merkulov, 1988, Sov. Phys. JETP **67**, 750.

Bhattacharjee, A.K., 1990a, 199Oa, in: 20th Int. Conf. Phys. Semicond., Thessaloniki (Greece), August 6–10, eds E.M. Anastassakis and J.D. Joannopulos (World Scientific, Singapore) p. 763.

Bhattacharjee, A.K., 1990b, Phys. Rev. B **41**, 5696.

Bhattacharjee, A.K., G. Fishman and B. Coqblin, 1983, Physica B+C **117–118**, 449.

Blinowski, J., and P. Kacman, 1990, in: 20th Int. Conf. Phys. Semicond., Thessaloniki (Greece), August 6–10, eds E.M. Anastassakis and J.D. Joannopulos (World Scientific, Singapore) p. 1827.

Bottka, N., J. Stankiewicz and W. Giriat, 1981, J. Appl. Phys. **52**, 4189.

Brandt, N.B., and V.V. Moshchalkov, 1984, Adv. Phys. **33**, 193.

Brandt, N.B., V.V. Moshchalkov, A.O. Orlov, L. Skrbek, I.M. Tsidil'kovskii and S.M. Chudinov, 1983, Zh. Eksp. Teor. Fiz. **84**, 1059.

Brum, J.A., G. Bastard and M. Voos, 1986, Solid State Commun. **59**, 561.

Brun del Re, R., T. Donofrio, J. Avon, J. Majid and J.C. Woolley, 1983, Nuovo Cimento D **2** 1911.

Bryja, L., and J.A. Gaj, 1988, Acta Phys. Pol. A **73**, 459.

Bunker, B.A., 1987, J. Vac. Sci. Technol. A **5**, 3003.

Butler, M.A., 1987, Solid State Commun. **62**, 45.

Butler, M.A., S.J. Martin and R.J. Baughman, 1986, Appl. Phys. Lett. **49**, 1053.

Bylsma, R.B., W.M. Becker, T.C. Bonsett, L.A. Kolodziejski, R.L. Gunshor, M. Yamanishi and S. Datta, 1985, Appl. Phys. Lett. **47**, 1039.

Bylsma, R.B., W.M. Becker, J. Kossut, U. Debska and D. Yoder-Short, 1986, Phys. Rev. B **33**, 8207.

Bylsma, R.B., J. Kossut, W.M. Becker, L.A. Kolodziejski, R.L. Gunshor and R. Frohne, 1987, J. Appl. Phys. **61**, 3011.

Byszewski, P., K. Szlenk, J. Kossut and R.R. Gałązka, 1979, Phys. Status Solidi B **95**, 359.

Byszewski, P., M.Z. Cieplak and A. Mongird-Górska, 1980, J. Phys. C **13**, 5383.

Caldas, M.J., A. Fazzio and A. Zunger, 1984, Appl. Phys. Lett. **45**, 671.

Chang, L.L., 1989, Superlattices and Microstructures **6**, 39.

Chang, S.-K., A.V. Nurmikko, J.-W. Wu, L.A. Kolodziejski and R.L. Gunshor, 1988, Phys. Rev. B **37**, 1191.

Chehab, S.F., and J.C. Woolley, 1985, J. Less-Common Met. **106**, 13.

Chehab, S.F., and J.C. Woolley, 1987, Phys. Status Solidi B **139**, 213.

Ching, W.Y., and D.L. Huber, 1982, Phys. Rev. B **25**, 5761.

Choi, J.B., R. Mani, H.D. Drew and P. Becla, 1990, Phys. Rev. B **42**, 3454.

Chou, H.H., and H.Y. Fan, 1974, Phys. Rev. B **10**, 901.

Claessen, L.M., A. Wittlin and P. Wyder, 1990, Phys. Rev. B **41**, 451.

Cochrane, R.W., F.T. Hedgcock, A.W. Lightstone and J.O. Ström-Olsen, 1974, AIP Conf. Proc., **24**, 71.

Corliss, L.M., J.M. Hastings, S.M. Shapiro, Y. Shapira and P. Becla, 1986, Phys. Rev. B **33**, 608.

Dai, N., H. Luo, F.C. Zhang, N. Samarth, M. Dobrowolska and J.K. Furdyna, 1992, Phys. Rev. Lett. **67**, 3824.

Davydov, A.B., L.M. Noskova, B.B. Ponikarov and L.A. Ogorodnikova, 1980, Fiz. Tekh. Poluprovodn. **14**, 1461.

de Gennes, P.G., 1962, J. Phys. Rad. **23**, 630.

de Jonge, W.J.M., A. Twardowski and

C.J.M. Denissen, 1987, in: Diluted Magnetic (Semimagnetic) Semiconductors, Mater. Res. Soc. Symp., Vol. 89, eds R.L. Aggarwal, J.K. Furdyna and S. von Molnar (Mater. Res. Soc., Pittsburgh) p. 153.

Deleporte, E., J.M. Berroir, G. Bastard, C. Delalande, J.M. Hong and L.L. Chang, 1990, Phys. Rev. B **42**, 5891.

Denissen, C.J.M., 1986, Ph.D. Thesis (Eindhoven) unpublished.

Denissen, C.J.M., H. Nishihara, J.C. van Gool and W.J.M. de Jonge, 1986, Phys. Rev. B **33**, 7637.

Denissen, C.J.M., Sun Dakun, K. Kopinga, W.J.M. de Jonge, H. Nishihara, T. Sakakibara and T. Goto, 1987, Phys. Rev. B **36**, 5316.

Dietl, T., 1983, J. Magn. & Magn. Mater. **38**, 34.

Dietl, T., 1987, Jpn. J. Appl. Phys. Suppl. **26**, suppl. 26-3 pt. 3, 1907.

Dietl, T., 1990, J. Cryst. Growth **101**, 808.

Dietl, T., and J. Spałek, 1983, Phys. Rev. B **28**, 1548.

Dietl, T., J. Antoszewski and L. Świerkowski, 1983, Physica B+C **117–118**, 491.

Diouri, J., J.P. Lascaray and M.El. Amrani, 1985, Phys. Rev. B **31**, 7995.

Dobrowolska, M., and W. Dobrowolski, 1981, J. Phys. C **14**, 5689.

Dobrowolska, M., W. Dobrowolski, R.R. Gałązka and A. Mycielski, 1981, Phys. Status Solidi B **105**, 477.

Dobrowolski, W., K. Dybko, A. Mycielski, J. Mycielski, J. Wróbel, S. Piechota, M. Palczewska, H. Szymczak and Z. Wilamowski, 1987, in: Proc. 18th. Conf. Phys. Semicond., Stockholm 1986, ed. O. Engström (World Scientific, Singapore) p. 1743.

Dobrowolski, W., K. Dybko, C. Skierbiszewski, T. Suski, E. Litwin-Staszewska, S. Miotkowska, J. Kossut and A. Mycielski, 1988, in: Proc. 19th. Int. Conf. Physics Semicond., Warsaw 1988, ed. W. Zawadzki (Institute of Physics Polish Academy of Science, Warsaw) p. 1247.

Dobrowolski, W., J. Kossut, B. Witkowska and R.R. Gałązka, 1989, in: High Magnetic Field in Semiconductor Physics II, Proc. of the Int. Conf., Wuerzburg Germany, 1988, ed. G. Landwehr (Springer, Berlin) p. 496.

Donofrio, T., G. Lamarche and J.C. Woolley, 1985, J. Appl. Phys. **57**, 1932.

Dugaev, V.K., and V.I. Litvinov, 1990, Phys. Rev. B **41**, 788.

Dynowska, E., et al., unpublished.

Dynowska, E., A. Sarem, B. Orłowski and A. Mycielski, 1990, Mater. Res. Bull. **25**, 1109.

Dzwonkowski, P., B.J. Kowalski, B.A. Orłowski and A. Mycielski, 1986, Acta Phys. Pol. A **69**, 1047.

Ehrenreich, H., K.C. Hass, N.F. Johnson, B.E. Larson and R.J. Lempert, 1987, in: Proc. 18th Int. Conf. Phys. Semicond., Stockholm, 1986, ed. O. Engström (World Scientific, Singapore) p. 1751.

Foner, S., Y. Shapira, D. Heiman, P. Becla, R. Kershaw, K. Dwight and A. Wold, 1989, Phys. Rev. B **39**, 11793.

Franciosi, A., 1987, in: Diluted Magnetic (Semimagnetic) Semiconductors, Mat. Res. Soc. Symp. Proc., Vol. 89, eds R.L. Aggarwal, J.K. Furdyna and S. von Molnar (Mater. Res. Soc., Pittsburgh) p. 175.

Franciosi, A., S. Chang, C. Caprile, R. Reifenberger and U. Debska, 1985a, J. Vac. Sci. Technol. A **3**, 926.

Franciosi, A., S. Chang, R. Reifenberger, U. Debska and R. Riedel, 1985b, Phys. Rev. B **32**, 6682.

Franciosi, A., A. Wall, Y. Gao, J.H. Weaver, M.-H. Tsai, J.D. Dow, R.V. Kasowski, R. Reifenberger and F. Pool, 1989, Phys. Rev. B **40**, 12009.

Furdyna, J.K., 1982, J. Appl. Phys. **53**, 7637.

Furdyna, J.K., 1988, J. Appl. Phys. **64**, R29.

Furdyna, J.K., and J. Kossut, 1986, Superlattices and Microstructures **2**, 89.

Furdyna, J.K., and J. Kossut, eds, 1988, Semiconductors and Semimetals, Vol. 25, Diluted Magnetic Semiconductors, series eds R.K. Willardson and A.C. Beer (Academic Press, New York).

Furdyna, J.K., J. Kossut and A.K. Ramdas, 1987, in: Optical Properties of Narrow-Gap Low-Dimensional Structures, Proc. of a NATO Adv. Research Workshop, 29 July–1 Aug. 1986, St. Andrews, Scotland, eds C.M. Sotomayor Torres and J.C. Portal (Plenum Press, New York) p. 135.

Furdyna, J.K., N. Samarth, R.B. Frankel and J. Spałek, 1988, Phys. Rev. B **37**, 3707.

Gaj, J.A., 1980, in: Proc. 15th Int. Conf. Phys. Semicond., Kyoto 1980, eds S. Tanaka and Y. Toyozawa (Phys. Soc. Japan, Tokyo) p. 797.

Gaj, J.A., 1985, in: Proc. 17th Int. Conf. Phys. Semicond., San Francisco 1984, eds J.D. Chadi and W.A. Harrison (Springer, New York) p. 1423.

Gaj, J.A., and A. Golnik, 1987, Acta Phys. Pol. A **71**, 197.

Gaj, J.A., R.R. Gałązka and M. Nawrocki, 1978a, Solid State Commun. **25**, 193.

Gaj, J.A., J. Ginter and R.R. Gałązka, 1978b, Phys. Status Solidi B **89**, 655.

Gaj, J.A., R. Planel and G. Fishman, 1979, Solid State Commun. **29**, 435.

Gałązka, R.R., 1978, in: Proc 14th Int. Conf. Phys. Semicond., Edinburgh 1978, ed. B.L.H. Wilson, Inst. Phys. Conf. Ser. 43 (Institute of Physics, London) p. 133.

Gałązka, R.R., 1987, in: Proc. 18th Int. Conf. Phys. Semicond., Stockholm 1986, ed. O. Engström (World Scientific, Singapore) p. 1727.

Gałązka, R.R., S. Nagata and P.H. Keesom, 1980, Phys. Rev. B **22**, 3344.

Gałązka, R.R., W. Dobrowolski, J.P. Lascaray, M. Nawrocki, A. Bruno, J.M. Broto and J.C. Ousset, 1988, J. Magn. & Magn. Mater. **72**, 174.

Gan, Z., 1986, Phys. Rev. B **34**, 7391.

Gel'mont, B.L., V.I. Ivanov-Omskii, I.T. Postolaki and V.A. Smirnov, 1988a, Sov. Phys. Semicond. **20**, 318.

Gel'mont, B.L., I.A. Merkulov, Yu.F. Ruzina and I.L. Beinikhes, 1988b, Sov. Phys. Solid State **30**, 1220.

Gel'mont, B.L., R.R. Gałązka, V.I. Ivanov-Omskii and V.A. Smirnov, 1988c, Semicond. Sci. Technol. **3**, 514.

Germanenko, A.V., G.M. Minkov, O.E. Rut and E.L. Rumyantsev, 1990, in: 20th Int. Conf. Phys. Semicond., Thessaloniki (Greece), August 6–10, eds E.M. Anastassakis and J.D. Joannopulos (World Scientific, Singapore) p. 1791.

Geyer, F.F., and H.Y. Fan, 1980, IEEE J. Quantum Electron. **QE-16**, 1365.

Giebultowicz, T., and T.M. Holden, 1988, in: Diluted Magnetic Semiconductors, volume eds J.K. Furdyna and J. Kossut, Vol. 25 of Semiconductors and Semimetals, series eds R.K. Willardson and A.C. Beer (Academic Press, New York) ch. 4, p. 125.

Giebultowicz, T., B. Lebech, B. Buras, W. Minor, H. Kepa and R.R. Gałązka, 1984, J. Appl. Phys. **55**, 2305.

Giebultowicz, T.M., J.J. Rhyne, W.Y. Ching and D.L. Huber, 1985, J. Appl. Phys. **57**, 3415.

Giebultowicz, T.M., J.J. Rhyne, W.Y. Ching, D.L. Huber and R.R. Gałązka, 1986, J. Magn. & Magn. Mater., **54**, 1149.

Giebultowicz, T.M., J.J. Rhyne and J.K. Furdyna, 1987, J. Appl. Phys. **61**, 3557.

Giebultowicz, T.M., J.J. Rhyne, W.Y. Ching, D.L. Huber, J.K. Furdyna, B. Lebech and R.R. Gałązka, 1989, Phys. Rev. B **39**, 6857.

Giebultowicz, T.M., J.J. Rhyne, J.K. Furdyna and P. Klosowski, 1990a, J. Appl. Phys. **67**, 5096.

Giebultowicz, T.M., P. Klosowski, J.J. Rhyne, T.J. Udovic, J.K. Furdyna and W. Giriat, 1990b, Phys. Rev. B **41**, 504.

Giebultowicz, T.M., P. Klosowski, N. Samarth, H. Luo, J.J. Rhyne and J.K. Furdyna, 1990c, Phys. Rev. B **42**, 2582.

Giriat, W., and J.K. Furdyna, 1988, in: Diluted Magnetic Semiconductors, volume eds J.K. Furdyna and J. Kossut, Vol. 25 of Semiconductors and Semimetals, series eds R.K. Willardson and A.C. Beer (Academic Press, New York) ch. 1, p. 1.

Giriat, W., and J. Stankiewicz, 1980, Phys. Status Solidi A **59**, K79.

Gluzman, N.G., L.D. Sabirzyanova, I.M. Tsidil'kovskii, L.D. Paranchich and S.Yu. Paranchich, 1986a, Fiz. Tekh. Poluprovodn. **20**, 94.

Gluzman, N.G., L.D. Sabirzyanova, I.M. Tsidil'kovskii, L.D. Paranchich and S.Yu. Paranchich, 1986b, Fiz. Tekh. Poluprovodn. **20**, 1994.

Golnik, A., J.A. Gaj, M. Nawrocki, R. Planel and C. Benoit a la Guillaume, 1980, in: Proc. 15th Int. Conf. Phys. Semicond., Kyoto 1980, eds S. Tanaka and Y. Toyozawa (Phys. Soc. Japan, Tokyo) p. 819.

Golnik, A., J. Ginter and J.A. Gaj, 1983, J. Phys. C **16**, 6073.

Goncalves da Silva, C.E.T., 1985, Phys. Rev. B **32**, 6962.

Goncalves da Silva, C.E.T., 1986, Phys. Rev. B **33**, 2923.

Górska, M., and J.R. Anderson, 1988, Phys. Rev. B **38**, 9120.

Grabecki, G., T. Dietl, P. Sobkowicz, J. Kossut and W. Zawadzki, 1984, Appl. Phys. Lett. **45**, 1214.

Grabecki, G., T. Suski, T. Dietl, T. Skośkiewicz and M. Glinski, 1987, in: High Magnetic Field in Semiconductor Physics, Proc. of the Int. Conf., Wuerzburg Germany, 1986, ed. G. Landwehr (Springer, Berlin) p. 127.

Grynberg, M., 1983, Physica B+C **117–118**, 461.

Gumlich, H.-E., 1981, J. Lumin. **23**, 73.

Gunnarsson, O., O.K. Andersen, O. Jepsen and J. Zaanen, 1989, Phys. Rev. B **39**, 1707.

Gunshor, R.L., L.A. Kolodziejski, N. Otsuka, B.P. Gu, D. Lee, Y. Hefetz and A.V. Nurmikko, 1987, Superlatt. Microstr. **3**, 5.

Harris, J.H., and A.V. Nurmikko, 1983, Phys. Rev.

Lett. **51**, 1472.
Hass, K.C., and H. Ehrenreich, 1983, J. Vac. Sci. Technol. A **1**, 1678.
Hass, K.C., B.E. Larson, H. Ehrenreich and A.E. Carlsson, 1986, J. Magn. & Magn. Mater. **54**, 1283.
Heiman, D., P.A. Wolff and J. Warnock, 1983, Phys. Rev. B **27**, 4848.
Heiman, D., Y. Shapira and S. Foner, 1984, Solid State Comunn. **51**, 603.
Heiman, D., A. Petrou, S.H. Bloom, Y. Shapira, E.D. Isaacs and W. Giriat, 1988, Phys. Rev. Lett. **60**, 1876.
Heremans, J., and D.L. Partin, 1988, Phys. Rev. B **37**, 6311.
Holden, T.M., G. Dolling, V.S. Fears, J.K. Furdyna and W. Giriat, 1982, Phys. Rev. B **26**, 5074.
Hui, P.M., H. Ehrenreich and K.C. Hass, 1989, Phys. Rev. B **40**, 12346.
Ikeda, M., K. Itoh and H. Sato, 1968, J. Phys. Soc. Jpn. **25**, 455.
Isaacs, E.D., D. Heiman, J.J. Zayhowski, R.N. Bicknell and J.F. Schetzina, 1986, Appl. Phys. Lett. **48**, 275.
Isaacs, E.D., D. Heiman, P. Becla, Y. Shapira, R. Kershaw, K. Dwight and A. Wold, 1988, Phys. Rev B **38**, 8412.
Ivanov-Omskii, V.I., B.T. Kolomiets, W.M. Mielnik and V.K. Ogorodnikov, 1969, Fiz. Tverd. Tela **11**, 2563.
Jaczyński, M., J. Kossut and R.R. Gałązka, 1978a, Phys. Status Solidi B **88**, 73.
Jaczyński, M., J. Kossut and R.R. Gałązka, 1978b, in: Phys. Narrow Gap Semicond. Proc. Int. Conf. Warsaw 1977, eds J. Raułuszkiewicz, M. Górska, and E. Kaczmarek (Panst. Wydawn. Nauk, Warsaw) p. 325.
Jaroszyński, J., and T. Dietl, 1985, Solid State Commun. **55**, 491.
Jaroszyński, J., T. Dietl, M. Sawicki, T. Wojtowicz and W. Plesiewicz, 1989, in: High Magnetic Field in Semiconductor Physics II, Proc. Int. Conf., Wuerzburg Germany, 1988, ed. G. Landwehr (Springer, Berlin) p. 514.
Johnson, W.B., J.R. Anderson and D.R. Stone, 1984, Phys. Rev. B **29**, 6679.
Jonker, B.T., J.J. Krebs, S.B. Qadri and G.A. Prinz, 1987, Appl. Phys. Lett. **50**, 848.
Jonker, B.T., J.J. Krebs and G.A. Prinz, 1988, Appl. Phys. Lett. **53**, 450.
Kaniewski, J., and A. Mycielski, 1982, Solid State Commun. **41**, 959.
Karczewski, G., and M. von Ortenberg, 1984, in: Proc. 17th Int. Conf. Phys. Semicond., San Francisco, 1984, eds J.D. Chadi and W.A. Harrison (Springer New York) p. 1435.
Karczewski, G., M. Klimkiewicz, I. Glass, A. Szczerbakow and R. Behrendt, 1982, Appl. Phys. A **29**, 49.
Karczewski, G., M. von Ortenberg, Z. Wilamowski, W. Dobrowolski and J. Niewodniczańska-Zawadzka, 1985, Solid State Commun. **55**, 249.
Kasuya, T., and A. Yanase, 1968, Rev. Mod. Phys. **40**, 684.
Kendelewicz, T., 1980, Solid State Commun. **36**, 127.
Kendelewicz, T., 1981, J. Phys. C **14**, L407.
Kett, H., W. Gebhardt, U. Krey and J.K. Furdyna, 1981, J. Magn. & Magn. Mater. **25**, 215.
Khattak, G.D., C.D. Amarasekara, S. Nagata, R.R. Gałązka and P.H. Keesom, 1981, Phys. Rev. B **23**, 3553.
Kim, R.S., Y. Mita, S. Takeyama and S. Narita, 1982, in: Physics of Narrow Gap Semiconductors, Lecture Notes in Physics, Vol. 152, eds E. Gornik, H. Heinrich and L. Palmetshofer (Springer, Berlin) p. 316.
Kolodziejski, L.A., R.L. Gunshor, N. Otsuka, B.P. Gu, Y. Hefetz and A.V. Nurmikko, 1986a, Appl. Phys. Lett. **48**, 1482.
Kolodziejski, L.A., R.L. Gunshor, N. Otsuka, S. Datta, W.M. Becker and A.V. Nurmikko, 1986b, IEEE J. Quantum Electron. **QE-22**, 1666.
Kossut, J., 1988, in: Diluted Magnetic Semiconductors, volume eds J.K. Furdyna and J. Kossut, Vol. 25 of Semiconductors and Semimetals, series eds R.K. Willardson and A.C. Beer (Academic Press, New York) ch. 5, p. 183.
Kossut, J., and J.K. Furdyna, 1987, in: Diluted Magnetic (Semimagnetic) Semiconductors, Mat. Res. Soc. Symp. Proc., Vol. 89, eds R.L. Aggarwal, J.K. Furdyna and S. von Molnar (Mater. Res. Soc., Pittsburgh) p. 97.
Kossut, J., W. Dobrowolski, Z. Wilamowski, T. Dietl and K. Świątek, 1990, Semicond. Sci. Technol. **5**, S260.
Krenn, H., 1986, Festkörperprobleme **26**, 183.
Krenn, H., W. Zawadzki and G. Bauer, 1985, Phys. Rev. Lett. **55**, 1510.
Krenn, H., K. Kaltenegger and G. Bauer, 1987, in: Proc. 18th Int. Conf. Phys. Semicond., Stockholm, 1986, ed. O. Engström (World Scientific, Singapore) p. 1477.
Krenn, H., K. Kaltenegger, T. Dietl, J. Spałek and G. Bauer, 1989, Phys. Rev. B **39**, 10918.
Kuivalainen, R., J. Sinkkonen, K. Kaski and

T. Stubb, 1979, Phys. Stat. Sol. B **94**, 181.
Langer, J.M., and H. Heinrich, 1985, Phys. Rev. Lett. **55**, 1414.
Larson, B.E., and H. Ehrenreich, 1989, Phys. Rev. B **39**, 1747.
Larson, B.E., K.C. Hass, H. Ehrenreich and A.E. Carlsson, 1985, Solid State Commun. **56**, 347.
Larson, B.E., K.C. Hass and R.L. Aggarwal, 1986, Phys. Rev. B **33**, 1789.
Larson, B.E., K.C. Hass, H. Ehrenreich and A.E. Carlsson, 1988, Phys. Rev. B **37**, 4137.
Lascaray, J.P., M. Nawrocki, J.M. Broto, M. Rakoto and M. Demianiuk, 1987, Solid State Commun. **61**, 401.
Lascaray, J.P., A. Bruno, J.C. Ousset, H. Rakoto, J.M. Broto and S. Askenazy, 1989, Physica B **155**, 353.
Lautenschlager, P., S. Logothetidis, L. Vina and M. Cardona, 1985, Phys. Rev. B **32**, 3811.
Le Van Khoi, A. Szczerbakow, G. Karczewski and R.R. Gałązka, 1991, Acta Phys. Polon. A **79**, 287.
Lee, V.-C., and L. Liu, 1983, Solid State Commun. **48**, 341.
Lee, Y.R., and A.K. Ramdas, 1984, Solid State Commun. **51**, 861.
Lee, Y.R., A.K. Ramdas and R.L. Aggarwal, 1986, Phys. Rev. B **33**, 7383.
Lee, Y.R., A.K. Ramdas and R.L. Aggarwal, 1987, in: Proc. 18th Int. Conf. Phys. Semicond., Stockholm, 1986, ed. O. Engström (World Scientific, Singapore) p. 1759.
Lee, Y.R., A.K. Ramdas and R.L. Aggarwal, 1988, Phys. Rev. B **38**, 10600.
Lenard, A., T. Dietl, M. Sawicki, W. Dobrowolski, K. Dybko, T. Skośkiewicz, W. Plesiewicz, S. Miotkowska, A. Witek and A. Mycielski, 1990, J. Low Temp. Phys. **80**, 15.
Lewicki, A., J. Spałek and J. Mycielski, 1987, J. Phys. C **20**, 2005.
Lewicki, A., J. Spałek, J.K. Furdyna and R.R. Gałązka, 1988, Phys. Rev. B **37**, 1860.
Lewicki, A., A.I. Schindler, J.K. Furdyna and W. Giriat, 1989, Phys. Rev. B **40**, 2379.
Ley, L., M. Taniguchi, J. Ghijsen, R.L. Johnson and A. Fujimore, 1987, Phys. Rev. B **35**, 2839.
Liu, L., and G. Bastard, 1982, Phys. Rev. B **25**, 487.
Liu, S.H., 1961, Phys. Rev. **121**, 451.
Liu, X., A. Petrou, J. Warnock, B.T. Jonker, G.A. Prinz and J.J. Krebs, 1989, Phys. Rev. Lett. **63**, 2280.
Liu, X., W.C. Chou, A. Petrou, J. Warnock, B.T. Jonker, G.A. Prinz and J.J. Krebs, 1990, in: 20th Int. Conf. Phys. Semicond., Thessaloniki (Greece), August 6–10, eds E.M. Anastassakis and J.D. Joannopulos (World Scientific, Singapore) p. 621.
Lubczyński, W., J. Cisowski, J. Kossut and J.C. Portal, 1991, Semicond. Sci. Technol. **6**, 619.
Lyapilin, I.I., and I.M. Tsidil'kovskii, 1985, Usp. Fiz. Nauk **146**, 35.
Madelung, O., ed., 1982, Landolt-Börnstein Tables: Physics of II–VI and I–VII Compounds, Semimagnetic Semiconductors, Vol. 17b (Springer, Berlin).
Masek, J., and B. Velicky, 1987, Phys. Status Solidi B **140**, 135.
Mermin, N.D., and H. Wagner, 1966, Phys. Rev. Lett. **17**, 1133.
Mikkelsen Jr, J.C., and J.B. Boyce, 1982, Phys. Rev. Lett. **49**, 1412.
Miller, M.M., and R. Reifenberger, 1988a, Phys. Rev. B **38**, 4120.
Miller, M.M., and R. Reifenberger, 1988b, Phys. Rev. B **38**, 3423.
Morales, J.E., W.M. Becker and U. Debska, 1985, Phys. Rev. B **32**, 5202.
Morales Toro, J.E., W.M. Becker, B.I. Wang, U. Debska and J.W. Richardson, 1984, Solid State Commun. **52**, 41.
Mycielski, A., 1987, in: Diluted Magnetic (Semimagnetic) Semiconductors, Mat. Res. Soc. Symp. Proc., Vol. 89, eds R.L. Aggarwal, J.K. Furdyna and S. von Molnar (Mater. Res. Soc., Pittsburgh) p. 159.
Mycielski, A., 1988, J. Appl. Phys. **63**, 3279.
Mycielski, A., C. Rigaux, M. Menant, T. Dietl and M. Otto, 1984, Solid State Commun. **50**, 257.
Mycielski, A., P. Dzwonkowski, B. Kowalski, B.A. Orłowski, M. Dobrowolska, M. Arciszewska, W. Dobrowolski and J.M. Baranowski, 1986, J. Phys. C **19**, 3605.
Mycielski, J., 1981, in: Recent Dev. Condens. Matter Phys., Vol. 1, ed. J.T. Devreese (Plenum Press, New York) p. 725.
Mycielski, J., 1986, Solid State Commun. **60**, 165.
Nagaev, E., 1983, Physics of Magnetic Semiconductors (MIR Publishers, Moscow).
Nagata, S., R.R. Gałązka, D.P. Mullin, H. Akbarzadeh, G.D. Khattak, J.K. Furdyna and P.H. Keesom, 1980, Phys. Rev. B **22**, 3331.
Nawrocki, M., R. Planel, G. Fishman and R.R. Gałązka, 1981, Phys. Rev. Lett. **46**, 735.
Nawrocki, M., J.P. Lascaray, D. Coquillat and M. Demianiuk, 1987, in: Diluted Magnetic

(Semimagnetic) Semiconductors, Mat. Res. Soc. Symp. Proc., Vol. 89, eds. R.L. Aggarwal, J.K. Furdyna and S. von Molnar (Mater. Res. Soc., Pittsburgh) p. 65.

Nawrocki, M., F. Hamdani, J.P. Lascaray, Z. Gołacki and J. Deportes, 1991, Solid State Commun. **77**, 111.

Neve, J.J., C.J.R. Bouvens and F.A.P. Blom, 1981, Solid State Commun. **38**, 27.

Neve, J.J., J. Kossut, C.M. van Es and F.A.P. Blom, 1982, J. Phys. C **15**, 4795.

Nhung, T., R. Planel, C. Benoit a la Guillaume and A.K. Bhattacharjee, 1985, Phys. Rev. B **31**, 2388.

Niewodniczańska-Zawadzka, J., G. Elsinger, L. Palmetshofer, E.J. Fanter, G. Bauer, A. Lopez-Otero and W. Zawadzki, 1983, Physica B+C **117–118**, 458.

Niewodniczańska-Zawadzka, J., T. Piotrowski and J. Kossut, 1985, J. Cryst. Growth **72**, 398.

Nowik, I., E.R. Bauminger, A. Mycielski and H. Szymczak, 1988, Physica B **153**, 215.

Nurmikko, A.V., X.-C. Zhang, S.-K. Chang, L.A. Kolodziejski, R.L. Gunshor and S. Datta, 1985, J. Lumin. **34**, 89.

Nurmikko, A.V., R.L. Gunshor and L.A. Kolodziejski, 1986, J. Quantum Electron. **QE-22**, 1785.

Nurmikko, A.V., Fu Qiang, D. Lee, L.A. Kolodziejski and R.L. Gunshor, 1988, in: Proc. 19th Int. Conf. Physics Semicond., Warsaw 1988, ed. W. Zawadzki (Institute of Physics Polish Academy of Science, Warsaw) p. 1523.

Oelhafen, P., M.P. Vecchi, J.L. Freeouf and V.L. Moruzzi, 1982, Solid State Commun. **44**, 1547.

Oka, Y., K. Nakamura, I. Souma, M. Kido and H. Fujisaki, 1987, J. Lumin. **38**, 263.

Orłowski, B.A., K. Kopalko and W. Chab, 1984, Solid State Commun. **50**, 749.

Oseroff, S., and F.G. Gandra, 1985, J. Appl. Phys. **57**, 3421.

Oseroff, S., and P.H. Keesom, 1988, in: Diluted Magnetic Semiconductors, volume eds J.K. Furdyna and J. Kossut, Vol. 25 of Semiconductors and Semimetals, series eds R.K. Willardson and A.C. Beer (Academic Press, New York) ch. 3, p. 73.

Oseroff, S.B., 1982, Phys. Rev. B **25**, 6584.

Paranchich, C.Y., L.D. Paranchich, V.N. Makogonienko and C.V. Lototzkaia, 1990, Fiz. Tekh. Poluprov. **24**, 225.

Pascher, H., E.J. Fanter, G. Bauer, W. Zawadzki and M. von Ortenberg, 1983, Solid State Commun. **48**, 461.

Pascher, H., P. Rothlein, G. Bauer and L. Palmetshofer, 1987, Phys. Rev. B **36**, 9395.

Pastor, K., M. Grynberg and R.R. Gałązka, 1979, Solid State Commun. **29**, 739.

Peterson, D.L., D.U. Bartholomew, U. Debska, A.K. Ramdas and S. Rodriguez, 1985, Phys. Rev. B **32**, 323.

Pidgeon, C.R., and R. Brown, 1966, Phys. Rev. **146**, 575.

Pietraszko, A., and K. Łukaszewicz, 1979, Phys. Status Solidi A **18**, 723.

Pool, F.S., J. Kossut, U. Debska and R. Reifenberger, 1987, Phys. Rev. B **35**, 3900.

Quintero, M., and J.C. Woolley, 1985, Phys. Status Solidi A **92**, 449.

Reifenberger, R., and J. Kossut, 1987, J. Vac. Sci. Technol. A **5**, 2995.

Reifenberger, R., and D.A. Schwarzkopf, 1983, Phys. Rev. Lett. **50**, 907.

Roth, L., and P.N. Argyres, 1966, in: Semiconductors and Semimetals, Vol. 1, eds R.K. Willardson and A.C. Beer (Academic Press, New York) p. 159.

Rozen, J.R., and D.D. Awschalom, 1986, Appl. Phys. Lett. **49**, 1649.

Samarth, N., and J.K. Furdyna, 1988, Solid State Commun. **65**, 801.

Samarth, N., H. Luo, J.K. Furdyna, S.B. Qadri, Y.R. Lee, A.K. Ramdas and N. Otsuka, 1989, Appl. Phys. Lett. **54**, 2680.

Sandauer, A.M., and P. Byszewski, 1982, Phys. Status Solidi B **109**, 167.

Sarem, A., B.J. Kowalski, J. Majewski, J. Górecka, B.A. Orlowski, A. Mycielski and K. Jezierski, 1990, Acta Phys. Polon. A **77**, 407.

Savage, H., J.J. Rhyne, R. Holm, J.R. Cullen, C.E. Carroll and E.P. Wohlfarth, 1973, Phys. Status Solidi B **58**, 685.

Sawicki, M., and T. Dietl, 1988, in: Proc. 19th Int. Conf. on Physics of Semicond., Warsaw, 1988, ed. W. Zawadzki (Institute of Physics Polish Academy of Science, Warsaw) p. 1217.

Sawicki, M., T. Dietl, J. Kossut, J. Igalson, T. Wojtowicz and W. Plesiewicz, 1986, Phys. Rev. Lett. **56**, 508.

Scalbert, D., J.A. Gaj, A. Mauger, J. Cernogora and C. Benoit a la Guillaume, 1989a, Phys. Rev. Lett. **62**, 2865.

Scalbert, D., J. Cernogora, A. Mauger, C. Benoit a la Guillaume and A. Mycielski, 1989b, Solid State Commun. **69**, 453.

Scalbert, D., M. Guillot, A. Mauger, J.A. Gaj, J. Cernogora, C. Benoit a la Guillaume and A. Mycielski, 1990, unpublished results.

Schrieffer, J.R., 1967, J. Appl. Phys. **38**, 1143.
Schrieffer, J.R., and P.A. Wolff, 1966, Phys. Rev. **149**, 491.
Schultz, M., and H. Weiss, eds, 1984, Landolt-Börnstein Tables: Technology of III–V, II–VI and Non-Tetrahedrally Bounded Compounds, Vol. 17d (Springer, Berlin).
Shapira, Y., 1990, J. Appl. Phys. **67**, 5090.
Shapira, Y., and N.F. Oliveira Jr, 1987, Phys.Rev., B **35**, 6888.
Shapira, Y., S. Foner, D.H. Ridgley, K. Dwight and A. Wold, 1984, Phys. Rev. B **30**, 4021.
Shapira, Y., S. Foner, P. Becla, D.N. Domingues, M.J. Naughton and J.S. Brooks, 1986, Phys. Rev. B **33**, 356.
Shapira, Y., S. Foner, D. Heiman, P.A. Wolff and C.R. McIntyre, 1989, Solid State Commun. **70**, 355.
Shapira, Y., T.Q. Vu, B.K. Lau, S. Foner, E.J. McNiff Jr, D. Heiman, C.L.H. Thieme, C.-M. Niu, R. Kershaw, K. Dwight and A. Wold, 1990, Solid State Commun. **75**, 201.
Shih, O.W., R.L. Aggarwal, Y. Shapira, S.H. Bloom, V. Bindilatti, R. Kershaw, K. Dwight and A. Wold, 1990, Solid State Commun. **74**, 455.
Shklovskii, B.I., and A.L. Efros, 1984, Electronic Properties of Doped Semiconductors (Springer, Berlin).
Skierbiszewski, C., T. Suski, E. Litwin-Staszewska, W. Dobrowolski, K. Dybko and A. Mycielski, 1989, Semicond. Sci. Technol. **4**, 293.
Skierbiszewski, C., T. Suski, W. Dobrowolski and J. Kossut, 1990a, J. Cryst. Growth **101**, 869.
Skierbiszewski, C., W. Dobrowolski, J. Kossut, P. van der Wel and J. Singleton, 1990b, in: Proc. IV Int. Conf., High Pressure in Semiconductor Physics, Chalkidiki, Porto Carras, Greece 1990, eds D.S. Kyriakos and O.V. Valassiades (Aristotle University of Thessaloniki) p. 120.
Spałek, J., A. Lewicki, Z. Tarnawski, J.K. Furdyna, R.R. Gałązka and Z. Obuszko, 1986, Phys. Rev. B **33**, 3407.
Spasojevic, V., A. Bajorek, A. Szytuła and W. Giriat, 1989, J. Magn. & Magn. Mater. **80**, 183.
Stępniewski, R., 1986, Solid State Commun. **58**, 19.
Story, T., R.R. Gałązka, R.B. Frankel and P.A. Wolff, 1986, Phys. Rev. Lett. **56**, 777.
Story, T., G. Karczewski, L. Świerkowski and R.R. Gałązka, 1990, Phys. Rev. B **42**, 10477.
Suski, T., J. Igalson and T. Story, 1987, J. Magn. & Magn. Mater. **66**, 325.
Swagten, H.J.M., 1990, Thesis (Department of Physics, Eindhoven University of Technology) unpublished.
Swagten, H.J.M., W.J.M. de Jonge, R.R. Gałązka, P. Warmenbol and J.T. Devrese, 1988a, Phys. Rev. B **37**, 9907.
Swagten, H.J.M., A. Twardowski, W.J.M. de Jonge, M. Demianiuk and J.K. Furdyna, 1988b, Solid State Commun. **66**, 791.
Swagten, H.J.M., C.E.P. Gerrits, A. Twardowski and W.J.M. de Jonge, 1990, Phys. Rev. B **41**, 7330.
Szuszkiewicz, W., W. Bardyszewski, Q. Dingrong, Z. Jiaming, C. Julien, M. Balkanski, B. Witkowska and A. Mycielski, 1990, in: 20th Int. Conf. Phys. Semicond., Thessaloniki (Greece), August 6–10, eds E.M. Anastassakis and J.D. Joannopulos (World Scientific, Singapore) p. 2255.
Takeyama, S., and R.R. Gałązka, 1979, Phys. Status Solidi B **96**, 413.
Takeyama, S., and S. Narita, 1980, Kotai Butsuri **15**, 634.
Takeyama, S., and S. Narita, 1986a, J. Phys. Soc. Jpn. **55**, 274.
Takeyama, S., and S. Narita, 1986b, Solid State Commun. **60**, 285.
Taniguchi, M., L. Ley, R.L. Johnson, J. Ghijsen and M. Cardona, 1986, Phys. Rev. B **33**, 1206.
Taniguchi, M., M. Fujimori, M. Fujisawa, T. Mori, I. Souma and Y. Oka, 1987, Solid State Commun. **62**, 431.
Testelin, C., A. Mauger, C. Rigaux, M. Guillot and A. Mycielski, 1989, Solid State Commun. **71**, 923.
Thibblin, U., 1989, Internat. J. Mod. Phys. B **3**, 337.
Tran, H.N., R. Planel, C. Benoit a la Guillaume and A.K. Bhattacharjee, 1985, Phys. Rev. B **31**, 2388.
Turner, A.E., R.L. Gunshor and S. Datta, 1983, Appl. Opt. **22**, 3152.
Twardowski, A., 1990a, J. Appl. Phys. **67**, 5108.
Twardowski, A., 1990b, Thesis (Warsaw University) unpublished.
Twardowski, A., 1991, in: Diluted Magnetic Semiconductors, ed. M. Jain (World Scientific, Singapore) ch. 8, p. 276.
Twardowski, A., M. Nawrocki and J. Ginter, 1979, Phys. Status Solidi B **96**, 497.
Twardowski, A., T. Dietl and M. Demianiuk, 1983, Solid State Commun. **48**, 845.
Twardowski, A., P. Świderski, M. von Ortenberg and R. Pauthenet, 1984, Solid State Commun.

50, 509.

Twardowski, A., H.J.M. Swagten, W.J.M. de Jonge and M. Demianiuk, 1987a, Phys. Rev. B **36**, 7013.

Twardowski, A., P. Głód, W.J.M. de Jonge and M. Demianiuk, 1987b, Solid State Commun. **64**, 63.

Twardowski, A., A. Lewicki, M. Arciszewska, W.J.M. de Jonge, H.J.M. Swagten and M. Demianiuk, 1988, Phys. Rev. B **38**, 10749.

Twardowski, A., H.J.M. Swagten and W.J.M. de Jonge, 1990a, Phys. Rev. B **42**, 2455.

Twardowski, A., K. Pakula, I. Perez, P. Wise and J.E. Crow, 1990b, Phys. Rev B **42**, 7567.

Twardowski, A., K. Pakula, M. Arciszewska and A. Mycielski, 1991, Solid State Commun. **73**, 601.

Varshni, Y.P., 1967, Physics **34**, 149.

Vaziri, M., and R. Reifenberger, 1985, Phys. Rev. B **32**, 3921.

Vaziri, M., D.A. Schwarzkopf and R. Reifenberger, 1985, Phys. Rev. B **31**, 3811.

Vecchi, M.P., W. Giriat and L. Videla, 1981, Appl. Phys. Lett. **38**, 99.

Velicky, B., J. Masek, V. Chab and B.A. Orłowski, 1986, Acta Phys. Pol. A **69**, 1059.

Venugopalan, S., L.A. Kolodziejski, R.L. Gunshor and A.K. Ramdas, 1984, Appl. Phys. Lett. **45**, 974.

von Molnar, S., 1987, in: Diluted Magnetic (Semimagnetic) Semiconductors, Mat. Res. Soc. Symp. Proc., Vol. 89, eds R.L. Aggarwal, J.K. Furdyna and S. von Molnar (Mater. Res. Soc., Pittsburgh) p. 39.

von Ortenberg, M., 1982, Phys. Rev. Lett. **49**, 1041.

von Ortenberg, M., N. Miura and W. Dobrowolski, 1990, Semicond. Sci. Technol. **5**, S274.

Wall, A., S. Chang, P. Philip, C. Caprile, A. Franciosi, R. Reifenberger and F. Pool, 1987, J. Vac. Sci. Technol. A **5**, 2051.

Wall, A., A. Franciosi, Y. Gao, J.H. Weaver, J.D. Dow and R.V. Kasowski, 1989, J. Vac. Sci. Technol. A **7**, 656.

Wang, X., D. Heiman, S. Foner and P. Becla, 1990, Phys. Rev. B **41**, 1135.

Warnock, J., D. Heiman, P.A. Wolff, R. Kershaw, D. Ridgley, K. Dwight, A. Wold and R.R. Gałązka, 1985, in: Proc. 17th Int. Conf. Phys. Semicond., San Francisco 1984, eds J.D. Chadi and W.A. Harrison (Springer, New York) p. 1407.

Webb, C., M. Kaminska, M. Lichtensteiger and J. Lagowski, 1981, Solid State Commun. **40**, 609.

Wei, S.-H., and A. Zunger, 1987a, in: Diluted Magnetic (Semimagnetic) Semiconductors, Mat. Res. Soc. Symp. Proc., Vol. 89, eds R.L. Aggarwal, J.K. Furdyna and S. von Molnar (Mater. Res. Soc., Pittsburgh) p. 197.

Wei, S.-H., and A. Zunger, 1987b, Phys. Rev. B **35**, 2340.

Wiedemeier, H., and A.G. Sigai, 1970, J. Electrochem. Soc. **117**, 551.

Wilamowski, Z., A. Mycielski, W. Jantsch and G. Hendorfer, 1988, Phys. Rev. B **38**, 3621.

Wilamowski, Z., K. Świątek, T. Dietl and J. Kossut, 1990, Solid State Commun. **74**, 833.

Williams, C.K., T.H. Glisson, F.R. Hauser and M.A. Littlejohn, 1978, J. Electron. Mater. **7**, 639.

Wiśniewski, P., and M. Nawrocki, 1983, Phys. Status Solidi B **117**, K43.

Wittlin, A., M. Grynberg, W. Knap, J. Kossut and Z. Wilamowski, 1980, in: Proc. 15th Int. Conf. Phys. Semicond., Kyoto 1980, eds S. Tanaka and Y. Toyozawa (Phys. Soc. Japan, Tokyo) p. 635.

Wojtowicz, T., T. Dietl, M. Sawicki, W. Plesiewicz and J. Jaroszyński, 1986, Phys. Rev. Lett. **56**, 2419.

Wolff, P.A., 1988, in: Semiconductors and Semimetals, Vol. 25, eds J.K. Furdyna and J. Kossut (Academic Press, New York) ch. 10, p. 413.

Woolley, J.C., S.F. Chchab, T. Donofrio, S. Manhas, A. Manoogian and G. Lamarche, 1987, J. Magn. & Magn. Mater. **66**, 23.

Woolley, J.C., A. Manoogian, R.J.W. Hodgson and G. Lamarche, 1989, J. Magn. & Magn. Mater. **78**, 164.

Wróbel, J., T. Wojtowicz, A. Mycielski, F. Kuchar, R. Meisels, A. Raymond and J.L. Robert, 1987, in: Proc. 18th Int. Conf. Phys. Semicond., Stockholm, 1986, ed. P. Engström (World Scientific, Singapore) p. 1795.

Wróbel, J., T. Dietl, G. Karczewski, J. Jaroszyński, W. Plesiewicz, A. Lenard, M. Dybiec and M. Sawicki, 1990, Semicond. Sci. Technol. **5**, S299.

Wu, J.-W., A.V. Nurmikko and J.J. Quinn, 1986, Solid State Commun. **57**, 853.

Yanase, A., 1972, Int. J. Magn. **2**, 99.

Yoder-Short, D.R., U. Debska and J.K. Furdyna, 1985, J. Appl. Phys. **58**, 4056.

Zasavitskii, I.I., and A.V. Sazonov, 1988, Sov. Phys. Solid State **30**, 962.

Ździanowicz, W., K. Kloc, A. Burian, B. Rzepa and

E. Źdanowicz, 1983, Cryst. Res. Technol. **18**, K25.

Zhang, X.-C., S.-K. Chang, A.V. Nurmikko, L.A. Kolodziejski, R.L. Gunshor and S. Datta, 1985, Phys. Rev. B **31**, 4056.

Zhang, X.-C., Y. Hefetz, S.-K. Chang, J. Nakahara, A.V. Nurmikko, L.A. Kolodziejski, R.L. Gunshor and S. Datta, 1986, Surf. Sci. **174**, 292.

Zheng, X.L., C.A. Huber, M. Shih, P. Becla, A.M. Rao and D. Heiman, 1990, in: 20th Int. Conf. Phys. Semicond., Thessaloniki (Greece), August 6–10, eds E.M. Anastassakis and J.D. Joannopulos (World Scientific, Singapore) p. 260.

Zhou, Y., C. Rigaux, A. Mycielski, M. Menant and N. Bontemps, 1989, Phys. Rev. B **40**, 8111.

Zunger, A., 1986, in: Solid State Physics, Vol. 39, eds H. Ehrenreich and D. Turnbull (Academic Press, New York) p. 276.

chapter 5

MAGNETIC PROPERTIES OF BINARY RARE-EARTH 3d-TRANSITION-METAL INTERMETALLIC COMPOUNDS

J. J. M. FRANSE and R. J. RADWAŃSKI

Van der Waals-Zeeman Laboratorium
University of Amsterdam
The Netherlands

This review has been prepared in the scope of the BRITE/EURAM contract BREU-0068-C(GDF) "BASIC INTERACTIONS IN RARE-EARTH MAGNETS" supported by the Commission of the European Communities within its Research&Development Programme

Handbook of Magnetic Materials, Vol. 7
Edited by K. H. J. Buschow

CONTENTS

1. Introduction

In this chapter basic concepts related to the intrinsic magnetic properties of the 3d-rich R_nT_m (R = rare earths; T = 3d heavy transition metals Mn, Fe, Co, Ni) intermetallic compounds are discussed. The extrinsic magnetic properties that are related to the microstructure of the material are left out of the present review.

The study of rare-earth transition-metal intermetallic compounds has a number of interesting aspects. Inspection of tables 1.1 and 1.2 shows that the number of compounds, available at present, amounts to nearly 200. Owing to the wide range of intermetallics and their different stoichiometries and variable rare-earth elements, modifications of magnetic properties of 3d transition-metal and 4f rare-earth ions can be investigated systematically. These investigations illuminate the rather complex interactions in which the 3d and 4f electrons are involved.

We are concerned in this chapter with rare-earth metals in their 'normal' state where the magnetic properties of the ion cores are well defined. The 4f electrons are positioned within the ion cores and hybridization with the conduction-band-electron states is negligible. This situation is realized for most iron- and cobalt-based compounds with 4f elements. The Ce and Yb ions, which sometimes demonstrate unusual properties connected with valence fluctuations, tend to behave quite normally in the compounds with iron or cobalt. Nevertheless, there are some anomalies in the Ce compounds that can be ascribed to a mixed-valence state of the cerium ion.

From a macroscopic point of view, the magnetic moment at 4.2 K varies substantially over the R_nT_m compounds. In terms of the moment per formula unit, however, the variation resembles the variation of the free-ion moment value as can be concluded by inspecting fig. 1.1 where the moment for the R_2Fe_{17}, R_2Co_{17} and RCo_5 series is shown. The large value of the magnetization of some typical hard-magnetic materials can be kept at temperatures well above room temperature as the magnetic ordering temperature is well above 600 K, see fig. 1.2.

In general, alloying of the 3d elements with rare-earth metals weakens the 3d magnetism. This effect is best illustrated for the yttrium compounds. In fig. 1.3, the magnetic moment per 3d ion is presented as a function of the concentration of the 3d atoms. It turns out that the 3d moment decreases gradually with increasing yttrium concentration. Fig. 1.3 can serve as the basis for a division of the rare-earth intermetallic compounds with the heavy 3d-transition-metal atoms into two groups. The first group contains compounds with large and stable 3d moments. The large and stable 3d moments guarantee a substantial value for the molecular field experienced

TABLE 1.1

Overview of existing (marked by +) 3d-rich R–T intermetallic compounds of rare earths (R) with 3d transition metals (T) (T = Mn, Fe, Co, Ni).

R	RT_{12} tetr	R_2T_{17}						RT_5 hex			R_6T_{23} cubic		R_5Co_{19} hex	R_2T_7				RT_3				RT_2				
		hex			rhomb									hex		rhomb		hex	rhomb			hex	cubic		
	Mn	Fe	Co	Ni	Fe	Co	Ni	Fe	Co	Ni	Mn	Fe		Co	Ni	Co	Ni	Ni	Fe	Co	Ni	Mn	Mn	Fe	Co	Ni
Y	+	+	+	+	+	+			+	+	+	+				+	+		+	+	+		+	+	+	+
La									+	+				+	+	+					+					+
Ce		+	+		+	+			+	+			+	+	+	+		+		+				+	+	+
Pr					+	+			+	+			+	+	+	+	+			+	+	+		+	+	+
Nd	+			+	+	+			+	+	+		+	+	+	+	+			+	+	+		+	+	+
Sm			+	+	+	+			+	+	+			+	+	+	+		+	+	+	+	+	+	+	+
Eu				+						+																
Gd	+	+	+	+	+	+			+	+	+	+		+	+	+	+		+	+	+		+	+	+	+
Tb	+	+	+	+	+	+			+	+	+	+			+	+	+		+	+	+		+	+	+	+
Dy	+	+	+	+	+	+			+	+	+	+			+	+	+		+	+	+		+	+	+	+
Ho	+	+	+	+		+			+	+	+	+				+	+		+	+	+	+	+	+	+	+
Er	+	+	+	+		+			+	+	+	+				+	+		+	+	+	+		+	+	+
Tm	+	+	+	+					+	+	+	+				+			+	+	+	+		+	+	+
Yb		+	+	+						+		+								+	+			+	+	+
Lu		+	+							+	+	+				+			+	+	+	+		+	+	+

TABLE 1.2
Overview of existing (marked by +) R-rich R–T intermetallic compounds (T = Mn, Fe, Co, Ni).

R	RNi	R_9Co_7	R_3T_2		$R_{24}T_{11}$	R_9Co_4	R_7Ni_3	R_3T	
			Co	Ni				Co	Ni
Y	+	+	+					+	+
La	+						+	+	+
Ce	+				+		+		
Pr	+						+	+	+
Nd	+						+	+	+
Sm	+					+		+	+
Eu									
Gd	+	+						+	+
Tb	+	+		+				+	+
Dy	+	+		+				+	+
Ho	+	+		+				+	+
Er	+	+		+				+	+
Tm	+	+		+					+
Yb	+								
Lu	+							+	

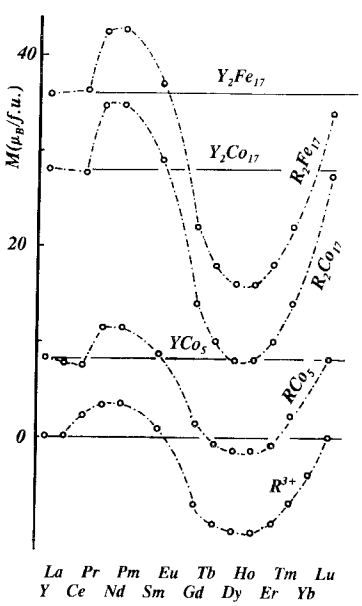

Fig. 1.1. Variation of the magnetic moment at 4.2 K of the R_2Fe_{17}, R_2Co_{17} and RCo_5 series with the R-ion partner. In the bottom part the contribution of the R ion to the total magnetic moment is shown.

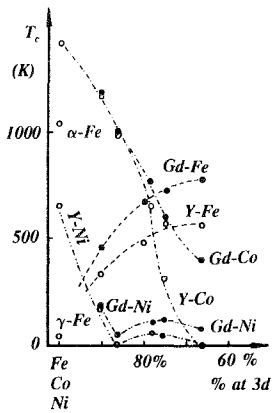

Fig. 1.2. Magnetic ordering temperature of the Y–Fe (Y_2Fe_{17}, Y_6Fe_{23}, YFe_3, YFe_2) and Gd–Fe series, the Y–Co (Y_2Co_{17}, YCo_5, Y_2Co_7, YCo_3, YCo_2) and Gd–Co series as well as the Y–Ni (Y_2Ni_{17}, YNi_5, YNi_3, YNi_2) and Gd–Ni series as a function of the 3d transition-metal atomic concentration. In addition the magnetic ordering temperature of α-Fe, γ-Fe, hcp-Co and fcc-Ni are shown.

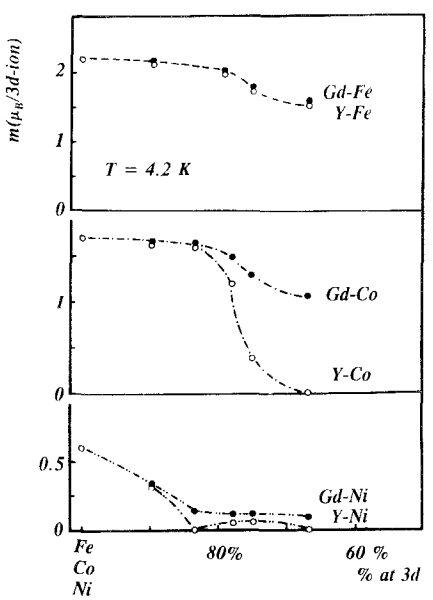

Fig. 1.3. The 3d magnetic moment at 4.2 K in the Y–Fe (Y_2Fe_{17}, Y_6Fe_{23}, YFe_3, YFe_2) and Gd–Fe series, the Y–Co (Y_2Co_{17}, YCo_5, Y_2Co_7, YCo_3, YCo_2) and Gd–Co series as well as the Y–Ni (Y_2Ni_{17}, YNi_5, YNi_3, YNi_2) and Gd–Ni series as a function of the 3d transition-metal atomic concentration. In addition the 3d magnetic moment of the α-Fe, hcp-Co and fcc-Ni are shown.

by the R ion, 63 T in case of Ho_2Co_{17} and as large as 230 T in case of $Pr_2Fe_{14}B$. As a consequence, the exchange effect on the rare-earth ion can be larger than the crystalline-electric-field (CEF) effect. To this group belong all R_nFe_m compounds and the Co-rich R_nCo_m compounds. In the second group, the 3d ions behave as a Pauli-paramagnetic system. In these compounds the CEF effect on the R ion can dominate the exchange-field effect. Most of the nickel compounds belong to this group. There is an intermediate region in which the 3d moments are sensitive to changes of the internal and external surroundings. RNi_5 and RCo_2 belong to this category. Some instabilities in the 3d moment are observed in 1:3 and 2:7 cobalt series as well. Substitution of Y by Gd in these compounds substantially enhances the 3d moment as well as T_c, see figs. 1.2 and 1.3. Most of the compounds of the group 1 belong, in first approximation, to the limiting case where the magnetic interactions dominate the crystal-field splitting. Both interactions, however, are equally important for a proper description of the rare-earth ions in 3d–4f intermetallics, and of the magnetization curves in particular.

In the last decade considerable progress in the understanding of the rare-earth 3d intermetallics has been achieved. This progress was possible by the growing availability of sizeable single-crystalline samples and by the application of more powerful experimental techniques. Here, the hexagonal ferrimagnetic compound Ho_2Co_{17} may serve as an example. Magnetization studies at 4.2 K on a monocrystalline spherical sample of 3 mm diameter in external fields up to 35 T (Franse et al. 1985), as shown in fig. 1.4, have revealed a breaking of the collinear magnetic structure of this ferrimagnetic compound in a field of 22 T applied along the easy direction of magnetization and at 29 T for the field along the hard axis within the hexagonal plane. The breaking of the collinear ferrimagnetic structure is also seen in magnetic measurements in which the specimen, a single-crystalline sphere or free powder particles, can freely rotate during the field course. In this case, however, the transition is smooth as seen in fig. 1.5. The observed magnetic transition has led to an unambiguous and direct evaluation of the exchange interactions between the 3d and 4f spins. Since these

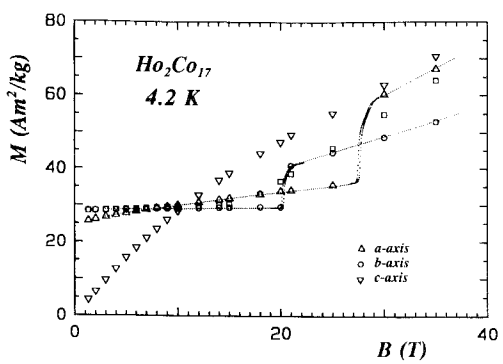

Fig. 1.4. Magnetization curves for single-crystalline Ho_2Co_{17} at 4.2 K for fields along the different crystallographic directions of the hexagonal cell; results for the 'free' single-crystalline sphere of Ho_2Co_{17} are also indicated (□). After Franse et al. (1992); see also Franse et al. (1985).

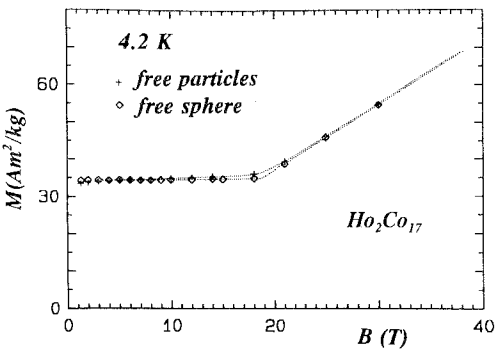

Fig. 1.5. Magnetization curve for a single-crystalline sphere and for powder particles of Ho_2Co_{17} that both are free to rotate with applied field. After Verhoef et al. (1990).

exchange interactions influence the magnetic ordering temperature as well, the study of T_c as a function of the rare-earth element in a particular R_nT_m series is relevant. In most cases the magnetic ordering temperature is maximal for R = Gd, a fact that has led de Gennes (1962) to correlate this maximum with the maximal value of the 4f spin. Comparison between the T_c values within a given series with a given stoichiometry but for different 3d partners allows for studies of the effect of the 3d partner. In the R_2T_{17} compounds, for instance, T_c amounts to about 400 K for iron compounds while T_c for the cobalt compounds is much higher, reaching values up to 1200 K. The lowest values for T_c in the R_2T_{17} series occur, for the compounds with Ni. Investigations of T_c as a function of the 3d-metal concentration reveal a nonmonotonic behaviour for the Fe compounds. With increasing iron concentration T_c decreases. This is associated with the magnetovolume effects visible especially in Fe-rich compounds like R_2Fe_{17} and $R_2Fe_{14}B$. Ferromagnetic order in the R_2T_{17} series exists for compounds with a nonmagnetic rare-earth partner (Y, La, Ce, Lu, Th), and for compounds with the light rare-earth elements. For the heavy rare-earth compounds, for Gd to Yb, the ordered magnetic state is ferrimagnetic. The same systematics exist for all other R_nT_m series where T = Fe, Co or Ni. A tilted magnetic structure can occur because of a competition between the higher-order and second-order CEF interactions in the determination of the easy magnetic direction. Nd and Ho compounds are good candidates for studies of these phenomena due to the relatively weak second-order 4f-charge-moment of these ions. In general, the tilt angle decreases with increasing temperature and becomes zero at a temperature denoted by T_{MR}. As an example we show in fig. 1.6 the magnetization curves of single-crystalline $Nd_2Fe_{14}B$ at 4.2 K measured in external fields up to 40 T along the principal tetragonal directions. All curves start with a nonzero magnetization value, indicating that the spontaneous moment direction does not lie along any principal direction. At room temperature the easy direction of magnetization for $Nd_2Fe_{14}B$ is directed along the tetragonal *c*-axis, resulting in much simpler magnetization curves as shown in fig. 1.7. An inspection of the magnetization curves shown in figs. 1.6 and 1.7 makes clear why

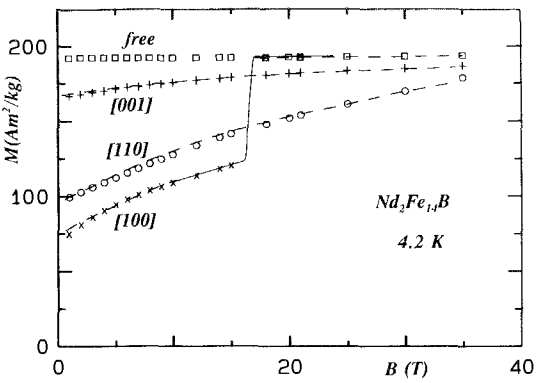

Fig. 1.6. Magnetization curves at 4.2 K for $Nd_2Fe_{14}B$ along the different crystallographic directions of the tetragonal cell and for the sphere that is free to rotate during the magnetization process. After Verhoef et al. (1988b).

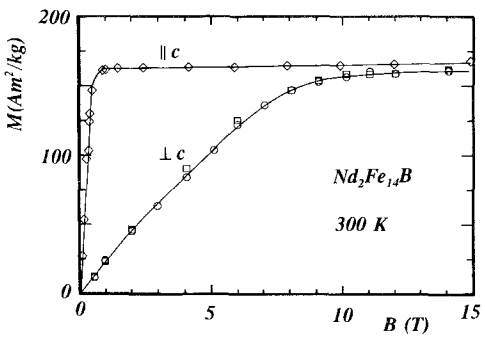

Fig. 1.7. Magnetization curves at 300 K for $Nd_2Fe_{14}B$ along the different crystallographic directions of the tetragonal cell.

low-temperature measurements revealing particularities in the magnetization process are indispensable for the evaluation of the magnetic interactions in full details.

The intrinsic magnetic properties of R_nT_m compounds can be qualitatively understood in terms of *exchange interactions* and *magnetocrystalline anisotropy*.

The *exchange interactions* take place between all unpaired spins in the 3d–4f system. These interactions are generally considered to be of the Heisenberg type. Because there are three kinds of spin pairs, the exchange interactions are formally described by three different exchange-interaction parameters: J_{TT}, J_{RT} and J_{RR}. The strength of these interactions in the iron- and cobalt-rich R_nT_m intermetallics decreases in the sequence mentioned. J_{TT} is positive and leads to the ferromagnetic coupling between the 3d spins. In the iron- and cobalt-based compounds this interaction turns out to be strong enough to produce an almost exact parallel alignment of the 3d magnetic moments at low temperatures. This interaction primarily governs the temperature

dependence of the 3d moment and the value of T_c of a 3d–4f compound. The interaction parameter J_{RT} is responsible for the internal magnetic structure. Its negative sign reflects an antiparallel coupling of the 4f and 3d spins and leads to a parallel alignment of the 3d and 4f moments in case of light rare earths and to an antiparallel alignment for the heavy rare earths. The 3d–4f interaction produces a dominant contribution to the molecular field experienced by the rare-earth moments. The corresponding molecular field determines the temperature dependence of magnetic moment and magnetocrystalline anisotropy of the rare-earth ions. The R–R interaction between the 4f spins is generally the weakest one in the 3d–4f compounds. Values for J_{RR} are small compared to those of J_{RT} and since the number of R–R bonds in the 3d-rich compounds is small as well, the effect of J_{RR} is difficult to detect. Values of 115, −8 and 2.3 K found in R_2Co_{17} with heavy R's can serve as approximate values for the J_{TT}/k_B, J_{RT}/k_B and J_{RR}/k_B exchange parameters (Radwański 1986a).

The *anisotropy energy* represents the anisotropic part of the free energy of the system. In magnetic systems it is observed by the preference of the magnetization to be oriented along a specific crystallographic direction. For a given structure this energy can be represented by phenomenological expressions in terms of even powers of $\sin\theta$ or of Legendre functions, where θ is the angle between the magnetization direction and a symmetry direction of the crystallographic structure. In the present class of magnetic materials, the magnetocrystalline anisotropy energy originates from both the rare-earth and 3d magnetic sublattices. The technical interest in this class of materials is closely connected to the huge magnetic anisotropy that is found in many of the 3d–4f intermetallics. This anisotropy largely originates from the rare-earth ions and is transferred by the 3d–4f exchange interactions to the 3d sublattice. This anisotropy is the fundamental parameter behind the coercive field. The magnetocrystalline energy can be most effectively studied in magnetic measurements on single-crystalline specimens by applying external fields along the specific crystallographic direction. If the measurements are done on free powder particles or on single-crystalline samples that are free to rotate under the action of the applied field all information about the magnetocrystalline anisotropy is lost, compare figs. 1.4 and 1.5.

The anisotropic magnetic properties of the rare-earth ions in the R–T intermetallics are connected with the existence of nonquenched orbital moments. In the quantum formalism, the 4f shell is represented by wave functions in the basis of the total angular momentum $\boldsymbol{J}$ and its components M_J: $|J, M_J\rangle$. The appropriate Hamiltonian, which determines these wave functions includes several terms associated with the various relevant interactions. The main part of the interactions of the 4f electrons with the surrounding electric charges is described in terms of the crystalline electric field (CEF). This field can eventually be modulated by magneto-elastic phenomena associated with magnetostriction. The interaction of the 4f electron spin with the surrounding spins is treated in terms of an (isotropic or anisotropic) Heisenberg-type of Hamiltonian that is approximated by an effective exchange field originating from the surrounding spins. The aim of the present chapter is to give a quantitative discussion of these basic (crystal-field and exchange) interactions.

Magnetism of the 3d ions is often discussed in terms of the energy-band parameters. Band-structure calculations, however, are still not able to reproduce the experimental

results for the 3d anisotropy. As a consequence, the 3d anisotropy is experimentally deduced from compounds with nonmagnetic rare-earth elements, for instance, from the Y_nT_m compounds. The magnetization curves of single-crystalline Y_nT_m are relatively simple but they illustrate the different course of the magnetization for external fields applied along the easy and hard magnetic axes. The saturation is reached along the hard axis at rather low field values. The outstanding value of 17 T that is observed for YCo_5 at 4.2 K for the saturation field corresponds to an energy difference between the hard and easy directions of magnetization of $+7.3\,MJ/m^3$. The 3d anisotropy contributes substantially to the overall anisotropy of all magnetic rare-earth compounds at elevated temperatures. The rare-earth contribution to the magnetocrystalline anisotropy is dominant at low temperatures whenever the 4f ions have nonzero orbital moments. This contribution, however, decreases rapidly with increasing temperature and at room temperature it is for most compounds comparable in magnitude to that of the 3d-ion sublattice. In case of competition between the rare-earth and 3d anisotropies, temperature-induced moment-reorientation (TIMR) phenomena can occur as a consequence of a mutual cancellation of the anisotropy contributions from the 4f and 3d sublattices. At temperatures above the moment-reorientation temperature, T_{MR}, the anisotropy is dominated by the 3d contribution.

This chapter is organized as follows. In section 2, the notation for describing the crystal-field and exchange interactions is introduced. In section 3, a review is presented of the most useful experimental techniques for investigating this class of materials. Some prototype compounds are discussed in this section in order to illustrate the advantage and disadvantage of the method under discussion. Section 4 reviews briefly the magnetism of the 3d sublattice as it can be deduced from compounds with nonmagnetic rare-earth partners. By comparing the yttrium compounds with the gadolinium compounds, the influence of the 4f spin on magnetic parameters of the 3d sublattice such as the spontaneous magnetization and the magnetic ordering temperature T_c is discussed. Section 5 presents a review of experiments that have been performed on the R_nT_m compounds and discusses the magnetic parameters for all series of existing compounds. Although the theoretical concepts behind the crystal-field and isotropic exchange interactions are rather simple, the evaluation of their numerical values is far from straightforward. An effort is made to collect characteristic values for the crystal-field and exchange parameters as completely as possible. Although a full evaluation of the CEF and exchange parameters is at present available for a few compounds only, the overall features of electronic and magnetic properties are now quite well understood for the whole series of the R_nT_m compounds.

Three general reviews that include a basic description of the magnetism of 3d–4f intermetallic compounds and that provide a good insight into the general properties of the compounds under discussion, have been written by Buschow (1977) ("Intermetallic compounds of rare-earth and 3d transition metals"), by Kirchmayr and Poldy (1979) ("Magnetic properties of intermetallic compounds of rare earth metals") and by Buschow (1980a) ("Rare earth compounds"). A review of experimental data and magnetic properties of the $R_2Fe_{14}B$ compounds has been presented by Buschow (1988) ("Permanent magnet materials based on 3d-rich ternary compounds"), by Burzo and Kirchmayr (1989) ("Physical properties of $R_2Fe_{14}B$-based alloys") and by Herbst

(1991) ("$R_2Fe_{14}B$ materials: intrinsic properties and technological aspects"). Ternary compounds of rare-earth and 3d elements with a variety of other elements have been reviewed by H. S. Li and Coey (1991) and Szytuła (1991) in volume 6 of this series. In that volume Wiesinger and Hilscher (1991) have reviewed magnetic properties of hydrogenated R_nT_m intermetallic compounds.

The units, used in the literature for describing magnetic materials are far from uniform. A comparison of the cgs and SI units is presented, for instance, in section 2.3 of the review by Buschow (1988). Moreover, one should realize the difference in the description of magnetic parameters from technical and 'scientific' points of view. In the former, the parameters refer to the unit of volume and then the magnetization M is expressed in A/m. Alternatively, the magnetic polarization $\mu_0 M$ is expressed in telsa. In the 'scientific' description all units are related to a given number of atoms, ions or formula units. In that case one should speak of the magnetic moment expressed in $A\,m^2$/mol or μ_B/f.u. The same holds for the anisotropy energy or the anisotropy constants where parameters in units of J/mol instead of J/m^3 better describe the intrinsic properties. There is a constant factor of 5.585 ($\sim N_A\mu_B$) between the magnetic moment in $A\,m^2$/mol and the magnetic moment in μ_B/f.u. A factor of 8.31 ($\sim N_A k_B$) enters into the transformation of the anisotropy energy expressed in J/mol to K/f.u.

The mass of the specimen is the easiest characteristic from an experimental and an accuracy point of view. Direct experimental magnetization data are mostly presented in values per unit of mass. To transform these results in atomic or molar units, the actual stoichiometry has to be known. For the 'technical' units, the density of the material enters.

2. Modelling of the magnetic interactions

The parameters that are relevant for a description of the free ions of the rare-earth series are well known both from a theoretical and an experimental point of view. For a description of the rare-earth ion in compounds an extra contribution to the free-ion energy has to be included that depends on its local surrounding in the given crystallographic structure. This contribution is parametrized in terms of the interactions of the 4f ion with its charge and spin surroundings. The CEF approach provides an elegant form for parametrization of the interactions that involve the charges, whereas the interactions that depend on the spin can be treated within the molecular-field approximation.

The magnetocrystalline anisotropy is the main source of information on the crystal-field parameters. In order to evaluate the crystal-field parameters from magnetization studies, other contributions to the magnetic anisotropy have to be considered as well. Dipolar interactions can easily be calculated and turn out, in general, to be relatively small. The shape anisotropy is a trivial effect. Contributions to the magnetic anisotropy induced by thermal treatments or applied stresses can be relevant for certain applications but should be avoided in studies of the intrinsic anisotropy. Magneto-elastic terms in the free energy are related with the magnetostriction and can be evaluated. Other intrinsic sources of magnetic anisotropy, that are not of single-ion origin, are the

quadrupolar interactions, the anisotropic exchange and the two-ion anisotropy. All these anisotropic terms have to be considered in making an appropriate analysis of the magnetocrystalline anisotropy. Quadrupolar interactions have been found to play a significant role in weakly magnetic compounds. A survey of the properties of 4f quadrupolar moments in a variety of rare-earth compounds has been given by Morin and Schmitt (1991) in volume 5 of this series.

Little is known about the anisotropic exchange. In principle, one expects the exchange interactions between neighbouring ions to be anisotropic because of the non-isotropic spatial distribution of nearest-neighbour ions. These effects, however, are hardly visible in the compounds discussed. Here, compounds are mentioned for which anisotropy contributions have been claimed that are not of single-ion origin. First of all, the compound $GdCo_5$ is discussed. The analysis of high-field magnetization curves up to 32 T obtained on a single-crystalline specimen by Ballou et al. (1986a, 1987a) and by Gerard and Ballou (1992) has resulted in an anisotropy associated with the Co sublattice that is 50% larger than that found in YCo_5. The authors have attributed this extra contribution of +20 K/f.u. to an anisotropic term in the exchange. The question arises why such a significant contribution from the anisotropic exchange is not visible in other Gd compounds like Gd_2Co_{17}, Gd_2Fe_{17} or $Gd_2Fe_{14}B$ (Radwański et al. 1992b). In all the three latter compounds the magnetic anisotropy is very close to that in the yttrium counterparts and a significant part of the (small) difference is due to normal dipole–dipole interactions. In later sections we return to this discrepancy. Next, a two-ion contribution to the anisotropy has been claimed for $PrCo_5$ (Andoh et al. 1982) and Nd_2Co_{17} (Kąkol and Figiel 1985). These latter authors derived a nonlinear concentration dependence of the anisotropy energy of aligned polycrystalline samples of $(Nd–Y)_2Co_{17}$ and called for a two-ion contribution. Magnetic experiments, however, on polycrystalline $PrCo_5$ by Ibarra et al. (1991) and on single-crystalline Nd_2Co_{17} by Radwański et al. (1988b) have been reported to be understandable within the single-ion model. Owing to the tilted magnetic structures occurring in these compounds, conclusions about a significant non-single-ion anisotropy seem to be premature.

2.1. Crystalline-electric-field interactions

The rare-earth ions in a lattice form a system to which the CEF formalism can be applied. Within this formalism the 4f electrons, being considered as well localized and separated from other positive and negative charges, experience an electrostatic potential $V_{CF}(r)$ that originates from the surrounding charge distribution. In case there is no overlap between this charge distribution and the wave functions of the 4f state, V_{CF} can be expanded in terms of the spherical harmonics, Y_n^m. The value of n in this expansion is limited to 6, as higher multipoles cannot cause electronic transitions between states of the 4f ion. For details see Hutchings (1964) and Fulde and Loewenhaupt (1985, 1988).

It is an experimental fact that for the rare-earth ions, the spin–orbit interaction is much larger than the crystal-field and exchange interactions. A review of experimental data of the spin–orbit interactions based on the observation of intermultiplet transi-

tions has been presented by Osborn et al. (1991). Most of the interpretations of experimental results on systems involving rare-earth ions are made within the ground-state multiplet. Eu^{3+} and Sm^{3+} are ions where the analysis requires the involvement of higher multiplets as the higher multiplet is only 530 and 1500 K above the ground multiplet, respectively. For this case Racah algebra has been employed. For details, see, e.g., de Wijn et al. (1976), where an analysis of $SmFe_2$ and $SmCo_5$ has been presented. Within the extended approach, the magnetic properties of $SmNi_5$ have recently been analysed by Ballou et al. (1988a). In fig. 2.1 the energy separation to the first excited multiplet is compared with the effect of crystal-field interactions in RCo_5 compounds. Owing to the predominant spin–orbit interactions resulting in a large energy distance to the first excited multiplet it is usually sufficient to consider the lower multiplet J, given by Hund's rules. This limitation results in a substantial simplification in computer calculations.

The crystal-field Hamiltonian that describes part of the electron–electron interactions in the solid due to the electrostatic interaction of the aspherical 4f charge distribution with the aspherical electrostatic field arising from the surrounding, can be written as:

$$\mathscr{H}_{\mathrm{CF}} = \sum_{n=0}^{\infty} \sum_{m=0}^{n} A_n^m \sum_i f_{nm}(r_i). \tag{2.1}$$

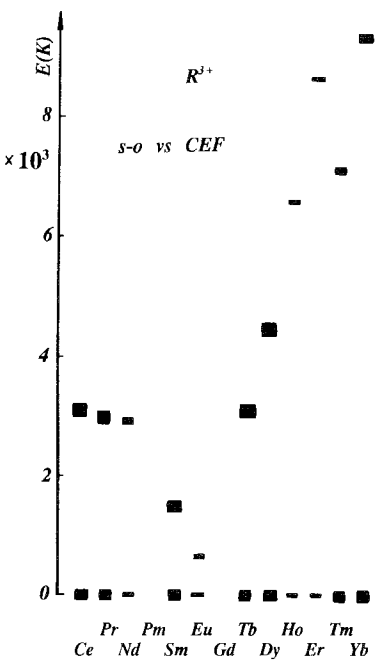

Fig. 2.1. Comparison of the spin–orbit and CEF energies in the RCo_5 compounds. The energy distance to the first excited multiplet for the trivalent rare-earth ions is taken from the R-doped LaF_3 compounds. After Osborn et al. (1991). The splitting of the multiplets due to the CEF interactions is indicated by the size of the symbols.

The f_{nm} are Tesseral harmonics describing the spatial distribution of the charge associated with the 4f electrons; the summation over i is over all 4f electrons. A_n^m describes the spatial distribution of the charge surrounding the 4f electrons.

The summation in eq. (2.1) over the 4f electrons leads within the Stevens formalism to matrix elements of the total angular momentum:

$$\sum_i f_{nm}(r_i) = \theta_n \langle r^n \rangle O_n^m(\boldsymbol{J}), \tag{2.2}$$

where the x, y and z coordinates of a particular electron in the functions $f_{nm}(r_i)$ are replaced by the components J_x, J_y and J_z of the multiplet $\boldsymbol{J}$. The O_n^m are the Stevens equivalent operators tabulated by Hutchings (1964). θ_n is the appropriate Stevens factor of order n which represents the proportionality between operator functions of x, y and z and operator functions of J_x, J_y and J_z. The notation of α_J, β_J and γ_J for the second-, fourth- and sixth-order factors, respectively, is used later. The sign of each θ_n factor reflects the type of asphericity associated with each O_n^m term describing the angular distribution of the 4f-electron shell. In particular, the factor α_J describes the ellipsoidal character of the 4f electron distribution. For $\alpha_J > 0$, the electron distribution associated with $J_z = J$ is prolate, i.e. elongated along the moment direction whereas for $\alpha_J < 0$ the 4f-electron-charge distribution is oblate, i.e. expanded perpendicular to the moment direction. For $\alpha_J = 0$, which is the case of the Gd^{3+} ion, the charge density has spherical symmetry. $\langle r_{4f}^n \rangle$ is the mean value of the nth power of the 4f radius. Values for the average value $\langle r_{4f}^n \rangle$ of the 4f wave function have been computed on the basis of Dirac–Fock studies of the electronic properties of the trivalent rare-earth ions by Freeman and Desclaux (1979) and are tabulated in table 2.1.

TABLE 2.1

The second-, fourth- and sixth-order multipole moments of the trivalent rare-earth ions. α_J, β_J and γ_J are the Stevens factors of the second, fourth and sixth order, respectively. The values for $\langle r_{4f}^2 \rangle$, $\langle r_{4f}^4 \rangle$ and $\langle r_{4f}^6 \rangle$ have been taken after Freeman and Desclaux (1979). The multipole moment values enter into the relations between the CEF parameters B_n^m and the CEF coefficients A_n^m.

R	J	$\langle r_{4f}^2 \rangle$ (a_0^2)	$\langle r_{4f}^4 \rangle$ (a_0^4)	$\langle r_{4f}^6 \rangle$ (a_0^6)	$\alpha_J \langle r_{4f}^2 \rangle$ $(10^{-3} a_0^2)$	$\beta_J \langle r_{4f}^4 \rangle$ $(10^{-4} a_0^4)$	$\gamma_J \langle r_{4f}^6 \rangle$ $(10^{-6} a_0^6)$
Ce	5/2	1.309	3.964	23.31	−74.8	+251.7	0
Pr	4	1.208*	3.396*	18.72*	−25.54	−24.95	+1141.66
Nd	9/2	1.114	2.910	15.03	−7.161	−8.471	−570.96
Sm	5/2	0.9743	2.260	10.55	+40.209	+56.527	0
Gd	7/2	0.8671	1.820	7.831	0	0	0
Tb	6	0.8220	1.651	6.852	−8.303	+2.021	−7.683
Dy	15/2	0.7814	1.505	6.048	−5.020	−0.891	+6.260
Ho	8	0.7446	1.379	5.379	−1.676	−0.459	−6.959
Er	15/2	0.7111	1.270	4.816	+1.831	+0.564	+9.969
Tm	6	0.6804	1.174	4.340	+6.976	+1.916	−24.33
Yb	7/2	0.6522	1.089	3.932	+21.04	−18.857	−581.94

*Values for Pr have been deduced from interpolation (data taken from Radwański and Franse 1989a).

These values for $\langle r_{4f}^2 \rangle$, $\langle r_{4f}^4 \rangle$ and $\langle r_{4f}^6 \rangle$ are larger than the values reported previously by Freeman and Watson (1962), by approximately 10%, 20% and 25%, respectively. As a consequence, the coefficients A_n^m evaluated by employing the $\langle r_{4f}^n \rangle$ values from Freeman and Desclaux (1979) are smaller than previously reported results. In the present review the more recent results are used. For literature data based on the older results, relevant corrections have been introduced.

Within the ground-state multiplet the crystal-field Hamiltonian of eq. (2.1) is written in the conventional form as

$$H_{CF} = \sum_{n}^{\infty} \sum_{m=0}^{n} B_n^m O_n^m(J), \tag{2.3}$$

where B_n^m are called the crystal-field parameters. Evaluation of these parameters is the subject of the analysis of experimental data. The parameters B_n^m can be written as

$$B_n^m = \theta_n \langle r_{4f}^n \rangle A_n^m, \tag{2.4}$$

in which expression terms related to the 4f ion, $\theta_n \langle r_{4f}^n \rangle$, and the term related to the surrounding charges, A_n^m, are separated. The coefficients A_n^m are referred to as the crystal-field coefficients. In eq. (2.4), the screening factors, that eventually occur in theoretical calculations of the crystal-field coefficients, are included in the coefficients A_n^m. Values for $\theta_n \langle r_{4f}^n \rangle$, that have the meaning of the multipole charge moments of the 4f shell are collected in table 2.1. The computation of the CEF coefficients, A_n^m, from microscopic, ab initio, calculations is a complex problem. The use of point-charge (PC) models, with electron (hole) charges centered at the ion positions in the lattice, is criticized, especially in case of metallic systems. A full band-structure calculation of the charge distribution over the unit cell and, consequently, of the full set of CEF coefficients, is lacking for almost all compounds. In the simplest approach to the R–T intermetallic compounds, the CEF coefficients are calculated by attributing a charge of 3+ to the R ion and zero charge to the 3d ions. With such a distribution of charges, the correct sign of the leading second-order coefficient, A_2^0, has been obtained for the RCo_5 and R_2Co_{17} compounds (Greedan and Rao 1973). These charges, however, do not lead to correct results for the higher-order coefficients. The correct sign of the coefficient A_6^6, for instance, can be obtained by attributing positive charges to the 3d ions (Radwański 1987). But even in this case, with realistic 3d charges, the value of A_6^6 is to small to reproduce the experimental results. In order to obtain a proper value for the coefficient A_6^6, a dominant contribution from conduction electrons has been postulated in this latter paper.

A number of attempts has been made to involve these conduction electrons into the evaluation of the coefficients A_n^m. Duthie and Heine (1979) show that for some compounds the conduction-electron contribution to the crystalline electric field can be the dominant term and eventually can lead to changes in sign of the coefficients A_n^m as deduced from PC calculations with charges located at the R sites. Schmitt (1979a,b) considered the direct and the exchange Coulomb contributions arising from the conduction electrons. Both contributions have been found to be significant in the cubic rare-earth intermetallics DyRh, DyCu and DyZn. The results are, however, not directly applicable to 3d–4f intermetallics. The contribution from conduction

electrons to the crystalline electric field in the Laves-phase compounds, RT_2, has been discussed by del Moral (1984). Kąkol et al. (1984) considered the shielding by the conduction electrons of the charges located at the 4f and 3d sites. This Thomas–Fermi type of shielding has been considered to be fully isotropic and only affects the intensity of the crystalline electric field originating from different coordination spheres. X. F Zhong and Ching (1989) performed first-principles calculations of the CEF parameters for another intermetallic compound, $Nd_2Fe_{14}B$, and showed the dominant role of electrons in the nearest distance of the 4f ion. This result is supported by band-structure calculations of Coehoorn (1989, 1991a,b) and of Coehoorn et al. (1990). These authors have calculated the second-order crystal-field coefficient A_2^0 for $Gd_2Fe_{14}B$ and find that this coefficient is mainly determined by the asphericity of the charge density of the Gd 5d and 6p valence shells. However, in calculations for $GdCo_5$ Coehoorn and Daalderop (1992) have found that though the on-site contribution to A_2^0 is the dominant effect the lattice contribution amounts to 60% of the on-site one. As these two contributions are of opposite signs the resultant calculated value is rather uncertain. In fact, the calculations for $GdCo_5$ predict the correct sign and the right order of magnitude for A_2^0 but the calculated value exceeds the one known from experiments by a factor of four.

The present review is dealing with experimental techniques by which the CEF parameters can be evaluated but leaves the problem of the origin of the crystalline electric field in intermetallic compounds out of the discussions.

There is only a limited number of compounds for which quantitative data for the CEF interactions are available. Discussions are still continuing even for the best-known systems like the cubic Laves-phase RT_2 or the hexagonal RNi_5 compounds. The situation becomes more complex for structures with several non-equivalent crystallographic sites for the rare-earth ions. Unfortunately, this situation occurs for most of the compounds under consideration, see table 2.2.

For cubic symmetry, the crystalline electric field is described by two parameters, B_4 and B_6,

$$H_{CF} = B_4(O_4^0 + 5O_4^4) + B_6(O_6^0 - 21O_6^4), \tag{2.5}$$

whereas for hexagonal symmetry, four parameters, B_2^0, B_4^0, B_6^0 and B_6^6 are needed:

$$H_{CF} = B_2^0O_2^0 + B_4^0O_4^0 + B_6^0O_6^0 + B_6^6O_6^6 \tag{2.6}$$

For rhombohedral symmetry, two extra terms appear in eq. (2.6): $B_4^3O_4^3$ and $B_6^3O_6^3$.

In fig. 2.2, a comparison of the CEF and exchange-field splittings is shown for the RCo_5 series, as an example. The exchange energy is largest in the middle of the 4f series where the spin of the 4f shell, S_R, is largest. In contrast, the crystal-field interactions are relatively large at the beginning and at the end of the 4f series. Many interesting phenomena in Ce, Yb and partly in Pr and Tm compounds, result from the intricate balance between crystal-field and exchange interactions.

2.1.1. Macro- and microscopic anisotropy parameters

The magnetocrystalline anisotropy energy, being that part of the free energy that depends on the orientation of the magnetic moment with respect to the crystallo-

TABLE 2.2
Types of crystallographic structures occurring in the 3d-rich rare-earth (R) transition-metal (T) intermetallics together with the numbers of nonequivalent crystallographic sites for the R and T atoms.

Compound	Symmetry	R sites	T sites
RT_{12}	tetr	1	3
R_2T_{17}	hex	2	4
	rhomb	1	4
$R_2T_{14}B$	tetr	2	6
RT_5	hex	1	2(4*)
R_6T_{23}	cubic	1	4
R_5T_{19}	hex	3	6
R_2T_7	hex	2	5
	rhomb	2	5
RT_3	hex	2	4
	rhomb	2	3
RT_2	cubic	1	1
	hex	1	2

*For T-rich off-stoichiometric compounds.

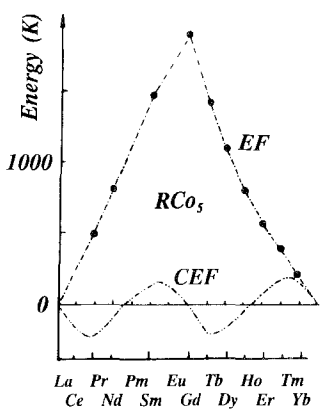

Fig. 2.2. Comparison between the crystal-field (CEF) and the exchange-field (EF) energies for the rare-earth ions in the RCo_5 series. A negative value of the CEF energy corresponds with an easy-plane preference of the 4f ion in this series. After Radwański et al. (1990a).

graphic axes, can be approximated by the expansion

$$E_a = \sum_{n=0}^{\infty} \sum_{m=0}^{n} K_n^m \sin^n\theta \cos m\phi. \tag{2.7}$$

The angles θ and ϕ are the polar and azimuthal angles of the magnetization with respect to the main symmetry directions of the elementary cell, respectively. The

number of nonzero terms is limited by symmetry. The coefficients K_n^m are called the anisotropy constants and are rather denoted for $m=0$ as K_i where $i=n/2$. For hexagonal symmetry the anisotropy energy takes the form:

$$E_a = K_1 \sin^2\theta + K_2 \sin^4\theta + K_3 \sin^6\theta + K_6^6 \sin^6\theta \cos 6\phi, \tag{2.8a}$$

whereas for the tetragonal symmetry

$$E_a = K_1 \sin^2\theta + K_2 \sin^4\theta + K_3 \sin^6\theta + K_4^4 \sin^4\theta \cos 4\phi + K_6^4 \sin^6\theta \cos 4\phi. \tag{2.8b}$$

In an alternative expansion, the associated Legendre functions $P_n^m(\cos\theta)$ are used,

$$E_a = \sum_{n=0}^{\infty} \sum_{m=0}^{n} \kappa_n^m P_n^m(\cos\theta) \cos m\phi, \tag{2.9}$$

in which expression the anisotropy coefficients κ_n^m enter. The Legendre functions employed in the present review are collected in appendix A.

The angular dependence of the anisotropy energy of the neodymium ions in Nd_2Co_{17} is presented in fig. 2.3 as an example. Individual contributions arising from different anisotropy coefficients are shown as well. This angular dependence has been derived from magnetization studies. A field of 35 T applied along the hard axis causes a rotation of the neodymium moment over nearly 90° making it possible to trace the anisotropy energy curve in the nearly full angular range. It allows to separate the different multipole contributions.

The expression for the anisotropy energy in terms of the coefficients κ_n^m in eq. (2.9) is obviously related to that given in terms of the anisotropy constants K_n^m in eq. (2.7).

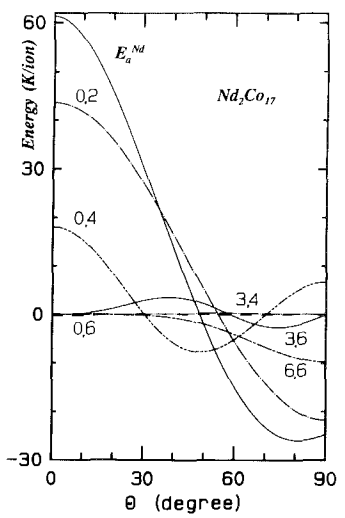

Fig. 2.3. Calculated angular dependence of the magnetocrystalline anisotropy energy, E_a^{Nd}, of the Nd sublattice in Nd_2Co_{17} (full line); the different multipole contributions $\kappa_n^m P_n^m(\cos\theta)$ are shown; values for (m,n) are indicated. After Radwański et al. (1988b).

The relations are given in appendix B. There are, however, some differences between these anisotropy parameters that have to be stressed. The anisotropy constants K_i, usually employed to represent the overall anisotropic behaviour of the intermetallic compounds, are especially convenient for a technical characterization of the magnetic material. The coefficients κ_n^m are used for a description of the rare-earth sublattice anisotropy, in particular. As a consequence, the coefficients κ_n^m are expected to manifest, for a given stoichiometry, single-ion correlation over the series of the rare-earth elements, whereas the anisotropy constants K_n^m are not expected to reveal such a systematic behaviour.

The rare-earth anisotropy coefficients κ_n^m reflect the CEF parameters B_n^m owing to the fact that the Legendre functions are classical equivalents of the Stevens operators. The relations between the coefficients κ_n^m and the parameters B_n^m can be expressed as

$$\kappa_2^0 = B_2^0\langle O_2^0\rangle, \qquad \kappa_4^0 = B_4^0\langle O_4^0\rangle, \qquad \kappa_6^0 = B_6^0\langle O_6^0\rangle, \tag{2.10}$$

where $\langle O_n^m\rangle$ denotes the expectation value of the Stevens operators of order n. For the ground state with J_z equal to its maximal value, i.e. $J_z = J$, the expectation values of the Stevens operators $\langle O_n^m(J_z)\rangle$ at 0 K can be expressed as

$$\langle O_2^0(J_z = J)\rangle = 2J_2, \qquad \langle O_4^0(J_z = J)\rangle = 8J_4, \qquad \langle O_6^0(J_z = J)\rangle = 16J_6, \tag{2.11}$$

where

$$J_2 = J(J - \tfrac{1}{2}), \qquad J_4 = J_2(J - 1)(J - \tfrac{3}{2}), \qquad J_6 = J_4(J - 2)(J - \tfrac{5}{2}). \tag{2.12}$$

Moreover

$$\kappa_4^4 = J_4 B_4^4, \qquad \kappa_6^4 = J_6 B_6^4, \qquad \kappa_6^6 = J_6 B_6^6. \tag{2.13}$$

Other terms, that appear for symmetries lower than the cubic and hexagonal ones, can be written in a similar manner. As the ground state with a dominant $J_z = J$ state in the presence of CEF interactions is realized in large magnetic fields, the relations (2.11) are applicable for the situation that is called the large-exchange limit. Values for J_n for all rare-earth elements are collected in table 2.3. Values for the product $\theta_n\langle r_{4f}^n\rangle J_n$ are collected in table 2.4. Provided that the strength of the CEF interactions is constant in an iso-structural series in which the lattice parameters do not change appreciably, the variation in the anisotropy coefficients over this iso-structural series at $T = 0$ should follow the variation of this product. Inspection of fig. 2.3 confirms the dominant role of the second-order term to the anisotropy energy. Provided this contribution is dominant, the easy direction of magnetization (EMD) in a given series should follow the sign of the second-order Stevens factor α_J. The RNi_5 compounds follow these systematics strictly, see table 2.5. Also nice agreement is found for the R_2Co_{17} series, see table 2.6. Within the R_2Fe_{17} series, the Er compound has been found to deviate from these expectations. This deviation is understood as the Er uniaxial anisotropy is overruled by the planar anisotropy of the Fe sublattice. At 4.2 K the 3d sublattice anisotropy is, in general, one order of magnitude weaker than that associated with the R sublattice. In case of the R_2Re_{17} compounds, however, the Fe anisotropy is substantial whereas the Er anisotropy is one of the weakest within the rare-earth series.

TABLE 2.3

Values for J_n in eq. (2.12) for the trivalent rare-earth ions. These factors enter into the relations between the anisotropy coefficients κ_n^m and the crystal-field parameters B_n^m in the large-exchange limit. J is the total angular momentum whereas $J_2 = J(J-1/2)$, $J_4 = (J-1)(J-3/2)J_2$ and $J_6 = (J-2)(J-5/2)J_4$. Note, that $\tilde{O}_2^0(J) = 2J_2$, $\tilde{O}_4^0(J) = 8J_4$ and $\tilde{O}_6^0(J) = 16J_6$, where $\tilde{O}_n^0(J)$ is the value of the Stevens operator for $J_z = J$.

R	J	J_2	J_4	J_6
Ce	5/2	5	7.5	0
Pr	4	14	105	315
Nd	9/2	18	189	945
Sm	5/2	5	7.5	0
Gd	7/2	10.5	52.5	78.75
Tb	6	33	742.5	10395
Dy	15/2	52.5	2047.5	56306.25
Ho	8	60	2730	90090
Er	15/2	52.5	2047.5	56306.25
Tm	6	33	742.5	10395
Yb	7/2	10.5	52.5	78.75

TABLE 2.4

Values for the second-, fourth- and sixth-order multipole parameters, $\theta_n\langle r^n\rangle J_n$ and $\theta_n\langle r^n\rangle\tilde{O}_n^0$, describing the interactions of the trivalent rare-earth ions with the crystalline-electric field in the frame of a single-ion approximation. These parameters enter into the approximate relations between the anisotropy coefficients κ_n^m and the crystal-field coefficients A_n^m, see eqs. (2.4) and (2.10); a_0 is the Bohr radius.

R	$\alpha_J\langle r_{4f}^2\rangle J_2$ $(10^{-2}a_0^2)$	$\beta_J\langle r_{4f}^4\rangle J_4$ $(10^{-2}a_0^4)$	$\gamma_J\langle r_{4f}^6\rangle J_6$ $(10^{-2}a_0^6)$	$\alpha_J\langle r_{4f}^2\rangle\tilde{O}_2^0$ $(10^{-2}a_0^2)$	$\beta_J\langle r_{4f}^4\rangle\tilde{O}_4^0$ $(10^{-1}a_0^4)$	$\gamma_J\langle r_{4f}^6\rangle\tilde{O}_6^0$ $(10^{-1}a_0^6)$
Ce	−37.40	+18.88	0	−74.80	+15.10	0
Pr	−35.76	−26.20	+35.96	−71.51	−20.96	+57.54
Nd	−12.89	−16.01	−53.96	−25.78	−12.81	−86.33
Sm	+20.10	+4.24	0	+40.21	+3.39	0
Gd	0	0	0	0	0	0
Tb	−27.40	+15.01	−7.99	−54.80	+12.00	−12.78
Dy	−26.36	−18.24	+35.24	−52.71	−14.59	+56.40
Ho	−10.06	−12.54	−62.69	−20.12	−10.03	−100.31
Er	+9.61	+11.55	+56.13	+19.23	+9.24	+89.81
Tm	+23.02	+14.23	−25.29	+46.04	+11.38	−40.47
Yb	+22.09	−9.90	+4.58	+44.18	−7.92	+7.33

In the cubic RFe_2 and RCo_2 compounds, the easy magnetic direction at low temperatures has been found to follow the sign of the factor β_J, see table 2.7. A positive sign of β_J in case of RFe_2 compounds results in an easy direction of the R moment along the body diagonal $\langle 111\rangle$.

Although the role of the second-order term in the uniaxial systems is dominant,

TABLE 2.5
Correlation between the experimentally observed easy direction of magnetization (EMD) at 4.2 K in the RNi_5 series and the second-order, α_J, and the sixth-order, γ_J, Stevens factors of the R ion.

Compound	Easy direction	α_J	EMD in plane	γ_J
Pr	plane	−	***b***	+
Nd	plane	−	***a***	−
Sm	*c* axis	+		
Gd				
Tb	plane	−	***a***	−
Dy	plane	−	***b*** (>6.5 K)	+
Ho	plane	−	***a***	−
Er	*c* axis	+	***b***	+
Tm	*c* axis	+	***a***	−
Yb	no data	+	no data	+

TABLE 2.6
Correlation between the experimentally observed easy direction of magnetization (EMD) at 4.2 K for the R_2Co_{17} series and the Stevens factors α_J and γ_J of the R ion. (t): EMD slightly tilted out from the basal plane. After Radwański and Franse (1992).

Compound	Easy direction	α_J	EMD in plane	γ_J
Y	plane	0		0
Pr	plane (t)	−	complex	+
Nd	plane (t)	−	***b***	−
Sm	*c* axis	+		0
Gd	plane	0		0
Tb	plane	−	***b***	−
Dy	plane	−	***a***	+
Ho	plane (t)	−	***b***	−
Er	*c* axis	+		+
Tm	*c* axis	+		−

the role of the higher-order terms is not negligible. Higher-order terms are manifest in easy-plane systems. For the hexagonal symmetry, the easy magnetic direction within the basal plane is governed by the sign of the sixth-order Stevens factor, γ_J. The RNi_5 compounds exactly follow these systematics. The same is found for the R_2Co_{17} and R_2Fe_{17} compounds, see table 2.6. In other series the evidence is not yet complete. Moreover, by inspection of table 2.4 one notices that for Nd and Ho ions the fourth-order term is relatively large compared to the second-order term. For these ions, a competition between the second- and the fourth-order terms may cause a deviation of the easy direction of magnetization from the main crystallographic direction. Tilted magnetic structures are observed in Nd_2Co_{17}, $Nd_2Fe_{14}B$, $Ho_2Fe_{14}B$ and $HoCo_5$, indeed.

TABLE 2.7

Correlation between the experimentally observed easy direction of magnetization in RFe_2 and RCo_2 compounds and the fourth-order Stevens factor β_J for the R ion. For a negative value of β_J, the easy direction points along the cubic edge, whereas for a positive value along the body diagonal. As for some compounds the EMD rotates with temperature, the easy directions for low and high temperatures are given. (t): EMD tilted out from a main crystallographic direction. After Radwański and Franse (1992).

Compound	Easy direction RFe_2		β_J	Easy direction RCo_2	
	low T	high T		low T	high T
Y	111	111			
Ce	100	(t)	+		
Pr	100	100	−	100	100
Nd	110	100	−	110	100
Sm	110	111	+	111	111
Gd			0	100	100
Tb	111	111	+	111	111
Dy	100	100	−	100	100
Ho	110	100	−	110	100
Er	111	111	+	111	111
Tm	110	111	+	111	111
Yb	100	100	−		

2.2. *Exchange interactions and the molecular and exchange field*

2.2.1. *4f–4f interactions*

These interactions are generally considered to be mediated by the conduction electrons as the inter-ionic distances, in combination with the spatial localization of the 4f electrons, make a direct overlap of the 4f functions of neighbouring R ions improbable. Two models have been proposed for this interaction: the RKKY model developed for rare-earth magnetism by de Gennes (1962) and a model put forward by Campbell (1972). Both models involve the 5d and 6s conduction electrons of the R ion and the 4s electrons of the T ion. In the model of Campbell the role of the 5d electrons is emphasized, whereas in the RKKY model the total density of conduction electrons enters into the relevant expressions.

Originally, the variation of T_c with the de Gennes factor, $G = (g_R - 1)^2 J(J+1)$, observed for *heavy* R elements in many rare-earth series was taken as a strong argument for the validity of the RKKY model. At present it is argued that such a behaviour is to be expected for any interaction that proceeds via the spins. Being more strict, as far as in a rare-earth ion J remains a good quantum number, the operator $(g_R - 1)\boldsymbol{J}$ serves as the spin-operator and, consequently, enters into the exchange interactions of the Heisenberg-type of Hamiltonian,

$$\mathscr{H} = -\sum_{i,j} J_{ij} \boldsymbol{S}_i \cdot \boldsymbol{S}_j, \tag{2.14}$$

where the summation is over all the magnetic ions in the lattice and where J_{ij} is the exchange parameter between local spins residing at the sites i and j.

Introducing

$$\boldsymbol{S}_R = (g_R - 1)\boldsymbol{J}_R \tag{2.15}$$

one arrives at the Hamiltonian

$$\mathscr{H} = -\sum_{i,j} J_{RR}(g_R - 1)^2 \boldsymbol{J}\cdot\boldsymbol{J} \tag{2.16}$$

where J_{RR} is an effective exchange parameter between the 4f-spins of the rare-earth ions at sites i and j.

In a mean-field approximation, all spin moments are replaced by their mean value, except the spin under discussion at the site i. In that case the exchange field acting on the spin moment is introduced,

$$B_{ex}^R = \frac{1}{2\mu_B}\sum_j J_{RR}\langle S_R\rangle, \tag{2.17}$$

where the summation runs over the surrounding spins. The equivalent molecular field, B_{mol}^R, that acts on the total 4f moment is given as

$$B_{mol}^R = \gamma_R B_{ex}^R, \tag{2.18}$$

where

$$\gamma_R = \frac{2(g_R - 1)}{g_R}. \tag{2.19}$$

The parameter γ_R defines the spin part of the total moment m_R of the rare-earth ion:

$$\langle m_R^s\rangle = \gamma_R\langle m_R\rangle, \tag{2.20}$$

where $\langle m_R\rangle = -g_R\mu_B\langle J_R\rangle$. The values for γ_R are tabulated in table 2.8 for all R^{3+} ions in the Hund-rules ground-state multiplet.

The molecular field, B_{mol}^R, can be estimated from the magnetic ordering temperature, T_c:

$$B_{mol}^R = \frac{3k_B T_c}{g_R(J+1)\mu_B}. \tag{2.21}$$

In the paramagnetic region the rare-earth susceptibility is expected to obey a Curie law with the Curie constant C_R given by

$$C_R = N_R\frac{g^2 J(J+1)\mu_B^2}{3k}, \tag{2.22}$$

where N_R is the number of R atoms per unit volume. Values of C_R for the trivalent rare-earth ions are collected in table 2.8. The molecular-field coefficient n_{RR} can be estimated from the magnetic ordering temperature as:

$$n_{RR} = \frac{T_c}{C_R}. \tag{2.23}$$

TABLE 2.8
Values for γ_R in eq. (2.19) and for the Curie constant C_R for the trivalent rare-earth ions in the ground-state multiplet given by Hund's rules.

Ion	J	g	γ_R	C_R	
				(K emu/mol)	(10^{-6} K m^3/mol)
Ce	5/2	6/7	−1/3	0.804	10.11
Pr	4	4/5	−1/2	1.601	20.12
Nd	9/2	8/11	−3/4	1.637	20.58
Sm	5/2	2/7	−5	0.092	1.12
Gd	7/2	2	1	7.88	99.04
Tb	6	3/2	2/3	11.82	148.55
Dy	15/2	4/3	1/2	14.17	178.17
Ho	8	5/4	2/5	14.07	176.85
Er	15/2	6/5	1/3	11.48	144.31
Tm	6	7/6	2/7	7.15	89.87
Yb	7/2	8/7	1/4	2.57	32.34

Applying the above-mentioned equations to gadolinium metal, a value for B_{mol}^{Gd} of 145 T and a corresponding value of 21 T/μ_B for n_{RR} are deduced. The evaluation of n_{RR} for other elements, however, is not straightforward because of the presence of crystal-field interactions. In intermetallics with a magnetic partner the R–R interaction is strongly dominated by the R–T exchange interactions. Most effectively, the 4f interactions can be studied in compounds with a nonmagnetic rare-earth partner. Some nickel compounds, for instance, are suited for a study of the R–R interaction. Examples are the RNi_5 and RNi_2 series, as nickel atoms have lost their spontaneous magnetic moment in these compounds. Application of eq. (2.23) to the series RZn, RAl_2 and RNi_5, results in the values for the exchange-field coefficient $\gamma_R^{-2} n_{RR}$ as presented in fig. 2.4. Although there are some ambiguities in the magnetic behaviour of the light R elements, the substantial increase of the exchange parameter with decreasing number of 4f electrons is certainly present in these series as has been originally pointed out by Belorizky et al. (1988a). As mentioned above, the 4f states are localized and direct overlap of the 4f functions is extremely small. The interaction between the 4f moments must involve conduction electrons. The most plausible mechanisms emphasize the role of the 5d electrons of the R ion. The localized 4f spin polarizes the 5d electrons. These electrons, subsequently, interact with 5d electrons of the neighbouring ions. In such a picture the effective parameter of the 4f–4f spin coupling J_{RR} contains information about the more fundamental interaction parameters J_{4f-5d} and J_{5d-5d}. The *intra-ionic* interaction J_{4f-5d} is found always to be positive. Brooks et al. (1989) have estimated this interaction from atomic calculations. They found increasing values for J_{4f-5d} from 947 K for Yb to 1420 K for Ce. The observed increase in the parameter $\gamma^{-2} n_{RR}$ found for RZn, RNi_5 and RAl_2 series as shown in fig. 2.4 is in satisfactory agreement with these theoretical calculations. Belorizky et al. (1988b) deduced a value for J_{4f-5d} of about 1440 K in Gd metal and in several Gd

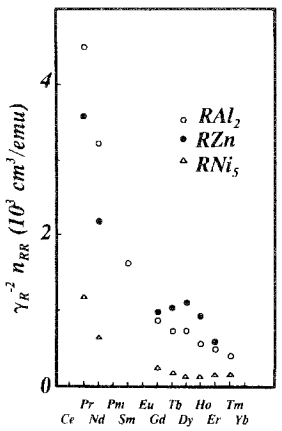

Fig. 2.4. Values for the exchange-field coefficient $\gamma_R^{-2} n_{RR}$ in the RAl_2, RZn and RNi_5 series. After Belorizky et al. (1988a).

compounds ($GdAl_2$, GdCd, Gd_3In and GdZn) by considering values for T_c and the susceptibility. H. S. Li et al. (1991) by means of self-consistent relativistic atomic calculation have found the exchange integral between the 4f electrons and conduction electrons J_{4f-c} to decrease from 1766 K for Pr^{3+} to 1140 K for Tm^{3+}. For the effective molecular-field coefficient n_{RR}, expressed as

$$n_{RR} = \gamma_R \chi_c n_{4f-c}^2, \tag{2.24}$$

where χ_c is the susceptibility of conduction electrons, an even larger decrease is found due to the simultaneous reduction of the number of 5d electrons.

2.2.2. 3d–3d interactions

The 3d subsystem in the 3d–4f intermetallic compounds is treated within the itinerant-electron model, similarly to the magnetism of the pure 3d metals. Band-structure calculations performed for Y–Fe, Y–Co and Y–Ni compounds by different authors are consistent (Cyrot and Lavagna 1979, M. Shimizu and Inoue 1986, 1987, Yamada and Shimizu 1986a, Coehoorn 1989) and, in general, reproduce the basic experimental results, e.g. the magnetic moment and the general shape of the density-of-states curves. Conditions required for the occurrence of ferromagnetism in cobalt compounds like Y_3Co, Y_3Co_2 and YCo_2 have been studied by Coles and Chhabra (1986). There is a significant hybridization of the 4d and 5s conduction electrons of yttrium, with the 3d electrons of the transition-metal elements. This hybridization becomes more effective for smaller concentrations of the 3d metals. Generally, the electronic structure can schematically be represented by one of the three DOS curves shown in fig. 2.5. In the first curve, illustrating the weak ferromagnetic case, the majority and minority sub-bands are both partly filled. To this category belong all iron compounds. For these compounds the Fermi level is situated in a region with a large density of states originating primarily from the 3d band of iron. In the second curve, illustrating the strong ferromagnetic case, the majority band is filled up but the Fermi level stays

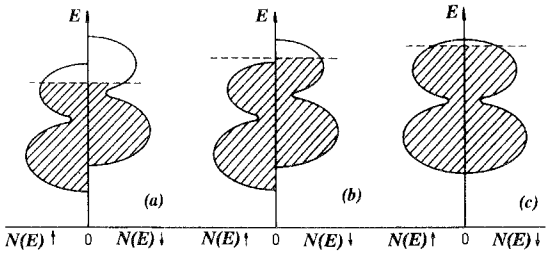

Fig. 2.5. Schematic representation of the density of states curves for 3d electrons with spin-up and spin-down in the 3d–4f intermetallics for (a) weak, (b) strong ferromagnetic, and (c) paramagnetic cases; the Fermi energy, E_F, is indicated by the broken lines.

within a large density of states region. To this class belong the cobalt-rich R_nCo_m compounds and the R_2Ni_{17} compounds. In the third curve, illustrating the paramagnetic case, the two subbands are filled up and the Fermi level is pulled out to a low density-of-states region originating from the conduction-electron band of the rare-earth ion. As an example of the first category, the electronic structure for the series Y–Fe compounds is shown in fig. 2.6. These compounds are found to be weak ferromagnets in the sense that the top of both sub-bands remains unfilled. In Y_2Fe_{17}, the Fermi energy, E_F, is situated just above a pronounced peak of antibonding states in the majority-spin band and just below this peak in the minority-spin band. This feature is characteristic for all Fe compounds.

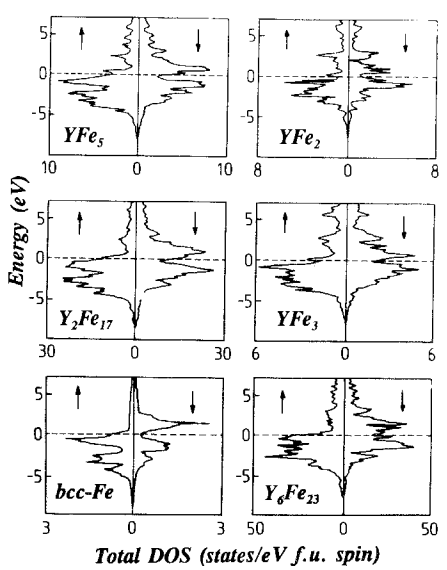

Fig. 2.6. Calculated total density of states for majority-spin (↑) and minority-spin (↓) electrons of the Y–Fe compounds; bcc-Fe is included for comparison; the energy is given with respect to the Fermi level (horizontal dashed line). After Coehoorn (1989).

The density-of-states values at the Fermi level that result from band-structure calculations are of the order of 1–3 eV^{-1} per spin-atom. Values for the susceptibility and the electronic-specific-heat coefficient γ that follow from band-structure calculations are collected in table 2.9. From these calculations for the YFe_3, YCo_3 and YNi_3 compounds it has been found that the shape of the density of states is very similar. Therefore, as a first approximation, a rigid-band model is considered to be applicable for the pseudobinary compounds of Y–Fe, Y–Co and Y–Ni compounds for the same stoichiometry, in good agreement with experimental observations.

Band-structure calculations for the Y–Fe compounds reveal a small moment on the Y site that is coupled antiparallelly to the 3d moments. Its value increases with increasing Y concentration, from $0.20\mu_B$ in Y_2Fe_{17} to $0.44\mu_B$ in YFe_2 (Coehoorn 1989). The result for YFe_2 is in good agreement with the calculated value reported by Mohn and Wohlfarth (1987). A magnetic moment of this size has been deduced by Dumelow et al. (1986) from the pressure dependence of NMR spectra on ^{89}Y nuclei. Ritter (1989) reported an even larger moment of $0.67\mu_B$ for Y on basis of polarized neutron studies of YFe_2. Brooks et al. (1989) calculated a value of $0.41\mu_B$ for the moment localized at the Lu site in $LuFe_2$. Bulk magnetization measurements, of course, are not able to separate the contributions originating from the different atoms, but the magnetic data can be compared with results of neutron experiments and theoretical calculations for the total magnetization.

In performing band-structure calculations, the mutual 3d interactions have to be somehow approximated. Usually, these calculations are performed within a molecular-field approximation with the 3d interactions expressed in terms of a molecular-field

TABLE 2.9

Results of band-structure calculations for the differential high-field susceptibility χ_{hf} and the linear-term coefficient γ in the low-temperature specific heat.

Compound	χ_{hf} (10^{-9} m^3/mol f.u.)	γ (mJ/K^2 mol f.u.)	Ref.*
Y_2Fe_{17}	56	86.9	[1]
Y_6Fe_{23}	66	123.7	[1]
YFe_3	4	12.6	[1]
YFe_2	5	7.5	[2]
Y_2Co_{17}	0.5	72.2	[1]
YCo_5	3.9	27.8	[1]
Y_2Co_7	8.4	49.2	[1]
YCo_3	8.0	20.2	[1]
YCo_2	5.0	13.7	[2]
YNi_2	1.8	4.7	[2]
YMn_2	5.9	12.7	[2]

*References:

[1] Inoue and Shimizu (1985).

[2] Yamada et al. (1984).

coefficient. The value of this coefficient is often considered to be dependent on the 3d atomic species but only slightly dependent on the 3d concentration. Values of 1.064, 1.19 and 0.85 (in units of 10^4 mol/emu) have been taken by Inoue and Shimizu (1985) and by Inoue (1988) for Y_2Fe_{17}, Y_2Co_{17} and Y_2Ni_{17}, respectively. The first value corresponds to a value of $5940\,T/\mu_B$ for the molecular-field coefficient n_{TT}. Coehoorn (1989) approximates the Fe–Fe interactions by the Stoner parameter, I, with a value of 0.925 eV. For Y_2Fe_{17} this value for I is equivalent with a value of $8000\,T/\mu_B$ for the molecular-field coefficient n_{TT}, following the relation

$$I = 2\mu_B^2 n_{TT}. \tag{2.25}$$

A value of 0.88 meV has been used by Brooks et al. (1989) to analyse $LuFe_2$. A serious problem appears as these values for n_{TT} lead to values of the Curie temperature that largely exceed the experimentally observed values. This discrepancy reveals the shortcomings of the mean-field approach to the 3d magnetism.

On the other hand, starting from the experimental values for T_c and accepting eq. (2.21) to be applicable to the 3d magnetism as well (with $g = 2$ and $J = S$), values for the molecular field for Y–Fe and Y–Co compounds can be derived as collected in table 2.10. These values illustrate the magnitude of internal fields present in 3d–4f compounds due to the 3d–3d interactions. In compounds with cobalt, B^T_{mol} decreases gradually. The exchange parameter J_{Co-Co}/k, calculated by means of the mean-field relation, remains virtually constant and takes a value of 115 K (Radwański 1986a, Coey 1987) despite of the fact that the magnetic moment gradually decreases. A different behaviour is observed for the iron compounds. The molecular field and the corresponding value for J_{Fe-Fe} is smallest for Y_2Fe_{17}, the Y–Fe compound with the

TABLE 2.10
Phenomenological characteristics of the 3d exchange: Curie temperature, T_c, quasi-spin of the 3d ion, S_T, and the molecular field experienced by 3d moment, B^T_{mol}.

Compound	T_c (K)	S_T	B^T_{mol} (T)
Co	1410	0.85	1700
Y_2Co_{17}	1186	0.82	1450
$Y_2Co_{14}B$	1015	0.70	1330
YCo_5	987	0.82	1210
Y_2Co_7	639	0.75	820
YCo_3	301	0.19	565
α-Fe	1043	1.11	1100
Y_2Fe_{17}	358	1.03	390
$Y_2Fe_{14}B$	558	1.10	590
Y_6Fe_{23}	496	1.00	554
YFe_3	569	0.85	690
YFe_2	542	0.77	680

highest concentration of iron. The variation in the value of exchange parameter J_{T-T} is in qualitative agreement with the systematics known as the Bethe–Slater curve.

In a description of the Curie temperature of 3d alloys and compounds by Mohn and Wohlfarth (1987), it is proposed that for most rare-earth transition-metal alloys the effect of spin fluctuations dominates the value of T_c. Good agreement between calculated and experimental values of T_c has been obtained for the Y_nCo_m and Y_nFe_m series but $Y_2Fe_{14}B$ and α-Fe do not follow the general trend. A magnetic valence model developed originally for binary transition-metal alloys by Williams et al. (1983) and for transition-metal metalloids alloys by Malozemoff et al. (1984) has been extended to the 3d–4f compounds by Gavigan et al. (1988). It attributes the variation of J_{TT} to the magnetic coordination number Z of the interacting 3d spins. It has been demonstrated that a larger number of Fe spins in the local surrounding of an Fe ion leads to smaller values of T_c. This model provides, for instance, a qualitative explanation for the antiferromagnetism of fcc γ-Fe with $Z = 12$ and for the ferromagnetism of bcc α-Fe with $Z = 8$.

Inspection of table 2.10 shows that the molecular field experienced by the 3d moments in most of 3d–4f compounds is two orders of magnitude larger than the external fields available at present. It explains the weak influence of external fields on the 3d magnetic moment. Indeed, the experimentally observed field-induced moment in the ordered state amounts to a few parts in thousand per tesla, see table 2.11, where the values for the differential high-field magnetic susceptibility are collected. These values as well as values of the experimentally observed electronic specific-heat coefficient γ are in reasonable agreement with band-structure results as one can conclude comparing tables 2.9 and 2.11 for the susceptibility data and tables 2.9 and 2.12 for the coefficient γ data. Discrepancies will be discussed in the next section in more detail.

The paramagnetic behaviour of the iron compounds is relatively simple, although its understanding is rather poor. For all the compounds above T_c, a linear part is found in the plot of χ^{-1} versus T. The value of the Curie constant, C_{Fe}, serves as a parameter describing the high-temperature magnetic behaviour of the iron sublattice. It has been used in analysing the values of the Curie temperature in the R–T compounds in order to evaluate the parameter n_{RT} (Belorizky et al. 1987, H. S. Li et al. 1991).

As was already mentioned, band-structure calculations can, in principle, reproduce the variation of the magnetic moment over the different stoichiometries. Two points should be mentioned here. Both of them are related to the critical region where the 3d magnetism vanishes. Band-structure calculations attribute the occurrence of magnetism in the compounds YNi_3 and Y_2Ni_7 to some peculiarities in the density of electron states. Y_2Ni_7 was reported to exhibit "thermal induced spontaneous magnetization" (Gignoux et al. 1981, Gignoux 1987). This phenomenon became manifest by the appearance of a spontaneous magnetization in the temperature range between 7 and 58 K. More careful examinations of the quality of the sample by Ballou et al. (1990a) have showed that the thermally induced ferromagnetism in Y_2Ni_7 has resulted from Gd impurities.

The magnetism of Mn compounds is still intriguing. Magnetic moments as large as $3\mu_B$ are reported for the manganese atoms. The antiferromagnetic coupling

TABLE 2.11
Experimental values for the differential high-field susceptibility as measured for fields along the easy direction of magnetization.

Compound	T (K)	χ_{hf}		Ref.*
		(10^{-9} m^3/mol f.u.)	($10^{-4}\mu_B$/T f.u.)	
Y_2Co_{17}	4.2	48	70	[1,2]
Ho_2Co_{17}	4.2	48	70	[1,2]
YCo_5	4.2	19	27	[3]
$Gd_2Co_{14}B$	4.2	70	100	[4]
Y_2Co_7	4.2	96	137	[5]
Gd_2Co_7	4.2	45	65	[5]
YCo_3	4.2	70	100	[6]
YCo_2	4.2	24	34	[7]
YCo_2	4.2	22	31	[8]
YCo_2	300	49	69	[9]
$LuCo_2$	4.2	15	21	[8]
$ScCo_2$	4.2	14	20	[8]
Co	4.2	2.6	3.7	[10]
Y_2Fe_{17}	4.2	120	170	[11]
Ho_2Fe_{17}	4.2	95	135	[1,2]
$Y_2Fe_{14}B$	4.2	116	165	[12]
$Gd_2Fe_{14}C$	4.2	70	100	[13]
$Lu_2Fe_{14}C$	4.2	200	280	[13]
YFe_3	4.2	16	23	[6]
Fe	4.2	2.5	3.6	[10]
YNi_5	4.2	29	40	[14]
$LaNi_5$	4.2	25	36	[14]
$GdNi_5$	4.2	38	54	[14]
$SmNi_5$	4.2	27	38	[15]
YNi_3	4.2	36	51	[6]
YNi_2	4.2	2.5	3.0	[16]
$LuNi_2$	4.2	5.0	7.0	[17]
Ni	4.2	1.2	1.7	[10]
YMn_2	4.2	12	17	[18]

*References:

[1] Sinnema (1988).
[2] Radwański et al. (1988a).
[3] Alameda et al. (1981).
[4] Radwański et al. (1990b).
[5] Ballou (1987).
[6] Kebe (1983).
[7] Schinkel (1978).
[8] Ikeda et al. (1984).
[9] Bloch et al. (1975).
[10] Pauthenet (1983).
[11] Averbuch-Pouchot (1987).
[12] Franse et al. (1990).
[13] Radwański et al. (1989a).
[14] Nait-Saada (1980).
[15] Ballou et al. (1988a).
[16] Burzo and Laforest (1972).
[17] Scrabek and Wallace (1963).
[18] Wada et al. (1985).

TABLE 2.12
Values for the coefficient γ of the electronic contribution to the specific heat and for the Debye temperature, θ_D, of R–T intermetallics.

Compound	γ (mJ/K^2 mol)	θ_D (K)	Ref.*
YCo_2	36	240	[1]
YCo_2	30.6–33.1	232–222	[2]
$LuCo_2$	26.6	238	[2]
$ScCo_2$	18.4	344	[2]
YCo_2	34	252	[3]
YCo_3	59	285	[4]
Th_2Co_7		320	[5]
YCo_5		370	[6]
Y_2Co_{17}	70		[7]
Ho_2Co_{17}	70	310	[8]
Er_2Co_{17}	70	310	[8]
YFe_2	12	300	[1]
$LuFe_2$	12.8	296	[9]
YNi_2	5.2	291	[10]
$LuNi_2$	5.4	241	[11]
YNi_5		400	[6]
$LaNi_5$	33	322	[12]
YMn_2	14	304	[3]
YMn_2	15	290	[13]
Lu_6Mn_{23}	277	270	[14]

*References:
[1] Muraoka et al. (1977), heat.
[2] Ikeda et al. (1984), heat 1.3–6 K.
[3] Wada et al. (1989), heat 1.5–7 K.
[4] Bartashevich et al. (1988), heat.
[5] Andreev et al. (1984a), thermal exp.
[6] Andreev et al. (1985b), thermal exp.
[7] Godwin et al. (1979), heat.
[8] Radwański et al. (1988b), heat.
[9] Butera et al. (1979), heat.
[10] Mori et al. (1982) (below 10 K).
[11] Deutz et al. (1989), heat.
[12] Nait-Saada (1980, p. 85), heat 5–300 K.
[13] N. Okamoto et al. (1987), heat above 7 K.
[14] Graves-Tompson et al. (1983), heat 1.7–18 K.

complicates the magnetic structure very much. Manganese moments are especially sensitive to their local surroundings. Neutron studies for the compound Y_6Mn_{23}, for instance, reveal magnetic-moment values that vary between 1.8 and 2.8μ_B (Delapalme et al. 1979). In the RMn_2 series, the magnetic moment has been followed across the rare-earth series. Mn does not carry a magnetic moment in $HoMn_2$, whereas in YMn_2, $TbMn_2$ and $GdMn_2$ a magnetic moment of about 2.7μ_B has been found (Yoshimura et al. 1986a). This large variation in the manganese moment is correlated

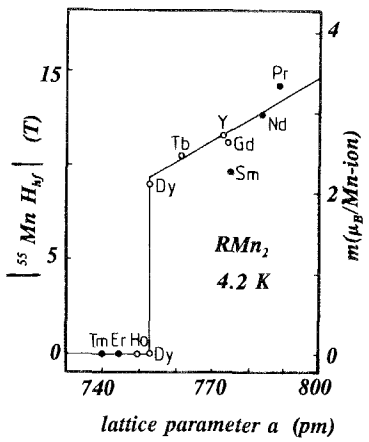

Fig. 2.7. Correlation between the ^{55}Mn hyperfine field and the lattice parameter at 4.2 K for the RMn_2 compounds; open and closed circles indicate results for the cubic and hexagonal compounds, respectively; the right-hand scale gives the Mn moment as deduced from the hyperfine fields with a value for the proportionality factor A in eq. (3.20) of 4.27 T/μ_B. Two values for the $DyMn_2$ compound correspond to two Mn sites. In the case of the hexagonal structure the effective cubic lattice parameter is defined as $\sqrt{(3/2)a^2c}$. After Yoshimura et al. (1986a).

with the variation of the lattice parameter in this Laves-phase series, see fig. 2.7. The large volume-dependence of the band-structure parameters of the d (3d and 5d) electrons came out from band-structure calculations of Yamada and Shimizu (1987a,b). The mutual Mn–Mn interactions have been approximated by a molecular-field coefficient of 2700 T/μ_B. This value is two times smaller than in Fe and Co compounds but still produces a significant band splitting (Yamada and Shimizu 1988).

Contrary to Fe and Co compounds, the presence of a magnetic R element does not change the magnetic ordering temperature of the RMn_2 compounds very much. The Néel temperature of YMn_2 as well as of $GdMn_2$ is in the vicinity of 100–110 K, indicating that this temperature reflects mainly the Mn–Mn interaction.

2.2.3. *3d–4f interactions*

In a number of compounds with magnetic rare-earth elements, the electronic structure around the Fermi level is not expected to differ significantly from the yttrium compounds with the same stoichiometry as the number of conduction electrons and the lattice parameters are rather similar. From a formal point of view, one can write the molecular field, acting on a R moment, as

$$B^{R}_{mol} = B^{R}_{mol,RT} + B^{R}_{mol,RR} = n_{RT}M_T + n_{RR}M_R, \tag{2.26}$$

and similarly for the molecular field on a T atom,

$$B^{T}_{mol} = B^{T}_{mol,TT} + B^{T}_{mol,RT} = n_{TT}M_T + n_{RT}M_R. \tag{2.27}$$

The more complex notation for the molecular fields has been introduced in order to distinguish the different parts. The sequence of the terms at the right-hand side

follows the strength of the internal fields. Although the 4f moments are often larger than the moments of the 3d transition metals, the internal field acting on the rare-earth moment and originating from the 3d sublattice dominates that originating from the 4f sublattice. This dominance is due to the much smaller value of the intra-sublattice molecular-field coefficient n_{RR} compared to that of inter-sublattice molecular-field coefficient n_{RT}. In the analysis of most of the rare-earth compounds with iron or cobalt, the contribution to the molecular field from the 4f–4f interactions is ignored. Since it is the spin rather than the total moment that is involved in the interactions, it is useful to introduce the exchange field, $B^{R}_{ex,RT}$ that acts on the rare-earth spin. The relation between $B^{R}_{mol,RT}$ and $B^{R}_{ex,RT}$ can be written in the form

$$B^{R}_{mol,RT} = \gamma_R B^{R}_{ex,RT}. \tag{2.28}$$

This relation results from a comparison between two expressions for the exchange energy:

$$E_{ex} = g_R \mu_B \boldsymbol{J} \cdot \boldsymbol{B}^{R}_{mol,RT}, \quad \text{and} \quad E_{ex} = 2(g_R - 1)\mu_B \boldsymbol{J} \cdot \boldsymbol{B}^{R}_{ex,RT}. \tag{2.29}$$

The exchange field measures the strength of the interaction between different species of the spins in the 3d–4f intermetallics. For gadolinium compounds, $B^{Gd}_{mol,RT} = B^{Gd}_{ex,RT}$ as the Gd moment is a spin moment only.

Within a molecular-field formalism, the exchange field can be expressed as

$$B^{R}_{ex,RT} = -\frac{1}{\mu_B} \sum_{T} J_{RT} S_T \tag{2.30}$$

where the summation runs over all transition-metal neighbours of the rare-earth spin. Here the negative sign appears in order to take into account the negative value of the coupling parameter J_{RT} reflecting the AF interactions between 3d and 4f spins.

In a further step this field is attributed to the interactions between nearest neighbours. Assuming, additionally, that this interaction is isotropic, one gets:

$$B^{R}_{ex,RT} = -\frac{J_{RT} S_T z_{RT}}{\mu_B}, \tag{2.31}$$

where J_{RT} is the exchange parameter between the 3d and 4f spins and where z_{RT} is the number of transition-metal spins in the nearest-neighbour surrounding to an R atom. The evaluation of the molecular field, the exchange field and the parameter J_{RT} is the main purpose of the analysis of the experimental data. The restriction to the nearest neighbours in eq. (2.31) gives the possibility to correlate the values for $B^{R}_{ex,RT}$ between different series.

From an experimental point of view, the situation around the values for the 3d–4f exchange interaction ($B^{R}_{ex,RT}$ or J_{RT}) has considerably been improved in the last decade. A constant value of J_{RT} within a given series has been inferred in a number of publications from an analysis of the Curie temperatures: Buschow and van Stapele (1972) for RFe_2, Pszczoła and Krop (1986) for the iron series, Sinnema et al. (1984) for $R_2Fe_{14}B$. In general, a satisfying correlation between the values for T_c and the de Gennes factor is found for the *heavy* rare-earth compounds.

Values of T_c for the light rare-earth compounds always reveal deviations from simple systematics. This deviation was taken as a characteristic feature of light rare-earth ions because of some peculiarities of the magnetic behaviour of Pr, Nd and Sm metals, possibly related to crystal-field phenomena. Belorizky et al. (1987, 1988a) were the first to attribute this deviation to a substantial increase of the 3d–4f interactions towards the light rare-earths.

Applying a molecular-field approach, the following expression for T_c is derived:

$$T_c = \tfrac{1}{2}[T_T + T_R + \sqrt{(T_T - T_R)^2 + 4T_{RT}^2}], \tag{2.32}$$

where T_T, T_R and T_{RT} represent the contributions to T_c arising from the T–T, R–R and R–T interactions, respectively. The characteristic temperatures are given by

$$T_T = n_{TT} C_T, \tag{2.33}$$

$$T_R = n_{RR} C_R, \tag{2.34}$$

$$T_{RT} = n_{RT} \sqrt{C_R C_T}, \tag{2.35}$$

where C_R and C_T are the Curie constants of the R and T sublattices involved, respectively. Both parameters enter in this expression because it is assumed that the temperature dependence of the magnetic susceptibility of the two subsystems contain both Curie constants. This assumption is of crucial importance for the 3d sublattice. T_{RT} is proportional to the de Gennes factor, G, of the R ion involved. Provided T_{RT} is much smaller than T_T ($T_c - T_T$) is in first approximation proportional to the value of G.

The temperature T_{RT} can also be expressed as:

$$T_{RT} = \sqrt{(T_c - T_T)(T_c - T_R)}. \tag{2.36}$$

Combination of eqs. (2.33) and (2.36) leads to (Belorizky et al. 1987)

$$n_{RT} = \sqrt{\frac{(T_c - T_T)(T_c - T_R)}{C_R C_T}}. \tag{2.37}$$

By employing eq. (2.37) for a given R series, values for n_{RT} can be derived. In fig. 2.8, the results for the $R_2Fe_{14}B$ and RCo_2 series are presented. The figure reveals a significant decrease of the exchange–coupling parameter $\gamma_R^{-1} n_{RT}$ with increasing number of the 4f electrons. This decrease has been correlated to the decrease of the distance between the radius of the 4f and 5d shells. The radius of the 4f shell, r_{4f}, decreases substantially going across the 4f series (Freeman and Desclaux 1979). The values for $\langle r_{4f} \rangle$ between Ce and Yb range from 1.1 to $0.8 a_0$, i.e., they differ by a factor of 1.4. The radius of the 5d shell also decreases following the lanthanide contraction but the reduction is only 4%. As a consequence, the overlap of the 5d and 4f functions decreases towards the heavy rare-earth ions. The distance between the 4f and 5d shells is plotted versus the number of 4f electrons in the bottom part of fig. 2.8. It has been concluded that the 4f–5d part of the effective 3d–4f exchange interaction is most affected going through the 4f series. The same conclusion can be drawn for the 4f–4f interactions. In that latter interaction the intra-ionic 4f–5d interaction enters

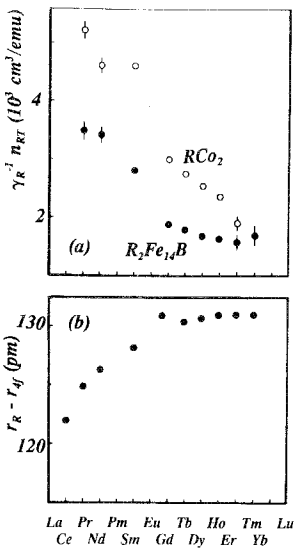

Fig. 2.8. (a) Values for the intersublattice exchange-field coefficient $\gamma_R^{-1} n_{RT}$ in the $R_2Fe_{14}B$ and RCo_2 series derived from an analysis of the values for the Curie temperature. (b) Values for $(r_R - r_{4f})$ across the 4f series; r_R is the ionic radius of the R element and r_{4f} is the radius of the 4f shell taken as $\sqrt{\langle r_{4f}^2 \rangle}$. After Belorizky et al. (1987).

twice, resulting in a stronger variation of the 4f–4f interaction. Comparison of figs. 2.4 and 2.8 supports this view.

In fig. 2.9, values for the exchange field are presented for different series of rare-earth compounds. These values have been derived from different types of experiments, in particular high-field magnetization and inelastic neutron scattering, and the above discussed increase is observed for all series.

Because of the spatial localization of the 4f shell, the direct overlap between the 3d and 4f spins is rather small. The model suggested by Campbell (1972) involves a direct on-site 4f–5d exchange. According to this scheme, the localized 4f spins create a positive localized 5d moment through the intra-ionic 4f–5d exchange with, subsequently, direct 5d–3d exchange as in normal transition metals. This interaction is negative. In combination with positive 4f–5d interactions, it leads to a parallel moment alignment for the light rare-earths and to an antiparallel moment alignment for the heavy rare-earths as schematized in fig. 2.10. Brooks et al. (1989) have calculated the exchange integrals J_{4f-5d} and J_{5d-3d} for the RFe_2 compounds with heavy rare earths and found a substantial but monotonic variation of the intra-atomic integral J_{4f-5d}. H. S. Li et al. (1991, 1992) have extended these calculations and considered also integrals with p and s conduction electrons. The values for J_{4f-6s} and J_{4f-6p}, however, are much smaller than that for J_{4f-5d}. The magnitude of J_{4f-5d} is in the range 1900–2700 K, whereas values for J_{4f-6s} and J_{4f-6p} are 450 and 180 K, respectively. All three integrals decrease across the rare-earth series due to the lanthanide contraction. The effective exchange integral between the 4f electrons and the conduction

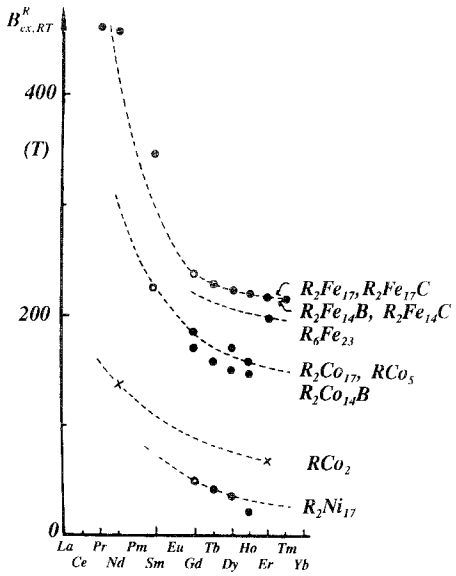

Fig. 2.9. Values for the exchange field $B^R_{ex,RT}$ experienced by the 4f spin moment in a number of R_nT_m series; high-field magnetization studies for R_2Fe_{17} and R_2Co_{17} (●); inelastic-neutron-scattering data (×); data obtained from T_c values (○); broken lines are guides to the eye. After Radwański et al. (1990a).

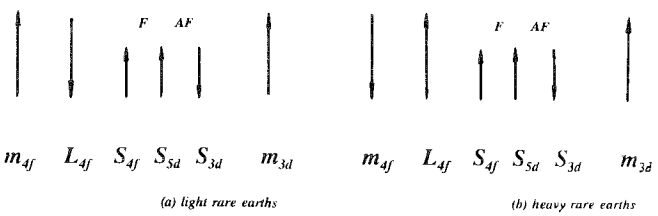

Fig. 2.10. Schematic diagram illustrating the transfer of the coupling between the spin moments of the rare-earth and 3d ions on the coupling between the R and T moments; F and AF indicate ferro- and antiferromagnetic spin–spin exchange interactions.

band electrons J_{4f-c}, defined as the weighted average contributions from 5d, 6s and 6p bands, decreases by 40% going from Ce^{3+} to Tm^{3+}. The parameter n_{RT} is defined in this conduction-electron mediated model as

$$n_{RT} = \gamma_R \chi_c n_{3d-c} n_{4f-c}. \tag{2.38}$$

The value for n_{RT} varies by a factor 2.1 going from Pr to Tm. This larger variation compared with that of J_{4f-c} results from a decrease by 25% of the number of 5d electrons n_{5d}. χ_c is the susceptibility of the conduction electrons. Brooks et al. (1991a,b, 1992) showed that the overall 3d–4f coupling parameter depends on the ratio of the

average 3d and 5d spin. For the RFe_2 series it is the 5d spin that changes substantially through the R series.

2.3. *Electronic structure of the 4f ions in the R_nT_m compounds*

The electronic properties of a 4f ion in the 3d–4f compounds can be described, in general, within a single-ion Hamiltonian that takes into account the spin–orbit, crystal-field and exchange interactions:

$$\mathscr{H}_R = \mathscr{H}_{s-o} + \mathscr{H}_{CF} + \mathscr{H}_{ex} + \mathscr{H}_z \tag{2.39}$$

where $\mathscr{H}_z$ stands for the Zeeman magnetostatic energy term in an external field $\boldsymbol{B}_0$. These terms are written in sequence of their importance. This Hamiltonian takes the explicit form:

$$\mathscr{H}_R = \lambda \boldsymbol{L}\cdot\boldsymbol{S} + \mathscr{H}_{CF} + g_s\mu_B \boldsymbol{S}\cdot\boldsymbol{B}^R_{ex} + \mu_B(g_L\boldsymbol{L} + g_s\boldsymbol{S})\cdot\boldsymbol{B}_0 \tag{2.40}$$

where λ denotes the spin–orbit coupling parameter and g_s and g_L are the spin ($=2$) and orbital ($=1$) gyromagnetic factors.

For most of the rare-earth ions, the spin–orbit interaction strongly dominates the other terms in eq. (2.39). Orbital and spin momenta, $\boldsymbol{L}$ and $\boldsymbol{S}$, are coupled and $\boldsymbol{J}$, the total angular momentum, becomes a good quantum number. The expectation value for the z-component of $\boldsymbol{J}$ varies between $|L-S|$ and $|L+S|$. As a consequence, $(2L+1)(2S+1)$ atomic levels are ordered in multiplets with different J values. Equation (2.40) indicates that the multiplets are separated by a value given by $\Delta E_{s-o} = \lambda(J+1)$. Hund's rules provide the selection rule for the ground state. In case of the light rare-earths it is a state with the lowest J, it means the multiplet with $J = |L-S|$ whereas for the heavy rare earths the multiplet with $L+S$ is the ground-state multiplet.

The spin–orbit coupling parameter λ amounts to -410 K for Sm^{3+} and $+650$ K for Dy. For the Sm ion, the first-excited multiplet lies 1500 K above the ground state and more than 4500 K for Dy, see fig. 2.1. With these large energy separations it is not surprising that calculations of the low-temperature electronic and magnetic properties within the ground-state multiplet provide much the same results as considerations involving the higher multiplets. In the case of samarium where the excited multiplet is relatively close to the ground state, extended calculations have been reported. Europium is a special case. Hund's rules for the trivalent ion lead to $J=0$ and here the extended calculations are unavoidable. In reality, europium exhibits mixed valence properties and the discussed procedures are useless for a treatment of this problem. As europium forms compounds with the 3d metals very rarely this problem does not enter into the present discussions.

The restriction to the ground-state multiplet, enlarges the efficiency of the computations enormously. In that case, the Stevens-equivalent operators can be introduced for the CEF Hamiltonian. Within the ground-state multiplet the Landé factor g_R, the angular momentum operators J_z, J_+ and J_- are defined and the Hamiltonian of eq. (2.40) can be rewritten as

$$\mathscr{H}_R = \sum_{n=0}^{6}\sum_{m=0}^{n} B_n^m O_n^m(J_+, J_-, J_z) + g_J\mu_B \boldsymbol{J}_R\cdot(\boldsymbol{B}^R_{mol} + \boldsymbol{B}_0). \tag{2.41}$$

Eigenvalues and eigenfunctions result in a straightforward way from the diagonalization of this Hamiltonian, provided that the relevant CEF and exchange field parameters are known. The eigenfunctions Γ_i can be expressed as linear combination of the eigenfunctions of the free ion associated with the different z components of J, $|\mathrm{LSJM}\rangle$:

$$|\Gamma_i\rangle = \sum_{M=-J}^{J} a_{iM}|M\rangle. \tag{2.42}$$

From the eigenfunctions, the expectation value of the magnetic moment $\boldsymbol{\mu}_i$ associated with each eigen-state can be calculated as

$$\boldsymbol{\mu}_i = -g_R\mu_B\langle\Gamma_i|\boldsymbol{J}|\Gamma_i\rangle. \tag{2.43}$$

Having obtained the eigenfunctions and eigenenergies, magnetic and electronic properties of the R ion can be calculated. First of all, the free energy is given by:

$$F^R(T,\boldsymbol{n}) = -kT\ln Z_R(\boldsymbol{n}), \tag{2.44}$$

where Z_R is the partition function over the available energy levels,

$$Z_R(\boldsymbol{n}) = \mathrm{Tr}\exp(-\mathscr{H}_R(\boldsymbol{n})/kT) = \sum_{i=0}^{2J+1}\exp(-E_i^R(\boldsymbol{n})/kT). \tag{2.45}$$

E_i denotes the energy of the levels with respect to the ground level, whereas $\boldsymbol{n}$ denotes the direction of the molecular field.

The free energy is a function of the direction $\boldsymbol{n}$ and the energy-level scheme is different for the different crystallographic directions. This is illustrated in figs. 2.11

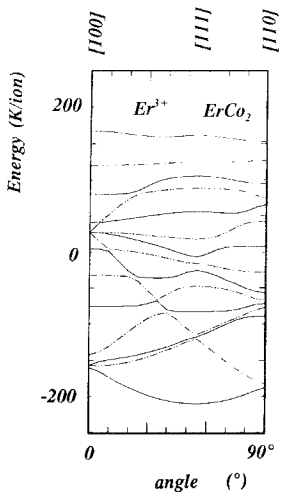

Fig. 2.11. The angular dependence of the energy level scheme of Er^{3+} in $ErCo_2$ calculated with the cubic CEF coefficients $A_4 = +46.0\,\mathrm{K}\,a_0^{-4}$ and $A_6 = -1.36\,\mathrm{K}\,a_0^{-6}$ and with the molecular field $B_{mol}^{Er} = 26.4\,\mathrm{T}$. The angle is between the direction of the field B_{mol}^{Er} and the $\langle 001\rangle$ direction within the (110) plane. The minimum at 54° indicates that the $\langle 111\rangle$ direction is the easy axis of the magnetization of the Er ion. After Radwański and Franse (1993).

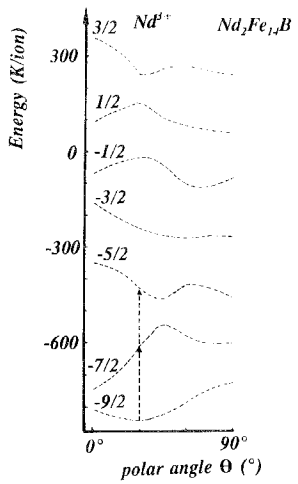

Fig. 2.12. The energy level scheme of the Nd^{3+} ion in $Nd_2Fe_{14}B$ under the combined action of the crystal and molecular fields for different directions of the molecular field B_{mol}^{Nd} (350 T). Arrows indicate excitations observed by inelastic-neutron-scattering experiments of Loewenhaupt et al. (1988). After Radwański and Franse (1989b).

and 2.12 where the energy-level scheme for the trivalent Er ion in $ErCo_2$ and for the Nd^{3+} ion in $Nd_2Fe_{14}B$ are presented. In the former case the body diagonal of the cubic Laves-phase structure is the preferred direction of the Er moment. The magneto-crystalline anisotropy is by definition the anisotropic part of the free energy. At zero temperature it is the anisotropic part of the ground-state energy. In case of $Nd_2Fe_{14}B$, a compound that crystallizes in an tetragonal structure, the Nd moment does not lie along a particular crystallographic direction and points to a direction tilted from the c axis by 30°. This tilting results from CEF interactions of higher order (Radwański and Franse 1989b). It can be shown easily that in the presence of large molecular fields, the second-order term produces minima either at $\theta = 0$ or 90°, the fourth-order term at $\theta = 54.7°$ or 0°, the sixth-order term at $\theta = 0°$, about 30.0° or 90°. Thus, CEF interactions can, in principle, produce any preferred magnetic direction. Moreover, for weak exchange interactions they can lead to a reduction of the 4f moment, an effect that is partly visible in the compounds under discussion in the RNi_5 series.

The easy direction of the R-ion magnetic moment in an R_nT_m compound is determined by the minimum of the free energy F for any specific crystallographic direction $\boldsymbol{n}$ provided the anisotropy associated with the T sublattice is negligible. In fact, the T anisotropy is at low temperatures an order of magnitude smaller. It can happen that the direction at which the free energy has its minimum varies with temperature, as at elevated temperature, higher levels become thermally populated, leading to temperature-induced moment-reorientation (TIMR) phenomena. This purely single-ion TIMR phenomenon is illustrated in fig. 2.13 where the temperature dependence of the free energy for the Nd^{3+} ion in $Nd_2Fe_{14}B$ is shown for different directions denoted by the polar angle. At 4.2 K the Nd moment is tilted out from the tetragonal

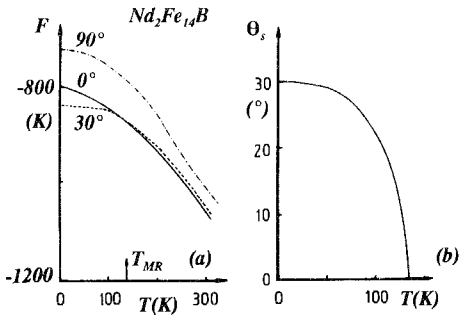

Fig. 2.13. (a) Temperature dependence of the free energy for the Nd^{3+} ion in $Nd_2Fe_{14}B$ for different directions of the molecular field; at low temperatures below the moment reorientation T_{MR} of 138 K, a tilted magnetic structure with tilt angle Θ_s is formed; (b) the tilt-angle Θ_s as a function of temperature. After Radwański and Franse (1989b).

axis by 30°; the tilt angle decreases with increasing temperature vanishing at 138 K. It has been mentioned in section 2.1 that the single-ion properties of the Ho^{3+} and Nd^{3+} ions are very similar. Indeed, $Ho_2Fe_{14}B$ manifests similar behaviour: the tilt angle is only slightly lower, 23°, and the tilted structure vanishes faster, at 58 K. More significant moment rotations occur in $NdCo_2$ and $HoCo_2$ where the EMD changes from the cubic ⟨110⟩ direction at helium temperature to the ⟨100⟩ direction at elevated temperatures, see fig. 2.14.

For a non-negligible anisotropy of the T sublattice that favours a direction different from the R sublattice, a non-collinear magnetic structure can occur. Indeed, Cadogan

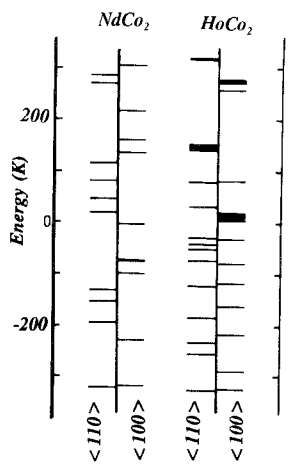

Fig. 2.14. The energy level scheme of Nd^{3+} in $NdCo_2$ and Ho^{3+} in $HoCo_2$ for the direction of the molecular field along ⟨001⟩ and ⟨110⟩. Both compounds reveal a moment reorientation at 42 and 16 K, respectively. At low temperatures the EMD is along the ⟨110⟩ direction whereas above the TIMR temperature the moment lies along the cube edge ⟨100⟩.

et al. (1988) have described the magnetic structure in $Nd_2Fe_{14}B$ at helium temperatures with five sublattices though the angles between the sublattices are small. The small values for the angles justify the use of the two-sublattice model.

A quantitative analysis of the CEF parameters and the exchange interactions from experimental data is not always straightforward. Experimental information is often too limited in view of the large number of parameters that is involved in the microscopic description even with the simple form of the Hamiltonian given by eq. (2.40) or (2.41). Combination of the results from different experimental techniques and inspection of the systematics across the 4f series is essential for getting reliable and physically meaningful sets of crystal-field and exchange parameters.

3. Experimental methods

In this chapter, the experimental methods that are used for studying the magnetic parameters of the R–T intermetallics are reviewed. The methods can be distinguished in macroscopic and microscopic ones. The macroscopic experimental techniques include magnetization, thermodynamic and transport studies. Neutron, Mössbauer and NMR experiments belong to the microscopic techniques that yield information concerning properties on an atomic scale. To illustrate the relevance of the different techniques, characteristic examples are presented of the type of information that can be obtained from the method under discussion.

3.1. Magnetization and magnetic susceptibility

The study of magnetization and magnetic susceptibility is a direct and relevant method to investigate the magnetic parameters of the R–T intermetallics. These investigations can contribute to the information about the microscopic parameters provided that they are performed on single-crystalline samples and in sufficiently large external fields. Semicontinuous fields of 40 T which are available at present, are in many cases not sufficient to reach saturation along the hard axes. The magnetization curves often reflect a complex interplay of CEF and exchange interactions. Field-oriented-powder samples provide a reasonable alternative for single-crystalline material in studying the magnetic anisotropy. Magnetization experiments on finely powdered samples that are free to rotate in the applied magnetic field are found to yield an accurate estimate for the intersublattice exchange interaction for the heavy rare-earth compounds. This section starts with a discussion of high-field magnetization processes.

3.1.1. High-field magnetization process

Detailed high-field magnetization measurements have been performed in static or semicontinuous magnetic field installations with fields up to 40 T. Experiments performed along the different crystallographic directions of single-crystalline samples, permit a full and quantitative analysis of the magnetization process up to the highest fields available under well-controlled conditions. The simplest magnetization curves are obtained for compounds with nonmagnetic rare-earth elements. For YCo_5, shown as an example in fig. 3.1, the saturation magnetization at 4.2 K, along the easy direction of magnetization, is reached for fields above the demagnetizing field that is not larger

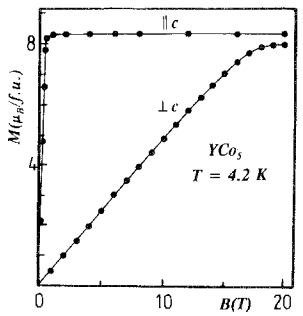

Fig. 3.1. Magnetization curves at 4.2 K of YCo_5 for fields applied parallel and perpendicular to the hexagonal c axis. After Alameda et al. (1981).

than 0.5 T for a spherical sample. For fields larger than the demagnetizing field, the magnetization is represented by

$$M(B, T) = M(0, T) + \chi_{hf}(0, T)B_0, \tag{3.1}$$

where χ_{hf} is the differential high-field susceptibility, which is of the order of $5 \times 10^{-4} \mu_B$/T per 3d ion. The values for χ_{hf} for some 3d–4f compounds have been collected in table 2.11. Band-structure calculations performed for compounds with yttrium yield a susceptibility of that order of magnitude, see table 2.9. For most compounds with magnetic rare-earth elements values for the easy-axis susceptibility of this order are obtained as well. Apparently, the rare-earth moment is hardly sensitive to external fields, indicating the realization of the full trivalent moment of the rare-earth ion. For ferrimagnetic compounds, this result is only obtained below certain critical fields above which spin-reorientation phenomena occur like in Ho_2Co_{17} at 22 T, see fig. 1.4.

Enhanced values for the differential high-field susceptibility usually indicate peculiarities. Moment instabilities like observed in Y_2Co_7 and YCo_3 or field-dependent noncollinear internal magnetic structures like observed in $HoCo_5$ are examples of these phenomena. In case of tilted magnetic structures, the susceptibility, measured along the main crystallographic directions, is substantial but again small along the easy direction of magnetization. Here, Nd_2Co_{17} or $Nd_2Fe_{14}B$ can serve as examples, see fig. 1.6.

The analysis of magnetization curves along the hard axis provides values for the anisotropy parameters appearing in the expansion of the magnetocrystalline-anisotropy energy in terms of even powers of $\sin\theta$. In order to derive values for the anisotropy constants K_n^m, usually an analysis is made in terms of the Sucksmith–Thompson (S–T) method by plotting B_0/M^2 versus M^2 (Sucksmith and Thompson 1954). The intercept of this plot with the vertical axis provides a value for K_1 whereas the slope yields K_2. The S–T method is based on the consideration of the free energy that consists of the sum of magnetostatic and anisotropy energies, i.e.,

$$E = E_a - \boldsymbol{M}_s \cdot \boldsymbol{B}_0, \tag{3.2}$$

where M_s represents the (constant) value for the spontaneous magnetization (observed along the easy axis). In this context, the concept of the saturation field is introduced as a field at which the magnetization along the hard direction reaches the value

measured along the easy direction. The saturation field along the hard axis of magnetization, B_K, is related to the difference in (anisotropy) energy, ΔE_a, between the two magnetization directions:

$$\Delta E_a = \int_0^{B_K} M \, dB. \tag{3.3}$$

The anisotropy field, B_A, by definition, is obtained as the crossing of the extrapolated low-field hard-axis magnetization curve with the easy-direction magnetization curve, see fig. 3.2. In case of one single second-order anisotropy constant of an uniaxial compound B_K coincides with B_A. The anisotropy energy for most of the Y–3d compounds is well represented by the first term of eq. (2.8a).

Alameda et al. (1981) extended the S–T method to the case of an anisotropy in the magnetic moment magnitude. This has been illustrated for YCo_5 in which compound the moment after full reorientation shows a 4% lower value than that measured for the field applied along the easy direction, see fig. 3.1.

The S–T method, or more generally eq. (3.2), is not applicable anymore for (ferri- or ferro-)magnetic systems that are composed of different magnetic sublattices coupled by intersublattice interactions. For these systems external fields disturb the magnetic configuration of the different sublattices. In that case, the parameters derived by the S–T method are effective parameters only, that are not simply related to the intrinsic magnetocrystalline anisotropy. But these parameters are still useful in a technical characterization of magnetic materials.

The effect of a field-induced noncollinearity can directly be observed in the high-field magnetization curves of the Gd compounds. The Gd ion itself is not expected to have a significant magnetocrystalline anisotropy because of the half-filled 4f shell and its S ground state. The anisotropy energy of, for instance, $GdCo_5$ derived by the S–T plot or equivalently by means of eq. (3.2) is found to be a factor of three smaller than that observed for YCo_5. This large difference proves the inapplicability of eq. (3.2) to ferrimagnetic compounds even for small values of the external field. The high-field behaviour for a number of Gd–Co compounds, that are ferrimagnets, has been analyzed within a two-sublattice model by Radwański (1986a). Fields of the order of 200 T are needed in order to attain the forced ferromagnetic state. The curves obtained for $GdCo_5$ and $GdCo_3$ are shown in fig. 3.3. These curves are representative for the high-field magnetization curves of anisotropic ferrimagnetic compounds.

Within a two-sublattice model, one considers two well-defined and well-developed

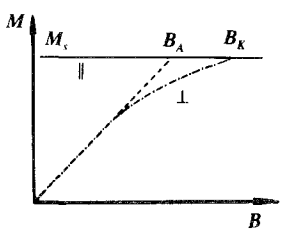

Fig. 3.2. Schematic magnetization curve for an ordered ferromagnetic 3d–4f compound. The anisotropy field, B_A, and the saturation field, B_K, are shown.

sublattices formed by different, R and T, moments. These two sublattices are coupled ferri- or antiferromagnetically due to the interactions between the 3d and 4f spins. As these interactions are of a finite strength, an external field disturbs this internal magnetic structure. In the two-sublattice model the energy of a magnetic system in an external field, B_0, takes the form

$$E_{RT} = E_a^T + E_a^R + n_{RT} M_T \cdot M_R - (M_T + M_R) \cdot B_0. \tag{3.4}$$

In this expression, terms related to the intrasublattice interactions do not enter. The T sublattice is not affected by the applied magnetic field (all T moments are supposed to rotate coherently) and, therefore, its intrinsic energy is conserved. In contrast, the 4f–4f interactions are weak and, in first approximation, neglected. The constraint of weak 4f–4f interactions is not a serious restriction. In case one is dealing with systems containing only one single R site within the elementary cell, all R moments can be assumed to rotate coherently as well.

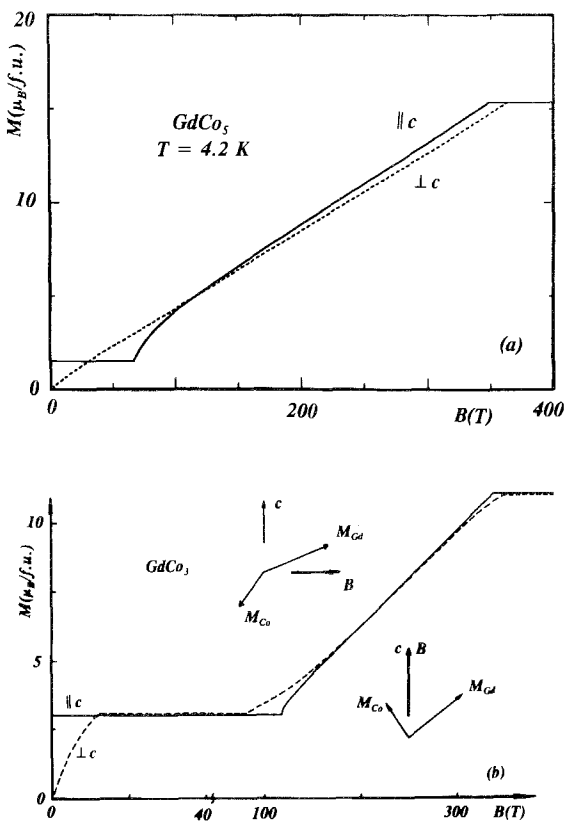

Fig. 3.3. Two examples of magnetization curves in the full field range for ferrimagnetic materials; (a) calculated with parameters relevant to $GdCo_5$ at 4.2 K; after Radwański et al. (1992b), and (b) to $GdCo_3$; after Radwański (1986a). For $GdCo_3$ the moment configurations for the field of 250 T applied parallel and for the field of 100 T perpendicular to the (easy) hexagonal axis are shown.

Under the assumption that there is no magnetocrystalline anisotropy present, the analysis of eq. (3.4) shows that there is a field region where a noncollinear magnetic structure is realized:

$$n_{RT}|\boldsymbol{M}_R - \boldsymbol{M}_T| < B < n_{RT}|\boldsymbol{M}_R + \boldsymbol{M}_T|. \tag{3.5}$$

In this field region, the magnetization curve is linear in field with a slope determined by the intersublattice interaction,

$$n_{RT}^{-1} = \mathrm{d}M/\mathrm{d}B. \tag{3.6}$$

The assumption of zero magnetocrystalline anisotropy is not realistic for R–T compounds that are known to exhibit anisotropies of substantial size. Verhoef et al. (1989) have shown that the magnetization curves of finely powdered polycrystalline samples with particles that are free to rotate in the applied magnetic field, follow eq. (3.6) quite well in sufficiently large fields. In these experiments, the anisotropy does not enter into the free-energy expression, due to the fact that the particles always orient their net magnetization direction along the direction of the external field. This can be realized as long as there is obviously no anisotropy but also in ferrimagnetic compounds where the anisotropy is associated with only one magnetic sublattice. In most of the 3d–4f compounds, the anisotropy of the R sublattice dominates the anisotropy of the 3d sublattice by one order of magnitude. By inspection of fig. 3.4, where the high-field magnetization curves of several $Er_2Fe_{14-x}Mn_xB$ compounds measured on fine particles obtained from polycrystalline material are shown, one observes a quite wide field region with an almost linear magnetization curve. In this particular case the Mn substitutions reduce the net magnetization and shift the regime of linear magnetization to lower field values. In fig. 3.5 the magnetic isotherms are presented for single-crystalline R_2T_{17} spheres that are free to orient themselves in the applied magnetic field.

The experimental conditions for these two methods, the fixed and the free sample

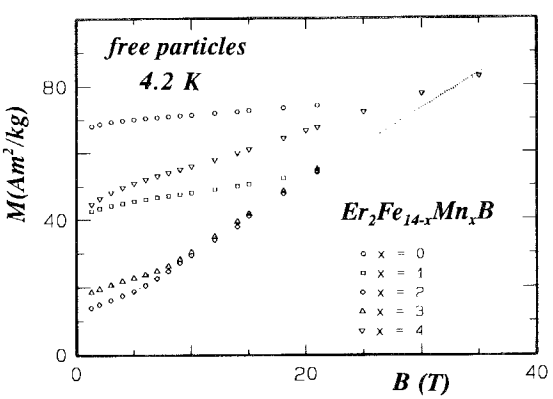

Fig. 3.4. Magnetic isotherms for various $Er_2Fe_{14-x}Mn_xB$ compounds at 4.2 K measured on powder particles that are free to rotate in the sample holder. After Verhoef et al. (1990).

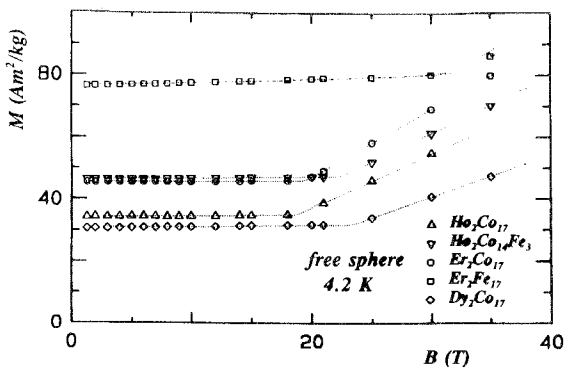

Fig. 3.5. High-field magnetization isotherms at 4.2 K for several R_2T_{17} single-crystalline spheres that are free to orient themselves in the applied magnetic field. After Verhoef et al. (1992c).

method, are compared in fig. 3.6. In both experiments, the resultant moment of the ferrimagnetic system reorients itself continuously during the magnetization process in order to coincide with the direction of the external field. In case of the free-sample experiments this coincidence is full and is realized by an actual rotation of the sample in order to keep M_R, characterized by a large magnetic anisotropy, along its easy direction. As a consequence, in these experiments no information about the magnetic anisotropy of the R sublattice can be obtained. In case of fixed-sample experiments both moments are pushed out from their easy direction over angles that depend on the strength of the applied field. In these experiments a part of the angular dependence of the free energy is probed from which the anisotropy parameters can be evaluated. Sometimes, anomalies are found in the magnetization curves. In this respect, the phenomenological model developed by Asti and Bolzoni (1980) and Asti (1990) is mentioned. First-order magnetization process (FOMP) transition can be analyzed in terms of eq. (3.2) with significant values for the higher-order anisotropy constants. Noncollinear structures are not considered in the FOMP model as the exchange energy does not enter into the description. This neglect is equivalent with the assumption of an infinite value for n_{RT}.

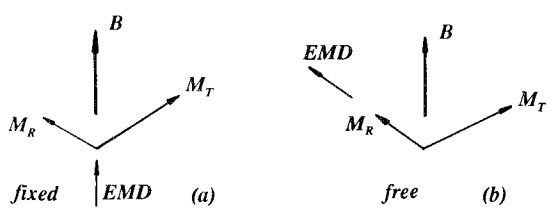

Fig. 3.6. Orientation of the external field, the moments and the easy direction of the R moment in the noncollinear region at (a) fixed-sample and (b) free-sample experiments. At fixed-sample experiments the R sublattice magnetization is pushed out from the preferred direction contrary to free-sample experiments where the R sublattice magnetization stays always along the preferred direction. The anisotropy of the T sublattice is assumed to be negligible.

The magnetization curves for $GdCo_5$ and $GdCo_3$ as presented in figs. 3.3a and b can serve as prototypes for single-crystal magnetization curves of ferrimagnetic R–T intermetallics. The main difference between these curves is seen for fields applied along the hard axis. For $GdCo_3$ there is an intermediate state with the magnetization close to that observed along the easy axis (hard-axis magnetization process of type I) that does not exist for $GdCo_5$. For this latter compound, the magnetization continuously increases to the forced ferromagnetic configuration (hard-axis magnetization process of type II). For fields applied along the easy direction the curves for both cases are similar. At low fields the resultant magnetization is constant its value being simply the difference of the two sublattice magnetizations. For intermediate fields a noncollinearity region exists. The forced ferromagnetic state with a value for the magnetization equal to $M_R + M_T$ is reached at sufficiently high fields, usually well above 100 T. The character of the hard-axis curve depends, in general, on the net magnetization of the ferrimagnetic system and the strength of the intersublattice coupling. For a large zero-field magnetization and a strong intersublattice coupling, the hard-axis magnetization curve is of type I. For the hard-axis magnetization curves of type II, the apparent 'anisotropy' field, B_K^{eff}, i.e. the crossing of easy- and hard-axis magnetization curves, is a complex function of the magnetic parameters. The evaluation of the intrinsic anisotropy parameters and the intersublattice coupling constant from the low-field part of these magnetization curves is an almost impossible task. The calculations show that even in small magnetic fields, the internal magnetic structure is modified, especially for ferrimagnetic compounds with a low value for the net resultant spontaneous magnetization. In that case the system behaves almost like an antiferromagnetic system. The calculated hard-axis magnetization curve for $GdCo_5$ is nearly a straight line up to a field roughly equal to $2B_{\text{mol}}^{\text{Gd}}$ at which field the ferromagnetic configuration is reached. The slope of this curve is approximately equal to n_{RT}^{-1}. This picture has indeed been verified for $GdCo_5$ by magnetization experiments (fig. 3.7). For a full experimental verification of this behaviour, magnetic fields of the order of 100 T are required. Model calculations again show that for sufficiently large

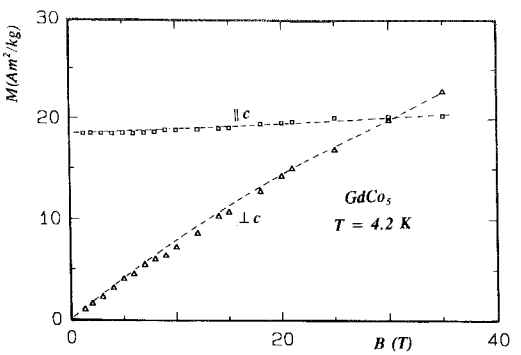

Fig. 3.7. Magnetization curves at 4.2 K for $GdCo_5$ measured up to 35 T for two main crystallographic directions. After Radwański et al. (1992b).

fields applied along the easy-axis direction, a breaking of the antiparallel moment alignment in Gd–Co compounds will occur. Recent experiments performed on another Gd compound, $Gd_2Co_{14}B$, show the breaking of the ferrimagnetic configuration along the easy direction at a field of 52 T (Radwański et al. 1990b).

For compounds consisting of a magnetic rare-earth element with a non-zero orbital moment, large magnetocrystalline anisotropies are present. The anisotropy energy arising from the rare-earth sublattice dominates, in general, that originating from the 3d sublattice by one order of magnitude or more as can be inferred by comparing the magnetization curves for Ho_2Co_{17}, see fig. 1.4, with those of Y_2Co_{17}. In Ho_2Co_{17} a variety of interesting phenomena is found in the high-field region.

The observed transitions in Ho_2Co_{17} at 22 and 29 T are typical for a ferrimagnetic *easy-plane system* and they can be quite easily understood. In most cases, the large number of parameters related with the different terms in the expressions for the magnetocrystalline anisotropy energy of the 4f and 3d ions, in combination with the unknown strength of the intersublattice interactions, make the analysis of magnetization curves a complex problem. In this compound, however, a dominant second-order anisotropy creates the conditions for both sublattice magnetizations to rotate under the action of the external fields within the basal plane. Moreover, the anisotropy-energy term of the hexagonal symmetry tries to keep the R moment along a certain direction within the basal plane. In that case, only the basal-plane anisotropy terms, K_6^6 of the R and T sublattices enter into eq. (3.4). The in-plane anisotropy of the 3d sublattice is negligibly small. Thus, in the analysis of these transitions one is left with two parameters only: n_{RT} and $\kappa_6^6 (= K_6^6)$ of the R sublattice. The anisotropy coefficient κ_6^6 restricts the R-moment direction to certain crystallographic directions. The transitions are associated with jumps of the R moment from its easy axis to a direction close to the next easy axis over an angle of about $\pi/3$. After the transition a noncollinear magnetic structure is formed, see fig. 3.8. At this first-order magnetic-reorientation (FOMR) transition, the gain of magnetostatic energy of the R sublattice compensates the loss in the intersublattice R–T exchange energy.

For an easy-plane ferrimagnetic hexagonal compound, one expects three transition fields in the magnetization curve for fields applied along the easy axis, whereas only two transitions are expected for fields applied along the hard axis in the easy plane. In fig. 3.9 the magnetization curves for Ho_2Co_{17} as derived from model calculations are presented over the full field range. After the first observation of this type of transition in Ho_2Co_{17} (Franse et al. 1985), transitions of the same type have been

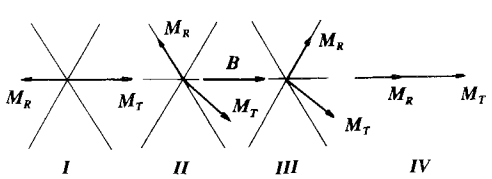

Fig. 3.8. Different configurations of the R and T moments for a ferrimagnetic easy-plane hexagonal compound. After Franse et al. (1988b).

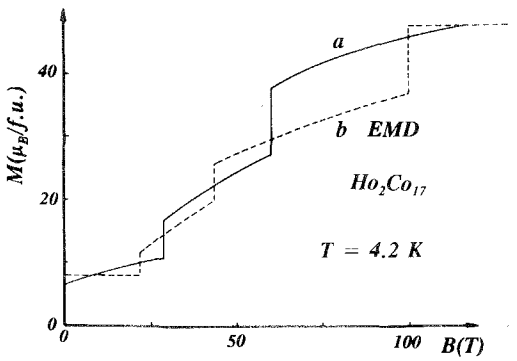

Fig. 3.9. Magnetization curves for Ho_2Co_{17} calculated within the two-sublattice model in the full field range for fields applied within the hexagonal plane. After Radwański and Franse (1992).

reported for Dy_2Co_{17} (Sinnema et al. 1986a), for $Ho_2Co_{14}Fe_3$ (Sinnema et al. 1987a) and for $TbCo_5$ (Ballou et al. 1989). Recently, the second transition in the easy-axis magnetization curve for Ho_2Co_{17} has been observed at 44 T (Tomiyama et al. 1991) in good agreement with the predicted value (Radwański et al. 1985c). The observation of these transitions gives strong support to the above-discussed model and confirms the results for the strength of the intersublattice interactions.

So far, we have been dealing with systems in which the magnetic moments are well defined and developed. There are, however, compounds, for which the magnetic moments are induced, either by the rare-earth partner or by the applied magnetic field. These phenomena can be studied within the 3d–4f compounds in the RNi_5 series and in RCo_2 in particular.

In the RNi_5 compounds the Ni 3d-band is completely filled due to hybridization of the 3d-band of Ni and 5s–4d band of Y (or 6s–5d band for other R elements). As a consequence, the Ni sublattice is nonmagnetic and exhibits Pauli paramagnetic behaviour as we can learn from YNi_5. In the presence of an externally applied field, B_0, a nickel moment is induced that starts to interact with its spin surroundings. The Ni-sublattice magnetization can be written as

$$M_{Ni} = \chi_{Ni} B_0 + \alpha M_R, \tag{3.7}$$

where the Pauli paramagnetic susceptibility, χ_{Ni}, is enhanced by the mutual nickel interactions. The rare-earth magnetization is calculated from the CEF Hamiltonian with the molecular field experienced by the R moment given by

$$B^R_{mol} = (1 + \alpha) B_0 + n M_R. \tag{3.8}$$

The parameter α equals $\chi_{Ni} n_{RT}$. The effective (enhanced) R–R exchange constant n is given by:

$$n = n_{RR} + \alpha n_{RT}. \tag{3.9}$$

In a fitting procedure the moments, the CEF parameters and the exchange parameters

are obtained self-consistently. A list of the these parameters is presented in section 5.5, where the RNi_5 compounds are discussed.

In RCo_2 compounds the susceptibility χ_{Co} is field dependent and increases with increasing field. This nonlinear magnetization finally leads to the formation of a stable cobalt moment of about $1\mu_B$ in RCo_2. An external field close to 70 T is needed in YCo_2 to induce this moment whereas in RCo_2 compounds this field is generated by the 3d–4f interactions. As a consequence, magnetization curves of RCo_2 compounds with a magnetic R partner can often be analyzed in terms of eq. (3.4).

3.1.2. Temperature dependence of magnetization

The temperature dependence of the spontaneous magnetization of the R–T intermetallics provides another possibility to evaluate the strength of the 3d–4f interaction. In this analysis, the magnetization is split into a 3d and 4f contribution. The temperature dependence of the magnetic moment of the 4f ion is described, in first approximation, by the Brillouin function:

$$M_R(T) = M_R(0)B_J(x), \quad \text{with } x = g\mu_B J B^R_{mol}/kT. \tag{3.10}$$

Values for the compensation temperature are also used for the determination of the 3d–4f exchange interactions. At the compensation point both sublattice contributions to the magnetization of a ferrimagnetic system cancel, resulting in a vanishing net magnetization. This phenomenon is understood by the different temperature variations of the two sublattice moments. In case of the 3d–4f compounds, the compensation point is observed for ferrimagnetic compounds in which at low temperatures the rare-earth magnetization dominates that of the 3d sublattice. Molecular-field coefficients are derived by the self-consistent solution of the equations

$$M_R(T) = g\mu_B J B_J(n_{RT}M_T + n_{RR}M_R), \tag{3.11}$$

$$M_T(T) = M_T(0)B_J(n_{TT}M_T + n_{RT}M_R). \tag{3.12}$$

Gadolinium compounds are especially suited for determination of the molecular field in this way due to the absence of CEF interactions. Still, the problem has to be solved how to deduce the temperature dependence of the gadolinium sublattice from the experimental magnetization data referring to the whole system. The temperature variation of the Gd moment in Gd_2Co_{17} is well approximated in the temperature range from 4.2–300 K by eq. (3.10), yielding a value for B^{Gd}_{mol} of 220 T, see fig. 3.10. Bogé et al. (1985) obtained a value of 280 T for the molecular field in $Gd_2Fe_{14}B$. In case of compounds with rare-earths with nonzero orbital moments, the molecular field B^R_{mol} derived from eq. (3.10) and the molecular-field coefficient n_{RT} derived from eqs. (3.11) and (3.12), are usually overestimated. The crystal-field effect is not taken into account in these equations. The crystalline electric field contributes to the energy-level splitting leading to a weaker temperature dependence of the rare-earth sublattice. Taking into account the crystal-field effects, values for the molecular field have been obtained that are consistent with those derived from other techniques.

3.1.3. Paramagnetic region

There is a variety of magnetic behaviour in the paramagnetic region. Only in a few cases, the temperature dependence of the susceptibility follows a simple Curie–Weiss

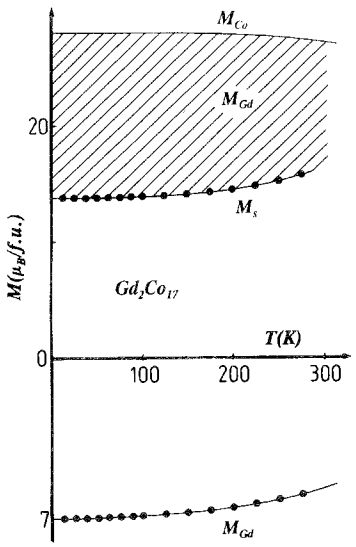

Fig. 3.10. Evaluation of the temperature dependence of the Gd moment, M_{Gd}, in ferrimagnetic Gd_2Co_{17} from the temperature dependence of the spontaneous magnetization, M_s, of Gd_2Co_{17}. The temperature variation of the Co moment is taken from Y_2Co_{17}. The temperature variation of the Gd moment is well approximated by a Brillouin function, $B_{7/2}(x)$ (full curve), yielding a value for the molecular field, B_{mol}^{Gd}, of 220 T.

relation,

$$\chi = \frac{C}{T - \Theta_p}, \tag{3.13}$$

where C is the Curie constant. More frequently, the magnetic susceptibility in the paramagnetic region can be represented by a modified Curie–Weiss (MC–W) law in the form

$$\chi = \chi_0 + \frac{C}{T - \Theta_p}, \tag{3.14}$$

where an extra term χ_0 appears. Usually χ_0 is a weakly temperature-dependent susceptibility.

An alternative expression is given by the more complex hyperbolic relation (HC–W) of the form:

$$\chi^{-1} = \chi_0^{-1} + \frac{T}{C} - \frac{\sigma}{T - \Theta_p}. \tag{3.15}$$

The parameters χ_0, Θ_p and σ occurring in eq. (3.15) are often just fitting parameters.

Generally, the C–W behaviour is manifest in compounds in which only one type of magnetic moment is present like YFe_2, YFe_3, Y_2Fe_{17} compounds. The MC–W behaviour is found for compounds where, besides the localized rare-earth moments,

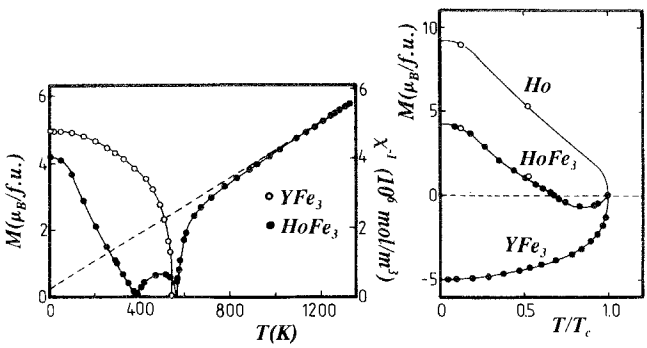

Fig. 3.11. Temperature dependence of the spontaneous magnetization for $HoFe_3$ (●) and YFe_3 (○) together with the thermal variation of the reciprocal magnetic susceptibility for $HoFe_3$. After Simmons et al. (1973).

there is a paramagnetic medium. Here, RNi_2 and RNi_5 compounds can serve as examples. In the former compounds the nickel ions are nonmagnetic already from the lowest temperatures. The Curie constant derived from the slope of the χ^{-1} versus T plot is close to the value expected for the trivalent ions, indicating a negligible contribution of nickel in the paramagnetic region. Values for the Curie constant, C_R, of the trivalent R ions have been collected in table 2.8. The hyperbolic behaviour is found in magnetic systems with two types of magnetic moments that still interact above the magnetic ordering temperature. Results for $HoFe_3$ are presented in fig. 3.11. In that case the coefficient C contains contributions from the 3d and R ions. Provided the R contribution is given by that of the trivalent ion, the iron contribution can be estimated. It turns out that in $HoFe_3$ the iron contribution to C is only slightly larger than that observed in YFe_3. This description has been also found to be applicable to RCo_2 compounds (Burzo 1972) although it is known that an itinerant description of the Co moment especially in these compounds is more appropriate due to its induced character. Earlier, Bloch and Lemaire (1970) could fit the paramagnetic susceptibility of compounds with the heavy rare-earths in terms of the localized R moment and an itinerant moment of Co. The successful description found in both approaches indicates that a more subtle analysis is needed to represent the Co magnetism.

All considered expressions do not take into account the CEF interactions. These interactions manifest themselves in anisotropic behaviour detectable for single-crystalline specimens. Some phenomenological expressions have been derived that correlate the anisotropy of the paramagnetic Curie temperature Θ_p with the second-order crystal-field parameter B_2^0. For a proper analysis of the magnetic behaviour in the paramagnetic region, at least the exchange and CEF interactions have to be taken into account.

Despite of these limitations we would like to put some attention to the description given by eq. (3.15). The parameters involved in the procedure are related to the molecular-field coefficients within a molecular-field approach. For $HoFe_3$, Simmons et al. (1973) have reported values of 115, 21 and 2 (in units of emu/mol) for the

molecular-field coefficients n_{Fe-Fe}, n_{Ho-Fe} and n_{Ho-Ho}, respectively. Their relative magnitudes confirm the general view on the strength of the different interactions in 3d–4f compounds. These results yield a value of 70 T for the field B^{Ho}_{mol} in which a dominant contribution of 60 T is due to $B^{Ho}_{ex,RT}$ that originates from the 3d–4f interactions. As there are no other data concerning this particular compound, the result for the field $B^{Ho}_{ex,RT}$ has to be compared with a value of 62 T estimated on the basis of the high-field magnetization results at 4.2 K for Ho_2Co_{17} (Radwański 1986b). The agreement is satisfactory taking into account the different approaches and the different temperature regions in which the experimental results have been analyzed.

3.2. *Neutron studies*

3.2.1. Neutron diffraction

Neutron-diffraction experiments belong to the frequently applied experimental methods to study magnetic structures and the magnetic moment distribution over the elementary cell. As the neutron carries a magnetic moment, elastic neutron scattering studies yield information about the spin distribution resulting in a spin density map. Polarized neutron experiments on YFe_2 and YCo_5 are mentioned in this respect. The studies of Ritter (1989) have revealed a moment at the Y site in YFe_2 of $0.67\mu_B$. By comparing the spectra obtained for the spin-up and the spin-down states and by studying the [220] reflection, which is exclusively determined by the Y-site, it is found that this moment is antiparallel to the Fe moment. This value for the yttrium moment leads to a value for the iron moment of $1.77\mu_B$ given the net moment of $2.9\mu_B$/f.u. deduced from magnetization studies. Earlier studies of Givord et al. (1980) on $LuFe_2$ have revealed an orbital contribution to the iron moment of $0.07\mu_B$. These experimental facts are at present well accounted for by band-structure calculations described elsewhere in this volume (Brooks and Johansson, chapter 3).

The hexagonal compound YCo_5 is another system that has been studied in order to determine the spin distribution over the elementary cell. The experiments reveal a substantial difference in the spatial spin distribution at the two Co sites (Schweizer and Tasset 1980). This observation has strongly supported the earlier conclusion drawn on basis of nuclear magnetic resonance studies by Streever (1977) that the dominant contribution to the large and uniaxial magnetocrystalline anisotropy of YCo_5 originates from the cobalt 2c site, rather than from the 3g site.

Considerable attention in neutron diffraction studies has been devoted to the magnetism in manganese compounds. As an example we shall discuss the series of Laves-phase compounds. In YMn_2, a Laves-phase compound with the C15-type structure, a helimagnetic structure of manganese moments has been found by Ballou et al. (1987b). This is in contrast to the collinear magnetic structures found in RFe_2 and RCo_2 compounds. The C15 structure consists of a compact packing of atoms of two different sizes that form triangular configurations. It is impossible to satisfy the antiferromagnetic coupling for all Mn–Mn pairs within these triangular configurations, even not within the nearest-neighbour surrounding. As a consequence, frustration of the antiferromagnetic exchange interactions occurs. The minimalization of the exchange energies is then realized by staggered directions of the moments or/and by variation

of the *moment amplitude*. It turns out that this variation in the moment minimizes the antiferromagnetic exchange interactions more effectively than the formation of noncollinear magnetic structures.

Similar effects have also been detected in $ThMn_2$, a Laves-phase system with the hexagonal C14-type structure. $ThMn_2$ serves as a representative for the study of the Mn–Mn exchange in the hexagonal RMn_2 family, as YMn_2 serves for the cubic RMn_2 series. Powder neutron diffraction studies of Deportes et al. (1987c) reveal an AF structure with a triangular configuration of the moments at the 6h sites at the subsequent hexagonal planes, $z = \frac{1}{4}$ and $z = \frac{3}{4}$ as will be discussed in more detail later. This magnetic structure is described by the propagation vector of $[\frac{1}{3}, \frac{1}{3}, 0]$. Some of the Mn ions in $ThMn_2$ are found to be *nonmagnetic*.

Neutron diffraction studies have enlighted the complex magnetic structures in the hexagonal compounds $PrMn_2$ and $NdMn_2$ (Ballou et al. 1988b,c). The neutron pattern can be resolved by two sets of peaks with different temperature dependencies and two different propagation vectors indicating the presence of two non-coupled sets of magnetic moments. In the formation of the magnetic structure local symmetry distortions play an important role. A spin-canted ferromagnetic structure has been found by Ritter et al. (1991) in the cubic compound $DyMn_2$.

3.2.2. *Inelastic neutron scattering*

Inelastic magnetic neutron scattering (INS) yields information on the dynamical magnetic response of both, 3d and R, subsystems. INS techniques enable to determine the CEF level scheme of the ground-state multiplet of a R^{3+} ion as the available neutron energies are of the order of this splitting. The molecular field, that is present in magnetically ordered systems, produces a complete splitting of the CEF levels and non-uniformly shifts the positions of all magnetic levels.

The scattering amplitude $S(\boldsymbol{q}, \omega)$ as a function of the momentum transfer $\boldsymbol{q}$ and the energy transfer $\hbar\omega$, depends on the matrix element that is given by

$$S(\boldsymbol{q}, \omega) \sim |\langle i|J_\perp|f\rangle|^2, \tag{3.16}$$

where $J_\perp$ is the component of the total angular momentum operator perpendicular to the scattering vector $\boldsymbol{q}$ (=momentum transfer), i and f denote the initial and final 4f-electron states (=CEF levels). Within the dipole approximation, the intensities for the transitions are determined by the corresponding dipole matrix elements, i.e., transitions with changes of $J_\perp$ by 0 (the longitudinal mode) or ± 1 (the transversal mode).

Full information about the energy and the momentum transfer is obtained from studies on single-crystalline samples in a triple-axis experiment. Large crystals of a few cubic centimeters are required. The neutron absorption by the sample under investigation is in some cases a serious problem that has to be solved, for instance, by using less absorbing isotopes of Gd, Dy or B. Useful information about the characteristic magnetic excitations of the system, the energy transfer in particular, can be drawn from neutron scattering spectra on polycrystalline samples. In that case, the $\boldsymbol{q}$-dependence is lost and the observed well-pronounced peaks in the energy scan are assigned to localized states of the R-ion involved.

The INS spectra of a material containing 4f ions depend very much on the relative strength of the CEF and exchange interactions. The spectra belonging to just CEF interactions contain a few well-defined peaks related to magnetic excitations between crystal-field levels. The number of the transitions as well as the probability for these transitions is determined by matrix elements between the crystal-field eigenstates. In principle, these are governed by the local symmetry of the CEF interactions. These transitions are typically single-site excitations. Including the exchange interactions, the transitions on neighbouring ions are coupled and lead to propagating modes. The spectra become more complex and the analysis is not straightforward. With increasing strength of the exchange interactions, the INS spectra become again simpler and for a dominant molecular-field system, the energy-level splitting becomes more and more Zeeman-like. In that case, the wave functions are essentially pure J_z states with the ground state $J_z = J$. As a consequence, the probability for excitations between adjacent levels in the ground-state J multiplet is much larger than those with $\Delta m > 1$. Neutron experiments at low temperatures give very limited information as often only *one* transition is observed associated with the ground state to the first-excited level excitation. Further excitations can be observed by performing experiments at elevated temperatures as then excited states become thermally populated. Obviously, in case of a purely Zeeman energy scheme these new excitations, having the same energy separation, fall practically into the same peak. Indeed, one single peak is observed for $Dy_2Fe_{14}B$ and $Er_2Fe_{14}B$ (Loewenhaupt et al. 1990, 1991). In reality, the higher excitations have different, usually smaller, energies, due to the presence of crystal-field effects and new peaks appear with increasing temperature.

A typical magnetic excitation scheme as observed for the ordered rare-earth transition-metal intermetallics is shown in fig. 3.12. By inspection of this figure one

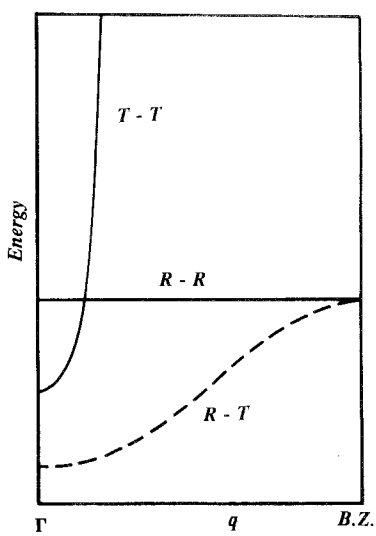

Fig. 3.12. Schematic representation for magnetic excitations in R–T intermetallics in the (q, E) space. B.Z. denotes the Brillouin zone.

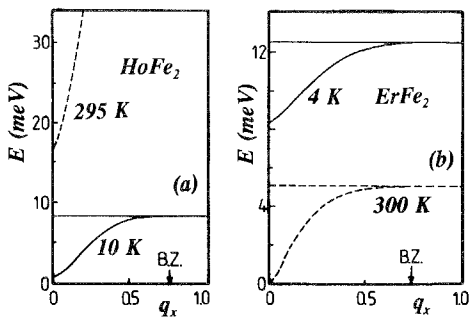

Fig. 3.13. (a) Inelastic neutron scattering spectra for $HoFe_2$ at 10 K revealing the single-ion excitations at the Ho ion. In addition, at room temperature the highly dispersive mode associated with the Fe spins has been observed. (b) Inelastic neutron scattering spectra for $ErFe_2$ at 4 K and 300 K. B.Z. denotes the Brillouin zone. After Koon and Rhyne (1981).

recognizes strongly dispersive modes and a nearly flat mode. The former are spin-wave-like and give smooth contributions to the E–q spectra. The flat mode manifests itself in the energy scale as a well-pronounced maximum and is related to single-ion excitations between crystal-field levels of the R ions. The energy variation of this mode is a direct measure for the inter-ionic R–R interaction. The mode denoted as T–T involves collective excitations of the T spins as observed in pure 3d elements. This mode is usually difficult to observe especially for $\boldsymbol{q}$ not close to the centre of the Brillouin zone. In $HoFe_2$ this mode has been only observed at room temperature, see fig. 3.13 where the INS spectra at 10 K and 295 K are shown. The stiffness parameter of 2.4 meV nm^2 being close to that observed in pure iron metal (2.8 meV nm^2) confirms that it is associated with excitations within the Fe sublattice.

The R–T mode involves spins of the R and T neighbours and has an energy gap Δ_2 at $q = 0$. Within ordinary spin-wave theory the energy gap Δ_2 in the (R–T) excitation spectrum is due to the R–T exchange interaction and is related to the J_{RT} parameter by (Koon and Rhyne 1981)

$$\Delta_2 = -z_{RT} J_{RT}(\langle J_R \rangle - 2\langle S_T \rangle), \tag{3.17}$$

where z_{RT} represents the number of nearest 3d neighbours of the rare-earth spin. In the cubic Laves-phase structure $z_{RT} = 12$. The parameter J_{RT} defines the exchange field by the relation (note that it is eq. (2.31) with $z_{RT} = 12$ relevant to the RT_2 structure):

$$B_{ex}^{R} = -12 J_{RT} \langle S_T \rangle / \mu_B. \tag{3.18}$$

Within ordinary spin-wave theory, and neglecting CEF interactions, the energy gap in the R–R mode is simply the separation between the subsequent energy levels of the J multiplet under the action of the molecular field and is given by

$$\Delta_{loc} = g \mu_B B_{mol}^{R}. \tag{3.19}$$

The value of 8.4 meV observed for Δ_{loc} in $HoFe_2$ points to a value of 116 T for B_{mol}^{Ho}. A

much bigger value of 182 T one gets using eq. (3.19) to the localized energy mode observed in $ErFe_2$. The INS results for this compound are shown in fig. 3.13b.

The validity of the eqs. (3.17)–(3.19) to R–T intermetallics is limited due to presence of substantial CEF interactions. The use of these expressions provide largely overestimated values for B_{mol}. Indeed, the analysis of the INS spectra within the CEF and exchange Hamiltonian, given by eq. (2.41), provide the value of 78 T for B_{mol}^{Er} in $ErFe_2$ (Koon and Rhyne 1981). Thus, the neglect of the CEF interactions in $ErFe_2$ lead to an incorrect, two-times larger value for the molecular field. With increasing temperatures additional modes appear with remarkable difference in the energy separations. More complex INS spectra than observed for $HoFe_2$ and $ErFe_2$ compounds have been observed by Koon and Rhyne (1981) in $ErCo_2$, see fig. 3.14. In this compound the CEF interactions become comparable with the exchange interactions. At 4.2 K two localized transitions are observed to the second and the fourth excited levels. Castets et al. (1982a) reported INS spectra for $HoCo_2$ that later have been analyzed by Yamada and Shimizu (1982). These authors extended the spin-wave description in order to take into account the itinerant behaviour of the Co moments in $HoCo_2$.

For the nickel compounds inelastic neutron scattering spectra have been reported for $PrNi_2$ (Greidanus et al. 1983), for $HoNi_2$ (Castets et al. 1982b) and for compounds with Pr, Nd, Tb, Ho, Er and Tm (Goremychkin et al. 1989). The localized states of Pr in $PrNi_5$ have also been studied by point-contact spectroscopy (Reiffers et al. 1989). In the R_2T_{17} series, inelastic neutron scattering experiments have been performed on single-crystalline samples of Ho_2Co_{17} and Ho_2Fe_{17} (Clausen and Lebech, 1982) and of Dy_2Co_{17} (Colpa et al. 1989a,b). The Ho_2Co_{17} results are presented in fig. 3.15. INS spectra on powder specimens of the $R_2Fe_{14}B$ series (R = Pr, Nd, Tb, Dy, Ho, Er, Tm) have been presented by Loewenhaupt et al. (1991).

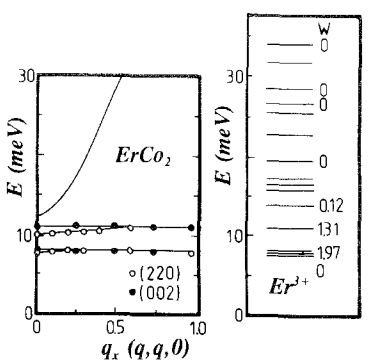

Fig. 3.14. Magnetic excitations at 4.2 K in $ErCo_2$; the open and closed circles represent data points observed around the (220) and (002) reciprocal lattice points, respectively; solid lines represent model calculations within the random-phase approximation (RPA) model; the highest Co–Co branch has not been observed; on the right-hand side, the energy level scheme of Er^{3+} with the calculated transition probabilities W from the ground state are shown; probabilities smaller than 0.03 are not indicated; forbidden transition are denoted by $W = 0$; the middle state of the low-lying triplet and the fourth state give rise to the observed dispersionless branches. After Rhyne (1987).

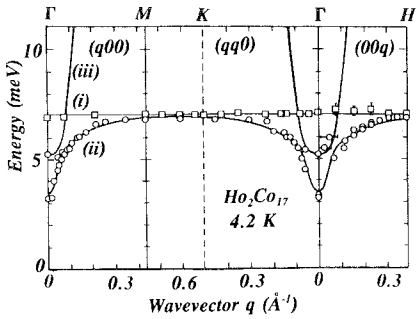

Fig. 3.15. Magnetic excitations at 4.2 K in Ho_2Co_{17} observed for a single-crystalline sample; experimental points (□ and ○) are observed around the (220) and (301) reciprocal lattice points, respectively. The full curves represent the results of a linear spin-wave model. (i), (ii) and (iii) denote the excitation mode Ho–Ho, Ho–Co and Co–Co, respectively. After Clausen and Lebech (1982).

For a review of the INS spectra on weakly magnetic materials see, for instance, Rhyne and Koon (1983), Fulde and Loewenhaupt (1985) and Stirling and McEwen (1987).

3.3. *Mössbauer, NMR and μSR spectroscopy*

Mössbauer spectroscopy and NMR probe the magnetic and electronic properties on a microscopic scale and provide information on at least two important parameters: the hyperfine field, $H_{\mathrm{hf}}^{\mathrm{eff}}$, and the quadrupolar splitting.

The hyperfine field is used to evaluate a value for the magnetic moment of the unfilled 3d or 4f shell, usually by taking the hyperfine field directly proportional to the magnetic moment. This latter assumption can be criticized as $H_{\mathrm{hf}}^{\mathrm{eff}}$ contains additional contributions originating from core polarization and conduction electrons. These additional contributions are also proportional to the expectation value $\langle J_z^{4\mathrm{f}} \rangle$ or $\langle S_z^{3\mathrm{d}} \rangle$ but can have a different sign compared to the dominant contribution. As long as these additional contributions are much smaller than those originating from the unfilled shell, the direct proportionality holds rather well. In that case the temperature dependence of $H_{\mathrm{hf}}^{\mathrm{eff}}$ reflects the temperature dependence of the (4f or 3d) magnetic moment. By analyzing the temperature variation of the 4f moment, the effective molecular fields can be derived. The CEF interactions are rather difficult to subtract from these effective molecular fields.

The quadrupolar splitting contains information about interactions between the quadrupolar moment of the nuclei and the gradient of the electric field. In a similar way as the hyperfine field, the gradient of the electric field at the rare-earth nuclei results partly from the quadrupolar moment of the 4f shell and partly from that of the surrounding charges. Having an estimate for the 4f-shell contribution, the quadrupolar splitting arising from the lattice-charge arrangement can be evaluated and transformed into the crystal-field coefficient A_2^0. Higher-order CEF coefficients cannot be determined by the Mössbauer technique because of the much lower intensity of the higher-order multipolar interactions.

Mössbauer as well as NMR experiments for Laves-phase compounds with the easy-axis direction along the ⟨100⟩ direction reveal a single spectrum whereas two subspectra with equal intensity are observed for compounds with the easy axis along the ⟨110⟩ direction. In case of the easy direction along the ⟨111⟩ axis, there are two subspectra with an intensity ratio of 3 : 1. In this way these techniques enable the detection of the easy direction of magnetization on polycrystalline samples. Details of temperature-induced moment-reorientation phenomena can be effectively studied. In experiments on $HoCo_2$ by Guimarães et al. (1987) two NMR lines that are characteristic for an easy magnetization direction along ⟨110⟩ gradually join with increasing temperature into one line characteristic for an easy magnetization direction along ⟨100⟩.

Complementary to Mössbauer and NMR spectroscopy is the muon-spin-rotation (μ^+SR) spectroscopy. In this method, the positive muon is used as a local magnetic probe to sense the magnetization (spin density) at interstitial sites. These interstitial sites are hardly accessible in other methods. The muon site in the host lattice is not known a priori. μSR experiments provide information on the local magnetism via the spin-procession frequency and on relaxation processes via the relaxation rate. μSR experiments have reported by Barth et al. (1986) for some cubic Laves-phase compounds (YFe_2, $LuFe_2$, $GdFe_2$, $ErFe_2$, $TmFe_2$ and $GdCo_2$) and by Yaouanc et al. (1990) for $GdNi_5$. In the former compounds the μ^+ frequency has been found to follow the 3d sublattice magnetization for all compounds investigated. In particular, it is not sensitive to the compensation of the resultant magnetization occurring in $ErFe_2$ and $TmFe_2$ compounds. The local hyperfine field in the $GdCo_2$ and $GdFe_2$ compounds has been found to be oriented parallel to the macroscopic magnetization, i.e., antiparallel to the 3d sublattice magnetization. Barth et al. (1986) have concluded that the main contribution to the muon hyperfine field comes from the 3d electrons suggesting a larger penetration of the interstitial space by 3d electrons than by 4f electrons. Muon spin spectroscopy for $DyMn_2$ and $TbMn_2$ compounds have been reported by Cywinski and Rainford (1992).

3.3.1. Hyperfine field at 3d nuclei

The approximate relation

$$m_T = \frac{1}{A_{hf}} H_{hf}^T \tag{3.20}$$

has been found to work surprisingly well for many intermetallic compounds. The parameter A_{hf} is known as the hyperfine interaction constant.

For iron compounds, the hyperfine field is detected by Mössbauer spectroscopy on ^{57}Fe nuclei. The parameter A_{hf} takes a value between 14.5 and 15.0 T/μ_B. By comparing the magnetic parameters of metallic iron with $H_{hf}^{Fe} = 33.0$ T and $\mu_{Fe} = 2.21\mu_B$, a value of 14.7 T/μ_B is deduced for the parameter A_{hf}.

For cobalt, the hyperfine field H_{hf}^{Co} is detected by the NMR technique on ^{59}Co nuclei. In this case, the parameter A_{hf} takes a value of $-13.0\,T/\mu_B$ according to Berthier et al. (1988b). A slightly lower value of $-11.5\,T/\mu_B$ has been reported by Panissod et al. (1982) and by Boehner et al. (1986). An even smaller value, of $-10\,T/\mu_B$ only, has been reported for YCo_2 (Yoshimura and Nakamura 1990). This value has

been found to be strongly reduced by Al substitutions in $Y(Co–Al)_2$ compounds. In first-principles calculations by C. Li et al. (1991), it has been found that the core electron contribution to the hyperfine field for the hcp Co surfaces is strictly proportional to the spin part of the local magnetic moment with a factor of $-14.5\,T/\mu_B$. The discrepancies between the above-mentioned values are due to the orbital contribution to the Co magnetic moment which is not completely quenched.

For Mn compounds, there is a less clear situation. A value of $4.27\,T/\mu_B$ is claimed for the hyperfine coupling constant by comparing the hyperfine field detected by NMR at ^{55}Mn nuclei with the value of the magnetic moment derived from magnetization and neutron studies in the RMn_2 compounds (Yoshimura and Nakamura 1983). In YMn_{12} a smaller value of $3.6\,T/\mu_B$ has been found (Yoshimura et al. 1990).

The effect of external pressures on the ^{57}Fe hyperfine field in Y–Fe compounds has been studied by Armitage et al. (1989). Mössbauer spectroscopy on ^{57}Fe in Y_2Fe_{17} in external magnetic fields has revealed an anisotropy effect of the external magnetic field on the values of the hyperfine field at the different crystallographic iron sites (Averbuch-Pouchot et al. 1987). The effect of external fields on the hyperfine field has been studied for a large number of RCo_5 compounds, see fig. 3.16 (Yoshie et al. 1987, 1988a) and for RCo_3 (Yoshie and Nakamura, 1988a, 1990).

NMR studies of RMn_2 on ^{55}Mn by Yoshimura et al. (1986a) reveal a large variation of the hyperfine field as a function of the R partner, see fig. 2.7, that has been correlated

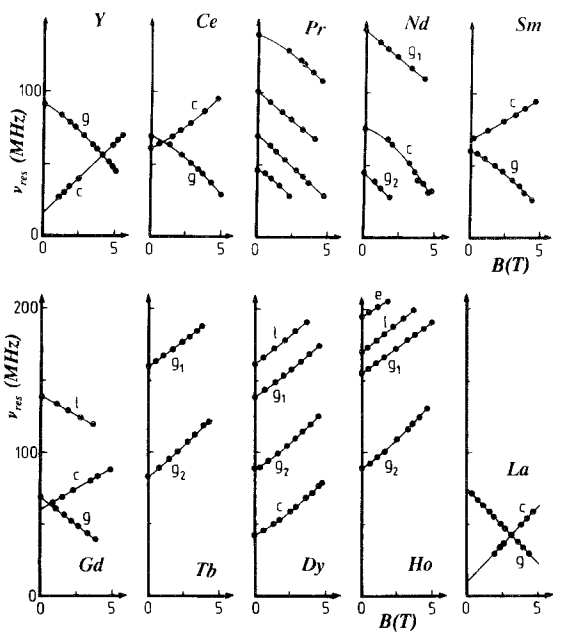

Fig. 3.16. Magnetic field dependence of the ^{59}Co NMR frequency at 4.2 K of RCo_5 for R = Y, Pr, Nd, Gd, Tb, Dy, Ho (after Yoshie et al. 1987, 1988a), Ce, Sm (after Yoshie et al. 1988b) and La (after Yoshie and Nakamura 1988b).

with the variation of the Mn moment. By applying external fields, for R_6Mn_{23} compounds with R = Y, Gd, Dy and Ho, the NMR signals coming out from nuclei located in domain walls are smeared out and the resonance frequency decreases with the increasing field for all measured compounds (Nagai et al. 1988a). N. Okamoto et al. (1987) studied RMn_{12} compounds for R = Gd, Tb, Dy and Ho whereas the relaxation and the temperature dependence of the NMR frequency of YMn_{12} has been reported by Yoshimura et al. (1990). Till now it is not clear how far these different values are due to the difference in the orbital contribution to the Mn magnetic moment in a similar way as for Co compounds.

3.3.2. Hyperfine field at rare-earth nuclei

It appears that the hyperfine field at the rare-earth nuclei differs about 20 to 30 T from the value that corresponds to the ground state of the 4f shell with the maximal J_z value ($=J$). This latter value is called the free-ion value and is known from atomic calculations. The excess hyperfine field, that is attributed to a transferred hyperfine field from the 3d sublattice on the rare-earth nuclei has been analyzed by Pszczoła and Krop (1986). In an analysis of the different contributions to the hyperfine field by Nowik et al. (1983) for $SmCo_5$, the experimentally observed value of -155 T is split into -168, -23 and $+36$ T as originating from the 4f shell, the core polarization and the conduction electrons. A similar situation occurs in Sm_2Co_{17}. An inspection of these values shows the dominant 4f-shell contribution.

The quadrupolar splitting contains information on the second-order crystal-field parameter. For these studies Mössbauer spectroscopy on the Gd nuclei is of utmost importance. Due to its S-state, the 4f-shell contribution to the gradient of the electric field vanishes for Gd and the measured electric-field gradient (EFG) is entirely due to the surrounding charges. In this way the EFG can be directly related to the CEF coefficient A_2^0 (Gubbens et al. 1987, 1989a) as

$$eV_{zz}^{\text{latt}} = -4S_H A_2^0 \tag{3.21}$$

for compounds with the easy direction of magnetization parallel to the uniaxial axis (c-axis), whereas in the case of easy-plane systems

$$eV_{zz}^{\text{latt}} = +2S_H A_2^0, \tag{3.22}$$

where $-|e|$ is the electronic charge and S_H is a factor containing shielding and anti-shielding Sternheimer factors. These factors have been reanalyzed by Bhattacharyya and Ghosh (1989) for rare-earth ions in ionic compounds. H. S. Li and Coey (1991) following Gubbens et al. (1989a) have calculated the second-order CEF coefficient in a number of ternary intermetallic compounds with S_H equal to 93. Band structure calculations of Coehoorn et al. (1990) reveal, however, a very limited validity of the proportionality between V_{zz} and A_2^0 in intermetallic compounds. The reason is that V_{zz} is determined mainly by the asphericity of the 6p shell, whose density near the nucleus is much larger than that of the 5d shell, whereas A_2^0 is determined by the asphericity of both shells. In conclusion, the electric field gradient given by Mössbauer spectroscopy being evaluated at the place of the nucleus is not simply related with the CEF coefficients describing the electrical potential at the place of the 4f orbitals.

Hyperfine interactions become visible in specific-heat experiments at low temperatures by an upturn with decreasing temperatures. This upturn is extremely pronounced in case of the magnetically ordered Ho compounds at temperatures below 5 K. Due to the nuclear contribution, for Ho_2Co_{17} a heat capacity at a temperature of 1.3 K as large as 2.3 J/K mol Ho has been observed (Radwański et al. 1988c).

An overview of NMR experimental data in samarium and neodymium compounds with iron and cobalt (Nd_2Co_{17}, $Nd_2Fe_{14}B$, $NdCo_4B$, Sm_2Co_{17}, Sm_2Fe_{17}) has been given by Figiel (1991) and Figiel et al. (1992). Theoretical background as well as an extensive review of experimental data on NMR in intermetallic compounds has been presented by Dormann (1991).

3.4. *Specific heat*

The specific heat of 3d–4f samples contains electronic, c_{el}, lattice (phonon), c_{ph}, magnetic, c_m, and nuclear, c_N, contributions:

$$c = c_{el} + c_{ph} + c_N + c_m. \tag{3.23}$$

The nuclear contribution to the heat capacity is related to the hyperfine interactions of the 4f shell with the nuclear moment of the 4f ion and is only significant at low temperatures for most of the 4f ions. The largest nuclear contribution is observed in ordered Ho compounds. In Ho_2C_{17} it reaches a value of 4.3 J/K mol f.u. at 1.37 K (Radwański et al. 1988c).

The electronic part is linear in temperature with the coefficient γ yielding information on the integrated density of states at the Fermi level. The phonon term is approximated by a Debye function with the Debye temperature as the characteristic temperature. At low temperatures this contribution is represented by βT^3. In compounds where other terms, like magnetic or crystal-field contributions, are expected to be important, a priori knowledge about the characteristic coefficients, γ and Θ_D, is desirable in order to separate the different contributions. Isostructural compounds with nonmagnetic rare-earth elements usually serve as the reference material. The number of these compounds, however, is limited as La or Lu compounds very often are not formed. The use of the Y compound, even with corrections for the atomic mass difference, does not always lead to a successful evaluation of the phonon contribution.

In table 2.12, some representative values for γ and Θ_D are collected. In the current literature there is a large scatter in values for Θ_D as derived by different techniques or by the same method from different temperature regions. Apparently one single parameter is not sufficient to account for the dynamics of the lattice over a large temperature region.

The values for the electronic coefficient γ should be compared with values from band-structure calculations, as collected in table 2.9. The enhancement of the experimental values for YCo_2 and $LuCo_2$ with respect to the calculated values is another manifestation of the moment instability. Ikeda et al. (1984, 1991) discussed it in terms of spin fluctuations which is supported by the T^2-term in the resistivity at low temperatures. The strong effect of external fields on γ for $ScCo_2$, YCo_2 and $LuCo_2$

is taken as a strong support for considering these compounds as spin-fluctuation ones. Values for Θ_D for the compounds $ScCo_2$, YCo_2 and $LuCo_2$ poorly follow the relation $\Theta_D \sim M^{-1/2}$, where M is the molar mass, expected from the Debye model.

In compounds with a magnetic R element the magnetic contribution, c_m, is associated with the increasing population of excited localized states. These localized states are due to CEF and molecular field interactions of the 4f ion which lift the $(2J+1)$-fold degeneracy of the ground multiplet. Having the energy-level scheme available it is straightforward to evaluate this contribution by making use of the general formula,

$$c_m(T) = -T\frac{\partial^2 F}{\partial T^2}, \tag{3.24}$$

where F is the free energy of the R system.

The reverse procedure is troublesome. Contributions like the electronic and lattice contributions have to be evaluated and subtracted. Moreover, the CEF contributions at higher temperatures are largely dominated by the phonon contributions making the evaluation of c_m rather problematic. In general, relevant information about the lower part of the energy level scheme can be drawn from the specific-heat measurements. In case of a small energy separation between the ground state and the first excited state, a very pronounced Schottky peak is detectable. This situation may occur for weak magnetic materials like $ErNi_5$. The magnetic and CEF contributions to the specific heat of this compound are presented in fig. 3.17. In case of the 3d-rich R–T intermetallics with T = Fe, Co there is always a significant molecular field present that causes large separations between the energy levels. The energy separation to the

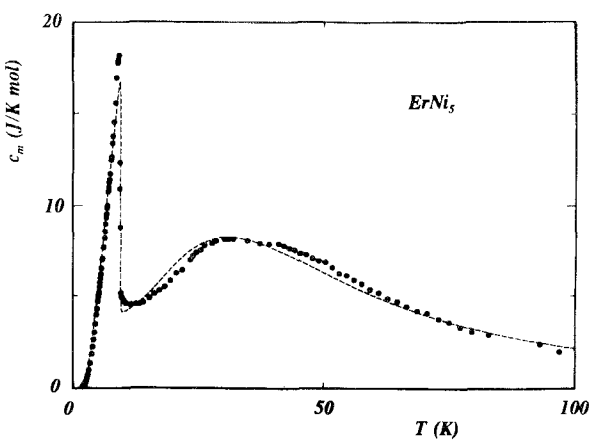

Fig. 3.17. Temperature variation of the contribution of the Er subsystem to the specific heat of $ErNi_5$ with the λ-type anomaly associated with the magnetic ordering, $T_c = 9.2$ K, and a Schottky-type anomaly with its maximum in the vicinity of 35 K. Full circles are experimental data measured by Radwański et al. (1992c). The broken curve shows data calculated by Radwański et al. (1992a) taking into account the CEF and exchange interactions.

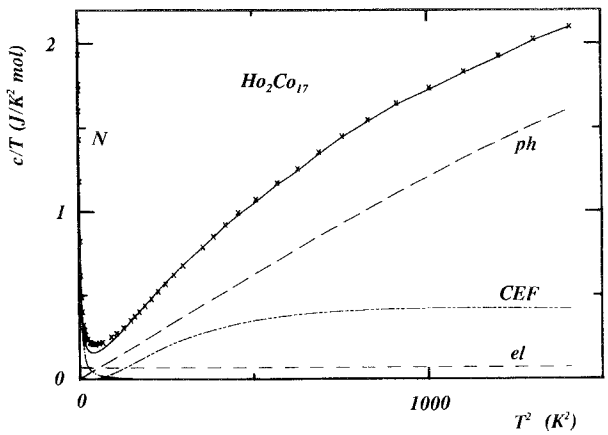

Fig. 3.18. Low-temperature specific heat for Ho_2Co_{17}. × are experimental data and the solid line is the sum of electronic, phonon, nuclear and CEF contributions. After Radwański et al. (1988c).

first excited level amounts to 144 K for $ErFe_2$ and to 82 K for Ho_2Co_{17}, for example. In the latter case the other levels lie at energies of 138 and 182 K above the ground state. Such large energy separations are the reason that the magnetic contribution is not clearly visible but is hidden in the lattice contribution. This is illustrated in fig. 3.18 for Ho_2Co_{17}.

Experiments in external magnetic fields can give further information as the applied field additionally shifts the energy levels. The shift is not uniform for all levels and is largely dependent on the direction of the applied field. This effect can be detected provided the specific-heat measurements are performed on single-crystalline samples.

3.5. *Electrical resistivity*

Resistivity studies have been found to be useful in studies of magnetic transitions where the electrical resistivity usually exhibits an anomaly. The series of RCo_2 compounds measured by Gratz et al. (1987) can serve as an example. In these compounds a significant and abrupt increase of the resistivity occurs at the temperature where a first-order transition from the magnetically ordered to the paramagnetic state takes place (see fig. 3.19 for $ErCo_2$ and $HoCo_2$). In case of a second-order transition, as observed in $TbCo_2$ for instance, the anomaly that accompanies the onset of magnetic order is not so spectacular. Influence of Y substitutions on the resistivity of $(R-Y)Co_2$ compounds has been studied by Duc et al. (1991). Some anomalies found at the low-temperature region have been discussed in terms of spin fluctuations in the Co matrix associated with the onset of the Co-ion moment. Resistivity measurements for YCo_2 have been reported by Ikeda et al. (1984). At low temperatures a T^2 dependence is found that changes into a rather strong linear dependence on T from 150 up to 1000 K (Gratz et al. 1987). A T^2 dependence of the resistivity has been reported by Kim-Ngan et al. (1992a) for the paramagnetic $LuMn_2$ below 50 K. With Nd substi-

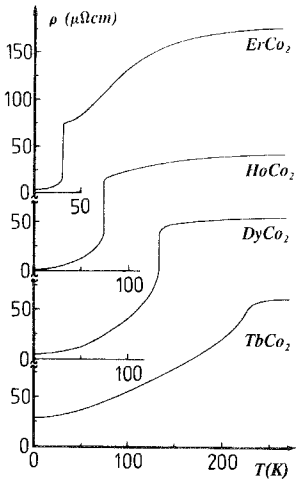

Fig. 3.19. Thermal variation of the resistivity for RCo_2 compounds. After Gratz and Zuckermann (1982).

tutions this quadratic dependence is lost. For antiferromagnet $NdMn_2$ the resistivity display an S-shaped rise at low temperature and an anomaly at a T_N of 104 K. A well-pronounced peak in the resistivity has been observed for $SmNi_5$ at T_c (Ballou et al. 1988a).

Transport properties like electrical resistivity, thermoelectric power and thermal conductivity for rare-earth intermetallics have been reviewed by Gratz and Zuckermann (1982).

3.6. Magnetostriction

An extensive review of experimental data concerning the magnetostriction in intermetallic compounds with the C15 structure: $RA1_2$, RCo_2 and RNi_2 has been given by Belov et al. (1983). Special attention has been devoted to the giant magnetostriction in RFe_2 compounds reviewed earlier by Clark (1979, 1980). Extensive theoretical studies of magnetostriction in rare-earth intermetallics as well as the comparison with experimental data for $RA1_2$, RNi_2 and $R_2Fe_{14}B$ have been presented by del Moral et al. (1991). Magnetostriction due to its inherent anisotropy leads to non-uniform distortion of the elementary cell of the crystal that can be studied by X-ray diffraction even on polycrystalline samples. In the case of the cubic symmetry one expects a rhombohedral distortion for EMD directed along the $\langle 111 \rangle$ axis and a tetragonal distortion for the EMD directed along the cubic edge $\langle 100 \rangle$. Approximate expressions for the magnetoelastic constants λ_{111} and λ_{100} can be written as (Levitin and Markosyan 1990)

$$\lambda_{111} = \Delta\alpha, \quad \text{and} \quad \lambda_{100} = \frac{2\Delta a}{3a}, \tag{3.25}$$

where $\Delta\alpha$ is the deviation of the angle between neighbouring edges of the distorted cube from $\pi/2$ whereas Δa is the difference between inequivalent distorted-cube edges. Such a situation is observed in RNi_2 compounds, indeed. $TbNi_2$ manifest a rhombohedral distortion due to its $\langle 111 \rangle$ easy axis ($\lambda_{111} = +1.6 \times 10^{-3}$), whereas $DyNi_2$ and $HoNi_2$ show a tetragonal distortion with $\lambda_{100} = -1.3$ and -1.0×10^{-3}, respectively. No trace of distortion was found in $ErNi_2$ which is likely due to its low value of T_c.

The correlation between the type of distortion and the EMD direction is nicely observed for $HoCo_2$. In this compound the EMD direction undergoes a temperature-induced spin reorientation around 18 K. Above this temperature but below T_c (= 78 K), the EMD lies along the $\langle 100 \rangle$ axis. Below 12 K, the $\langle 110 \rangle$ direction becomes the EMD. At 12 K an *orthorhombic* distortion has been detected by Levitin and Markosyan (1990).

Magnetostriction in RFe_3 and R_6Fe_{23} compounds has been measured by Abbundi et al. (1980) and Herbst and Croat (1982, 1984) and is found to be much weaker than in the RFe_2 compounds. A single-ion model, related to rare-earth ions, has been employed to explain these results.

According to this model the anisotropic-magnetostriction constants can be represented as

$$\lambda_i = C\alpha \langle r_{4f}^2 \rangle J_2, \tag{3.26}$$

where C is a numerical factor that is expected to be much the same for all R partners within an isostructural series. The magnetostriction constants should be proportional to the factor $\alpha_J \langle r_{4f}^2 \rangle J_2$, values of which have been tabulated in table 2.4. One obviously notices that the same dependency is expected for the magnetocrystalline anisotropy coefficient κ_2^0. The large magnetocrystalline anisotropy within the RFe_2 series ($\lambda_{111} = +4.4 \times 10^{-3}$) observed from the terbium compound supports the predictions. At present most of the results on the magnetostriction of the 3d–4f intermetallics are analyzed within the single-ion model. This was done for the RCo_5 series by Andreev et al. (1983) and for the $R_2Fe_{14}B$ series by Ibarra et al. (1986).

In the series RCo_2, the constant λ_{111} follows the single-ion model prediction quite well. The constant λ_{100}, however, is rather independent on the R element. As magnetostrictive deformations of the same size have already been observed for $GdCo_2$ ($\lambda_{100} = -1.2 \times 10^{-3}$) its origin must be predominantly due to the cobalt subsystem (Levitin et al. 1982). In the isostructural compounds $GdNi_2$ and $GdFe_2$, λ_{100} is less than 5×10^{-5}.

4. 3d Magnetism in R_nT_m compounds

4.1. Introduction

By decreasing the concentration of 3d atoms in the Y–Fe, Y–Co, and Y–Ni compounds, the magnetic moment of the 3d atom is reduced. The reduction is attributed to the increasing hybridization of the 5s and 4d conduction electrons of Y (6s and 5d in case of other rare-earth metals) with the 3d and 4s electrons of the 3d atoms. This hybridization is clearly visible in fig. 2.6, where the electronic structure for a number

of Y–Fe compounds is presented. The calculated shape of the DOS curve in the different stoichiometries keeps its overall shape, whereas the Fermi level is gradually pushed out from the high DOS region, that originates from the d band of the 3d atom, to a low-density-of-states region, originating from the conduction band of the R element. Obviously, different structures and different surroundings of the 3d atoms modify the DOS curve since a rigid-band model cannot account for all observed magnetic moment variations in detail.

4.2. Magnetic moment and magnetic anisotropy of the 3d sublattice

Although the magnetization curves for the uniaxial Fe- and Co-rich compounds are rather simple, the experimental data reported by different authors differ considerably even for single crystalline samples. These differences are connected with small off-stoichiometries that frequently occur in these crystallographic structures. A small deviation from stoichiometry can have a large effect on the magnetic properties, especially in instability regions. Here Co-rich YCo_5, Co-poor YCo_3 compounds and all Ni compounds can be mentioned. For Co-rich YCo_5, the magnetrocrystalline anisotropy rapidly changes with deviations from the 1 : 5 ratio, whereas the magnetic moment is hardly affected. Contrary, in Co-poor YCo_3 it is the magnetic moment that changes considerably upon changing composition.

YCo_5 is known for its large magnetocrystalline anisotropy. A field of 16.5 T is needed to reach saturation along the hard axis, see fig. 3.1. An anisotropy in the cobalt moment, of about 4% (Alameda et al. 1981), is evident as the moment for the hard direction after saturation is lower than that observed for the easy axis. No moment anisotropy has been observed for Y_2Co_{17} (Matthaei et al. 1988) for which compound the magnetocrystalline anisotropy is more than ten times smaller than that of YCo_5. Magnetic moment anisotropy has been reported for other uniaxial Y–Co compounds as well: Y_2Co_7 (fig. 4.1) and YCo_3 (fig. 4.2). In compounds with iron, a significant moment anisotropy is observed in Y_2Fe_{17} (fig. 4.3) (Deportes et al. 1986, Matthaei et al. 1988) and a rather small one for YFe_3 (fig. 4.4). The large moment anisotropy in Y_2Fe_{17} is concomitant with a remarkably large value of the MCA. Y_2Fe_{17} exhibits the largest magnetocrystalline anisotropy of the iron

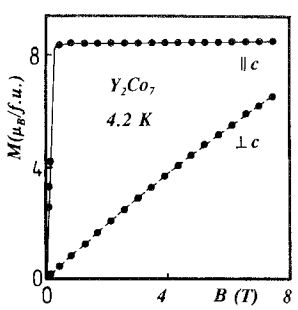

Fig. 4.1. Magnetization curves at 4.2 K for Y_2Co_7 for fields applied parallel and perpendicular to the hexagonal c axis. After Ballou (1987, p. 70).

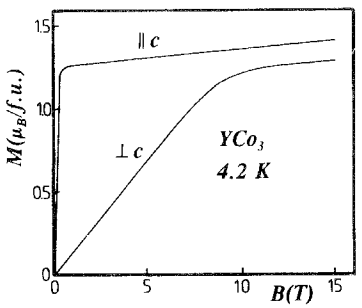

Fig. 4.2. Magnetization curves at 4.2 K for YCo_3 in fields applied parallel and perpendicular to the hexagonal c axis. After Ballou (1987, p. 112).

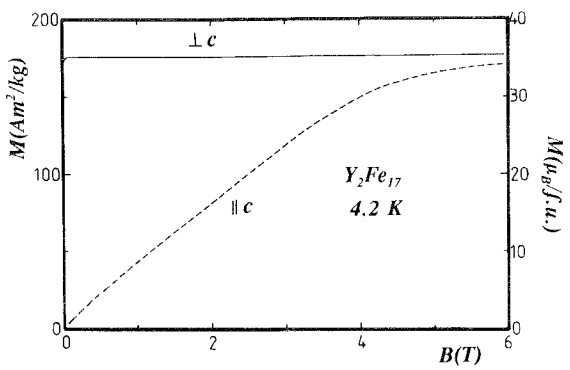

Fig. 4.3. Magnetization vs. internal field B_i at 4.2 K for Y_2Fe_{17} for fields applied parallel and perpendicular to the hexagonal c axis. After Matthaei et al. (1988).

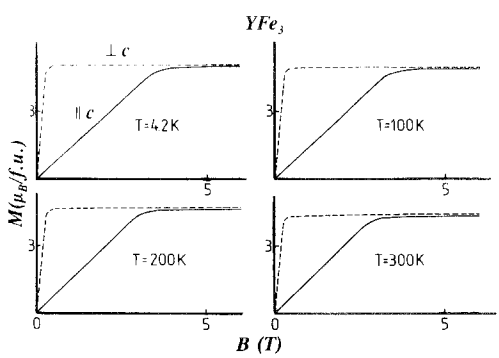

Fig. 4.4. Magnetization curves for YFe_3 for fields applied parallel and perpendicular to the hexagonal c axis at different temperatures. After Kebe (1983, p. 62).

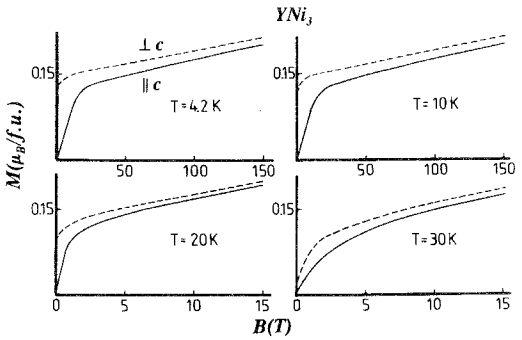

Fig. 4.5. Magnetization curves at 4.2 K for YNi_3 for fields applied parallel and perpendicular to the hexagonal c axis at different temperatures. After Kebe (1983, p. 65).

compounds with a nonmagnetic R partner. In compounds with Ni, moment anisotropies have been reported as well. An example is YNi_3, see fig. 4.5. In table 2.11 the magnetic parameters for the Y–Co and Y–Fe series are collected. The differential susceptibility χ_{hf} for Co-rich compounds for fields applied along the easy direction of magnetization is small, see table 2.12. It indicates that the moments are hardly sensitive to external fields even at fields up to 35 T. The field of 40 T in case of Y_2Co_{17} enlarges the Co moment by 1.0% only. The value of 48×10^{-9} m^3/mol as observed for this compound corresponds to a density of states of 6 eV^{-1} atom^{-1} which value slightly exceeds band-structure results. The significantly larger susceptibility observed for Fe-rich and RCo_2 compounds indicates an instability of the 3d magnetism.

The temperature variation of the 3d sublattice magnetization at low temperatures can be approximated by the expression

$$M(T) = M(0)\left[1 - b\left(\frac{T}{T_c}\right)^n\right] \tag{4.1}$$

or by means of the Brillouin function, eq. (3.12). Both relations are not able to describe the thermal variation over the full temperature range. The Brillouin function is more appropriate for the rare-earth moment. Indeed, the temperature variation of the ^{57}Fe hyperfine field in Y_2Fe_{17}, for instance, does not follow the Brillouin function at all (Gubbens and Buschow 1982). Instead, the data up to $0.8T_c$ can be well represented by eq. (4.1) with $n = 2$ and with a value for the parameter b of 0.5. As this T^2 behaviour is also found in Nd_2Fe_{17} and Dy_2Fe_{17} it has been concluded that the Fe sublattice magnetization is not affected by the presence of the 4f moment. Sinnema (1988) investigated the temperature dependence of the magnetization for single-crystalline Y_2Fe_{17} and Y_2Co_{17} samples and found a value for the exponent of $\frac{3}{2}$ more appropriate than a value of 2. Values for b of 0.45 and 0.20, respectively, are found. These latter values should be compared with the values for α-Fe and γ-Co of 0.12 and 0.08, respectively (Pauthenet 1983). A similar behaviour has been reported for $Y_2Fe_{14}B$ by Gavigan et al. (1988) who found values for the exponent and for b of $\frac{3}{2}$ and 0.43, respectively. The different results for the exponent point to different origins of the

TABLE 4.1
Characteristics of the magnetic properties at 4.2 K for Y–Co and Y–Fe compounds.

Compound	M_s (μ_B/f.u.)	B_A (T)	E_a (K/f.u.)	K_1 (K/f.u.)	K_2 (K/f.u.)	Ref.*
Y_2Co_{17}	28.0	1.6	−9.0	−8.65	−0.38	[1]
Y_2Co_{17}	28.0	1.6	−8.3	−6.8	−1.8	[2]
YCo_5	8.33	16.5	+47	+47	–	[3]
Y_2Co_7	9.6	10.5	+34	+34		[4]
Y_2Co_7	8.6	9.7	+28	+28	–	[5]
$Y_2Co_{6.7}$	6.1	9.3	+19	+19	–	[6]
YCo_3	1.2	8.0	+3.2	+5.0	–	[5]
$Y_2Co_{14}B$	19.4	2.6	−17	−17		[7]
Y_2Fe_{17}	35.2	4.5	−53.2	−57.9	+4.7	[1]
$Y_2Fe_{14}B$	29.8	1.55	+11.0	+11.0	–	[7,8]
Y_6Fe_{23}	39.3	0.5	+9.0	+9.0		[9]
YFe_3	5.0	3.5	−5.9	−5.9	–	[10]

*References:
[1] Matthaei et al. (1988) from magnetization.
[2] Matthaei et al. (1988) from magn. torque.
[3] Alameda et al. (1981).
[4] Andreev et al. (1985a).
[5] Ballou (1987, p. 71).
[6] Ballou (1989), Ballou and Lemaire (1988).
[7] Hirosawa et al. (1987).
[8] Sinnema et al. (1984).
[9] Andreev et al. (1990).
[10] Kebe (1983, p. 61).

magnetic excitations in the 3d system. A T^2 dependence is usually associated with single-particle excitations whereas a $T^{3/2}$ dependence points to collective excitations of the spin-wave type.

The magnetocrystalline anisotropy energy of the 3d sublattice is derived by applying eq. (3.2) to the magnetization curves of 3d compounds with yttrium, lanthanium or lutetium. Results are collected in table 4.1. The anisotropy energy varies very much, manifesting its dependence on the crystallographic structure and local surroundings. The anisotropy is largest for YCo_5. The presence of a significant magnetocrystalline anisotropy in yttrium compounds proves that the orbital moment of the 3d ion is far from quenched. This anisotropy is one to two orders of magnitude larger than in the pure 3d elements. The temperature dependence of the 3d anisotropy energy is much faster than expected according to the Callen–Callen equation (H. B. Callen and Callen 1966),

$$\kappa_n^m(T) = \kappa_n^m(0)\left(\frac{m(T)}{m(0)}\right)^n, \tag{4.2}$$

and resembles that found for the pure 3d metals.

The anisotropy energy of YCo_5 is very much the same as that of $LaCo_5$ as expected since both R elements are nonmagnetic, see fig. 4.6. At first sight this does not seem to hold for $GdCo_5$ although Gd ions are in the S-state. The evaluation of the anisotropy energy of $GdCo_5$ with the Sucksmith–Thompson method provides an effective anisotropy that is not the simple sum of the Co and Gd anisotropy. If the finite strength of

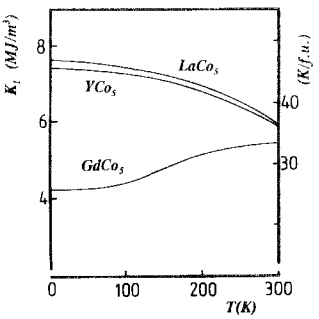

Fig. 4.6. Thermal variation of the anisotropy constant K_1 of YCo_5, $LaCo_5$ and $GdCo_5$. After Ballou et al. (1986a).

the intersublattice interactions is taken into account, as discussed in more detail in section 3, the Co anisotropy in $GdCo_5$ is much the same as in YCo_5 (Radwański et al. 1992b).

4.3. Magnetovolume phenomena

As mentioned in section 2.2.2, T_c decreases considerably with decreasing 3d concentration in the Y–Co and Gd–Co compounds. In contrast, in Y–Fe compounds, the lowest value for the Curie temperature of 324 K occurs for Y_2Fe_{17}, a compound consisting for nearly 90% of Fe. A more than 200 K larger value is observed for YFe_2. This large variation in T_c is a manifestation of magnetovolume effects that are present in many iron-based compounds. The different magnetic properties of α-Fe and γ-Fe are related to the same effects. A consequence of the large magnetovolume effect is the substantial pressure dependence of magnetic properties such as the magnetic ordering temperature, the magnetic moment, the hyperfine field.

Values for the pressure dependence of T_c are collected in table 4.2. The largest decrease of T_c is observed in Fe-rich compounds, a fact that makes these compounds the best candidates for studying magnetovolume effects. The effect is analyzed usually in terms of the volume dependence of the exchange interactions. Comparison of YFe_2 and $ZrFe_2$ illustrates the influence of the electron concentration as Zr bears one electron more than Y. Although, both compounds have Curie temperatures and magnetic moments very close to each other (T_c equal to 540 and 620 K, m_{Fe} to 1.5 and 1.6μ_B, respectively) the pressure dependence of T_c is largely different: large and negative for $ZrFe_2$, $dT_c/dp = -3.4\,K\,kbar^{-1}$, and small and positive for YFe_2, $dT_c/dp = +0.5\,K\,kbar^{-1}$ (Buschow 1980a).

Within the Stoner–Edwards–Wohlfarth (SEW) theory, dT_c/dp can be expressed as

$$dT_c/dp = \frac{-\alpha}{T_c} + \beta T_c. \tag{4.3}$$

A dominance of the second term in eq. (4.3) points to localized-magnetism behaviour, as observed, for instance, in R–Ni compounds where dT_c/dp has been found to be

TABLE 4.2
Values for T_c and for the relative pressure dependence of T_c and the magnetization.

Compound	T_c (K)	dT_c/dp (K kbar^{-1})	$d\ln M/dp$ (10^{-4} kbar^{-1})	Ref.*
Y_2Fe_{17}	324		−41.6	[1]
Er_2Fe_{17}	310	−4.0		[2]
Dy_2Fe_{17}	371	−4.8		[3]
Y_6Fe_{23}	483		−18.5	[1]
$Y_2Fe_{14}B$			−19	[4]
$Nd_2Fe_{14}B$		−2.65		[5]
YFe_2	540	+0.5	−8.4	[6, 1]
$ZrFe_2$	620	−3.4		[7]
YCo_5			−6	[8]
Y_2Co_7			−16	[8]
YCo_3			−40	[8]
$GdCo_2$	400	−2.3		[9]
YMn_2	105	−10		[10]

*References:
[1] Armitage et al. (1989).
[2] Brouha et al. (1974).
[3] Radwański et al. (1985a).
[4] Gavigan et al. (1988).
[5] Kamarad et al. (1987).
[6] Brouha et al. (1974).
[7] Hilscher and Rais (1978).
[8] Ballou (1987 p. 69) at 50 K and 2 T.
[9] Yoshida et al. (1988).
[10] Oomi et al. (1987).

roughly proportional to T_c (Jaakkola et al. 1983). In iron or cobalt compounds the first term in eq. (4.3) dominates with values for α/k of 1.25×10^6 K^2 and 2.9×10^6 K^2, respectively (κ is the compressibility). Sometimes, the dimensionless magnetic Grüneisen parameter is introduced,

$$\gamma_m = -\frac{d\ln T_c}{d\ln V}. \tag{4.4}$$

The value for this parameter in R_2Fe_{17} can be as large as 20 (Radwański et al. 1988a). By applying an external pressure of 4.2 GPa, T_c of $Y_2Fe_{14}B$ decreases from 566 to 316 K, i.e. by nearly 50% (Kamarad et al. 1987, Nagata et al. 1987). The corresponding value for $d\ln T_c/dp$ amounts to -0.13 GPa^{-1}. With a value of 0.8 Mbar^{-1} for the compressibility, it results in a value of 16 for the magnetic Grüneisen parameter. External pressures applied to $Y_2Fe_{14}B$ largely reduce the iron-sublattice moment (Gavigan et al. 1988). This reduction is also seen for other iron-rich compounds in the pressure dependence of the ^{57}Fe hyperfine field, see fig. 4.7 Gavigan et al. (1988) and Coey (1986) have attributed the variation of T_c with the pressure/volume to a change of the iron moment, rather than a change in the exchange interaction parameter J_{TT}. A strong volume dependence of the iron moment in Y_2Fe_{17} is found in band structure calculations, indeed (Coehoorn 1989). Fe moment instabilities in 3d alloys have been discussed by Wassermann et al. (1990) and Wassermann (1991) in connection with the fcc–bcc structural transition and moment-volume instabilities. The mag-

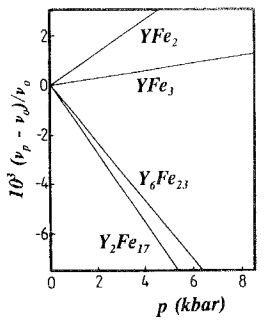

Fig. 4.7. The pressure dependence of the ^{89}Y hyperfine field of Y–Fe compounds at 4.2 K. After Armitage et al. (1989).

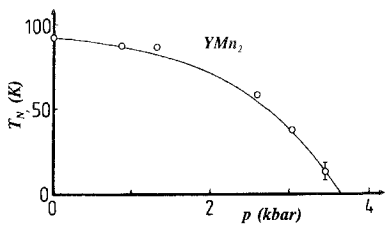

Fig. 4.8. Pressure dependence of T_N of YMn_2. After Oomi et al. (1987).

netic properties of fcc–Fe has been reanalyzed by Takahashi and Shimizu (1990) in terms of a strong dependence of the exchange interactions on the volume.

YMn_2 exhibits very dramatic pressure effects. The magnetic ordering disappears under pressures of 3.7 kbar (Oomi et al. 1987), fig. 4.8, indicating that the interactions involved in the formation of the antiferromagnetism of the manganese ions are weak and that the Mn moment itself is in a delicate state.

4.4. Magnetostriction

The spontaneous magnetostriction is usually derived from thermal expansion measurements by comparing the lattice parameters (or volume of the elementary cell) in the magnetic state, V_m, with that obtained by extrapolation from the paramagnetic region, V_p, and given as $\omega_s = (V_m - V_p)/V$. This evaluation is not always straightforward because of uncertainties in the magnetic contribution to the volume in the paramagnetic state. The spontaneous magnetostriction is very large in iron-rich compounds. For R_2Fe_{17} and $R_2Fe_{14}B$, ω_s at 4.2 K amounts to 1.6% (Givord and Lemaire 1974) and 2.5% (Andreev et al. 1985c, Buschow 1986, Graham and Flanders 1986), respectively. Similar values for ω_s are observed in compounds with nonmagnetic R partners as well. Apparently, the spontaneous volume magnetostriction must be attributed to the 3d system. The spontaneous volume magnetostriction can lead to very small and

even negative values for the thermal-expansion coefficient in specific temperature intervals. The Invar alloy, $Fe_{65}Ni_{35}$, is a well-known example. Values for ω_s decrease with decreasing iron concentration.

In Co-rich compounds, the spontaneous magnetostriction is hardly visible in the temperature dependence of the lattice parameters, partly because of the large values of T_c in these compounds. By systematic studies of the $Y(Co_{1-x}Ni_x)_5$ series, the spontaneous magnetostriction of YCo_5, has been estimated to amount to 0.68% (Andreev et al. 1985b). Upon substitution of nickel for cobalt, the spontaneous magnetostriction decreases, vanishing already when half of the cobalt atoms has been replaced. It is found that ω_s varies with the square of the magnetic moment: $\omega_s = C\mu_s^2$. The value for the magnetoelastic coupling parameter C is found to be around $4 \times 10^{-3}\mu_B^{-2}$, see table 4.3.

In compounds with magnetic rare-earths the magnetostriction of the 3d sublattice is overruled by that associated with the R sublattice. For the description of the R sublattice magnetostriction, the single-ion model has been often found to be applicable as already discussed in section 3.6. An extensive review of experimental data concerning the magnetostriction in intermetallic compounds with the C15 structure like RAl_2, RCo_2 and RNi_2 has been given by Belov et al. (1983). Magnetostriction in RFe_2 compounds has been reviewed earlier by Clark (1979, 1980).

The spontaneous and forced magnetostriction are obviously related to each other. Indeed, attributing the spontaneous magnetostriction of 16.2×10^{-3} as observed in Y_2Fe_{17} to the internal field of 390 T one gets $d\omega/dB = 43 \times 10^{-6}\,T^{-1}$ (Radwański 1985). This value is in good agreement with the experimentally observed value for the forced magnetostriction coefficient (Armitage et al. 1989). In the R_2Fe_{17} compounds, the spontaneous magnetostriction is found to be independent of the rare-earth element whereas the forced magnetostriction reflects the resultant magnetization

TABLE 4.3

Forced magnetostriction $h\,(=d\omega_s/dB)$ and spontaneous volume magnetostriction ω_s for R_nT_m compounds at 4.2 K.

Compound	h $(10^{-6}\,T^{-1})$	ω_s (10^{-4})	μ_T (μ_B/3d-atom)	C $(10^{-4}\mu_B^{-2})$	Ref.*
Y_2Fe_{17}	+43	170	2.1	38	[1,2]
Dy_2Fe_{17}		162	2.2	33	[3]
Y_6Fe_{23}	+16.7	102	1.7	35	[1,4]
$Y_2Fe_{14}B$	+13	290	2.2	45	[5,6]
YFe_2	+4.5				[1]
YCo_5		68	1.65	25	[7]
$GdCo_2$	22				[8]

*References:

[1] Armitage et al. (1989).
[2] Givord and Lemaire (1974).
[3] Radwański and Krop (1983).
[4] Andreev et al. (1990).
[5] Graham and Flanders (1986).
[6] Andreev et al. (1985c).
[7] Andreev et al. (1985b).
[8] Markosyan and Snegirev (1985).

course (Garcia-Landa et al. 1992). For Er_2Fe_{17}, for instance, both curves (magnetostriction and magnetization) undergo a sharp transition at 5 T. An adequate description of the anisotropic magnetostriction in the band-magnetism model is still lacking.

4.5. Magnetic susceptibility

In the paramagnetic region the magnetic susceptibility of Y–Fe compounds is well approximated by the Curie–Weiss law, eq. (3.13). Attributing the usual meaning to the Curie constant, a value for the effective paramagnetic moment μ_{eff} is derived which is substantially larger than the spontaneous moment in the ordered state. In YFe_2, for instance the Curie constant,C, amounts to 2.28 K emu/mol (Burzo et al. 1985) yielding a value for μ_{eff} equal to $3.0\mu_B$. The effective spin involved in that moment amounts to 1.1 and is 50% larger than the spin obtained from the spontaneous moment measured at low temperatures. Values for the Curie constant of 4.41 and 27.70 K emu/mol observed in YFe_3 and $Y_2Fe_{14}B$ point to effective moments of 3.2 and $4.0\mu_B$, respectively (Burzo et al. 1985). The above analysis is based on a localized picture of the 3d magnetism and values for the effective moment have a limiting physical meaning.

The differential high-field susceptibility in the ordered state at 4.2 K for yttrium compounds with Fe, Co and Ni is presented in fig. 4.9. The susceptibility of the Co moment of $4 \times 10^{-4}\mu_B$/T as observed in the Co-rich compounds is accounted well by a very reasonable value for the density of states of $1.6\,eV^{-1}\,at^{-1}\,spin^{-1}$. Two peculiarities are, however, found in the concentration dependence of the differential susceptibility. In the Y–Fe series, a maximum is found for Y_2Fe_{17}, which is related to magnetovolume phenomena. The second peculiarity is connected with the onset of 3d magnetism in Co compounds.

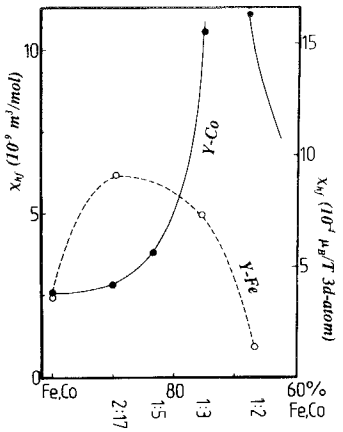

Fig. 4.9. The magnetic susceptibility of Y–Co and Y–Fe compounds at 4.2 K vs. 3d transition-metal concentration. After Radwański et al. (1988a).

4.6. 3d magnetic moment in Gd_nT_m compounds

The Gd compounds offer a good opportunity to investigate the effects of the localized R spins on the magnetic properties of the 3d ions. The Gd ion has a localized moment without an orbital component. In principle, in Gd compounds some enhancement of the 3d magnetism compared to Y compounds is expected. The Curie temperature of the Gd compound is largest in all R–T series with Fe, Co and Ni. The net spontaneous magnetization is small because of the antiparallel alignment of the Gd and 3d moments. With a value for the Gd moment as expected for a trivalent ion, a value of the 3d magnetization is obtained that is close to that observed for the yttrium compounds. In Gd_2Co_{17}, the Gd spins induce an extra molecular field of about 100 T on the Co moment. Provided that the susceptibility is equal to that measured in high fields, see table 2.11, one expects the cobalt moment to be increased by $0.04\mu_B$ only. Due to uncertainties in the exact stoichiometry of the compounds studied, this result is difficult to confirm. The enhancement of the moment starts to be detectable for Gd_2Co_7 and is very pronounced for $GdCo_3$ and $GdCo_2$, see fig. 1.3. The Co moment in $GdCo_3$ amounts to $1.33\mu_B$ whereas in YCo_3 to $0.38\mu_B$ only. Magnetic parameters for the Gd compounds with cobalt are collected in table 4.4.

In fig. 4.10, the magnetization curves at 4.2 K are shown for Y_2Co_{17} and Gd_2Co_{17}. The anisotropy energy of Gd_2Co_{17} is lower than that of the Y compound. Part of this reduction is due to dipolar interactions between the Gd moments (Colpa 1992). A more detailed study of the magnetic isotherm at 4.2 K reveals an abrupt transition at 1.2 T. The transition indicates the presence of higher-order anisotropy constants. These have been quantified by magnetic torque measurements, indeed (Matthaei et al. 1988). The microscopic origin of the higher-order constants is, however, not clear. Dipolar interactions are unlikely to be the source of such contributions. This view

TABLE 4.4
Characteristics of the magnetic properties at 4.2 K for Gd–Co and Gd–Fe compounds.

Compound	M_s (μ_B/f.u.)	B_A^{eff} (T)	E_a (K/f.u.)	K_1^{eff} (K/f.u.)	K_2^{eff} (K/f.u.)	Ref.*
Gd_2Co_{17}	13.70	1.6	−6.8	−5.1	−2.4	[1]
$GdCo_{5.14}$	1.90	41	25			[2, 3]
$Gd_{0.99}Co_{5.02}$	1.50	31				[4]
Gd_2Co_7	4.2	21	+30	+30		[5]
Gd_2Co_7	3.5	34				[6]
$GdCo_3$	3.0	12	+10.8	+6.6	+4.2	[7]
Gd_2Fe_{17}	22.9	8	−53.2	−57.8	+4.6	[4]

*References:

[1] Matthaei et al. (1988).
[2] Ballou et al. (1986a).
[3] Ballou et al. (1987a).
[4] Radwański et al. (1992b).
[5] Andreev et al. (1985a).
[6] Ballou et al. (1992a).
[7] Ballou (1987, p. 117).

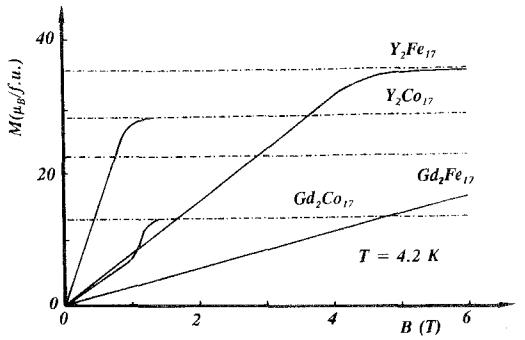

Fig. 4.10. Magnetization vs. internal field at 4.2 K for Y_2Co_{17} and Gd_2Co_{17} as well as for Y_2Fe_{17} and Gd_2Fe_{17} for fields applied parallel (full lines) and perpendicular (dashed lines) to the hexagonal c axis. After Matthaei et al. (1988).

is supported by the strong temperature dependence: at 250 K the higher-order contributions are absent as the peculiarities on the magnetization curve disappears. These contributions are possibly related to band-structure effects and reflect small details of the band-structure of the Gd ion near the Fermi level.

In contrast to Gd_2Co_{17} and Y_2Co_{17}, for which compounds the magnetic anisotropy is nearly the same, the anisotropy energy of $GdCo_5$ is much lower than that observed in YCo_5 at cryogenic temperatures, see fig. 4.6. The effective anisotropy of $GdCo_5$ evaluated from the initial slope of the hard-axis magnetization curve is only indirectly related to the intrinsic anisotropy. As discussed before in section 3.1.1, in case of a nearly compensated ferrimagnetic system this slope reflects the intersublattice coupling of the Co and Gd sublattice rather than the magnetocrystalline anisotropy.

4.7. Evaluation of the exchange field from the Curie temperature of Y and Gd compounds

A first attempt to estimate the strength of the intersublattice exchange field, $B^{R}_{ex,RT}$, can be made by comparing Curie temperatures within a given series. A mean-field approximation leads to the relation (Radwański et al. 1990a)

$$B^{R}_{ex,RT} = \frac{3k}{2\mu_B} \frac{\sqrt{T^{R}_{c}(T^{R}_{c} - T^{Y}_{c}) z_{RT} S_T}}{z_{TR}(S_T + 1)G}, \tag{4.5}$$

where G is the de Gennes factor. T^{R}_{c} and T^{Y}_{c} denote the Curie temperature of the compound with a magnetic rare-earth partner and a nonmagnetic rare-earth partner, respectively. z_{RT} (z_{TR}) stands for the number of T (R) nearest neighbours of the R (T) ion. S_T is a pseudo-spin of the 3d ion taken as half the value of the 3d moment. Values for $B^{R}_{ex,RT}$ are presented in table 4.5 for most of the R–T compounds. The nearest-neighbour number, z_{RT}, is determined by the crystallographic structure but a strict value for this number is not obvious. Gubbens et al. (1988a), for instance, used numbers for z_{RT} and z_{TR} for Gd_2Co_{17} of 19 and 2, respectively. These are slightly different from the numbers given in table 4.5 and obviously lead to different values for the

TABLE 4.5
Evaluation of the 3d–4f exchange field, B_{ex}^{Gd}, in R_nT_m compounds from values for the Curie temperatures.

Series	T_c^{Gd} (K)	$T_c^{Gd} - T_c^{Y}$ (K)	S_T	z_{RT}	z_{TR}	B_{ex}^{Gd} (T)
Gd_2Co_{17}	1218	32	0.82	19	2.1	225
$Gd_2Co_{14}B$	1050	35	0.7	18	2.5	186
$GdCo_5$	1014	27	0.82	18	2	188
Gd_2Fe_{17}	466	108	1.1	19	2.1	275
$Gd_2Fe_{17}C$	582	80	1.1	19	2.1	265
$Gd_2Fe_{14}B$	630	135	1.13	18	2.1	350
Gd_6Fe_{23}	659	178	1.0	16	3	272
$GdFe_3$	729	160	0.87	18	4	278
$GdFe_2$	790	245(Y)	0.75	12	6	230
$GdFe_2$	790	194(Lu)	0.75	12	6	200
Gd_2Ni_{17}	196	36	0.3	19	2.1	51

exchange field. The value of 225 T is close to that found from low-temperature magnetization measurements. For $GdCo_5$, however, the difference between the chosen value for z_{TR} is more significant. With a value of 2 for z_{TR} as given in table 4.5 one arrives for $B_{ex,RT}^{Gd}$ to a value of 188 T that is close to the experimentally observed value of 195 T (Radwański et al. 1992b). Taking, however, a more proper (according to the composition) value of 3.5 instead of 2, one deduces an exchange field of 246 T that, however, exceeds the experimentally observed value of 195 T (Radwański et al. 1992b). On the basis of a similar analysis (but with a value for z_{RT} of 16 and for z_{TR} of 2.3), Coey (1986) obtained a value for the exchange field of 300 T for $Gd_2Co_{14}B$, a value that is rather different from the value reported in table 4.5. A value of 175 T has been derived from an observed high-field transition at 52 T in the low-temperature magnetization curve (Radwański et al. 1990b, Kohashi et al. 1991).

Brommer (1991) has argued that the ratio of z_{RT}/z_{TR} is fixed by the composition of the R_nT_m compound and equals m/n. Although evaluation of the 3d–4f exchange interactions through the mean-field analysis of the corresponding T_c values has a rather limited validity, the good agreement with low-temperature high-field magnetization results somehow manifests the consistency of the mean-field description.

4.8. Onset of 3d magnetism

The onset of 3d magnetism can be investigated in case of the cobalt magnetism in the RCo_2 compounds and, a fortiori, in case of the nickel magnetism in the R_2Ni_{17} compounds. The series with Co is best documented. The compound YCo_2 does not order magnetically but exhibits strongly enhanced paramagnetism. The magnetic susceptibility of YCo_2 at 4.2 K is more than four times larger than that observed in Y_2Co_{17}. It increases with increasing temperature passing at 250 K through a flat maximum of 50×10^{-9} m^3/mol (Lemaire 1966b, Ikeda et al. 1984), see fig. 4.11. The

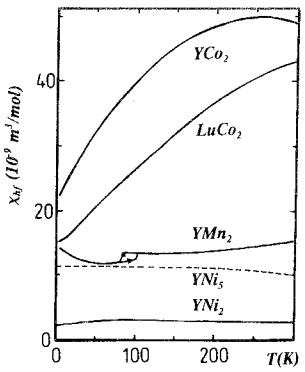

Fig. 4.11. Temperature variation of the magnetic susceptibility for exchange-enhanced paramagnetic YCo_2 and $LuCo_2$ (after Ikeda et al. 1984), for Pauli-paramagnetic YNi_2 (after Burzo and Laforest 1972), for antiferromagnetic YMn_2 with a T_N of 110 K (after Buschow 1977). The susceptibility for exchange-enhanced paramagnetic YNi_5, divided for reasons of comparison by a factor of 2.5, is included.

compounds $LuCo_2$ and $ScCo_2$ show very similar behaviour, indicating that it is an inherent property of the Co sublattice. For these two latter compounds the maximum occurs at higher temperature: about 370 and 600 K, respectively (Ikeda et al. 1984). The susceptibility of Ni, Fe and Mn counterparts is one order of magnitude smaller.

Ikeda et al. (1984, 1991) discussed the YCo_2 phenomenon in terms of spin fluctuations. From the susceptibility measurements an enhancement factor as large as 25 is derived for YCo_2 taking the DOS results from Cyrot and Lavagna (1979). Combining the experimental susceptibility, shown in table 2.12, with that given by band-structure calculations, table 2.9, one arrives at a value for the Stoner product of 0.75. Thus, the Stoner criterion for the occurrence of ferromagnetism is not fulfilled confirming the nonmagnetic ground state for Co ions in YCo_2.

In RCo_2 compounds with a magnetic rare-earth element, cobalt moments up to $1\mu_B$ are observed. This moment is understood to be fully induced by the presence of localized 4f spins, see fig. 4.12. Thus , the high-field behaviour of YCo_2 is of particular interest. This compound undergoes a collective-electron metamagnetic transition originally discussed by Wohlfarth and Rhodes (1962). Theoretical findings for the metamagnetic field show a large scatter. Yamada et al. (1984) report a value of 150 T on the basis of band-structure calculations, somewhat larger than the value of 100 T presented by Cyrot and Lavagna (1979). Calculations by Schwarz and Mohn (1984) led to a value as large as 350 T, whereas a recently calculated value of Yamada and Shimizu (1989) amounts to 89 T. Such different values are mainly related with the evaluation of the molecular field produced by the 3d–4f interactions. An estimate of the 3d–4f interactions in Ho_2Co_{17} has led to a value of 20 T for the molecular field, $B^{Er}_{mol,RT}$, in $ErCo_2$ (Radwański 1986b) which, in return, points to an extra molecular field experienced by the Co ion in $ErCo_2$ of 90 T. Since, the cobalt moment in this compound is already close to $1\mu_B$ the molecular field due to the Er spins is obviously large enough to induce a cobalt moment. The value of 90 T can be considered as the upper value

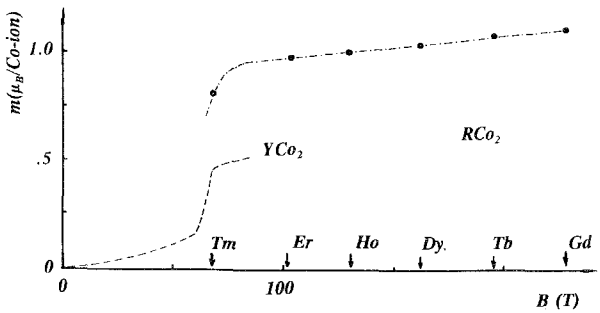

Fig. 4.12. The cobalt magnetic moment at 4.2 K in RCo_2 as a function of the internal magnetic field due to the presence of the localized R spin. The dashed line represents the experimentally observed high-field behaviour of YCo_2 whereas the dashed–dotted line is a guide for the eye.

for the metamagnetic field. With this value one arrives at a value of 270 T for the extra molecular field, $B^{T}_{mol,RT}$, acting on the Co ion in $GdCo_2$ due to the Gd moments. Knowing this value the correspondence between the Co moment in the RCo_2 compounds and the internal field is established as is shown in fig. 4.12.

Another special feature of the exchange-enhanced paramagnetism of YCo_2 is the ferromagnetic behaviour of alloys in which cobalt is substituted by nonmagnetic elements like Al, see fig. 4.13. A Co moment of $0.14\mu_B$ and a T_c value of 26 K has been observed for 15% Al substitutions (Yoshimura and Nakamura 1985). A giant increase of T_c for RCo_2 compounds by small substitutions of cobalt by Al has been reported by Aleksandryan et al. (1984a). The ferromagnetic state can also be induced by hydrogenation. The magnetic moment of $YCo_2H_{3.5}$ at 4.2 K in a field of 8 T amounts to $0.58\mu_B$/f.u. (Fujiwara et al. 1990). Both effects point to a large volume dependence of the ferromagnetic state since interstitial hydrogen and substitutional Al both enlarge the elementary cell volume.

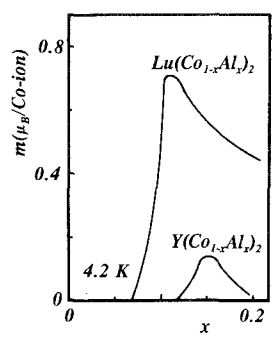

Fig. 4.13. Concentration dependence of the Co magnetic moment at 4.2 K in $Y(Co_{1-x}Al_x)_2$ and $Lu(Co_{1-x}Al_x)_2$. After Wada et al. (1990).

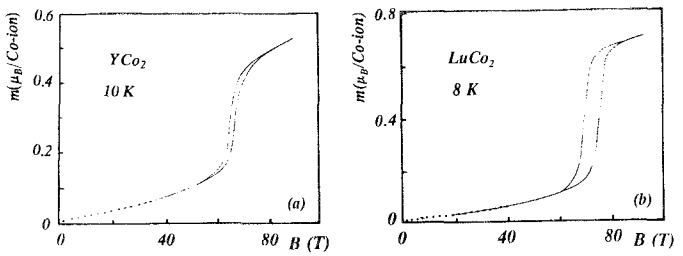

Fig. 4.14. Magnetization curve at low temperatures in magnetic fields up to 94 T of (a) YCo_2 and (b) $LuCo_2$ revealing the metamagnetism of the collective electrons. After Goto et al. (1990).

Some metamagnetic-like peculiarities have been observed in magnetization curves of Y_2Ni_{17} by Gignoux et al. (1980a) and of $ThCo_5$ by Givord et al. (1979b) and Andreev et al. (1984a). They have been discussed in terms of 3d-moment instabilities induced at some crystallographic sites (Gignoux 1987).

Experiments in pulsed fields up to 100 T by Goto et al. (1990) have revealed that at 4.2 K the metamagnetic transition in YCo_2 occurs at 69 T, fig. 4.14. The transition is associated with an increase of the cobalt moment by $0.27\mu_B$ indicating a not completed formation of the cobalt moment. Above the transition the system is still very susceptible and attains at 90 T a moment $0.5\mu_B$/Co ion. A similar transition occurs for $LuCo_2$ at 75 T.

4.9. Atomic scale 3d magnetism

In the discussions so far, the internal structure of the 3d sublattice has not been considered. Owing to the different crystallographic sites and different local surroundings one could expect different properties at different sites. Some experiments indicate a significant dependence of the magnetic properties of the 3d ions on the local environment. Of the experimental methods that are able to reveal these local environment effects, the spectroscopic methods based on the Mössbauer effect and on nuclear magnetic resonance on the 3d nuclei are particularly useful.

^{57}Fe Mössbauer spectra contain a number of the subspectra that are associated with Fe nuclei situated at different crystallographic sites with different local surroundings. The number of subspectra is equal to the number of non-equivalent Fe sites or frequently it is even larger due to further subdivision of the crystallographic sites caused by a lower magnetic symmetry. The average hyperfine fields experienced by the ^{57}Fe nuclei in Y_2Fe_{17} at 4.2 K are close to the value of 33 T that is observed for bcc iron. The hyperfine fields at the non-equivalent sites of Y_2Fe_{17} differ by nearly 20% (Deportes et al. 1986). A significant variation has also been detected in NMR studies on ^{59}Co for a number of Y_nCo_m compounds (Yoshie et al. 1987, 1988a,b). Care must be taken in the evaluation of the 3d moment from the Mössbauer or NMR experiments, since the moment is not directly measured.

Different local magnetic moments are also observed in polarized-neutron experiments. Moreover, these experiments on YCo_5 have revealed that the cobalt magnetic moment

at the site 2c has a substantial orbital contribution as well as a significant asphericity (Schweizer and Tasset 1980). These facts have been correlated with the large magnetocrystalline anisotropy observed in YCo_5. The sum of the moments derived from polarized-neutron experiments often does not agree with the resultant moment measured by magnetization measurements. Usually this sum is higher. This difference originates from the existence of a negative spin background. From neutron experiments on Er_2Co_{17} (Kumar and Yelon, 1990), cobalt moments between 1.7 and 2.15μ_B, even larger than in the Co metal, have been reported whereas the single-crystalline magnetization studies provide a mean cobalt moment close to 1.65μ_B. Despite these limitations, neutron experiments give unambiguous evidence of site-to-site variations in the moment.

Values for the magnetic moments at the different crystallographic sites have also been evaluated in band-structure calculations. These calculations reveal a substantial difference of the local density-of-states at the different sites of, for instance, Y_2Fe_{17}, as is shown in fig. 4.15. Values for the total magnetic moment as obtained by different authors are consistent and, in general, reproduce the experimental (magnetization) results. Calculations for the $Y_2Fe_{14}B$ compound reproduce the site-to-site variation of the iron moment quite well (Coehoorn et al. 1990). A more detailed account of band-structure calculations of R–T intermetallics is given by Brooks and Johansson in chapter 3 of this volume.

Band calculations, in general, only provide the spin contribution to the moment. To include the orbital moment, the spin–orbit coupling has to be taken into account. In doing so, in principle, phenomena like the magnetic anisotropy of the 3d sublattice can be discussed. Results of band-structure calculations (Eriksson et al. 1988a, Brooks et al. 1989) point to an orbital contribution of a few percent, in agreement with the

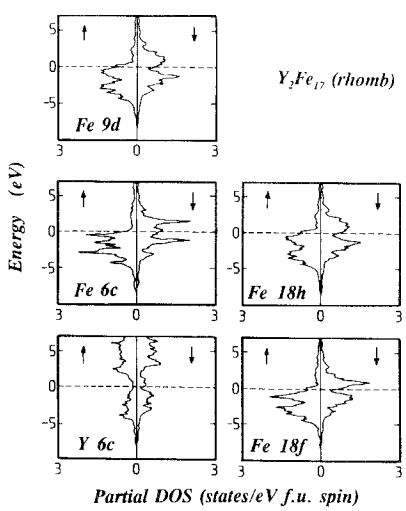

Fig. 4.15. Partial densities of states for the different crystallographic sites in Y_2Fe_{17} with the rhombohedral Th_2Zn_{17}-type of structure. After Coehoorn (1989).

rather small anisotrophy effects observed experimentally. Calculations performed later on by Eriksson et al. (1990) and Johansson et al. (1991) have led to even smaller values of 0.06, 0.14 and $0.07\mu_B$ for bcc-Fe, hcp-Co and fcc-Ni, respectively. If the calculations are performed for the same structure, a monotonic decrease is obtained: 0.14, 0.12 and $0.05\mu_B$ for the fcc structure. The small value of the orbital moment in 3d systems is a consequence of the quenching of the orbital moment due to the crystalline electric field in combination with the weak spin–orbit coupling parameter. The calculated values are found in good agreement with values deduced from experiments. Anyhow, these calculations confirm the general view that the orbital moment of the 3d ions is small and very sensitive to the crystal structure.

Strong evidence for a nonnegligible orbital contribution comes from Mössbauer studies in externally applied magnetic fields. Studies on ^{57}Fe nuclei in $Y_2Fe_{18.9}$ have been performed at a field of 9 T (Deportes et al. 1986) which field is sufficiently large to orient the magnetization along the hard direction. The hyperfine field contains at least three contributions: an isotropic spin contribution, an anisotropic part directly related to the orbital contribution and an anisotropic contribution due to dipolar interactions. The latter contribution can easily be calculated and taken into account. In the experiments of Deportes et al., Mössbauer spectra have been taken at 4.2 K with the external field applied along two main hexagonal directions. The hyperfine field was found to be larger along the c direction, i.e. along the hard direction. The largest anisotropy (3.1 T) occurs for the Fe ion in the dumbbell site (site 4f) for which the symmetry is uniaxial. The larger value for the hyperfine field for the magnetization along the hard direction has been explained by a reduction of the orbital contribution. The orbital contribution is antiparallel to the dominant spin contribution. Similar phenomena have been observed for Tm_2Fe_{17} (Gubbens et al. 1989b) and $ErFe_3$ (van der Kraan et al. 1975). In both compounds a temperature-induced reorientation of the magnetization occurs due to a competition between the R and Fe anisotropies. Anomalies in the thermal variation of the hyperfine field exist at the MR temperature. Averbuch-Pouchot et al. (1987) discussed the anisotropy of the Fe moment in $Y_2Fe_{18.9}$ as arising from a reduction of the orbital contribution in case the iron moments are forced to lie along their hard direction.

Band-structure calculations for the local magnetocrystalline anisotropy of the 3d ions are just starting. Preliminary results within relativistic spin-polarized scattering theory for Ni metal have been presented by Strange et al. (1989). A phenomenological explanation of the anisotropy energy in YCo_5 as well as in RCo_5 has been given in terms of the ratio c/a (Szpunar and Lindgard 1979). This explanation is based on the point-charge model. Within this model, the value of the second-order CEF parameter for the hcp structure is determined by a deviation of the ratio c/a from the ideal value. This explanation has been used later on to explain the anomalous temperature dependence of the anisotropy energy in $Y_2Fe_{14}B$. Indeed, the maximum in the plot of E_a^{Fe} versus temperature observed at room temperature coincides well with that observed in the ratio c/a. In an alternative explanation, the anomalous behaviour of the iron anisotropy has been attributed to the different temperature dependences of contributions arising from 3d ions at different non-equivalent sites. The overall anisotropy in this approach is the resultant of different 3d-ion contributions

which largely cancel. The individual site contributions have been evaluated from the composition dependence of the anisotropy energy in the isostructural series $Y_n(Co_xFe_{1-x})_m$ (Thuy and Franse 1986, Thuy et al. 1988). The occupancy factors indispensable for these calculations have been taken mainly from neutron diffraction studies.

The individual-site-anisotropy picture is based, in principle, on the model developed for the rare-earth anisotropy, i.e., on a localized picture. Although such an approach can be critisized for the 3d magnetism, it offers a very elegant explanation for the experimental fact that the anisotropy energy of the Co and Fe sublattices is of *opposite sign for most of the series*, see table 4.1. This phenomenon can be understood by assuming a $3d^6$ or more likely $3d^7$ configuration for the Fe ion and a $3d^8$ configuration for the Co ions. In these ionic states the relevant second-order Stevens factor of the Fe and Co ions are of opposite sign, $-2/21$ ($3d^6$) or $-2/105$ ($3d^7$) and $+2/105$ ($3d^8$), respectively (Hutchings 1964).

Although the discussion about the ionic configurations of 3d metals in the R–T intermetallics is rather irrelevant, the general view about the local anisotropy is supported by neutron studies. As mentioned in section 3.2.1. these studies on YCo_5 reveal a large difference in the spatial spin distribution at the two Co sites (Schweizer and Tasset 1980). A value of $+8.0$ K and 2.2 K is inferred for the local anisotropy at the site 2c and 3g, respectively (Franse et al. 1988b). Such a picture explains, for instance, also the rotation of the easy direction of magnetization in the $Y_2(Co_{1-x}Fe_x)_{17}$ system with iron concentration observed by Perkins and Nagel (1975). A dominant c-axis contribution to the magnetocrystalline anisotropy of YCo_5 from the site 2c has been obtained by Daalderop et al. (1992) by means of ab initio calculations within the local-spin-density approximation.

5. Magnetic properties of R_nT_m compounds (T = Fe, Co, Ni, Mn)

5.1. *Introduction*

Most of the crystallographic structures of rare-earth compounds with 3d transition metals are close-packed structures on the basis of the hexagonal close-packed structure of the $CaCu_5$-type. All compounds with the stoichiometry 1 : 5 have this structure. The compositions less rich in the T element than RT_5 follow a simple replacement rule:

$$n\mathrm{RCo_5} + \mathrm{R - Co} \rightarrow \mathrm{R_{n+1}Co_{5n-1}}. \tag{5.1}$$

For $n = 1, 2$ and 3 the compositions RCo_2, RCo_3 and R_2Co_7 are found, respectively. Higher values of n correspond to compositions that are closer to the RCo_5 composition. A value for n of 4 corresponds to the compound R_5Co_{19}. Indeed, this composition has been found for Co compounds with Ce, Pr and Nd.

Compositions in the Co-richer side are found to follow a rule in which one specific R ion with a large volume (about 24.4 Å^3) is replaced by a pair of Co ions (with a volume of about 8.2 Å^3):

$$n\mathrm{RCo_5} - \mathrm{R} + 2\mathrm{Co} \rightarrow \mathrm{R_{n-1}Co_{5n+2}}. \tag{5.2}$$

For $n = 3$ the composition R_2Co_{17} is obtained. Compositions with other values of n are hardly formed. The case $n = 2$ corresponds to RT_{12}, which composition is found in compounds of Mn. In compounds with Fe this phase is stabilized by small amounts of other metals such as the light 3d or 4d transition metals Ti, V, Cr and Mo. Higher values of n in eq. (5.2) again correspond to compositions that are closer to the RCo_5 composition from the Co-rich side. The compounds RCo_5 become progressively richer in Co towards the end of the rare-earth series. The 1:5 compound with erbium, for instance, is found with a composition close to $ErCo_6$, corresponding to $n = 8$ in eq. (5.2). An alternative way of characterizing compositions within the 1:5 and 2:17 range is to use a formula composition in which the excess Co pairs are given that substitute for R according to the equation

$$RCo_{5+x} \rightarrow R_{1-s}Co_{5+2s}. \tag{5.3}$$

The 2:17 composition is obtained for $s = \frac{1}{3}$. Comparing eqs. (5.2) and (5.3) one notices that the parameter s is just the reverse of n.

The systematics in the formation of the different compositions makes it clear that single-crystalline samples easily may contain inhomogeneous parts associated with concentration fluctuations that match due to the structural similarities discussed above to the crystal structures. In the analysis of the electronic and magnetic properties in terms of microscopic parameters the local symmetry and the local surrounding play decisive roles. The analysis becomes more complex in case the number of inequivalent crystallographic and magnetic sites for the ions involved increases. The notation of the non-equivalent crystallographic sites for the 3d and 4f ions in the Y_nT_m compounds is collected in table 5.1. In fig. 5.1, the variation of the Curie temperature with the R-ion involved is shown for the R_nT_m series with iron and for the series with cobalt in fig. 5.2. The maximum value of T_c is observed in all series for the Gd compounds indicating the effect of the spin of the rare-earth ion on T_c.

TABLE 5.1

Notation of the non-equivalent crystallographic sites for the R and T atoms in R_nT_m compounds according to the Wyckoff symbols.

Compound	Symmetry	R_1	R_2	T_1	T_2	T_3	T_4	T_5	T_6
RT_{12}	tetr	2a	–	8f	8i	8j	–	–	–
R_2T_{17}	hex	$2b_1$	$2b_2$	6g	12j	12k	4f	–	–
	rhomb	6c	–	6c	9d	18f	18h	–	–
$R_2T_{14}B$	tetr	4f	4g	4e	4c	$8j_1$	$8j_2$	$16k_1$	$16k_2$
RT_5	hex	1a	–	2c	3g	61*	2e*	–	–
R_6T_{23}	cubic	24e	–	4b	24d	$32f_1$	$32f_2$	–	–
R_5T_{19}	hex	3a	$6c_1, 6c_2$	3b	$6c_1$	$6c_2$	$6c_3$	$18h_1$	$18h_2$
R_2T_7	hex	4f	4f	2a	4e	4f	6h	12k	
	rhomb	$6c_1$	$6c_2$	3b	$6c_1$	$6c_2$	9e	18h	
RT_3	hex	2c	4f	2a	2b	2d	12k		
	rhomb	3a	6c	3b	6c	18h	–	–	–
RT_2	cubic	8a	–	16d	–	–	–	–	
	hex	4f	–	2a	6h	–	–	–	

*For T-rich off-stoichiometric compounds.

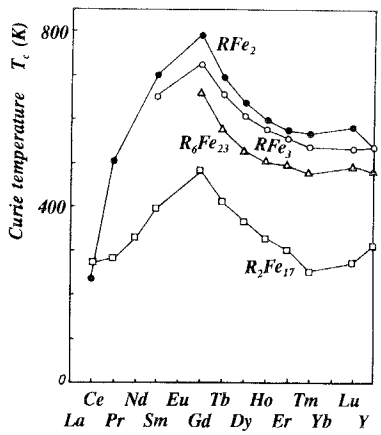

Fig. 5.1. Variation of the Curie temperature in R_nFe_m compounds with the R partner.

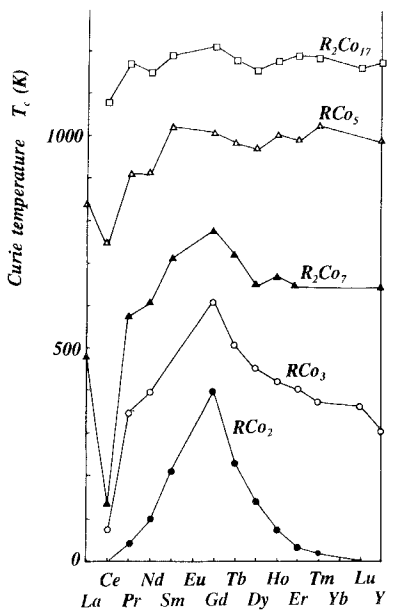

Fig. 5.2. Variation of the Curie temperature in R_nCo_m compounds with the R partner.

5.2. *RT_2 compounds (T = Fe, Co, Ni, Mn)*

All RT_2 compounds with Fe, Co and Ni crystallize in the cubic $MgCu_2$-type of Laves-phase structure (C15, space group Fd 3m). These compounds have extensively been studied in the past decades. The simple structure with a single crystallographic site for the R and T ions makes these compounds especially suited for an extensive

analysis of the basic magnetic interactions as a function of the rare-earth element and of the 3d partner. The local symmetry for the R ion is cubic and trigonal for the T ions. The $MgCu_2$ unit cell contains eight formula units. Each R ion has 12 T nearest neighbours, at a distance of $\frac{1}{8}\sqrt{11}a$, and four R ions at a distance of $\frac{1}{4}\sqrt{3}a$, where a denotes the lattice parameter. Each T ion has six T ions in the nearest-neighbour shell with a radius of $\frac{1}{4}\sqrt{2}a$ and six R ions at $\frac{1}{8}\sqrt{11}a$ as next-nearest neighbours. The lattice parameter of the cubic RT_2 compounds changes between 706 and 740 pm. In the various RT_2 series it decreases almost linearly with increasing number of 4f electrons. Some anomalies that are found for Ce and Yb compounds are indicative for their mixed-valence properties.

The RMn_2 compounds with Y, Sm, Gd, Tb, Dy, Ho crystallize in the same cubic C15 structure whereas the Pr, Nd, Sm Ho, Er, Tm and Lu compounds form the hexagonal $MgZn_2$ (C14) structure. These hexagonal and cubic structures are closely related as they result from different stacking of subsequent atomic layers. Contrary to the cubic structure where the T ions occupy only a single crystallographic site, in the hexagonal structure there are two Mn sites, (a) and (h). In both structures there is only one single site for the R ions. The Sm and Ho compounds have been found in both forms, depending on the heat treatment. The variation in the lattice parameter for the RMn_2 compounds across the rare-earth series is much more pronounced than in the Fe, Co or Ni series and provides arguments that the Mn valency is not preserved across the series. In fig. 5.3, the two structures are compared. The triangular arrangement of the 3d ions in the hexagonal structure leads to frustration effects in the exchange interactions with the nearest neighbours.

The magnetocrystalline anisotropy for a cubic system is conveniently expressed in terms of the directional cosines α_i of the magnetization vector with respect to the crystallographic axes:

$$E_a = K_0 + K_1^c(\alpha_1^2\alpha_2^2 + \alpha_2^2\alpha_3^2 + \alpha_3^2\alpha_1^2) + K_2^c(\alpha_1^2\alpha_2^2\alpha_3^2), \tag{5.4}$$

where K_i^c are the cubic anisotropy constants.

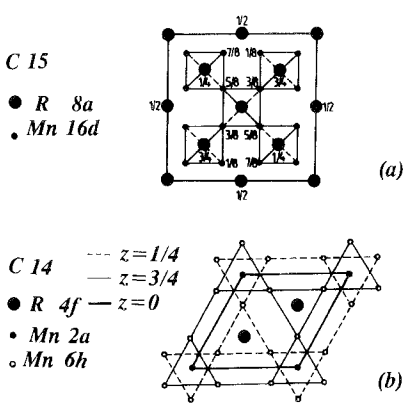

Fig. 5.3. Projection of the cubic C15 (a) and hexagonal C14 (b) crystallographic structures of the Laves-phase RT_2 compounds into the basal plane.

TABLE 5.2
Renormalization factors F_4 and F_6 for the R^{3+} ion occurring in the CEF Hamiltonian relevant for the crystal field interactions of the cubic symmetry. The number of CEF levels of the R^{3+} ion and of the allowed transitions in INS experiments is also given.

Ion	J	F_4	F_6	CEF levels	INS transitions
Ce/Sm	5/2	60	–	2	1
Pr/Pm	4	60	1260	4	4
Nd	9/2	60	2520	3	3
Gd/Yb	7/2	60	1260	3	2
Tb/Tm	6	60	7560	6	9
Dy/Er	15/2	60	13860	5	9
Ho	8	60	13860	7	16

The crystalline electric field for the 4f ion in the cubic symmetry as expressed by eq. (2.3) is often rewritten in the form (Lea et al. 1962)

$$H_{CF} = Wx(O_4^0 + 5O_4^4) + (1 - |x|)(O_6^0 - 21O_6^4). \tag{5.5a}$$

The parameters W and x are related to the crystal-field parameters B_n^m by:

$$Wx = F_4 B_4^0, \qquad W(1 - |x|) = F_6 B_6^0. \tag{5.5b}$$

F_4 and F_6 are numerical factors that have been collected for all rare-earth ions in table 5.2. The description by eq. (5.5) allows for a parametrization of the cubic CEF interactions by one single parameter since W is a scaling factor.

The anisotropy constants of the 4f sublattice can be deduced from the angular dependence of the energy level scheme of the 4f ion. The following relations hold:

$$4(F[110] - F[100]) = K_1^c \quad \text{and} \quad 3(F[111] - F[100]) = K_1^c + \tfrac{1}{9}K_2^c. \tag{5.6}$$

In case of $ErCo_2$, for instance, the energy difference between the easy and the hard axes, $F[111] - F[100]$, amounts to -50 K, whereas $F[111] - F[110]$ amounts to -22 K, see fig. 2.10. These values correspond to $K_1^{c,Er}$ and $K_2^{c,Er}$ at zero temperature of -112 K (-3.4 J/g) and -342 K (-10.4 J/g), respectively. In the RFe_2 and RCo_2 compounds these values are at least two orders of magnitude larger than those associated with the Fe or Co sublattice. Magnetoelastic studies in a wide temperature region have been reported for RNi_2 by Markosyan (1981a, 1982) and by Ibarra et al. (1984a,b), for RCo_2 by Lee and Pouranian (1976a,b), Markosyan (1981b) and Markosyan and Snegirev (1985). Magnetovolume effects in RCo_2 have been studied by Y. Nakamura (1983) and Muraoka et al. (1983, 1984) and analyzed in terms of the formation of the Co moment in the series Gd–YCo_2.

5.2.1. *RFe_2 compounds*

In the RFe_2 series, the compounds with La, Pm and Eu have not yet been reported to exist, whereas the compounds with Pr, Nd and Yb have been synthesized using high pressure and high temperature (80 kbar and 1300°C, Meyer et al. 1979, 1981). The compounds with Ce and Yb are of interest because of the anomalies related to

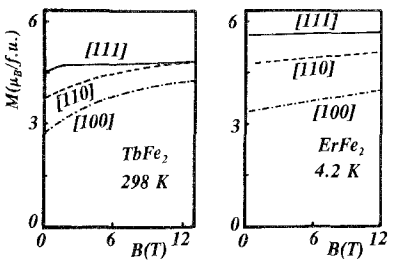

Fig. 5.4. Magnetization curves for single-crystalline $TbFe_2$ at 298 K and for $ErFe_2$ at 4.2 K along different cubic crystallographic directions. After Clark (1980).

the rare-earth valency that differs from 3+, as generally observed for the normal rare-earth ions.

Magnetization curves for single-crystalline samples in fields up to 12 T have been reported for $TbFe_2$ at 300 K and for $ErFe_2$ at 4.2 K by Clark (1979, p. 245), see fig. 5.4. The temperature dependence of the spontaneous moment has been presented by Clark (1979, p. 241) and Clark (1980, pp. 553–555) for single-crystalline $TbFe_2$, $DyFe_2$, $HoFe_2$, $ErFe_2$ and $TmFe_2$ over a wide range of temperatures. The iron sublattice moment, calculated from the spontaneous moment under the assumption of a full trivalent moment of the rare-earth ions, is close to the value of $3.0 \pm 0.1 \mu_B$/f.u. in compounds with the heavy rare-earth elements. The iron sublattice moment observed in these compounds agrees well with the value observed for YFe_2, confirming that the moment of the heavy rare-earth ions is very close to their maximal value and that the magnetic properties of the 3d sublattice are much the same for these compounds. A value for the iron moment of $1.85 \mu_B$ is obtained if one takes into account the moment of $-0.67 \mu_B$ that is induced at the Y site according to Ritter (1989).

The easy-axis direction derived by magnetization studies on single-crystalline samples confirms earlier results on polycrystalline samples by means of Mössbauer spectroscopy. Mössbauer as well as NMR spectra consist of a single subspectrum only when the easy-axis direction is along the $\langle 100 \rangle$ direction. Two subspectra with equal intensity are found for compounds in which the easy axis is along the $\langle 110 \rangle$ direction. In case the easy direction is along the $\langle 111 \rangle$ axis there are two subspectra but now with the intensity ratio of 3 : 1. In this way, details of the temperature-induced moment-reorientation phenomena can be effectively studied on polycrystalline samples with cubic symmetry. In experiments on $HoCo_2$ by Guimarães et al. (1987) the two NMR lines that are characteristic for the easy $\langle 110 \rangle$ direction gradually go over with increasing temperature into one line that is characteristic for the easy $\langle 100 \rangle$ direction. The direction of the easy axis of magnetization in the RT_2 compounds follows at low temperatures the sign of the fourth-order Stevens factor β_J, see table 2.7. A positive sign of β_J results in an easy direction along the body diagonal $\langle 111 \rangle$.

Moment reorientations are observed in Ce, Nd, Sm, Gd and Ho compounds at elevated temperatures. The temperature-induced moment-reorientation phenomena occurring in the RFe_2 compounds with Nd, Sm and Ho can be explained in terms

of single-ion crystal-field interactions. The difference in the easy-axis direction between YFe_2 and $GdFe_2$ points to an extra contribution due to the gadolinium ions. The gadolinium anisotropy probably has a band-structure origin like in Gd metal, where a temperature induced rotation of the easy axis of magnetization is also observed. Part of this anisotropy is due to dipolar interactions.

The cubic Laves-phase compounds were the first rare-earth intermetallics for which inelastic-neutron-scattering studies have been performed. Of the iron compounds, $ErFe_2$ (Koon and Rhyne 1981), $HoFc_2$ and $TbFe_2$ (Rhyne 1987, Koon nd Rhyne 1981) were studied, see figs. 3.14 and 3.15. Substantial CEF interactions are visible in the INS spectra. The energy levels are not equally separated as would be expected in the absence of CEF interactions.

The presence of substantial crystal-field effects in the RFe_2 compounds is also evident from specific heat data. Specific-heat measurements have been performed for RFe_2 compounds of the heavy-rare earth elements (Germano and Butera 1981). The crystal-field contribution to the specific heat as well as the magnetic entropy at 300 K have been deduced using $LuFe_2$ as a reference system. The magnetic entropy at 300 K is smaller than the theoretical value of $R\ln(2J+1)$ that is expected for the entropy related to thermal excitations over all levels of the ground-state multiplet. It indicates that the overall splitting of the 4f levels is of the order of or larger than 300 K. A unique set of crystal-field coefficients has not been found: A_4^0 varies between $+20\,\mathrm{K}\,a_0^{-4}$ and $+50\,\mathrm{K}\,a_0^{-6}$ and A_6^0 between -0.7 and $-2.6\,\mathrm{K}\,a_0^{-6}$. These crystal-field coefficients reproduce the magnetic heat capacity rather poorly. For these calculations the exchange field was assumed to have a constant value of 245 T.

The exchange field or rather the intersublattice molecular-field coefficient has been evaluated from free-powder high-field magnetization studies (Liu et al. 1991c). These studies lead to meaningful results only for ferrimagnetic compounds. Therefore only the compounds $(R-Y)Fe_2$ with heavy R partners have been studied. Y substitutions have been made in order to bring the noncollinearity region into the experimentally accessible field regime. These studies resulted in an exchange parameter J_{RFe} of -22.0 K for $Gd_{0.40}Y_{0.60}Fe_2$ and -19.1 K for $Er_{0.4}Y_{0.6}Fe_2$.

Systematic theoretical studies of the magnetocrystalline anisotropy in the Laves-phase RFe_2 compounds have been performed by Atzmony and Dariel (1976). The values for the coefficients A_4 and A_6, equal to $+32\,\mathrm{K}\,a_0^{-4}$ and $-1.2\,\mathrm{K}\,a_0^{-6}$ respectively, have been assumed to be constant through the series. For the exchange field, B_{ex}, a constant value of 225 T has been taken. These parameters satisfactorily reproduce many properties like the easy direction of magnetization, the rotation of the easy direction with temperature as well as the easy-axis phase diagram in $(R, R')T_2$ pseudo-binary compounds.

Magnetostriction properties have been summarized by Clark (1979, 1980) and Belov et al. (1983). The anisotropic part of the magnetostriction has been explained for most of the compounds within a single-ion model.

Transport measurements for RFe_2 compounds have been reported by Gratz et al. (1998). The thermopower as well as the resistivity show a pronounced decrease when passing T_c. This is the case for all compounds of heavy R elements. As the same behaviour is observed for YFe_2 and $LuFe_2$ it has been concluded that the Fe 3d

electrons play a dominant role in determining the transport properties. The correlation of the electronic structure of YFe_2 with that of other Laves-phase compounds of Fe with nonmagnetic partners such as Zr, Nb and Sc, have been discussed by Asano and Ishida (1987).

5.2.1.1. YFe_2. The value reported for T_c of YFe_2 amounts to 542 K. The easy direction of magnetization is along $\langle 111 \rangle$; the cubic anisotropy constant K_1^c at 4.2 K is equal to $-0.6\,J\,cm^{-3}$ (-2.0 K/f.u.). Magnetization studies on YFe_2 provide a value for the magnetic moment of $2.9\mu_B$/f.u. Attributing this moment to the iron atoms only, a moment of $1.45\mu_B$/(Fe ion) is obtained. Polarized neutron studies performed by Ritter (1989) reveal a moment at the yttrium site as large as $0.67\mu_B$ and antiparallel to the iron moment that has been found to be equal to $1.77\mu_B$. These results again reproduce the experimental value for M_s. The yttrium moment is in good agreement with theoretical calculations (Schwarz and Mohn 1984, Yamada et al. 1984, Brooks and Johansson, chapter 3 of this volume) and with ^{89}Y NMR studies (Armitage et al. 1986, 1989, Dumelow et al. 1986). The paramagnetic susceptibility yields a Curie constant of 2.28 K emu/mol and a value for Θ_p of 550 K (Burzo et al. 1985). NMR experiments give one single line at 45.94 MHz corresponding to a hyperfine field of 22.0 T (Alves et al. 1986). With a value for the proportionality factor of $14.8\,T/\mu_B$, this hyperfine field results in a value for the Fe moment of $1.5\mu_B$. The pressure derivative of the hyperfine field is negative for Fe and positive for Y (Riedi and Webber 1983). Muon resonance spectroscopy for the compounds with Y, Lu, Gd, Er and Tm has been reported by Barth et al. (1986). From these studies it is concluded that the main contribution to the hyperfine field experienced at the interstitial muon site originates from the 3d electrons.

5.2.1.2. $CeFe_2$. The compound $CeFe_2$ shows mixed-valence behaviour. A valency larger than three is inferred from the reduced spontaneous moment, of about $2.30\mu_B$/f.u. at 4.2 K, and from the reduced value for T_c of 230 K compared to the other RFe_2 compounds. Moreover, CeT_2 compounds with Fe, Co and Ni show an anomalously small lattice parameter compared with the other RT_2 compounds. The value of the hyperfine field at ^{57}Fe of 16.0 T (Pszczoła et al. 1990) is also significantly lower than the value of 22.0 T observed in $DyFe_2$, for instance. Polarized neutron experiments have been reported by Deportes et al. (1981). The thermal variation of the paramagnetic susceptibility measured up to 1000 K roughly follows the C–W law (Brown et al. 1982). Attributing the Curie constant fully to the iron moments, one derives a value of $3.7\mu_B$/Fe-ion, substantially larger than that observed for YFe_2, indicating the presence of a cerium contribution. This is consistent with computations of Eriksson et al. (1988a,b) and Johansson et al. (1991) who considered the hybridization between 3d and rare-earth conduction electron bands suggesting that the total moment of $CeFe_2$ consists of a moment of $1.43\mu_B$ per iron atom and a moment of $0.7\mu_B$ per Ce atom, antiferromagnetically coupled to the iron moment. The Curie temperature is decreased rapidly by Al substitutions. Moreover, the ferromagnetic state changes into the antiferromagnetic state when the Al substitutions exceeds 7% (Kido et al. 1990). Kennedy et al. (1988) have reported a transition from the ferro- to the antiferromagnetic

state in the Ce(Fe–Co)$_2$ series. The EMD for $CeFe_2$ is along $\langle 001 \rangle$ below 132 K above which temperature the Fe moments deviate from the cubic edge by about 20° (Forsthuber et al. 1990). The CEF interactions have been studied by Atzmony et al. (1976) in order to explain magnetic anisotropic properties. By comparing the magnetic and transport properties, the interatomic distances and the electronic specific-heat coefficients of the RFe_2 compounds it has been concluded that, within this series, $CeFe_2$ exhibits exceptional behaviour with features similar to UFe_2 (Rastogi et al. 1988). Actually, the coefficient γ amounts to 53 mJ/K^2 mol (Roy and Coles 1989) and is four times larger than that observed in YFe_2 and close to the value of 45 mJ/K^2 mol reported for UFe_2 by Franse et al. (1981). Paramagnetic neutron scattering experiments performed above the ordering temperature point to the existence of short-range ferromagnetic correlations between iron moments of the order of $0.5\mu_B$ (Lindley et al. 1988). Croft et al. (1987) have reported a Ce-ion valency of 3.3 on the basis of L_{III} X-ray absorption experiments.

5.2.1.3. $PrFe_2$. A polycrystalline sample has been prepared under high pressure and high temperature by Meyer et al. (1979, 1981) and by Shimotomai et al. (1980). Mössbauer spectroscopy indicates that the easy axis is along the $\langle 100 \rangle$ direction (Meyer et al. 1979, 1981). Shimotomai et al. (1980) have reported a value for the magnetic moment at 78 K in an external field of 1.5 T of $4.7\mu_B$/f.u., indicating ferromagnetic alignment of the Fe and Pr moments. An anomaly in the vicinity of 200 K has been attributed by Shimotomai and Doyama (1983) to a moment reorientation. For T_c a value of 543 K has been reported (Meyer et al. 1981).

5.2.1.4. $NdFe_2$. For the compound $NdFe_2$, values for T_c of 578 K and for M_s of $4.6\mu_B$/f.u. at 78 K and at 1.5 T have been reported by Meyer et al. (1981) and Shimotomai et al. (1980). The ^{57}Fe Mössbauer spectra of $NdFe_2$ exhibit two subspectra with an intensity ratio of 1 : 1, characteristic for a magnetization direction along $\langle 110 \rangle$. With increasing temperature the two subspectra change into a single spectrum around 160 K, suggesting a rotation of the magnetization from $\langle 110 \rangle$ towards $\langle 100 \rangle$. Similar phenomena have also been observed for $NdCo_2$ and explained by CEF interactions at the Nd site. NMR experiments at ^{143}Nd nuclei indicate that the Nd-ion moment is close to saturation, although the hyperfine field of 339 T is considerably smaller than the free-ion value, of 425.3 T. This difference has been attributed by Meyer et al. (1981) to a substantial contribution of the transferred hyperfine field. The effect of Y substitutions on the TIMR have been studied by Baranov et al. (1983) on the (Nd–Y)Co_2 compounds. A weak variation of the MR temperature is well understood within the CEF and exchange interactions. A value of $3.6\mu_B$/f.u. has been reported for M_s at 4.2 K for $NdCo_2$.

5.2.1.5. $SmFe_2$. For a polycrystalline sample of $SmFe_2$, a value for the spontaneous moment at 4.2 K of $2.25\mu_B$/f.u. has been reported by Clark (1980, p. 556). It is much smaller than expected for a parallel alignment of Fe and Sm moments. An explanation has been provided by de Wijn et al. (1976) in terms of J mixing that may lead to an antiparallel alignment of the Fe and Sm moments, as observed for the heavy R's.

The moment-reorientation with increasing temperature near 180 K from ⟨110⟩ to ⟨111⟩ can be accounted for by the single-ion model with values: $A_4^0 = +44\,\mathrm{K}\,a_0^{-4}$, $A_6^0 = -9.5\,\mathrm{K}\,a_0^{-6}$ and $B_{ex}^{Sm} = 195\,\mathrm{T}$. Atzmony and Dariel (1976) have used different values for A_4 and A_6: $+32\,\mathrm{K}\,a_0^{-4}$ and $-1.2\,\mathrm{K}\,a_0^{-6}$, respectively. In these calculations a value of 150 K for $\mu_B B_{ex}^{Sm}$ was used. The moment reorientation is accompanied by a sharp minimum in the temperature dependence of the elastic constants (Clark 1980, p. 569).

5.2.1.6. $GdFe_2$. The EMD of $GdFe_2$ is along ⟨100⟩ which is different from what is observed in YFe_2. This fact, in combination with the temperature-induced moment-reorientation transition indicates an extra gadolinium contribution that is likely of a band-structure origin.

5.2.1.7. $TbFe_2$. Magnetization measurements at 298 K on a single-crystalline sample of $TbFe_2$ performed by Clark (1979, 1980) are shown in fig. 5.4. INS experiments performed by Koon and Rhyne (1981) have allowed for quantification of CEF interactions of the Tb^{3+} ion as shown in table 5.3. These CEF parameters can fully account for the moment orientation phase diagram observed in the (Tb–Ho)Fe_2 series (Koon et al. 1991). Hyperfine interactions of the Tb ion have been quantified by NMR studies on ^{159}Tb (de Azevedo et al. 1985, K. Shimizu 1987).

TABLE 5.3
Crystal-field parameters and the exchange field in the RFe_2 and RCo_2 compounds with the cubic Laves-phase structure C15.

Compound	W(K)	x	A_4 (K a_0^{-4})	A_6 (K a_0^{-6})	B_{ex}^R (T)	Ref.*
RFe_2			+32	−1.2	225	[1]
$SmFe_2$			+44	−9.5	195	[2]
$ErFe_2$	−0.277	−0.4019	+32.9	−1.20	233	[3]
$TbFe_2$			+36.6	−1.39	240	[4]
$HoFe_2$			+36.6	−1.39	240	[4]
RCo_2			+32	−1.2	150	[5]
$HoCo_2$	+0.6	−0.4687	+101	−3.3	85	[6, 7]
$TbCo_2$	+0.75	+0.8	+49.5	−2.5	147	[6]
$NdCo_2$	+2.9	−0.18	+10.2	−1.65	165	[8]
$NdCo_2$	+4.0	−0.20				[9]
PCM			+24.0	−0.2		[6]
$ErCo_2$			+44.2	−1.4	79	[3, 10]
$ErAl_2$			+23.0	−1.3		[11]

*References:

[1] Atzmony and Dariel (1976).
[2] de Wijn et al. (1976).
[3] Koon and Rhyne (1981).
[4] Koon et al. (1991).
[5] Dublon and Atzmony (1977).
[6] Gignoux et al. (1979b).
[7] Aubert et al. (1978).
[8] Gignoux et al. (1975).
[9] Baranov et al. (1983).
[10] Rhyne (1987).
[11] Boucherle et al. (1989).

5.2.1.8. $DyFe_2$. In $DyFe_2$ the value for the ^{57}Fe hyperfine field of 22 T at 4.2 K (Pszczoła et al. 1990) points to an Fe moment of $1.5\mu_B$. Magnetic properties of $Dy(Fe–Al)_2$ have been studied by Bara et al. (1982a).

5.2.1.9. $HoFe_2$. INS experiments on $HoFe_2$, presented by Koon and Rhyne (1981) and by Rhyne (1987), reveal a strongly dispersive mode that has a $q = 0$ intercept Δ_2 of 9.0 meV at 300 K and of approximately 17 meV at 10 K, see fig. 3.15. The stiffness parameter D of 2.4 meV nm^2 assigns this mode to excitations of the 3d spins. INS spectra have been analyzed within the single-ion Hamiltonian of the 4f ions and result in a set of CEF parameters and in a value for the parameter J_{RT}. The magnetic structure has been established by Fuess et al. (1979) by means of neutron-diffraction experiments. NMR experiments on ^{165}Ho in $(Gd, Ho)Fe_2$ have been performed by Prakash et al. (1983).

5.2.1.10. $ErFe_2$. Single-crystal magnetization studies on $ErFe_2$ at 4.2 K by Clark (1980) are presented in fig. 5.4. Inelastic neutron scattering experiments performed by Koon and Rhyne (1981) and Rhyne (1987) have been presented in fig. 3.16. At 4.2 K there are two lowest energy modes: a $\boldsymbol{q}$-independent mode with $\Delta_{loc} = 12.4$ meV and an acoustic mode with a Δ_2 of 8.3 meV. The INS spectra are highly temperature dependent. At 300 K the flat mode has an energy gap of 5 meV whereas the acoustic branch has a very small energy gap. New peaks appear that are due to excitations from the second and subsequently the third level to higher excited Er levels. These peaks appear at much lower energies indicating substantial CEF interactions. The compensation of the magnetization occurs at 486 K.

5.2.1.11. $TmFe_2$. A value for T_c of 599 K has been reported for $TmFe_2$. The easy direction of the magnetization is along $\langle 111 \rangle$. The Tm moment is found to be close to the free-ion value. A compensation of the magnetization occurs at 225 K. The nearly full Tm moment in $TmFe_2$ has been revealed by ^{169}Tm Mössbauer spectroscopy by Bleaney et al. (1982).

5.2.1.12. $YbFe_2$. Samples of $YbFe_2$ have been prepared under extreme conditions: 80 kbar and 1200°C (Meyer et al. 1979, 1981). Magnetic measurements show that $YbFe_2$ is a ferrimagnet compound with a value for T_c of 543 K. The compensation temperature is found to be 31 ± 7 K. The occurrence of compensation proves that the Yb-ion is trivalent in $YbFe_2$ with a moment close to $4\mu_B$. This is further confirmed by the value for the hyperfine field on ^{170}Yb of 444 T, a value that is slightly higher than the free-ion value of 417 T. According to the ^{57}Fe Mössbauer spectra the easy magnetic direction is along $\langle 100 \rangle$. Above 50 K, however, the easy direction seems to slightly deviate from that direction. The temperature dependence of the hyperfine field H_{eff} at the ^{170}Yb nuclei drops rapidly with increasing temperature from a value of 444 T at 4.2 K. This temperature dependence has been found to follow a Brillouin curve, yielding a value of 111 K for $\mu_B H_{ex}$. On the basis of these results, Meyer et al. (1981) concluded that the crystalline electric field in $YbFe_2$ is fairly small.

5.2.1.13. $LuFe_2$. The value for the Curie temperature of $LuFe_2$ is substantially larger than in the Y compound: 596 and 535 K, respectively. Taking into account the lanthanide contraction, this difference is consistent with a strong volume dependence of T_c. Band-structure calculations of Brooks et al. (1989, 1991b) have revealed a small orbital moment of iron $0.07\mu_B$ and a dominant spin moment of $1.56\mu_B$. Moreover, there is a moment of $-0.41\mu_B$ at the Lu site, similar to that at the Y site in YFe_2. The presence of an iron orbital moment is in agreement with polarized neutron experiments (Givord et al. 1980). The temperature behaviour of the local field detected by means of μSR experiments follows closely the macroscopic magnetization (Barth et al. 1986). Butera et al. (1979) have found from specific-heat experiments values of 12.8 mJ/K^2 mol and 296 K for γ and Θ_D, respectively.

5.2.2. RCo_2 Compounds

The RCo_2 compounds have attracted much attention for more than 25 years due to some peculiar phenomena related to the metamagnetism of the cobalt moment. YCo_2 is an exchange-enhanced paramagnetic compound, whereas in compounds with a magnetic rare-earth element, cobalt moments up to $1\mu_B$ are observed. In RCo_2, the Co moment is induced by exchange interactions between the 3d and 4f spins.

The transition from the paramagnetic to the magnetically ordered state has been found for the compounds with Pr, Nd, Dy, Ho, Er to be accompanied by a large and sudden increase in volume that is characteristic for a first-order transition and by smooth volume changes for $GdCo_2$ and $TbCo_2$, for which compounds the transition is second-order. This difference between first- and second-order transitions has been related to the value of T_c. With increasing ordering temperature the transition becomes second order. A value of 200 K for T_c is regarded as the border temperature below which the transition is first order. In more advanced studies, the order of the transition has been attributed to the sign of the coefficient, a_3, of the fourth-order term in the expansion of the free energy in terms of the 3d magnetization M_d (Bloch et al. 1975) or of the total magnetization M (Inoue and Shimizu 1988). A generalization of the Inoue–Shimizu model for the multicomponent magnetic system has been provided by Brommer (1989). By the replacement of Co by Al atoms in the RCo_2 compounds with R = Dy, Ho and Er the first-order transition changes to a second-order one. The effect has been discussed by Duc et al. (1991) in terms of the Inoue–Shimizu model by considering a concentration dependence of the coefficient a_3. In these calculations the value of 2.1×10^6 mol/m^3 (= 15.0 T f.u./μ_B) for the intersublattice molecular-field coefficient n_{Ho-Co} has been used.

The Curie temperature reaches its maximal value of 395 K for $GdCo_2$ and rapidly decreases with lower spin values of the rare-earth element, being only 32.6 K for $ErCo_2$. The decrease is much faster than expected from the de Gennes factor. This faster decrease has been explained by a substantial variation of the 3d susceptibility with temperature (Duc et al. 1988a,b), consistent with the maximum in the susceptibility of YCo_2 at 300 K (Lemaire 1966b, Ikeda et al. 1984). The paramagnetic behaviour of RCo_2 compounds formed with the heavy rare-earths has been analyzed by Burzo (1972) and by Bloch and Lemaire (1970) by taking into account the localized R moment and the itinerant character of the Co moment.

YCo_2 undergoes a collective-electron metamagnetic transition as discussed in section 4.8. A nonlinear magnetic response of YCo_2 has been observed at 4.2 K in fields above 30 T (Schinkel 1978). Later on the pronounced metamagnetic transition has been observed at 69 T (Goto et al. 1990). The same kind of transition for $LuCo_2$ occurs at 75 T. The large increase of T_c for RCo_2 compounds, in which small amounts of cobalt have been replaced by Al, has been discussed in terms of a strong volume dependence of the band parameters (Aleksandryan et al. 1984a).

The specific heat has been measured for YCo_2 (Muraoka et al. 1977), for (R–Y)Co_2 (Hilscher et al. 1988, Pillmayr et al. 1987, 1988), for (Tb–Y)Co_2 (Berthier et al. 1986) and for (Y–Er)Co_2 (Duc et al. 1988a). The electronic specific heat can be approximated by a γ value of 36–38 mJ/K^2 mol. The Debye temperature has been found to be 270 K in YCo_2. Values for the Debye temperature up to 300 K are reported for the compounds with magnetic R partners. NMR studies at 4.2 K in external fields have been performed by Hirosawa and Nakamura (1982) for R = Pr, Nd, Sm, Gd, Tb, Dy, Ho, Er and Tm. The correlation between the type of NMR spectrum and the easy magnetic direction as well as the influence of external fields on the NMR spectrum of the RCo_2 compounds have been discussed by Englich et al. (1990). Resistivity data in the numerous (R–Y)Co_2 compounds have been discussed by Duc et al. (1991) in terms of spin fluctuations in the Co matrix associated with the onset of the Co moment. Magnetostriction studies on RCo_2 and the Fe substituted compounds have been reported by Aleksandryan et al. (1984b, 1987).

Inelastic neutron scattering experiments have been reported for $HoCo_2$ (Castets et al. 1982a) and $ErCo_2$ (Koon and Rhyne 1981, Rhyne 1987). By the direct observation of localized excitations these studies have significantly contributed to the evaluation of the CEF and exchange interactions. The single-ion rare-earth anisotropy has been calculated by Dublon and Atzmony (1977) assuming values for the CEF coefficients $A_4 = +32\,\mathrm{K}\,a_0^{-4}$ and $A_6 = -1.2\,\mathrm{K}\,a_0^{-6}$. A constant value for the exchange field of 150 T has been assumed. In principle, these parameters explain in a satisfactory way the EMD through the series as well as the magnitude of the anisotropy and its temperature dependence. As far as the relative magnitude of the exchange and CEF interactions is concerned, the RCo_2 compounds fall into the class of compounds with comparable strength of these interactions.

Magnetostriction of $R_xR'_{1-x}Co_2$ compounds with R = Tb, Dy and Er have been studied by Aleksandryan et al. (1984b). Moment-reorientation phenomena have been found to be accompanied by large magnetostriction effects. The anisotropic part in the magnetostriction has been evaluated by Levitin and Markosyan (1988, 1990). A rhombohedral or tetragonal distortion has been found depending on the direction of the easy axis. The latter has in turn been related to the sign of the fourth-order Stevens factor β_J as it has been discussed in section 2.3.

5.2.2.1. YCo_2. The compound YCo_2 is an exchange-enhanced Pauli paramagnet. A collective-electron metamagnetic transition, as discussed in section 4.8, has been observed at 4.2 K at a field of 69 T (Goto et al. 1990). The cobalt moment in a field of 90 T amounts to $0.5\mu_B$, see fig. 4.14. Ferromagnetism in YCo_2 can be induced by Al substitutions, see fig. 4.13, and by hydrogenation (Yoshimura and Nakamura 1985,

Wada et al. 1990). The magnetization at 4.2 K of $YCo_2H_{3.5}$ in a field of 8 T amounts to $0.58\mu_B$/f.u. (Fujiwara et al. 1990). The specific heat at low temperatures can be approximated by $\gamma = 36\,mJ/K^2\,mol$ and $\Theta_D = 270\,K$ (Muraoka et al. 1977). Slightly different values have been reported by Ikeda et al. (1984) and by Wada et al. (1989), see table 2.12. The temperature variation of the metamagnetic transition in $YCo_{0.9}Al_{0.1}$ has been studied by Sakakibara et al. (1991).

5.2.2.2. $CeCo_2$. The compound $CeCo_2$ is an exchange-enhanced paramagnetic material with a value of 0.95 for the Stoner product (Eriksson et al. 1988a,b, Johansson et al. 1991). The valency of the Ce ion has been derived to be 3.3 from L_{III} X-ray absorption studies (Croft et al. 1987). Band-structure calculations lead to $\gamma = 14.7\,mJ/K^2\,mol$ in fairly good agreement with the experimental value of $21\,mJ/K^2\,mol$ (Sa et al. 1985).

5.2.2.3. $PrCo_2$. The transition from ferro- to paramagnetism in $PrCo_2$ occurs at 49 K and is accompanied by a substantial but smooth anomaly in the thermal expansion indicating a second-order transition (Lee and Pouranian 1976a,b). A much lower value for T_c of 40 K has been reported by de Jongh et al. (1981) on the basis of ac susceptibility measurements. The magnetization curve at 4.2 K of the polycrystalline specimen reported by these authors gradually increases reaching $3.9\mu_B$/f.u. at 30 T. This value can be understood by the value of $2.2\mu_B$/f.u. found for Pr^{3+}-ion moment from hyperfine specific heat and the cobalt moment of $0.85\mu_B$. The easy direction of magnetization is along $\langle 100 \rangle$, indicating the dominancy of the B_4 CEF term.

5.2.2.4. $NdCo_2$. A spin reorientation from $\langle 110 \rangle$ to $\langle 100 \rangle$ occurs in $NdCo_2$ at 42 K which can be understood as a CEF effect at the Nd site (Gignoux et al. 1975). The TIMR is accompanied by a sharp peak in the specific heat. The energy level scheme of the Nd^{3+} ion is shown in fig. 2.14. At helium temperature only the lowest level is occupied only and its energy is the lowest for the direction $\langle 110 \rangle$. With increasing temperature the minimum of the free energy shifts to the $\langle 100 \rangle$ direction. The TIMR is indicative for a substantial contribution to the anisotropy from the sixth-order CEF interactions. Similar phenomena occur in $HoCo_2$ and possibly in $NdFe_2$. The effect of Y substitutions on the temperature of the moment reorientation has been studied by Baranov et al. (1983) on the (Nd–Y)Co_2 compounds. The weak variation of this temperature found experimentally indicates that the CEF interactions of the Nd ion are not significantly modified with the Y substitutions. The authors reported a value of $3.6\mu_B$/f.u. for the spontaneous moment at 4.2 K.

5.2.2.5. $GdCo_2$. Magnetization measurements on $GdCo_2$ have been performed on a single-crystalline specimen by Gignoux et al. (1975). The high-field susceptibility measured up to 14 T by Kaneko et al. (1988) amounts to $5 \times 10^{-3}\mu_B$/T f.u. Additional magnetization measurements on a single-crystalline sample at temperatures above 78 K have been reported by Katayama and Shibata (1981). The ferromagnetic–paramagnetic transition is second-order which has been related by Bloch et al. (1975) to the high value for T_c of 395 K. The formation of the Co moment in RCo_2 compounds

has been studied by Y. Nakamura (1983) and Muraoka et al. (1983, 1984) by observing the magnetovolume effect as a function of the Gd content in the series (Y–Gd)Co_2. The moment reorientation at 180 K from ⟨100⟩ to ⟨110⟩ has been studied by NMR (Karnachev et al. 1986). The presence of the TIMR transition in $GdCo_2$ has to be attributed to anisotropy effects within the Co subsystem. The 3d moment of Gd(Co–Ni)$_2$ has been reported by Kaneko et al. (1988) to decrease linearly with the Ni concentration.

5.2.2.6. $TbCo_2$. The transition from the magnetic to the paramagnetic state in $TbCo_2$ is second order, contrary to the compounds with heavier rare-earth partners. Single-crystal magnetization curves, reported by Gignoux et al. (1979a), are shown in fig. 5.5. The EMD lies along cube diagnoal for which direction a value for M_s of $6.83\mu_B$/f.u. at 4.2 K has been found. This value for the spontaneous moment is accounted for by Tb and Co moments of 8.93 and $1.12\mu_B$, respectively. Along the easy magnetization direction a substantial susceptibility of $5.7 \times 10^{-2}\mu_B$/T f.u. has been reported. A value of 98 T has been derived for the molecular field B_{mol}^{Tb}. The CEF coefficients are shown in table 5.3. The specific heat of (Tb–Y)Co_2, studied by Berthier et al. (1986), reveals a complex behaviour at low temperatures, leading to a nonregular dependence of the coefficient γ on the Y content. This nonmonotonic behaviour is likely due to CEF effects. A rhombohedral distortion of the cubic elementary cell has been reported by Abd El-aal et al. (1987). The effect of other heavy rare-earth elements on the magnetostriction constants of $TbCo_2$ has been studied by Levitin and Markosyan (1990). The results have been discussed in terms of the 4f single-ion properties.

5.2.2.7. $DyCo_2$. The magnetic transition of $DyCo_2$ at T_c (= 140 K) is first-order. By a 7.5% replacement of the Co atoms by Al the first-order transition changes into the second-order one as has been revealed by magnetization, thermal-expansion and electrical-resistivity measurements (Duc et al. 1991). The effect has been discussed within the Inoue–Shimizu model. In the calculations values of 19.3 T f.u./μ_B and 3.4 T f.u./μ_B have been used for the molecular-field coefficients n_{Dy-Co} and n_{Dy-Dy}, respectively. The tetragonal distortion of the cubic cell due to the magnetostriction has been studied by Levitin and Markosyan (1990).

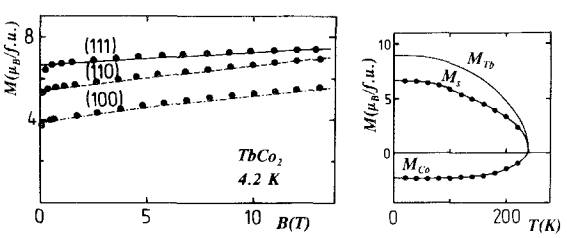

Fig. 5.5. (a) Magnetization curves at 4.2 K for single-crystalline $TbCo_2$ along different cubic crystallographic directions; full circles: experimental points; drawn curves: calculated results. (b) The thermal variation of the spontaneous moment of $TbCo_2$ split into that of the Co and Tb moments. After Gignoux et al. (1979a).

5.2.2.8. $HoCo_2$. A temperature-induced spin reorientation has been observed in $HoCo_2$ from the $\langle 110 \rangle$ direction at low temperatures to the $\langle 100 \rangle$ direction above 20 K. Aubert et al. (1978) have interpreted the spin reorientation by a crystal-field approach with $W = 0.6$ K, $x = -0.4665$ and $B_{mol}^{Ho} = 33.4$ T. Similar parameters have also been found by Gignoux et al. (1975). Details of the temperature-induced spin reorientation have been investigated by NMR experiments on ^{59}Co nuclei (Guimarães et al. 1987). The reorientation sets in between 18 and 20 K as indicated by the gradual change of the NMR spectra from two lines of equal intensity to one resonance line with increasing temperature. Inelastic neutron scattering experiments on $HoCo_2$ have been performed by Castets et al. (1982a). These authors analyzed the spectra with the same values for the crystal-field parameters as obtained by Aubert et al. (1978) from magnetization studies. The fit is not satisfactory. Yamada and Shimizu (1982) incorporated the itinerant character of the Co moment in $HoCo_2$ into the spin-wave model but still details of the magnetic excitations remain unsatisfactorily described. Transport properties have been measured by Gratz et al. (1987).

5.2.2.9. $ErCo_2$. Single-crystal magnetization curves of $ErCo_2$ up to 6 T have been reported by Aleksandryan et al. (1988). The EMD lies along the $\langle 111 \rangle$ direction; the value for M_s at 4.2 K is equal to $7.7\mu_B$/f.u. The $\langle 100 \rangle$ direction is the hard axis. At T_c, $ErCo_2$ undergoes a first-order transition connected with the collapse of the Co moment. The INS spectra presented in fig. 3.14 have been analyzed within the single-ion Hamiltonian (Koon and Rhyne 1981, Rhyne 1987). Specific-heat measurements show a large peak at T_c (Duc et al. 1988a) that is related with the first-order phase transition. The magnetic entropy up to 40 K amounts to 16–17 J/K mol and indicates that seven to eight levels of the 15/2 multiplet are involved in the magnetic transition. Specific-heat measurements on the $(Er–Y)Co_2$ series have been reported for the Er-rich side by Duc et al. (1988a) and for the Y-rich side by Pillmayr et al. (1988). A spin-glass-like behaviour has been claimed by the latter authors. A further analysis of these data within the single-ion Hamiltonian resulted in an evaluation of CEF and exchange field interactions of the trivalent Er ion (Radwański and Franse 1993). The angular dependence of the energy-level scheme of the erbium ion with a value of 26.4 T for the molecular field has been presented in fig. 2.11. The overall molecular field splitting amounts to 315 K whereas the overall CEF splitting amounts to 110 K only. The first excited level is situated 90 K above the ground state causing a small contribution to the low-temperature specific heat. The molecular field of 26.4 T derived for B_{mol}^{Er} is in good agreement with the estimated value of 20 T for $B_{mol,RT}^{Er}$ (Radwański 1986b). The contribution from the R–R interaction to B_{mol}^{Er} has been estimated to be smaller than 4 T. Any magnetic field (internal or external) drastically changes the energy-level scheme. This strong field dependence is responsible for the complex temperature dependence of the electronic and magnetic properties of $ErCo_2$ and their complex concentration dependence in the $(Y–Er)Co_2$ compounds.

5.2.2.10. $TmCo_2$. Polarized-neutron experiments on $TmCo_2$ at 4.2 K performed by Gignoux et al. (1976) have provided values for the Tm and cobalt moments of 5.4 and $0.8\mu_B$, respectively. A value for M_s of $4.3\mu_B$/f.u. found by these authors for a

single-crystalline $TmCo_2$ is not directly consistent with the above-mentioned neutron results. Mössbauer studies performed by Gubbens et al. (1982) confirm the first-order character of the transition from ferro- to paramagnetism at 20 K.

5.2.2.11. $LuCo_2$. The compound $LuCo_2$ has similar properties as YCo_2. A collective-electron metamagnetic transition has been observed at 75 T which is at slightly higher fields than in YCo_2, see fig 4.14. The jump of the Co moment at the transition is substantially larger than in YCo_2, 0.27 vs 0.49 μ_B, respectively. The onset of induced ferromagnetism has previously been observed by Al substitution (Gabelko et al. 1987, K. Endo et al. 1987, 1988). A cobalt moment as large as 0.7 μ_B has been found for an Al concentration of 10%, see fig. 4.12. Ikeda et al. (1991) discussed electronic and magnetic properties of $LuCo_2$, the influence of external magnetic fields on specific heat in particular, in terms of strongly exchange-enhanced paramagnetic properties with the Stoner enhancement factor S of 17.

5.2.3. RNi_2 compounds

Single-crystal magnetization measurements (Gignoux et al. 1975, Gignoux and Givord 1977, 1983) have revealed that for the RNi_2 compounds the easy direction of magnetization is along the $\langle 100 \rangle$ direction for Pr, Ho and Dy and along the $\langle 111 \rangle$ direction for Tb and Er. The magnetic susceptibility in the paramagnetic region is well approximated by the Curie–Weiss law with the Curie constant accounted for by the R^{3+}-ion value (Burzo and Laforest 1972). Magnetostriction measurements on polycrystalline RNi_2 compounds have been performed for the Pr, Nd, Sm, Tb, Dy, Ho, Er and Tm compounds by Ibarra et al. (1984a,b) and Ibarra and del Moral (1990) following earlier studies of Markosyan (1981a, 1982). The anisotropic contribution has been correlated with the single-ion properties of the R ion involved.

Inelastic-neutron-scattering spectra have been reported for $PrNi_2$ (Greidanus et al. 1983, Mühle et al. 1989), for $HoNi_2$ (Castets et al. 1982b) and for compounds with Pr, Nd, Tb, Ho, Er and Tm (Goremychkin et al. 1989). CEF coefficients for RNi_2 compounds are collected in table 5.4. Although the values show a substantial variation, both coefficients A_4^0 and A_6^0 keep their sign independent of the R partner.

5.2.3.1. YNi_2. The compound YNi_2 is a weakly exchange-enhanced Pauli paramagnet with $\chi(4.2\,\mathrm{K}) = 2.5 \times 10^{-9}\,\mathrm{m^3/mol}$. Specific-heat measurements by Mori et al. (1982) in the temperature region 1.5–10 K yield $\gamma = 6.0\,\mathrm{mJ/K^2\,mol}$ and $\Theta_D = 264\,\mathrm{K}$. Deutz et al. (1989) have reported a value of $5.2\,\mathrm{mJ/K^2\,mol}$ and 291 K for γ and Θ_D, respectively. The electronic properties of YNi_2 have been discussed in terms of a substantial hybridization of 4d and 3d bands. NMR experiments on $Y(Ni,Co)_2$ compounds have been reported by Nagai et al. (1988b).

5.2.3.2. $LaNi_2$. Specific-heat experiments on $LaNi_2$ by Sahling et al. (1982) yield: $\gamma = 15.9\,\mathrm{mJ/K^2\,mol}$ and $\Theta_D = 231\,\mathrm{K}$.

5.2.3.3. $CeNi_2$. The compound $CeNi_2$ behaves as a mixed-valence system or weakly enhanced paramagnet which properties have been widely discussed by Johansson

TABLE 5.4
CEF parameters of the R^{3+} ion in RNi_2 compounds. A_n in units of $K a_0^{-n}$.

Compound	W(K)	x	A_4	A_6	Ground state	Ref.*
$PrNi_2$	−2.20	+0.62	+9.1	−1.72	Γ_3	[1]
$PrNi_2$	−2.09	0.58	+9.0	−0.61	Γ_3	[2, 3]
$NdNi_2$	+3.25	+0.28	+56.9	−2.4	Γ_6	[2]
$TbNi_2$			+48	−2.6		[4]
$TbNi_2$	−0.77	−0.73	+46.1	+3.6	Γ_1	[2]
$DyNi_2$	−0.8	+0.49	+73	−4.6		[5]
$HoNi_2$	0.62	−0.5				[6]
$HoNi_2$	0.27	−0.5				[7]
$HoNi_2$	+0.24	−0.44	+39.0	−1.4	$\Gamma_5^{(1)}$	[2]
$ErNi_2$	−1.0	−0.35				[8]
$ErNi_2$	−0.39	−0.54	+62.9	−1.31	$\Gamma_8^{(3)}$	[2]
$TmNi_2$	+0.64	+0.38	+21.15	−2.16		[9]
	+0.65	+0.71	+40.14	−1.02		[9]
$TmNi_2$	+0.71	+0.62	+38.2	−1.5	Γ_1	[2]

*References:
[1] Greidanus et al. (1983).
[2] Goremychkin et al. (1989).
[3] Mühle et al. (1989).
[4] Ibarra et al. (1984a).
[5] Gignoux and Givord (1977).
[6] Gignoux et al. (1975).
[7] Castets et al. (1982b).
[8] Gignoux and Givord (1983).
[9] Deutz et al. (1989).

et al. (1991). A valency of 3.3 has been derived for the cerium ion by Weidner et al. (1985) and Croft et al. (1987) by means of L_{III} X-ray absorption experiments. The same value has been found for $CeCo_2$ and $CeFe_2$ compounds. The linear specific-heat coefficient γ of 11 mJ/K^2 mol found by Sa et al. (1985) is reproduced well by band-structure calculations of Eriksson et al. (1988a): 10.5 mJ/K^2 mol. A full tetravalent Ce state has been inferred by Dijkman (1982) on the basis of magnetic studies as the susceptibility in the temperature range 50 to 300 K is temperature independent with a value of 8.5×10^{-9} m^3/mol. An upturn at low temperatures, with χ values up to 13×10^{-9} m^3/mol at helium temperature has been interpreted in terms of the presence of some trivalent Ce impurities with a concentration of 3.2%.

5.2.3.4. $PrNi_2$. The anomalously small value for T_c in $PrNi_2$ of 0.27 K points to a nonmagnetic CEF level as the ground state. Specific heat measurements have been performed by Mori et al. (1982) and by Greidanus et al. (1983). These experimental data have been analyzed within a single-ion Hamiltonian leading, however, to different ground states. The former yields to the nonmagnetic singlet Γ_1. The latter work results in the nonmagnetic doublet Γ_3 as the ground state. Inelastic-neutron-scattering experiments reported by Mühle et al. (1989) rather confirm Γ_3 as the ground state.

5.2.3.5. $NdNi_2$. Inelastic neutron scattering experiments on $NdNi_2$ reported by Goremychkin et al. (1989) yield the doublet Γ_6 as the ground state.

5.2.3.6. $GdNi_2$. Kaneko et al. (1988) have reported for $GdNi_2$ a value of 139 Am^2/kg for M_s, a value that is consistent with the Gd^{3+}-ion moment. The high-field susceptibility estimated from measurements up to 14 T amounts to $7 \times 10^{-4} \mu_B$/T f.u. and is seven times smaller than in $GdCo_2$. The compound $GdNi_2$ shows the highest value for T_c of 85 K. It is weakly pressure dependent as found by Jaakkola et al. (1983). The same behaviour has been found also for other Ni compounds with the heavy rare earths.

5.2.3.7. $TbNi_2$. Inelastic neutron scattering experiments on $TbNi_2$ reported by Goremychkin et al. (1989) have resulted in an evaluation of the CEF interactions. NMR studies of hyperfine interactions on ^{159}Tb nuclei by K. Shimizu et al. (1988) point to a substantial Tb moment.

5.2.3.8. $DyNi_2$. Single-crystal magnetization curves of $DyNi_2$ are presented in fig. 5.6. The spontaneous moment at 4.2 K along the $\langle 100 \rangle$ direction of 8.8μ_B/f.u. indicates a small value of the Ni moment (Gignoux and Givord 1977). The paramagnetic susceptibility is well approximated by the C–W law with $C = C(Dy^{3+})$ and $\Theta_p = 28$ K.

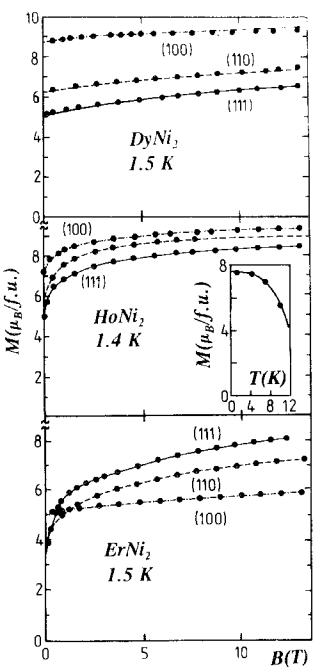

Fig. 5.6. Magnetization curves at low temperatures for single-crystalline RNi_2 compounds along different cubic crystallographic directions: $DyNi_2$ (after Gignoux and Givord 1977), $HoNi_2$ (after Gignoux et al. 1975) and $ErNi_2$ (after Gignoux and Givord 1983).

5.2.3.9. $HoNi_2$. Single-crystal magnetization curves of $HoNi_2$ are shown in fig. 5.6. Values for the crystal-field parameters as deduced from magnetization studies have been reported to be: $W = 0.62$ K and $x = -0.5$ with $B_{mol} = 5$ T (Gignoux et al. 1975). These parameters, however, cannot account for the inelastic neutron scattering spectra obtained by Castets et al. (1982b) who derived the following parameters: $W = 0.27$ K, $x = -0.5$ and $B_{mol} = 8.5$ T. These latter results are in agreement with the INS data reported by Goremychkin et al. (1989).

5.2.3.10. $ErNi_2$. The magnetization curves for $ErNi_2$ at 1.5 K are complex, see fig 5.6. At fields below 0.6 T the largest value for the magnetic moment is measured along the $\langle 100 \rangle$ direction: $5.0\mu_B$/f.u., a value much smaller than the free trivalent ion value (Gignoux and Givord 1983). Along this direction the magnetization increases slowly and almost linearly with field; at 13 T its value is not more than $5.9\mu_B$/f.u. The magnetic moments at zero field along the $\langle 110 \rangle$ and $\langle 111 \rangle$ directions are 3.5 and $2.9\mu_B$/f.u., respectively, as expected for an easy axis along the $\langle 100 \rangle$ direction. The moment along the $\langle 111 \rangle$ direction, however, develops very fast, reaching a value of $8.16\mu_B$/f.u. in a field of 13 T. The values for the crystal-field coefficients are close to the values observed in the other RNi_2 and RCo_2 compounds and always result in the $\langle 111 \rangle$ direction as the easy axis. Inelastic neutron scattering experiments performed by Goremychkin et al. (1989) result in the quartet $\Gamma_8^{(3)}$ as the ground state.

5.2.3.11. $TmNi_2$. The specific heat of $TmNi_2$ has been measured in the temperature range 45 mK–100K by Deutz et al. (1986, 1989). The specific-heat data point to a ferromagnetic transition at 1.1 K and to a crystal-field singlet ground state. The singlet ground state Γ_1 is confirmed by inelastic neutron scattering experiments (Goremychkin et al. 1989). For the analysis of the specific heat, values for γ and Θ_D of 5.4 mJ/K^2 mol and 241 K, respectively, have been taken from $LuNi_2$. Several sets of crystal-field parameters have been discussed taking into account possible trigonal and orthorhombic distortions by including extra terms proportional to B_2^0 and B_2^2. On the basis of the magnetization and specific-heat studies, the first excited level is found to be 3 K above the singlet ground state whereas the next level is at 14 K. The molecular-field coefficient n_{RR} was found to be $0.084\ T/\mu_B$. In the temperature region from 4 to 250 K the susceptibility shows a MC–W behaviour with $\Theta_p = 1.05$ K and $C = 9.0 \times 10^{-5}$ K m^3/mol. The latter value corresponds to the free-ion value of Tm^{3+}.

5.2.3.12. $LuNi_2$. The specific heat of $LuNi_2$, measured by Deutz et al. (1989) in the temperature range from 1.7 to 100 K, yields $\gamma = 5.4$ mJ/K^2 mol and $\Theta_D = 241$ K. These values are close to those found for YNi_2.

5.2.4. RMn_2 compounds

The presence of a magnetic moment on the Mn ion in YMn_2 has been demonstrated by neutron-diffraction studies and in particular by NMR investigations on the ^{55}Mn nuclei, following the studies of Nakamura (1983). By means of systematic NMR studies across the 4f series, Yoshimura and Nakamura (1983, 1984) and Yoshimura et al. (1986a) have established that manganese atoms carry a moment of $2–3\mu_B$ in

compounds with the light rare-earth elements, whereas in compounds beyond Ho the manganese moment disappears, see fig. 2.7. This observation has been correlated with the interatomic distance between Mn atoms. A distance of 267 pm is postulated as a critical distance below which the manganese atoms have no magnetic moment (Wada et al. 1987b). For $DyMn_2$, where the distance between the Mn ions is close to the critical distance, there are Mn ions with zero and nonzero value for the magnetic moment (Ritter et al. 1991). The antiferromagnetism in YMn_2 is delicate. A small amount of Sc substituted for Y suppresses antiferromagnetism and the paramagnetic state in $Y_{0.97}Sc_{0.03}Mn_2$ is stabilized down to 4.2 K (H. Nakamura et al. 1988a,b). Replacement of Mn by 5% Fe or Co cancels the manganese moment as well. In contrast, Al substitutions have been reported to maintain the moment at the Mn site (Yoshimura et al. 1986b). These facts have been explained in terms of a shrinkage (by Co and Fe substitutions) or expansion (by Al substitution) of the lattice. Direct pressure measurements confirm the strong volume dependence of the Mn magnetism: the value for T_N is dramatically reduced with pressure. A pressure of 3.7 kbar suppresses the antiferromagnetism of YMn_2, see fig. 4.8. A lower value of 2.7 kbar has been reported by Mondal et al. (1992). In case of $GdMn_2$ a pressure of 15 kbar converts the system into paramagnetic (S. Endo et al. 1992).

The suscpetibility of YMn_2 is weakly temperature dependent with a slight step-like anomaly in the vicinity of 105 K (see fig. 4.11) that is identified as the transition from the antiferromagnetic state to the paramagnetic one; $\chi(4.2\,\mathrm{K}) = 15 \times 10^{-9}\,\mathrm{m}^3/\mathrm{mol}$. The transition from the antiferro- to the paramagnetic state is accompanied by a large temperature hysteresis, characteristic for a first-order transition, as evidenced by thermal expansion (Shiga et al. 1988), susceptibility (Y. Nakamura et al. 1983) and resistivity (Kamimura et al. 1987) measurements. The exchange interactions between the 3d and 4f spins apparently are small in the RMn_2 compounds or not effective as the magnetic ordering temperature depends on the rare-earth partner in a minor way only. The Néel temperatures for YMn_2 and GMn_2 are nearly the same and both are in the range 100 to 110 K. This is in sharp contrast to compounds of the RT_2 systems with Fe and Co, for which the presence of a rare-earth spin largely enhances T_c.

All RMn_2 compounds with the heavy magnetic rare earths have been found to order magnetically at temperatures much lower than that of YMn_2. Values of 54, 35, 24, 15 and 8 K have been reported for R = Tb, Dy, Ho, Er and Tm, respectively. The magnetic phase transitions in case of Gd and Tb compounds are first-order and accompanied by a large anomaly in the thermal expansion curve. The transition in the case of the other compounds are second-order (Labroo et al. 1990a,b). The first-order transition is believed to be associated with the collapse of the Mn moment. The values for the transition temperature of the heavy RMn_2 compounds agree well with the de Gennes rule. This observation supports the suggestion that in this case the magnetism is primarily driven by the rare-earth ion with a low or zero value of the Mn moment. In case of $GdMn_2$, $TbMn_2$ and the light rare earths, a Mn moment with a substantial value appears and the magnetism in these compounds is largely controlled by the manganese sublattice.

The properties of hydrogenated RMn_2 compounds have been reviewed by

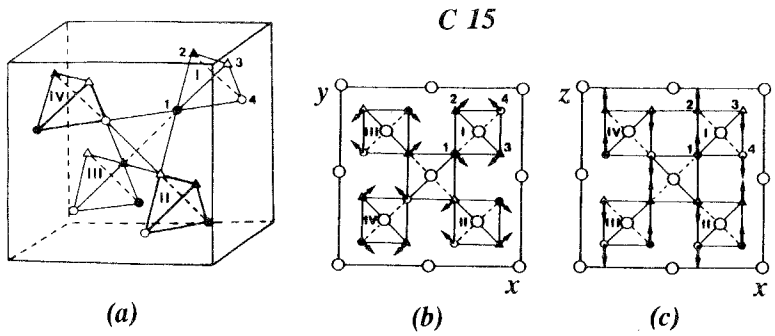

Fig. 5.7. Magnetic structure of YMn_2. The Mn atoms are shared out in two sublattices with different magnetic directions (circles and triangles). Within each sublattice the Mn moments are antiparallel (black and white symbols). (a) Schematic representation of tetrahedrals of Mn ions in the cubic C15 structure; (b) and (c) components of Mn moments at y–x and z–x planes. After Ballou et al. (1988b,c).

Wiesinger and Hilscher (1991). The uptake of hydrogen strengthens remarkably the magnetism. Values for T_c of 284 and 260 K have been found in YMn_2H_x and $GdMn_2H_x$, respectively.

5.2.4.1. YMn_2. A helimagnetic structure of manganese moments, as shown in fig. 5.7, has been established on basis of neutron-diffraction studies of Ballou et al. (1987b). It indicates complex interactions in which a Mn ion is involved owing to the simple collinear magnetic structure occurring in YFe_2, for instance. The complex magnetic structure of YMn_2 results from frustration effects in the antiferromagnetic interactions between the nearest-neighbour Mn spins (Ballou et al. 1988b,c). The C15 structure consists of a compact packing of atoms of two different sizes forming triangular configurations as shown in fig. 5.3. In this compact atomic packing, it becomes impossible to satisfy the antiferrromagnetic coupling for all Mn–Mn pairs within the nearest-neighbour surrounding. Frustration of the antiferromagnetic exchange interactions leads to a ground state that includes several minima close in energy that are associated with a variety of complex magnetic structures. It turns out that the variation of the moment amplitude minimizes the antiferromagnetic exchange interactions more effectively than the formation of antiferromagnetic or noncollinear magnetic structures. Indeed, more detailed neutron-diffraction experiments by Ballou et al. (1988c) revealed a variation of the Mn moment between 2.3 and 2.9μ_B in YMn_2. Properties of YMn_2 and related compounds have been discussed by Rainford et al. (1992) in terms of spin fluctuations.

Similar effects have also been detected in $ThMn_2$, a Laves-phase system with the C14-type of structure. Th compounds show properties that are very similar to the Y compounds. $ThMn_2$ is representative for the study of the Mn–Mn exchange in the hexagonal RMn_2 compounds. Powder neutron diffraction studies of Deportes et al. (1987c) reveal an AF structure with the propagation vector of $[\frac{1}{3}, \frac{1}{3}, 0]$. A triangular configuration of the moments at the 6h sites at the subsequent hexagonal planes, $z = \frac{1}{4}$ and $z = \frac{3}{4}$ is shown in fig. 5.8. The Mn moment at the 6h site is close to 1.6μ_B.

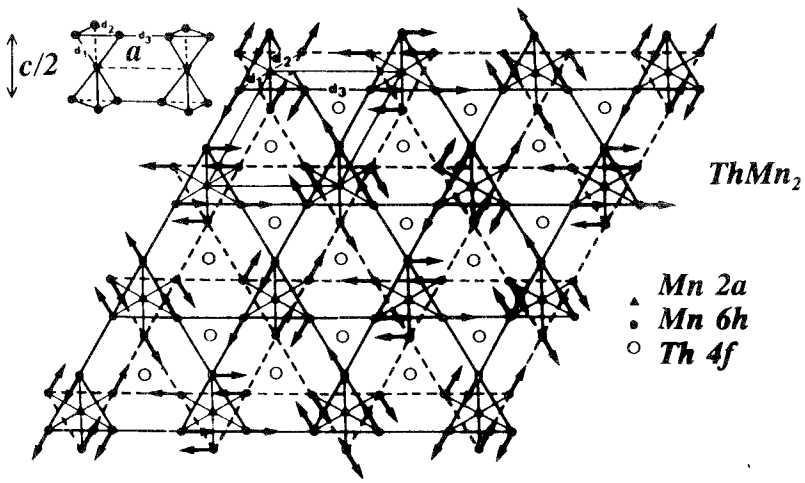

Fig. 5.8. Magnetic structure of $ThMn_2$ with the hexagonal structure C14 presented by the projection of the moments into the basal plane. The Mn ions at the site 2a are nonmagnetic. After Deportes et al. (1987c).

The Mn ions at the site 2a are found to be *nonmagnetic*. The triangular configuration causes a full cancellation of the exchange field at this site. Further studies of the temperature dependence of the susceptibility of these ions indicate that they are indeed nonmagnetic and not just non-oriented as could be expected from a simple cancellation of the exchange field. An unusual increase with increasing temperature of the effective Mn moment has been detected by paramagnetic scattering of polarized neutrons on YMn_2. It amounts to 1.6, 1.7 and 1.9μ_B at 120, 200 and 300 K, respectively (Deportes et al. 1987a,b).

At T_N, the compound YMn_2 undergoes a first-order magnetic transition accompanied by an enormous volume change of 5% (Shiga et al. 1983, 1987). Gaidukova et al. (1983) have reported on a tetragonal distortion developed in the ordered state. Specific-heat measurements performed by T. Okamoto et al. (1987) have revealed a γ value of 15 mJ/K^2 mol and a pronounced peak at T_N. The magnetic entropy, ΔS, associated with this peak is equal to 3.9 J/K mol and is much smaller than one could expect from the disorder of a well-defined localized moment. This points to an itinerant character of the Mn moments that has been analyzed theoretically by Terao and Shimizu (1984, 1987), by Yamada and Shimizu (1987a,b) and by Yamada et al. (1984). A T^2 dependence below 100 K in the resistivity has been found by Kim-Ngan et al. (1992c). The paramagnetic sample $Y_{0.97}Sc_{0.03}Mn_2$ shows a value for the electronic specific heat coefficient γ of 140 mJ/K^2 mol (Wada et al. 1987a, 1989). Thermal expansion measurements have been reported by Shiga et al. (1987) and Oomi et al. (1987).

5.2.4.2. $PrMn_2$ and $NdMn_2$. The complex magnetic structures in the hexagonal compounds $PrMn_2$ and $NdMn_2$ (Ballou et al. 1988b,c) have been unravelled by neutron diffraction studies. The neutron pattern can be resolved into two sets of

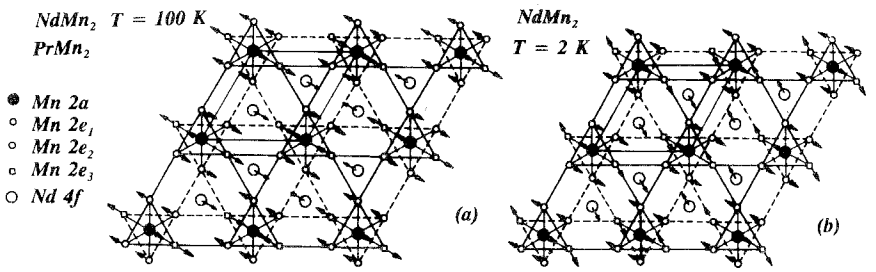

Fig. 5.9. Magnetic structure of $NdMn_2$ and $PrMn_2$ presented by the projection of the moments into the basal hexagonal plane. (a) The magnetic structure of $PrMn_2$ and of $NdMn_2$ at 100 K; (b) the magnetic structure of $NdMn_2$ at 2 K. After Ballou et al. (1988b).

peaks with different temperature dependencies and two different propagation vectors indicating the presence two non-coupled sets of magnetic moments. The inferred magnetic structure is schematized in fig. 5.9. Due to the symmetry breaking by the monoclinic distortion, the 6h Mn ions are distributed over the three sites $2e_1$, $2e_2$ and $2e_3$. The first set of peaks is associated with manganese moments located at the 2a, $2e_1$ and $2e_2$ sites, whereas the second one contains the Mn-$2e_3$ ions and the R moments. At 100 K, i.e. just below T_N, the magnetic structure formed by the two sets of moments is collinear. With decreasing temperature, however, the second set of the moments undergoes a reorientation to a direction tilted by 30° out of the preferred direction of the set 1. This reorientation results from crystal-field effects on Nd^{3+} ions favouring the [100] direction (Ballou et al. 1988c). The crystal-field interactions have not been analyzed in a quantitative way. The magnetic structure of $PrMn_2$ is similar to the high-temperature structure of $NdMn_2$ and does not change with temperature. Magnetic, thermal and transport properties of (Nd–Lu)Mn_2 compounds have been studied by Kim-Ngan et al. (1990, 1992a). A nonlinear magnetization curve for $NdMn_2$ has been found. The field of 38 T is not able to saturate the Nd moment, a value of $2.1\mu_B$/f.u. only is observed in this field value. The susceptibility above 110 K can be well described a modified Curie–Weiss law. A very sharp peak in the specific heat is observed at 104 K due to the appearance of the antiferromagnetic order of the manganese moments. A broad peak observed around 20 K most probably originates from Nd^{3+} energy levels.

5.2.4.3. $GdMn_2$. The compound $GdMn_2$ orders magnetically at about 110 K, a temperature that is very close to that observed in YMn_2. The magnetization at 4.2 K in a field of 6 T results in a moment of about $3.9\mu_B$, see fig. 5.10. ^{55}Mn spin-echo NMR spectra at 1.7 K in zero field indicate that the Mn hyperfine field is 11.2 T, pointing to a Mn moment of $2.6\mu_B$. In order to reconcile these different experimental results, T. Okamoto et al. (1986) proposed a canted structure for the Gd moments and an antiferromagnetic structure for the Mn moments in $GdMn_2$. The canting angle of the Gd moments is estimated to be about 130°. In contrary, Yamada and Shimizu (1986b) proposed for $GdMn_2$ a noncollinear magnetic structure with gadolinium

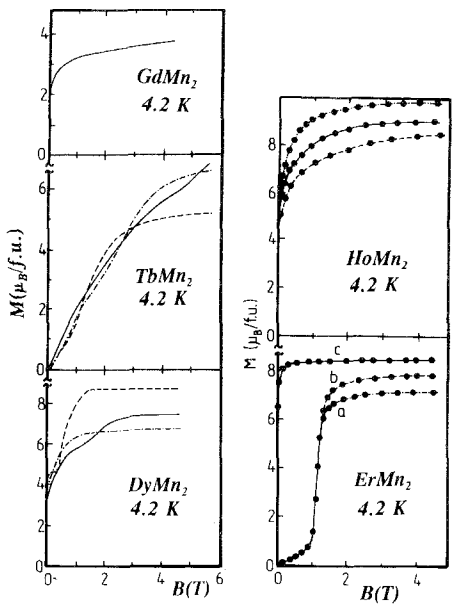

Fig. 5.10. Magnetization vs effective field for single-crystalline RMn_2 (R = Gd, Tb, Ho and Er) at 4.2 K along different crystallographic directions. For R = Gd, Tb, Dy and Ho the structure is cubic C15; ⟨111⟩–solid line; ⟨110⟩–dashed line; ⟨100⟩–dashed–dotted line. $ErMn_2$ has a hexagonal structure and the curves are measured for the field direction parallel to the *a*, *b* and *c* axes. After Makihara et al. (1983).

moments parallel to each other whereas the manganese moments are divided in two sublattices that make an angle of 67°. The mean manganese moment is antiparallel to the Gd moment. The antiferromagnetism in $GdMn_2$ is very sensitive to external pressure. Voiron et al. (1991) has reported a linear decrease of T_N with a value for dT_N/dp of -5.4 K/kbar. The magnetization increases with pressure. Under 6 kbar and an applied field of 6.5 T the magnetization reaches a value of $4.3\mu_B$/f.u. More extended pressure experiments of S. Endo et al. (1992) up to 10.7 kbar and a chemical pressure of 14.8 kbar (by Sc substitutions) have revealed a critical pressure of 14.8 kbar below which the Mn sublattice magnetic moment in $GdMn_2$ disappears. This pressure, when converted to the lattice parameter, corresponds to a critical lattice parameter of 760 pm. The specific heat reported T. Okamoto et al. (1987) shows a pronounced peak at T_N.

5.2.4.4. $TbMn_2$. Ballou et al. (1990b) have reported that the temperature dependence of the susceptibility of $TbMn_2$ above 20 K, but below T_N, can be analyzed with a modified Curie law yielding an effective moment of $9.78\mu_B$, a value that is very close to the free-ion Tb^{3+} value. Magnetic properties of $(Tb–Y)Mn_2$ have been studied by Belov et al. (1989). Small substitutions of Tb to YMn_2 destroy the helimagnetic structure of YMn_2 as $Y_{0.9}Tb_{0.1}Mn_2$ has been reported by Berthier et al. (1988a) to be purely antiferromagnetic. Tanaka et al. (1991) have found on basis of magnetization

measurements under hydrostatic pressure that a pressure of 5.3 kbar changes the magnetic state of $TbMn_2$ from helimagnetic to a simple ferromagnetism in the low temperatures below 50 K. This change in the magnetic structure can be attributed to the disappearance of the magnetic moment of the manganese atoms by application of the pressure. A metastable magnetic multiphase state with two different propagating vectors has been found by Ballou et al. (1992b,c) in single-crystal neutron-diffraction studies. NMR experiments of Yoshimura et al. (1986a) result in a value for the Mn moment of $2.5\mu_B$.

5.2.4.5. $DyMn_2$. It has been established on the basis of powder neutron diffraction and magnetization studies of Ritter et al. (1991) that the Dy moments in $DyMn_2$ form a spin-canted ferromagnetic structure with $8.8\mu_B$ per Dy atom. Although all Mn sites within the unit cell of the C15-type of structure are chemically equivalent, only 25% of Mn ions are found to carry a magnetic moment of $1.4\mu_B$. This result is consistent with the conclusion drawn by Yoshimura et al. (1986a) on the basis of NMR studies. The NMR spectrum contains two resonance peaks ascribed to M ions with different values of the magnetic moment. At 36 K a moment reorientation is observed that is accompanied by a small thermal expansion anomaly. The Curie temperature of $DyMn_2$ is found to be 45 K. The magnetization curves, measured by Makihara et al. (1983) are presented in fig. 5.10.

5.2.4.6. $HoMn_2$. Neutron diffraction studies by Hardman et al. (1982) on $HoMn_2$ have revealed a collinear magnetic structure with Ho and Mn moments staying within the hexagonal plane and antiparallel to each other. The Ho moment amounts to $9.4\mu_B$ and $8.1\mu_B$ at the hexagonal and cubic sites, respectively. The moments of manganese have been found to be $-0.8\mu_B$ for the cubic, and -0.6 and $-1.0\mu_B$ at the a and h sites for the hexagonal structure, respectively. NMR studies of Yoshimura et al. (1986a), shown in fig. 2.7, indicate that the Mn moment is close to zero. At 4.2 K, a localized excitation of 30.7 K above the ground state has been observed in INS experiments for both the hexagonal and cubic sites (Hardman et al. 1982).

5.2.4.7. $ErMn_2$. In the compound $ErMn_2$, the Mn ions do not carry a magnetic moment as is deduced from neutron and NMR experiments (Yoshimura et al. 1986a). The Er moments in this compound behave as a simple c-axis ferromagnet with a moment only slightly reduced compared with the free-ion value. Single crystal magnetization curves measured by Makihara et al. (1983) are shown in fig. 5.10. A λ-type anomaly in the specific heat is observed at T_c ($=15$ K) which is indicative for a second-order transition (T. Okamoto et al. 1987). Analysis of the specific heat within the CEF Hamiltonian leads to the following values for the CEF coefficients: $B_2^0 = +0.1$ K, $B_4^0 = +0.72$ mK, $B_6^0 = +4.1$ μK and $B_6^6 = +6.8$ μK. These parameters describe, however, the temperature dependence of the magnetic specific heat rather poorly. Magnetization curves measured on single-crystalline samples by Makihara et al. (1983) are complex. Magnetization curves at high fields are continuously increasing indicating large effect of external fields on the internal magnetic structure. The magnetization process has not been analyzed in detail so far.

5.2.4.8. $LuMn_2$. This is a Pauli paramagnet with a susceptibility of 11×10^{-9} m^3/mol at 4.2 K as has been reported by Kim-Ngan et al. (1992a) on the basis of high-field magnetization measurements up to 38 T. The resistivity up to 50 K shows a T^2 dependence. The specific heat reported by these authors in the temperature range from 1.5 to 300 K shows regular behaviour that can be approximated by a value for Θ_D of 250 K. The electronic specific-heat coefficient amounts to 30 mJ/K^2 mol.

5.3. RT_3 compounds (T = Fe, Ni, Co)

Most RT_3 compounds with Fe, Co and Ni crystallize in the rhombohedral $PuNi_3$-type of structure, space group R3m. $CeNi_3$ is an exception as it crystallizes in a hexagonal structure. Both structures are closely related as both of them originate from the hexagonal $CaCu_5$-type of structure. The RT_3 structure is obtained by systematic replacements of Cu ions by R ions in every second basal plane of the $CaCu_5$ structure according to the formula

$$2\,RCo_5 + R - Co \rightarrow 3\,RCo_3. \tag{5.7}$$

The hexagonal and rhombohedral structures differ in the way of stacking of the same atomic blocks, similar to the hcp and fcc stacking variants or the C14 and C15 structures. The rhombohedral structure is usually described within the hexagonal

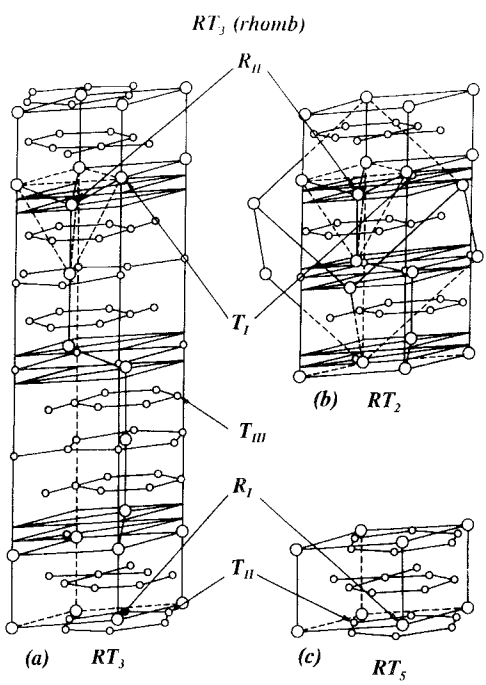

Fig. 5.11. Construction of the rhombohedral structure of RT_3 from the RT_2 and RT_5 blocks. RT_3, RT_2 and RT_5 structures are shown in (a), (b) and (c), respectively.

frame. The above-described construction of the elementary cell is reflected in the values of the lattice parameters. The basal-plane parameter is approximately the same as in YCo_5, i.e., about 495 pm. The elementary cell is elongated along the c-axis. The parameter c amounts to 2435 pm for rhombohedral YCo_3, which is approximately six times larger than the c-parameter value of YCo_5. In case of the hexagonal structure the c-parameter value is approximately four times larger.

In the rhombohedral structure, the R atoms are situated at two different crystallographic sites, 3a (I) and 6c (II), whereas the 3d atoms are distributed over three different sites, see fig. 5.11. In first approximation, the local arrangement of the R_I site is that of the hexagonal RCo_5 structure whereas the local arrangement of the R_{II} site resembles that of the cubic RT_2 Laves-phase structure. Thus, quite different magnetic behaviour can be expected for R ions placed at the different sites. The same holds for the Co ions where one expects to find Co ions in the paramagnetic state as in YCo_2 and in the magnetic state like in YCo_5 with the occupancy ratio 1 to 2. Indeed, instabilities of the Co moment in YCo_3 have been experimentally observed by Goto et al. (1992).

5.3.1. RFe_3 compounds

Compounds with La, Ce, Pr, Nd, Eu and Yb have not been reported to exist. In YFe_3, the iron ion carries a moment of $1.75\mu_B$ at low temperatures. Roughly the same value is found in $GdFe_3$. In compounds with the heavy R's, a compensation temperature for the magnetization exists since the rare-earth sublattice moment at low temperatures is larger than that of the Fe sublattice. The compensation temperature, T_{comp}, amounts to 618, 512, 546, 393 and 236 K for the Gd, Tb, Dy, Ho and Er compounds, respectively. The decreasing values for T_{comp} reflect the decreasing value of the molecular field experienced by the R-ion moment. T_c varies from 569 K for YFe_3 to 729 K for $GdFe_3$. Attributing this increase to the 3d–4f interactions, a value of 278 T is obtained for $B^{Gd}_{RT,ex}$, see table 4.5. The intersublattice interactions have been quantified more directly by Liu et al. (1991c) by means of free-powder high-field magnetization studies on ferrimagnetic samples (i.e., from Gd to Er) with relevant Y substitutions in order to be closer to the moment compensation. The experimental magnetization curves are presented in fig. 5.12. The exchange parameter J_{RFe} has been found to change from -14.4 K for $Gd_{0.75}Y_{0.25}Fe_3$ to -16.7 K for $Er_{0.45}Y_{0.55}Fe_3$. The former value corresponds to a value of 255 T that can serve as representative for the exchange field in the heavy rare-earth RFe_3 compounds.

The Fe sublattice moment prefers the hexagonal plane as is known from the planar anisotropy of YFe_3. As a consequence, for the Sm, Er and Tm compounds a temperature-induced moment reorientation, due to the competition of the R and the Fe anisotropy, is expected. For $ErFe_3$, a TIMR transition has been detected at 50 K, indeed. Magnetostriction has been measured in the temperature range from 80 to 300 K for RFe_3 compounds with R = Sm, Tb, Dy, Ho, Er and Tm by Abbundi et al. (1980). The room-temperature magnetostriction $\lambda_\parallel - \lambda_\perp$ has been found by Herbst and Croat (1982) to follow the Stevens factor α_J of the R ion involved.

5.3.1.1. YFe_3. Single-crystal magnetization studies of YFe_3 at 4.2 K performed by Kebe (1983) have resulted in a value for M_s of $5.0\mu_B$/f.u. (see fig. 4.4). B_a amounts to

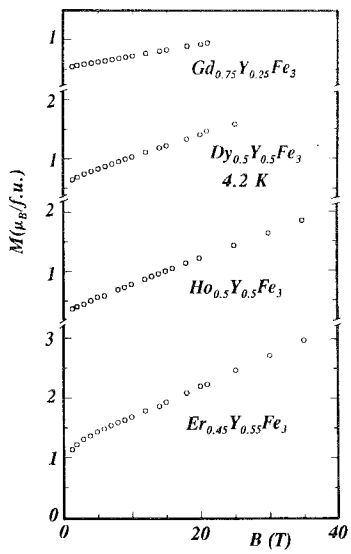

Fig. 5.12. High-field free-powder magnetization curves at 4.2 K for some nearly compensated ferrimagnetic (R–Y)Fe_3 compounds. After Liu et al. (1991c).

3.5 T pointing to $K_1 = -5.9$ K/f.u. The anisotropy field slowly decreases with temperature and amounts to 3 T at room temperature. The Curie temperature amounts to 569 K. The easy direction of magnetization lies in the hexagonal plane; the in-plane anisotropy is negligibly small. The concentration dependence of the magnetic anisotropy in the Y(Fe–Co)$_3$ series has been interpreted within the individual-site model by Hong et al. (1989). Hydrogenation of YFe_3 leads to an increase of the magnetic moment and of T_c. For YFe_3H_5 a moment of $1.95\mu_B$/Fe-ion has been reported by Bartashevich et al. (1988).

5.3.1.2. $SmFe_3$. For the compound $SmFe_3$ the easy magnetic direction stays along the c axis up to T_c. An anisotropy field of 14 T at room temperature has been reported by Schultz et al. (1991) and by Schultz and Katter (1991).

5.3.1.3. $GdFe_3$. High-field magnetization studies at 4.2 K on free powder particles of $Gd_{0.75}Y_{0.25}Fe_3$ have revealed a value of 50 T f.u./μ_B for the molecular-field coefficient n_{GdFe} (Liu et al 1991c).

5.3.1.4. $TbFe_3$. A value of 32.7 T f.u./μ_B for n_{TbFe} has been found by Liu et al. (1991c) from free-powder magnetization studies at 4.2 K up to 35 T on $Tb_{0.6}Y_{0.4}Fe_3$. The magnetic structure has been established by James et al. (1979a) by means of neutron-diffraction experiments. Hydrogen uptake strongly reduces the value for T_c from 648 K for $TbFe_3$ (Herbst and Croat 1982) to about 300 K for the hydrogenated compound (Malik et al. 1983). Similar to $TbFe_2$, the compound $TbFe_3$ shows large magnetostriction effects with $\lambda_\parallel - \lambda_\perp$ equal to 1.7×10^{-3} at 80 K and to 1.0×10^{-3} at room temperature.

5.3.1.5. $DyFe_3$. Magnetization measurements by Pĺusa et al. (1984) on a polycrystalline sample of $DyFe_3$ at 4.2 K yield $M_s = 4.25\mu_B$/f.u. and $K_1 = -1.2\,\mathrm{MJ\,m^{-3}}$. Compensation for the two sublattice magnetizations occurs in the vicinity of 525 K. At room temperature the EMD lies along the ***b*** axis, as is expected, whereas at low temperatures the Mössbauer studies of Japa et al. (1979) indicate a direction within the *ac* plane. The hyperfine field at the Dy nucleous amounts to 927 T (Bara et al. 1982b) and indicates the full value of the Dy moment. A value of 27 T f.u./μ_B for the coefficient n_{DyFe} has been found from free powder studies at 4.2 K on $Dy_{0.5}Y_{0.5}Fe_3$ (Liu et al. 1991c).

5.3.1.6. $HoFe_3$. The compound $HoFe_3$ exhibits a TIMR transition within the hexagonal plane in the vicinity of 85 K from the ***a*** direction to the ***b*** direction above this temperature. Although the CEF parameters are not yet available the TIMR transition is likely to be of the single-ion type (type II) similar to that found in $HoCo_2$. An analysis of the paramagnetic susceptibility, shown in fig. 3.12 according to eq. (3.15), yields values for n_{FeFe} of 64 T f.u./μ_B, for n_{Ho-Fe} of 11.7 T f.u./μ_B and for n_{Ho-Ho} of 1.1 T f.u./μ_B (Simmons et al. 1973). Applying the molecular-field relations one arrives at values of 70 T for the molecular field experienced by the Ho moment, B_{mol}^{HO}, and of 430 T for that experienced by the iron moment. In the value of B_{mol}^{Ho}, a contribution of 60 T is due to the Ho–Fe interactions, which largely dominate the R–R interaction. High-field free-powder studies at 4.2 K on $Ho_{0.5}Y_{0.5}Fe_3$ yield a rather large value of 23 T f.u./μ_B for n_{HoFe} (Liu et al. 1991c). Provided that the derived parameters are correct it could indicate that the exchange interactions in the paramagnetic region are two times smaller than at low temperatures.

5.3.1.7. $ErFe_3$. Magnetization studies on a single-crystalline sample of $ErFe_3$ by Kebe (1983) at 4.2 K have revealed a value for the spontaneous magnetic moment M_s of 3.7μ_B/f.u. The magnetization curves are presented in fig. 5.13. The value for M_s can be split into $M_{Er} = 9\mu_B$ and $M_{Fe} = 1.75\mu_B$/Fe. Neutron studies by Ballou et al. (1986b) point to a collinear structure at 4.2 K and confirm the magnetization results for

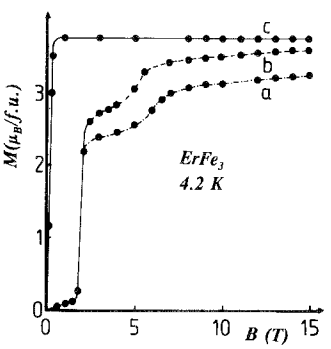

Fig. 5.13. Magnetization curves at 4.2 K for single-crystalline $ErFe_3$ along different hexagonal crystallographic directions. After Kebe (1983).

the magnetic moment. With increasing temperatures, however, three magnetic phases are observed. At low temperatures below 42 K, all moments are collinear with the c direction, whereas above 220 K the magnetic arrangement is again collinear but now within the c plane. At intermediate temperatures, a noncollinear structure exists resulting from the competition of the local anisotropies. The erbium moments at the sites I and II favour different directions, one of them the c axis. The iron sublattice moment favours the direction perpendicular to the c axis as known from YFe_3. The TIMR at low temperatures has also been detected by Mössbauer studies by Van der Kraan et al. (1975). Extended Mössbauer spectroscopy studies reported by Tharp et al. (1992) indicate a magnetic structure canted by 57° from the c axis at 85 K. The compensation of the two sublattice moments at 240 K is accompanied by a well-pronounced minimum in the magnetostriction (Abbundi et al. 1980). A significant reduction of the compensation temperature to 81 K has been reported by Malik et al. (1983) for $ErFe_3H_{3.5}$. High-field magnetization measurements on free powder of $Er_{0.45}Y_{0.55}Fe_3$ by Liu et al. (1991c) at 4.2 K yield a value of 19.3 T f.u./μ_B for n_{ErFe}. Tharp et al. (1987) by means of neutron diffraction experiments have found that there is a nonstatistical site occupation in the Ni substituted $ErFe_3$ compound.

5.3.1.8. $TmFe_3$. The compensation of the magnetization in $TmFe_3$ at a temperature of 78 K is manifest in magnetostriction measurements by a significant anomaly (Abbundi et al. 1980). Making use of this value for the compensation temperature and assuming that the decrease of the Tm moment is described by the Brillouin function one gets a quite reasonable value of 46 T for the molecular field. Malik et al. (1983) have reported that hydrogenation reduces the compensation temperature to 13 K for $TmFe_3H_3$.

5.3.2. RCo_3 compounds

The Co sublattice moment prefers the c axis as can be concluded from experiments on YCo_3 and $GdCo_3$; $K_1 = +3.2$ K/f.u. in YCo_3. The Co moment varies from $0.38\mu_B$ in YCo_3 to $1.33\mu_B$ in $GdCo_3$ due to the presence of localized 4f spins. The easy-axis direction of the magnetization follows the Stevens factor α_J. For negative values of α_J, the easy direction is within the hexagonal plane. $SmCo_3$ has been reported in NMR studies to violate this rule (Yoshie and Nakamura 1990). Magnetic structures for the RCo_3 compounds (R = Pr, Nd, Tb, Ho and Er) have been studied by Yakinthos and Rossat-Mignod (1972) in neutron diffraction experiments on polycrystalline specimens. Nuclear magnetic resonance measurements on ^{59}Co nuclei have been performed at 4.2 K by Yoshie and Nakamura (1990) in fields up to 5 T for RCo_3 compounds with R = Y, Nd, Sm, Gd, Tb, Dy and Ho. A large orbital moment at the site 6c is found for the Y, Nd and Sm compounds and at the site 3b for compounds with the heavy rare earths. In the $PuNi_3$ structure, there are three inequivalent Co sites. In case the magnetization of RCo_3 has a c-plane component, the 18h site is magnetically subdivided into the sites $6h_1$ and $12h_1$. Temperature dependences of the electrical resistivity of ferrimagnetic $DyCo_3$, $ErCo_3$ and $TmCo_3$ and of ferromagnetic YCo_3 and $CeCo_3$ have been reported by du Plessis and Germishuyse (1992).

5.3.2.1. YCo_3. Single-crystal magnetization data for YCo_3 at 4.2 K as shown in fig. 4.2 reveal the easy direction of magnetization to be along the *c* axis with a value for M_s of $1.45\mu_B$/f.u. A moment of $1.8\mu_B$/f.u. has been reported in another study of a single-crystalline sample by Shcherbakova et al. (1986). Different values for T_c of 264 and 310 K have been obtained from magnetization studies (Kebe 1983, p. 68). This difference reflects the instability of the Co moment in this compound similarly as observed in the RCo_2 compounds. The substantial differential susceptibility at low temperatures is indicative for this instability. A strong dependence of the cobalt moment on the local surrounding is revealed by neutron measurements. The Co moment amounts to 0.73, 0.94 and $0.47\mu_B$ at the sites 3b, 6c and 18h, respectively. Metamagnetic-like anomalies have been observed in the magnetization measurements on a powder sample in ultra-high external fields. These anomalies at 60 and 82 T have been recognized as field-induced moment transitions in the Co ions. The variation of the Co moment in the $(Gd-Y)Co_3$ compounds has been analyzed by Burzo and Seitabla (1981) in terms of an induced cobalt moment due to the presence of the localized 4f moment. From NMR studies, Yoshie and Nakamura (1990) concluded that the orbital moment is largest at the site 6c and equal to $0.16\mu_B$. The NMR frequency of 43 MHz has been associated by Fontes et al. (1992) to Co ions in the 18h sites. The variation of the anisotropy in the $Y(Co-Fe)_3$ series has been analyzed in the individual-site model by Hong et al. (1989). Electron spin resonance studies have been performed by Turek et al. (1987). Hydrogen absorption studies performed by Bartashevich et al. (1988) have revealed a stable phase with four hydrogen atoms per formula unit. With the absorption of hydrogen, the magnetic order of the Co moments is reported to change from ferro- with T_c of 301 K to antiferromagnetic with T_N of 215 K for $YCo_3D_{3.8}$. High-field studies of Bartashevich et al. (1992b) up to 40 T have revealed at 15 T a metamagnetic transition. The moment after the transition amounts to $1.95\mu_B$/f.u.

5.3.2.2. $CeCo_3$. This compound has been reported by Lemaire (1966b) to be ferromagnetic with T_c of 78 K and M_s of $0.2\mu_B$/f.u. and by Buschow (1980b) to be Pauli paramagnetic with an almost temperature-independent susceptibility down to low temperatures. The latter author has reported that Pauli paramagnetic $CeCo_3$ is converted to a ferromagnet after the absorption of hydrogen. This phenomenon has been correlated with the formation of the trivalent Ce states. $CeCo_3$ exhibits large temperature dependent resistivity as measured by du Plessis and Germishuyse (1992).

5.3.2.3. $NdCo_3$. At 4.2 K the EMD of $NdCo_3$ is within the hexagonal plane indicating the dominant Nd contribution to the overall anisotropy at low temperatures. This view is consistent with the observation of the moment reorientation in the temperature range between 225 and 252 K (Marusi et al. 1991). NMR studies have been reported by Yoshie and Nakamura (1990) and NMR parameters have been compared with those observed in the other Nd compounds by Figiel et al. (1991).

5.3.2.4. $SmCo_3$. From NMR studies the magnetization direction in $SmCo_3$ is found to be perpendicular to the *c* axis (Yoshie and Nakamura 1990).

5.3.2.5. $GdCo_3$. Single-crystal magnetization data for $GdCo_3$ at 4.2 K yield a value for M_s of $3.0\mu_B$/f.u. Assuming the full gadolinium moment, this result leads to a value of $1.33\mu_B$ for the cobalt moment. The value for T_c is quite high and amounts to 612 K. From magnetization measurement up to 15 T Kebe (1983, p. 75) has found the coefficient n_{Gd-Co} to be equal to 31 K/μ_B^2 corresponding to a value of 186 T for $B_{ex,RT}^{Gd}$. NMR studies by Yoshie and Nakamura (1988a) have revealed three well-defined lines associated with the 3b, 6c and 18h sites with values for the hyperfine fields of +8.0, −5.8 and −8.0 T, respectively. The positive sign at the 3b site has been taken as indicative for the large orbital contribution to the Co moment at this site.

5.3.2.6. $TbCo_3$ and $DyCo_3$. For the compounds $TbCo_3$ and $DyCo_3$, single-crystal magnetization measurements up to 9 T have been reported by Shcherbakova and Ermolenko (1985). In the Tb compound the compensation of magnetization is found at 411 K. Hydrogenation of $DyCo_3$ leads to a dramatic decrease of T_c. A value for T_c of 18 K has been reported by Malik et al. (1978) for $DyCo_3H_{4.3}$.

5.3.2.7. $HoCo_3$. For the compound $HoCo_3$ Shcherbakova and Ermolenko (1982) have observed a metamagnetic transition at 4.2 K for a field of 5 T applied along the *c* axis, the hard axis of the system, see fig. 5.14a. Beyond the transition the magnetization is still substantially lower than the easy-direction value of $6.2\mu_B$/f.u. The easy-direction magnetization points to the full Ho moment and a cobalt moment of $1.3\mu_B$ like in $GdCo_3$. At 4.2 K the EMD is along the *b* axis. At 55 K TIMR starts to a complex noncollinear magnetic structure, due to the competition of anisotropies at the rare-earth and Co sublattices, that exists up to 200 K (Bartashevich et al. 1992a). Above this temperature the EMD becomes parallel to the *c* axis. Studies of (Y–Ho)Co_3 have been reported by Shcherbakova et al. (1986). For $HoCo_3H_{4.2}$ a value of 15 K has been reported by Malik et al. (1978) for T_c.

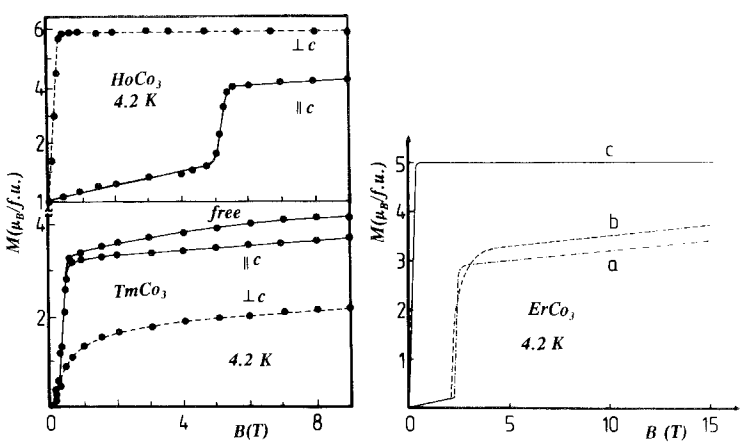

Fig. 5.14. Magnetization curves at 4.2 K (a) for single-crystalline $HoCo_3$ and $TmCo_3$ (after Shcherbakova and Ermolenko 1982), and (b) for $ErCo_3$ along different crystallographic directions (after Kebe 1983).

5.3.2.8. $ErCo_3$. For the compound $ErCo_3$ a value for M_s of $5.0\mu_B$/f.u. has been determined from single-crystal magnetization studies at 4.2 K, see fig. 5.14. With the moment of the trivalent Er ion, this result leads to a value for the cobalt moment of $1.33\mu_B$. The magnetization curve for field directions within the hexagonal plane, shows abrupt transitions in the vicinity of 2 T that resemble the transitions observed for $ErFe_3$ (Kebe 1983). With increasing temperature, the transitions become weaker and at 100 K there is only a small anomaly left (Bartashevich et al. 1992a). For $ErCo_3$, the easy axis of magnetization is always along the *c* direction as the Co sublattice, in contrast to the Fe sublattice in $ErFe_3$, favours the *c* direction. Crystal-field and exchange-field parameters have not yet been determined.

5.3.2.9. $TmCo_3$. For the compound $TmCo_3$ single-crystal magnetization measurements at 4.2 K in fields up to 9 T have been reported by Shcherbakova and Ermolenko (1982). These experiments reveal a tilted magnetic structure as the EMD does not lie along one of the main crystallographic directions. The compensation of the magnetization at 118 K points to a value of 37 T for the molecular field (Radwański 1986c). Studies on hydrogenated compounds have been reported by Malik et al. (1981).

5.3.3. RNi_3 compounds

Magnetic moments of the Ni ions in the RNi_3 compounds as small as $0.05\mu_B$ have been reported by Gignoux et al. (1980b). Band-structure calculations by M. Shimizu and Inoue (1986, 1987) can account for a re-entrance of the 3d magnetism in these Ni compounds. The highest value for T_c occurs for $GdNi_3$ and amounts to 115 K. The pressure dependence of T_c has been measured by Jaakkola et al. (1983) for R = Gd, Tb and Dy. The largest effect is obtained for $DyNi_3$ with $\partial T_c/\partial p = -0.20$ K/kbar.

5.3.3.1. YNi_3. The small spontaneous moment of $0.15\mu_B$/f.u. in single-crystalline YNi_3 at 4.2 K disappears above 31 K (Gignoux et al. 1980b). The magnetization curves are shown in fig. 4.5. The large value of the differential susceptibility of $51 \times 10^{-4}\mu_B$/T f.u. indicates moment instabilities. The anisotropy energy is small and takes a value of -2.3×10^3 J/m^3. Values for M_s of $0.13\mu_B$/f.u. and of 28 K for T_c have been reported by Dubenko et al. (1990). Band-structure calculations by M. Shimizu et al. (1984) yield different moments at different crystallographic sites, in agreement with experimental neutron data of Gignoux et al. (1980b, 1981). The thermal variation of the reciprocal susceptibility between 30 and 300 K is not linear, showing at temperatures below 150 K a deviation characteristic for ferromagnetic interactions. The resistivity gradually increases from 23 μΩ cm at the lowest temperatures to about 120 μΩ cm at 300 K. The thermal variation of the specific heat in the temperature interval between 1.5 and 300 K is well approximated by a value for Θ_D of 335 K and by a value for γ of 31 mJ/K^2 mol (Gignoux et al. 1980b). A suppression of the magnetic properties upon charging with hydrogen gas has been observed by Buschow et al. (1982). Al substitution for nickel has a similar effect: for 1.5% of Al the system becomes paramagnetic (Dubenko et al. 1990).

5.3.3.2. $CeNi_3$. In the compound $CeNi_3$, the Ce ions are tetravalent and do not carry a magnetic moment. Moreover the 3d-electron magnetism disappears. Hydrogen

absorption, however, leads to a change in valence of Ce ions from near 4 to near 3 as is evidenced by the temperature dependence of the susceptibility. The Curie–Weiss constant of the hydrogenated compound has been reported to be close to that expected for the Ce^{3+} ion (Buschow 1980b, Buschow et al. 1982a).

5.3.3.3. $TbNi_3$. Magnetization studies at 4.2 K on single-crystalline $TbNi_3$ by Hashimoto et al. (1987) have revealed the easy direction of magnetization to be along the *b* axis. The magnetization curves are shown in fig. 5.15. The value for the spontaneous magnetic moment, M_s, is equal to $7.52\mu_B$/f.u. Powder neutron diffraction measurements by Yakinthos and Paccard (1972) have not revealed a Ni magnetic moment. In the paramagnetic region the susceptibility obeys the MC–W law yielding an effective moment of $9.81\mu_B$ which indicates an almost zero Ni contribution. The large anisotropy in the values for the paramagnetic Curie temperature ($\theta_\perp = 63$ K and $\theta_\parallel = 9$ K) points to a remarkably large value of the second-order CEF parameter. Owing to the complex magnetization curves a canted magnetic structure of the Tb moments has been suggested by Hashimoto et al. (1987), resulting from the competition between the different easy directions at the different sites. A mean-field analysis, including crystal-field interactions, of the magnetization curves results in values for the crystal-field coefficients at the two inequivalent Tb sites of -806 and $+135$ for the coefficient A_2^0, -19 and -17 for A_4^0 and -2.5 and -141 for A_4^3 (in units of $K a_0^{-n}$), respectively (Hashimoto et al. 1987). Moreover, the exchange parameter between the R spins has been found to be quite different at the different sites.

5.3.3.4. $HoNi_3$. For the compound $HoNi_3$ the spontaneous magnetic moment determined for a single-crystalline sample at 4.2 K amounts to $8.2\mu_B$/f.u. with the easy direction of magnetization along the *b* axis. The magnetization curve measured by Hashimoto (1988) along the *c* axis that turned out to be the hard axis shows a complex behaviour with three steps. The magnetization curves are presented in fig. 5.15, $T_c =$

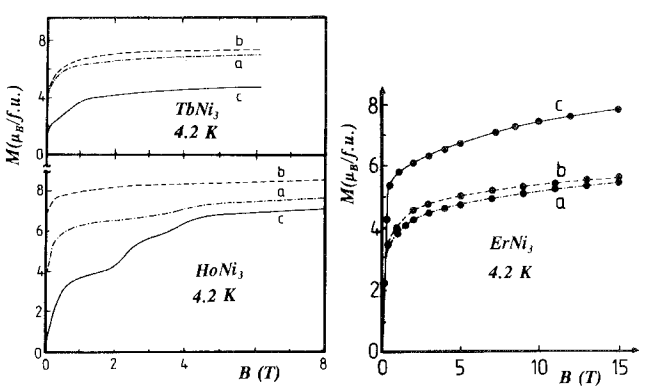

Fig. 5.15. Magnetization curves at 4.2 K (a) for single-crystalline $TbNi_3$ (after Hashimoto et al. 1987) and $HoNi_3$ (after Hashimoto 1988), and (b) for $ErNi_3$ (after Kebe 1983) along different hexagonal crystallographic directions.

56 K. Powder neutron diffraction measurements by Yakinthos and Paccard (1972) indicate that the compound orders ferromagnetically with partially quenched moments of $9.3\mu_B$ and $7.9\mu_B$ at the two Ho sites. In this compound nickel does not carry a moment. A plot of the inverse susceptibility versus temperature along the principal axes, indicates MC–W behaviour with an effective moment of $10.7\mu_B$, close to that of the Ho^{3+} ion. An anisotropy in the paramagnetic Curie temperature ($\Theta_\perp = 35$ K and $\Theta_\parallel = 6$ K) indicates substantial crystal-field effects; B_2^0 is estimated to be 0.236 cm^{-1} (0.34 K). The CEF coefficients derived from magnetization studies by Hashimoto (1988) seem to be unrealistically large. The values for the crystal-field coefficients reported for $TbNi_3$ do not describe the magnetic isotherms of $HoNi_3$. A preferential site occupation in $Er(Ni–Fe)_3$ compounds has been found by Tharp et al. (1987) by means of neutron-diffraction experiments.

5.4. R_2T_7 compounds ($T = Co, Ni$)

5.4.1. R_2Co_7 compounds

These compounds crystallize in a rhombohedral structure, belonging to the space group $R\bar{3}m$. There are two crystallographic sites for the R atoms whereas cobalt atoms are distributed over five different sites. The structure is obtained by relevant replacements of the Cu ions by the Ca ions in every third basal plane of the $CaCu_5$ structure according to the formula:

$$3RCo_5 + R - Co \rightarrow 2R_2Co_7$$

As a consequence, the lattice parameter a equals approximately that observed for RCo_5 compounds, i.e., about 495 pm whereas the parameter c for the rhombohedral Y_2Co_7 amounts to 3621 pm, approximately nine times that of YCo_5.

Although at first sight complex, the rhombohedral R_2T_7 structure can be schematized as an alternative stacking along the trigonal axis of two kinds of building blocks. It is illustrated fig. 5.16. The first block contains three cobalt sites (Co_{II}, Co_{III}, Co_{IV}) with a nearest-neighbour surrounding similar as in hexagonal YCo_5. In the block with the two remaining sites (Co_I and Co_V), cobalt atoms have a nearest-neighbour surrounding close to that in YCo_2. On basis of these crystallographic considerations one expects to find in the R_2Co_7 compounds two types of Co moments (with the ratio 1 : 1): stable and highly unstable similar to those observed in YCo_5 and in YCo_2, respectively. By band structure calculations Inoue and Shimizu (1985) found that Y_2Co_7 is close to the saturated ferromagnetic state.

The magnetic properties can be briefly summarized as follows: (i) the cobalt moment varies from about $1.3\mu_B$ in Y_2Co_7 to $1.5\mu_B$ in Gd_2Co_7; (ii) the Co sublattice magnetization exhibits a preference for the c axis; (iii) the mean value of the CEF coefficient A_2^0 of the two nonequivalent 4f sites is negative corresponding to the planar preference for the R ions with $\alpha_J < 0$ and to the uniaxial preference for the ions with $\alpha_J > 0$. A basal-plane preference is observed in the Nd and Tb compounds, indeed. The same is expected for the Pr, Dy and Ho compounds. For all these compounds temperature-induced moment reorientations are expected due to the competition between the 4f and Co anisotropy. For Tb_2Co_7 this transition has been observed at 440 K, indeed.

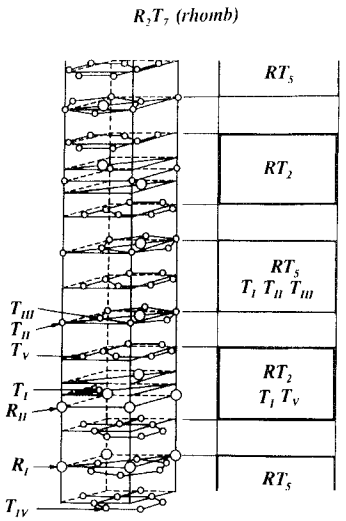

Fig. 5.16. Distribution of the R and T ions within the crystallographic structure of the R_2T_7 compound together with the construction of the R_2T_7 structure from the RT_5 and RT_2 blocks. After Ballou (1989).

The magnetic measurements have not yet resulted in a set of CEF parameters for the rare-earth ions. Zhou et al. (1992) have reported magnetization curves at 4.2 K up to 35 T on free particles of the ferrimagnetic $(R-Y)_2Co_7$ compounds with R = Gd, Tb, Dy, Ho, Er and Tm, see fig. 5.17. For compounds with a composition close to compensation, a linear increase of the magnetization with field has been observed that allows for the evaluation of the coupling parameter. The tendency for the parameter J_{RCo} to decrease from R = Gd towards the end of the lanthanide series has been found to be less pronounced than observed in other intermetallics. However, a strong variation of n_{RT} as a function of the Y substitutions has been observed for all the $R_{2-x}Y_xCo_7$ series. For instance, values of 20.3, 18.3 and 17.9 T f.u./μ_B have been found for $x = 0.7$, 0.6 and 0.5 of the $Gd_{2-x}Y_xCo_7$ series. An extrapolation of these values to $x = 0$ leads to a value of 14.4 T f.u./μ_B that has been found in high-field magnetization studies on single-crystalline Gd_2Co_7 (Ballou et al. 1992a). Thus, it can be concluded that the value of 152 T found by these latter authors for the exchange field in Gd_2Co_7 is representative for the heavy rare-earth compounds. It corresponds to a value for J_{RFe} of -7.40 K. Thermal expansion in a wide temperature range have been studied by Andreev et al. (1988a).

5.4.1.1. Y_2Co_7. Values of 8.5μ_B/f.u. and 9.6μ_B/f.u. have been reported for M_s from single-crystal magnetization studies on Y_2Co_7 at 4.2 K by Ballou (1987, p. 71) and Andreev et al. (1985a), respectively. This substantial difference likely originates from different stoichiometries. There is a large coexistence range for Y_2Co_7 in the phase diagram. A deviation from the 2:7 stoichiometry towards the Co-poor side has large effects on M_s. For a single crystal with a composition of $Y_2Co_{6.7}$ a value for M_s of

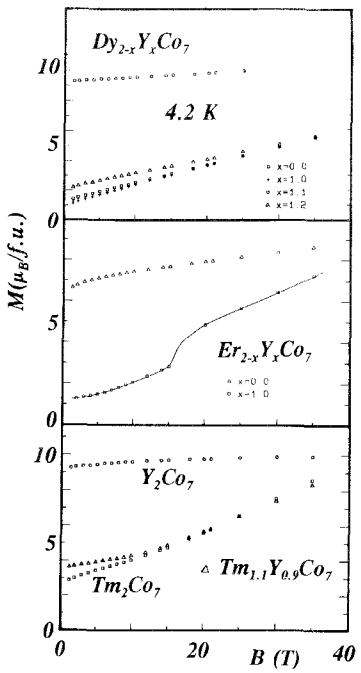

Fig. 5.17. High-field magnetization curves at 4.2 K for free powder particles of some ferrimagnetic $R_{2-x}Y_xCo_7$ compounds. After Zhou et al. (1992).

6.1μ_B has been reported by Ballou and Lemaire (1988). The observed anomalous temperature dependence of the anisotropy constants has been considered by Ballou (1989) to be due to metamagnetic instabilities of the cobalt moment. This metamagnetic behaviour has been attributed to the cobalt ions at the sites I and V. These sites have local surroundings similar to that in the cubic C15 structure and are expected to behave similarly to those of YCo_2. Single-crystalline $Y_2Co_7H_6$ has been reported by Andreev et al. (1986a) to be antiferromagnetic with a metamagnetic transition to ferromagnetism at fields above 2 T. Magnetic studies on Th_2Co_7 have been reported by Andreev et al. (1984b).

5.4.1.2. La_2Co_7. Buschow and de Chatel (1979) have reported a reduction of the Co moment upon hydrogenation from 1.0μ_B in La_2Co_7 to 0.6μ_B in $La_2Co_7H_5$.

5.4.1.3. Ce_2Co_7. A substantial increase of both T_c and the spontaneous magnetization has been observed after hydrogenation by Buschow (1980b). The value for T_c of 50 K increases to about 230 K for $Ce_2Co_7H_7$. This effect has been explained as due to the recovery of the trivalent state of the Ce ion after hydrogenation.

5.4.1.4. Nd_2Co_7. The compound Nd_2Co_7 is a planar system with the EMD at 4.2 K along the *a* axis. The value for M_s along that direction amounts to 14.6μ_B/f.u.

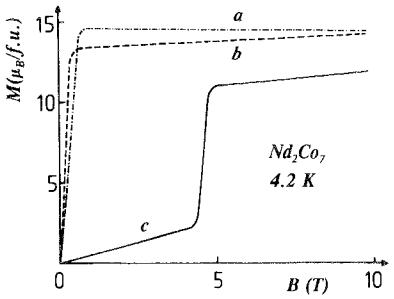

Fig. 5.18. Magnetization curves at 4.2 K for single-crystalline Nd_2Co_7. After Andreev et al. (1988b).

(Bartashevich et al. 1992a). Magnetization studies up to 75. T on a single-crystalline sample performed by Andreev et al. (1988b) have revealed a sharp and significant magnetic transition at 5 T for the field applied along the hard hexagonal c axis. The magnetization curves are presented in fig. 5.18. The magnetization after the transition does not reach saturation pointing to the formation of a local energy minimum at an angle of 45° with respect to the c axis. These phenomena are associated with the Nd ions. The temperature-induced moment reorientation transition from the plane to the c axis occurs in the temperature range between 211 and 258 K (Marusi et al. 1991). Andreev et al. (1988b) have reported that hydrogenation dramatically reduces T_c from 613 to 35 K only for $Nd_2Co_7H_{8.5}$. This reduction is accompanied by the reduction of the spontaneous magnetization to $3.7\mu_B$/f.u.

5.4.1.5. Gd_2Co_7. For the compound Gd_2Co_7 a value for M_s of $4.2\mu_B$/f.u. has been reported for a single-crystalline sample at 4.2 K by Andreev et al. (1985a). A much lower value of $3.5\mu_B$/f.u. has been found by Ballou et al. (1992a). The difference is likely due to imperfections of the former single crystal that contains substantial amounts of the 1 : 3 phase. Magnetization curves up to 35 T reported by Ballou et al. (1992a) and shown in fig. 5.19 are very close to earlier two-sublattice model calculations performed by Radwański (1986a). The analysis of high-field magnetization curves within the two-sublattice model have resulted in: $M_{Co} = 10.5\mu_B$/f.u., $M_{Gd} = 14\mu_B$/f.u., $K_1^{Co} = +52$ K/f.u., $E_a^{Gd} = 0$ and $B_{mol,RT}^{Gd} = 152$ T. Yoshie et al. (1992) have found the hyperfine fields of +8.8, +6.7, −7.2 and −6.9 T for the 3b, 12c, 9e and 18h sites, respectively. The positive sign would indicate that the Co ions at the 3b and 12c sites have a large orbital contribution to the magnetic moment. Andreev et al. (1985a) have reported that hydrogenation reduces T_c but increases M_s. For single-crystalline $Gd_2Co_7H_{7.7}$ T_c amounts to about 420 K, a value that is 60% of that observed for the pure compound.

5.4.1.6. Tb_2Co_7. For the compound Tb_2Co_7 a value for the spontaneous moment at 4.2 K of $7.3\mu_B$/f.u. has been reported by Andreev et al. (1982). With the full Tb^{3+}-ion moment this value results in a moment per cobalt atom of $10.7\mu_B$/f.u., close to that observed in Gd_2Co_7. T_c amounts to 720 K. The moment reorientation at 440 K is

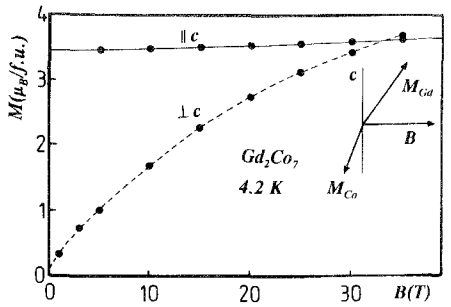

Fig. 5.19. Magnetization curves at 4.2 K for single-crystalline Gd_2Co_7. The moment configuration at 30 T for $\boldsymbol{B} \perp \boldsymbol{c}$ is shown. After Ballou et al. (1992a).

due to the competition between the c-axis preference of the Co sublattice magnetization and the planar anisotropy of the Tb sublattice.

5.4.1.7. Ho_2Co_7. Apostolov et al. (1988) have reported that the value for T_c of 670 K for Ho_2Co_7 is reduced by hydrogenation to about 200 K ($Ho_2Co_7H_{2.6}$).

5.4.1.8. Er_2Co_7. The value of 140 K for the compensation temperature of Er_2Co_7 in combination with the spontaneous moment of $7.5\mu_B$/f.u. yields a value for the molecular field experienced by the Er^{3+}-ion moment of 46 T (Radwański 1986c).

5.4.2. R_2Ni_7 compounds

These compounds have attracted significant attention because of the unique phenomenon of the temperature-induced ferromagnetism originally reported for Y_2Ni_7 by Gignoux et al. (1981). In principle, theoretical works have shown the possibility for these phenomena by the formation of a special shape of the DOS (M. Shimizu et al. 1984, Misawa 1988). The formation of a paramagnetic ground state at low temperatures has been, however, questioned by theoretical studies of Irkhin and Rosenfeld (1985) and by Vonsovsky et al. (1988) as well as by experimental studies of Buschow (1984). Actually, recent studies by Ballou et al. (1990a) have found that the temperature-induced ferromagnetism in Y_2Ni_7 had originated from Gd impurities. Dubenko et al. (1990) have reported the spontaneous magnetization of Y_2Ni_7 at 4.2 K as $0.43\mu_B$/f.u. and a value of 60 K for T_c. These authors have found that substitution of aluminium for nickel suppresses rapidly the ferromagnetism: both M_s and T_c decrease drastically and at 3–5 at.% of aluminium the compound is already paramagnetic. Limited cobalt substitutions transform Y_2Ni_7 into a paramagnetic material. Buschow (1984a,b) has found that hydrogenation of Y_2Ni_7 causes a remarkable increase of T_c to 98 K. In contrary, La_2Ni_7 becomes Pauli paramagnetic upon hydrogen charging.

Among the compounds with a magnetic rare-earth partner the highest value for T_c of 116 K occurs for the gadolinium compound. The pressure dependence of T_c measured by Jaakkola et al. (1983) for R = Gd, Tb, Dy and Nd has revealed that pressure effects are small.

5.5. R_6T_{23} compounds ($T = Fe, Mn$)

These compounds crystallize in the Th_6Mn_{23}-type of structure, space group Fm3m. There is only one site available for the R ions whereas the Fe or Mn atoms are distributed over four different sites, see table 5.1. The structure can be considered as a face-centered cubic arrangement of the R octahedron surrounded by 3d atoms. The crystal symmetry is cubic but the local symmetry of the rare-earth site is uniaxial (4mm), with a fourfold axis, due to the octahedral arrangement of the R atoms in the cell.

5.5.1. R_6Fe_{23} compounds

Only compounds with Y and the heavy rare-earths are formed. Single-crystalline results have been reported for Y_6Fe_{23}. Free-powder high-field magnetization studies at 4.2 K up to 35 T have been reported by de Boer et al. (1990) for Er_6Fe_{23}. The studies result in a value of 1.70 T f.u./μ_B for n_{ErFe}. With the iron sublattice moment of 46.5μ_B/f.u. it yields a value of 240 T for the exchange field, a value that is representative for the heavy rare-earth compounds. Similarly, a value of 2.0μ_B is representative for the Fe moment in R_6Fe_{23}.

Hydrogen uptake up to 16 (25) hydrogen atoms per formula unit can be realized. In case of the Fe compounds the hydrogen enhances strongly the magnetism of the Fe sublattice. T_c of 485 K for Y_6Fe_{23} increases to 743 K in the hydrogenated compound (Pedziwiatr et al. 1983). The Fe moment itself is enhanced which is reflected in the increase of the ^{57}Fe hyperfine field (Wallace et al. 1987). Studies of Rhyne et al. (1983, 1987) and Wallace et al. (1987) have revealed that the increase of the Fe sublattice magnetization by hydrogenation leads in case of ferrimagnetic compound like Ho_6Fe_{23} to a substantial decrease of the spontaneous magnetization and of the compensation temperature. The hydrogen effects have been discussed by Gubbens et al. (1984a) as due to an enhancement of the Fe–Fe interactions in combination with a pronounced weakening upon hydrogen uptake of the R–Fe interactions. Properties of hydrogenated compounds have been reviewed by Wiesinger and Hilscher (1991).

Magnetostriction has been measured in the R_6Fe_{23} compounds between 80 and 300 K by Abbundi et al. (1980) for R = Ho, Er, Tm. The sign of $\lambda_{\parallel} - \lambda_{\perp}$ follows the Stevens factor α_J of the R ion involved (Herbst and Croat 1984). It means that the anisotropic magnetostriction of the iron sublattice is of minor importance. Indeed, the anisotropic magnetostriction constant λ_{100} for Y_6Fe_{23} is at 5 K less than 5×10^{-5} (Andreev et al. 1990). The volume magnetostriction of this compound, is, however, substantial and amounts at 5 K to 10.2×10^{-3}. For Ho and Er compounds, the magnetostriction shows a well-pronounced peak at 193 and 100 K, respectively, associated with the compensation temperature (Herbst and Croat 1984, Croat 1980). For Tm_6Fe_{23} no anomaly has been observed above liquid-nitrogen temperature and the compensation point is expected to be below 40 K.

5.5.1.1. Y_6Fe_{23}. From magnetization studies at 4.2 K on a single-crystalline Y_6Fe_{23} sample, values for M_s of 39.3μ_B/f.u. and for T_c of 483 K have been determined by

Andreev et al. (1990). The easy direction of magnetization lies along the cubic axis. The cubic anisotropy constant K_1 amounts to $+3.6 \times 10^{-5}$ J m^{-3}. Thermal expansion measurements point to a small value for λ_{100}. NMR studies by Armitage et al. (1989) have revealed five signals in the range 30–50 MHz. The most intensive signal at 39.1 MHz (corresponding with a hyperfine field of −18.7 T) originates from the ^{89}Y nuclei. In external magnetic fields the NMR signals are shifted to lower frequencies indicating the presence of negative local fields on the Y nuclei.

5.5.1.2. Dy_6Fe_{23}. For the compound Dy_6Fe_{23}, T_c amounts to 536 K and $M_s = 14.90\mu_B$/f.u. (Bara et al. 1982b). These authors have reported Mössbauer measurements on ^{57}Fe and ^{161}Dy. The hyperfine field at the ^{161}Dy nuclei amounts to 905 MHz. These studies indicate that the EMD lies along the ⟨111⟩ direction. The compensation of the magnetization occurs at 273 K. Assuming a Brillouin function for the temperature dependence of the Dy sublattice magnetization and taking a value of $42\mu_B$/f.u. for the Fe sublattice at the compensation temperature (10% reduction of the zero-temperature value) one gets a molecular field of 112 T.

5.5.1.3. Er_6Fe_{23}. Magnetization measurements at 4.2 K by Frings et al. (1983) on a polycrystalline sample of Er_6Fe_{23} yield a value for M_s of 16 A m^2/kg ($6.6\mu_B$/f.u.). A slightly larger value of $7.5\mu_B$/f.u. has been reported by de Boer et al. (1990). With the full trivalent erbium moment this latter value results in a value of $46.5\mu_B$/f.u. for M_{Fe} and an Fe moment of $2.02\mu_B$. Frings et al. (1983) have derived from high-field magnetization measurements at 4.2 K up to 35 T on a polycrystalline sample, a value for n_{RT} of 0.595 T kg/A m^2 (= 1.45 T f.u./μ_B). A higher value of $1.70\mu_B$/T f.u. has been found from the slope of the magnetization curve for free powder particles in the field interval of 15 to 35 T by de Boer et al. (1990). This latter value corresponds with a value for the exchange field of 240 T. The high-field magnetization curves for free powder particles of Er_6Fe_{23} and Er_5YFe_{23} are presented in fig. 5.20.

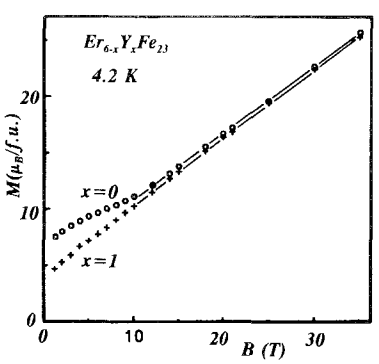

Fig. 5.20. Magnetization curves for free powder particles of Er_6Fe_{23} and Er_5YFe_{23}. After de Boer et al. (1990).

5.5.1.4. Tm_6Fe_{23}. Values of 480 K and $12\mu_B$/f.u. have been reported for T_c and M_s in Tm_6Fe_{23}, respectively. Gubbens et al. (1984a) derived a value of 103 T for B_{mol}^{Tm} from the thermal variation of the ^{169}Tm hyperfine field and of the quadrupolar splitting measured by means of the Mössbauer effect. This value is too large compared with that expected on the basis of the high-field studies of Er_6Fe_{23} likely due to the presence of CEF interactions.

5.5.1.5. Lu_6Fe_{23}. Magnetic properties and ^{57}Fe Mössbauer effect in this compound have been studied by Gubbens et al. (1981). The Fe magnetic moment increases upon hydrogen charging from $1.54\mu_B$ to $1.64\mu_B$ in $Lu_6Fe_{23}H_8$.

5.5.2. R_6Mn_{23} compounds

Magnetism of these compounds is not understood well yet. The highest Curie temperature occurs for the Y compound in contrary to general systematics found in Fe, Co and Ni compounds where the highest value for T_c occurs for the Gd compounds. The values for the magnetic ordering temperature around 450 K indicate that the magnetism is primarily controlled by interactions between manganese ions. The anisotropy is, however, related with rare-earth ions. CEF parameters are not yet available. The interplay of exchange interactions between the different Mn ions and CEF interactions leads to complex magnetic structures. It is marked by nonlinear magnetization curves observed even for Gd_6Mn_{23}.

Magnetic properties of these compounds have been compared by Buschow et al. (1982a,b) with properties of hydrogenated compounds. Hydrogen uptake up to 25 hydrogen atoms per the formula unit can be realized. The influence of hydrogen is complex. For Y_6Mn_{23} the absorption of hydrogen leads to a complete loss of magnetic order down to helium temperature though moderate absorption increases T_c of Y_6Mn_{23} from about 490 K to about 700 K for $Y_6Mn_{23}H_{20}$ (Crowder and James 1983). The hydrogen uptake converts Th_6Mn_{23} from a Pauli paramagnetic material into a magnetically ordered hydride with T_c as high as 329 K (Malik et al. 1977, Boltich et al. 1982). In case of the compounds with magnetic rare-earth hydrogen uptake leads to a substantial reduction of both Curie temperature and spontaneous magnetization (Buschow et al. 1982a,b). See the review of Wiesinger and Hilscher (1991) for more details.

Specific heat for R_6Mn_{23} compounds with R = Lu, Gd, Dy and Er has been measured by Graves-Thompson et al. (1983). In all cases the temperature dependence of the heat capacity in the temperature range from 1.7 to 18 K does not show anomalies. For Lu_6Mn_{23} the c/T versus T^2 plot is well approximated by a straight line with $\gamma = 277$ mJ/K^2 mol and $\Theta_D = 270$ K. For Y_6Mn_{23} the NMR spectrum contains three resonance lines at 90, 112 and 130 MHz (Berthier et al. 1988a). NMR studies reported by Nagai et al. (1988a) have revealed that the resonance frequency on the ^{55}Mn nuclei in Dy_6Mn_{23}, Ho_6Mn_{23} and Gd_6Mn_{23} decreases with the applied field. The transferred hyperfine fields in the Dy and Ho compounds are small in magnitude and comparable with those observed in Y_6Mn_{23}.

5.5.2.1. Y_6Mn_{23}. Single-crystal magnetization measurements on Y_6Mn_{23} reported by Delapalme et al. (1979) have revealed the EMD to be along the cube axis

with $M_s = 13.8\mu_B$/f.u. at 4.2 K and $9.9\mu_B$/f.u. at room temperature. The ferrimagnetic arrangement of the Mn moments is confirmed by polarized neutron experiments. These experiments have revealed different manganese moments at the different crystallographic sites. At 4.2 K, moments of -2.8, -2.1, $+1.8$, $+1.8\mu_B$ have been found by Delapalme et al. (1979) by means of polarized neutron studies for the sites b, d, f_1 and f_2, respectively. The negative value for the moments at the site b and d show that these moments are oriented antiparallel to the bulk magnetization. Systematically smaller values are observed at 300 K. The low-temperature values are accounted for by band-structure calculations of Inoue and Shimizu (1985). These authors concluded, that the concentration dependence of T_c, the magnetic moment and the specific-heat coefficient γ in $Y_6(Mn–Fe)_{23}$ as has been found by James et al. (1979b) cannot be explained by a rigid-band model. Neutron-diffraction studies on $Y_6(Fe–Mn)_{23}$ by Hardman-Rhyne and Rhyne (1983) have revealed a complex magnetic structure. Mössbauer studies of $Y_6Mn_{23}H_x$ and $Gd_6Fe_{23}H_x$ have been reported by Kozłowski et al. (1990) and Wortmann and Zukrowski (1989), respectively. Absorption of hydrogen gas leads to the loss of magnetic order in Y_6Mn_{23} and to Pauli paramagnetism (Buschow et al. 1982a,b). The reversed process has been observed for Th_6Mn_{23}.

5.5.2.2. Gd_6Mn_{23}. Magnetization studies by Delapalme et al. (1979) on Gd_6Mn_{23} have revealed a spontaneous moment, M_s, of $38.5\mu_B$/f.u. at 4.2 K. However, the magnetization increases strongly with field indicating complex magnetic structures that are sensitive to external conditions. The magnetization curves are presented in fig. 5.21. At high fields the magnetization approaches saturation at a level of $54.5\mu_B$/f.u. They do not show anisotropy as is expected for an S-state 4f ion.

5.5.2.3. Dy_6Mn_{23} and Er_6Mn_{23}. A significant anisotropy has been observed by Hardman et al. (1979) for single-crystalline Dy_6Mn_{23} and Er_6Mn_{23}. The easy direction of the magnetization is along $\langle 110 \rangle$ for the Dy compound and along $\langle 100 \rangle$ for the Er compound (Hilscher and Rais 1978). No conclusive quantitative analysis of the magnetization process in these manganese compounds is available at present. Pouranian et al. (1980a,b) have reported that the hydrogenated compounds $Dy_6Mn_{23}H_{23}$ and $Er_6Mn_{23}H_{23}$ do not show any magnetic ordering down to helium temperature. Magnetic order, however, has been observed by Stewart et al. (1981) in $Er_6Mn_{23}H_{21}$ below 85 K by means of ^{57}Fe (0.5% substitution of the Mn atoms) and ^{166}Er Mössbauer spectroscopy. The value of the ^{166}Er hyperfine field indicates the Er^{3+}-ion moment in Er_6Mn_{23} to be $7.6\mu_B$. After hydrogenation the value of the hyperfine field decreases only by 3% indicating the same value for the Er-ion moments in $Er_6Mn_{23}H_{21}$ that largely cancel themselves due to the antiferromagnetic structure.

5.5.2.4. Ho_6Mn_{23}. Pouranian et al. (1980a) have found a value for M_s of $59.8\mu_B$/f.u. and for T_c of 434 K. These authors have reported that hydrogenation transforms the system to paramagnetic. A noncollinear antiferromagnetic structure, however, has been revealed at 9 K by neutron-diffraction studies of $Ho_6Mn_{23}D_{22}$ by Littlewood et al. (1986). The structure is no longer cubic but tetragonal, P4/mmm. Ho moments with rather low values, close to $3.5\mu_B$, have been found on all sites. Mn moments differ substantially from site to site and range from 0 to $3.5\mu_B$.

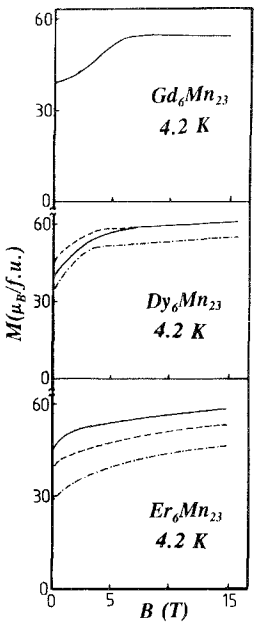

Fig. 5.21. Magnetization curves at 4.2 K for R_6Mn_{23} (R = Gd, Dy, Er), along different cubic crystallographic directions; ⟨111⟩: solid curve; ⟨110⟩: dashed curve; ⟨100⟩: dash–point curve. After Delapalme et al. (1979).

5.6. *RT_5 compounds (T = Co, Ni)*

The cobalt and nickel compounds that are formed with this composition crystallize in the hexagonal $CaCu_5$-type of structure. In compounds with cobalt, there is an increasing tendency for the heavy rare earths to form compounds richer in Co: RCo_{5+x}. Non-stoichiometric compounds have been reported for $GdCo_{5.14}$, $TbCo_{5.1}$, $DyCo_{5.2}$, $HoCo_{5.5}$, $ErCo_6$. The additional Co atoms are statistically located at the rare-earth site in the form of dumbbell-pairs. These dumbbells are characteristic for the 2:17 structure in which structure they occupy fixed positions. The extra Co sites are denoted as 6i and 2e. For the actual composition one can write: $R_{1-s}Co_{5+2s}$, where s denotes the number of dumbbells formed. In $ErCo_6$, for instance, $s = \frac{1}{8}$. In this compound more than 12% of the places occupied by R atoms in the ideal $CaCu_5$ structure, are replaced by Co pairs. For $s = \frac{1}{3}$ the composition becomes equal to that of 2:17 compounds.

5.6.1. *RCo_5 compounds*

In the RT_5 compounds with Co, T_c is of the order of 1000 K and the cobalt moment, as deduced from magnetization studies, is approximately $1.64\mu_B$, a value that is only slightly lower than that observed in Co metal. Within the RCo_5 series, $SmCo_5$ has attracted most interest because of its extraordinary large anisotropy that makes the compound suited for permanent-magnet applications. The anisotropy field has been reported to be as large as 60 T at 4.2 K, implying a value for the anisotropy energy

of about 40 MJ m^{-3}. A substantial part of this anisotropy still exists at room temperature due to the large value of B_{mol}^{Sm}. Compounds with the heavy rare earths exhibit rather small values for the spontaneous magnetization because of the antiparallel moment alignment. The cobalt anisotropy in RCo_5 compounds is extraordinary large and favours the c axis, $K_1 = +47.0$ K/f.u. The second-order CEF term of the R ions is dominant and the easy magnetic direction follows the Stevens factor(s). For R ions with a negative value for the second-order Stevens factor α_J (Pr, Nd, Tb, Dy and Ho), the R anisotropy competes with the Co anisotropy in determining the easy direction of the net magnetization. In that case, tilted and noncollinear magnetic structures can be expected. Indeed, in Pr and Ho compounds the EMD direction is tilted away from the hexagonal axis by 23° and 72°, respectively. In other compounds, i.e., with Nd, Tb and Dy, TIMR phenomena occur at ambient temperatures. The main features of these phenomena are well accounted for by the single-ion anisotropy in combination with an exchange field of 160 T (Radwański 1986d) which value is representative for the heavy RE's. In the reorientation region, magnetoelastic properties exhibit peculiarities (del Moral et al. 1987). Compounds with the heavy rare earths are very sensitive to external fields as the net magnetization is small. The case of $GdCo_5$ has been discussed in section 3.1.

Polarized neutron experiments have enlightened the origin of the large anisotropy of YCo_5. Experiments by Schweizer and Tasset (1980) reveal that the spin density at the site 2c has a larger spatial distribution than that at the site 3g. It is concluded that the 2c ions give the dominant contribution to the anisotropy energy. This view is supported by NMR studies in which a substantial difference in the values for the hyperfine field is observed for these two sites as already mentioned in section 3.3.1. Pirogov et al. (1986) evaluated the cobalt anisotropy at the site c and g as +11.8 and +6.4 K, respectively.

The first analysis of the rare-earth contribution to the magnetocrystalline anisotropy of the RCo_5 series was performed by Greedan and Rao (1973). Values for the crystal-field coefficients A_2^0 of $-180\,\mathrm{K}\,a_0^{-2}$ (derived on the basis of a point-charge model with R^{3+} ions only) and for the exchange field B_{ex}^{R} of 315 T were taken constant across the RCo_5 series. It was found that the sign of the crystal-field parameter B_2^0 determines the direction of the easy axis of magnetization: for negative values of B_2^0 the hexagonal c axis is the easy axis whereas for a positive value of B_2^0 the easy direction lies within the hexagonal plane. The model has been extended in order to take into account the spin-reorientation phenomena observed for Pr, Nd, Tb, Dy and Ho compounds (Radwański 1986d). The temperature dependence of the rare-earth contribution to the magnetocrystalline anisotropy of RCo_5 is shown in fig. 5.22. The predicted easy direction of the magnetization in the RCo_5 series are in agreement with those observed experimentally except for the Pr and Ho compounds for which tilted structures occur with the easy direction slightly deviating from the hexagonal plane. These tilted structures cannot be accounted for by one single CEF parameter and at present they are supposed to result from higher-order crystal-field contributions. The zero-temperature anisotropy of the R sublattice as well as its temperature dependence can be represented well by a value of $-190\,\mathrm{K}\,a_0^{-2}$ for A_2^0. The model calculations, however, should be extended in order to take into account all four CEF parameters related

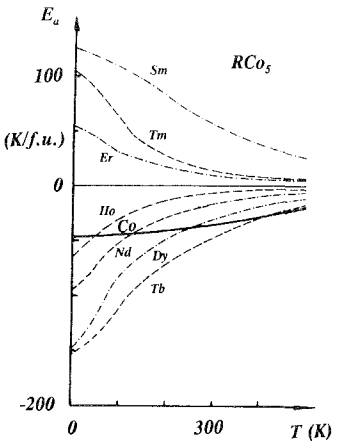

Fig. 5.22. The temperature dependence of the rare-earth contribution to the magnetocrystalline anisotropy of RCo_5 compounds. The heavy full line represents the temperature dependence of the Co-sublattice anisotropy. The moment reorientation occurs in the neighbourhood of the temperature where the absolute values of the R- and Co-sublattice anisotropy are equal. After Radwański (1986d).

with the hexagonal symmetry. Liu et al. (1991a) have evaluated the 3d–4f exchange interactions by means of high-field magnetization studies on free powder particles of ferrimagnetic compounds. Some of these magnetization curves are presented in fig. 5.23. Values for $-J_{RT}/k_B$ have been found to decrease from 9.5 K for the Tb compound to 7.8 K for the Tm compound.

5.6.1.1. YCo_5. The compound YCo_5 is a simple ferromagnet with a value for T_c of 980 K. The compound shows an extraordinary large anisotropy, in fact the largest among all compounds in which only 3d ions are involved, leading to a value for the anisotropy field of 16.5 T (see fig. 3.1) and a value for K_1 of +9.4 K/ion. The value for M_s of $8.2\mu_B$/f.u. at 4.2 K points to a cobalt moment of $1.64\mu_B$. The small value for the differential susceptibility in high magnetic fields of $\chi_{hf} = 27 \times 10^{-4}\,\mu_B$/T f.u. points to a stable cobalt moment. It is worth noting that in an off-stoichiometric $ThCo_5$ compound, a metamagnetic transition of the same origin as in YCo_2 has been observed by Givord et al. (1979b), Gignoux (1987) and Andreev et al. (1984a). The latter authors estimated the values for the local susceptibility of the Co moment as 61 and $79 \times 10^{-4}\mu_B$/T at the sites 2c and 3g, respectively. These values are much larger than in YCo_5. NMR spectra contain two lines at +1.5 T and −9.2 T that have been attributed by Yoshie et al. (1988a) to the sites 2c and 3g, respectively. A positive sign at the site 2c is unusual and has been related with a large orbital contribution to the hyperfine field at this site. These results support an earlier conclusion from NMR studies of Streever (1977) and from polarized neutron measurements of Schweizer and Tasset (1980) that the dominant magnetocrystalline anisotropy in YCo_5 originates from the 2c site. The Co-sublattice anisotropy has been studied by Drzazga et al. (1991) in boron-substituted YCo_5 and $GdCo_5$ compounds.

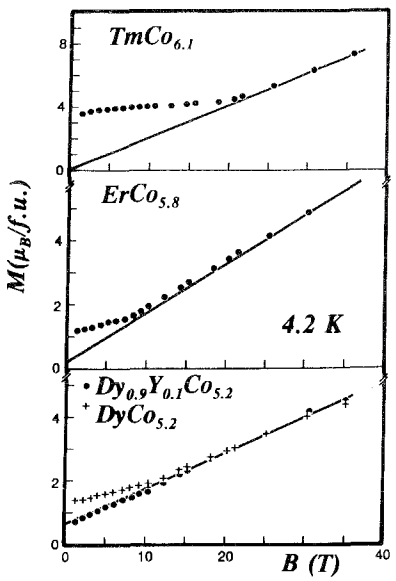

Fig. 5.23. High-field free-powder magnetization curves for some ferrimagnetic RCo_5 compounds at 4.2 K. After Liu et al. (1991a).

5.6.1.2. $LaCo_5$. The compound $LaCo_5$ shows properties that are much the same as those of YCo_5. The magnetocrystalline anisotropy energy at 4.2 K amounts to 7.5 MJ m^{-3} and is weakly temperature dependent (Ermolenko 1979). NMR spectra have been measured by Yoshie and Nakamura (1988b).

5.6.1.3. $CeCo_5$. For the compound $CeCo_5$, mixed-valence properties have been reported on the basis of NMR experiments by Yoshie et al. (1988b). The tetravalent ion does not carry a magnetic moment and does not contribute to the anisotropy. The Ce^{3+} ion carries a moment and in the RCo_5 structure should exhibit planar anisotropy. The anisotropy energy of 10 MJ m^{-3} reported by Ermolenko (1979) and Andreev et al. (1985d) is larger than that of YCo_5 and indicates that some Ce ions are in the trivalent state. A significant amount of Ce^{4+} ions in $CeCo_5$ has been revealed by L_3 X-ray absorption spectroscopy (Croft et al. 1987).

5.6.1.4. $PrCo_5$. Single-crystal magnetization studies for $PrCo_5$ performed by Andoh et al. (1982) have revealed that in zero magnetic field, the spontaneous magnetization makes an angle of 23° with the hexagonal *c* axis, which angle vanishes in the vicinity of 107 K (Pareti et al. 1988). The tilted structure results from a competition between the planar anisotropy of the Pr ions and the uniaxial anisotropy of the Co sublattice. As a consequence, the magnetic structure, that in general is collinear, is likely to be noncollinear with the canting angle depending on the local anisotropy and the intersublattice coupling. Single-crystal magnetization curves are presented in fig. 5.24.

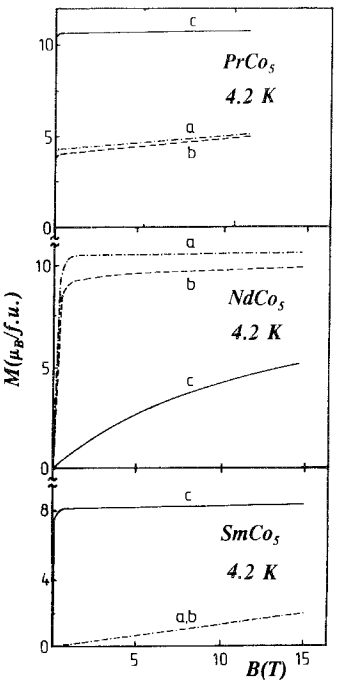

Fig. 5.24. Magnetization curves at 4.2 K for single-crystalline $PrCo_5$ (after Andoh et al. 1982), $NdCo_5$ (after Lu 1981, p. 25) and $SmCo_5$ (after Laforest 1981, p. 45,47) along different hexagonal crystallographic directions.

Andoh et al. (1982) claim a substantial two-ion contribution to the magnetocrystalline anisotropy in this compound following an earlier suggestion of Karpenko and Irkhin (1973). This view is not supported by the analysis of magnetization data on $(Pr–Nd)Co_5$ compounds by Ibarra et al. (1991) and on single-crystalline $PrCo_3Ni_2$ by Ballou et al. (1991). The magnetic phenomena like the tilted magnetic structure and the temperature-induced moment reorientation have been accounted for by the single-ion approach. CEF interactions in $PrCo_5$ have been, however, found to be significantly smaller than in $NdCo_5$, see table 5.5. NMR spectra are rather complex due to the tilted structure, see fig. 3.16. The assignment of the NMR spectra to the different Co sites is still under discussion (Yoshie et al. 1987).

5.6.1.5. $NdCo_5$. Magnetization studies on a single-crystalline sample of $NdCo_5$ by Alameda et al. (1981) reveal a value for the spontaneous magnetization at 4.2 K of $10.5\mu_B$/f.u. along the *a* axis, see fig. 5.24. This moment is considered to be the sum of a cobalt moment, M_{Co}, of $8.2\mu_B$/f.u. and a neodymium moment, M_{Nd}, of $2.3\mu_B$/f.u. Polarized neutron studies give a similar value for the Nd moment (Boucherle et al. 1982, Alameda et al. 1981) but a cobalt moment as large as $1.90\mu_B$. A negative moment contribution from a polarization of the conduction-band electrons has been

TABLE 5.5
CEF coefficients, in units of $K a_0^{-n}$, of the trivalent R ions and the exchange field acting on the R^{3+} ion in RCo_5 compounds.

Compound	A_2^0	A_4^0	A_6^0	A_6^6	B_{ex}^R	Ref.*
$PrCo_5$	+106	−26.5	–	–	260	[1]
$PrCo_5$	−48	−9.6	+0.9	–	328	[2]
$NdCo_5$	−433	+26.0	–	+26.0	267	[1, 3]
$NdCo_5$	−419	−1.9	–	–	330	[2]
$SmCo_5$	−205	0	+4.7	0	360	[4]
$SmCo_5$	−205	0	+4.7	0		[5]
$SmCo_5$	−205	0	+4.7	0	260	[6, 7]
$GdCo_5$					220	[8]
$Gd_{0.93}Co_{5.14}$					219	[9]
$GdCo_5$					235	[10]
$GdCo_5$					195	[11]
$GdCo_{4.5}Ni_{0.5}$					200	[10]
$TbCo_5$					210	[12]
$TbCo_{5.1}$	−205	−12.9	–	+27.3	174	[13]
$DyCo_{5.2}$	−259	−1.5	–	+17.6	156	[1]
$DyCo_{5.2}$					172	[10]
$HoCo_{5.6}$	−412	−30	−0.6	–	800	[14]
$HoCo_{5.5}$	−388	−17	–	–	135	[15]
$HoCo_{5.4}$			–	–	188	[10]
$(Ho–Er)(Co–Ni)_5$	−200	–	–	–	–	[16]
$ErCo_{5.8}$					182	[10]
$ErCo_6$					180	[1]
$TmCo_{6.1}$					170	[10]

*References:

[1] Ermolenko (1982a).
[2] Ibarra et al. (1991).
[3] Ermolenko (1982b).
[4] Sankar et al. (1975).
[5] de Wijn et al. (1976).
[6] Boucherle et al. (1979).
[7] Laforest (1981).
[8] Ermolenko (1979, 1980).
[9] Ballou et al. (1986a, 1987a).
[10] Liu et al. (1991a).
[11] Radwański et al. (1992b).
[12] Ballou et al. (1989).
[13] Ermolenko (1985).
[14] Decrop et al. (1982, 1983).
[15] Ermolenko & Rozhda (1982).
[16] Drzazga and Mydlarz (1988).

suggested in order to reach agreement between the magnetization and neutron results. At increasing temperature up to 300 K, the spontaneous moment is only weakly reduced. At room temperature the moment equals $9.1 \mu_B$/f.u. This small reduction of the moment is related to the large value for B_{ex}^{Nd} estimated by Lu (1981) to be 372 T. The temperature-induced moment reorientation at about 250 K can be understood within the two-sublattice model as resulting from a competition between the Co uniaxial anisotropy and the planar anisotropy of the Nd sublattice. The moment reorientation takes place over a wide temperature range. Two particularities in the thermal variation of the magnetoelastic constant C_{33}, at 248 and 292 K, have been observed by Patterson et al. (1986). The anomalies reported by Sousa et al. (1990)

at 242 and 283 K on basis of resistivity measurements mark the beginning and the end of the moment-reorientation transition. Magnetic measurements of Moze et al. (1990b) and Ibarra et al. (1991) on the (Nd–Pr)Co_5 series have resulted in an evaluation of the CEF and exchange parameters as shown in table 5.5. In the CEF analysis of (Nd–Sm)Co_5 series Han et al. (1991) has considered the variation of the coefficient A_2^0 with temperature. The origin of this variation has not been discussed.

5.6.1.6. $SmCo_5$. Single-crystal magnetization studies for $SmCo_5$, see fig. 5.24, performed by Laforest (1981) reveal a value for M_s at 4.2 K of 8.11 μ_B/f.u., which is smaller than the corresponding value in YCo_5. J-mixing has been suggested to cause the Sm moment to be antiparallel to the cobalt moment. The value of the susceptibility measured along the c axis, $\chi_{hf} = 38 \times 10^{-4} \mu_B$/T f.u., is almost the same as that observed for YCo_5. At a field of 15 T applied perpendicular to the c axis, the magnetization reaches a value of 2.0 μ_B only (Givord and Nozieres 1991). It points to an anisotropy field of 60 T and a value for K_1 of $+26$ J/cm^3 ($+162$ K/f.u.), a four times larger value than in YCo_5. With increasing temperature, the magnetization decreases reaching at room temperature a value of 7.5 μ_B/f.u. (Laforest 1981, p. 46). The temperature dependence of the anisotropy energy has been measured by Klein et al. (1975) and analyzed within a single-ion Hamiltonian by Sankar et al. (1975), de Wijn et al. (1976) and Radwański (1986d). The higher J multiplets are taken into account with a value for the spin–orbit coupling constant λ of -410 K. Exchange and CEF parameters derived from magnetization studies and polarized neutron measurements are collected in table 5.5. Polarized neutron studies performed by Boucherle et al. (1979) have revealed a change in character of the Sm moment with temperature: at 4.2 K the orbital contribution is dominant whereas with increasing temperature the spin character becomes more pronounced. The spin and orbital contributions to the magnetic moment of $SmCo_5$ have been discussed by Richter and Eschring (1991).

Mössbauer studies performed by Nowik et al. (1983) on low concentrations of ^{153}Eu and ^{57}Fe have allowed for a separation of the different contributions to the hyperfine field, see section 3.2. The 4f contribution has been found as expected, to be dominant. A value of 340 T for the exchange field has been deduced from the temperature dependence of the hyperfine field. NMR spectra (Yoshie et al. 1988b) are simple as expected for a uniaxial system.

5.6.1.7. $GdCo_5$. Magnetization studies on a single-crystalline sample of $GdCo_5$ with the off-stoichiometric composition $Gd_{0.93}Co_{5.14}$ ($s = 0.07$) (Ballou et al. 1986a, 1987a) reveal a value for M_s of 1.9 μ_B/f.u. at 4.2 K, which in combination with $m_{Gd} = 7 \mu_B$ leads to a value for the cobalt moment of 1.64 μ_B. The magnetization at a field of 30 T applied perpendicular to the c axis does not reach the spontaneous-moment value. A standard analysis yields an effective anisotropy energy which is three times smaller than that found in YCo_5, an unexpected fact because of the S state of the Gd^{3+} ion. As $GdCo_5$ is close to the compensation of the sublattice moments as is seen from the small value of the resultant moment, the canting effect due to external fields is rather pronounced. A two-sublattice analysis with a value for the intersublattice molecular-field coefficient calculated from the value for $B_{ex,RT}^{Gd}$ of 219 T, results in a cobalt-

sublattice anisotropy that is 50% larger than that observed in YCo_5 (Ballou et al. 1986a, 1987a, Gerard and Ballou 1992). On this basis, the authors claim that this extra contribution to the MCA energy originates from an anisotropic exchange. Recent studies on single-crystalline $GdCo_5$ with the better stoichiometry of $s = 0.02$ do not confirm this extra contribution that has been estimated not to exceed 15% (Radwański et al. 1992b). The magnetization curves up to 35 T have been presented in fig. 3.7. The parameters derived for this sample are: $M_s = 18.6\,\mathrm{A\,m^2/kg} = 1.50\,\mu_B$/f.u. and $K_1^{Co} = +52 \pm 7$ K/f.u. The value of 15.5 K f.u./μ_B points to a value for $B_{ex,RT}^{Gd}$ of 195 T. A value of 220 T has been reported for this exchange field by Ermolenko (1980). Yamagushi et al. (1983) have reported that hydrogenation reduces both T_c and M_s. For $GdCo_5H_{2.8}$ T_c amounts to about 480 K, i.e., one half of that observed for the pure compound.

5.6.1.8. $TbCo_5$. Values for M_s at 4.2 K of $0.55\mu_B$/f.u. for $TbCo_{5.1}$ (Ermolenko 1985) and of $0.25\mu_B$/f.u. for $TbCo_{5.2}$ (Ballou et al. 1989) have been reported. The small value for the spontaneous moment M_s results from a cancellation of the two sublattice moments. For a free single-crystalline sample, a transition at 6.2 T has been observed by Ermolenko (1985) and Pirogov et al. (1984). The magnetization curves are shown in fig. 5.25. An abrupt transition has also been observed for a fixed sample in magnetic fields applied along the easy axis, see fig. 5.26. $TbCo_5$ is a planar system with the easy direction of magnetization along the *a* axis. The transition is of the FOMR-type as discussed in section 3.1. A value of 16.6 T f.u./μ_B has been derived for the parameter n_{RT} by Ballou et al. (1989). This value corresponds to a value of 140 T for $B_{mol,RT}^{Tb}$. This value is consistent with the systematics observed in the RCo_5 series as it yields a value for the exchange field of 210 T. The moment compensation occurs in the vicinity of 90–110 K, a value that depends on the actual stoichiometry of the sample. In the sample of Ballou et al. at 90 K the magnetization curves for all principal hexagonal directions gradually increase with field, see fig. 5.26. In the temperature range 395–410 K, the compound undergoes a TIMR transition to the *c* direction that is preferred by the Co sublattice. The TIMR transition is accompanied by an increase of the net magnetization indicating a directional dependence of the Tb moment. For NMR results, see fig. 3.16.

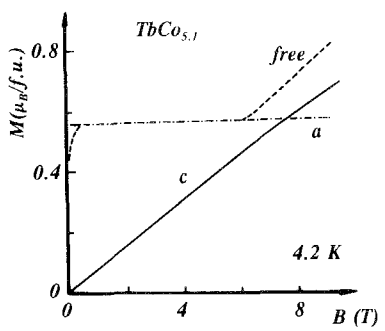

Fig. 5.25. Magnetization curves for single-crystalline $TbCo_{5.1}$ at 4.2 K along different hexagonal crystallographic directions. In addition the curve for the sample that is free to rotate in the applied field is shown. After Ermolenko (1985).

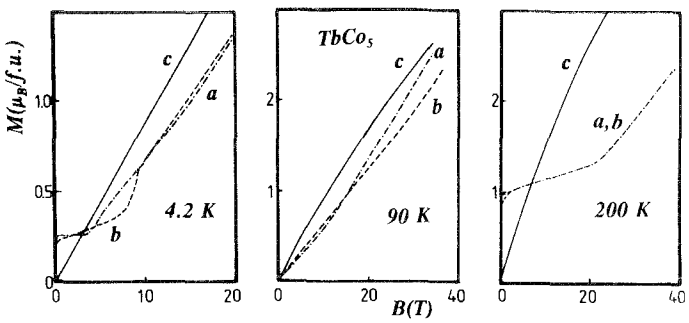

Fig. 5.26. Magnetization curves for single-crystalline $TbCo_5$ at 4.2 K, 90 K (the compensation temperature) and at 200 K along different hexagonal directions. After Ballou et al. (1989).

5.6.1.9. $DyCo_5$. Magnetic data have been reported for a sample of $DyCo_5$ with presumably 2.8% of Co pairs extra, i.e., $DyCo_{5.2}$. For this sample M_s at 4.2 K amounts to $1.0\mu_B$/f.u. (Ermolenko 1976). The occurrence of a noncollinear magnetic structure in external fields has been reported by Berezin et al. (1980) for $DyCo_{5.3}$. Berezin and Levitin (1980) have found a value for the molecular field of 95 T. The moment compensation occurs at 124 K. A TIMR transition occurs between 325 and 367 K as a consequence of the competition between the planar Dy anisotropy and the uniaxial Co anisotropy (Gignoux and Schmitt 1991). The TIMR transition is accompanied by an increase of the magnetization caused by a partial quenching of the Dy moment in its unfavourite direction.

5.6.1.10. $HoCo_5$. The noncollinear magnetic structure occurring in $HoCo_5$ below 180 K has been studied by magnetization, Mössbauer and neutron-diffraction measurements by Decrop et al. (1982). Magnetization measurements on a large single-crystalline sample ($3 \times 3 \times 3\,mm^3$) with composition $HoCo_{5.6}$ at 4.2 K have revealed nonzero values for the spontaneous magnetization measured along the c axis as well as within the hexagonal plane: $M_{\perp c} = 1.7\mu_B$ and $M_{\parallel} = 0.55\mu_B$. At liquid helium temperature, the magnetization vector makes an angle of 72° with respect to the c axis. This angle is reduced with temperature and vanishes at 180 K. In the reorientation region the magnetic structure is noncollinear as shown by Mössbauer measurements on a polycrystalline sample in which 3% of the Co atoms are replaced by ^{57}Fe. From the thermal variation of the experimentally observed values for the holmium moment and from the temperature dependence of the directions of the cobalt and holmium moments, values for the CEF coefficients ($A_2^0 = -412\,K\,a_0^{-2}$, $A_4^0 = -30\,K\,a_0^{-4}$, $A_6^0 = -0.6\,K\,a_0^{-6}$) and the intersublattice molecular-field coefficient n_{Ho-Co} of 24 K/μ_B^2 have been derived (Decrop et al. 1982, 1983). This value for n_{RT} results in an unrealistically large exchange field of 800 T which does not make the formation of a noncollinear structure favourable. Ermolenko and Rozhda (1982) reported a value for $B^{Ho}_{mol,RT}$ of 54 T ($B^{Ho}_{ex,RT} = 135$ T) only on the basis of single-crystal magnetization measurements up to 9 T. This value is in good agreement with the value of 159 T for the exchange field in Ho_2Co_{17} derived from magnetic studies up to 35 T by Franse et al. (1985). The magnetization curves are

complex, reflecting the large sensitivity of the internal magnetic structure of this largely compensated ferrimagnet on external fields. At 4.2 K, the holmium moment is larger than the Co sublattice moment and a compensation temperature is expected. Although the Ho and Co magnetizations become equal around 85 K, a full compensation of the two moments does not occur because of the noncollinearity of two sublattice moments. The magnetic phase diagram for the $Ho(Co–Ni)_5$ series has been presented by Chuyev et al. (1983). A field-induced magnetization in $(Ho–Er)(Co–Ni)_5$ has been successfully analyzed by Drzazga and Mydlarz (1988) in terms of CEF and exchange interactions. NMR experiments have been performed by Yoshie et al. (1988a).

5.6.1.11. $ErCo_5$. For a single-crystalline sample of $ErCo_5$, magnetization studies have been performed by Ermolenko and Rozhda (1983). Mössbauer experiments on the Er and Tm compounds performed by Gubbens et al. (1989a) have led to the evaluation of the electric-field gradient that has been transformed into the CEF parameter B_2^0. These parameters have been compared with those obtained others RCo_5 compounds and a fair agreement was concluded. Drzazga and Drzazga (1987) have analyzed magnetic properties of the $Er(Co–Ni)_5$ series within the single-ion approach.

5.6.2. RNi_5 compounds

The RNi_5 series is a unique series for which very detailed and long-lasting studies exist. These studies do not, however, lead to an unambiguous evaluation of the CEF and exchange interactions in the RNi_5 series although a number of experimental results has been successfully interpreted. The magnetization of these compounds is considered, as usual, to originate from the R and Ni sublattices. Both 3d subbands of nickel are equally occupied and nearly full, see fig. 2.5. The magnetic properties of the nickel sublattice can be taken from YNi_5 or $LaNi_5$ compounds. YNi_5 is found to be an exchange-enhanced Pauli paramagnet with a susceptibility at 4.2 K that is five times larger than in Ni metal. Band-structure calculations for Y–Ni compounds have been performed by M. Shimizu et al. (1984). These calculations indicate a rather temperature independent susceptibility for YNi_5. Actually, the susceptibility decreases monotonously with increasing temperature and reaches at 300 K a value of 87% of that observed at zero temperature.

The RNi_5 compounds are magnetically ordered with the exception of $PrNi_5$. The highest value for T_c of 32 K is found for $GdNi_5$. The RNi_5 compounds are different from the RT_5 compounds discussed so far in which the magnetic moments are well defined and developed. In the RNi_5 series, the Ni moment is entirely induced either by the rare-earth moment or by the applied magnetic field. This series can serve as a model system for studies of the magnetization processes in weakly magnetic materials. In principle, the analysis of these compounds is based on the same assumptions as those for the iron and cobalt compounds. In RNi_5 compounds again three kinds of the exchange interactions are distinguished, Ni–Ni, R–R and R–Ni exchange interactions. Due to hybridization of the 3d-band of Ni and the 5s–4d band of Y (or 6s–5d band for other R elements) the Ni sublattice is nonmagnetic and exhibits Pauli

paramagnetic behaviour as we can learn from YNi_5. In the presence of an externally applied field, B_0, a nickel moment is induced that starts to interact with its spin surroundings. The Ni-sublattice magnetization can be written as

$$M_{Ni} = \chi^0_{Ni}(B_0 + n_{TT}M_{Ni}), \tag{5.8}$$

where χ^0_{Ni} denotes the bare nickel susceptibility in the absence of exchange interactions. The Ni–Ni exchange interactions are described within the molecular-field approximation with n_{TT} as the molecular-field coefficient. Equation (3.7) can be rewritten in the form

$$M_{Ni} = \chi_{Ni}B_0, \tag{5.9}$$

where

$$\chi_{Ni} = \frac{\chi^0_{Ni}}{1 - n_{TT}\chi^0_{Ni}} \tag{5.10}$$

is the exchange-enhanced nickel susceptibility. The enhancement of the Pauli susceptibility is the result of the existence of Ni–Ni exchange interactions. For YNi_5, χ_{Ni} is equal to $40 \times 10^{-4}\,\mu_B$/T f.u. at 4.2 K. With increasing temperature, it decreases slightly and monotonously as shown in fig. 4.11. Rather similar values for χ_{Ni} are derived for compounds with magnetic rare-earth partners from high-field magnetization studies.

The molecular field acting on a R moment can be written as

$$B^R_{mol} = n_{RR}M_R + n_{RT}M_T. \tag{5.11}$$

The Ni-sublattice magnetization in this case is given by the modified expression (5.9):

$$M_{Ni} = \chi_{Ni}(B_0 + n_{RT}M_R), \tag{5.12}$$

where an extra field due to the existence of the R moment is taken into account. Substituting eq. (5.12) into eq. (5.11) one obtains:

$$B^R_{mol} = (1 + n_{RT}\chi_{Ni})B_0 + (n_{RR} + n_{RT}\chi_{Ni}n_{RT})M_R. \tag{5.13}$$

Equations (5.12) and (5.13) can be rewritten as

$$M_{Ni} = \chi_{Ni}B_0 + \alpha M_R, \tag{5.14}$$

$$B^R_{mol} = (1 + \alpha)B_0 + nM_R, \tag{5.15}$$

where $\alpha = \chi_{Ni}n_{RT}$ and where the effective (enhanced) R–R exchange constant n contains the R–T interaction parameter as given by eq. (3.9). Values for the exchange parameter derived from the magnetization studies are collected in table 5.6. The nickel susceptibility is practically the same in all compounds indicating a linear magnetic response of the Ni sublattice to the internal magnetic field. The intersublattice interactions, after taking into account the spin moment, show an increase going from Gd towards the light rare-earth elements. Such an increase has been detected in other 3d–4f series as well. The results are, however, not conclusive for the interactions between the R spins.

Values for the electric-field gradient derived by means of Mössbauer studies by Gubbens et al. (1989a) are in fair agreement with those derived from magnetization

TABLE 5.6
Exchange interaction parameters in the RNi_5 series derived from magnetic measurements. α denotes $n_{RNi}\chi_{Ni}$.

Compound	χ_{Ni} ($10^{-4}\mu_B$ f.u./T)	n_{RNi} (T f.u./μ_B)	n_{RR} (T f.u./μ_B)	α	Ref.*
Y	41	–	–	–	[1]
La	37	–	–	–	[1]
Pr	37	−16.2	1.125	−0.06	[1]
Sm	38	−4.7	2.5		[1]
Gd	40	−15.6	1.0		[2]
Gd	54	−21.0	−0.04	−0.11	[2]
Er	39	−10.8	−0.28	−0.042	[3]
Tm	37	−9.45	−0.196	−0.037	[1]

*References:
[1] Barthem (1987).
[2] Szewczyk et al. (1992).
[3] Radwański et al. (1992a).

measurements proving the ability of Mössbauer spectroscopy for the evaluation of the second-order CEF parameters. Systematic magnetic, neutron and specific-heat studies have resulted in the evaluation of CEF interactions in all the compounds. The CEF interactions expressed by the CEF coefficients are collected in table 5.7. Inspecting the results one can notice on one hand substantial differences between the coefficients in different compounds but on the other hand some systematics can be found. Except for the coefficient A_6^0 of the Tm compound there is full agreement in the *sign* of the CEF coefficients across the series.

5.6.2.1. YNi_5. In the compound YNi_5 the Ni subsystem is found to be a Pauli-enhanced paramagnet. The susceptibility at 4.2 K amounts to 29×10^{-9} m^3/mol ($40 \times 10^{-4}\mu_B$/T f.u.). It decreases monotonously with increasing temperature as shown in fig. 4.11.

5.6.2.2. $LaNi_5$. Like YNi_5 the compound $LaNi_5$ is Pauli enhanced paramagnetic. Specific heat measurements of Sahling et al. (1982) yield $\gamma = 39$ mJ/K^2 mol and $\Theta_D = 393$ K. Values of 33 mJ/K^2 mol and 322 K have been derived by Nait-Saada (1980), respectively. The discrepancy in the values for Θ_D shows again that one single parameter is not able to describe the lattice dynamics over a large temperature range. Radwański et al. (1992c) have deduced a nonmonotonic variation of the Debye temperature with temperature from a detailed analysis over different temperature regions of the specific heat of $LaNi_5$ measured in the temperature range between 1.5 and 250 K on a single-crystalline sample. This analysis has revealed a significant softening of the lattice at 22 K. The variation of Θ_D ranging between 322 to 270 K has been correlated with the nonstandard complex phonon spectrum that has been revealed by point-contact spectroscopy measurements performed by Akimenko et al. (1986). A value for γ of

TABLE 5.7
CEF coefficients, in units of $K a_0^{-n}$, of the trivalent R ions in the RNi_5 compounds. PCM denotes a point-charge model result. After Radwański et al. (1992c).

Compound	T_c	A_2^0	A_4^0	A_6^0	A_6^6	Ref.*
$PrNi_5$	–	−229	−18.2	+0.78	+27.5	[1]
$PrNi_5$	–	−227	−20.8	+0.7	+27.1	[2]
$NdNi_5$	8	−468	−17.1	+0.61	+23.6	[3]
$SmNi_5$	27	−370	−181	+11.4	0.0	[4]
$GdNi_5$	32					[5]
$TbNi_5$	23	−385	−13.4	+5.8	+13.0	[6]
$TbNi_5$		−442	−9.0	+1.5	+47.7	[7]
$TbNi_5$		−462	−11.9	+0.79	+47.7	[8]
$DyNi_5$	12	−458	−24.7	+1.8	+45.0	[9]
$HoNi_5$	5	−686	−56	0.3	+55.0	[6]
$ErNi_5$		−382	−17.7	+5.0	+30.0	[10]
$ErNi_5$		−349	−40.0	+2.4	+13.7	[7]
$ErNi_5$	9	−336	−44.3	+2.3	+13.7	[11]
$TmNi_5$	5	−545	−65.8	−7.52	+31.2	[12]
RNi_5 (PCM)		−300	−10.0	−0.06	−0.39	[6]
$SmNi_5$ (PCM)		−422	−11.0	−0.07	−0.43	[4]

*References:

[1] Barthem et al. (1988a).
[2] Reiffers et al. (1989).
[3] Barthem et al. (1989b).
[4] Ballou et al. (1988a).
[5] Szewczyk et al. (1992).
[6] Gignoux et al. (1979b).
[7] Goremychkin et al. (1984).
[8] Gignoux and Rhyne (1986).
[9] Aubert et al. (1981).
[10] Escudier et al. (1977).
[11] Radwański et al. (1992a).
[12] Barthem et al. (1989a).

36 mJ/K^2 mol has been derived by Radwański et al. (1992c). Thermopower measurements have been performed by Sakurai et al. (1987). The resistivity for $LaNi_5$ shows a smooth increase from 26 μΩ cm at 4.2 K to 35 μΩ cm at 60 K. The resistivity is only little affected by the presence of the localized 4f spin as can be inferred from the studies of the (La–Sm)Ni_5 series (Ballou et al. 1988a). The magnetic susceptibility is very similar to that observed for YNi_5. Electronic structure calculations performed by Gupta (1987) have revealed that the Fermi energy falls in the rapidly decreasing part of the density of states originating of the Ni d bands. The calculated DOS at E_F is large and corresponds to a specific-heat γ value of 28 mJ/K^2 mol. The outstanding hydrogen-storage properties of $LaNi_5$ have been reviewed by Wiesinger and Hilscher (1991).

5.6.2.3. $CeNi_5$. The compound $CeNi_5$ is regarded as an intermediate valence compound. From L_3 X-ray absorption spectroscopy a valency of 3.3 for the Ce ions was deduced by Alekseev et al. (1988a). INS experiments by Alekseev et al. (1988b) do not reveal localized excitations indicating that the Ce ions seem to be in a state with a valency close to four. However, point-contact spectroscopy measurements by Akimenko et al. (1986) have revealed, besides a complex phonon contribution as in

$LaNi_5$, two peaks at energies 1.8–2 and 4–5 meV. The origin of these peaks is not clear as CEF levels of the Ce^{3+} ions are expected to be at a much larger energy distance (above 15 meV). Thermopower experiments have been reported by Sakurai et al. (1987).

5.6.2.4. $PrNi_5$. The compound $PrNi_5$ has extensively been studied because of its nonmagnetic singlet ground state that is determined by the CEF interactions. There is no magnetic ordering of the 4f spins down to the lowest temperatures although exchange interactions between Pr ions are appreciable. The thermal variation of several properties like the susceptibility and the specific heat, exhibit pronounced maxima around 15 K. The thermal expansion is strongly anisotropic and shows a maximum within the hexagonal plane and a minimum along the hexagonal axis (Barthem et al. 1988b) in both cases with an extremum near 13 K. Magnetization studies on a single-crystalline sample by Barthem et al. (1988a) have resulted in a full set of CEF parameters, as tabulated in table 5.7. The magnetization curves are presented in fig. 5.27. In the paramagnetic region the susceptibility contains contributions from the Pr^{3+} ions and the Ni atoms. Due to the small value of the Curie constant

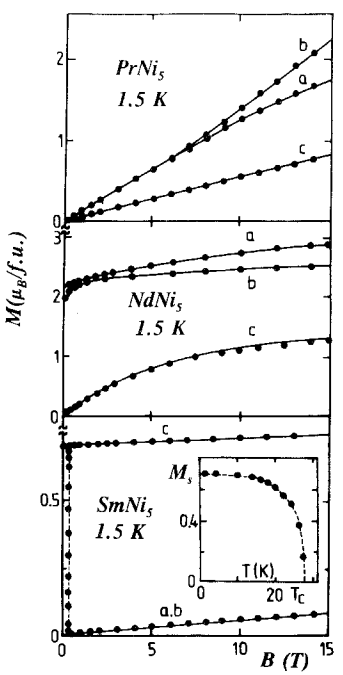

Fig. 5.27. Magnetization vs. internal field at 1.5 K for single-crystalline compounds of RNi_5 with light rare earths for the field applied along three main crystallographic directions of the hexagonal cell. Full lines are calculated results. The inset for $SmNi_5$ shows the observed temperature dependence of the spontaneous magnetization. $PrNi_5$ (after Barthem et al. 1988a), $NdNi_5$ (after Barthem et al. 1989a), $SmNi_5$ (after Ballou et al. 1988a).

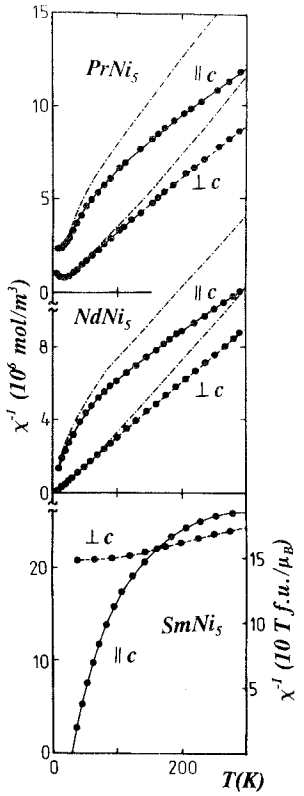

Fig. 5.28. Temperature dependence of the reciprocal susceptibility measured parallel and perpendicular to the hexagonal c axis for single-crystalline $PrNi_5$ (after Barthem et al. 1988a), $NdNi_5$ (after Barthem et al. 1989a) and $SmNi_5$ (after Ballou et al. 1988a). Points are experimental data. Dashed–dotted lines show the calculated Pr and Nd contribution to the susceptibility whereas full lines are the calculated results taking into account the nickel contribution to the susceptibility.

for the Pr^{3+} ion the Ni susceptibility contributes substantially to the overall suceptibility from the lowest temperatures. In fig. 5.28 experimental data for the susceptibility of $PrNi_5$ are shown together with the calculated Pr^{3+}-ion susceptibilities (dashed–dotted lines in fig. 5.28). Very good agreement is obtained when the Ni susceptibility of the size detected in YNi_5 is taken into account. INS measurements have been performed by Alekseev et al. (1980, 1988a). Reiffers et al. (1989) have succeeded in the detection of the excitations at the Pr site by point-contact spectroscopy allowing for the refinement of the CEF parameters. The parameters are slightly different from those derived earlier. Nevertheless, the specific-heat studies of Andres et al. (1979), the point-contact spectroscopy and the magnetization studies all result in the singlet $\Gamma_4 = |+3\rangle - |-3\rangle$ as the ground state. The first excited level $|0\rangle$ is separated from the ground-state level by 38 K (from point-contact spectroscopy) or by 22 K as given by the parameters of Barthem et al. (1988a). The possibility of field-induced phase transitions during the magnetization process on the basis of the CEF parameters of Reiffers et al. (1989) has been examined by Ishii et al. (1990). Improved CEF parameters on the

basis of INS experiments have been provided by Amato et al. (1992): $B_2^0 = +5.916$ K, $B_4^0 = +46.4$ mK, $B_6^0 = +0.905$ mK and $B_6^6 = +30.2$ mK.

5.6.2.5. $NdNi_5$. Single-crystal magnetization curves for $NdNi_5$ yield values for T_c of 7 K and for M_s of 2.14 μ_B/f.u. at 1.5 K with the EMD along the *a* axis. The magnetization curves are presented in fig. 5.27. The magnetization data have been analyzed by Barthem et al. (1989b) within a molecular-field approximation including CEF interactions. The set of CEF coefficients derived from these studies is shown in table 5.7. It results, in the absence of the exchange, in the energy level scheme that contains five doublets with $\Gamma_8^{(2)}$ as the ground level. These CEF interactions give rise to the dipolar transitions $\Gamma_8^{(2)}$–$\Gamma_9^{(2)}$, $\Gamma_9^{(2)}$–Γ_7 and $\Gamma_8^{(2)}$–$\Gamma_8^{(1)}$ at energies of 18.2, 32.2 and 163.8 K, respectively, in reasonable agreement with INS results of Goremychkin et al. (1985).

5.6.2.6. $SmNi_5$. Single-crystal magnetization studies on $SmNi_5$ by Ballou et al. (1988a) yield values for T_c of 27 K and for M_s of 0.7 μ_B/f.u. at 1.5 K with the EMD along the hexagonal *c* axis. The magnetization curves at 1.5 K are presented in fig. 5.27. An analysis of magnetization data performed with the Hamiltonian given by eq. (2.10) and with a value of -410 K for the spin–orbit coupling parameter, λ, yields a value for the coefficient n_{Sm-Ni} of -4.7 T f.u./μ_B and values for the CEF parameters as collected in table 5.7. It has been noted that the value of the coefficient A_2^0 can be reproduced by the PC-model with a charge of 3+ on Sm and with zero charge on Ni ions. The nickel susceptibility, $\chi_{Ni} = 38 \times 10^{-4}$ μ_B/T f.u., is much the same as in the yttrium compound. This susceptibility is responsible for the increase in the magnetization along the easy axis. The domain structure has been analyzed by Szymczak et al. (1988). The enormously large anisotropy causes extremely narrow domain walls that are manifest in the abrupt magnetization process measured on virgin samples for fields applied along the easy axis. In case the anisotropy is much larger than the exchange interactions, the domain wall extends over a few interatomic distances and can be moved only if the applied field is larger than a critical value. At 1.5 K this critical field amounts to 0.3 T. The value for T_c of 27.5 K is too large by a factor of two compared to the value that is deduced from the strength of the 4f–4f interactions for $GdNi_5$ (Barthem 1987). This discrepancy has been attributed to CEF effects in $SmNi_5$ and is characteristic for an energy level scheme where the ground state, being a purely $|\pm J_z\rangle$ state, is well separated from the excited states (about 210 K in this case). Large second-order CEF interactions create the conditions for a one-dimensional Ising-like behaviour of the Sm ions in this compound. Similar phenomena occur in $TmNi_5$.

At low temperatures the susceptibility is very anisotropic, see fig. 5.28. The temperature dependence of the susceptibility does not follow the C–W law, even not at temperatures around 300 K (Ballou et al. 1988a). The large and negative curvature of the reciprocal susceptibility along the *c* axis is partly due to a nickel contribution but the main part arises from the CEF effect. Moreover, a 'cross-over' of the *c* axis and the in-plane susceptibility, at 160 K, is another peculiarity of $SmNi_5$ indicating a change of the 'easy magnetization direction' in the *paramagnetic state* (parallel to the *c* axis at low temperatures and perpendicular to it above 160 K). The origin for this cross-over is the CEF effect that makes that the first excited level lies much closer to the ground

state for the direction perpendicular to the c axis than for the direction along the c axis. The mechanism is similar to the TIMR as discussed in section 2.3 for $NdCo_2$ and $HoCo_2$. The resistivity, measured by Ballou et al. (1988a) in the temperature region 1.5–300 K, reveals an anomaly at 27.5 K which is related to the Curie temperature. The value of ρ of 26.5 μΩ cm at helium temperature is only slightly larger than that detected for $LaNi_5$.

5.6.2.7. $GdNi_5$. For the compound $GdNi_5$, values for T_c and M_s at 4.2 K amount to 32 K and $6.2\mu_B$/f.u., respectively. Nickel itself does not carry a spontaneous magnetic moment. An induced Ni moment of $0.16\mu_B$ is calculated on the basis of the full Gd^{3+} moment. In the paramagnetic region this small Ni moment is not detectable. The Curie constant is well accounted for by the Gd^{3+} contribution. Anisotropic exchange interactions have been concluded to be negligible on the basis of magnetization studies (Barthem 1987, p. 131). Specific-heat measurements up to 48 K have been performed by Szewczyk et al. (1992). These experiments result in a value for Θ_D of 296 K and for γ of 36 ± 3 mJ/K^2 mol. The magnetic entropy calculated up to 40 K amounts to $R \ln 8$, indicating, as expected, that all levels of the ground-state multiplet are populated above T_c. The following exchange parameters have been derived:

$$n_{GdNi} = -21\,\text{T f.u.}/\mu_B, \qquad \alpha = -0.11, \qquad n = 2.27\,\text{T f.u.}/\mu_B.$$

The effective exchange interactions between the Gd moments as described by the parameter n are positive and lead to the ferromagnetic alignment of the Gd moments despite of the antiferromagnetic coupling parameter n_{RR}. The corresponding molecular field B_{mol}^{Gd} amounts at 0 K to 15.9 T. At zero temperature the energy levels are equally split with an energy distance of 21.4 K. van Steenwijk et al. (1977) have reported a value of $+10.3 \times 10^{21}$ V m^{-2} for V_{zz} at the ^{155}Gd nuclei. This value is slightly larger than a value of $+8.2 \times 10^{21}$ V m^{-2} found for $GdCo_5$ by Tomala et al. (1977) and indicates substantial CEF interactions in the RNi_5 compounds. μSR experiments have been reported by Yaouanc et al. (1990).

5.6.2.8. $TbNi_5$. Single-crystal magnetization studies for $TbNi_5$ by Gignoux et al. (1979b) reveal values for T_c of 23 K and for M_s of $7.6\mu_B$/f.u. at 4.2 K. The analysis of these data results in the set of CEF coefficients presented in table 5.7. These coefficients, however, are unable to account for the INS spectra (Gignoux and Rhyne 1986). The refined CEF coefficients, shown also in table 5.7, yield the state $|0\rangle$ as the ground state. Muon spectroscopy studies have been reported by Dalmas de Réotier et al. (1992). Only one muon precession frequency of 80 MHz at the lowest temperatures has been detected.

5.6.2.9. $DyNi_5$. Single-crystal magnetization measurements for $DyNi_5$ yield a value for T_c of about 11 K and for M_s of $9.5\mu_B$/f.u. (see fig. 5.29) with the easy magnetic direction at 4.2 K along the b axis (Aubert et al. 1981). With increasing temperature a TIMR transition occurs at 6.5 K at which the moments rotate to the a axis. It has been explained by Aubert et al. (1980) as a CEF effect of the Dy ion. The ground state for the ***b*** direction is slightly lower than for the a axis but the first excited level lies much closer to the ground state for the ***a*** direction.

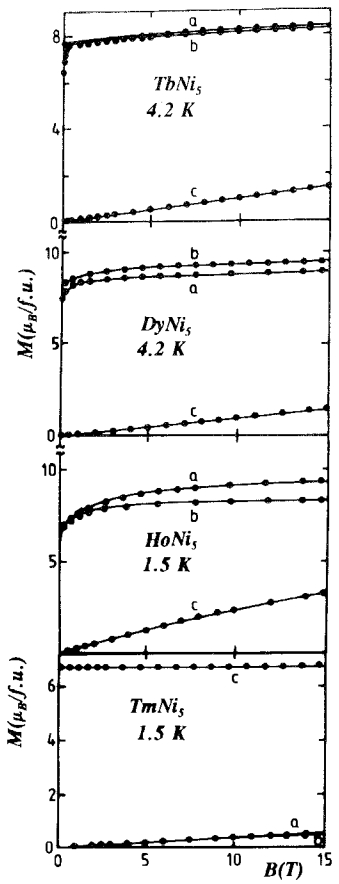

Fig. 5.29. Magnetization vs. internal field for single-crystalline RNi_5 compounds with heavy rare earths for the field applied along different hexagonal crystallographic directions: R = Tb and Ho (after Gignoux et al. 1979b), R = Dy (after Aubert et al. 1981) and R = Tm (after Gignoux et al. 1981).

5.6.2.10. $HoNi_5$. Single-crystal magnetization measurements for $HoNi_5$ have resulted in values for T_c of 5 K, and for M_s at 1.5 K with a field of 15 T along the easy direction of magnetization (*b* axis) of $9.2\mu_B$/f.u. (Gignoux et al. 1979b). The second-order CEF coefficient is extraordinary large compared with that observed for other RNi_5 compounds, see table 5.7. The substantial magnetic anisotropy is visible in the paramagnetic region as well, see fig. 5.30. The magnetic phase diagram of the $Ho(Ni–Co)_5$ series has been studied by Chuyev et al. (1983).

5.6.2.11. $ErNi_5$. Single-crystal magnetization measurements on $ErNi_5$ have resulted in values for T_c of 9 K and for M_s at 1.5 K of $8.62\mu_B$/f.u. with the easy direction of magnetization along the *c* axis, see fig. 5.31. Previous magnetization studies up to 15 T by Escudier et al. (1977) yielded a value for M_s of $7.2\mu_B$ only. The analysis of these latter results gives the Γ_7 doublet with a dominant $|\pm 13/2\rangle$ component as the ground

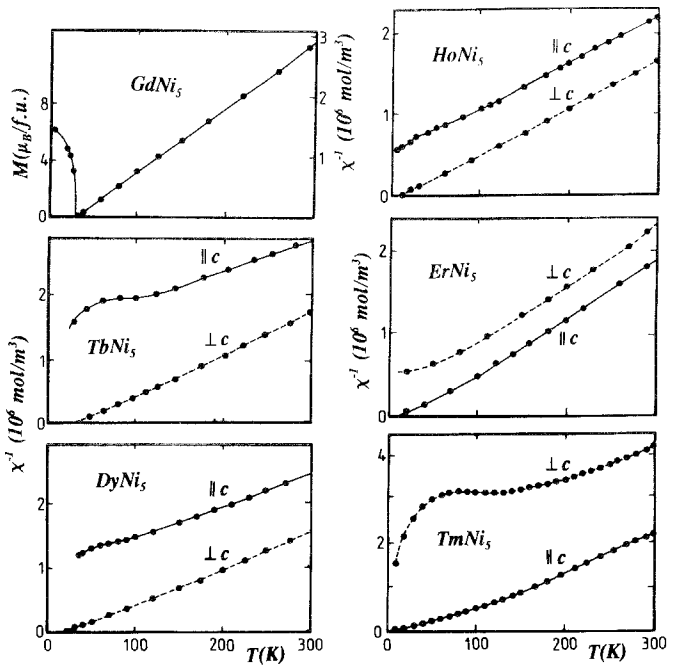

Fig. 5.30. Temperature dependence of the reciprocal susceptibility measured parallel and perpendicular to the hexagonal c axis for single-crystalline RNi_5 for R = Gd (after Nait Saada 1980, p. 28), R = Tb and Ho (after Gignoux et al. 1979b), R = Dy (after Aubert et al. 1981), R = Er (after Escudier et al. 1977) and R = Tm (after Gignoux et al. 1981). For $GdNi_5$ the temperature dependence of the spontaneous moment is shown as well.

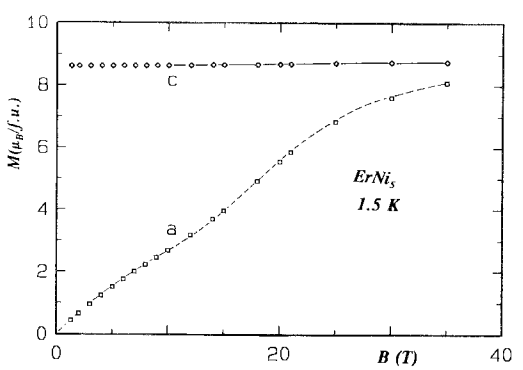

Fig. 5.31. Magnetization curves at 1.5 K for single-crystalline $ErNi_5$ for the field applied along two main crystallographic directions of the hexagonal cell. After Radwański et al. (1992a).

state. This ground state has been questioned by INS studies of Goremychkin et al. (1984) who inferred a Γ_9 doublet with a dominant $|\pm 15/2\rangle$ component as the ground state. High-field magnetization studies up to 35 T by Radwański et al. (1992a) have supported the INS result. The magnetization studies have resulted in the evaluation of the full set of CEF parameters relevant to the hexagonal symmetry that is shown in table 5.7. The exchange coupling parameters have been determined as follows:

$$n_{\mathrm{RNi}} = -10.8\,\mathrm{T\,f.u./}\mu_{\mathrm{B}}, \qquad \chi_{\mathrm{Ni}} = 39 \times 10^{-4}\mu_{\mathrm{B}}/\mathrm{T\,f.u.}, \qquad \alpha = -0.042,$$
$$n = 0.17\,\mathrm{T\,f.u./}\mu_{\mathrm{B}}, \qquad n_{\mathrm{RR}} = -0.28\,\mathrm{T\,f.u./}\mu_{\mathrm{B}}.$$

The effective exchange interaction between the Er moments is ferromagnetic resulting from the AF interactions of the R and Ni moments. The value of $0.17\,\mathrm{T\,f.u./}\mu_{\mathrm{B}}$ for the effective molecular-field coefficient between the Er moments is only by 15% lower than the value that can be derived from the molecular-field expressions in eq. (2.21). Exchange interactions of this size produce a molecular field experienced by the Er-ion moment at the lowest temperatures of 1.5 T.

The energy level scheme of the Er^{3+} ion in $ErNi_5$ is shown in fig. 5.32 together with the associated eigen-functions. The CEF interactions of the hexagonal symmetry split the $^4I_{15/2}$ multiplet into eight doublets as the Er^{3+} ion, with $J = 15/2$, is a Kramers

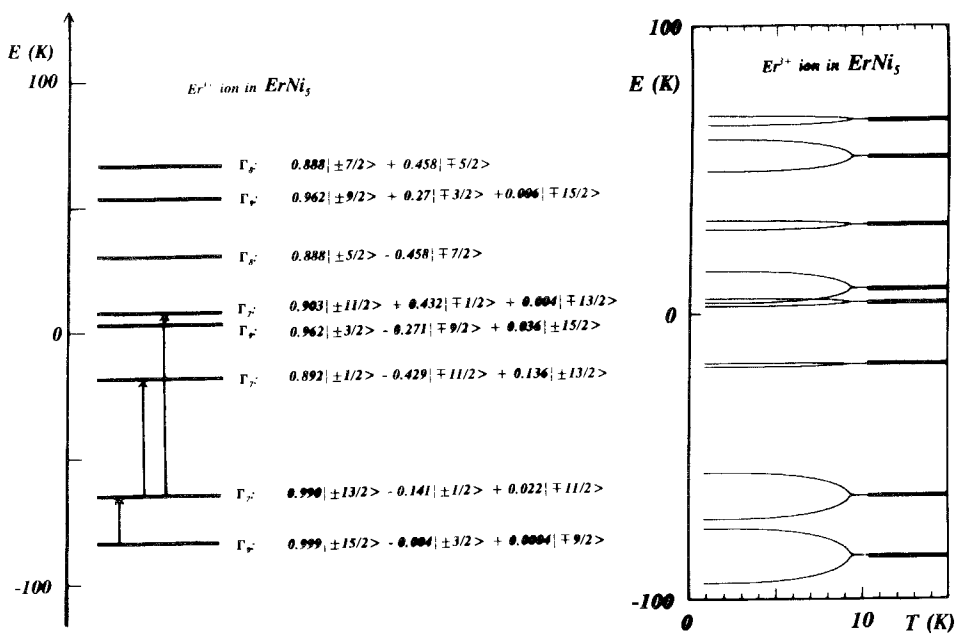

Fig. 5.32. (a) Energy level scheme of the Er^{3+} ion in $ErNi_5$ under the action of the CEF interactions together with the associated eigen-functions. All the levels are doublets as the Er^{3+} ion with $J = 15/2$ is a Kramers ion. The arrows show the transitions observed in inelastic-neutron-scattering experiments. (b) Temperature dependence of the energy-level scheme. As the effect of the exchange interactions the doublets are split in the magnetically ordered state. $T_c = 9.2$ K. After Radwański et al. (1992c).

ion. The eigen-function of the ground-state doublet Γ_9 is given by

$$\psi = +0.999|\pm 15/2\rangle - 0.04|\pm 3/2\rangle + 0.0004|\mp 9/2\rangle,$$

where the dominant $|\pm 15/2\rangle$ contribution is clearly seen. The quantization axis is taken along the hexagonal axis. This energy-level scheme provides the INS excitations at energies of 21.0 K (1→2), 46.0 K (2→3) and 72.6 K (2→5). These excitations have been observed by Goremychkin et al. (1984), indeed. Actually, in the ordered state all the levels are split by the exchange interactions but their splitting is small. As is seen from fig. 5.32b, where temperature dependence of the energy-level scheme is presented, the exchange interactions do not cause a mixing of the levels determined by the CEF interactions. The calculated specific heat of the Er subsystem is shown in fig. 3.17. The specific heat measurements of Radwański et al. (1992c) on single-crystalline samples of $ErNi_5$ and $LaNi_5$ have been reduced to the temperature dependence of the specific heat of the Er subsystem. An inspection of fig. 3.17 shows that the calculated specific heat resembles very well the measured one. The entropy associated with the Er subsystem amounts to 21.5 ± 1 J/K mol at 150 K and is quite close to that expected for the $(2J + 1)$-fold degeneracy of the ground-state multiplet, i.e. 23.0 J/K mol. It indicates that the magnitude of the CEF interactions in $ErNi_5$ is of the order of 150 K.

The temperature dependence of the susceptibility of $ErNi_5$ is largely determined by the susceptibility of the Er subsystem (Radwański et al. 1992a). The temperature dependences along the hard and easy axes above 100 K follow the Curie–Weiss low very well. Both curves show nearly the same value for paramagnetic moment but the paramagnetic Curie temperatures differ by 54 K ($\Theta_{\parallel} = +28$ K and $\Theta_{\perp} = -26$ K) as the result of substantial CEF interactions.

5.6.2.12. $TmNi_5$. The magnetic behaviour of $TmNi_5$ is extremely anisotropic. At a field of 15 T applied within the hexagonal plane, 8% of the easy-axis magnetization value is attained only. The easy-axis (c-axis) magnetization at 1.5 K amounts to $6.8\mu_B$/f.u. which is very close to the full Tm^{3+} moment (Barthem et al. 1989a). T_c amounts to 4.5 K. CEF interactions lead to a pseudo-doublet $|+6\rangle - |-6\rangle$ and $|+6\rangle + |-6\rangle$ as the ground state. Such a ground-state results from predominant second-order CEF interactions. As the doublet is slightly split, a pronounced λ-type peak in the specific heat at 4 K is observed. The ground-state doublet is well separated from the first excited doublet that was observed by INS at 143 K (Nait-Saada 1980, p. 111). The magnetostriction for this hexagonal compound is large (Barthem et al. 1989a). The forced as well as the spontaneous magnetostriction contributions have been evaluated within the single-ion model. A satisfactory agreement with experimental data has been found. Mössbauer effect studies have been reported by Gubbens et al. (1989a).

5.7. *R_2T_{17} compounds (T= Fe, Co, Ni)*

These compounds are formed for Fe, Co and Ni. The structure is closely related to the structure of the RCo_5 compounds. The composition is obtained by a replacement of

a specific R ion by a pair of 3d ions according to the formula

$$3RCo_5 - R + Co_2 \rightarrow R_2 + Co_{17}. \tag{5.16}$$

Since the substitutions of every third R ion are made within the hexagonal plane a new enlarged hexagon becomes the basis of the elementary cell with the a parameter equal to roughly $\sqrt{3}$ times that observed in the RCo_5 compounds.

The easy magnetic direction at helium temperature follows for the R_2T_{17} series the sign of the second-order Stevens factor α_J of the R ions involved, see table 2.6 for the R_2Co_{17} and table 5.8 for the R_2Fe_{17} series. An inspection of the tables shows that a negative value of α_J in these hexagonal and rhombohedral compounds is associated with planar anisotropy. In case of planar anisotropy, the EMD within the basal plane alternates as the sign of the sixth-order Stevens factor γ_J. Almost all Co compounds follow these α_J and γ_J systematics as the cobalt-sublattice anisotropy is small. The cobalt-sublattice magnetization prefers weakly the hexagonal plane as can be learned from Y_2Co_{17}; K_1 amounts to -11 K/f.u. The moment of Sm, Er, Tm and Yb ions in these structures favours the hexagonal axis, whereas other rare-earth ions show planar anisotropy. In compounds with iron the 3d anisotropy is much larger. The anisotropy of Y_2Fe_{17} is five times larger than the anisotropy of the cobalt counterpart. Due to the dominant Fe anisotropy the c-axis preference is observed for Tm_2Fe_{17} only below 72 K. The absence of TIMR processes in Er_2Fe_{17} can be understood as the uniaxial R anisotropy is overruled by the iron planar anisotropy over the whole temperature range below T_c.

Greedan and Rao (1973) used the point-charge model by considering the 3+ charges for the R ions and found a value for A_2^0 of $-55\,\text{K}\,a_0^{-2}$ for the Th_2Zn_{17} structure. Values of $-420\,\text{K}\,a_0^{-2}$ and $+310\,\text{K}\,a_0^{-2}$ for A_2^0 were found for the sites b and d in the Th_2Ni_{17}-type structure, respectively. These results suggest that there is a substantial competition between the rare-earth ions in determining the easy

TABLE 5.8

Correlation between the experimentally observed easy direction of magnetization (EMD) at low temperatures for the R_2Fe_{17} series and the Stevens factors α_J and γ_J. (t): EMD slightly tilted out from the basal plane.

Compound	Easy direction	α_J	EMD in plane	γ_J
Y	plane	0		0
Pr	plane (t)	−	complex	+
Nd	plane (t)	−	***b***	−
Sm	plane	+		0
Gd	plane	0		0
Tb	plane	−	***b***	−
Dy	plane	−	***a***	+
Ho	plane (t)	−	***b***	−
Er	plane	+	***a***	+
Tm	c-axis (<72 K)	+		−

direction of both moments. Andreev et al. (1985e) extended the PC-model calculations in order to obtain the CEF coefficients for the R_2Fe_{17} compounds with the heavy rare-earths (i.e. for Th_2Ni_{17} type of structure). The following values for the CEF coefficients have been reported: $A_2^0 = -150\,\mathrm{K}\,a_0^{-2}$, $A_4^0 = -0.05\,\mathrm{K}\,a_0^{-4}$ and $A_6^0 = -0.006\,\mathrm{K}\,a_0^{-6}$. The unrealistically small values for the higher-order coefficients show the shortcomings of the PC model. The CEF interactions orient the magnetic moments for the compounds with Pr, Nd, Tb, Dy and Ho within or close to the hexagonal plane. After the first observation of the FOMR transition in Ho_2Co_{17} (Franse et al. 1985) a number of other magnetic transitions to a noncollinear ferrimagnetic structure has been observed. High-field magnetization studies on single-crystalline R_2T_{17} compounds have been reviewed by Franse et al. (1991, 1992). The intersublattice interaction results in values for the molecular field acting on the Gd moment in Gd_2Co_{17} and Gd_2Fe_{17} of approximately 200 and 290 T, respectively.

For the $R_2(Co, Fe)_{17}$ compounds with R = Y, Pr, Sm, Gd, Dy and Er the results for the easy magnetic direction have been summarized in magnetic-anisotropy phase diagrams by E. Callen (1982) and Chen et al. (1989). All these phenomena are semi-quantitatively understood within a single-ion description of the 4f ions although the CEF interactions have not been fully evaluated yet. The occurrence of two different rare-earth sites with presumably substantial different anistropic behaviour is the main obstacle for it.

5.7.1. R_2Fe_{17} compounds

Single-crystal magnetization curves have been presented by Andreev et al. (1985e) for compounds with Y, Gd, Tb, Dy, Er and Tm in fields up to 6 T. The anisotropy coefficients of the R ions, derived from an analysis of these magnetization curves, do not show the expected single-ion correlation. Sinnema (1988) reported magnetization curves at 4.2 K up to 35 T for single-crystalline samples of Y, Dy, Ho and Er compounds. In addition, Verhoef (1990) performed the same type of measurements on single-crystalline Gd and Tb compounds and extended the measurements for Er_2Fe_{17} up to 50 T. Magnetic parameters of the R_2Fe_{17} compounds are collected in table 5.9. Within the compounds discussed, a FOMR transition within the hexagonal plane has been detected only for Er_2Fe_{17}, being a planar system due to the dominant Fe anisotropy. For other ferrimagnetic planar systems (Tb, Dy, Ho) the FOMR transitions are expected to occur at fields exceeding 40 T (Franse et al. 1988a).

The easy magnetization directions follow the α_J and γ_J rules rather well, see table 5.8. Er_2Fe_{17} and Sm_2Fe_{17} are exceptions. In these compounds the c-axis preference of the Er ions is overruled by the planar preference of the Fe moments. The Fe sublattice anisotropy is remarkably large as deduced from Y_2Fe_{17}. Magnetostriction measurements have been reported for single-crystalline samples of the heavy rare-earths in the temperature range between 4.2 and 300 K in fields up to 20 T by Andreev et al. (1985e) and for single-crystalline samples of Y and Er by Garcia-Landa et al. (1992).

The crystallographic structures and magnetic properties of the $R_2Fe_{17}C$, $R_2Fe_{17}N_x$ and $R_2Fe_{17}H$ interstitial R_2Fe_{17} compounds with C, N and H (in the form of deuterium) have been presented by X. P. Zhong et al. (1990a), by Buschow et al. (1990) and Isnard et al. (1992), respectively. All these interstitial elements cause a significant

TABLE 5.9
Magnetic parameters for R_2Fe_{17} compounds.

Compound	M_s		T_c (K)	$B^R_{ex,RT}$ (T)	Ref.*
	(A m²/kg)	(μ_B/f.u.)			
Y_2Fe_{17}	174.2	35.2			[1]
Y_2Fe_{17}		34.0	327		[2]
Ce_2Fe_{17}		30.0	225		[3]
Nd_2Fe_{17}		38.0	326		[3]
Sm_2Fe_{17}		34.0			[4]
Gd_2Fe_{17}		24.0	478		[2]
Gd_2Fe_{17}	101.4	22.9		290	[5,6]
Tb_2Fe_{17}		19.0	410		[2]
Tb_2Fe_{17}	81.9	18.6			[5]
Dy_2Fe_{17}		16.8	370		[2]
Dy_2Fe_{17}	74.0	16.9		214	[5]
Ho_2Fe_{17}		16.4	335		[8]
Ho_2Fe_{17}	81.5	18.7		219	[9]
$Ho_2Co_{14}Fe_3$	45.7	10.8			[9]
Er_2Fe_{17}		19.0	310		[2]
Er_2Fe_{17}	75.9	17.5		190	[7]
Tm_2Fe_{17}		23.0	306		[2]

*References:
[1] Matthaei et al. (1988).
[2] Andreev et al. (1985e).
[3] Isnard et al. (1992).
[4] X. P. Zhong et al. (1990b).
[5] Verhoef (1990).
[6] Radwański et al. (1992a).
[7] Sinnema (1988).
[8] Clausen and Nielsen (1981).
[9] Sinnema et al. (1987a).

increase of the magnetic ordering temperature and of the magnetization at room temperature making these interstitial compounds promising candidates for permanent-magnet applications.

5.7.1.1 Y_2Fe_{17}. The compound Y_2Fe_{17} is ferromagnetic with a value for M_s at 4.2 K of 35.2μ_B/f.u. (Sinnema 1988). Attributing this moment to the iron sublattice one gets a moment of 2.07μ_B per Fe ion. A value for T_c of 324 K is commonly accepted. For the hexagonal off-stoichiometric compound $Y_2Fe_{18.9}$ a much higher value of 386 K has been reported by Averbuch-Pouchot et al. (1987). For this latter compound a Fe moment of 2.01μ_B has been given. The occurrence of the hexagonal or rhombohedral structure depends on the heat treatment. The anisotropy field of 5.0 T at 4.2 K corresponds to a value for ΔE_a of -392 J/kg (-53.2 K/f.u.) that has been split into $K_1 = -427$ J/kg and $K_2 = +35$ J/kg (Matthaei et al. 1988). A much smaller value of -19 K/f.u. for ΔE_a has been reported for $Y_2Fe_{18.9}$ by Deportes et al. (1986) revealing the large effect of non-stoichiometry on the anisotropy energy. The para-magnetic susceptibility can be described by the MC–W law with p_{eff} close to 4μ_B/Fe-atom

(Burzo et al. 1985). Such behaviour is accounted for by the band-structure calculations of Inoue and Shimizu (1985). All band-structure calculations (Coehoorn 1989, Szpunar et al. 1987, Mohn and Wohlfarth 1987, Beuerle et al. 1991) have revealed a strong volume dependence of the 3d magnetism in Y_2Fe_{17}. Values for the local Fe (spin) moment of 2.41, 2.35, 2.12 1.91μ_B have been calculated by Beuerle et al. (1991) at the sites f, j, k and g of the hexagonal structure, respectively. A similar variation has been observed by Gubbens et al. (1987) for the hyperfine field detected by ^{57}Fe Mössbauer spectroscopy. Direct evidence for an orbital contribution to the iron moment has been provided by Mössbauer and NMR studies. Mössbauer studies on the ^{57}Fe nuclei in external fields applied along the hard and easy directions by Averbuch-Pouchot et al. (1987) and Deportes et al. (1986) have revealed anisotropies of the hyperfine field at the different crystallographic sites. The orbital contribution to the iron moment is estimated as 0.05μ_B. Moreover, NMR studies in external field by Armitage et al. (1986, 1989) have revealed a moment located at the Y sites of 0.4μ_B antiparallel to the Fe moment. Band-structure calculations can account for this result. Nikitin et al. (1991) have reported a pressure-induced magnetic phase transition. This phase transition has been associated with the development of antiferromagnetic interactions that lead to the formation of a complex helimagnetic structure like it is present in Lu_2Fe_{17}. It has been argued that under pressures of 2 GPa, the elementary-cell volume of Y_2Fe_{17} is reduced by 2% and becomes equal to the unit cell volume of Lu_2Fe_{17}. The magnetostriction in fields up to 20 T has been studied by Andreev et al. (1985e) and Garcia-Landa et al. (1992). Spontaneous magnetostriction studies of Y_2Fe_{17} and carbonated compound have been reported by Andreev et al. (1992).

5.7.1.2. Ce_2Fe_{17}. In the compound Ce_2Fe_{17}, Ce behaves largely as tetravalent ion that does not carry a magnetic moment. Complex, helimagnetic and fan structures within the Fe sublattice have been inferred from neutron diffraction studies by Givord and Lemaire (1974). Besides diffraction peaks that are characteristic for the rhombohedral Th_2Zn_{17}-type structure, new magnetic peaks have appeared indicating the formation of a magnetic structure incommensurate with the lattice. According to the authors, the noncollinearity of Fe moments is a characteristic feature of the iron 2:17 compounds with the smallest rare-earth ions (Ce^{4+}, Tm^{3+} and Lu^{3+}). The low value for T_c of 225 K and the relatively low value for M_s of 30μ_B/f.u. (Isnard et al. 1992) are further indications that Ce ions are for a substantial part in the tetravalent state. The iron magnetism is enhanced by absorption of hydrogen; Isnard et al. (1992) have reported values for T_c of 444 K and for M_s of 35μ_B/f.u. for $Ce_2Fe_{16.5}D_{4.8}$.

5.7.1.3. Pr_2Fe_{17} and Nd_2Fe_{17}. For the compounds Pr_2Fe_{17} and Nd_2Fe_{17} single-crystal data have not been reported yet. For Nd_2Fe_{17} a value of 40.0μ_B/f.u. has been found for M_s at 4.2 K by means of free-particle high-field magnetization measurements (Radwański et al. 1993). The anisotropy field exceeds 40 T. T_c amounts to 326 K. Absorption of hydrogen enhances magnetism as is seen from the values of 40.2μ_B/f.u. for M_s and of 525 K for T_c reported for $Nd_2Fe_{16.5}D_{4.8}$ by Isnard et al. (1992). Neutron diffraction studies by Herbst et al. (1982) on Co-substituted compounds of

$Nd_2(Fe–Co)_{17}$ have revealed a preferential site occupation: the c sites (dumbbells) are preferentially occupied by the Fe ions whereas the d and h sites have a Co occupation larger than those predicted by the stoichiometry and the random distribution. Mössbauer studies of Nd_2Fe_{17} and the nitrogenated sample have been reported by Pringle et al. (1992). The increase of T_c by ca. 400 K in $Nd_2Fe_{17}N_{2.6}$ has been correlated by these authors with the weakening of the AF exchange between iron ions mainly at the 6c sites.

5.7.1.4. Sm_2Fe_{17}. Single-crystal data for Sm_2Fe_{17} are not available. Although the Sm moment seems to prefer the *c* axis, the compound shows planar anisotropy likely due to the strong Fe sublattice anisotropy. Uniaxial anisotropy is obtained when the material is carbonized (X. P. Zhong et al. 1990b) or nitrided (Coey and Sun 1990). Both these processes improve substantially the hard magnetic properties at room temperature since T_c increases by more than 300 K. For $Sm_2Fe_{17}N_{2.7}$, a value for the anisotropy field of 14 T at room temperature has been reported by Katter et al. (1991). This substantial value for the anisotropy field as well as the value of 25 T at 4.2 K have been satisfactory explained within the single-ion approach by H. S. Li and Cadogan (1992). For this sample a multiplet transition at 170 meV has been observed by Mozc et al. (1990a,b) by means of inelastic neutron scattering. The spin-echo NMR spectra on Sm nuclei at 4.2 K reported by Kapusta et al. (1992a) contain two septet subspectra located at 468 and 568 MHz. They are ascribed to the two Sm isotopes, ^{149}Sm and ^{147}Sm, respectively.

5.7.1.5. Gd_2Fe_{17}. A value of $22.9\mu_B$/f.u. has been obtained at 4.2 K for a single-crystalline sample of Gd_2Fe_{17} by Verhoef (1990) on the basis of high-field magnetization studies. With the value of $7\mu_B$ for the Gd moment, one arrives at an Fe moment of $2.17\mu_B$. A substantial part of the difference with the moment in Y_2Fe_{17} is due to the presence of the Gd spins that produce an extra field of 110 T, which is experienced by the Fe moment. The hard-axis magnetization curve can be described well within the two-sublattice model with zero Gd anisotropy, $K_1^{Fe} = -57.8$ K/f.u., $K_2^{Fe} = +4.6$ K/f.u. and a molecular field $B_{mol,RT}^{Gd}$ of 290 T (Radwański et al. 1992a). High-field magnetization studies on fine particles of $Gd_2(Fe–Al)_{17}$ and $Gd_2(Fe–Mn)_{17}$ have been reported by Jacobs et al. (1992a) who found that the compensation of the magnetization occurs for 5.5 and 8.2 Fe atoms substituted by Mn and Al, respectively. For samples with a composition close to the compensation a value for the parameter n_{Gd-Fe} of about 8.7 T f.u./μ_B has been deduced from the measurements in fields above 20 T.

5.7.1.6. Tb_2Fe_{17}. For the compound Tb_2Fe_{17}, magnetization curves on a single-crystalline sphere have been measured by Verhoef et al. (1992b) at 4.2 K in fields up to 35 T. The EMD lies along the *b* axis. The magnetization curves are presented in fig. 5.33. A large basal-plane anisotropy and two transitions at fields of 3.9 and 10 T applied along the *c* axis are visible. Beyond these two transitions the magnetization reaches the same magnetization value as measured along the easy axis. The low-field transitions have been studied before by Andreev et al. (1985e). These authors evaluated

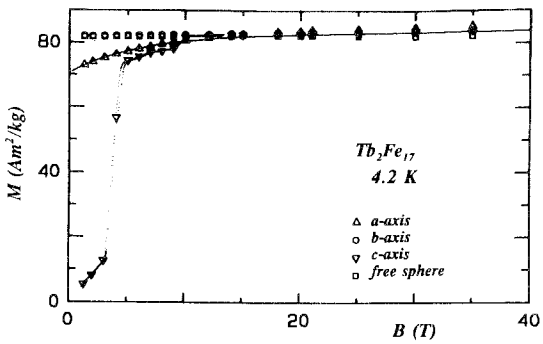

Fig. 5.33. Magnetization curves at 4.2 K for Tb_2Fe_{17} along different hexagonal crystallographic directions and for a free monocrystalline sample. After Verhoef et al. (1992b).

the CEF coefficients with the following results: $A_2^0 = +5.3\,\mathrm{K}a_0^{-2}$, $A_4^0 = -0.24\,\mathrm{K}\,a_0^{-4}$ and $A_6^0 = -7.8\,\mathrm{K}\,a_0^{-6}$. These values are rather small and are not able to describe details of the transitions. The ***a*** magnetization curve, the hard-axis within the hexagonal plane, fitted within the two-sublattice model provides a value for the coefficient $n_{\mathrm{Tb-Fe}}$ of 0.875 T kg/Am^2 (Verhoef et al. 1992b). It corresponds to a value for $J_{\mathrm{Tb-Fe}}/k_{\mathrm{B}}$ of -7.0 ± 0.1 K. The planar anisotropy has been evaluated as $+30$ J/kg, yielding a value for B_6^6 of $+140\,\mu$K.

5.7.1.7. Dy_2Fe_{17}. For the compound Dy_2Fe_{17}, a value of 260 T for the molecular field, $B_{\mathrm{mol}}^{\mathrm{Dy}}$, has been derived by Bogé et al. (1979) on the basis of Mössbauer spectroscopy. Subsequent studies of the temperature dependence of the hyperfine field at the Dy nuclei by Gubbens and Buschow (1982) yield, however, only half of this value, i.e. 128 T. A value of 107 T has resulted from high-field magnetization studies in fields up to 35 T performed by Sinnema (1988). The high-field magnetization curves are presented in fig. 5.34. From magnetization measurements up to 6 T, Andreev et al. (1985e) derived values of -0.97, -4.6 and $+0.06$ (in units of $\mathrm{K}a_0^{-n}$) for the CEF-coefficients A_2^0, A_4^0 and A_4^4, respectively. T_c is highly sensitive to pressure. It has been found by Radwański et al. (1985a) that a pressure of 15 kbar reduces T_c from 370 to 308 K. The same authors have discussed the pressure effect in the $Dy_2(Fe{-}Al)_{17}$ series in terms of magnetovolume effects.

5.7.1.8. Ho_2Fe_{17}. Magnetization curves at 4.2 K on single-crystalline Ho_2Fe_{17} have been reported by Sinnema et al. (1987a), see fig. 5.34, who found a value of $18.7\mu_{\mathrm{B}}$/f.u. for M_s. A smaller value of $16.4\mu_{\mathrm{B}}$/f.u. has been reported by Clausen and Nielsen (1981). The easy direction of magnetization lies along the ***b*** direction and the hard-axis curve is concave which is ascribed to the development of a noncollinearity of the Ho and Fe sublattice magnetic moments. In fields up to 35 T, in contrary to Ho_2Co_{17}, no transitions have been observed. According to the model calculations of Franse et al. (1988a) these transitions are expected to occur at fields larger than 35 T. The compound $Ho_2Co_{14}Fe_3$ that has a lower net magnetization exhibits FOMR transitions at 29 and 38 T for fields along the *b* and *a* axis, respectively (Sinnema et al. 1987a). The

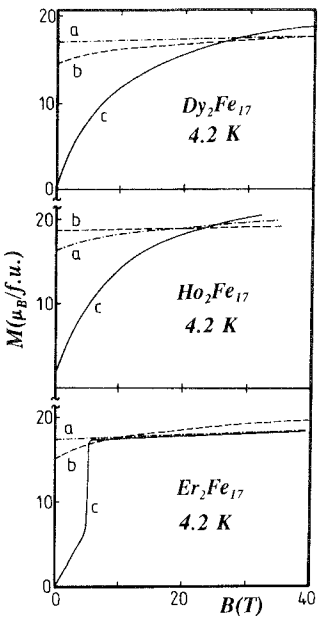

Fig. 5.34. Magnetization curves at 4.2 K along different hexagonal crystallographic directions for single crystalline R_2Fe_{17} compounds with R = Dy, Ho and Er. After Sinnema (1988) and Franse et al. (1992).

transitions in Ho_2Fe_{17} can be brought to experimentally accessible fields by relevant substitutions. The high-field measurements on fine particles of $Ho_2Fe_{17-x}Al_x$ performed by Jacobs et al. (1992b) have revealed transitions in the vicinity of 15 T for $x = 3$ and 4. $Ho_2Fe_{12}Al_5$ is at 4.2 K an almost compensated ferrimagnet and shows a linear magnetization curve, see fig. 5.35, with a slope of 2.8 T f.u./μ_B.

INS experiments performed by Clausen and Lebech (1982) have revealed at elevated temperatures, excitations to the first three CF levels with energies of 96, 163 and 219 K. The CEF coefficients deduced from these INS results are: $B_2^0 = +1.5$ K,

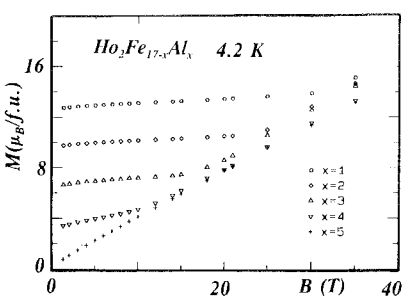

Fig. 5.35. High-field free-powder magnetization curves at 4.2 K for ferrimagnetic $Ho_2(Fe–Al)_{17}$ compounds. After Jacobs et al. (1992b).

$B_4^0 = +1.4\,\text{mK}$, $B_6^0 = +24.1\,\mu\text{K}$ and $B_6^6 = +11.6\,\mu\text{K}$. These parameters should be taken with some reservation as they were derived in combination with an unrealistically small value of 58.5 T for the molecular field. A value of 88 T has been derived by Franse and Radwański (1988) from high-field magnetization studies. This value corresponds to a value of -7.1 K for the parameter $J_{\text{Ho-Fe}}$ and fits well to the value for the exchange coupling observed for other R–T intermetallics, in particular to Ho_2Co_{17} where a value of -6.8 K has been deduced (Radwański et al. 1985b). The CEF parameters of Clausen and Lebech (1982) are enormously large compared to the ones derived for other the R_2T_{17} compounds as one can see by inspecting table 5.10. Hydrogen absorption as studied by Isnard et al. (1992) has resulted in values for T_c of 500 K (335 K) and for M_s at 300 K of 24.6(18.0)μ_B/f.u. for $Ho_2Fe_{18}D_{3.8}$ (Ho_2Fe_{18}).

5.7.1.9. Er_2Fe_{17}. The compound Er_2Fe_{17} does not follow the systematics of the Stevens factor α_J for the easy direction of magnetization within the R_2Fe_{17} series. Given the planar anisotropy observed in compounds with Tb, Dy and Ho, the single-ion model requires that the Er moment favours the c axis. The planar anisotropy of Er_2Fe_{17} results from the dominant Fe anisotropy. The resultant anisotropy is weak as is confirmed by magnetization studies at 4.2 K. Andreev et al. (1985e), Sinnema (1988) and Franse et al. (1992) have reported that a field of 4.8 T applied along the hard c axis is sufficient to reorient both sublattice moments. Beyond the transition, the magnetization coincides with that measured for the easy direction in the field

TABLE 5.10

CEF coefficients, in units of $K a_0^{-n}$, for the R_2Co_{17} and the R_2Fe_{17} compounds with the hexagonal structure of the Th_2Ni_{17} type. PCM denotes a point-charge model result.

Compound	Site	A_2^0	A_4^0	A_6^0	A_6^6	Ref.*
R_2Co_{17} (PCM)	2b	−420	–	–	–	[1]
	2d	+310	–	–	–	[1]
R_2Fe_{17} (PCM)	–	−150	−0.05	−0.006	–	[2]
Dy_2Co_{17}	–	−71	−3.1	0	−45.4	[3]
Ho_2Co_{17}	–	−69	+20	−1.4	−4.1	[4]
Ho_2Co_{17}	2b	−348	−13.1	+1.9	−19.7	[5]
	2d	−121	+17.8	+2.6	−19.7	[5]
Tb_2Fe_{17}	–	+5.3	−0.24	−7.8	–	[2]
Dy_2Fe_{17}	–	−0.97	−4.6	+0.06	–	[2]
Ho_2Fe_{17}	–	−900	−30.0	−3.4	−1.7	[4]
Er_2Fe_{17}	–	+17.9	−8.9	–	–	[2]
Tm_2Fe_{17}	–	−61.0	−4.3	–	–	[2]

*References:

[1] Greedan and Rao (1973).
[2] Andreev et al. (1985e).
[3] Colpa et al. (1989a,b).
[4] Clausen and Lebech (1982).
[5] Radwański and Franse (1989a).

interval up to 35 T. This fact, together with the very small high-field susceptibility indicates that after the transition both moments are forming a strictly antiparallel configuration. Model calculations of Franse et al. (1988a) have anticipated transitions in fields just above the capability of the Amsterdam High-Field Installation (Gersdorf et al. 1983). Indeed, measurements at fields above 40 T performed in later years at the High-Field Installation of Osaka University reveal transitions at 36 and 43 T for fields along the easy axis (*a*) and at 45 T along the *b* axis (Verhoef et al. 1992a). The transitions at 36 and 45 T have been associated by the latter authors with the FOMR transitions within the hexagonal plane whereas the transition at 43 T with a reorientation of the moments within the *a*–*c* plane. Andreev et al. (1985e) have deduced from magnetization studies up to 6 T, values of +17.9 and −8.9 (in units of K a_0^{-n}) for A_2^0 and A_4^0, respectively. A value of 258 T for $B_{ex,RT}^{Er}$ has been found by de Boer et al. (1990) by means of high-field magnetization studies on free-powder particles. Neutron-diffraction studies at 8 K performed by Kumar and Yelon (1990) on a sample with the actual composition $Er_{1.91}Fe_{18.25}$ have revealed different values for the magnetic moments for the Er moment at the sites b and d of 7.49 and 8.94μ_B, respectively. A pronounced magnetovolume effect is seen by the large negative pressure dependence of T_c that has been studied up to 33 kbar by Brouha et al. (1974). Silicon substitution causes a substantial increase of T_c as has been reported by Alp et al. (1987). For $Er_2Fe_{14}Si_3$, T_c equals 498 K, a much higher value compared with 305 K observed for the nonsubstituted compound. This effect is quite striking owing to the fact that silicon substitutions decrease the volume of the elementary cell.

5.7.1.10. Tm_2Fe_{17}. The compound Tm_2Fe_{17} is the only iron compound with the 2:17 structure that has an easy *c* axis at 4.2 K. A TIMR transition occurs at 72 K (Gubbens et al. 1987). The transition is caused by the competition of the Tm and Fe anisotropies. Magnetization studies up to 6 T by Andreev et al. (1985e) on a single-crystalline specimen revealed the *c* axis to be the easy direction of magnetization. There is a transition at 3 and 3.5 T for fields along the ***a*** and ***b*** directions, respectively. The magnetization studies yield values of -61 K a_0^{-2} and -4.32 K a_0^{-4} for the CEF coefficients A_2^0 and A_4^0 of Tm^{3+}, respectively. Mössbauer spectra reported by Gubbens et al. (1987) distinguish the two different R sites that have different values for the ^{169}Tm hyperfine field (755 and 739 T). From the quadrupolar splitting, values for the coefficient A_2^0 at the two different sites have been determined. Within the experimental error the values for both sites are equal in absolute value, i.e., -71 and $+71$ K a_0^{-2}, resulting in a negligibly small resultant Tm anisotropy. However, a Tm-sublattice anisotropy of about 80 K/f.u. at 4.2 K has to exist in order to overrule the Fe-sublattice anisotropy below 72 K. The temperature dependence of the ^{169}Tm hyperfine field has been fitted with a value of 201 T for $B_{ex,RT}^{Tm}$. The TIMR transition is accompanied by an anomaly in the thermal variation of the ^{57}Fe hyperfine field which is visible in particular for the site 4f. This anomaly is ascribed to the nonzero orbital contribution to the Fe magnetic moment.

5.7.1.11. Yb_2Fe_{17}. From the unit-cell volume consideration the Yb ion has been inferred to be in the trivalent state in Yb_2Fe_{17}. ^{174}Yb Mössbauer spectra reported

by Buschow et al. (1989) have been dissolved. The magnitude of the hyperfine field of 4.48 MOe is slightly larger than the free-ion value indicating the full Yb^{3+}-ion moment. Two parameters – different in sign – for the quadrupolar interactions give evidence that the second-order crystal-field parameters at the two crystallographically different R sites are opposite in sign. The resultant anisotropy of the Yb sublattice is small as the anisotropy energies of the Yb ions at the two sites nearly cancel. The easy direction of magnetization is determined by the iron sublattice. The Fe sublattice probably gives rise to a fan-type magnetic structure, as in Lu_2Fe_{17}, with the Fe moments remaining within the hexagonal plane.

5.7.1.12. Lu_2Fe_{17}. From single-crystal magnetization measurements at 4.2 K it is known that the hard axis is the *c* axis. At 4.2 K a field of 4.5 T is needed to orient the Fe moments along this direction. A complex, helimagnetic structure of the Fe moments has been claimed by Givord and Lemaire (1974) on the basis of neutron studies. The authors have argued that the helimagnetic arrangement of the Fe moments is a compromise between ferro- and antiferromagnetic interactions between the Fe spins at the different crystallographic sites. The AF interactions become stronger with decreasing Fe–Fe distance. Indeed, the volume of the elementary cell of Lu_2Fe_{17} is lower by 2.1% compared with that of Y_2Fe_{17}. A reduction of T_c in Lu_2Fe_{17} by 40 K compared with Y_2Fe_{17} is given as further proof for the development of the AF interactions in Lu_2Fe_{17}. This view is consistent with the substantial high-field susceptibility of the Lu_2Fe_{17} compound for fields applied along the easy (***b***) direction. Influence of C, N and H on ^{57}Fe NMR spectra have been studied by Kapusta et al. (1992b).

5.7.2. R_2Co_{17} compounds

The results of point-charge calculations by Greedan and Rao (1973) for the CEF coefficients of the Co compounds are the same as reported earlier for the Fe compounds. For the hexagonal structure two different R-ion sites exist that, so far, not have been detected in INS experiments on Ho_2Co_{17} (Clausen and Lebech 1982, Jensen 1982). Magnetic parameters for the R_2Co_{17} compounds have been collected in table 5.11. Radwański and Franse (1989a) have shown by analyzing high-field magnetization, specific heat and INS experimental data of Ho_2Co_{17} that, irrespective of the quite different CEF interactions at the two sites, the lower part of the energy level schemes at the two sites is essentially the same. Magnetization curves up to 35 T have been measured by Sinnema (1988) for single-crystalline specimens for the R_2Co_{17} compounds with R = Y, Pr, Nd, Gd, Tb, Dy, Ho and Er. Verhoef (1990) have extended the measurements for the Ho and Er compounds up to fields of 50 T.

The single-ion origin of the anisotropy is manifest in the systematic variation of the EMD across the 4f series as seen in table 2.6. The planar/axis preference follows exactly the α_J rule. Of the compounds under discussion, Pr_2Co_{17} is found to be an exception of the γ_J systematics since the *a* axis instead of the *b* axis is the easy axis of magnetization. An external field of 3 T, however, is already sufficient to reorient the moment from the *a* to the *b* axis.

TABLE 5.11
Values for the magnetic parameters of single-crystalline R_2Co_{17} compounds.

Compound	M_s		$B^R_{ex,RT}$ (T)	Ref.*
	($A\,m^2/kg$)	(μ_B/f.u.)		
Y_2Co_{17}	132.5	28.0		[1]
Pr_2Co_{17}	145.6	33.5		[2]
Nd_2Co_{17}	146.8	33.9		[3]
Sm_2Co_{17}			340	[4]
Gd_2Co_{17}	58.1	13.7		[1]
Tb_2Co_{17}	42.5	10.0	189	[5]
Dy_2Co_{17}(S)	31.1	7.4	166	[7]
Dy_2Co_{17}(S)	31.1	7.4	166	[7, 8]
Dy_2Co_{17}(R)	35.5	8.4	166	[8]
Ho_2Co_{17}(S)	33.6	8.0	159	[9, 10]
Ho_2Co_{17}(R)	28.4	6.8		[8]
Er_2Co_{17}	48.3	11.6	150	[5]

*References:
[1] Matthaei et al. (1988).
[2] Verhoef et al. (1988a).
[3] Radwański et al. (1988a).
[4] Perkins and Strassler (1977).
[5] Sinnema (1988).
[7] Sinnema et al. (1986a).
[8] Verhoef (1990).
[9] Franse et al. (1985).
[10] Radwański and Franse (1989a).

5.7.2.1. Y_2Co_{17}. For the compound Y_2Co_{17} Sinnema (1988) has found for a single-crystalline sample values for the magnetization and the differential susceptibility at 4.2 K of 28.0μ_B/f.u. and $70 \times 10^{-4}\mu_B$/T f.u., respectively. The value for the anisotropy field B_A of 1.6 T at 4.2 K points to a value of K_1 of −9.0 K/f.u. Magnetic torque measurements reported by Matthaei et al. (1988) yield $K_1 = -6.8$ K/f.u. and $K_2 = -1.8$ K/f.u. Temperature weakly affects the magnetic properties below room temperature since T_c is as high as 1200°C. At 250 K the magnetization is reduced to 27.6μ_B/f.u., i.e. by 1.5%, whereas the anisotropy energy is reduced by 23% (Sinnema 1988). The decrease of the anisotropy energy is much faster than expected from the Callen–Callen model (H.B. Callen and Callen 1966). According to the phase diagram of Chen et al. (1989), Y_2Co_{17} undergoes a TIMR transition. At temperatures above 1000 K, the planar anisotropy changes into the axial one. The uniaxial anisotropy in Y_2Co_{17} can be induced even at helium temperature by substitutions of small amounts of Fe (Perkins and Nagel 1975) or Mn (Kąkol and Figiel 1986). These latter authors evaluated the contributions to the magnetocrystalline anisotropy from the different Co sites. An extended analysis of the anisotropy of the $Y_2(Co–Fe)_{17}$ within the individual site model has been presented by Franse et al. (1988b).

5.7.2.2. Ce_2Co_{17}. For the compound Ce_2Co_{17} two crystallographic structures, the hexagonal and rhombohedral, can occur depending on the heat treatment.

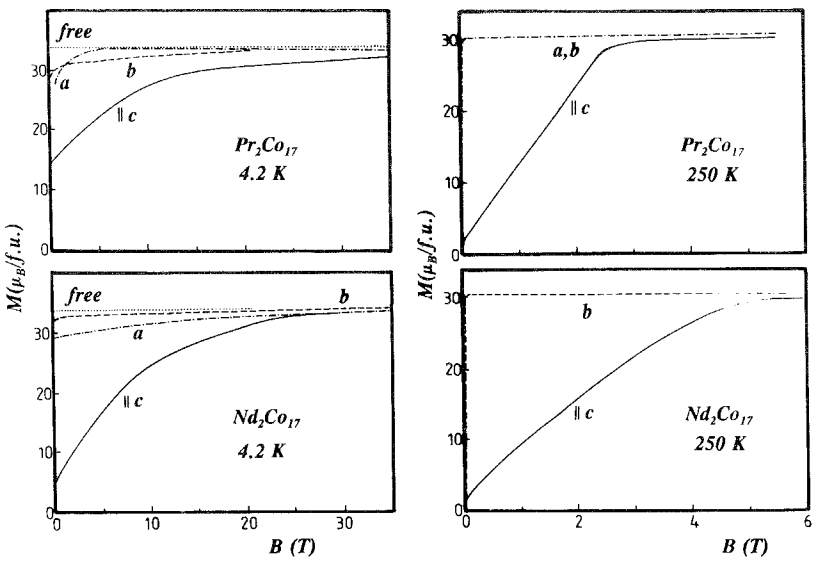

Fig. 5.36. Magnetization curves for single-crystalline Pr_2Co_{17} and Nd_2Co_{17} at 4.2 K and 250 K along different hexagonal crystallographic directions. After Verhoef et al. (1988a).

5.7.2.3. Pr_2Co_{17}. Single-crystal magnetization studies for Pr_2Co_{17} at 4.2 K up to 35 T as shown in fig. 5.36 have revealed that the magnetization does not lie along a specific crystallographic direction as all magnetization curves along the main crystallographic directions start at zero field with nonzero values. A tilt angle of 74° with respect to the *c* axis has been deduced by Verhoef et al. (1988a). In fields above 3 T along the *a* axis, the magnetization lies along the ***a*** direction satisfying the systematics of the sixth-order Stevens factor within the 2:17 series. The origin of the tilted magnetic structure seems to be higher-order CEF interactions of the Pr^{3+} ion. Verhoef et al. (1988a) have reported that the tilted structure persists up to at least 250 K.

5.7.2.4. Nd_2Co_{17}. High-field magnetization curves at 4.2 K shown in fig. 5.36 have revealed that a field of 35 T along the *c* axis is still not able to fully orient the neodymium moment along the field direction. A tilted magnetic structure with a tilt angle of 82.5° with respect to the *c* axis is deduced at 4.2 K from the magnetic isotherms (Verhoef et al. 1988a). Radwański et al. (1988b) have shown that this tilted structure results from CEF interactions of higher order. The authors succeeded in evaluation of the contributions to the magnetocrystalline anisotropy originating from all six CEF coefficients relevant to the rhombohedral symmetry $R\bar{3}m$. The angular dependence of the magnetocrystalline anisotropy of the Nd sublattice as well as the different contributions have been shown in fig. 2.3. The set of CEF parameters is shown in table 5.12. Neutron diffraction studies on a powder sample have been performed by Herbst et al. (1982). A substantial two-ion contribution to the anisotropy has been concluded by Kąkol and Figiel (1985) on the basis of magnetization studies on

TABLE 5.12
CEF coefficients, in units of $K a_0^{\,n}$, for the R_2Co_{17} compounds with the rhombohedral structure of the Th_2Zn_{17} type. PCM denotes a point-charge model result.

Compound	A_2^0	A_4^0	A_6^0	A_6^6	A_4^3	A_6^3	Ref.*
R_2Co_{17} (PCM)	−55	–	–	–	–	–	[1]
Sm_2Co_{17}	−94	–	–	–	–	–	[2]
Nd_2Co_{17}	−169	−14.2	+0.035	−14.0	+4.7	−5.2	[3]

*References:
[1], Greedan and Rao (1973).
[2] Perkins and Strassler (1977).
[3] Radwański et al. (1988a).

polycrystalline $(Nd–Y)_2Co_{17}$ samples since the dependence of the anisotropy on the Y concentration has been found to have a quadratic variation. The spin-echo NMR studies at 4.2 K by Figiel et al. (1990) have revealed a well-resolved spectrum located at 562 MHz associated with the ^{145}Nd isotope. A value for the Nd-ion moment of $3.0\mu_B$ in Nd_2Co_{17} has been deduced by Figiel et al. (1992).

5.7.2.5. Sm_2Co_{17}. A value for M_s at 4.2 K of $27.8\mu_B$/f.u. has been reported for single-crystalline Sm_2Co_{17} by Deryagin et al. (1982). The EMD lies along the c axis and the anisotropy of the Sm sublattice dominates that of the Co sublattice. The anisotropy constant K_1 derived for a polycrystalline sample amounts to $+6.6\,J/cm^3$ ($+120$ K/f.u.) (Perkins and Strassler 1977). This value as well as the temperature dependence of the anisotropy constant has been described within a single-ion Hamiltonian with an exchange field $\mu_B H_{ex}$ of 221 K and with $\langle r^2\rangle A_2^\circ = -104$ K. The magnetization curve in the hard direction is markedly curved. Deryagin et al. (1982) described this noncollinearity in terms of the anisotropy constants K_1 and K_2 with values of $+770$ and $+230$ J/kg, respectively. Radwański et al. (1987) have attributed this curvature to a field-induced noncollinearity of the Sm and Co sublattices. Magnetostriction measurements on the $(Sm–Y)_2Co_{17}$ series have been reported by Kudrevatykh et al. (1984). Mössbauer studies on diluted ^{153}Eu in Sm_2Co_{17} by Nowik et al. (1983) yield a hyperfine field of -159 T experienced by the Sm nucleus. The different contributions to the hyperfine field have been separated, see section 3.3.2. The spin echo NMR experiments on Sm nuclei reported by Figiel et al. (1991) contain two septet subspectra located at 496 and 600 MHz associated with two Sm isotopes: ^{149}Sm and ^{147}Sm. The lattice contribution to the EFG at the Sm site has been estimated as $1.1 \times 10^{21}\,V\,m^{-2}$. This value is of similar magnitude as observed in $SmCo_5$ indicating CEF interactions of a similar size.

5.7.2.6. Gd_2Co_{17}. For the compound Gd_2Co_{17} the EMD at 4.2 K stays within the hexagonal plane. Magnetization curves indicate a small value for the anisotropy energy, slightly lower, in absolute value, compared with that observed for Y_2Co_{17}.

A peculiarity of the hard-axis magnetization curve at 4.2 K shown in fig. 4.10 is a transition at 1.2 T. Sinnema (1988) has shown that the transition can be described within the FOMP model of Asti and Bolzoni (1980) and is due to an appreciable value of K_2. An anomalously large value for the anisotropy constant K_2 has been found in magnetic torque measurements, indeed (Matthaei et al. (1988). The origin of this significant value of K_2 in Gd_2Co_{17} is unclear as the anisotropy energy of Y_2Co_{17} can well be described by the K_1 term only. A noncollinearity of the Co and Gd moments is improbable due to the large 3d–4f exchange in Gd–Co compounds. A suggestion has been made by Matthaei et al. (1988) that the anisotropy in Gd_2Co_{17} is of the same origin as in Gd metal and in both cases of the order of magnitude of 0.5 K. A two-ion contribution to the anisotropy energy by dipolar interactions cannot be excluded in this compound as the overall anisotropy is rather small. The strong temperature dependence of the K_2 term, however, cannot be explained by the dipole–dipole interaction. At 250 K this term is already absent whereas the Gd moment itself is only slightly reduced. Dipolar interactions have been analyzed by Colpa (1992) who has shown that the difference in the anisotropy between Gd_2Co_{17} and Y_2Co_{17} is due to extra dipolar interactions caused by the presence of the Gd moments. These studies, however, do not explain the origin of the FOMP-like transition at 1.6 T. At temperatures above 950 K the anisotropy is reported to be uniaxial (Chen et al. 1989). This uniaxial anisotropy can also be induced at helium temperature by adding small amounts (above 3%) of Fe and persists to an Fe concentration of 50% as has been found by Perkins and Nagel (1975).

5.7.2.7. Tb_2Co_{17}. High-field magnetization studies at 4.2 K performed by Sinnema (1988) on a single-crystalline sample of Tb_2Co_{17} do not reveal specific transitions in the field range up to 35 T. The high-field magnetization curves are presented in fig. 5.37. The large value of the apparent anisotropy field of 28 T indicates a strong intersublattice coupling. A value for $B^{Tb}_{ex,RT}$ of 130 T has been derived from the magnetization curves along the hard-axis. Two-sublattice model calculations of Franse et al. (1988a) indicate FOMR transitions in fields well above 40 T.

5.7.2.8. Dy_2Co_{17}. High-field magnetization studies at 4.2 K on a single-crystalline sample have been performed by Sinnema et al. (1986a). The results are shown in fig. 5.37. An analysis within the two-sublattice model, presented by Sinnema et al. (1986a), have revealed a molecular field of 82 T. This value differs largely from the value of 330 T reported by Bogé et al. (1979) on the basis of Mössbauer-effect studies. The lower value is in good agreement with the systematics found within the 2:17 series and has been further supported by the analysis of magnetic excitations observed by Colpa et al. (1989a,b) by means of inelastic neutron scattering. An interpretation of the INS spectra, shown in fig. 5.38, within a linear spin-wave theory has resulted in an evaluation of microscopic parameters, i.e. the Heisenberg-like exchange and the CEF parameters. The parameters are found to be in good agreement with the parameters derived from high-field studies. The CEF coefficients are shown in table 5.10. As Dy_2Co_{17} is an easy-plane ferrimagnetic system, FOMR transitions are to be expected. The lowest one has been estimated by Radwański (1985) to occur

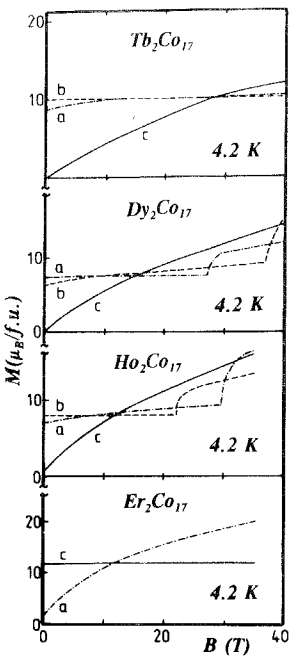

Fig. 5.37. Magnetization curves for single-crystalline R_2Co_{17} compounds with R = Tb, Dy (after Sinnema et al. 1986b), R = Ho (after Franse et al. 1985) and R = Er (after Sinnema 1988) along different hexagonal crystallographic directions.

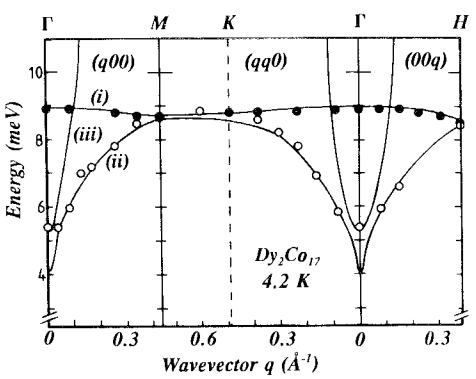

Fig. 5.38. Magnetic excitations at 4.2 K in Dy_2Co_{17} observed for a single-crystalline sample; experimental points (○ and ●) are observed around the (220) and (301) reciprocal lattice points, respectively. The full lines represent the results of a linear spin-wave model. (i), (ii) and (iii) denote the excitation mode Dy–Dy, Dy–Co and Co–Co, respectively. After Colpa et al. (1989a, b).

at 26 T for fields applied along the easy direction of magnetization. Indeed, two FOMR transitions have been detected later on by Sinnema et al. (1986a). For the crystal denoted by Verhoef (1990) by S two transitions occur for fields applied within the hexagonal plane: at 26 T for the ***a*** direction and 38 T for the ***b*** direction. The transition fields result in values for n_{RT} of 2.0 K f.u./μ_B^2 and for $K_6^{6,Dy}$ of -200 J/kg (Sinnema et al. 1986a). For another single-crystalline sample (denoted by R) Verhoef (1990) has found the transition at 31 and 42 T (Verhoef 1990). These different results originate from small differences in the composition that have, however, a significant impact on the spontaneous magnetic moment: 31.1 A m^2/kg in the case of the sample S and 35.5 A m^2/kg in the case of the sample R. Despite this difference the values for the parameter n_{RT} as derived for both samples are very similar.

5.7.2.9. Ho_2Co_{17}. Magnetization studies at 4.2 K reported by Franse et al. (1985) in fields up to 35 T on a single-crystalline sample Ho_2Co_{17} (referred to as sample S) have revealed a value for M_s of 33.6 A m^2/kg ($=8.0\mu_B$/f.u.). In combination with the Ho-ion moment of $10\mu_B$ this value corresponds to a cobalt moment of $1.65\mu_B$. For another single-crystalline sample (sample R), a much smaller value is reported, $M_s = 28.4$ A m^2/kg (Verhoef 1990). For a single-crystalline sample Clausen and Nielsen (1981) have reported the value $8.4\mu_B$/f.u. These different values have to be ascribed to a slight off-stoichiometry of the compound that is allowed by the homogeneity region in the phase diagram. Indeed, the actual composition of sample R has been found by microprobe studies as $Ho_{2.05}Co_{16.90}$. These imperfections hamper the exact analysis of experimental results and the high-field magnetization data, in particular. The differential susceptibility of sample S along the easy (*b*) axis amounts to $\chi_{hf} = 70 \times 10^{-4}\mu_B$/T f.u. in the field range up to 21 T. This value is much the same as the value for χ_{hf} found for Y_2Co_{17}. It indicates that the Ho-ion moments in Ho_2Co_{17} are not affected by external fields, a fact that points to a ground state of the Ho ions with the full moment. The transitions observed at 22 T for fields applied along the easy (*b*) axis and at 29 T for fields applied along the hard-in plane (*a*) axis, see fig. 5.37, are transitions of the FOMR type. In these first-order moment-reorientation transitions the two-sublattice moments reorient within the hexagonal plane as it has been discussed in section 3.1. The transition-field value depends on the value of the in-plane anisotropy coefficient κ_6^6 but mainly on the value of the intersublattice molecular-field coefficient. The studies in fields up to 50 T by Tomiyama et al. (1991) have revealed a next transition at 44 T identified as the second FOMR transition, see fig. 3.9, confirming the model predictions (Radwański et al. 1985b). It is worth noting that the magnetization curves for the *c* axis and for the *a* and *b* axes provide values for the parameter n_{RT} that are almost the same. For sample R the transitions are observed at lower fields (20.6 and 27.6 T) (Verhoef 1990). These lower fields are consistent with the lower value of the net magnetic moment. The effect of temperature on the FOMR transition has been studied by Sinnema et al. (1987b). With increasing temperature the transition becomes smooth and at 77 T does not occur any longer. It is related with the strong temperature dependence of the in-plane anisotropy that is governed by the sixth-order CEF parameter B_6^6.

INS experiments performed by Clausen and Lebech (1982) have revealed excitations

from the ground state to the first excited CEF level at an energy distance of 82 K. Two other excitations, at 138 and 182 K, have been observed by Clausen and Lebech (1982) in the experiments at increased temperatures. These authors derived the following values for the CEF parameters: $B_2^0 = +0.116\,\mathrm{K}$, $B_4^0 = -0.93\,\mathrm{mK}$, $B_6^0 = +10\,\mu\mathrm{K}$ and $B_6^6 = +28\,\mu\mathrm{K}$. A value for 3d–4f coupling parameter J_{RT}^* of 0.147 meV has been found. J_{RT}^* refers to the Hamiltonian $J_{\mathrm{RT}}^* S_{3\mathrm{d}} J_{4\mathrm{f}}$. The above-mentioned results reproduce the energy separations but are not able, however, to describe the high-field magnetization curves in full detail. Nevertheless, the value of the molecular field $B_{\mathrm{mol}}^{\mathrm{Ho}}$ of 61.5 T that can be derived from the value of J_{RT}^* is found to be in good agreement with the value derived from the high-field magnetization studies (63.5 T, Franse et al. 1985). Results of specific heat measurements have been reported by Radwański et al. (1988b). The electronic, lattice and CEF contributions to the specific heat have been separated. An extended analysis of the magnetic properties of Ho_2Co_{17} has been given by Radwański and Franse (1989a) on the basis of the experimental data from specific-heat, Mössbauer, INS and high-field magnetization studies. In fig. 5.39 the angular dependence of the magnetocrystalline anisotropy energy of the Ho sublattice derived from high-field magnetization studies is presented together with the contributions originating from different CEF parameters as well as originating from the two non-equivalent sites of the Ho ions. The CEF coefficients are shown in table 5.10. It turns out that, despite the quite different values for the CEF coefficients at the two nonequivalent crystallographic sites b and d, the bottom part of the energy level scheme of the trivalent holmium ion is essentially the same for both sites, see fig. 5.40. It provides a plausible explanation that only one spectrum is detectable in the INS experiments (Clausen and Lebech 1982, Jensen 1982).

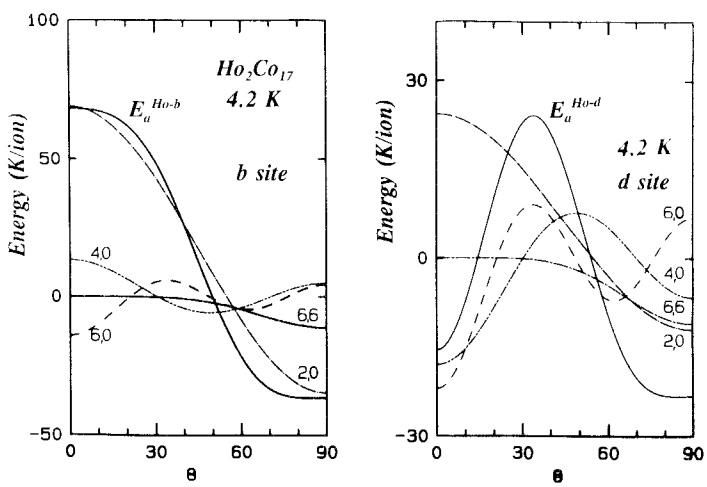

Fig. 5.39. The angular dependence of the magnetocrystalline anisotropy energy of the holmium ion at 4.2 K for the two different crystallographic sites, b and d, in Ho_2Co_{17}. The different multipole contributions $\kappa_n^m P_n^m(\cos\Theta)$ are shown: values for (n,m) are indicated. After Radwański and Franse (1989a).

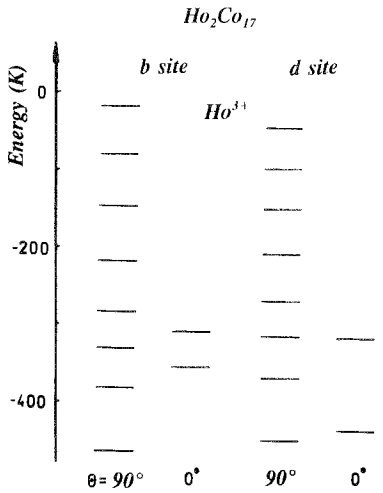

Fig. 5.40. The energy-level scheme of the trivalent holmium ion in Ho_2Co_{17} at the two different crystallographic sites, b and d, under the combined action of the crystal field and the molecular field, acting along the polar angle Θ. The angle Θ is indicated. Only eight lowest levels for the easy direction ($\Theta = 90°$) and two for the hard direction ($\Theta = 0°$) are shown. After Radwański and Franse (1989a).

5.7.2.10. Er_2Co_{17}. For the compound Er_2Co_{17}, single-crystal magnetization curves, presented in fig. 5.37, point to a value for M_s at 4.2 K of 48.3 A m^2/kg. With the full trivalent erbium moment it yields a quite large value of 1.74μ_B for the cobalt moment. This result indicates that a compound richer in cobalt than Er_2Co_{17} has been formed. Indeed, assuming a composition $Er_2Co_{18.4}$ values of 9.0 and 1.65μ_B can be obtained for the Er and Co ions, respectively (Radwański and Franse 1993). Extraordinary large values for the Co magnetic moment between 1.70 and 2.15μ_B at 300 K have been reported by Kumar and Yelon (1990) on the basis of neutron diffraction measurements. In contrary, smaller but more reasonable values for the Co moment of 2.6, 1.6, 1.9 and 1.2μ_B at the site 4f, 6g, 12j and 12k, respectively have been found by polarized neutron diffraction studies at 5 K carried out on a single-crystalline sample by Moze et al. (1992). Magnetic measurements on $Er(Co_{0.4}Fe_{0.6})_{17}$ reported by Andreev et al. (1986b) have revealed a metamagnetic transition that can be interpreted within the FOMP description. Magnetostriction measurements for this compound have been reported by Kudrevatykh et al. (1986).

5.7.2.11. Tm_2Co_{17}. Mössbauer studies on Tm_2Co_{17} by Gubbens et al. (1987) have revealed that the two R sites have quite different values for the second-order CEF coefficient; −130 and −40 K a_0^{-2}. The temperature dependence of the hyperfine field has been fitted with a value for B_{ex} of 178 T. This result agrees with the values obtained from high-field magnetization studies on other 2:17 compounds. Mössbauer studies lead to a ground state that is nearly a pure $|J_z = -6\rangle$ state like in the Fe and Ni counterparts.

5.7.3. R_2Ni_{17} compounds

Single crystalline samples of this series have not been reported to exist so far. The nickel moment in these compounds amounts to $0.3\mu_B$ as has been concluded by Laforest et al. (1967) and X. P. Zhong et al. (1990c) on the basis of magnetization studies on the compound Y_2Ni_{17}. The Ni magnetism is very sensitive to the exact composition as has been proved by band-structure calculations of M. Shimizu et al. (1984). The exchange interactions in Y_2Ni_{17} can be reduced by lowering the Ni concentration within the homogeneity region of the Th_2Ni_{17}-phase. Lowering Ni concentration causes that some of the Ni atoms become very close to the Stoner limit. Y_2Ni_{16} exhibits a step-like magnetization process as has been found by Gignoux et al. (1980a). This nonlinear magnetization process has been related with the collective-electron metamagnetism, as has been discussed in section 4.8. The large value for the differential high-field susceptibility, of $12 \times 10^{-3}\mu_B$/T f.u. at 4.2 K observed by X. P. Zhong et al. (1990c) for Y_2Ni_{17} in fields up to 35 T is consistent with this view.

The pressure dependence of T_c has been analyzed by Jaakkola et al. (1983). A value of $-0.45\,\mathrm{K\,kbar^{-1}}$ has been derived for dT_c/dp, independent of the R partner. All ferrimagnetic compounds, i.e. those formed with heavy R elements, exhibit a compensation point in the magnetization versus temperature curves. Values for the parameter J_{RT} derived from the compensation temperature are found to be consistent with those found from free-powder high-field magnetization measurements (X. P. Zhong et al. 1990c). These authors have evaluated the intersublattice interaction by means of the free-powder method applied to the $(R{-}Y)_2Ni_{17}$ samples. The results are collected in table 5.13. Relevant Y substitutions have been made in order to bring the noncollinear regime to lower fields. The Ni sublattice magnetization in Gd_2Ni_{17} amounts to $5.5\mu_B$/f.u. (X. P. Zhong et al. 1990c). This value is higher by $0.4\mu_B$/f.u. than that of the Y counterpart. This difference in the spontaneous moment is likely due to the presence of Gd spins producing an extra molecular field of 100 T. The Pauli susceptibility equals $4 \times 10^{-3}\mu_B$/T f.u. This is a reasonable value although it is three times smaller

TABLE 5.13

Values for the magnetic parameters of R_2Ni_{17} compounds. M_s is the spontaneous magnetization whereas $M_\parallel$ is the magnetization in the forced ferromagnetic state obtained in large external fields. After X. P. Zhong et al. (1990c).

Compound	M_s	$M_\parallel$ (μ_B/f.u.)	M_{Ni}	n_{RNi} (T f.u./μ_B)	$B^R_{cx,RT}$ (T)
Y_2Ni_{17}	5.1	–	5.1	...	...
Gd_2Ni_{17}	8.5		5.5		
$Gd_{0.7}Y_{1.3}Ni_{17}$	–	–	–	5.17	28
$Tb_{0.6}Y_{1.4}Ni_{17}$		9.9		2.83	23
$Dy_{0.55}Y_{1.45}Ni_{17}$	–	–	–	1.98	21
$Ho_{0.55}Y_{1.45}Ni_{17}$		10.0		1.43	19
$Er_{0.6}Y_{1.4}Ni_{17}$	–	–	–	1.15	18
$Tm_{0.8}Y_{1.2}Ni_{17}$				0.74	

than the differential high-field susceptibility observed for polycrystalline specimens. A significant part of this discrepancy has to be attributed to imperfections of the polycrystalline samples.

Crystal-field interactions have not been studied yet. Mössbauer studies on Dy_2Ni_{17} by Bogé et al. (1979) reveal two R sites, which is characteristic for the hexagonal Th_2Ni_{17}-type structure. An analysis has led to different values for the molecular field at these sites: 45 and 16 T. The average value points to a value for $B^{Dy}_{ex,RT}$ of 60 T. These two sites have not been seen in Mössbauer studies on ^{169}Tm in Tm_2Ni_{17} (Gubbens et al. 1986, 1987). Here a single hyperfine-field value of 720 T, equal to the free-ion value, as well as a single CEF coefficient A_2^0 of $-250\,K\,a_0^{-2}$ has been found. The two sites have been investigated by Mössbauer studies on ^{155}Gd in Gd_2Ni_{17} by van Steenwijk et al. (1977) where two values of $+5.1$ and $+7.5 \times 10^{21}\,V\,m^{-2}$ have been found for V_{zz}. These values are smaller than the value of $+10.3 \times 10^{21}\,V\,m^{-2}$ found for $GdNi_5$ but still indicates significant CEF interactions in the R_2Ni_{17} compounds.

Single-crystal magnetization data are not yet available. Model calculations for high-field magnetization curves of Ho_2Ni_{17} performed by Marquina et al. (1992) are presented in fig. 5.41. Ho_2Ni_{17} is supposed to be an easy-plane system like Ho_2Co_{17} and Ho_2Fe_{17}. With increasing fields it should exhibit two FOMR transitions at which the Ho moment is pushed out from the preferred direction in order to lower the total energy during the rotation of the Ni moment towards the applied field. The FOMR process in Ho_2Ni_{17} differs from that found in Ho_2Co_{17} as in the former compound the Ho moment dominates the Co moment. The transitions observed for

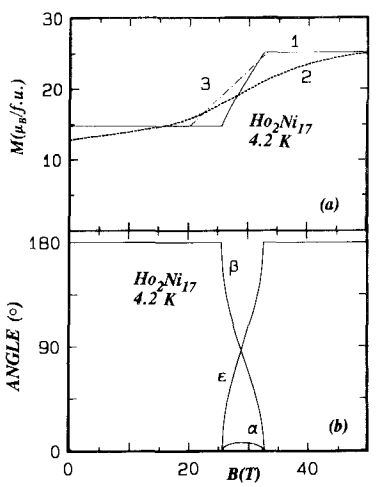

Fig. 5.41. (a) The magnetization curve at 4.2 K for Ho_2Ni_{17} calculated within the two-sublattice for fields applied within the hexagonal plane along the EMD direction (1) and the hard direction within the plane (2) calculated within the two-sublattice model. Curve 3 shows the magnetization curve of the free powder. (b) The variation of the direction of the Ho (α) and Ni (β) sublattice magnetization for the field applied along the EMD. α and β are the angles with respect to the field direction. ε is the canting angle of the two sublattice magnetizations. After Marquina et al. (1992).

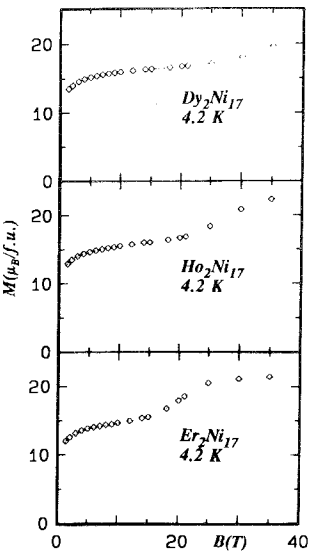

Fig. 5.42. High-field free-powder magnetization curves at 4.2 K for ferrimagnetic R_2Ni_{17} compounds with R = Dy, Ho and Er. After Marquina et al. (1992).

a free particle sample are smeared out, as one can see in fig. 5.42 where magnetization curves at 4.2 K up to 35 T are presented for Dy_2Ni_{17}, Ho_2Ni_{17} and Er_2Ni_{17}.

Systematic high-field magnetization studies at 4.2 K performed by de Boer and Buschow (1992) on free powder particles of R_2T_{17} compounds (T = Fe, Co and Ni) have resulted in convincing evidence that (i) the exchange interactions decreases from R = Gd towards the end of lanthanide series for all series and that (ii) the exchange coupling in the Fe and Co compounds is essentially the same, whereas (iii) in the Ni compounds the exchange coupling is substantially weaker compared to that in the compounds with Fe and Co. This is illustrated in fig. 5.43. As far as the 3d–4f exchange interactions between the different series are compared the absolute value of the exchange coupling parameter J_{RT} increases with increasing the rare-earth metal concentration. It is illustrated in fig. 5.44 for the Er–Fe series. The exchange parameter J_{RT}/k_B varies monotonically from about −6.8 K in Er_2Fe_{17} to about −18.0 K in $ErFe_2$ (de Boer and Buschow 1992). Duc et al. (1992c) have correlated the values for J_{RT} with values of the magnetic moment of the 3d ion involved in the interaction. An approximate correlation is found: the smaller the 3d-ion moment the larger exchange the parameter is.

5.8. *RT_{12} compounds (T = Fe, Mn)*

The RT_{12} compounds crystallize in the $ThMn_{12}$ structure. The elementary cell of this structure is tetragonal and contains two formula units. It can be described by the space group I4/mmm. The R atoms occupy one Th site, 2a, with the tetragonal

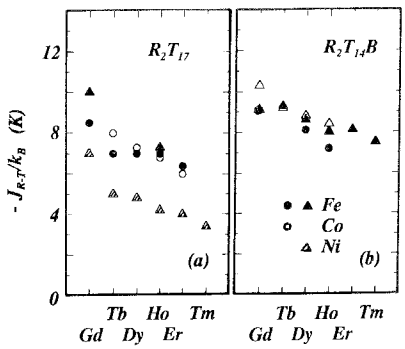

Fig. 5.43. Variation of the exchange coupling parameter J_{RT} in (a) R_2T_{17} and (b) $R_2T_{14}B$ compounds (T = Fe, Co, Ni) with the R ion involved. The circles denote results obtained from measurements on single crystals whereas the triangles represent measurements on free powders. The filled symbols correspond to Fe compounds, the open symbols to Co compounds and the shaded symbols to Ni compounds. After de Boer and Buschow (1992).

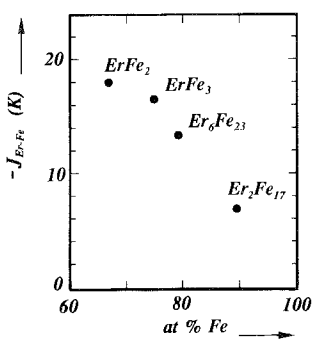

Fig. 5.44. Variation of the exchange coupling parameter J_{RT} with the Fe concentration within the Er–Fe series. After de Boer and Buschow (1992).

point symmetry 4/mmm, whereas the 3d atoms are distributed over the three different manganese sites 8i, 8j and 8f. Yang et al. (1988) have shown that the $ThMn_{12}$-structure is related to the $CaCu_5$ by a certain regular substitution of R atoms by a dumbbell of two transition metal atoms according to the formula

$$2RT_5 - R + T_2 \rightarrow RT_{12}. \tag{5.17}$$

By these substitutions, the hexagonal symmetry of the $CaCu_5$ elementary cell is not preserved. The c axis of the hexagonal $CaCu_5$ cell becomes the a axis of the tetragonal $ThMn_{12}$ cell with the consequence that the tetragonal c axis of the $ThMn_{12}$-structure is perpendicular to that of the $CaCu_5$-structure.

Binary iron compounds of the RFe_{12} type are not formed. The RFe_{12} phase, however, is stabilized by adding small amounts of metals like Si, V, Cr, Mo and W

according to the formula $RFe_{12-x}X_x$. For X = Si, V and Cr, x is close to 1, whereas for X = Ti and W, x is close to 2. The magnetic properties of ternary 1:12 phases have been reviewed in volume 6 of this series by H. S. Li and Coey (1991). The $RFe_{12-x}X_x$ compounds are ferromagnetic with Curie temperatures for the $RFe_{11}Ti$ compounds in the range of 488 K (Lu) to 607 K (Gd). These values for T_c are approximately 200 K larger than for the R_2Fe_{17} compounds. The Curie temperatures can further be increased by substitution of cobalt for iron. The iron sublattice magnetization in $RFe_{12-x}X_x$ exhibits a preference for the tetragonal c axis as can be learned from magnetic studies on aligned powder of $YFe_{10}V_2$ (de Boer et al. 1987). For this latter compound the anisotropy field at 4.2 K has been estimated to be 4 T. The saturation moment of $17\mu_B$/f.u. observed for this compound at 4.2 K results in a value of $1.7\mu_B$ for the Fe-ion moment, a value that is substantially smaller than that observed for other iron-rich compounds like, for instance, Y_2Fe_{17} and $Y_2Fe_{14}B$. The magnetization data are consistent with Mössbauer data on ^{57}Fe nuclei that provide a value of 23 T for the average hyperfine field (Gubbens et al. 1988a). Values of 1.99, 1.75 and $1.51\mu_B$ have been reported for the Fe moment in $RFe_{11}Ti$ at 4.2 K by Hu et al. (1989) for the site i, j and f, respectively. A substantial variation of the iron moment at different sites has been also revealed by Trygg et al. (1992) in ab initio calculations of the magnetism for the hypothetical compound $GdFe_{12}$. However, in these calculations all Fe moments are by 35% larger. Mössbauer studies on the rare-earth nuclei (^{155}Gd, ^{161}Dy, ^{166}Er and ^{169}Tm) by Gubbens et al. (1988b) in $RFe_{10}V_2$ and by Dirken et al. (1989) in the compounds with Ti and W, have revealed values for the hyperfine fields that are quite close to the free-ion value pointing to a dominant role of the exchange interactions. Indeed, the full R^{3+}-ion moment is found in magnetic measurements.

Magnetic measurements on a single-crystalline $DyFe_{11}Ti$ by Hu et al. (1990) allowed for the determination of a set of CEF coefficients: $A_2^0 = -32.3\,\text{K}\,a_0^{-2}$, $A_4^0 = -12.4\,\text{K}\,a_0^{-4}$, $A_4^4 = +118\,\text{K}\,a_0^{-4}$, $A_6^0 = +2.56\,\text{K}\,a_0^{-6}$, $A_6^6 = +0.64\,\text{K}\,a_0^{-6}$. The EMD for $DyFe_{11}Ti$ lies within the tetragonal plane. It exhibits a TIMR. Below 58 K the spontaneous magnetization is parallel to the $\langle 100 \rangle$ direction, whereas above 200 K it lies along the tetragonal axis. Between these temperatures a complex canted magnetic structure occurs. The EMD phase diagram for the $RFe_{11}Ti$ series and $RFe_{10}V_2$ is complex, see fig. 5.45, because of significant higher-order CEF interactions. Hu et al. (1990) have claimed that the above-mentioned set of CEF coefficients can account for most features of this phase diagram.

The magnetic isotherms for free particles of the $RFe_{12}V_x$ (R = Ho and Er) compounds at 4.2 K in fields up 38 T have been measured by X. P. Zhong et al. (1990d). The magnetization curves for compensated ferrimagnetic compounds, i.e. with x close to 3.5, are presented in fig. 5.46. The parameter n_{RT} as derived from the slope in the high-field region has been found to be 5.8 and 4.2 T f.u./μ_B for the Ho and Er compounds, respectively. The authors have derived values of +52 and −8.5 K for the exchange parameters J_{FeFe} and J_{RFe}, respectively. Both values are close to those observed in other binary compounds. For more details regarding the $RFe_{12-x}X_x$ compounds the reader is referred to the review of H. S. Li and Coey (1991) in volume 6 of this series.

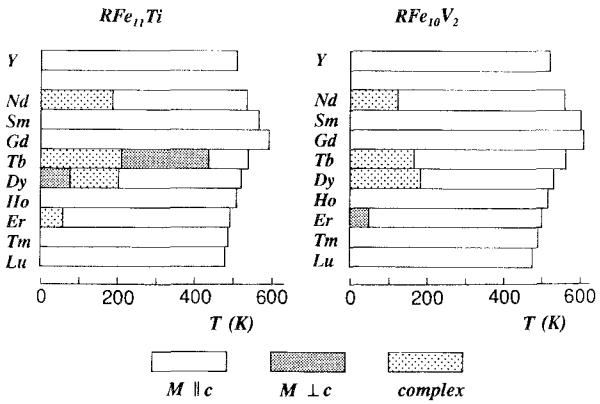

Fig. 5.45. Temperature variation of the easy magnetic direction of the $RFe_{11}Ti$; after Hu et al. (1989) and the $RFe_{10}V_2$ compounds.

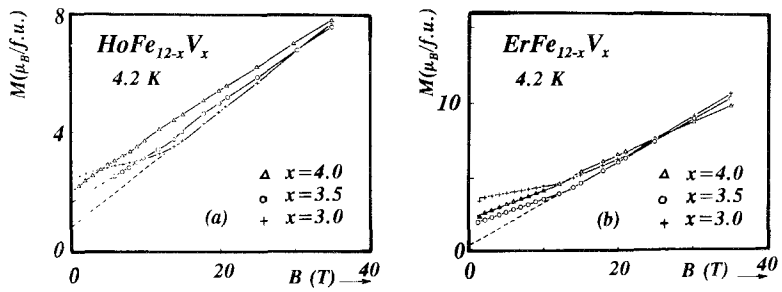

Fig. 5.46. Field dependence of the magnetic moment at 4.2 K in various nearly-compensated ferrimagnetic $HoFe_{12-x}V_x$ (a) and $ErFe_{12-x}V_x$ (b) compounds obtained on free powder particles. After X. P. Zhong et al. (1990d).

The compound YMn_{12} is an antiferromagnetic material with $T_N = 94$ K. Neutron diffraction experiments by Deportes and Givord (1976) and Deportes et al. (1977) have provided values of 0.42, 0.42 and $0.14\mu_B$ for the manganese moment at the i, j and f sites, respectively. The three times smaller value for the moment at the site f has been confirmed by ^{55}Mn NMR studies in the magnetically ordered state. For this site, the resonance field amounts to 5 MHz and is indeed three times smaller than that observed for the other sites. Correlating these results, yields a value for the hyperfine coupling constant $|A_{hf}|$ of $3.6\,T/\mu_B$ (Yoshimura et al. 1990). This value is lower than that observed in RMn_2 compounds (Yoshimura and Nakamura 1983). The origin of this reduction is not clear.

In compounds with magnetic R ions the R moments couple ferromagnetically below T_c (about 5 K) and Mn moments couple antiferromagnetically below T_N (about 100 K)

(Deportes et al. 1977). Amako et al. (1992) have reported for $GdMn_{12}$ and $TbMn_{12}$ values for T_c of 9.4 and 8.3 K, respectively. $GdMn_{12}$ has been reported by N. Okamoto et al. (1987) to have a spontaneous moment at 1.3 K of $4.2\mu_B$/f.u. whereas Amako et al. (1992) give a value of $5.5\mu_B$/f.u. These authors have found a value of $6.0\mu_B$/f.u. for the saturation magnetization of $TbMn_{12}$. The NMR frequencies of about 20 and 3 MHz observed for this latter compound have been associated to the 8i/8j and 8f sites, respectively. With increasing external field the values for the NMR frequencies linearly increase.

6. Concluding remarks

In the last decade, substantial progress has been made in the understanding of the electronic and magnetic properties of rare-earth 3d-transition-metal intermetallic compounds. This progress was possible due to improved sample quality, more powerful experimental techniques and extended computation facilities all developed in the eighties. In sophisticated experiments for some specific compounds, significant correlations have been obtained between the results from macroscopic and microscopic measurements. Inelastic neutron-scattering experiments should be mentioned among the microscopic techniques and high-field magnetization studies in semicontinuous magnetic fields up to 40 T and in short-pulse experiments up to 60 or even 90 T among the macroscopic techniques.

In discussing the electronic and magnetic properties of the R_nT_m systems, two interacting electronic subsystems have to be taken into account. The physical properties of the rare-earth subsystem result from the interplay of exchange and CEF interactions. In the compounds under discussion a broad spectrum of interplay is encountered: from exchange-dominated to CEF-dominated systems. The exchange interactions between the 3d and 4f spins have been evaluated for several series of the R_nT_m intermetallics. The substantial increase of the 3d–4f interactions going from the heavy to the light rare earths is an interesting finding of large theoretical impact. The crystalline electric-field interactions have been investigated for the rare-earth ions with nonzero orbital moments. Systematic trends could be observed in several series of compounds. The lack of systematics in special cases reflects the difficulties in quantifying the electric-field interactions, especially as far as higher order contributions are concerned.

The above-mentioned findings can be regarded as forward steps towards a unified picture of the electronic and magnetic properties of the 3d–4f intermetallic compounds. There remain, however, numerous topics for further detailed investigations. The crystalline electric field in intermetallic compounds in terms of the electron-density distribution, especially in relation to higher-order CEF interactions, the detailed mechanism of the exchange interactions including the role of the 5d electrons of 4f ions, the formation of 3d and 4f magnetic moments in the presence of the exchange and crystal-field interactions, the metamagnetism of the collective electrons, the 3d magnetocrystalline anisotropy and the orbital moment of the 3d ion remain among others topics for further studies.

Acknowledgements

The present review has been prepared in the scope of an European Programme on Basic Interactions in Rare-Earth Magnets supported by the Commission of the European Communities within its Research and Development programme BREU-0068-C(GDF). The authors kindly acknowledge the frequent discussions with their colleagues at the Van der Waals–Zeeman Laboratory and the cooperation within the European programme with the Laboratory Louis Neél in Grenoble, the Institute MASPEC in Parma and the University of Zaragoza.

Appendix A. Legendre functions

The Legendre functions $P_n^m(\cos\theta)$ are used in this chapter for the description of the magnetocrystalline anisotropy energy as given in eq. (2.9). These functions have been taken from Hutchings (1964). The normalization factors in the functions with a nonzero value of m are put equal to 1 for reasons of convenience.

$$P_2^0(\cos\theta) = \tfrac{1}{2}(3\cos^2\theta - 1),$$
$$P_2^2(\cos\theta) = (1 - \cos^2\theta),$$
$$P_4^0(\cos\theta) = \tfrac{1}{8}(35\cos^4\theta - 30\cos^2\theta + 3),$$
$$P_4^2(\cos\theta) = (1 - \cos^2\theta)(7\cos^2\theta - 1),$$
$$P_4^3(\cos\theta) = (1 - \cos^2\theta)^{3/2}\cos\theta,$$
$$P_4^4(\cos\theta) = (1 - \cos^2\theta)^2,$$
$$P_6^0(\cos\theta) = \tfrac{1}{16}(231\cos^6\theta - 315\cos^4\theta + 105\cos^2\theta - 5),$$
$$P_6^2(\cos\theta) = (1 - \cos^2\theta)(33\cos^4\theta - 18\cos^2\theta + 1),$$
$$P_6^3(\cos\theta) = (1 - \cos^2\theta)^{3/2}(11\cos^3\theta - 3\cos\theta),$$
$$P_6^4(\cos\theta) = (1 - \cos^2\theta)^2(11\cos^2\theta - 1),$$
$$P_6^6(\cos\theta) = (1 - \cos^2\theta)^3.$$

Appendix B. Anisotropy coefficients and anisotropy constants

By making use of the definition given by eqs. (2.7) and (2.9) relations between the anisotropy coefficients κ_n^m and the anisotropy constants can be found. In case of the hexagonal symmetry eq. (2.7) becomes

$$E_A(\theta, \phi) = K_1 \sin^2\theta + K_2 \sin^4\theta + K_3 \sin^6\theta + K_4 \sin^6\theta \cos 6\phi,$$

and the relations between the K_n and κ_n^m are given by

$$K_1 = -\tfrac{1}{2}(3\kappa_2^0 + 10\kappa_4^0 + 21\kappa_6^0),$$
$$K_2 = \tfrac{1}{8}(35\kappa_4^0 + 189\kappa_6^0),$$
$$K_3 = -(231/16)\kappa_6^0$$

and

$$K_4 = \kappa_6^6.$$

In the case of tetragonal symmetry eq. (2.7) becomes

$$E_A(\theta, \phi) = K_1 \sin^2\theta + K_2 \sin^4\theta + K_3 \sin^6\theta + (K_4 \sin^4\theta + K_5 \sin^6\theta)\cos 4\phi,$$

and the relations between the K_n and κ_n^m are given by:

$$K_1 = -\tfrac{1}{2}(3\kappa_2^0 + 10\kappa_4^0 + 21\kappa_6^0),$$
$$K_2 = \tfrac{1}{8}(35\kappa_4^0 + 189\kappa_6^0), \qquad K_3 = -(231/16)\kappa_6^0,$$
$$K_4 = \kappa_4^4 + 10\kappa_6^4 \quad \text{and} \quad K_5 = -11\kappa_6^4.$$

Abbreviations

CEF	crystalline electric field
EMD	easy magnetic direction
FOMP	first-order magnetization process
FOMR	first-order moment reorientation
MR	moment reorientation
TIMR	temperature-induced moment reorientation

List of symbols

a_0	Bohr radius
A_n^m	CEF coefficients
B_n^m	CEF parameters
B_A	anisotropy field
B_0	external magnetic field ($=\mu_0 H$)
$B_{\text{mol}}^{\text{R}}$	molecular field acting on the R moment in R metals
$B_{\text{mol}}^{\text{T}}$	molecular field acting on the T moment in Y_nT_m compounds
$B_{\text{ex,RR}}^{\text{R}}$	exchange field acting on the R-spin moment due to the intrasublattice (R–R) interactions in 3d–4f compounds
$B_{\text{mol,RR}}^{\text{R}}$	molecular field acting on the R moment due to the intrasublattice (R–R) interactions in 3d–4f compounds
$B_{\text{ex,RT}}^{\text{R}}$	exchange field acting on the R-spin moment due to the intersublattice (R–T) interactions in 3d–4f compounds
$B_{\text{mol,RT}}^{\text{R}}$	molecular field acting on the R moment due to the intersublattice (R–T) interactions in 3d–4f compounds
$B_{\text{mol,RT}}^{\text{T}}$	molecular field acting on the T moment due to the intersublattice (R–T) interactions in 3d–4f compounds
$B_{\text{mol,TT}}^{\text{T}}$	molecular field acting on the T moment due to the intrasublattice (T–T) interactions in 3d–4f compounds
g_s	spin gyromagnetic factor

g_R Landé (gyromagnetic) factor
$\boldsymbol{J}$ the total angular momentum for the 4f ions
J quantum number of the total angular momentum $\boldsymbol{J}$ for the 4f ions
J_{ij} spin–spin coupling parameter
J_{RR} spin–spin coupling parameter between R spins
J_{RT} spin–spin coupling parameter between R and T spins
J_{TT} spin–spin coupling parameter between T spins
J_2, J_4, J_6 functions of the total angular momentum, see table 2.3
k_B Boltzmann constant
K_i^c cubic anisotropy constant
K_n^m anisotropy constant
K_i anisotropy constant for uniaxial systems
κ_n^m anisotropy coefficients
$\boldsymbol{L}$ the orbital angular momentum
m_i magnetic moment per ion
m_R magnetic moment per R ion
m_T magnetic moment per T ion
M_i sublattice magnetization
M_R magnetization of the R sublattice
M_T magnetization of the T sublattice
M_s spontaneous magnetization
n_{RR} intrasublattice molecular-field coefficient
n_{RT} intersublattice molecular-field coefficient
n_{TT} intrasublattice molecular-field coefficient
p pressure
P_n^m Legendre functions
S_R quasi-spin of the 4f ion, component of the R spin along the direction of $\boldsymbol{J}$
T_c Curie temperature
T_{MR} temperature of the moment reorientation
T_N Néel temperature
α_J second-order Stevens factor
β_J fourth-order Stevens factor
γ_J sixth-order Stevens factor
γ_R the spin part of the magnetic moment (for the 4f ions)
γ linear specific-heat coefficient
θ polar angle
θ_D Debye temperature
ϕ azimuthal angle

References

Abbundi, R., A.E. Clark, H.T. Savage and O.D. McMasters, 1980, J. Magn. & Magn. Mater. **15–18**, 595.

Abd El-Aal, M.M., A.S. Ilyushin and V.I. Chechernicov, 1987, J. Magn. & Magn. Mater. **69**, 325.

Akimenko, A.I., N.M. Ponomarenko and I.K. Yanson, 1986, Fiz. Tverd. Tela **28**(4) [Sov. Phys. Solid State **28**(4), 615].

Alameda, J.M., D. Givord, R. Lemaire and Q. Lu, 1981, J. Appl. Phys. **52**, 2079.

Aleksandryan, V.V., K.P. Belov, R.Z. Levitin, A.S. Markosyan and V.V. Snegirev, 1984a, Pis'ma Zh. Eksp. Teor. Fiz. **40**(2), 77–80 [JETP Lett **40**(2)].

Aleksandryan, V.V., R.Z. Levitin and A.S. Markosyan, 1984b, Fiz. Tverd. Tela **26**, 1921–1925 [Sov. Phys. Solid State **26**(7), 1165–1168].

Aleksandryan, V.V., R.Z. Levitin, A.S. Markosyan, V.V. Snegirev and A.D. Shchurova, 1987, Zh. Eksp. Teor. Fiz. **92**(3), 889–901 [Sov. Phys. JETP **65(3)**, 502–508].

Aleksandryan, V.V., N.V. Baranov, A.I. Kozlov and A.S. Markosyan, 1988, Fiz. Met. Metalloved. **66**(4), 682 [Phys. Met. Metall. **66**(4), 50].

Alekseev, P.A., A. Andreeff, H. Griessmann, L.P. Kaun, B. Lippold, W. Matz, I.P. Sadikov, O.D. Chistyakov, I.A. Markova and E.M. Savitskii, 1980, Phys. Status Solidi B **97**, 87.

Alekseev, P.A., V.N. Lazukov, A.Y. Rumyantsev and I.P. Sadikov, 1988a, J. Magn. & Magn. Mater. **75**, 323.

Alekseev, P.A., V.N. Lazukov and I.P. Sadikov, 1988b, J. Magn. & Magn. Mater. **76–77**, 423.

Alp, E.E., A.M. Umarji, S.K. Malik, G.K. Shenoy, M.Q. Huang, E.B. Boltich and W.E. Wallace, 1987, J. Magn. & Magn. Mater. **68**, 305.

Alves, K.M.B., N. Alves, A.P. Guimarães, I.S. Mackenzie and J.W. Ross, 1986, J. Magn. & Magn. Mater. **54–57**, 501.

Amako, Y., H. Nagai, T. Nomura, H. Yoshie, I. Oguro, T. Shinohara and K. Adachi, 1992, J. Magn. & Magn. Mater. **104–107**, 1451.

Amato, A., W. Bührer, A. Grayevsky, F.N. Gygax, A. Furrer, N. Kaplan and A. Schenck, 1992, Solid State Commun. **82**(10), 767.

Andoh, Y., H. Fujii, H. Fujiwara and T. Okamoto, 1982, J. Phys. Soc. Jpn. **51**, 435.

Andreev, A.V., and S.M. Zadvorkin, 1990, Fiz. Met. Metalloved. **69**(4), 89 [Phys. Met. Metall. **69**(4), 85].

Andreev, A.V., E.N. Tarasov, A.V. Deryagin and S.M. Zadvorkin, 1982, Phys. Status Solidi A **71**, K245.

Andreev, A.V., A.V. Deryagin and S.M. Zadvorkin, 1983, Zh. Exp. Teor. Fiz. **85**(3), 974–979 [Sov. Phys. JETP **58**(3), 566–569].

Andreev, A.V., A.V. Deryagin, S.M. Zadvorkin, R.Z. Levitin, R. Lemaire, J. Laforest, A.S. Markosyan and V.V. Snegirev, 1984a, Zh. Eksp. Teor. Fiz. **87**(6), 2214–2222 [Sov. Phys. JETP **60**(6), 1280–1284].

Andreev, A.V., M.I. Bartashevich and A.V. Deryagin, 1984b, Zh. Eksp. Teor. Fiz. **87**(2), 623–628 [Sov. Phys. JETP **60**(2), 356–359].

Andreev, A.V., M.I. Bartashevich, A.V. Deryagin and E.N. Tarasov, 1985a, Zh. Eksp. Teor. Fiz. **89**(3), 959–966 [Sov. Phys. JETP **62**(3), 551–555].

Andreev, A.V., A.V. Deryagin and S.M. Zadvorkin, 1985b, Fiz. Met. Metalloved. **59**(2), 339–343 [Phys. Met. Metall. **59**(2), 116] also Fiz. Met. Metalloved. **60**(4), 730–735 [Phys. Met. Metall. **60**(4), 96].

Andreev, A.V., A.V. Deryagin, S.M. Zadvorkin and S.V. Terentyev, 1985c, Fiz. Tverd. Tela **27**(6), 1641–1645 [Sov. Phys. Solid State **27**(6), 987–990].

Andreev, A.V., A.V. Deryagin, S.M. Zadvorkin and G.M. Kvashnin, 1985d, Fiz. Tverd. Tela **27**(10), 3164–3166 [Sov. Phys. Solid State **27**(10), 1905–1906].

Andreev, A.V., A.V. Deryagin, S.M. Zadvorkin, N.V. Kudrevatykh, V.N. Moskalev, R.Z. Levitin, Yu.F. Popov and R.Yu. Yumaguzhin, 1985e, in: Fizika Magnitnykh Materialov (Physics of Magnetic Materials), in Russian, ed. D.D. Nishin (Sverdlovsk State Univ.) p. 21–49.

Andreev, A.V., M.I. Bartashevich, A.V. Deryagin and E.N. Tarasov, 1986a, Fiz. Met. Metalloved. **62**(5), 905–910 [Phys. Met. Metall. **62**(5), 66–71].

Andreev, A.V., A.V. Deryagin, S.M. Zadvorkin, G.M. Kvashnin and N.V. Kudrevatykh, 1986b, Fiz. Met. Metalloved. **61**(4), 744–749 [Phys. Met. Metall. **61**(4), 107–112].

Andreev, A.V., M.I. Bartashevich, A.V. Deryagin, S.M. Zadvorkin and E.N. Tarasov, 1988a, Zh. Exp. Teor. Fiz. **94**(4), 218–230 [Sov. Phys. JETP **67**(4), 771–778].

Andreev, A.V., M.I. Bartashevich, A.V. Deryagin, S.M. Zadvorkin and E.N. Tarasov, 1988b, Fiz. Met. Metalloved. **65**(3), 519–526 [Phys. Met. Metall. **65**(3), 61].

Andreev, A.V., M.I. Bartashevich and V.A. Vasilkovsky, 1990, J. Less-Common Met. **167**, 101.

Andreev, A.V., F.R. de Boer, T.H. Jacobs and K.H.J. Buschow, 1992, J. Magn. & Magn. Mater. **104–107**, 1305.

Andres, K., S. Darack and H.R. Ott, 1979, Phys. Rev. B **19**, 5475.

Apostolov, A., L. Bozukov, N. Stanev and T. Mydlarz, 1988, J. Phys. (Paris) **49**, C8–517.

Armitage, J.G.M., T. Dumelow, R.H. Mitchell, P.C. Riedi, J.S. Abell, P. Mohn, K. Schwarz, 1986, J. Phys. F **16**, L141.

Armitage, J.G.M., T. Dumelow, P.C. Riedi and J.S. Abell, 1989, J. Phys.: Condens. Matter **1**, 3987.

Asano, S., and S. Ishida, 1987, J. Magn. & Magn. Mater. **70**, 39.

Asano, S., and S. Ishida, 1988, J. Phys. F **18**, 501.

Asti, G., 1990, in: Ferromagnetic Materials, Vol. 5, eds K.H.J. Buschow and E.P. Wohlfarth (North-Holland, Amsterdam) p. 398.

Asti, G., and F. Bolzoni, 1980, J. Magn. & Magn. Mater. **20**, 29.

Atzmony, U., and M.P. Dariel, 1976, Phys. Rev B **13**, 4006.

Atzmony, U., M.P. Dariel and G. Dublon, 1976, Phys. Rev. B **14**, 3713.

Aubert, G., D. Gignoux, F. Givord, R. Lemaire and B. Michelutti, 1978, Solid State Commun. **25**, 85–87.

Aubert, G., D. Gignoux, B. Michelutti and A. Nait-Saada, 1980, J. Magn. & Magn. Mater. **15–18**, 551.

Aubert, G., D. Gignoux, B. Hennion, B. Michelutti and A. Nait-Saada, 1981, Solid State Commun. **37**, 741.

Averbuch-Pouchot, M.T., R. Chevalier, J. Deportes, B. Kebe and R. Lemaire, 1987, J. Magn. & Magn. Mater. **68**, 190.

Ballou, R., 1987, Thesis (Grenoble).

Ballou, R., 1989, Physica B **156–157**, 727.

Ballou, R., and R. Lemaire, 1988, J. Phys. (Paris) **49**, C8–249.

Ballou, R., J. Deportes, B. Gorges, R. Lemaire and J.C. Ousset, 1986a, J. Magn. & Magn. Mater. **54–57**, 465.

Ballou, R., J. Deportes, B. Kebe and R. Lemaire, 1986b, J. Magn. & Magn. Mater. **54–57**, 494.

Ballou, R., J. Deportes and R. Lemaire, 1987a, J. Magn. & Magn. Mater. **70**, 306.

Ballou, R., J. Deportes, R. Lemaire, Y. Nakamura and B. Ouladdiaf, 1987b, J. Magn. & Magn. Mater. **70**, 129.

Ballou, R., V.M.T.S. Barthem and D. Gignoux, 1988a, Physica B **149**, 340.

Ballou, R., J. Deportes, R. Lemaire and B. Ouladdiaf, 1988b, J. Appl. Phys. **63**, 3487.

Ballou, R., J. Deportes, R. Lemaire, B. Ouladdiaf and P. Rouault, 1988c, in: Physics of Magn. Materials, eds W. Gorzkowski, H.K. Lachowicz and H. Szymczak (World Scientific, Singapore) p. 427–443.

Ballou, R., B. Gorges, R. Lemaire, H. Rakoto and J.C. Ousset, 1989, Physica B **155**, 266.

Ballou, R., B. Gorges, P. Mohlo and P. Rouault, 1990a, J. Magn. & Magn. Mater. **84**, L1–4.

Ballou, R., J. Deportes, R. Lemaire, P. Rouault and J.L. Soubeyroux, 1990b, J. Magn. & Magn. Mater. **90–91**, 559.

Ballou, R., B. Michelutti and J. Voiron, 1991, J. Appl. Phys. **69**, 5705.

Ballou, R., R.J. Radwański, R. Lemaire and J.J.M. Franse, 1992a, Physica B **177**, 262.

Ballou, R., P.J. Brown, J. Deportes, A.S. Markosyan and B. Ouladdiaf, 1992b, J. Magn. & Magn. Mater. **104–107**, 935.

Ballou, R., I.Yu. Gaydukova, A.S. Markosyan and B. Ouladdiaf, 1992c, J. Magn. & Magn. Mater. **104–107**, 1465.

Bara, J.J., A.T. Pędziwiatr, W. Zarek, D. Konopka and U. Gacek, 1982a, J. Magn. & Magn. Mater. **27**, 159.

Bara, J.J., A.T. Pędziwiatr and W. Zarek, 1982b, J. Magn. & Magn. Mater. **27**, 168.

Baranov, N.V., E. Gratz, H. Novotny and W. Steiner, 1983, J. Magn. & Magn. Mater. **37**, 206.

Bartashevich, M.I., O.A. Ivanov, V.V. Kelarev, N.V. Kudrevatykh, I.Y. Proshkin and V.V. Chuyev, 1988, Zh. Eksp. Teor. Fiz. **94**(9), 302–308 [Sov. Phys. JETP **67**(9), 1906–1909].

Bartashevich, M.I., T. Goto and M.T. Yamaguchi, 1992a, J. Magn. & Magn. Mater. **111**, 83.

Bartashevich, M.I., T. Goto, M.T. Yamaguchi, I. Yamamoto and A.V. Andreev, 1992b, Solid State Commun. **82**(3), 201.

Barth, S., E. Albert, G. Heiduk, A. Mösslang, A. Weidinger, E. Recknagel and K.H.J. Buschow, 1986, Phys. Rev. B **33**, 430.

Barthem, V.M.T.S., 1987, Thesis (Grenoble).

Barthem, V.M.T.S., D. Gignoux, A. Nait-Saada and D. Schmitt, 1988a, Phys. Rev. B **37**, 1733.

Barthem, V.M.T.S., G. Creuzet, D. Gignoux and D. Schmitt, 1988b, J. Phys. (Paris) **49**, C8–527.

Barthem, V.M.T.S., D. Gignoux, D. Schmitt and G. Creuzet, 1989a, J. Magn. & Magn. Mater. **78**, 56.

Barthem, V.M.T.S., D. Gignoux, A. Nait-Saada, D. Schmitt and A.Y. Takeuchi, 1989b, J. Magn. & Magn. Mater. **80**, 142.

Belorizky, E., and Y. Berthier, 1986, J. Phys. F **16**, 637.

Belorizky, E., M.A. Frémy, J.P. Gavigan, D. Givord and H.S. Li, 1987, J. Appl. Phys. **61**, 3971.

Belorizky, E., J.P. Gavigan, D. Givord and H.S. Li, 1988a, Europhysics Lett. **5**, 349.

Belorizky, E., J.P. Gavigan, D. Givord and H.S. Li, 1988b, J. Phys. (Paris) **49**, C8–411.

Belov, K.P., G.I. Kataev, R.Z. Levitin, S.A. Nikitin and V.I. Sokolov, 1983, Usp. Fiz. Nauk **140**, 271–313 [Sov. Phys. Usp. **26**(6), 518–542].

Belov, K.P., I.S. Dubenko, A.S. Markosyan and V.V. Snegirev, 1989, Fiz. Met. Metalloved. **67**(1), 108–114 [Phys. Met. Metall. **67**(1), 108].

Berezin, A.G., and R.Z. Levitin, 1980, Zh. Eksp. Teor. Fiz. **79**, 1109–1119 [Sov. Phys. JETP **52**(3), 561–567].

Berezin, A.G., R.Z. Levitin and Yu.F. Popov, 1980, Zh. Eksp. Teor. Fiz. **79**, 268-280 [Sov. Phys. JETP **52**(1), 135–142].

Berthier, Y., D. Gignoux, R. Kuentzler and A. Tari, 1986, J. Magn. & Magn. Mater. **54–57**, 479.

Berthier, Y., J. Deportes, M. Horvatic and P. Rouault, 1988a, J. Phys. (Paris) **49**, C8–261.

Berthier, Y., N. Nassar and T. Vadieu, 1988b, J. Phys. (Paris) **49**, C8–585.

Beuerle, T., P. Braun and M. Fähnle, 1991, J. Magn. & Magn. Mater. **94**, L11.

Bhattacharyya, S., and D. Ghosh, 1989, J. Magn. & Magn. Mater. **80**, 276.

Bleaney, B., G.J. Bowden, J.M. Cadogan, R.K. Day and J.B. Dunlop, 1982, J. Phys. F **12**, 795.

Bloch, D., and R. Lemaire, 1970, Phys. Rev. B **2**, 2648.

Bloch, D., D.M. Edwards, M. Shimizu and J. Voiron, 1975, J. Phys. F **5**, 1217.

Boehner, W., H. Lütgemeier and W. Zinn, 1986, J. Magn. & Magn. Mater. **62**, 152.

Bogé, M., J. Chappert, A. Yaouanc and J.M.D. Coey, 1979, Solid State Commun. **31**, 987.

Bogé, M., J.M.D. Coey, G. Czjzek, D. Givord, C. Jeandey, H.S. Li and J.L. Oddou, 1985, Solid State Commun. **55**, 295.

Boltich, E.B., W.E. Wallace, F. Pouranian and S.K. Malik, 1982, J. Magn. & Magn. Mater. **25**, 295.

Boucherle, J.X., D. Givord, J. Laforest, J. Schweizer and F. Tasset, 1979, J. Phys. (Paris) **40**, C5–180.

Boucherle, J.X., J. Schweizer, D. Givord, A.R. Gregory and J. Schweizer, 1982, J. Appl. Phys. **53**, 1950.

Boucherle, J.X., A.R. Gregory, J. Schweizer and G. Will, 1989, Physica B **156–157**, 734.

Brommer, P.E., 1989, Physica B **154**, 197.

Brommer, P.E., 1991, Physica B **173**, 277.

Brooks, M.S.S., O. Eriksson and B. Johansson, 1989, J. Phys.: Condens. Matter **1**, 5861.

Brooks, M.S.S., L. Nordström and B. Johansson, 1991a, Physica B **172**, 95.

Brooks, M.S.S., O. Eriksson and B. Johansson, 1991b, J. Phys.: Condens. Matter **3**, 2357.

Brooks, M.S.S., T. Gasche, S. Auluck, L. Nordström, L. Severin, J. Trygg and B. Johansson, 1992, J. Magn. & Magn. Mater. **104–107**, 1381.

Brouha, M., K.H.J. Buschow and A.R. Miedema, 1974, IEEE Trans. Mag. **MAG-10**, 182.

Brown, P.J., J. Deportes, D. Givord and K.R.A. Ziebeck, 1982, J. Appl. Phys. **53**, 1973.

Burzo, E., 1972, Int. J. Mag. **3**, 161.

Burzo, E., and H.R. Kirchmayr, 1989, in: Handbook on the Physics and Chemistry of Rare Earths, Vol. 12, eds K.A. Gschneidner Jr and L. Eyring (North-Holland, Amsterdam) p. 71.

Burzo, E., and J. Laforest, 1972, Int. J. Mag. **3**, 171.

Burzo, E., and D. Seitabla, 1981, Solid State Commun. **37**, 663.

Burzo, E., E. Oswald, M.Q. Huang, E.B. Boltich and W.E. Wallace, 1985, J. Appl. Phys. **57**, 4109.

Buschow, K.H.J., 1977, Rep. Prog. Phys. **40**, 1179.

Buschow, K.H.J., 1980a, in: Ferromagnetic Materials, Vol. 1, ed. E.P.Wohlfarth (North-Holland, Amsterdam) p. 297.

Buschow, K.H.J., 1980b, J. Less-Common Met. **72**, 257.

Buschow, K.H.J., 1981, Solid State Commun. **40**, 207.

Buschow, K.H.J., 1984a, in: Handbook on the Physics & Chemistry of Rare Earths, Vol. 6, eds K.A. Gschneidner Jr and L. Eyring (North-Holland, Amsterdam) p. 1.

Buschow, K.H.J., 1984b, J. Less-Common Met. **97**, 185.

Buschow, K.H.J., 1986, Mater. Sci. Rep. **1**, 1.

Buschow, K.H.J., 1988, in: Ferromagnetic Materials, Vol. 4, eds. E.P. Wohlfarth and K.H.J. Buschow (North-Holland, Amsterdam) p. 1.

Buschow, K.H.J., and P.F. de Chatel, 1979, Pure & Appl. Chem. **52**, 135.

Buschow, K.H.J., and R.P. van Stapele, 1972, J. Appl. Phys. **41**, 4066.

Buschow, K.H.J., P.C.P. Bouten and A.R. Miedema, 1982a, Rep. Prog. Phys. **45**, 937.

Buschow, K.H.J., P.C.M. Gubbens, W. Ras and A.M. van der Kraan, 1982b, J. Appl. Phys. **53**, 8329.

Buschow, K.H.J., J.W.C. de Vries and R.C. Thiel, 1985, J. Phys. F **15**, L93.

Buschow, K.H.J., G. Czjzek, H.-J. Bornemann and R. Kmiec, 1989, Solid State Commun. **71**, 759.

Buschow, K.H.J., R. Coehoorn, D.B. de Mooij, K. de Waard and T.H. Jacobs, 1990, J. Magn. & Magn. Mater. **92**, L35.

Butera, R.A., T.J. Clinton, A.G. Moldovan, S.G. Sankar and K.A. Gschneidner Jr, 1979, J. Appl. Phys. **50**, 7492.

Cadogan, J.M., J.P. Gavigan, D. Givord and H.S. Li, 1988, J. Phys. F **18**, 779.

Callen, E., 1982, J. Appl. Phys. **53**, 2367.

Callen, H.B., and E. Callen, 1966, J. Phys. Chem. Solids **2**, 1271.

Campbell, I.A., 1972, J. Phys. F **2**, L47.

Castets, A., D. Gignoux and B. Hennion, 1982a, Phys. Rev. B **25**, 337.

Castets, A., D. Gignoux, B. Hennion and R.M. Nicklow, 1982b, J. Appl Phys. **53**, 1979.

Chen, H., W-W. Ho, S.G. Sankar and W.E. Wallace, 1989, J. Magn. & Magn. Mater. **78**, 203.

Chuyev, V.V., V.V. Kelarev, A.N. Pirogov, S.K. Sidorov and V.S. Koryakova, 1983, Fiz. Met. Metalloved. **55**(3), 510–519 [Phys. Met. Metall. **55**(3), 80–89].

Clark, A.E., 1979, in: Handbook on the Physics and Chemistry of Rare Earths, Vol. 2, eds K.A. Gschneidner Jr and L. Eyring (North-Holland, Amsterdam) p. 231.

Clark, A.E., 1980, in: Ferromagnetic Materials, Vol. 1, ed. E.P. Wohlfarth (North-Holland, Amsterdam) p. 531.

Clausen, K.N., and B. Lebech, 1982, J. Phys. C **15**, 5095.

Clausen, K.N., and O.V. Nielsen, 1981, J. Magn. & Magn. Mater. **23**, 237.

Coehoorn, R., 1989, Phys. Rev. B **39**, 13072.

Coehoorn, R., 1991a, J. Magn. & Magn. Mater. **99**, 55.

Coehoorn, R., 1991b, in: Supermagnets, Hard Magnetic Materials, eds G.J. Long and F. Grandjean, NATO ASI Series C-331 p. 133.

Coehoorn, R., and G.H.O. Daalderop, 1992, J. Magn. & Magn. Mater. **104–107**, 1081.

Coehoorn, R., K.H.J. Buschow and M.W. Dirken, 1990, Phys. Rev. B **42**, 4645.

Coey, J.M.D., 1986, J. Less-Common Met. **126**, 21.

Coey, J.M.D., 1987, Physica Scripta **T19**, 426.

Coey, J.M.D., and H. Sun, 1990, J. Magn. & Magn. Mater. **87**, L251.

Coles, B.R., and A.K. Chhabra, 1986, J. Magn. & Magn. Mater. **54–57**, 1039.

Colpa, J.H.P., 1992, J. Magn. & Magn. Mater. **104–107**, 1211.

Colpa, J.H.P., S. Sinnema, J.J.M. Franse, R.J. Radwański and P.H. Frings, 1989a, Physica B **156**, 731.

Colpa, J.H.P., S. Sinnema, P.H. Frings, J.J.M. Franse and R.J. Radwański, 1989b, J. Phys.: Condens. Matter **1**, 2047.

Croat, J.J., 1980, J. Magn. & Magn. Mater. **15–18**, 597.

Croft, M., R. Neifield, B. Qi, G. Liang, I. Perez, S. Gunapala, F. Lu, S.A. Shaheen, E.G. Spencer, N. Stoffel and M. den Boer, 1987, in: 5th Int. Conf. Valence Fluctuations, eds S.K. Malik and L.C. Gupta (Plenum Press, New York) p. 217.

Crowder, C., and W.J. James, 1983, J. Less-Common Met. **95**, 1.

Cyrot, M., and M. Lavagna, 1979, J. Phys. (Paris) **40**, 763.

Cywinski, R., and B.D. Rainford, 1992, J. Magn. & Magn. Mater. **104–107**, 1424.

Daalderop, G.H.O., P.J. Kelly and M.F.H. Schuurmans, 1992, J. Magn. & Magn. Mater **104–107**, 737.

Dalmas de Réotier, P., A. Yaouanc, P.C.M. Gubbens, D. Gignoux, B. Gorges, D. Schmitt, O. Hartmann, R. Wäppling and A. Weidinger, 1992, J. Magn. & Magn. Mater. **104–107**, 1267.

Darby, M.I., and E.D. Isaacs, 1974, IEEE Trans. Mag. **MAG-10**, 259.

de Azevedo, W.M., I.S. Mackenzie and Y. Berthier, 1985, J. Phys. F **15**, L243.

de Boer, F.R., and K.H.J. Buschow, 1992, Physica B **177**, 199.

de Boer, F.R., Y.K. Huang, D.B. de Mooij and K.H.J. Buschow, 1987, J. Less-Common Met. **135**, 199.

de Boer, F.R., X.P. Zhong, K.H.J. Buschow and T.H. Jacobs, 1990, J. Magn. & Magn. Mater. **90–91**, 25.

de Gennes, P.G., 1962, J. Phys. Radiat. **23**, 510.

de Jongh, L.J., J. Bartolome, F.J.A.M. Greidanus, H.J.M. de Groot, H.L. Stipdonk and K.H.J. Buschow, 1981, J. Magn. & Magn. Mater. **25**, 207.

de Wijn, H.W., A.M. van Diepen and K.H.J. Buschow, 1976, Phys. Status Solidi B **76**, 11.

Decrop, B., J. Deportes, D. Givord, R. Lemaire and J. Chappert, 1982, J. Appl. Phys. **53**, 1953.

Decrop, B., J. Deportes and R. Lemaire, 1983, J.Less-Common Met. **94**, 199.

del Moral, A., 1984, J. Phys. F **14**, 1477.

del Moral, A., P.A. Algarabel and M.R. Ibarra, 1987, J. Magn. & Magn. Mater. **69**, 285.

del Moral, A., M.R. Ibarra, P.A. Algarabel and J.I. Arnaudas, 1991, in: Physics of Magnetic Materials, eds W. Gorzkowski, M.Gutowski, H.K.Lachowicz and H. Szymczak (World Scientific, Singapore) p. 90.

Delapalme, A., J. Deportes, R. Lemaire, K. Hardman and W.J. James, 1979, J. Appl. Phys. **50**, 1987.

Deportes, J., and D. Givord, 1976, Solid State Commun. **19**, 845.

Deportes, J., D. Givord, R. Lemaire and N. Nagai, 1977, Physica B **86–88**, 69.

Deportes, J., D. Givord and K.R.A. Ziebeck, 1981, J. Appl. Phys. **52**, 2074.

Deportes, J., B. Kebe and R. Lemaire, 1986, J. Magn. & Magn. Mater. **54–57**, 1089.

Deportes, J., B. Ouladdiaf and K.R.A. Ziebeck, 1987a, J. Magn. & Magn. Mater **70**, 14.

Deportes, J., B. Ouladdiaf and K.R.A. Ziebeck, 1987b, J. Phys. (Paris) **48**, 1029.

Deportes, J., R. Lemaire, B. Ouladdiaf, E. Rouault and F. Sayetat, 1987c, J. Magn. & Magn. Mater. **70**, 191.

Deryagin, A.V., N.V. Kudrevatykh and V.N. Moskalev, 1982, Fiz. Met. Metalloved. **54**(3), 473–477 [Phys. Met. Metall. **54**(3), 49–53].

Deutz, A.F., H.B. Brom, H. Deelen, L.J. de Jongh, W.J. Huiskamp and K.H.J. Buschow, 1986, Solid State Commun. **60**, 917.

Deutz, A.F., H.B. Brom, C.D. Wentworth, W.J. Huiskamp, L.J. de Jongh and K.H.J. Buschow, 1989, J. Magn. & Magn. Mater. **78**, 176.

Dijkman, W.H., 1982, Thesis (University of Amsterdam).

Dirken, M.W., R.C. Thiel and K.H.J. Buschow, 1989, J.Less-Common Met. **146**, L15.

Dirken, M.W., R.C. Thiel, R. Coehoorn, T.H. Jacobs and K.H.J. Buschow, 1991, J. Magn. & Magn. Mater. **94**, L15.

Dormann, E., 1991, in: Handbook on the Physics and Chemistry of Rare Earths, Vol. 14, eds K.A. Gschneidner Jr and L. Eyring (North-Holland, Amsterdam) p. 63.

Drzazga, Z., and M. Drzazga, 1987, J. Magn. & Magn. Mater. **65**, 21.

Drzazga, Z., and T. Mydlarz, 1988, J. Phys. (Paris) **49**, C8–515.

Drzazga, Z., K. Białas-Borgieł and W. Borgieł, 1991, J. Magn. & Magn. Mater. **101**, 399.

Drzazga, Z., E. Popiel and A. Winiarska, 1992, J. Magn. & Magn. Mater. **104–107**, 1437.

Du Plessis, P. de V., and T. Germishuyse, 1992, J. Magn. & Magn. Mater. **104–107**, 1349.

Dubenko, I.S., R.Z. Levitin, A.S. Markosyan, A.B. Petropavlosky and V.V. Snegirev, 1990, J. Magn. & Magn. Mater. **90–91**, 715.

Dublon, G., and U. Atzmony, 1977, J. Phys. F **7**, 1069.

Duc, N.H., 1991, Phys. Status Solidi B **164**, 545.

Duc, N.H., T.D. Hien, P.E. Brommer and J.J.M. Franse, 1988a, J. Phys. F **18**, 275.

Duc, N.H., T.D. Hien, P.E. Brommer and J.J.M. Franse, 1988b, Physica B **149**, 352.

Duc, N.H., T.D. Hien, P.P. Mai and P.E. Brommer, 1991, Physica B **172**, 399.

Duc, N.H., T.D. Hien, P.E. Brommer and J.J.M. Franse, 1992a, J. Magn. & Magn. Mater. **104–107**, 1252.

Duc, N.H., T.D. Hien, R.Z. Levitin, A.S. Markosyan, P.E. Brommer and J.J.M. Franse, 1992b, Physica B, to be published.

Duc, N.H., T.D. Hien and D. Givord, 1992c, J. Magn. & Magn. Mater. **104–107**, 1344.

Dumelow, T., P.C. Riedi, P. Mohn, K. Schwarz and Y. Yamada, 1986, J. Magn. & Magn. Mater. **54–57**, 1081.

Dumelow, T., P.C. Riedi, J.S. Abell and O. Prakash, 1988, J. Phys. F **18**, 307.

Duthie, J.C., and V. Heine, 1979, J. Phys. F **9**, 1349.

Endo, K., M. Iijima, A. Shinogi and K. Ishiyama, 1987, J. Phys. Soc. Jpn. **56**, 1316.

Endo, K., M. Iijima, T. Sakakibara and T. Goto, 1988, J. Phys. F **18**, L119.

Endo, S., R. Tanaka, S. Nakamichi, F. Ono, H. Wada and M. Shiga, 1992, J. Magn. & Magn. Mater. **104–107**, 1441.

Englich, J., H. Stepankova, V. Sechovsky, I. Dvorakova and H. Lütgemeier, 1990, Hyperf. Interact. **59**, 489.

Eriksson, O., L. Nordström, M.S.S. Brooks and B. Johansson, 1988a, Phys. Rev. Lett. **60**, 2523.

Eriksson, O., L. Nordström, M.S.S. Brooks and B. Johansson, 1988b, J.Phys. **49**, C8–693.

Eriksson, O., B. Johansson, R.C. Albers, A.M. Boring and M.S.S. Brooks, 1990, Phys. Rev. B **42**, 2707.

Ermolenko, A.S., 1976, IEEE Trans. Mag. **MAG-12**, 992.

Ermolenko, A.S., 1979, IEEE Trans.Mag. **MAG-15**, 1765.

Ermolenko, A.S., 1980, Fiz. Met. Metalloved. **50**(4), 741–746 [Phys. Met. Metall. **50**(4), 57–62].

Ermolenko, A.S., 1982a, Proc 6th Int. Workshop

on Rare-Earth-Cobalt Permanent Magnets, ed. J. Fidler (Technical Univ. Vienna) p. 771.
Ermolenko, A.S., 1982b, Fiz. Met. Metalloved. **53**(4), 706 [Phys. Met. Metall. **53**(4), 74].
Ermolenko, A.S., 1985, Fiz. Tverd. Tela **27**(1), 246–248 [Sov. Phys. Solid State. **27**(1), 148].
Ermolenko, A.S., and A.F. Rozhda, 1980, Fiz. Met. Metalloved. **50**(6), 1186 [Phys. Met. Metall. **50**(6), 53].
Ermolenko, A.S., and A.F. Rozhda, 1982, Fiz. Met. Metalloved. **54**(4), 697–704 [Phys. Met. Metall. **54**(4), 64–71].
Ermolenko, A.S., and A.F. Rozhda, 1983, Fiz. Met. Metalloved. **55**(2), 267–272 [Phys. Met. Metall. **55**(2), 53–58].
Escudier, P., D. Gignoux, D. Givord, R. Lemaire and A.P. Murani, 1977, Physica B **86–88**, 197.
Figiel, H., 1991, Magn. Reson. Rev. **16**, 101.
Figiel, H., N. Spiridis, Cz. Kapusta, J. Zukrowski, P.C. Riedi and R.G. Graham, 1990, Proc. 25th Congress Ampere (Stuttgart) p. 482.
Figiel, H., N. Spiridis, P.C. Riedi and R.G. Graham, 1991, J. Magn. & Magn. Mater. **101**, 401.
Figiel, H., Cz. Kapusta, N. Spiridis, G. Stoch, P.C. Riedi and M. Rosenberg, 1992, J. Magn. & Magn. Mater. **104–107**, 1198.
Fontes, M.B., A.P. Guimarães, R.G. Graham and P.C. Riedi, 1992, J. Magn. & Magn. Mater. **104–107**, 1315.
Forsthuber, M., F. Lehner, G. Wiesinger, G. Hilscher, T. Huber, E. Gratz and G. Wortmann, 1990, J. Magn. & Magn. Mater. **90–91**, 471.
Franse, J.J.M., and R.J. Radwański, 1988, in: Physics of Magnetic Materials, eds W. Gorzkowski, H.K. Lachowicz and H. Szymczak (World Scientific, Singapore) p. 336.
Franse, J.J.M., and R.J. Radwański, 1991, in: Semiconductors and Rare Earth Based Materials, eds C.A.J. Ammerlaan, F.F. Bekker, J.J.M. Franse, Nguyen Van Hieu and T.D. Hien (World Scientific, Singapore) p. 215.
Franse, J.J.M., P.H. Frings, F.R. de Boer and A.A. Menovsky, 1981, in: Physics of Solids under High Pressure, eds J.S. Schilling and R.N. Shelton (North-Holland, Amsterdam) p. 181.
Franse, J.J.M., F.R. de Boer, P.H. Frings, R. Gersdorf, A.A. Menovsky, F.A. Muller, R.J. Radwański and S. Sinnema, 1985, Phys. Rev. B **31**, 4347.
Franse, J.J.M., R.J. Radwański and S. Sinnema, 1988a, J. Phys. (Paris) **49**, C8–505.
Franse, J.J.M., N.P. Thuy and N.M. Hong, 1988b, J. Magn. & Magn. Mater. **72**, 361.
Franse, J.J.M., R.J. Radwański and R. Verhoef, 1990, J. Magn. & Magn. Mater. **84**, 299.
Franse, J.J.M., R. Verhoef and R.J. Radwański, 1991, in: Physics of Magnetic Materials, eds W. Gorzkowski, M. Gutowski, H.K. Lachowicz and H. Szymczak (World Scientific, Singapore) p. 144.
Franse, J.J.M., F.E. Kayzel, C. Marquina, R.J. Radwański and R. Verhoef, 1992, J. Alloys & Compounds **181**, 95.
Freeman, A.J., and J.P. Desclaux, 1979, J. Magn. & Magn. Mater. **12**, 11.
Freeman, A.J., and R.E. Watson, 1962, Phys. Rev. **127**, 2058.
Frings, P.H., J.J.M. Franse and G. Hilscher, 1983, J. Phys. F **13**, 175.
Fuess, H., D. Givord, A.R. Gregory and J. Schweizer, 1979, J. Appl. Phys. **50**, 2000.
Fujiwara, K., 1988, J. Phys. Soc. Jpn. **57**, 2133.
Fujiwara, K., K. Ichinose, H. Nagai and A. Tsujimura, 1990, J. Magn. & Magn. Mater. **90–91**, 561.
Fulde, P., and M. Loewenhaupt, 1985, Adv. Phys. **34**, 589.
Fulde, P., and M. Loewenhaupt, 1988, in: Spin Waves and Magnetic Excitations, Vol. 22.1, eds A.S. Borovik-Romanov and S.K. Sinha (North-Holland, Amsterdam) ch. 6, p. 367.
Gabelko, I.L., R.Z. Levitin, A.S. Markosyan and V.V. Snegirev, 1987, Pis'ma Zh. Eksp. Teor. Fiz. **45**(7), 360–362 [JETP Lett. **45**(7), 459–461].
Gaidukova, I.Yu., and A.S. Markosyan, 1982, Fiz. Met. Metalloved. **54**(1), 168–170 [Phys. Met. Metall. **54**(1), 168–170].
Gaidukova, I.Yu., S.B. Kruglyashov, A.S. Markosyan, R.Z. Levitin, Yu.G. Pastushenkov and V.V. Snegirev, 1983, Zh. Eksp. Teor. Fiz. **84**(5), 1858–1867 [Sov. Phys. JETP **57**(5), 1083–1088].
Gaidukova, I.Yu., A.S. Markosyan and A.V. Tsvyashchenko, 1987, Fiz. Met. Metalloved. **64**(3), 486–491 [Phys. Met. Metall. **64**(3), 62].
Garcia-Landa, B., M.R. Ibarra, P.A. Algarabel, F.E. Kayzel, T.H. Anh and J.J.M. Franse, 1992, Physica B **177**, 227.
Gavigan, J.P., D. Givord, H.S. Li and J. Voiron, 1988, Physica B **149**, 345.
Gerard, P., and R. Ballou, 1992, J. Magn. & Magn. Mater. **104–107**, 1463.
Germano, D.J., and R.A. Butera, 1981, Phys. Rev. **24**, 3912.
Gersdorf, R., F.R. de Boer, J.C. Wolfrat, F.A. Muller and L.W. Roeland, 1983, in: High

Field Magnetism, ed. M. Date (North-Holland, Amsterdam) p. 277.
Gignoux, D., 1987, J. Magn. & Magn. Mater. **70**, 81.
Gignoux, D., and F. Givord, 1977, Solid State Commun. **21**, 499.
Gignoux, D., and F. Givord, 1983, J. Magn. & Magn. Mater. **31–34**, 217.
Gignoux, D., and J.J. Rhyne, 1986, J. Magn. & Magn. Mater. **54–57**, 1179.
Gignoux, D., and D. Schmitt, 1991, J. Magn. & Magn. Mater. **100**, 99.
Gignoux, D., F. Givord and R. Lemaire, 1975, Phys. Rev. B **12**, 3878.
Gignoux, D., D. Givord, F. Givord, W.C. Koehler and R.M. Moon, 1976, Phys. Rev. B **14**, 162.
Gignoux, D., F. Givord, R. Perrier de la Bâthie and F. Sayetat, 1979a, J. Phys. F **9**, 763.
Gignoux, D., A. Nait-Saada and R. Perrier de la Bâthie, 1979b, J. Phys. (Paris) **40**, C5–188.
Gignoux, D., R. Lemaire and P. Mohlo, 1980a, J. Magn. & Magn. Mater. **21**, 119.
Gignoux, D., R. Lemaire, P. Mohlo and F. Tasset, 1980b, J. Magn. & Magn. Mater. **21**, 307.
Gignoux, D., R. Lemaire, P. Mohlo and F. Tasset, 1981, J. Appl. Phys. **52**, 2087.
Givord, D., and R. Lemaire, 1974, IEEE Trans. Magn. **MAG-10**, 109.
Givord, D., and J.P. Nozières, 1991, in: Semiconductors and Rare Earth Based Materials, eds C.A.J. Ammerlaan, F.F. Bekker, J.J.M. Franse, Nguyen Van Hieu and T.D. Hien (World Scientific, Singapore) p. 147.
Givord, D., J. Laforest, J. Schweizer and F. Tasset, 1979a, J. Appl. Phys. **50**, 2008.
Givord, D., J. Laforest and R. Lemaire, 1979b, J. Appl. Phys. **50**, 7489.
Givord, D., A.R. Gregory and J. Schweizer, 1980, J. Magn. & Magn. Mater. **15–18**, 293.
Givord, D., J. Laforest, R. Lemaire and Q. Lu, 1983, J. Magn. & Magn. Mater. **31–34**, 191.
Godwin, L.M., H.W. White and W.J. James, 1979, J. Appl. Phys. **50**, 1165.
Goremychkin, E.A., E. Mühle, P.G. Ivanitskii, V.T. Krotenko, M.V. Pasechnik, V.V. Slisenko, A.A. Vasilkevich, B. Lippold, O.D. Chistyakov and E.M. Savitskii, 1984, Phys. Status Solidi B **121**, 623.
Goremychkin, E.A., E. Mühle, I. Natkaniec, M. Popescu and O.D. Chistyakov, 1985, Fiz. Tverd. Tela **27**(8), 1986 [Sov. Phys. Solid State **27**(8), 1195].
Goremychkin, E.A., I. Natkaniec, E. Mühle and O.D. Chistyakov, 1989, J. Magn. & Magn. Mater. **81**, 63.
Goto, T., T. Sakakibara, K.K. Murata, H. Komatsu and K. Fukamichi, 1990, J. Magn. & Magn. Mater. **90–91**, 700.
Goto, T., H. Aruga Katori, T. Sakakibara and M.T. Yamaguchi, 1992, Physica B **177**, 255.
Graham Jr, C.D., and P.J. Flanders, 1986, IEEE Trans. Mag. **MAG-22**, 749.
Gratz, E., and M.J. Zuckermann, 1982, in: Handbook on the Physics and Chemistry of Rare Earths, Vol. 5, eds K.A. Gschneidner Jr and L. Eyring (North-Holland, Amsterdam) ch. 42, p. 117.
Gratz, E., E. Bauer and H. Novotny, 1987, J. Magn. & Magn. Mater. **70**, 118.
Gratz, E., E. Bauer, S. Pöllinger, H. Novotny, A.T. Burkov and M.V. Vedernikov, 1988, J. Phys. (Paris) **49**, C8–511.
Graves-Tompson, R.J., H.W. White, K. Hardman and W.J. James, 1983, J. Appl. Phys. **54**(5), 2838.
Greedan, J.E., and V.U.S. Rao, 1973, J. Solid State Chem. **6**, 587.
Greidanus, F.J.A.M., L.J. de Jongh, W.J. Huiskamp, A. Furrer and K.H.J. Buschow, 1983, Physica B **115**, 137.
Gschneidner Jr, K.A., and K. Ikeda, 1980, Phys. Rev. Lett. **45**, 1341.
Gschneidner Jr, K.A., and K. Ikeda, 1983, J. Magn. & Magn. Mater. **31–34**, 265.
Gubbens, P.C.M., and K.H.J. Buschow, 1982, J. Phys. F **12**, 15.
Gubbens, P.C.M., A.M. van der Kraan and K.H.J. Buschow, 1981, Solid State Commun. **37**, 635.
Gubbens, P.C.M., A.M. van der Kraan and K.H.J. Buschow, 1982, J. Magn. & Magn. Mater. **29**, 113.
Gubbens, P.C.M., W. Ras, A.M. van der Kraan and K.H.J. Buschow, 1983, Phys. Status Solidi B **117**, 277.
Gubbens, P.C.M., A.M. van der Kraan and K.H.J. Buschow, 1984a, J. Phys. F **14**, 235.
Gubbens, P.C.M., A.M. van der Kraan and K.H.J. Buschow, 1984b, J. Phys. F **14**, 2195.
Gubbens, P.C.M., A.M. van der Kraan, J.J. van Loef and K.H.J. Buschow, 1986, J. Magn. & Magn. Mater. **54–57**, 483.
Gubbens, P.C.M., A.M. van der Kraan, J.J. van Loef and K.H.J. Buschow, 1987, J. Magn. & Magn. Mater. **67**, 255.
Gubbens, P.C.M., A.M. van der Kraan and K.H.J. Buschow, 1988a, J. Phys. (Paris) **49**, C8–591.

Gubbens, P.C.M., A.M. van der Kraan and K.H.J. Buschow, 1988b, Hyperf. Interact. **40**, 389.
Gubbens, P.C.M., A.M. van der Kraan and K.H.J. Buschow, 1989a, Phys. Rev. B **39**, 12548.
Gubbens, P.C.M., A.M. van der Kraan, T.H. Jacobs and K.H.J. Buschow, 1989b, J. Magn. & Magn. Mater. **80**, 265.
Guimarães, A.P., K.M.B. Alves, N. Alves and E. Gratz, 1987, J. Appl. Phys. **61**, 3985.
Gupta, M., 1987, J. Less-Common Met. **130**, 219.
Han, X.-F., T.-S. Zhao and H.-M. Jin, 1991, J. Magn. & Magn. Mater. **102**, 151.
Hardman, K., W.J. James, J. Deportes, R. Lemaire and R. Perrier de la Bâthie, 1979, J. Phys. (Paris) **40**, C5–204.
Hardman, K., J.J. Rhyne, S.K. Malik and W.E. Wallace, 1982, J. Appl. Phys. **53**, 1944.
Hardman-Rhyne, K., and J.J. Rhyne, 1983, J. Less-Common Met. **94**, 23.
Hardman-Rhyne, K., J.J. Rhyne, E. Prince, C. Crowder and W.J. James, 1984, Phys. Rev. B **29**, 416.
Hashimoto, Y., 1988, J. Phys. (Paris) **49**, C8–421.
Hashimoto, Y., H. Fujii, T. Okamoto and Y. Makihara, 1987, J. Magn. & Magn. Mater. **70**, 291.
Herbst, J.F., 1991, Rev. Mod. Phys. **63**(4), 819.
Herbst, J.F., and J.J. Croat, 1982, J. Appl. Phys. **53**, 4304.
Herbst, J.F., and J.J. Croat, 1984, J. Appl. Phys. **55**, 3023.
Herbst, J.F., J.J. Croat, P.W. Lee and W.B. Yelon, 1982, J. Appl. Phys. **53**, 250.
Hien, T.D., N.H. Duc and J.J.M. Franse, 1984, J. Magn. & Magn. Mater. **54–57**, 471.
Hilscher, G., and H. Rais, 1978, J. Phys. F **8**, 511.
Hilscher, G., N. Pillmayr, C. Schmitzer and E. Gratz, 1988, Phys. Rev. B **37**, 3480.
Hirosawa, S., and Y. Nakamura, 1982, J. Magn. & Magn. Mater. **25**, 284.
Hirosawa, S., K. Tokuhara, H. Yamamoto, S. Fujimura, M. Sagawa and H. Yamauchi, 1987, J. Appl. Phys. **61**, 3571.
Hong, N.M., J.J.M. Franse and N.P. Thuy, 1989, J. Magn. & Magn. Mater. **80**, 159.
Hu, B.P., H.S. Li, J.P. Gavigan and J.M.D. Coey, 1989, J. Phys.: Condens. Matter **1**, 755.
Hu, B.P., H.S. Li, J.M.D. Coey and J.P. Gavigan, 1990, Phys. Rev. B **41**, 2221.
Hutchings, M.T., 1964, Solid State Phys. **16**, 227.
Ibarra, M.R., and A. del Moral, 1990, J. Magn. & Magn. Mater. **83**, 121.
Ibarra, M.R., A. del Moral and J.S. Abell, 1984a, J. Magn. & Magn. Mater. **46**, 157.
Ibarra, M.R., J.I. Arnaudas, P.A. Algarabel and A. del Moral, 1984b, J. Magn. & Magn. Mater. **46**, 167.
Ibarra, M.R., E.W. Lee, A. del Moral and J.S. Abell, 1986, J. Magn. & Magn. Mater. **54–57**, 879.
Ibarra, M.R., L.A. Morellón, P.A. Algarabel and O. Moze, 1991, Phys. Rev. B **44**, 9368.
Ikeda, K., K.A. Gschneidner Jr, R.J. Stierman, T-W.E. Tsang and O.D. McMasters, 1984, Phys. Rev. B **29**, 5039.
Ikeda, K., S.K. Dhar, M. Yoshizawa and K.A. Gschneidner Jr, 1991, J. Magn. & Magn. Mater. **100**, 292.
Inoue, J., 1988, Physica B **149**, 376.
Inoue, J., and M. Shimizu, 1982, J. Phys. F **12**, 1811.
Inoue, J., and M. Shimizu, 1985, J. Phys. F **15**, 1511.
Inoue, J., and M. Shimizu, 1986, J. Magn. & Magn. Mater. **54–57**, 991.
Inoue, J., and M. Shimizu, 1988, J. Phys. F **18**, 2487.
Irkhin, Yu.P., and E.V. Rosenfeld, 1985, J. Magn. & Magn. Mater. **51**, 357.
Ishii, H., S. Aoyama and N. Okamoto, 1990, J. Magn. & Magn. Mater. **90–91**, 59.
Ishio, S., F. Aubertin, T. Limbach, H. Engelman, L. Dezsi, U. Gonser, S. Fries, M. Takahashi and M. Fujikura, 1988, J. Phys. F **18**, 2253.
Isnard, O., S. Miraglia, D. Fruchart and J. Deportes, 1992, J. Magn. & Magn. Mater. **103**, 157.
Jaakkola, S., S. Parviainen and S. Penttilä, 1983, J. Phys. F **13**, 491.
Jacobs, T.H., K.H.J. Buschow, G.F. Zhou, J.P. Liu, X. Li and F.R. de Boer, 1992a, J. Magn. & Magn. Mater. **104–107**, 1275.
Jacobs, T.H., K.H.J. Buschow, G.F. Zhou, X. Li and F.R. de Boer, 1992b, J. Magn. & Magn. Mater. **116**, 220.
James, W.J., K. Hardman, W.B. Yelon, J. Keem and J.J. Croat, 1979a, J. Appl. Phys. **50**, 2006.
James, W.J., K. Hardman, W.B. Yelon and B. Kebe, 1979b, J. Phys. (Paris) **40**, C5–206.
Japa, S., K. Krop, R.J. Radwański and J. Wolinski, 1979, J. Phys. (Paris) **40**, C2–193.
Jensen, J., 1982, J. Magn. & Magn. Mater. **29**, 47.
Johansson, B., O. Eriksson, L. Nordström, L. Severin and M.S.S. Brooks, 1991, Physica B **172**, 101.

Kąkol, Z., and H. Figiel, 1985, Physica B **130**, 312.
Kąkol, Z., and H. Figiel, 1986, Phys. Status Solidi B **138**, 151.
Kąkol, Z., H. Figiel and K. Turek, 1984, IEEE Trans. Mag. **MAG-20**, 1605.
Kamarad, J., Z. Arnold and J. Schweizer, 1987, J. Magn. & Magn. Mater. **67**, 29.
Kamimura, H., J. Sakurai, Y. Komura, H. Nakamura, M. Shiga and Y. Nakamura, 1987, J. Magn. & Magn. Mater. **70**, 145.
Kaneko, T., K. Marumo, S. Miura, G. Kido, S. Abe, H. Yoshida, K. Kamigaki and Y. Nakagawa, 1988, Physica B **149**, 334.
Kapusta, Cz., M. Rosenberg, R.G. Graham, P.C. Riedi, T.H. Jacobs and K.H.J. Buschow, 1992a, J. Magn. & Magn. Mater. **104–107**, 1333.
Kapusta, Cz., M. Rosenberg, H. Figiel, T.H. Jacobs and K.H.J. Buschow, 1992b, J. Magn. & Magn. Mater. **104–107**, 1331.
Karnachev, A.S., T.V. Maksimchuk, V.A. Reymer, E.V. Sinitsyn and E.E. Solovyev, 1986, Fiz. Met. Metalloved. **61**(5), 910–914 [Phys. Met. Metall. **61**(5), 70–74].
Karpenko, V.P., and Yu.P. Irkhin, 1973, Zh. Eksp. Teor. Fiz. **64**(2), 756–759 [Sov. Phys. JETP **37**(2), 383–385].
Katayama, T., and T. Shibata, 1981, J. Magn. & Magn. Mater. **23**, 173.
Katter, M., J. Wecker, L. Schultz and R. Grössinger, 1991, J. Magn. & Magn. Mater. **92**, L14.
Kebe, B., 1983, Thesis (Grenoble).
Kelarev, V.V., V.V. Chuyev, A.N. Pirogov and S.K. Sidorov, 1983, Phys. Status Solidi A **79**, 57.
Kennedy, S.J., A.P. Murani, B.R. Coles and O. Moze, 1988, J. Phys. F **18**, 2499.
Kido, G., Y. Nakagawa, Y. Nishihara and F. Iga, 1990, J. Magn. & Magn. Mater. **90–91**, 75.
Kim-Ngan, N.H., F.F. Bekker, P.E. Brommer and J.J.M. Franse, 1990, Physica B **160**, 388.
Kim-Ngan, N.H., Z. Tarnawski, F.E. Kayzel, P.E. Brommer and J.J.M. Franse, 1992a, Physica B **177**, 302.
Kim-Ngan, N.H., Z. Tarnawski, N.P. Thuy, T.D. Hien, F.F. Bekker, P.E. Brommer and J.J.M. Franse, 1992b, J. Magn. & Magn. Mater. **104–107**, 1298.
Kim-Ngan, N.H., P.E. Brommer, T.D. Hien and J.J.M. Franse, 1992c, Physica B **182**, 27.
Kirchmayr, H.R., and C.A. Poldy, 1979, in: Handbook on the Physics and Chemistry of Rare Earths, Vol. 2. eds K.A. Gschneidner Jr and L. Eyring (North-Holland, Amsterdam) p. 55.
Klein, H.P., A. Menth and R.S. Perkins, 1975, Physica B **80**, 153.
Kohashi, M., M. Ono, M. Date, A. Yamagishi, X.P. Zhong, Q. Wang, F.M. Yang, R.J. Radwański and F.R. de Boer, 1991, J. Appl. Phys. **69**, 5542.
Koon, N.C., and J.J. Rhyne, 1981, Phys. Rev. B **23**, 2078.
Koon, N.C., C.M. Williams and B.N. Das, 1991, J. Magn. & Magn. Mater. **100**, 173.
Kozłowski, A., G.A. Stewart, Z. Obuszko and J. Zukrowski, 1990, J. Magn. & Magn. Mater. **92**, 155.
Krop, K., 1989, Physica B **159**, 66.
Kudrevatykh, N.V., E.W. Lee and D. Melville, 1984, Fiz. Met. Metalloved. **58**(4), 709 [Phys. Met. Metall. **58**(4)].
Kudrevatykh, N.V., E.W. Lee and D. Melville, 1986, Fiz. Met. Metalloved. **61**(5), 898–903 [Phys. Met. Metall. **61**(5), 59–64].
Kumar, R., and W.B. Yelon, 1990, J. Appl. Phys. **67**, 4641.
Labroo, S., N. Ali and P. Robinson, 1990a, J. Appl. Phys. **67**, 5292.
Labroo, S., F. Willis and N. Ali, 1990b, J. Appl. Phys. **67**, 5295.
Laforest, J., 1981, Thesis (Grenoble).
Laforest, J., R. Lemaire, D. Paccard and R. Pauthenet, 1967, Acad. Sci. Paris **264**, 676.
Lea, K.R., M.J.M. Leask and W.P. Wolf, 1962, J. Phys. Chem. Sol. **23**, 1381.
Lee, E.W., and F. Pouranian, 1976a, Phys. Status Solidi A **33**, 483.
Lee, E.W., and F. Pouranian, 1976b, Phys. Status Solidi A **34**, 383.
Lemaire, R., 1966a, Cobalt **32**, 132.
Lemaire, R., 1966b, Cobalt **33**, 201.
Levitin, R.Z., and A.S. Markosyan, 1988, Usp. Fiz. Nauk **155**(4), 623–657 [Sov. Phys. Usp. **31**(8), 730–749].
Levitin, R.Z., and A.S. Markosyan, 1990, J. Magn. & Magn. Mater. **84**, 247.
Levitin, R.Z., A.S. Markosyan and V.V. Snegirev, 1982, Pis'ma Zh. Eksp. Teor. Fiz. **36**(10), 367–369 [JETP Lett. **36**(10), 446–448].
Li, C., A.J. Freeman and C.L. Fu, 1991, J. Magn. & Magn. Mater. **94**, 134.
Li, H.S., and J.M. Cadogan, 1992, J. Magn. & Magn. Mater. **103**, 53.
Li, H.S., and J.M.D. Coey, 1991, in: Handbook of Magnetic Materials, Vol. 6, ed. K.H.J. Buschow

(North-Holland, Amsterdam) chapter 1, p. 1.
Li, H.S., Y.P. Li and J.M.D. Coey, 1991, J. Phys.: Condens. Matter **3**, 7277.
Li, H.S., Y.P. Li and J.M.D. Coey, 1992, J. Magn. & Magn. Mater. **104–107**, 1444.
Lindley, E.J., B.D. Rainford and D.McK. Paul, 1988, J. Phys. (Paris) **49**, C8–279.
Littlewood, N.T., W.J. James and W.B. Yelon, 1986, J. Magn. & Magn. Mater. **54–57**, 491.
Liu, J.P., X.P. Zhong, F.R. de Boer and K.H.J. Buschow, 1991a, J. Appl. Phys. **69**, 5536.
Liu, J.P., K. Bakker, F.R. de Boer, T.H. Jacobs, D.B. de Mooij and K.H.J. Buschow, 1991b, J. Less-Common Met. **170**, 109.
Liu, J.P., F.R. de Boer and K.H.J. Buschow, 1991c, J. Magn. & Magn. Mater. **98**, 291.
Loewenhaupt, M., M. Prager, A.P. Murani and H.E. Hoenig, 1988, J. Magn. & Magn. Mater. **76–77**, 408.
Loewenhaupt, M., I. Sosnowska and B. Frück, 1990, Phys. Rev. B **42**, 3866.
Loewenhaupt, M., I. Sosnowska, A.D. Taylor and R. Osborn, 1991, J. Appl. Phys. **69**, 5593.
Lu, Q., 1981, Thesis (Grenoble).
Makihara, Y., Y. Andoh, Y. Hashimoto, H. Fujii, M. Hasuo and T. Okamoto, 1983, J. Phys. Soc. Jpn. **52**, 629.
Makihara, Y., H. Fujii, K. Hiraoka, T. Kitai and T. Hihara, 1988, J. Phys. (Paris) **49**, C8–1087.
Malik, S.K., and W.E. Wallace, 1981, J. Magn. & Magn. Mater. **24**, 23.
Malik, S.K., T. Takeshita and W.E. Wallace, 1977, Solid State Commun. **23**, 599.
Malik, S.K., W.E. Wallace and T. Takeshita, 1978, Solid State Commun. **28**, 977.
Malik, S.K., E.B. Boltich and W.E. Wallace, 1981, Solid State Commun. **37**, 329.
Malik, S.K., F. Pouranian and W.E. Wallace, 1983, J. Magn. & Magn. Mater. **40**, 27.
Malozemoff, A.P., A.R. Williams and V.L. Moruzzi, 1984, Phys. Rev B **29**, 1620.
Markosyan, A.S., 1981a, Fiz. Tverd. Tela **23**(4), 1153–1155 [Sov. Phys. Solid State **23**(4), 670–671].
Markosyan, A.S., 1981b, Fiz. Tverd. Tela **23**(6), 1656–1661 [Sov. Phys. Solid State **23**(6), 965–967].
Markosyan, A.S., 1982, Fiz. Met. Metalloved. **54**(6), 1109–1114 [Phys. Met. Metall. **54**(6), 59–65.].
Markosyan, A.S., and V.V. Snegirev, 1985, Fiz. Met. Metalloved. **59**(6), 1151–1157 [Phys. Met. Metall. **59**(6), 99].
Marquina, C., F.E. Kayzel, T.H. Anh, R.J. Radwański and J.J.M. Franse, 1992, J. Magn. & Magn. Mater. **104–107**, 1323.
Marusi, G., L. Pareti and M. Solzi, 1991, J. Magn. & Magn. Mater. **101**, 333.
Matthaei, B., J.J.M. Franse, S. Sinnema and R.J. Radwański, 1988, J. Phys. (Paris) **49**, C8–533.
McMorrow, D.F., M.A.H. McCausland, Z.P. Han and J.S. Abell, 1989, J. Phys.: Condens. Matter **1**, 10439.
Meyer, C., F. Hartmann-Boutron, Y. Gros, B. Srour and J.J. Capponi, 1979, J. Phys. (Paris) **40**, C5–191.
Meyer, C., F. Hartmann-Boutron, Y. Gros, Y. Berthier and J.L. Buevoz, 1981, J. Phys. (Paris) **42**, C6–605.
Misawa, S., 1988, J. Phys. (Paris) **49**, C8–255.
Mohn, P., and E.P. Wohlfarth, 1987, J. Phys. F **17**, 2421.
Mondal, S., S.H. Kilcoyne, R. Cywinski, B.D. Rainford and C. Ritter, 1992, J. Magn. & Magn. Mater. **104–107**, 1421.
Mori, H., T. Satoh, H. Suzuki and T. Ohtsuka, 1982, J. Phys. Soc. Jpn. **51**, 1785.
Morin, P., and D. Schmitt, 1991, in: Handbook of Magnetic Materials, Vol. 5, eds K.H.J. Buschow and E.P. Wohlfarth (North-Holland, Amsterdam) p. 1.
Motoya, K., T. Freltoft, P. Boni and G. Shirane, 1987, J. Phys. Soc. Jpn. **56**, 885.
Moze, O., R. Caciuffo, H.S. Li, B.P. Hu, J.M.D. Coey, R. Osborn and A.D. Taylor, 1990a, Phys. Rev. B **42**, 1940.
Moze, O., M.R. Ibarra, A. del Moral, G. Marusi and P.A. Algarabel, 1990b, J. Phys.:Condens. Matter **2**, 6031.
Moze, O., R. Caciuffo, B. Gillon and F.E. Kayzel, 1992, J. Magn. & Magn. Mater. **104–107**, 1394.
Mühle, E., E.A. Goremychkin and I. Natkaniec, 1989, J. Magn. & Magn. Mater. **81**, 72.
Muraoka, Y., M. Shiga and Y. Nakamura, 1977, J. Phys. Soc. Jpn. **42**, 2067.
Muraoka, Y., M. Shiga and Y. Nakamura, 1983, J. Magn. & Magn. Mater. **31–34**, 121.
Muraoka, Y., H. Okuda, M. Shiga and Y. Nakamura, 1984, J. Phys. Soc. Jpn. **53**, 331.
Nagai, H., K. Kojima and H. Yoshie, 1988a, J. Phys. (Paris) **49**, C8–535.
Nagai, H., M. Takigawa and H. Yasuoka, 1988b, J. Phys. Soc. Jpn. **57**, 3690.
Nagata, H., S. Hirosawa, M. Sagawa, A. Ishibashi and S. Endo, 1987, J. Magn. & Magn. Mater. **70**, 334.
Nait-Saada, A., 1980, Thesis (Grenoble).

Nakamura, H., H. Wada, K. Yoshimura, M. Shiga, Y. Nakamura, J. Sakurai and Y. Komura, 1988a, J. Phys. F **18**, 981.

Nakamura, H., Y. Kitaoka, K. Yoshimura, Y. Kohori, K. Asayama, M. Shiga and Y. Nakamura, 1988b, J. Phys. (Paris) **49**, C8–257.

Nakamura, Y., 1983, J. Magn. & Magn. Mater. **31–34**, 829.

Nakamura, Y., M. Shiga and S. Kawano, 1983, Physica B **120**, 212.

Narasimha, C.V., H. Wada, M. Shiga and Y. Nakamura, 1987, J. Magn. & Magn. Mater. **70**, 151.

Nikitin, S.A., A.M. Tishin, M.D. Kuzmin and Yu.I. Spichkin, 1991, Phys. Lett. A **153**, 155.

Nishihara, Y., 1987, J. Magn. & Magn. Mater. **70**, 75.

Nowik, I., I. Felner, M. Seh, M. Rakavy and D.I. Paul, 1983, J. Magn. & Magn. Mater. **30**, 295.

Oesterreicher, H., and F.T. Parker, 1980, Phys. Status Solidi A **58**, 585.

Okamoto, N., H. Nagai, H. Yoshie, A. Tsujimura and T. Hihara, 1987, J. Magn. & Magn. Mater. **70**, 299.

Okamoto, T., H. Fujii, Y. Makihara, T. Hihara and Y. Hashimoto, 1986, J. Magn. & Magn. Mater. **54–57**, 1087.

Okamoto, T., H. Nagata, H. Fujii and Y. Makihara, 1987, J. Magn. & Magn. Mater. **70**, 139.

Oomi, G., T. Terada, M. Shiga and Y. Nakamura, 1987, J. Magn. & Magn. Mater. **70**, 137.

Osborn, R., S.W. Lovesey, A.D. Taylor and E. Balcar, 1991, in: Handbook on the Physics and Chemistry of Rare Earths, Vol. 14, eds K.A. Gschneidner Jr and L. Eyring (North-Holland, Amsterdam) p. 1.

Ouladdiaf, B., 1986, Thesis (Grenoble).

Panissod, P., J. Durand and J.I. Budnick, 1982, Nucl. Instr. & Meth. **199**, 99.

Pareti, L., O. Moze, M. Solzi and F. Bolzoni, 1988, J. Appl. Phys. **63**, 172.

Parthé, E., and R. Lemaire, 1975, Acta Crystallogr. **331**, 1879.

Patterson, C., D. Givord, J. Voiron and S.B. Palmer, 1986, J. Magn. & Magn. Mater. **54–57**, 891.

Pauthenet, R., 1983, in: High Field Magnetism, ed. M. Date (North-Holland, Amsterdam) p. 77.

Pędziwiatr, A.T., E.B. Boltich, W.E. Wallace and R.S. Craig, 1983, J. Solid State Chem. **46**, 342.

Perkins, R.S., and H. Nagel, 1975, Physica B **80**, 143.

Perkins, R.S., and S. Strassler, 1977, Phys. Rev. B **15**, 477.

Pillay, R.G., A.K. Grover, V. Balasubramanian, A.K. Rastogi and P.N. Tandon, 1988, J. Phys. F **18**, L63.

Pillmayr, N., C. Schmitzer, E. Gratz and G. Hilscher, 1987, J. Magn. & Magn. Mater. **70**, 162.

Pillmayr, N., G. Hilscher, E. Gratz and V. Sechovsky, 1988, J. Phys. (Paris) **49**, C8–273.

Pirogov, A.N., V.V. Kelarev and V.V. Chuyev, 1984, Fiz. Met. Metalloved. **58**(4), 615 [Phys. Met. Metall. **58**(4), 55].

Pirogov, A.N., A.S. Ermolenko, V.V. Kelarev and S.K. Sidorov, 1986, Fiz. Met. Metalloved. **62**(5), 1035–1037 [Phys. Met. Metall. **62**(5), 196–198].

Płusa, D., R. Pfranger and B. Wysłocki, 1984, J. Magn. & Magn. Mater. **40**, 271.

Pouranian, F., E.B. Boltich, W.E. Wallace, R.S. Craig and S.K. Malik, 1980a, J. Magn. & Magn. Mater. **21**, 128.

Pouranian, F., E.B. Boltich, W.E. Wallace and S.K. Malik, 1980b, J. Less-Common Met. **74**, 153.

Prakash, O., M.A. Chaundry, J.W. Ross and M.A.H. McCausland, 1983, J. Magn. & Magn. Mater. **36**, 271.

Pringle, O.A., G.J. Long, F. Grandjean and K.H.J. Buschow, 1992, J. Magn. & Magn. Mater. **104–107**, 1123.

Pszczoła, J., and K. Krop, 1986, J. Magn. & Magn. Mater. **59**, 95.

Pszczoła, J., D. Best, L. Klimek and M. Forker, 1990, J. Magn. & Magn. Mater. **92**, 101.

Radwański, R.J., 1985, J. Phys. F **15**, 459.

Radwański, R.J., 1986a, Physica B **142**, 57.

Radwański, R.J., 1986b, Phys. Status Solidi B **137**, 487.

Radwański, R.J., 1986c, Z. Phys. B **65**, 65.

Radwański, R.J., 1986d, J. Magn. & Magn. Mater. **62**, 120.

Radwański, R.J., 1987, J. Phys. F **17**, 267.

Radwański, R.J., and J.J.M. Franse, 1989a, Physica B **154**, 181.

Radwański, R.J., and J.J.M. Franse, 1989b, J. Magn. & Magn. Mater. **80**, 14.

Radwański, R.J., and J.J.M. Franse, 1992, Physica B **177**, 193.

Radwański, R.J., and J.J.M. Franse, 1993, to be published.

Radwański, R.J., and K. Krop, 1983, Physica B **119**, 180.

Radwański, R.J., J.J.M. Franse, K. Krop, R. Duraj and R. Zach, 1985a, Physica B **130**, 286.
Radwański, R.J., J.J.M. Franse and S. Sinnema, 1985b, J. Magn. & Magn. Mater. **51**, 175.
Radwański, R.J., J.J.M. Franse and S. Sinnema, 1985c, J. Phys. F **15**, 969.
Radwański, R.J., J.J.M. Franse and S. Sinnema, 1987, J. Magn. & Magn. Mater. **70**, 313.
Radwański, R.J., J.J.M. Franse and K. Krop, 1988a, Physica B **149**, 306.
Radwański, R.J., J.J.M. Franse, S. Sinnema, H.J.M. Heerooms and J.H.P. Colpa, 1988b, J. Magn. & Magn. Mater. **76–77**, 182.
Radwański, R.J., J.J.M. Franse, J.C.P. Klaasse and S. Sinnema, 1988c, J. Phys. (Paris) **49**, C8–531.
Radwański, R.J., F.R. de Boer, J.J.M. Franse and K.H.J. Buschow, 1989, Physica B **159**, 311.
Radwański, R.J., J.J.M. Franse and R. Verhoef, 1990a, J. Magn. & Magn. Mater. **83**, 127.
Radwański, R.J., X.P. Zhong, F.R. de Boer and K.H.J. Buschow, 1990b, Physica B **164**, 131.
Radwański, R.J., R. Verhoef and J.J.M. Franse, 1990c, J. Magn. & Magn. Mater. **83**, 141.
Radwański, R.J., J.J.M. Franse, D. Gignoux, F.E. Kayzel, C. Marquina and A. Szewczyk, 1992a, Physica B **177**, 291.
Radwański, R.J., J.J.M. Franse, P.H. Quang and F.E. Kayzel, 1992b, J. Magn. & Magn. Mater. **104–107**, 1321.
Radwański, R.J., N.H. Kim-Ngan, F.E. Kayzel, J.J.M. Franse, D. Gignoux, D. Schmitt and F.Y. Zhang, 1992c, J. Phys.: Condens. Matter **4**, 8853.
Radwański, R.J., et al., 1993, to be published.
Rainford, B.D., S. Dakin and R. Cywinski, 1992, J. Magn. & Magn. Mater. **104–107**, 1257.
Rastogi, A.K., G. Hilscher, E. Gratz and N. Pillmayr, 1988, J. Phys. (Paris) **49**, C8–277.
Reiffers, M., Yu.G. Naidyuk, A.G.M. Jansen, P. Wyder and I.K. Yanson, 1989, Phys. Rev. Lett. **62**, 1560.
Rhyne, J.J., 1987, J. Magn. & Magn. Mater. **70**, 88.
Rhyne, J.J., and N.C. Koon, 1983, J. Magn. & Magn. Mater. **31–34**, 608.
Rhyne, J.J., K. Hardman-Rhyne, H.K. Smith and W.E. Wallace, 1983, J. Less-Common Met. **94**, 95.
Rhyne, J.J., K. Hardman-Rhyne, H.K. Smith and W.E. Wallace, 1987, J. Less-Common Met. **129**, 207.
Richter, M., and H. Eschrig, 1991, Physica B **172**, 85.
Riedi, P.C., and G.D. Webber, 1983, J. Phys. F **13**, 1057.
Ritter, C., 1989, J. Phys.: Condens. Matter **1**, 2765.
Ritter, C., S.H. Kilcoyne and R. Cywinski, 1991, J. Phys.: Condens. Matter **3**, 727.
Roy, S.B., and B.R. Coles, 1989, J. Phys.: Condens. Matter **1**, 419.
Sa, M.A., J.B. Oliviera, J.M. Machado da Silvia and I.R. Harris, 1985, J. Less-Common Met. **108**, 263.
Sahling, A., P. Frach and E. Hegenbarth, 1982, Phys. Status Solidi B **112**, 243.
Sakakibara, T., H. Mitamura, G. Kido and T. Goto, 1991, Physica B **177**, 251.
Sakurai, J., H. Kamimura, T. Ohyama, Y. Komura, D. Gignoux and R. Lemaire, 1987, J. Magn. & Magn. Mater. **70**, 383.
Sankar, S.G., V.U.S. Rao, E. Segal, W.E. Wallace, W.G.D. Frederick and H.J. Garrett, 1975, Phys. Rev. B **11**, 435.
Sarkis, A., and E. Callen, 1982, Phys. Rev. B **26**, 3870.
Schinkel, C.J., 1978, J. Phys. F **8**, L87.
Schmitt, D., 1979a, J. Phys. F **9**, 1745.
Schmitt, D., 1979b, J. Phys. F **9**, 1759.
Schultz, L., and M. Katter, 1991, in: Supermagnets, Hard Magnetic Materials, eds G.J. Long & F. Grandjean, NATO ASI Series C-331 p. 227.
Schultz, L., K. Schnitzke, J. Wecker, M. Katter and C. Kuhrt, 1991, J. Appl. Phys. **70**, 3666.
Schwarz, K., and P. Mohn, 1984, J. Phys. F **14**, L129.
Schweizer, J., and F. Tasset, 1980, J. Phys. F **10**, 2799.
Scrabek, E.A., and W.E. Wallace, 1963, J. Appl. Phys. **34**, 1356.
Shcherbakova, E.V., and A.S. Ermolenko, 1982, Fiz. Met. Metalloved. **54**(6), 1103 [Phys. Met. Metall. **54**(6), 53].
Shcherbakova, E.V., and A.S. Ermolenko, 1985, Fiz. Met. Metalloved. **59**(2), 344–348 [Phys. Met. Metall. **59**(2), 120].
Shcherbakova, E.V., A.S. Ermolenko and A.V. Korolev, 1986, Fiz. Met. Metalloved. **62**(1), 89–94 [Phys. Met. Metall. **62**(1), 77].
Shiga, M., H. Wada and Y. Nakamura, 1983, J. Magn. & Magn. Mater. **31–34**, 119.
Shiga, M., H. Wada, H. Nakamura, K. Yoshimura and Y. Nakamura, 1987, J. Phys. F **17**, 1781.
Shiga, M., H. Wada, Y. Nakamura, J. Deportes and K.R.A. Ziebeck, 1988, J. Phys. (Paris) **49**, C8–241.
Shimizu, K., 1987, J. Magn. & Magn. Mater. **70**, 178.

Shimizu, K., K. Sato and H. Nagano, 1988, Physica B **149**, 319.

Shimizu, M., and J. Inoue, 1986, J. Magn. & Magn. Mater. **54–57**, 963.

Shimizu, M., and J. Inoue, 1987, J. Magn. & Magn. Mater. **70**, 61.

Shimizu, M., J. Inoue and S. Nagasawa, 1984, J. Phys. F **14**, 2673.

Shimotomai, M., and M. Doyama, 1983, J. Magn. & Magn. Mater. **31–34**, 215.

Shimotomai, M., H. Miyake and M. Doyama, 1980, J. Phys. F **10**, 707.

Simmons, M., J.M. Moreau, W.J. James, F. Givord and R. Lemaire, 1973, J. Less-Common Met. **30**, 75.

Sinnema, S., 1988, Thesis (University of Amsterdam).

Sinnema, S., R.J. Radwański, J.J.M. Franse, D.B. de Mooij and K.H.J. Buschow, 1984, J. Magn. & Magn. Mater. **44**, 333.

Sinnema, S., J.J.M. Franse, A.A. Menovsky and R.J. Radwański, 1986a, J. Magn. & Magn. Mater. **54–57**, 1639.

Sinnema, S., J.J.M. Franse, A.A. Menovsky, F.R. de Boer and R.J. Radwański, 1986b, in: Physics of Magnetic Materials, eds W. Gorzkowski, H.K. Lachowicz and H. Szymczak (World Scientific, Singapore) p. 324.

Sinnema, S., J.J.M. Franse, R.J. Radwański, A.A. Menovsky and F.R. de Boer, 1987a, J. Phys. F **17**, 233.

Sinnema, S., J.J.M. Franse, A.A. Menovsky and F.R. de Boer, 1987b, J. Less-Common Met. **127**, 105.

Smit, H.H.A., R.C. Thiel and K.H.J. Buschow, 1988, J. Phys. F **18**, 295.

Sousa, J.B., J.M. Moreira, A. del Moral, P.A. Algarabel and M.R. Ibarra, 1990, J. Phys.: Condens. Matter **2**, 3897.

Stewart, G.A., J. Zukrowski and G. Wortmann, 1981, Solid State Commun. **39**, 1017.

Stirling, W.G., and K.A. McEwen, 1987, in: Methods of Experimental Physics, Vol. 23C, eds K. Sköld and D.L. Price (Academic Press, New York) ch. 20, p. 159–240.

Strange, P., H. Ebert, J.B. Staunton and B.L. Gyorffy, 1989, J. Phys.: Condens. Matter **1**, 3947.

Streever, R.L., 1977, Phys. Rev. B **16**, 1796.

Sucksmith, W., and J.E. Thompson, 1954, Proc. Roy. Soc. **225**, 362.

Szewczyk, A., R.J. Radwański, J.J.M. Franse and H. Nakotte, 1992, J. Magn. & Magn. Mater. **104–107**, 1319.

Szpunar, B., and P.A. Lindgard, 1979, J. Phys. F **9**, L55.

Szpunar, B., W.E. Wallace and J.A. Szpunar, 1987, Phys. Rev. B **36**, 3782.

Szymczak, R., H. Szymczak, A. Szewczyk, J. Zawadzki, D. Gignoux, B. Gorges and R. Lemaire, 1988, J. Phys. (Paris) **49**, C8–329.

Szytuła, A., 1991, in: Handbook of Magnetic Materials, Vol. 6, ed. K.H.J. Buschow (North-Holland, Amsterdam) p. 85.

Tagawa, Y., J. Sakurai, Y. Komura, H. Wada, M. Shiga and Y. Nakamura, 1985, J. Phys. Soc. Jpn. **54**, 591.

Takahashi, I., and M. Shimizu, 1990, J. Magn. & Magn. Mater. **90–91**, 725.

Tanaka, R., S. Nakamichi, S. Endo, H. Wada, M. Shiga and F. Ono, 1991, Solid State Commun. **78**, 489.

Terao, K., and M. Shimizu, 1984, Phys. Lett. A **104**, 113.

Terao, K., and M. Shimizu, 1987, J. Magn. & Magn. Mater. **70**, 57.

Tharp, D.E., Y.C. Yang and W.J. James, 1987, J. Appl. Phys. **61**, 4249.

Tharp, D.E., G.J. Long, O.A. Pringle, W.J. James and F. Grandjean, 1992, J. Magn. & Magn. Mater. **104–107**, 1477.

Thuy, N.P., and J.J.M. Franse, 1986, J. Magn. & Magn. Mater. **54–57**, 915.

Thuy, N.P., J.J.M. Franse, N.M. Hong and T.D. Hien, 1988, J. Phys. (Paris) **49**, C8–499.

Tomala, K., G. Czjzek, J. Fink and H.J. Schmidt, 1977, Solid State Commun. **24**, 857.

Tomiyama, F., M. Ono, M. Date, A. Yamagishi, R. Verhoef, F.R. de Boer, J.J.M. Franse and X.P. Zhong, 1991, J. Appl. Phys. **69**, 5539.

Trygg, J., B. Johansson and M.S.S. Brooks, 1992, J. Magn. & Magn. Mater. **104–107**, 1447.

Turek, K., Z. Kąkol and A. Kołodziejczyk, 1987, J. Magn. & Magn. Mater. **66**, 337.

van der Kraan, A.M., P.C.M. Gubbens and K.H.J. Buschow, 1975, Phys. Status Solidi A **31**, 495.

van Steenwijk, F.J., H.Th. Lefever, R.C. Thiel and K.H.J. Buschow, 1977, Physica B **92**, 52.

Verhoef, R., 1990, Thesis (University of Amsterdam).

Verhoef, R., J.J.M. Franse, F.R. de Boer, H.J.M. Heerooms, B. Matthaei and S. Sinnema, 1988a, IEEE Trans. Magn. **MAG-24**, 1948.

Verhoef, R., J.J.M. Franse, A.A. Menovsky, R.J. Radwański, S-Q. Ji, F.M. Yang, H.S. Li and J.P. Gavigan, 1988b, J. Phys. (Paris) **49**, C8–565.

Verhoef, R., F.R. de Boer, J.J.M. Franse, C.J.M. Denissen, T.H. Jacobs and K.H.J. Buschow, 1989, J. Magn. & Magn. Mater. **80**, 41.

Verhoef, R., R.J. Radwański and J.J.M. Franse, 1990, J. Magn. & Magn. Mater. **89**, 176.

Verhoef, R., F.R. de Boer, S. Sinnema, J.J.M. Franse, F. Tomiyama, M. Ono, M. Date and A. Yamagishi, 1992a, Physica B **177**, 223.

Verhoef, R., P.H. Quang, R.J. Radwański, C. Marquina and J.J.M. Franse, 1992b, J. Magn. & Magn. Mater. **104–107**, 1473.

Verhoef, R., S. Sinnema, P.H. Quang and J.J.M. Franse, 1992c, J. Magn. & Magn. Mater. **104–107**, 1325.

Voiron, J., R. Ballou, J. Deportes, R.M. Galera and E. Lelievre, 1991, J. Appl. Phys. **69**, 5678.

Vonsovsky, S.V., U.P. Irkhin, U.V. Irkhin and M.I. Katsnelson, 1988, J. Phys. (Paris) **49**, C8–253.

Wada, H., K. Yoshimura, M. Shiga, T. Goto and Y. Nakamura, 1985, J. Phys. Soc. Jpn. **54**, 3543.

Wada, H., H. Nakamura, E. Fukami, K. Yoshimura, M. Shiga and Y. Nakamura, 1987a, J. Magn. & Magn. Mater. **70**, 17.

Wada, H., H. Nakamura, K. Yoshimura, M. Shiga and Y. Nakamura, 1987b, J. Magn. & Magn. Mater. **70**, 134.

Wada, H., M. Shiga and Y. Nakamura, 1989, Physica B **161**, 187.

Wada, H., M. Shiga and Y. Nakamura, 1990, J. Magn. & Magn. Mater. **90–91**, 727.

Wallace, W.E., F. Pouranian, A.T. Pędziwiatr and E.B. Boltich, 1987, J. Less-Common Met. **130**, 33.

Wassermann, E.F., 1991, J. Magn. & Magn. Mater. **100**, 346.

Wassermann, E.F., M. Acet and W. Pepperhoff, 1990, J. Magn. & Magn. Mater. **90–91**, 126.

Weidner, P., K. Keulerz, R. Löhe, B. Roden, J. Röhler, B. Wittershagen and D. Wohlleben, 1985, J. Magn. & Magn. Mater. **47–48**, 75.

Wiesinger, G., and G. Hilscher, 1991, in: Handbook of Magnetic Materials, Vol. 6, ed. K.H.J. Buschow (North-Holland, Amsterdam) p. 511.

Williams, A.R., V.L. Moruzzi, A.P. Malozemoff and K. Terakura, 1983, IEEE Trans. Mag. **MAG-19**, 1983.

Wohlfarth, E.P., 1977, Physica B **91**, 305.

Wohlfarth, E.P., and P. Mohn, 1988, Physica B **149**, 145.

Wohlfarth, E.P., and P. Rhodes, 1962, Phil. Mag. **7**, 1817.

Wortmann, G., and J. Zukrowski, 1989, Z. Phys. Chem. Neue Folge **163**, 661.

Yakinthos, J., and D. Paccard, 1972, Solid State Commun. **10**, 989.

Yakinthos, J., and J. Rossat-Mignod, 1972, Phys. Status Solidi B **50**, 747.

Yamada, H., 1988, Physica B **149**, 390.

Yamada, H., and M. Shimizu, 1982, J. Phys. F **12**, 2413.

Yamada, H., and M. Shimizu, 1986a, J. Phys. F **16**, 1039.

Yamada, H., and M. Shimizu, 1986b, Phys. Lett. A **117**(6), 313.

Yamada, H., and M. Shimizu, 1987a, J. Magn. & Magn. Mater. **70**, 47.

Yamada, H., and M. Shimizu, 1987b, J. Phys. F **17**, 2249.

Yamada, H., and M. Shimizu, 1988, J. Phys. (Paris) **49**, C8–247.

Yamada, H., and M. Shimizu, 1989, Physica B **155**, 369.

Yamada, H., and M. Shimizu, 1990, J. Magn. & Magn. Mater. **90–91**, 703.

Yamada, H., J. Inoue, K. Terao, S. Kanda and M. Shimizu, 1984, J. Phys. F **14**, 1943.

Yamada, H., J. Inoue and M. Shimizu, 1985, J. Phys. F **15**, 169.

Yamaguchi, M.T., T. Ohta and T. Katayama, 1983, J. Magn. & Magn. Mater. **31–34**, 211.

Yang, Y.C., H. Sun, L.S. Kong, J.L. Yang, Y.F. Ding, B.S. Zhang, C.T. Ye, L. Jin and H.M. Zhou, 1988, J. Appl. Phys. **64**, 5968.

Yaouanc, A., P. Dalmas de Réotier, B. Chevalier and Ph. L'Héritier, 1990, J. Magn. & Magn. Mater. **90–91**, 575.

Yoshida, H., T. Komatsu, T. Kaneko, S. Abe and K. Kamigaki, 1988, J. Phys. (Paris) **49**, C8–275.

Yoshie, H., and Y. Nakamura, 1988a, J. Phys. Soc. Jpn. **57**, 3157.

Yoshie, H., and Y. Nakamura, 1988b, J. Phys. Soc. Jpn. **57**, 3649.

Yoshie, H., and Y. Nakamura, 1990, Hyperf. Interact. **59**, 423.

Yoshie, H., K. Ogino, H. Nagai, A. Tsujimura and Y. Nakamura, 1987, J. Magn. & Magn. Mater. **70**, 303.

Yoshie, H., K. Ogino, H. Nagai, A. Tsujimura and Y. Nakamura, 1988a, J. Phys. Soc. Jpn. **57**, 1063.

Yoshie, H., K. Ogino, H. Nagai, A. Tsujimura and Y. Nakamura, 1988b, J. Phys. Soc. Jpn. **57**, 2525.

Yoshie, H., S. Ozasa, K. Adachi, H. Nagai,

M. Shiga and Y. Nakamura, 1992, J. Magn. & Magn. Mater. **104–107**, 1449.
Yoshimura, K., and Y. Nakamura, 1983, J. Magn. & Magn. Mater. **40**, 55.
Yoshimura, K., and Y. Nakamura, 1984, J. Phys. Soc. Jpn. **53**, 3611.
Yoshimura, K., and Y. Nakamura, 1985, Solid State Commun. **56**, 767.
Yoshimura, K., and Y. Nakamura, 1990, J. Magn. & Magn. Mater. **90–91**, 697.
Yoshimura, K., M. Shiga and Y. Nakamura, 1986a, J. Phys. Soc. Jpn. **55**, 3585.
Yoshimura, K., M. Takigawa, H. Yasuoka, M. Shiga and Y. Nakamura, 1986b, J. Magn. & Magn. Mater. **54–57**, 1073.
Yoshimura, K., M. Nakamura, M. Takigawa, H. Yasuoka, M. Shiga and Y. Nakamura, 1987, J. Magn. & Magn. Mater. **70**, 142.
Yoshimura, K., H. Yasuoka and Y. Nakamura, 1990, J. Magn. & Magn. Mater. **90–91**, 706.
Zhong, X.F., and W.Y. Ching, 1989, Phys. Rev. B **39**, 12018.
Zhong, X.P., R.J. Radwański, F.R. de Boer, R. Verhoef, T.H. Jacobs and K.H.J. Buschow, 1990a, J. Magn. & Magn. Mater. **83**, 143.
Zhong, X.P., R.J. Radwański, F.R. de Boer, T.H. Jacobs and K.H.J. Buschow, 1990b, J. Magn. & Magn. Mater. **86**, 333.
Zhong, X.P., F.R. de Boer, T.H. Jacobs and K.H.J. Buschow, 1990c, J. Magn. & Magn. Mater. **92**, 46.
Zhong, X.P., F.R. de Boer, D.B. de Mooij and K.H.J. Buschow, 1990d, J. Less-Common Met. **163**, 123.
Zhou, G.F., F.R. de Boer and K.H.J. Buschow, 1992, Physica B **176**, 288.

chapter 6

NEUTRON SCATTERING ON HEAVY FERMION AND VALENCE FLUCTUATION 4f-SYSTEMS

M. LOEWENHAUPT and K. H. FISCHER

Institut für Festkörperforschung
Forschungszentrum Jülich GmbH
Postfach 1913, D-5170 Jülich
Germany

Handbook of Magnetic Materials, Vol. 7
Edited by K. H. J. Buschow

CONTENTS

1. Introduction

Valence fluctuation (VF) and heavy fermion (HF) systems have been widely studied in the past two decades (for review articles, see Wohlleben and Coles 1973, Wohlleben 1976, Jefferson and Stevens 1978, Robinson 1979, Grewe et al. 1980, Lawrence et al. 1981, Stewart 1984, Varma 1985, Steglich 1985, Lee et al. 1986, Moshchalkov and Brandt 1986, Newns and Read 1987, Ott 1987, Bickers 1987, Fulde et al. 1988, Schlottmann 1989, Grewe and Steglich 1991). These systems contain either rare-earth (R) elements such as Ce, Sm, Eu, Tm or Yb or actinides such as U or Np. They can be diluted or can form concentrated alloys or compouds with other systems. In both VF and HF systems, the 4f or 5f electrons partly delocalize due to the mixing with the conduction or valence electrons of the outer shells or of the host. In this way they become itinerant in a similar way as the d-electrons in transition metals.

Rare-earth VF or 'intermediate valence' systems are characterized by a non-integral valence or a quantum mechanical mixture of the two ground-state configurations $(4f)^n$ and $(4f)^{n+1}$ with different valences. Due to the Coulomb interactions these states are highly correlated. The mixing with the conduction electrons leads to anomalous properties such as an isostructural phase transition with a large volume change (in SmS), strong pressure, temperature or alloying dependence and anomalies in the thermal, magnetic and transport properties.

In a 'normal' compound the R ions are in a trivalent state and most of them order magnetically at low temperatures. This is in contrast to Ce compounds with the configurations $4f^1$ and $4f^0$ and the valences 3 and 4, and Sm, Eu, Tm and Yb with the valences 3 and 2. For Yb the corresponding configurations are $4f^{13}$ and $4f^{14}$. In the solid state the second ionic configuration has nearly the same ground-state energy as the configuration with valence 3. Together with the hybridization with the conduction electrons, this leads to strong fluctuations of the 4f charge. In addition, one has an effective exchange between the spins of the 4f and conduction electrons that leads to spin fluctuations. The corresponding exchange interaction has a profound effect on most physical properties of these alloys or compounds. It leads to the 'Kondo effect' with a characteristic 'Kondo' temperature T_K, which can vary between a fraction of a degree and several hundred K. In VF systems T_K is considerably larger than in HF systems. At temperatures $T \gg T_K$ all VF and HF systems behave like systems with a stable magnetic moment (leading to a Curie or Curie–Weiss susceptibility). At $T \ll T_K$ this moment either disappears (is 'quenched') or is strongly reduced. The Kondo effect is due to the mixing of 4f and conduction electrons, the degeneracy of

the f-electron ground state and the strong Coulomb repulsion between electrons in a single f-shell.

In the limit of weak hybridization of the 4f and conduction electrons the charge fluctuations are strongly suppressed and there remain only spin fluctuations. In this 'Kondo limit' the f-electron level width is small compared to the (negative) f-electron energy ε_f and compared to the Coulomb energy U. At low temperatures these systems exhibit an unusually high electronic specific heat coefficient γ or a large effective electron mass m^* and are therefore called heavy fermion systems.

At low temperatures ($T \ll T_K$), most HF systems order magnetically. Possible exceptions are $CeAl_3$, $CeCu_6$, $CeRu_2Si_2$ and a few other systems. However, even in these systems, one observes antiferromagnetic correlations and/or a metamagnetic transition in a magnetic field. In addition, HF systems can become superconducting. The HF superconductors presently known are $CeCu_2Si_2$, the only Ce-based system, and UPt_3, URu_2Si_2, UBe_{13}, UPd_2Al_3, and UNi_2Al_3. Some of these systems also order antiferromagnetically at higher temperature or show in a magnetic field a transition to a metamagnetic (metastable) state. VF systems do not order magnetically and do not become superconducting (exception: antiferromagnetic order in TmSe).

Our understanding of VF and HF compounds is based on theoretical and experimental results for *dilute* magnetic alloys (including transition metals) that are summarized in section 3.1. The basic properties involve the Kondo effect, crystal field (CF) effects and effects due to spin–orbit coupling of the 4f electrons. A characteristic property of the Kondo effect is a sharp peak of the 4f electron density of states at or very near to the Fermi energy. This 'Kondo resonance' builds up by strong correlations between 4f- and conduction-electron spins and is connected to a resonance in the scattering of the conduction electrons by the 4f-ions. The Kondo-resonance is strongest at $T = 0$, broadens considerably at T_K and vanishes at high temperatures. However, the Kondo effect is a true many-body effect, and the formation of this resonance cannot be understood in a single-electron picture. In sufficiently dilute systems it leads to a maximum of the impurity resistivity at $T = 0$ and this maximum is shifted to finite temperatures in more concentrated systems. In concentrated alloys and compounds one has in addition *collective* effects at low temperatures ($T < T_K$), the most spectacular of them being superconductivity as observed in the six systems listed above. HF superconductors have been discussed in detail by Lee et al. (1986), Moshchalkov and Brandt (1986), Fulde et al. (1988) and Grewe and Steglich (1991) and will not be considered in this chapter.

A second collective effect is the magnetic order. There is a competition between the Kondo effect, which tries to enforce a nonmagnetic singlet state, and indirect magnetic interactions of the Rudermann–Kittel–Kasuya–Yosida (RKKY) type, which tend to align the 4f moments into some magnetic order and to destroy the Kondo effect. This destruction is due to the fact that the internal (or external) magnetic field lifts the degeneracy of the 4f ground state (see section 3.2).

The third collective effect (which exists only in compounds with lattice periodicity of the 4f ions) is a quasiparticle band structure at low temperatures, which exhibits itself in the splitting of the Kondo resonance according to the symmetries of the R ion lattice. This periodic structure leads to a 'coherence' of the electron waves like

in other itinerant paramagnetic metals and to a vanishing resistivity at $T = 0$. This is because the local magnetic moments either disappear due to the Kondo effect or form a periodic magnetic structure far below the characteristic temperature. At temperatures $T > T_K$ the quasiparticle bands no longer exist and the coherence is destroyed since one has scattering by the local moments. At extremely high temperatures the Kondo effect disappears completely and the moments scatter incoherently, leading to the 'Yosida limit' (Yosida 1957) in the resistivity.

In both diluted and concentrated systems one has a characteristic temperature that separates the magnetic high temperature state from a nonmagnetic low temperature Fermi liquid state (apart from the magnetic order at still lower temperatures due to a small residual magnetic moment). It turns out that many properties scale in a large concentration range as a function of this temperature. For this reason we call this characteristic temperature in all cases the 'Kondo temperature' T_K, where T_K depends on the concentration of 4f ions. In this chapter we summarize shortly the basic properties of VF and HF systems, focussing particularly on the presentation of neutron scattering data.

2. Neutron scattering experiments

The differential cross section for magnetic neutron scattering is proportional to the imaginary part of the dynamic susceptibility or the magnetic excitation spectrum,

$$\frac{\mathrm{d}^2\sigma}{\mathrm{d}\Omega\,\mathrm{d}\omega} = \frac{k_1}{k_0}\frac{1}{2\pi}\left(\frac{g_N e^2}{mc^2}\right)^2 S(\omega, \boldsymbol{Q}, T), \tag{1}$$

with the scattering function

$$S(\omega, \boldsymbol{Q}, T) = [1 - \exp(-\beta\hbar\omega)]^{-1}\,\mathrm{Im}\,\chi(\omega, \boldsymbol{Q}, T). \tag{2}$$

Here, $\beta^{-1} = k_B T$, $\boldsymbol{Q}$ is the momentum transfer and $\hbar\omega$ the energy transfer, $\hbar\boldsymbol{k}_0$ and $\hbar\boldsymbol{k}_1$ are the momenta of the incoming and outgoing neutrons, and m is the electron mass. The Kramers–Kronig relations (White 1970) yield the sum rule

$$\chi(\boldsymbol{Q}, T) = \frac{1}{\pi}\int\frac{\mathrm{d}\omega}{\omega}\,\mathrm{Im}\,\chi(\omega, \boldsymbol{Q}, T), \tag{3}$$

which connects $\mathrm{Im}\,\chi(\omega, \boldsymbol{Q}, T)$ with the static susceptibility $\chi(\boldsymbol{Q}, T)$. The latter is often written in the form

$$\chi(\boldsymbol{Q}, T) = F^2(\boldsymbol{Q}, T)\chi(T), \quad F(\boldsymbol{Q} = 0) = 1, \tag{4}$$

with the magnetic form factor $F(\boldsymbol{Q}, T)$. In the limit $\omega = T = 0$ there is another exact relation between the local static susceptibility $\chi(T)$ and $\mathrm{Im}\,\chi(\omega, 0, T)$ due to Shiba (1975) for dilute systems with a nonmagnetic singlet ground state,

$$\frac{\mu_{\mathrm{eff}}^2}{3}\left.\frac{\mathrm{Im}\,\chi(\omega, 0, T)}{\omega}\right|_{\omega = T = 0} = \frac{\pi}{N}\chi^2(0), \tag{5}$$

with $\mu_{\mathrm{eff}} = g_j\mu_B\sqrt{j(j+1)}$.

Often one assumes that the excitation spectrum $\mathrm{Im}\,\chi(\omega, \boldsymbol{Q}, T)$ can be approximated by a single relaxation process with the relaxation rate $\Gamma(\boldsymbol{Q}, T)/2$. This leads to a quasielastic line for the scattering function

$$S(\omega, \boldsymbol{Q}, T) = [1 - \exp(-\beta\hbar\omega)]^{-1} \chi(\boldsymbol{Q}, T) \frac{\omega\Gamma(\boldsymbol{Q}, T)/2}{\omega^2 + (\Gamma(\boldsymbol{Q}, T)/2)^2}, \tag{6}$$

where $\Gamma(\boldsymbol{Q}, T)$ is the linewidth. As discussed below, such a Lorentz function is sometimes a rather poor approximation for HF and VF systems at low temperatures. It fulfils the sum rule, eq. (3). However, the integral $\int \mathrm{d}\omega\, \mathrm{Im}\,\chi(\omega, \boldsymbol{Q}, T)$ is not convergent. This would imply a diverging total cross-section and shows that eq. (6) does not hold at high frequencies and that $\mathrm{Im}\,\chi(\omega, \boldsymbol{Q}, T)$ has to decay faster than ω^{-1} for large ω. If eq. (6) holds (apart from the high-frequency region), the width $\Gamma(\boldsymbol{Q} = 0, T)$ of the quasielastic line can be expressed by the relaxation time $T_1(T)$ measured in NMR experiments. In particular, for dilute systems with a Q-independent susceptibility (Fulde and Loewenhaupt 1986) one has

$$\frac{1}{T_1} = \frac{k_B T}{\mu_B^2} \gamma_n^2 (H_{hf}^{4f})^2 \lim_{\omega \to 0} [\omega^{-1}\, \mathrm{Im}\,\chi(\omega, T)], \tag{7}$$

where γ_n is the nuclear moment and H_{hf}^{4f} the hyperfine coupling constant to 4f electrons. The limit $\mathrm{Im}\,\chi(\omega) \sim \omega$ for $\omega \to 0$ holds for all Fermi liquid systems. For concentrated systems T_1 depends on a certain Q-average over $\mathrm{Im}\,\chi(\omega, \boldsymbol{Q}, T)$.

At high temperatures or in the classical regime ($k_B T \gg \hbar\omega \approx \Gamma/2$), the scattering function, eq. (6), has a maximum at $\omega = 0$ ('quasi-elastic' scattering). In many HF and VF systems and at low temperatures ($T \ll T_K$) the spectrum $\mathrm{Im}\,\chi(\omega)$ peaks more sharply than in the Lorentzian of eq. (6), though one has still $\mathrm{Im}\,\chi(\omega) \sim \omega$ for $\omega \to 0$. This leads to a 'bump' or 'hump' in $\mathrm{Im}\,\chi(\omega)/\omega$, i.e., the maximum of this function is shifted to finite energies. Depending on $\Gamma(T)$ and T_K one might have inelastic or quasielastic scattering, though the difference might often be within the experimental resolution.

Up to now there is no *comprehensive* review on neutron scattering experiments involving VF and HF 4f-systems. Most of the existing reviews were given as invited talks at conferences and deal mainly with those systems investigated by the authors themselves. We list here some of these reviews in chronological order: Shapiro et al. (1978), Loewenhaupt and Holland-Moritz (1979a,b), Holland-Moritz et al. (1982), Loewenhaupt (1984a), Boucherle and Schweizer (1985), Goldman (1985), Holland-Moritz (1985), Shapiro (1986), Buyers (1986), Stassis (1986), Vettier et al. (1987), Murani (1987b), Rossat-Mignod et al. (1988) and Holland-Moritz (1992).

We should also mention the following reviews that deal at least partly with VF and HF systems in connection with NMR (Dormann 1991), ESR (Elschner and Schlott 1988), and light scattering (Zirngiebl and Güntherodt 1991).

2.1. Cerium-based heavy fermion systems

Most of the neutron scattering experiments on heavy fermion and valence fluctuation 4f-systems involve Ce-based compounds. The huge amount of Ce systems investigated

in this field during the last two decades makes it impossible to discuss all of them. We therefore select characteristic systems for the two groups (HF and VF) which we will discuss in more detail.

Magnetic neutron scattering can give information on the local *magnetic* properties but it cannot answer the question about the *origin* of the magnetic phenomena: are they driven by fast charge fluctuations or by the Kondo effect or by other mechanisms? We think that the Anderson model is the most appropriate model up to now for the description of HF and VF phenomena (see section 3). The separation of the discussion on Ce-based compounds into HF and VF systems follows more from a practical point of view than from theoretical insight. We call Ce compounds VF systems, if all $N = 6$ levels of the $^2F_{5/2}$ multiplet are involved in the determination of the ground state properties. We call them HF systems if only a fraction of the six states are involved. In the latter case the ground state may be a doublet ($N = 2$, this is the case for most cubic and all low symmetry systems) or a quartet ($N = 4$, this is the case for some cubic systems), often well separated from the remaining excited states. Crystal field effects (the origin of the splitting) therefore play an important role in the discussion of HF systems, but are negligible ('wiped out') in VF systems.

Usually the HF systems have much lower Kondo temperatures than the VF systems. Because of this small Kondo energy the RKKY interaction no longer can be ignored. Hence in HF systems one has to consider also spin–spin interactions which in VF systems practically are absent (the 5d–4f coupling seen in the form factor of some VF compounds takes place *on site* at each Ce ion). The spin–spin interactions in HF systems produce either long-range magnetic order or short-range spin correlations. In both cases the magnetic response is drastically modified at low temperatures compared to the spectrum of non-interacting Kondo spins. Spin correlations can be identified by $\boldsymbol{Q}$-dependent measurements on single crystals. Magnetic order is easily seen in neutron diffraction on polycrystalline samples if the ordered moments are sufficiently large ($\geqslant 0.2\mu_B$). Very small ordered moments ($10^{-2}\mu_B$) can only be detected by diffraction from single crystals.

A non-interacting $S = \frac{1}{2}$ Kondo spin ($N = 2$) exibits a quasielastic magnetic response of Lorentzian shape [eq. (6)] down to $T = 0$. By setting the residual width $\Gamma_0/2$ equal to $k_B T_K^N$ we define a neutron deduced Kondo temperature T_K^N which should roughly agree with the (not very precisely) defined transition of the static susceptibility from a Curie–Weiss law to Pauli behavior. In *more concentrated* systems and/or for $S > \frac{1}{2}$ ($N \geqslant 4$) the connection between magnetic response and Kondo temperature is much more complicated (see the theoretical discussion in section 3). Inelastic features are often seen in the low temperature magnetic response. They can be due to (in increasing order of energy for a typical Ce compound):

– magnons in a magnetically ordered phase or pseudo-magnons due to spin correlations above the ordering temperature or in nearly ordering systems,
– Kondo or VF response for $N \geqslant 4$,
– crystal field transitions,
– spin–orbit transitions.

However, it is often very difficult to identify the individual sources for inelasticity

(see, e.g., the discussion of results for $CeRu_2Si_2$ from single crystal and polycrystal data).

We have subdivided the discussion on HF Ce systems into parts dealing with superconducting, non-ordering, antiferromagnetic and ferromagnetic ordering compounds.

2.1.1. Superconducting $CeCu_2Si_2$

So far the only known cerium HF superconducting compound is $CeCu_2Si_2$ (Steglich et al. 1979a). The superconducting properties of Ce- and U-based HF compounds are discussed in detail by Grewe and Steglich (1991). The appearance of superconductivity depends strongly on stoichiometry (copper-deficient samples are *not* superconducting while copper-excess samples have $T_c \approx 0.5$–0.7 K) and for the nominally stoichiometric samples on sample preparation like annealing temperature, cooling rate, etc. $CeCu_2Si_2$ has the tetragonal $ThCr_2Si_2$ structure with $a = 4.09$ Å and $c = 9.91$ Å. For this symmetry we expect a CF splitting of the $^2F_{5/2}$ Ce^{3+} ground state into three doublets. An early inelastic neutron scattering investigation on a nominally stoichiometric polycrystalline sample by Horn et al. (1981a) revealed a CF level scheme with a doublet at 12 meV as first excited state and a second doublet at 31 meV. This level scheme was questioned as specific heat, magnetic susceptibility and resistivity data of $CeCu_2Si_2$ seem to favor a quasi-quartet located around 32 meV (Steglich 1985). The latter scheme is supported by recent neutron investigations by Goremychkin and Osborn (1991b) (quasi-quartet at 30 meV) while neutron investigations by Holland-Moritz et al. (1989a) on copper-deficient $CeCu_{1.8}Si_2$ (0–21–33 meV) and on copper-excess $CeCu_{2.2}Si_2$ (0–17–33 meV) seemed to confirm the first proposed scheme. Even experiments with polarized neutrons (Stassis et al. 1986, Johnson et al. 1985) were not able to locate unambiguously the position of the first excited state. In any case, all data agree on the fact that the ground state of $CeCu_2Si_2$ is a doublet, well separated (at least 12 meV) from the excited states with a total CF splitting around 31 meV. No long-range magnetic order could be detected down to 30 mK by neutron diffraction on a polycrystalline sample (Horn et al. 1981a). Also no significant spatial spin correlations were found in a polarized neutron experiment by Johnson et al. (1985) at 70 mK. The magnetic response, integrated in this experiment over an energy window of ± 20 meV, is essentially Q independent, signalling the local character of the underlying magnetism. From form factor measurements on a (Cu-rich) $CeCu_2Si_2$ single crystal by Stassis et al. (1985) it was concluded that the induced magnetization at 4.2 K is predominantly of 4f electronic character. No indication of a 5d contribution was found in $CeCu_2Si_2$ in contrast to the situation in VF $CeSn_3$ at low temperatures.

The temperature dependence of the quasielastic linewidth of $CeCu_2Si_2$ was investigated by Horn et al. (1981a) and Stassis et al. (1986) between 5 K and room temperature. The results are shown in fig. 1 together with those of $CeAl_3$. The linewidth follows roughly a $T^{1/2}$-law with an extrapolated residual width around 1 meV for $T \to 0$. Data on Cu-deficient and Cu-excess samples towards lower temperatures show a change from the quasielastic line shape ($T = 1.5$ K: $\Gamma/2 \approx 0.8$ meV) to an inelastic line shape below 1 K (Holland-Moritz et al. 1989a). From the low-temperature data a Kondo temperature of about 8 K can be estimated. A similar result for T_K was obtained from the analysis of a polarized neutron scattering experiment by Uemura

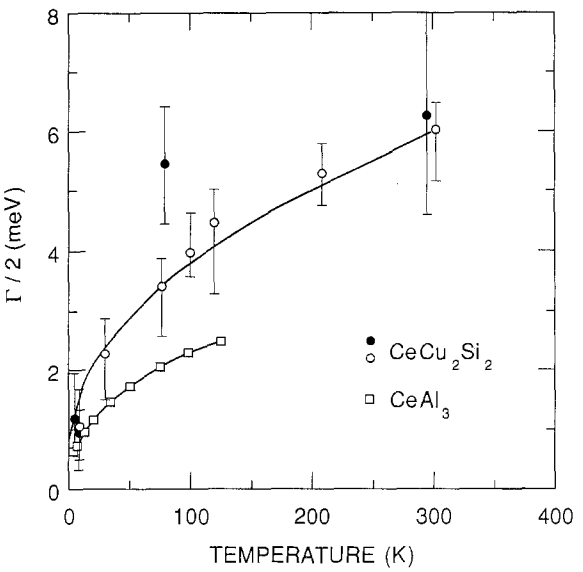

Fig. 1. Temperature dependence of the quasielastic linewidth of $CeCu_2Si_2$ (open circles from Horn et al. 1981a, full circles from Stassis et al. 1986) and of $CeAl_3$ (open squares, Murani et al. 1980). Solid line corresponds to $T^{1/2}$-law.

et al. (1986) at $T = 2.5$ K performed at different external magnetic fields between 0 and 2 T.

Finally we want to note that when passing the superconducting transition temperature no change in the inelastic magnetic response was observed (Holland-Moritz et al. 1989a). Also the search for anomalies in the phonon density of states did not reveal any indications for a strong coupling between the phonos and the Ce 4f electrons (Gompf et al. 1987). The phonon spectra of both $CeCu_2Si_2$ and its non-superconducting reference compound $LaCu_2Si_2$ turned out to be quite similar.

In view of the detailed results obtained on a single crystal of $CeCu_6$ (existence of spin correlations, discrimination between single-site quasielastic and intersite inelastic scattering; see section 2.1.2) it would be of great importance to perform similar experiments on $CeCu_2Si_2$ single crystals. This may then shed some light on the origin of the *inelastic* line observed in $CeCu_2Si_2$ at low temperatures yielding an unphysical degeneracy of six when fitted with the Kuramoto–Müller-Hartmann formula [eq. (30)] (Holland-Moritz et al. 1989a). For a doublet ground state with $S_{\text{eff}} = \frac{1}{2}$ a *quasielastic* line shape is expected in the Kondo limit down to the lowest temperatures. Inelasticity in this case requires the existence of spin correlations as in $CeCu_6$ and $CeRu_2Si_2$ or of a gap.

2.1.2. Non-ordering compounds

For one of these compounds ($CeAl_3$) magnetic ordering with very small ordered moments had been proposed but the bulk of the present experimental evidence is against this suggestion.

$CeAl_3$ crystallizes in the hexagonal Ni_3Sn structure with $a = 6.545$ Å and $c = 4.609$ Å (Taylor 1971). For this symmetry the Ce^{3+} ground state spilts into three doublets with the pure wave functions $|\pm 1/2\rangle$,$|\pm 3/2\rangle$, and $|\pm 5/2\rangle$. There are only two inelastic transitions (between $|\pm 1/2\rangle$ and $|\pm 3/2\rangle$, and between $|\pm 3/2\rangle$ and $|\pm 5/2\rangle$) with nonzero matrix elements of 16/3 and 10/3, respectively. Murani et al. (1977) and Murani (1987b) observed at $T = 5$ K on a polycrystalline sample of $CeAl_3$ two CF transitions at $\Delta_1 = 6$ meV and $\Delta_2 = 8$ meV, though not well separated from each other. If there are really two transitions from the ground state then the ground state has to be the $|\pm 3/2\rangle$ doublet. This implies that the quasielastic scattering which is also observed in $CeAl_3$ must originate from J^z matrix elements (all $J^{\pm}$ matrix elements are zero for this doublet). The temperature dependence of the quasielastic linewidth has been measured by Murani et al. (1980) between 60 mK and 125 K. The results are shown in fig. 1 together with those for $CeCu_2Si_2$. For $T \geqslant 1$ K the linewidth follows nicely a $T^{1/2}$-law and is constant below 1 K with $\Gamma/2 = 0.5$ meV yielding $T_K^N = 6$ K for $CeAl_3$. The line shape is quasielastic down to the lowest measured temperature as expected for an $S_{eff} = \frac{1}{2}$ ground-state doublet. The value of the Kondo temperature of the ground-state doublet as deduced from the neutron data is in fairly good agreement with T_K values obtained from susceptibility measurements on small-sized single crystals of $CeAl_3$ ($T_K^{\chi} = 4.6$ K, Jaccard et al. 1988) and from specific heat data ($\gamma = 1620$ mJ/K^2 mol, Andres et al. 1975). On the other hand, there is a discrepancy between the spin relaxation rates obtained from the quasielastic linewidths of the neutron data and those deduced from NMR, from which the existence of ferromagnetic correlations is inferred (Lysak and MacLaughlin 1985).

The inter-multiplet transition $^2F_{5/2} \rightarrow {}^2F_{7/2}$ was observed by Osborn et al. (1990) who found, surprisingly, *two*, equally intense, lines at 260 and 291 meV with rather large widths of 49 meV, compared to an estimated resolution of 12 meV. The unusually large splitting and linewidth of the excited $^2F_{7/2}$ multiplet compared to the much lower crystal field splitting ($\leqslant 8$ meV) and the small residual quasielastic linewidth of 0.5 meV of the ground-state $^2F_{5/2}$ multiplet is discussed by Osborn et al. (1990) in terms of hybridization-mediated enhanced exchange between f- and conduction electrons.

$CeCu_6$ has an orthorhombic crystal structure at room temperature ($a = 8.11$ Å, $b = 5.10$ Å, $c = 10.16$ Å, Cromer et al. 1960) and becomes monoclinic below $T \approx 220$ K ($a^* = 5.08$ Å, $b^* = 10.12$ Å, $c^* = 8.07$ Å, $\beta = 91.36°$ at 65 K, Asano et al. 1986). It should be noted that most publications on $CeCu_6$ use the orthorhombic notation even at low temperatures. To avoid confusion we use a, b, c, for the orthorhombic and ($a^* = b$, $b^* = c$, $c^* = a$) for the monoclinic notation. In both structures the low local symmetry of the Ce ions splits the ground state into three doublets. $CeCu_6$ seems to be the most thoroughly investigated HF Ce compound. We will therefore present in detail results on CF splitting, quasielastic linewidths, spin correlations, etc., for this compound. Walter et al. (1986) propose a CF level scheme 0–5.5–11 meV while Goremychkin and Osborn (1991a) find a slightly different scheme 0–7–13.8 meV. Figure 2 shows in the upper part the original data of Goremychkin and Osborn (1991a) for polycrystalline $CeCu_6$ (open circles) measured with an incident neutron energy of 40 meV at $T = 20$ K for low-Q values and the

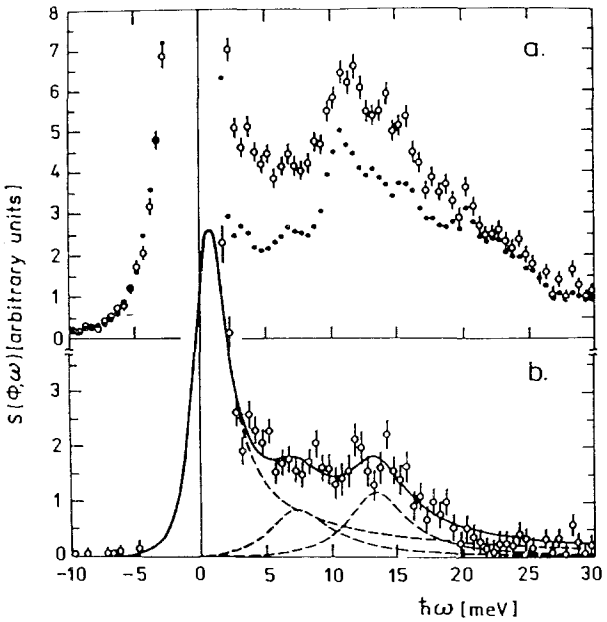

Fig. 2. (a) Neutron spectra of polycrystalline $CeCu_6$ at $T = 20\,K$ measured at 7° scattering angle with $E_0 = 40\,meV$ (open circles). The closed circles show the phonon contribution estimated by multiplying the high-angle data by a scaling function deduced from $LaCu_6$ data. (b) The magnetic response of $CeCu_6$ estimated by subtracting the phonon contribution. The solid line is a fit to three Lorentzians centered at 0, 7.0 and 13.8 meV, shown individually as the dashed lines (Goremychkin and Osborn 1991a).

estimated phonon contribution as deduced from the high-Q data (closed circles). The lower part shows the difference spectrum which is believed to represent the magnetic response of $CeCu_6$ together with a fit involving a quasielastic line and two inelastic CF transitions of Lorentzian line shape. The ground-state doublet is well separated from the excited states which is important for the discussion of the low temperature properties. The temperature dependence of the quasielastic linewidth which was also measured on a polycrystalline sample but with better energy resolution (Walter et al. 1986), follows a $T^{1/2}$-law with a residual width around 0.5 meV (fig. 3). There is no long-range order nor superconductivity down to 10 mK. Below 3 K, however, *short-range* spin correlations become observable as reported by Aeppli et al. (1986) and by Rossat-Mignod et al. (1988). The latter performed a rather detailed neutron scattering investigation on a *single crystal* of $CeCu_6$ in the low temperature region (25 mK to 5 K) which we will discuss in the following.

The anisotropic magnetic behavior seen in susceptibility and magnetization data (Amato et al. 1987) is also reflected in the neutron data when measuring the magnetic response for $\boldsymbol{Q}$ along different symmetry directions. Energy scans for $\boldsymbol{Q}$ along the b^* direction do not show any sizeable magnetic intensity which indicates that the ground-state doublet has an Ising-type anisotropy along the b^*-axis with negligible *transverse* fluctuations (note: neutrons sample only fluctuations perpendicular to $\boldsymbol{Q}$).

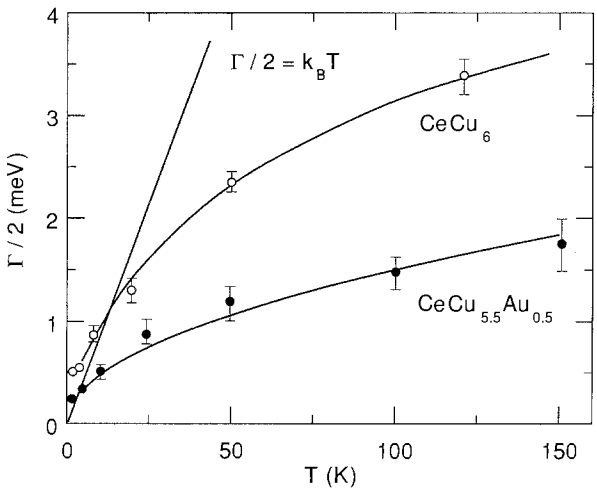

Fig. 3. Temperature dependence of the quasielastic linewidths of polycrystalline $CeCu_6$ (open circles, Walter et al. 1986) and of $CeCu_{5.5}Au_{0.5}$ (closed circles, Stroka et al. 1992). The solid line corresponds to $T^{1/2}$-law.

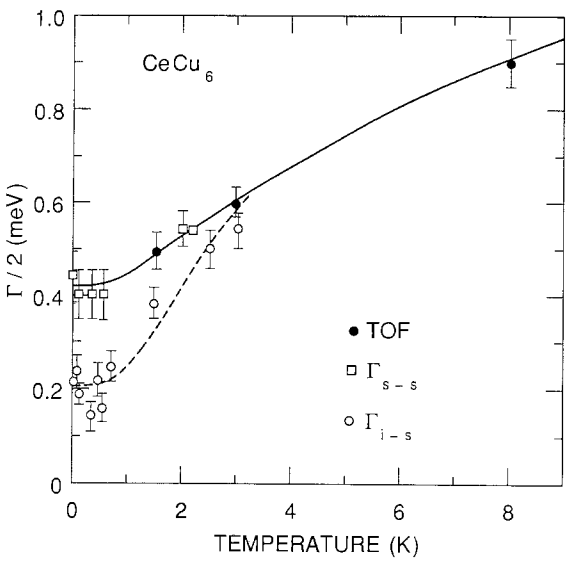

Fig. 4. Temperature dependence of the linewidths for the quasielastic single-site contributions (open squares, Γ_{s-s}) and for the inelastic intersite contributions (open circles, Γ_{i-s}) obtained on a $CeCu_6$ single crystal (Rossat-Mignod et al. 1988). Also shown are the quasielastic linewidths measured on a polycrystalline sample (full circles, Walter et al. 1986).

Energy scans with $\boldsymbol{Q}$ along the a^* and c^* direction, however, show magnetic scattering with a maximum around 0.2–0.3 meV originating from *longitudinal* fluctuations along the b^*-axis. Rossat-Mignod et al. (1988) subdivide the magnetic response into a single-site, $\boldsymbol{Q}$-independent, Kondo-type contribution and an intersite, $\boldsymbol{Q}$-dependent contribution from antiferromagnetic spin correlations.

The single-site fluctuations can be described by a quasielastic line of Lorentzian shape. At 25 mK the half linewidth is $\Gamma_{s-s}/2 = 0.42 \pm 0.04$ meV defining a Kondo temperature of $T_K^N = 5 \pm 0.5$ K. For increasing temperatures Γ_{s-s} fits well to the quasielastic linewidth deduced from time-of-flight measurements on polycrystalline $CeCu_6$ samples as shown in fig. 4. The single-site contribution amounts to about 90% of the spectral weight if integrated over $\boldsymbol{q}$-space within a Brillouin zone. The remaining 10% stems from the intersite correlations which are strongly peaked in $\boldsymbol{q}$-space (figs. 5 and 6) and inelastic in energy. From the peak positions Rossat-Mignod et al. (1988) infer the existence of two different antiferromagnetic spin correlations. There are commensurate correlations along c^* with a propagation vector $\boldsymbol{k}_1 = (0,0,1)$

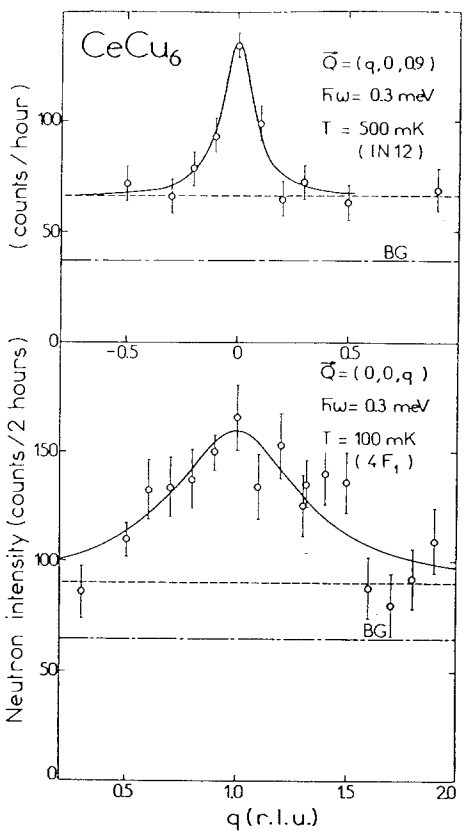

Fig. 5. $\boldsymbol{q}$-Scans around $\boldsymbol{Q} = (0,0,1)$ performed on $CeCu_6$ at a finite energy transfer of 0.3 meV along the directions [001] and [100] at $T = 0.1$ and 0.5 K, respectively (Rossat-Mignod et al. 1988).

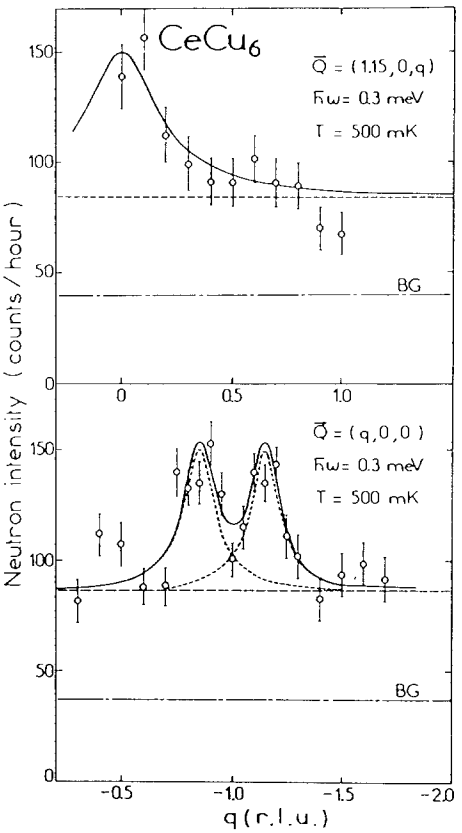

Fig. 6. q-Scans around $Q = (1,0,0)$ performed on $CeCu_6$ at a finite energy transfer of 0.3 meV along the directions [001] and [100] at $T = 0.5$ K (Rossat-Mignod et al. 1988).

and there are also incommensurate correlations along a^* with a propagation vector $k_2 = (0.85,0,0)$. Furthermore, the correlation lengths are anisotropic as can be deduced from the different widths of scans in different q-directions. One obtains at the lowest temperatures: $\xi(a^*) = 9 \pm 1$ Å, extending up to second neighbors, and $\xi(c^*) = 3.5 \pm 0.5$ Å, extending only up to the first neighbor. The temperature dependence of the correlations lengths is shown in fig. 7.

The energy width of the inelastic intersite response Γ_{i-s} is also strongly Q-dependent but with the product $[\chi(Q,T)$ times $\Gamma(Q,T)]$ being roughly constant in the low temperature region. The minimal values for the position and the width in energy at $T = 25$ mK measured at $Q = (0,0,0.9)$ and $(1.15,0,0)$ are $\hbar\omega_0 \approx \Gamma_{i-s}/2 \approx 0.2$ meV. With increasing temperature Γ_{i-s} stays roughly constant up to $T = 1$ K, but increases strongly above 1 K (see fig. 4). Thus the width becomes much larger than the energy which means that the inelastic character of the intersite excitations is lost. Γ_{i-s} and Γ_{s-s} become equal above 3 K where also the magnetic correlations

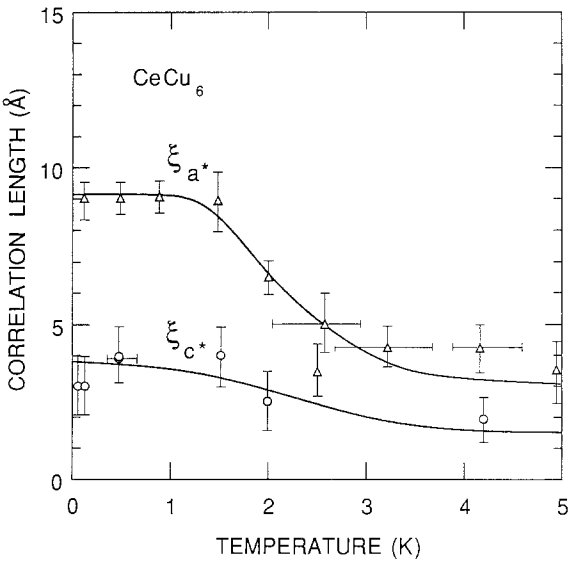

Fig. 7. Magnetic correlation lengths along the a^* and c^*-directions as a function of temperature for $CeCu_6$ (Rossat-Mignod et al. 1988).

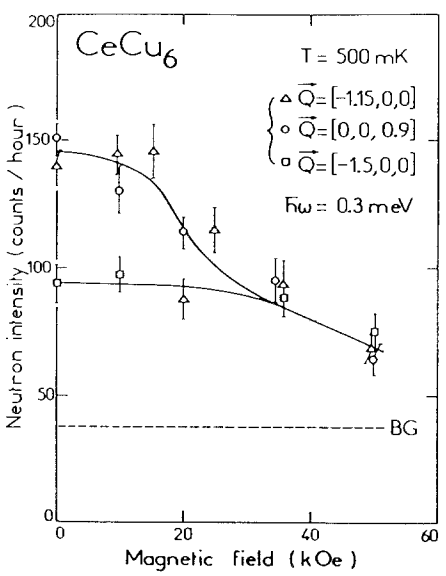

Fig. 8. Magnetic intensities measured on $CeCu_6$ at $T = 0.5$ K as a function of a magnetic field applied along the b^*-direction. The scattering vectors were choosen to follow intensities on the peaks associated with the wave vectors $k_1 = (0, 0, 1)$, $k_2 = (0.85, 0, 0)$, and in between (squares) (Rossat-Mignod et al. 1988).

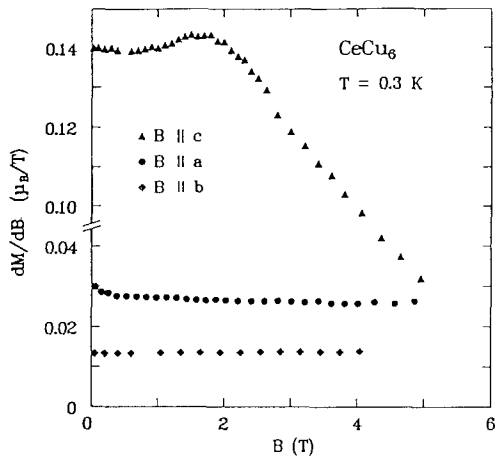

Fig. 9. Susceptibility dM/dB of $CeCu_6$ at $T = 0.3$ K versus B oriented along the different crystalline axes in orthorhombic notation (Schröder et al. 1991).

begin to collapse (see fig. 7). The intersite correlations can also be suppressed by the application of an external field. Figure 8 shows the evolution of the inelastic magnetic intensities in magnetic fields along the easy b^*-axis. The intensity measured at $\boldsymbol{Q} = (-1.5,0,0)$ corresponds to the single-site contribution. At $\boldsymbol{Q} = (0,0,0.9)$ and $(-1.15,0,0)$ both the sigle-site and the intersite contribution are measured. From the suppression of the intersite contribution with field a metamagnetic-like transition at 2.5 T is deduced by Rossat-Mignod et al. (1988). This is supported by the observation of a metamagnetic transition in magnetization measurements along the $c\,(b^*)$ direction by Schröder et al. (1992). They observe a broad maximum in the field dependence of the susceptibility $\chi_c(B) = dM(B)/dB$ around 1.7 T at $T = 0.3$ K (fig. 9). Though less significant, there is also a decrease of single-site intensity with increasing field (fig. 8) which can be correlated with the decrease of the linear term γ of the specific heat in $CeCu_6$ if a magnetic field is applied in the $c\,(b^*)$ direction (Amato et al. 1987).

The low Kondo temperature of $T_K^N = 5$ K and the presence of magnetic correlations at low temperatures indicates that $CeCu_6$ is near a magnetic instability. Negative pressure (i.e. by appropriate alloying to expand the lattice) usually drives a Kondo system towards the magnetic limit. Long-range magnetic order was predicted from specific heat data on $CeCu_{6-x}Au_x$ by Germann and Löhneysen (1989) for $x > 0.1$ and verified by neutron diffraction on polycrystalline $CeCu_{5.5}Au_{0.5}$ (Chattopadhyay et al. 1990). Figure 10 shows the diffraction patterns of $CeCu_{5.5}Au_{0.5}$ ($T_N = 0.9$ K) at $T = 0.05$ and 1 K and the difference pattern (where the magnetic reflections are marked by arrows). Surprisingly, the magnetic Bragg peaks of $CeCu_{5.5}Au_{0.5}$ do not appear at the positions of the short-range correlations of $CeCu_6$. The crystal field level scheme of $CeCu_{5.5}Au_{0.5}$ (Stroka et al. 1992) is only slightly modified (0–8–14 meV) compared to $CeCu_6$ (0–7–13 meV) and thus cannot account for the different magnetic ordering phenomena at low temperatures. It is rather the subtle interplay between

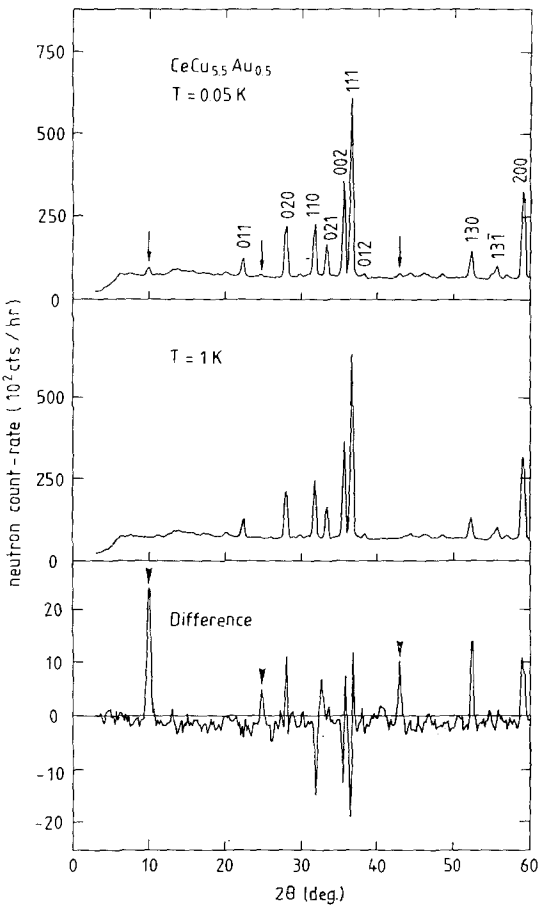

Fig. 10. Diffraction patterns of $CeCu_{5.5}Au_{0.5}$ at $T = 0.05$ and 1 K and the difference pattern. The magnetic reflections are marked by arrows (Chattopadhyay et al. 1990).

RKKY exchange and Kondo energy which produces long-range magnetic order in $CeCu_{5.5}Au_{0.5}$ and short-range correlations in $CeCu_6$. Therefore it is not the CF level scheme that affects the details of the magnetism but it is the different width of the quasielastic and inelastic response of the two HF systems. A comparison of the quasielastic linewidths and of the CF transition between the ground state and the first excited state for $CeCu_6$ and $CeCu_{5.5}Au_{0.5}$ is shown in figs. 3 and 11, respectively.

$CeRu_2Si_2$ has the tetragonal $ThCr_2Si_2$ structure with $a = 4.197$ Å and $c = 9.797$ Å (Hiebl et al. 1983). The crystal field splitting has not yet been determined but it seems likely that the ground state is a doublet, well separated ($\leqslant 20$ meV) from the other two excited doublets (Grier et al. 1988, Severing et al. 1989a). $CeRu_2Si_2$ neither becomes superconducting nor orders magnetically down to 20 mK in zero field. Two

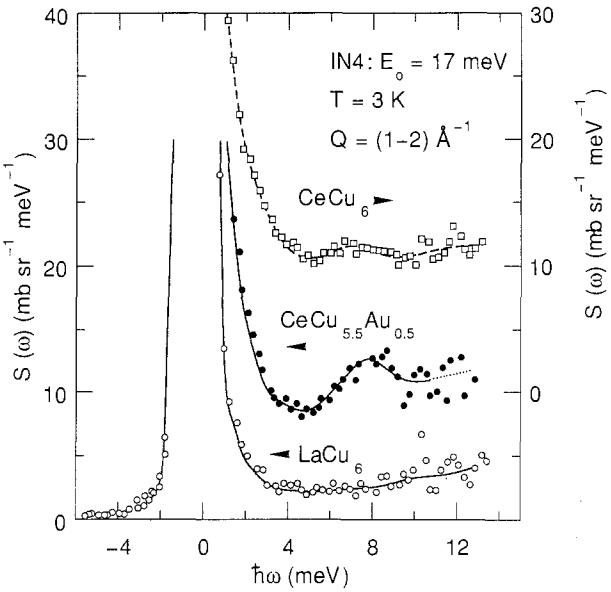

Fig. 11. Neutron spectra of $CeCu_6$, $CeCu_{5.5}Au_{0.5}$ and $LaCu_6$ at $T = 3$ K (Stroka et al. 1992). The spectrum of $LaCu_6$ shows the nonmagnetic background.

maxima in the specific heat at 11 and 84 K can be attributed to a Kondo effect on the ground state doublet ($T_K = 24$ K) and to a Schottky anomaly from an excited state at 220 K (Besnus et al. 1985), respectively. The low temperature susceptibility is very anisotropic ($\chi_c \approx 15\chi_{a,b}$) and at $T = 1.5$ K a metamagnetic transition occurs at $H_c = 8$ T (Haen et al. 1987).

Severing et al. (1989b) performed inelastic neutron scattering experiments on a polycrystalline sample of $CeRu_2Si_2$ and report a *linear* temperature dependence of the quasielastic linewidth between 50 and 250 K. Below 50 K the magnetic response becomes Q-dependent and at 1.5 K the spectra are better fitted with a broad inelastic line ($\Delta \approx \Gamma/2 \approx 1$–$1.5$ meV, depending on Q) than with a quasielastic line. A fit with the analytic function of Kuramoto and Müller-Hartmann [eq. (30)] looks also acceptable but yields an unrealistic large degeneracy of 3.85 ± 0.74 for the ground state in contrast to the expected value of 2 for a doublet. No attempt has been made by Severing et al. (1989b) to fit the low-temperature spectra by a superposition of a (Q-independent) quasielastic and a (Q-dependent) inelastic line. However, this has been done by Rossat-Mignod et al. (1988), Jacoud et al. (1989), and Regnault et al. (1990) who analyzed their data obtained on a *single crystal* of $CeRu_2Si_2$ in analogy to the situation in $CeCu_6$. The quasielastic part then originates from single-site fluctuations, its residual linewidth being $\Gamma/2 \approx 2$ meV. This yields $T_K^N = 23$ K in good agreement with estimates from other measurements. Intersite correlations develop below 50 K and are identified by additional Q-dependent inelastic magnetic intensity. At low temperatures the spectral weight of this intensity is about 40% of the total

intensity (for comparison: 10% in $CeCu_6$). The inelastic intensity is peaked at the incommensurate wave vectors $\boldsymbol{q}_1 = (0.3,0,0)$ and $\boldsymbol{q}_2 = (0.3,0.3,0)$ indicating competing in-plane couplings between first- and second-nearest neighbors. Position and linewidth of the corresponding inelastic response are slightly dispersive with the minimum for both at $\boldsymbol{q}_1$ and $\boldsymbol{q}_2$. The range of values at $T = 1.4\,\mathrm{K}$ is $\Delta = 1.2$–$1.6\,\mathrm{meV}$ and $\Gamma/2 = 0.8$–$2\,\mathrm{meV}$. The inelastic linewidth at $\boldsymbol{q}_2$ and the quasielastic linewidth merge above 30 K (compare: 3 K for $CeCu_6$). The polycrystalline data from Severing et al. (1989b) agree with the single-crystal data around 50 K but give a slightly steeper and linear increase towards higher temperatures.

As in $CeCu_6$ the magnetic correlations in $CeRu_2Si_2$ can be suppressed by the application of an external field (in c-direction). The intersite contribution disappears above the metamagnetic transition at 8.3 T and at the highest investigated field of 10 T the scattering becomes $\boldsymbol{Q}$-independent and purely quasielastic. The single-site response is only little affected by the application of the external field. It is evident that the behavior of the two non-ordering HF compounds $CeCu_6$ and $CeRu_2Si_2$ is very similar except for an increase of the characteristic energy scale from $CeCu_6$ to $CeRu_2Si_2$ by roughly a factor of five. This is also reflected in the *decrease* of γ from $1600\,\mathrm{mJ/K^2\,mol}$ for $CeCu_6$ to $350\,\mathrm{mJ/K^2\,mol}$ for $CeRu_2Si_2$.

$CeRu_2Si_2$ is also close to a magnetic instability. Alloying [(Ce, La)Ru_2Si_2: Mignot et al. 1990; $CeRu_2(Si,Ge)_2$: Mignot et al. 1991, Dakin et al. 1992] which corresponds to *negative* pressure produces long-range magnetic order at low temperatures with roughly the same incommensurate wave vector $\boldsymbol{q}_1 = (0.31,0,0)$ that describes the short-range correlations in the pure compound. An inelastic neutron study of a single crystal of $Ce_{0.8}La_{0.2}Ru_2Si_2$ ($T_N = 5.7\,\mathrm{K}$) by Jacoud et al. (1992) at $T = 1.5\,\mathrm{K}$ shows that single-site fluctuations ($\Gamma/2_{s-s} = 0.7\,\mathrm{meV}$, i.e. $T_K^N = 8\,\mathrm{K}$) are even present in the long-range ordered state. The simultaneous presence of a single-site and of an intersite response has also been observed in inelastic neutron scattering data on polycrystalline samples of $CeRu_2Si_{2-x}Ge_x$ by Rainford et al. (1992) in the paramagnetic region.

$CeNi_2Ge_2$ is tetragonal with $a = 4.150\,\text{Å}$ and $c = 9.854\,\text{Å}$ (Knopp et al. 1988a). Like $CeRu_2Si_2$ it does not order nor becomes superconducting and seems to have a doublet ground state. Yet the CF splitting itself has not been determined. The low-temperature specific heat data taken at $B = 4\,\mathrm{T}$ (to suppress coherence effects in zero field) can be quantitatively fitted with a $S_{\mathrm{eff}} = \frac{1}{2}$ impurity Kondo model yielding $T_K = 29\,\mathrm{K}$ ($\gamma = 300\,\mathrm{mJ/K^2mol}$, Knopp et al. 1988a). Knopp et al. also report on the temperature dependence of the quasielastic part of the magnetic response measured on a polycrystalline sample with cold ($E_0 = 3.15\,\mathrm{meV}$) and thermal ($E_0 = 12.5\,\mathrm{meV}$) neutrons between 5 and 200 K. They describe all spectra with just one quasielastic line of Lorentzian shape. For $T \geqslant 40\,\mathrm{K}$ the linewidth increases smoothly with temperature reaching 6 meV at 200 K. At 30 K there is a shallow minimum ($\Gamma/2 \approx 3.5\,\mathrm{meV}$) and again a smooth increase of the linewidth towards the low-temperature limit ($\Gamma_0/2 = 4\,\mathrm{meV}$). For an $S = \frac{1}{2}$ Kondo system, however, no minimum in the $\Gamma(T)$ curve is expected. It is therefore likely that the observed minimum is an artifact of the fitting procedure because of the restriction to just one quasielastic Lorentzian line. A similar difficulty was discussed for the polycrystalline data of $CeRu_2Si_2$. There the fit of the magnetic response with just one function also

led to inconsistencies. Again, single-crystal data are necessary to elucidate the situation in $CeNi_2Ge_2$.

$CePt_2Si_2$ has the tetragonal $CaBe_2Ge_2$-type structure with $a = 4.25$ Å and $c = 9.79$ Å (Hiebl and Rogl, 1985). Though its valence is near 3+ (Röhler, 1987) its properties seem to ly in between those of HF and VF compounds. Resistivity and susceptibility exhibit a broad maximum around 76 and 60 K, respectively. Single-crystal data show that the behavior of $CePt_2Si_2$ is anisotropic with even different temperatures for the maxima in ***a*** and ***c*** directions: 55 and 85 K for the resistivity curves, 55 and 65 K for the susceptibility curves (Gignoux et al. 1988a). Specific heat data interpreted by Ayache et al. (1987) in terms of an $S_{\text{eff}} = \frac{1}{2}$ Kondo contribution with $T_K = 70$ K and a Schottky peak near 90 K arising from a doublet ground state and an excited doublet at $\Delta = 240$ K(20.7 meV). The low-temperature specific heat yields a linear coefficient γ around 100 mJ/K^2 mol (with a maximum of 130 mJ/K^2 mol at $T = 1.4$ K). From all this one would expect a magnetic response consisting of a quasielastic line with residual width around 6–8 meV and inelastic CF transitions around 20 meV. Two groups have performed inelastic neutron scattering experiments on polycrystalline samples of $CePt_2Si_2$. Both observe at all temperatures between 5 and 200 K only a rather broad (15–20 meV) magnetic response with no indications of well defined inelastic CF transitions (Grier et al. 1988, Gignoux et al. 1988b). The unusual temperature dependence of the spectral width exhibiting a minimum around 100 K, however, seems to indicate that the magnetic response must contain inelastic features reminiscent of CF transitions though presumably considerably broadened. This point should be checked by neutron scattering on single crystals.

2.1.3. Antiferromagnetic-ordering compounds

Most of the HF compounds show magnetic order at low temperatures and from these compounds again the majority orders antiferromagnetically (including also more complicated types of magnetic order like modulated or spiral structures). Even in the ordered state the specific heat data show a rather large linear T term though typically reduced by a factor of 10 ($CeAl_2$: 130 to 180 mJ/K^2 mol; CeB_6: 260 mJ/K^2 mol; $CeCu_2$: 82 mJ/K^2 mol, Bredl 1987) if compared to a non-ordering Ce compound with similar T_K($CeCu_6$: 1600 mJ/K^2 mol). An exception is $CePb_3$ with $\gamma =$ 1400 mJ/K^2 mol (Lin et al. 1987). Most of the antiferromagnetically ordering HF compounds exhibit in addition a metamagnetic transition and have rather complicated phase diagrams in the H–T and p–T planes. Usually the ordered magnetic moment is reduced if compared to the free CF ground state moment ('Kondo compensation'). In some cases, however, the exact CF ground state is not known or modified by other interactions (e.g., quadrupolar, CeB_6). This makes the comparison, of course, impossible. Inelastic neutron scattering experiments cover

- the ordered region (magnons),
- quasielastic scattering above T_N, and
- crystal field transitions including CF–phonon interactions.

$CeAl_2$ has the cubic Laves-phase structure with $a = 8.06$ Å. The Ce ions form a diamond lattice which can be viewed as two interpenetrating fcc lattices shifted by

$(\frac{1}{4},\frac{1}{4},\frac{1}{4})$. The local cubic symmetry is expected to split the $J = 5/2$ Ce^{3+} ground state into a low lying Γ_7 doublet and an excited Γ_8 quartet. Instead of the expected *single* inelastic $\Gamma_7 \rightarrow \Gamma_8$ transition, however, *two* inelastic transitions were observed in $CeAl_2$ by neutron scattering (Loewenhaupt et al. 1979) and explained by the formation of a bound state between the crystal field transition and a phonon (Thalmeier and Fulde 1982, Thalmeier 1984). The influence of this strong coupling on the lattice dynamics (unusual frequency shifts and line broadenings with temperature) have been reported by Reichardt and Nücker (1984) and Loewenhaupt et al. (1987). Reviews of this phenomenon can be found in Fulde and Loewenhaupt (1986) and Thalmeier and Lüthi (1991) and will therefore not be discussed further in this chapter. The energies of the two CF transitions are around 9 and 17 meV and the energy of the interacting phonon varies between 11 meV (at 6 K) and 13 meV (at 300 K). Hence the low-temperature properties of $CeAl_2$ are mainly determined by the Γ_7 ground-state doublet. The Kondo temperature is estimated to be $T_K = 5 \pm 2$ K (Steglich et al. 1979b) analysing the residual quasielastic linewidth and specific heat data on diluted (La,Y) and concentrated $CeAl_2$. The Kondo temperature is of the same order as the antiferromagnetic ordering temperature $T_N = 3.8$ K. The ordering is incommensurate with wave vectors of the form $(\frac{1}{2}+\delta, \frac{1}{2}-\delta, \frac{1}{2})$ where $\delta = 0.11$ (Barbara et al. 1977, 1979). Barbara et al. proposed a single-q collinear structure with (111) moment direction and a long-period sinusoidally modulation ($\delta^{-1} \approx 9$ atomic layer spacings) of the *value* of the moments. The absence of higher order satellites down to $T_N/10$ was taken as evidence for the existence of Kondo compensated moments (at the nodes of the modulation) even for $T \rightarrow 0$. Any moment value between zero and $0.89\mu_B$ can be realized in this structure with an average value of $0.63\mu_B$. The average value corresponds to the free Γ_7 value ($0.71\mu_B$) reduced by 10%. A triple-q structure was proposed by Shapiro et al. (1979) to explain the observation of intensity at the $(\frac{1}{2},\frac{1}{2},\frac{1}{2})$ position. This latter model, however, was disproved by Barbara et al. (1980) and Boucherle et al. (1981) who showed that the $(\frac{1}{2},\frac{1}{2},\frac{1}{2})$ intensity belongs to another phase of $CeAl_2$ which can be stabilized by defects or pressure. To account for the pressure effects different T–p phase diagrams were proposed by Barbara et al. (1977) and Schefzyk et al. (1984).

For a long time the question of magnetic structure of $CeAl_2$ seemed to be settled in favor of the single-q collinear modulated structure proposed by Barbara et al. (1977). Later, however, Forgan et al. (1990) produced in an applied field a single-domain $CeAl_2$ single crystal and reported that even in this state there are two (coupled) modulations. This excludes a single-q structure. They therefore propose a double-q, spiral structure which is nonchiral (i.e., the moments in different sublattices rotate in different senses). Furthermore there are no zero moments in this structure. All moment values for the spiral structure lie between 0.53 and $0.75\mu_B$ with the same average value of $0.63\mu_B$ as given for the sinusoidally modulated structure.

The magnetic excitations (magnons) in the ordered state at $T = 1.2$ K have been measured in zero field on a (multidomain) single crystal by Osborn et al. (1987). The spectra consist of broadened bands which can be characterized by two (overlapping) Gaussian peaks. The two bands were interpreted as originating from an acoustic magnon branch centered at 0.7 meV and with a FWHM of 0.4 meV and from an

optic magnon branch centered at 1.2 meV and with a FWHM of 0.8 meV. Both branches show little dispersion except near the ordering wave vectors where the acoustic branch softens. A complete softening could not be observed, presumably due the presence of several domains. Therefore the reported value of 0.45 meV for the magnon gap may not be the true gap value (if there is a gap at all). Specific heat measurements at low temperatures (Steglich et al. 1979b) yield a linear term in T with $\gamma = 130\,\mathrm{mJ/K^2\,mol}$ and a T^3 term indicating the presence of *gapless* antiferromagnetic magnons. At $T_N = 3.8\,\mathrm{K}$ the entropy is only $\frac{1}{2}R\ln 2$, reaching the full value of $R\ln 2$ for a doublet not below 15 K. This shows the existence of short-range spin correlations in $CeAl_2$ far above the ordering temperature which was also inferred from the Q-dependence of the quasielastic response measured with relaxed energy resolution (Steglich et al. 1979b). An experiment with improved energy resolution (Loewenhaupt 1984b) shows that the low-energy response ($\leqslant 2$ meV) contains at $T = 5\,\mathrm{K}$ beside the quasielastic also an inelastic component. This reminds of the situation for the non-ordering HF compounds $CeCu_6$ and $CeRu_2Si_2$ as reported by Rossat-Mignod et al. and discussed in section 2.1.2. Unfortunately, there are no investigations of the short-range order in $CeAl_2$ above T_N using a single crystal which might then be directly compared with the other results.

The evolution of the quasielastic linewidth of $CeAl_2$ with temperature was reported by Horn et al. (1981b) and is shown together with that of CeB_6 in fig. 12. Above 15 K ($\Gamma/2 = 0.5$ meV) up to room temperature ($\Gamma/2 = 5$ meV) the linewidth has a nonlinear temperature dependence. If approximated by a $T^{1/2}$-law (solid line in fig. 12) there are, however, considerable deviations from this law around 50 to 100 K. Below 15 K the quasielastic linewidth is temperature independent (Steglich et al. 1979b) if

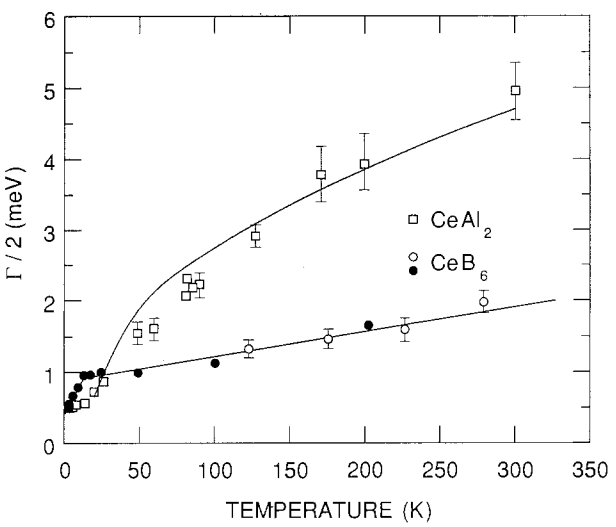

Fig. 12. Temperature dependence of the quasielastic linewidth of $CeAl_2$ (open squares: Horn et al. 1981b, the solid line corresponds to $T^{1/2}$-law) and of CeB_6 (open circles: Horn et al. 1981c; closed circles: Neuhaus 1987).

measured with moderate energy resolution. But we have to keep in mind that the magnetic response in this temperature region is Q-dependent and develops additional inelastic features and thus a description with just a quasielastic line is certainly not adequate. These complications do not arise for dilute samples of the type $Ce_{1-x}M_xAl_2$ with M = La, Y for $x \leqslant 0.6$ and with M = Sc for $x \leqslant 0.4$ (Horn et al. 1981b). For all samples a $T^{1/2}$-law has been claimed in the temperature range from 2.5 to 60 K. Dilution with La (producing *negative* chemical pressure) reveals smaller linewidths compared to $CeAl_2$ while for Y and Sc diluted samples (*positive* chemical pressure) the linewidths become larger. For $Ce_{1-x}Sc_xAl_2$ and $x \geqslant 0.5$ the strong lattice pressure even seems to drive the Ce ions into a VF state (Loewenhaupt et al. 1981) exhibiting a considerably larger and nearly temperature independent quasielastic linewidth (for $x = 0.5$: $\Gamma/2 \approx 20$ meV).

CeB$_6$ crystallizes in the cubic CaB_6 structure with $a = 4.135$ Å. This structure can be viewed as a bcc CsCl structure with Ce^{3+} ions at the body-centered positions and boron octahedra at the cube corners. The Kondo behavior of the *dilute* system (CeLa)B_6 ($T_K = 1$ K) has been nicely demonstrated by resistivity (see fig. 56) and specific heat (see fig. 57) measurements. The behavior of the full compound CeB_6, on the other hand, was considered to be mysterious for quite some time (see, e.g., Komatsubara et al. 1983). The clue for a better though not yet complete understanding of the magnetic properties of CeB_6 was the observation of an unexpectedly large (47 meV) crystal field splitting with a Γ_8 ground state and a Γ_7 excited state and an additional splitting of the Γ_8 quartet deduced indirectly from an energy shift of the $\Gamma_8 \rightarrow \Gamma_7$ transition at temperatures below 20 K (Zirngiebl et al. 1984, Loewenhaupt et al. 1985). Strong quadrupolar interactions yield in zero field at $T_Q = 3.3$ K a transition to long-range antiferro-quadrupolar ordering, followed at $T_N = 2.3$ K by a transition to a noncollinear, commensurate, double-q magnetic structure (Effantin et al. 1985). The latter transition is suppressed by a magnetic field of 1.5 T, whereas the former transition is shifted to higher temperatures in high magnetic fields. A similar phase diagram is found for dilute $Ce_{0.75}La_{0.25}B_6$ but with reduced $T_Q \approx T_N \approx 1.6$ K and increased metamagnetic transition field of 2.6 T (Erkelens et al. 1987). The ordered magnetic moment ($0.28\mu_B$) of CeB_6 is strongly reduced compared to the free Γ_8 moment ($1.57\mu_B$). The entropy determined from specific heat data is only R ln 2 at T_N, it reaches R ln 3 around 10 K but R ln 4 not below 50 K (Peysson et al. 1986). This led Kunii (1988) to propose a somewhat peculiar splitting of the Γ_8 quartet into a ground-state doublet and two excited singlets at 0.78 meV (9 K) and 8.2 meV (95 K). Any splitting of the Γ_8 state in the paramagnetic phase, however, could not yet be observed directly.

The temperature dependence of the quasielastic linewidth was thought to follow a $T^{1/2}$-law (Horn et al. 1981c) between 5 K ($\Gamma/2 = 0.4$ meV) and 280 K ($\Gamma/2 = 2$ meV). Figure 12 shows some of these results deduced from low-resolution data together with those of a later experiment with better energy resolution (Neuhaus 1987). A closer inspection of the low-temperature region, however, reveals instead of the claimed overall $T^{1/2}$ dependence a *kink* in the $\Gamma(T)$ curve at $T = 20$ K separating a *steep linear* increase below 20 K from a *flat linear* increase above 20 K (solid line through CeB_6 data points in fig. 12). From the residual widths one obtains for CeB_6 $T_K^N = 3$–4.5 K depend-

ing on the extrapolation scheme ($T^{1/2}$ or linear). The results for *dilute* $Ce_{0.5}La_{0.5}B_6$ (Neuhaus 1987) give in general lower values for the line widths. There is a kink around 15 K and the residual width yields $T_K^N = 2.3$ K (for linear extrapolation). The reduced Kondo temperature for $Ce_{0.5}La_{0.5}B_6$ is in line with $T_K = 1$ K for the dilute limit of (CeLa)B_6. The kink in both curves is further an (indirect) indication of the Γ_8 splitting in the paramagnetic state. It may be smaller in $Ce_{0.5}La_{0.5}B_6$ than in CeB_6. Down to $T_N = 2.3$ K, including the antiferro-quadrupolar ordered region below T_Q, the magnetic response of CeB_6 is quasielastic (Neuhaus 1987). These results obtained for a polycrystalline sample agree with the observation of Regnault et al. (1988) that there is no inelastic feature in the magnetic spectrum of a single crystal in zero field at $T = 2.3$ K. Application of 4 T, however, produces dispersive magnetic excitations in the antiferro-quadrupolar phase ar $T = 2.3$ K with energies up to 1 meV (Regnault et al. 1988). In the magnetically ordered phase at $T = 1.5$ K, well below T_N, the magnon density of states measured on the polycrystalline sample peaks at 0.5 meV and 1 meV which can be interpreted as originating from acoustic and optic magnon branches. These inelastic features (magnons) soften towards T_N and disappear above T_N (Neuhaus 1987).

$CeCu_2$ crystallizes in the orthorhombic $CeCu_2$-type structure with $a = 4.43$ Å, $b = 7.06$ Å, and $c = 7.47$ Å (Larson and Cromer 1961). Electrical resistivity (ln T law) and other properties classify this compound as Kondo lattice (Gratz et al. 1985, Onuki et al. 1985b). Below $T_N = 3.5$ K $CeCu_2$ orders in a simple antiferromagnetic structure (fig. 13) with the moments of the two Ce ions of the primitive unit cell in opposite

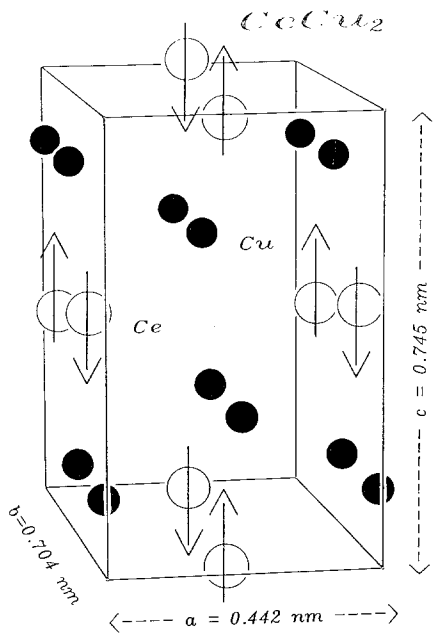

Fig. 13. Magnetic structure of $CeCu_2$ (Trump et al. 1991).

directions and along the c-axis (Trump et al. 1991, Nunez et al. 1992). Surprisingly, this structure is much simpler than those of the 'normal' RCu_2 compounds (see, e.g., Lebech et al. 1987) and of the other antiferromagnetic Ce HF compounds discussed in this section. The susceptibility and the magnetization are very anisotropic in the ordered as well as in the paramagnetic phase of $CeCu_2$ with the easy axis in the $\boldsymbol{a}$-direction, the hard axis in the $\boldsymbol{b}$-direction, and the $\boldsymbol{c}$-direction in between. The strong magnetic anisotropy is mainly due to single-ion crystal field effects. The low-symmetry crystal field splits the $J = 5/2$ ground state of Ce^{3+} into three doublets. Inelastic neutron scattering experiments on the polycrystalline sample yield a level scheme 0–9–23 meV from which, however, only the position of the 23 meV level could be determined directly (Loewenhaupt et al. 1988). The position of the first excited level was inferred indirectly from the temperature dependence of the intensity of the 23 meV transition and from the evolution of the entropy with temperature ($\frac{2}{3} R \ln 2$ at T_N, $R \ln 2$ at 16 K, $R \ln 4$ around 50 K; Loewenhaupt et al. 1990). Furthermore, there seems to be a strong coupling between the crystal field transition from the first to the second excited level ($23 - 9 = 14$ meV) and a phonon around 14 meV (Loewenhaupt et al. 1988, 1990). This is a similar situation as the CF–phonon bound state in $CeAl_2$ except that in $CeCu_2$ the involved CF transition connects *excited* levels and hence this effect can only be observed at elevated temperatures.

The magnons have been measured at $T = 1.4$ K, well below T_N, on a single crystal of $CeCu_2$ in all main symmetry directions (Trump 1991). The dispersion relations in [010] and [001] direction are shown in fig. 14. There are two magnon branches: an acoustic and an optic branch. The acoustic magnons exhibit at the Γ-point a small gap of 0.06 meV (in agreement with specific heat data of Takayanagi et al. 1990), followed by a steep increase in energy at low q-values and with an extended flat portion towards the zone boundary with energies around 0.5 meV. The optic branch is strongly dispersive with energies between 0.8 and 1.5 meV. The magnon dispersion curves can

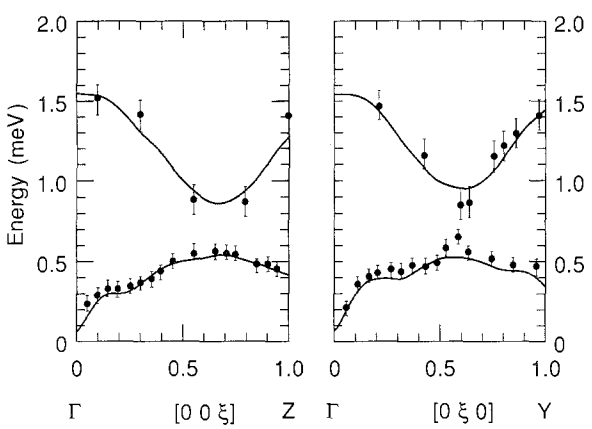

Fig. 14. Magnon dispersion relations of $CeCu_2$ in [010] and [001] direction at $T = 1.4$ K. Solid line is fit with model as described in the text (Trump, 1991).

be fitted with an anisotropic Heisenberg model with dominant antiferromagnetic exchange for short distances and weaker ferromagnetic exchange of long-range character (solid lines in fig. 14). Above T_N the low-energy magnetic response becomes quasielastic with mainly Gaussian line shape at low temperatures and changing around 50 K to mainly Lorentzian line shape at higher temperatures (Loewenhaupt et al. 1990). A good fit of the spectra is obtained allowing for a superposition of both types of lineshapes with an increasing ratio of Lorentzian to Gaussian intensity with increasing temperatures. The Gaussian width is nearly independent of temperature ($\Gamma/2 = 0.8$ meV). It is interpreted as being due to short-range spin correlations which show also up in the Q-dependence of the quasielastic intensity and in strong contributions to the specific heat above T_N (Takayanagi et al. 1990). The Lorentzian width increases linearly with temperature ($T = 5$ K: $\Gamma/2 = 0.4$ meV; $T = 200$ K: $\Gamma/2 =$ 1.4 meV) and is identified with lifetime effects of single-ion relaxation processes of the Ce paramagnetic moments. The residual width of Lorentzian shape may be reminiscent of the Kondo effect ($T_K^N = 4$ K) though strongly modified by the presence of spin correlations.

$CePb_3$ has the simple cubic Cu_3Au structure with $a = 4.87$ Å. This compound has drawn much attention since Lin et al. (1985) reported that it exhibits besides its HF properties and magnetic ordering at $T_N \approx 1.1$ K also a magnetic-field induced superconducting transition. The observation of superconductivity in $CePb_3$, however, turned out to be an impurity effect. The magnetic ordering was investigated in zero field on a multidomain single crystal by Vettier et al. (1986). At $T = 30$ mK, well below $T_N = 1.16$ K, they observe magnetic Bragg peaks at eight incommensurate positions around the X-point $(0, 0, \frac{1}{2})$, corresponding to propagation vectors of the form $(\mu_1, \mu_2, \frac{1}{2})$ with $\mu_1 = 0.135$ and $\mu_2 = 0.058$. *Assuming* a single-q structure (although couplings between different components cannot be ruled out) they propose a sinusoidally modulated structure with a modulation amplitude of $m_0 = (0.55 \pm 0.10)\mu_B$ and the moments along the (001) direction. This type of structure is similar to the single-q modulated structure proposed by Barbara et al. (1977) for $CeAl_2$ which, however, was disapproved by Forgan et al. (1990). As in $CeAl_2$ there were no higher-order harmonics observed in $CePb_3$ indicating a pure sine wave modulation of the moments in a single-q structure and hence the presence of Kondo compensated zero moments at the nodes. For this structure, however, the moment directions (001) do not coincide with the axis of easy magnetization (111). It is therefore more likely that the magnetic structure of $CePb_3$ is of triple-q type rather than of single-q type (Welp 1988). Unfortunately, the validity of the assumption of a single-q structure was not yet checked in a diffraction experiment on a single-domain $CePb_3$ crystal. Neutron diffraction under pressure reveals a transition from the incommensurate structure at 0.7 GPa to a simple type-II structure, which corresponds to alternating ferromagnetic [111]-planes (Morin et al. 1988). T_N decreases to 0.6 K at 0.7 GPa, followed by an increase and a possible maximum around 1.3 GPa with $T_N \approx 1$ K (Kirsch et al. 1992).

Inelastic neutron scattering experiments on the single crystal at $T = 200$ mK (Vettier et al. 1986) revealed a broadened $\Gamma_7 \rightarrow \Gamma_8$ transition at 1.5 THz (= 6.2 meV) in agreement with inelastic neutron data on a polycrystalline sample at $T = 4$ K ($\Delta = 5.8 \pm 0.2$ meV with $\Gamma/2 = 1.9 \pm 0.2$ meV) by Renker et al. (1987). From intensity considerations it was

concluded that Γ_7 is the ground state. The temperature dependence of the Lorentzian quasielastic linewidth was reported by Balakrishnan et al. (1989) for temperatures between 2 and 128 K. It follows a $T^{1/2}$-law with a residual width of only 0.17 meV yielding a Kondo temperature of $T_K^N = 2$ K. No evidence could be found for any Q-dependence (beyond the single-ion magnetic form factor) of the magnetic intensity over the range 0.2 to 2.4 $Å^{-1}$ at any investigated temperature. This is surprising in view of the results for the other ordering compounds as discussed in this section but it is in line with the single-ion Kondo behavior of the whole series (Ce, La)Pb_3 from the very dilute limit to the full compound (Lin et al. 1987).

CeT_2Si_2 compounds crystallize in the tetragonal $ThCr_2Si_2$ structure. The magnetic ordering has been investigated with neutron diffraction for T = Au, Ag, Pd and Rh by Grier et al. (1984) where also the lattice parameters can be found. All four compounds order antiferromagnetically with $T_N = 10$ K for T = Au, Ag and Pd and $T_N = 39$ K for T = Rh and ordered moments of $1.29\mu_B$ (Au), $0.73–0.93\mu_B$ (Ag, assuming sine wave or square wave modulation) and 0.62 (Pd). Though the structures of these three compounds are different in detail they have in common that there are ferromagnetic planes with the moments perpendicular to the planes but along the direction of antiferromagnetic coupling or modulation. The fourth compound $CeRh_2Si_2$, shows a second phase transition around 27 K and a different antiferromagnetic type of ordering (of which the low temperature structure is not yet clear). The first three compounds (Au, Ag, Pd) show well-defined crystal field transitions (Severing et al. 1989a) with a doublet ground state sufficiently separated from the next excited doublet ($\geqslant 8.8$ meV) and total splittings around 20 meV. The Lorentzian quasielastic linewidth follows above T_N roughly a $T^{1/2}$-law with values for the linewidths at 10 K increasing from Au (0.15 meV) to Ag (0.45 meV) to Pd (0.9 meV). This yields Kondo temperatures T_K^N of 1.7 K (Au), 5 K (Ag) and 10 K (Pd). It should be noted that for the first two compounds where $T_K \ll T_N$ an additional quasielastic line with Gaussian shape was necessary to fit the measured spectra in the low temperature region. These Gaussian contributions are also observed in the quasielastic response of other magnetically ordering polycrystalline Kondo compounds and can be associated with (critical) spin fluctuations which occur as precursors of the magnetic order. In the ordered state the spectra become inelastic with typically two peaked regions (in the energy range up to 3 meV) originating from the density of states of the acoustic and optic magnon branches (Grier et al. 1988, Severing et al. 1989b, Loidl et al. 1989). On a $CePd_2Si_2$ single crystal Hippert et al. (1992) have performed an inelastic neutron study of the magnetic excitations (magnons) at $T = 1.6$ K, well below $T_N = 10$ K. They observe two dispersive inelastic modes with substantial broadening (linewidth ≈ 0.5 meV) which they ascribe to Kondo-type local fluctuations. For $CeRh_2Si_2$ there exist only inelastic neutron data with low incident energies (Severing et al. 1989b). The quasielastic linewidth is around 3 to 4 meV above T_N and the magnetic intensity in the available energy window ($\leqslant 2$ meV) decreases rapidly below T_N. The experimental conditions did not allow to determine the CF level scheme nor to characterize the magnetic response in the ordered state.

CeT_2Ge_2 compounds have the same crystal structure as the CeT_2Si_2 compounds discussed above. There is a trend that the f-conduction electron hybridization is smaller for the Ge-based compounds compared to the corresponding Si-based compounds.

Direct comparison is possible for T = Au, Ag, and Cu because there exist inelastic neutron scattering data at least for the quasielastic response for all systems. If magnetic ordering effects [$T_N = 15, 5, 4.1$ K for CeT_2Ge_2 with T = Au, Ag, Cu (Böhm et al. 1988, Knopp et al. 1989)] are taken into account by an additional *Gaussian* quasielastic line above T_N and the Kondo relaxation effects by a *Lorentzian* quasielastic line then the following results are obtained for the residual Lorentzian linewidths: $\Gamma/2 \leqslant 0.1$ meV (Au, Loidl et al. 1989), 0.15 meV (Ag, Knopp et al. 1987, 1988b), 0.35 meV (Cu, Knopp et al. 1989). This yields Kondo temperatures T_K^N of $\leqslant 1, 2, 4$ K for the Ge-based compounds while $T_K^N = 1.7, 5, 8$ K was obtained for the Si-based compounds (see previous discussions). This underlines the trend of increasing hybridization when going from Ge to Si and also from Au to Ag to Cu within both series. For $CeAg_2Ge_2$ and $CeCu_2Ge_2$ only one inelastic crystal field transition was observed at 11 meV and at 16.5 meV, respectively, and interpreted as transition from a doublet ground state to an excited quasi-quartet (Knopp et al. 1987, 1989). From this proposed level scheme a moment of about $1.6\mu_B$ is expected for the ground state. This value is roughly observed for the ordered moment in $CeAg_2Ge_2$ (Knopp et al. 1988b) but only half this value in $CeCu_2Ge_2$ (Knopp et al. 1989). The reduction of the moment in the latter compound seems to be related to the observation of quasielastic intensity of Lorentzian shape well below T_N besides inelastic intensity from the magnon density of states (Knopp et al. 1989). This latter point, however, needs further clarification from single-crystal data to separate intensity due to low-lying magnon modes from true quasielastic scattering. Finally, we should mention a very interesting investigation of the evolution of the magnetic ordering when $CeCu_2Ge_2$ is alloyed with the non-ordering compound $CeNi_2Ge_2$ (Steglich et al. 1990). These alloying experiments are expected to cover the whole span from local moment magnetism with ordered moments of the order of μ_B (though reduced by the Kondo effect) to heavy fermion band magnetism with possibly very small ordered moments of the order of 10^{-1} to $10^{-2}\mu_B$ (Steglich 1991).

2.1.4. Ferromagnetic-ordering compounds

CeAg has the cubic CsCl structure with $a = 3.77$ Å at room temperature and undergoes a martensitic phase transition into a tetragonal phase around 15 K (Ihrig and Methfessel 1976). A new interpretation of this phase transition was proposed later by Morin (1988) in terms of a quadrupolar ordering. The cubic crystal field ground state is Γ_8, well separated from the Γ_7 excited state at 23 meV (Frick et al. 1983). The tetragonal distortion or the quadrupolar ordering may split the Γ_8 quartet into two doublets. This splitting, however, was not observed directly. It must be rather small, if it exists at all. At $T_C = 5.3$ K CeAg orders ferromagnetically with a moment of only $0.7\mu_B$ (from magnetization data extrapolated to $T = 0$ K, Takke et al. 1981b) or $0.8\mu_B$ (from neutron diffraction at $T = 1.8$ K, Schmitt et al. 1978). Single-crystal magnetization data yield a somewhat larger saturation moment of $1.25\mu_B$ (Morin 1988). In any case, the experimentally observed magnetic moment is smaller than the value for a free Γ_8 ground state ($1.57\mu_B$). The reduction is thought to be due to the Kondo effect and not to the possible splitting of the Γ_8 ground state (Takke et al. 1981b). Application of pressure first increases the Curie temperature towards a maximum ($T_{C,max} = 7.6$ K at $p = 0.7$ GPa) followed by a decrease and reaching the zero pressure value of T_C at

$p \approx 2.5$ GPa as inferred from resistivity measurements (Eiling and Schilling 1981). Inelastic neutron scattering on a CeAg polycrystal under pressure reveals an increase of the residual quasielastic linewidth from 0.55 meV at zero pressure to 1.1 meV at 2.3 GPa (Frick et al. 1983). If other contributions to the linewidth can be neglected one obtains $T_K^N = 6$ K at zero pressure and $T_K^N = 12$ K at 2.3 GPa. The Curie temperature is about the same for both pressures and should therefore not have a big influence on the linewidth. The temperature dependence of the quasielastic linewidth for both pressures differs from the usual behavior of Kondo systems ($T^{1/2}$-law or linear): a flat portion at low temperatures is followed by a steep increase at elevated temperatures above 100 K. The reason for this different behavior is not yet clear. Unfortunately, the relaxed energy resolution did not allow to identify and to separate different contributions of Gaussian or Lorentzian shape to the quasielastic response.

$CeSi_x$ crystallizes in the tetragonal α-$ThSi_2$ type structure for $1.8 \leqslant x \leqslant 2$ and in the orthorhombic α-$GdSi_2$ type structure for $1.6 < x < 1.8$ (see Kohgi et al. 1990a, and references therein). For $1.85 < x \leqslant 2$ the compound shows HF behavior with no magnetic ordering down to 0.1 K while for $x < 1.85$ it becomes ferromagnetic with Curie temperatures around 10 K. The Kondo mechanism is also effective in the ferromagnetically ordered regime leading to finite magnon linewidths ($x = 1.7$: Hippert et al. 1988; $x = 1.8$: Kohgi et al. 1987) and reduced ordered moments ($0.45\mu_B$). There is a smooth variation of the crystal field splitting over the whole series. It increases monotonously from $CeSi_{1.7}$ (0–15–28 meV) to $CeSi_2$ (0–25–48 meV) (Kohgi et al. 1990b, 1991, Galera et al. 1989). The residual quasielastic linewidth of the non-ordering $CeSi_x$ compounds also increases with x ($x = 1.85$: $\Gamma_0/2 = 1.7$ meV; $x \approx 2$: $\Gamma_0/2 = 3.5$ meV, Galera et al. 1989) yielding Kondo temperatures T_K^N of 19 and 40 K, respectively. The increase of T_K is in line with the decrease of the linear coefficient γ of the specific heat from 234 mJ/K^2 mol for $x = 1.85$ to 104 mJ/K^2 mol for $x \approx 2$ (Yashima et al. 1982). All conclusions concerning the linewidths (magnons, quasielastic, CF transitions), however, should be critically looked at, because it is rather difficult to separate the contribution from the Kondo effect from lattice disorder effects even if similar experiments on corresponding $CeGe_x$ compounds are used for comparison (magnons: Hippert et al. 1988; CF: Kohgi et al. 1990b, Lahiouel et al. 1987). There are also doubts whether stoichiometric $CeSi_2$ exists at all. Dhar et al. (1987) give an upper limit of $x \approx 1.95$.

$CeRu_2Ge_2$ belongs to the large group of CeT_2M_2 compounds with the $ThCr_2Si_2$-type structure. But unlike the other members which are antiferromagnetic or non-ordering HF and VF compounds $CeRu_2Ge_2$ orders ferromagnetically with $T_C = 7.5$ K (Böhm et al. 1988; note: at 8.5 K there is a second transition of yet unknown origin). The low-temperature specific heat (Böhm et al. 1988) contains a linear T term with a rather low γ value of only 20 mJ/K^2 mol and a $T^{3/2}\exp(-\Delta/T)$ term indicative of ferromagnetic magnons with gap ($\Delta = 10$ K). From the high-temperature specific heat Felten et al. (1987) propose a CF level scheme 0–43–65 meV. Inelastic neutron scattering has only been performed with low incident neutron energies and was thus not able to determine the crystal field splitting. Loidl et al. (1989) report the temperature dependence of the quasielastic Lorentzian linewidth. It shows a *linear* temperature dependence with small values similar to the antiferromagnet $CeAu_2Ge_2$. Also the residual width is very small and resolution limited ($\Gamma_0/2 < 0.1$ meV). From this:

$T_K^N < 1$ K. It therefore seems that the low-temperature properties of $CeRu_2Ge_2$ are dominated by RKKY-type interactions and not by Kondo fluctuations.

2.2. *Cerium-based valence fluctuation systems*

As already mentioned in the foreword of the section on Ce-based heavy fermion compounds we have taken the degeneracy of the ground state as a criterion whether a Ce system is a HF ($N = 2$ or 4) or VF ($N = 6$) system. The lower degeneracy of HF systems has its origin in crystal field effects which split the sixfold $^2F_{5/2}$ ground state multiplet of Ce^{3+} into three doublets or into a doublet and a quartet (depending on the local symmetry). CF effects, however, survive only if the Kondo temperature is considerably smaller than the CF splitting. In VF systems we have the opposite situation. CF effects are wiped out due to the considerably larger Kondo temperature of the VF systems. This situation is also reflected in the observation of one broad quasielastic line in VF systems, indicative of unusual fast spin fluctuations at elevated temperatures. Even faster charge fluctuations are believed to be the origin of the fast spin fluctuations. The charge fluctuations themselves, however, cannot be seen directly in neutron scattering experiments. An inelastic feature ('bump or hump') that appears in the low-temperature magnetic response of VF systems is not due to inelastic CF transitions (as in HF systems) but can be explained by electronic excitations in the framework of the Anderson model (Bickers et al. 1987, Kuramoto and Müller-Hartmann 1985). In line with the change of the shape of the magnetic response from room temperature to low temperatures is also the change of the magnetic form factor of VF Ce compounds with temperature. While the form factor is purely 4f-like at elevated temperatures there are distinct deviations from the 4f form factor at low temperatures. The measured magnetic form factor of VF Ce systems at 4 K is interpreted as originating from a coherent coupling of 4f and 5d wave functions on each Ce site. This observation should not be mixed up with the occurrence of a $\boldsymbol{Q}$-dependence of the magnetic response in HF systems due to spin–spin correlations (involving 4f moments on different sites). Finally we should mention the observation of phonon anomalies in VF Ce systems. Their experimental detection was difficult though successful in the end.

In this section we first give for each VF Ce compound some information about the crystal structure and other important properties for its characterization like valence, susceptibility, resistivity, specific heat. The discussion of neutron data involves all available elastic measurements (form factor) and, of course, all inelastic measurements (quasielastic and inelastic magnetic scattering and phonon scattering, if related to VF phenomena). We think that our list of VF compounds is more or less complete while this is certainly not the case for the huge and still rapidly growing list of HF compounds in the preceding section.

$CePd_3$ is *the* archetypical valence fluctuation compound. It has a cubic crystal structure of Cu_3Au type with $a_0 = 4.13$ Å. Early estimates for the valence from lattice parameter systematics by Harris et al. (1972) gave a value of 3.45. This value was revised to 3.23 by Bauchspiess et al. (1982) and to 3.15 by Perez et al. (1990) employing L_3 X-ray absorption measurements. In any case, the valence of Ce in $CePd_3$ is

considerably different from the integer value of 3+ (keeping in mind the present upper limit of 3.3 for VF Ce systems, Röhler 1987, and the obvious difficulty to define a valence in these systems at all, Baer and Schneider 1987). Thus $CePd_3$ can still be considered a typical valence fluctuator even if the f-count as deduced from the experimental data has steadily increased over the years.

$CePd_3$ was the first compound where unusual fast spin fluctuations had been observed. The time-scale of the spin fluctuations was directly measured by the width of the magnetic response deduced from an inelastic neutron scattering experiment performed on a polycrystalline sample of $CePd_3$ by Holland-Moritz et al. (1977, 1982). Figure 15 shows the spectra of $CePd_3$ and YPd_3 at $T = 145$ and 240 K measured on a time-of-flight spectrometer with unpolarized, cold neutrons with an incident energy of $E_0 = 3.5$ meV. The spectra of nonmagnetic YPd_3 serve to show the contribution of phonon and elastic nuclear scattering. The clearly visible additional scattering in $CePd_3$ can be interpreted as magnetic scattering from the Ce ions. Its shape, however, is completely different of what one expects from a stable rare-earth 3+ moment. Instead of a narrow ($\leqslant 1$ meV) quasielastic component and a sharp inelastic line around an energy transfer of the order of 10 meV (crystal field transition) the magnetic scattering of $CePd_3$ exhibits only a very broad ($\geqslant 10$ meV) quasielastic component. The underlying power spectrum is of the Lorentzian shape, eq. (6),

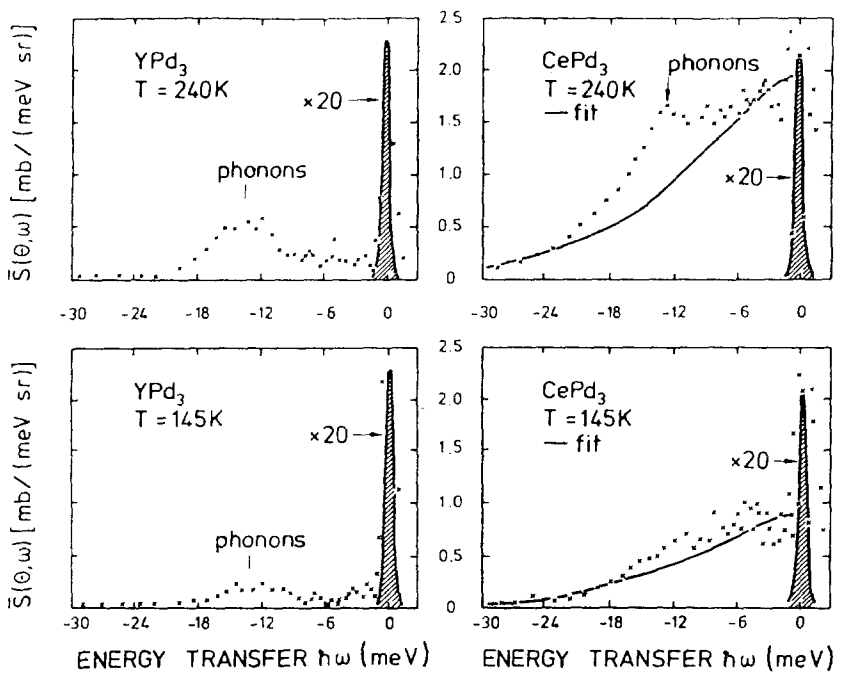

Fig. 15. Inelastic neutron spectra of YPd_3 and $CePd_3$ taken with $E_0 = 3.5$ meV at a constant scattering angle of $2\Theta = 20°$ and two different temperatures. The solid line is a fit with one broad quasielastic line (Holland-Moritz et al. 1982).

corresponding to a relaxational process of the spin self-correlation function in time. The solid line in fig. 15 is a fit of the magnetic scattering in $CePd_3$ with such a Lorentzian power spectrum centered at zero energy transfer. The two parameters to be determined are intensity and linewidth. The Q-dependence of the intensity at $T = 240\,K$ is shown in fig. 16. It follows the square of the free ion Ce^{3+} form factor indicating the local character of the magnetic response. Furthermore, if extapolated to $Q = 0$ and put on an absolute scale by a standard vanadium calibration, it corresponds within experimental error to the measured static susceptibility including its temperature dependence (see fig. 17). For the other parameter, the linewidth, no Q-dependence could be detected, consistent with the local character of the magnetic

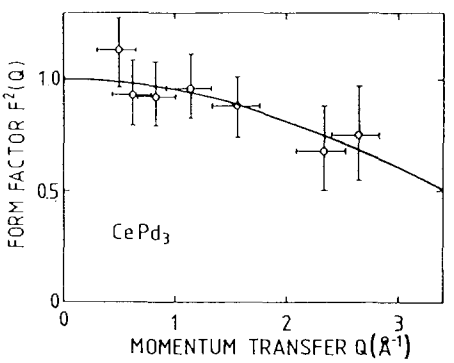

Fig. 16. Q-dependence of the inelastic magnetic scattering in $CePd_3$ deduced from the intensity in the energy window from -1 to $-6\,meV$ at $T = 240\,K$ (Holland-Moritz et al. 1982).

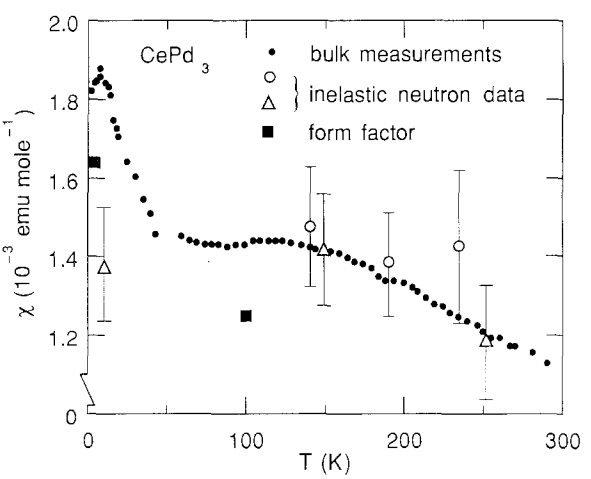

Fig. 17. Comparison of bulk susceptibility and the susceptibility of $CePd_3$ as deduced from neutron data. Open triangles from neutron data by Galera et al. (1987), open circles from neutron data by Holland-Moritz et al. (1982), full squares from form factor measurements by Stassis et al. (1982). The bulk susceptibility (full circles) was measured on the sample used by Galera et al. (1987).

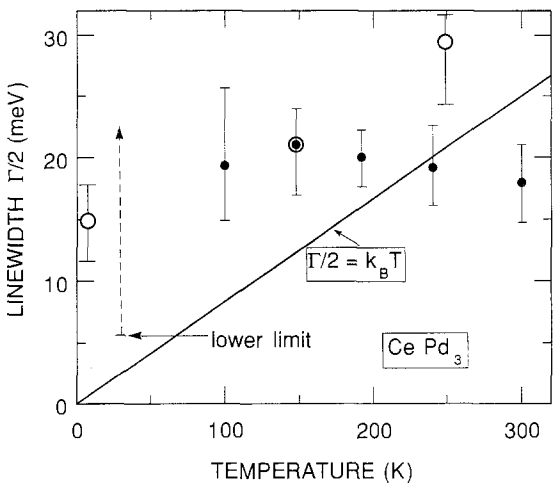

Fig. 18. Temperature dependence of the quasielastic linewidth of $CePd_3$. Full circles: Holland-Moritz et al. (1982); open circles: Galera et al. (1987).

response as already deduced from the Q-dependence of the intensity. The temperature dependence of the linewidth is shown in fig. 18 (full circles). The linewidths are nearly temperature independent from room temperature down to about 100 K with a value around 20 meV. This value of $\Gamma/2$ corresponds to an unusual short relaxation time of 10^{-13} s or to a thermal energy $k_B T_{SF}$ with $T_{SF} = 232$ K, where T_{SF} can be defined as the spin fluctuation temperature. Here we use the expression 'spin fluctuation temperature' synonymously with 'Kondo temperature'. A characteristic *charge* fluctuation temperature usually corresponds to considerably higher energies and cannot be seen directly in neutron scattering experiments. The high value of $T_{SF} = 232$ K for $CePd_3$ is consistent with the large exchange coupling constant J, as discussed in section 3.2. The constant linewidth in $CePd_3$, however, is in strong contrast to the much smaller absolute value and the *linear* temperature dependence (Korringa law) of the quasielastic linewidth for a stable moment rare-earth ion in a metallic compound (e.g., for $TbPd_3$ the slope of $\Gamma/2(T)$ is 10^{-3} meV/K). From this we encounter the picture of *fast relaxing, local spins* to describe the spin dynamics of a valence fluctuating system at elevated temperatures ($\geqslant 100$ K). The fast relaxation prevents the observation of inelastic crystal field transitions in $CePd_3$ on an energy scale smaller than the quasielastic linewidth. In this connection we also want to mention a neutron study at room temperature of the system $CePd_3B_x$ by Culverhouse et al. (1992) who demonstrated the recovery of sharp CF transitions when going from a VF to a more stable moment configuration for $x = 0.32$.

The aforementioned neutron scattering experiments on $CePd_3$ employing cold neutrons of $E_0 = 3.5$ meV, however, were unable to give conclusive information on the shape of the magnetic response below 100 K. The observable energy window in a neutron scattering experiment is confined to the incident neutron energy E_0 (for practical reasons $0.9E_0$) for processes where the neutron loses energy to the sample (positive energy transfers) and roughly to three to four times $k_B T$ for processes where

the neutron gains energy from the sample (negative energy transfers). From the strong reduction of the magnetic intensity in the observable energy window for temperatures below 100 K it could only be inferred that the quasielastic linewidth must stay broad (a lower limit of 5 meV was given for $T = 30$ K; see fig. 18) and/or that the magnetic response develops inelastic features at higher energy transfers.

To explore this region several inelastic neutron scattering experiments have been performed employing different techniques:

– time-of-flight experiments with unpolarized neutrons with different incident energies up to 115 meV on a polycrystalline sample (Severing and Murani 1990),
– triple-axis experiments with unpolarized neutrons on a single crystal (Shapiro et al. 1989),
– triple-axis experiments with very coarse energy resolution but polarized neutrons and polarization analysis on a polycrystalline sample (Galera et al. 1985a,b, 1987).

The advantage to use polarized neutrons and perform a polarization analysis lies in the *unambiguous* determination of magnetic scattering. The trade-off is usually a rather coarse energy resolution and poor counting statistics. Figure 19 shows the magnetic neutron scattering of $CePd_3$ obtained by this method by Galera et al. (1987) at $T = 10, 150$ and 250 K. We have also included in the figure earlier results by the same group for $T = 5.5$ and 280 K (Galera et al. 1985a,b). At high temperatures (250 K/280 K) the spectrum can be fitted with just one broad quasielastic line, confirming the aforementioned results. At $T = 150$ K there is still considerable quasielastic intensity with a linewidth of 22 meV. But, in addition a broad inelastic line at $\Delta = 55 \pm 5$ meV with $\Gamma/2 = 30 \pm 5$ meV is observed. At the lowest temperatures this inelastic line becomes the dominant feature of the magnetic response. The intensity in the low-energy region ($\leqslant 20$ meV) is drastically reduced. From the data, however, it cannot be decided whether there still exists a quasielastic line (dashed line with $\Gamma/2 = 15$ meV) or not. Galera et al. (1987) have included the quasielastic line in their fit and calculated from the neutron data a value of 1.4×10^{-3} emu/mol for the static susceptibility at 10 K (see fig. 17). The measured value of 1.9×10^{-3} is somewhat larger. Agreement can only be achieved if the upturn in χ below 50 K is neglected. The question, however, whether the upturn in the static susceptibility is an intrinsic property of $CePd_3$ or not, could not be satisfactorily answered up to now.

Using unpolarized neutrons the existence of a broad *inelastic* line at low temperatures was also deduced from time-of-flight data on $CePd_3$ by Severing and Murani (1990). The authors claim that the intensity of the inelastic line at 50 meV with a linewidth of 40 meV *alone* accounts for a static susceptibility of 1.4×10^{-3} emu/mol. They argue that there is *no* quasielastic scattering left at $T = 5$ K and explain the low-energy magnetic intensity as being totally due to impurity magnetic scattering.

Galera et al. (1985a,b, 1987) and Severing and Murani (1990), however, agree on the observation that the low-temperature magnetic response of $CePd_3$ is dominated by the broad inelastic line ['bump or hump' as mentioned below eq. (7)] at about 50 meV energy transfer and 30 to 40 meV wide, and furthermore, that the intensity in the quasielastic region is strongly reduced. This is in contrast to the findings of Shapiro et al. (1989). They claim that at 10 K magnetic scattering is observed over the *whole*

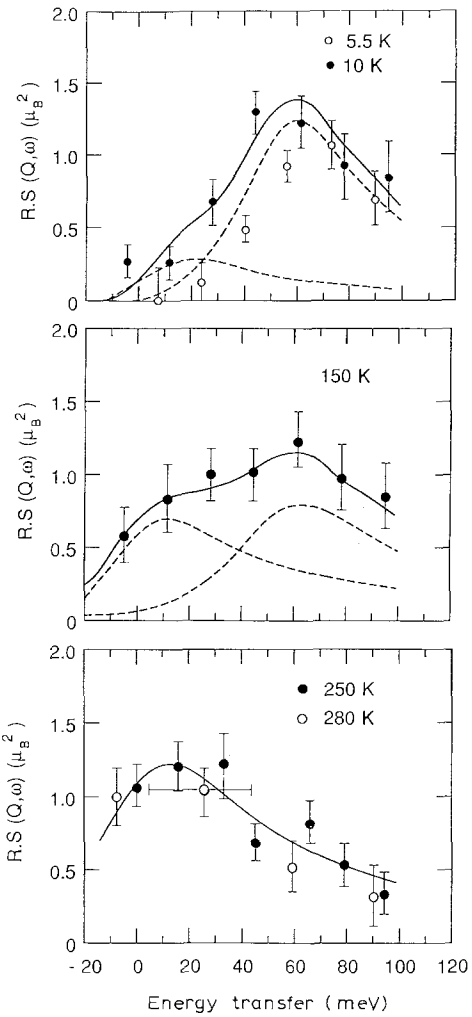

Fig. 19. Magnetic cross sections for $CePd_3$ at different temperatures and $Q = 2.57\,\text{Å}^{-1}$. The lines are fits involving quasielastic and inelastic scattering convoluted with the energy resolution of the spectrometer (FWHM $\approx$ 40 meV). Full circles: Galera et al. (1987); open circles: Galera et al. (1985a, b).

energy range up to 80 meV, being strongest at low energy transfers and decaying slowly towards higher energies with no indication of an inelastic structure around 50 meV.

The Q-dependence of the magnetic form factor as deduced from inelastic measurements is often not very accurate and limited in Q-range (see fig. 16). This usually leads to the rather weak statement that the data are *consistent* with a 4f, 3d, etc., form factor. There is, however, a much more accurate method to measure the form factor over a wide Q-range, though restricted to the Q-values of nuclear Bragg reflections. Using polarized neutrons and a single crystal one can measure for each Bragg reflection the ratio of

the peak intensities for the two neutron spin orientations, parallel and antiparallel to an external magnetic field. After minor corrections and normalization to the known nuclear structure factors one obtains the static susceptibility $\chi(\boldsymbol{Q}, T)$ and from its Fourier transform the spatial distribution of the magnetization induced by the external field. Figure 20 shows the results of such an experiment on a single crystal of $CePd_3$ by Stassis et al. (1982) at $T = 4.2$ and 100 K. The data points at 100 K can be fitted quite well with the theoretical form factor of the Ce^{3+} free ion calculated from relativistic electronic wave functions. This implies that at 100 K the field-induced magnetization has a spatial distribution which is characteristic of the localized 4f electronic density of the Ce^{3+} ion. At 4.2 K the experimental results exhibit deviations from the 4f form factor at low scattering angles. The induced moment must contain an additional component whose spatial distribution is more extended than that of the 4f electrons. Stassis et al. could fit their data at 4.2 K assuming that the induced moment consists

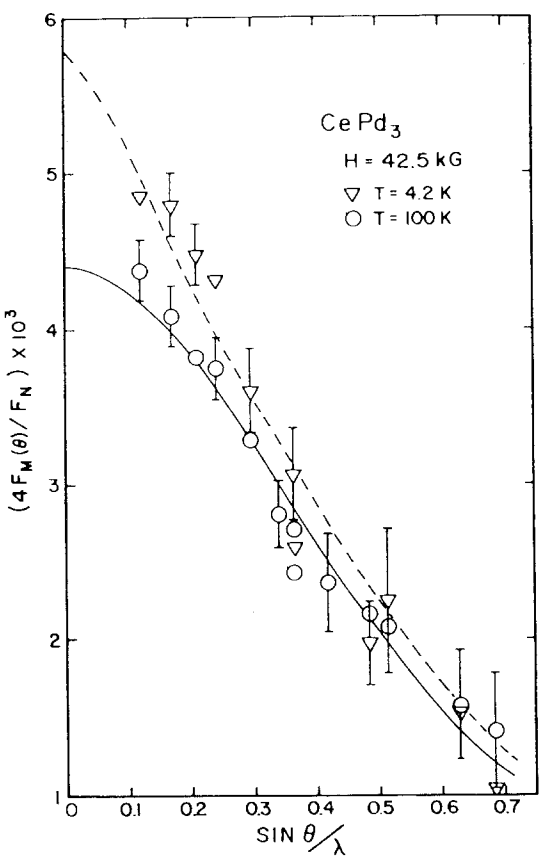

Fig. 20. Paramagnetic form factors of $CePd_3$ at 4.2 and 100 K plotted versus $\sin\theta/\lambda = Q/4\pi$. The solid line has been obtained by fitting the 100 K data to the 4f-magnetic form factor of Ce^{3+}. The dashed line was obtained assuming a 83% 4f–17% 5d distribution of the induced moment (Stassis et al. 1982).

of a 83% 4f–17% 5d Ce component. The extrapolation to $Q = 0$ gives for the susceptibility 1.64×10^{-3} emu/mol at 4.2 K and 1.25×10^{-3} emu/mol at 100 K. The increase of χ at low temperatures is mainly due to the additional 5d component; the 4f component is nearly identical for the two temperatures. Both χ values deduced from the form factor extrapolation, however, are considerably smaller than the measured static bulk susceptibility (see fig. 17; χ measured on the sample which was used for the form factor measurements is very similar to that shown here, Thompson et al. 1982). The discrepancy between neutron deduced χ and bulk χ is assumed to be due to additional contributions of s and p character which are not sensed in the neutron measurements. This discrepancy is not found in the inelastic data. They sense the 4f component only, therefore they are not tracking the upturn in χ below 50 K. Their absolute values, however, exhibit a much larger systematic error.

Finally we discuss the influence of valence fluctuations on the phonon spectra of $CePd_3$. A detailed study has been undertaken by Severing et al. (1988). The effects associated with valence fluctuations were difficult to detect, but evident:

– a *breathing* mode had to be taken into account to reproduce the dispersion relations,
– certain phonons show unusual temperature dependent line shifts, broadenings and splittings.

The crystallographic structure of $CePd_3$ gives rise to 12 phonon branches in each of the three main symmetry directions. The transverse modes in the [100] and [111] directions are twofold degenerate. The results for the room-temperature dispersion curves are shown in fig. 21. The data points are best fitted by a 16-parameter Born–von Kármán model with an additional breathing term (solid and dashed lines). The dotted lines indicate the dispersion curves as obtained with the same set of parameters but *without* breathing term. The breathing term accounts for an extra degree of freedom due to the breathing deformability of the Ce atom when undergoing valence fluctuations. It does *not* occur in 'normal' compounds with Cu_3Au structure. The strongest influence of the breathing term is seen in the LA branch in the [100] direction at the zone boundary and in the LA branches of the [110] and [111] directions in the middle of the Brillouin zone. At these positions the phonons also exhibit the unusual temperature dependence. The data reflect two different temperature regions: the low-temperature region ($T \leqslant 80$ K) with normal line shapes and a weak, linear decrease of the phonon energies with increasing temperature, and the region $T \geqslant 100$ K with anomalous softening, intrinsic linewidths, and mode splittings. An attempt to explain the splittings has been given by Liu (1989). It should be noted that also in the magnetic response there is a considerable shift of intensity from the high energy region (60 meV at 10 K) to the quasielastic region (0 to 20 meV) around this temperature as discussed above.

However, Loong et al. (1988) concluded in another study of the phonon dispersion curves at room temperature that there are *no* significant anomalies neither in the phonon frequencies nor in the linewidths. Though the results of both groups (Severing et al. and Loong et al.) agree in general, there are significant differences in the interpretation of details and in their conclusions.

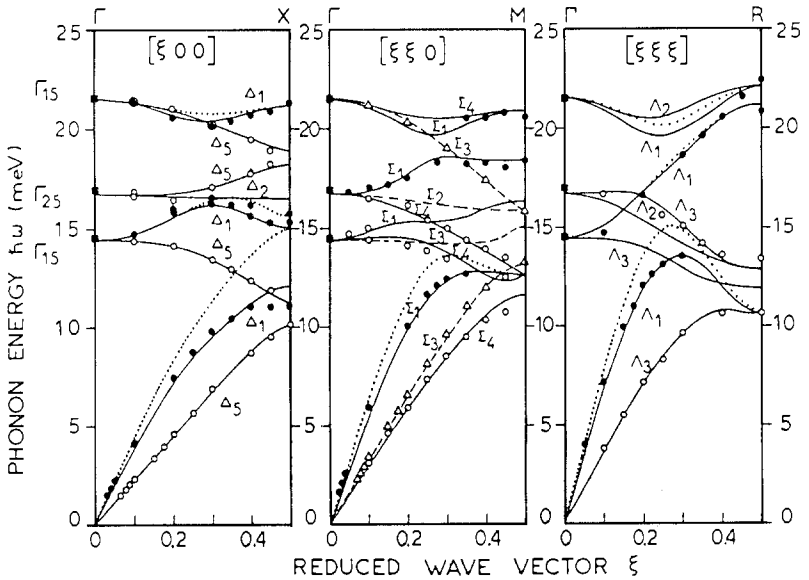

Fig. 21. Phonon dispersion curves for $CePd_3$ at room temperature. Full symbols are longitudinal modes, open symbols transverse modes. In the [110] direction: Δ, transverse polarized in (110) plane; ○, transverse polarized in (100) plane. Results of Born–von Kàrmàn fit including breathing term are shown as solid and dashed lines (latter for Δ data points). Dotted lines: if breathing term is neglected (Severing et al. 1988).

The physical properties of $CeSn_3$ resemble those of $CePd_3$ in many aspects. The crystal structure is also of Cu_3Au-type yet the nearest-neighbor Ce–Ce distance is much larger in $CeSn_3$ (4.72 Å) than in $CePd_3$ (4.13 Å). The bulk susceptibility has a broad maximum around 130 K and an upturn at low temperatures. As in $CePd_3$ there is a controversy whether the upturn is of intrinsic nature or not. Similar behavior is also observed for the resistivities (maximum around 130 K) but with a different effect on both compounds if nonmagnetic impurities are added [drastic change of $\rho(T)$ for $CePd_3$, minor effects on $\rho(T)$ for $CeSn_3$]. The results of inelastic magnetic neutron scattering and of form factor measurements which will be discussed below also make both compounds look very similar. There is, however, one big difference: the valence of Ce in $CeSn_3$ is very near to the integral value of 3+ (3.02, Röhler 1987) while for $CePd_3$ the valence is *considerably* away from this value ($\geqslant 3.15$, depending on method and author). This may be the reason why no phonon anomalies have been observed for $CeSn_3$ in contrast to $CePd_3$.

Inelastic neutron scattering experiments to study the temperature dependence of the magnetic response of $CeSn_3$ have been performed by several groups employing different techniques (all experiments were done on polycrystalline samples):

– time-of-flight experiments with unpolarized *cold* neutrons by Holland-Moritz et al. (1982),

– time-of-flight experiments with unpolarized *thermal* neutrons with incident energies up to 82 meV by Murani (1983a,b),

– triple-axis experiments with very coarse energy resolution but polarized neutrons and polarization analysis by Capellmann et al. (1985).

All authors agree on the observation that at high temperatures the spectral response consists only of one broad quasielastic line of Lorentzian shape. This was first discovered by Holland-Moritz et al. (1982). In the temperature range from 100 to 300 K, the range where cold neutrons can give valuable information, the linewidths are nearly temperature independent with values around 25 meV. These values were confirmed by the measurements with thermal neutrons by Murani (1983a,b). At $T = 300$ K Murani could fit the data with just one broad quasielastic line. At $T = 100$ K there is, however, already in addition to the quasielastic line ($\Gamma/2 = 23$ meV) an inelastic line positioned at 40 meV and with halfwidth $\Gamma/2 \approx 35$ meV. For decreasing temperatures the inelastic feature becomes more pronounced as it was also observed for $CePd_3$. At $T = 5$ K there is clearly visible a quasielastic contribution and an inelastic contribution. Murani fitted the data at $T = 5$ K with a quasielastic line and an inelastic line at 40 meV, both having a linewidth around 10–15 meV. The spectra of Capellmann et al. (1985) obtained with polarized neutrons at 30, 115 and 290 K are presented in fig. 22. The authors have published only the experimental data with no fitting curve. Therefore we have tried to draw some theoretical curves through the data points in analogy to the curves in $CePd_3$ (fig. 19). Qualitative agreement for this interpretation of the data with the results of the aforementioned experiments with unpolarized neutrons can be stated. At $T = 30$ K there is a quasielastic line with width around 15 meV and an inelastic line positioned at about 45 meV. For increasing temperatures both lines broaden. The spectral weight of the inelastic line is diminishing while the weight of the quasielastic line is increasing with temperature. At room temperature both lines have merged into one quasielastic line with a width around 20–30 meV. In the interpretation of the data, however, we do not agree with Capellmann et al. (1985) that there is *no* quasielastic intensity at low temperatures. The disagreement relies mainly on the interpretation and significance of the data point at $\omega = 0$. A similar conclusion has been drawn by Murani (1986).

The temperature dependence of the quasielastic linewidth of $CeSn_3$ is shown in fig. 23 up to room temperature. There is an increase of linewidth between $T = 5$ K and 100 K by a factor of two. Beyond 100 K the linewidth stays nearly constant. Comparing fig. 18 ($CePd_3$) and fig. 23 ($CeSn_3$) it is evident that the temperature dependence and even the absolute values of the quasielastic linewidths in both compounds are very similar.

The Q-dependence of the inelastic magnetic scattering in $CeSn_3$ follows the free ion Ce^{3+} form factor at all temperatures (Murani 1983a,b, Capellmann et al. 1985). Some minor deviations were only observed at $T = 5$ K by Murani.

The temperature dependence of the static susceptibility as deduced from the inelastic magnetic scattering follows the 4f-part of the bulk susceptibility (smooth variation of $\chi(T)$ with a broad maximum around 130 K, the upturn at low temperatures being neglected). The results of Murani (1983a,b) are shown in fig. 24 together with the bulk

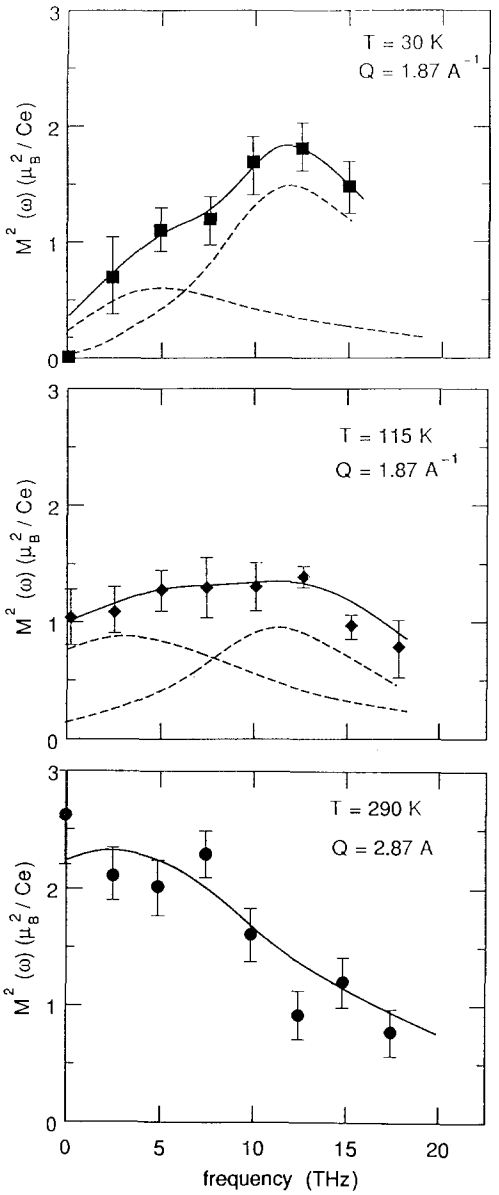

Fig. 22. Frequency dependence of the magnetic scattering of $CeSn_3$ at different temperatures from Capellmann et al. (1985), data points only. The lines have been added by the present authors. Quasielastic and inelastic contributions are shown separately for $T = 30$ and 115 K. For $T = 290$ K there is only a quasielastic line. The energy resolution of the spectrometer is 10 THz = 41.3 meV (FWHM).

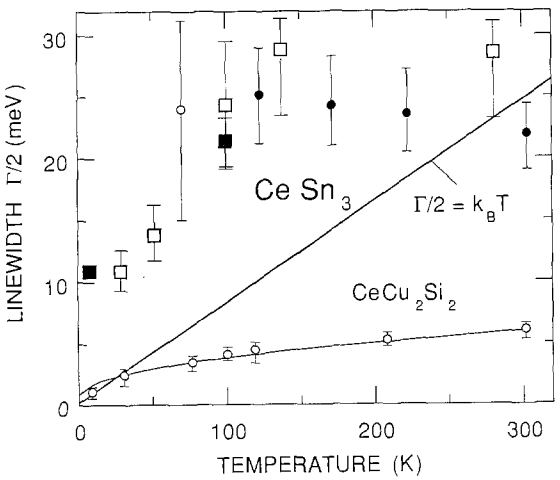

Fig. 23. Temperature dependence of quasielastic linewidth of $CeSn_3$. Full circles: from Holland-Moritz et al. (1982); squares: from Murani (1983a,b), open and filled for $E_0 = 50$ and 82 meV, respectively. For comparison: results for HF superconductor $CeCu_2Si_2$ (Horn et al. 1981a).

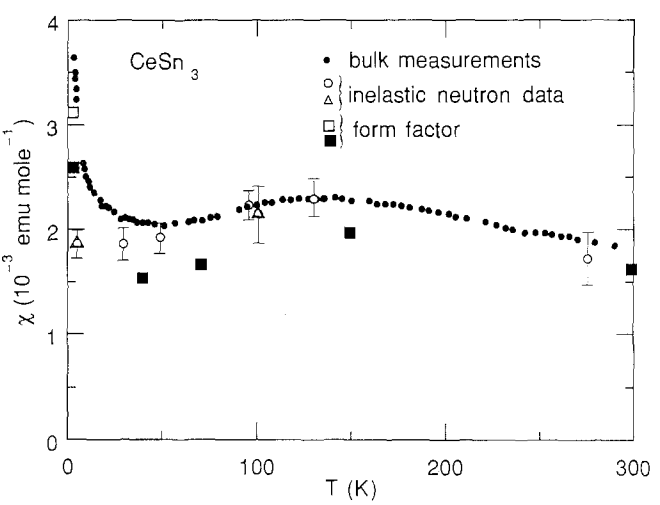

Fig. 24. Comparison of bulk susceptibility and the susceptibility of $CeSn_3$ as deduced from neutron data. Open circles and triangles: from inelastic neutron scattering by Murani (1983a,b) with $E_0 = 50$ and 82 meV, respectively. The neutron data have no absolute calibration, but are normalized to the bulk susceptibility at 130 K. Full circles give bulk susceptibility as measured on part of the sample used by Murani. Squares: χ from form factor measurements by Stassis et al. (1979b) on different single crystals, open and full squares for 2 and 4 mm thick crystal, respectively.

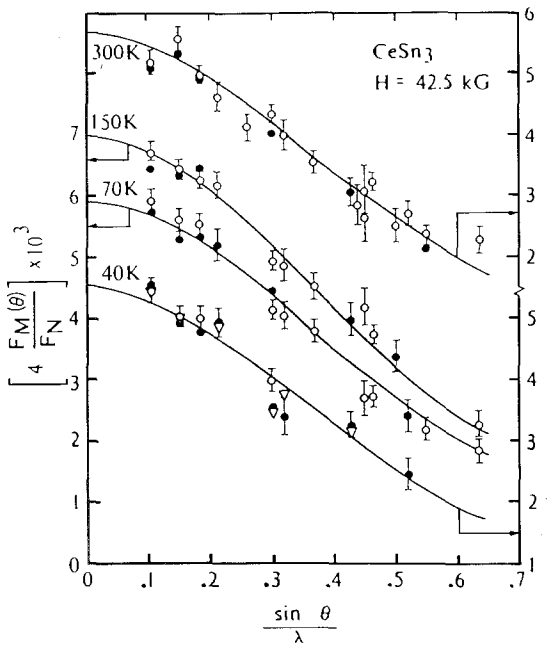

Fig. 25. Magnetic form factor data for $CeSn_3$ obtained with a 4 mm (open circles) and 2 mm (full circles) thick crystal at 40, 70, 150 and 300 K with the field parallel to the [110] direction. The triangles are data obtained with the 2 mm thick crystal at 40 K with the field parallel to the [100] direction (after Stassis et al. 1979b).

susceptibility as measured on a part of the sample used by Murani and with the results of form factor measurements by Stassis et al. (1979a,b). The form factor of $CeSn_3$ shows a different behavior at low temperatures and at elevated temperatures. For temperatures of 40 K and above all data obtained on two different single crystals and for different directions of the applied magnetic field (parallel to [100] or [110]) give practically the same results. Part of the data are presented in fig. 25. The Q-dependence of the induced moment follows quite well the theoretical form factor of the Ce^{3+} free ion. The values of the static susceptibility as obtained from an extrapolation to the forward direction, however, are always lower than those of the bulk susceptibility measurements (even if compared to those measured on the crystals used by Stassis et al. 1979b). This discrepancy is interpreted by Stassis et al. as an indication of an additional contribution to the bulk susceptibility of s or p electronic character which is not sensed in the neutron measurements because of the limited, finite Q-range.

At temperatures below 40 K large deviations were observed from a 4f form factor. The data obtained at 4.2 K for both crystals with the field applied in the [110] direction are plotted in fig. 26. The data do not follow a smooth curve indicating a large anisotropy in the spatial distribution of the induced magnetization. A good fit can be achieved if a Ce 5d contribution of e_g character is added coherently to the 4f

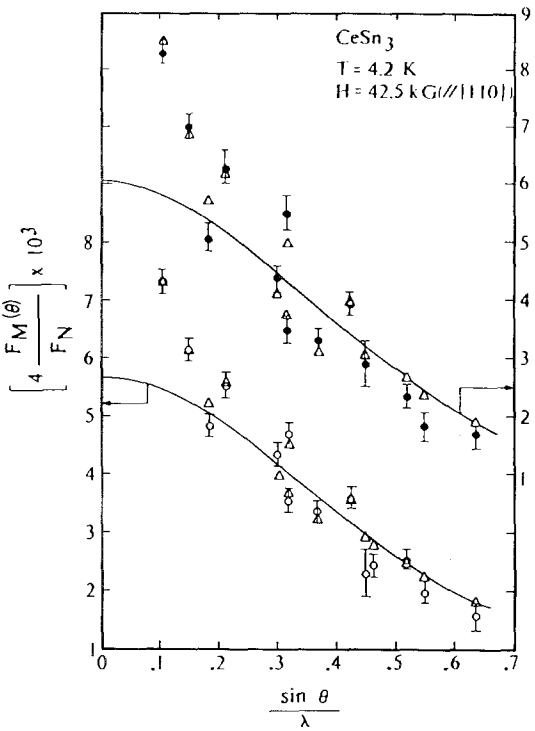

Fig. 26. Magnetic form factor data for $CeSn_3$ obtained with a 4 mm (open circles) and 2 mm (full circles) thick crystal at 4.2 K with the field parallel to the [110] direction. The triangles are calculated values assuming the induced moment consists of a 4f and a 5d Ce component of e_g symmetry. The solid lines represent the 4f contribution (from Stassis et al. 1979b).

component (triangles in fig. 26). The amount of the additional 5d contribution is different for both samples, which is also reflected in their different bulk susceptibility at low temperatures. Thus the occurrence of the additional 5d contribution is intimately connected with the upturn at low temperatures of the bulk susceptibility. This does not mean, however, that the upturn and the 5d contribution cannot be an intrinsic property of $CeSn_3$. Boucherle et al. (1990) investigated the form factor of stoichiometric and off-stoichiometric $CeSn_3$ at low temperatures. They found that *only the stoichiometric* single crystal showed the additional 5d contribution, though with smaller amount (24%) than the two crystals investigated by Stassis et al. (1979b) (38% for the 4 mm and 49% for the 2 mm crystal). The 4f contribution was about the same for all investigated crystals. Above we said that the *inelastic* neutron scattering experiments did not reveal any significant deviation from a 4f form factor. This is not in contradiction to the form factor measurements which show the deviation due to the additional 5d component. The Q-range of the inelastic data of Murani (1983a,b) is from 0.2 to 0.5 in units of $\sin(\theta)/\lambda$. The significant deviation in the form factor data of Stassis et al., however, is seen for $\sin(\theta)/\lambda \leqslant 0.2$, outside the Q-range of Murani's inelastic

data. Capellmann et al. (1985) measured the Q-dependence of the magnetic scattering with the energy window of the spectrometer set at $\omega = 0 \pm 5$ THz. At high temperatures they state consistency with the 4f form factor in agreement with all other experiments. At low temperatures the magnetic intensity was drasticaly reduced for this configuration making any determination of the Q-dependence impossible.

No phonon anomalies such as unusual line shifts or linewidths have been observed up to date in $CeSn_3$ (Pintschovius et al. 1980, 1983) in contrast to $CePd_3$. Also a study of phonon frequency shifts induced by external pressure gave no conclusive evidence for an unusual breathing deformability in $CeSn_3$ due to valence fluctuations (Blaschko et al. 1984).

The different behavior of $CeSn_3$ and $CePd_3$ concerning phonon anomalies is at first sight surprising. Both exhibit similar spin dynamics as discussed here in detail. The fast spin fluctuations at room temperature give a quasielastic linewidth around 20–25 meV corresponding to a spin fluctuation temperature of $T_{SF} = 232$–290 K (T_{SF} seems to be somewhat smaller for $CePd_3$ than for $CeSn_3$, compare figs. 18 and 23). T_{SF} is for both compounds of the same order as the Debye temperature ($\Theta_D = 205$ K for $CeSn_3$ and $\Theta_D = 292$ K for $CePd_3$, Takke et al. 1981a). There is a slight tendency that for $CeSn_3$ $\Theta_D \leqslant T_{SF}$ while for $CePd_3$ $\Theta_D \geqslant T_{SF}$. This, however, does not yet explain the absence and the presence of phonon anomalies in $CeSn_3$ and $CePd_3$, respectively. The only explanation up to date is the difference in valence (3.02 for $CeSn_3$ and $\geqslant 3.15$ for $CePd_3$). As mentioned before, charge fluctuations are always faster than the corresponding spin fluctuations and the ratio depends on the valence. In the case of Ce this means that the nearer the valence is to the integral value of 3 the larger is the ratio of charge to spin fluctuations. This would imply that the charge fluctuations are much faster in $CeSn_3$ than in $CePd_3$ and the lattice is unable to follow.

In connection with $CeSn_3$ we will also discuss the experiments performed on the intermetallic alloys $CeSn_{3-x}In_x$. Whereas $CeSn_3$ has weak VF properties, $CeIn_3$ behaves as a Kondo or HF compound. There have been extensive investigations of the magnetic properties (Lawrence 1979, Dijkman et al. 1980), heat capacity and resistivity (Elenbaas et al. 1980). Some of the results of the different authors are collected in fig. 27 showing the evolution of a characteristic temperature T_K^χ [as defined by Lawrence (1979) through the scaling behavior of the effective moment $\mu^2 = T\chi/C$ by the condition $\mu^2(T_K^\chi) = 0.5$] and of T_{max} [the temperature of the maximum in $\chi(T)$]. Also shown is the evolution of the linear coefficient γ of the specific heat and the x-dependence of the aniferromagnetic ordering temperature T_N for the In-rich side. Three distinct concentration regimes seem to exist:

– ($0 \leqslant x \leqslant 1$): the characteristic temperatures T_K^χ and T_{max} decrease almost linearly with increasing x, accompanied by a linear increase of γ,

– ($1 \leqslant x \leqslant 2.6$): γ peaks around $x \approx 1$; then there is a steady decrease of γ with x and a nearly constant characteristic temperature (with minor variations due to alloying effects as also found in $LaSn_{3-x}In_x$); in the first two regimes no long-range magnetic ordering has been found,

– ($2.6 \leqslant x \leqslant 3$): γ and T_K^χ stay constant with x; long-range antiferromagnetic order appears with T_N steeply increasing with x; $T_N = 10$ K for $CeIn_3$.

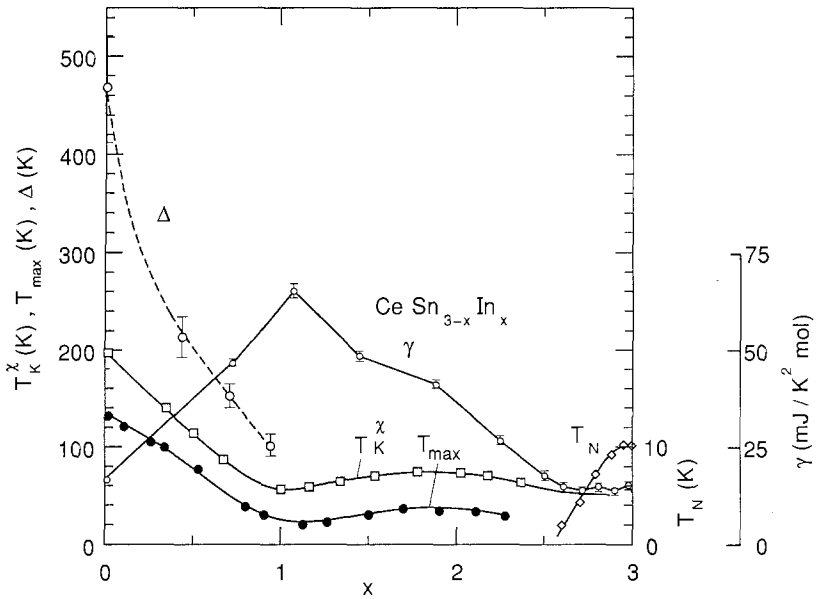

Fig. 27. Evolution of T_K^{χ} (Lawrence 1979) and T_{max} (Dijkman et al. 1980) from susceptibility measurements, of γ and T_N (Elenbaas et al. 1980) from specific heat data with x for $CeSn_{3-x}In_x$. Also shown (big open circles): position Δ of hump as observed in inelastic neutron scattering by Murani (1987a,b).

Neutron investigations have been performed mainly in the first regime and for $CeIn_3$. We discuss first the results of inelastic magnetic scattering. Murani (1987a,b) has shown that the position Δ of the hump in the low-temperature spectra moves towards smaller values for increasing x (up to $x = 1$) in line with the decrease of T_K^{χ} and T_{max} (fig. 27). There seems to be a scaling relation ($\Delta \approx 3T_{max}$) between the position Δ of the hump and T_{max}, the temperature, where $\chi(T)$ has a maximum. In addition to the reduction of the hump position Murani claims that there is also a reduction of quasielastic intensity for increasing x. An experiment performed on a $CeSn_2In$ *single crystal* at $T = 5$ K by Murani et al. (1990a) reveals only an inelastic line of Lorentzian shape with $\Delta = 8 \pm 1$ meV and $\Gamma/2 = 7 \pm 1$ meV and *no* quasielastic scattering. The value of Δ as deduced from the single-crystal experiment is consistent within error with the value given above for the polycrystalline sample for $x = 1$. The magnetic response of the single crystal was measured at different $\boldsymbol{Q}$ values. The shape of the magnetic response seemed to be independent of $\boldsymbol{Q}$. There was, however, a slight, $\boldsymbol{Q}$ dependence of the intensities indicating the possible presence of short-range spin correlations. Temperature-dependent measurements on all samples showed the characteristic evolution of the inelastic features into a broad quasielastic response at elevated temperatures as usually observed for VF compounds.

Preliminary neutron data for the $^2F_{5/2} \rightarrow {}^{2F}F_{7/2}$ spin–orbit transition in $CeSn_{3-x}In_x$ obtained with high incident neutron energies of 600 meV by Murani et al. (1990b) are shown in fig. 28. The energy of the spin–orbit transition for a free ion Ce is

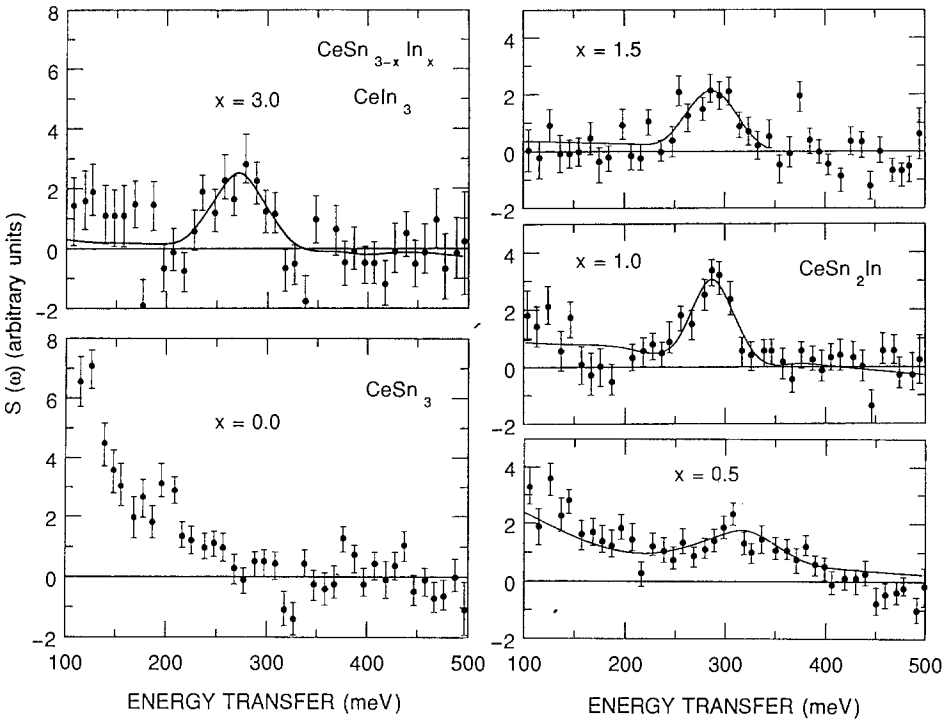

Fig. 28. Spin–orbit transition in $CeSn_{3-x}In_x$ measured at $T = 20\,K$ with $E_0 = 600\,meV$ (redrawn from Murani et al. 1990b).

280 meV (see Osborn et al. 1991). An inelastic transition with about this energy is observed for $x = 1$ to 3 ($CeSn_2In$ up to $CeIn_3$). For $x = 0.5$ there is still an inelastic transition visible, though already considerably broadened and shifted to higher energies (315 meV). In addition, a tail on the low-energy side is developing for increasing Sn concentration. It is reminiscent of the broad magnetic scattering within the $J = 5/2$ ground-state multiplet. For $CeSn_3$ the tail is the only observed scattering intensity. No inelastic line seems visible. It is not clear whether the spin–orbit transition is totally absent in $CeSn_3$ or whether it is present but even further broadened or shifted and is thus lost in the statistical scatter of the data.

Form factor measurements have been performed on $CeSn_2In$ (Benoit et al. 1985) and $CeIn_3$ (Boucherle et al. 1983, Boucherle and Schweizer 1985). In contrast to $CeSn_3$ there is no *significant* 5d-like contribution at low temperatures for both compounds. Data taken at 5.5 and 75 K on a $CeSn_2In$ single crystal can be fitted essentially with a 4f form factor. There is a slight deviation from the 4f form factor for the data point of the (001) reflection (within error bars for $T = 75\,K$, just outside error bars for $T = 5.5\,K$). This corresponds to a 5d contribution of *at most* 10% to the total magnetization density. There is also only a small upturn in the susceptibility at low temperatures measured on the same sample. No anisotropies of the form factor

due to crystal field effects have been reported. The same isotropic behavior was found for $CeSn_3$ and $CePd_3$, indicating that all six levels from the $^2F_{5/2}$ multiplet are involved in the formation of the ground state wave function. This is not the case for $CeIn_3$ which we already have identified as HF compound. There are signatures in $CeIn_3$ that its ground state is split by the cubic crystal field into a low-lying Γ_7 and an excited Γ_8 level around 10–15 meV. The form factor measured in the magnetically ordered state at 1.8 K is strongly anisotropic (fig. 29). All (h 00) reflections lie above and all (0 kk) reflections lie below the average 4f form factor. This is what one expects from a Γ_7 crystal field ground state (the opposite anisotropy is expected for a Γ_8 ground state or isotropic behavior for the full $J = 5/2$ multiplet). This interpretation is strongly supported by the fact that the magnetic entropy per mol Ce is close to R ln 2 at the ordering temperature (Elenbaas et al. 1980) as expected for a Γ_7(doublet) in contrast to R ln 4 for Γ_8(quartet) or R ln 6 for the full multiplet. From the slight discrepancy between calculated and measured form factor for the two low-Q reflections (111) and (200) Boucherle et al. (1983) estimate an additional 5d contribution of 18% to the total magnetization density in $CeIn_3$. No error is quoted for this estimate, but the error must be rather large as it relies on discrepancies for reflections where the 5d contribution is already very weak. No data are given for the more decisive reflections (001) and (011). These reflections are rather weak (because the nuclear scattering lengths of Ce and In are nearly equal) and thus difficult to be measured. We are also

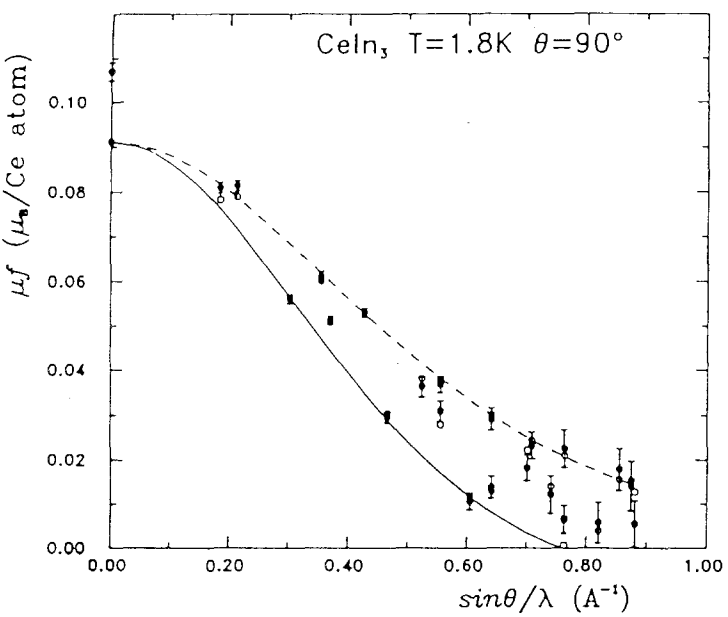

Fig. 29. Magnetic form factor for $CeIn_3$ at $T = 1.8$ K in the magnetically ordered phase. Full circles: data points; open circles: calculated with Γ_7 ground-state wave function. Dashed and solid line: upper and lower boundary for anisotropy (Boucherle and Schweizer 1985).

not aware of any form factor measurements at elevated temperatures that can give information whether the 5d contribution is still present or not.

The magnetic structure of $CeIn_3$ has been determined by Lawrence and Shapiro (1980) and by Benoit et al. (1980). $CeIn_3$ is a simple antiferromagnet with propagation vector $(\frac{1}{2},\frac{1}{2},\frac{1}{2})$, i.e., the Ce moments are aligned in opposite directions in adjacent (111) planes. The spin directions within the planes could not be determined from the experiments. Lawrence and Shapiro report for the Ce moments a value of $(0.65 \pm 0.1)\mu_B$ at $T = 5$ K, Benoit et al. a value of $(0.48 \pm 0.08)\mu_B$ at $T = 3$ K. Both values are somewhat smaller than the expected $0.71\mu_B$ for a Γ_7 state. Lawrence and Shapiro also investigated the critical scattering around $T_N = 10.2$ K. They observed a strong suppression of critical fluctuations and nearly mean-field behavior.

Finally we discuss the inelastic magnetic response of $CeIn_3$. The $\Gamma_7 \rightarrow \Gamma_8$ crystal field transition was measured by Lawrence and Shapiro (1980) as a function of temperature. They observed a rather broad inelastic line at 15 meV with width around 10 meV at low temperatures (5, 15 K) shifting to 11–12 meV at elevated temperatures (50, 160 K). The width of the crystal field transition was originally interpreted by Lawrence and Shapiro as a measure of a spin fluctuation energy $k_B T_{SF}$ with $T_{SF} \approx$ 100 K. This value, however, seems to be much too high for $CeIn_3$. The quasielastic scattering, which could not be resolved in the experiments by Lawrence and Shapiro, was measured by Lassailly et al. (1985) with better energy resolution at $T = 60$, 140, and 240 K. The width and the intensity of the quasielastic line are strongly Q-dependent and temperature dependent. This behavior suggests that spin–spin correlations are the main origin for the spin dynamics while line broadening due to hybridization effects is of minor importance in $CeIn_3$. A typical value for the linewidth in the region around 1–2 $Å^{-1}$ is 1 meV at $T = 60$ K and 2–3 meV at $T = 140$ and 240 K. The value of 1 meV at 60 K is of the same order as $k_B T_N$ (10.2 K $\approx$ 0.9 meV). Unfortunately there are no data for the quasielastic scattering below 60 K which might allow to extract a residual width due to Kondo broadening in comparison to spin–spin interactions. From the data of Lassailly et al. we can only estimate an upper limit of the Kondo temperature of $CeIn_3$ of $T_K \leqslant 10$ K.

While $CePd_3$ and $CeSn_3$ have been studied very thoroughly over the past 15 years there are only few data available for *$CeBe_{13}$* though it exhibits similar magnetic properties. $CeBe_{13}$ was already very early classified as VF compound with an (overestimated) valence of 3.2–3.3 from lattice parameter systematics (Borsa and Olcese 1973, Krill et al. 1980). New estimates of the valence from L_3 X-ray absorption give 3.04 (Röhler 1987), a value much more close to the integral valence of 3+, similar to $CeSn_3$. The crystal structure is of cubic $NaZn_{13}$ type with the Ce ions forming a simple cubic lattice. The shortest Ce–Ce distance is 5.1 Å. There are no Ce–Ce near-neighbors as Be ions from cages around the Ce ions. The structure may be viewed as Ce ions embedded in Be metal.

The susceptibility of $CeBe_{13}$ is rather flat at low temperatures with a very broad maximum at $T_{max} = 140$ K and a paramagnetic Curie temperature $\Theta_p = 200$ K (Kappler and Meyer 1979). Inelastic neutron scattering experiments have been performed by Holland-Moritz et al. (1982) on polycrystalline samples with cold neutrons ($E_0 =$ 3.5 meV). The spectra could be fitted with just one broad quasielastic line. The line-

width is 17 meV at room temperature and *increases* with decreasing temperatures reaching a value around 28 meV at 100 K. For lower temperatures it could only be stated that the magnetic response must stay broad and/or develops inelastic features. Unfortunately no inelastic neutron data are available at low temperatures with sufficiently high incident energies. There are, however, NMR data reported as function of temperature from 300 K down to 4 K (Panissod et al. 1988). NMR basically probes the imaginary part of the dynamic susceptibility $\chi''(\omega)/\omega$ as does neutron scattering. But while NMR probes a Q-average of this quantity at very low energy ($\omega \approx \mu$eV, nuclear Larmor frequency) neutron scattering probes it for different Q-values and in a much higher energy range (0.1–100 meV, depending on spectrometer). If an electronic relaxation rate (corresponding to a quasielastic linewidth) is deduced from NMR-T_1 measurements usually two important assumptions are made:

– there are no correlations between different spins, i.e., the magnetic response is independent of Q, and

– the magnetic response is of purely relaxational form (quasielastic spectrum of Lorentzian shape).

For $CeBe_{13}$ the NMR data yield a linewidth around 70 meV for temperatures between 4 and 50 K. It then decreases with increasing temperatures to 55 meV (100 K), 35 meV (200 K) and 25 meV (300 K). This is the same behavior as observed for the linewidths deduced from neutron scattering but with larger absolute values for the NMR-deduced linewidths. The discrepancy between the values for both methods increases for decreasing temperatures. It is rather unlikely that correlation effects are the origin for the discrepancies. It is more likely that the shape of $\chi''(\omega)$ changes with temperature. We therefore suspect that the magnetic response of $CeBe_{13}$ changes from a more or less quasielastic spectrum at high temperatures to a spectrum with quasielastic and inelastic features at low temperatures, as it was observed in $CePd_3$ and $CeSn_3$.

Ce metal in its various phases (α, β and γ) exhibits already the wide span of properties of the Ce-based compounds ranging from well localized moment via Kondo lattice to valence fluctuating and nonmagnetic behavior. Vice versa, the behavior of Ce compounds has been classified as α-, β- and γ-like. Simple measurements, however, as on the temperature dependence of the magnetic response of a certain phase are hampered by the peculiarities of the phase diagram. At ambient pressure and room temperature it is possible to produce Ce samples in the β-phase (dhcp, $a_0 = 3.68$ Å, $c_0 = 11.92$ Å) and in the γ-phase (fcc, $a_0 = 5.16$ Å). For decreasing temperatures both transform into the α-phase (fcc, $a_0 = 4.85$ Å). At room temperature γ-Ce transforms upon application of pressure into α-Ce around 8 kbar. For more details of the phase diagram and the description of even further phases we refer the reader to the review articles by Koskenmaki and Gschneidner (1978) and by Gschneidner and Daane (1988). To overcome the limitations of the phase diagram and allow, e.g., temperature-dependent measurements over a wide range of temperatures a simple trick has been applied: alloying. For instance, alloying with Y *stabilizes* the β-phase while alloying with Th *prevents* the formation of the β-phase. (Ce, Th)-alloys therefore show only the $\gamma \rightarrow \alpha$ phase transition. Further addition of La to (Ce, Th) then even allows some

'fine tuning' of the $\gamma \rightarrow \alpha$ transition and eventually the suppression of the transition. Alloying, however, always introduces disorder, different local environments, etc. These effects often complicate the interpretation of work on alloys compared to experiments on chemically ordered intermetallic compounds. We therefore discuss only briefly neutron investigations perfomed on Ce metal and its alloys with Sc, Y, La and Th in its different phases.

β-phase. In β-Ce the 4f electron can be considered as well localized. Rapid quenching to low temperatures allows to deduce that β-Ce orders antiferromagnetically around 12–13 K (Burghardt et al. 1976). For $Ce_{1-x}Y_x$ the ordering temperature decreases with x (Panousis and Gschneidner 1972). On a polycrystalline sample of $Ce_{0.75}Y_{0.25}$ neutron diffraction experiments by Gibbons et al. (1987) yield an antiferromagnetic ordering below $T_N = 7$ K with a propagation vector of 0.5 τ_{100}. Inelastic neutron scattering by Gibbons et al. (1989) on the same sample shows narrow quasielastic scattering (width = 1.3 meV at $T = 20$ K) and well-defined crystal field transitions at 8 and 16.5 meV. Gibbons et al. (1989) analyse this in terms of a Γ_7 ground state and an excited Γ_8 state at 16.5 meV (197 K) for the cubic sites and a $|\pm 1/2\rangle$ ground state and a $|\pm 3/2\rangle$ excited state at 8 meV (97 K) for the hexagonal sites. This model explains why the ordered moments lie in the basal plane (as found in the diffraction experiment), but predicts somewhat larger moments ($1.29\mu_B$ and $0.71\mu_B$) than found experimentally ($0.91\mu_B$ and $0.38\mu_B$ for the hexagonal and cubic sites, respectively).

γ-phase. The lattice and spin dynamics of a γ-Ce single crystal have been studied at room temperature by Stassis et al. (1979c). If compared to the phonon dispersion curves of Th a relative phonon softening of some branches had been stated. Yet it was not clear whether this observation could be uniquely related to a valence fluctuation effect. The magnetic response could be fitted with just one broad quasielastic line of Lorentzian shape and a width of 16 meV. Rainford et al. (1977) reported a width of 10 meV deduced from an experiment on a polycrystalline sample. Form factor measurements by Stassis et al. (1978) revealed at room temperature a 4f free ion Ce^{3+} form factor.

For obvious reasons there are no measurements of γ-Ce at low temperatures. It is, however, believed that the residual quasielastic linewidth would only be a few meV and an inelastic crystal field transition would be observable. This can be inferred from the results of inelastic neutron scattering experiments $Ce_{0.9-x}La_xTh_{0.1}$ (for $x = 0.14, 0.20, 0.40$) by Grier et al. (1980, 1981). The addition of La suppresses the $\gamma \rightarrow \alpha$ transition of $Ce_{0.9}Th_{0.1}$. The spectra below 110 K were fitted with a quasielastic and an inelastic line of same width. The inelastic line was interpreted as a $\Gamma_7 \rightarrow \Gamma_8$ crystal field transition with an energy around 12, 14 and 15 meV and a width around 5, 6 and 8 meV for $x = 0.40, 0.20$ and 0.14, respectively. Position and width are nearly temperature independent for all x for temperatures between 40 and 110 K. Below 40 K a moderate increase of position and linewidth is observed for the samples with $x = 0.40$ and 0.20 while a drastic increase is observed for the 0.14 sample ($\Delta = 21$ meV, width = 12 meV at 5 K). The different behavior of the 0.14 sample is connected to the still present $\gamma \rightarrow \alpha$ transition (though of second order instead of first order as in Ce-metal). Grier et al. (1981), however, emphasize that the increase in crystal field splitting cannot be understood quantitatively on these grounds.

$\gamma \rightarrow \alpha$ transition. $Ce_{0.74}Th_{0.26}$ undergoes a first-order valence transition at $T = 150$ K. For this sample detailed neutron investigations have been performed. Inelastic neutron scattering experiments are reported by Shapiro et al. (1977) between 100 and 250 K using thermal neutrons and by Loong et al. (1987) between 10 and 200 K using epithermal neutrons with incident energies up to 1.2 eV. In both phases (α below, γ above 150 K) the magnetic response consists of a broad quasielastic spectrum with no indication of inelastic crystal field transitions. In both phases the linewidth increases with *decreasing* temperatures. It is typically 20 meV in the γ-phase and around 100 meV in the α-phase. At $T = 10$ K the magnetic response of the α-phase is somewhat better described by a broad *inelastic* line at $\Delta = 140$ meV and a width of 90 meV. This reminds of the hump observed at low temperatures in the excitation spectra of $CePd_3$ and $CeSn_3$.

A form factor measurement by Moon and Koehler (1979) on $Ce_{0.74}Th_{0.26}$ revealed a 4f free ion Ce^{3+} form factor in the γ-phase at $T = 180$ K and deviations from the 4f form factor at the two low-Q reflections (111) and (200) in the α-phase at $T = 50$ K. The results at 50 K suggest that the induced moment in the α-phase has two components, one 4f-like and the other 5d-like as also found for $CePd_3$ and $CeSn_3$.

α-phase. The determination of the magnetic response in α-Ce has been a challenge for neutron scatterers for many years. There is no final answer yet, but there is agreement that there *is* magnetic scattering intensity in the α-phase of Ce and that the magnetic response is very broad in energy, presumably, extending up to the eV region. Fillion et al. (1985) report an inelastic scattering experiment at $T = 8$ K with polarized neutrons and polarization analysis. They obtain very weak magnetic intensity for all data points between 0 and 180 meV followed by a steplike increase of magnetic intensity for three data points at 200, 230 and 250 meV (the upper limit of the experiment). The steplike increase of intensity between 180 and 200 meV is somewhat surprising in view of the very coarse energy resolution of 150 meV (FWHM) in this region, which should produce a much smoother variation of intensity with energy transfer (even if the underlying scattering law would be a step function). Fillion et al. conclude from their data that the magnetic response in α-Ce is essentially inelastic and rule out a purely quasielastic response (of width around 200 meV). This is consistent with the observation of Loong et al. (1987) for α-$Ce_{0.74}Th_{0.26}$ at $T = 10$ K. Furthermore, the tail of the inelastic magnetic response in α-$Ce_{0.74}Th_{0.26}$ seems to extend well beyond 500 meV. A similar conclusion concerning the extend of the response to high energy transfers was drawn by Murani et al. (1990b) from the results of an experiment with $E_0 = 2$ eV on a $Ce_{0.93}Sc_{0.07}$ sample. Exploiting the hysteretic nature of the $\alpha \leftrightarrow \gamma$ transition Murani et al. managed to measure the magnetic response of the same sample in the α- and in the γ-phase at the same temperature (125 K). A difference spectrum reveals a narrow ($\leqslant 50$ meV) response of the γ-phase and a very broad response of the α-phase again extending to energy transfers far beyond 500 meV.

2.3. *Ytterbium-based systems*

Making a particle–hole inversion one can connect the properties of Ce-based VF compounds with those of Yb-based VF compounds. Ce^{3+} ($4f^1$) and Yb^{3+} ($4f^1 = 4f^{14-1}$)

have a magnetic ground state with one electron or one hole in the f-shell, and Ce^{4+} and Yb^{2+} have no f-electron or a magnetic-inactive filled f-shell, respectively. The average valence in VF Ce compounds, however, never covers the full range from 3+ to 4+ (3.3 being the maximum, see section 2.2) while it does so for Yb compounds (from 3+ to 2+, of course). Also the magnetic ground-state multiplets of Ce^{3+} and Yb^{3+} are not identical due to Hund's rule for the coupling of L and S to J ($J = |L - S|$ for the light rare earths and $J = |L + S|$ for the heavy rare earths). Thus for Ce^{3+} the ground-state multiplet is $^2F_{5/2}$ ($N = 6$) with the excited $^2F_{7/2}$ state at about 280 meV while for Yb^{3+} the ground-state multiplet is $^2F_{7/2}$ ($N = 8$) with the excited $^2F_{5/2}$ state at about 1300 meV.

There are not so many Yb-based systems investigated by neutron scattering as there are Ce-based systems. Also the division into VF and HF Yb-based systems is not as straightforward as for the Ce-based systems. In most cases crystal field and HF/VF effects are of comparable strength in Yb systems and therefore the interpretation of the magnetic response as seen by neutron scattering is often controversial (see, e.g., Polatsek and Bonville 1992).

$YbAl_3$ has the cubic Cu_3Au structure with $a = 4.20$ Å. The lattice parameter if compared with the neighboring $TmAl_3$ and $LuAl_3$ indicates that Yb is more or less trivalent in this compound (Havinga et al. 1973). Walter et al. (1991) derive a somewhat smaller average valence of 2.85 ± 0.1 when considering a variety of valence-dependent properties. $YbAl_3$ does not order magnetically nor becomes superconducting at low temperatures (Havinga et al. 1970, Walter et al. 1991). The temperature dependence of the susceptibility (with a maximum around 120 K) and of the resistivity (with a steep slope around 120 K) resemble those of the VF compounds $CePd_3$ and $CeSn_3$ (Havinga et al. 1973).

Inelastic neutron scattering experiments on a polycrystalline sample of $YbAl_3$ were reported by Murani (1985a,b) employing unpolarized neutrons with incident energies of 50 and 115 meV. The shape of the magnetic response of $YbAl_3$ at elevated temperatures (70 to 200 K) can fairly well be described by a broad quasielastic line centered at zero energy transfer with a halfwidth of 40 ± 10 meV. As in the case of the VF Ce compounds there is a drastic change of the shape of the magnetic response for decreasing temperatures. The intensity in the low-energy region ($\leqslant 30$ meV) is reduced and an inelastic feature develops. At $T = 6$ K it seems that there is a *gap* in the magnetic excitation spectrum with a resolution-limited steplike increase of intensity at 32 meV and a rather smooth decrease of intensity towards higher energies. The existence of a gap in the excitation spectrum of $YbAl_3$, however, has been questioned by Walter et al. (1991) who performed an inelastic neutron investigation with cold neutrons. Instead, these authors claim to have observed a Kondo resonance in $YbAl_3$ at 18 meV (if extrapolated to $T = 0$). Unfortunately, the evidence for the 18 meV excitation is only indirect. Because of the low incident energy of the cold neutrons the relevant energy region can only be covered at elevated temperatures ($T \geqslant 50$ K) and the response at low temperatures can only be *extrapolated* from these high-temperature data.

Preliminary experiments on the $^2F_{7/2} \rightarrow {}^2F_{5/2}$ spin–orbit transition by Osborn and Goremychkin (1991) locate the spin–orbit transition at 1374 ± 12 meV with an unusual large FWHM of 340 meV. The large width is taken as evidence for the strong hybridization of the f-shell with the conduction band.

$YbCu_2Si_2$ (valence 2.9, Röhler 1987, $\gamma = 135\,\mathrm{mJ/K^2\,mol}$, Sales and Viswanathan 1976) was the first Yb-based VF compound to be investigated by inelastic neutron scattering (Holland-Moritz et al. 1978). It showed the typical broad, nearly temperature-independent response which was first analyzed with a quasielastic line only, with width around 6–10 meV. Subsequent measurements with different incident neutron energies and a more careful phonon subtraction led to inconsistencies if only a quasielastic line was used to fit the magnetic part of the spectra (Holland-Moritz 1982). Better consistency for all data was obtained assuming a crystal field splitting of the $J = 7/2$ ground-state multiplet of Yb^{3+} into four doublets. This is expected for the tetragonal symmetry of the Yb ions in this crystal structure ($ThCr_2Si_2$ type, $a = 3.92$ Å, $c = 9.99$ Å, Rogl 1984). The excited doublets were placed at 18, 23 and 31 meV. The low-energy part was fitted with a quasielastic line of width 4–5 meV in the temperature range from 5 to 300 K (Holland-Moritz et al. 1982). The spectra at $T = 5$ K, taken with $E_0 = 12.5$ and 51.5 meV, are shown in fig. 30. Unfortunately the magnetic part of the high-energy spectrum is considerably masked by phonon and multi-phonon scattering. No attempts have been made at that time to fit the low-energy part of the magnetic response (< 10 meV) with an inelastic line instead of a quasielastic line.

An inelastic neutron scattering study on a *single crystal* of $YbCu_2Si_2$ was performed at $T = 4.3$ K by Currat et al. (1989) on a triple-axis instrument covering a range of energy transfers between 8 and 50 meV. The results are shown in fig. 31 for different $\boldsymbol{Q}$-vectors along the two principal directions $\boldsymbol{a}$ and $\boldsymbol{c}$. The magnetic part of the response is indicated by the thin lines under the data points (the thick lines through the data points are the sum of magnetic and phonon scattering, the latter being obtained by scaling of data measured at equivalent lattice vectors with high Q-values). Though the static susceptibility of $YbCu_2Si_2$ is rather anisotropic at low temperatures ($\chi_\parallel : \chi_\perp \approx 3:1$; Shimizu et al. 1987) the magnetic response for the measured $\boldsymbol{Q}$-vectors is only slightly different, exhibiting two broad inelastic peaks around 12–16 meV and 30 meV. This supports the interpretation of Holland-Moritz et al. (1982) of the powder spectra in fig. 30 in terms of a Kondo temperature of 50 K (= quasielastic linewidth) for the ground-state doublet (this region is not covered by the single-crystal experiment) and strong transition matrix elements to the first and third excited doublets

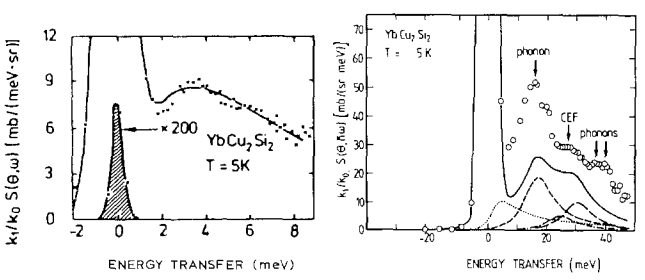

Fig. 30. Inelastic neutron spectra of polycrystalline $YbCu_2Si_2$ at $T = 5$ K taken with $E_0 = 12.5$ meV (left) and 51.5 meV (right). The full line is the magnetic part obtained from a complete fit (magnetic plus phonon) of the measured spectrum. Right spectrum: the quasielastic (dotted line) and the three crystal field transitions (dashed lines) are shown separately (Holland-Moritz 1980, Holland-Moritz et al. 1978, 1982).

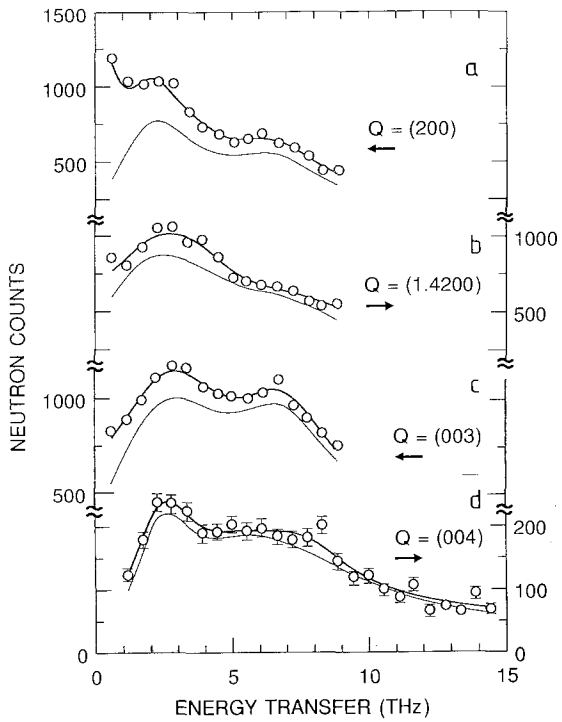

Fig. 31. Inelastic neutron scattering cross-section of single crystal $YbCu_2Si_2$ at $T = 4.3$ K and at four different wave vector transfers. The thin line is the magnetic contribution and the full line is the sum of the magnetic and phonon parts, fitted to the data. Note the different scale for (d). The count rate is lower because a different configuration was used to access the higher energy transfers (Currat et al. 1989).

at 18 and 32 meV (corresponding to the peaks around 12–16 and 30 meV in the single-crystal data).

This interpretation of the magnetic response is, however, in contrast to the assumptions made by Zevin et al. (1988a,b) and by Rasul and Schlottmann (1989a,b) to explain the unusual temperature dependence of the 4f quadrupole moment in $YbCu_2Si_2$ measured by the Mössbauer effect (Bonville and Hodges 1985, Tomala et al. 1990). Both theories assume a considerably larger Kondo temperature (~ 200 K) and a crystal field level scheme with pure $|\pm J_z\rangle$ states, with $|\pm 7/2\rangle$ being lowest. In the absence of spin and charge fluctuations this would yield only one crystal field transition with a nonzero matrix element for neutron scattering at low temperatures, namely from the ground-state doublet to the first excited doublet $|\pm 5/2\rangle$ at 4 meV (Rasul and Schlottmann) or at 10 meV (Zevin et al.). Zwicknagl et al. (1990) calculated the magnetic response including crystal field *and* strong spin and charge fluctuations. They obtain an excitation spectrum with one broad peak with different positions for $\chi''_{\parallel}(\omega)$ and $\chi''_{\perp}(\omega)$ reflecting the CF anisotropy. This model, however, does not explain the low-energy response ($\leqslant 6$ meV, see fig. 30) and the presence of two broad inelastic peaks in the single crystal spectra for all $\boldsymbol{Q}$-vectors (see fig. 31).

$YbPd_2Si_2$ exhibits similar physical properties as $YbCu_2Si_2$: $ThCr_2Si_2$ structure ($a = 4.09$ Å, $c = 9.87$ Å, Rogl 184), a valence around 2.9 (Röhler 1987), a maximum in the susceptibility around 40 K, and a large specific heat $\gamma = 203\,\mathrm{mJ/K^2}$ mol. From specific heat and NMR measurements by Besnus et al. (1988) and from Mössbauer effect measurements by Bonville et al. (1990) it was concluded that $YbPd_2Si_2$ has a Kondo temperature of about 65 K involving, however, only the two low-lying doublets ($N = 4$) which are well separated in energy from the two other doublets. No specific values for the splittings are given except that the splitting between the two low-lying doublets is small compared to 65 K while the separation between the quasi-quartet ground state and the remaining two excited doublets is large compared to 65 K. Inelastic neutron scattering experiments are reported by Weber et al. (1989b) for polycrystalline $YbPd_2Si_2$ in the temperature range from 1.5 to 250 K. For temperatures between 100 and 250 K the VF-typical broad quasielastic response with width 11–13 meV is observed. At $T \approx 50$ K an inelastic excitation at 21 meV becomes visible; its intensity increases with decreasing temperature. In the same temperature range ($T < 50$ K) the quasielastic linewidth decreases rapidly and at $T = 5$ K the quasielastic response is transformed into a second *inelastic* feature at about 4.7 meV. The width of this inelastic low-energy excitation fits well to the temperature dependence of the quasielastic linewidth for $T > 5$ K. Weber et al. note that a simple explanation of their observations on the basis of a crystal field model is not possible. They speculate that the existence of a high-energy and of a low-energy excitation may be due to a different relaxation behavior along different crystallographic axes. This can only be checked by an experiment on a single crystal. We want to offer here, however, another explanation on the ground of the aforementioned description given by Besnus et al. (1988) and Bonville et al. (1990, 1991). Then the high-energy excitation (21 meV) is a crystal field transition from the quasi-quartet ground state to one or both of the high-lying doublets. It is visible in the experiment because the transition energy (21 meV) is larger than the Kondo energy (65 K $\approx$ 6 meV). The transition energies within the quasi-quartet are smaller than the Kondo energy leading to the observation of a quasielastic line with residual width (5 meV) of the order of the Kondo energy. Finally, at low temperatures ($T = 5$ K) the quasielastic line transforms into an inelastic feature though involving only $N = 4$ states of the total $N = 8$ states of Yb^{3+}.

YbCuAl is also one of the very early VF compounds studied with inelastic neutron scattering and compared to NMR data (Mattens et al. 1980, MacLaughlin et al. 1979, Murani et al. 1985). It crystallizes in the hexagonal Fe_2P-type structure with $a = 6.92$ Å and $c = 4.00$ Å. The valence from lattice parameter is close to 3, from L_3 absorption spectra a value of 2.95 is obtained. The susceptibility has a maximum around 30 K and the specific heat γ is $260\,\mathrm{mJ/K^2}$ mol. YbCuAl shows the typical broad quasielastic line with a width of 6–10 meV in the temperature range from 30 to 250 K, directly obtained from the neutron data and deduced from NMR data assuming relaxational behavior and the absence of correlations. Again, at low temperatures ($T = 5$ K) inelastic features at 10 and 23 meV seem to appear in the magnetic response yet on top of a still present broad quasielastic response with $\Gamma/2 = 7.5$ meV. No simple explanation of the inelastic features could be given, a crystal field description had been ruled out (Murani et al. 1985).

From the analysis of Mössbauer effect and susceptibility data Bonville et al. (1990) estimate a Kondo temperature of 90 K and a rather small total crystal field splitting of only 20 K. Adopting these values it is tempting to relate the broad inelastic features at 10 and 23 meV in the magnetic response of YbCuAl at $T = 5$ K to the two broad maxima for $\chi''_{\parallel}(\omega)$ and $\chi''_{\perp}(\omega)$ in the model of Zwicknagl et al. (1990) as originally calculated for $YbCu_2Si_2$. As was already the case for $YbCu_2Si_2$ there is, however, in this model no explanation for the quasielastic intensity. We should also note that there is some ambiguity about the origin of the two broad inelastic peaks in the neutron scattering data as their position coincides also with sharp maxima in the phonon density of states. Yet the detailed analysis of Murani et al. (1985) seems to prove their magnetic origin. Unfortunately, no single crystals of this compound are available to investigate the direction dependence of the magnetic response which is predicted in the model of Zwicknagl et al. (1990).

Preliminary experiments on diluted samples $Yb_{1-x}Y_xCuAl$ with $x = 0.2$ and 0.7 still show the inelastic peaks below $T = 30$ K (Murani 1987b).

$YbXCu_4$ compounds with X = Ag, Au, Pd and In crystallize in the cubic $AuBe_5$ structure with Strukturbericht notation C15b. In this structure the Yb and X ions form well-ordered sublattices. The local symmetry of the Yb ion is cubic and the Yb–Yb distance is rather large and of the order of 5 Å. The compounds with X = Au and Pd appear to order antiferromagnetically at 0.6 and 0.8 K, respectively, whereas $YbAgCu_4$ does not show any sign of magnetic order down to 0.45 K (Rossel et al. 1987). $YbInCu_4$ undergoes a first-order valence transition around 40–50 K with no sign of magnetic order at low temperatures (Felner et al. 1987, Yoshimura et al. 1988, K. Kojima et al. 1989). All compounds are in a nearly trivalent state at room temperature. While the compounds with X = Ag, Au and Pd stay trivalent down to low temperatures, the valence transition in $YbInCu_4$ yields at $T = 45$ K a sudden change in valence by about 0.1 f electrons to ~ 2.9.

Inelastic neutron scattering experiments on polycrystalline samples using time-of-flight techniques with incident energies between 3 and 67 meV have been reported for the compounds with X = Ag, Au and Pd by Severing et al. (1990a) and for X = In, covering the valence transition, by Severing et al. (1990b).

The results for $YbAuCu_4$ and $YbPdCu_4$ resemble those obtained for Ce-based HF or Kondo lattices which show magnetic order at low temperatures. Inelastic crystal field transitions are well separated from quasielastic scattering. For $YbAuCu_4$ a crystal field level scheme is deduced from the neutron data with a level sequence Γ_7–Γ_8(3.89 meV)–Γ_6(6.88 meV). The spectra of $YbPdCu_4$ are also interpreted in a crystal field scheme but the inelastic transitions are considerably broader while the quasielastic line is even narrower than for $YbAuCu_4$. The unusual width of the inelastic transitions is explained by the presence of a large amount of *disordered* $Yb_{1-x}Pd_{1+x}Cu_4$ phases with Strukturbericht notation C15 which does not exhibit the cubic site symmetry of the Yb ions of the ordered C15b phase. The narrower quasielastic linewidth reflects the weaker hybridization in the compound with X = Pd with respect to X = Au. The overall crystal field splitting is of the same order for both compounds.

The magnetic response of the third compound, $YbAgCu_4$, is markedly different.

Though an interpretation of the spectra in terms of crystal field theory cannot be ruled out it would require a much larger overall splitting for $YbAgCu_4$ than for the other two compounds. This is just opposite to the trend observed in the isostructural, stable moment compounds $ErXCu_4$ where the overall crystal field splitting *decreases* in the sequence $X = Pd \rightarrow Au \rightarrow Ag$. Thus Severing et al. (1990a) have put forward an interpretation of the temperature dependence of the magnetic response of $YbAgCu_4$ in terms of theories describing the magnetic relaxation behavior of unstable 4f moments. Figure 32 shows the spectra of $YbAgCu_4$ at $T = 5\,K$ measured with neutrons of incident energies of 12.5 and 50 meV and fitted with the Kuramoto–Müller-Hartmann function [eq. (30)]. The variables in the function are α/π, the ratio of the 4f occupancy to the degeneracy of the ground state (n_f/N), and the Kondo energy $\tilde{\varepsilon}_f$ (the position of the renormalized 4f level relative to the Fermi level). The low-energy part of the spectrum (< 6 meV) was excluded from the fitting range since the Kuramoto–Müller-Hartmann function *underestimates* the real spectrum by as much as 20% for $\omega \rightarrow 0$. The resulting fit parameters are $\alpha/\pi = 0.147\ (\pm 15\%)$ and $\tilde{\varepsilon}_f/k_B = 96\,K\ (\pm 8\%)$. Assuming $n_f = 1$, a value of $N = 6.8 \pm 1$ for the ground state degeneracy is obtained. Within the uncertainty, this value of N is consistent with the full degeneracy of the $2J + 1 = 8$

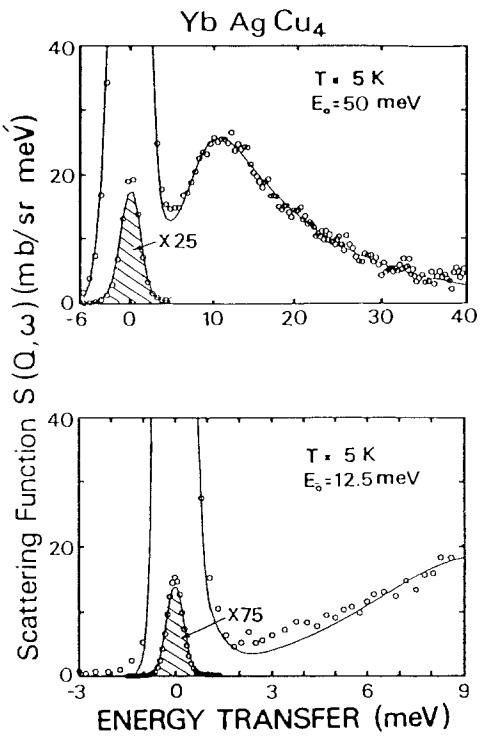

Fig. 32. Inelastic neutron spectra of $YbAgCu_4$ at $T = 5\,K$ and $E_0 = 50$ and 12.5 meV. The spectra are fitted with the Kuramoto–Müller-Hartmann function, eq. (30). Elastic incoherent scattering is marked by the hatched area (Severing et al. 1990a).

of an Yb^{3+} ion. This indicates that the overall crystal field splitting is small compared to the Kondo energy in agreement with the aforementioned trend for the crystal field splittings in this series. Hence crystal field transitions are not resolved in the magnetic spectra of $YbAgCu_4$.

For increasing temperatures the inelastic feature of the magnetic response of $YbAgCu_4$ merges into a broad quasielastic line around $T \approx 75$ K. Figure 33 shows the temperature dependence of the inelastic ($T < 75$ K) and of the quasielastic ($T \geqslant 75$ K) linewidth of $YbAgCu_4$ and of the quasielastic linewidth of the more stable moment compounds $YbAuCu_4$ and $YbPdCu_4$. A forced fit of the spectra of $YbAgCu_4$ for $T < 75$ K with a quasielastic line yields increasing linewidths for decreasing temperatures (full data points in fig. 33). For $T \geqslant 75$ K the quasielastic linewidth increases slightly with temperature. This produces a minimum of the linewidth at a temperature $T_0 \approx 75$ K which is interpreted in the theory of Bickers et al. (1987) as the Kondo temperature defined above. Employing different (single-ion) theories for the interpretation of the inelastic neutron data including susceptibility and specific heat data yields characteristic temperatures (energies) around 100 K for $YbAgCu_4$ as collected in table 3 of the paper of Severing et al. (1990a). The relatively good agreement among the variously determined values for the characteristic temperature suggests that the observed magnetic response of $YbAgCu_4$ can be understood in terms of a VF, single-ion model. The quasielastic linewidths of the magnetically ordering compounds $YbAuCu_4$ and $YbPdCu_4$ follow roughly a $T^{1/2}$ power law. The Kondo temperatures for the latter compounds are much smaller than for $YbAgCu_4$ and of the order of 1 K, a value of the same order as the RKKY interactions in these compounds.

$YbInCu_4$ exhibits the features of both types of $YbXCu_4$ compounds discussed above:

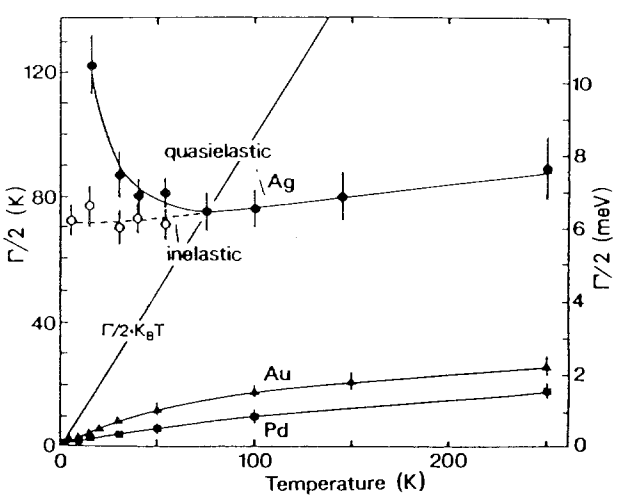

Fig. 33. Temperature dependence of the quasielastic Lorentzian linewidth of $YbPdCu_4$ (full squares), $YbAuCu_4$ (full triangles) and $YbAgCu_4$ (full circles). The open circles represent the width of an alternative fit of the $YbAgCu_4$ data below 75 K with an inelastic Lorentzian (Severing et al. 1990a).

– a VF behavior similar to $YbAgCu_4$ below T_v, the valence transition temperature, and

– a behavior similar to $YbAuCu_4$ and $YbPdCu_4$ for temperatures above T_v (Severing et al. 1990b).

For comparison, also the magnetic response of $YbInNi_4$ has been studied. The spectra of $YbInNi_4$, measured between 5 and 50 K, can be analysed in terms of an ordinary crystal field splitting with a level sequence 0–2.9–4.1 meV. Quasielastic and inelastic lines are well seperated. This is also the case for the spectra of $YbInCu_4$ above T_v where a similar level scheme is deduced with the level sequence 0–3.2–3.8 meV. Below T_v, however, the spectra of $YbInCu_4$ are completely different. In the VF phase the crystal field transition and the quasielastic scattering are absent (except for a small amount due to magnetic impurities) and, instead, a broad inelastic line centered around 40 meV and with a width of 18 meV appears. Measurements at various temperatures in the VF phase (5, 20, 35 K) show that the magnetic signal is nearly temperature independent in this state.

The three HF Yb compounds *$YbBe_{13}$*, *YbPd* and *Yb_3Pd_4* have in common that they order magnetically at low temperatures ($T_N = 1.28$, 0.5 and 3.1 K for $YbBe_{13}$, YbPd and Yb_3Pd_4, respectively) and that they show well-defined crystal field splittings as deduced from inelastic neutron scattering on polycrystalline samples by Walter et al. (1985) and by Walter and Wohlleben (1987). The behavior of these Yb compounds is similar to the behavior of Ce-based Kondo and HF compounds.

$YbBe_{13}$ has the cubic $NaZn_{13}$ structure (as $CeBe_{13}$) with $a = 10.195$ Å. The crystal field level scheme is Γ_7–Γ_8(3.2 meV)–Γ_6(4.4 meV) (Walter et al. 1985). The quasielastic linewidth shows a linear temperature dependence with a residual width of only 0.2 meV (2 K). The absolute values and the slope (~ 1 meV/300 K) of the quasielastic linewidth, though being small on the scale of non-ordering Yb-based VF compounds, are anomalously large if compared to the stable moment $TbBe_{13}$ compound (slope < 0.1 meV/300 K). Near the magnetic phase transition the quasielastic line is more of Gaussian than of Lorentzian shape.

A similar behavior as for $YbBe_{13}$ is observed for cubic YbPd (CsCl structure, $a =$ 3.44 Å) and trigonal Yb_3Pd_4 (Pb_3Pd_4 structure, $a = 12.917$ Å, $c = 5.664$ Å) by Walter and Wohlleben (1987). Yet, surprisingly, for both compounds nearly the same (cubic) level scheme is deduced from the neutron data [Γ_8–Γ_7(4–5 meV)–Γ_6(12–13 meV)]. Unfortunately, all results are obtained only with low-energy neutrons (3 meV) and on (partially) multiphase samples. We therefore hesitate to believe that the authors have really observed some novel features like two different quasielastic linewidths or 'magnetophonons' unless these are confirmed by new experiments. Also the interpretation of part of the data in terms of 'selection rules' for matrix elements between the nonmagnetic $4f^{14}$ configuration and the various crystal field states of the $4f^{13}$ configuration has been questioned from theoretical grounds (Schmidt and Müller-Hartmann 1989).

YbX compounds with X = N, P, As and Sb have the cubic rocksalt structure and a nearly integral 3+ valence for the Yb ions. Details of their physical properties depend on sample preparation and stoichiometry (see, e.g, Dönni et al. 1990a). Their main properties are:

– a large crystal field splitting with the level sequence Γ_6–Γ_8–Γ_7 and the first excited state at least 13 meV above the ground state,

– antiferromagnetic order with small Néel temperatures ($\leqslant 1$ K), being much lower than expected from the RKKY exchange interaction,

– reduced ordered magnetic moments ($\leqslant 0.9\mu_B$), much lower than expected for a Γ_6 ground state ($1.33\mu_B$).

The crystal field splitting has been investigated by two groups (Dönni et al. 1990a,b,c for X = N, P and Sb, and by Kohgi et al. 1990c for X = N, P and As). They agree on the level sequence Γ_6–Γ_8–Γ_7 but disagree on the position of the exited Γ_7 level and on the interpretation of the resulting crystal field parameters. For YbN Dönni et al. (1990b) and Kohgi et al. (1990c) observe a 6–7 meV *additional splitting* of the $\Gamma_6 \rightarrow \Gamma_8$ transition with a stronger peak at 30 (31.7) meV and a weaker peak at 37 (38) meV. The temperature dependence of this unusual splitting is investigated in more detail by Ohoyama et al. (1992). Returning to the discussion of the level scheme we have to mention that there is no matrix element for the $\Gamma_6 \rightarrow \Gamma_7$ transition so that the position of the Γ_7 level can only be obtained by the observation of the $\Gamma_8 \rightarrow \Gamma_7$ transition at elevated temperatures when the Γ_8 level is sufficiently populated. Dönni et al. place the Γ_7 level at 81 meV while Kohgi et al. place it at 50 meV due to differences in the interpretation of the high-temperature spectra (phonon scattering). Similarly for YbP, Dönni et al. (1990a) give Γ_6–Γ_8(19 meV)–Γ_7(43 meV) while Kohgi et al. give Γ_6–Γ_8(20 meV)–Γ_7(35 meV). For YbAs there are only published data by Kohgi et al. which propose a level sequence Γ_6–Γ_8(18 meV)–Γ_7(42 meV). Finally for YbSb there are only data by Dönni et al. (1990c). They again observe a splitting of the $\Gamma_6 \rightarrow \Gamma_8$ transition with a stronger peak at 13 meV and a weaker peak at 18 meV and place the Γ_7 level at 39 meV. The splitting of the $\Gamma_6 \rightarrow \Gamma_8$ transition in YbN and YbSb may be of similar origin as that observed in $CeAl_2$ (crystal field–phonon interaction).

In any case the ground-state Γ_6 doublet is well separated from the first excited Γ_8 quartet. The magnetic moment connected with Γ_6 is $1.33\mu_B$. In contrast to this expectation the ordered moments of YbN, YbP and YbAs as deduced from neutron diffraction by Dönni et al. (1990c) are only $0.39\mu_B$, $1.03\mu_B$ and $0.86\mu_B$. YbSb does not show magnetic ordering down to 7 mK. Slightly different results are obtained from specific heat (Ott et al. 1985) and Mössbauer effect measurements (Bonville et al. 1988) indicating the aforementioned sample dependence. Similar slight differences were also found for the values of the ordering temperatures by the different groups.

2.4. *Samarium-based systems*

Sm ions show low-lying spin–orbit coupled states which have to be included in the discussion of the magnetic response measured by inelastic neutron scattering when considering VF systems. The energy levels of 2+ and 3+ free Sm ions and CF split Sm ions are shown schematically in fig. 34. The following states have to be taken into account:

– For Sm^{2+} ($4f^6$): the nonmagnetic $J = 0$ ($^7F_0$) ground state and the $J = 1$ ($^7F_1$) excited state at 36.4 meV (free ion value); there is no splitting in cubic CF fields for both states.

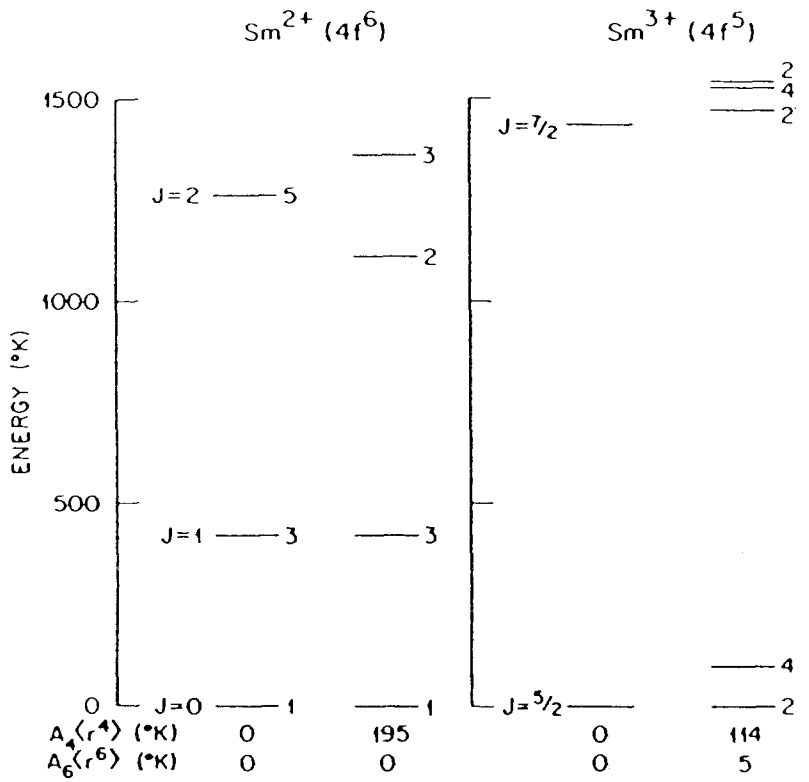

Fig. 34. Energy levels for free Sm ions and for Sm ions in crystal fields expected for SmS (with the CF parameters given below the scheme). Degeneracies are shown to the right of the levels (Moon et al. 1978).

– For Sm^{3+} ($4f^5$): the $J = 5/2$ ($^6H_{5/2}$) ground state and the $J = 7/2$ excited state at 130 meV; a cubic CF splits the ground state into a doublet and a quartet (same as for Ce^{3+}).

The strongest magnetic scattering stems from the $^7F_0 \rightarrow {}^7F_1$ transition with an inelastic magnetic cross-section of 7.3 b. The second largest cross-section is the quasi-elastic scattering within the $^7F_1$ excited state (2.72 b). Its observation, however, depends on its population, hence on temperature and valence. Both these cross-sections belong to the Sm^{2+} ion. On the other hand, the *total* magnetic scattering intensity from the $^6H_{5/2}$ ground state of Sm^{3+} is only 0.43 b (nine times smaller than for the $J = 5/2$ ground state of Ce^{3+}). If the state is split by a crystal field the intensity is furthermore divided into a quasielastic and an inelastic part. Besides the low magnetic intensities there is another handicap for the neutron investigation of Sm compounds: the rather high absorption cross-section. This requires the use of isotope-enriched samples. Therefore only few systems have been investigated. Mostly, also the quality of the data is not good enough to identify all expected contributions to the magnetic response. The situation is similar for Eu-based VF compounds.

SmS, $Sm_{0.75}Y_{0.25}S$ and YS have the simple NaCl structure with $a = 5.97$, 5.70 and 5.50 Å, respectively. SmS undergoes a first-order, isostructural phase transition around

0.65 GPa (6.5 kbar) at room temperature from the semiconducting, 'black' Sm^{2+} state to the metallic, 'gold', mixed valent state. At the phase transition the volume shrinks by 15% ($a_0 = 5.66$ Å in the gold phase of SmS). From the lattice parameter a ratio of 20/80 for the Sm^{2+}/Sm^{3+} mixing is estimated. Lattice pressure in the $Sm_{1-x}Y_xS$ alloys drives the Sm ions already at ambient pressure into the VF state for $x \geqslant 0.15$. The alloy $Sm_{0.75}Y_{0.25}S$, which was the only one investigated by neutron scattering, has a mixing ratio of $\sim 40/60$ for Sm^{2+}/Sm^{3+} at room temperature increasing to $\sim$ 70/30 at 2 K (with the dominant change around 200 K).

The $^7F_0 \rightarrow {}^7F_1$ excitation at 36 meV in SmS at ambient pressure was studied in detail by Shapiro et al. (1975) on a single crystal and by Mook et al. (1978a) on a polycrystalline sample as function of temperature. All data (dispersion, intensities) could be satisfactorily explained by the paramagnetic singlet–triplet model in MF–RPA (mean-field–random-phase approximation) assuming sharp transitions which are only limited by resolution. Applying pressure the situation is unchanged up to 0.6 GPa (McWhan et al. 1978). At 0.65 GPa in the VF phase, however, there is no evidence for *sharp* transitions from either the Sm^{2+} or the Sm^{3+} configuration. Yet, the accuracy of the experiments was not sufficient to detect *broadened* transitions which are expected in a VF system. These were observed in the VF alloy $Sm_{0.75}Y_{0.25}S$. Mook et al. (1978a) report a broad $^7F_0 \rightarrow {}^7F_1$ transition (FWHM $\approx$ 15 meV) centered around 32 meV. The temperature dependence of its intensity is claimed to be inconsistent with the expected temperature dependence for the singlet–triplet model (which worked so well for SmS). Mook et al.'s findings, however, are revised by recent experiments by Holland-Moritz et al. (1988). Due to better experimental resolution they observe a fine structure (four peaks) of the broad $^7F_0 \rightarrow {}^7F_1$ transition with individual linewidths of only 2 meV and a temperature dependence of the total intensity consistent with the expectations of the singlet–triplet model. The fine structure is explained in terms of a resonant coupling of optical phonons to the dispersive magnetic exciton built from the localized $^7F_0 \rightarrow {}^7F_1$ transition by magnetic intersite coupling. Clearly, single-crystal data are necessary to approve or disapprove this explanation. On the same polycrystaline sample of $Sm_{0.75}Y_{0.25}S$ Weber et al. (1989a) could also detect quasielastic scattering above $T = 100$ K. It stems from the $^6H_{5/2}$ ground state of the Sm^{3+} component and from transitions within the excited $^7F_1$ state of the Sm^{2+} component. Its width is about 7 ± 2 meV, and temperature independent between 100 and 250 K. As in other VF compounds the broad quasielastic magnetic response at elevated temperatures may become inelastic at low temperatures, but the experimental conditions (cold neutrons with $E_0 = 3.15$ meV) do not allow to draw any decisive conclusions from the data below 100 K. Also no indication of a crystal field splitting of the $^6H_{5/2}$ could be detected in this experiment. This shows that the low-energy magnetic response in $Sm_{0.75}Y_{0.25}S$ resembles strongly those of typical Ce- and Yb-based VF compounds.

Because of the drastic difference of the shape of the magnetic form factors of Sm^{2+} (monotonous decrease with Q) and Sm^{3+} (maximum at finite Q) interesting effects were expected from form factor measurements in VF Sm compounds. The results of Moon et al. (1978), however, indicate no visible change of the form factor of SmS when going from the 2+ low pressure to the VF high pressure phase as presented

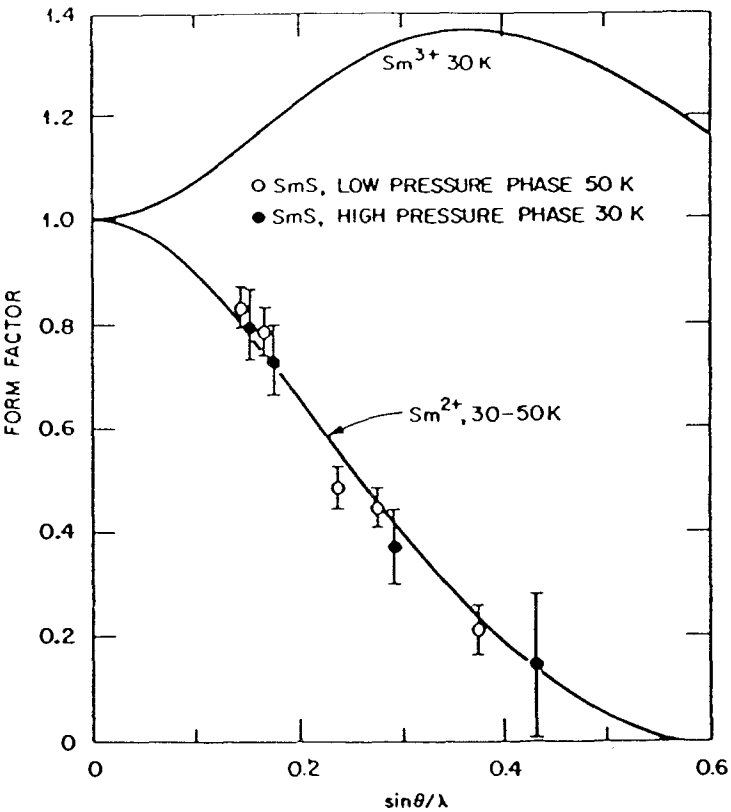

Fig. 35. Form factor of the high-pressure (VF) phase of SmS compared with the low-pressure results and the ionic calculations. The Sm^{3+} calculation is based on $A_4\langle r^4\rangle = 114\,K$, $A_6\langle r^6\rangle = 5\,K$ and $J_{ex} = 7\,K$ (Moon et al. 1978).

in fig. 35. Also more precise data from a single crystal of $Sm_{0.76}Y_{0.24}S$ (Moon et al. 1978, 1983) can only be fitted assuming an unreasonably small fraction of Sm^{3+} in the VF state. Moon et al. argue that the Curie term which gives rise to the finite Q maximum in the Sm^{3+} form factor is strongly suppressed in the VF state. This assumption is in line with susceptibility data of these Sm systems and furthermore supported by the observation of a broad quasielastic (or possibly inelastic) line in $Sm_{0.75}Y_{0.25}S$ as discussed above.

In contrast to the more subtle effects on the magnetic form factor and the difficulty to observe the influence on the inelastic magnetic response there are strong phonon anomalies associated with the VF state in SmS under pressure and in $Sm_{0.75}Y_{0.25}S$. Figure 36 shows the acoustic phonon dispersion curves of SmS in [111] direction at room temperature in the 2+ ('black', semiconducting) state at ambient pressure and in the VF ('gold', metallic) state at 0.7 GPa. Mook et al. (1982) observe a dramatic softening of the LA branch in the middle of the [111] direction while there is little change in the [100] and [110] directions. The unusual behavior of the LA mode in

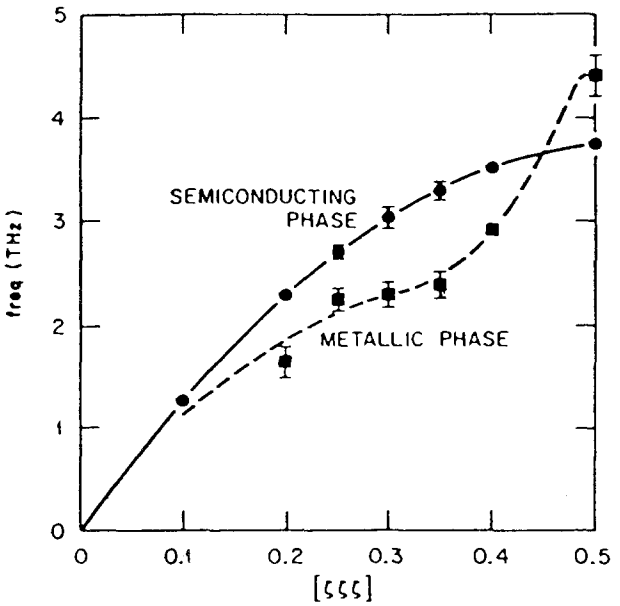

Fig. 36. LA phonon dispersion curves for the [111] direction for metallic (VF) and semiconducting SmS (Mook et al. 1982).

[111] direction is even more pronounced in the VF alloy $Sm_{0.75}Y_{0.25}S$ as measured by Mook et al. (1978b) and shown in fig. 37. Here the LA mode lies partly even *below* the TA mode. In addition, the phonons exhibit intrinsic linewidths. Temperature-dependent measurements by Mook and Nicklow (1979) reveal that the largest phonon softening and the largest phonon linewidths are observed around 200 K where $Sm_{0.75}Y_{0.25}S$ shows the steepest change in valence or Sm^{2+}/Sm^{3+} mixing. These findings could be explained quite satisfactorily by lattice dynamical models which take into account the peculiarities of the NaCl structure and the VF character of the Sm ions ('breathing' modes). The models were developed by Grewe and Entel (1979), Bennemann and Avignon (1979), Bilz et al. (1979), Wakabayashi (1980) and Mishchenko and Kikoin (1991).

SmB_6 crystallizes in the cubic CaB_6 structure with $a = 4.134$ Å (Alekseev et al. 1989). Its valence is ~ 2.6 as deduced from lattice parameter, Mössbauer isomer shift, and L_3 absorption edge. The resistivity of SmB_6 is small at room temperature but increases drastically below 30 K (by a factor of 10^4, depending on sample quality). Thus we can call SmB_6 a small-gap VF semiconductor with an activation energy of around 3 meV. Czycholl (1982) has calculated in the alloy approximation of the Anderson lattice model the dynamical magnetic response for SmB_6. At low temperatures he obtains an inelastic feature due to excitations across the hybridization gap. For increasing temperatures the inelastic feature weakens and quasielastic intensity appears. The whole response becomes quasielastic at sufficiently high temperatures (a few

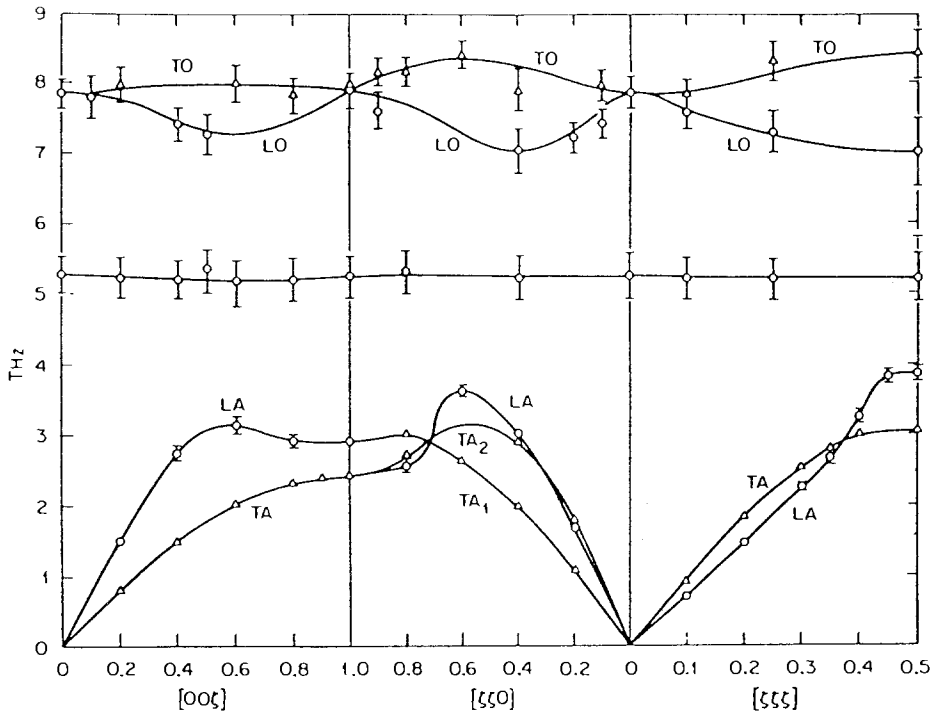

Fig. 37. Phonon dispersion curves for $Sm_{0.75}Y_{0.25}S$ measured at room temperature. The flat mode near 5 THz is the local Y mode (Mook et al. 1978b).

hundred K). This is what one typically observes for *metallic* VF compounds (e.g. $CePd_3$, $CeSn_3$) but it could not be verified for SmB_6 because the inelastic neutron scattering experiments are strongly hampered by poor statistics. The only available data (Holland-Moritz and Kasaya 1986, Alekseev et al. 1978b, 1992) show at $T = 5$ K a very weak inelastic line with intensity of only 0.1 b and positioned around 15 meV. It seems to be of magnetic origin but shows some peculiar Q-dependence (it broadens and merges for increasing Q into the 11 meV phonon line). We think that this inelastic line is a CF transition within the $^6H_{5/2}$ ground-state multiplet of Sm^{3+} interacting with the strong phonon density of states around 11 meV. Extrapolation of the CF parameters of CeB_6, PrB_6 and NdB_6 (Loewenhaupt and Prager 1986) would yield for Sm^{3+} a Γ_8 ground state and a Γ_7 excited state around 11 meV. The quasielastic scattering could not be detected in the above experiments due to insufficient energy resolution. Also the $^7F_0 \rightarrow {}^7F_1$ transition from the Sm^{2+} state was hardly visible, presumably due to strong line broadening. Its position is estimated to lie between 30 meV and 40 meV (Alekseev et al. 1992), close to the free ion value of 36 meV.

More successful than these measurements on polycrystalline samples of SmB_6 searching for the magnetic excitations were measurements of the phonon dispersion

relations on a single crystal of double isotope $^{154}Sm^{11}B_6$ by Alekseev et al. (1989, 1992). Starting from the dispersion of LaB_6 (Smith et al. 1985) the strong softening of the SmB_6 modes can only be explained if VF-specific breathing (Γ_1^+) and dipole (Γ_{15}^-) modes are added to the usual phonon modes. In addition there is a flat mode (at 4.75 THz $\hat{=}$ 20 meV). Temperature-dependent measurements indicate that the flat mode does not exist at T = 1.8 K.

2.5. *Europium-based systems*

In Eu-based VF systems the two valence states Eu^{2+} and Eu^{3+} have to be considered when discussing neutron scattering experiments. They yield:

– for Eu^{2+} ($4f^7$) a spin-only $^8S_{7/2}$ ground-state multiplet with negligible CF splitting and a rather large magnetic cross-section of 38 b (same as Gd^{3+}), and

– for Eu^{3+} ($4f^6$) a $J = 0$ $^7F_0$ nonmagnetic ground-state multiplet and a $J = 1$ $^7F_1$ magnetic excited state at 46 meV (free ion value), both being connected by an inelastic spin–orbit transition with 7.3 b (same as Sm^{2+}).

These properties would suggest that Eu VF compounds are good candidates for the study of the magnetic response with neutrons. A huge handicap, however, is the large absorption cross-section of natural Eu (2450 b for $E_0 = 30$ meV). The use of an isotope (^{153}Eu: 390 b for 30 meV) improves somewhat the situation but reduces drastically the number of investigated compounds (presently: two) even if there exists a much larger number of interesting Eu VF compounds.

$EuNi_2P_2$ has the tetragonal $ThCr_2Si_2$ structure with $a = 3.938$ Å and $c = 9.469$ Å (at room temperature). The valence changes only slightly with temperature: 2.53 at 16 K, 2.47 at 53 K and 2.35 at room temperature as deduced from Mössbauer data (Perscheid et al. 1985, Holland-Moritz et al. 1989b). The only inelastic neutron experiments, performed on a polycrystalline sample with ^{153}Eu isotope, are reported by Holland-Moritz et al. (1989b). Only the response from the Eu^{2+} state could be detected as function of temperature between 5 and 270 K. There was no indication of the $^7F_0 \rightarrow {}^7F_1$ transition of the Eu^{3+} state in the spectra with $E_0 = 50$ meV. This transition would have been observed if it had an energy of 38 meV or less (as in $EuPd_2Si_2$). But it would lie outside the accessible energy range if its energy were around 46 meV or larger (corresponding to the free ion value of the $^7F_0 \rightarrow {}^7F_1$ transition). It is thus not clear whether this Eu^{3+} transition was not observed due to intrinsic effects (e.g., line broadening) or due to experimental limitations.

We now discuss the Eu^{2+} response in more detail. Between 100 and 270 K a temperature independent broad quasielastic response with $\Gamma/2 \approx 6$ meV is observed. Its intensity corresponds roughly to the fraction of Eu^{2+} ions. Its Q-dependence is consistent with the Eu^{2+} magnetic form factor. Below 100 K the magnetic response splits into a quasielastic line and an inelastic line as shown in fig. 38. For decreasing temperatures the quasielastic component narrows and decreases in intensity while the inelastic line gains intensity and moves to higher energies. The temperature dependence of the linewidth of the quasielastic line and of the position of the inelastic line are reproduced in fig. 39. This behavior is similar to that found for TmSe.

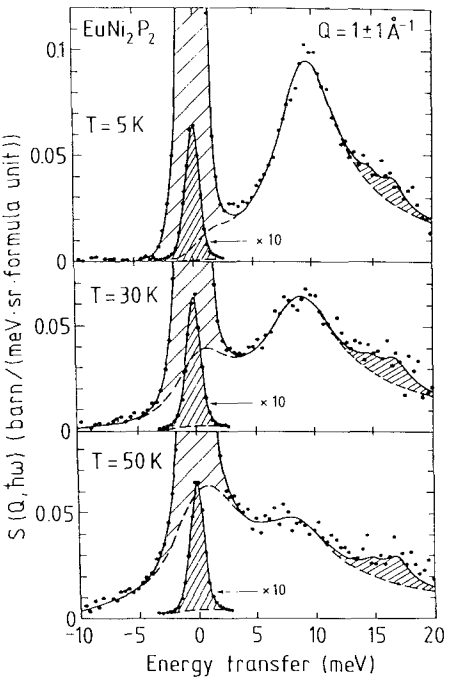

Fig. 38. Inelastic neutron spectra of $EuNi_2P_2$ at $T = 5, 30$ and 50 K obtained with $E_0 = 30$ meV. The hatched areas represent the elastic nuclear and the inelastic phonon scattering. The magnetic response (dashed or full line) involves a quasielastic and an inelastic line of Lorentzian shape (Holland-Moritz et al. 1989b).

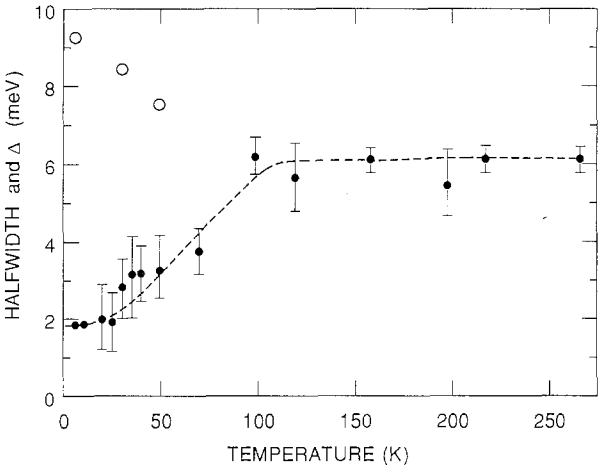

Fig. 39. Temperature dependence of the quasielastic magnetic linewidth (full circles) and of the position of the inelastic line (open circles) in $EuNi_2P_2$ (Holland-Moritz et al. 1989b).

Deviations of the Q-dependence of the intensity from the Eu^{2+} form factor at low temperatures (at $T = 5$ K, especially for the inelastic lines for $Q \leqslant 1$ Å^{-1}) were also reported by Holland-Moritz et al. (1989b) and assumed to be due to 5d-electrons (similar to $CeSn_3$).

$EuPd_2Si_2$ crystallizes in the $ThCr_2Si_2$ structure with $a = 4.10$ Å and $c = 9.88$ Å (Rogl 1984). As is found in many other VF Eu compounds the valence changes considerably with temperature. It is around 2.75 at 15 K and 2.3 at room temperature, exhibiting the largest change around $T = 150$ K. The only inelastic neutron scattering experiment was performed by Holland-Moritz et al. (1987) for different temperatures between 5 and 250 K on a polycrystalline sample enriched with ^{153}Eu isotope. The low temperature spectra ($T < 100$ K) are dominated by the response from the Eu^{3+} state: the $^7F_0 \rightarrow {}^7F_1$ transition (see fig. 40). The energy of this transition is considerably lower than the free ion value (38 meV in $EuPd_2Si_2$ compared to 46 meV) and its linewidth is only 2 meV. The response of the Eu^{2+} state cannot be seen directly in the spectra. It can only be deduced indirectly. Assuming an upper limit of 2.85 for the valence at 5 K and a quasielastic shape for the Eu^{2+} response, a lower limit of 25 meV for the linewidth is estimated by Holland-Moritz et al. (if this line exists at all at low temperatures). On the other hand, the spectra at high temperatures ($T \geqslant 200$ K) are dominated by the response from the Eu^{2+} state: quasielastic scattering with $\Gamma/2 \approx 4$ meV. No inelastic intensity from the $^7F_0 \rightarrow {}^7F_1$ transition is visible in this temperature region.

This yields a picture of $EuPd_2Si_2$ for the two temperature regions below and above the steep valence change of a VF system with not too fast spin fluctuations in both regions (2 and 4 meV, if the inelastic and the quasielastic linewidth are taken as measure). Furthermore, only the magnetic response of the dominant valence state is observed in each region. At intermediate temperatures (100–200 K) where the steep valence change takes place it seems that the response of both valence states is observed

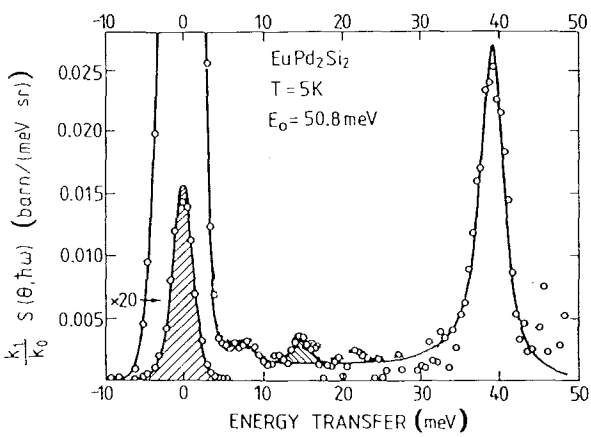

Fig. 40. Inelastic neutron spectrum of $EuPd_2Si_2$ at $T = 5$ K obtained with $E_0 = 50.8$ meV (Holland-Moritz et al. 1987).

simultaneaously. Both signals change, however, dramatically within a small temperature region. The quasielastic line broadens with *decreasing* temperature and becomes undetectable below 100 K while the inelastic $^7F_0 \rightarrow {}^7F_1$ transition broadens and shifts to lower energies with *increasing* temperature and becomes undetectable above 140 K.

2.6. *Thulium-based systems*

The peculiarity of Tm-based VF systems is the fact that both valence states have magnetic ground-state multiplets [Tm^{2+} ($4f^{13}$): $^2F_{7/2}$ ($N = 8$), same as Yb^{3+}, and Tm^{3+} ($4f^{12}$): $^3H_6$ ($N = 13$)]. The CF ground state of Tm^{2+} is at least a doublet, Tm^{3+} may have a CF singlet ground state. A large number of neutron investigations has been performed on TmSe and will be discussed here in detail. As far as other Tm compounds are concerned we are only aware of neutron data on the Kondo-lattice TmS (Lassailly et al. 1983, Holtzberg et al. 1985) and on pressure-dependent neutron scattering experiments on TmTe (Walter et al. 1992).

Stoichiometric *TmSe* has the simple rocksalt structure with $a = 5.71$ Å at room temperature. The sample preparation has been a problem from the beginning, especially for growing large single crystals. The valence is estimated to be around 2.6 (L_3 edges). Nonstoichiometric Tm_xSe shows the tendency towards 3+ for decreasing x in connection with a decreasing lattice parameter ($x = 0.87$: $a = 5.63$ Å, Batlogg et al. 1979).

Bjerrum-Møller et al. (1977) investigated the magnetic structure of a stoichiometric single crystal of TmSe by neutron diffraction. Surprisingly, they found a simple type-I antiferromagnetic structure below $T_N = 3.2$ K, yet with a rather small ordered moment of $(1.7 \pm 0.2)\mu_B$. Applying a magnetic field of about 0.4 T they observe a first-order phase transition from the antiferromagnetic state to a ferromagnetic state. The H–T phase diagram can be understood using a classical spin Hamiltonian with a weak and antiferromagnetic J_{nn}, a strong and ferromagnetic J_{nnn}, and a small anisotropy term. Bonnet et al. (1986) measured the magnetic form factor in the antiferromagnetic state, in the ferromagnetic state and in the paramagnetic state. While for the latter two states of TmSe they observe a purely f-like form factor, the form factor in the antiferromagnetic state deviates at low angles. This shows that only in the antiferromagnetic state the outer electrons of Tm (5d) are polarized (i.e., coupled to the 4f-magnetization), similar to the observations for VF Ce compounds (see section 2.2).

Neutron diffraction studies as function of external pressure were reported by Ribault et al. (1980) and Debray et al. (1981). The AF type-I structure is stable up to pressures of 3 GPa (with T_N first increasing with increasing pressure, passing a maximum around 1.5 GPa and then decreasing). For higher pressures (> 3 GPa) the structure changes to type-II AF. In the region between 1.5 and 3 GPa there seems to exist a mixture of both structure types (depending on sample). The type-II structure is also observed at ambient pressure for understoichiometric TmSe (sample 2, Shapiro et al. 1978) with $T_N \approx 4.7$ K. But even for 1.6 K the long-range order in this sample is not fully developed (correlation length ≈ 100 Å).

The interpretation of the dynamical response of TmSe is still rather controversial. It seems that the response of stoichiometric TmSe consists at low temperatures

(but above $T_N = 3.2\,K$) of a narrow quasielastic line ($\Gamma/2 \approx 0.5\,meV$ at $T = 5\,K$) well separated from an inelastic line at $\Delta = 10\,meV$. This was observed on a polycrystalline sample (Loewenhaupt and Holland-Moritz 1979b) and on a single crystal (Shapiro and Grier 1982) with room temperature lattice parameters of 5.711 and 5.714 Å, respectively. In all other experiments the sharp 10 meV inelastic line was not observed (sample 2, Shapiro et al. 1978, also Furrer et al. 1981) presumably due to the understoichiometry of the investigated sample. The sensitivity of the 10 meV line on the stoichiometry is shown in fig. 41 comparing the low temperature inelastic response of a single crystal of stoichiometric TmSe ($a = 5.714$ Å) with that of slightly understoichiometric $Tm_{0.99}Se$ ($a = 5.690$ Å). In the latter sample the inelastic structure is

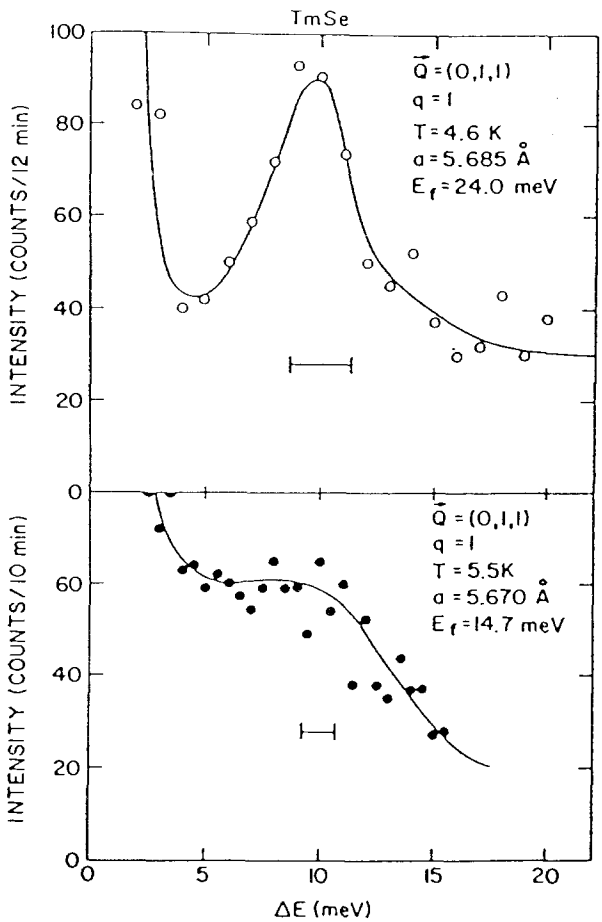

Fig. 41. Inelastic neutron spectra measured on two single crystals of TmSe at low temperatures. The top portion is for stoichiometric TmSe and the lower portion is for $Tm_{0.99}Se$. The concentrations were determined by the room temperature lattice constants. The lattice constants given in the figures are those at the low temperatures (Shapiro and Grier 1982).

already considerably broadened. We now come back to discuss the magnetic response of the stoichiometric compound in more detail: its Q, temperature and magnetic field dependence. Figure 42 shows the inelastic spectrum of TmSe at $T = 4.6$ K for several Q values along the [100] direction. Shapiro and Grier (1982) observe some dispersion (2 meV) and a drastic intensity variation within a Brillouin zone which deviates from the single ion Tm magnetic form factor. They explain their findings within a model of Fedro and Sinha (1981). In this model the 10 meV line is an excitation across a hydridization gap originating from the coupling between the localized f electrons and bandlike d electrons (as shown schematically in the inset in fig. 42). This interpretation has been doubted by Holland-Moritz (1983). He has observed an inelastic line also in the low temperature spectra of $TmSe_{0.85}Te_{0.15}$ and *dilute* $Tm_{0.05}Y_{0.95}Se$ and $Tm_{0.05}La_{0.95}Se$ favoring a *single ion origin* of the excitation. A model on this basis has been put forward by Mazzaferro et al. (1981) and Schlottmann (1984).

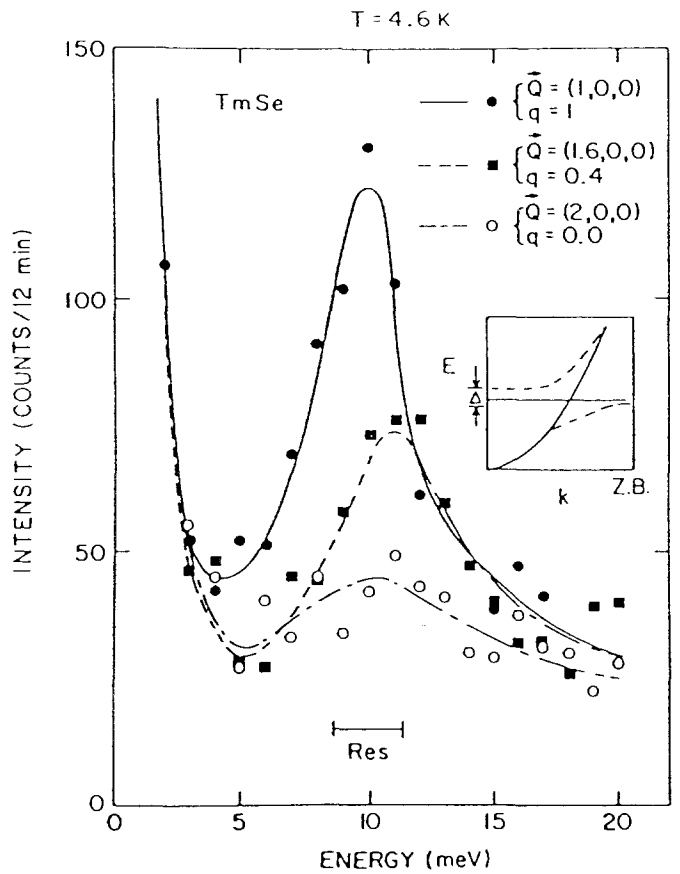

Fig. 42. Inelastic neutron spectra of TmSe measured at $T = 4.6$ K for different values of q along the $[q\,00]$ direction. The inset is a schematic form of uncoupled f and d bands (solid lines) and the result when they are coupled giving rise to a hybridization gap Δ (Shapiro and Grier 1982).

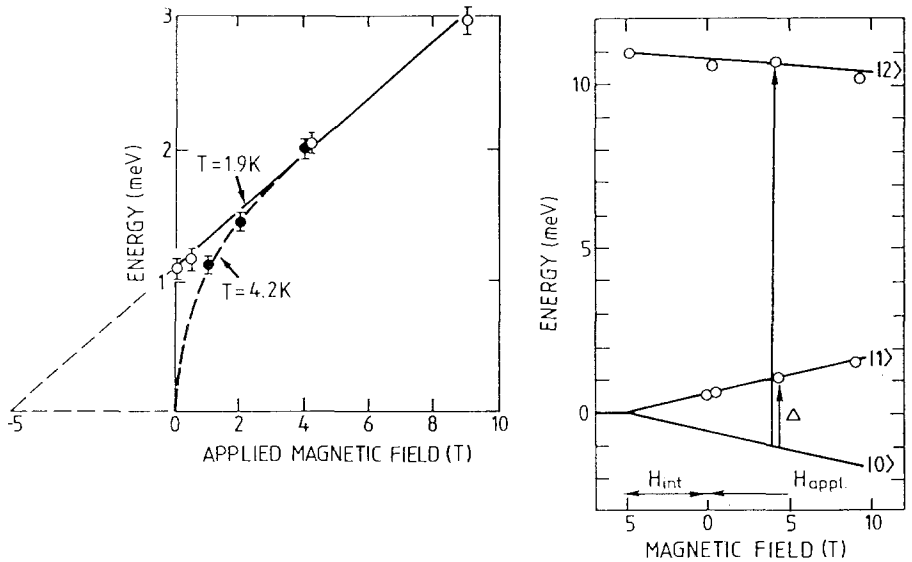

Fig. 43. Left: magnetic field dependence of the low energy excitation in TmSe at $T = 1.9$ K (below T_N) and at 4.2 K (above T_N). The extrapolation of the excitation energy for the data at 1.9 K (dashed line) yields the value of the internal field in the ordered state. Right: proposed level scheme for stoichiometric TmSe at low temperature. Levels 0 and 1 are singlets, the degeneracy of level 2 is unknown, but expected to be very large (Loewenhaupt and Bjerrum-Møller 1981).

No measurable effect on the 10 meV line is observed when TmSe is cooled below $T_N = 3.2$ K (Holland-Moritz and Loewenhaupt 1979, Shapiro and Grier 1982). The quasielastic line, however, becomes inelastic ($\Delta = 1$ meV) indicative of magnon-like excitations within the ground state. A field-dependent measurement of the magnetic spectra at $T = 1.9$ and 4.2 K by Loewenhaupt and Bjerrum-Møller (1981) reveals a strong field response of the magnon-like excitation while the 10 meV line is only little affected even in fields of 10 T (fig. 43). The ground-state splitting can be described by an effective spin $S = \frac{1}{2}$ and an effective g-factor of 3.8. The assumption of a doublet ground state ($N = 2$) is supported by specific heat data which show that the entropy has reached $0.5R \ln 2$ at T_N and $R \ln 2$ around 8 K (Berton et al. 1981). The temperature dependence of the magnetic response above T_N is almost identical for the polycrystalline sample and the single crystal (fig. 44). It shows a broadening and a shift of the inelastic line and a broadening of the quasielastic line. For temperatures around 80–120 K both lines merge into one broad quasielastic line with $\Gamma/2 \approx 7$ meV. Its width stays constant up to room temperature. The evolution of the quasielastic linewidth and of the position of the inelastic line (if present) is shown in fig. 45 for TmSe.

Finally we want to mention that also phonon anomalies have been observed in TmSe (Mook and Holtzberg 1981) and in dilute $Tm_{0.05}Y_{0.95}S$ (Holland-Moritz and Severing 1986) similar to those found in SmS under pressure and in $Sm_{0.75}Y_{0.25}S$.

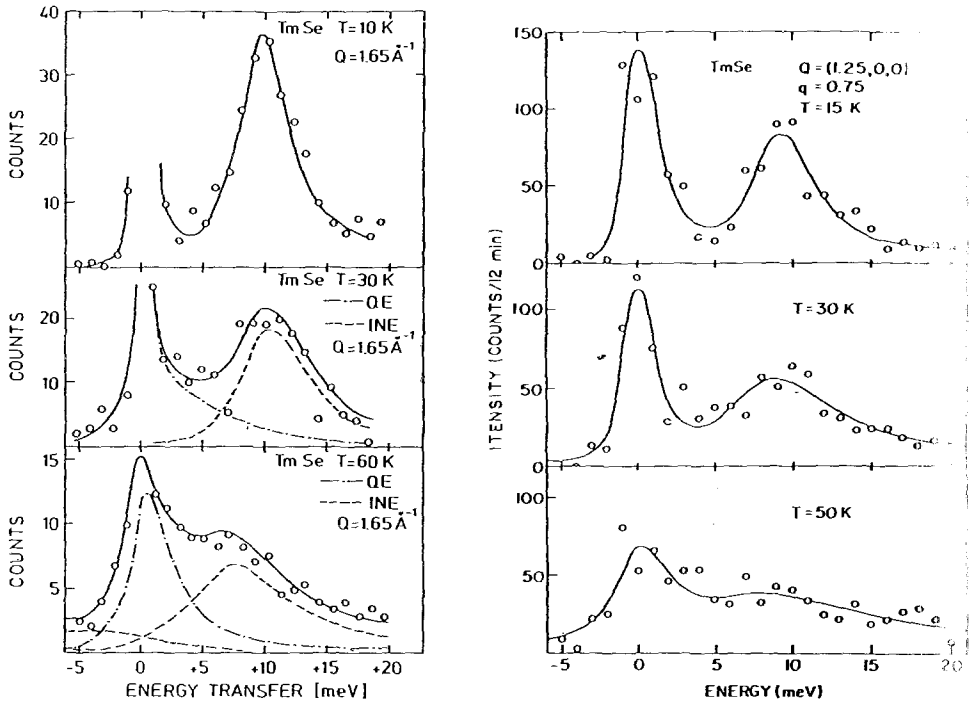

Fig. 44. Inelastic neutron spectra at different temperatures for stoichiometric TmSe in form of a polycrystalline sample (left, from Loewenhaupt and Holland-Moritz 1979b) and of a single crystal (right, from Shapiro and Grier 1982).

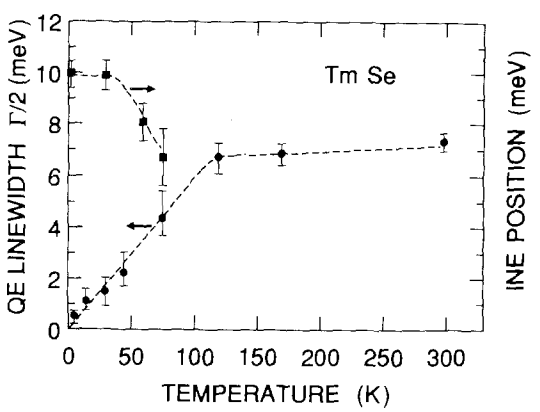

Fig. 45. Temperature dependence of the quasielastic linewidths (full circles) and of the excitation energies (full squares) of TmSe (from Loewenhaupt and Holland-Moritz 1979b, and Holland-Moritz 1983).

3. Survey over theoretical concepts

3.1. Dilute systems

Of the various models proposed to explain the VF and HF phenomena the Anderson model is the only one that has been investigated in great detail. If one includes CF and spin–orbit coupling, this model describes most properties fairly well despite its simplifications. In this model the conduction or valence electrons are assumed to form a single band. In R alloys and compounds this band is formed by 5d and 6s electrons, together with the conduction electrons of the other components of the system. The 4f electrons of a single R ion interact strongly via a screened Coulomb interaction. For a Ce ion this energy is of the order of $U \approx 5\,\text{eV}$ (Herbst et al. 1978, Johansson 1979). The exchange between these 4f electrons is usually neglected. The direct overlap of 4f wave functions between different sites is small and is also ignored. The 4f electrons hybridize with the conduction electrons, which makes them to a certain extent itinerant.

The eigenstates of a R ion in a free electron gas can be described by spherical coordinates with the quantum numbers k, l, l_z, σ where $k = |\boldsymbol{k}|$ is the momentum, l the total orbital angular momentum, l_z its z-component and σ the spin quantum number. However, in the presence of spin–orbit coupling only the total angular momentum $j = l \pm \frac{1}{2}$ is conserved. For the magnetic quantum number m we have $-j \leqslant m \leqslant j$. We introduce the states $|k, j, m\rangle = a|k, l, l_z - \frac{1}{2}, \uparrow\rangle + b|k, l, l_z + \frac{1}{2}, \downarrow\rangle$, where a and b are Clebsch–Gordon coefficients. For Ce ions one has in the $4f^1$ configuration $j = 5/2$, or a degeneracy $N = 2j + 1 = 6$. This multiplet can split in the solid by CF effects into multiplets with $N = 2$ and $N = 4$. With these basis states the Anderson model for a single impurity reads

$$H = \sum_{k,m} \varepsilon_k c^+_{km} c_{km} + \varepsilon_f \sum_m f^+_m f_m + V \sum_{k,m} (f^+_m c_{km} + c^+_{km} f_m) + U \sum_{m>m'} f^+_m f_m f^+_{m'} f_{m'}. \tag{8}$$

Here, f^+_m creates an f-electron with quantum number $j_z = m$, c^+_{km} a conduction electron in the state $|k, 5/2, m\rangle$; ε_k is the conduction electron energy, ε_f the 4f-electron energy [with $\varepsilon_f \approx -2\,\text{eV}$ below the Fermi level for Ce (Johansson and Rosengren 1975, Johansson 1979, Herbst et al. 1978)] and $V_k = \langle f^1, 5/2, m|V|f^0, k, 5/2, m\rangle \approx V$ the hopping matrix element which usually is assumed to be constant. The parameter V_k would vary on an energy scale of the bandwidth (of a few eV) whereas the energy scale of the Kondo effect is $k_B T_K$ corresponding to a few K. For Yb impurities one has $j = 7/2$ and has to replace electrons by holes since for the f^{14} configuration the 4f shell is completely filled and for f^{13} it has one hole.

The parameters of the model are the bandwidth D (with the Fermi energy assumed to be zero), the 4f electron energy ε_f, the f-electron interaction energy U and the mixing energy V. An important new parameter is the 4f-electron level width for $U = 0$,

$$\Delta = \pi N_c(0) V^2, \tag{9}$$

where $N_c(0)$ is the conduction electron density of states for both spin directions at

the band energy $\omega = 0$. In the case of VF systems one has $|\varepsilon_f| \leqslant \Delta$, which leads to strong charge fluctuations. For HF systems one has $-\varepsilon_f \gg \Delta$ with $\varepsilon_f < 0$. In both types of systems the conduction band extends to still lower energies (Herbst et al. 1978).

For $-\varepsilon_f \gg \Delta$, $U \gg \Delta$ and $U + 2\varepsilon_f = 0$ the Anderson Hamiltonian, eq. (8), can be transformed into the Coqblin–Schrieffer (CS) Hamiltonian. In this 'Kondo limit' charge fluctuations are completely suppressed and the model describes an effective 4f-electron spin j which interacts via exchange with the conduction electrons

$$H_{CS} = \sum_{k,m} \varepsilon_k c^+_{km} c_{km} - J \sum_{kk'mm'} c^+_{k'm'} f^+_m f_{m'} c_{km}. \tag{10}$$

The exchange coupling constant for electrons at the Fermi surface,

$$J = V^2 \frac{U}{\varepsilon_f(\varepsilon_f + U)}, \tag{11}$$

is negative for Ce impurities with $\varepsilon_f < 0$, $\varepsilon_f + U > 0$. For $j = \frac{1}{2}$, $m \pm \frac{1}{2}$ (or spin $\frac{1}{2}$), the model of eq. (10) can be identified with the Kondo Hamiltonian

$$H_K = \sum_{k,\sigma} \varepsilon_k c^+_{k\sigma} c_{k\sigma} - J \sum_{kk'\sigma\sigma'} \boldsymbol{S} c_{k'\sigma'} \boldsymbol{\sigma} c_{k\sigma}, \tag{12}$$

with the Pauli matrices $\boldsymbol{\sigma}$ and the spin quantum numbers σ, σ'. The generalization of the Kondo model [eq. (12)] for a lattice (see section 3.2) describes for instance $CeAl_3$ and $CeCu_2Si_2$. In these systems the sixfold degeneracy of the Ce $j = 5/2$ state is split by the CF into three doublets. At sufficiently low temperatures only the lowest doublet is effective, corresponding to $S = \frac{1}{2}$.

For the nonsymmetric Anderson model with $U + 2\varepsilon_f \neq 0$, one has in the Coqblin–Schrieffer and Kondo Hamiltonians in addition to the exchange a potential scattering term. The Kondo resonance is no longer at the Fermi energy $\varepsilon_F = 0$ but is shifted. This shift leads to a smaller resistivity $\rho(T)$, the maximum of which, however, is still at $T = 0$. The potential scattering has a dramatic effect on the thermoelectric power which vanishes in the symmetric case $U + 2\varepsilon_f = 0$ but has a huge peak near T_K for $U + 2\varepsilon_f \neq 0$.

In the case of crystal field (CF) effects one has to add to the Hamiltonians of eq. (8), (10) or (12) a term which for the lowest multiplet (j, m) can be written as

$$H_{CF} = \sum_{lm} B^m_l O^m_l, \tag{13}$$

with the CF parameters B^m_l and where the 'Stevens operator equivalents' O^m_l depend on the crystal symmetry. Magnetic excitations in CF-split systems are discussed in detail by Fulde and Loewenhaupt (1986).

Both the Anderson and the Kondo (or Coqblin–Schrieffer) models have been solved exactly for thermodynamic properties such as the 4f-electron valence, specific heat, static magnetic and charge susceptibilities, and the magnetization as a function of temperature and magnetic field $\boldsymbol{B}$ by means of the Bethe ansatz (see Schlottmann 1989 and references therein). This method allows also to calculate the zero-temperature resistivity as a function of $\boldsymbol{B}$. Non-equilibrium properties such as the finite temperature resistivity, thermopower, heat conductivity or dynamic susceptibility could be

calculated in a self-consistent approximation (the 'noncrossing' approximation) which works very well and is based on an $1/N$ expansion where N is the degeneracy of the 4f level,

$$N = 2j + 1 \tag{14}$$

(see Bickers 1987, and references therein). Spectroscopic properties have been calculated for the ground state by means of a variation method (Gunnarsson and Schönhammer 1987).

In all theories emerges a characteristic temperature, the Kondo temperature, which is approximately

$$T_K = (D/k_B)\exp[\pi\varepsilon_f/N\Delta], \tag{15}$$

where D is the conduction electron bandwidth (see, for instance, Newns and Read 1987, eq. 31). In a more rigorous expression (Schlottman 1989, eq. 4.29) the prefactor of the exponential in eq. (15) depends also on the quantum number j. For temperatures far above T_K all theories predict a magnetic state with a Curie susceptibility and $\ln T$ terms in the susceptibility, specific heat, resistivity, etc. Far below T_K one has Fermi liquid behavior with simple power laws of all quantities as a function of the temperature, the excitation energy ω and the magnetic field B. In this regime all $\ln T$ singularities vanish. At all temperatures one has scaling: most quantities are functions of T_K, T/T_K, ω/T_K or B/T_K and do not depend explicitly on the model parameters J or U, ε_f and Δ. The ground state is a singlet, i.e., the impurity moment is 'quenched' or 'compensated' by the spins of the surrounding conduction electrons.

For a *non-interacting* electron gas one has the linear coefficient γ of the specific heat per R ion for $T \to 0$

$$\gamma = \frac{\pi^2}{3} k_B^2 N N_c(0), \tag{16}$$

where $N_c(\omega)$ is the electron density of states per R atom and per channel m. The corresponding zero temperature susceptibility reads (Newns and Read 1987)

$$\chi(0) = \tfrac{1}{3} N \mu_{eff}^2 N_c(0), \quad \mu_{eff}^2 = g_j^2 \mu_B^2 j(j+1), \tag{17}$$

with the Landé factor g_j for the total angular momentum j and the Bohr magneton μ_B. Equations (16) and (17) lead to the Wilson ratio

$$R = \frac{\chi(0)/\mu_{eff}^2}{\gamma/\pi^2 k_B^2} = 1. \tag{18}$$

In the Kondo limit $U \to \infty$, $|\varepsilon_f| \gg \Delta$ one has from Bethe ansatz (Andrei and Loewenstein 1981, Andrei et al. 1983, Tsvelick and Wiegmann 1982, 1983) the exact result

$$\chi(0) = \frac{\mu_{eff}^2}{3T_K}, \quad \gamma = \frac{\pi^2}{3} k_B^2 \frac{1}{T_K} \frac{N-1}{N} \tag{19}$$

(with a properly defined characteristic temperature T_K) which leads to the Wilson ratio $R = N/(N-1)$. Note that R reaches for $N = 2$ its maximum value $R = 2$ and

for $N \to \infty$ (which corresponds to the mean field theory discussed below) the value $R = 1$, eq. (18). For non-integer valences $n_f < 1$ or VF systems the correction $1/(N-1)$ to the mean field value $R = 1$ yields a smaller value (Newns and Read 1987). For most dilute HF alloys one observes indeed R of the order of unity. The result of eq. (19) can be interpreted as the susceptibility and the coefficient γ of independent quasi-particles in a Fermi liquid. It can be compared with eq. (17) if we define a quasi-particle density of states $N_f(\omega)$ which is mostly of f-character and which replaces $N_c(0)$ in eq. (17). This leads to $NN_f(0) = T_K^{-1}$ and with $NN_c(0) \sim T_F^{-1}$ and the Fermi temperature $T_F = \hbar^2 k_F^2/2m$ to a huge effective mass m^* proportional to mT_F/T_K or to a strongly enhanced specific heat and susceptibility in the Fermi liquid state since $T_F/T_K \gg 1$.

The large f-electron density of states $N_f(0)$ is due to the Kondo resonance which exists in both VF and HF systems. Figure 46 shows a schematic plot of the 4f electron density of states of a Ce ion at temperatures $T \ll T_K$ with the energy ω measured from the Fermi level. One has at energy $\varepsilon_f < 0$ a broad peak due to the transition of a conduction electron into the empty 4f level ($f^1 \to f^0$) and a similar broad peak centered around the energy $\varepsilon_f + U$ due to a transition $f^1 \to f^2$. These peaks can be obtained in the lowest decoupling approximation of an equation of motion and have the width $N\Delta$ with Δ from eq. (9) (Kittel 1963). The sharp Kondo resonance appears only for $T < T_K$ and has at $T = 0$ the width of order $\pi k_B T_K/N$ (Bickers 1987). For Ce alloys the density of states $N_f(\omega)$ has its maximum at the energy $\varepsilon_m > 0$. For the symmetrical Anderson model or for the Kondo model $\varepsilon_m = 0$.

The Kondo resonance is a many-body effect. It can be traced to the fact that a sudden perturbation of an electron gas creates an infinite number of electron–hole pairs with the excitation energy $\omega \to 0$. In our case the perturbation is caused by spin flip or by the exchange of a 4f and a conduction electron. In the simplest process a single conduction electron goes into the f^0 level, leading to an f^1 state and leaving a hole in the conduction electron band. In the intermediate state and at $T = 0$, this leads to electron–hole excitations of arbitrarily small energies. At finite temperatures the Fermi surface no longer is sharp and the Kondo resonance is 'washed out'. A complementary picture is the result of high-temperature perturbation or T-matrix

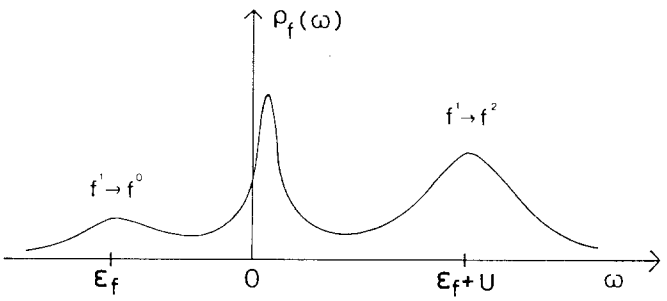

Fig. 46. Schematic 4f-density of states for a Ce ion in a simple metal. The energy ω is measured from the Fermi level. The two broad peaks are due to $4f^1 \to 4f^0$ and $4f^1 \to 4f^2$ transitions. The peak close to $\omega = 0$ is the Kondo resonance.

theory of the Kondo model (Fischer 1970) or of renormalization group calculations (Wilson 1975, Nozières 1974). Both approaches show that with decreasing temperature the system can be described by an increasingly strong effective exchange interaction $J_{\text{eff}}(T)$. This leads for $T \to 0$ to a singlet state which is formed by the impurity spin and spins of the surrounding conduction electrons and which leads to a disappearance of the impurity spin degree of freedom in thermodynamic properties. Evidence for this is the transition from Curie to Pauli behaviour of the susceptibility. However, there are still low-energy magnetic excitations of the 4f-electrons (which form this singlet state) which are observed in inelastic neutron scattering in the form of a quasielastic scattering peak of the width of the order $k_B T_K$. In addition, the increasingly stronger exchange leads to increasingly stronger scattering of the conduction electrons and to a maximum in the resistivity at $T = 0$. For the symmetric Anderson model and $T = 0$ (or for the Kondo resonance at $\omega = 0$) this scattering reaches its maximum possible value for a single scattering channel or the 'unitarity' limit (Grüner and Zawadowski 1974).

The Kondo effect, including a Kondo resonance, exists also in VF systems where one has in contrast to HF systems also sizeable charge fluctuations. In the following we list theoretical results for both systems, as obtained from the Bethe ansatz (for a review, see Schlottmann 1989) and from a self-consistent perturbation theory with respect to the hopping-matrix element V, the so-called noncrossing approximation (NCA), which is essentially an expansion with respect to the inverse of the 4f degeneracy N, eq. (14) (Keiter and Kimball 1971, Kuramoto 1983, Keiter and Czycholl 1983, Grewe 1983, Zhang and Lee 1983, 1984, Coleman 1984, 1987a, Bickers et al. 1987, Bickers 1987). The highest-order terms of this expansion can also be obtained in a

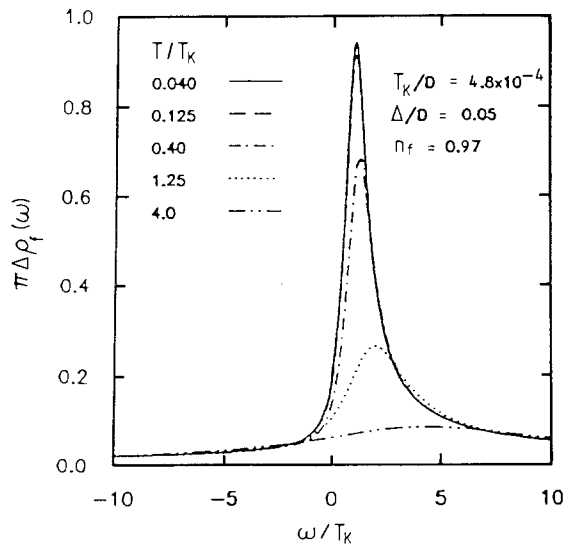

Fig. 47. Temperature dependence of the 4f density of states in NCA. The density of states is normalized by $\pi\Delta$. The Kondo scale is in this case 100 times smaller than the hybridization width Δ (Bickers et al. 1987).

mean field theory which leads to the Wilson ratio $R = 1$. Both methods yield for thermodynamic properties fairly similar results even for $N = 4$ and $N = 6$ (see below). However, the NCA allows also for the calculation of transport properties, in contrast to the Bethe ansatz.

In this survey over VF and HF phenomena we discuss only the most important results of both methods, apart from neutron data which have been dealt with separately in section 2 and on the end of section 3.2.

The Kondo resonance in the f-electron density of states shows a strong temperature dependence. It is largest at $T = 0$ and is already strongly reduced and broadened at temperatures $T \approx T_K$ (fig. 47). At least at $T = 0$, it is fairly insensitive to the average number n_f of f-electrons or holes per R ion with $n_f \approx 1$ for Ce and Yb alloys (fig. 48). Hence, VF systems with n_f distinctly lower than unity have nearly the same resonance as HF systems with $n_f \approx 1$. However, the energy scale T_K is considerably smaller in HF systems than in VF systems. The valence n_f itself depends on temperature (fig. 49). Smaller n_f-values increase fairly rapidly near T_K and approach at high temperatures the value of HF systems. This expresses the fact that for $T \gg T_K$ perturbation theory with respect to the hybridization V is valid and in zeroth order one can put $V = 0$. One is then dealing with an ensemble of independent ions and band electrons. The results shown in figs. 47–49 and in the following figs. 50–52 have been obtained by solving the NCA equations numerically for the degeneracy $N = 6$ corresponding to Ce ions with $l = 3$ and $j = 5/2$.

The temperature dependence of the magnetic impurity resistivity $\rho_{imp}(T)$ [normalized to its value $\rho_{imp}(0)$ at $T = 0$] and of the corresponding specific heat $c_m(T)$ is plotted

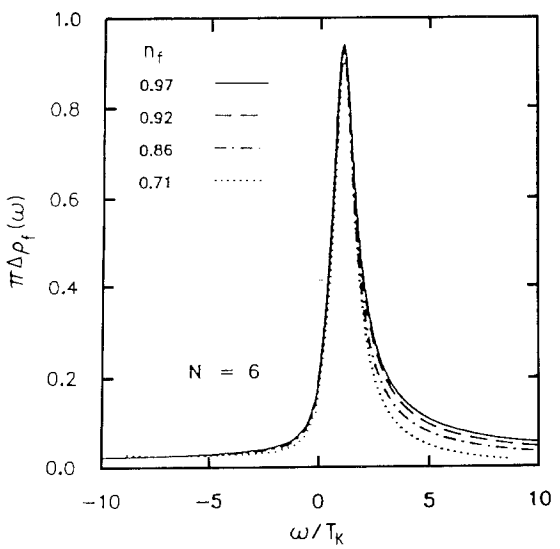

Fig. 48. 4f density of states for $T \to 0$ and various valences (or average numbers of 4f-electrons per R ion) n_f in NCA. The 4f level degeneracy is $N = 6$ (Bickers et al. 1987).

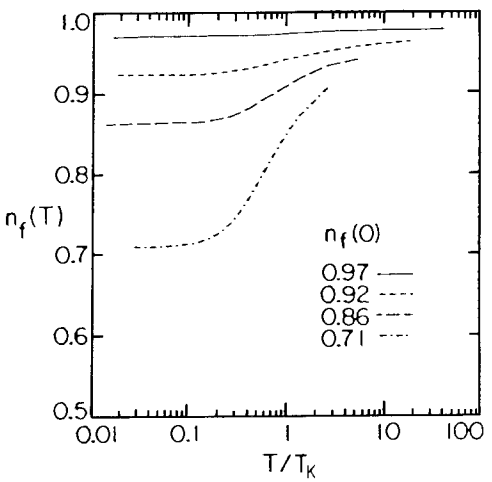

Fig. 49. Temperature dependence of the 4f-electron valence n_f in NCA (Bickers et al. 1987).

in figs. 50 and 51, respectively. Both $\rho_{imp}(T)$ and $c_m(T)$ scale with T/T_K and do not differ strongly for VF systems with $n_f = 0.71$ and HF systems with $n_f \approx 1$. The resistivity has its maximum at $T = 0$ and varies within about one decade around T_K as $\ln(T/T_K)$. It reaches its asymptotic (constant) value as given by the Born approximation only at temperatures $T > 100T_K$, i.e., outside the temperature range shown in fig. 50. In the Kondo limit $n_f \to 1$ the zero temperature resistivity $\rho_{imp}(0)$ can be calculated exactly. From the Friedel sum rule one has (Langreth 1966, Newns and Read 1987,

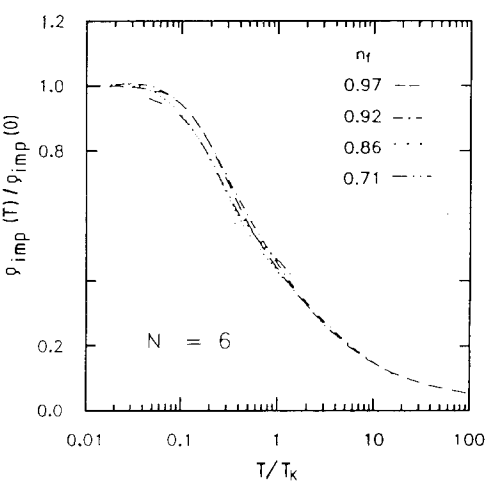

Fig. 50. Temperature dependence of the impurity resistivity for $N = 6$ and various values for the valence n_f in NCA (Bickers et al. 1987).

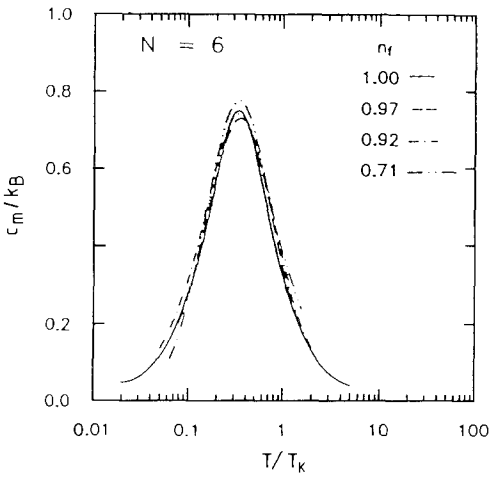

Fig. 51. Temperature dependence of the impurity (or magnetic) specific heat for $N = 6$ and various values for n_f in NCA. The result for $n_f = 1$ and the characteristic temperature T_K are calculated by means of the Bethe ansatz (Bickers et al. 1987).

Cox and Grewe 1988)

$$\rho_{\text{imp}}(0) = \frac{2\pi n_i}{ne^2 k_F} N \sin^2(\pi n_f / N). \tag{20}$$

Here n_i is the impurity concentration and n the concentration of conduction electrons.

The specific heat as a function of $\ln(T/T_K)$ shows a broad maximum below T_K.

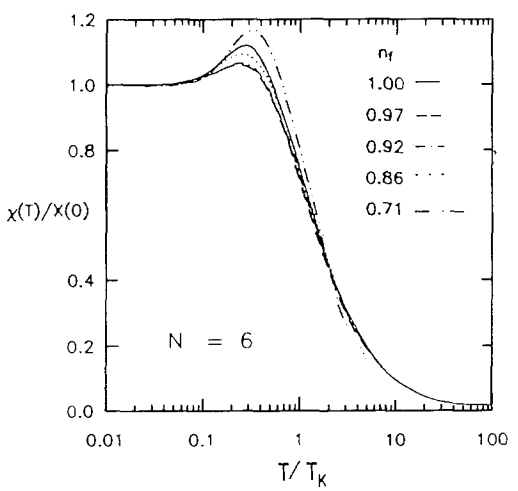

Fig. 52. Temperature dependence of the magnetic susceptibility for $N = 6$ in NCA. The curve $n_f = 1$ is a Bethe ansatz result. The susceptibility exhibits a weak maximum at $T/T_K \approx 0.5$ which depends on n_f (Bickers et al. 1987).

For $T \ll T_K$, both $\rho_{imp}(T)$ and $c_m(T)$ show Fermi liquid behavior with $\rho_{imp}(T) = \rho_{imp}(0)[1 - A(T/T_K)^2]$ and $c_m(T) = \gamma T$, where $A = \pi^2(1 - 8/3N)$ to order $1/N$ (Houghton et al. 1987) and where γ is given by eq. (19).

The susceptibility $\chi(T)/\chi(0)$ with $\chi(0)$ from eq. (19) is shown in fig. 52. It is again similar for VF and HF systems, apart from a peak near T_K, which is more pronounced for VF systems. This peak depends strongly on the 4f level degeneracy N and vanishes in the Kondo model with $N = 2$ or effective spin $S = \frac{1}{2}$. Figure 53 shows this behavior

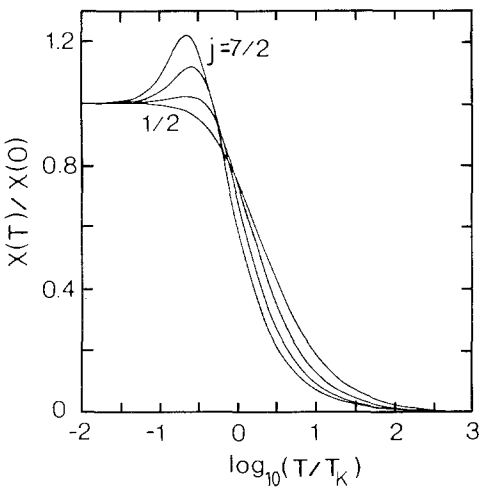

Fig. 53. Temperature dependence of the magnetic susceptibility for impurities with total angular momenta $j = 1/2, 3/2, 5/2, 7/2$ and $n_f = 1$, calculated with the Bethe ansatz for the Coqblin–Schrieffer model [eq. (2.3)] (Rajan 1983).

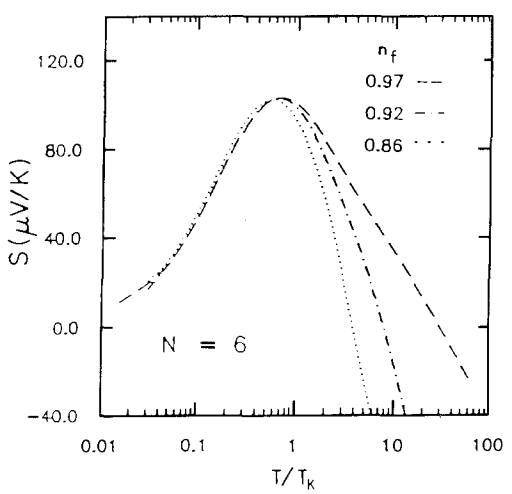

Fig. 54. Temperature dependence of the impurity thermopower $S(T)$ for $N = 6$ in NCA. For $T > T_K$ the thermopower depends strongly on n_f (Bickers et al. 1987).

for the susceptibility in the Coqblin–Schrieffer model [eq. (10)] (in which charge fluctuations are ignored) for various values of the total angular momentum j.

The temperature dependence of the thermopower $S_d(T)$ of VF and HF systems is very similar for $T < T_K$ but differs considerably for $T > T_K$ (fig. 54). For $N = 6$ it has a huge peak roughly at $T = T_K$ of order 100 μV/K whereas in typical metals it is of the order 1 μV/K. At low temperatures one has Fermi liquid behavior and the exact result

$$S_d = 2\gamma \frac{\pi}{|e|N} T \cot(\pi n_f/N), \quad T \to 0, \tag{21}$$

with the specific heat coefficient γ of eq. (19). The thermopower of Ce-based HF systems is positive, for Yb-based systems negative (Houghton et al. 1987, Fischer 1989b).

A crystal field (CF) can strongly modify these 'standard' properties of VF or HF systems if the CF level splitting is of the order of $k_B T_K$. Figure 55 shows a shift and the deformation of the Kondo peak and also a Schottky peak in the specific heat due to cubic CF splitting for this case.

The theoretical results based on the NCA (or $1/N$ expansion) and on the Bethe ansatz presented so far are generally in rather good agreement with experimental data for dilute R systems. For such a comparison we present a few examples and refer for a more extended (but still rather incomplete) collection of experimental data for HF systems to Stewart (1984) and Grewe and Steglich (1991).

The impurity resistivity $\rho_{imp}(T)/\rho_{imp}(0)$ of the dilute HF system (CeLa)B_6 agrees very well with the results of the NCA for $N = 4$ over more than three temperature decades (fig. 56). The agreement with the data for the specific heat of (CeLa)B_6 is less

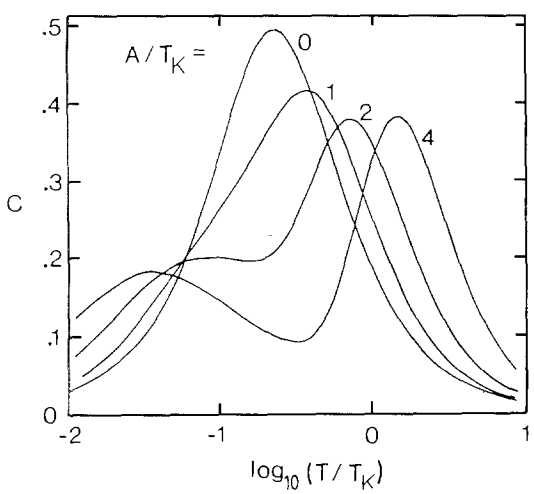

Fig. 55. Specific heat of a $j = 3/2$ Coqblin–Schrieffer impurity as a function of temperature for various CF strengths A where the CF splits a quadruplet into two Kramers doublets (Desgranges and Rasul 1985, Schlottmann 1989).

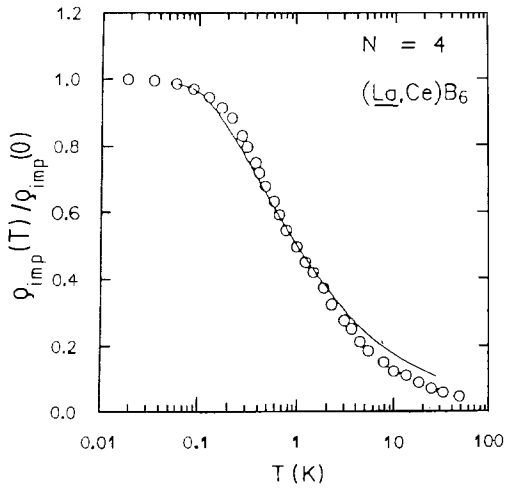

Fig. 56. Comparison of the results of the NCA for $N = 4$ with experimental data for dilute (CeLa)B_6: electrical resistivity (Bickers et al. 1987).

satisfactory. Figure 57 shows these data (including data with a magnetic field) and the theoretical results for the Coqblin–Schrieffer model with $S = \frac{3}{2}$. In fig. 58 the data for the susceptibility and specific heat of the VF system YbCuAl are compared with results from the Bethe ansatz with $N = 8$. For the specific heat the difference between YbCuAl and the nonmagnetic analog LuCuAl is presented in order to eliminate

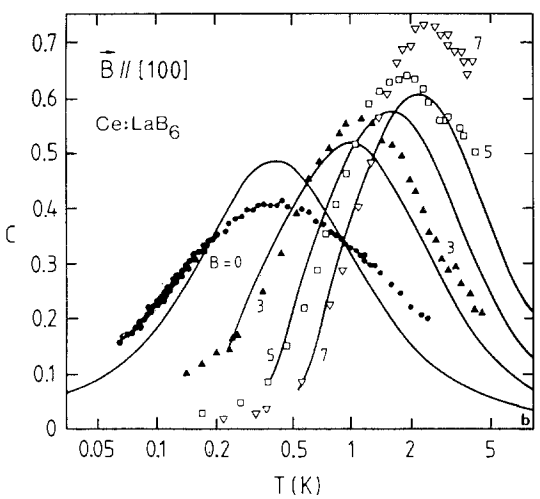

Fig. 57. Comparison of results from the Bethe ansatz for the Coqblin–Schrieffer model with $S = \frac{3}{2}$ and $T_K = 0.86$ K with the specific heat of dilute (CeLa)B_6 as a function of temperature for various magnetic fields (in tesla). Part of the discrepancy between theory and experiment might be due to CF effects (Schlottmann 1989).

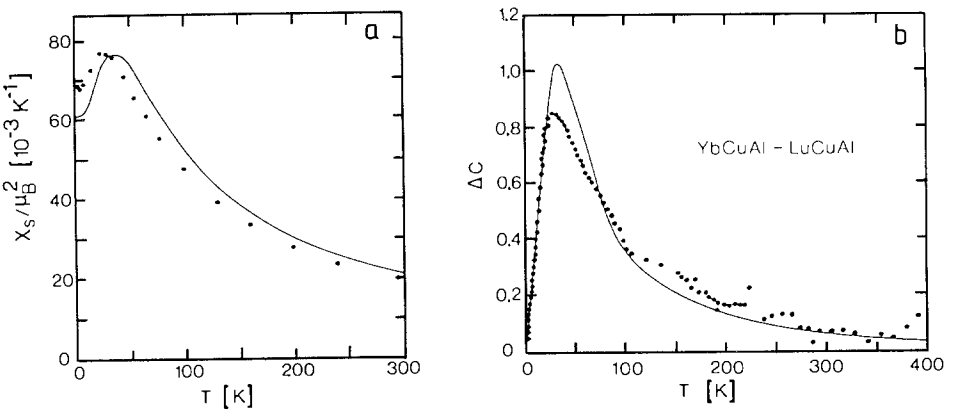

Fig. 58. Temperature dependence of (a) the susceptibility of YbCuAl, and (b) the specific heat difference between YbCuAl and the nonmagnetic analog LuCuAl compared with theoretical results from the Bethe ansatz for a Coqblin–Schrieffer impurity with $N = 8$, $\Delta = 527$ K and $g_j = 8/7$ (Schlottmann 1989).

phonon contributions. Part of the difference between experimental and theoretical results again can be explained by CF effects. In addition, one might have impurity interactions in this nondilute system.

3.2. *Concentrated systems and compounds*

The physical properties of concentrated VF and HF systems and of compounds are much less understood than those of dilute systems. In the case of transition metals in a nonmagnetic host one has already for rather small concentrations (of the order of one percent) magnetic order or spin glass structure due to direct or indirect exchange interactions. In R systems direct exchange is small, but the Rudermann–Kittel–Kasuya–Yosida (RKKY) interactions can also lead to magnetic order or spin glass properties. As first pointed out by Doniach (1977), there is a competition between the Kondo effect (which leads to the formation of singlet states and hence to a nonmagnetic ground state) and the RKKY interactions. The internal fields due to these interactions tend to destroy the singlet formation or the Kondo effect. One expects a phase transition from a nonmagnetic to a magnetic state as a function of concentration of the R ions or of the ratio J/D where D is the width of the conduction electron band. The Kondo temperature of eq. (15) with eqs. (9) and (11) varies exponentially with the exchange constant J. One has for $N = 2$ or $S = \frac{1}{2}$ (note that $2N_c(\omega)$ is the conduction electron density of states for both spin directions)

$$T_K = (D/k_B)\exp[1/J2N_c(0)], \quad J < 0, \tag{22}$$

and for the RKKY interaction (Moshchalkov and Brandt 1986)

$$T_{RKKY} \approx J^2/k_B D. \tag{23}$$

The dependence of both characteristic temperatures on $|J|N_c(0)$ is indicated in fig. 59. One has three regimes. (a) For extremely small values of $|J|N_c(0)$ the RKKY interaction

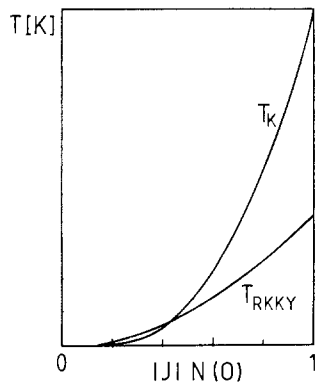

Fig. 59. Dependence of the Kondo temperature T_K and the RKKY interaction temperatures T_{RKKY} on the coupling constant (Aliev et al. 1984).

'wins' and the system has stable moments at all temperatures. (b) For somewhat larger values, but still $|J|N_c(0) \ll 1$ one has $T_K \gtrsim T_{RKKY}$. The system shows the Kondo effect but there is a delicate interplay between both interactions and the ground state depends also on the band structure and other details if the interactions are of the same order of magnitude. (c) For $|J|N_c(0)$ of the order unity one has very large Kondo temperatures, but also charge fluctuations. In this VF regime the magnetic interactions become unimportant and one has a nonmagnetic ground state, as is also observed. However, strictly speaking, the Kondo model becomes invalid in this regime. More rigorous results for a one-dimensional Kondo model have been obtained by Doniach (1977) who predicted a second-order phase transition at $T = 0$ from a non-magnetic Kondo to an AF state as a function of J/D. Experimentally, one indeed observes magnetic order at low temperatures ($T < T_K$) in most of the HF compounds (see section 2). In all these cases the magnetic moment is strongly reduced. At present there is no theory which predicts this behavior in detail. For the observed antiferro-magnetic order band structure effects are also important.

The various properties of VF and HF systems depend in a different way on the concentration of magnetic ions, though one has always Fermi liquid properties (or simple power laws as function of T and $\boldsymbol{B}$) at low temperatures. The magnetic specific heat $c_m(T)$ and magnetic susceptibility $\chi(T)$ of $Ce_xLa_{1-x}Cu_6$ scale very well as a function of concentration x. For $c_m(T)$ this is observed for $x = 1, 0.8$ and 0.5 (Andrei et al. 1983) and for $\chi(T)$ for the concentrations $1 \leqslant x \leqslant 0.1$ (Onuki and Komatsubara 1987). The behavior of the magnetic resistivity $\rho_m(T)$ is different. Figure 60 shows $\rho_m(T)$ for $Ce_xLa_{1-x}Cu_6$ for x between 0.094 and 1 as a function of $\ln(T/T_K)$. For small concentrations x the resistivity reaches its maximum at $T = 0$ (compare fig. 50). With increasing concentration the maximum shifts to finite temperatures.

For $x = 1$ the resistivity due to the magnetic moments vanishes at $T = 0$ and one has

$$\rho_m(T) = A_1(T/T_K)^2. \tag{24}$$

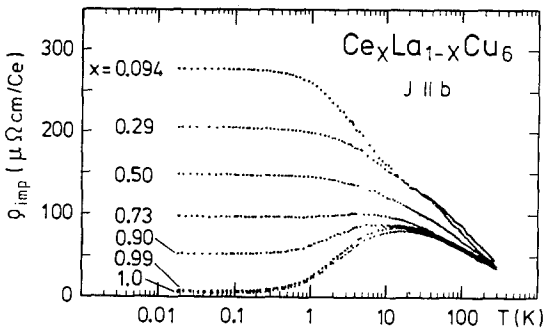

Fig. 60. Temperature dependence of the magnetic resistivity of dilute and concentrated $Ce_xLa_{1-x}Cu_6$ per mol cerium (Onuki and Komatsubara 1987).

The R ions form a periodic lattice which leads for the 4f electrons together with the conduction electrons to the formation of 'quasiparticle' bands, i.e., the electrons are in a 'coherent' state. Since the magnetic moments either vanish (in the nonmagnetic Kondo state) or form themselves a periodic magnetic structure (Kondo systems with magnetic order) there is no elastic scattering of the conduction electrons and therefore $\rho_m(0) = 0$. This is different at high temperatures, where even in a periodic lattice one has disordered moments which scatter elastically. The coefficient A_1 can be calculated analytically. One has $A_1 = j(j+1)\pi^4\rho_{ul}/9n^3$ with the resistivity in the unitarity limit $\rho_{ul} = h/(2j+1)e^2k_F$ (h is the Planck constant) (Fischer 1989a, Coleman 1987b). For small concentrations one has at low temperatures the Fermi liquid behavior mentioned below eq. (20) and at intermediate concentrations $\rho_{imp} = \rho_{imp}(0)[1 - A'(T/T_K)^2]$, where $\rho_{imp}(0)$ and A' depend on the R ion concentration (Moshchalkov and Brandt 1986).

Sometimes one defines a 'coherence' temperature $T_{coh} \approx 0.1T_K$ for periodic systems above which eq. (24) becomes invalid. Deviations from eq. (24) are interpreted as 'incoherent' scattering or the beginning of elastic scattering for which the spin compensation or quenching of the 4f moments no longer is complete. The temperature T_{coh} also marks the breakdown of Fermi liquid behavior with simple power laws for all physical quantities. For $T > T_{coh}$ the sharp pseudo-gap near the Fermi level due to the Kondo resonance is not fully developed (Kaga et al. 1988). Experimentally, one finds that T_{coh} roughly coincides with the temperature at which the Sommerfeld coefficient $\gamma = c_m(T)/T$ of the specific heat shows a maximum (Bredl et al. 1984, Brodale et al. 1986, Fujita et al. 1982).

The thermopower of concentrated VF systems or compounds shows the huge Kondo peak (see fig. 54) and in addition a low temperature peak of opposite sign (Franz et al. 1978) which can be explained by inelastic spin flip scattering between the 4f and conduction electrons and is due to the RKKY interactions (Fischer 1989b). The thermopower can also strongly depend on CF effects and seems to be far from universal.

The basis for our understanding of VF and HF compounds is the periodic Anderson

model

$$H = \sum_{k,m} \varepsilon_k c^+_{km} c_{km} + \varepsilon_f \sum_{m,i} f^+_{im} f_{im} + V \sum_{k,m,i} [e^{ik\cdot R_i} c^+_{km} f_{im} + \text{h.c.}] + U \sum_{m>m',i} f^+_{im} f_{im} f^+_{im'} f_{im'}, \tag{25}$$

where in contrast to eq. (8) one sums over all lattice sites $\boldsymbol{R}_i$. In the simplest approach one constructs a mean field theory for $U \to \infty$. In this limit (which seems reasonable for Ce and Yb compounds), double occupancy of the 4f states is forbidden and one can replace the last term on the r.h.s. of eq. (25) by the constraint $\sum_m \langle f^+_{im} f_{im} \rangle = \langle n^i_f \rangle \leqslant 1$. This constraint is taken into account by introducing a boson field b^+_i ('slave bosons') at each site i which creates a hole on the corresponding 4f orbital. In MFA (mean field approximation) the Bose operators b^+_i, b_i are treated as site-independent c-numbers (Coleman 1984, 1987a, Read et al. 1984, Auerbach and Levin 1986a,b, Millis and Lee 1987, Newns and Read 1987). This leads to strongly renormalized parameters $\tilde{\varepsilon}_f$ and $\tilde{V}$ with

$$|\tilde{\varepsilon}_f| = k_B T_K, \quad \tilde{\Delta} = \pi N_c(0) \tilde{V}^2 = \pi T_K / N \tag{26}$$

[see eq. (9)] and quasiparticle bands with the dispersion

$$E^{\pm}_k = \tfrac{1}{2}\{\tilde{\varepsilon}_f + \varepsilon_k \pm [(\tilde{\varepsilon}_f - \varepsilon_k)^2 + 4\tilde{V}^2]^{1/2}\}, \tag{27}$$

as indicated in fig. 61. The chemical potential μ is determined by the number of quasiparticles with $\mu < \tilde{\varepsilon}_f$ for a less than half-filled band, and the wave vector k_h is defined by $\mu = k_h^2/2m$. Due to the flatness of the bands near μ and $\tilde{\varepsilon}_f$ one has a sharp Kondo resonance in the quasiparticle density of states which is now split into two peaks. Such a split resonance has been obtained also by Kaga et al. (1988) in a somewhat different approximation. If one takes into account the conduction electron

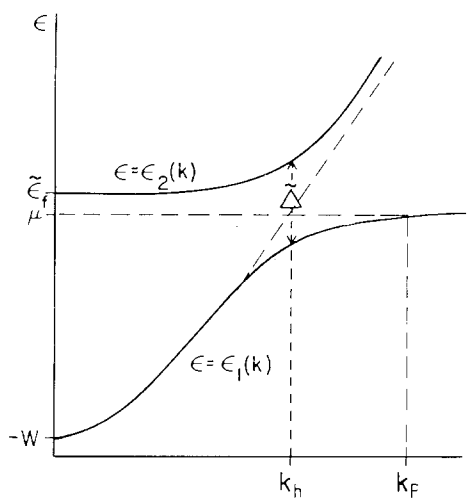

Fig. 61. Sketch of the dispersion relation $\varepsilon(k)$ for quasiparticle bands, as derived from the periodic Anderson model in a mean field approximation (Millis and Lee 1987).

band structure, the shape of the Kondo resonance becomes more complicated and reflects the symmetry of the crystal (see Fulde et al. 1988).

The MFA yields bands of independent quasiparticles. Fluctuation corrections to the MFA lead to interactions between these quasiparticles, that are responsible for a frequency and temperature dependent resistivity, spin fluctuations and modifications of the mean field result for specific heat and susceptibility (Coleman 1987a, Auerbach et al. 1988, Millis and Lee 1987, Doniach 1987, Houghton et al. 1988). Modified models have also been considered which take into account intersite coupling or RKKY interactions explicitly (Zhang et al. 1987, Kaga and Yoshida 1988, 1989, Grewe 1988, Grewe and Welslau 1988, Grewe et al. 1988, Irkhin and Katsnelson 1989, Ohkawa 1989).

Depending on the ratio $T_{\mathrm{RKKY}}/T_{\mathrm{K}}$ one has quite different low-temperature properties. Strong RKKY interactions lead to magnetic order below $T_m > T_{\mathrm{K}}$, where T_m is the ordering temperature. Since the RKKY interaction is oscillating one can have antiferromagnetic, ferromagnetic or more complicated magnetic order including spin density waves (Doniach 1987), spiral order or also a spin glass structure. Depending on parameters such as the lattice structure, crystal fields, crystal anisotropy and the quasiparticle band structure all these structures can be observed. For $T_m \gg T_{\mathrm{K}}$ the local moments are little reduced from their high-temperature values and the Kondo renormalization process [which would lead at $T = 0$ to an infinite exchange constant in the Kondo Hamiltonian, eq. (12)] stops at the temperature T_m (Doniach 1977). Examples are $CeAl_2$ (Barbara et al. 1977) or $CeCu_2Ge_2$ (Steglich et al. 1990).

In the opposite limit of weak RKKY interactions one has no magnetic order. However, there are still magnetic short-range correlations between the quasiparticles and a strongly enhanced Pauli susceptibility. The latter is essentially due to the Kondo effect. Spatial correlations can be due to spin–orbit coupling (Zou and Anderson 1986, Kaga 1989, Evans 1990) and RKKY interactions. The latter can be included in the framework of the Anderson lattice model if one goes beyond the independent quasiparticle approximation (Grewe et al. 1988, Grewe and Welslau 1988, Welslau and Grewe 1990, Kuramoto 1989). A model in which the RKKY interactions have been added explicitely to the Anderson lattice also has been investigated by Coleman and Andrei (1989) and Irkhin and Katsnelson (1990, 1991). In both approaches one obtains in mean field approximation a Stoner-like expression for the dynamic susceptibility in which the intrasite interaction U of the Stoner theory is replaced by an effective intersite RKKY interaction $I(q)$

$$\chi(q,\omega) = \{[\chi_{\mathrm{L}}(q,\omega)]^{-1} - I(q)\}^{-1}, \tag{28}$$

where χ_{L} is the susceptibility in the absence of the RKKY interaction. If $I(q)\chi_{\mathrm{L}}(q,0) > 1$ one has a magnetic instability and the magnetic structure is determined by the q-value for which $I(q)\chi_{\mathrm{L}}(q,0)$ has a maximum. In the approach of Coleman and Andrei (1989) and Irkhin and Katsnelson (1990, 1991) one assumes a constant ferromagnetic interaction I which leads to a Stoner gap due to spin splitting. In addition one has a gap in the quasiparticle spectrum due to the split Kondo resonance, and the magnetic properties depend on the position of the Kondo gap with respect to the Fermi energy and the relative size of both gaps. Both approaches describe itinerant magnetism due

to quasiparticles and hold only in the Fermi liquid region $T < T_{coh}$ as defined below eq. (24).

So far we considered the limits of local moment and itinerant magnetism. Experimentally, one can study the transition between both limits either by applying hydrostatic pressure or by alloying. An example is $Ce(Cu_{1-x}Ni_x)_2Ge_2$ where $CeCu_2Ge_2$ is a local moment system and where $CeNi_2Ge_2$ does not order (Grewe and Steglich 1991, Steglich 1991). A change of the lattice constant (or volume) might also be the mechanism for a metamagnetic transition in a magnetic field (see fig. 8) as observed in $CeCu_6$, $CeRu_2Si_2$ (see section 2.1.2) and UPt_3 and discussed by Ohkawa (1989) and Lacroix (1991).

Finally, we discuss the theories of VF and HF systems which deal with the neutron scattering function of eq. (2) or the corresponding excitation spectrum. For non-interacting stable R ions (without hybridization with the conduction electrons), the excitation spectrum $\mathrm{Im}\,\chi(\omega)$ consists of a series of δ-functions $\delta(\Delta_j - \Delta_i - \omega)$, where Δ_i is the energy of the CF level i (see Fulde and Loewenhaupt 1986). The interaction of the 4f electrons of such ions with the conduction electrons of a metallic host can be described by the Kondo Hamiltonian, eq. (12), in which the exchange interaction J is replaced by $2(g_j - 1)J$ and the spin S by the total angular momentum. In addition, one has the CF term of eq. (13). For positive exchange there is no Kondo effect. Since $J/\varepsilon_F \ll 1$, where ε_F is the Fermi energy, the exchange interaction can be treated in the Born approximation. This leads to an excitation spectrum consisting of two Lorentzians [eq. (6)] with a Korringa-like linewidth $\Gamma(T)$. For two CF levels of distance $\Delta \equiv \Delta_j - \Delta_i$ one has for the quasielastic line,

$$\Gamma(T)/2 = 4\pi\alpha[(g_j - 1)JN_c(0)]^2 k_B T, \tag{29}$$

with $\alpha = 1$ for $\Delta \ll k_B T$ and $\alpha = 25/9$ for $\Delta \gg k_B T$ and for Ce with a Γ_7 ground state and a Γ_8 excited state. For the inelastic linewidth one has an additional term due to the decay of the CF excitation into electron–hole pairs which does not vanish for $T = 0$ (Fulde and Loewenhaupt 1986). The Korringa relation corresponds to $\alpha = 1$. For VF and HF systems the Born approximation is not sufficient and the linewidth $\Gamma(T)$ is no longer proportional to T.

Very extended calculations of various physical properties [including $\mathrm{Im}\,\chi(\omega, T)$ and $\Gamma(T)$] of HF systems have been performed by Bickers et al. (1987) and Bickers (1987) in the framework of the single impurity Anderson model in NCA. Figure 62 shows $\mathrm{Im}\,\chi(\omega)$, normalized to its maximum value and compared with a Lorentzian and experimental data for $CePd_3$ at 5 K from Galera et al. (1985a,b). For $T \geqslant T_K$ the theoretical results can be fitted by a Lorentzian whereas for $T < T_K$ the theory predicts strong deviations. Hence, for $T < T_K$ a unique linewidth $\Gamma(T)$ does no longer exist. One defines rather arbitrarily either the slope for $\omega \to 0$, eq. (7), or the position of the peak of $\mathrm{Im}\,\chi(\omega)$ as an effective linewidth. The latter definition leads to the linewidth presented in fig. 63 for the degeneracy $N = 6$ which shows a $T^{1/2}$ power law above T_K, increases with decreasing temperature for $T < T_K$, and for $T \to 0$ tends to $\Gamma(0)/2 \approx 1.4T_K$. In contrast, the width Γ_1 defined from the slope of $\mathrm{Im}\,\chi(\omega)$ for $\omega \to 0$ [see eq. (7)] extrapolates for $T \to 0$ to $\Gamma_1(0)/2 \approx 2.1T_K$ (Cox et al. 1986).

The narrowing of the spectrum $\mathrm{Im}\,\chi(\omega)$ for $T \to 0$ as indicated in fig. 62 leads to a

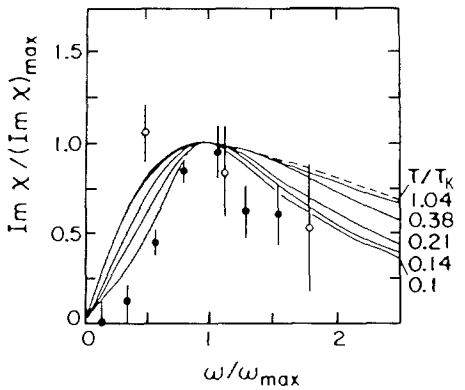

Fig. 62. Dynamic magnetic susceptibility $\mathrm{Im}\,\chi(\omega)$, normalized to its maximum value, as a function of frequency ω. Full lines are result of the NCA, the dashed line corresponds to the quasielastic lineshape, eq. (6), and the dots are experimental data for $CePd_3$ (solid circles at 5 K, open circles at 280 K from Galera et al. 1985a, b) (Bickers et al. 1987).

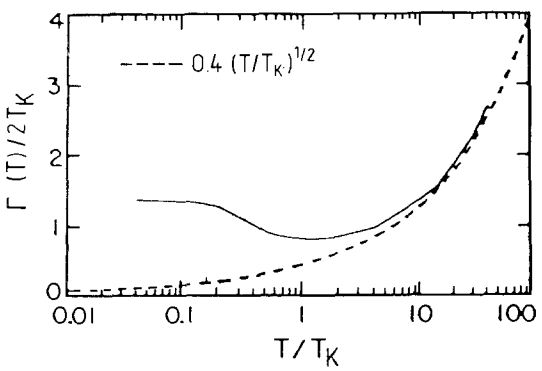

Fig. 63. Neutron scattering linewidth $\Gamma(T)$ as a function of temperature from the NCA. Here, $\Gamma/2$ is defined operationally as the position of the peak in $\mathrm{Im}\,\chi(\omega)$, fig. 62. At high temperature one obtains a $T^{1/2}$ power law (dashed line).

'bump' in $\mathrm{Im}\,\chi(\omega)/\omega$ as indicated in fig. 64. Here, the parameters are $N = 6$ and $T_K = 44$ K. At low energies and $T = 0$ the NCA fails, and the correct values of $\mathrm{Im}\,\chi(\omega)/\omega$ as obtained from eq. (5) are indicated as a dashed line. For $T \geqslant T_K$ the spectrum is again Lorentzian.

A simple analytic expression for $\mathrm{Im}\,\chi(\omega)/\omega$ for dilute HF and VF systems at $T = 0$, based on the NCA and an additional approximation, has been proposed by Kuramoto and Müller-Hartmann (1985). It reads

$$\mathrm{Im}\,\chi(\omega) = C\frac{N\omega}{\pi\tilde{\varepsilon}_f^2}\frac{\sin\alpha}{u^2(u^2+4\sin^2\alpha)} \times\left\{\sin\alpha\ln[(1-u^2)^2+4u^2\sin^2\alpha]+u\left[\frac{\pi}{2}-\tan^{-1}\left(\frac{1-u^2}{2u\sin\alpha}\right)\right]\right\}, \quad (30)$$

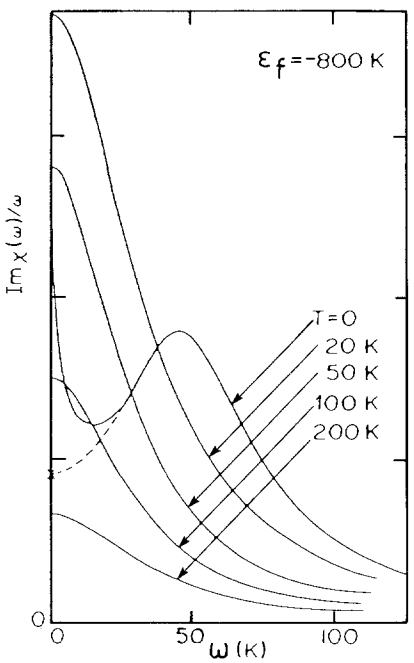

Fig. 64. Dynamic susceptibility divided by the frequency $\mathrm{Im}\,\chi(\omega)/\omega$ as a function of frequency from the NCA for $N = 6$ and $\varepsilon_f = -800$ K. The peak at $T = 0$ with a power-law divergency of $\mathrm{Im}\,\chi(\omega)/\omega$ for $\omega = 0$ is an artifact of the NCA. The exact value of $\mathrm{Im}\,\chi(\omega)/\omega$ for $\omega = 0$ from eq. (5) is indicated by a cross, the dashed line is an interpolation (Kuramoto and Kojima 1985).

with the Curie constant $C = (g_j\mu_B)^2 j(j+1)/3$, $u = \omega/\tilde{\varepsilon}_f$, $\alpha = \pi n_f/N$ and $\tilde{\varepsilon}_f$ the renormalized $4f^1$ level relative to the Fermi level, where n_f is the 4f-electron number. We showed in fig. 53 that the peak in the *static* susceptibility $\chi(T)$ depends strongly on the degeneracy N and vanishes for $N = 2$ or spin $S = \frac{1}{2}$. Unfortunately, the possibility of a similar trend in $\mathrm{Im}\,\chi(\omega)/\omega$ has not yet been investigated. A simple approximation scheme based on the NCA for the single impurity Anderson model has been proposed by Zwicknagl et al. (1990, 1991) and possibly allows to answer this question.

The width $\Gamma(T)$ at low temperatures is of the order of the Kondo temperature T_K. In VF systems this characteristic temperature is rather high (several hundred K) which leads in these systems to a very weak temperature dependence of $\Gamma(T)$. On the other hand, the temperature region $T < T_K$ in these systems is experimentally more easily accessible. One has essentially the same features as in HF systems such as a Lorentzian in $\mathrm{Im}\,\chi(\omega)$ for $T \geqslant T_K$ and an inelastic peak of $\mathrm{Im}\,\chi(\omega)/\omega$ for $T \ll T_K$ (H. Kojima et al. 1984). Earlier calculations of Schlottmann (1982) based on the Mori technique, though not completely reliable, indicate a small maximum in $\Gamma_1(T)$ (as obtained from the slope of $\mathrm{Im}\,\chi(\omega)$ for $\omega \to 0$) in HF systems and a considerably stronger hump in VF systems. Possibly, this is an indication of stronger deviations from the Lorentzian at low temperatures in VF systems compared to HF systems.

The theories considered so far deal with HF or VF systems consisting of a singlet

and a degenerate ground state. The Tm ion differs from the Ce, Yb, Sm and Eu ions considered so far in that its two valence states, f^{12} and f^{13}, are both magnetic with degeneracies 13 and 8, respectively. The dynamic susceptibility of Tm-based VF systems can be well fitted by a Lorentzian with a relaxation rate $\Gamma(T)$ which below 100 K is roughly proportional to T. However, the proportionality constant is considerably larger than expected for the Korringa law. At high temperatures $\Gamma(T)$ seems to saturate as expected for VF systems (Müller-Hartmann 1984). Similar results have been obtained earlier by a mode–mode coupling approach (Schlottmann 1984).

A comparison of these results based on a single-impurity model with experimental data on concentrated HF and VF systems or compounds is not completely justified. However, we discussed earlier in this section several physical properties that remained *qualitatively* unchanged if scaled with the characteristic temperature T_K. This is true for the static susceptibility $\chi(T)$ and possibly holds for $\mathrm{Im}\,\chi(\omega, Q=0, T)$ (Auerbach et al. 1987). However, due to the quasiband structure $\mathrm{Im}\,\chi$ now becomes Q-dependent. The Q-dependence of the static susceptibility and of the width Γ has been calculated by Tachiki et al. (1987) for the Anderson lattice and compared with experimental data on $CeCu_6$, assuming a simplified band structure. Similar calculations for some typical cubic band structures, assuming a spherical Fermi surface, lead to antiferromagnetic peaks in $\mathrm{Im}\,\chi(\omega, Q, T)/\chi(Q, T)$ at the zone boundary. At temperatures $T \geqslant 0.5T_K$ the large-Q peaks can be fitted by the Lorentzian of eq. (6) with $\Gamma/2 = k_B T_K^N$, but at $T=0$ and a sufficiently large Fermi momentum a shifted Lorentzian would yield a better fit (Auerbach et al. 1987). The Q-dependent dynamic susceptibility of HF systems which order magnetically at low temperatures (see section 2) has not yet been calculated. However, Kuramoto (1987) showed that the Shiba relation, eq. (5), approximately holds also for finite Q-values. This leads with eq. (6) to the relation

$$\chi(\boldsymbol{Q}, T)\Gamma(\boldsymbol{Q}, T)/2 = \mu_{\mathrm{eff}}^2 N/3\pi = \text{const.}, \tag{31}$$

which connects the static susceptibility with the linewidth. Equation (31) holds for a Lorentzian lineshape, above the temperature at which the Kondo peak in the density of states becomes $\boldsymbol{Q}$-dependent and for $T \ll T_K$. Equation (31) is in fair agreement with neutron scattering data on $CeCu_6$ (Rossat-Mignod et al. 1988).

The Kondo effect with additional CF splitting has been discussed already for the specific heat (see fig. 55). Depending on the CF parameters the Kondo peak in the specific heat can be deformed, shifted or split into several peaks. Similar effects are observed in the dynamic susceptibility. Maekawa et al. (1985a,b) calculated the neutron scattering function $S(\omega, T)$ for a small concentration of Ce^{3+} ions in a cubic crystal with a Γ_7 ground state in the framework of the Coqblin–Schrieffer model [eq. (10)]. Figure 65 shows two peaks (quasielastic and inelastic) which both depend on temperature. The CF peak at $\omega \approx \Delta_0$ decreases strongly with increasing temperature. Here, Δ_0 is the crystal field splitting. The temperature dependence of the quasielasic linewidth $\Gamma(T)$ (fig. 66) agrees for $\Delta_0 = 150$ K fairly well with the experimental data for $Ce_{0.7}La_{0.3}Al_2$ (Loewenhaupt and Steglich 1977). In particular, the decrease of $\Gamma(T)$ at low temperatures can be explained by CF effects. However, due to the approximation made in the calculation (a self-consistent ladder approximation), the theory is not completely reliable at temperatures below the Kondo temperature. The latter is assumed to be $T_K = 5.5$ K for $\Delta_0 = 150$ K.

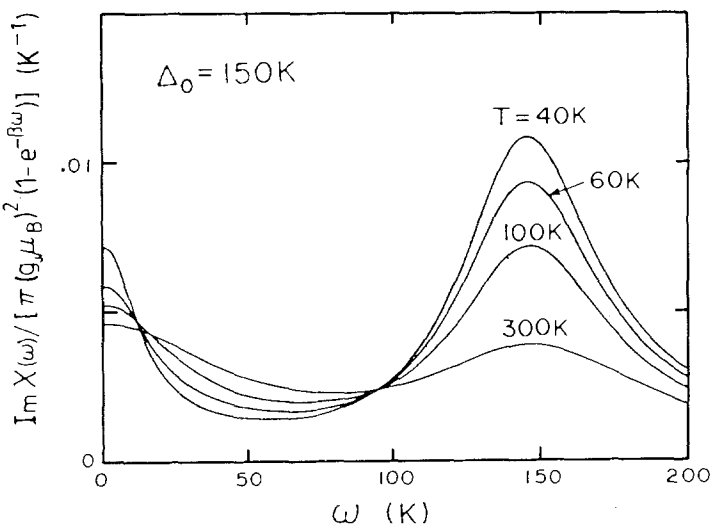

Fig. 65. Neutron scattering for a Ce^{3+} ion in a cubic crystal with the Γ_7 ground state for the parameters $T_K = 5.5$ K and the CF energy $\Delta_0 = 150$ K, calculated from a self-consistent ladder approximation (Maekawa et al. 1985a,b).

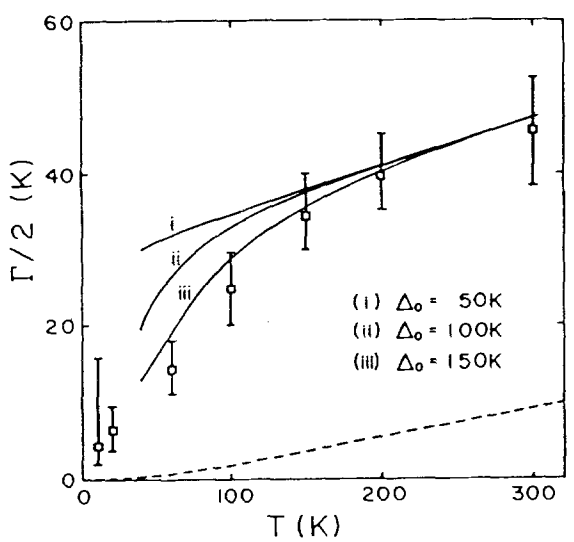

Fig. 66. Quasielastic neutron scattering linewidth as a function of temperature for a Ce^{3+} ion with the Γ_7 ground state, $T_K = 5.5$ K and the CF energies $\Delta_0 = 50$, 100 and 150 K from a self-consistent ladder approximation. Indicated are also experimental results for $Ce_{0.7}La_{0.3}Al_2$ (Loewenhaupt and Steglich 1977) and (as dashed line) the results of second-order perturbation theory (Maekawa et al. 1985c).

The influence of spin–orbit and crystal-field splitting effects on the static susceptibility of HF compounds have been calculated by Evans (1990) in the slave boson approach (which is equivalent to the leading term in a $1/N$ expansion). Fair agreement is obtained for χ_x/χ_z at $T = 0$ for $CePt_2Si_2$, $CeCu_2Si_2$, $CeRu_2Si_2$, $CeAl_3$ and $CeSi_{1.86}$. A more phenomenological model for the spin–orbit coupling (which leads to a $\boldsymbol{q}$-dependent susceptibility) is due to Zou and Anderson (1986) and Kaga (1989).

An attempt to explain experimental data for the neutron scattering function $S(\omega, T)$ of the γ- and α-phases of metallic Ce on the basis of CF and spin–orbit effects (without taking into account the interaction between 4f and conduction electrons) is due to Orlov (1988). The effect of spin–orbit splitting on the dynamic susceptibility of VF systems within the framework of the NCA has been considered by Cox et al. (1986).

4. Summary

This chapter deals with valence fluctuation and heavy fermion 4f-systems such as Ce, Sm, Eu, Tm and Yb alloys and compounds. In sections 1 and 3 we summarize the most important physical properties of these systems, based on the main theoretical results achieved so far and on representative data.

In the main part (section 2) we summarize neutron scattering data of HF and VF systems. By means of neutrons one can measure the magnetic structure of a system (elastic magnetic scattering) and magnetic and nonmagnetic excitations such as relaxational modes (quasielastic excitations), magnons, crystal field and spin–orbit transitions and phonons. Some of these excitations have been observed in all HF or VF systems. Both HF and VF systems exhibit a quasielastic line due to spin fluctuations or the Kondo effect. Both expressions are used synonymously, but in VF systems the quasielastic line is very broad, corresponding to a high characteristic energy, and is fairly temperature independent. Here one talks in general about spin fluctuations. In HF systems the quasielastic line is narrower, temperature dependent, and has at low temperatures the halfwidth $\Gamma/2 \approx k_B T_K^N$. A typical quasielastic line can be fitted by a Lorentzian and corresponds to a single relaxation time. In most *HF compounds* the line becomes $\boldsymbol{Q}$-dependent at low temperatures indicating spin correlations that often lead at still lower temperatures to magnetic order. These spin correlations, on the other hand, lead already to deviations from the Lorentz shape above the spin ordering temperature. In *VF compounds* spin correlations do not play a role, but the high-temperature quasielastic line also changes its shape and becomes narrower and inelastic at low temperatures.

Ce-based HF systems have been investigated by many groups, whereas few data exist for the corresponding VF systems and for Yb-, Sm-, Eu- and Tm-based VF and HF systems. As a consequence, our survey over Ce-based VF and Yb, Sm, Eu and Tm systems is rather complete, whereas for Ce-based HF systems we could only select representative examples. Part of this strong research activity on Ce compounds is due to the fact that $CeCu_2Si_2$ becomes superconducting, and it is an enormous challenge to find other superconducting HF systems. In addition, one has in these systems a variety of magnetic structures such as ferromagnetic, antiferromagnetic and

spiral order and metamagnetism. In many cases the detection of these structures is hampered by moments that are strongly reduced by the Kondo effect.

In addition to the Kondo effect one has in HF systems strong crystal field effects, and the corresponding 4f-levels can be determined by neutron scattering experiments. The interplay between Kondo and CF effects varies from system to system, and the corresponding information is part of the content of this chapter. Since in HF systems the Kondo temperature is typically rather small, one observes at low temperatures mainly the properties of the lowest CF level.

Valence fluctuations couple to phonons, and our review gives a rather complete survey of the corresponding anomalies. In addition, one has phonon anomalies due to the CF–phonon interaction, since a lattice deformation around an R ion modifies the crystalline electric field. Finally, we mention the spin–orbit interaction, which is modified in VF and HF systems due to the hybridization between f and conduction electrons. The few neutron scattering experiments on spin–orbit transitions in VF and HF systems show unexpected splittings, line shifts, and line broadenings if compared to the free ion case.

Abbreviations

AF	anti-ferromagnetic
CF	crystal field
FWHM	full width at half maximum
HF	heavy fermion
LA	longitudinal acoustic
LLW	Lea–Leask–Wolf
MFA	mean field approximation
NCA	noncrossing approximation
NMR	nuclear magnetic resonance
R	rare earth
RKKY	Ruderman–Kittel–Kasuya–Yosida
TA	transverse acoustic
VF	valence fluctuation

List of symbols

a, b	Clebsch–Gordon coefficients
$b_i^+ (b_i)$	slave boson creation (annihilation) operator
c_m	magnetic specific heat
$c_{km}^+ (c_{km})$	conduction electron creation (annihilation) operator
$f_m^+ (f_m)$	f-electron creation (annihilation) operator
g_j	electron Landé factor for total angular momentum
g_N	neutron g-factor
$\hbar k_0, \hbar k_1$	momentum of incoming (outgoing) neutron
i	lattice site

j, J	total angular momentum
$k = \|\boldsymbol{k}\|$	wave vector
k_B	Boltzmann constant
k_F	Fermi wave vector
k_h	wave vector defined by $\mu = k_h^2\ 2m$
l	total orbital angular momentum
l_z	z-component of l
m	magnetic quantum number, bare electron mass
m^*	effective electron mass
n	conduction electron concentration
n_f	average number of f-electrons per R ion
n_i	impurity concentration
x	concentration
$\boldsymbol{B}$	magnetic field
C	Curie constant
D	conduction electron bandwidth
E_k	quasi-particle energy
$F(\boldsymbol{Q}, T)$	magnetic form factor
H	Anderson Hamiltonian
H_{CS}	Coqblin–Schrieffer Hamiltonian
H_{CF}	crystal field Hamiltonian
H_K	Kondo Hamiltonian
H_{hf}^{4f}	hyperfine coupling constant for 4f electrons
Im	imaginary part
J (J_{eff})	(effective) exchange coupling constant
N	degeneracy of 4f ground state
$N_c(\omega)$	conduction electron density of states
$N_f(\omega)$	quasi-particle density of states
$\boldsymbol{Q}$	momentum transfer
R	Wilson ratio
$\boldsymbol{R}$	lattice vector
Re	real part
$\boldsymbol{S}, S$	total spin (eigenvalue)
$S(\omega, \boldsymbol{Q}, T)$	scattering function
S_d	thermopower
T_C	Curie temperature
T_{coh}	coherence temperature
T_F	Fermi temperature
T_K	Kondo temperature
T_K^N	Kondo temperature deduced from neutron data
T_N	Néel temperature
T_{SF}	spin fluctuation temperature
U	Coulomb energy of 4f electrons
$V_k \approx V$	hopping matrix element
$\tilde{V}$	renormalized matrix element

β	$= 1/k_B T$
$\gamma = c_m(T)/T$	Sommerfeld coefficient
γ_n	nuclear moment
$\Gamma(\boldsymbol{Q}, T)/2$	relaxation rate for Lorentzian lineshape (Γ is the linewidth)
$\Gamma_6, \Gamma_7, \Gamma_8$	crystal field states
Δ	4f electron level width for $U = 0$; energy of inelastic transition
$\tilde{\Delta}$	renormalized level width
Δ_i	energy of crystal field level i
ε_f ($\tilde{\varepsilon}_f$)	f-electron energy (renormalized)
ε_F	Fermi energy
ε_k	conduction electron energy
ε_m	energy of the maximum of the density of states $N_f(\omega)$ (Kondo peak)
μ	chemical potential
μ_B	Bohr magneton
μ_{eff}	effective magnetic moment
ρ_{imp}	impurity resistivity
ρ_m	magnetic resistivity
ρ_{ul}	unitarity limit of impurity resistivity
$\boldsymbol{\sigma}$	Pauli spin matrices
σ	spin quantum number
Θ_D	Debye temperature
$\chi(\omega)$	dynamic susceptibility
$\chi(T), \chi(\boldsymbol{Q}, T)$	static susceptibilities
ω	band energy (excitation energy)
$\hbar\omega$	energy transfer in neutron scattering

References

Aeppli, G., H. Yoshizawa, Y. Endoh, E. Bucher, J. Hufnagl, Y. Onuki and T. Komatsubara, 1986, Phys. Rev. Lett. **57**, 122.

Alekseev, P.A., A.S. Ivanov, B. Dorner, H. Schober, K.A. Kikoin, A.S. Mishchenko, V.N. Lazukov, E.S. Konovalova, Y.B. Paderno, A.Y. Rumyantsev and I.P. Sadikov, 1989, Europhys. Lett. **10**, 457.

Alekseev, P.A., A.S. Ivanov, V.N. Lazukov, I.P. Sadikov and A. Severing, 1992, Physica B **180+181**, 281.

Aliev, F.G., N.B. Brandt, V.V. Moshchalkov and S.M. Chudinov, 1984, J. Low Temp. Phys. **57**, 61.

Amato, A., D. Jaccard, J. Flouquet, F. Lapierre, J.L. Tholence, R.A. Fisher, S.E. Lacy, J.A. Olsen and N.E. Phillips, 1987, J. Low Temp. Phys. **68**, 371.

Andrei, N., and J.H. Loewenstein, 1981, Phys. Rev. Lett. **46**, 356.

Andrei, N., K. Furuya and J.H. Loewenstein, 1983, Rev. Mod. Phys. **55**, 331.

Andres, K., J.E. Graebner and H.R. Ott, 1975, Phys. Rev. Lett. **35**, 1779.

Asano, H., M. Umino, Y. Onuki, T. Komatsubara, F. Izumi and N. Watanabe, 1986, J. Phys. Soc. Jpn. **55**, 454.

Auerbach, A., and K. Levin, 1986a, Phys. Rev. Lett. **57**, 877.

Auerbach, A., and K. Levin, 1986b, Phys. Rev. B **34**, 3524.

Auerbach, A., J.H. Kim and K. Levin, 1987, Physica B **148**, 50.

Auerbach, A., J.H. Kim, K. Levin and M.R. Norman, 1988, Phys. Rev. Lett. **60**, 623.

Ayache, C., J. Beille, E. Bonjour, R. Calemczuk, G. Creuzet, D. Gignoux, A. Najib, D. Schmitt, J. Voiron and M. Zerguine, 1987, J. Magn. & Magn. Mater. **63–64**, 329.

Baer, Y., and W.-D. Schneider, 1987, in:

Handbook on the Physics and Chemistry of Rare Earths, Vol. 10, eds K. A. Gschneidner Jr and L. Eyring (North-Holland, Amsterdam) p. 1.

Balakrishnan, G., D.McK. Paul and N.R. Bernhoeft, 1989, Physica B **156–157**, 815.

Barbara, B., J.X. Boucherle, J.L. Bouevoz, M.F. Rossignol and J. Schweizer, 1977, Solid State Commun. **24**, 481.

Barbara, B., M.F. Rossignol, J.X. Boucherle, J. Schweizer and J.L. Bouevoz, 1979, J. Appl. Phys. **50**, 2300.

Barbara, B., M.F. Rossignol, J.X. Boucherle and C. Vettier, 1980, Phys. Rev. Lett. **45**, 938.

Batlogg, B., H.R. Ott, E. Kaldis, W. Thöni and P. Wachter, 1979, Phys. Rev. B **19**, 247.

Bauchspiess, K.R., W. Boksch, E. Holland-Moritz, H. Launois, R. Pott and D. Wohlleben, 1982, in: Valence Fluctuations in Solids, eds L.M. Falicov, W. Hanke and M.B. Maple (North-Holland, Amsterdam) p. 417.

Bennemann, K.H., and M. Avignon, 1979, Solid State Commun. **31**, 645.

Benoit, A., J.X. Boucherle, P. Convert, J. Flouquet, J. Palleau and J. Schweizer, 1980, Solid State Commun. **34**, 293.

Benoit, A., J.X. Boucherle, J. Flouquet, J. Sakurai and J. Schweizer, 1985, J. Magn. & Magn. Mater. **47–48**, 149.

Berton, A., J. Chassy, B. Cornut, J. Flouquet, J. Odin, J. Peyrard and F. Holtzberg, 1981, Phys. Rev. B **23**, 3504.

Besnus, M.J., J.P. Kappler, P. Lehmann and A. Meyer, 1985, Solid State Commun. **55**, 779.

Besnus, M.J., M. Benakki, A. Braghta, H. Danan, G. Fischer, J.P. Kappler, A. Meyer and P. Panissod, 1988, J. Magn. & Magn. Mater. **76–77**, 471.

Bickers, N.E., 1987, Rev. Mod. Phys. **59**, 846.

Bickers, N.E., D.L. Cox and J.W. Wilkins, 1987, Phys. Rev. B **36**, 2036.

Bilz, H., G. Güntherodt, W. Kleppmann and W. Kress, 1979, Phys. Rev. Lett. **43**, 1988.

Bjerrum-Møller, H., S.M. Shapiro and R.J. Birgeneau, 1977, Phys. Rev. Lett. **39**, 1021.

Blaschko, O., G. Krexner, L. Pintschovius, W. Assmus and G. Ernst, 1984, Solid State Commun. **51**, 971.

Böhm, A., R. Caspary, U. Habel, L. Pawlak, A. Zuber, F. Steglich and A. Loidl, 1988, J. Magn. & Magn. Mater. **76–77**, 150.

Bonnet, M., J.X. Boucherle, J. Flouquet, F. Holtzberg, D. Jaccard, J. Schweizer and A. Stunault, 1986, Physica B **136**, 428.

Bonville, P., and J.A. Hodges, 1985, J. Magn. & Magn. Mater. **47–48**, 152.

Bonville, P., J.A. Hodges, F. Hulliger, P. Imbert, G. Jehanno, J.B. Marimon da Cunha and H.R. Ott, 1988, J. Magn. & Magn. Mater. **76–77**, 473.

Bonville, P., J.A. Hodges, P. Imbert, D. Jaccard, J. Sierro, M.J. Besnus and A. Meyer, 1990, Physica B **163**, 347.

Bonville, P., J. Hammann, J.A. Hodges, P. Imbert, G. Jehanno, M.J. Besnus and A. Meyer, 1991, Z. Phys. B **82**, 267.

Borsa, F., and G. Olcese, 1973, Phys. Status Solidi A **17**, 631.

Boucherle, J.X., and J. Schweizer, 1985, Physica B **130**, 337.

Boucherle, J.X., J.L. Buevoz, S. Horn, M. Loewenhaupt, H. Scheuer, J. Schweizer and F. Steglich, 1981, Solid State Commun. **38**, 669.

Boucherle, J.X., J. Flouquet, Y. Lassailly, J. Palleau and J. Schweizer, 1983, J. Magn. & Magn. Mater. **31–34**, 409.

Boucherle, J.X., G. Fillion, J. Flouquet, F. Givord, P. Lejay and J. Schweizer, 1990, Physica B **163**, 635.

Bredl, C.D., 1987, J. Magn. & Magn. Mater. **63–64**, 355.

Bredl, C.D., S. Horn, F. Steglich, B. Lüthi and R.M. Martin, 1984, Phys. Rev. Lett. **52**, 1982.

Brodale, G.E., R.A. Fisher, C.M. Lisse, N.E. Phillips and A.S. Edelstein, 1986, J. Magn. & Magn. Mater. **54–57**, 416.

Burghardt, P., K.A. Gschneidner Jr, D.C. Koskenmaki, D.K. Finnemore, J.O. Moorman, S. Legvold, C. Stassis and T.A. Vyrostek, 1976, Phys. Rev. B **14**, 2995.

Buyers, W.J.L., 1986, Physica B **137**, 53.

Capellmann, H., P.J. Brown, S.M. Johnson, K.R.A. Ziebeck and J.G. Booth, 1985, J. Magn. & Magn. Mater. **49**, 137.

Chattopadhyay, T., H. v. Löhneysen, T. Trappmann and M. Loewenhaupt, 1990, Z. Phys. B **80**, 159.

Coleman, P., 1984, Phys. Rev. B **29**, 3035.

Coleman, P., 1987a, Phys. Rev. B **35**, 5072.

Coleman, P., 1987b, J. Magn. & Magn. Mater. **63–64**, 245.

Coleman, P., and N. Andrei, 1989, J. Phys.: Condens. Matter **1**, 4057.

Cox, D.L., and N. Grewe, 1988, Z. Phys. B **71**, 321.

Cox, D.L., N.E. Bickers and J.W. Wilkins, 1986, J. Magn. & Magn. Mater. **54–57**, 333.

Cromer, D.T., A.C. Larson and R.B. Roof, 1960,

Acta Cryst. **13**, 913.
Culverhouse, S.R., B.D. Rainford and D. McK. Paul, 1992, J. Magn. & Magn. Mater. **108**, 121.
Currat, R., R.G. Lloyd, P.W. Mitchell, A.P. Murani and J.W. Ross, 1989, Physica B **156–157**, 812.
Czycholl, G., 1982, Phys. Rev. B **25**, 3413.
Dakin, S., G. Rapson and B.D. Rainford, 1992, J. Magn. & Magn. Mater. **108**, 117.
Debray, D., R. Kahn, D.L. Decker, A. Werner, M. Loewenhaupt, E. Holland-Moritz and D.K. Ray, 1981, in: Valence Fluctuations in Solids, eds L.M. Falicov, W. Hanke and M.B. Maple (North-Holland, Amsterdam) p. 183.
Desgranges, H.-U., and J.W. Rasul, 1985, Phys. Rev. B **32**, 6100.
Dhar, S.K., K.A. Gschneidner Jr, W.H. Lee, P. Klavins and R.N. Shelton, 1987, Phys. Rev. B **36**, 341.
Dijkman, W.H., F.R. de Boer, P.F. de Chatel and J. Aarts, 1980, J. Magn. & Magn. Mater. **15–18**, 970.
Doniach, S., 1977, Physica B **91**, 231.
Doniach, S., 1987, Phys. Rev. B **35**, 1814.
Dönni, A., P. Fischer, A. Furrer, P. Bonville, F. Hulliger and H.R. Ott, 1990a, Z. Phys. B **81**, 83.
Dönni, A., P. Fischer, A. Furrer, W. Bacsa and P. Wachter, 1990b, Z. Phys. B **80**, 269.
Dönni, A., A. Furrer, P. Fischer, F. Hulliger, P. Wachter and H.R. Ott, 1990c, J. Magn. & Magn. Mater. **90–91**, 143.
Dormann, E., 1991, in: Handbook on the Physics and Chemistry of Rare Earths, Vol. 14, eds K.A. Gschneidner Jr and L. Eyring (North-Holland, Amsterdam) p. 63.
Effantin, J.M., J. Rossat-Mignod, P. Burlet, H. Bartholin, S. Kunii and T. Kasuya, 1985, J. Magn. & Magn. Mater. **47–48**, 145.
Eiling, A., and J.S. Schilling, 1981, Phys. Rev. Lett. **46**, 364.
Elenbaas, R.A., C.J. Schinkel and C.J.M. van Deudekom, 1980, J. Magn. & Magn. Mater. **15–18**, 979.
Elschner, B., and M. Schlott, 1988, J. Magn. & Magn. Mater. **76–77**, 444.
Erkelens, W.A.C., L.P. Regnault, P. Burlet, J. Rossat-Mignod, S. Kunii and T. Kasuya, 1987, J. Magn. & Magn. Mater. **63–64**, 61.
Evans, S.M.M., 1990, J. Phys.: Condens. Mat. **2**, 9097.
Fedro, A.J., and S.K. Sinha, 1981, in: Valence Fluctuations in Solids, eds L.M. Falicov, W. Hanke and M.B. Maple (North-Holland, Amsterdam) p. 329.
Felner, I., I. Nowik, D. Vaknin, U. Potzel, J. Moser, G.M. Kalvius, G. Wortmann, G. Schmiester, G. Hilscher, E. Gratz, C. Schmitzer, N. Pillmayr, K.G. Prasad, H. de Waard and H. Pinto, 1987, Phys. Rev. B **35**, 6956.
Felten, R., G. Weber and H. Rietschel, 1987, J. Magn. & Magn. Mater. **63–64**, 383.
Fillion, G., R.M. Galera, D. Givord, J. Pierre, J. Schweizer and C. Vettier, 1985, J. Appl. Phys. **57**, 3179.
Fischer, K.H., 1970, Springer Tracts in Modern Physics **54**, 1.
Fischer, K.H., 1989a, Z. Phys. B **74**, 475.
Fischer, K.H., 1989b, Z. Phys. B **76**, 315.
Forgan, E.M., B.D. Rainford, S.L. Lee, J.S. Abell and Y. Bi, 1990, J. Phys.: Condens. Mat. **2**, 10211.
Franz, W., E. Griessel, F. Steglich and D. Wohlleben, 1978, Z. Phys. B **31**, 7.
Frick, B., M. Loewenhaupt, D. Debray and W. Just, 1983, Z. Phys. B **52**, 223.
Fujita, T., K. Satoh, Y. Onuki and T. Komatsubara, 1982, J. Magn. & Magn. Mater. **47–48**, 66.
Fulde, P., and M. Loewenhaupt, 1986, Adv. Phys. **34**, 589.
Fulde, P., J. Keller and G. Zwicknagl, 1988, Solid State Phys. **41**, 1.
Furrer, A., W. Bührer and P. Wachter, 1981, Solid State Commun. **40**, 1011.
Galera, R.M., D. Givord, J. Pierre, A.P. Murani, C. Vettier and K.R.A. Ziebeck, 1985a, J. Magn. & Magn. Mater. **47–48**, 139.
Galera, R.M., D. Givord, J. Pierre, A.P. Murani, J. Schweizer, C. Vettier and K.R.A. Ziebeck, 1985b, J. Magn. & Magn. Mater. **52**, 103.
Galera, R.M., A.P. Murani, J. Pierre and K.R.A. Ziebeck, 1987, J. Magn. & Magn. Mater. **63–64**, 594.
Galera, R.M., A.P. Murani and J. Pierre, 1989, Physica B **156–157**, 801.
Germann, A., and H. v. Löhneysen, 1989, Europhys. Lett. **9**, 367.
Gibbons, E.P., E.M. Forgan and K.A. McEwen, 1987, J. Phys. F **17**, L101.
Gibbons, E.P., E.M. Forgan, K.A. McEwen and A.P. Murani, 1989, Physica B **156–157**, 777.
Gignoux, D., D. Schmitt and M. Zerguine, 1988a, Phys. Rev. B **37**, 9882.
Gignoux, D., D. Schmitt, M. Zerguine and A.P. Murani, 1988b, J. Magn. & Magn. Mater. **76–77**, 401.
Goldman, A.I., 1985, Physica B **135**, 9.

Gompf, F., E. Gering, B. Renker, H. Rietschel, U. Rauchschwalbe and F. Steglich, 1987, J. Magn. & Magn. Mater. **63–64**, 344.

Goremychkin, E.A., and R. Osborn, 1991a, report RAL-91-072; Phys. Rev. B, to be published.

Goremychkin, E.A., and R. Osborn, 1991b, report RAL-91-073; Phys. Rev. B, to be published.

Gratz, E., E. Bauer, B. Barbara, S. Zemirli, F. Steglich, C.D. Bredl and W. Lieke, 1985, J. Phys. F **15**, 1975.

Grewe, N., 1983, Z. Phys. B **52**, 193; **53**, 2711.

Grewe, N., 1988, Solid State Commun. **66**, 1053.

Grewe, N., and P. Entel, 1979, Z. Phys. B **33**, 331.

Grewe, N., and F. Steglich, 1991, in: Handbook on the Physics and Chemistry of Rare Earths, Vol. 14, eds K.A. Gschneidner Jr and L. Eyring (North-Holland, Amsterdam) p. 343.

Grewe, N., and B. Welslau, 1988, Solid State Commun. **65**, 437.

Grewe, N., H.J. Leder and P. Entel, 1980, in: Festkörperprobleme XX. Advances in Solid State Physics, ed. H. Treusch (Vieweg, Braunschweig) p. 413.

Grewe, N., T. Pruschke and H. Keiter, 1988, Z. Phys. B **71**, 75.

Grier, B.H., S.M. Shapiro, C.F. Majkrzak and R.D. Parks, 1980, Phys. Rev. Lett. **45**, 666.

Grier, B.H., R.D. Parks, S.M. Shapiro and C.F. Majkrzak, 1981, Phys. Rev. B **24**, 6242.

Grier, B.H., J.M. Lawrence, V. Murgai and R.D. Parks, 1984, Phys. Rev. B **29**, 2664.

Grier, B.H., J.M. Lawrence, S. Horn and J.D. Thompson, 1988, J. Phys. C **21**, 1099.

Grüner, G., and A. Zawadowski, 1974, Rep. Prog. Phys. **37**, 1497.

Gschneidner Jr, K.A., and A.H. Daane, 1988, in: Handbook on the Physics and Chemistry of Rare Earths, Vol. 11, eds K.A. Gschneidner Jr and L. Eyring (North-Holland, Amsterdam) p. 409.

Gunnarsson, O., and K. Schönhammer, 1987, in: Handbook on the Physics and Chemistry of Rare Earths, Vol. 10, eds K.A. Gschneidner Jr and L. Eyring (North-Holland, Amsterdam) p. 103.

Haen, P., J. Flouquet, F. Lapierre, P. Lejay, J.M. Mignot, A. Ponchet and J. Voiron, 1987, J. Magn. & Magn. Mater. **63–64**, 320.

Harris, I.R., M. Norman and W.E. Gardner, 1972, J. Less-Common Met. **29**, 299.

Havinga, E.E., H. Damsma and M.H. Vanmaaren, 1970, J. Phys. Chem. Solids **31**, 2653.

Havinga, E.E., K.H.J. Buschow and H.J. van Daal, 1973, Solid State Commun. **13**, 621.

Herbst, J.E., R.E. Watson and J.W. Wilkins, 1978, Phys. Rev. B **17**, 3089.

Hiebl, K., and P. Rogl, 1985, J. Magn. & Magn. Mater. **50**, 39.

Hiebl, K., C. Howarth, P. Rogl and M.J. Sienko, 1983, J. Magn. & Magn. Mater. **37**, 287.

Hippert, F., B. Hennion, F.L. Chui, M. Kohgi and T. Satoh, 1988, J. Magn. & Magn. Mater. **76–77**, 417.

Hippert, F., B. Hennion, J.M. Mignot and P. Lejay, 1992, J. Magn. & Magn. Mater. **108**, 177.

Holland-Moritz, E., 1982, in: Valence Instabilities, eds P. Wachter and H. Boppart (North-Holland, Amsterdam) p. 347.

Holland-Moritz, E., 1983, J. Magn. & Magn. Mater. **38**, 253.

Holland-Moritz, E., 1985, J. Magn. & Magn. Mater. **46–47**, 127.

Holland-Moritz, E., 1992, in: Frontiers in Solid State Sciences, Vol. on Magnetism, eds L.C. Gupta and M.S. Multani (World Scientific, Singapore).

Holland-Moritz, E., and M. Kasaya, 1986, Physica B **136**, 424.

Holland-Moritz, E., and M. Loewenhaupt, 1979, J. Phys. Colloq. (Paris) **40**, C5-359.

Holland-Moritz, E., and A. Severing, 1986, Z. Phys. B **63**, 313.

Holland-Moritz, E., M. Loewenhaupt, W. Schmatz and D. Wohlleben, 1977, Phys. Rev. Lett. **38**, 983.

Holland-Moritz, E., D. Wohlleben and M. Loewenhaupt, 1978, J. Phys. Colloq. (Paris) **39**, C6-835.

Holland-Moritz, E., D. Wohlleben and M. Loewenhaupt, 1982, Phys. Rev. B **25**, 7482.

Holland-Moritz, E., E. Braun, B. Roden, B. Perscheid, E.V. Sampathkumaran and W. Langl, 1987, Phys. Rev. B **35**, 3122.

Holland-Moritz, E., E. Zirngiebl and S. Blumenröder, 1988, Z. Phys. B **70**, 395.

Holland-Moritz, E., W. Weber, A. Severing, E. Zirngiebl, H. Spille, W. Baus, S. Horn, A.P. Murani and J.L. Ragazzoni, 1989a, Phys. Rev. B **39**, 6409.

Holland-Moritz, E., W. Weber, G. Michels, W. Schlabitz, A. Mewis, C. Sauer and H. Mutka, 1989b, Z. Phys. B **77**, 105.

Holtzberg, F., J. Flouquet, P. Haen, F. Lapierre, Y. Lassailly and C. Vettier, 1985, J. Appl. Phys. **57**, 3152.

Horn, S., E. Holland-Moritz, M. Loewenhaupt, F. Steglich, H. Scheuer, A. Benoit and J. Flouquet, 1981a, Phys. Rev. B **23**, 3171.

Horn, S., F. Steglich, M. Loewenhaupt and E. Holland-Moritz, 1981b, Physica B **107**, 103.
Horn, S., F. Steglich, M. Loewenhaupt, H. Scheuer, W. Felsch and K. Winzer, 1981c, Z. Phys. B **42**, 125.
Houghton, A., N. Read and H. Won, 1987, Phys. Rev. B **35**, 5123.
Houghton, A., N. Read and H. Won, 1988, Phys. Rev. B **37**, 3782.
Ihrig, H., and S. Methfessel, 1976, Z. Phys. B **24**, 381.
Irkhin, V.Yu., and M.I. Katsnelson, 1989, Z. Phys. B **75**, 67.
Irkhin, V.Yu., and M.I. Katsnelson, 1990, J. Phys.: Condens. Mat. **2**, 8715.
Irkhin, V.Yu., and M.I. Katsnelson, 1991, Z. Phys. B **82**, 77.
Jaccard, D., R. Cibin, A. Bezinge, J. Sierro, K. Matho and J. Flouquet, 1988, J. Magn. & Magn. Mater. **76–77**, 255.
Jacoud, J.L., L.P. Regnault, J. Rossat-Mignod, C. Vettier, P. Lejay and J. Flouquet, 1989, Physica B **156–157**, 818.
Jacoud, J.L., L.P. Regnault, J.M. Mignot, J. Rossat-Mignod, J. Flouquet and P. Lejay, 1992, J. Magn. & Magn. Mater. **108**, 131.
Jefferson, J.M., and K.W.H. Stevens, 1978, J. Phys.: Condens. Mat. **11**, 3919.
Johansson, B., 1979, Phys. Rev. B **20**, 1315.
Johansson, B., and A. Rosengren, 1975, Phys. Rev. B **11**, 2836.
Johnson, S.M., J.A.C. Bland, P.J. Brown, A. Benoit, H. Capellmann, J. Flouquet, H. Spille, F. Steglich and K.R.A. Ziebeck, 1985, Z. Phys. B **59**, 401.
Kaga, H., 1989, Phys. Rev. B **39**, 9296.
Kaga, H., and T. Yoshida, 1988, Phys. Rev. B **38**, 12047.
Kaga, H., and T. Yoshida, 1989, Physica C **159**, 727.
Kaga, H., H. Kubo and T. Fujiwara, 1988, Phys. Rev. B **37**, 341.
Kappler, J.P., and A. Meyer, 1979, J. Phys. F **9**, 143.
Kawakami, N., and A. Okiji, 1985, J. Magn. & Magn. Mater. **52**, 220.
Keiter, H., and G. Czycholl, 1983, J. Magn. & Magn. Mater. **31**, 477.
Keiter, H., and J.C. Kimball, 1971, Int. J. Magn. **1**, 233.
Kirsch, T., A. Eichler, P. Morin and U. Welp, 1992, Z. Phys. B **86**, 83.
Kittel, C., 1963, in: Quantum Theory of Solids (John Wiley, New York) ch. 18, p. 360.
Knopp, G., H. Spille, A. Loidl, K. Knorr, U. Rauchschwalbe, P. Felten, G. Weber, F. Steglich and A.P. Murani, 1987, J. Magn. & Magn. Mater. **63–64**, 88.
Knopp, G., A. Loidl, R. Caspary, U. Gottwick, C.D. Bredl, H. Spille, F. Steglich and A.P. Murani, 1988a, J. Magn. & Magn. Mater. **74**, 341.
Knopp, G., A. Loidl, K. Knorr, H. Spille, F. Steglich and A.P. Murani, 1988b, J. Magn. & Magn. Mater. **76–77**, 420.
Knopp, G., A. Loidl, K. Knorr, L. Pawlak, M. Duczmal, R. Caspary, U. Gottwick, H. Spille, F. Steglich and A.P. Murani, 1989, Z. Phys. B **77**, 95.
Kohgi, M., F. Hippert, L.-P. Regnault, J. Rossat-Mignod, B. Hennion, T. Satoh, F.L. Chui, T. Miura and H. Takei, 1987, Jpn. J. Appl. Phys. **26**, 559.
Kohgi, M., M. Ito, T. Satoh, H. Asano, T. Ishigaki and F. Izumi, 1990a, J. Magn. & Magn. Mater. **90–91**, 433.
Kohgi, M., T. Satoh, K. Ohoyama, M. Arai and R. Osborn, 1990b, Physica B **163**, 137.
Kohgi, M., K. Ohoyama, A. Oyamada, T. Suzuki and M. Arai, 1990c, Physica B **163**, 625.
Kohgi, M., T. Satoh, K. Ohoyama and M. Arai, 1991, Physica B **169**, 501.
Kojima, H., Y. Kuramoto and M. Tachiki, 1984, Z. Phys. B **54**, 293.
Kojima, K., H. Hayashi, A. Minami, Y. Kasamatsu and T. Hihara, 1989, J. Magn. & Magn. Mater. **81**, 267.
Komatsubara, T., N. Sato, S. Kunii, I. Oguro, Y. Furukawa, Y. Onuki and T. Kasuya, 1983, J. Magn. & Magn. Mater. **31–34**, 368.
Koskenmaki, D.C., and K.A. Gschneidner Jr, 1978, in: Handbook on the Physics and Chemistry of Rare Earths, Vol. 1, eds K.A. Gschneidner Jr and L. Eyring (North-Holland, Amsterdam) p. 337.
Krill, G., J.P. Kappler, M.F. Ravet, A. Amamou and A. Meyer, 1980, J. Phys. F **10**, 1031.
Kunii, S., 1988, J. Magn. & Magn. Mater. **76–77**, 337.
Kuramoto, Y., 1983, Z. Phys. B **53**, 37.
Kuramoto, Y., 1987, Solid State Commun. **63**, 467.
Kuramoto, Y., 1989, Physica B **156–157**, 789.
Kuramoto, Y., and H. Kojima, 1985, J. Magn. & Magn. Mater. **47–48**, 329.
Kuramoto, Y., and E. Müller-Hartmann, 1985, J. Magn. & Magn. Mater. **52**, 122.
Lacroix, C., 1991, J. Magn. & Magn. Mater. **100**, 90.
Lahiouel, R., R.M. Galera, J. Pierre, E. Siaud and

A.P. Murani, 1987, J. Magn. & Magn. Mater. **63–64**, 98.
Langreth, D.C., 1966, Phys. Rev. **150**, 712.
Larson, A.C., and D.T. Cromer, 1961, Acta Crystallogr. **14**, 73.
Lassailly, Y., C. Vettier, F. Holtzberg, J. Flouquet, C.M.E. Zeyen and F. Lapierre, 1983, Phys. Rev. B **28**, 2880.
Lassailly, Y., S.K. Burke and J. Flouquet, 1985, J. Phys. C **18**, 5737.
Lawrence, J.M., 1979, Phys. Rev. B **20**, 3770.
Lawrence, J.M., and S.M. Shapiro, 1980, Phys. Rev. B **22**, 4379.
Lawrence, J.M., P.S. Riseborough and R.D. Parks, 1981, Rep. Prog. Phys. **44**, 1.
Lebech, B., Z. Smetana and V. Sima, 1987, J. Magn. & Magn. Mater. **70**, 97.
Lee, P.A., T.M. Rice, J.W. Serene, L.J. Sham and J.W. Wilkins, 1986, Comments in Condensed Mat. Phys. **12**, 99.
Lin, C.L., J. Teter, J.E. Crow, T. Mihalisin, J. Brooks, A.I. Abou-Aly and G.R. Stewart, 1985, Phys. Rev. Lett. **54**, 2541.
Lin, C.L., A. Wallash, J.E. Crow, T. Mihalisin and P. Schlottmann, 1987, Phys. Rev. Lett. **58**, 1232.
Liu, S.H., 1989, Phys. Rev. B **39**, 1403.
Loewenhaupt, M., 1984a, in: Moment Formation in Solids, ed. W.J.L. Buyers (Plenum, New York and London) p. 215.
Loewenhaupt, M., 1984b, unpublished data.
Loewenhaupt, M., and H. Bjerrum-Møller, 1981, Physica B **108**, 1349.
Loewenhaupt, M., and E. Holland-Moritz, 1979a, J. Magn. & Magn. Mater. **14**, 227.
Loewenhaupt, M., and E. Holland-Moritz, 1979b, J. Appl. Phys. **50**, 7456.
Loewenhaupt, M., and M. Prager, 1986, Z. Phys. B **62**, 195.
Loewenhaupt, M., and F. Steglich, 1977, in: Crystal Field Effects in Metals and Alloys, ed. A. Furrer (Plenum, New York) p. 198.
Loewenhaupt, M., B.D. Rainford and F. Steglich, 1979, Phys. Rev. Lett. **72**, 1709.
Loewenhaupt, M., S. Horn and F. Steglich, 1981, Solid State Commun. **39**, 295.
Loewenhaupt, M., J.M. Carpenter and C.-K. Loong, 1985, J. Magn. & Magn. Mater. **52**, 245.
Loewenhaupt, M., W. Reichardt, R. Pynn and E. Lindley, 1987, J. Magn. & Magn. Mater. **63–64**, 73.
Loewenhaupt, M., M. Prager, E. Gratz and B. Frick, 1988, J. Magn. & Magn. Mater. **76–77**, 415.
Loewenhaupt, M., E. Gratz, N. Pillmayr and H. Müller, 1990, Physica B **163**, 427.
Loidl, A., G. Knopp, H. Spille, F. Steglich and A.P. Murani, 1989, Physica B **156–157**, 794.
Loong, C.-K., B.H. Grier, S.M. Shapiro, J.M. Lawrence, R.D. Parks and S.K. Sinha, 1987, Phys. Rev. B **35**, 3092.
Loong, C.-K., J. Zarestky, C. Stassis, O.D. McMasters and R.M. Nicklow, 1988, Phys. Rev. B **38**, 7365.
Lysak, M.J., and D.E. MacLaughlin, 1985, Phys. Rev. B **31**, 6963.
MacLaughlin, D.E., F.R. de Boer, J. Bijvoet, P.F. de Chatel and W.C.M. Mattens, 1979, J. Appl. Phys. **50**, 2094.
Maekawa, S., S. Takahashi, S. Kashiba and M. Tachiki, 1985a, J. Appl. Phys. **57**, 3169.
Maekawa, S., S. Takahashi, S. Kashiba and M. Tachiki, 1985b, J. Phys. Soc. Jpn. **54**, 1955.
Maekawa, S., S. Takahashi, S. Kashiba and M. Tachiki, 1985c, J. Magn. & Magn. Mater. **52**, 149.
Mattens, W.C.M., F.R. de Boer, A.P. Murani and G.H. Lander, 1980, J. Magn. & Magn. Mater. **15–18**, 973.
Mazzaferro, J., C.A. Balseiro and B. Alascio, 1981, Phys. Rev. Lett. **47**, 274.
McWhan, D.B., S.M. Shapiro, J. Eckert, H.A. Mook and R.J. Birgeneau, 1978, Phys. Rev. B **18**, 3623.
Mignot, J.M., J.L. Jacoud, L.P. Regnault, J. Rossat-Mignod, P. Haen, P. Lejay, Ph. Boutrouille, B. Hennion and D. Pettigrand, 1990, Physica B **163**, 611.
Mignot, J.M., Ph. Boutrouille, L.P. Regnault, P. Haen and P. Lejay, 1991, Solid State Commun. **77**, 317.
Millis, A.J., and P.A. Lee, 1987, Phys. Rev. B **35**, 3394.
Mishchenko, A.S., and K.A. Kikoin, 1991, J. Phys.: Condens. Matter **3**, 5937.
Mook, H.A., and F. Holtzberg, 1981, in: Valence Fluctuations in Solids, eds L.M. Falicov, W. Hanke and M.B. Maple (North-Holland, Amsterdam) p. 113.
Mook, H.A., and R.M. Nicklow, 1979, Phys. Rev. B **20**, 1656.
Mook, H.A., T. Penny, F. Holtzberg and M.W. Shafer, 1978a, J. Phys. Colloq. (Paris) **39**, C6-837.
Mook, H.A., R.M. Nicklow, T. Penny, F. Holtzberg and M.W. Shafer, 1978b, Phys. Rev. B **18**, 2925.
Mook, H.A., D.B. McWhan and F. Holtzberg, 1982, Phys. Rev. B **25**, 4321.
Moon, R.M., and W.C. Koehler, 1979, J. Appl.

Phys. **50**, 2089.
Moon, R.M., W.C. Koehler, D.B. McWhan and F. Holtzberg, 1978, J. Appl. Phys. **49**, 2107.
Moon, R.M., S.H. Liu and K. Werner, 1983, J. Magn. & Magn. Mater. **31–34**, 387.
Morin, P., 1988, J. Magn. & Magn. Mater. **71**, 151.
Morin, P., C. Vettier, J. Flouquet, M. Konczykowski, Y. Lassailly, J.M. Mignot and U. Welp, 1988, J. Low Temp. Phys. **70**, 377.
Moshchalkov, V.V., and N.B. Brandt, 1986, Sov. Phys. Usp. **29**, 725.
Müller-Hartmann, E., 1984, Z. Phys. B **57**, 281.
Murani, A.P., 1983a, J. Phys. F **16(33)**, 6359.
Murani, A.P., 1983b, Phys. Rev. B **28**, 2308.
Murani, A.P., 1985a, Phys. Rev. Lett. **54**, 1444.
Murani, A.P., 1985b, J. Magn. & Magn. Mater. **47–48**, 142.
Murani, A.P., 1986, J. Magn. & Magn. Mater. **61**, 212.
Murani, A.P., 1987a, Phys. Rev. B **36**, 5705.
Murani, A.P., 1987b, in: Theoretical and Experimental Aspects of Valence Fluctuations and Heavy Fermions, eds L.C. Gupta and S.K. Malik (Plenum, New York and London) p. 287.
Murani, A.P., K. Knorr and K.H.J. Buschow, 1977, in: Crystal Field Effects in Metals and Alloys, ed. A. Furrer (Plenum, New York) p. 268.
Murani, A.P., K. Knorr, K.H.J. Buschow, A. Benoit and J. Flouquet, 1980, Solid State Commun. **36**, 523.
Murani, A.P., W.C.M. Mattens, F.R. de Boer and G.H. Lander, 1985, Phys. Rev. B **31**, 52.
Murani, A.P., R. Currat, A. Severing and R. Raphel, 1990a, Physica B **163**, 717.
Murani, A.P., W.G. Marshall, A.D. Taylor and R. Osborn, 1990b, ISIS experimental report ULS 85/1, p. A164.
Neuhaus, W., 1987, Berichte der KFA Jülich, Jül-2165.
Newns, D.M., and N. Read, 1987, Adv. Phys. **36**, 799.
Nozières, P., 1974, J. Low Temp. Phys. **17**, 31.
Nunez, V., R. Trump, P.J. Brown, T. Chattopadhyay, M. Loewenhaupt and F. Tasset, 1992, J. Phys.: Condens. Matter **4**, 1115.
Ohkawa, F.J., 1989, Solid State Commun. **71**, 907.
Ohkawa, F.J., and T. Yamamoto, 1987, Physica B **148**, 87.
Ohoyama, K., M. Kohgi, T. Nakane, M. Arai, A.D. Taylor, A. Oyamada and T. Suzuki, 1992, Physica B **180+181**, 250.
Onuki, Y., and T. Komatsubara, 1987, J. Magn. & Magn. Mater. **63–64**, 281.
Onuki, Y., Y. Shimizu, M. Nishihara, Y. Machii and T. Komatsubara, 1985a, J. Phys. Soc. Jpn. **54**, 1964.
Onuki, Y., Y. Machii, Y. Shimizu, T. Komatsubara and T. Fujita, 1985b, J. Phys. Soc. Jpn. **54**, 3562.
Orlov, V.G., 1988, Solid State Commun. **67**, 689.
Osborn, R., and E.A. Goremychkin, 1991, ISIS report 1991, Vol. II, p. A208.
Osborn, R., M. Loewenhaupt, B.D. Rainford and W.G. Stirling, 1987, J. Magn. & Magn. Mater. **63–64**, 70.
Osborn, R., K.A. McEwen, E.A. Goremychkin and A.D. Taylor, 1990, Physica B **163**, 37.
Osborn, R., S.W. Lovesey, A.D. Taylor and E. Balcar, 1991, in: Handbook on the Physics and Chemistry of Rare Earths, Vol. 14, eds K.A. Gschneidner Jr and L. Eyring (North-Holland, Amsterdam) p. 1.
Ott, H.R., 1987, in: Progress in Low Temperature Physics, Vol. XI, ed. D.F. Brewer (North-Holland, Amsterdam) p. 215.
Ott, H.R., H. Rudigier and F. Hulliger, 1985, Solid State Commun. **55**, 113.
Panissod, P., M. Benakki and A. Qachaou, 1988, J. Phys. Colloq. (Paris) **49**, C8-685.
Panousis, N.T., and K.A. Gschneidner Jr, 1972, Phys. Rev. B **5**, 4767.
Perez, I., G. Liang, J.B. Zhou, H. Jhans, S.A. Shaheen and M. Croft, 1990, Physica B **163**, 618.
Perscheid, B., E.V. Sampathkumaran and G. Kaindl, 1985, J. Magn. & Magn. Mater. **47–48**, 410.
Peysson, Y., C. Ayache, J. Rossat-Mignod, S. Kunii and T. Kasuya, 1986, J. Phys. (Paris) **47**, 113.
Pintschovius, L., E. Holland-Moritz, D. Wohlleben, S. Stöhr and J. Liebertz, 1980, Solid State Commun. **34**, 953.
Pintschovius, L., E. Holland-Moritz, D. Wohlleben, S. Stöhr, J. Liebertz, W. Assmus, C. Stassis, C.-K. Loong, J. Zarestky and R.M. Moon, 1983, Solid State Commun. **47**, 663.
Polatsek, G., and P. Bonville, 1992, Z. Phys. B **88**, 189.
Rainford, B.D., B. Buras and B. Lebech, 1977, Physica B **86–88**, 41.
Rainford, B.D., S. Dakin and A. Severing, 1992, J. Magn. & Magn. Mater. **108**, 119.
Rajan, V.T., 1983, Phys. Rev. Lett. **51**, 308.
Rasul, J.W., and P. Schlottmann, 1989a, Phys. Rev. B **39**, 3065.
Rasul, J.W., and P. Schlottmann, 1989b, Phys. Rev. Lett. **62**, 1325.
Read, N., D.M. Newns and S. Doniach, 1984, Phys. Rev. B **30**, 3841.

Regnault, L.P., W.A.C. Erkelens, J. Rossat-Mignod, C. Vettier, S. Kunii and T. Kasuya, 1988, J. Magn. & Magn. Mater. **76–77**, 413.

Regnault, L.P., J.L. Jacoud, J.M. Mignot, J. Rossat-Mignod, C. Vettier, P. Lejay and J. Flouquet, 1990, Physica B **163**, 606.

Reichardt, W., and N. Nücker, 1984, J. Phys. F **14**, L135.

Renker, B., E. Gering, F. Gompf, H. Schmidt and H. Rietschel, 1987, J. Magn. & Magn. Mater. **63–64**, 31.

Ribault, M., J. Flouquet, P. Haen, F. Lapierre, J.M. Mignot and F. Holtzberg, 1980, Phys. Rev. Lett. **45**, 1295.

Robinson, J.M., 1979, Phys. Rep. **51**, 1.

Rogl, P., 1984, in: Handbook on the Physics and Chemistry of Rare Earths, Vol. 7, eds K.A. Gschneidner Jr and L. Eyring (North-Holland, Amsterdam) p. 1.

Röhler, J., 1987, in: Handbook on the Physics and Chemistry of Rare Earths, Vol. 10, eds K.A. Gschneidner Jr and L. Eyring (North-Holland, Amsterdam) p. 453.

Rossat-Mignod, J., L.P. Regnault, J.L. Jacoud, C. Vettier, P. Lejay, J. Flouquet, E. Walker, D. Jaccard and A. Amato, 1988, J. Magn. & Magn. Mater. **76–77**, 376.

Rossel, C., K.N. Yang, M.B. Maple, Z. Fisk, E. Zirngiebl and J.D. Thompson, 1987, Phys. Rev. B **35**, 1914.

Sales, B.C., and R. Viswanathan, 1976, J. Low Temp. Phys. **23**, 449.

Schefzyk, R., W. Lieke, F. Steglich, T. Goto and B. Lüthi, 1984, J. Magn. & Magn. Mater. **45**, 229.

Schlottmann, P., 1982, Phys. Rev. B **25**, 2371.

Schlottmann, P., 1984, Phys. Rev. B **29**, 4468.

Schlottmann, P., 1989, Phys. Rep. **181**, 1.

Schmidt, H.J., and E. Müller-Hartmann, 1989, Z. Phys. B **75**, 331.

Schmitt, D., P. Morin and J. Pierre, 1978, J. Magn. & Magn. Mater. **8**, 249.

Schröder, A., H.G. Schlager and H. v. Löhneysen, 1992, J. Magn. & Magn. Mater. **108**, 47.

Severing, A., and A.P. Murani, 1990, Physica B **163**, 699.

Severing, A., W. Reichardt, E. Holland-Moritz, D. Wohlleben and W. Assmus, 1988, Phys. Rev. B **38**, 1773.

Severing, A., E. Holland-Moritz, B.D. Rainford, S.R. Culverhouse and B. Frick, 1989a, Phys. Rev. B **39**, 2557.

Severing, A., E. Holland-Moritz and B. Frick, 1989b, Phys. Rev. B **39**, 4164.

Severing, A., A.P. Murani, J.D. Thompson, Z. Fisk and C.-K. Loong, 1990a, Phys. Rev. B **41**, 1739.

Severing, A., E. Gratz, B.D. Rainford and K. Yoshimura, 1990b, Physica B **163**, 409.

Shapiro, S.M., 1986, Physica B **136**, 365.

Shapiro, S.M., and B.H. Grier, 1982, Phys. Rev. B **25**, 1457.

Shapiro, S.M., R.J. Birgeneau and E. Bucher, 1975, Phys. Rev. Lett. **34**, 470.

Shapiro, S.M., J.D. Axe, R.J. Birgeneau, J.M. Lawrence and R.D. Parks, 1977, Phys. Rev. B **16**, 2225.

Shapiro, S.M., H. Bjerrum-Møller, J.D. Axe, R.J. Birgeneau and E. Bucher, 1978, J. Appl. Phys. **49**, 2101.

Shapiro, S.M., E. Gurewitz, R.D. Parks and L.D. Kupferberg, 1979, Phys. Rev. Lett. **43**, 1748.

Shapiro, S.M., C. Stassis and G. Aeppli, 1989, Phys. Rev. Lett. **62**, 94.

Shiba, H., 1975, Prog. Theor. Phys. **54**, 967.

Shimizu, T., H. Yasuoka, Z. Fisk and J.L. Smith, 1987, J. Phys. Soc. Jpn. **56**, 4113.

Smith, H.G., G. Dolling and T. Goto, 1985, Solid State Commun. **53**, 15.

Stassis, C., 1986, Physica B **137**, 61.

Stassis, C., C.-K. Loong, G.R. Kline, O.D. McMasters and K.A. Gschneidner Jr, 1978, J. Appl. Phys. **49**, 2113.

Stassis, C., C.-K. Loong, O.D. McMasters and R.M. Moon, 1979a, J. Appl. Phys. **50**, 2091.

Stassis, C., C.-K. Loong, B.N. Harmon, S.H. Liu and R.M. Moon, 1979b, J. Appl. Phys. **50**, 7567.

Stassis, C., T. Gould, O.D. McMasters, K.A. Gschneidner Jr and R.M. Moon, 1979c, Phys. Rev. B **19**, 5746.

Stassis, C., C.-K. Loong, J. Zarestky, O.D. McMasters, R.M. Moon and J.R. Thompson, 1982, J. Appl. Phys. **53**, 7890.

Stassis, C., J.D. Axe, C.F. Majkrzak, B. Batlogg and J.P. Remeika, 1985, J. Appl. Phys. **57**, 3087.

Stassis, C., B. Batlogg, J.P. Remeika, J.D. Axe, G. Shirane and Z.J. Uemura, 1986, Phys. Rev. B **33**, 1680.

Steglich, F., 1985, in: Theory of Heavy Fermions and Valence Fluctuations, eds T. Kasuya and T. Saso (Springer, Berlin, Heidelberg, New York, Tokyo) p. 23 and references therein.

Steglich, F., 1991, J. Magn. & Magn. Mater. **100**, 186.

Steglich, F., J. Aarts, C.D. Bredl, W. Lieke, D. Meschede, W. Franz and H. Schäfer, 1979a, Phys. Rev. Lett. **43**, 1892.

Steglich, F., C.D. Bredl, M. Loewenhaupt and K.D. Schotte, 1979b, J. Phys. Colloq. (Paris) **40**, C5-301.

Steglich, F., U. Alheim, C. Schank, C. Geibel, S. Horn, M. Lang, G. Sparn, A. Loidl and A. Krimmel, 1990, J. Magn. & Magn. Mater. **84**, 271.

Stewart, G.R., 1984, Rev. Mod. Phys. **56**, 755.

Stroka, B., A. Schröder, T. Trappmann, H. v. Löhneysen, M. Loewenhaupt and A. Severing, 1992, Z. Phys. B (in print).

Tachiki, M., S. Takahashi and T. Koyama, 1987, Jpn. J. Appl. Phys. Suppl. **26-3**, 493.

Takayanagi, S., I. Umehara, K. Sato, Y. Onuki and N. Wada, 1990, J. Magn. & Magn. Mater. **90–91**, 479.

Takke, R., M. Niksch, W. Assmus, B. Lüthi, R. Pott, R. Schefzyk and D. Wohlleben, 1981a, Z. Phys. B **44**, 33.

Takke, R., N. Dolezal, W. Assmus and B. Lüthi, 1981b, J. Magn. & Magn. Mater. **23**, 247.

Taylor, K.N.R., 1971, Adv. Phys. **20**, 551.

Thalmeier, P., 1984, J. Phys. F **17**, 4153.

Thalmeier, P., and P. Fulde, 1982, Phys. Rev. Lett. **49**, 1588.

Thalmeier, P., and B. Lüthi, 1991, in: Handbook on the Physics and Chemistry of Rare Earths, Vol. 14, eds. K.A. Gschneidner Jr and L. Eyring (North-Holland, Amsterdam) p. 225.

Thompson, J.R., S.T. Sekula, C.-K. Loong and C. Stassis, 1982, J. Appl. Phys. **53**, 7893.

Tomala, K., D. Weschenfelder, G. Czjzek and E. Holland-Moritz, 1990, J. Magn. & Magn. Mater. **89**, 143.

Trump, R., 1991, Dissertation (University of Cologne) unpublished.

Trump, R., S. Thierfeld, M. Loewenhaupt and T. Chattopadhyay, 1991, J. Appl. Phys. **69**, 4699.

Tsvelick, A.M., and P.B. Wiegmann, 1982, J. Phys. F **15**, 1707.

Tsvelick, A.M., and P.B. Wiegmann, 1983, J. Phys. F **16**, 2281 and 2321.

Uemura, Y.J., C.F. Majkrzak, G. Shirane, C. Stassis, G. Aeppli, B. Batlogg and J.P. Remeika, 1986, Phys. Rev. B **33**, 6508.

Varma, C.M., 1985, Comments Solid State Phys. **11**, 221.

Vettier, C., P. Morin and J. Flouquet, 1986, Phys. Rev. Lett. **56**, 1980.

Vettier, C., P. Burlet and J. Rossat-Mignod, 1987, J. Magn. & Magn. Mater. **63–64**, 18.

Wakabayashi, N., 1980, Phys. Rev. B **22**, 5833.

Walter, U., and D. Wohlleben, 1987, Phys. Rev. B **35**, 3576.

Walter, U., Z. Fisk and E. Holland-Moritz, 1985, J. Magn. & Magn. Mater. **47–48**, 159.

Walter, U., D. Wohlleben and Z. Fisk, 1986, Z. Phys. B **62**, 325.

Walter, U., E. Holland-Moritz and Z. Fisk, 1991, Phys. Rev. B **43**, 320.

Walter, U., E. Holland-Moritz and U. Steigenberger, 1992, Z. Phys. B **89**, 169.

Weber, W., E. Holland-Moritz and K. Fischer, 1989a, Europhys. Lett. **8**, 257.

Weber, W., E. Holland-Moritz and A.P. Murani, 1989b, Z. Phys. B **76**, 229.

Welp, U., 1988, Dissertation (University of Konstanz), unpublished.

Welslau, B., and N. Grewe, 1990, Physica B **165–166**, 387.

White, R.M., 1970, in: Quantum Theory of Magnetism (McGraw-Hill, New York).

Wilson, K.G., 1975, Rev. Mod. Phys. **47**, 773.

Wohlleben, D., 1976, J. Phys. Colloq. (Paris) **C-4**, 231.

Wohlleben, D., and B.R. Coles, 1973, in: Magnetism, Vol. 5, ed. H. Suhl (Academie Press, New York) p. 3.

Yashima, H., N. Sato, H. Mori and T. Satoh, 1982, Solid State Commun. **43**, 595.

Yoshimura, K., T. Nitta, M. Mekata, T. Shimizu, T. Sakakibara, T. Goto and G. Kido, 1988, Phys. Rev. Lett. **60**, 851.

Yosida, K., 1957, Phys. Rev. **107**, 396.

Zevin, V., G. Zwicknagl and P. Fulde, 1988a, Phys. Rev. Lett. **60**, 3221.

Zevin, V., G. Zwicknagl and P. Fulde, 1988b, J. Magn. & Magn. Mater. **76–77**, 475.

Zhang, F.C., and T.K. Lee, 1983, Phys. Rev. B **28**, 33.

Zhang, F.C., and T.K. Lee, 1984, Phys. Rev. B **30**, 1556.

Zhang, F.C., T.K. Lee and Z.B. Su, 1987, Phys. Rev. B **35**, 4728.

Zirngiebl, E., and G. Güntherodt, 1991, in: Handbook on the Physics and Chemistry of Rare Earths, Vol. 14, eds K.A. Gschneidner Jr and L. Eyring (North-Holland, Amsterdam) p. 163.

Zirngiebl, E., B. Hillebrands, S. Blumenröder, G. Güntherodt, M. Loewenhaupt, J.M. Carpenter, K. Winzer and Z. Fisk, 1984, Phys. Rev. B **30**, 4052.

Zou, Z., and P.W. Anderson, 1986, Phys. Rev. Lett. **57**, 2073.

Zwicknagl, G., V. Zevin and P. Fulde, 1990, Z. Phys. B **79**, 365. Erratum: 1991, Z. Phys. B **83**, 153.

SUBJECT INDEX

MATERIALS INDEX